Number 7 Volume 21 1957

P11

BULLETIN

of the

Academy of Sciences of the USSR

- Physical Series -

(Izvestiia Akademii Nauk SSSR)
(Seriia fizicheskaia)

Reproduction rights reserved

by

Columbia Technical Translations
5 Vermont Avenue
White Plains, New York

Single Issues

$20

Annual Subscription

$215

Transactions of the

Seventh All-Union Conference on Nuclear Spectroscopy

(To be continued in Vol.21, No.12)

ALPHA-DECAY OF Pu^{238}

- L.N.Kondrat'ev, G.I.Novikova, V.B.Dedov & L.L.Gol'din

Knowing the α-decay intensities to successive levels of one rotational band, we can draw certain conclusions regarding the shape of the daughter nucleus[1]. In view of this, accumulation of experimental material on α-decays is of considerable interest.

The most accurate values of α-decay intensities are obtained through direct measurement of the intensity of α-transitions by means of a magnetic α-spectrometer or ionization chamber. Investigation of the intensities by other procedures (for example γ-γ coincidences) sometimes leads to substantial errors.

In view of the low intensity of the transitions to 4^+, 6^+ and higher levels it is expedient to choose relatively short-lived materials for α-spectrometer measurements.

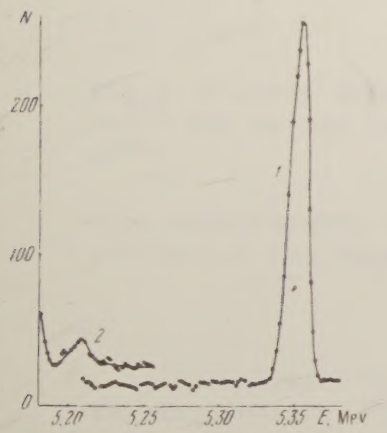

Fig.1. α-Spectrum of Pu^{238} in the 5.3 Mev region (the leading edge of the principal α-lines of Pu^{239} and Pu^{240} appears at the left: 1) 40 hour exposure, 2) 110 hour exposure.

In the present work we investigated the highest excited rotational states of U^{234} evinced in α-decay of Pu^{238}. The work was carried out on the magnetic α-spectrometer of the USSR Academy of Sciences. Prior to the present study only the transitions to the ground level of U^{238} and to the two excited levels at 43.5 and 143 kev had been investigated by means of an α-spectrometer[2]. Two other excited levels lying at 96 kev (Ref.2) and 499 kev (Ref.3) had been detected by γ-γ coincidence measurements.

The Pu^{238} was obtained as a product of α-decay of Cm^{242} formed by slow neutron bombardment of Am^{241}. The elements were separated by the chromatographic method. The separation of the plutonium from the americium was so thorough that no trace of the Am^{241} α-lines appeared in the recorded spectra. We carried out two series of measurements with exposures of 40 and 110 hours. The recorded α-spectra are shown in Fig.1. We detected α-lines with energies of 5.3521 and 5.208 Mev. The intensities of the corresponding transitions are $0.13 \pm 0.01\%$ and $(5 \pm 1)\cdot 10^{-3}\%$. No other lines having an intensity greater than $2\cdot 10^{-3}\%$ appear in the energy interval from 5.210 to 5.350 Mev.

The weak line at 5.208 Mev cannot be explained by any impurities in the source. It undoubtedly belongs to Pu^{238}.

In addition, we redetermined the energy of the fundamental α-line of Pu^{238} relative to Pu^{210}; we took 5.2978 Mev as the energy of the Po^{210} α-particles[4]. The results of all our measurements are summarized in the accompanying table.

Line	α-line energy, Mev	Level energy, kev	Transition intensity, %	Spin and parity
α_0	5,4912±0,001	0	71,1 ±1,2	0^+
α_{44}	5,4482±0,001	43,7±1	28,7 ±1,2	2^+
α_{142}	5,3521±0,001	141,5±1	0,13±0,01	4^+
α_{288}	5,208 ±0,005	288 ±5	$(5\pm1)\cdot10^{-3}$	6^+

The ambiguity in the above Po^{210} α-particle energy is not included in the indicated experimental uncertainties.

The detected levels fit well into the usual rotational scheme for even-even nuclei. The experimental ratios of the energies of the successive levels are 1:3.24:6.6, which is in good agreement with the theoretical 1:3.3:7.0. On the basis of this agreement, we assume that all the detected levels are rotational and hence have the following spins and parities: 0+, 2+, 4+ and 6+.

The 499 kev level[3] also fits well into the rotation scheme if one accepts the 8+ assignment for it.

In their work Asaro & Perlman[2] investigated the total conversion coefficients of the γ-rays accompanying α-decay of Pu^{238}. According to their data, the γ-transitions from the 43.5 kev level to the ground level and from the 143 kev level to the 43.5 kev level are E2, which is in agreement with the 2+ and 4+ assignments for these levels.

The characteristics of the 2+ level were also determined by E.F.Tret'iakov (private communication) from the ratio of the abundance of the $(L_I + L_{II})$ to abundance of the L_{III} conversion electrons. The level scheme for U^{234}, constructed on the basis of all now known data, is shown in Fig.2.

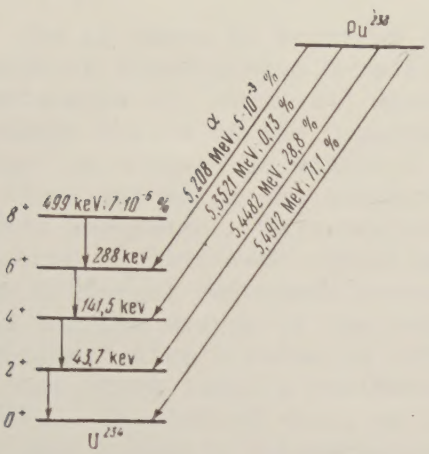

Fig.2. α-decay scheme for Pu^{238} and energy levels of U^{234}.

We take this occasion to thank E.F.Tret'iakov for carrying out β-spectroscopic identification measurements and I.I.Agapkin, G.I.Grishuk and V.V.Titov for their aid in performing the measurements and processing the results.

References

1. G.M.Adel'son-Vel'skii, A.P.Birzgal, A.D.Piliia, L.L.Gol'din & K.A. Ter-Martirosian, Doklady na VII ezhefodnom soveshchanii po iadernoi spektroskopii (Report at the Seventh Conference on Nuclear Spectroscopy) 1957.

2. F.Asaro & I.Perlman, Phys.Rev., 94, 381 (1954).

3. I.Perlman & J.O.Rasmussen, UCRL-3424.

4. I.I.Agapkin & L.L.Gol'din, Report at the Seventh Conference on Nuclear Spectroscopy). (See following article in the present issue of the Bulletin).

Digitized by the Internet Archive
in 2024

https://archive.org/details/russian-academy-of-sciences-physics-bulletin_1957_21_7

ENERGY OF α-PARTICLES FROM Po^{210}

- I. I. Agapkin & L. L. Gol'din

Introduction

As is known, by means of a magnetic α-spectrometer one can compare the energy of investigated α-particles with the energy of α-particles emitted by a reference of "standard" source with an accuracy of a fraction of a kev. The absolute values of the α-particle energies from a number of "standards" are listed in tables[1] to within 1 kev; moreover, it is usually assumed that the relative values of the standard source energies are known with appreciably higher precision. Nevertheless, the results for the same group of α-particles obtained by different investigators sometimes diverge appreciably, particularly when different reference sources are used. By way of illustration, we note that for the energy of the principal Am^{241} α-particle group, Asaro, Reynolds & Perlman[2] give a value of 5476.6 ± 2 kev (standard - Em^{222} (Rn)), while Gol'din, Tret'iakov & Novikova[3] give a value of 5482.0 ± 0.6 kev (standard - Po^{210}). In view of this, we felt it would be desirable to undertake a new and more accurate determination of the energy of the Po^{210} α-particles.

1. Experimental part

The measurements were carried out on the magnetic α-spectrometer of the USSR Academy of Sciences, which has been described earlier[4]. This spectrometer is well adapted for relative energy measurements inasmuch as both the source and the α-particle collector are located within the magnetic field region (this eliminates the uncertainty connected with the entry and emergence of the particles from the field), the intensity of the magnetic field is relatively low (6000-7000 oersted) and the instrument has provision for varying the magnetic field so that the compared α-particles follow identical paths during the exposures. The radial inhomogeneities of the magnetic field, connected with the use of double focusing, do not, however, allow of making absolute measurements.

The source holder had two arms each of which carried one source. Either of the sources could be moved in front of the entrance slit. The photographic cassette had five plate holders only two of which were used. Each source was exposed on a separate plate.

Each measurement consisted of four exposures, carried out in the following order: 1) source A was exposed on the plate in the first holder, 2) source B was exposed on the plate in the second holder, 3) the plates were replaced by new ones, 4) source B was exposed on the plate in the first holder and, finally, 5) source A was exposed on the plate in the second holder. In shifting from source A to B and vice versa, the magnetic field was adjusted so that the peak would fall at the center of the exposed plate.

Averaging the coordinates of the peaks of exposures 1 and 5 for source A and exposures 2 and 3 for source B automatically excluded dependence of the position of the peaks on the number of the plate holder and eliminated errors connected with possible slow temperature-induced changes of the field configuration.

The positions of the peaks were determined by counting the number of tracks on the plates. To enhance the statistics the number of tracks was averaged over three strips[4], each 0.2 mm wide. The energy was evaluated by extrapolating the leading edge of the peaks using the section of the peak between 0.2 and 0.8 of the total height for this purpose.

The field intensity was measured by means of a suitable coil equipped with a counterweight and mirror[4]. The current through the coil was measured by a potentiometer. In calculating the peak energies we utilized the experimentally determined "value" of 1 mm displacement on the photographic plate, equal to $0.970 \cdot 10^{-3}$ the energy corresponding to the center of the plate. The peaks were never shifted by more than 2 mm from the center of the plate.

The sources were prepared by vacuum evaporation of the radioactive materials (Po^{210} and Ra^{224}) from a heated filament onto a glass support.

In all the measurements the reference "standard" was Ra^{224} (ThX), the energy of the α-particles from which according to Ref.1 is 5681.4 ± 1.1 kev.

2. Results and discussion

The most substantial source of possible error may be disparity between the mean value of the magnetic field H_{av} traversed by the α-particles and the field H_l at the point where it is sensed by the field meter coil. It can hardly be imagined, however, that these values were not proportional to each other, which is the only thing that matters in relative measurements. Inasmuch as such a nonproportionality could arise only due to unequal saturation of different sections of the pole pieces, it should obviously be more strongly manifest at high field values. To check this we measured the energy of α-particles from Po^{216} (ThA) and obtained a value of 6775.6 kev (the tabular value[1] is 6774.6 ± 1.3 kev). The excellent agreement of the results for particles of such high energy substantiated the proportionality of H_{av} and H_l.

Table 1

Results of Po^{210} α-particle energy measurements

Exper. No.	Measured energy, kev	width of slit at source, mm	Mean line half-width, mm		Half-width difference
			Po^{210}	Ra^{224}	
1	5297,6 ± 1,4	0,83	2,24	2,31	−0,56±0,33
2	5298,5±0,6	0,83	2,15	2,33	−0,90±0,16
3	5296,4±0,2	0,83	2,29	2,06	+1,02±0,14
4	5294,9±0,2	1,49	2,43	2,19	+1,03±0,23
5	5299,9±0,3	0,99	1,91	1,93	−0,27±0,37

Special experiments showed that the measured energy of the α-particles did not depend on which of the holders the source was mounted in. We also checked the dependence of the measured energy on the age of the sources. Comparison of the energy values obtained for two fresh polonium sources showed agreement within 0.3 kev. On the other hand, in the comparison of two old sources, one prepared 30 days, the other 90 days prior to the experiment, the measured energy values differed by all of 5 kev and the half-widths of the peaks were 1.88 and 2.36 mm respectively.

The results of our Po^{210} α-particle energy measurements are shown in Table 1. In the last column of the table we give the difference Δ between the intrinsic half-widths of the Po^{210} and Ra^{224} peaks calculated according to the formula

$$\Delta = \sqrt{(\Delta Po^{210})^2 - (\Delta Ra^{224})^2}.$$

This formula takes into account that the measured width of the α-line is comprised of the sum (of the squares) of the apparatus width (principal part) and the inherent width of the source.

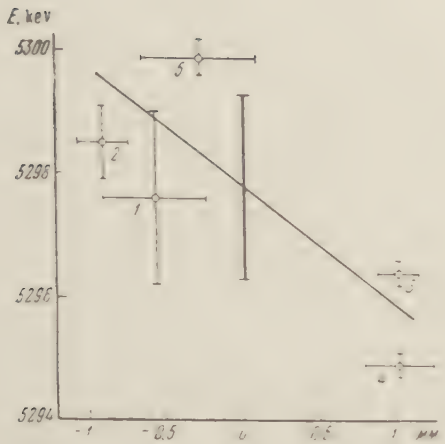

Fig.1. Plot of measured Po^{210} α-particle energy values vs difference between the half-widths of the Po^{210} and Ra^{224} α-lines (the indicated uncertainties are the statistical error).

The results of the experiments are shown in Fig.1 where the difference between the half-width of the α-lines of Po^{210} and Ra^{224} is plotted against the measured Po^{210} α-particle energy. A comparison carried out for equal half-widths of the peaks yield a value of 5297.8 ± 1.5 kev for the energy of the α-particles from Po^{210} (taking into account the tabular uncertainty of 1.1 kev in the energy of the α-particles from Ra^{224} which served as our standard). The tabular value[1] for the Po^{210} energy is 5300.6 ± 2.6 kev.

The results obtained in measuring the energy of α-particles from Em^{220} (Tn) with reference to the same standard (Ra^{224}) are shown in Table 2. In the last column we list the half-widths normalized to a 0.83 mm exit slit width. Inasmuch as "normalization" of the line widths introduces errors difficult of evaluation, the results of experiments 4 and 5 must be treated with a certain degree of circumspection.

Table 2

Results of measurement of Em^{220} (Tn) α-particle energy

Exper. No.	Measured energy, kev	Width of slit at source, mm	Mean line half-width, mm		Reduced line half-width, mm
			Em^{220}	Ra^{224}	
1	6285.7±1.7	0.83	2.39	2.31	2.39±0.15
2	6288.1±1.2	0.83	2.51	2.33	2.51±0.07
3	6284.5±0.7	0.83	2.17	2.05	2.17±0.06
4	6283.9±1.0	1.49	2.33	2.19	1.97±0.06
5	6286.9±0.7	0.99	2.14	1.93	2.07±0.06

As will be evident from Table 2, the line half-width for the daughter element Em^{220} is always greater than the half-width for the parent Ra^{224}; the variation of the half-width difference from experiment to experiment lies within the limits of experimental error. This precludes the possibility of unambiguous comparison of the energies of Em^{220} and Ra^{224}.

The variation of the measured α-particle energy of Em^{220} with the half-width of the α-line is plotted in Fig.2. The curve shows how careful one must be in identifying the measured value with the true energy.

Extrapolation of the curve to the apparatus half-width of the line (1.5 mm) yields a value of 6282.4 kev for the Em^{220} α-particle energy, which is in excellent agreement with the tabular value of 6282.3 ± 1.3 kev. It should be noted, however, that infinitely thin sources do not necessarily give the best energy value, for infinitely thin in this case is only the distribution of the parent Ra^{224} and not of the daughter Em^{220}. In the case of thick sources the difference in the distributions of the parent and daughter isotopes is no longer a significant factor but the difference in absorption of particles of different energies begins to play an appreciable role.

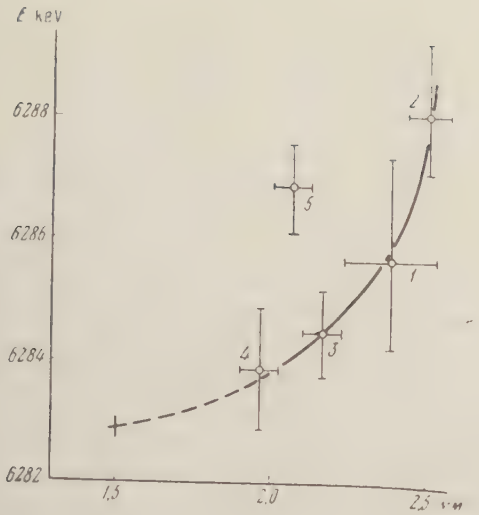

Fig.2. Plot of measured Em^{220} (Tn) α-particle energy values vs the half-width of the α-line (the indicated uncertainties are the statistical experimental error).

Our data gives reason to think that true energy values of the α-particles from Em^{220} and, probably, from other "daughter" α-emitters may lie somewhat higher than the tabular values. This may explain the above noted divergence between the Am^{241} α-particle energies obtained by different investigators.

We suggest the value of 5297.8 ± 1.5 kev for the Po^{210} α-particle energy.

References

1. G.H.Briggs, Rev.Mod.Phys., 26, 1 (1954).

2. F.Asaro, F.L.Reynolds & I.Perlman, Phys.Rev., 87, 277 (1952).

3. L.Gol'din, E.Tret'iakov & G.Novikova, Sessiia Akademii nauk po mirnomu ispol'zovaniiu atomnoi energii (Meeting of the USSR Academy of Sciences on the Peaceful Uses of Atomic Energy), M., 1955.

4. L.Gol'din & E.Tret'iakov, Izv. AN SSSR, Ser.fiz., 20, 859 (1956). (Trans. Bulletin, 20, No.8, 781.)

A GRID TYPE IONIZATION CHAMBER

- S.A.Baranov, A.G.Zelenkov & Iu.F.Rodionov

In recent years there have been developed a number of different spectrometric instruments based on the ionization principle. In particular, ionization chambers with a grid[1-5] have gained wide acceptance. The grid serves primarily to eliminate the influence of positive ions, so that the height of the electron pulses becomes independent of the direction of ejection of the particles from the target.

An instrument of this type was developed in our laboratory in 1952-3. The diagram of this ionization chamber is shown in Fig.1. Its design provided for successive measurement of four α-active sources without disturbing the physical conditions of the experiment. The pulses from the collecting electrode are fed to the input of an amplifier and then to a discriminator which allows of clipping part of the pulse height and amplifying the remainder to the requisite value. The need for amplitude discrimination is dictated by the fact that the energies of α-particles from different radioactive isotopes frequently differ by only a few percent. From the discriminator output the pulses go to a multichannel differential pulse height analyzer.

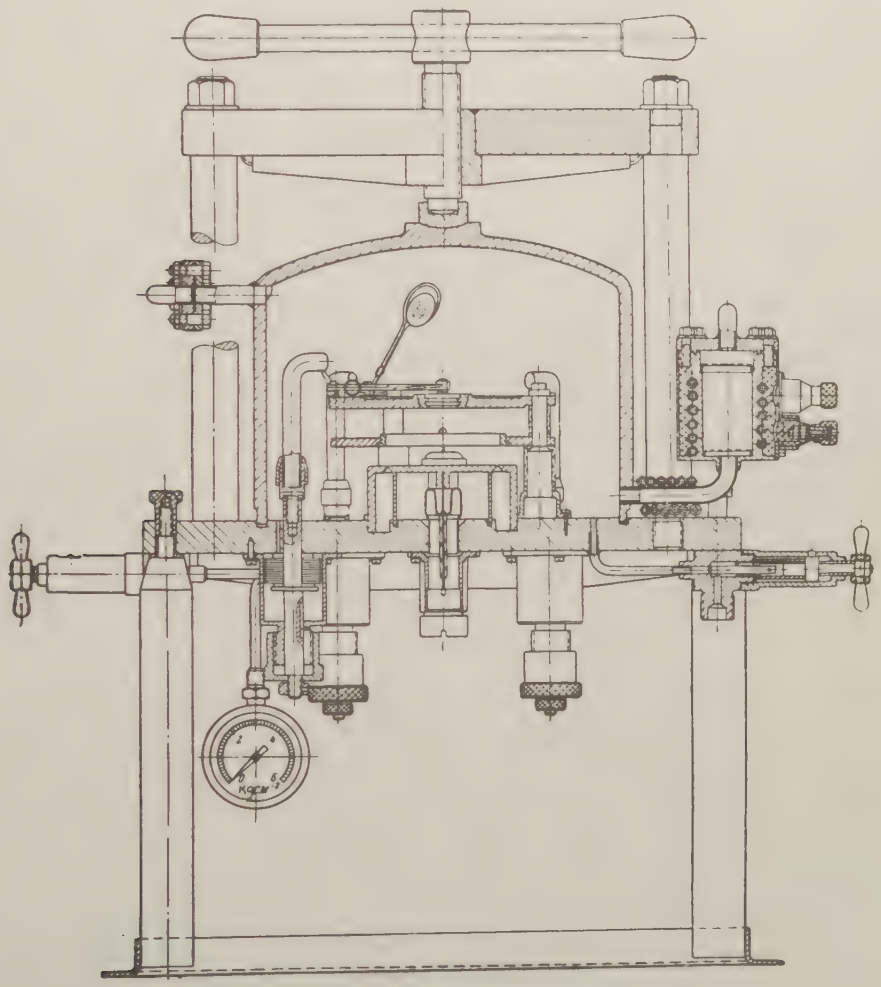

Fig.1. Diagram of ionization chamber with grid.

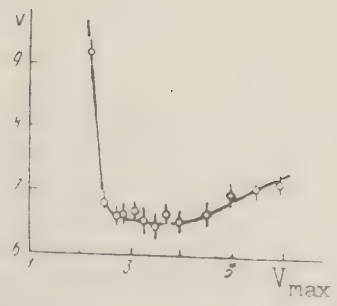

Fig.2. Dependence of the reduced value of the noise on the filament voltage of the first preamplifier tube.

A positive feature of ionization chambers, in general, is their large effective aperture or acceptance angle (up to 50% of 4π). The basic characteristic in rating such instruments is their resolution. The limit as regards resolution is set by ionization straggling, the magnitude of which according to Fano[8] is approximately 8 kev (root mean square fluctuation) for 5 Mev α-particles. Other factors limiting or influencing the resolution of the set-up are the noise in the input tube of the amplifier, the absorption of α-particles in the target, the formation of negative ions, variations of the amplifier gain depending on the rise time of the pulses and incomplete extraction of the electrons from the collimator by the electric field.

The resolution of the apparatus is determined to an appreciable extent by the noise level of the first amplifier tube. The principal contribution here is that of the Schottky effect, the magnitude of which is proportional to the capacitance of the amplifier input circuit. To reduce the hum we used direct current for the preamplifier filament supply. The first tube (6Zh1P) was connected as a triode, since it was found that the noise in this case was about 30% lower. We recorded the variation of the noise level as a function of the filament voltage of the first tube (Fig.2). On the basis of these tests, we decided to use a filament voltage of 3.5 v; further reduction of the filament voltage is undesirable inasmuch as it is connected with an appreciable reduction of the amplification coefficient. An appreciable reduction of the noise level can also be attained by narrowing the passband of the amplifier. The optimal frequency characteristic was selected on the basis of the minimum half-width of the distribution in height of the pulses due to α-particles from a polonium target (Figs.3 & 4). The effect of noise on the resolving power of the instrument was determined in the following manner. Pulses of ~1 mv amplitude from a special generator were applied to the amplifier input connected with the chamber through a 1 $\mu\mu$f capacitor or directly to the chamber grid. The amplitude stability of the generator pulses was checked separately. This height was selected because it is approximately equal to the height of the pulses due to α-particles from a polonium source. By this method it was possible to measure accurately the contribution of noises to the resolution of

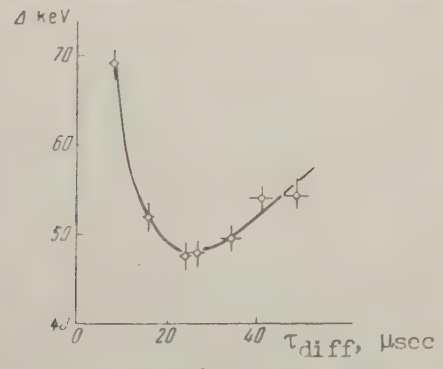

Fig.3. Dependence of the half-width of the amplitude distribution Δ of the pulses due to α-particles from Po^{210} on the time constant τ of the differentiating circuit with C_{int} = = 100 $\mu\mu$f.

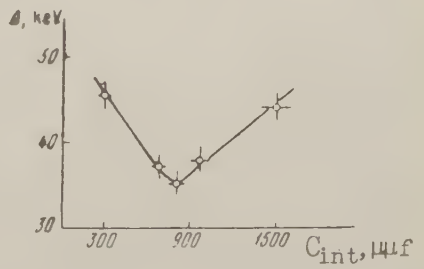

Fig.4. Dependence of the half-width of the amplitude distribution Δ of the pulses due to α-particles from Po^{210} on the upper limit of the amplifier passband with τ_{diff} = 25 μsec. C_{int} = capacitance of the integrating circuit.

the instrument. In the case of our particular set-up, the "standard deviation" in the distribution of the artificial pulses amounted to 9.0 ± 0.5 kev (~3 μv).

Another significant factor influencing the resolution of an ionization chamber is the formation of negative ions due to "sticking" of electrons to the molecules of any electronegative gases present. It turned out that the "chemically pure" argon supplied by the domestic industry, that we used for filling our chamber, contains an appreciable amount of such electronegative impurities. It was found that over a period of measurement the height of the pulses gradually decreased by several percent and the resolution deteriorated. In order to investigate the influence of the formation of negative ions we recorded the variation of the pulse heights and resolution of the set-up with the ratio of the potentials on the electrodes. These measurements allowed of determining experimentally the optimal potential ratio and the magnitude of the effect of formation of negative ions (~40%). The optimal ratio of the potentials on the grid and on the high voltage electrode (V_g/V_a) was found to be 0.49, which is in good agreement with the results of calculations according to Bunemann's[1] formula: $V_g/V_a \geq 0.48$. Here V_g is the voltage on the grid and V_a is the voltage on the high voltage electrode referred to the collecting electrode. The distance from the high voltage electrode to the grid in our chamber is 25 mm; that from the grid to the collecting electrode is 15 mm. The gas pressure in the chamber was 3 atmospheres. In order to reduce the effect of formation of negative ions, we increased the voltages on the chamber electrodes and eliminated all organic materials from inside the chamber. As a further improvement, we added a calcium purifier, containing metallic calcium, heated to 350-400°. The operation of the purifier is based on convection. The introduction of this unit makes it possible to purify the argon further in the process of operation. It was found that after such decontamination (3-4 hours), the height of the pulses increases appreciably and then remains constant for at least a week. The curves characterizing the dependence of the pulse height on the ratio of the voltages on the chamber electrodes are shown in Fig.5 (A & B). It will be seen that the curves go through a maximum. The sharp falling off of the curves on the left is due to capture of part of the electrons by the grid; the falling off on the right is due to the formation of negative ions. It will be seen that the latter effect was appreciably reduced by the above mentioned measures (curve B is for the improved version of the chamber) and according to our evaluation does not exceed 5%.

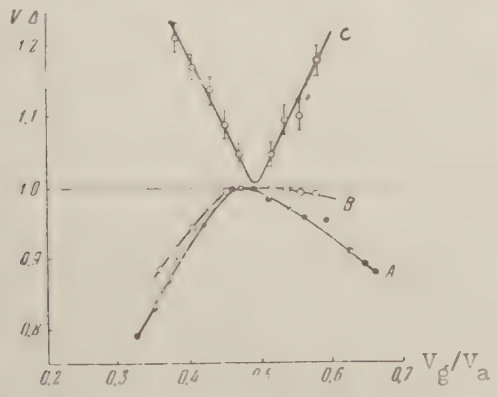

Fig.5. Dependence of the height V of the pulses due to α-particles from Po^{210} (A & B) and the half-width of their distribution Δ (C) on the ratio of the potential on the grid (V_g) to the potential on the high voltage electrode (V_a). A - for original chamber design; B & C - for new, modified chamber design.

Curve C in Fig.5 shows the variation of the resolving power of the improved chamber with the ratio of the potentials on the electrodes. It will be seen that the best resolution is obtained with a maximum pulse height.

In order to assure a high resolution it is important to reduce to a minimum self-absorption of the α-particles on the target; hence great care must be exercized in preparing the targets. Usually we prepared the target layer by electrolysis[7]. In other cases we used the ethylene glycol technique to obtain

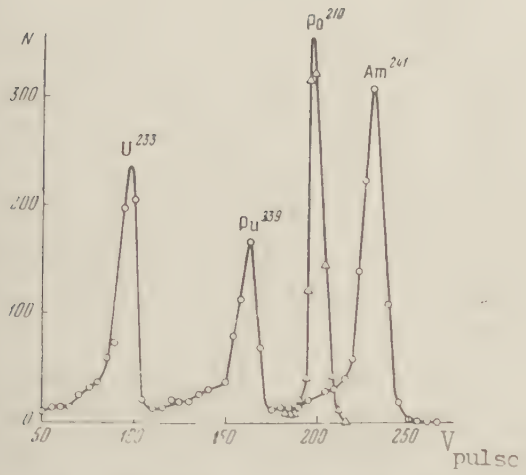

Fig.6. α-Particle spectra of U^{233}, Pu^{239}, Am^{241} and Po^{210}.

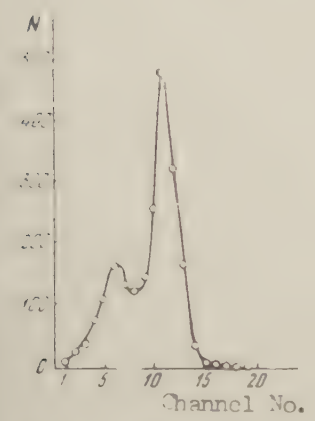

Fig.7. Spectrum of α-particles from Th^{230}.

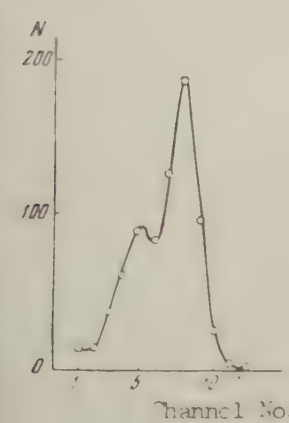

Fig.8. Spectrum of α-particles from Pu^{238}.

a uniform coating. Absorption of α-particles in the active layer leads to a shift of the pulse distribution curve to the side of lower energies and the distortion of its shape. Substantial improvement of the resolution in working with fairly thick sources (several micrograms per cm^2) can be realized by using collimators. Collimators serve to eliminate the α-particles emitted at small angles to the target surface, i.e., the particles for which the greatest energy losses obtain. We used a number of different collimators with wall thicknesses ranging from 0.3 to 1 mm and openings from 0.3 to 1 mm in diameter. The choice of collimator depends on the nature of the experimental problem involved, the solution required and the activity of the source. We also collimated the α-particle beam by placing a 1 mm thick disc with a 10 mm diameter opening over the target. By means of such a collimator we obtained a Po^{210} α-particle distribution with a half-width of 50 kev (standard deviation 20-21 kev). It was noted that even in the case of relatively thin sources there is observed a shift of the distribution in energy curve amounting to several tens of kev, depending on the particular type of collimator used. This can be explained only by incomplete extraction of the electrons from the collimator aperture. In order to minimize this effect it is expedient to use collimators of minimal thickness. By way of such minimal thickness collimators we used specially etched screens similar to those described by Engelkemeir & Magnusson[5]. The thickness of the screens was 50-60 μ, diameter of the screen openings 140-160 μ. The use of such screens led to an appreciable improvement of the resolution. In Fig.6 we give the α-particle spectra of U^{233} (E_α = 4.83 Mev), Pu^{239} (5.15 Mev) and also of Am^{241} (5.47 Mev), which we used as a standard. In the same figure we give the energy distribution of the α-particles from Po^{210} (5.30 Mev). Evaluation of the standard deviation of this distribution gave 15.0 ± ± 0.5 kev (half-width ~35 kev). By way of illustration of the resolving power attained, in Figs.7 & 8 we show the recorded α-particle spectra of Pu^{238} and Th^{230}, each of which comprises two fine structure groups ($\Delta E_1 \approx 40$ and $\Delta E_2 \approx 70$ kev).

Thus at present the principal factors contributing to the width of the distribution in height of the α-particle pulses from a polonium source are the ionization straggling (8 kev) and the amplifier noise (9 kev). All the other factors make a contribution of only about 9 kev. To attain the limiting resolution of the instrument (~8 kev) one should appreciably reduce the noise of the amplifier which would involve special research on the amplifier design.

In its present form the apparatus is a satisfactory instrument which has proved highly useful in a number of investigations and, particularly, for analysis of microquantities of α-active isotopes. By virtue of its high admission and relatively good resolution the instrument can be used for investigations that cannot at present be performed with other instruments. Thus, A.A.Van'kov, student at Moscow State University, carried out in our laboratory a series of measurements of α-γ coincidences in the decay of Np^{237}. The α-particles were recorded by means of the ionization chamber; the γ-rays were detected by a scintillation spectrometer. Only the pulses due to α-particles in coincidence with γ-rays of a certain energy entered the multichannel analyzer. This procedure allows of obtaining valuable data on the decay scheme of long-lived α-active isotopes and on the multipole order of the corresponding transitions of the daughter nucleus.

References

1. O.Bunemann, T.E.Granshaw & J.C.Harvey, Can.J.Res. A27, 191 (1949).
2. T.E.Granshaw & J.A.Harvey, Can.J.Res. A26, 243 (1948).
3. A.Chiorso, A.H.Jaffey, M.Robinson & B.Weissbourd, The Transuranium Elements, 1949.
4. The Actinide Elements. Edited by G.T.Seaborg & J.J.Katz (1954).
5. D.W.Engelkemeir & L.B.Magnusson, Rev.Sc.Instr., 26, No.3, 295 (1955).
6. U.Fano, Phys.Rev., 72, 26 (1947).
7. G.I.Iakovlev, P.M.Chulkov, V.B.Dedov, V.N.Kosiakov & Iu.P.Sobolev, Atomnaia energiia (Atomic energy), 5, 131 (1956).

CONVERSION ELECTRON SPECTRA OF NEUTRON-DEFICIENT THULIUM ISOTOPES

- K. Ia. Gromov, B. S. Dzhelepov & B. K. Preobrazhenskii

Introduction

The samples were prepared by bombardment of tantalum targets with fast (660 Mev) protons, followed by chemical separation of rare earth elements and, finally, chromatographic separation of the thulium fraction[1]. Conversion electron spectra were investigated by means of the Radium Institute Ketron[2] under the following conditions: width of receiving slit 0.5 mm; film over counter window transparent to >3.5 kev electrons; relative apparatus line half-width R = 0.6%. The sources were prepared by evaporation of thulium lactate, deposited on one side of an aluminum strip measuring 1 x 10 x 0.005 mm. For these measurements the instrument was calibrated with reference to the conversion lines of In^{114}, Ce^{144} and Yb^{169}, the energies of which have been carefully determined by Cork and his coworkers[3-6] and Porter & Cook[7]. The mean deviation of the calibration points from a smooth curve was 0.3%.

Table 1

Data on the neutron-deficient thulium isotopes from Seaborg's Table of Isotopes

A	Degree of certainty of assignment	Type decay	Period
165	A	K	29 hours
166	A	K,β^+	7.7 hours
167	A	K	9.6 days
168	A	K,β^-	85 days

The proton bombardment of the tantalum targets and separation of the thulium fraction were carried out three times. The first and second irradiations were about 1 hour each; the third extended over several months. The chromatographic separation in the first two cases was carried out about 30 hours after irradiation; in the third case, about a week after irradiation. The measurements on the Ketron started some 3-5 hours after separation. Lines with periods of

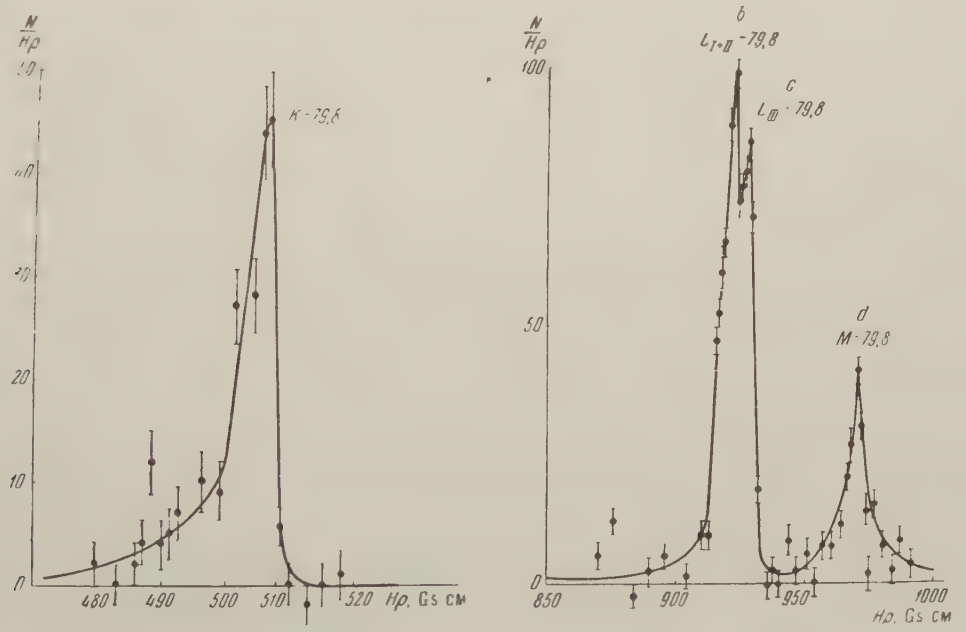

Fig. 1. Conversion from Tm^{168}.

<10 hours, ~ 29 hours, ~ 9 days and ~ 55 days were observed in the conversion electron spectra of the thulium fraction. These periods are rather close to the periods listed in Seaborg's tables[8] (Table 1); this simplified identification of the lines.

1. Conversion Electron Spectrum of Tm^{168}

We begin our examination of the results with the longest lived isotope Tm^{168}. The clearest data for this isotope were obtained with the third sample (long irradiation). After all the short-lived activities of the thulium fraction had died down sufficiently, four weak lines were distinguishable in the electron conversion spectrum. The strongest of these produced only 75 pulses per min in the spectrometer counter. All these lines are shown in Fig.1; the pertinent data are listed in Table 2. Even a cursory examination of Fig.1 indicates that the lines in the figure are the K-, L- and M-lines of same transition. The most distinctly recorded are the lines a and d, which we shall assume to be the K- and M- lines.

Table 2

Experimental results of investigation of the electron conversion lines shown in Fig. 1

	Electron energy, kev				Relative intensity of conversion lines
	Line *a*	Line *b*	Line *c*	Line *d*	
Series I	— *	70,1	70,1	77,4	(—)*:1,53:1,66:1,0
Series II	22,4	70,6	71,4	77,6	1,47:1 66:2,16:1,0
Average value	22,4	70,3	71,3	77,5	(1,47±0,15):(1,60± ± 0,16) : (1,91 ± ±0,16):1
Binding energy (Z = 68)	57,5	9,3	8,4	2,2	
Transition energy	79,9	79,6	79,7	79,7	
Average value from K- and L-lines			79,8		

*The *a* line was not observed in the first series of measurements.

From the magnitude of the difference K-M (55.1 kev), it is evident that the transition occurs in the nucleus with Z = 68. Taking Z = 68 (Er), we obtain for the transition energy $h\nu = 79.8$ kev. Let us now turn to the lines b and c shown in Fig.2. Arrows indicate the positions of the L_I, L_{II} and L_{III} lines calculated on the basis of $h\nu = 79.8$ kev and Z = 68. The figure shows that the b and c lines must be interpreted as due to electron conversion on the L_{II} and L_{III} subshells.

The experimentally determined intensity ratios of the K:L:M:N conversion lines are (0.71 ± 0.03):1:(0.24 ± 0.02):(0.07 ± 0.01). A notable feature here is the low value of the K/L ratio. The experimental value is juxtaposed with the theoretical value of this ratio for different multipole orders in Table 5. It will be seen that the experimental value is closest to the theoretical one for E3. Mixtures, however, are also possible. Inasmuch as different methods of interpolation can give values differing by as much as 30%, basing our identification only on the K/L ratio one cannot exclude transitions for which

$$\Delta I = 3, \text{ "yes"} - (E3 + M4),$$
$$\Delta I = 3, \text{ "no"} - (E4 + M3),$$
$$\Delta I = 4, \text{ "yes"} - (E5 + M4).$$

To choose between these possibilities we must turn to other indications.

Table 5

Comparison of the experimental value of K/L with the theoretical values for Z = 68 and hν = 207.5 kev

Experimental					
	M1	M2	M3	M4	M5
	6,2	4,3	2,6	1,2	0,3

Table 6

Comparison of the experimental and theoretical values of the partial half-life of the 207.5 kev state of Tm^{167} with respect to the γ-radiation

Transition	$T_{1/2}$ *, sec	$T_{1/2}$ **, sec
E3	0,5	5
E4	$1,9 \cdot 10^{10}$	23
M3	22,0	25
M4	$1,4 \cdot 10^{6}$	110

A. The spin of Er^{167} was measured by Bleaney & Scovil[21] and proved to be 7/2. Inasmuch as excited states with spin 15/2 are not encountered for nuclei in this region, the third possibility is automatically excluded.

B. The width of the integral L-line calculated for both the first two assumptions proves to be close to the experimental and hence is of no help in making the choice.

C. In their report Campbell et al[18] give an experimental value of the conversion coefficient for the 210 kev transition on the K-shell: $\alpha_K = 0.55 \pm 0.10$. This value is in good agreement with the theoretical one for a pure E3 transition, namely, 0.49 (for M3 radiation, $\alpha_K = 6.3$). In their work, Wilkinson & Hicks give the experimental value of the ratio of the number of conversion electrons to the number of 210 kev γ-rays as 7.5. This value differs very considerably from the value of 1.45 based on α_K and K/(L + M + N); hence we believe that the value given by Wilkinson & Hicks is in error.

D. We carried out a comparison of the experimental and theoretical values of the half-life of the 207 kev state with respect to the γ-transition. The values are listed in Table 6.

---

*Theoretical values calculated according to the formulas given by Mos'tskovskii in Ref.10.

**Experimental values calculated according to the formula $T_{exp} = T(1 + \alpha)$, where T is the experimental value of the half-life of the state (Ref.18,19), equal to 2.5 sec and α is the total conversion coefficient (the theoretical value for each multipole order).

This isotope was discovered by Wilkinson & Hicks[11]; according to their 1949 measurements its half-life is 85 ± 2 days.

On the basis of their absorption curves, Wilkinson & Hicks asserted that the emission spectrum of Tm^{168} comprises electrons of energies 160 and 500 kev and 210 and 850 kev γ-rays. In our measurements no conversion electrons with the indicated energies were observed (the upper limit for the possible intensity of a ~500 kev line is 2% with reference to the 79.8 kev L-line; we cannot evaluate the upper limit for the 160 kev electrons inasmuch as in our experiments there were also present in this energy region the 150 kev electrons from 9-day Tm^{167}.

The chromatographic separation technique is such that one can always fear the presence of a certain amount of isotopes with Z 1 or 2 greater than that of the investigated fraction. Hence we had to make sure that our samples were reasonably free of Yb^{169} (33-day) and $Lu^{171,173,174}$ (>150 days) (all the other isotopes of Yb and Lu have periods much shorter than 9 days). Evaluations of the maximum possible content of Yb and Lu carried out with reference to the 178 kev K-line of Yb^{169} (Ref.12) and the 79.7 kev K-line of Lu^{173} (Ref.13) showed that the contribution of Yb and Lu to the experimentally observed lines of Tm^{168} did not exceed 3% for the 79.8 kev L-line and 0.75% for the 79.8 K-line.

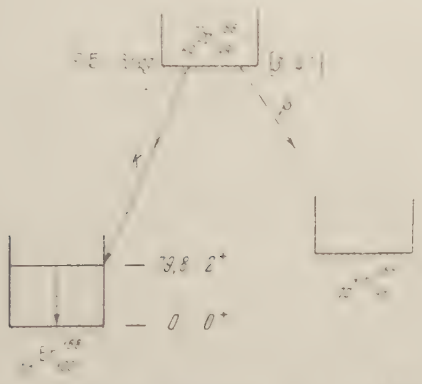

Fig.3. Decay scheme for Tm^{168}.

Inasmuch as the observed conversion electrons are associated with only the 79.8 kev transition, it may be assumed that the decay of Tm^{168} is characterized by the scheme shown in Fig.3. There is nothing surprising about the location of the first level of Tm^{168}: the first excited level in all even-even nuclei in this region of Z lies at about 80 kev.

With Coulomb excitation of Er by α-particles, we observed a 79 kev γ-line. In view of the fact that a mixture of isotopes was irradiated, one cannot assert that the observed γ-line belonged to Er^{169}; it is probable that it pertained to all the isotopes ($Er^{162,164,166,168,170}$) including Er^{168}. There is also nothing exceptional about the E2 identification: all the first excited states of even-even nuclei have spin and parity 2+ and, consequently, the transition to the ground level must be of the E2 type.

It remains unclear whether the K-capture goes to the ground level or to the 4+ level of Er^{168}. The answer to this question can be given by an investigation of the Auger electrons (in our measurements no Auger electrons from Tm^{168} were detected) or measurements of the relative intensities of the 79.8 kev γ-line and the K and L x-ray lines. The intensity ratio of the last two might indicate the role played by L-capture. This may make it possible to determine the exact energy of the transition.

We note that the spin of Tm^{168} can be predicted by the method proposed by Peker[14]. The nucleus of this isotope comprises 69 protons and 99 neutrons. The spin of Tm^{169} which also has 69 protons is 1/2, while the spin of Er^{167} which has 99 neutrons is 7/2. According to Peker, the spin of Tm^{168} should be 3 or 4. In view of this it may be assumed that capture to the ground level of Tm^{168} (0+) is much less probable than to the 79.8 kev excited level. One could expect with greater probability excitation of a second rotational

level of Tm^{168} (its spin and parity assignment would be 4+). The absence of such excitement is indicative of the small mass difference between Tm^{168} and Er^{168}.

According to our measurements, the intensity of the K-line associated with the 184 kev transition is less than 5% relative to the intensity of the 79.8 K-line. Taking into account the conversion coefficients for the 79 kev and 184 kev transitions, we can assert that the abundance of the 184 kev transition is not greater than 30% relative to the abundance of the 79.8 kev transition. Further investigation of the Tm^{168} γ-ray spectrum should verify or refine our evaluation. It is possible, incidentally, that the 264 kev level is not excited.

The relative probability of β^--decay of Tm^{168} remains obscure. It must not be forgotten that Yb^{168} is stable and that consequently a β^--branch must exist.

2. Conversion electron spectrum of Tm^{167}

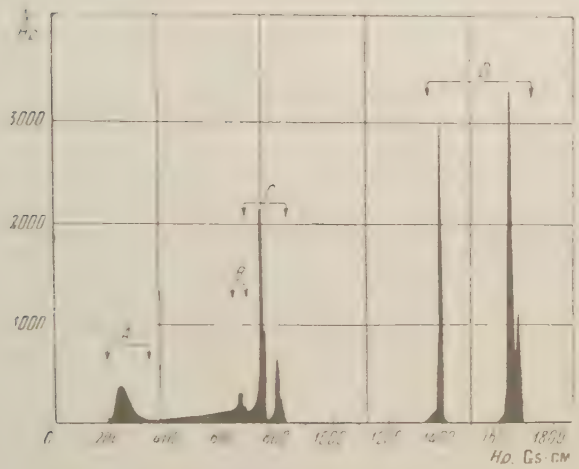

Fig. 4. Conversion electrons from Tm^{167}.

In the conversion electron spectra of all three specimens there were observed lines whose intensity fell off with a period of about 9 days. It is reasonable to attribute these lines to Tm^{167}, whose half life is 9.6 ± 0.1 days according to the measurements of Wilkinson & Hicks[11] or 9.4 days according to Handley & Olson[15]. The mass number has been established by Michel & Templeton[16] on a mass spectrometer on the basis of time-of-flight measurements. At the time of initiation of this investigation, it is known that the γ-spectrum of Tm^{167} consists of lines of 49, 115, 202, 515 and 720 kev energy, having relative intensities of 1.0, 0.02, 0.29, 0.09 and 0.18 respectively. These data were obtained by Nervik & Seaborg[17] by means of a scintillation spectrometer. An excited state of Er^{167} with an energy of 210 kev and a lifetime of 2.5 sec was found in 1956 in irradiating Er with fast neutrons[18] and with hard gammas[19]. Two γ-transitions in Er^{167} having energies of 350 and 700 kev were observed by Handley et al[20] in studying the β^--decay of Ho^{167}.

The conversion electron spectrum of 9-day thulium obtained with the third specimen (long irradiation) and normalized to a 9.6 day period is shown in Fig.4. The lines were fairly intense: for the strongest the counting rate amounted to 10,000 pulses per min. The contribution from Tm^{168} in the region of the lines in question is negligibly small (less than 0.01%). No short-lived activities were in evidence: there was no measureable count above the background at the position of the strongest line of Tm^{165} (185 kev). The upper bound of Yb and Lu impurities was evaluated on the basis of the 178 kev K-line of Yb^{169} (Ref.12) and the 78.7 K-line of Lu^{173} (Ref.13) and proved to be less than 0.1%. The observed spectrum comprised two groups of Auger electrons (A and B) and two groups of conversion lines (C and D).

Group D. We begin our description with Group D (Fig.5 and Table 4). The average spread of energy values is only 0.2 kev; the accuracy of energy determination taking into account the calibration uncertainty is 0.6 kev. It is immediately evident that the lines of group D are associated with conversion on the K, L, M and N shells. It is apparent from the magnitude of the difference K - M (56.2 kev) that the transition occurs in a nucleus with Z = 68.

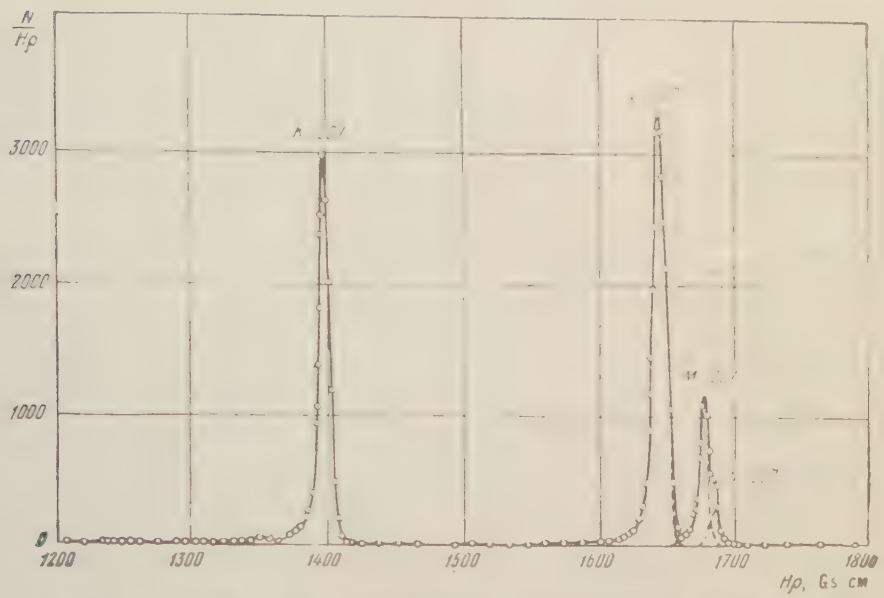

Fig.5. Group D of conversion electrons from Tm^{167}.

The 210 kev γ-transition originates from the excited state of the Er^{167} nucleus, reported by Campbell et al[18] and Stewart et al[19]. Adding the K shell binding energy to the energy of the K-line we obtain the energy of this transition: 207.5 ± 0.6 kev.

Table 4

Experimental results obtained from the D group of conversion lines of Tm^{167}.

Irradiation Number	% $R_{inst.}$	K-line $R_{exp.}$ %	K-line E_{e^-}	L-line $R_{exp.}$ %	L-line E_{e^-}	M-line E_{e^-}	N-line E_{e^-}	$I_K : I_L : I_M : I_N$
I (short)	0,9	0,9	149,7	1,0	198,5	205,9	—	0,68 : 1 : 0,29*
II (short)	0,6	0,8	149,7	0,8	198,8	206,0	207,5	0,74 : 1 : 0,24 : 0,08
III (long)	0,6	0,5	150,3	0,65	199,2	206,3	207,8	0,72 : 1 : 0,25 : 0,06
Average electron energy value			150,0		198,8	206,1	207,8	(0,71±0,03) : 1 : : (0,24±0,02) : : (0,07±0,01)
Binding energy (Z = 68)			57,5		9,3	2,2	0,4	
Energy γ-rays			207,5		208,1	208,3	208,2	

*In experiment I the M- and N-lines were not resolved; the indicated value (0.29) pertains to M + N.

The experimentally determined intensity ratios of the K:L:M:N conversion lines are (0.71 ± 0.03):1:(0.24 ± 0.02):(0.07 ± 0.01). A notable feature here is the low value of the K/L ratio. The experimental value is juxtaposed with the theoretical value of this ratio for different multipole orders in Table 5. It will be seen that the experimental value is closest to the theoretical one for E3. Mixtures, however, are also possible. Inasmuch as different methods of interpolation can give values differing by as much as 30%, basing our identification only on the K/L ratio one cannot exclude transitions for which

$\Delta I = 3$, "yes" - (E3 + M4),
$\Delta I = 3$, "no" - (E4 + M3),
$\Delta I = 4$, "yes" - (E5 + M4).

To choose between these possibilities we must turn to other indications.

Table 5

Comparison of the experimental value of K/L with the theoretical values for Z = 68 and hν = 207.5 kev

Experimental					
6,2	4,3	2,6	1,2	0,3	

Table 6

Comparison of the experimental and theoretical values of the partial half-life of the 207.5 kev state of Tm^{167} with respect to the γ-radiation

Transition	*	**
E3	0,5	5
E4	$1,9 \cdot 10^{10}$	23
M3	[illegible]	25
M4	$1,4 \cdot 10^{10}$	110

A. The spin of Er^{167} was measured by Bleaney & Scovil[21] and proved to be 7/2. Inasmuch as excited states with spin 15/2 are not encountered for nuclei in this region, the third possibility is automatically excluded.

B. The width of the integral L-line calculated for both the first two assumptions proves to be close to the experimental and hence is of no help in making the choice.

C. In their report Campbell et al[18] give an experimental value of the conversion coefficient for the 210 kev transition on the K-shell: $\alpha_K = 0.55 \pm \pm 0.10$. This value is in good agreement with the theoretical one for a pure E3 transition, namely, 0.49 (for M3 radiation, $\alpha_K = 6.3$). In their work, Wilkinson & Hicks give the experimental value of the ratio of the number of conversion electrons to the number of 210 kev γ-rays as 7.5. This value differs very considerably from the value of 1.45 based on α_K and K/(L + M + N); hence we believe that the value given by Wilkinson & Hicks is in error.

D. We carried out a comparison of the experimental and theoretical values of the half-life of the 207 kev state with respect to the γ-transition. The values are listed in Table 6.

---

*Theoretical values calculated according to the formulas given by Mos'tskovskii in Ref.10.

**Experimental values calculated according to the formula $T_{exp} = T(1 + \alpha)$, where T is the experimental value of the half-life of the state (Ref.18,19), equal to 2.5 sec and α is the total conversion coefficient (the theoretical value for each multipole order).

As may be seen from the table the theoretical and experimental values are close for E3 and M3 and differ considerably for M4 and E4 type transitions; consequently, in the possible mixed types indicated above (E3 + M4 or E4 + M3) the admixtures of M4 and E4, if present, must be small.

Thus the arguments adduced under C and D above lead us to conclude that the 207.5 kev transition is either pure E3 or E3 with a small admixture of M4; in other words, the transition involves a spin change of 3 and change of parity. According to the Mottelson & Nilsson model, the spin and parity of the ground state of Er^{167} are 7/2+. Thus for the 207.5 kev level of Er^{167} we have the choice between 13/2- and 1/2-. We opt for the latter (1/2-) inasmuch as a) not a single 13/2 state is known in this nuclear region and b) in the case of spin 13/2, it would be difficult to explain the absence of a normal electric dipole transition to the 172 kev level of Er^{167} for which the assignment is apparently 11/2+.

Group C. The experimental results of our investigation of the conversion lines in Group C are listed in Table 7; the spectrum is shown in Fig.6. The energy spread does not exceed 0.2 kev; the accuracy of energy determination taking into account the calibration uncertainty is 0.4 kev. The lines of Group C apparently consist of the lines associated with interval conversion on the L_I, L_{II} and L_{III} subshells (these lines are not fully resolved) and the lines associated with conversion on the M and N shells.

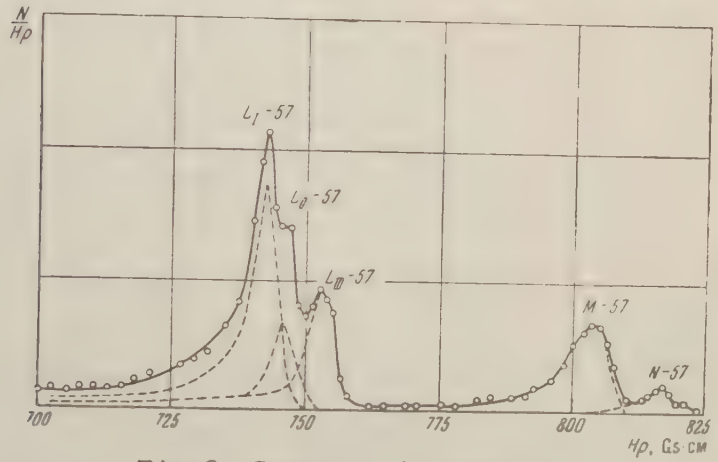

Fig.6. Group C of conversion electrons from Tm^{167}.

The experiments of Gorodinskii, Murin & Pokrovskii[22] showed that there are observed γ-γ coincidences between the pulses in scintillation spectrometers when each is gated to separate out a 40-60 kev interval of the spectrum. These coincidences can be regarded as coincidences of 56.7 kev γ-rays with x-rays. This means that the 56.7 kev transition occurs in Er and not in Tm. If one takes into account the binding energy for all the shells, as was done in Table 7, we obtain $h\nu = 56.7 \pm 0.1$ kev or taking into account the calibration uncertainty 56.7 ± 0.4 kev.

In attempting to locate the 56.7 kev transition in the Tm^{167} decay scheme one must take into account the following circumstances.

Er^{167} apparently has a group of rotational levels at 0 (7/2+), 80 kev (9/2+). and 172 kev (11/2+). The first level has not been detected in Coulomb excitation of Er inasmuch as it coincides with the first level of more abundant Er isotopes (its height was calculated from that of the second level); the second level has been detected by Temmer & Heydenburg[23] in Coulomb excitation experiments. It is obvious that there is no difference close to 56.7 kev between any of these levels and the 207.5 kev level. We cannot assume that the 56.7 kev level is the first excited state of Er^{167}, for if the spin of this level were $<7/2$, the 207.5 kev level of Er^{167} would decay it; while if the spin were $>7/2$, it would not be excited in the decay of Er^{167} either directly (inasmuch as the levels with 9/2+ and 11/2+ are not excited) or

Table 7

Experimental results obtained for the C group of conversion lines of Tm^{167}.

Irradiation number	Line	L_I-line		L_{II}-line		L_{III}-line		N-line		M-line	
		I_e	I	I_e	I	I_e	I	I_e	I	I_e	I
II (short)	0,6	47,2	2,7			48,5	1,1	54,9	1	56,3	0,16
III (long)	0,6	46,9	2,1	47,3	0,66	48,3	0,85	54,6	1	56,3	0,16
Average value		47,0	2,1±0,1	47,3	0,7±0,1	48,4	1,0±0,2	54,7	1	56,1	0,16±0,02
Binding energy (Z = 69)		9,8		9,5		8,4		2,2		0,45	
Transition energy		56,8		56,6		56,8		56,9		56,6	

through higher levels (there are no sufficiently intense γ-rays). Likewise, one cannot locate it above the 80 and 172 kev levels, for in this case there would be intense γ-rays of 80 or 172 kev energy. Nor can it be located much above the 207.5 kev level, for again there are no corresponding intense γ-rays. Hence we have no choice but to put this transition immediately above the 207.5 kev level, thereby introducing a 264.2 ± 1.0 kev excited state.

In order to elucidate the type of 56.7 kev transition we must turn first to the intensity ratios of the group C lines. Assuming that the shape of the L_I, L_{II}, L_{III} and N lines is similar to that of the M-line, which stands out clearest in the curve of Fig.5, one can deduce the following relationship for the intensities of the lines in group C:

$$L_I:L_{II}:L_{III}:M:N = (2.1 \pm 0.1):(0.7 \pm 0.1):(1.0 \pm 0.2):1:(0.16 \pm 0.02).$$

The ratio of $L_I:L_{II}:L_{III}$ can be compared with the theoretical ratios for different quantum characteristics of the 264.2 kev level of Er^{167}. These ratios, evaluated from the tables of Dranitsyna, are listed in Table 8; it may be concluded from these data that the assignments 1/2- and 7.2+ may be excluded inasmuch as it is impossible to find a mixture of transition types for which the theoretical ratios would be consistent with the experimental.

In Table 9 we list the data on the number of 56.7 kev γ-rays per decay of Er^{167} and the intensity of the 207.5 kev γ-rays relative to the total intensity of the 56.7 kev γ- and x-rays, calculated for different possible spin and parity assignments for the 264.2 kev level. The calculations were carried out on the basis of our relative intensities of the conversion lines assoicated with the 56.7 and 207.5 kev transitions,

$$(I_{L_I} + I_{L_{II}} + I_{L_{III}})_{56.7} : I_{L\text{-}207.5} = 0.75,$$

and the theoretical values of the conversion coefficients. Comparison of the calculated data with the experimental values (see Ref.22) indicates that the most probable assignment for the 264.2 kev level is 3/2-.

The exclusion of the 7/2-, 5/2- and 5/2+ assignments is also supported by the following arguments.

Table 8

Theoretical values of the ratios $L_I:L_{II}:L_{III}:\gamma$ for different quantum characteristics of the 264.2 kev level

Assignment	Type of transition to the 207.5 kev level	$L_I : L_{II} : L_{III} : \gamma$		
		For first type in Column 2	For second type in Column 2	For best mixtures
1/2	$E1 + M0$	1 : 0,39 : 0,63 : 7,7	No conversion	100% $E1$ 1 : 0,39 : 0,63 : 7,7
1/2	$E0 + M1$	1 : $<10^{-2}$: 0 : 0	1 : 0,11 : 0,46 : 0,5	99,9% $E1 + 0,1\%$ $M1$
3/2	$E1 + M2$	1 : 0,39 : 0,63 : 7,7	1 : 0,12 : 0,28 : 0,02	1 : 0,31 : 0,54 : 5,5
3/2	$E2 + M1$	1 : 14 : 9 : 0,25	1 : 0,11 : 0,46 : 0,5	2% $E2 + 98\%$ $M1$ 1 : 0,32 : 0,28 : 0,44
5/2	$E3 + M2$	1 : 120 : 27 : 0,1	1 : 0,12 : 0,28 : 0,02	1% $E3 + 99\%$ $M2$ 1 : 0,33 : 0,14 : 0,016
5/2	$E2 + M3$	1 : 14 : 9 : 0,25	1 : 0,013 : 0,36 : 10^{-4}	65% $E2 + 35\%$ $M3$ 1 : 0,65 : 0,38 : 0,12
7/2	$E3 + M4$	1 : 120 : 27 : 0,1	1 : 0,105 : 1,8 : 10^{-6}	
7/2	$E4 + M3$	1 : 3000 : 360 : 10^{-5}	1 : 0,013 : 0,36 : 10^{-4}	80% $E4 + 20\%$ $M3$ 1 : 0,28 : 0,32 : 10^{-4}

*Experimental ratios $L_I : I_{II} : L_{III} = 1 : 0,33 : 0,48$.

1. There is no converting crossover γ-transition of 264.2 kev energy in Er^{167} (or at any rate the L-conversion electrons from this transition are at least a thousand times fewer in number than the electrons from the 207.5 kev transition in Er^{167}).

If the level characteristic were 5/2- or 5/2+, the transition would be either E1 + M2 or E2 + + M1 and would probably be noticeable. This argument is somewhat weakened by the possibility that the 264.2 kev and 0 kev levels of Er^{167} may be systems with different K-shells, which, if true, might greatly lower the transition probability.

2. From a comparison of the relative intensities of the conversion lines (Fig.4) and the intensities of the γ-transitions as reported by Nervik & Seaborg[17], it is apparent that the probabilities of K-capture leading to the 207.5 kev level (1/2-) and the 264.2 kev level of Er^{167} are close. This precludes the 7/2± assignments.

3. The β-decay of Er^{167} which readily goes to the ground level (7/2+) does not go to the 264.2 kev level. This also precludes the possibility of the 264.2 kev level being either 7/2+ or 7/2-.

In the last column of Table 9 we list relative numbers of K-captures to the 264.2 and 207.5 kev levels evaluated for the different assignments. For 3/2- this ratio is 34:66.

Groups A and B. The groups of unresolved lines designated A and B (Fig.4) are due to Auger electrons. The energy position of group A is in satisfactory agreement with the energy values for L-2M, L-MN and so on Auger electrons, while the position of the B group is consistent with the energy of K-2L Auger electrons. The K-LM and K-LN

Data for evaluating the spin and parity of the 264.2 kev level of Er^{167}

Table 9

Spin & parity	Best mixture	Number of 56.7 kev γ-rays per decay of Tm^{167}	Intensity ratio (56.7 + X) to 207.5 kev γ-rays	K-capture branching ratio to the 264.2 and 207.5 kev levels
		Theory		
1/2+	100% $E1$	0,75	1 : 0,2	100 : 0
3/2+	95% $E1$ + 5% $M2$	0,66	1 : 0,2	84 : 16
3/2-	25% $E2$+75% $M1$	0,07	1 : 0,35	34 : 66
5/2+	15% $E3$+85% $M2$	0,002	1 : 0,37	22 : 78
5/2-	65% $E2$+35% $M3$	0,012	1 : 0,37	22 : 78
7/2-	80% $E4$+20% $M3$	10^{-4}	1 : 0,37	22 : 78
		Experiment		
Nervik & Seaborg[17]		(≥0,05) *	1 : 0,29	
Gorodinskii et al[22]		0,09±0,02		

*The number of 56.7 kev gammas per disintegration of Tm^{167} was evaluated from the data of Nervik & Seaborg on the assumption that the 115 kev peak observed by them was due to 56.7 γ-rays and x-rays.

Auger electrons fall in the energy region where the L_I, L_{II} and L_{III} lines of group C are located. Their relative number, however, is small and, consequently, they were not taken into account in calculating the intensities of the L_I, L_{II} and L_{III} lines. The ratio of the intensities of the K-2L and L-207 lines is (0.13 ± 0.05):1. It cannot be given with greater accuracy inasmuch as one cannot separate the tails of the K-2L and L-57 lines any more reliably.

From the indicated ratio one can evaluate the conversion coefficient for the 207.5 kev transition. According to Burhop[24] the intensity of the K-2L Auger electrons amounts to 55% relative to all the K Auger electrons. Burhop gives this value for silver, but having no more precise data we will apply it to erbium. Thus the relative intensity of all the K Auger electron lines is

$$I_{K\text{-Auger}} : I_{L\text{-}207} = 0.25 \pm 0.09.$$

On the other hand, the number of K Auger electrons equals the number n_v of vacancies in the K shell multiplied by the Auger yield η_K, which for Er (Z = 68) is reported to be equal to 0.07 ± 0.01. The number n_v of vacancies on the K shell equals the number of K-captures plus the number of K-conversion electrons (in this case undoubtedly the K shell is filled before the conversion with a period of 2 sec occurs). Inasmuch as in the conversion electron spectrum of Tm^{167} there is only one K conversion line (K-207), the number of K conversion transitions will be characterized by this line alone.

The number of K-captures can be evaluated as follows. Obviously, the total number of captures of atomic electrons is not less than the number of 207 kev transitions. For the purpose of our evaluation we can neglect capture of electrons on the L, M and higher shells. Thus the number of vacancies in the K shell, on the one hand, equals the number of K Auger electrons divided by the Auger yield,

$$n_\nu = \frac{I_{K\text{-Auger}}}{\eta_K}, \qquad (1)$$

on the other hand, this number is greater than the sum of the number of conversions on the K shell for the 207 kev transition and the total number of 207 kev transitions:

$$n_\nu \geqslant I_{K\text{-}207} + (I_{K\text{-}207} + I_{L\text{-}207} + I_{M\text{-}207} + I_{N\text{-}207} + I_{\gamma\text{-}207}) \qquad (2)$$

From (1) and (2), we obtain

$$I_{\gamma\text{-}207} \leqslant \frac{I_{K\text{-Auger}}}{\eta_K} - (2I_{K\text{-}207} + I_{L\text{-}207} + I_{M\text{-}207} + I_{N\text{-}207})$$

or

$$I_{\gamma\text{-}207} \leqslant +0.85 \pm 1.8$$

The conversion coefficient for the 207 kev transition on the K shell is $\alpha_K = I_{K\text{-}207}/I_{\gamma\text{-}207}$. It follows from the above that $\alpha_K \geqslant 0.71/0.95 = 0.75$ and $\alpha_L \geqslant 1/0.95 = 1.05$.

The theoretical conversion coefficient most consistent with these values are those for an E3 transition; the respective theoretical values are $\alpha_K = 0.49$ and $\alpha_L = 0.54$.

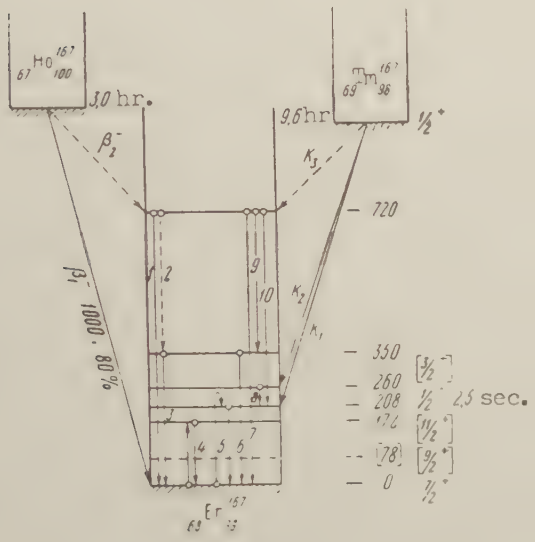

Fig.7. Levels of Tm^{167}. γ-Rays: 1 - 720 kev, 2 - 370 kev and 3 - 350 kev - detected in β-decay of Ho^{167}, 5 - 208 kev, 6 - 350 kev, 7 - 720 kev, 8 - 56 kev, 9 - 370 kev, 10 - 515 kev - detected in the decay of Tm^{167}; 4 - 172 kev detected with Coulomb excitation. The 208 kev γ-rays (5) were also observed in resonance excitation of Er by γ-rays and in bombardment of Er with fast neutrons.

No conversion lines corresponding to 115, 515 and 720 kev γ-transitions[11] were detected. From the results of our measurements, it may be asserted that the intensity of the L-115 line, if it exists, is less than 0.1% of the intensity of the L-207.5 line, and the total intensities of the conversion lines associated with the 515 and 720 kev γ-rays are less than 0.03% relative to the intensity of the L-207.5 line. Dividing these limiting intensity values by the minimum conversion coefficient at the given energy (for E1 transitions), we obtain the upper bound for the ratios of the abundances of these transitions to the abundance of the 207.5 kev transition; the ratios evaluated in this manner are listed in Table 10.

Table 10

E, kev	$I_t/I_{207,5}$, %
115	<0.5
515	<2
720	<4

The decay scheme for Tm^{167} that appears most plausible to us in the light of the present data, is shown in Fig.7.

3. Conversion Electron Spectrum of Tm^{165}

We also detected in the conversion electron spectrum of the thulium fraction lines whose intensity fell off with a period of about 29 hours. A thulium isotope with about this half-life has been mentioned by Handley & Olson[25] (T = 24.5 hours) and Michel & Templeton[16] (T = 29 hours). Our data on the period are in better agreement with the 29 hour period. Michel & Templeton, who used a mass spectrometer, established that the mass number of the thulium isotope is 165. As a result of capture of an atomic electron by the Tm^{165} nucleus there is formed[26,27] 10-hour Er^{165}, which in turn converts by K-capture to the stable isotope Ho^{165}.

Thus our preparations, in addition to Tm^{165}, contained an equilibrium amount of Er^{165}. In order to distinguish reliably between their radiations it was necessary to separate the isotopes chemically. This was done by B.K. Preobrazhenskii: the thulium fraction was again separated chromatographically. The activity of the separated out material actually did decay with a period of about 10 hours in agreement with the tabular values for Er^{165}. Hitherto little was known regarding the radiation of Er^{165}. Butement[26] asserts that it emits no γ-rays, while Wilkinson & Hicks report observing γ-rays of 1.1 Mev energy (absorption measurements).

Gorodinskii, Murin & Pokrovskii investigated the radiation of the Er^{165} material separated out by Preobrazhenskii on a scintillaion γ-spectrometer and found that there is only one line of 47 kev energy. The 1100 kev line, if it exists at all, is very weak. There can be no doubt that the 47 kev line is primarily due to x-rays emitted in the decay of Er^{165}. On the basis of this experiment alone one cannot preclude the possible existence of nuclear γ-rays of ~47 kev energy. However, the first excited states of Ho^{165} are well known: these are rotational states having energies of 94 and 216 kev. Thus the ~47 kev transition cannot be the lowest; nor can it lie above the cited levels inasmuch as in the decay of Er^{165} there are no 94 and 216 γ-rays. In view of the conflicting data on the 1100 kev γ-rays, we provisionally assume that no γ-rays are produced in the decay of Er^{165} and, therefore, ascribe all the 29-hour conversion lines to the decay of Tm^{165}.

We investigated the conversion electron spectrum of Tm^{165} twice. In both experiments we studied thulium fractions separated from tantalum subjected to brief proton bombardment. The spectra comprised lines due to conversion electrons from Tm^{165} (29 hours) and Tm^{167} (9 days). In order to obtain the conversion electron spectrum of Tm^{165}, it was obviously necessary to subtract the conversion lines of Tm^{167}. This was done in the following manner. After the conversion lines of Tm^{165} disappeared entirely (i.e., after ~15 days), we investigated the conversion electron spectrum of 9-day Tm^{167}. Then to obtain the number of counts associated with the decay of Tm^{165}, we subtracted the number of counts associated with Tm^{167}, reduced to the measurement time for the given point, from the total number of counts. The conversion electron spectrum obtained in this manner and reduced to the instant of beginning of measurement (assuming a period of 29 hours) is shown in Fig.8. It must be noted that this operation of subtracting the Tm^{167} spectrum yields satisfactory results only in the energy regions where there are no intense Tm^{167} lines. In those regions of the spectrum where there are intense Tm^{167} lines it is impossible to obtain reliable results and because of this these sections of

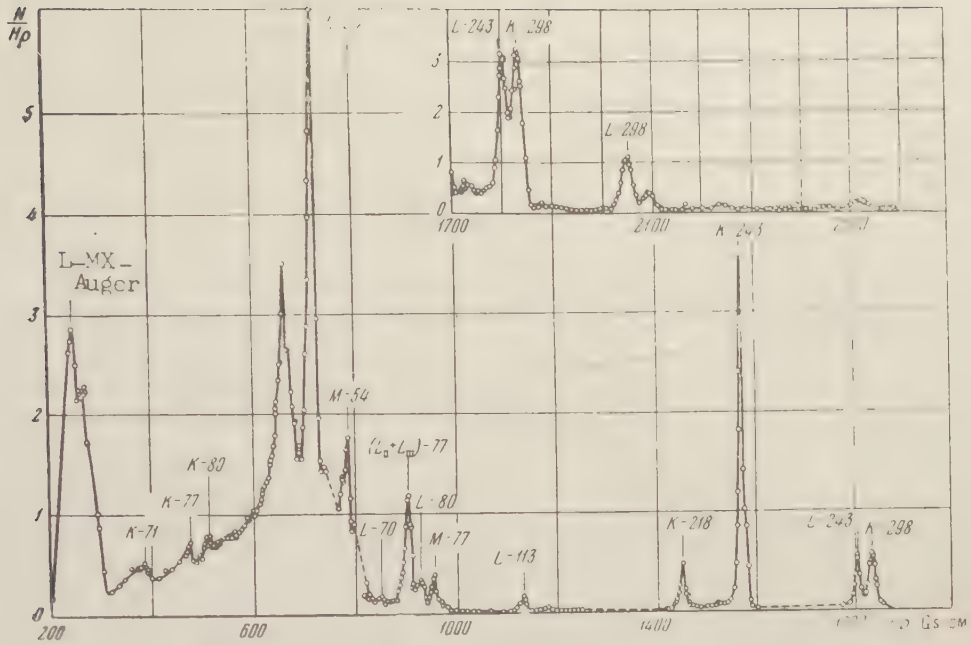

Fig.8. Conversion electrons from Tm^{165}.

Table 11

Experimental results obtained for the conversion electron lines of Tm^{165}

Electron energies, kev				Hρ	Identification	E_γ	Relative intensity
First exper.	Second experiment						
	Series I	Series II	Series III				
13,3				387	K-71?	70,8	~8
19,9	22,7	22,8	22,9	476	K-77	77,4	~14
24,8				510	K-82?	82,3	~10
36,9				655			—
37,7	37,0	37,6	37,4	662	K—2L-Auger		—
38,7				671			—
40,4				687			
44,7	44,1	44,1	44,0	724	L-53		~200
46,6				740			
51,4	51,7	51,0	51,1	780	M-53		~47
52,3				786			
60,7	—	—	—	851	L-71?		~2
67,5				902	L_{II}-77	76,8	24,2
68,7	68,2	68,0	67,9	910	L_{III}-77	77,1	26,7
71,5	71,4	71,2	71,7	929	L-82?		11
75,4	75,4	74,8	74,7	956	M-77	—	44
76,7	—	—	—	967	N-77	—	—
78,2	78,2	78,2	78,2	975	—	—	—
103,2	104,1	102,7	102,6	1134	N-113?		5,4
107,9	—	—	—	1162	—	—	0,6
111,7	—	—	—	1184	M-113?		1,3
160,9	161,1	161,3	161,7	1463	K-218,7	218,7	14,7±0,5
173,8	—	—	—	1523	—		~2
185,6	185,5	185,7	185,2	1576	K-243	243,0	100
233,8	233,7	233,9	233,7	1805	L-243		18,3±0,5
240,0	240,5	241,0	240,1	1833	K-298	297,6	18±2
	290,0	288,6	290,0	2049	L-298		6,2±0,3
	299,5	299,0		2093	—		<2
	401,7	401,7	400,9	2523	K-459	458,7	1,6±0,2

the spectrum are omitted in the figure (indicated by dash lines). Both the first and second experiments were carried out under the same conditions as the determination of the Tm^{167} spectrum, i.e., with an instrument resolution of ~0.6%; in the second experiment, however, due to less satisfactory preparation of the source the resolution at ~150 kev proved to be only 1.2%. The electron conversion spectrum of Tm^{165} shown in Fig.8 is that based on the results of the first experiment. In view of the fact, however, that in the first experiment the spectrum was measured only up to 250 kev, we also give in the insert of Fig.8 the conversion electron spectrum in the interval from 250 to 500 kev, as derived from the results of the second experiment.

The experimental results are listed in Table 11. There can be no doubt that there are present conversion lines associated with γ-transitions of 53-54, 77, 243 and 298 kev energy. The ~36.9, 37.7 and ~38.7 kev lines can be ascribed to K-2L Auger electrons from erbium and holmium. In addition there are 11 electron lines, the identification of which requires some discussion (see below) (E_e = 13.3, 24.8, 60.7, 71.5, 78.2, 103.2, 107.9, 111.7, 160.9, 299.4, 401.4).

53.2 kev transition. There were observed lines with E_e = 44.1 and 51.3 kev; in the first experiment carried out with a thinner source, the first line was slightly resolved into three components. The indicated lines are apparently the L and M lines of the same 53 kev transition; there may be no K line for this transition. Assuming (for Z = 68) a mean value of 9.1 kev for the L shell binding energy and 1.8 kev for M shell energy, we obtain the refined value of 53.2 kev for this transition. The 52.3 kev conversion line is possibly the N line of the same transition. Inasmuch as the L line may comprise an admixture of K-MX type Auger electrons, the intensity determination may be somewhat inaccurate.

77.4 kev transition. In the first experiment we observed lines with E_e = 19.9, 67.5, 68.7, 75.5 and 76.7 kev. They may be identified as the K, L_{II}, L_{III}, M and N lines associated with the same transition. From the difference K - M, equal to 55.5 kev, we can unambiguously establish that the transition occurs in a nucleus with Z = 68. Taking this value of Z (Er), we obtain from the position of the K line that the transition energy is 77.4 kev. The experimental relative intensities of the K, L_{II} and L_{III} lines for this transition are compared with the theoretical values for different multipole orders in Table 12.

Table 12

Relative intensities of the conversion lines for the 77.4 kev γ-transition

	K	L_I	L_{II}	L_{III}
Experimental	1	–	1,6	1,9
E1	1	0,09	0,02	0,03
E2	1	0,07	0,72	0,51
E3	1	0,83	34,5	13,5
M1	1	1,30	0,12	0,15
M2	1	0,65	0,07	0,16

It will be seen from the table that the experimental values are consistent with an E2 assignment. The results of the second experiment carried out, as was noted above, under worse conditions, cannot be utilized for identifying this transition; they do not, however, conflict with the above assignment.

243 kev transition. In both the first and second experiments we observed conversion lines with E_e = 185.5 and 233.8 kev. These lines may be identified as the K and L lines of the same transition. The M line associated with this transition was not observed inasmuch as is should be located at the energy of the most intense K line from the 297.6 kev transition. Although we did not observe structure of the L line, from the difference K - L

Table 13

Values of the K/L ratio for the 243.0 kev transition

Experimental	Theoretical					
	E1	E2	E3	M1	M2	M3
5,5±0,2	7,0	3,0	1,2	6,1	4,6	2,6

(48.3 ± 0.3 kev), it may be asserted that this transition occurs in a nucleus with Z = 68.

Again assuming Z = = 68 (Er), we obtain from the position of the K line a value of 243.0 ± 1.0 kev for the energy of the transition. Comparison of the experimental value of the ratio K/L with the theoretical values for different multipole orders (Table 13) does not allow of an unambiguous identification of the type of the 243.0 kev transition. Within the limits of the accuracy with which the theoretical K/L ratios are known (30%), the 243.0 kev transition may be E1, M1, M2 or a mixture of M1 + E2 or E1 + M2.

297.6 kev transition. In the second experiment we detected conversion lines with E_e = 240.2 and 289.5 kev. It is logical to identify these as the K and L lines of the same transition. The M line of this transition was not observed. From the magnitude of the difference K - L (49.0 ± 1 kev), it would appear probable that this transition occurs in a nucleus with Z = 68, but this identification is not unambiguous (Z = 69 is possible). Assuming Z = 68 (Er), we obtain from the position of the K line a value of 297.6 ± 1.2 kev for the energy of this transition. In determining the ratio of the intensities of the K and L lines it should be borne in mind that the K line of the 297.6 kev transition is superposed on the M and N lines associated with the 243.0 kev transition and that consequently the observed intensity for the K-297.6 line is probably somewhat higher than the actual value. The experimental value of the ratio K/L is compared with the theoretical values for different multipole orders in Table 14.

Table 14

Values of the K/L ratio for the 297.6 kev transition

Experimental	Theoretical					
	E1	E2	E3	M1	M2	M3
2,9	7,5	3,2	1,5	6,2	5,3	3,4

From a comparison of the experimental with the theoretical values of the K/L ratio the 297.6 kev transition may be characterized as E2, M3 or a mixture of M2 + E3.

The conversion line with E_e = 161.2 + 0.2 kev is apparently the K line of the 218.7 kev γ-transition. The ratio K/L in the region of γ-transition energies from 100 to 250 kev for all multipole orders from 1 to 5 is not less than 0.1. If we take the 161.2 kev line to be the L line, there must be a corresponding K conversion line at an energy of about 112 kev. The detected 111.7 kev line apparently cannot be the K line of this transition inasmuch as its intensity is less than 0.1 the intensity of the 161.2 kev line (if this should be the K line, then the multipole order of the transition is 5 or higher) If we take the 161.2 kev line to be the K line, then the corresponding L line should appear at 209 kev. Thus, in this case the L line falls into the energy region where we have the M and N lines of the 207.5 kev transition in Tm^{167} and hence would not be observable in our experiments. Adding the energy of the

161.2 kev line to the K binding energy we obtain a value of 218.7 ± 1.3 kev for the probable energy of the γ-transition.

The weak conversion lines at 103 and 111.7 kev could be identified as the L and M lines associated with the 113 kev γ-transition; this assignment, however, is not unambiguous in view of the fact that one cannot identify the corresponding K conversion line. Our data do not allow of identifying the 401.3 ± 0.7 kev line, but Gorodinskii, Murin & Pokrovskii[22], investigating the γ-ray spectrum of Tm^{165}, observed γ-rays with an energy of 460-480 kev. In view of this the 401.3 kev line can probably be identified as the K line associated with a 458.7 ± 2.0 kev γ-transition. The L line of this transition was not detected. Taking into account the statistical errors of measurement, it may be said that the K/L ratio is equal to or greater than 3. The 299.2 kev conversion line is close in energy to the M and N line of the 297.6 γ-transition; nevertheless its energy is greater than the energy of these lines by an amount exceeding our measurement error. We refrain from giving any identification for this line and the very weak 107.9 and 173.8 kev lines.

In the region of electron energies below 80 kev there is a large number of poorly resolved conversion lines. Susceptible of exact identification in this region are only the above discussed lines associated with the 53.2 and 77.1 kev γ-transitions and the group of lines at 37 kev which is wholly or partially due to K-2L Auger electrons. As possible identifications we suggest

71 kev transition - K line, E_e = 13.3 kev; L line, E_e = 60.7 kev;
82 kev transition - K line, E_e = 24.8 kev; L line, E_e = 71.4 kev.

Thus as a result of our investigation of the conversion electron spectrum we have detected six γ-transitions and established the possible characteristics of three of them. We infer the existence of three other transitions which cannot be reliably identified. It is worth noting, however, that the sums of the energies of the following transitions

(53.2 ± 1.0) kev + (243.0 ± 1.0) kev = (296.2 ± 2.0) kev;
(77.1 ± 0.5) kev + (218.7 ± 1.3) kev = (295.8 ± 1.8) kev

are close to the energy of the 297.6 kev transition.

According to Mottelson & Nilsson[29] the spin of the ground state of Tm^{165} must be the same as that of Tm^{169} (both nuclei have an even number of neutrons and 69 protons), i.e., 1/2+. The Er^{165} nucleus has 68 protons and 97 neutrons, i.e., must have the same spin and parity as Dy^{163}, which also has 97 neutrons. The spin of Dy^{163}, however, according to Murakawa & Kamei[30] is 7/2, while according to Cook & Park[31] it equals 5/2. The latter value appears to be more plausible. Hence we shall assume that the ground state of Er^{165} is characterized by 5/2-. In Fig.9 we give the decay scheme for Tm^{165} constructed on the basis of our experimental data, utilizing the scheme of Mottelson & Nilsson. We make no claim for the complete reliability of this scheme, but we feel that the following data speak in favor of it.

1. The level characteristics taken from the Mottelson-Nilsson scheme (hole excitation) do not conflict with our multipole order assignments.

2. According to this scheme there must be a 24 kev transition between the 243 and 218 kev levels. It is possible that the conversion lines at 13.3, 19.9 and 24.8 kev are partially due to this transition.

3. In Table 15 we list the total abundances of the transitions indicated in the scheme of Fig.9, calculated from the intensities of the K and L conversion lines assuming the multipole orders of the transitions indicated in scheme.

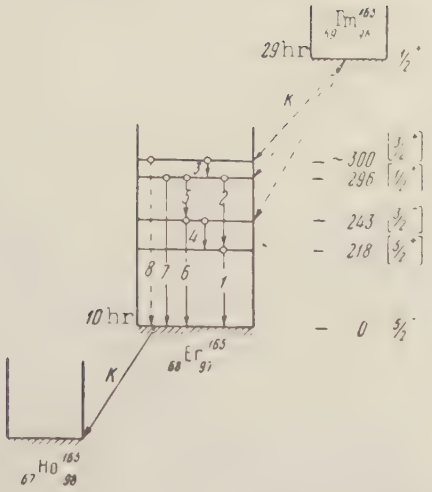

Fig.9. Possible decay scheme for Tm^{165}. γ-Rays: 1 - 218 kev, 2 - 77 kev, 3 - (5 kev), 4 - (24 kev), 5 - 54 kev, 6 - 243 kev, 7 - 296 kev, 8 - (300 kev).

In the case of mixed transitions we indicate the transition intensities evaluated for each component alone. As may be seen from the table, at the 243 kev level the intensities may be reconciled by an appropriate choice of the M1 + E2 mixture. Somewhat strange is the fact that the intensity of the 219 kev transition is several times higher than the intensity of the 77 kev transition. This might indicate that K-capture goes to the 218 kev level (5/2+), which would be strange inasmuch as in this case there should be an equal probability of K-capture from the 1/2+ level to levels with 1/2+ and 5/2+. It may be assumed that the intensity at the 218 kev level may to an extent be balanced by the ~24 kev transition.

4. It is possible that the 82 kev transition is a transition from the first rotational 300 kev level (1/2+, 3/2+) to the 5/2+ level. In this case there may also be 300 kev (E1) and 5 kev (M1 + E2) transitions.

In order to determine to what extent the proposed scheme is correct it would be desirable to have information on the relative intensities of the γ-rays and γ-γ coincidences in Tm^{165}.*

4. Conversion Electron Spectrum of Tm^{166}.

In studying the conversion electron spectrum of Tm^{165}, in one series of measurements we observed two groups of conversion lines which almost entirely vanished in the next series of measurements carried out some 24 hours later (Fig.10). Inasmuch as these lines were observed a few hours after chromatographic separation and vanished during the succeeding 24 hours, it is obvious that they belong to a Tm isotope with a period of a few hours. Only one thulium isotope with such a period is known, namely, Tm^{166} (7.7 hours). During the 30-40 hours elapsing between the end of irradiation and beginning of measurement a major portion

Table 15
Intensities of γ-rays and transitions in the decay of Tm^{165}

E_γ	I_K	I_L	I_γ		I_t	
77	14	51	14		80	
53	—	200	750		1000	
219	15	—	430		450	
243	100	18	*M*1	*E*2	*M*1	*E*2
			510	1000	630	1100
298	18	6	*M*2	*E*3	*M*2	*E*3
			38	180	62	204

*Note added in proof: The results of an investigation of $e^- - e^-$ coincidences in Tm^{165} obtained by Dzhelepov & Sergienko in the Scientific Research Institute for Physics at Leningrad State University support our identification of the 161.2 kev conversion line as K-218.7. They also observed coincidences between the conversion electrons associated with the 53 & 243 kev and the 77 & 218.7 kev γ-transitions, which is also evidence in favor of the decay scheme shown in Fig.9.

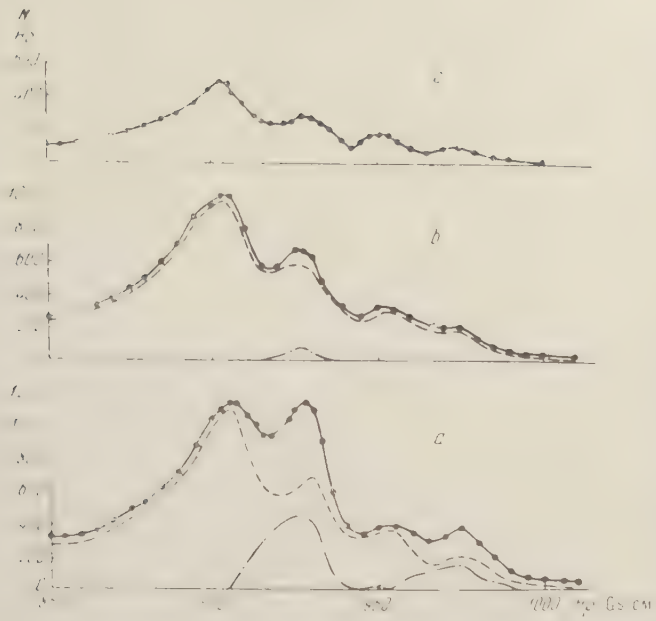

Fig.10. Conversion electrons from Tm^{166}: a - first series of measurements, b - second series of measurements carried out 24 hours after the first series, c - third series of measurements carried out 48 hours after the first series. The dash curves in a and b represent the conversion electron spectrum of Tm^{165} based on the results of the third series of measurements, reduced to the respective times of the given series of measurements. The dash-dot lines are the spectra obtained as a result of subtracting the dash curve from the solid curve, i.e., are the spectra ascribed to Tm^{166}.

of the Tm^{166} produced in the reaction on tantalum has time to decay, but an additional amount is formed in the decay of Yb^{166} (60 hour) and pure decay occurs only after separation of the isotopes in the chromatographic column. The conversion electrons observed from Tm^{166} had energies of 71.7, 78.1 and 126.6 kev. The first two lines are, apparently, the L and M lines associated with the 80-81 kev transition in Er^{166}. This transition of Er^{166} was observed in the decay of Ho^{166}. Its energy was determined as 81 kev. It was also established that this is an E2 transition. It is generally assumed that the 81 kev level is the first excited state, has the quantum characteristic 2+ and is the lowest level of the rotational band - 80 kev (2+), 264 kev (4+) and 546 kev (6+) (experimental energy ratios 1:3.30:6.83, instead of the theoretical 1:3.3:7.00). In the transition between the 4+ and 2+ levels there must obviously be released an energy of 184 kev and the corresponding K conversion electrons should therefore have an energy of 126.5 kev. This is precisely the energy of the third line observed by us.

Thus our data fit well into the scheme of rotational transitions shown in Fig.11, based on β-decay studies of the long-lived isomer Ho^{166} ($\sim$30 years)[39]. In view of this we may assume that the 80 and 184 kev transitions are both pure E2. This enables us 1) to identify the L line observed in the region of 71.2 kev - this line is apparently primarily due to electrons resulting from conversion on the L_{II} and L_{III} shells - and 2) to refine the energy value of the transition by adding the mean binding energy on the L_{II} and L_{III} shells to the energy of the line, i.e., $E_\gamma = 71.2 + 8.81 = 80.1$ kev.

The spin of Tm^{166} can also be determined by the method of Peker[14]. This nucleus contains 69 protons and 97 neutrons. The 69th proton in Tm^{169} produces a spin of 1/2, while the 97th neutron in Dy^{163} gives 5/2. Hence the spin of the Tm^{166} nucleus must be 2 or 3. Hence transitions to the third rotational state of Er^{166}, if at all possible, are characterized by a low probability, while transitions to the 80 and 264 kev levels are more probable. An obvious question is: what is the ratio of the probabilities of capture to the 80 and 264 kev levels of Er^{166}? This question could be answered if we had been able to measure with sufficient accuracy the intensities of 71.9 and 126.6 kev electron lines. It was impossible to do this, however, because these lines were observed together with the lines of Tm^{166} and Tm^{167}.

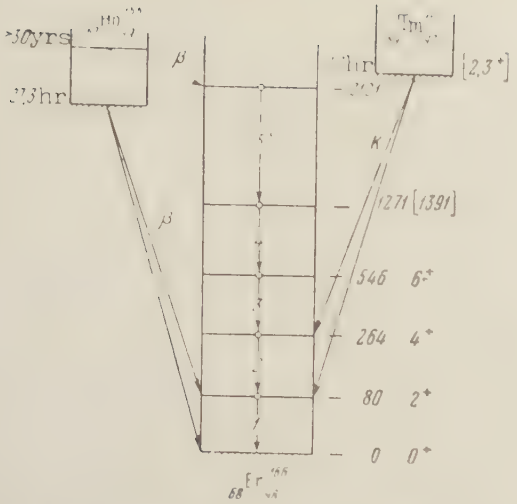

Fig.11. Decay scheme for Tm^{166}. γ-Rays: 1 - 80 kev, 2 - 184 kev, 3 - 282 kev, 4 - 625 kev (745 kev), 5 - 850 kev.

The approximate ratio is $N_e(71.2) : N_e(126.6) = 1:02$.

Using the theoretical values of the conversion coefficients, we obtain for the ratio of the total transition probabilities:

$$W_{80} : W_{184} = 1 : 0.8.$$

It follows from this relationship that the branching ratio for capture to the 80 and to the 264 kev levels is $W_{K-80} : W_{K-264} = 20 : 80$.

Thus according to our rough evaluation K-capture goes primarily to the second excited (264 kev) level of Er^{166} (4+). This seems rather strange inasmuch as with the above indicated spin (2 or 3) of the Tm^{166} nucleus, electron capture should go mainly to the 80 kev level (2+).

5. General Conclusions Regarding the Thulium Fraction

In Fig.12 we show the variation with time of the counting rate at the peaks of all the principal lines of the short-term (1 hour) irradiation thulium fraction. From this figure one can find the relative intensities of the conversion lines at any given time.

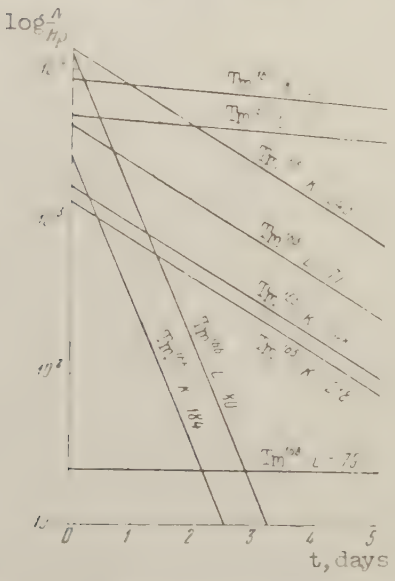

Fig.12. Variation with time of the counting rate at the peaks of the principal lines of the thulium fraction.

Extrapolating these straightline plots to the time of chromatographic separation and utilizing the proposed decay schemes, we can find the relative content of the different thulium isotopes at the instant of separation. In order to find subsequently the relative reaction yields we must extrapolate the plots to the instant of irradiation, taking into account the genetic relationship of the isotopes.

The Tm^{168} nucleus is a shielded one (Yb^{168} and Er^{168} are stable). Hence extrapolating its relative content to the instant of irradiation, we obtain the relative yield of this isotope from the spallation reaction. Tm^{165} and Tm^{167} nuclei are both formed as such and are also accumulated in the decay of nuclei with $Z > 69$. In connection with the fact, however, that the periods of the parent nuclei are very short (less than 20 min), one can, by extrapolating with respect to the periods of the thulium isotopes, obtain the yields for the given mass numbers. We evaluated the relative yield for the mass number 166 on the assumption that during the time from the end of irradiation to the instant of chromatographic separation equilibrium was established in the decay of Yb^{166} (60 hours) to Tm^{166} (7.7 hours).

Table 16

Relative yields of nuclei with different A in the spallation reaction*

Mass number	165	166	167	168
Relative activity at time of chromatographic separation	8.1	0.75	1	$1.3 \cdot 10^{-3}$
Relative content at time of chromatographic separation	1	0,025	1	$1.1 \cdot 10^{-2}$
Relative yield	2,1	(0,27)	1	$1 \cdot 10^{-2}$

*1. The number of decays per sec (activity) of Tm^{167} was calculated on the basis of the conversion lines associated with the 207 kev transition. 2. The activities of Tm^{167} and Tm^{168} were calculated from the L conversion lines of the 80 kev transitions. 3. The activity of Tm^{165} was evaluated from the K = 243 conversion line.

"V.G.Khlopin" Radium Institute of the Academy of Sciences of the USSR

We desire to express our deep gratitude to V.P.Dzhelepov, Director of the Laboratory for Nuclear Problems of the Joint Institute for Nuclear Research for assistance in the work. We are indebted to the service personnel of the JINR synchrocyclotron for carrying out the irradiation of the tantalum specimens and to V.D.Pluzhenkov, V.N. Mekhedov and V.A.Khalkin for facilitating the prolonged irradiation. We thank G.M.Gorodinskii, A.N.Murin and V.N.Pokrovskii for communicating the results of their γ-spectra investigation prior to publication and L. K. Peker for valuable discussion of the results.

References

1. B.K.Preobrazhenskii, O.M.Lilova, A.N.Dobronravova & E.D.Teterin, Zhur. neorg.khim (J.Inorgan.Chem.), 1, 2294 (1956).
2. P.P.Zarubin, Izv.AN SSSR, Ser.fiz., 18, 563 (1954).(Trans.Bulletin, 18, No.4, 244).
3. J.M.Cork, R.G.Schreffer & C.M.Fowler, Phys.Rev., 74, 1657 (1948).
4. J.M.Cork, M.K.Brice & L.C.Schmid, Phys.Rev., 96, 1295 (1954).
5. J.M.Cork & M.K.Brice, Phys.Rev., 100, 1237 (1955).
6. J.M.Cork, H.B.Keller, W.C.Rutledge & A.E.Stoddard, Phys.Rev., 78, 95 (1950).
7. F.T.Porter & C.S.Cook, Phys.Rev., 87, 464 (1952).
8. J.M.Hollander, I.Perlman & G.T.Seaborg, Table of Isotopes, Revs. Mod. Phys., 25, 469 (1953). (Cited in Russian Trans., M.1956).
9. L.A.Sliv & I.M.Band, Tablitsy koeffitsientov vnutrennei konversii (Tables of internal conversion coefficients) M.1956.
10. K.Siegbahn, Editor, Beta- and Gamma-Spectroscopy. Amsterdam, 1955.
11.G.Wilkinson & H.G.Hicks, Phys.Rev., 75, 1687 (1949).
12. K.Ia.Gromov, B.S.Dzhelepov & B.K.Preobrazhenskii, Report presented at the Seventh All-Union Conference of Nuclear Spectroscopy, 1957.
13. Iu.G.Bobrov, K.Ia.Gromov, B.S.Dzhelepov & B.K.Preobrazhenskii, Present issue of the Bulletin (next article).
14. L.K.Peker, Present issue of the Bulletin, p. 1030.

15. T.Handley & E.Olson, Phys.Rev., 94, 968 (1954).
16. M.C.Michel & P.H.Templeton, Phys.Rev., 93, 1422 (1954).
17. W.E.Nervik & G.T.Seaborg, Phys.Rev., 97, 1092 (1955).
18. E.Campbell, J.Kahn & M.Goodrich, Nu.Sc., 10, 256 (1956).
19. M.G.Stewart, A.M.Bureau & C.L.Hammer, Bull.Am.Phys.Soc., 1, 206 4(R2) (1956); Nucl.Sci., 10, 256 (1956).
20. T.Handley, W.Lyon & E.Olson, Phys.Rev., 98, 688 (1955).
21. B.Bleaney, H.E.D.Scovil, Proc.Phys.Soc., 64A, 204 (1951).
22. G.M.Gorodinskii, A.N.Murin, V.N.Pokrovskii & B.K.Preobrazhenskii, Present issue of the Bulletin.
23. G.M.Temmer & N.P.Heydenburg, Phys.Rev., 100, 150 (1955).
24. E.H.S.Burhop, The Auger Effect, p.50, Cambridge, 1952.
25. T.H.Handley & E.L.Olson, Phys.Rev., 92, 1260 (1953).
26. F.D.S.Butement, Proc.Phys.Soc., 63A, 775 (1950).
27. D.N.Kundu, J.D.Service, M.L.Pool & G.E.Boyd, Phys.Rev., 87, 203 (1952).
28. G.Wilkinson & H.Hicks, UCRL-744, June, 1950.
29. B.R.Mottelson & S.G.Nilsson, in Problemy sovremennoi fiziki (Problems of Modern Physics), 1 (1956).
30. K.Murakawa & T.Kamei, Phys.Rev., 92, 325 (1953).
31. A.H.Cook & J.G.Park, Proc.Phys.Soc., 69A, 282 (1956).
32. J.W.Michelich & E.L.Church, Phys.Rev., 85, 690 (1951).
33. K.Siegbahn & H.Slatis, Arc.f.Fys., 1, 559 (1950).
34. F.K.McCowan, Phys.Rev., 85, 151 (1952).
35. J.M.Cork, H.B.Keller & A.Stoddard, Phys.Rev., 76, 986 (1949).
36. N.M.Anton'eva, A.A.Bashilov, B.S.Dzhelepov & A.V.Zolotavin, Doklady AN SSSR, 70, 397 (1950).
37. R.L.Graham, J.L.Wolfson, & M.A.Clark, Phys.Rev., 98, 1173 (1955).
38. A.W.Sunyar, Phys.Rev., 93, 1345 (1954).
39. J.C.D.Millon, J.S.Fraser & G.M.Milton, Phys.Rev., 98, 1173 (1955).

CONVERSION ELECTRON SPECTRA OF NEUTRON-DEFICIENT LUTETIUM ISOTOPES

- Iu.G.Bobrov, K.Ia.Gromov, B.S.Dzhelepov & B.K.Preobrazhenskii

Introduction

The lutetium samples were prepared in the same manner as the thulium samples in the investigation of Ref.1 (see preceding article - 660 Mev proton bombardment of Ta, followed by chemical and then ion column separation). The measurements were carried out under the same experimental conditions.

We investigated the conversion electron spectra of two lutetium samples. The first sample was obtained from a tantalum target which was proton bombardment for about 3 months. The chromatographic separation was carried out a week after the end of bombardment. Measurements on this sample began three weeks after the end of bombardment and were continued over a period of almost one and a half years.

The second sample was obtained from a Ta target bombarded for one and a half hours. The chromatographic separation was carried out 30 hours after irradiation. The measurements were begun 3 hours after separation and continued over about 2 months.

Lutetium has two stable isotopes: Lu^{175} and Lu^{176}. The following information is available in the literature on the neutron-deficient isotopes of Lu. Wilkinson & Hicks[2] in 1951 found a number of lutetium isotopes. The data on these isotopes listed in lines 2 through 8 of Table 1 have been taken from Seaborg's Table of Isotopes.[3] The mass numbers were determined by the method of cross reactions; the nuclear radiation energies by absorption measurements.

Nervik & Seaborg[4], investigating the lutetium fraction obtained by spallation of tantalum, detected in it, in addition to others, a 32-day activity, which they ascribed to Yb^{169} formed as the daughter of Lu^{169}. The cross

Table 1

Neutron-deficient lutetium isotopes according to the data in the literature

Isotope	Reliab. of ident.*	Type of decay	Period	Energies, Mev: Particles	Energies, Mev: γ-rays	Method of obtaining
Lu^{169}	A		1,7 days			Ta + p; from parent Yb^{169} (32days)
Lu^{170}	B	EC **	1,7 days		~2,5	Tm — α — $3n$
Lu^{171}	B	EC	8,5 days		~1,2	Tm — α — $2n$; Yb — p — n; from Hf^{171}
Lu^{171}	D	EC	~600 days		~1	Tm — α — $2n$
Lu^{172}	B	EC	6,7 days		1.2	Tm — α — n; Yb — p — n; from Hf^{172}
Lu^{172}	B	?, EC?	4 hours	1.2		Tm — α — n; Yb — p — n; Lu — p — $p3n$;
Lu^{173}	B	EC	~500 days		~0,2;0,8	Yb — p — n; Lu — p — $p2n$; from Hf^{173}
Lu^{174}	A	EC-80% β—20%	165 days	~0,6	~1	Lu — n — $2n$; Lu — d — $p2n$; Lu — p — pn; Hf — d — α

*Degree of certainty of determination of A and Z as indicated by Seaborg.[3]

** EC = electron capture

sections for the formation of the 32-day and 1.7-day activities are close and this suggests that the 1.7 day period belongs to Lu^{169}. Gorodinskii et al[5] investigated the γ-ray spectrum of a preparation of ytterbium separated from the lutetium fraction and established that this γ-spectrum is identical with the γ-spectrum of Yb^{169}; this substantiates the hypothesis of Nervik & Seaborg. Thus, either the Wilkinson & Hicks mass number determination for 1.7 day lutetium is erroneous or in addition to 1.7 day Lu^{170} there exists Lu^{169} with a close half-life. The conversion electron spectra of the lutetium isotope listed in Table 1 were investigated for the first time in the present study. Many conversion lines were observed in the electron spectra of the two investigated lutetium samples. The observed lines may be divided into three groups on the basis of the observed decay period:

1) conversion lines whose intensity falls off with a period of 150-200 days (~0.5 year)

2) conversion lines with a decay period of~8 days and

3) conversion lines with a period of about 2 days.

The lutetium sample obtained by prolonged bombardment (~3 months) was investigated over a period of almost one and a half years, during which time seven series of spectral measurements were carried out. The first four series of measurements were made within one month; in these we observed the lines of the first and second groups. The next three series of measurements were separated by intervals of 1-1.5 months; in them we observed only the lines of the first group.

The short-term (1.5 hours) bombardment lutetium sample was investigated over a period of 2 months. During this time we carried out eight series of spectral measurements. During the first 2-3 weeks the conversion spectrum comprised electrons of the second and third groups. In the last series of measurements we observed electrons of the second group; at the very end of the measurements there became noticeable the strongest 17.4 kev line of the first group of conversion electrons. In addition, the spectrum of this sample comprised conversion electrons from Yb^{169} formed as a result of decay of one of the 2-day isotopes.

1. Conversion electrons from Lu isotopes with a period of 150-200 days

As was noted above in the 5th, 6th and 7th series of measurements on the long bombardment sample there were observed only the conversion electrons of the first group (T = 150-200 days). The general appearance of the spectrum did not vary from series to series. The average value of T was 170 days (the individual values have a spread from 120 to 250 days). A month after separation the count at the strongest line was still 2000 pulses per min.

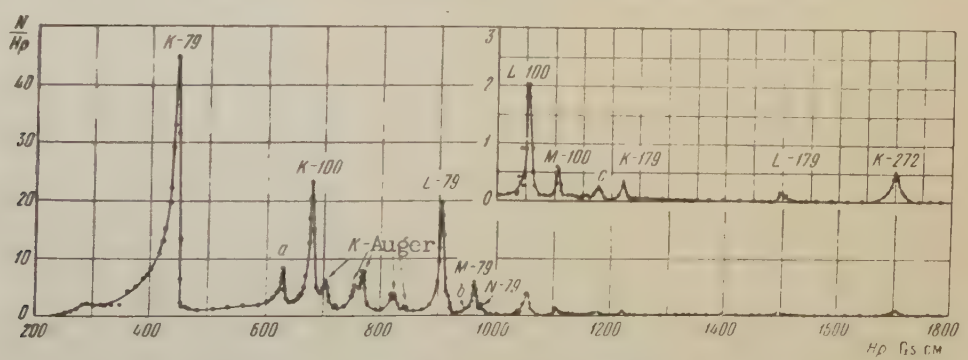

Fig.1. Conversion electron spectrum of Lu isotopes with T = 150-200 days.

Table 2

Relative intensities of the conversion lines of Lu having a period of ~170 days (average value for 3 series of measurements)

№	Electron energy, kev	Identification	Relative intensity
446	17,4±0,2	K-79	33±5
627	34,1±0,2	(a)	2,2±0,2
678	39,4±0,2	K-101 $K - L_I L_{II}$	6,7±0,5
703	42,2±0,2	$K - L_{II} L_{III}$	
754	48,2±0,4	K - LM	1,7±0,4
767	49,9±0,2		3,2±0,4
822	56,7±0,1	K-MM	1,5±0,3
833	58,8±0,3	K-MN	0,39±0,12
906	68,2±0,2	$(L_I + L_{II})$-79	6,2±0,5
916	69,6±0,1	L_{III}-79	0,29±0,08
947	74,2±0,1	(b)	0,10±0,04
962	76,2±0,3	M-79	1,38±0,09
975	78,4±0,2	N-79	0,56±0,14
1054	90,2±0,2	L-101	1,00
1105	98,6±0,2	M-101	0,26±0,05
1175	110,1±0,1	(c)	0,16±0,02
1221	118,2±0,2	K-179	0,16±0,02
1499	170,3±0,3	L-179	0,08±0,02
1700	211,3±0,3	K-272	0,19±0,02
1933	262±0,3	L-272	0,047±0,002

Our data on the energies and relative intensities of the conversion lines of the first group are shown in Table 2. Conversion electron spectrum of these Lu isotopes is plotted in Fig. 1. We attribute the 42.2, 48.2, 49.9, 56.7 and 58.8 kev lines to K--XY Auger electrons. It is not impossible, also, that part of the intensity of the 39.4 kev line (K-100) is due to K-2L Auger electrons.

We identified the 17.4, 68.2, 19.6, 76.2 and 78.4 kev lines as the K, $(L_I + L_{II})$, L_{III}, M and N lines associated with the 78.7 ± 0.7 γ-transition. From the experimental difference between the energies of the K and M conversion lines one can establish the atomic number of the nucleus in which the said transition occurs:

X-ray value of K - M for Z = 69 - from 57.0 to 58.0 kev,
" " Z = 70 - from 58.9 to 59.8 kev,
" " Z = 71 - from 60.8 to 61.7 kev;

The experimental value of K - M is 58.8 kev. Consequently, the transition presumably occurs in the nucleus with Z = 70 (Yb).

Knowing the atomic number of the nucleus in which the transition occurs, one can readily show that our identification of the close unresolved 68.2 and 69.6 kev lines as $(L_I + L_{II})$ and L_{III} is correct. Invoking the binding energies on the K and L shells, we can deduce the exact energy value of the transition: 78.8 ± 0.7 kev.

To determine the type of the transition we compared the experimental ratios of the conversion line intensities to the theoretical values for different multipole orders. The theoretical values of the K/L ratio were computed in the same way as in the investigation of Ref.1. As may be seen from Table 3, the experimental values of the ratios K/L and $L_{III}/(L_I + L_{II})$ for the 78.7 kev transition are most consistent with the theoretical values for an M1 transition; it will be noted, however, that the experimental value of $L_{III}/(L_{II} + L_I)$ is approximately half the theoretical one for M1. This divergence limits the possible admixture of E2; even with a 10% admixture of E2, the divergence between experiment and theory becomes greater than 3-fold.

We identified the 100.7 kev transition from the 39.4 (K), 90.2 (L) and 98.6 kev (M) lines. The experimental value of K - M, equal to 58.8 kev, shows that the transition occurs in a Z = 70 nucleus (see above). The experimental value of the difference K - L for the 100.7 kev transition is 50.7 kev (the tabular values for Z = 70 are $K - L_I = 50.8$, $K - L_{II} = 51.3$ and $K - L_{III} = 52.4$ kev); in view of this it may be assumed that the conversion occurs

primarily on the L_I shell. With Z = 70 and $h\nu$ = 100.7 kev, $\alpha_{L_I} > \alpha_{L_{II}}$ and $\alpha_{L_{III}}$ for E1, M1 and M3 type transitions. Even with 10% admixture of M2 in the first case and 25% E2 in the second and third cases, the intensities of the L_{II} and L_{III} conversion lines, according to the theoretical conversion coefficient, should be comparable to the intensity of the L_I line. Presumably the $K\text{-}L_IL_I$ and $K\text{-}L_IL_{II}$ Auger electron lines, having energies of 40.3 and 40.8 kev, should be superimposed on the K line (39.4 kev) of the 100.7 kev transition. An attempt to determine the fraction of Auger electrons in the 39.4 kev K line, made utilizing the data on the relative intensities of K Auger electrons for silver (Z = 49) (from Ref.6) and our data on the intensities of the K-LM and K-MX Auger lines (Table 2), led to the result that the entire 39.4 kev line is produced by Auger electrons. This result is probably erroneous in view of the following facts.

1. The energy of the 39.4 kev line differs too much from the energy of the $K\text{-}L_IL_I$ and $K\text{-}L_IL_{II}$ Auger electrons (40.3 and 40.8 kev) for it to be wholly due to the Auger electrons.

2. In the conversion electron spectrum of Tm^{167} the group of K-2L Auger electrons is well separated in energy from the other conversion lines and hence it may be assumed that in this case the shape of the K-2L Auger electron peak is not distorted - see group B in Fig.4 of Ref.1. It will be seen from that figure that in the K-2L Auger electron group there are evident two peaks but that both are of approximately the same intensity.

In view of this it appears more probable to us that the principal part of the intensity of the 39.4 kev line is nevertheless due to conversion electrons of the 100.7 kev transition. Obviously, under the circumstances, the intensity of the K-100.7 line can be determined only approximately. The experimental value of the ratio K/L is, apparently, somewhat less than 6.7. The theoretical values of the K/L ratio for different multipole orders are listed in Table 3.

Table 3

Comparison of the experimental values of K/L and $L_{III}/(L_I + L_{II})$ with the theoretical values for different multipole orders

Transition, kev	Ratio	Experimental value	E1	E2	E3	M1	M2	M3
78,7	K/L	5,2±0,9	6,1	0,49	0,02	5,75	2,75	0,65
	$L_{III}/(L_{II}+L_I)$	0,047±0,014	0,26	0,72	0,22	0,09	0,26	0,44
100,7	K/L	<6,7	5,8	0,91	0,1	6,7	1,6	1,4
179,5	K/L	2,0±0,3	5,7	1,7	0,8	6,1	3,9	2,7
272,5	K/L	≥10	5,8	3,2	1,0	6,0	4,7	3,7

Table 4

Comparison of the experimental value of K - L with the theoretical values for different atomic numbers

$K-L_i$	Theoretical Z=70	Theoretical Z=71	Experimental $h\nu$ = 179.5 kev
$K-L_I$	50,8	52,4	
$K-L_{II}$	51,3	53,0	
$K-L_{III}$	52,4	54,1	52,1±0,3

We identified the 118.2 and 170.3 kev conversion lines as the K and L lines associated with the 179.5 ± 0.7 kev transition. The experimental value of the energy difference between these lines does not allow of establishing the atomic number of the nucleus in which the transition occurs; it appears most probable, however, that Z = 70 (Yb) (see Table 4).

This deduction is further substantiated by the fact that the 179.5 kev transition energy is almost exactly equal to the sum of the energies of the 78.7 and 100.7 kev transitions which we know occur in the nucleus

with Z = 70. The experimental value of the conversion ratio K/L for the 179.5 kev transition within the limits of experimental error equals the theoretical value of this ratio for an E2 type transition.

One cannot reliably identify the 211.35 kev conversion lines as the K line of a 272.5 kev γ-transition on the basis of our data alone. The L line of this transition was observed by us only once (in the 6th series of measurements). However, our identification is upheld by the fact that Gorodinskii et al[7], investigating the γ-ray spectrum of the same lutetium fraction on a scintillation γ-spectrometer, detected γ-rays with an energy of about 270 kev. The ratio of the intensities of the K and L conversion lines according to our data is greater than 10. This value is not consistent with any of the theoretical values of the ratio but is closest to the values for E1 and M1 type transitions (Table 3). At present we refrain from any attempt at identification of the a, b and c electron lines in Fig.1, having energies of 34.1, 74.2 and 110.1 kev.

We must now turn to the question of what lutetium isotopes the observed conversion lines belong to and what may be the character of the decay schemes of these isotopes. Closest to the observed 150-200 day activities is the period of Lu^{174} (165 days). Hence we will begin our analysis with this isotope. Lu^{174} must convert to Yb^{174}. The first excited level of even-even nuclei in this region is situated at about 80 kev. It is natural to assume that the detected 78.7 kev transition is associated with the de-excitation of this level. In Yb^{174}, just as in neighboring even-even nuclei, there should be evident a rotational band comprised of 2+, 4+ and 6+ type levels with excitation energies in the proportion 1:3.29: 6.78 (average value for Er^{166} and Hf^{176}). In the case of Lu^{174} the excitation energies should be 78.7, 258.9 and 533.5 kev. The transitions should be of the E2 type and have energies of 78.7, 180.2 and 274.6 kev. These values are very close to the experimentally observed ones of 179.5 and 272.5 kev; if we take into account the error in determining the level energies (0.7 kev) and the theoretical energy ratios (3.29 ± 0.01 and 6.78 ± 0.04) one might say that the values coincide. In view of this one might attempt to describe the decay by the scheme shown in Fig.2. A number of difficulties arise however.

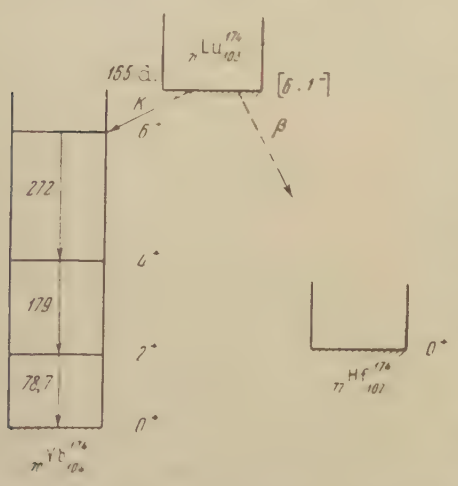

Fig.2. Possible decay scheme for Lu^{174}.

1. Gorodinskii et al[7] observed coincidences between the 78.7 and 100.7 kev γ-rays and coincidences of all the γ-rays (78.7, 100.7, 179.5 and 272.5 kev) with the x-rays. No other coincidences were observed.

2. In the decay scheme of Fig.2 all the transitions must be E2 whereas actually M1, E2 and E1 or M1 type transitions are observed.

3. Inasmuch as in the decay of Lu^{174} there forms a state with 6+, presumably the spin of Lu^{174} must be great. It can be determined by means of Peker's rule[8]. Inasmuch as the spins of Lu^{175} and Yb^{173} are 7/2 and 5/2, respectively, the spin of Lu^{174} must be 6 or 1. Of these two alternatives, apparently, the first is realized. If this is the case, the principal decay goes to the 6+ level, while the transition probabilities to the 4+, 2+ and 0+ levels are low. Taking into account conversion, it may be deduced that the relative intensities of the γ-rays should be

$$\gamma_{79}: \gamma_{179}: \gamma_{272} = 1.0 : 5.0 : 6.0.$$

Yet according to the data of Gorodinskii et al[7] the actual ratios are

$$\gamma_{79}: \gamma_{179}: \gamma_{272}: \gamma_{101} = 1.00 : 0.42 : 1.85 : 0.51.$$

The relative intensities of the conversion lines must be

$K_{79}: L_{79}: K_{179}: L_{179}: K_{272} = 1.00 : 2.04 : 0.79 : 0.39 : 0.30 : 0.09$
while the observed ratios are $1.00 : 0.20 : 0.005 : 0.002 : 0.006 : 0.0006.$

Thus we see that there is no agreement as regards the relative intensities of the γ-rays and the conversion lines. Taking into account these circumstances as well as the presence of the intense 100.7 kev γ-ray which does not fit into the scheme, we must admit that all the experimental facts cannot be explained by means of the scheme pictured in Fig.2. At the same time there can be no doubt that the scheme of Fig.2 is to some degree applicable to Lu^{174}. It may be assumed that part of the observed radiation does occur according to the scheme of Fig.2, but the absence of coincidences between the strongest 78.7 and 272 kev γ-rays shows that this part cannot be a major fraction.

We must, consequently, take into account the possibility that the identification proposed by Wilkinson & Hicks on the basis of nuclear reactions is erroneous and that the activity close to 170 days belongs not to Lu^{174} but to some other Lu isotope. It should be added that the existence of other long-lived even-even isotopes of Lu, such as Lu^{172} or Lu^{170}, would not help explain the established facts inasmuch as they would have a similar sequence of excited states. Therefore, let us assume that the sought isotope is Lu^{173} decaying into Yb^{173}. Regarding Yb^{173} it is known[9] that the ground state spin is 5/2; no excited states of Yb^{173} are known. In the rotational band region of the rare earths ($152 \leqslant A \leqslant 190$) rotational levels are observed in many odd nuclei. There are, however, only two known nuclei in this region with a ground state spin of 5/2. These are Eu^{153} and Dy^{161}. The 7/2 and 9/2 spin levels of these isotopes lie at 84 & 194 and 74.8 & 166 kev. The energy of the rotational levels in a nucleus with spin $I \neq 1/2$ can be written

$$E_1 I(I+1) + E_2 I^2 (I+1)^2.$$

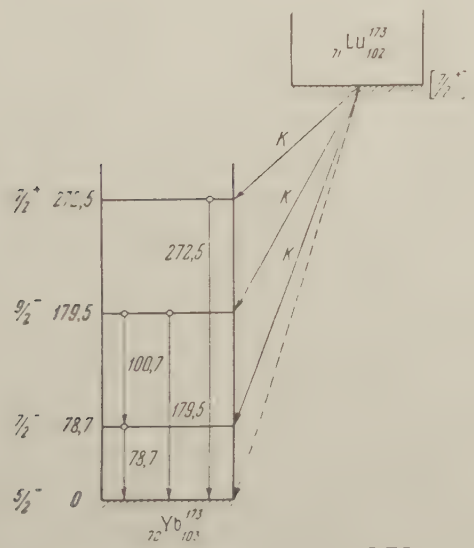

Fig.3. Decay scheme for Lu^{173}

If we neglect the second correction term, the energy of the levels must be characterized by the series 7, 16, 27, 40..., i.e., the energy ratios must be 1 : 2.28 : 3.86. In Eu^{153} and Dy^{161} the energy ratios of the first two levels are close to 2.28-2.31 and 2.22 respectively; this means that the second term is actually very small and can be disregarded.

Applying the indicated series to Yb^{173}, we obtain the level sequence 78.7, 179 and 304 kev. We immediately note that the first two values and the difference between them correspond exactly to the energy of the three observed transitions. They fit into the scheme shown in Fig.3.

According to the scheme of Fig.3 the 179.5 kev transition must be E2. This is in agreement with our experimental data. The 100.7 and 78.7 kev transitions must be of the M1 type with an admixture of E2, which is also not in conflict with the experimental results.

We now have to determine the origin of the 272.5 kev transition. The third rotational level of Yb^{173} must have an energy of about 300 kev. Obviously, the 272.5 kev transition cannot be associated with this level. On the other hand, it cannot be a transition between rotational levels inasmuch as then there would be coincidences of the γ_{79} and γ_{272} rays. The vibrational levels in these nuclei lie considerably higher. Hence we have no other course than to assume that this transition is associated with a single particle level of Yb^{173}. It must be a cross-over transition to the ground state of Yb^{173} inasmuch as the 272.5 γ-ray does not yield coincidences with any other γ-ray.

On the basis of the scheme of Fig.3 the 179.5 kev of transition must be of type E2 and hence it would be convenient to utilize it for relating the γ-rays and the conversion electrons. The conversion electron spectrum, however, comprises a 110.1 kev line for which we cannot exclude the identification K = 171.4. In this case the intensity of the γ-rays ascribed by Gorodinskii et al[7] to the 179 kev transition pertains both to the 179.5 kev transition and to the 171.4 kev transition. In view of this, for establishing correlation between the γ-rays and the conversion electrons we chose the 78.7 kev transition, regarding which it was shown above on the basis of the K/L and $L_{III}/(L_I + L_{II})$ values that it is either pure M1 or M1 plus an admixture of up to 10% E2. Taking the intensity of the γ-rays of this transition as 1.00 and utilizing the theoretical conversion coefficients for a type M1 transition, we evaluated the relative intensities of the γ-rays and conversion electrons; the results are shown in Table 5.

Table 5

Comparison of the relative intensities of the γ-rays and conversion electrons (α_K for the 78.7 kev transition taken equal to 5.7)

Transition energy, kev	Intensity					α_K (experimental)	α_K (theoretical)	
	γ-rays	Electrons			Transition			
		K	L	M				
78.7	1,00	5,7	1,1	0,3	8,1	-	M1 5,7	
100.7	0,51	1,0	0,17	0,04	1,7	1,96	M1—3,1	E2—1,0
179,5	0,42	0,028	0,014	-	0,46	0,067	E2—0,21	
272,5	1,85	0,033	0,033	-	1,9	0,018	E1—0,021	M1 0,18

In the same table we list the experimental coefficients for conversion on the K shell, which are, of course, the intensity ratios of the K conversion electrons to the γ-rays. From a comparison of the experimental value of α_K for the 272.5 kev transition with the theoretical valuesit is evident that the transition is E1. The experimental value of the K shell conversion coefficient for the 179.5 kev transition is three times smaller than the theoretical value for the E2 type transition. It is possible that this is due to the presence of the above mentioned 171.4 kev γ-rays. In determining the intensity of the K conversion electrons associated with the 100.7 kev transition, we took the total intensity of the 39.4 kev line, neglecting the contribution of the K-2L Auger electrons. Since the assumed K electron intensity is overvaluated, the deduced value of α_K for this transition must be an overestimate. The experimental value of α_K for the 100.7 kev transition (1.96) differs appreciably from the theoretical value for an M1 type transi-

tion (3.1). This could be explained by an appreciable admixture of E2 (>30%). Utilizing the theoretical ratio of the intensities of quadrupole γ-radiation from the second rotational level to the first level and the ground state[10], one can evaluate the percent admixture of quadrupole radiation in the 100.7 kev transition. Evaluated in this manner, the admixture of E2 does not exceed 5%. Thus there appears to be no satisfactory explanation for the high experimental value of α_K for the 100.7 kev transition.

Utilizing the data on the total number of transitions, we obtain the following ratios for the numbers of electron captures to the levels of Yb^{173}:

$$W_{272.5} : W_{179.5} : W_{78.7} = 1.9 : 2.2 : 6.5.$$

In order to evaluate the number of captures to the ground level of Yb^{173} one must know the relative intensity of the x-ray radiation.

Comparison of the relative intensities of the γ-rays and conversion electrons on the assumption that the 78.7 kev transition is mixed (90% M1 + 10% E2) leads to identical results.

2. Conversion electrons from Lu isotopes with a period of 7-8 days

Conversion lines associated with the 1-week isotopes were observed in the spectra of both the long and short-term bombardment samples. The conversion electron spectra of the long-term bombardment sample were investigated seven times over a period of one and a half years. The electron lines of both the half-year and week period isotopes were observed in the first four series of measurements. In the last three series only the electrons from the half-year isotopes were present. The conversion electron spectrum of the half-year isotopes was reduced to the time of the first or second series measurements and subtracted from the latter spectrum. The difference spectrum obtained in this manner is shown in Fig.4. It should be noted that for obvious reasons such subtraction leads to reliable results only in those parts of the spectrum where there are no intense conversion electrons of the first group. Hence the sections of the spectrum where there were present intense lines associated with the half-year isotopes are omitted in Fig.4 (dash lines).

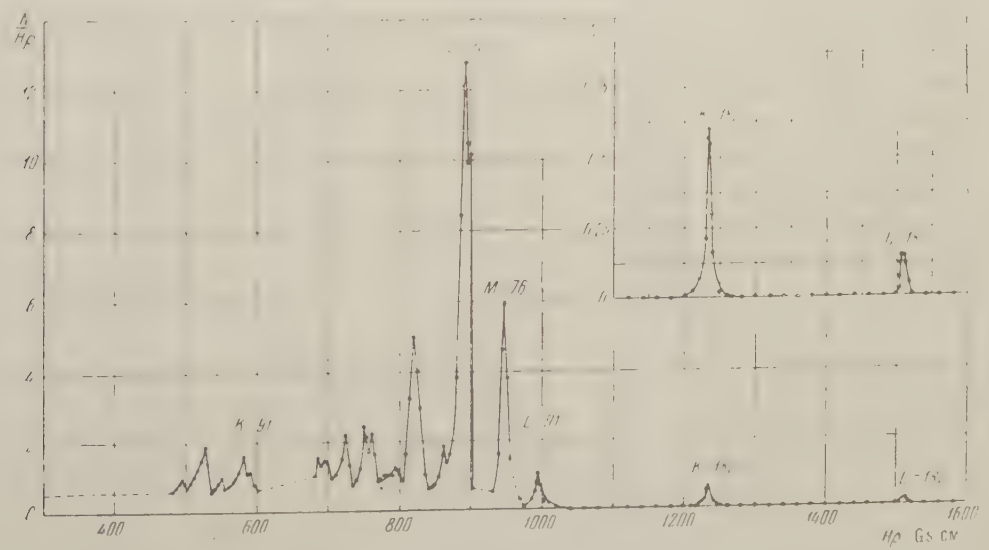

Fig. 4. Conversion electron spectrum of ~8-day lutetium isotopes.

The conversion electron spectrum of the short-term bombardment sample was studied over a period of two months. During the first 2 weeks conversion electrons from 1-week and 2-week isotopes were observed in the spectrum. In the last series of measurements we obtained the spectrum of the 1-week isotopes, essentially identical with the spectrum shown in Fig.4.

The experimental results obtained for the conversion lines of the 1-week isotopes are summarized in Table 6. As may be seen from the table we identified three γ-transitions, while 14 lines remained undeciphered. The 75.8 kev γ-transition was identified with reference to the 14.5 (K), 66.1 ($L_I + L_{II}$), 67.3 (L_{III}) and 74.2 kev (M) lines. The 14.5 kev line as regards energy position is close to the most intense conversion electron line of the half-year isotopes (17.4 kev) and hence was virtually unnoticeable in the spectrum of the long-term bombardment sample. In the spectrum of the short-term bombardment sample, this line was clearly discernible (see, for example, Fig.6). The other lines associated with this transition are clearly evidenced in the spectra of both samples. Obviously, from the value of the difference K - M one can unambiguously establish that the transition occurs in a nucleus with Z = 70 (Yb):

X-ray value of K - M for Z = 69 - from 57.0 to 57.9 kev,
" " " Z = 70 - from 58.9 to 58.8 kev,
" " " Z = 71 - from 60.8 to 61.7 kev.
Experimental value of K - M = 59.7 kev.

Table 6

Energy and relative intensities of the conversion line of Lu isotopes with a period of ~8 days

No.	Electron energies, kev: short-term irradiation	long-term irradiation	Average value	Hρ	I	Identification
1	14,5±0,1	14,4	14,5±0,1	407	~7	K-76
2		21,2±0,2	21,2±0,2	493	<0,5	
3	24,3±0,1	24,4±0,4	24,3±0,2	528	4,5±0,2	
4		26,2±0,2	26,2±0,2	549	<0,5	
5	29,3±0,1	29,3±0,2	29,3±0,1	582	1,6±0,1	K-91
6		30,2±0,2	30,2±0,2	590	<0,5	
7		40,2±0,2	40,2±0,2	686	–	
8		42,1±0,2	42,1±0,2	698	–	K—2L-Auger
9	45,4±0,1	45,2±0,1	45,3±0,2	730	7,2±1,3	
10		48,0±0,2	48,0±0,2	751	–	K—LM-
11		49,6±0,2	49,6±0,2	761	–	Auger
12	53,5±0,4	53,4±0,1	53,4±0,2	795	0,8±0,1	
13	56,7±0,2	56,6±0,1	56,6±0,2	823	~15	K—2M-Auger
14	58,1±0,3		58,1±0,3	831		
15	62,1±0,2	62,1±0,1	62,1±0,2	861	1,3±0,1	
16	67,8		67,8	881	–	
17	66,2±0,1	66,0±0,1	66,1±0,2	891	16,8±0,6	(L_I+L_{II})-76
18	67,2±0,2	67,4±0,3	67,3±0,2	900	21,6±0,8	L_{III}-76
19	69,0±0,2		69,0±0,2	911	–	
20	70,2±0,2		70,2±0,2	920	–	
21	74,2±0,2	74,2±0,1	74,2±0,2	947	13,5±0,5	M-76
22	80,6±0,3	81,2±0,3	80,9±0,3	992	2,8±0,2	L-91
23	88,5±0,2		88,5±0,2	1042	–	M-91
24	120,4±0,1	120,5±0,2	120,4±0,2	1234	1,0	K-182
25	171,8±0,2	172,1±0,3	171,9±0,2	1507	0,41±0,01	L-182
26	209,9±0,5		209,9±0,5	1690	<0,1	
27	753,7±0,5		753,7±0,5	3854	<0,1	
28	845,6±0,5		845,6±0,5	4188	<0,1	
29	903,1±1,0		903,1±1,0	4396	<0,1	

Adding the energy of the K line to the binding energy on the K shell of Yb, we obtain the value of 75.8 ± 0.3 kev for the energy of the transition. Comparison of the experimental and theoretical values of the K/L and $(L_I + L_{II})/L_{III}$ ratios (Table 7) shows that the 75.8 kev transition is of the E2 type.

Table 7

Comparison of experimental and theoretical values of K/L and $(L_I + L_{II})/L_{III}$

Transition (kev)	Ratio	Experimental	Theoretical					
			E1	E2	E3	M1	M2	M3
75,8	K/L	0,15	5,7	0,5	0,02	5,3	2,8	0,4
75,8	$(L_I + L_{II})/L_{III}$	0,78	3,6	1,3	1,0	11	4,3	1,7
90,6	K/L	0,58±0,07	6,4	0,74	0,06	6,6	3,1	1,3
181,7	K/L	2,44±0,08	5,7	1,7	0,8	6,1	3,9	2,7

We attribute the 29.3, 80.8 and 88.5 kev lines to the 90.6 kev γ-transition. In view of the experimental value of the difference K - M (59.2 kev), it may be asserted that the transition occurs in a nucleus with Z = 70 (Yb). Taking Z = 70, we obtain from the K-line and binding energies, a value of 90.6 ± 0.5 kev for this transition. Comparison of the experimental and theoretical conversion ratios indicates that this transition is probably E2.

We attribute the 120.4 (K) and 171.9 kev (L) lines to the 181.7 kev γ-transition. Again, the magnitude of the difference K - L (51.8 kev) allows us to assert that the transition occurs in a nucleus with Z = 70 (Yb). The energy of the transition evaluated on the basis of the K line energy and the binding energy equals 181.7 ± 0.7 kev. Comparison of the theoretical and experimental values of K/L (Table 7) indicates that the 181.7 kev transition may be either E2 or M3; it may also be a mixture of M1 + E2 or E2 + M3.

The energies of the 40.2 and 42.4 kev electron lines coincide with the energies of the K-2L Auger electrons from ytterbium; the energies of the 48.0 and 49.6 kev lines are consistent with the energy of the K-MM Auger electrons. These lines are apparently due partly or entirely to Auger electrons.

Goroginskii, Murin et al[5] investigating the γ-spectrum of Lu isotopes with a period of 7-8 days detected the following γ-rays: 180-190, 300-350, 480, 720, 900, 980 and 1080 kev (they did not investigate the region of the spectrum below 150 kev). In view of the existence of ~900 and ~980 kev γ-rays, it may be inferred that the 845.6 and 903.1 kev conversion lines are the K lines associated with these transitions. In this case the respective refined transition energies are 906.9 ± 3.0 kev and 964.5 ± 3.0 kev.

The presently available data are insufficient for identification of the other lines listed in Table 6.

We also investigated a lutetium sample separated from hafnium formed as a result of spallation of tantalum. From the results of our investigation of the conversion electron spectrum we feel safe in asserting that the Nos. 13, 14, 15, 17, 18, 21 and 22 lines (Table 6) are associated with Lu^{171}. To what nuclides the other lines belong remains unclear.

3. Conversion electrons from Lu isotopes with a period of ~2 days

The conversion electrons of the third group (~2-day activity) were observed only in the spectrum of the short-term bombardment sample. As was noted above, in the spectrum of the short bombardment sample we observed conversion electron lines of the 1-week and 2-week Lu isotopes as well as a

Table 8

Comparison of the energies and relative intensities (based on counting rate at the peak) of the conversion lines observed for the lutetium sample with the energies and intensities of the lines of Yb^{169}

Identification, kev		Lu source		Yb^{169} source	
		Hρ	I	Hρ	I
	110	1112	0,55	1113	0,48
K	178	1221	0,82	1220	0,86
K	198	1336	1	1337	1
	178	1485	0,15	1487	0,11
	198	1500	0,15	1502	0,15

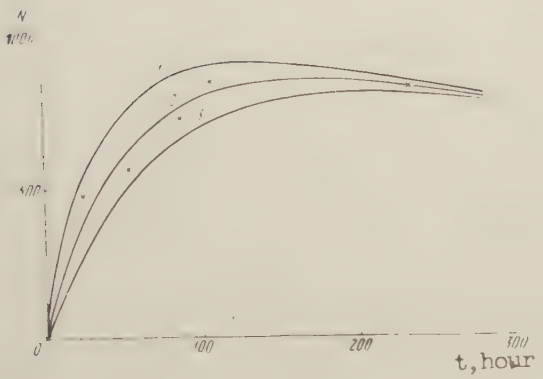

Fig.5. Accumulation and decay of Yb^{169} in the short term bombardment sample. Curves plotted on the assumption of parent activities 1) 1 day, 2) 1.5 day, 3) 2 day.

number of conversion electron lines that, on the basis of their energy and relative intensity, must be attributed to Yb^{169} (Table 8) (we carried out a special study of the conversion electron spectrum of an Yb^{169} source under the same conditions). The intensity of the lines attributed by us to Yb^{169} at first increased for several days and then fell off with a period of about 32 days.

In Fig.5 we have plotted the curves characterizing the rise and decay of the daughter activity (32-day Yb^{169}) for three different values of the parent activity (1, 1.5 and 2 days). In the same figure the points (crosses) indicate the experimental variation of the intensity of the K--198 conversion line. The calculated curves have been plotted to intersect at the experimental point for t = 666 hours (not shown in the figure). It will be seen that the experimental points fit closest to the theoretical curve for a parent activity of 1.5 days. Thus our data substantiate the deduction of Gorodinskii, Murin et al that in the spallation of tantalum there is formed the isotope Lu^{169} with a half-life close to 2 days. Does Lu^{170} form in the reaction? Can the entire 2-day activity detected by Nervik & Seaborg and Gorodinskii et al in their lutetium fractions be associated with the decay of Lu^{169}? Our data supply an answer to these questions.

Table 9

Conversion electron lines of Lu isotopes with a period of ~2 days

Hρ	E_{e^-}, keV	Identification	E_γ, keV	Hρ	E_{e^-}, keV	Identification	E_γ, keV
513	23,0	K-84	84,3	1088	95,5	K_1	156,8
549	26,2			1114	99,7		
649	36,3			1137	103,3	K_2	164,6
689	40,6			1171	109,5	K_3	170,8
703	42,3			1287	129,4	K_4	190,7
730	45,4			1301	131,8	K_5	193,1
743	47,0			1355	142,2	K_6	203,5
948	74,2	(L_I+L_{II})-84		1382	147,3	L_1	
956	75,4	L_{III}-84		1424	155,3	L_2	
1001	82,4	M-84		1460	162,1	L_3	
1013	83,4	N-84		1555	180,5	L_4	
1060	90,1			1608	183,8	L_5	
				1612	192,9	L_6	

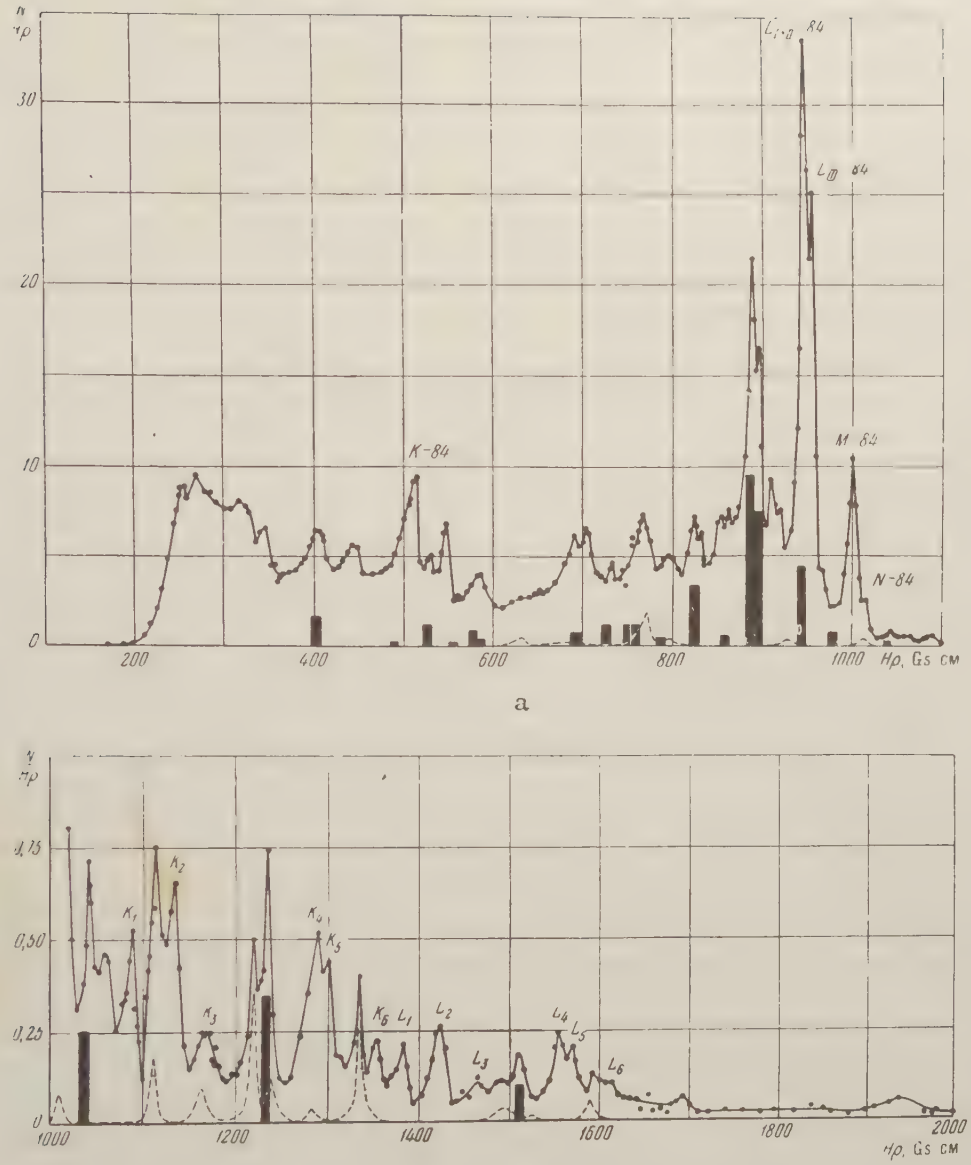

Fig.6. Conversion electron spectrum of the ~2-day Lu isotopes. The vertical bars indicate the lines of 8-day Lu; the dash line is the conversion spectrum of Yb^{169}.

The observed conversion lines of the third group are listed in Table 9. Fig.6 shows the conversion electron spectrum obtained in the second series of measurements on the short-term bombardment sample. The vertical bars along the horizontal axis indicate the conversion lines that we class in the second group; the heights of the bars are approximately equal to half the height of the corresponding peak. The dash-line in Fig.6 represents the conversion electron spectrum of Yb^{169}, plotted on the basis of our measurements of the above mentioned ytterbium source; the intensity is referred to the K-198 line. As may be seen from Table 9 the data of the conversion lines of the third group allow of identifying seven γ-transitions.

Table 10

Comparison of the experimental and theoretical K/L and $(L_I + L_{II})/L_{III}$ ratios for the 84.3 kev transition

	Exper. value	E1	E2	E3	M1	M2	M3
K/L	0,15	6,1	0,49	0,02	5,7	2,7	0,6
$(L_I+L_{II})/L_{III}$	0,8	3,9	1,4	4,5	11	4,3	1,7

Table 11

Comparison of the experimental values of the difference K - L with the x-ray values

Ly	Z = 70			Z = 71		
	$K-L_I$	$K-L_{II}$	$K-L_{III}$	$K-L_I$	$K-L_{II}$	$K-L_{III}$
X-ray	50,8	51,3	52,4	52,4	53,0	54,1
156,8		51,8				
164,6			52,0			
170,8			52,6			
190,7		51,1				
193,1			52,0			
203,5	50,7					

The 84.3 kev transition was identified as the transition giving rise to the 23.0 (K), 74.2 ($L_I + L_{II}$), 75.4 (L_{III}), 82.4 (M) and 83.4 kev (N) electron lines. Comparing the experimental value of the difference K - M (59.4 kev) with the x-ray values, one can readily show (see above under Section 1) that this transition occurs in a nucleus with Z = 70 (Yb). Adding the energy of the K line to the binding energy on the K shell of Yb, we obtain a value of 84.3 ± 0.3 for the energy of the transition. In view of the complexity of the spectrum, it is difficult to determine accurately the K/L ratio; it is of the order of 0.15. Evaluation of $(L_I + L_{II})/L_{III}$ yields approximately 0.8. Comparison of these experimental ratios with the theoretical ones (Table 10) shows unambiguously that the 84.3 kev transition is of the E2 type.

An E2 type 84.8 kev γ-transition was observed in the β-decay of Tm^{170} by Michelich & Church[9]; they found that the experimental values of the conversion ratios were K/L = 0.15 and $L_I:L_{II}:L_{III}$ = 0.1:0.83:1.00 and established that this transition goes from the first rotational level to the ground level of Yb^{170}. There can be little doubt that we have detected the same transition occurring in the disintegration of Lu^{170} by K-capture. Thus we can now give an answer to the above question: the Lu isotope with mass number 170 was present in our sample.

In Table 11 the experimental values of the difference K - L for the other six γ-transitions are compared with the tabular values for two atomic numbers. It appears highly probable that all these transitions occur in the nucleus with Z = 70 (Yb). In view of the fact that the conversion electron spectrum shown in Fig.6,b is very complicated, we did not attempt to resolve the individual lines and did not determine the relative intensities. It is obvious from the general appearance of the spectrum that the K/L ratio for all these transitions is greater than unity. Hence it may be asserted that among the six γ-transitions listed in Table 11 there are no transitions with a multipolarity higher than quadrupole. On the basis of our evaluation of the period of the conversion lines of the third group (Table 9), it may be asserted that all the conversion lines of the third group are associated with the decay of two lutetium isotopes, namely, Lu^{169} and Lu^{170}. As already

noted, the 84.3 kev γ-transition undoubtedly belongs to Lu^{170} and is a transition between the first rotational level and the ground state of Yb^{170}. The energy of the transition between the second and first rotational states must be $84.3 \cdot 2.33 = 196$ kev. It is possible that one of the three detected γ-transitions - 190.7, 193.1 or 203.5 kev - is this transition. At present we can draw no further inferences regarding the nuclides responsible for the other conversion lines listed in Table 11.

We wish to express our deep appreciation to V.P.Dzhelepov, Director of the Lboratory of Nuclear Problems of the Joint Institute for Nuclear Research, for assistance in the work. We owe a debt of gratitude to the service personnel of the JINR synchrocyclotron for carrying out the irradiation of the tantalum samples and to V.D.Pluzhenkov, V.I.Mekhedov and V.A.Khalkin who facilitated the prolonged bombardments. We also desire to thank G.M.Gorodinskii, A.N.Murin & V.N.Pokrovskii for communicating the results of their investigation of the γ-ray spectrum prior to publication and L.K.Peker for discussion of the results.

"V.G.Khlopin" Radium Institute of the
Academy of Sciences of the USSR

References

1. K.Ia.Gromov, Dzhelepov & B.K.Preobrazhenskii, Present issue of the Bulletin, p. 920.
2. G.Wilkinson & H.G.Hicks, Phys.Rev., 75, 1370 (1949); 81,540 (1950).
3. J.M.Hollander, I.Perlman & G.T.Seaborg, Table of Isotopes, Revs. Mod. Phys., 25, 469 (1953). (Cited in Russian trans., M.1956).
4. W.E.Nervik & G.T.Seaborg, Phys.Rev., 97, 1092 (1955).
5. G.M.Gorodinskii, A.N.Murin, B.N.Pokrovskii, B.K.Preobrazhenskii & I.E.Titov, Doklady AN SSSR, 112, 3 (1956).
6. J.Laberrique-Frolow & P.Radvanyi, J.Phys.rad., 17, 944 (1956).
7. G.M.Gorodinskii, A.N.Murin, V.N.Pokrovskii & B.K.Preobrazhenskii, Present issue of the Bulletin, p. 1005.
8. L.M.Peker, Present issue of the Bulletin, p.1030.
9. J.Michelich & E.Church, Phys.Rev., 85, 690 (1952).
10. N.Heydenburg & G.Temmer, Phys.Rev., 104, 981 (1956).

INTERNAL CONVERSION ELECTRON SPECTRUM OF RADIOTHORIUM. Part III
(Hρ = 1380-2700 and 3500-9000 gauss-cm regions)

- V.D.Vorob'ev, K.I.Il'in, T.I.Kol'chinskaia, G.D.Latyshev, A.G.Sergeev, Iu.N.Trofimov & V.I.Faleev

Introduction

The present report is the third in this series giving the results of our investigation of the internal conversion spectrum of the RaTh active deposit. Part I (Ref.1) was devoted to the high energy section of the spectrum (Hρ $>$ 2600 gauss-cm), while Part II (Ref.2) was concerned with the low energy region (Hρ $<$ 1380 gauss-cm). The measurements were carried out on a magnetic Ketron type spectrometer with a resolution of 0.25%. The magnetic field was measured and stabilized by the method of proton magnetic resonance[3]. For determining the conversion electron energies the instrument was calibrated with reference to a number of RaTh active deposit lines whose Hρ values are known with great accuracy from the studies of Refs.4 & 5. The calibration curve for the Ketron is given in Ref.2. The accuracy of determination of Hρ for the intense lines is evaluated as 1 part in $(2\text{-}3)\cdot 10^4$.

1. Conversion lines intensities

In determining the relative intensities of the conversion lines we took into account the fact that part of the ThC'' atoms leave the target due to α-recoil in the ThC $\xrightarrow{\alpha}$ ThC'' decay. As a result, the intensity of all the conversion lines produced in the ThC'' $\xrightarrow{\beta}$ ThD decay is reduced by about 30% as compared with the intensity of the lines pertaining to other nuclei.[6] For this reason the intensities of all the lines arising in the ThC'' $\longrightarrow$ ThD decay were evaluated with reference to the L line from the same decay. The intensities of the other lines were found relative to the I line from ThB $\longrightarrow$ ThC. In order to establish a relationship between the two sets of intensity values, we found the ratio of the intensities of the L and I lines with the source covered by an appropriate film ($\sim$10 μg/cm^2) precluding the escape of the recoil atoms. We also calculated the absolute intensities of the conversion lines, i.e., the number of electrons per ThB decay. The calculations were made with reference to the X line, the absolute intensity of which is $1.7\cdot 10^{-3}$ electrons per ThC'' decay event. This value follows from the theoretical conversion coefficient[7] for an E3 transition. That this is the multipole order of the transition in question is demonstrated in Refs.6 & 8.

In order to check our calibration as regards absolute intensities, we carried out a comparison of our data on the intensity of the 40 kev γ-transition of the known value for the excitation probability of the 40 kev level of ThC'' in the α-decay of ThC; 70% of the α-decays in the ThC $\longrightarrow$ ThC'' process go to this level. In addition, this level is excited in γ-transition from the upper levels of ThC''; according to our data the percentage of such transitions is 2%. Thus the probability of excitation of the 40 kev level of ThC'' is 0.72. The number of transitions from this level to the ground level is

$$N = N_{L_I} + N_{L_{II}} + N_{L_{III}} + N_M + N_N + N_O + N_\gamma,$$

where N_{L_I}, $N_{L_{II}}$...are the numbers of conversion electrons from the 40 kev γ-transition per ThC $\longrightarrow$ ThC'' and N_γ is the number of quanta with 40 kev energy.

Conversion of the 40 kev γ-transition on L_I shell of Tl^{208} (ThC'') gives rise to a strong A line. This A line, however, has an appreciable admixture of K electrons from the conversion of the 115 kev γ-rays from Bi^{212} (ThC).* The magnitude of this admixture can be calculated inasmuch as the intensity of the E line associated with conversion of the 115 kev γ-rays on the L_I shell of Bi^{212} is known. From the ratio L_I/L_{II} it follows that the 115 kev transition is M1, and for M1 the value of the K/L ratio is 6.3. It was found that the contribution made by the K conversion electrons to the A line is 15%. Taking this into account, we have $N_{L_I} = 0.446$. The number of conversion electrons on the other subshells is

$$N_{L_{II}} + N_{L_{III}} + N_M + N_N + N_O = 0.208.$$

The number N_γ of transitions with γ-radiation can readily be computed from the theoretical conversion coefficient on the L_I shell. From the $L_I:L_{II}:L_{III}$ ratio it follows that the 40 kev transition is pure M1. Utilizing Rose's[10] conversion coefficient corrected for finite nuclear size[11], we obtain $N_\gamma = 0.031$.

Thus the intensity of all the transitions from the 40 kev level is N = =0.685 electrons per ThC $\longrightarrow$ ThC'' decay, which differs by only 5% from the excitation probability (0.72) of this level. The agreement may be considered good particularly if we take into account the fact that N_{L_I}, $N_{L_{II}}$, etc. were determined by means of the X line (E_γ = 2615 kev) located at the other end of the spectrum.

The absolute intensities for some of the strongest conversion lines from RaTh have been measured by Martin & Richardson[12] and Flammersfeld[13]. Our data differ from those of Martin & Richardson by 8% on the average and from the data of Flammersfeld by 5%. We evaluate the accuracy of our absolute intensity determinations as 5-10% for the most intense lines.

2. Conversion spectrum in the Hρ = 1380-2600 gauss-cm region

Three series of measurements were made in investigating this region of the spectrum. In each series we determined both the positions and intensities of the lines. The average Hρ and line intensity values are listed in Table 1 together with the electron energies and corresponding γ-transitions, identifications of the lines and the comparative data from Refs. 12-15. It will be noted that our data on the Hρ values and particularly on the intensities differ appreciably from the data of Refs.13 & 14 in which photographic recording of the electrons was employed.

We did not observe the six lines - F2, Fb1, G1, H1, Ia2 and Ja3 - detected by Surugue[15]. Presumably the Fb1 and G1 lines were masked by the strong Fb and G lines. For the other lines we indicate in Table 1 the upper bounds of the intensities which, according to our data, lie below the upper bounds indicated in Refs.14 & 15. At the same time we discovered four new lines in this region: Fa1, Jc3a, Jc3b and L1. The Jc3a and L1 lines are due to conversion of 312.6 and 437.7 γ-rays, respectively on the L shell of Tl^{208} (ThC'').

---

*The presence of an admixture of K electrons in the A line was shown by us in Ref.9. The amount of the K electron admixture determined therein is not accurate inasmuch as in the graphic resolution of the A line we did take into account the high energy L_I-line tail due to the Doppler effect.

Table 1

Conversion Electron Spectrum of Radiothorium Active Deposit in the Hρ = 1380 to 2700 gauss-cm Region

Designation after Ellis	Our data								Ellis[14]		Surugue[15]		Flammersfeld[13]		Martin & Richardson[12]	
	Hρ, Gs. см	E_e, keV	Transition	Z	Level	E_γ, keV	Inten. rel. to I line	$P_\alpha \cdot 10^2$	Hρ	I	Hρ	I	I	$P_\alpha \cdot 10^2$	I	$P_\alpha \cdot 10^2$
F	1388,44	148,108	$B \to C$	83	*K*	238,601	5,94	28,4	1385,8	6,7	1388	8,6	5,54	28,4	5,49	31,3
F1	1436	157,2	—	83	—		0,001	0,005	1428,6	0,002	1436	0,005				
F2	—	—	—	—	—	—	<0,001	<0,005	—	—	1439	0,005				
Fa	1452,97	160,3	$B \to C$	—	L_I	176,7	0,0034	0,016	1446,6	0,014	1452	0,017				
Fa1	1458	161,5	—	83	—	—	0,0015	0,007	—	—	—	—				
Fb	1473,8	164,54	$C'' \to D$	—	*K*	252,54	0,0310	0,146	1469,3	0,024	1472	0,025	0,23	0,12		
Fb1	—	—	—	82	—	—	—	—	1479,0	0,003	1476	0,005				
G	1597,5	189,35	$C'' \to D$	—	*K*	277,35	0,199	0,94	1593,8	0,13	1595	0,17	0,18	0,92	0,17	0,99
G1	—	—	—	82	—	—	—	—	1611,8	—	1598	0,005				
G2	1628	195,7	$C'' \to D$	—	L_I	211,5	0,002	0,008	—	—	1624	0,005				
Ga	1661,8	202,66	$C \to C''$	82	*K*	288,18	0,023	0,107	1656,8	0,026	1658	0,017	0,021	0,11		
H	1694,7	209,59	$B \to C$	81	*K*	300,12	0,224	1,06	1691,0	0,24	1695	0,25	0,21	1,06		
H1	—	—	—	83	—	—	<0,001	<0,005	1710,9	—	1719	0,005			0,21	1,27
H2	1732	217,6	$C'' \to D$	—	L_I	233,5	0,0024	0,011	—	—	1729	0,005				
I	1753,91	222,21	$B \to C$	82	L_I	238,60	0,896	4,23	1751,0	1	1752	1	1	5,13	1	5,7
Ia	1757,07	222,90	$B \to C$	83	L_{II}	238,6	0,104	0,491	1754,0		1755					
Ia1	1766,85	225,0	$B \to C$	83	L_{III}	238,4	0,0059	0,028	1761,8	0,003	1764	0,005				
Ia2	—	—	—	83	—	—	<0,002	<0,008	1804,1	—	1785	0,005				
J	1811,11	234,61	$B \to C$	—	M_I	238,61	0,213	1,00	1807,7	0,24	1809	0,25				
J1	1812,6	234,93	$B \to C$	83	M_{II}	238,63	0,025	0,12	—	—	1812	<0,065				
J2	1821	236,7	$C'' \to D$	83	L_I	252,6	0,007	0,03	—	—	1816	<0,005	0,31	1,58		
Ja	1825,5	237,76	$B \to C$	82	*N*	238,65	0,073	0,34	1821,3	0,067	1822	0,077				
Ja1	1829,4	238,61	$B \to C$	83	*O*	238,76	0,015	0,071	1842,1	0,007	1825	<0,005				

Table 1 (Continued)

Designation after Ellis	Our data								Ellis[14]		Surugue[15]		Flammersfeld[13]		Martin & Richardson[12]	
	$Hρ$, Gs. cm	E_e, keV	Transition	Z	Level	$E_γ$, keV	Inten. rel. to I line	$P_α \cdot 10^3$	$Hρ$	I	$Hρ$	I	I	$P_α \cdot 10^3$	I	$P_α \cdot 10^3$
Ja2	1847,1	242,50	$C \rightarrow C''$	81	K	328,02	0,007	0,033	—	—	1843	0,005				
Ja3	—	—	—	—	—	—	$<$0,0005	$<$0,0025	1905,2	—	1907	$<$0,005				
Ja4	1916	257,9	—	—	—	—	0,0005	0,0025	1915,2	—	1919	$<$0,005				
Jb	1932,6	261,53	$C'' \rightarrow D$	82	L_I	277,40	0,037	0,17	1929,1	0,026	1932	0,025	0,027	0,14	0,028	0,16
Jb1	1985	273,4	$C \rightarrow C''$	81	L_I	288,2	0,0045	0,021	1980,2	0,007	1978	0,008				
Jb2	—	—	$C'' \rightarrow D$	82	M	277,3	0,0085	0,040	—	—	1981	0,008				
Jb3	1998,4	276,43	$C'' \rightarrow D$	82	N	277,33	0,0023	0,011	—	—	1995	$<$0,005				
Jb4	2009	278,8	—	—	—	—	0,0005	0,002	—	—	2008	$<$0,005				
Jc	2030,54	283,79	$B \rightarrow C$	83	L_I	300,18	0,039	0,18	2025,7	0,033	2026	0,025	0,035	0,18	0,035	0,2
Jc1	2034,9	284,8	—	—	—	—	0,003	0,01	—	—	2029	$<$0,005				
Jc2	2084,5	296,25	$B \rightarrow C$	83	M	300,25	0,0087	0,041	2081,4	0,007	2079	0,008				
Jc3	2098,0	299,40	$B \rightarrow C$	83	N	300,34	0,0025	0,012	—	—	2093	$<$0,005				
Jc3a	2154	312,6	$C \rightarrow C''$	81	L_I	327,9	0,0009	0,005	—	—	—	—				
Jc3b	2206	324,7	$B \rightarrow C$	83	K	415,2	0,0006	0,003	—	—	—	—				
Jc4	2304	348,1	$C \rightarrow C''$	81	K	433,6	0,0004	0,002	2296,6	0,002	2296	$<$0,005				
Jc5	2383,4	367,46	$C \rightarrow C''$	81	K	452,98	0,0075	0,035	2376,8	0,002	2379	$<$0,005				
Jc6	2465	387,5	$C \rightarrow C''$	81	K	473,0	0,0012	0,006	2457,4	—	2455	$<$0,005				
Jc7	2507	397,9	$C'' \rightarrow D$	82	K	485,9	0,0008	0,004	—	—	2493	$<$0,005				
Jc8	2547	407,7	$C \rightarrow C''$	81	K	493,2	0,0006	0,003	—	—	2537	$<$0,005				
L	2607,17	422,84	$C'' \rightarrow D$	82	L	510,84	0,142	0,67	2603,1	0,04	2607	0,08	0,15	0,76	0,12	0,688
L1	2666	437,7	$C \rightarrow C''$	81	L_I	453,0	0,0016	0,008	—	—	—	—				

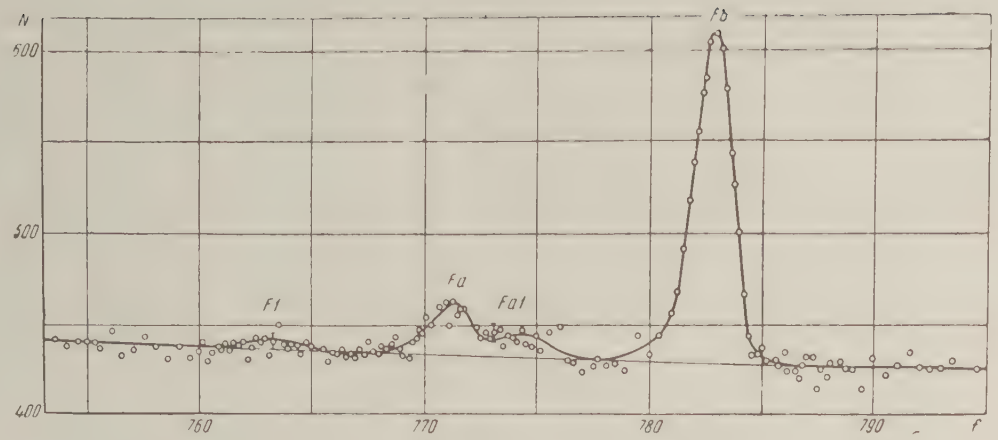

Fig.1. Hρ = 1400 to 1500 gauss-cm section of the spectrum (the Fa line was resolved into two components: Fa and Fa1); f = proton resonance frequency.

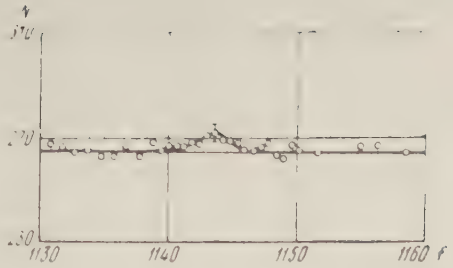

Fig.3. Section of the spectrum comprising the newly detected Jc3a line associated with conversion of the 312.6 kev γ-ray on the L shell of Tl^{208} (ThC'').

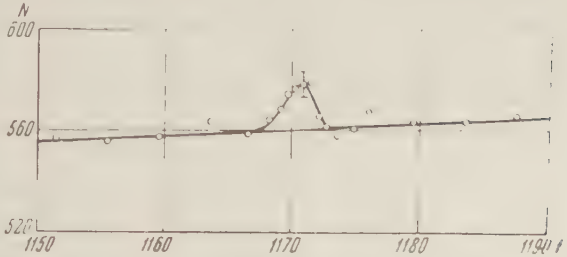

Fig.4. Section of the spectrum comprising the newly detected Jc3b line associated with conversion of the 415.2 kev γ-ray on the K shell of Bi^{212} (ThC).

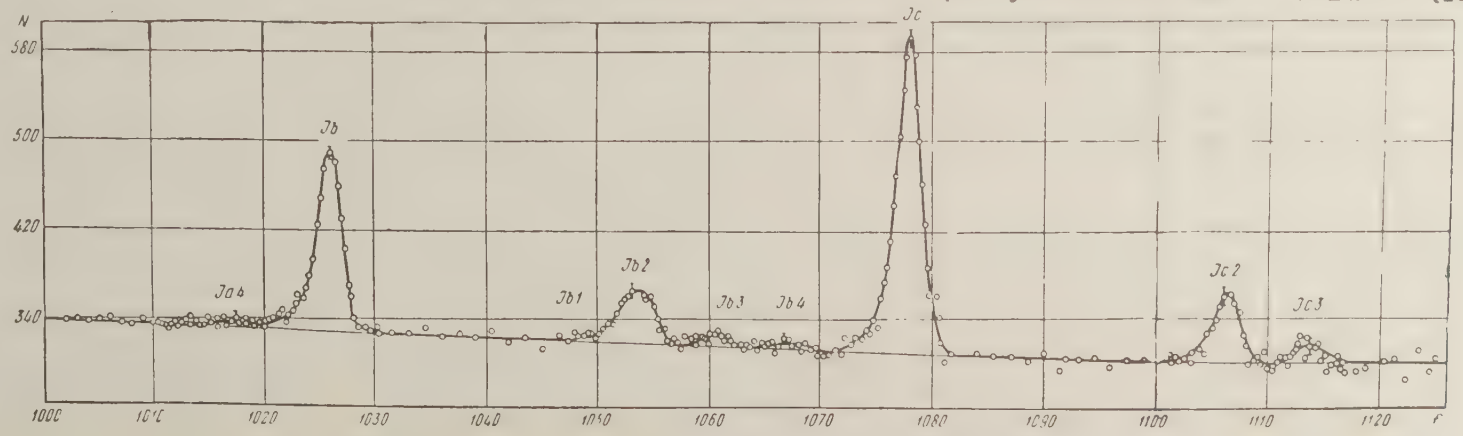

Fig.2. Hρ = 1880 to 2130 gauss-cm section of the spectrum.

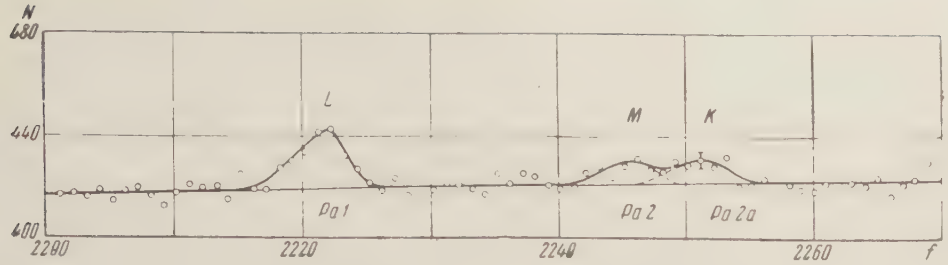

Fig.5. Hρ = 4140 to 4280 gauss-cm section of the spectrum (the Pa2 line was resolved into two components: Pa2 & Pa2a).

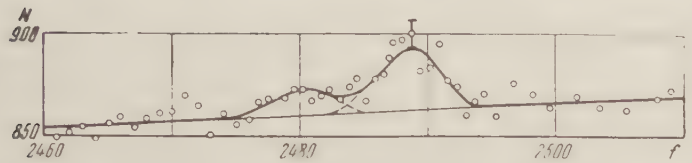

Fig.6. Hρ = 4630 to 4760 gauss-cm section of the spectrum containing two of the newly detected lines (after plotting of the Ra line according to the standard shape, in all four series of measurements there remained in its left-hand tail an appreciable excess of points above the background which we attributed to the R line).

The possibility that such a transition exists follows from the ThB → ThC decay scheme. We can give no identification for the Fal line.

We did not measure the intensities of the Ia, Ial and Jl lines in the present investigation; their intensities are taken from Ref.16. The J2 and Jc2 lines are located at the sides of the stronger Ja and Jc lines. In evaluating their intensities we carried out a graphic resolution of the lines employing the standard line shape. The Jbl and Jb2 lines are merged into one broad line. We determined its integral intensity. In order to determine the intensities of each of the components we proceeded as follows. The Jb2 line is associated with conversion of the 277.3 kev γ-transition on the M shell of Pb^{208}. The value of the K/L ratio for this transition indicates that it is Ml. In this energy region there are known to be two strong Ml γ-transitions, namely, the 238.6 and 300 kev transitions (ThB → ThC). For these transitions L/M = 4.3 and from the known intensity of the L (Jb) line found the intensity of the Jb2 line and then, by subtraction, the intensity of the Jbl line. Some sections of the conversion electron spectrum in the Hρ region from 1380 to 2600 gauss-cm are reproduced in Figs.1,2,3 & 4.

3. Conversion electron spectrum in the high energy region

In the first part of the work (Ref.1) we investigated the sections of the spectrum in the Hρ range from 2600 to 10,000 gauss-cm that were known to contain conversion lines[14,15]. In view of the fact that our procedure has a somewhat higher sensitivity in the high energy region than the photographic technique employed by Ellis and Surugue, we decided to carry out a search for conversion lines over the entire spectral range from Hρ = 4000 to Hρ = 9000 gauss-cm (E = 800 to 2200 kev). We detected a number of new very weak lines in this energy region: Oa4, Pa2a, R, Ra and S. The sections of the spectrum where these lines appeared were carefully rescanned two or three times. Some of the lines discovered by us are shown in Figs.5,6 & 7. Their energies and intensities are listed in Table 2.

We determined the nuclei to which the newly discovered lines as well as the hitherto unidentified (Oa, Oa3, Pa and Pa3) lines pertain. In the given energy region (E > 700 kev), the lines can belong only either to ThC' or to ThD. In order to facilitate identification, each lines was recorded twice,

Table 2

Conversion Electron Spectrum of Radiothorium Active Deposit in the Hρ = 3500 to 7200 gauss-cm Region

Designation	Our data								Ellis[14]		Surugue[15]	
	Hρ, Gs·cm	E_e, keV	Transition	Z	Level	E_γ	I	$P_\alpha \cdot 10^2$	Hρ	I	Hρ	I
O2	3570,8	675,23	$C'' \rightarrow D$	82	K	763,23	0,0048	0,023	3566,1	0,001	3567	<0,005
O3	—	—	—	—	—	—	—	—	3594,1	0,0004	3613	<0,005
Oa	3633,8	692,29	$C \rightarrow C'$	84	K	785,40	0,0078	0,037	3629,0	0,042	3623	0,005
Oa1	3701,4	710,66	$C \rightarrow C'$	84	L	727,61	0,0036	0,017	3700,1	0,002	3713	<0,005
Oa2	3748	723,3	$C \rightarrow C'$	84	M	727,4	0,0007	0,003	3741,1	0,001	3753	<0,005
Oa3	3836	747,4	$C'' \rightarrow D$	82	L	763,3	0,001	0,005	3875,9	—	3895	<0,005
Oa4	3913	768,5	$C \rightarrow C'$	84	L	785,4	0,001	0,005	—	—	—	—
P	3927,13	772,46	$C'' \rightarrow D$	82	K	860,46	0,023	0,109	3924,4	0,013	3931	0,009
Pa	4028,3	800,33	$C \rightarrow C'$	84	K	893,43	0,002	0,010	4010,7	0,001	4014	<0,005
Pa1	4188,2	844,61	$C'' \rightarrow D$	82	L	860,47	0,0043	0,020	4194,1	0,0005	4199	<0,005
Pa2	4232	856,8	$C'' \rightarrow D$	82	M	860,6	0,001	0,005	4224,8	0,0005	4228	<0,005
Pa2a	4242	859,6	$C \rightarrow C'$	84	K	952,7	0,0014	0,007	—	—	—	—
Pa3	4303	876,5	$C \rightarrow C'$	84	L	893,4	0,0005	0,003	4272,4	—	4279	<0,005
R	4674	980,6	$C \rightarrow C'$	84	K	1073,7	0,0008	0,004				
Ra	4691	985,4	$C \rightarrow C'$	84	K	1078,5	0,0020	0,010				
S	6210	1419,5	$C \rightarrow C'$	84	K	1512,6	0,0012	0,006				
Sa	6582	1527,3	$C \rightarrow C'$	84	K	1620,4	0,0020	0,009	6591	*		
Sb	7200	1707,1	$C \rightarrow C'$	84	K	1800,2	0,0011	0,005	7207	*		

*Ellis[14] gives $P_\alpha \cdot 10^2$ = 0.009 and 0.004, respectively, for these lines.

Fig.7. Hρ = 6130 to 6250 gauss-cm section of the spectrum comprising the S line (E_e = 1419.5 kev).

once with the usual unshielded source and once with the source covered with a film to prevent escape of the ThC'' atoms due to α-recoil. An increase of 30% in the intensity of the line in the latter case as compared to the former means that the line belongs to ThC''--ThD. Thus it was shown that the 02 line pertains to ThC''⟶ ThD, while the Oa, Pa and Ra lines are from ThC ⟶ ThC'. The identification of the other lines was effected with reference to the decay schemes.

Physics Faculty of the
Leningrad Institute of Railway Transport Engineers

References

1. E.Krisiuk, A.Vitman, V.Vorob'ev, G.Latyshev & A.Sergeev, Izv. AN SSSR, Ser.fiz., 20, 877 (1956). (Trans. Bulletin, 20, No.8, 797.)

2. A.Zhernovoi, E.Krisiuk, G.Latyshev, A.Remennyi, A.Sergeev & V.Fadeev, Zhur.eksp.i teor.fiz., 32, 682 (1957).

3. Iu.Egorov, G.Latyshev, PTE (Instruments and Technique of Experiment), No.2, 80 (1956); Iu.Egorov, G.Latyshev & Iu.Trulev, PTE, No.5 (1957).

4. K.Siegbahn & K.Edvarson, Nucl.Physics, 1, 137 (1956).

5. G.Lindström, Phys.Rev., 87, 678 (1952).

6. E.Krisiuk, A.Vitman, V.Vorob'ev, I.Vorob'ev, K.Il'in, G.Latyshev, M. Listengarten & A.Sergeev, Izv.AN SSSR, Ser.fiz., 20, 883 (1956). (Trans. Bulletin, 20, No.8, 803).

7. L.Sliv & I.Band, Tablitsy koeffitsientov vnutrennei konversee γ-izlucheniia (Tables of internal conversion coefficients) Part I, M.1956).

8. L.Elliott, R.Graham, J.Walker & J.Wolfson, Phys.Rev., 93, 356 (1954).

9. E.Krisiuk, G.Latyshev & A.Sergeev, Izv.AN SSSR, Ser.fiz., 20, 367 (1956). (Trans.Bulletin, 20, No.3, 335.)

10. M.Rose, Beta- and Gamma-Spectroscopy, Siegbahn, Editor, Amsterdam, 1955.

11. L.Sliv & M.Listengarten, Zhur.eksp.i teor.fiz., 22, 29 (1952).

12. D.Martin & H.Richardson, Proc.Roy.Soc., A195, 287 (1948).

13. A.Flammersfeld, ZS.f.Phys., 124, 227 (1939).

14. G.Ellis, Proc.Roy.Soc., A138, 318 (1932); G.Ellis, Proc.Roy.Soc., A143, 350 (1934).

15. F.Surugue, Ann.Phys., 8, 484 (1937); F.Surugue, J.Phys.et Rad., 9, 438 (1938).

16. E.Krisiuk, G.Latyshev, M.Listengarten, L.Ostretsov & A.Sergeev, Izv. AN SSSR, Ser.fiz., 20, 363 (1956). (Trans. Bulletin, 20, No.3, 332.)

SPECTRUM OF CONVERSION ELECTRONS FROM Ho^{160}

- B.S.Dzhelepov, B.K.Preobrazhenskii, I.M.Rogachev & P.A.Tishkin

We investigated the conversion electron spectra of the erbium and holmium fractions separated from tantalum bombarded with 660 Mev protons by means of two different spectrometers.

I

The erbium fraction was investigated on a single lens spectrometer with a solid acceptance angle of 0.5% of 4π and a line half-width of 2%.

The observed spectrum comprised one conversion line (44 kev) whose intensity fell off with a period of several hours, 21 lines with a period of about 28 hours and a few weak lines with a period of about 12 days. We were not able to establish the origin of the 44 kev line; possibly it was associated with residues of Er^{161} (3.6 hours).

The conversion electron spectrum of the 1-day isotope was recorded a number of times until the activity of the source died out. One day after separation of the source material the spectrum had the appearance shown in Fig.1. The counting rate in this case at the most intense line was 41,000 pulses/min.

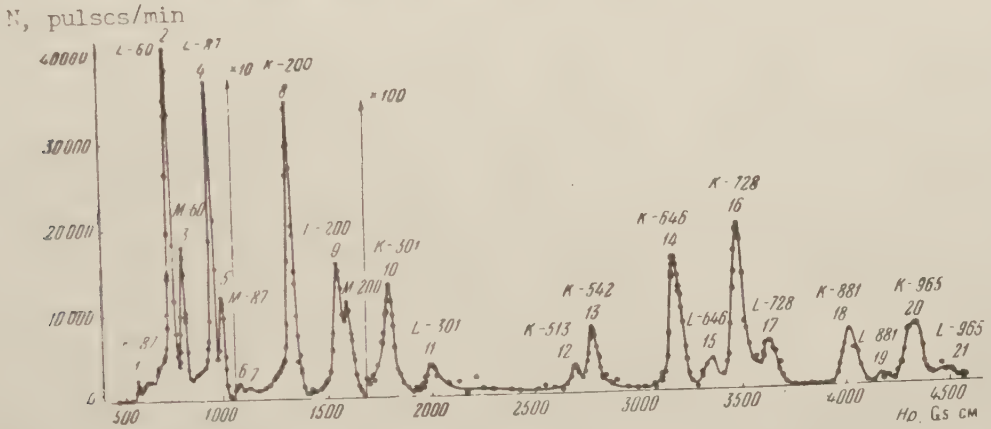

Fig.1. Conversion electron spectrum of Ho^{160} (erbium fraction).

The decay periods of the lines listed in Table 1 lie between the limits of 25 and 30 hours. The closeness of these values gives reason to assume that all these lines belong to the same isotope. The mean period is 28 ± 2 hours. Comparison with the data in the literature[1] indicates that the observed activity is probably due to Er^{160} (according to the data in the literature T = 30 hours).

Nervik & Seaborg[2] and Gorodinskii, Murin et al[3] have shown that in the decay of Er^{160} the isotope Ho^{160} is formed in the ground (22 min) and isomeric (5 hour) states. The energy of the isomeric transition is 60 kev (Mihelich et al[4]). There is no evidence of decay of Er^{160} to other states of Ho^{160}. The 5-hour isotope Ho^{160} emits γ-rays of energies 87, 194, 650, 730, 890 and 970 kev according to Nervik & Seaborg[2] or 90, 205, 290, 500-510, 650, 710 and 900 kev according to Gorodinskii, Murin et al[3].

The fact that these lines are attributable to the 5-hour Ho^{160} isomer is proved by observation of their increasing intensity in the erbium fraction[2] and decay with a period of 5 hours in the holmium fraction[2,3]. Whether these

Table 1

Conversion electrons from Ho^{160} (erbium fraction)

No.	Hρ, gauss.cm	Electron energy, kev	Identification	Intensity	$\frac{K}{L+M}$
1	615	32±1,0	*K*-87	—	—
2	780	51,0±0,5	*L*-60	1700±200	—
3	841	58,8±0,5	*M*-60	770±100	
4	981	78,6±0,5	*L*-87	1200±100	
5	1024	85,1±0,5	*M*-87	420±10	—
6	1108	99±1	—	3,6±0,4	—
7	1176	110±3	—	2,0±0,7	—
8	1368	143±1	*K*-197	100	1,25
9	1610	191,8±2	*L* + *M*-197	80±10	
10	1862	246±1	*K*-300	5,4±0,4	2,34
11	2080	295±3	*L* + *M*-300	2,3±0,6	
12	2744	457±5	*K*-511	1,0±0,3	—
13	2857	486±3	*K*-540	3,1±0,3	—
14	3256	591±3	*K*-645	5,6±0,4	4,0
15	3434	638±5	*L* + *M*-645	1,4±0,3	
16	3561	672±5	*K*-726	7,8±4	3,0
17	3752	724±5	*L* + *M*-726	2,6±0,5	
18	4221	826±5	*K*-880	3,8±0,2	6,3
19	4298	875±10	*L* + *M*-880	0,6±0,2	
20	4420	909±5	*K* + 963	4,0±0,2	4,0
21	4588	956±5	*L* + *M*-963	1,0±0,3	

γ-radiations are emitted directly in capture of electrons by the 5-hour Ho^{160} or after the $Ho^{160*} \rightarrow Ho^{160}$ isomeric transition is not known.

Inasmuch as the measurements were begun 24 hours after separation of the Er, it must be assumed that both the Ho^{160} isomers in the source were in equilibrium with Er^{160}. Without further experimentation one cannot determine whether the lines listed in Table 1 are associated only with the 5-hour or with both Ho^{160} isomers.

After the activity of the Er^{160} + Ho^{160} mixture had died out, there was observed a weak conversion electron spectrum of an activity having a period of about 12 days (counting rate at the maximum about 300 pulses/min). This spectrum consisted of seven electron lines. Four of them can be attributed to γ-transitions with energies of 58.3 ± 0.5 and 207.4 ± 1 kev. We found K/(L + M) = 0.53 for the 207.4 kev transition. These data indicate that the source contained a small amount of Tm^{167}. The thulium fraction from proton bombardment tantalum was the subject of a separate investigation[5]. Comparing our Tm^{167} lines with the corresponding lines observed in the thulium fraction, we deduce that our erbium fraction contained about 4.5% Tm. In addition there were present in our source Tm^{165} (29 hours), Tm^{166} (7.7 hours), and Tm^{168} (85 days). Assuming that the ratios of the activities of these isotopes in our sample were the same as in the thulium fraction, we made the appropriate corrections in our results on the basis of the data of Ref.5.

In the spectrum of the "residue" there were also discernible three weak electron lines with E_e = 66.3 ± 1, 72 ± 2 and 141 ± 3 kev. Their half life was of the order of 10 days. So far these lines have not been identified.

II

The holmium fraction was investigated by means of a two-lens spectrometer. The film over the counter window passed > 2 kev electrons. The activity was applied in the form of a thin layer on a lightly aluminized collodion film; the diameter of the active spot was 5 mm.

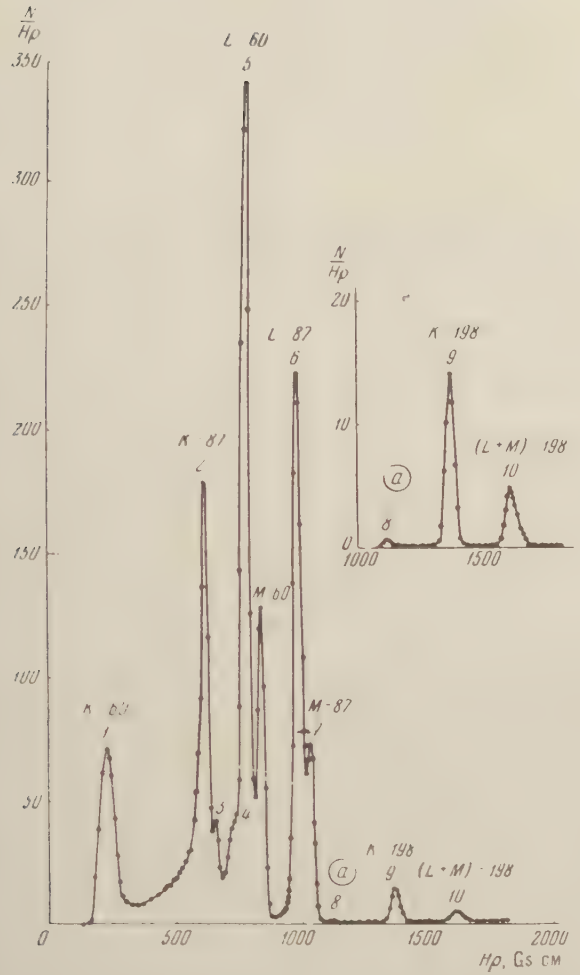

Fig.2. Conversion electron spectrum of Ho^{160} in the interval from 2 to 240 kev (pure Ho^{160}).

Actually two samples were investigated. In the first, in addition to Ho^{160}, there were present an admixture of Er^{160} which converted to the same Ho^{160}; consequently, the decay curves were complicated. The second source was repurified: first the erbium fraction was separated out and then 25 hours later the holmium was separated from it. This source proved to be pure Ho^{160}: the intensity of all the lines fell off with a period of 5.3 ± 0.2 hours.

With this source we carried out four series of measurements in the energy range from 2 to 200 kev. The general appearance of the electron spectrum observed is shown in Fig.2. The detected lines with their energies and identifications are listed in Table 2.

According to our identification, the 32, 79.5 and 86 kev conversion lines are associated with the 87 kev γ-transition, while the 4.8, 51.5 and 59 kev electron lines are the K, L and M conversion electron lines of the 60 kev γ-transition.

We could not observe the activity of the short-lived isotopes Ho^{164} and Ho^{161} inasmuch as the measurements on both samples were started three days after the end of irradiation of the tantalum targets. We did not detect the long-lived isotopes Ho^{163} and Ho^{162} in the measurements with the first sample (holmium fraction) although one cannot positively assert that they were absent inasmuch as in the series of measurements obtained 25-30 days after separation of the fraction there were observed weak electron lines with energies of 5.5, 34, 39, 50, 70, 100, 118, 141, 153 and 205 kev; these have not been identified so far.

Table 2

Conversion and Auger electrons from Ho^{160} (pure Ho^{160} source)

No.	Hρ, gauss.cm	electron energy, kev	Tentative identification	Relative intensity
1	233	4,8±0,2	K-60; $L-XY$	780±50
2	618	32,5±0,5	K-87	1000±50
3	660	37	$K-LL$	
4	720	44	$K-LM$	
5	784	51,5±0,5	L-60	2200±100
6	842	58,9±0,5	M-60	750±50
7	984	79,0±0,5	L-87	1400±100
8	1030	86,0±0,5	M-87	500±30
9	1118	100±1	Not identified "a"	5±1
10	1367	141±1	K-198	100
11	1615	192±4	$L-M$-198	5±1

We desire to thank the personnel of the Laboratory of Nuclear Problems of the Joint Institute for Nuclear Research for irradiating the tantalum and K.Ia.Gromov for organizational help as well as graduate students N.Babenko, A.Bogdanov and A.Iashuk who participated in the measurements.

"A.A.Zhdanov" Leningrad State University

References

1. J.M.Hollander, I.Perlman & G.T.Seaborg, Table of Isotopes, Revs.of Mod. Phys., 25, 469 (1953). (Cited in Russian trans., M.1956.)

2. W.E.Nervik & G.T.Seaborg, Phys.Rev., 97, 1092 (1955).

3. G.M.Gorodinskii, A.N.Murin, V.N.Pokrovskii & B.K.Preobrazhenskii, Present issue of the Bulletin, p.1005.

4. J.W.Mihelich, B.Hermatz, T.H.Handley & J.S.Pinajcra, Bull.Am.Phys.Soc., 1, 330 (1956).

5. K.Ia.Gromov, B.S.Dzhelepov & B.K.Prebrazhenskii, Present issue of the Bulletin, p. 920.

GAMMA-RADIATION FROM $Eu^{152,154}$

- B.S.Dzhelepov, N.N.Zhukovskii, V.G.Nedovesov & G.E.Shchukin

The decay of the long-lived isotopes Eu^{152} and Eu^{154} obtained by prolonged irradiation of europium with thermal neutrons has been investigated by many authors[1-44]. The γ-radiation from Eu^{152} and Eu^{154} was investigated in our laboratory in 1954 on the Elotron[37], a γ-spectrometer with improved focusing, utilizing recoil electrons. In view of the complex character of the γ-spectrum and the particular interest presented by the Eu^{152} nucleus, in 1956 we carried out a repeat investigation of the γ-spectrum of the $Eu^{152,154}$ mixture by means of the Elotron operated under new improved conditions.

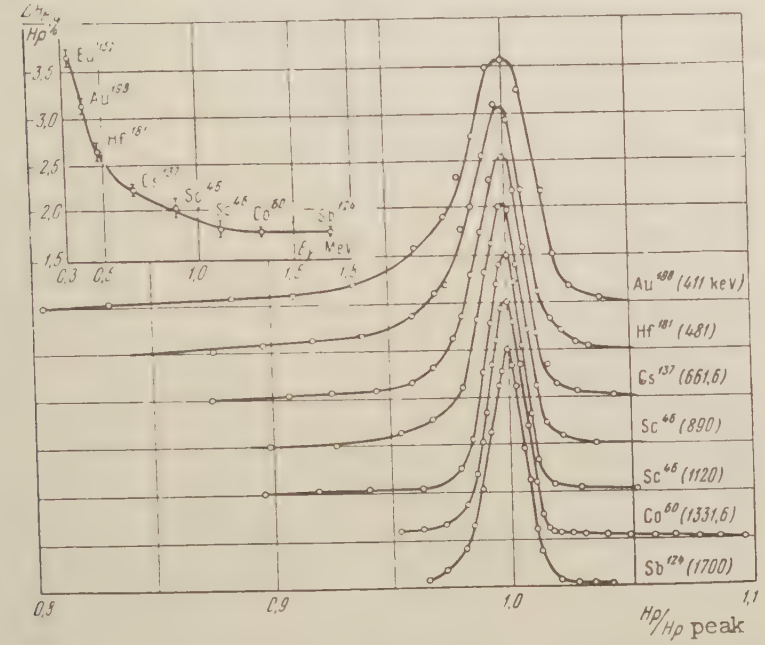

Fig.1. Experimental calibration γ-lines obtained on the Elotron. The lines are normalized to the same height and shifted vertically for clarity. Insert - energy dependence of the relative line half-width.

The measurements were carried out under conditions close to those realized in the investigation of the γ-spectrum of Sb^{124} and described in Ref.45. However, since the presence of gas in the instrument produced an appreciable broadening of the γ-lines, particularly in the region below 1 Mev, the instrument was converted to a separate vacuum regime: the instrument chamber was under continuous evacuation, while the counters were filled with a 60% argon plus 40% methane mixture at a pressure of 10 cm Hg. This resulted in an appreciable improvement of the resolution of the instrument; the transmission factor was also increased somewhat. Under the new conditions the line half-width in the energy region above 1 Mev is 1.7-1.8%, whereas under equal operating conditions but with gas present in the instrument chamber the line half-width was 2.5-2.7%. An even greater improvement was obtained in the region of low energies: thus the half-width of the 411.8 kev γ-line of Au^{198} was reduced from 6.5 to 3.3%. Conversion to the new improved operating regime required new calibration of the spectrometer in energy and new determinations of the experimental shape of the lines and the spectral sensitivity. The line shape and energy calibration were obtained by investigating the well-known single γ-lines of Au^{198} (411.8 kev), Hf^{181} (481 kev), Cs^{137}

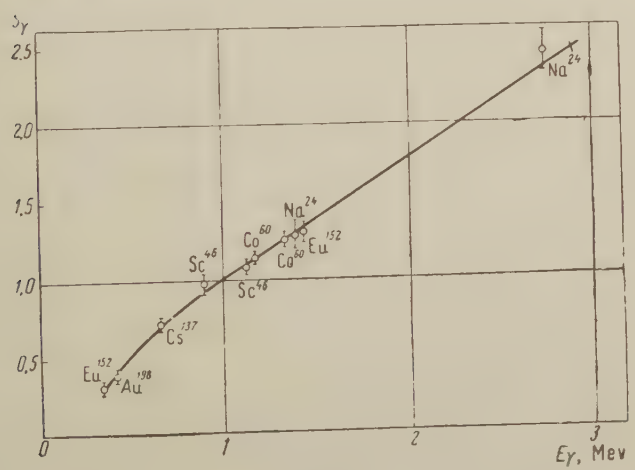

Fig.2. Experimental spectral sensitivity curve for the Elotron.

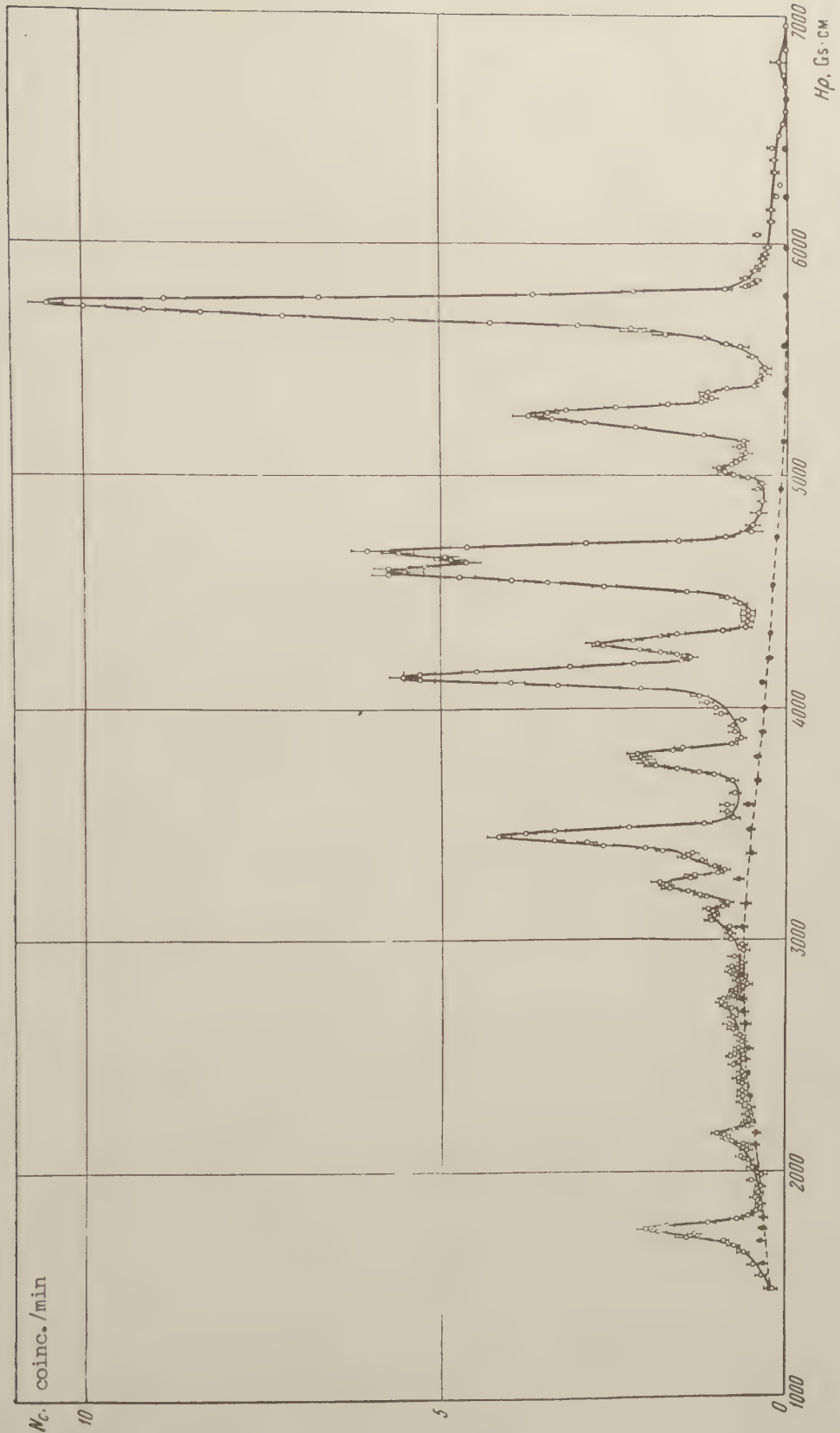

Fig. 3. Experimental γ-spectrum of $Eu^{152,154}$. Solid dots - background.

(661.6 kev), Sc^{46} (890 and 1120 kev), Co^{60} (1171.5 and 1331.6 kev) and Sb^{124} (603 and 1700 kev). These lines, normalized to arbitrary coordinates, are shown in Fig.1.

The spectral sensitivity curve for the instrument, shown in Fig.2, was plotted on the basis of the calorimetric measurements of the activity of the γ-emitters Eu^{198}, Cs^{137} and Co^{60} carried out by E.A.Khol'nov in the VNIIMe (All-Union Scientific Research Institute of Metrology), the data on the relative intensities of the 344 and 1411 kev γ-lines of Eu^{152} obtained on the Ritron by Iu.V.Khol'nov and his co-workers and the results of a special investigation of the 1580 and 2740 kev cascade lines of Na^{24}. We also show in the figure the two points obtained for Sc^{46} which is known to have two γ-lines (890 and 1120 kev) of approximately equal intensity. The uncertainties indicated in the figure include the uncertainties of the calorimetric data as well as the statistical errors in recording the γ-lines.

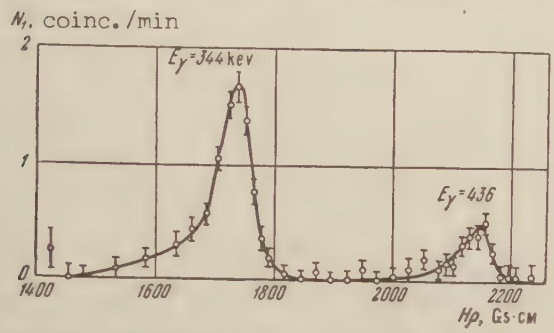

Fig.4. Resolution of the γ-spectrum of $Eu^{152,154}$ in the Hρ = 1400-2200 gauss-cm region. N_1 - number of coincidences per minute (background subtracted).

The experimental γ-spectrum obtained for $Eu^{152,154}$ is shown in Fig.3. The elimination of gas from the instrument chamber appreciably reduced the background, i.e., the number of coincidences with the target (radiator) withdrawn from the beam. At energies above 1.2 Mev the background is virtually nil; the count amounts to less than 1 coincidence per hour.

The γ-spectrum after subtraction of the background was resolved into its individual components taking into account the energy dependence of the line shape (Fig.1). The results of such resolution for different intervals of the spectrum are shown in Figs.4,5, 6 & 7. The integral curve (sum of the

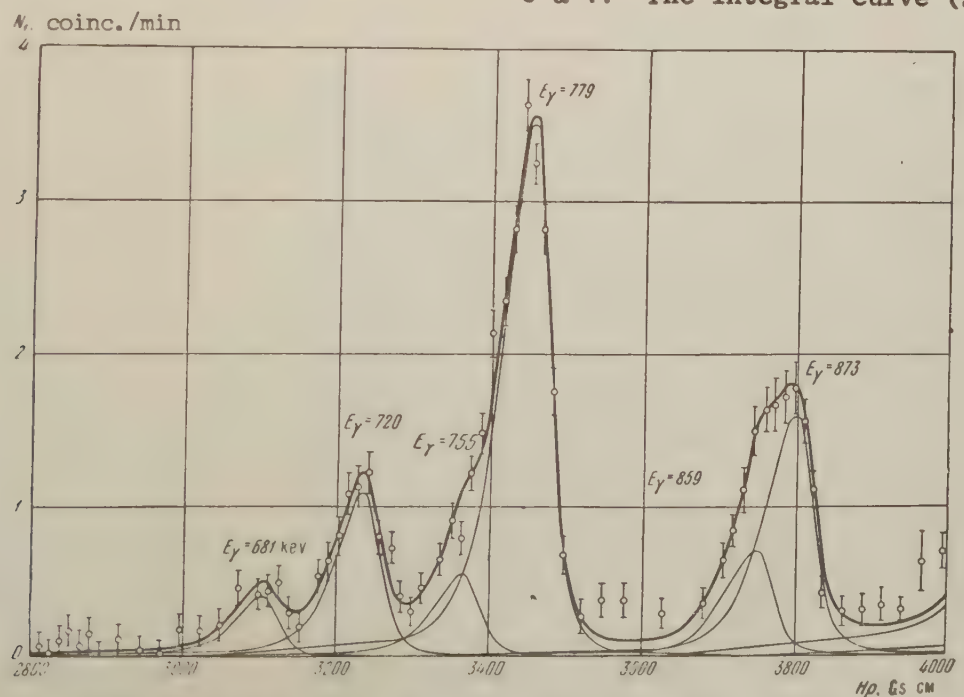

Fig.5. Same as Fig.4 but for the Hρ = 2800-4000 gauss-cm region.

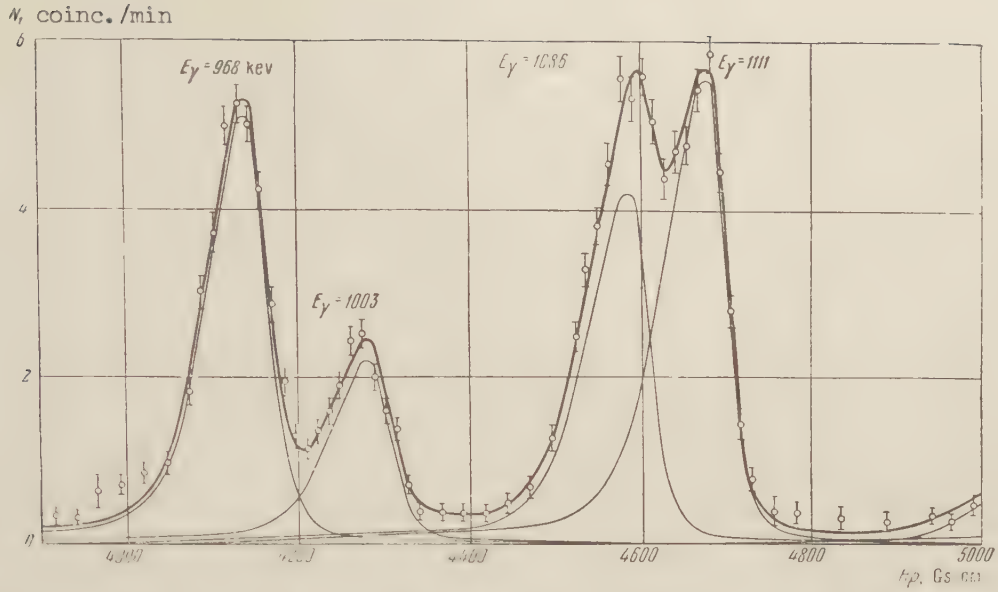

Fig.6. Same as Fig.4 but for the Hρ = 4000-5000 gauss-cm region.

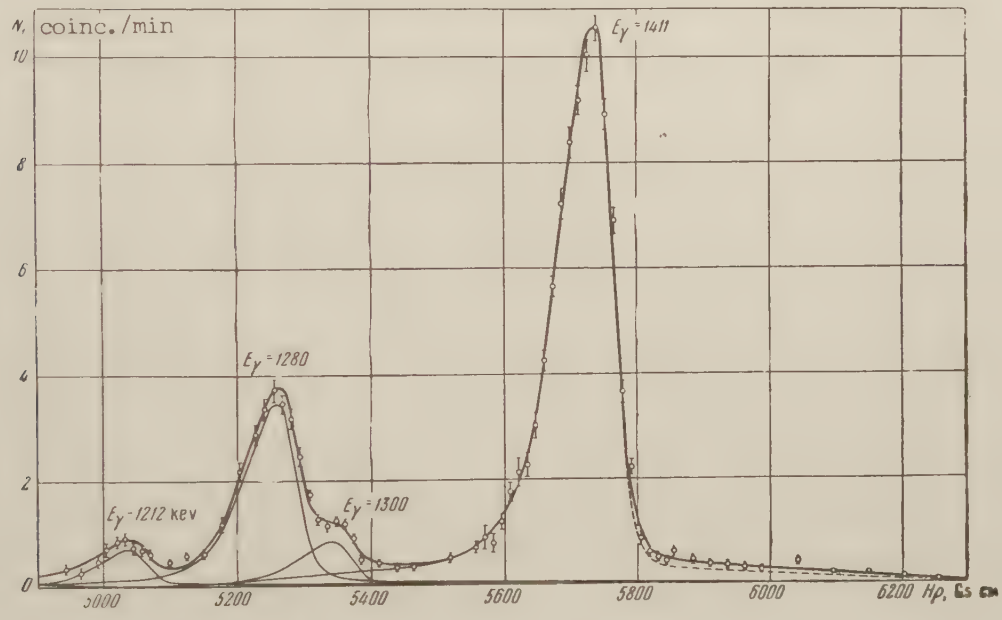

Fig.7. Same as Fig.4 but for the Hρ = 5000-6200 gauss-cm region.

individual components indicated by the light lines) agree within the limits of the statistics with the experimental points. Exceptions are the two Hρ intervals 1) 1800 to 3200 gauss-cm (Fig.3) and 2) 3600 to 4000 gauss-cm (Fig.5). In the first interval ($h\nu \approx$ 350-700 kev) there presumably exist a number of weak γ-lines[25]; however, we were able to identify only three lines with energies 436, 583 and 681 kev. In the second interval there may also exist some weak γ-rays.

The high-energy tail of the 1411 kev γ-line is interesting. As may be seen in Fig.7 the experimental points fall above tha apparatus line, indicated by the dash line. It may be assumed that in this region (1.4-1.5 Mev) there is present a γ-line, although it is impossible to evaluate its energy and

Table 1

Energies and relative intensities of the γ-lines of the long-lived Eu^{152} and Eu^{154} activity obtained by different investigators

Dzhelepov et al[37]		Nathan[43]		Grodzins[42]		Our data	
hν, kev	Energy, kev	hν, kev	Relative intensity	hν, kev	Energy, kev	hν, kev	Relative intensity
341	86	344	111	344	108	344	118±7
				408	10		
427	14	420	4	442	20	436	23±6
593	7			550	~2	583*	8±6
				690	1,2	681*	8±2
717	14			720	4	720*	21±2
						755*	10±4
779	43	775	44	778	36	779	61±4
		860	17	866	24	862	11±2
871	25					873*	24±2
958	73	965	67	963	56	968	61±4
						1003*	29±2
		1090	56	1085	52	1086	50±7
				1100	6	1111	63±7
1106	101			1110	48		
		1200	22	1210	8	1212	7±2
1281	41	1280	13	1240	8	1280*	35±3
						1300	8±3
1409	100	1415	100	1410	100	1411	100

*Lines belonging to Eu^{154}

relative intensity. The γ-line energies and intensities obtained by us are shown in Table 1 together with the results reported by other authors.

The difference between the intensity values in the low energy region obtained by us in the present investigation and in the earlier study[37] is explained by inaccuracies of evaluating the spectral sensitivity of the Elotron under the old operating conditions.

The investigations of Grodzins[40] and Nathan & Waggoner[43] were carried out by means of scintillation spectrometers. The latter authors evaluate the accuracy of their relative intensity determinations as ~30%. Our data are appreciably more accurate.

Grodzins[42] work was carried out with a source enriched with Eu^{152}. Our source contained a higher proportion of Eu^{154} and, consequently, we obtained 583, 581, 720, 755, 873, 1003 and 1280 kev γ-lines of relatively higher intensities than Grodzins. A number of recent investigations [40-43,47,48] and the work of Stephens[44] carried out with an Eu^{154} source obtained by fission have helped clear up a number of obscurities in the decay of Eu^{152} and Eu^{154}; it is, however, still impossible to construct the definitive decay scheme for these isotopes.

Our data on the relative intensities of the γ-lines taken together with the data of Nathan & Waggoner[43] on the relative intensities of the K conversion lines make it possible to determine the multipole orders of the γ-transitions. It is known that the 344 kev γ-transition is associated with the deexcitation of the excited state of Gd^{152} and is of the E2 type. According to Sliv & Band[46] the conversion coefficient for this transition $\alpha_K = 30.9 \cdot 10^{-3}$.

The results of our multipolarity determinations are shown in Table 2.

We desire to thank E.A.Khol'nov for the calorimetric measurements, Iu.V. Khol'nov for the data on the relative intensities of the 344 and 1411 kev γ-lines of Eu^{152} and V.G.Chumin and Iu.G.Kondakov for help in carrying out the measurements.

Table 2

Energy, kev	Relative γ-line intensity	Ident. of transition *	Relat. intensity K-line **	Assumed exp. value $\alpha_K \cdot 10^3$	Theoretical conversion coefficient, $\alpha_K \cdot 10^3$ (Ref. 46)					Probable multipole order
					E1	*E2*	*E3*	*M1*	*M2*	
344	100	Gd^{152}	100,0	30,9	–	30,9	–	–	–	*E2*
435	20	Sm^{152}	2,7	4,4	4,90	14,5	38,8	25,1	81,3	*E1*
583	6,8	Gd^{154}	1,4	6,2	2,76	7,59	18,2	14,2	42,6	*E2*
681	7,1	Sm^{154}	5,1	22,5	1,86	4,68	10,9	7,95	22,9	*M2*
755	8,4	Gd^{154}	1,0	3,9	1,58	4,07	9,33	7,58	20,0	*E2*
779	52	Gd^{152}	2,4	1,4	1,51	3,89	8,70	7,08	18,2	*E1*
862	9,2	Sm^{152}	2,3	7,6	1,15	2,76	6,04	4,68	11,7	*E3 – M2*
968	51	Sm^{152}	3,2	1,9	0,93	2,24	4,68	3,72	9,34	*E2*
1003	24	Gd^{154}	1,6	2,0	0,96	2,34	4,68	3,80	9,34	*(E2, M1?)*
1086	42	Sm^{152}	1,1	0,81	0,76	1,78	3,72	2,88	7,09	*E1*
1111	53	Sm^{152}	2,2	1,3	0,73	1,70	3,55	2,70	6,60	*(E2?)*
1212	6,2	Sm^{152}	<0,3	1,5	0,63	1,48	2,95	2,24	5,37	*(E2?)*
1280	29	Gd^{154}	<0,3	0,32	0,53	1,48	2,70	2,22	5,25	*(E1?)*
1411	84	Sm^{152}	1,4	0,51	0,49	1,07	2,14	1,55	3,63	*E1*

*Refs. 40–44, 47 & 48.
**Ref. 43.

"V.G.Khlopin" Radium Institute of the
Academy of Sciences of the USSR

References

1. S.Sugden, Nature, 135, 469 (1935).
2. J.Marsh & S.Sugden, Nature, 136, 102 (1935).
3. G.Hevesy & H.Levi, Nature, 136, 103 (1935).
4. G.Hevesy & H.Levi, Nature, 137, 185 (1936).
5. A.Alichanian, A.Alichanov & B.Dzelepov, Physik Zeits, 11, 204 (1937).
6. H.Scheinberger, Anz.Akad.Wiss.Wien, 75, 108 (1938).Mat.-naturwiss, Klasse.
7. M.Pool & L.Quill, Phys.Rev., 53, 437 (1938).
8. J.Richardson, Phys.Rev., 53, 942 (1938).
9. J.Richardson, Phys.Rev., 55, 609 (1939).
10. A.Tyler, Phys.Rev., 55, 1136 (1939); Phys.Rev., 56, 125 (1939).
11. K.Fajans & D.Stewart, Phys.Rev., 56, 625 (1939).
12. K.Fajans & A.Voigt, Phys.Rev., 60, 533 (1941).
13. R.Hayden & M.Inghram, Phys.Rev., 70,89 (1946).
14. W.Bothe, ZS Naturf., 1, 179 (1946).
15. M.Inghram & R.Hayden, Phys.Rev., 71, 130 (1947).
16. M.Wiedenbeck & K.Chu, Phys.Rev., 72, 1164 (1947).
17. J.Cork, R.Shreffler & C.Fowler, Phys.Rev., 72, 1209 (1947).
18. J.Cork, R.Shreffler & C.Fowler, Phys.Rev., 73, 78 (1948).
19. N.Krisberg & M.Pool, Phys.Rev., 74, 44 (1948).
20. J.Cork, R.Shreffler & C.Folwer, Phys.Rev., 74, 240 (1948).
21. F.Shull, Phys.Rev., 74, 917 (1948).
22. R.Hayden, J.Reinolds & M.Inghram, Phys.Rev., 75, 1500 (1949).
23. J.Hill & L.Shepherd, Proc.Phys.Soc., Lond., 63, 126, 960 (1950).
24. C.Fowler & R.Shreffler, Rev.Sci.Instr., 21, 740 (1950).

25. J.Cork, H.Keller, W.Rutledge & A.Stoddard, Phys.Rev., 77, 848 (1950).
26. L.Shavtvalov, Zhur.eksp.i teor.fiz., 21, 1123, (1951).
27. W.Wright & M.Deutsch, Phys.Rev., 82, 272 (1951).
28. H.Keller & J.Cork, Phys.Rev., 84, 1079 (1951).
29. R.Katz & M.Lee, Phys.Rev., 85, 1038 (1952).
30. L.Shavtvalov, Zhur.eksp.i teor.fiz., 23, 611 (1952).
31. D.Karraker, R.Hayden & M.Inghram, Phys.Rev., 87, 901 (1952).
32. E.Lockett & R.Thomas, Nucleonics, 11, 3, 14 (1953).
33. J.Kastner, Can.J.Phys., 31, 169 (1953).
34. M.Lee & R.Katz, Phys.Rev., 93, 155 (1954).
35. E.Church & M.Goldhaber, Phys.Rev., 95, 626 (1954).
36. R.Slattery, D.Lu & M.Wiedenbeck, Phys.Rev., 96, 465 (1954).
37. B.Dzhelepov, N.Zhukovskii & V.Nedovesov, Izv.AN SSSR, Ser.fiz., 19, 296 (1955). (Trans.in Bulletin, 19, No.3, 269.)
38. A.Sunyar, Phys.Rev., 98, 653 (1956).
39. B.Andersson, Proc.Phys.Soc., London, 69A, 415 (1956).
40. L.Grodzins, Bul.Am.Phys.Soc., 1, 4, 163 (1956).
41. H.Kendall, & L.Grodzins, Bul.Am.Phys.Soc., 1, 4, 164 (1956).
42. L.Grodzins & H.Kendall, Nucl.Sci.Abstr., 10, 12B, 253 (1956).
43. O.Nathan & M.Waggoner, Nuclear Phys., 2, 548 (1956/57).
44. F.Stephens, Thesis (1955), UCRL - 2970.
45. B.Dzhelepov, N.Zhukovskii, V.Nedovesov, I.Uchevatkii & V.Chumin, Izv. AN SSSR, Ser.fiz., 20, 925 (1956). (Trans. Bulletin, 20, No.8, 838.); Nuclear Phys., 2, 1, 408 (1956/57).
46. L.Sliv & N.Band, Tablitsy koeffitsientov vnutrennei konversee γ-izlucheniia (Tables of internal conversion coefficients), M., 1956.
47. J.Cork, M.Price, R.Helmer & D.Sarason, Bull.Am.Phys.Soc. II, 2, 16; E3 (1957).
48. B.Bobykin & K.Novik, Doklady AN SSSR, 115, 2 (1957).

GAMMA-RADIATION FROM Ag^{110}

- B.S.Dzhelepov, N.N.Zhukovskii & Iu.G.Kondakov

The decay of Ag^{110} has been studied by many investigators.[1-45] The principal data regarding the decay scheme, available to date, are shown in Fig.1.

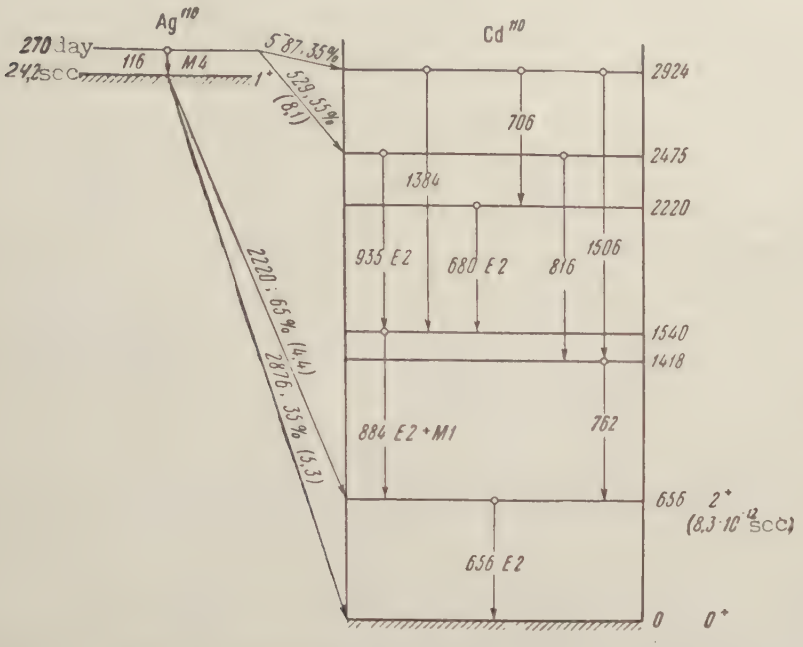

Fig.1. Decay scheme for Ag^{110} proposed by Siegbahn[24] and refined on the basis of subsequent investigations. The multipole orders have been determined only on the basis of the K/L ratios.

In the present investigation we determined the relative intensities of 12 γ-lines of Ag^{110}. This made it possible to check the intensity balance for different levels and to determine the multipole order of a number of transitions.

We investigated the γ-radiation of Ag^{110} by means of the Elotron[46,47], a γ-spectrometer with improved focusing utilizing recoil electrons. The measurements were carried out under the same conditions as the investigation of the γ-spectrum of $Eu^{152,154}$ (see preceding article). The source was a neutron-activated silver strip weighing 7.9 g. At the beginning of measurement the activity of the source was ~700 millicuries. The measurements were carried out 3 months after preparation of the source.

The general appearance of the observed spectrum of Ag^{110} is shown in Fig.2.

Relative intensities of the Ag^{110} γ-lines — Table 1

Most probable E_γ values	Our E_γ values	Relative intensities: Ref.15 (photoelectr.)	Ref.24 (photoelectr.)	Ref.32 (recoil electr.)	Ref.45 (scint. counter)	Our data
656±1	656±2	100	100	100	100	100
680±2	681±10	—	—	—	-	13±2
705±2	706±10	—	—	—	-	18±2
741±3	743±6	—	—	—	-	6±2
762±3	764±5	—	—	—	-	23±2
816±3	818±5	—	—	—	7	9±1
884±3	884±4	107	81	103	100	75±4
935±3	936±5		31		55	32±2
1384±4	1384±4	—	33	26	30	28±2
1480±5	1481±5	20	—	22	-	6±1
1506±4	1508±4		17			15±1
—	1560±10	—	—	—	—	1,3±0,2

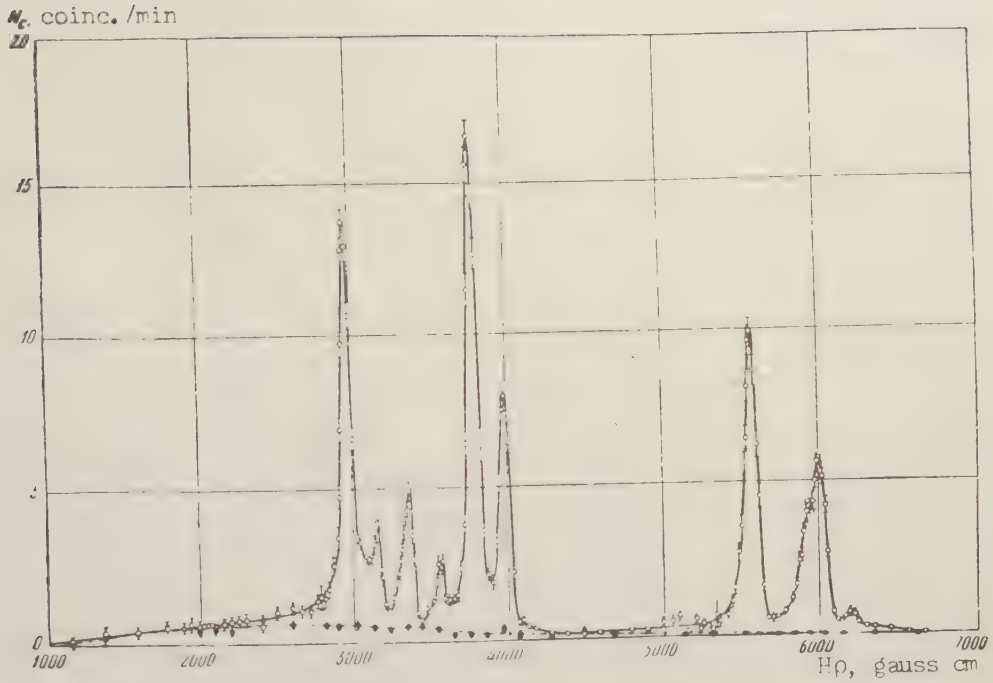

Fig.2. Experimental γ-spectrum of Ag^{110}. Solid points - background.

The circle points indicate the number of coincidences per minute when the target was in the γ-ray beam; the solid dots give the background, i.e., the count with the target (radiator) withdrawn from the beam. After subtraction of the background the spectrum was resolved into components taking into account the energy dependence of the apparatus line shape. The results of such resolution for different regions of the spectrum are shown in Figs.3,4 & 5. In the figures the light lines indicate the components; the heavy lines the integral curve, i.e., the sum of the components. The indicated energy values are in kev according to our calibration. As noted above 12 γ-lines were observed in the spectrum. The 1560 kev line has been detected for the first time in this investigation, but we cannot prove that it belongs to Ag^{110} inasmuch as no radiochemical analysis of the source was performed. Careful investigation of the hard part of the γ-spectrum three months after the first measurements showed, however, that the intensity of this line fell off with a period of 270 days. The other γ-lines have been observed earlier. Our results, together with the results of other authors, are listed in Table 1. The uncertainty in our evaluation of the relative intensities is determined by the uncertainty in plotting the spectral sensitivity curve (~5%), the statistical errors of measurement and the inaccuracies in resolving the spectrum into components.

A check of the γ-ray intensity balances for the excited levels of Cd^{110} substantiates the decay scheme proposed by Siegbahn[24] for the most intense γ-lines. The 1560 kev γ-line discovered by us can be attributed to a γ-transition between the 2220 and 656 kev levels.

The sum of the energies of the equal intensity 741 and 1480 kev γ-rays is close to the excitation energy of the 2220 kev level of Cd^{110}. If these two γ-rays are in cascade, the corresponding transitions can be logically inserted into the decay scheme between the 2220 kev excited level and the ground level

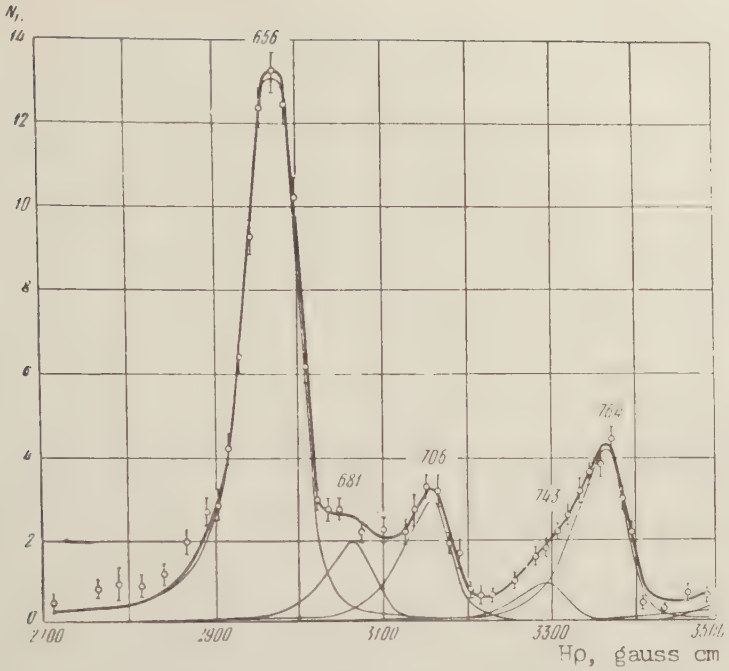

Fig.3. Resolution of the γ-spectrum of Ag^{110} in the $H\rho$ = 2700 to 3500 gauss-cm interval. N_1 - number of coincidences (background subtracted).

of Cd^{110}, postulating the existence of an excited 1480 kev level in Cd^{110}, inasmuch as the existence of a 741 kev level would be in conflict with the regularities characterizing the distribution of levels in even-odd nuclei predicted by the unified nuclear model.

Utilizing our relative intensity values for the γ-transitions and the values of the relative intensities of the corresponding K conversion lines given in Ref.31, one can determine the multipole order of the trans-

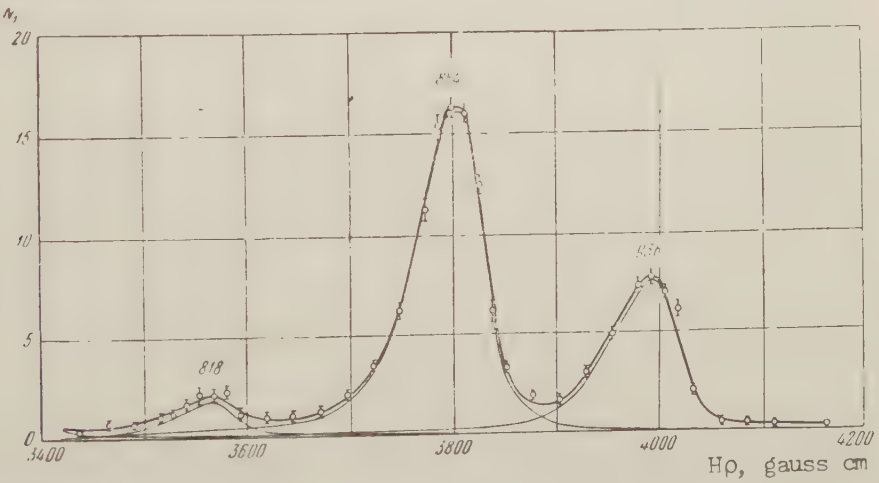

Fig.4. Same as Fig.3 but for the $H\rho$ = 3400 to 4200 gauss-cm region.

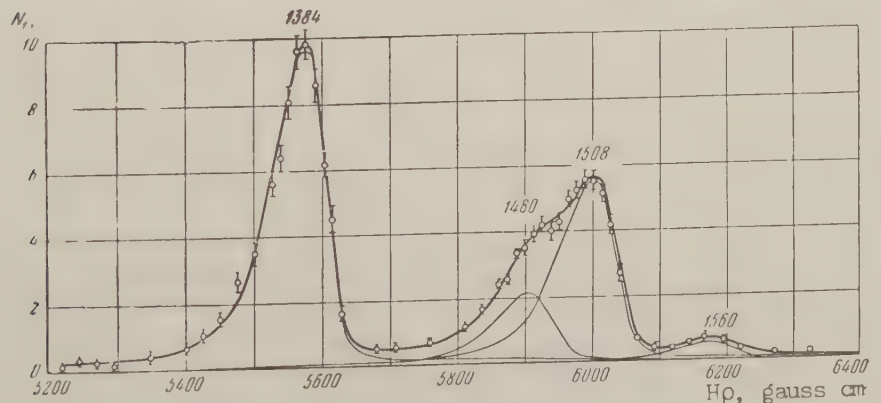

Fig.5. Same as Fig.3 but for the $H\rho$ = 5200 to 6400 gauss-cm region.

itions, provided the multipole order for some one of them is known. According to a number of investigators[24,31,44,45] the 656 kev transition between the first excited level and the ground state of Cd^{110} is of the E2 type. The K shell conversion coefficient for this transition according to Sliv and Band[49] is $2.76 \cdot 10^{-3}$, which is in good agreement with the experimental value[24,45]. Assuming that this transition is pure E2, we determined the probable multipole orders of the different transitions. The results are listed in Table 2.

Probable type of γ-transitions — Table 2

γ-transition energy	Relative γ-line intensity	Relative K conversion line intensity (Ref. 31)	Experimental conversion coefficient $\alpha_K \cdot 10^3$	Theoretical values of $\alpha_K \cdot 10^3$			Probable multipole order
				E1	*E2*	*M1*	
656	100	100	2,76	1,00	2,76	3,02	*E2*
680	13	8	1,7	0,935	2,51	2,76	?
705	18	16	2,45	0,870	2,34	2,51	*M1*
741	6	3	1,38	0,776	2,09	2,39	(*E2*)
762	23	16	1,92	0,740	1,90	2,14	*E2*
816	9	3,7	1,13	0,630	1,67	1,82	(*E2*)
884	75	32	1,18	0,537	1,38	1,55	*E2*
935	32	13	1,10	0,479	1,20	1,32	*E2*
1384	28	6,5	0,651	0,234	0,525	0,537	*E2, M1*
1480	6	0,8	0,367	0,209	0,457	0,490	(*E2*)
1506	15	2,5	0,460	0,199	0,436	0,478	*E2, M1*

The relative intensities of the weaker conversion lines are now known with sufficient accuracy[31] to permit of unambiguous determination of the multipole orders of the corresponding γ-transitions.

"V.G.Khlopin" Radium Institute of the
Academy of Sciences of the USSR

References

1. A.Alichanow, A.Alichanian & B.Dzelepov, Nature, 136, 257 (1935).
2. E.Gartner, J.Turin & J.Gray, Phys.Rev., 49, 793 (1936).
3. J.Krays & J.Cork, Phys.Rev., 51, 383 (1937).
4. J.Jackson & H.Kuhn, Proc.Roy.Soc., 158A, 372 (1937).
5. K.Alekseeva, Doklady AN SSSR, 18, 553 (1938).
6. M.Pool, Phys.Rev., 53, 116 (1938).
7. H.Raddeman & F.Strakman, Naturwiss, 26, 187 (1938).
8. A.Mitchell, Phys.Rev., 53, 269 (1938).
9. J.Livingood & G.Seaborg, Phys.Rev., 54, 88 (1938).
10. N.Godzinskii, I.Gol'tsvan & A.Danilenko, Zhur.eksp.i teor.fiz., 9, 516 (1939).
11. R.Krishman, Proc.Cambr.Phyl.Soc., 36, 500 (1940).
12. M.Deutsch, A.Roberts & L.Elliott, Phys.Rev., 61, 389 (1942).
13. L.Hurt & M.Pool, Phys.Rev., 65, 351 (1944).
14. O.Hirzel & H.Waffler, Helv.Phys.Acta, 19, 214 (1946).
15. W.Rall & R.Wilkinson, Phys.Rev., 71, 321 (1947).

16. M.Deutsch, Phys.Rev., 72, 527 (1947).
17. J.Cork, R.Shreffler & C.Fowler, Phys.Rev., 74, 1657 (1948).
18. K.Siegbahn, Phys.Rev., 75, 1277 (1949).
19. Yu Fu-Chan, Lin-Cheng & J.Kurbatov, Phys.Rev., 75, 1287 (1949).
20. W.Emmerish & J.Kurbatov, Phys.Rev., 76, 1446 (1949).
21. J.Grum, L.Thompson & M.Pool, Phys.Rev., 76, 184 (1949).
22. W.Eminerish & J.Kurbatov, Phys.Rev., 76, 454 (1949).
23. F.Maienschein & J.Meem, Phys.Rev., 76, 899 (1949).
24. K.Siegbahn, Phys.Rev., 77, 233 (1950).
25. E.Meteosian & M.Goldhober, Phys.Rev., 78, 326 (1950).
26. J.Miskel, Phys.Rev., 79, 403 (1950).
27. R.Wilson, Phys.Rev., 79, 1004 (1950).
28. W.Rutledge, A.Stoddard, C.Brangan, J.LeBlanc & J.Cork, Phys.Rev., 79, 237 (1950).
29. J.Cork, W.Rutledge, C.Bronyon, A.Stoddard, W.Childs & J.LeBlanc, Phys. Rev., 80, 286 (1950).
30. J.Crum & M.Pool, Phys.Rev., 80, 315 (1950).
31. N.Anton'eva, A.Bashilov & B.Dzhelepov, Doklady, AN SSSR, 77, 41 (1951).
32. B.Dzhelepov, N.Zhukovskii & Iu.Khol'nov, Doklady AN SSSR, 77, 597 (1951).
33. V.Shpinel' & N.Forafontov, Zhur.eksp.i teor.fiz., 21, 1376 (1951).
34. W.Mims, H.Halban, Proc.Roy.Soc., 64A, 311 (1951).
35. M.Goodrich, Phys.Rev., 82, 759 (1951).
36. S.Johansson & S.Almquist, Arkiv Fysik, 5, 427 (1952).
37. W.Kelly, Phys.Rev., 85, 101 (1952).
38. T.Azuma, Phys.Rev., 94, 638 (1954).
39. F.Boley, Phys.Rev., 94, 1078 (1954).
40. R.Rohr & K.Borkhoff, Phys.Rev., 98, 1266 (1955).
41. T.Azuma, J.Phys.Soc., Japan, 10, 167 (1955).
42. B.Dzhelepov & I.Iaritsyna, Izv.AN SSSR, Ser.fiz., 20, 343 (1956). (Trans.Bulletin, 20, No.3, 314.)
43. A.Bashilov, Nuclear Physics, 1, 629 (1956).
44. G.Temmer & N.Heydenburg, Phys.Rev., 98, 1308 (1955); 99, 617 (1955).
45. R.Thomas,Jr., W.Whitaker & C.Peakock, Bull.Am.Phys.Soc., 1, 86D3 (1956).
46. N.Zhukovskii, A.Karamian & S.Shestopalova, Izv.AN SSSR, Ser.fiz., 17, 518 (1953).
47. B.Dzhelepov, N.Zhukovskii, V.Nedovesov, I.Uchevatkin & V.Chumin, Izv.AN SSSR, Ser.fiz., 19, 296 (1955). (Trans.Bulletin, 19, No.3, 269.)
48. B.Dzhelepov, N.Zhukovskii, V.Nedovesov & G.Shchukin, Present issue of the Bulletin, p. 968.
49. L.Sliv & N.Band, Tablitsy koeffitsientov vnutrennei konversii γ-izlucheniia (Tables of internal conversion coefficients) M., 1956.

POSITRONS IN THE RADIATION FROM RADIOACTIVE In^{114}

- B.S.Dzhelepov, O.E.Kraft & V.B.Zhinkina

Introduction

Radioactive In^{114} is one of the isotopes in which competing β^+ and β^- decay is possible. This isotope lies between the two stable isobars Cd^{114}_{48} and Sn^{114}_{50} differing by two units as regards charge.

Investigation of cases of β^+—β^- decay is of great interest from the point of viewing of establishing the factors that may influence the degree of forbiddenness in β-transitions. The point is that in all cases of β^+—β^- decay the end isobars are nuclei with even A and Z in which the ground state must have spin 0 and an even wave function. Regardless of the spin and parity of the intermediate nucleus, the changes in these characteristics in the β^+ and β^- decays must be the same. If the probability of transition depends only on the change in spin and parity, as was assumed to be the case until recently, the β^+ and β^--transitions belong in the same category, i.e., must have equal values of the product $f\tau$. Actually the values of $f\tau$ proved to be close but not identical[1].

In a contribution published in 1956, Bohr & Mottelson[2] showed that deformation of the nucleus may affect the probability of β-decay.

In a recent publication, Peker and one of the present authors[1] made an attempt to relate the inequality of $f\tau$ for the two decay branches with different degrees of change in nuclear deformation. Analyzing the dependence of the deformation parameter and the number of nucleons in the filling shell, the authors come to the conclusion that deformation in the case of a transition approaching the nucleus to a state with a closed shell changes less than in a transition taking the nucleus further from the closed shell state. A lower transition probability and, consequently, a higher value of $f\tau$ corresponds to greater changes in the shape of the nucleus. Hence in the case of competing β^+ and β^- decays the magnitude of $f\tau$ must be greater for the transition which takes the nucleus further from the state with the closed shell. Analysis of the experimental data carried out by the authors[1] largely substantiates the deduction.

The isotope In^{114}_{49} is of interest precisely because in its electron decay there is obtained a nucleus with a closed proton shell: Sn^{114}_{50}. Hitherto the competing β^+—β^- decay in In^{114} has not been adequately studied; investigation of this decay was the purpose of the present work.

Survey of the data on the decay of In^{114}

Radioactive In^{114} has two isomers with periods of 50 days and 72 sec. The 50-day isomer converts to the ground state of In^{114} emitting either a 192 kev γ-ray or a conversion electron. The value of $N_e/(N_e + N_\gamma)$ for this transition according to measurements of Boehm & Preiswerk (Ref. 3) is 0.80 ± 0.05.

From its ground state In^{114} transforms by electron decay with a period of 72 sec to the ground state of Sn^{114}_{50}. Measurements of the electron spectrum of In^{114} led Lawson & Cork[4] and Boehm & Preiswerk[3] to the conclusion that the β-spectrum is a simple one and belongs in the category of allowed spectra. The end-point energy of the β-spectrum has been determined with greatest accuracy by Johns et al[5] who give 1.984 ± 0.004 Mev.

In 1956 Johns and his co-workers[6] found that the 1300 kev γ-line, discovered earlier by Maienschein & Meem[7] and having a relative intensity of

$2 \cdot 10^{-3}$ photons per decay, yields β-γ coincidences with the continuous β^- spectrum with an end-point energy 710 ± 50 kev and not with the 556 kev conversion line associated with the K capture branch as was earlier assumed[5].

This result was substantiated by Grodzins & Motz[8], who also detected coincidences between the 1300 kev γ-line and the electron spectrum whose end-point energy they determined as 675 ± 40 kev. The intensity of the 1300 kev γ-line according to these authors is $(9 \pm 1) \cdot 10^{-4}$ photons per decay. Thus it would appear that the β^--spectrum of In^{114} is complicated and consists of two components: a hard one of 1.984 Mev end-point energy and a soft with an end-point energy of about 0.7 Mev, leading to an excited level of Sn^{114}.

In addition to the electron decay branch, In^{114} also has an electron capture branch. It has been established by a number of authors[8-10] that K capture occurs both in the isomeric state of In^{114} and in the ground state. The K capture in the isomeric state, which accounts for 3.5% of the decays, goes to an excited level of Cd^{114} and is accompanied by cascade γ-rays with energies of 0.722 and 0.556 Mev. Electron capture by the ground state of In^{114} occurs in 1.9% of the decays and leads directly to the ground level of Cd^{114}.

In 1949 Boehm & Preiswerk[3], investigating the disintegration of In^{114} by means of a trochoidal analyzer in conjunction with photographic recording, detected a small number of positrons. According to these authors the end-point energy of the positrons is 650 ± 100 kev; the number of positrons per disintegration $\sim 1 \cdot 10^{-4}$. These authors inferred that the positron decay goes to the second excited level of Cd^{114}.

Subsequently, the positron branch in the decay of In^{114} was observed by Johns and his co-workers[5,11]. These authors recorded the positron annihilation radiation by means of anthracene counters connected in coincidence. Inasmuch as In^{114} also emits cascade γ-rays, the authors were forced to measure the coincidences due to the annihilation photons in the presence of a rather strong background. A value of $(4 \pm 1) \cdot 10^{-5}$ is given for the number of positrons per decay in Ref.11. In addition to evaluating the intensity, Johns and his co-workers attempted to determine the end-point energy of the positrons. For this purpose they used a source of indium foil surrounded by an absorber (aluminum). From the variation of the coincidence rate for annihilation photons with the absorber thickness the authors concluded that the end-point energy of the positron spectrum lies between 1 and 1.4 Mev. This result is in conflict with the data of Boehm & Preiswerk[3] who give an end-point energy value 650 ± 100 kev. Inasmuch as the energy difference between the ground states of In^{114} and Cd^{114}, as determined from the threshold of the Cd^{114} (p,n) In^{114} reaction by McGinnis[12] is 2.07 ± 0.2 Mev, Johns et al concluded that the positron decay goes to the ground level of Cd^{114}: $(1.2 \pm 0.2) + 1.022 \approx 2.2 \pm 0.2$ Mev.

At the time we began our investigation of the competing $\beta^+ - \beta^-$ decay of In^{114}, there were no other published data on the positron spectrum of In^{114}. It will be evident from what has been said above that whereas the fact of the existence of positrons had been firmly established there was serious disagreement regarding the end-point energy and intensity of the positron spectrum. Moreover, there was no information at all regarding the shape of the positron spectrum. By the time of the writing of this report, however, there appeared the contribution of Grodzins & Motz[8]; the results of these authors regarding the positron spectrum of In^{114} agree with our results although they were obtained by an entirely different procedure.

Experimental part

We investigated the β-spectrum of In^{114} by means of the magnetic β-spectrometer with triple focusing of the beam, described by Dzhelepov & Kraft[13]. The source was an indium foil having a superficial density of 9 mg/cm^2 irradiated by slow neutrons. The β-particles, emerging from the source at an angle to the plane of the magnet pole pieces, moved along helical trajectories and passed successively through two GM counters, located one above the other and connected in coincidence. The thickness of the films over the counter windows was 0.5 mg/cm^2; the vacuum in the instrument was $5 \cdot 10^{-2}$ mm Hg.

The experimental spectrum of positrons from In^{114} is shown in Fig.1. To measure the background the direct β-particle beam was cut off by a special shutter inserted under the source.

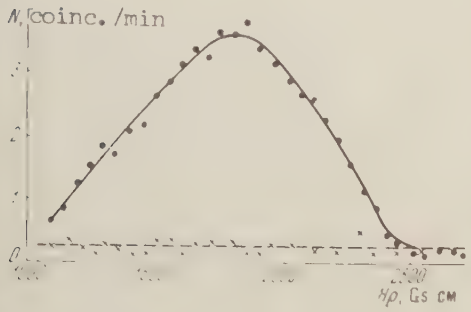

Fig.1. Experimental In^{114} positron spectrum. Dash line - coincidence background.

The "processed" positron spectrum is shown in Fig.2. Here we have taken into account the coincidence background, introduced suitable corrections for absorption in the source and the counter windows and replotted the spectrum to equal energy intervals. As may be seen from Fig.2 the end-point energy of the positron spectrum is ~400 kev.

As was indicated in Ref.13, our instrument distorts the particle spectra in the region of low energy. In order to obtain the true shape of the spectrum, it is necessary to introduce special corrections which differ for different sources. In the case of In^{114} the introduction of corrections for the positron spectrum is particularly important inasmuch as the entire spectrum lies in the energy region where the instrument distortion is particularly great. In order to determine the requisite correction we measured the β^--spectrum of In^{114} under exactly the same conditions as employed for studying the positron spectrum.

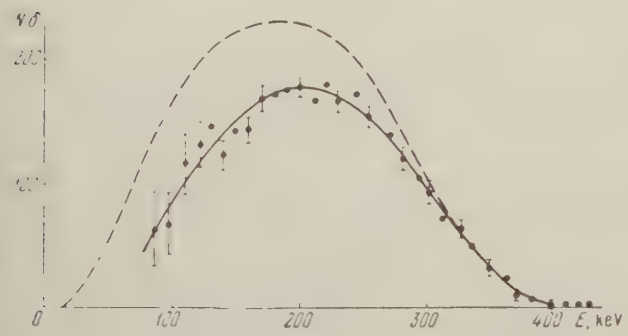

Fig.2. Processed In^{114} positron spectrum. The solid line indicates the β^+-spectrum prior to correction for distortion in the instrument; dash line represents the corrected spectrum.

The β^--spectrum in processed form is shown in Fig.3. The Fermi (Kurie) plot of the β^--spectrum of In^{114} is given in Fig.4. At energies above 800 kev all the points fit a straight line giving an end-point energy of ~ 1.960 Mev. Below 800 Mev there is some deviation, at first upward and then below the Fermi plot.

It is known that the β^--spectrum of In^{114} is not simple: in addition to the spectrum with end-point energy 1.984 Mev, there are present electrons with an end-point energy of about 0.7 Mev and characterized by an intensity of about $9 \cdot 10^{-4}$ electrons per decay. The presence of so soft a component cannot produce a significant deviation from the Fermi shape of the spectrum; in the investigations of Boehm & Preiswerk[3] and Lawson & Cork[4], in which the conditions for studying the spectrum were more favorable, the points fell on the straight-line Fermi plot down to 300 kev. Hence it may be assumed that the deviations

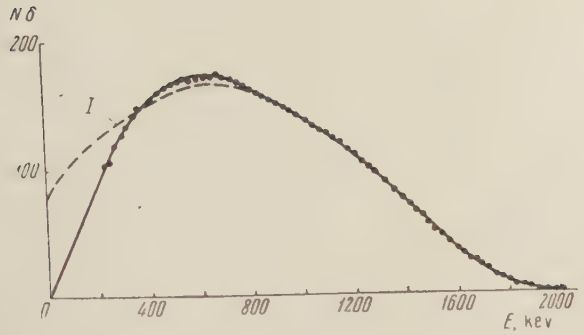

Fig.3. β^--spectrum of In^{114} in processed form. The solid line in the energy region below 200 kev represents extrapolation of the spectrum to zero energy; the dash line gives the Fermi shape of the spectrum.

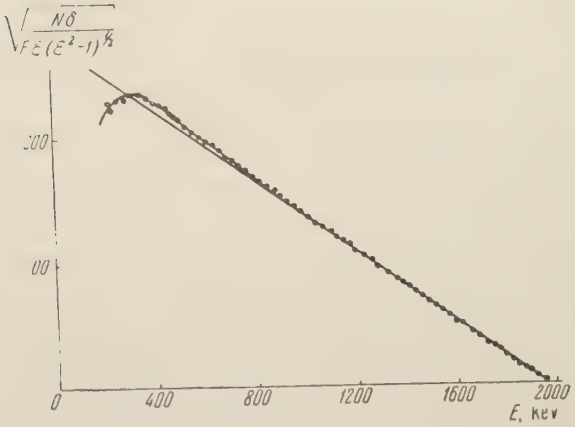

Fig.4. Fermi plot for the electron spectrum of In^{114}.

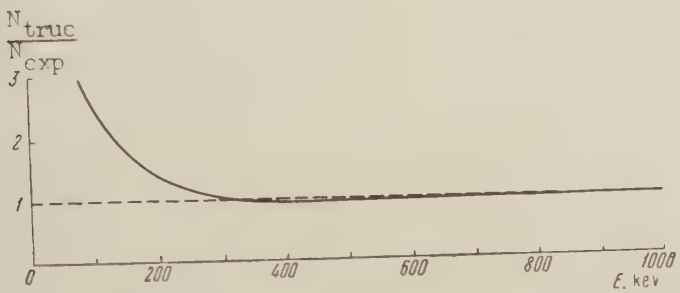

Fig.5. Energy dependence of the ratio N_{true}/N_{exp}.

observed by us are connected with the instrument and the source and can therefore serve for determining the corrections. The energy dependence of the correction, i.e., the ratio N_{true}/N_{exp} obtained from a comparison of the two curves in Fig.3 is shown in Fig.5. The corrections determined in this manner were used to establish the true shape of the positron spectrum, although strictly speaking the corrections may be somewhat different for spectra of different shapes and end-point energies.

We note that the corrections introduced by us in the energy region below 200 kev might be questioned. Admittedly, the extrapolation of the electron spectrum under the 0.192 Mev line is somewhat arbitrary. To test the validity of our corrections, we introduced them into the ordinates of the conversion line of In^{114}. The conversion line of In^{114} obtained through such processing is shown in Fig.6 by the solid line II. The dash line in Fig.6 shows the continuous spectrum in this energy region.

Further, we determined the ratio of the area under the total conversion line to the area under the electron spectrum (98% of the decays). The fraction of conversion electrons in the decay of In^{114*} proved to be 0.75. According to data of Boehm & Preiswerk this value is 0.80 ± 0.05. The good agreement indicates that the corrections introduced by us in the region to 100 kev are reasonably accurate.

The positron spectrum obtained after introduction of the above mentioned corrections is shown in Fig.2 by the dash line. The ratio of the areas under this line to the area under the electron spectrum (I in Fig.3) gives us the number of positrons per decay of In^{114}. Inasmuch as the experimental points begin at 90 kev in the β^+-spectrum and with 200 kev in the β^--spectrum, the spectra have to be extrapolated into the low energy region. Since the Kurie

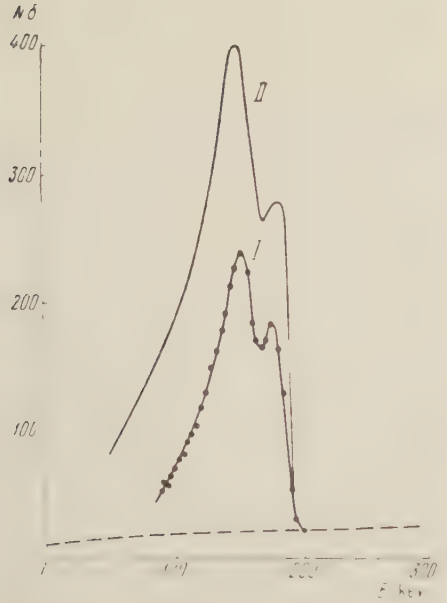

Fig.6. Conversion line of 0.192 Mev energy: I - conversion line without corrections, II - corrected conversion line. Dash line - continuous spectrum.

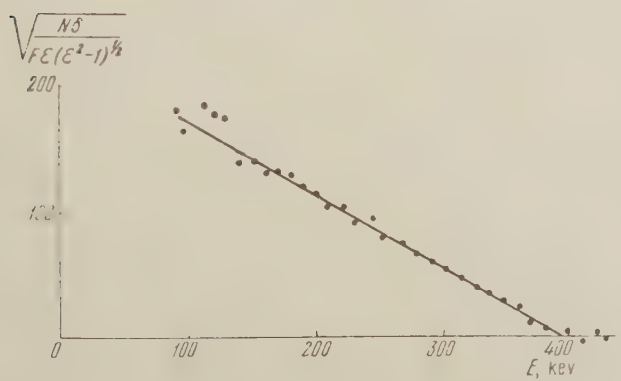

Fig.7. Fermi plot for the positron spectrum of In^{114}.

plots (Figs.4 & 7) proved to be sufficiently rectilinear, the extrapolation into the low energy region was made on the basis of the Fermi shape.

The ratio of the areas proved to be $(3.9 \pm 1.5)\cdot 10^{-5}$. This result is in good agreement with the data of Johns et al[11] - $(4 \pm 1)\cdot 10^{-5}$ - as well as with the results obtained by Grodzins & Motz[8]. The latter authors used the scintillation procedure for investigating the positrons from In^{114}. They obtained a value of $(3.5 \pm 1.0)\cdot 10^{-5}$ for the number of positrons per decay.

The end-point energy of our electron spectrum is 1.96 ± 0.05 Mev, which is in good agreement with the data of other authors[4,5]. The end-point energy of the positrons, as may be seen from the Fermi plot, is 395 ± 20 kev. This value differs markedly from the data of Johns et al (1-1.4 Mev) and of Boehm & Preiswerk (650 ± 100 kev), but is in good agreement with the positron end-point energy obtained by Grodzins & Motz[8] by means of a three-crystal technique (400 ± 25 kev).

We now have the question of whether this β^+-transition goes to the ground state or an excited level of Cd^{114}.

Our measurements in the >400 kev energy region showed that the positron spectrum has no harder component; or in any case the upper bound for its intensity is less than 3% relative to the soft component.

This leads us to conclude that the mass difference In^{114}-Cd^{114} is 1.022 + 0.395 = 1.417 ± 0.20 Mev. We believe that this value is more reliable than that determined from nuclear reactions (Zweifer[14] - 2.07 ± 0.20 Mev).

Using our data and the tables of Dzhelepov & Kudriavtseva[13], we determined the value of log $f\tau$ for the positron spectrum. It proved to be 4.68 ± 0.24, i.e., close to the value of log $f\tau$ for the electrons. Although the difference lies within the limits of the experimental error, the determined value of log $f\tau$ for the positron spectrum is somewhat greater than for the electron spectrum, which is in agreement with the predictions of Ref.1.

The question of the probability of K capture in the ground state of In^{114} is also of interest. Experimental determinations[18,10] of the number of Cd K x-ray quanta indicate that K capture occurs in 1.9% of the disintegrations of In^{114}. This figure includes capture transitions both the the ground level

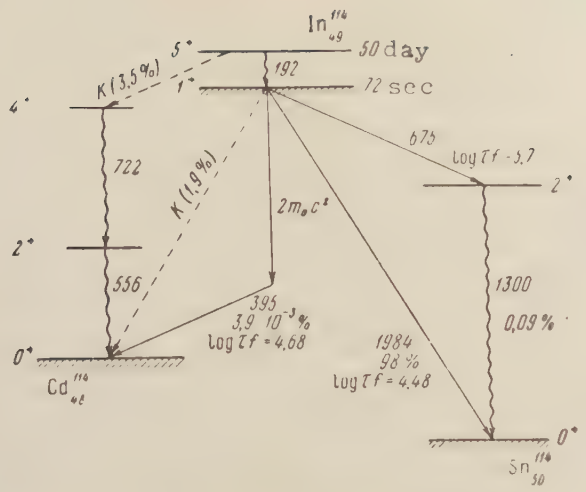

Fig. 8. Decay scheme for In^{114}.

of Cd^{114} and to the excited 556 and 1278 kev levels; the transition probability to the excited levels, however, is much lower than to the ground level, first owing to the lower (2.7 times for the 556 kev level) decay energy and, second because the reduced probability ($\log f\tau$) is always several times smaller for transitions to excited levels. If we assume that the 1.9% figure pertains wholly to capture to the ground level, then for this transition $\log f\tau \approx 4.2$, which is consistent for an allowed transition. The experimental value of the ratio $K/\beta^+ = 490$. In his analysis of capture probabilities, Zweifel[14] calculated the theoretical values of the ratio of the probabilities of K capture and positron decay W_K/W^+ for allowed transitions. For Z = 49 and a positron end-point energy of 395 kev, the theoretical ratio is 120. The reasons for this great divergence are not clear.

Our refined scheme for the decay of In^{114} is shown in Fig.8. The configurations indicated at the levels have been assigned on the basis of the following facts and considerations.

1. The ground states of Cd^{114} and Sn^{114} are assumed to be 0+ as in all even-even nuclei.

2. Direct measurements have shown that the spin of 50-day In^{114} is 5 (Goodman & Wexler[15]).

3. From the Coulomb excitation experiments of Temmer & Heydenburg[16] it follows that the configuration of the 556 kev state of Cd^{114} is 2+.

4. From analysis of the directional and polarization correlation of the 722 and 556 kev γ-rays, it follows[9,17,18] that the 1278 kev state of Cd^{114} is 4+; this is substantiated by the existence of allowed K capture from 50-day In^{114}. Given the above determined mass difference for In^{114}-Cd^{114}, we obtain for the transition from 50-day In^{114} to the 1278 kev level of Cd^{114} $\log f\tau = 7.4$. Despite the large value of $f\tau$, this is still an allowed decay inasmuch as in all other cases allowed β-decay to high-lying excited levels is associated with a high value of $f\tau$.[19]

5. From the last fact it follows that the parity of 50-day In^{114} is even (5+).[20] Since the principal β^--decay of In^{114} is allowed ($\log f\tau = 4.48$), it follows that the assignment for 72-sec In^{114} must be either 0+ of 1+. Of the two alternatives, we must select the second, inasmuch as 0+ would require a very high order of multipolarity for the transition from 50-day to 72 sec In^{114}, whereas from the experimental value of the K/L ratio[3,24], from the conversion on the L_I, L_{II} and L_{III} shells[12] and from the lifetime of the isomer it is evident that this transition is of the E4 type.

6. Inasmuch as the β^--decay of 72-sec In^{114} to the 1300 kev level of Sn^{114} is allowed ($\log f\tau = 5.7$), the spin of this level must be either 1+ or 2+. Again the second alternative must be given preference inasmuch as in even-even nuclei no even levels with odd spin are observed[23].

The authors desire to thank L.K.Peker for valuable discussion of the decay scheme.

"A.A.Zhdanov" Leningrad State University

References

1. B.S.Dzhelepov & L.K.Peker, Doklady AN SSSR, 104, 626 (1956).
2. A.Bohr & B.Mottelson, Kgl.Danske Videnkab Selskab. Mat.-fys Med., 27, 16 (1953).
3. F.Boehm & P.Preiswerk, Helv.Phys.Acta, 22, 331 (1949).
4. L.Lawson & J.Cork, Phys.Rev., 57, 982 (1940).
5. M.Johns, C.Cox, R.Donelly & C.McMullen, Phys.Rev., 87, 1135 (1952).
6. M.Johns, J.Williams & D.Brodie, Can. J. Phys., 34, 147 (1956).
7. F.Maienschein & L.Meem, Phys.Rev., 76, 899 (1949).
8. L.Grodzins & H.Motz, Phys. Rev., 102, 761 (1956).
9. R.Steffen & J.Brazos, Phys.Rev., 99, 1646 (1955).
10. J.Brazos & R.Heffen, Phys.Rev., 102, 753 (1956).
11. M.Johns, C.McMullen, R.Donnelly & S.Nablo, Can.J.Phys., 32, 35 (1954).
12. C.McGinnis, Phys.Rev., 81, 734 (1951).
13. B.Dzhelepov & O.Kraft, Izv.AN SSSR, Ser.fiz., 20, 318 (1956). (Trans. Bulletin, 20, No.3, 293.)
14. P.Zweifel, Phys.Rev., 96, 1572 (1954).
15. L.Goodman & S.Wexler, Bull.Am.Phys.Soc., 30, 18 (1955).
16. C.Temmer & N.Heydenburg, Phys.Rev., 98, 1308 (1955).
17. R.Steffen, Phys.Rev., 83, 166 (1951).
18. J.Brazos & R.Steffen, Phys.Rev., 99, 1645 (1955).
19. L.Sliv & L.Peker, Izv.AN SSSR, Ser.fiz., 19, 355 (1955). (Trans. Bull. 19, No.3, 319.)
20. J.Mei, A.Mitchell & D.Zaffarano, Phys.Rev., 76, 1883 (1949).
21. V.Shpinel' & N.Farafontov, Zhur.eksp.i teor.fiz., 21, 1376 (1951).
22. V.Kel'man, R.Metskhvarishvili, V.Romanov, L.Rusinov & K.Konoplev, Doklady AN SSSR, 107, 394 (1956).
23. M.Glaubman, Phys.Rev., 90, 1000 (1953).

GAMMA-SPECTRUM OF In^{114*}

- I.B.Golovanov, B.S.Dzhelepov, L.S.Lebedev, V.P.Prikhodtseva & Iu.V.Khol'nov

In the present investigation the relative intensities of the γ-rays from 49-day In^{114*} were determined by means of the Ritron[1] under new experimental conditions[2]. The distribution of recoil electrons in $H\rho$ (background subtracted) is shown in the accompanying figure. Four peaks corresponding to the 191, 556, 772 and 1300 kev γ-rays from In^{114*} are clearly discernible. For determining the relative numbers of photons of different energies from the areas under the peaks one must take into account the spectral sensitivity of the instrument[1,2].

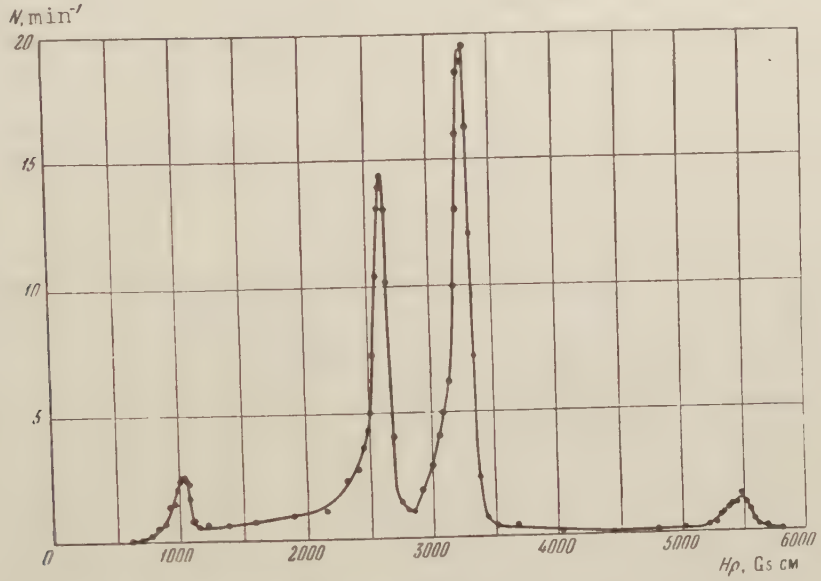

Distribution in $H\rho$ of recoil electrons ejected from target by In^{114*}

It must be noted that this investigation was the first in which the "soft" γ-line - 119 kev - was studied on the Ritron. We had no points for the spectral sensitivity curve in this energy region. We utilized the In^{114*} sample in order to obtain such a point.

It is evident from the decay scheme for In^{114*} that the principal disintegration chain (96%) is $In^{114*} \xrightarrow{\gamma^{191}} In^{114} \xrightarrow{\beta^- 1984} Sn^{114}$; in the process hard ($\sim$2000 kev) β^--particles are emitted. We utilized this circumstance and determined the activity of the source on a calorimeter.

Knowing the activity of the source and the conversion coefficient for the 191 kev transition, we could readily determine the number of photons of this energy emitted by the sample per unit time (the activity of the sample was 1.1 curie). Having determined the ratio of this number to the area under the line obtained by means of the Ritron, we were able to plot another point for the sensitivity curve[2] at 191 kev energy ($S\gamma$ = 0.084). The uncertainty here is of the order of 10%, the principal contribution to it being the uncertainty in the value of the conversion coefficient for the isomeric transition.

The spectrum was resolved using standard single lines. The results of our analysis are shown in the accompanying table.

It will be evident from the table that the ratio of the intensities of the 556 and 722 kev γ-lines is close to unity. From this it may be concluded that not infrequently the decay by orbital electron capture occurs not to the

Energies and intensities of the γ-rays from In^{114*}

E_γ, kev	Relative intensity	No. quanta per decay of In^{114*}
191	4,00	0,167
556	1,07	0,045
722	1,00	0,042
1300	0,039	0,0017

first excited level bu to the second level or the ground state of Ct^{114}. We calculated the numbers of quanta per decay for all the γ-transitions from the known conversion coefficients for the 191 and 722 kev transitions and our relative intensity values. These results are listed in the table.

After subtraction of the standard lines there remains in the region between the 190 and 556 kev γ-lines a certain excess of recoil electrons associated with the continuous γ-ray spectrum. A rough evaluation shows that this excess can, apparently, be attributed to bremsstrahlung produced by the hard β-particles.

We desire to thank E.A.Khol'nov for the calorimetric measurements of the activity of the In^{114*} sample.

"V.G.Khlopin" Radium Institute of the
Academy of Sciences of the USSR

References

1. B.Dzhelepov, N.Zhukovskii & Iu.Khol'nov, Izv.AN SSSR, Ser.fiz., 18, 599 (1954). (Trans.Bulletin, 18, No.5, 285.)

2. B.Dzhelepov, V.Prikhodtseva, A.Feoktistov & Iu.Khol'nov, Izv.AN SSSR, Ser.fiz., 20, 1361 (1956). (Trans. Bulletin 20, No.12a, 1245.)

REFINEMENT OF THE RELATIVE INTENSITIES OF THE LINES IN THE GAMMA-SPECTRUM OF Ta^{182}

- O.I.Sumbaev

The relative intensities of the lines in the γ-radiation spectrum of Ta^{182} were first measured on a curved crystal diffraction spectrometer by the DuMond group[1,2] and later by the writer[3] by means of a similar spectrometer[4] at the Leningrad Institute of Metrology. As may be seen from Table 1 the results obtained in these investigations differ appreciably. The presence of a large number of closely spaced low-energy lines makes it impossible to investigate the γ-spectrum of Ta^{182} by observing recoil electrons. On the other hand, the presence of intense high-energy lines greatly hampers photoelectron measurements by giving rise to the strong Compton electron background in the soft region[2]. Thus the crystal diffraction spectrometer procedure is the only one applicable to measurement of the relative line intensities in the spectrum of Ta^{182}.

Table 1

Relative intensities of a number of γ-lines in the Ta^{182} spectrum

E, kev (Ref.2)	Relative intensities			
	Ref.1	Ref.2	theoretical spectral sens. curve (Ref.3)	experimental spectral sensitivity curve
152,41	12,5	35	13,9	18,2
156,37	4,0	11,5	5,8	7,2
179,36	5,4	16	6,9	8,7
198,31	2,6	7,5	3,4	4,5
222,05	12,8	35	18,6	21,4
229,27	6,8	20	7,9	9,8
264,09	7,7	22	7,2	9,1
1122	100	100	100	100
1155	—	6,5	9,0	7,1
1189	44,6	45	59,5	56,8
1222	95	145	156	161
1231				

The spectral sensitivity curves in the investigations of the DuMond group and our early study were calculated theoretically taking into account the wavelength dependence of the following factors: 1) self-absorption in the source, 2) the coefficient of reflection of γ-radiation from the curved quartz crystal (reflection from the 1340 plane) and 3) the efficiency of the scintillation counter used as the detector for the diffracted radiation. The most significant proved to be the variation with wavelength of the coefficient of reflection. Measurements made by West, Lind & DuMond[5] showed that this dependence is close to the quadratic, i.e., $\Gamma \approx \lambda^n$, where n is somewhat smaller than 2.

Our measurements[3,4] substantiated the nearly quadratic character of the dependence and led to the relationship

$$\Gamma \approx \lambda^{1.85 \pm 0.04}, \qquad (1)$$

where ± 0.04 is the root mean square error obtained in processing the results of measurement by the method of least squares.

The error in theoretical calculation of the spectral sensitivity curve proves to be appreciable: 20-30%. It is due primarily to the uncertainty as regards the exponent in (1).

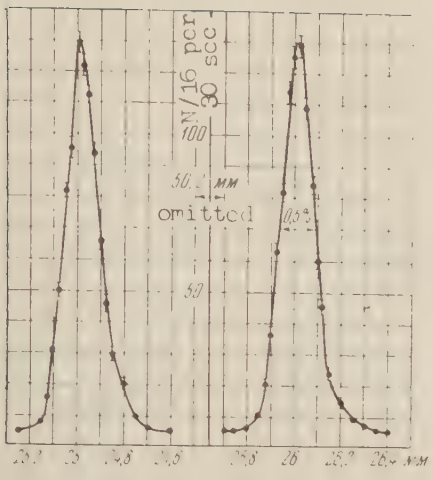

Fig.1. Right and left 412 kev mirror lines of Au^{198}. Abscissae - readings on instrument scale.

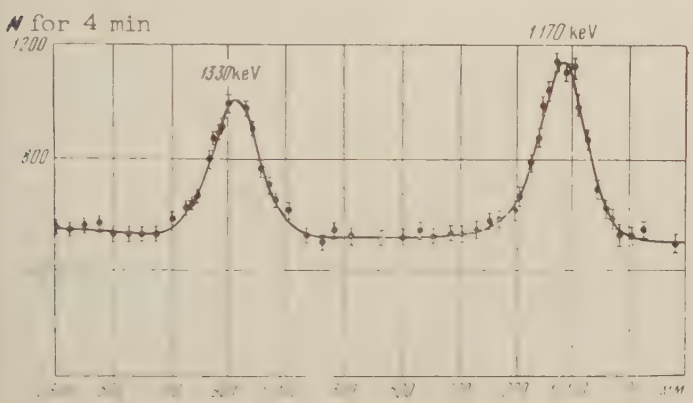

Fig.2. Spectral lines of Co^{60}. Abscissae - readings on instrument scale.

Hence in order to insure more reliable results we felt it would be desirable to check the calculated spectral sensitivity curve by a more direct procedure. The activity of Au^{198} and Co^{60} sources of standard size (30 x 50 x x 0.1 mm) was measured on a γ-calorimeter[7]. We then calculated the number of 412, 1170 and 1330 kev γ-rays emitted by the sources per unit time on the basis of the well-known decay schemes for these isotopes. Next we measured the areas under the spectral lines obtained for these sources on the crystal diffraction spectrometer (Figs.1 & 2). The ratio of these quantities obviously gives the value of the transmission factor of the instrument at 412, 1170 and 1330 kev.* The theoretical and experimental values are compared in Table 2.

In view of the higher accuracy (we evaluate the maximum error in our experimental values as 8-10%) and the greater reliability of the experimental points, the calculated spectral sensitivity curve was shifted so as to obtain the best agreement with experiment.

The relative line intensities in the γ-spectrum of Ta^{182} recalculated with reference to experimentally corrected spectral sensitivity curve are listed in Table 1.

In Table 3 we give the relative intensities of a number of γ-lines in the spectrum of Ir^{192}, also recalculated with reference to the corrected spectral sensitivity

*The transmission factor as defined here obviously has the dimension of a division on the scale of the spectrometer (in our case a millimeter). Inasmuch as the line shape virtually does not vary with the energy and the ratio of the number of counts at the maximum to the area under the line remains approximately constant (in our case this ratio was about 5 mm^{-1}), one can readily compute the transmission factor (detecting efficiency) as usually defined, i.e., the ratio of the number of counts at the line maximum to the total number of γ-quanta of given energy emitted by the source.

Table 2

Theoretical and experimental transmission factors of the spectrometer

E, kev	ε_{thco}, mm	$\varepsilon_{exp.}$, mm	$\frac{\varepsilon_{thco} - \varepsilon_{exp.}}{\varepsilon}$ %
412	$4,13 \cdot 10^{-10}$	$3,90 \cdot 10^{-10}$	+6
1170	$3,78 \cdot 10^{-11}$	$4,54 \cdot 10^{-11}$	−18
1330	$2,73 \cdot 10^{-11}$	$3,58 \cdot 10^{-11}$	−27

Table 3

Relative intensities of a number of lines in the γ-spectrum of Ir^{192}

E, kev (Ref.11)	Relative intensities				
	Ref.8	Ref.9	Ref.10	Ref.11	Our data
205,75	0,27	—	0,25	0,23	0,32
295,94	3,0	—	1,88	2,12	2,32
308,45	3,1 } 13,8	} 9,09	2,02 } 9,45	2,06 } 10,1	2,38 } 11,1
316,46	7,7		5,55	5,90	6,38
467,98	4,1	4,58	4,10	3,78	3,92
484,75	—	—	0,37	0,23	0,36
588,4	0,33	—	0,47	0,42	0,41
604,5	1,0 } 1,74	} 1,74	0,72 } 1,74	0,82 } 1,74	0,76 } 1,74
612,9	0,41	—	0,55	0,50	0,57

curve. The satisfactory agreement of these data with the data obtained from conversion electrons through the conversion coefficients[8], from recoil electrons[9] and photoelectron measurements[10,11] serves as further confirmation of the correctness of the experimentally adjusted spectral sensitivity curve.

The writer desires to express his indebtedness to E.A.Khol'nov who carried out the measurements on the γ-calorimeter.

"D.I.Mendeleev" All-Union Scientific Research Institute of Metrology

References

1. D.Muller, H.Hoyt, D.Klein & J.DuMond, Phys.Rev., 88, 775 (1952).
2. J.Murray, F.Boehm, P.Harmier & J.DuMond, Phys.Rev., 97, 1007 (1954).
3. O.Sumbaev, Zhur.eksp.i teor.fiz., 32, 247 (1957); Izmeritel'naia tekhnika (The technique of measurement) No.2 (1957).
4. P.Lukirskii & O.Sumbaev, Izv.AN SSSR, Ser.fiz., 20, 903 (1956). (Trans. in Bulletin 20, No.8, 820).
5. D.Lind, W.West & J.DuMond, Phys.Rev., 77, 475 (1950).
6. O.Sumbaev, Zhur.eksp.i teor.fiz., 32, 1276 (1957).
7. K.Aglintsev & E.Khol'nova, Doklady AN SSSR, 98, 3 (1954).
8. A.Bashilov, N.Anton'eva & B.Dzhelepov, Izv.AN SSSR, Ser.fiz, 16, 264 (1952).
9. M.Glazunov, B.Dzhelepov & Iu.Khol'nov, Izv., AN SSSR, Ser.fiz., 19, 294 (1955). (Trans. Bulletin 19, No.3, 267.)
10. M.Johns & S.Nablo, Phys.Rev., 96, 1599 (1954).
11. L.Baggerly, P.Marmier, F.Boehm & J.DuMond, Phys.Rev., 100, 1364 (1955).

INVESTIGATION OF THE GAMMA-SPECTRUM OF RaC

- B.S.Dzhelepov & S.A.Shestopalova

Introduction

The spectrum of γ-rays from RaC has been investigated repeatedly[1-5]. RaC is one of the decay products of radium; it is responsible for almost the entire high-energy part of the γ-spectrum of radium in equilibrium with its decay products. Radium is the principal radioactive substance utilized in metrology as a standard; for this reason it has drawn the consistent attention of investigators.

The spectrum of RaC is so complicated that every advance in experimental technique has revealed new details. At present more than 35 lines are known. The γ-ray energies are determined with the highest accuracy from the conversion electron spectrum. The relative intensities of the rays are best determined by observation of recoil electrons. Such investigations under satisfactory conditions have been performed twice. In 1940 Latyshev and his co-workers[2] investigated the spectrum of RaC by means of a magnetic spectrometer with a resolution >10% in the 1 Mev region. In 1954 Mladjenovic & Hedgran[3] studied the spectrum by means of a magnetic spectrometer with a resolution of ~3.5% in the 1 Mev region.

By means of the Elotron[6] we were able to carry out an investigation of the γ-spectrum of RaC with an even better (approximately one and a half times) resolution.*

1. Shape and size of the source

The source was 4 grams of radium in the form of $RaBr_2$ enclosed in 24 glass ampoules 4-5 mm in diameter and 40 mm in length. The ampoules were loaded into 4 containers of copper foil 50 μ thick: six ampoules, three in a row, in each container. The containers were stacked one behind the other. They were mounted with respect to the collimator as shown schematically in Fig.1. The $RaBr_2$ did not completely fill the ampoules. The ampoules were angled so that direct rays (parallel to the axis) from any point of the source could impinge on the target. The "empty" ends of the ampoules were therefore in an unfavorable position, but by a special experiment it was established that the γ-radiation from the active radon deposit on the inside walls of an ampoule amounted to less than 1.5% of the total γ-radiation of the given ampoule. With the described arrangement of the ampoules the effective length of the source was 13.5 cm. The closest end of the source was 3 cm from the edge of the collimator. An aluminun plate 2 mm thick was mounted between the source and the collimator.

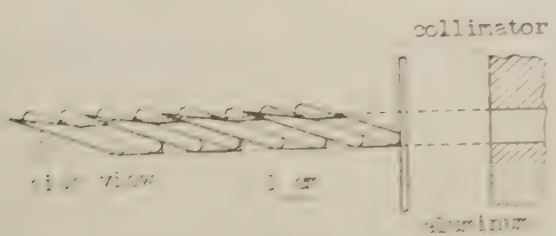

Fig.1. Arrangement of the source relative to the entrance opening of the collimator.

---

*The results of measurement and preliminary calculation of the relative intensities were reported at the Fifth All-Union Conference on Nuclear Spectroscopy.

2. Analysis of the sample for RaTh content

As is known, many radium preparations contain mesothorium and radiothorium. The presence of these impurities would distort the γ-spectrum. Although according to the accompanying certificate our sample was free of these impurities, we felt it desirable to double check for the absence of radiothorium. This check was carried out by the photoneutron procedure and directly on the Elotron by observing the high energy part of the γ-spectrum. In the first procedure, the photoneutron source was one of the ampoules and heavy water; the detector was a uranium chamber.

Photoneutrons are produced by γ-rays of energies exceeding 2.23 Mev, the threshold of the deuterium photodisintegration reaction. In the case of radium this is principally the weak 2450 kev γ-ray of RaC (0.02 photons per decay); in the case of radiothorium (in equilibrium with the decay product) this is the strong 2416 kev γ-ray of ThC'' (0.35 photons per disintegration of RaTh). This allows of detecting even small amounts of radiothorium in radium. The set-up was calibrated with reference to a radium source known to be pure. The relative probability of photoneutron production by the γ-rays from Ra and RaTh was taken from Ref.7. The results of measurement indicated that the amount of impurities present in the investigated sample was less than 1% (γ-equivalent basis).

In the case of the second procedure we investigated the energy region wherein the most intense 2614 kev γ-line of ThC'' is located by means of the Elotron, using the above described ampoule array as the source. The counting rate at the position of the peak of this line was <0.06 pulses/min. It may therefore be concluded that our radium sample contained less than 0.2% radiothorium impurity (on the basis of the number of disintegrations).

3. Experimental curve

The experimental curve we obtained for the γ-spectrum of RaC is shown in Fig.2 (solid dot).[8] The abscissae are the values of the energy E_γ calculated according to the formulas

$$E_\gamma = \frac{1}{2} m_0 c^2 (E_\beta + \sqrt{E_\beta^2 + 2E_\beta}), \quad \text{and} \quad E_\beta = \sqrt{1 + \left(\frac{e}{m_0 c^2}\right)^2 (H\rho)^2} - 1,$$

where H is the measured field and ρ is the radius of curvature of the circular electron trajectory in the instrument. The abscissae are coincidence counting rates in arbitrary units. The circle points give the background, i.e., counting rate with the target out of the beam. The average measuring time for the background points was 1.5 hours; that for the spectrum points was 4 hours each.

4. Background

The background in our instrument is made of the following components: 1) chance discharge coincidences in both counters, 2) Compton electrons ejected by the γ-rays from the gas (helium and methane) in the vicinity of the target, 3) stray electrons from the electron gas formed as the result of multiple scattering of the γ-rays and electrons in the space before the first slit, and 4) coincidences due to cosmic particles.

The counting rate due to chance coincidences can be calculated from the counter load and the resolution of the amplifiers; it depends little on the magnetic field intensity and amounts to $\sim$0.8 pulses/min. The cosmic ray background by virtue of the great separation between the counters is very low, namely, $\sim$1 pulse/hour.

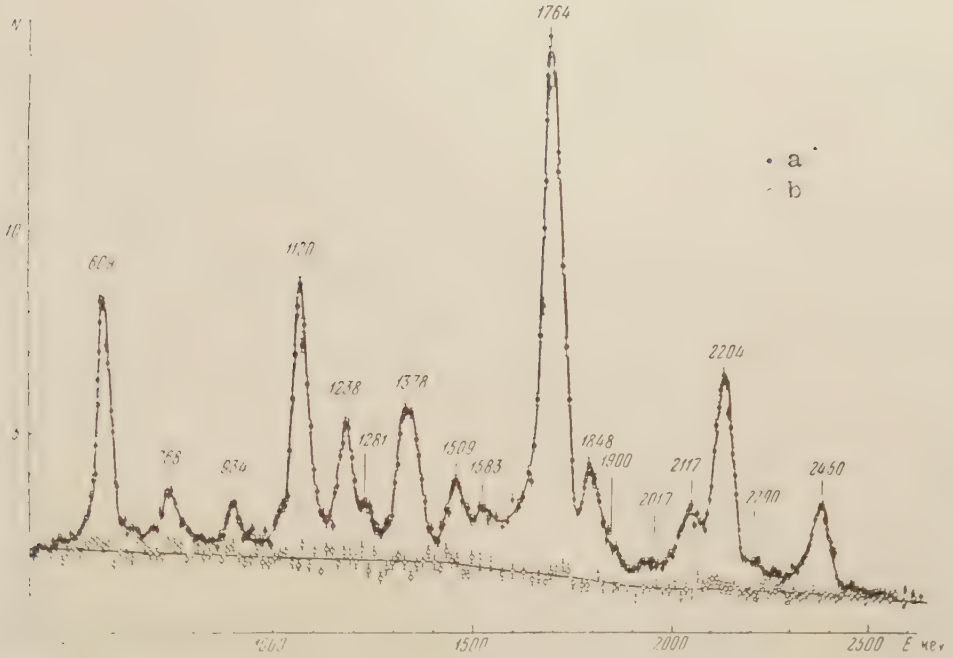

Fig.2. Experimental γ-spectrum of RaC: a - coincidences with the target in the beam; b - coincidences with the target out of the beam (background).

The second component of the background (Compton electrons ejected from the gas) was clearly observed in the Ritron[9]. The background repeated to a greatly reduced scale the main line: background count rose noticeably under or somewhat to the left of the peaks of the γ-lines. In our instrument we cannot reliably separate this component of the background: there are some indications of maxima under the 609, 1764 and 2204 kev lines but they lie almost within the limits of the statistics. Hence we attribute the observed background to the other factors and assume that it varies as a smooth function of H.

In the energy range from 500 to 1400-1500 kev the background slowly decreases, remaining equal to about two coincidence per min. In the region from 1500 to 1900 kev the background falls off by a factor of almost 1.5 and then decreases more slowly up to 2500 kev. If one assumes that the background varies smoothly as a function of H, one can dispense with the onerous operation of measuring the background individually at each point of the experimental spectrum and determine it simply from the smooth curve drawn through the experimental background points. Even though the experimental background points are further apart than the spectrum points and have a greater uncertainty, the averaging effect of the described procedure reduces the actual error in the final results to an insignificant amount.

The experimental background curve is such that it can be replaced by four straight lines. The straight lines shown in Fig.2 were obtained by the method of least squares. As a result of these calculations the background under the most intense lines is determined with an error of 0.2-0.3 counts/min. At other locations (where there are no indications of a rise in background) this

error is presumably not over 0.1 counts/min. Thus, for example, in the 2250-2600 kev region the error is approximately 0.06 counts/min.

5. Processing of the experimental curve

For determining the relative γ-line intensities the experimental spectrum was processed as follows. 1) The background was subtracted. 2) The appropriate corrections for the variation of the efficiency of the counter system with the electron energy were introduced; the efficiency vs energy curves were plotted on the basis of the work of McClure[10]; under our conditions the counter efficiency changed by about 7% in the electron energy range from 400 to 2000 kev. 3) The results were reduced to equal Hρ intervals. 4) The curve was then resolved into standard shape components and the area of each component determined. 5) The area of each component was multiplied by the appropriate coefficient associated with the absorption of the given γ-rays in the source and walls of the instrument and divided by the spectral sensitivity of the instrument. The final resultant values were taken as the relative line intensities. The values of E_γ were converted to E_{true} by means of the calibration curve given in Ref.6. In this earlier contribution we also discussed the results of our investigation of the line shape. In connection with the present investigation we undertook a repeat study of the line shape with particular attention to the low- and high-energy tails. The results obtained (Fig.3) agree with the earlier data on the line shape[6] except that the rise on the high-energy side for the Co^{60} and Zn^{65} lines begins somewhat earlier than for the γ-line of Cs^{137}. The line shapes for other energies were determined by linear extrapolation of the observed rises.

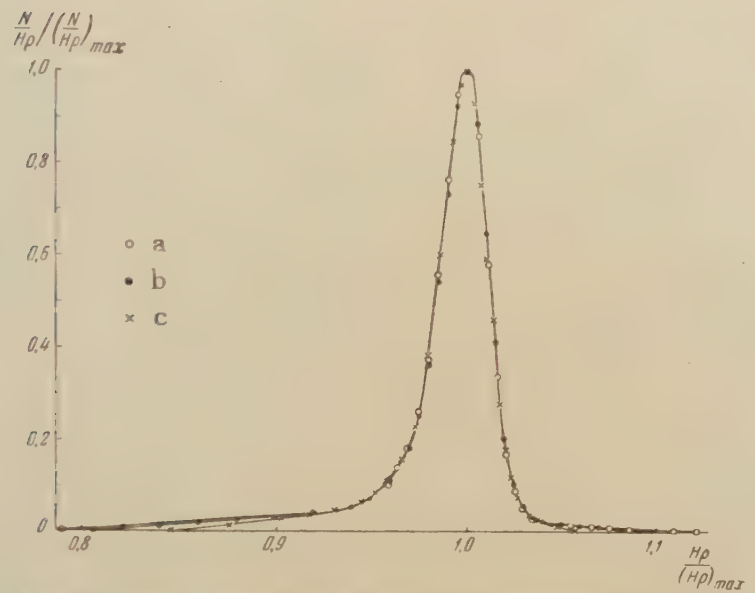

Fig.3. Apparatus line shape in reduced coordinates: a) 1332.5 kev line of Co^{60}, b) 1120 kev line of Zn^{65}, c) 661.6 kev line of Cs^{137}.

The spectral sensitivity of the instrument (Fig.4) was determined on the basis of measurements of the spectra of Cs^{137}, Co^{60} and Na^{24}. The activity of the Cs^{137} and Co^{60} sources was determined for us by the calorimetric method by E.A.Khol'nova.

6. Resolution of the recoil electron spectrum into components.

The procedure employed in resolving the recoil electron spectrum into components was the following. First we determined what γ-lines are already known in a given energy interval, both from recoil electron spectra[2,3] and conversion electron spectra[4,5]. As regards the latter, we paid particular attention to results of Mladjenovic & Slatis[5], taking into account both the

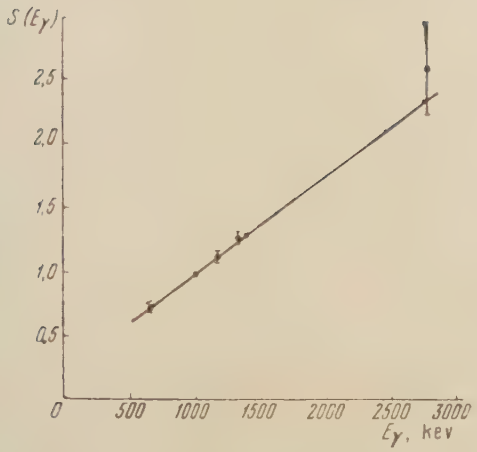

Fig.4 Experimental spectral sensitivity curve for the Elotron.

identified and the unidentified lines mentioned by these authors. The energy positions of the γ-lines determined from conversion electrons[5] were assumed to be correct. The line intensity was chosen so as to secure the best fit of experimental points. After this it was found that in some locations the experimental points lay above the composite curve representing the sum of the known components. In a number of cases in the region of high energies, where the rise of the experimental points above the composite curve was far beyond the limits of the statistical error, we postulated the existence of previously unknown lines.

The section of the spectrum from 1820 to 2600 kev is shown in Fig.5. In addition to the well-known intense γ-lines of 1840, 2204 and 2450 kev energy, there are evident in our spectrum weaker lines, not previously observed in recoil electron spectra. Two of them - 2016.7 and 2117.0 kev - have been observed from conversion electrons and identified by Mladjenovic & Slatis.[5] The conversion electron table given by these authors includes a number of unidentified lines. Among these is the line they list under No. 137 (Hρ = 7412.22).

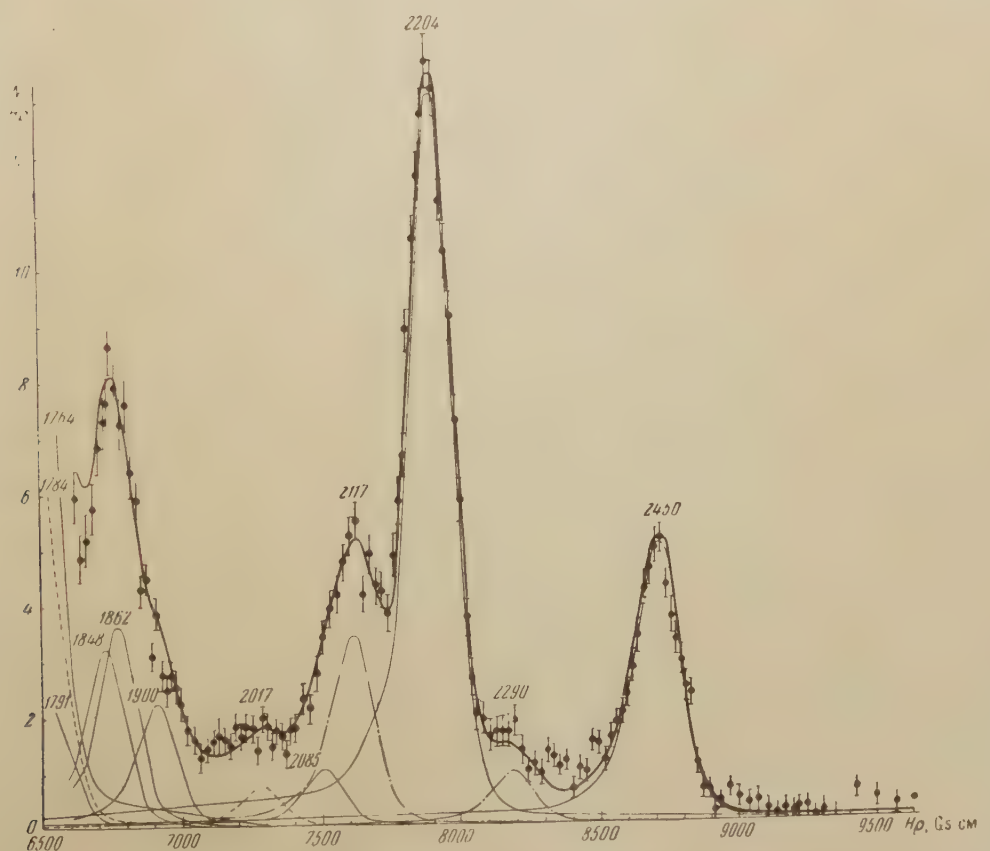

Fig.5. Resolution of the γ-spectrum of RaC in the 1820-2600 kev region.

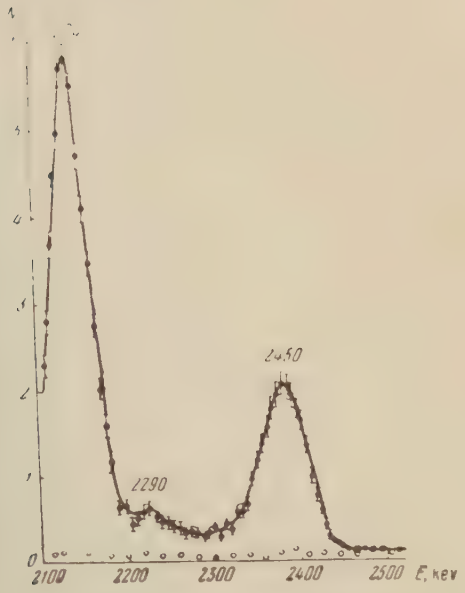

Fig.6. Experimental curve for the 2204-2450 kev section of the γ-spectrum of RaC obtained under improved conditions. Circles - background.

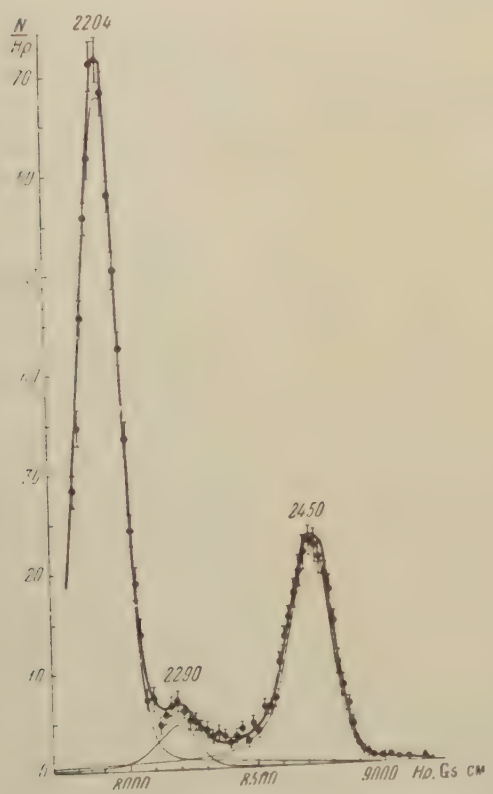

Fig.7. Resolution of the RaC γ-spectrum in the 2204 to 2450 kev region.

If we assume that this line is due to the K conversion electrons from RaC, the energy of the associated γ-line is found to be 1862.3 kev. After plotting the enumerated six lines, it became evident that there was an appreciable excess of coincidences near 1900, 2100 and 2300 kev. To explain this excess we assumed the existence of three weak γ-lines with energies of 1900, 2085 and 2290 kev; the most intense of these (1900 kev) is two times weaker than the 2450 kev line and appears only in 0.9% of the disintegrations. In the recoil electron spectrum published by Latyshev[2] there is indicated a 2090 kev γ-line; at the same time the three-times more intense 2117 kev line is not mentioned. Apparently, the two 2085 and 2117 kev lines merged in the spectrum of Latyshev and were attributed the 2090 kev energy value.

After addition of the above-mentioned lines there still remained the following divergences between the composite curve and the experimental one.

1. In the 2500 to 2700 kev region there is a persistent excess of the counting rate above the background; it cannot be explained by the influence of the neighboring 2450 kev line. It is possible that there exists other γ-lines on the high-energy side of the 2450 kev line; this question will be discussed in another contribution.

2. The experimental points lie above the composite curve in the interval between the 2290 and 2450 kev lines. This excess could be explained by the existence of a very weak (0.003 photons per disintegration) line with an energy of 2340 kev. To check this we reinvestigated the 2204 to 2450 kev section of the spectrum under improved conditions, using a new amplifier (reduced background). The results of this investigation are shown in Figs. 6 & 7. As may be seen from the curves, the existence of the γ-line at 2290 kev was confirmed, while the assumption of the presence of a 2340 kev line was not substantiated.

In Fig.8 we show the section of the spectrum from 1480 to 1820 kev. In addition to the peaks corresponding to the well-known 1509.3 and 1764.4 kev γ-lines, a peak in the vicinity of 1580 kev is clearly discernible in the experimental curve. Among the unidentified lines in the conversion electron study of Mladjenovic & Slatis[5] are their lines Nos.123 & 126. If we assume that these are the K and

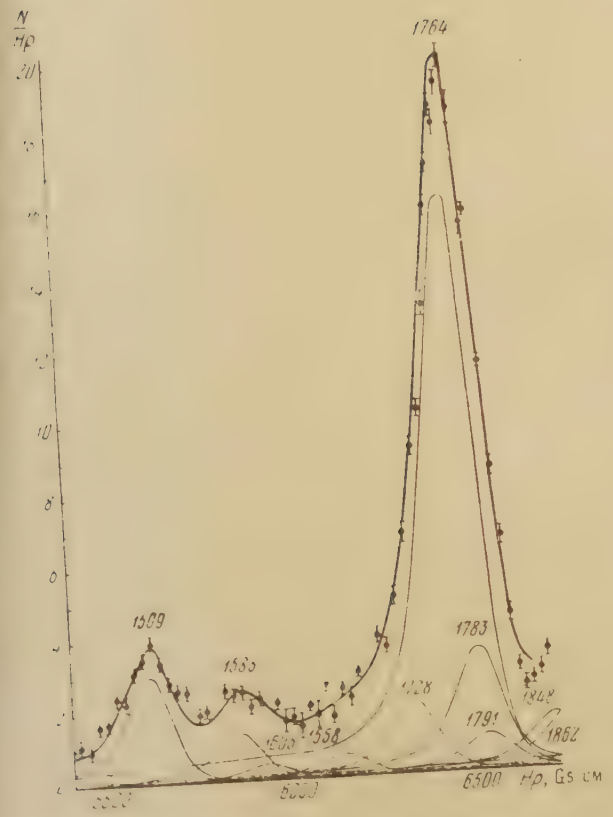

Fig.8. Resolution of the γ-spectrum of RaC in the 1480-1820 kev interval.

$L_{I,II}$ conversion electron lines, we obtain a value of 1582.9 kev for the energy of the associated γ-line. The excess of recoil electrons near the 1764.4 kev line on the side of low energies can be explained by the presence of γ-lines with energies of 1728.3, 1668.4 and 1605.2. The first is known from the conversion electron spectrum; the energies of the second and third were deduced on the assumption that the unidentified Nos.127 and 130, 124 and 128 lines of Mladjenovic & Slatis[5] are due to the K and L_I conversion electrons from RaC. The excess of recoil electrons near the 1764.4 kev line on the side of higher energies can be explained by the presence of γ-lines of energies 1783.8 and 1790.7 kev; these energy values were obtained on the assumption that the unidentified Nos.132 and 133 lines of Ref.5 were produced by the K conversion electrons from RaC. It must be noted that the accuracy in determining $(N/H\rho)_{max}$ for the above lines is not high inasmuch as they appear against the background of a very intense line; a small change in the actual height of the 1764.4 kev line would have an appreciable effect on the value of $(N/H\rho)_{max}$ for these lines and, consequently, on the areas under them. There appears to be no need to plot new lines in this part of the spectrum.

In Fig.9 we show the section of the spectrum in the region extending from 450 to 1480 kev. The well-known intense lines at 609.3, 768.7, 934.8, 1120.4, 1238.3 and 1378.2 kev do not wholly account for the experimental curve.

The excess of recoil electrons between the 609.3 and 768.7 kev lines can be explained by the presence of γ-lines of energies 652.4, 660.9 and 703.2 kev, whose energies we have evaluated on the assumption that the unidentified lines Nos.81, 82 and 88 of Mladjenovic & Slatis[5] are due to K conversion electrons from RaC. The unusual shape of the 768.7 kev line (comparatively flat slope on the high-energy side) is probably due to the presence of three close lines having energies of 787.1, 806.3 and 821.3 kev. The energies of these lines were also determined on the assumption that the Nos.91, 92 and 93 lines of Ref.5 are produced by K electrons from RaC. In order to account for the shape of the experimental curve in this region, we were forced to introduce two additional lines of 1155.3 and 1207.1 kev energy between the intense 1120 and 1238 kev lines. The energy of the first (1155.3 kev) is known from conversion electron measurements, while the second was found among the unidentified lines listed in Ref.5. On the high-energy side of the 1238.3 kev line there is clear evidence of the 1281.3 kev line which was observed by Mladjenovic & Slatis in the conversion electron spectrum. After plotting and adding up all the above enumerated lines, there still remains some divergence:

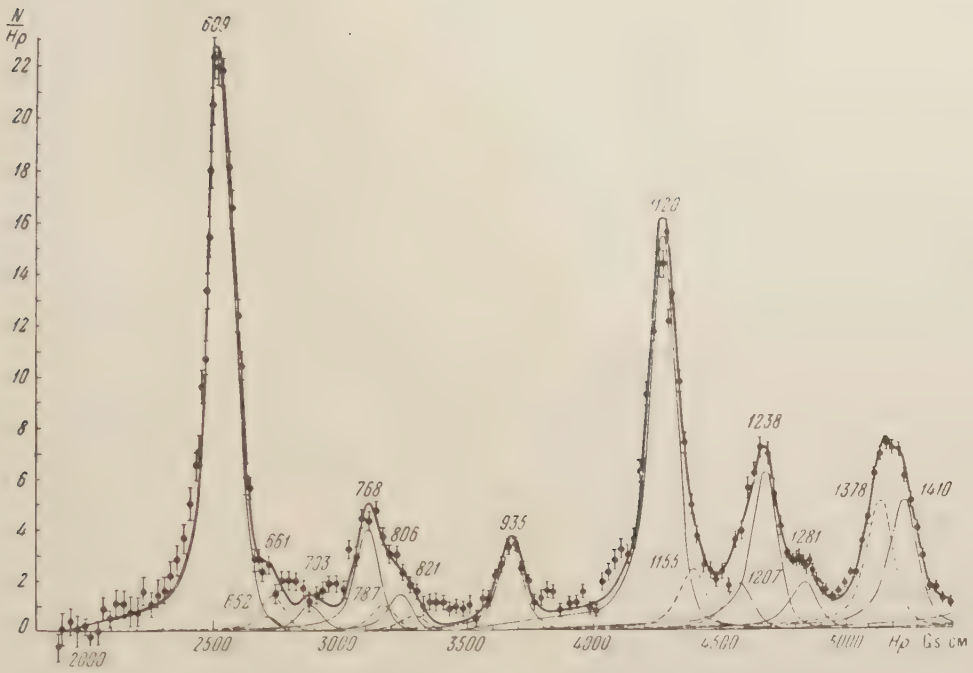

Fig.9. Resolution of the γ-spectrum of RaC in the 450-1480 kev region.

near 720 kev and in the 840-890 and 960-1040 kev intervals the experimental points lie well above the composite curve. Further investigations are needed to interpret these divergences.

The section of the γ-spectrum of RaC from 1350 to 1450 kev was analyzed in detail in Ref.11.*

The relative intensities of the γ-lines of RaC are listed in Table 1 and shown graphically in Fig.10.

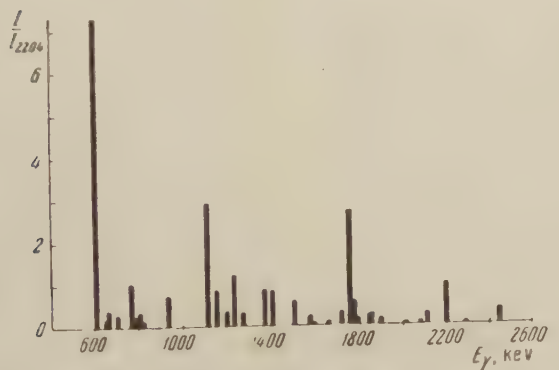

Fig.10. Relative line intensities in the γ-spectrum of RaC.

Regarding the accuracy of our determination of the relative line intensities we can state the following.

a) For the "strong" lines with relative intensities above 0.4 the error is determined not by the statistical uncertainty but primarily by the possible error in plotting the spectral sensitivity curves (±15% in the interval from 600 to 2200 kev). It should be recalled that the relative intensities of close lines are known with high accuracy.

b) For some lines there is an additional uncertainty due to the tails of close-lying strong lines. This pertains, for example, to the 1155, 1281, 1509, 1583 and 2117 kev lines.

c) For the weak lines one must add the statistical uncertainty to the above errors.

d) In the case of very closely spaced lines an appreciable error may be

---

*See Note at end of report.

Energies and relative intensities of the γ-lines of RaC

Table 1

Number	E_γ, kev	Relative intensities: Our data	Mladjenovic & Hedgran (Ref. 3)	Latyshev (Ref. 2)
1	609,3	7,31	5,13	–
2	652,4	0,56		
3	665,9			
4	703,2	0,30		–
5	768,7	1,02		–
6	787,1	0,25	1,11	–
7	806,3	0,33		–
8	821,3	0,14		–
9	934,8	0,74	0,54	–
10	1120,4	2,92	3,9	1,76
11	1155,3	0,44		
12	1207,1	0,37		
13	1238,3	1,23	1,42	0,41
14	1281,3	0,34		
15	1378,2	0,86	1,66	1,32
16	1385,3			
17	1391,1			
18	1396,5			
19	1401,7	0,84		
20	1408,0			
21	1438,0			
22	1509,3	0,60	0,56	0,56
23	1582,9	0,24		
24	1605,2	0,07		
25	1668,4	0,11		
26	1728,3	0,34	3,14	2,51
27	1764,4	2,73		
28	1783,8	0,58		
29	1790,7	0,16		
30	1848,5	0,25	0,33	0,32
31	1862,3	0,28		
32	1900	0,17		
33	2016,7	0,06		
34	2085	0,08		
35	2117,0	0,28		
36	2204,2	1	1	1
37	2290	0,07		
38	2450	0,36	0,36	0,34

*Note: The energies of the γ-lines Nos.1,5,9,10,11,13,14,15,22,26,27,30, 33,35 & 36 in our table are given on the basis of the conversion electron measurements of Mladjenovic & Slatis[5]. These authors also list a number of lines not identified by them. These are their lines Nos.81,82,88,90,91,92, 93,102,112-116,118,123,124,126-128,130,132,133 and 137 which we have identified and listed in Table 1 under Nos.2,3,4,6,7,8,12,16-21,23,24,25,28,29 & 31. The energies of the γ-lines Nos.32,34,37 & 38 were determined by us. The relative intensities indicated by Mladjenovic & Hedgran and Latyshev pertained to groups of unresolved lines; we have used braces to indicate the probable groups, but have indicated the corresponding intensity value at the energy given by the respective authors.

introduced by the uncertainties of resolution into components.

The accuracy of determination of the relative intensities of such lines as those at 787, 806, 821, 1207, 1605, 1668, 1784, 1791, 1900, 2017 and 2085 kev does not exceed 50%.

7. Determination of the number of quanta per disintegration

Knowing the relative intensities (N_γ) of the γ-lines in the spectrum and the total energy Q carried off by the γ-rays per disintegration we can readily determine the number of quanta per disintegration for each γ-line from the following relationship $\sum N_\gamma k E_\gamma = Q$, where $N_\gamma k$ is the number of quanta per disintegration associated with the γ-line of energy E_γ. It must be noted that the values of $N_\gamma k$ determined in this manner may be overestimates inasmuch as the summation is carried out over all the known γ-lines, while there may also be some still unknown ones. In the case of RaC, however, the γ-spectrum has been investigated fairly thoroughly in all energy regions, hence the indicated overestimates can only be minor.

The value of Q is taken from thermal or ionization measurements. For radium this quantity has been determined repeatedly.[12] The best calorimetric determination of the total energy carried off by the γ-rays of 1 gram of radium per unit time was carried out by Zlotowski[13] in 1935. Zlotowski gives $Q_0 = 9.1 + 0.15$ cal g^{-1} $hour^{-1}$; this energy value pertains to the radiation from radium (B + C); the effect from the γ-rays from radium itself amounts to only 0.02 cal g^{-1} $hour^{-1}$ (Hahn & Meitner[14]), i.e., lies well within the limits of the error in determining Q_0. In determining the number of quanta per disintegration, it is convenient to express Q in Mev per disintegration. Converting, we obtain Q = 1.81 Mev. (In our calculations we assumed that the number of disintegrations per second in 1 gram of radium is $3.65 \cdot 10^{10}$; this is given as the most accurate value by Whyte[15].) As noted, this energy pertains to the radiation from radium (B + C). The γ-rays from RaB account for 0.11 of the total energy emitted by radium (B + C). This value is given by Rutherford et al[16] as the most accurate one. Consequently, the total energy emitted in the form of γ-rays per disintegration of RaC equals 1.81 (1 - 0.11) = 1.6. Mev. The results of computations based on our relative intensity values and the indicated value of Q are listed in Table 2.

Table 2

Evaluated numbers of quanta per disintegration for RaC

	E_γ, kev	N_γ	$N_\gamma k$, number quanta per decay	$N_\gamma k E_\gamma$ number carried off by given gammas
1	609,3	7,31	0,398	0,242
2	652,4	0,56	0,030	0,020
3	660,9			
4	703,2	0,30	0,016	0,011
5	768,7	1,02	0,056	0,043
6	787,1	0,25	0,013	0,011
7	806,3	0,33	0,018	0,014
8	821,3	0,14	0,008	0,006
9	934,8	0,74	0,040	0,037
10	1120,4	2,92	0,159	0,178
11	1155,3	0,44	0,024	0,028
12	1207,1	0,37	0,020	0,024
13	1238,3	1,23	0,067	0,083
14	1281,3	0,34	0,018	0,023
15	1378,2	0,86	0,047	0,065
16—21	1410	0,84	0,046	0,065
22	1509,3	0,60	0,033	0,050
23	1582,9	0,24	0,013	0,020
24	1605,2	0,07	0,004	0,006
25	1668,4	0,11	0,006	0,010
26	1728,3	0,34	0,019	0,033
27	1764,4	2,73	0,149	0,263
28	1783,8	0,58	0,032	0,057
29	1790,7	0,16	0,009	0,015
30	1848,5	0,25	0,014	0,026
31	1862,3	0,28	0,015	0,028
32	1900	0,17	0,009	0,017
33	2016,7	0,06	0,003	0,006
34	2085	0,08	0,004	0,009
35	2117,0	0,28	0,015	0,032
36	2204,2	1	0,054	0,120
37	2290	0,07	0,004	0,009
38	2450	0,36	0,020	0,048
		Totals	1.36	1.60 Mev/decay

We take this occasion to express our gratitude to E.A.Khol'nova for the calorimetric measurements, I.A. Iaritsyna for aid in the photoneutron measurements for the purpose of checking the purity of our sample, I.F.Uchevatkin and graduate students Iu.Starostenko, N.Gluchkova and B.Ovchinnikov who participated in the measurements.

"D.I.Mendeleev" All-Union Scientific Research Institute of Metrology

---

Erratum note regarding Ref.11: In Ref.11 certain arithmetical errors crept into the calculation of λ_{e^-} and λ (Russ.pp.938 & 939; trans.pp.849 & 850, Bulletin, Vol.20, No.8). On the former page the text from the middle of the page should read:

"For our 806 kev case, $\lambda_{..} = 6.9 \cdot 10^{10}$ sec and, consequently, $\lambda_{e^-} = \lambda_{\gamma_{806}} \frac{N_{e^-}}{N_{\gamma_{806}}} = 2.0 \cdot 10^{10}$ sec and $T_{e^-} = 3.5 \cdot 10^{-11}$ sec.

The corresponding overlap parameter of the wave function is $\rho \approx 0.13$. The deduced value of T_{e^-} is in agreement with the evaluations of Bethe and Drell."

On the latter page, read:

"... $(\Pi_1 - \Pi_0)$, where Π_1 is computed by means of the same formula (2) as Π_0 but for ... = 2. As a result, we obtain ... = $7.3 \cdot 10^4$ sec^{-1} and the ratio ... = $2.3 \cdot 10^5$."

The calculated value of ... is in fairly good agreement with the experimental one.

References

1. G.Latyshev, Rev.Mod.Phys., 19,132 (1947); O.von Baeyer, O.Hahn, L. Meitner, Phys.ZS.,12,1099 (1911); E.Rutherford, H.Robinson, Phils.Mag., 26, 717 (1913); C.Ellis & G.Aston, Proc.Roy.Soc., A105,165 (1924); K.Siegbahn, Arkiv f.Mat.Astr.och.Fysid, 30A,20 (1944); S.Kageyama, J.Phys.Soc.Japan, 7,93 (1952); J.Itoh & Y.Watase, Phys.Math.Soc.Japan, 20,142 (1938); K.Mann & M.Ozeroff, Can.J.of Research, 7,164 (1949).

2. G.Latyshev, A.Kompaneets, N.Borisov & P.Gusak, Journ.Phys.USSR,3,251, (1940); G.Latyshev, Zhur.eksp.i teor.fiz., 14, 65 (1944).

3. M.Mladjenovic & A.Hedgran, Arc.för.Fiz., 8,49 (1954); Phisica, 18,1242 (1952).

4. C.Ellis, Proc.Roy.Soc., A143,350 (1934); J.Cork, C.Branyan, A.Stoddard, H.Keller, J.LeBlanc & W.Childs, Phys.Rev., 83,681 (1951).

5. M.Mladjenovic & H.Slatis, Arc. för.Fys., 8,65 (1954).

6. B.Dzhelepov & S.Shestopalova, Izv.AN SSSR, Ser.fiz., 20,328 (1956). (Trans. Bulletin, 20, No.3, 302.)

7. K.Aglintsev, Dozimetriia ioniziruiushchikh ezluchenii (Dosimetry of ionizing radiations), L., 1950.

8. B.Dzhelepov & S.Shestopalova, Nuovo Cim., 3 Suppl., 1,54 (1956).

9. B.Dzhelepov, N.Zhukovskii & Iu.Khol'nov, Doklady AN SSSR, 77,233 (1951).

10. G.W.McClure, Phys.Rev., 90,796 (1953).

11. B.Dzhelepov & S.Shestopalova, Izv.AN SSSR, Ser.fiz., 20,933 (1956). (Trans.Bulletin, 20, No.8, 845.)

12. E.Rutherford & H.Robinson, Phil.Mag., 25,312 (1913); C.Ellis, W.Wooster, Phil.Mag.,50,521 (1925); L.Gray, Proc.Roy.Soc., 159,263 (1937).

13. J.Zlotowski, J.Phys.et Rad., 6, 242 (1935).

14. O.Hahn & L.Meitner, ZS.f.Phys., 26, 161 (1924).

15. G.Whyte, Canad.J.of Physics, 30,442 (1952).

16. E.Rutherford, J.Chadwick & C.Ellis, "Radiations from Radioactive Substances", Cambridge, 1930.

NEW LINES IN THE SPECTRUM OF RaC

- I.F.Uchevatkin & S.A.Shestopalova

In their report, Dzhelepov & Shestopalova[1] (see preceding article) note that in investigating the γ-spectrum of RaC they observed in the region extending from the 2450 kev line up to about 2700 kev a rise in the number of coincidences above the background that cannot be explained by the influence of neighboring lines. We decided to investigate this section of the spectrum on the Elotron under enhanced transmission conditions. The usual cellophane target was replaced by a beryllium target 330 μ thick and the defining slits in front of the counters were increased to twice the width and height employed under standard conditions[2]. This led to an increase of the transmission by a factor of about 30 with an accompanying decrease of the resolution by a factor of 2.2 (at E_γ = 2700 kev). In order to determine the line shape under these conditions, we carefully investigated the 2614 kev line of ThC'' and the 2758 kev line of Na^{24}.

In investigating the spectrum of RaC in the region above 2450 kev, we observed a systematic appreciable excess of coincidences above the background up to about 3200 kev; the background in this region of the spectrum amounted to ~10% of the effect (coincidence count with the target in the beam). A substantial reduction of the background was realized by replacing the lead collimator by a lead plugged tungsten collimator and using an amplifier with $\tau \approx 10^{-6}$ sec.

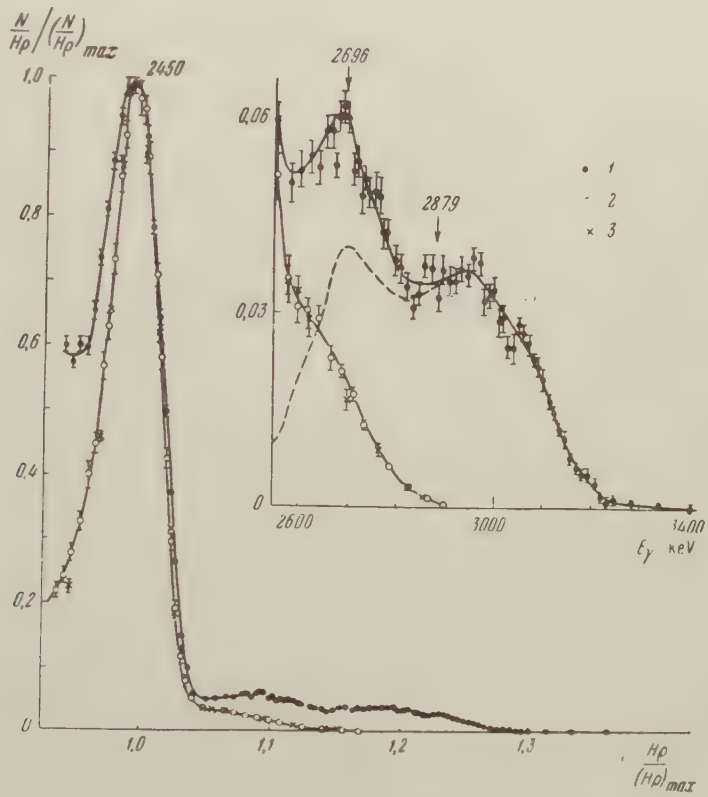

Gamma-spectrum of RaC in the 2450-3400 kev region: 1) spectrum of RaC, 2) 2614 kev line of ThC'', 3) 2758 kev line of Na^{24}. The insert shows the 2550-3400 kev section of the spectrum to an enlarged scale. Dash lines - RaC spectrum with the high-energy tail of the 2450 kev line subtracted.

The results of measurement are shown in the accompanying figure together with the records of the ThC" 2614 kev and Na^{24} 2758 kev lines.

For convenience of comparison the spectra are plotted in "relative" coordinates. It will be obvious from the figure that the high-energy tail of the 2450 kev RaC line, assuming it to be similar to tails of the ThC" and Na^{24} lines, lies well below and ends before the observed excess of recoil electrons from RaC. In the insert we show this excess with the "tail" of the 2450 kev line subtracted (dash line). The figures (2696 and 2879) above the arrows give the energies in kev of the two excited levels of RaC' known in this region from the long-range α-particle measurements of Rutherford et al[3]. It may be inferred from our results that the excess of recoil electrons is due to γ-lines that have not been hitherto detected.

In 1950, Bishop, Wilson & Halban[4] reported on their search for RaC γ-lines in the region of 3 Mev by observation of photoprotons produced by disintegration of deuterium. These authors did not succeed in detecting any γ-lines in this energy region; they indicate only the upper bound for the number of quanta per disintegration: $\leq 10^{-4}$.

We evaluated the total intensity of the detected "residue": it is 10 times weaker than the 2450 kev line or roughly $2 \cdot 10^{-3}$ quanta per decay.

B.M.Ovchinnikov of Leningrad Polytechnical Institute participated in the measurements of the RaC spectrum and the ThC" 2614 kev line. The authors acknowledge their obligation to B.S.Dzhelepov for discussion of the results and A.A.Pavlov for constructing the coincidence amplifier.

"D.I.Mendeleev" All-Union Scientific Research Institute of Metrology

References

1. B.S.Dzhelepov & S.A.Shestopalova, Present issue of the Bulletin, p.992.
2. B.S.Dzhelepov & S.A.Shestopalova, Izv.AN SSSR, Ser.fiz., 20,328 (1956). (Trans.Bulletin, 20, No.3, 302.)
3. E.Rutherford, W.Lewis & B.Bowden, Proc.Roy.Soc., A143, 347 (1933).
4. G.R.Bishop, R.Wilson & H.Halban, Phys.Rev., 77, 416 (1950).

NEUTRON DEFICIENT ISOTOPES OF THE RARE EARTH ELEMENTS FORMING AS A RESULT OF SPALLATION OF Ta UNDER BOMBARDMENT WITH 660 Mev PROTONS. Part 1.

- G.M.Gorodinskii, A.N.Murin, V.N.Pokrovskii & B.K.Preobrazhenskii

The spallation reaction on tantalum bombarded with 340 Mev protons was studied by Nevrik & Seaborg[1]. We undertook an investigation of the spallation products formed in the bombardment of Ta with 660 Mev protons. For the specific purposes of this study we chose the rare earth elements inasmuch as the neutron deficient lanthanide isotopes have been little studied and are partly unknown.

The tantalum targets were irradiated in the synchrocyclotron of the Joint Institute for Nuclear Research. The irradiation was carried out either in the intrinsic beam (1-2 hours) or in the scattered beam (several months). Such prolonged irradiation was necessary for accumulation of sufficient long-lived activities. The separation of the rare earth elements was realized by the chromatographic procedure described by Preobrazhenskii et al[2]. The high quality separation afforded by this procedure greatly facilitated our task.

The individual fractions were investigated primarily by scintillation techniques by means of a specially constructed γ-spectrometer and a γ-γ coincidence set-up. We also made use of data on the half-lives obtained through measurements with an end-window counter and information on the type of radiation and β-particle energies derived from measurements made on a simple Danish type magnetic spectrometer.

The scintillation γ-spectrometer, constructed in our laboratory, is based on the conventional single crystal, one channel design. It employs a non-jamming amplifier with pulse shaping in a shorted artificial line. Particular attention was paid to stability of operation, particularly stability of the discrimination thresholds in designing the set-up. The use of different auxiliary measures and devices (such as automatic shifting of the discriminator gate after a given time, alternate recording of the number of pulses by two mechanical registers, automatic recording of the γ-spectra, etc.) greatly facilitated the work and appreciably enhanced the "productivity" of the set-up. A standard NaI(Tl) crystal measuring 30 by 20 mm and a FEU-S type photomultiplier were used in the spectrometer. The relative half-width of the Cs^{137} γ-line (662 kev) was 8.6 or 9.3%, depending on the experimental geometry (see below).

The γ-γ coincidence discrimination in energy set-up was also based on the scintillation principle (NaI(Tl) crystals and FEU-11 type photomultipliers) and had the following characteristics: resolving time - $8 \cdot 10^{-7}$ sec; half-width of the Cs^{137} γ-line - 10% in each channel. A detailed description of the γ-spectrometer and the γ-γ coincidence circuit will be published later.

Among our aims was determination of the relative γ-line intensities. Hence we gave a great deal of attention to determining the line shape and eliminating the back-scattering peak.

Our best results (virtually complete absence of a back-scattering peak) were obtained by using a lead collimator with a tapered aperture. To eliminate x-ray fluorescence of the lead the truncated-cone opening was lined with successive layers of tantalum, tin and copper foil (0.5 mm Ta + 0.25 mm Sn + 0.3 mm Cu). With this experimental geometry the half-width of the Cs^{137} γ-line was 9.3%.

Inasmuch as the activity of some of the sources was insufficient for working with this geometry, these were placed in the immediate proximity of the crystal - so-called "0"-geometry. The back-scattering peak is reduced as the source is brought nearer to the crystal which facilitates working with this

geometry. It proved possible to avoid x-ray fluorescence of the lead in this case through suitable arrangement of the lead shielding; in this case the half-width of Cs^{137} line was 8.6%.

The line shapes were investigated with both geometries. For this purpose we chose the single γ-lines of such isotopes as Ce^{141} (145 kev), Hg^{203} (279 kev), Cr^{51} (320 kev), Au^{198} (411 kev), and Cs^{137} (662 kev) as well as their x-ray radiations. The results obtained allowed of resolving the spectrum into individual lines at all intermediate energies. The experimental technique for determining the line shape has obvious advantages over the procedure of theoretically calculating the line shape, frequently employed in scintillation γ-spectrometery (see, for example, Ref.3).

With the aim of determining the detecting efficiency of the crystal as regards γ-rays of different energies, we recorded the γ-spectra of β^--active isotopes having single γ-lines. We determined the corresponding number of decays by β measurements with a "4π" counter. From the known number N of decays per unit time and the number of pulses per unit time at the photopeak taken from the experimental spectrum (i.e., from the experimentally determined area under the photopeak - S_γ) one can readily determine the recording efficiency K_γ for photons of the given energy:

$$K_\gamma = S_\gamma / N_\gamma. \tag{1}$$

Here N_γ is the number of γ-quanta, a quantity that can readily be determined if the character of the decay scheme and the values of the conversion coefficient are known.

Further we took advantage of the fact that the x-ray radiation of our samples appears only due to conversion of the γ-rays. In view of this the relationship between the number N_x of x-ray quanta (K-line) and the number of γ-transitions is described by

$$N_x = \alpha_K \omega_K N_\gamma,$$

where α_K is the K shell conversion coefficient and ω_K is the fluorescence yield on the K shell. Then the detection efficiency for x-rays is

$$K_x = \frac{S_x}{N_x} = \frac{1}{\alpha_K \omega_K} \cdot \frac{S_x}{S_\gamma} K_\gamma. \tag{2}$$

Thus we were able to evaluate the efficiency of the crystal as regards detection of x-rays.

Inasmuch as the shape of the photopeak is very nearly gaussian[4], one can readily write the analytic expression for S, namely

$$S = \frac{1}{2} \sqrt{\frac{\ln 2}{\pi}} n \Delta E,$$

where n is the number of pulses per unit time measured at the maximum of the photopeak (per 1 kev) and ΔE is the half-width of the photopeak for the given energy in kev.

Expressions (1) and (2) were used to calculate the detection efficiencies for x-rays and γ-quanta of energies 36 kev (Ce^{141} K x-rays), 73 kev (Hg^{203} K x-rays), 145 kev (Ce^{141}), 279 kev (Hg^{203}) and 662 kev (Cs^{137}). The efficiency for 411 kev (Au^{198}) was determined from Eq.(2) taking the value of K_x from the previous measurements.

The results obtained for the efficiency of the 30 x 20 mm NaI(Tl) crystal are shown in Fig.1. The drop in efficiency in the low energy region is connected with absorption in the aluminum container and the MgO layer surrounding the crystal. Inasmuch as we did not know the effective thicknesses of these absorbers, we checked this assumption in the following manner. We determined the thickness of an aluminum layer that would yield equal detection efficiencies for 36 and 73 kev quanta (the efficiency of the crystal itself in the 100 kev region is commonly assumed to be energy independent). The order of magnitude obtained (~2 mm Al) and the fact that this agreed with our estimates of the approximate effective absorber thickness for the different geometries confirmed the validity of our inferences. After introducing the correction for absorption, we can evaluate the solid angle viewed by the crystal with the different geometries. Obviously, it is characterized by the maximum possible efficiency value with the given geometry and amounts to 0.183 for the "0"-geometry and 0.003 for the geometry with the collimator.

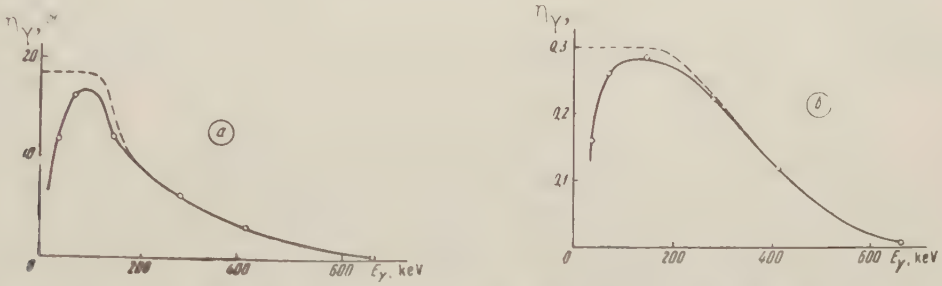

Fig.1. Efficiency η_γ of the 30 x 20 mm NaI(Tl) crystal as a function of the energy. η_γ is given in % of the total (in 4π) number of quanta. The solid curve is drawn through the experimental points; the dash-line curve is plotted taking into account the absorption in the container and the MgO surrounding the crystal. a) "0"-geometry; b) geometry with collimator.

The general appearance of the efficiency curves (Fig.1) and the increase in relative efficiency for hard γ-rays as the source is moved further from the crystal are in agreement with the results of the theoretical calculations of Liden & Starfelt[5] and the data of Johansson[6]. In view of the fact that it was impossible to eliminate certain experimental uncertainties, the accuracy of determination of relative line intensities with reference to the curves of Fig.1 does not exceed 20%. In the energy region below 70 kev evaluation of the intensities is further hampered by apparatus short-comings (low resolution, inadequate number of experimental points at the photopeak, etc.). Hence for the most part we did not calculate the intensities in this region. We hope that improvements in technique will enable us in the future to enhance substantially the accuracy of intensity determination.

We note that cascade γ-rays can yield an aggregate pulse and that thus there can appear in the spectrum an additional peak with the total energy of the coinciding γ-rays. Naturally, such coincidences are evinced only with a sufficiently large solid angle. Under our conditions, they were clearly recorded with the "0"-geometry. This effect proved useful in interpreting the spectrum. First, we were able to check the results obtained on the γ-γ coincidence set-up (a similar idea was utilized by Lu and Wiedenbeck[7]); and, second, we were able to evaluate the intensity of the coinciding γ-rays. Thus the number of photopeak coincidences for two γ-lines (i.e., the area

under the coincidence peak) $S_{1,2}$ according to the general coincidence formula is given by

$$S_{1,2} = \frac{N_1 N_2 \varepsilon_1 \varepsilon_2}{N} \qquad (3)$$

where N is the number of cascade transitions. Obviously, when N_1, N is known one can readily determine N_2 from (3). We shall make use of Eq.(3) below.

Let us now turn to the results of measurement. For convenience we shall proceed in order of decreasing mass number. In the present communication we shall consider the isotopes of Lu, Yb and Tu with A from 173 to 165.

A = 173. In the Lu fraction (short-term bombardment) there were detected[8] traces of a long-lived activity. According to the tables of Seaborg[9], it could be ascribed to Lu^{174} or Lu^{173}. From the γ-γ coincidence measurements it may be concluded that the Lu^{174} content does not exceed 10% of the Lu^{173} content (thus, for example, the absence of coincidences of the 79 and 180 kev γ-rays indicates the absence of the γ-spectrum associated with the rotational band of the even-even Yb^{174} nucleus). Gromov & Dzhelepov[10] came to the same conclusion. Hence in processing our results, there was assumed to be no Lu^{174} impurity present.

Lu^{173} has a period of ~200 days (not 500 days as indicated in Ref.9). We consider that our value is reliable inasmuch as it agrees with that obtained by Bobrov et al[10]. The Lu^{173} spectrum (Fig.2) consists of γ-lines having energies of 77, 101, 177 and 274 kev. These values are in good agreement with the data of Bobrov et al[10]: 78.7, 100.7, 179.5 and 272.5 kev. The relative intensities of the enumerated γ-lines, according to our measurements, are 1.95 : 1.0 : 0.81 : 3.62. Our coincidence measurements showed that the 77 and 101 kev γ-rays coincide in time, that the 177 and the 274 kev γ-rays are not in coincidence and, finally, that all the γ-lines coincide with the x-ray radiation.

On the basis of the data of Bobrov et al[10] and our results one can construct the level scheme, characteristic of even-odd nuclei (Yb^{173}), shown in Fig.3.

The first two levels are the levels of the familiar even-odd nucleus rotational band in which the cross-over transition (180 kev) has the multipole order E_2, while the cascade transitions (79 and 101 kev) are predominantly M1. This is substantiated by the data of Bobrov et al[10]. Taking the conversion

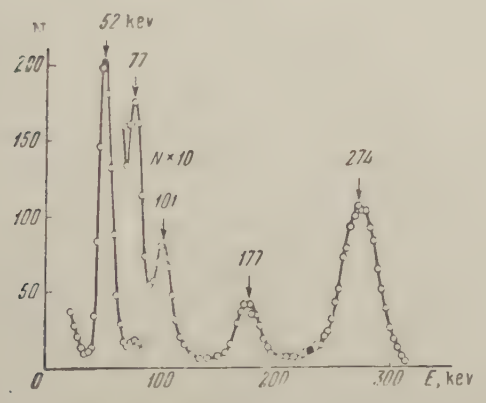

Fig.2. γ-Spectrum of Lu^{173} (geometry with collimator).

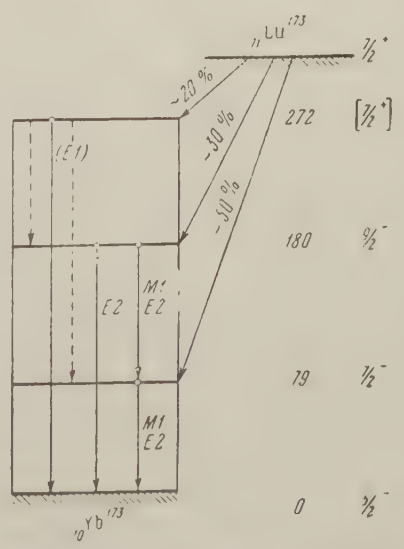

Fig.3. Decay scheme for Lu^{173}.

coefficient values listed by these authors, one can obtain the relative abundances of the direct and cascade transitions from the 180 kev level and therefrom (see Ref.11), for example) evaluate the admixture of E2 in the 101 and 79 kev transitions. Calculation yields a value of ~5% for the E2/M1 ratio, which is in good agreement with the evaluation of Bobrov et al based on the K/L ratio.

The 272 kev level is in all probability a single particle one. The possible spin and parity assignments (7/2+ or 7/2-, see Ref. 10) are in agreement with the scheme of Mottelson & Nilsson[12]. The fact that there are no transitions from this level to the rotational levels is also evidence in favor of the assumption that the 272 kev level is a single particle one. The spin and parity assignment for this level can be made more precise in the following manner. Taking $\alpha_K = 0.21$ for the 180 kev transition (the theoretical value for E2) and utilizing the data of Bobrov et al[10] on the relative intensities of the K lines of the 272 and 180 kev transitions (0.16 : 0.19) and our data on the relative intensities of the corresponding γ-lines (0.81 : 3.62), one can evaluate α_K for the 272 kev transition. Calculation yields $\alpha_K \approx 0.05$, which is more consistent with the value for E3 (0.02) than for M1 (0.18). This being the case the 7/2+ assignment for the 272 kev level is preferable.

Taking the theoretical conversion coefficients for the indicated multipole orders (neglecting the mixture of E2 in the cascade transitions), one can deduce the relative abundances of the transitions from each level and from this evaluate the population of the levels. The values obtained in this way are shown in Fig.3. Absence of transitions to the ground level is indicated by comparison of the x-ray radiation intensity as calculated from the total number of transitions (deduced as explained above) with the experimentally determined intensity. The last proved to be some 25% less than the calculated value; in view of our experimental uncertainties the agreement may be considered satisfactory.

Regarding the distinctive features of the decay scheme for Lu^{173}, namely, the absence of transitions to the ground level of Yb^{173} and the relatively low population of the single particle 272 kev level, it may be noted that the first can apparently be explained by the supplementary selection rules given by Alaga[13], while the second is explicable from energy considerations.

A = 172 & 171. The activity with a period of 7-8 days detected in the Lu fraction can, according to Nervik & Seaborg[1] and Gorodinskii et al[8], be ascribed to Lu^{172} or Lu^{171}, or a mixture thereof. We are unable at present to differentiate between these isotopes or give reliable information on the γ-spectrum of their mixture. We can only note that the most noticeable lines in the γ-spectrum of Lu^{172} + Lu^{171} are observed at ~180, 730 and 1100 kev. The existence of these lines has been substantiated by Bobrov et al[10].

A = 170 & 169. We also observed a 1.5-2 day activity in the Lu fraction. According to Seaborg's tables[9] it may belong to Lu^{170}. As has been noted by Nervik & Seaborg[1], however, and substantiated by our earlier measurements[8], Lu^{169} should also have a half-life in this range; the existence and approximate period of this isotope have been firmly established by us by means of repeated chromatographic separation of the daughter element Yb^{169}. We refrain from giving our data on the decay of Yb^{169} here inasmuch as they are in good agreement with the information in the literature.

Thus the 2-day activity must be attributed to either Lu^{169} or a mixture of Lu^{170} and Lu^{169}. Investigation of the γ-spectrum of Lu^{170} + Lu^{169} is rendered difficult not only by the complicated character of this spectrum itself but also by the presence of Lu^{172} and Lu^{171} in the lutetium fraction (see above); study of this spectrum is further hampered by the intense lines

of the daughter isotope Yb^{169}. At present we can only indicate that the γ-spectrum of Lu^{170} + Lu^{169} lies mainly in the low energy region (< 300 kev).

A = 168. In the Tm fraction we detected a long-lived activity with a half of ~100 days which one might be inclined to ascribe to Tm^{168}. Analysis of the γ-spectrum showed, however, that the observed γ-lines (~80,100,200, 350,800 and 1100 kev) do not fit into the simple rotational band scheme that should obtain for the even-even Er^{168} nucleus. The inadequate activity of our sources did not allow of carrying out the essential γ-γ coincidence experiments and evaluating the relative γ-line intensities. It is possible that we were dealing here with an admixture of the β^--emitter Tm^{170} or the presence of some isomer.

A = 167. This mass number corresponds to one of the neutron deficient Tm isotopes. The γ-spectrum of 9.6-day Tm^{167} was investigated by Nervik & Seaborg[1], who give the following line energies: 49 (x-rays), 115, 202, 515 and 720 kev. In our measurements the 515 and 720 kev lines were not detected; if they exist at all, their relative intensities must be at least one order of magnitude lower than indicated by Nervik & Seaborg. The γ-spectrum of Tm^{167} in the low-energy region is shown in Fig.4. It will be seen that the peak in the vicinity of 115 kev is due to surposition of the back-scattering peak from the 207 kev line and the 105 kev peak due to coincidences of the x-rays from Er^{167} (49 kev) with the 57 kev radiation.

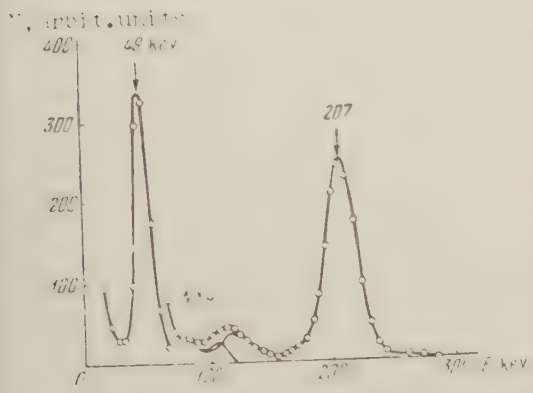

Fig.4. γ-Spectrum of Tm^{167} ("0"-geometry). The inscribed lines in the 100 kev region show the resolution of the spectrum into the back-scattering peak (from the 207 kev gammas) and the peak due to coincidences of the 49 and 57 kev radiations.

That the 57 kev line does exist was shown by Gromov, Dzhelepov & Preobrazhenskii (Ref.14). This line cannot be distinguished directly on the scintillation γ-spectrometer due to inadequate resolution in this energy region; nevertheless its existence may be regarded as firmly established. First, it is evinced in the character of the photopeak due to coincidences of this line with x-ray radiation. The actual existence of this peak was checked in the following manner. The γ-spectrum of Tm^{167} was recorded through a 0.12 mm Sn + 0.3 mm Cu absorber which appreciably attenuated the x-ray radiation but had virtually no effect on the intensity of the 207 kev line. With such an absorber the 57 and 49 kev quanta coincidences should disappear, while the back scattering peak due to the 207 kev line should persist. This is precisely what our experiment showed. Second, the existence of the 57 kev line was substantiated by direct γ-γ coincidence experiments.

In order not to return to the coincidence experiments, we note here that the 207 kev line does not yield coincidences with the x-ray radiation.

Thus according to our data, the γ-spectrum of Tm^{167} consists of lines with energies of 49 (x-rays), 57 and 207 kev. Direct evaluation of their relative intensities is difficult (we recall that in the ~70 kev region our line intensity data must be used with circumspection). We can circumvent this difficulty, however, by turning to the data on the coincidences between the 49 and 57 kev quanta in the "0"-geometry. Thus, invoking Eqs.(1) and (3), we can write

$$S_{\gamma_{207}} = K_{207} N_{\gamma_{207}},$$

and

$$S_{\text{coinc.}} = \frac{K_{49} N_{49} K_{57} N_{\gamma_{57}}}{N'} = \omega_K K_{49} K_{57} N_{\gamma_{57}}$$

(inasmuch as $N_{49}/N' = \omega_K$, where N' is the number of decays to the level from which the 57 kev transition originates), whence

$$\frac{N_{\gamma_{57}}}{N_{\gamma_{207}}} = \frac{K_{207}}{\omega_K K_{49} K_{57}} \frac{S_{\text{coinc.}}}{S_{\gamma_{207}}}.$$

Substituting our experimental values, we obtain $N_{\gamma_{57}}/N_{\gamma_{207}} = 0.22$.

The decay scheme for Tm^{167}, proposed by Gromov, Dzhelepov & Preobrazhenskii (Ref.14) and refined with reference to our data is shown in Fig.5. From analysis of the conversion electron spectra these authors came to the conclusion that the possible assignments for the 264 kev level are 1/2+, 3/2+ or 3/2-. The number of 57 kev photons per disintegration for different spin and parity assignments was calculated on the basis of the theoretical conversion coefficients and relative conversion line intensities. For 1/2+ this number is 0.75, for 3/2+ it is 0.66 and for 3/2- it is 0.07 photons per decay.

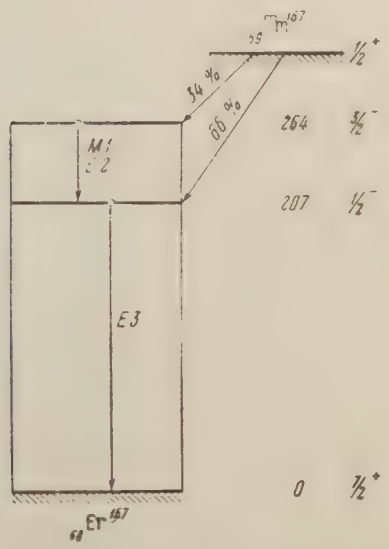

Fig.5. Decay scheme for Tm^{167}.

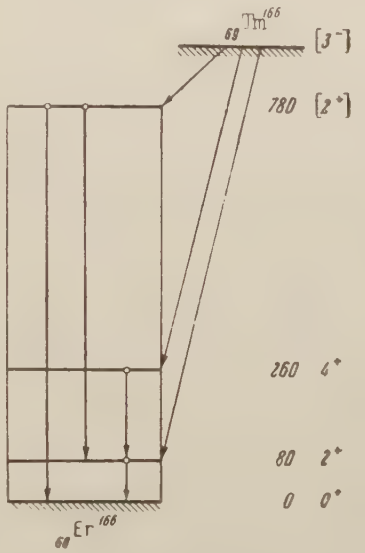

Fig.6. Tentative decay scheme for Tm^{166}.

Taking advantage of the fact that the number of transitions from the 207 kev level equals the total number of disintegrations and knowing the conversion coefficients for this transition (see Ref.14), one can calculate the number of 57 kev photons per disintegration. According to our data

$$\frac{N_{\gamma_{57}}}{N} = \frac{N_{\gamma_{57}}}{N_{\gamma_{207}}} \frac{1}{1+\alpha_{207}} = 0.09 \pm 0.02,$$

where α_{207} is the total conversion coefficient for the 207 kev transition and N is the total number of disintegrations. The indicated uncertainty is estimated in accord with the maximum and minimum number of coincidences evaluated in resolution of the γ-spectrum. Knowing the $N_{\gamma_{57}}/N$ ratio, we can unambiguously indicate the assignment for the 264 kev level (3/2-) and determine the population of the levels (see Fig.5).

A = 166. We observed two isotopes with this mass number: Yb^{166} (~60 hours) and its daughter Tm^{166} (8 hours). Nervik & Seaborg[1] investigated the γ-spectrum of the Yb^{166} + Tm^{166} mixture and report γ-rays of 80, 112, 140, 180, 670, 800 and 1320 kev energy.

We separated Tm^{166} chromatographically from the Yb fraction. Its γ-spectrum consisted of lines having energies of 80, 180, 690 and 780 kev and a doubtful line at ~470 kev. The γ-spectrum of Tm^{166} was studied at the initial stage of the investigation with a crystal of somewhat smaller size than subsequently used. Hence we cannot at present give the relative line intensities. It may be that we failed to detect the high-energy ~1300 kev line owing to the lower efficiency of the small crystal. In view of the short half-life of Tm^{166}, we were unable to carry out γ-γ coincidence measurements.

Nevertheless, we feel that we are justified in supplementing the decay scheme for Tm^{166} proposed in Ref.7 by introduction of a 780 kev level (Fig.6). The 780 kev level is, in all probability, a γ-vibrational one; its spin and parity are given on the basis of the review presented by L.A.Sliv at the Seventh Conference on Nuclear Spectroscopy. The assignment for the ground state was made according to Peker[15].

The γ-spectrum of Yb^{166} consists of two lines at 110 and 140 kev; observation of this spectrum was hampered by the intense lines of Yb^{169} in this region.

A = 165. The observed isotopes with this number were Tm^{165} (1-day) and its daughter Er^{165} (10 hours). According to our measurements the γ-spectrum of Tm^{165} certainly comprises lines at 240, 300, 457, 830 and 1160 kev. According to the results of Gromov, Dzhelepov & Preobrazhenskii[14] there are present in the γ-spectrum of Tm^{165} lines with energies of 54, 80, 218, 243, 298 and 459 kev. The 54 kev line could not be resolved by us; the 80 kev line was only weakly discernible but in view of the data of Ref.14 one can be certain that it exists. The 218 kev line could not be detected in our experiments inasmuch as it is too close to the 207 kev line of Tm^{167}. The presence of a mixture of isotopes in the Tm fraction greatly hampered both evaluation of the relative γ-line intensities of Tm^{165} and the γ-γ coincidence measurements.

The spectrum of Er^{165} in the energy range to 1 Mev contains no γ-lines (Er^{165} is reported to decay with the emission of x-rays).

We wish to express our obligation to V.P.Dzhelepov and the entire technical personnel of the Joint Institute for Nuclear Research synchrocyclotron for their assistance and to V.N.Mekhedov and V.A.Khalkin for facilitating the long-term irradiations. We thank K.Ia.Gromov and B.S.Dzhelepov for communicating their data prior to publication and for valuable discussions. We are grateful to L.K.Peker for his interest in the work and participation in discussion of the results.

"V.G.Khlopin" Radium Institute of the
Academy of Sciences of the USSR

References

1. W.E.Nervik & G.T.Seaborg, Phys.Rev., 97, 1092 (1955).
2. B.K.Preobrazhenskii, O.M.Lilova, A.N.Dobronravova & E.D.Teterin, Zh.N. Kh. (J.Inorgan.Chem.), 1, 2294 (1956).
3. D.Maeder, R.Müller & V.Wintersteiger, Helv.Phys.Acta, 27, 1 (1954).
4. G.F.J.Garlick & G.T.Wright, Proc.Phys.Soc., B65, 415 (1952).
5. K.Liden & N.Starfelt, Ark.Fys., 7, 427 (1954).
6. K.E.Johansson, Ark.Fys., 10, 247 (1956).
7. D.C.Lu & M.L.Wiedenbeck, Phys.Rev., 94, 501 (1954).
8. G.M.Gorodinskii, A.N.Murin, V.N.Pokrovskii, B.K.Preobrazhenskii & N.E.Titov, Doklady AN SSSR, 112, 405 (1957).
9. J.M.Hollander, I.Perlman & G.T.Seaborg, Table of Isotopes, Revs.Mod. Phys., 25, 469 (1953). (Cited in Russian trans.)
10. Iu.G.Bobrov, K.Ia.Gromov, B.S.Dzhelepov & B.K.Preobrazhanskii, Present issue of the Bulletin, p.942.
11. N.P.Heidenburg & G.M.Temmer, Phys.Rev., 104, 981 (1956).
12. B.Mottelson & S.G.Nilsson, Probl.sovr.fiziki (Problems of Modern Physics), 1, 186 (1956).
13. G.Alaga, Phys.Rev., 100, 432 (1955).
14. K.Ia.Gromov, B.S.Dzhelepov & B.K.Preobrazhenskii, Present issue of the Bulletin, p.920.
15. L.K.Peker, Present issue of the Bulletin, p.1030.

ROTATIONAL LEVELS OF Mg^{24}

- L.K.Peker, L.V.Gustova & O.V.Chubinskii

It is obviously of interest to verify the inference from the unified (Bohr-Mottelson-Nilsson) nuclear model that the conditions leading to the ellipsoidal equilibrium shape of the nucleus are realized not only in the region of heavy nuclei ($150 \leqslant A \leqslant 190$ and $A \geqslant 222$) but also in the region of light nuclei, in particular, near A = 24.[1,2] In certain light nuclei one might expect to find rotational levels.

Attempts have been made in a number of recently published reports[1,3-5] to identify some of the lower levels of Mg^{24}, Mg^{25}, Al^{25} and Al^{28} as rotational levels.

The purpose of the present work was to clarify the character of the higher ($E > 4.12$ Mev) excited levels of Mg^{24}.

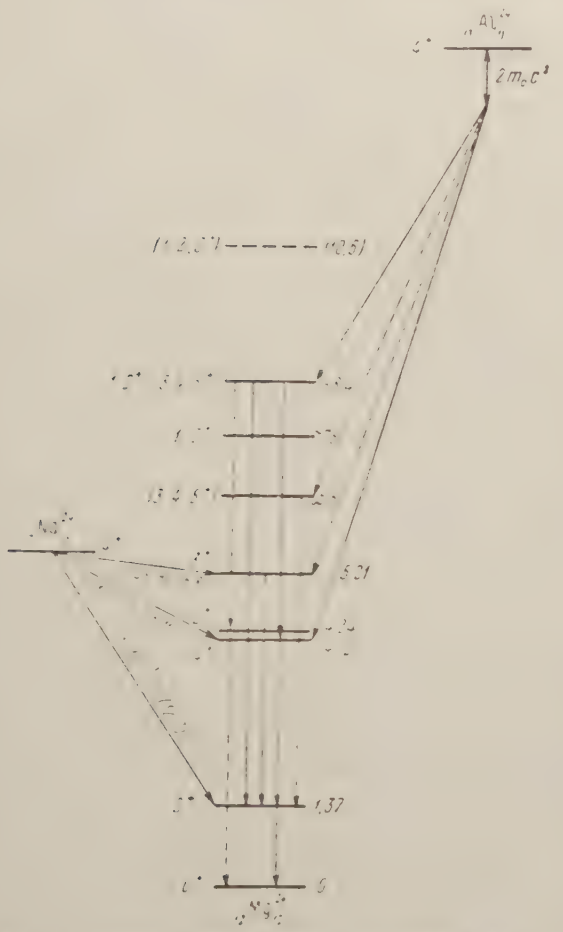

Fig.1. Decay and level scheme for Mg^{24}. The indicated energies are in Mev.

Let us analyze the experimental data on the states of the Mg^{24} nucleus up to 9 Mev energy (Fig.1 and the accompanying table). These data on the excited states of Mg^{24} have been obtained as the result of investigation of β-decay of the two isobars (Na^{24} (β^-) and La^{24} (β^+)) and different nuclear reactions.

The ~8.4 level is of particular interest. It follows from the data on the directional distribution of neutrons[14] from the (d,n) reaction on Na^{23} that the spin and parity of this level are 1+ or 2+. At the same time the β^+-decay data for Al^{24} lead to 3+, 4+ or 5+ for this level[6,12,13]. It may therefore be reasonably assumed that actually there are two different levels in the 8.4 Mev region: one with the configuration 1+ or 2+, the other with 3+, 4+ or 5+.

Bohr & Mottelson[1] infer that the 0 Mev (0+), 1.37 Mev (2+) and 4.12 Mev (4+) levels comprise a rotational band associated with the ground state of Mg^{24}, for which K = 0+ (K is the projection of the total angular momentum of the nucleus on the symmetry axis). Evidence in favor of this is the spin sequence 0+, 2+ and 4+ and the value of the energy ratio $E_{4+}/E_{2+} \approx 3$.

Let us hypothesize that higher-lying levels can also be rotational ones. If we assume that the 4.24 Mev (2+) and 5.21 Mev (3+) levels are the first levels of a rotational band with $I_0 = K = 2+$, then, as may be seen from the table one can also attribute to this band the ~6.5 and 8.4 Mev levels with the assignments 4+ and 5+, respectively. This is consistent with the available experimental data.

Table

Levels of Mg^{24}

Experimental data				Theoretical data					
E, Mev	Measurement procedure	I, π	Measurement procedure	E, Mev	I, π		E, Mev	I, π	
0	[6]	0^+	[6]	0	0^+	First rotational band (Equation (1))			
1,37	[6]	2^+	[6]	1,37	2^+				
4,12	[6]	4^+	[6]	4,60	4^+				
4,24±0,02	Nuclear reaction [7, 8, 9, 10]	2^+	γ–γ correlation [8, 11]	4,24	2^+	Second rotational band (Equation (2))			
	β^+ [6, 12, 13]	1,2^+	(d, n) [14]						
5,21±0,04	β^- [15] β^+ [6, 12, 13] Nuclear reaction [7, 8, 11, 16]	3^+	γ–γ correlation [8, 11] β^- [15]	5,21	3^+				
~6,5	β^+ [6] Nuclear reaction [7, 16, 17]	(3, 4, 5^+)	β^+ [6, 12, 13]	6,5	4^+				
~7,5	Nuclear reaction [7, 18, 19]	1, 2^+	(d, n) [14]	—	—		7,5	1^+	
~8,4	Nuclear reaction [7, 18, 19] β^+ [6, 12, 13]	3, 4, 5^+	β^+ [6, 12, 13]	8,1	5^+				Third rotational band (Eq. (2))
		1, 2^+	(d, n) [14]				8,4	2^+	
(10,6)	(p, γ) [7]	(1, 2, 3^+)	(p, γ) [7]				10—10,5	3^+	

$$E_{rot} = \frac{\hbar^2}{2J} I(I+1),\ I = 0,\ 2,\ 4,\ \ldots \quad (1)$$

$$E_{rot} = \frac{\hbar^2}{2J} [I(I+1) - I_0(I_0+1)],\ I = I_0,\ I_0+1,\ I_0+2,\ \ldots \quad (2),$$

where I is the spin of the level, I_0 is the spin of the lowest state of the rotational band and J is the moment of inertia.

The numbers in brackets are references.

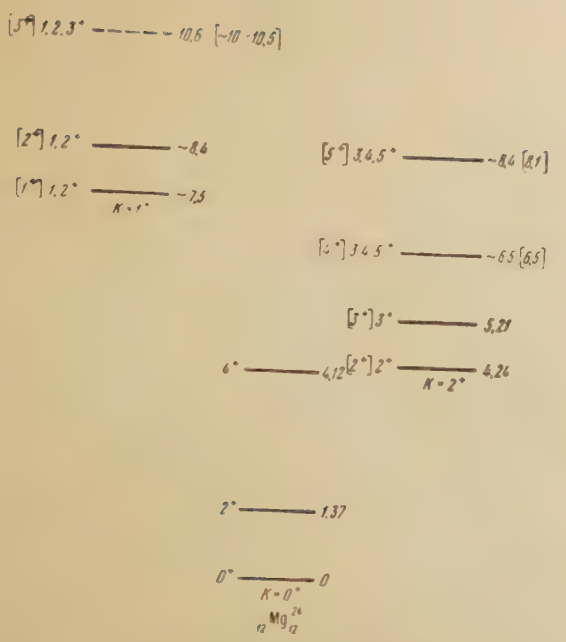

Fig.2. Level diagram for Mg^{24}. At right - energies; at left - spin and parities. The theoretical energy, spin and parity values shown in brackets. The levels pertaining to different rotational bands are shifted relative to each other.

The ~7.5 (1 or 2+) and ~8.4 Mev (1 or 2+) levels may be identified as the first two levels of the first rotational band with K = 1+. In this case the ~7.5 Mev level must have the configuration 1+, and the ~8.4 Mev level should be 2+. The energy of the third excited (3+) level according to Eq.(2) (see under the table), must be of the order of 10-10.5 Mev. Possibly this was the level observed by Turner[7] in the (p,γ) reaction (Turner gives 10.6 Mev).

The energy diagram for Mg^{24} is shown in Fig.2. The levels belonging to different rotational bands have been shifted relative to each other, i.e., arranged in vertical columns. It must be noted that all the known excited levels of Mg^{24} up to 9 Mev energy* fit into the indicated rotational bands.

If the higher excited states (up to 9 Mev) of Mg^{24} are rotational, one can explain some of the distinctive features in the level diagram for Mg^{24} and the β-decay scheme for Na^{24}.

1. It is known that the β-transitions to the rotational levels are unfavored transitions.[1,20] This being so, one can readily explain the low probability of the allowed β^--transitions of Na^{24} to the 5.21 Mev (log ft = = 6.8) and 4.24 Mev (log ft = 6.11) levels of Mg^{24}.**

2. The even parities of the 5.21 Mev (3+) and ~7.5 Mev (1+) levels do not conflict with Glaubman's rule[21], according to which levels with odd spins must have odd parities, inasmuch as this rule pertains only to spherical nuclei.

3. As may be seen from the table, the observed energy value for the 4.12 Mev level is lower than the theoretical one (4.60 Mev). This may be explained by the influence of the two rotational bands with $K \neq 0$.

It is interesting to note that the moment of inertia of the second rotational band is somewhat larger than that of the first. This increase in the value of the moment of inertia might indicate that the excited 4.24 Mev level is a single particle one. If the lowest state of the second rotational band (the 4.24 Mev level) is a single particle one, then one can explain the K = 2+ value for this band by means of Nilsson's scheme.

Identification of the higher excited levels of Mg^{24} as rotational levels is, therefore, consistent with the deduction from the unified model that the Mg^{24} nucleus has an axially symmetric equilibrium shape.

---

*The level at 5.5-5.9 Mev, mentioned by Fisher[16] and Fulbright & Bush[19], cannot as yet be reliably attributed to Mg^{24} inasmuch as the proton scattering experiments in question were carried out on a natural mixture of Mg isotopes.

**Excessively high probability of β^+-decay of Al^{24} to the ~8.4 Mev level of Mg^{24} is, however, inexplicable.

References

1. A.Bohr & B.Mottelson, Kong.Danske Vidensk. Selsk. Mat. Fys. Medd., 30, 1 (1955).
2. S.G.Nilsson, Kong.Danske Vidensk. Selsk. Mat. Fys. Medd.,29,16 (1955).
3. A.E.Litherland, E.B.Paul, G.A.Batholomew & H.E.Gove, Phys.Rev., 102, 208 (1956).
4. A.E.Litherland, E.B.Paul, G.A.Batholomew & H.E.Gove, Bull.Amer.Phys. Soc., 1,29 (1956); H.Gove, A.E.Litherland, E.B.Paul, G.A.Batholomew, Bull. Amer.Phys.Soc., 1,29 (1956).
5. R.K.Sheline, Nucl.Phys.2,382 (1956).
6. P.M.Endt & J.C.Kluyver, Rev.Mod.Phys., 26,95 (1954).
7. O.H.Turner, Austr.J.Phys., 6,4,380 (1953).
8. J.O.Newton, Phys.Rev., 96,241 (1954).
9. R.R.Carlson, E.H.Greer & E.B.Nelson, Phys.Rev., 94,1311 (1954).
10. H.J.Hausman, A.J.Allen, J.S.Arthur, R.S.Bender & C.J.McDole, Phys.Rev., 88, 1296 (1952).
11. P.J.Grant, J.C.Rutherglen, F.C.Flack & G.W.Hatchinson, Pros.Phys.Soc., 68A, 369 (1955).
12. S.W.Breckon, A.Henrickson, W.M.Martin & J.S.Foster, Canad.J.Phys., 32, 223 (1954).
13. N.W.Glass & J.R.Richardson, Phys.Rev., 98, 1251 (1955).
14. J.M.Culvert, A.A.Jaffe, A.E.Litherland & E.E.Maslin, Pros.Phys.Soc., 68A, 1008 (1955).
15. O.V.Chubinskii, L.V.Gustova, B.S.Dzhelepov & P.F.Ermolov, Report at the Fourth All-Union Conference on Nuclear Spectroscopy, 1956.
16. G.E.Fisher, Phys.Rev., 96, 704 (1954).
17. C.J.Baker, J.N.Dodd & D.H.Simmons, Phys.Rev., 85,1051 (1952).
18. C.E.Mandeville, Phys.Rev., 76, 436 (1949).
19. H.W.Fulbright & R.R.Bush, Phys.Rev., 74, 1323 (1948).
20. L.K.Peker, Thesis, FTI, USSR Academy of Sciences, 1956.
21. M.J.Glaubman, Phys.Rev., 90, 1000 (1953).

INVESTIGATION OF THE (α,n) REACTION ON OXYGEN

- I.A.Serdiukova, A.G.Khabakhpashev & E.M.Tsenter

Natural oxygen consists of the three isotopes O^{16}, O^{17} and O^{18}, whose relative abundances are 99.759, 0.037 and 0.204%. The (α,n) reactions on these isotopes have the following Q-values: -12.1 Mev on O^{16}, +0.52 Mev on O^{17} and -0.7 Mev on O^{18}.

Thus with all known α-emitters, the (α,n) reaction can proceed only on the isotopes O^{17} and O^{18}.

The neutron yield from the bombardment of natural oxygen with α-particles shows that at least one of these isotopes has a large cross section for the (α,n) reaction. It does not necessarily follow, however, from the published data[1,2] on the O^{18} (α,n) Ne^{21} reaction that O^{18} is the isotope with the large cross section.

We felt it would be of interest to determine which isotope is responsible for the high neutron yield, evaluate the cross section and also investigate the γ-radiation accompanying this reaction.

Source	Concentration, %		Amount of Jan.1 1957, millicurie	Yield, neutrons per sec
	O^{18}	O^{17}		
1	1.35		29	325
2	6.4	0.7	22	1060
3	19.8	1.3	180	29 000
4	0.204	0.037	126	280

In order to determine the O^{18} concentration dependence of the neutron yield, we prepared four similar sources consisting of a solution of polonium in 2N nitric acid with different concentrations of the heavy oxygen isotopes (see table).

The relative yields of the sources were measured in a paraffin plate on a BF_3-filled proportional counter. The absolute yield of source No.3 was determined with a long counter by comparison with a Pu-Be standard.

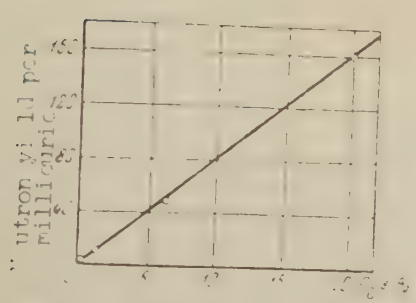

Fig.1. Neutron yield as a function of the O^{18} concentration in the source.

The variation of the neutron yield as a function of the O^{18} concentration is shown in Fig.1. It will be seen that the neutron yield is directly proportional to the O^{18} concentration, from which it may be concluded that the (α,n) reaction occurs principally on O^{18}. On the basis of the observed variations and the data on the O^{17} concentration, we estimate that the upper bound of cross section for the (α,n) reaction on O^{17} is ~10% of the cross section for the reaction on O^{18}.

The neutron yield for the case of a "thick target" of pure O^{18} can be calculated from the neutron yield measurements, the known O^{18} concentration in source No.3 and the relative stopping powers of H, N and O. Computation gives a value of 31 neutrons per 10^6 α-particles from polonium.

Comparing this result with the yield from other elements[3], we note that the cross section for the (α,n) reaction on O^{18} is second only to the cross section for the reaction on beryllium (50-80 neutrons per 10^6 α-particles).

The γ-radiation accompanying the O^{18} (α,n) Ne^{21} reaction was investigated on an automatic scintillation spectrometer with an NaI crystal. Inasmuch as in the case of source No.3 the Po yielded almost 3 γ-rays per emitted neutron, for detecting the γ-radiation accompanying the reaction we compared the spectra of sources Nos.3 & 4. The neutron emission from source No.4 can be neglected; hence after making the appropriate correction for the amount of Po in the

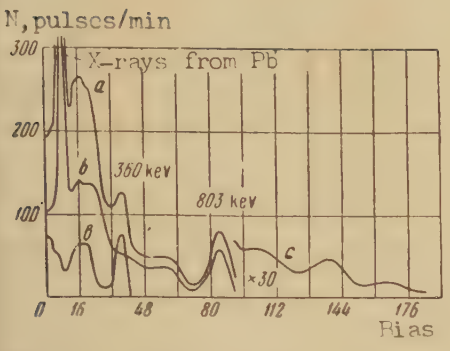

Fig.2. γ-Ray spectra of sources Nos.3 (O^{18} concentration - 19.8%) and 4 (O^{18} concentration - 0.204%). a) source No.3, b) source No.4, c) difference.

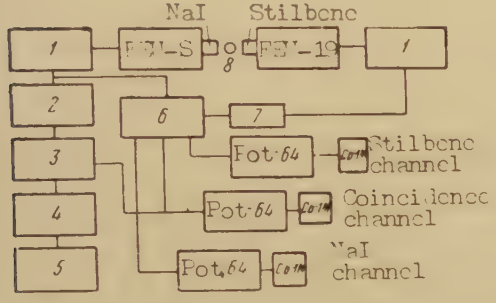

Fig.3. Block diagram of set-up for recording γ-radiations coinciding with the neutrons: 1) cathode follower, 2) amplifier, 3) gating circuit, 4) expander, 5) 5-channel analyzer, 6) coincidence circuit, 7) delay line, 8) source; FEU-S & FEU-19 - photomultipliers.

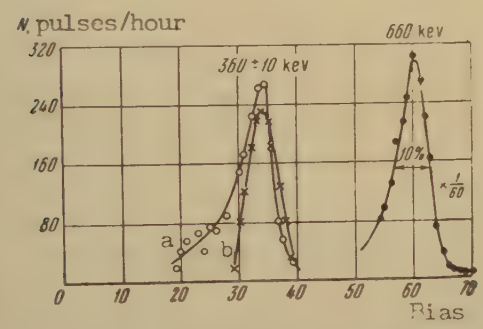

Fig.4. a) spectrum of γ-rays coinciding with neutrons (source No.3); b) spectrum recorded with lead shield between source and stilbene crystal. At right - 660 kev line of Cs^{137} used for calibration.

source and subtracting one spectrum from the other, we obtained the spectrum of the γ-radiation actually accompanying the O^{18} (α,n) Ne^{21} reaction. The three spectra are shown in Fig.2. In the figure one can readily discern the 360 kev γ-line which is associated with de-excitation of the first excited level of Ne^{21} (Ref.4). Evaluation of the intensity of this line yields 0.3±0.1 γ-rays per neutron.

The spectrum of the No.3 source has, in addition, a rather long tail, which could be due to γ-rays of more than 800 kev energy and/or neutron capture by the iodine. The level energy diagram for Ne^{21} shows that there may occur γ-transitions of 1.73 and 2.84 Mev energy as well as cascade transitions. Evaluation of the upper bounds for the intensity of these transitions, carried out with reference to the tail in the spectrum of source No.3, yielded a value of 0.14 γ-rays per neutron; of these no more than 0.03 can be attributed to the transition from the 2.84 Mev level.

The γ-radiation accompanying the (α,n) reaction was also investigated in coincidence with neutrons. The block diagram of the set-up employed for this purpose is shown in Fig.3. The neutrons were detected by a stilbene crystal. The neutron pulses were delayed $7\cdot10^{-8}$ sec and fed to the coincidence circuit which had a resolving time of $5\cdot10^{-8}$ sec. The delay time was selected experimentally. To check the operation of the counters we recorded pulses in all three channels. Source No.3 gave 50 coincidences per min. The number of chance coincidences was 2 per min.

The γ-spectrum recorded on this set-up is shown in Fig.4(curve a). In the same figure we show the spectrum of Cs^{137} (660 Mev line) recorded for calibration purposes. Here again the 360 kev line is clearly discernible. In order to prove that this peak is due to neutrons and that scattered γ-radiation makes no significant contribution to it, the stilbene crystal was shielded with 15 mm lead. The spectrum recorded with this shielding is shown in the same figure (curve b). Next the analyzer was adjusted for detecting the 1.73 and 1.38 Mev γ-rays, but these lines were too weak to be observed. Evaluation of the upper bounds for the intensity of these lines from the results of measurement on this set-up yielded values of 0.04 and 0.03 γ-rays per neutron, respectively.

Conclusions

As a result of the investigation, it has been established that the neutron yield from α-bombarded oxygen targets is due to the heaviest oxygen isotope, namely, O^{18}. The cross section for the O^{18} (α,n) Ne^{21} reaction is appreciably greater than the cross section for the reaction on all other elements except beryllium. The experimental data indicate that the yield from a thick O^{18} target should be 31 neutrons per 10^6 α-particles.

The compound Ne^{22} nucleus decays to the ground (70%) and first excited (30%) levels of Ne^{21}. The transition probability to the second and third excited levels is less than 10%. The energy of the first excited level is 360±10 kev.

We desire to thank O.Samadashvili and I.Karpenko for performing the analysis for O^{17}.

Moscow Engineering-Physical Institute

References

1. W.F.Hornyak, T.Lauritsen, P.Morrison & W.A.Fowler, Rev.Mod.Phys.,22, 291 (1950).

2. T.W.Bonner, A.A.Kraus, J.B.Marion & J.P.Schiffer, Phys.Rev., 102, 1348 (1956).

3. E.Serge, Experimental Nuclear Physics, Vol.2, (Cited in Russian trans. M. 1955).

4. F.Ajzenberg & T.Lauritsen, Revs.Mod.Phys., 24,321 (1952).

PROCEDURE FOR MEASURING THE ACTIVITY OF NUCLEI UNDERGOING K-CAPTURE

- M. Ia. Kuznetsova & V. N. Mekhedov

In the present report we shall describe the technique for detection of isotopes undergoing K-capture developed in our laboratory for the purposes of radiochemical investigation.[1,2] As is known, the predominant part of the products of interaction of nuclei with particles having energies in the hundred Mev range is comprised of neutron-deficient isotopes. In the case of medium and heavy elements such isotopes disintegrate for the most part by K-capture. Hence for investigating fission of such nuclei induced by fast particles one must have means for determining the absolute number of K-capture events. In view of the specific character of isotope formation at high particle energies and the nature of the K-capture process itself, the detecting-recording procedure in order to be useful must meet a number of specific requirements, namely, a) the procedure must insure reliable detection of weakly penetrating and weakly ionizing radiation (10-100 kev), b) the detecting efficiency must be sufficiently high and insofar as possible the same for different initial elements, b) in addition to x-rays or Auger electrons, the equipment must record competing positron and negatron emissions as well as the accompanying γ-rays (preferably separating out the 0.1-3 Mev range), and c) the procedure must provide for the possibility of checking the correlation between the recorded radiation and the K-capture in the investigated elements.

In developing our equipment and procedure, of the two forms of radiation emitted in K-capture - Auger electrons and x-rays - we deemed it preferable to detect the latter and by way of detecting device, chose a Geiger counter. The detecting unit consists of an electromagnet and two end-window counters. For the sake of brevity we shall refer to this unit as the magnetic analyzer. Below we shall describe the latest improved version of the equipment which is diagramed in Fig.1.

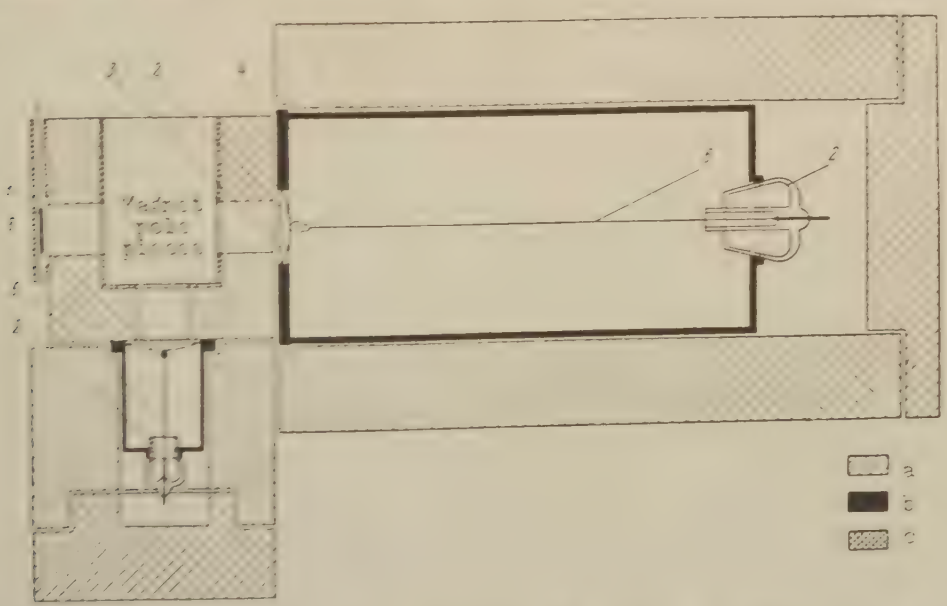

Fig.1. Diagram of magnetic analyzer (M 1:1): 1) target, 2) glass, 3) mica 3.5 mg/cm^2, 4) krypton counter, 5) small counter, 6) molybdenum filament 0.05 mm in diameter; a - lead, b - copper, c - plexiglass.

The electromagnet with 60 x 60 mm pole pieces and a gap of 25 mm is capable of producing a magnetic field of up to ~2000 oersteds. The large end-window counter serves for measuring the general radiation as well as the electromagnetic radiation with the magnetic field applied. This counter is filled with a mixture of krypton (330 mm Hg) and ether (20 mm Hg). It has a virtually flat plateau of over 200 v; the operating potential is 1800 v.

The fraction of x-rays in the total electromagnetic radiation is found by means of a lead absorber 0.2 mm thick mounted between the magnet pole pieces. This thickness of lead is adequate for virtually complete absorption of the x-rays emitted by the investigated elements. The positron:electron ratio is determined by separate measurements on the small counter with different strengths and polarities of the current through the electromagnet windings. The small counter was filled with a mixture of argon and alcohol (10%) at a pressure of 100 mm Hg. Generally the decay of each radiation component is followed separately.

The observed activities of the corpuscular radiations were corrected for absorption in air, mica and the nonsensitive part of the counter. Absorption of the sample was not, as a rule, taken into account in view of the thinness of the sources used (10-20 mg/cm^2). The following corrections were made in determining the number of K-capture events from the recorded number of x-ray quanta.

1. Correction for self-absorption of the x-rays in the sample. The value of the attenuation factor μ (absorption coefficient) was calculated for the given composition of the target on the basis of tabular values[3,4] of the atomic absorption coefficients.

2. Correction for x-ray absorption in air and the counter window. For elements close to silver and heavier than it, this correction was small and for the most part was disregarded. It was taken into account for light elements.

3. Correction for absorption in the nonsensitive volume of the counter. The noneffective or nonsensitive volume was assumed to be the layer of gas 8-12 mm thick between the window and the beginning of the active part of the filament.

4. Correction for recording efficiency. The efficiency of the krypton counter was calculated from the absorption in the sensitive volume of x-rays of different wavelengths, the absorption coefficients for krypton being taken from the work of Compton & Allison[3]. It should be noted that the collimating lead shields prevent the x-rays from striking the cylinder walls of the counter. This simplifies calculation of the efficiency inasmuch as it may be assumed that all the x-ray photons follow the same path and are absorbed only by the krypton. The value of the absorption coefficient near the jump (K-edge) was found to be extrapolation of the μ vs Z curve. The minimal value of μ was taken for the characteristic radiation of Sr (0.88 A). The curve characterizing the calculated x-ray detecting efficiency is shown in Fig.2 together with the curve for the variation of the correction for absorption in the nonsensitive volume as a function of Z.

5. Correction for the fluorescence yield. This correction takes into account the fraction of x-rays not emerging from the atom due to the Auger effect.[5]

The uncertainty of determining all the above enumerated corrections is evaluated to be 20% for the light elements and attains 30% for elements with $Z > 40$. The fact that we did not have to deal with any isotopes with strongly converting γ-radiation allowed us to dispense with the correction for the

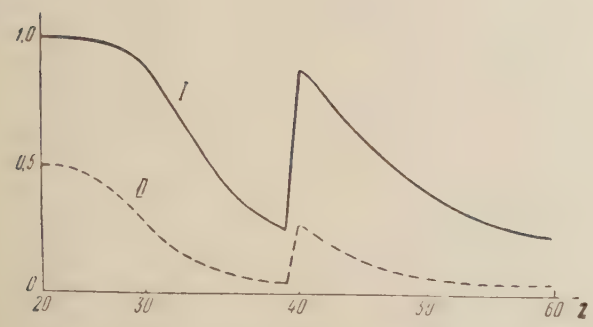

Fig.2. Curves characterizing the variation of the detecting efficiency (I) and the correction for absorption in the nonsensitive volume of the counter (II) for different proton numbers.

admixture of x-rays due to conversion of gammas.

The utilized procedure for discriminating the electromagnetic radiation involves the danger of errors due to mistakenly counting soft γ-rays as x-rays. In order to preclude this possibility we made it mandatory to obtain the absorption curve of the electromagnetic radiation in aluminum. Resolution of this absorption curve made it possible to bring out and exclude the admixture of soft γ-radiation and to determine the energy of the x-rays from the magnitude of the absorption coefficient. The observed wavelengths agreed with the tabular wavelength of the characteristic radiation in each case within the limits of the experimental error. It must be noted, however, that this method of identification does not allow of distinguishing between hard x-rays and soft γ-quanta in the case of small differences in wavelength.

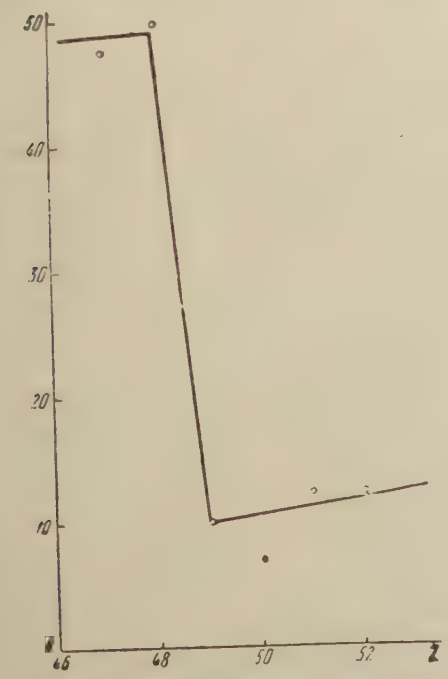

Fig.3. Values of the mass absorption coefficient for I^{125} x-rays in different elements.

In cases of low and moderate radiation intensities, we employed the method of identifying x-rays from the jump in the absorption coefficient (the differential absorption technique). To this end we carried out measurements of the absorption of the electromagnetic radiation in absorbers of a number of neighboring elements. The metals were taken in the form of foils; the other elements were taken in the form of finely ground powders mixed with beryllium oxide. The powders were placed into plexiglass containers. The absorption effect due to the container and beryllium oxide was determined by separate measurements. We calculated the mass attenuation factor μ for each element and plotted a curve for μ vs Z. The identification of the x-rays as belonging to one or another element was made by comparing the experimental curve with the curve plotted from the tabular data. For example, in the case of K-capture in iodine we have the characteristic sharp increase in μ in going from an indium to a cadmium absorber[3,4] illustrated in Fig.3.

The effective solid angle of our magnetic analyzer is 0.01. In cases where it was impossible to obtain activities sufficiently high for the analyzer, the radiation from the target was measured by means of a small krypton counter. This counter had a mica window and was filled with a mixture of krypton and ether to a pressure of 40 mm Hg. It was "calibrated" with reference to pure emitters (Pb^{103} and I^{125}), measured beforehand on the magnetic analyzer. Quantitative data were obtained for isotopes decaying only by K-capture.

K-capture data

Isotope	Period	Wavelength, Å		Percent K-capture			
		Mean.	Tab.	Exp.	Theor.	Literature	
J^{129}	30min	0,46	0,455	5—10	10	—	
J^{121}	1,6hr	0,46	0,455	58	82	—	
J^{124}	4,5day	0,46	0,455	58	46	~70	[7]
J^{126}	13day	—	—	50	—	~58	[7]
$Ag^{103}+Ag^{104}$	1,2hr	0,57					
		0,58	0,59	70	—	—	
Ag^{103}	70min	0,58	0,59	70	~57	-	
Pd^{101}	9 hr	0,53	0,61	97	~90	90	[7]
Rb^{95}	1,65 hr	0,65	0,67	75	72	—	
Mo^{90}	6,3 hr	—	—	≥75	—	—	
Nb^{90}	15—16 hr						
	16,0 hr	0,8	0,79	~50	55	—	
Zr^{89}	79 hr	0,8	0,83	~60	58	~75	[7]
Sr^{83}	1,5 day	0,96	0,93	80	~50	—	
$Rb^{81}+Rb^{82}$	6 hr	—	—	~87	—	Average~90	[7]
Br^{76}	17,2hr	1,03	1,1	20	—	—	
Br^{75}	1,6 hr	1,2	1,1	~15	19	—	
Se^{73}	6,7—7,1 hr						
	7,1 hr	1,2	1,18	40	32	37	[8]
Ga^{66}	9,4 hr	—	—	~30	20	36	[7]
Cu^{61}	3,3 hr	—	—	32	21	32	[7]
Cu^{64}	12,8 hr	—	—	46	—	42	[7]

Use of the described procedure made it possible to define the K-capture branch intensity values for a number of isotopes and to establish the presence of K-capture in a number of cases where it had not been previously detected. Our most recent data are summarized in the accompanying table; some of the results have been published earlier[1,2]. In addition, we list in the table the expected theoretical values and the corresponding data in the literature.

The theoretical values for some of the isotopes have been taken from the work of Dzhelepov & Kudriavtseva[6]. For the other nuclei they have been calculated according to the formulas given by these authors (in the case of a complicated β-spectra, we used weighted mean energy values). In columns 3 & 4 we list the measured and expected (tabular)[3] x-ray wavelengths. The fact that our experimental data agree closely with the tabular values shows that our detecting efficiency curve was correctly calculated and that the correction enumerated above were properly evaluated.

As may be seen from the table, our experimental values for the fraction of K-capture agree within the limits of the experimental error with the theoretical values, except for the isotopes I^{121}, I^{124}, Sr^{83} and Ga^{66}. The fact that the experimental value was higher than the theoretical one for the last three isotopes is not surprising and can be explained by the considerations set forth by Dzhelepov & Kudriavtseva[6]. The high theoretical value for I^{121} apparently indicates that the equations of Ref.6 are not applicable in this case.

By means of the described equipment we also detected among the fission products of different nuclei about 20 radioactive isotopes disintegrating only by orbital electron capture. For some of them the branching ratios have not been determined, while others have never previously been observed.

Thus the described procedure appears to be fully suitable for work in a wide range of elements up to the rare earths. It fully satisfies the requirements listed above and is competitive with other techniques for absolute

determination of the number of K-capture events. It is superior to other procedures as regards simplicity of the equipment and reliability of identification of the radiations. Detection of x-rays by means of proportional or scintillation counters involves the use of a considerable amount of complicated and expensive associated electronic equipment.

One shortcoming of the procedure, namely, the small solid acceptance angle of the analyzer, can possibly be eliminated with further improvement of the apparatus. The other shortcoming - the fact that one cannot distinguish between soft γ-quanta and x-rays of close energies - is common to other techniques. This shortcoming, however, is not a very serious one. Cases of emission of soft γ-rays are not very frequent, while cases of x- and γ-rays with close energies are even rarer.

In conclusion, it may be noted that although the described equipment was not developed for work with heavy elements, it may not be useless in this region. Here the low efficiency as regards detection of K radiation will, to some extent, be compensated for by the almost 100% efficiency in detection of L radiation. It will be recalled that beginning with approximately Hf ($Z = 72$ and higher) the wavelength of the x-rays emitted upon filling of the L shell is about the same as the wavelength of the K radiation from light elements. Hence equipment of this type can be used for detecting orbital electron capture in heavy nuclei as well, although admittedly, with appreciably lower efficiency in view of the fact that the intensity of L-radiation is four times lower than that of K radiation.

Laboratory of Nuclear Problems,
Joint Institute for Nuclear Research

References

1. B.V.Kurchatov, V.N.Mekhedov, N.I.Borisova, M.Ia.Kuznetsova, L.N.Kurchatova & L.V.Chistiakov, Transactions of the Meeting of the USSR Academy of Sciences on the Peaceful Uses of Atomic Energy, M., 1955.

2. V.N.Mekhedov, Thesis, 1954.

3. A.H.Compton & S.K.Allison, X-Rays in Theory and Experiment, New York, 1939.

4. K.K.Aglintsev, Dozimetriia ioniziriuishchikh izluchenii (Dosimetry of Ionizing Radiations), M, 1950.

5. P.R.Gray, Phys.Rev., 101, 1306 (1956).

6. B.S.Dzhelepov & A.V.Kudriavtseva, Zhur.eksp.i teor.fiz., 19, 761 (1949).

7. J.M.Hollander, I.Perlman & G.T.Seaborg, Tables of Isotopes, Revs.Mod. Phys., 25, 469 (1953). (Cited in Russian trans.).

8. F.R.Scott, Phys.Rev., 84, 659 (1951).

CHARACTERISTICS OF THE JUMPS IN THE EQUILIBRIUM SHAPE OF NUCLEI

- L.K.Peker

Nuclei with A = 150 to 190 have an ellipsoidal equilibrium shape.[1] The equilibrium shape depends on the filling of the nuclear shells and, consequently, on the number of neutrons and protons in the nucleus. It has now been established that transformation of the equilibrium shape from the spherical to the ellipsoidal occurs in going from nuclei with N = 88 to nuclei with N = 90. This transformation is readily noticed inasmuch as in going from 88 to 90 neutrons we observe an appreciable change in the energy of the first collective level, the Coulomb excitation cross section and the probability of electric γ-transitions, quadrupole moments and isotope shifts[2,4] (Fig.1).

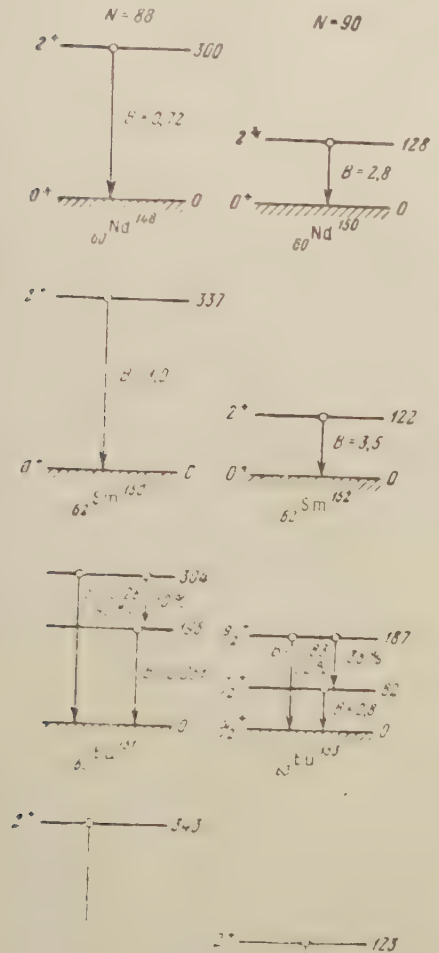

Fig.1. Diagrams of the lower collective levels of nuclei with 88 and 90 neutrons: B - reduced probability of Coulomb excitation.

No such anomaly in the variation of the nuclear properties is observed in nuclei with other neutron numbers. Consequently, difficulties have been encountered in attempts to establish the dependence of the equilibrium shape on Z (in nuclei with A = 150) or on Z and N (in nuclei with A = 190) and, in fact, the values of Z and N at which the deformation occurs have not yet been precisely established.

The purpose of the present article is to clarify the role of protons and neutrons separately in the process of the transformation of the equilibrium shape and to establish the values of N and Z at which the transformation occurs.

With a view to determining the boundaries of the region of deformed nuclei let us recall that the principal indication of a given equilibrium shape is the character of the excited levels (collective and single particle). In ellipsoidal nuclei the low-lying collective levels are always rotational ones, while the single particle levels in nuclei with odd A are described by Nilsson's[4] scheme for an axially symmetric potential. In contrast, in spherical nuclei the low-lying collective levels in most cases are vibrational (except for nuclei with a closed shell), while the single particle levels must be described in the framework of Mayer's scheme for a spherically symmetric potential. Rotational levels in such nuclei cannot be excited. Hence hereinafter we shall judge of the equilibrium shape of the nucleus exclusively on the basis of the character of the ground and excited states. Let us examine the variation of the equilibrium shape in the vicinity of nuclei with A = 150. We have already noted that the influence of neutrons here is very strong. In nuclei wherein the equilibrium shape is determined by the neutrons ($N \leqslant 88$ and $N \geqslant 90$)

the influence of protons is almost unnoticeable. Fig.2 shows the variation of the nuclear potential with the deformation parameter $\beta \approx \Delta R/R$. Nuclei with Z = 60, 62 and 64 may be either spherical (Nd^{148}, Sm^{150}, Gd^{152}) or ellipsoidal (Nd^{150}, Sm^{152}, Gd^{154}).

In order to detect the influence of protons one must select conditions in which the nucleus under the influence of neutrons alone would be in a state of "indifferent" equilibrium, characterized by curve III of Fig.2. One may hypothesize that in such nuclei the stability of the equilibrium shape will be determined by the protons. These conditions are satisfied by nuclei with N = = 89: Nd^{149}, Pm^{150}, Sm^{150}, Eu^{152}, Gd^{153} and Tb^{154}. Analysis of odd-odd nuclei is at present hindered by the presence of two unpaired nucleons (except for Eu^{152} - Ref.5), in view of which we shall herein consider only nuclei with odd A. Excited levels of Nd^{149} and Gd^{153} have as yet not been observed and the available experimental data[6] on the γ-transitions in Sm^{151} are inadequate for constructing a more or less complete energy level diagram. From analysis of the decay schemes given by Davis et al[6] one can, however, evaluate the spins and parities of their ground state: for Nd^{149} and Sm^{151} we find 9/2 (7/2-), while for Gd^{153} we obtain 3/2±. Comparing these assignments with the level schemes of Mayer and Nilsson, we find that in the first two cases the ground states are described in Mayer's scheme as $h_{9/2}$ (or $f_{7/2}$),while the ground state of Gd^{153} is described only by Nilsson's scheme. Hence it may be assumed that the change in the equilibrium shape of the nucleus under the influence of protons occurs in going from nuclei with Z = 62 to nuclei with Z = 64. The nucleus with Z = 63 and N = 89 (Eu^{152}) is in the state of "indifferent" equilibrium as regards both the number of neutrons and the number of protons.

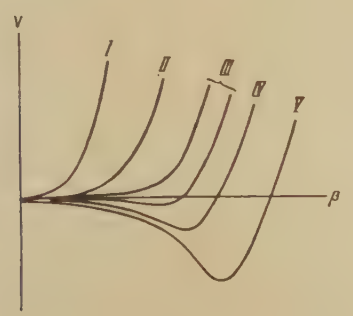

Fig.2

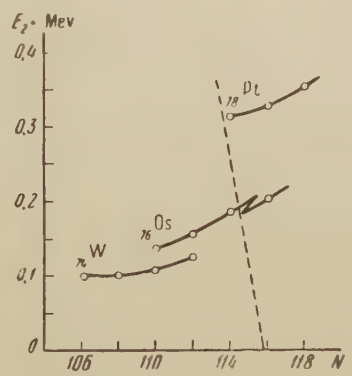

Fig.3

Fig.2. Variation of the potential energy of the nucleus with the deformation parameter. Curves I-V schematically illustrate the behavior of the energy surface as we go further from a closed shell.

Fig.3. Variation of the energy of the first level of even-even nuclei (2+) with the number of neutrons (A ≈ 190). The dash-line separates the region with rotational from the region with vibrational structure of the lower excited levels. Its slope indicates the dependence of the equilibrium shape on the number of protons in the nucleus.

Let us now turn to nuclei with A ≈ 190 in which we observe the reverse transition, i.e., from the ellipsoidal to the spherical shape.

In these nuclei the equilibrium shape can be determined from the character of the excited levels inasmuch as here such attributes as the energy of the first collective level (Fig.3), the Coulomb excitation cross section, etc.

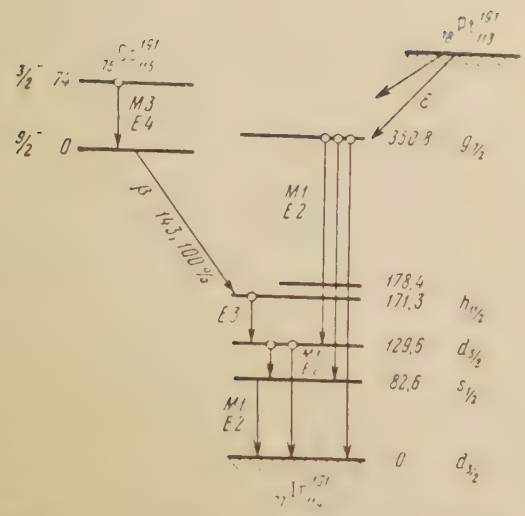

Fig.4. Level scheme for Ir^{191} and Os^{191}.

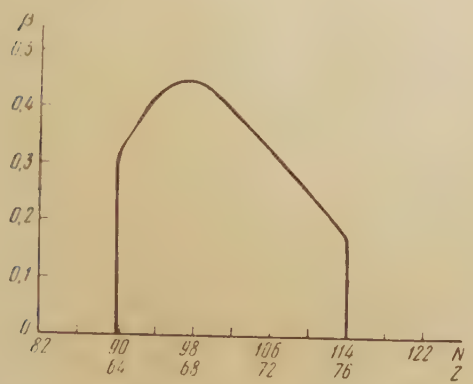

Fig.5. Variation of the deformation parameter β with the number of neutrons or protons in the nucleus (A = 132 to 208). In nuclei with $N \leqslant 88$, $N \geqslant 116$, $Z < 60$ and $Z \geqslant 78$, the parameter $\beta = 0$. Nuclei with N = 89, 114 or 115 and Z = 60-64 or Z = 76-77 may have $\beta \approx 0$ or $\beta \approx 0.2$.

vary relatively slowly and gradually, i.e., exhibit no noticeable discontinuities. The jump in going from Z = 76 (Os) to Z = 78 (Pt) is appreciably sharper than going from N = 114 (Os^{190}) to N = 116 (Os^{192}). The available experimental data on the spectra of even-even nuclei[6] are inadequate for precise determination of the boundary values of N and Z. We know only that in Pt^{192} the low-lying levels are vibrational.

A large number of γ-transitions has been observed in Os^{190} and Os^{192}. Several different decay schemes for each isotope can be constructed on the basis of the experimental data; in particular, for Os^{190} one can construct a scheme comprising a system of rotation levels, while for Os^{192} one can lay out a system of vibrational levels. Only the first levels (2+) of Os^{186} and Os^{188} are known. The second 4+ levels with energy values that would allow of proving the existence of a rotational band have not yet been observed in these nuclei.

In view of these difficulties we cannot draw any definitive deductions regarding the boundaries of the region of deformed nuclei. We can only assume that the transformation of the equilibrium shape apparently occurs at Z = 76 to 78 and N = 114 to 116. For a more precise determination of the boundary values of Z and N let us turn to data on nuclei with odd A, namely, Os^{191} and Ir^{191} (Ref.7); these are shown in Fig.4. The multipolarity of the isomeric transitions in both nuclei and the character of the β^--decay of Os^{191} uniquely determine the spin and parity values indicated in the figure. It will readily be seen that the levels of Os^{191} are described only by Nilsson's scheme; consequently, this nucleus has the ellipsoidal equilibrium shape. Attempts to apply Nilsson's scheme to the lower levels of Ir^{191} are vain inasmuch as this scheme does not correctly describe the 129 kev level with 5/2+. It has been suggested that the 129 kev level is a rotational one and, consequently, cannot be described by Nilsson's scheme. In this case, however, with Coulomb excitation there should be observed a second rotational level at 310 kev (7/2+). Experiment shows that there is no such level in Ir^{191}, but that a level with an appreciably higher energy (350 kev) is excited.

Since rotational levels cannot be excited in Ir^{191}, this nucleus must be spherical. This deduction is substantiated by the fact that all the lower levels of Ir^{191} can be described in the framework of Mayer's scheme as single particle levels with the configurations $s_{1/2}$, $d_{5/2}$, $h_{11/2}$ and $g_{7/2}$. From the above

considerations regarding the equilibrium shape of Os^{191} and Ir^{191} and the data for even-even nuclei, one can evaluate the precise values of N and Z at which transformation from the ellipsoidal to the spherical shape occurs: Z = 76-78 and N = 114-116. It will readily be noted that in contrast to nuclei with $A \approx 150$, in the case of nuclei with $A \approx 190$ the influence of protons on the equilibrium shape is comparable to that of neutrons and may even be somewhat stronger. For example, it is sufficient to add one proton to Os^{190} (i.e., go to Ir^{191}) for the equilibrium shape to change, whereas the addition of one neutron (i.e., going to Os^{191}) does not alter the shape. The weak dependence of the equilibrium form on Z in the beginning of the region of deformed nuclei and its appreciably stronger influence at the end of the region are, apparently, connected with the shell nature of the nuclear structure. Although in going through the boundary values of N and Z the deformation parameter $\beta \approx \Delta R/R$ goes to zero (Fig.5), the deforming effect of the protons and neutrons (proportional to their number outside the closed shell) changes very little. From this it follows that with filling of the shells by protons and neutrons, collective nuclear characteristics such as the energy of the first collective 2+ level, the Coulomb excitation cross section, etc. (with the exception of the structure of the levels) should change slowly and gradually without exhibiting noticeable jumps even when the equilibrium shape alters. This is precisely the behavior of nuclei with $A \approx 190$, wherein at the point of the alteration of the equilibrium shape, the proton and neutron shells are relatively far from being closed (Z = 76-78 and N = 114-116).

The change in the equilibrium shape in the case of nuclei with $A \approx 150$ occurs under different conditions. The distinguishing feature of these nuclei is that in them the protons almost completely fill the $g_{7/2}$ and $d_{5/2}$ levels, which constitute a distinct Z = 64 subshell, and, consequently, make almost no contribution to polarization of the nucleus. The neutrons, on the other hand, begin to fill a new shell and their deforming effect, which at N = 84 and N = 86 is still very weak, is rapidly strengthened with further increase in number. This leads directly to a rapid change in such collective properties as the energy of the first 2+ level, the Coulomb excitation cross section, the quadrupole moments, etc. This change in going from N = 88 to N = 90 is so great that we perceive it as a sharp jump pertaining to the transformation of the equilibrium nuclear shape.

I wish to express my gratitude to L.A.Sliv and B.S.Dzhelepov for detailed discussion of the work.

"M.Gorki" Library of the
Academy of Sciences of the USSR

References

1. A.Bohr & B.Mottelson, Dan.Mat.Fys.Medd., 27, 16 (1953); Dan.Mat.Fys. Medd., 30, 1 (1955).
2. K.Ford, Phys.Rev., 95, 1250 (1954).
3. N.P.Heydenburg & G.M.Temmer, Phys.Rev., 104, 981 (1956).
4. S.G.Nilsson, Dan.Mat.Fys.Medd., 29, 16 (1955).
5. L.K.Peker, Zhur.eksp.i teor.fiz., 32, 6 (1957).
6. B.S.Dzhelepov & L.K.Peker, Skhemy raspada radioaktivnykh izotopov (Decay schemes of radioactive isotopes), M.1957.
7. R.H.Davis, A.S.Divatia, D.A.Lind & R.D.Moffat, Phys.Rev., 103, 1801 (1956).

SPINS AND PARITIES OF DEFORMED ODD-ODD NUCLEI

- L. K. Peker

In deformed nuclei the state of a nucleon is characterized by the quantum number Ω (the component of the nucleon's total momentum along the nuclear symmetry axis). In odd-A nuclei the total angular momentum of the nucleus in the ground state is equal to the value of the momentum of the last odd nucleon: $I = \Omega$.

In odd-odd deformed nuclei, where there are two unpaired nucleons, the total angular momentum of the nucleus is given by the expression[1]

$$I_{1,2} \quad \Omega_p \pm \Omega_n \,. \tag{1}$$

At present, one cannot indicate beforehand what sign will hold for the ground state, but it is known that there exist in the nucleus states corresponding to both signs (+ and -). To determine I one must first find Ω_p and Ω_n. One cannot utilize Nilsson's scheme[2] for this purpose, inasmuch as for each specific Z and N this scheme gives two or even three possible values of Ω.[3] This indeterminacy as regards Ω would lead to an even greater indeterminacy in calculating the spins I_1 and I_2 of odd-odd nuclei.

In order to circumvent this difficulty, let us assume that the neutron and proton orbits in deformed nuclei are filled independently, so that the addition of one or more neutrons does not change the state of the protons and vice versa (provided the deformation parameters of the nuclei in question are approximately equal). The nucleonic orbits in odd-odd nuclei will, in this case, be filled in the same sequence as the orbits of neighboring nuclei with odd A.

We note that this hypothesis is admittedly not valid near the boundary of the region of deformed nuclei, where the addition of even one nucleon results in an appreciable change of the deformation and, consequently, a change in the order of filling of the nucleonic levels.

Experimental values of the spins and parities of odd A nuclei[3,4]

Table 1

Nucleus	Spin and parity	Nucleus	Spin and parity	Nucleus	Spin and parity
$_{63}Eu^{153}$	5/2+	$_{64}Gd^{153}_{89}$	3/2−	$_{74}W^{183}_{109}$	1/2−
$_{65}Tb^{159}$	3/2+	$_{64}Gd^{155}_{91}$	3/2−	$_{74}W^{185}_{111}$	3/2−
$_{67}Ho^{165}$	7/2−	$_{64}Gd^{157}_{93}$	3/2−	$_{76}Os^{189}_{113}$	3/2−
$_{69}Tu^{169}$	1/2+	$_{66}Dy^{161}_{95}$	5/2−	$_{76}Os^{191}_{115}$	9/2−
$_{71}Lu^{175}$	7/2+	$_{66}Dy^{163}_{97}$	5/2−	$_{90}Th^{229}_{139}$	5/2+
$_{73}Ta^{181}$	7/2+	$_{68}Er^{167}_{99}$	7/2+	$_{92}U^{233}_{141}$	5/2+
$_{75}Re^{185}$	5/2+	$_{70}Yb^{171}_{101}$	1/2−	$_{92}U^{235}_{143}$	7/2−
$_{75}Re^{187}$	5/2+	$_{70}Yb^{173}_{103}$	5/2−	$_{94}Pu^{239}_{145}$	1/2+
$_{89}Ac^{227}$	3/2+	$_{72}Hf^{177}_{105}$	7/2−	$_{96}Cm^{243}_{147}$	5/2+
$_{91}Pa^{231}$	3/2−	$_{72}Hf^{179}_{107}$	9/2+		
$_{93}Np^{237}$	5/2+				
$_{95}Am^{241}$	5/2−				
$_{95}Am^{243}$	5/2−				

Table 2

Spins and parities of deformed odd-odd nuclei[5,7]

Nucleus	Ω_p	Ω_n	$I=\lvert\Omega_p \pm \Omega_n\rvert$		I_{exp} (ground state)	I_{exp} (excited state)
$_{11}Na^{22}_{11}$	3/2+	3/2+	3+	0+	3+	
$_{11}Na^{24}_{13}$	3/2+	5/2+	4+	1+	4+	1+
$_{13}Al^{24}_{11}$	5/2+	3/2+	4+	1+	(4+)	
$_{13}Al^{26}_{13}$	5/2+	5/2+	5+	0+	5+	0+
$_{63}Eu^{152}_{89}$	(3/2−)		3−	0−		
$_{63}Eu^{154}_{91}$	5/2+	3/2+	4−	1−	3−	1−*
	(3/2−)	3/2−	(3+)	(0+)	3	
$_{63}Eu^{156}_{93}$	5/2+	3/2−	4−	1−	(4−)	
$_{65}Tb^{156}_{91}$	3/2+	3/2−	3−	0−	(3)	$I_1-I_2\geqslant 3$
$_{65}Tb^{160}_{95}$	3/2+	5/2−	4−	1−	4−	
$_{67}Ho^{160}_{93}$	7/2−	3/2−	5+	2+	(5)	$I_1-I_2\geqslant 3$
$_{67}Ho^{164}_{97}$	7/2−	5/2−	6+	1+	>5	1+
$_{67}Ho^{166}_{99}$	7/2−	7/2+	7−	0−	0−	⩾6
$_{69}Tu^{166}_{97}$	1/2+	5/2−	3−	2−	(3)	
$_{69}Tu^{170}_{101}$	1/2+	1/2−	1−	0−	1−	
$_{69}Tu^{172}_{103}$	1/2+	5/2−	3−	2−	(2)	
$_{71}Lu^{176}_{105}$	7/2+	7/2−	7−	0−	(⩾7−)	1 (0)−
$_{73}Ta^{180}_{107}$	7/2+	9/2+	8+	1+	>6	1±
$_{73}Ta^{182}_{109}$	7/2+	1/2−	4−	3−	3, 4	6,7, (4,3)
$_{73}Ta^{186}_{113}$	7/2+	3/2−	5−	2−	(2−)	
$_{75}Re^{186}_{111}$	5/2+	3/2−	4−	1−	1−	
$_{75}Re^{188}_{113}$	5/2+	3/2−	4−	1−	1−	4
$_{75}Re^{190}_{115}$	5/2+	9/2−	7−	2−	(>5)	
$_{77}Ir^{188}_{111}$	3/2+	3/2−	3−	0−	3−	
$_{77}Ir^{190}_{113}$	3/2+	3/2−	3−	0−	(3)	⩾8+
$_{77}Ir^{192}_{115}$	3/2+	9/2−	6−	3−	4, 5	7, 8**
$_{89}Ac^{228}_{139}$	3/2+	5/2−	4−	1−	1−(2−)	
$_{89}Ac^{230}_{141}$	3/2+	5/2−	4−	1−	1+	
$_{91}Pa^{228}_{137}$	3/2−	(5/2+)	4−	1−	1−(2−)	
$_{91}Pa^{230}_{139}$	3/2−	5/2−	4+	1+	1+	
$_{91}Pa^{232}_{141}$	3/2−	5/2−	4+	1+	1+	
$_{91}Pa^{234}_{143}$	3/2−	7/2−	5+	2+	(5)	1−, 2+***
$_{93}Np^{236}_{143}$	5/2+	7/2−	6−	1−	>5	1−
$_{93}Np^{238}_{145}$	5/2+	1/2+	3+	2+	3+	
$_{93}Np^{240}_{147}$	5/2+	5/2+	5+	0+	0,1±	>4±
$_{85}Am^{242}_{147}$	5/2−	5/2+	5−	0−	⩾5−	1,0−

---

*The equilibrium shape of the 9.2-hour isomeric state of Eu^{152} may be spherical.[4]

**Ir^{192} is a spherical nucleus; the spins of its ground and isomeric states should therefore not be described by Eq.(1).

***The 1- level of Pa^{234} may be formed incident to transition of a neutron to the first level with $\Omega_n = 1/2+$ (in U^{235} the ground state is 7/2- and the ~3 kev level is 1/2-). In this case, $I = |(3/2) \pm (1/2)| = 2$ or 1.

Table 3

Tabular values of Ω_p and Ω_n

Z	Ω_p	N	Ω_n	Z	Ω_p	N	Ω_n
11	3/2+	11	3/2+	77	3/2+	105	7/2−
13	5/2+	13	5/2+			107	9/2+
63	(3/2+)	89	3/2+			109	1/2−
	5/2+	91	3/2+			111	3/2−
65	3/2+	93	3/2−			113	3/2−
67	7/2+	95	5/2−			115	9/2−
69	1/2−	97	5/2−	89	3/2−	139	5/2−
71	7/2+	99	7/2+	91	3/2−	141	5/2−
73	7/2+	101	1/2+	93	5/2−	143	7/2−
75	5/2+	103	5/2−	95	5/2+	145	1/2+
				99	(7/2−)	147	5/2−

Table 4

Spins and parities of odd-A nuclei (A = 150 to 190) obtained from analysis of the decay schemes[7]

Nucleus	Spin & parity	Nucleus	Spin & parity
$_{62}Sm^{153}_{91}$	3/2−	$_{71}Lu^{173}_{102}$	7/2+
$_{63}Eu^{150}_{87}$	5/2+	$_{71}Lu^{177}_{106}$	7/2+
$_{64}Gd^{153}_{89}$	3/2+	$_{72}Hf^{173}_{101}$	1/2−
$_{64}Gd^{159}_{95}$	(5/2−)	$_{72}Hf^{175}_{103}$	5/2−
$_{65}Tb^{161}_{96}$	3/2+	$_{72}Hf^{181}_{109}$	1/2−
$_{66}Dy^{165}_{99}$	7/2+	$_{73}Ta^{179}_{106}$	7/2+
$_{67}Ho^{165}_{98}$	(7/2−)	$_{73}Ta^{183}_{110}$	7/2+
$_{67}Ho^{167}_{100}$	7/2−	$_{74}W^{179}_{105}$	7/2+
$_{68}Er^{165}_{97}$	(5/2−)	$_{74}W^{181}_{107}$	9/2+
$_{68}Er^{169}_{101}$	1/2−	$_{74}W^{185}_{111}$	3/2−
$_{68}Er^{171}_{103}$	5/2−	$_{74}W^{187}_{113}$	3/2−
$_{69}Tm^{167}_{98}$	1/2+	$_{75}Re^{183}_{108}$	5/2+
$_{69}Tm^{171}_{102}$	1/2+	$_{76}Os^{185}_{109}$	1/2−
$_{70}Yb^{169}_{99}$	7/2+	$_{76}Os^{191}_{115}$	9/2−
$_{70}Yb^{173}_{103}$	7/2−		
$_{70}Yb^{177}_{107}$	9/2−		

Bearing this limitation in mind, let us attempt to find I_1 and I_2, using for Ω_p and Ω_n the experimentally determined spins of deformed nuclei with odd-A in the A ≈ 24, A = 150 to 190 and A > 222 regions (Table 1). In Table 2 the theoretically calculated values of I_1 and I_2 are compared with the experimental data on the spins and parities of the ground states of odd-odd nuclei found from analysis of the corresponding decay schemes. As may be seen from the table, there is a serious discrepancy in the case of Eu^{154} and Ir^{192}. At present, it is difficult to explain the anomalous value (3) of the spin for Eu^{154}; it should be noted however that this nucleus lies right at the boundary of the region of deformed nuclei and that the sequence of filling of the nucleonic orbits in it may be different from that in neighboring nuclei. This effect is particularly clearly discernible in Eu^{152} where Ω_p is, apparently, equal to 3/2± (Ref.16) and not to 5/2+ as in Eu^{153}.

It will also be seen from the table that Eq.(1) does not describe the spin of the Ir^{192} ground state. This divergence can readily be understood, for nuclei with A = 192 are spherical and, consequently, this formula is not applicable to them.

The good agreement of the other experimental and theoretical spin and parity values supports our hypothesis that the neutron and proton orbits are filled independently of each other and that the sequence of filling of the nucleonic orbits in neighboring nuclei (with close deformation parameters) is the same.

This allows us to select the values of Ω_p and Ω_n on the basis of the experimentally measured spins of odd-A nuclei and hereinafter we shall only use these tabular values (Table 3). The possibility of unambiguous selection of Ω_p and Ω_n is substantiated by spin and parity data obtained from analysis of the decay schemes for unstable odd-A nuclei. In all cases where these can be evaluated, the most probable experimental spin and parity values agree with our tabular values for Ω (Table 4).

In the case of two nuclei, namely Np^{239} and Os^{187} (Ref.10), the experimental spins (1/2 in each case) do not agree with the tabular values 5/2+ and 3/2±, respectively. As regards Np^{239}, a number of authors have called attention to the fact that the experimental value of 1/2 is not consistent with the other properties of this nucleus. The character of the α-decay of Am^{243}

(Ref.11), the β-decay of Np^{239} (Ref.12), the multipole orders of the γ-transitions in Np^{239} and, particularly, the structure of the rotational levels are all in conflict with the 1/2 assignment and indicate 5/2.

In Os^{187}, formed by the decay of Ir^{187}, there is apparently excited a level at 135 kev.[13] Its energy is equal to the energy of the first rotational level of Os^{187}, computed on the assumption that the spin of the ground state of Os^{187} is 3/2 and that the moment of inertia is equal to that of neighboring even-even nuclei.

It may therefore be assumed that the spins of Np^{239} and Os^{187} are not 1/2 and 1/2 but actually 5/2+ and 3/2-, respectively, which fully agrees with the tabular values.

In light of what has been said above it would appear desirable to review the decay schemes of certain heavy isotopes. By way of example, illustrating the desirability of such review, one might cite the decay schemes for Th^{231} and Th^{233}. From the decay scheme in the literature[14,15] it follows that the spin of Th^{231} is 7/2, while the tabular value of Ω_n for N = 141 is 5/2. As a matter of fact, recent data[16] on α-γ directional correlation in α-decay of U^{235} appear to preclude the possibility of the 7/2 assignment.

In the case of Th^{233}, the tabular values of Ω for the initial and final nuclei require that the β-decay go only to the excited levels of Pa^{233}, inasmuch as decay to the ground state is twice forbidden, while log ft = 5.9. The intensity of the γ-transitions reported by Wagner et al[9] is, however, inconsistent with this requirement. It is possible that there are intense γ-lines in the low-energy part of the spectrum that have not been detected because they are masked by other forms of radiation.

Let us turn to the question of the spins and parities of the low-lying excited levels of deformed odd-odd nuclei. We have indicated above that in such nuclei there should be two classes of states: states with $I_1 = |\Omega_p + \Omega_n|$ and states with $I_2 = |\Omega_p - \Omega_n|$. The energies of the I_1 and I_2 levels differ by an amount of the order of the rotational energy.[1] Inasmuch as this energy is usually less than the energy of excitation of single particle levels, we can expect that if the spin of the ground state is I_1, the first excited state will have spin I_2. In the last column of Table 2 we list the experimental data on the spins and parities of the first excited level (or of the first two excited levels for some nuclei). It will be seen that in most cases the values agree with either I_1 or I_2.

Even in cases when the available experimental data do not allow of evaluating these spins, there are indications that the ground and first excited states of deformed odd-odd nuclei are the components of a doublet with $I = |\Omega_p \pm \Omega_n|$. The condition $\Delta I = |I_1 - I_2| \geqslant 3$ is almost always fulfilled in these nuclei and, consequently, isomeric states should frequently be encountered among them. This qualitative inference is, of course, supported by the experimental data. It is known that isomeric states are more frequently encountered in deformed odd-odd nuclei than in spherical nuclei.[5,7]

In heavy nuclei, however, the density of the nucleonic levels is great and in some cases the separation between them is definitely less than the rotational energy. In particular, according to the data of Novikova et al[17], the first single particle excited 1/2+ level of U^{235} is only 3 kev above the 7/2- ground state. Hence in some nuclei we may expect to find between the doublet-component levels with spins I_1 and I_2, one or two intermediate levels associated with excitation of one of the unpaired nucleons. This may explain the discrepancies appearing in the table between the theoretical and experimental values of the spin for the first excited level. The reason for this

divergence is particularly clearly evident in the case of Pa^{234} which has the same number of neutrons as U^{235} (N = 143). In this nucleus the doublet with spins 5+ and 2+ is comprised by the ground state and the second excited level at 60 kev.[7] The first excited level of Pa^{234} at 40 kev (1-) may form upon excitation of the 143rd neutron to the lowest single particle level with $\Omega_n = 1/2-$. The spin of this level $I = \Omega_p \pm \Omega_n$ may be 2- or 1-, which agrees with the experimental value.

In conclusion I feel it incumbent upon me to express my gratitude to K. Ia.Gromov, B.S.Dzhelepov & L.A.Sliv for discussion of the work.

"A.M.Gorki" Library of the
Academy of Sciences of the USSR

References

1. A.Bohr & B.Mottelson, Kgl.Danske Videnskab.Selskab; Mat.Fys.Medd., 27,16 (1953).
2. S.G.Nilsson, Kgl.Danske Videnskab. Salskab; Mat.Fys.Medd., 29,16 (1955).
3. B.R.Mottelson & S.G.Nilsson, Phys.Rev., 99, 1615 (1955).
4. L.K.Peker, Zhur.eksp.i teor.fiz., 32, 6 (1957).
5. J.M.Hollander, I.Perlman & G.T.Seaborg, Table of Isotopes, Rev.Mod.Phys., 25, 469 (1953). (Cited in Russian trans.)
6. J.G.Conway & R.McLaughlin, Phys.Rev., 96, 541(1954).
7. B.S.Dzhelepov & L.K.Peker, Skhemy raspada radioaktivnykh izotopov (Decay schemes of radioactive isotopes), M. 1957.
8. R.W.Kedzie, M.Abraham & C.Jeffries, Bull.Am.Phys.Soc., 1, 390 (1956).
9. F.Wagner, M.S.Friedman, D.Engelkemeir & J.R.Huizenga, Phys.Rev., 89, 502 (1953).
10. K.Murakawa, NSA, 9, 24B (1955); 10, 12B (1956).
11. F.Stephens, J.Hummel, F.Asaro & I.Perlman, Bull.Am.Phys.Soc., 29, 8, 13 (1954).
12. J.M.Hollander, W.G.Smith & J.W.Mihelich, Phys.Rev., 102, 740 (1956).
13. W.G.Smith & J.M.Hollander, Phys.Rev., 98, 1258 (1955).
14. J.P.Mise & J.W.Starner, Bull.Am.Phys.Soc., 1, 4, 171 (1956).
15. D.Strominger & J.O.Rasmussen, Phys.Rev., 100, 844 (1955).
16. Iu.I.Filimonov & G.A.Petrov, Abstracts in Program of the Seventh Conference on Nuclear Spectroscopy, 1957.
17. G.I.Novikova, L.N.Kondrat'ev, Iu.P.Sobolev & L.L.Gol'din, Abstracts in Program of the Seventh Conference on Nuclear Spectroscopy, 1957.

AMPLITUDE AND TIME CHARACTERISTICS OF A NEW PHOTOMULTIPLIER

- G.S.Vil'dgrube, A.P.Zharkov & E.D.Teterin

Introduction

It has hitherto been generally assumed that one cannot obtain short current pulse rise times in a "louvre type" photomultiplier. This assumption was based on investigations of the time characteristics of extant "louvre type" photomultipliers.

Analysis of the electron transit time straggling in the multiplying system of photomultipliers, however, leads to the following conclusions. The spread of transit times observed at the photomultiplier output is comprised of two components: 1) the straggling in the gap between the photocathode and the first dynode (hereinafter referred to as the "first stage") and 2) the straggling in the remaining stages, i.e., in the rest of the multiplying system.

The first component is the most substantial and "nonreversible". It, together with the uncertainty of the instant of appearance of the first or q-th photoelectron, from the photocathode, determines the spread in the initial instants of the pulses. This component of the time straggling cannot be reduced by "circuitry" modifications.

The second component is "reversible" in the sense that, with sufficient amplification in the photomultiplier, one can utilize only the initial part of the leading edge of the pulse at the output for measurements (by means of appropriate circuitry).

It is, of course, desirable that the transit time straggling be minimal in the multiplying system as well, but this requirement does not impose a rigid limitation on the possible time resolution.

From the standpoint of transit time straggling in the first stage even the FEU-11 (FEU-12) photomultiplier tube is an entirely satisfactory system. Thus with a potential difference of only 400 v between the photocathode and the first dynode, the maximum spread of the transit times of photoelectrons from the 50 mm diameter cathode to the first dynode does not exceed $3 \cdot 10^{-9}$ sec, according to the measurements of A.M.Bonch-Bruevich.

However, the relatively long current pulse rise time in the multiplying system of the FEU-11 (FEU-12) does not allow of realizing (with the inadequate amplification of the multipliers) of a satisfactory time characteristic of the first stage of these tubes. Even for the FEU-11 (FEU-12) photomultipliers it was found that with increasing potential (up to 300 v per stage) the rise time of the output pulses decreases. This indicated that the secondary electron collecting efficiency of the dynode stages in these tubes did not fall off with increasing potential but remained close to 100%. In view of this, in designing the new photomultiplier tubes it was deemed expedient to increase the electric field gradient between the stages and reduce the area of the dynodes with a view to reducing the time straggling.

1. New design features of the photomultipliers

The following modifications, as compared with the FEU-11, were introduced into the design of the new tubes. The width of the dynode "blades" was reduced by a factor of 2 and the separation between the stages by a factor of 1.5. The photomultipliers are made with Bi-Ag-Cs and Cs-Sb photocathodes 20 and 50 mm in diameter. Reduction of the area of the emitting surfaces lowered (as compared with the FEU-11) the mean value of the current at the output (to 10 ma).

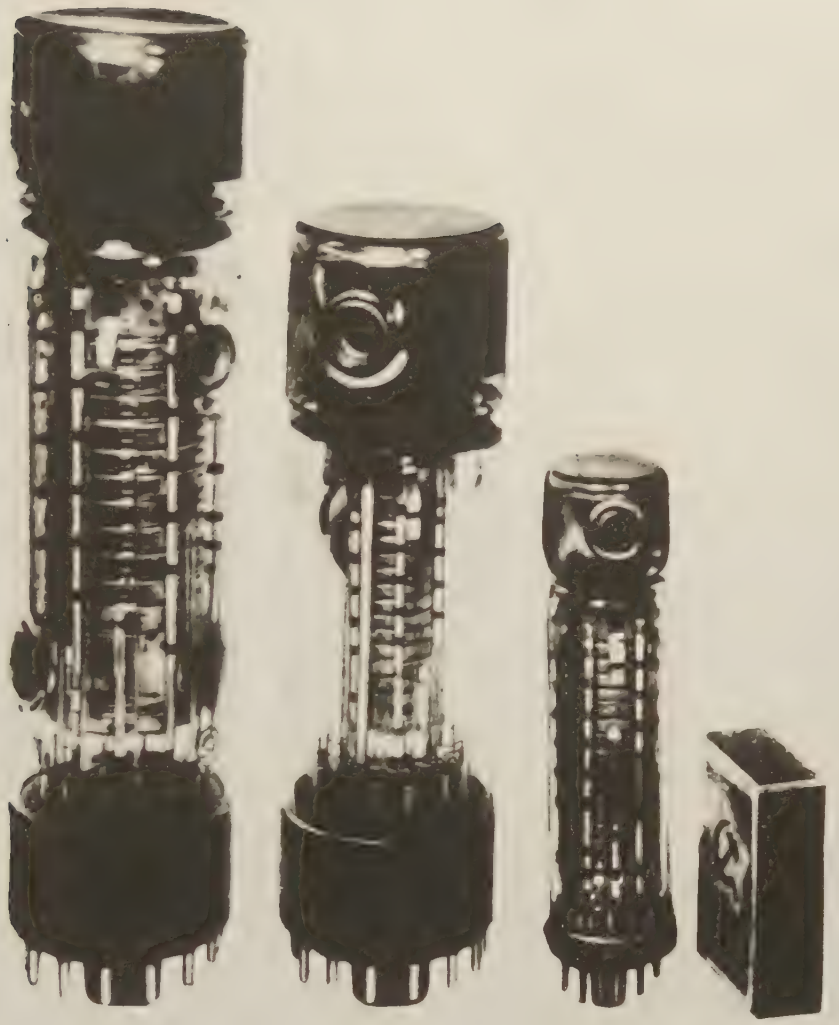

FEU-11 photomultiplier (1) and the new "louvre type" miniaturized photomultipliers: with 50 mm diameter cathode (2) and 20 mm diameter cathode (3). At right, safety match box for comparison.

All the other design characteristics of these multipliers are the same as those of the FEU-11.[1] As regards stability of operation they are equal to the FEU-11 tube. The new tubes together with the FEU-11 are shown in the accompanying photograph.

Although no special measurements of the maximum allowable current in pulse operation were made, it may be stated that a pulse current (pulse duration $6 \cdot 10^{-9}$ sec) of 0.15-0.2 amp can be maintained with no impairment as regards quality of operation of the photomultiplier.

2. Time characteristics

The shape of the current pulses at the output of the photomultiplier was investigated by the method of delayed self-coincidences. A plastic terphenyl-in-styrene scintillator was used in the measurements. The measurements showed that the current pulse rise time is $(2-3)\cdot10^{-9}$ sec for both the 20 and 50 mm diameter cathode tubes. Under conditions of actual coincidences the width of the recorded resolution curve was $3.5\cdot10^{-9}$ sec. This result gives reason to assume that the transit time straggling in the first stage is small. The operating voltages range from 2500 to 3000 v; no noticeable variation in the pulse front duration was observed in the investigated voltage range. The voltage distribution among the stages was uniform, except for the first stage where the potential difference was 1.5 times higher than in the other stages.

3. Amplitude characteristics

Modern experimental requirements often call for good time and amplitude characteristics to be combined in one and the same photomultiplier. In recording the 660 kev γ-line of Cs^{137} the new photomultipliers give a relative line half-width of 10-11% with the photomultiplier viewing a standard NaI(Tl) crystal. In "time regime" operation, the 8th or 9th dynode is used as the "amplitude" output. In conventional "amplitude regime" operation (1600-1800 v) the noise level does not exceed 5.7 kev in the scale of the NaI(Tl) crystal. As the voltage is increased to 2500-3000 v the noise level rises in proportion to the amplification.

Conclusions

The results of our measurements show that the described photomultipliers can be used for amplitude-time measurements.

It should be noted that the possibilities of the "louvre" system of multiplication from the viewpoint of reduction of transit time straggling have not been exhausted: further reduction of straggling is feasible even through purely geometric modifications. It would also be desirable to increase the amplification of the photomultipliers to 10^8.

"V.G.Khlopin" Radium Institute of the
Academy of Sciences of the USSR

References

1. Iu.A.Nemilov, V.M.Ovchinnikov, A.N.Pisarevskii & E.D.Teterin, Atomnaia energiia (Atomic energy), 4, 51 (1956).

Bulletin of the Academy of Sciences of the USSR - Physical Series
Vol. 21, No. 7 - Transactions of the Seventh All-Union Conference on Nuclear Spectroscopy -- Leningrad, 25-31 January 1957
(To be continued in Vol. 21, No. 12)

TABLE OF CONTENTS

	Page Orig.	Trans.
Alpha decay of Pu^{238} - L.N.Kondrat'ev, G.I.Novikova, V.B.Dedov & L.L.Gol'din	907	909
Energy of α-particles from Po^{210} - I.I.Agapkin & L.L.Gol'din	909	911
A grid type ionization chamber - S.A.Baranov, A.G.Zelenkov & Iu.F.Rodionov	913	915
Conversion electron spectra of neutron-deficient thulium isotopes - K.Ia.Gromov, B.S.Dzhelepov & B.K.Preobrazhenskii	918	920
Conversion electron spectra of neutron-deficient lutetium isotopes - Iu.G.Bobrov, K.Ia.Gromov, B.S.Dzhelepov & B.K.Preobrazhenskii	940	942
Internal conversion electron spectrum of radiothorium. Part III. ($H\rho$ = 1380-2700 and 3500-9000 gauss-cm regions). - V.D.Vorob'ev, K.I.Il'in, T.I.Kol'chinskaia, G.D.Latyshev, A.G.Sergeev, Iu.N.Trofimov & V.I.Fadeev	954	956
Spectrum of conversion electrons from Ho^{160} - B.S.Dzhelepov, B.K.Preobrazhenskii, I.M.Rogachev & P.A.Tishkin	962	964
Gamma-radiation from $Eu^{152,154}$ - B.S.Dzhelepov, N.N.Zhukovskii, V.G.Nedovesov & G.E.Shchukin	966	968
Gamma-radiation from Ag^{110} - B.S.Dzhelepov, N.N.Zhukovskii & Iu.G.Kondakov	973	975
Positrons in the radiation from radioactive In^{114} - B.S.Dzhelepov, O.E.Kraft & V.B.Zhinkina	978	980
Gamma-spectrum of In^{114*} - I.B.Golovanov, B.S.Dzhelepov, L.S.Lebedev, V.P.Prikhodtseva & Iu.V.Khol'nov	985	987
Refinement of the relative intensities of the lines in the gamma-spectrum of Ta^{182} - O.I.Sumbaev	987	989
Investigation of the gamma-spectrum of RaC - B.S.Dzhelepov & S.A.Shestopalova	990	992
New lines in the spectrum of RaC - I.F.Uchevatkin & S.A. Shestopalova	1002	1003

Neutron-deficient isotopes of the rare earth elements forming as a result of spallation of Ta under bombardment with 660 Mev protons. Part I - G.M.Gorodinskii, A.N.Murin, V.N.Pokrovskii & B.K.Preobrazhenskii 1004 1005

Rotational levels of Mg^{24} - L.K.Peker, L.V.Gustova & O.V. Chubinskii 1013 1014

Investigation of the (α,n) reaction on oxygen - I.A.Serdiukova, A.G.Khabakhpashev & E.M.Tsenter 1017 1018

Procedure for measuring the activity of nuclei undergoing K-capture - M.Ia.Kuznetsova & V.N.Mekhedov 1020 1021

Characteristics of the jumps in the equilibrium shape of nuclei - L.K.Peker 1025 1026

Spins and parities of deformed odd-odd nuclei - L.K.Peker 1029 1030

Amplitude and time characteristics of a new photomultiplier - G.S.Vil'dgrube, A.P.Zharkov & E.D.Teterin 1034 1035

Translated in 1958 by
Columbia Technical Translations
5 Vermont Ave., White Plains, N.Y.

Transactions of the Third Conference

on the

Physics of Magnetic Phenomena

Continued from Vol.21, No.6; to be continued in Vol.21, No.9

Translation Editor's Note

The original of this issue of the Bulletin contains a report entitled "Magnetic Properties of Some Orthoferrites and Cyanides at Low Temperatures" by R.M.Bozorth, H.J.Williams and Dorothy E.Walsh. Inasmuch as it has been published in Phys.Rev. 103, 572 (1956), we are omitting it from this issue of the Bulletin. We take this occasion to thank Dr.Bozorth for calling our attention to the Phys.Rev. publication.

We again wish to acknowledge the kindness and cooperation of the several authors whose papers were presented in English at the Conference. We are deeply indebted to them for furnishing copies of their manuscripts and granting permission to print.

The onus of any errors that may have crept into the reports in the process of editing and typing should, of course, be laid at the already sagging shoulders of

Your editor,

E.J.R.

White Plains, N.Y.
October 1958

INFLUENCE OF THE STRUCTURAL CHARACTERISTICS OF FERROMAGNETS ON THE TEMPERATURE DEPENDENCE OF THE SPONTANEOUS MAGNETIZATION

- K.P.Belov and A.N.Goriaga

Introduction

Sucksmith[1], Guilland[2] and Went[3] have reported significant differences between the temperature variation of the spontaneous magnetization in alloys as compared with the variation in pure ferromagnetic metals. All these authors investigated the temperature dependence of the spontaneous magnetization in temperature intervals somewhat removed from the Curie point. The said differences should, however, be particularly appreciable in the immediate vicinity of the Curie point, where the spontaneous magnetization is very sensitive both to external influences and to structural factors.

We know of no systematic experimental data in the literature relative to the influence of structural factors on the temperature dependence of the spontaneous magnetization in alloys near the Curie point.

In the present report we give the results of experimental investigation and analysis of the true magnetization curves for a number of nickel alloys in the vicinity of the Curie point. We determined the temperature dependence of the spontaneous magnetization near the Curie point from these curves by the following two methods:

1) The "lines of equal magnetization method" proposed by Weiss and Forrer. The procedure consists of plotting $H(T)_{\sigma = \text{const}}$ curves for different values of the magnetization and then finding the spontaneous magnetization by extrapolating these curves to H = 0. This procedure yields approximately the same results as that based on extrapolation of magnetocaloric effect curves.

2) The so-called "method of thermodynamic coefficients"[4], which is based on reduction of the true magnetization curves by means of the thermodynamic equation

$$\alpha\sigma + \beta\sigma^3 = H$$

where $\sigma = J/\rho$ is the specific magnetization (J is the magnetization and ρ is the density) and α and β are thermodynamic coefficients.

From this equation, for H = 0, we obtain the following formula for calculating the spontaneous magnetization at various temperatures near the Curie point

$$\sigma_s^2 = -\frac{\alpha}{\beta}. \qquad (1)$$

Having the values of α and β from experiment, we can calculate the temperature dependence of σ_s^2. The thermodynamic coefficients method gives the temperature variation of the magnetic long range order, and thereby makes it possible to determine correctly the actual temperature of the Curie point.[5]

Comparison of the results obtained by means of the two methods makes it possible to bring out the basic characteristics of the behavior of the spontaneous magnetization near the Curie point, in particular, to determine "residue" or "tail" of the spontaneous magnetization.[5]

In order to be able to compare the temperature dependences of the spontaneous magnetization in different alloys, as well as in the same alloys before and after heat treatment, we plotted all the curves in "reduced" (σ_s/σ_0), (T/θ) coordinates; where for σ_0 we took the specific saturation magnetization

of the alloys at the boiling point of helium*. Analysis of the spontaneous magnetization curves, as determined both by the "lines of equal magnetization" method and the "method of thermodynamic coefficients", allowed us to check the familiar relation, ensuing from model and thermodynamic concepts[6]:

$$\left(\frac{\sigma_s}{\sigma_0}\right)^2 = \xi\left(1-\frac{T}{\theta}\right). \qquad (2)$$

Here the coefficient ξ characterizes the steepness of the $(\sigma_s/\sigma_0)^2$ vs T/θ curve at the approach to the Curie temperature. Recently, values of for pure metals have been discussed by Dorfman[7] and Vonsovskii & Vlasov[8]. In the present investigation we attempted to evaluate ξ for some nickel alloys.

1. Ni-Cu Alloys

A series of nickel-copper alloys was prepared specifically for the investigation. All the alloys were given a preliminary homogenizing heat treatment: annealed at 1000° for 20 hours. After this we recorded the magnetization curves near the Curie point in fields from 300 to 2500 oersted (the measurement procedure has been described earlier[9]). Finally the temperature variation of the spontaneous magnetization in the vicinity of the Curie point was determined by the two methods mentioned above from these curves.

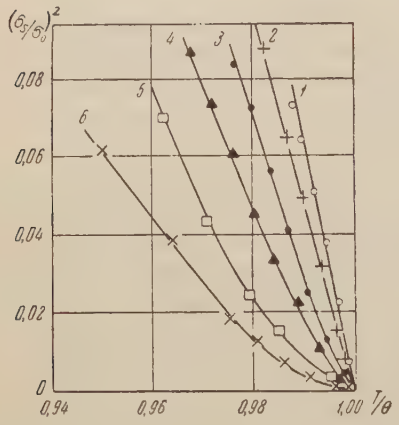

Fig.1. Variation of the square of the spontaneous magnetization with the temperature in "reduced" coordinates near the Curie point for Ni-Cu alloys annealed for 20 hours at 1000°: 1) 0%, 2) 5%, 3) 8%, 4) 15%, 5) 20% and 6) 25% Cu.

Fig.1 shows the variation of $(\sigma_s/\sigma_0)^2$ with T/θ for the investigated Ni-Cu alloys and pure nickel. It will be seen that for pure nickel and alloys with a low copper content the curves are straight lines in accord with theory. In alloys with a high copper content, on the other hand, the variation is nonlinear. Although the Ni-Cu alloys are ostensibly mutual solid solutions, a certain amount of liquation occurs in the process of solidification so that as a rule the distribution of copper atoms in the nickel matrix is not uniform. This inevitably leads to fluctuation of the exchange interaction over the volume of the sample; in consequence, the ferromagnetic transformation is smeared out, i.e., instead of a single Curie point the alloy has a whole series of slightly different Curie points. Obviously, the variation of $(\sigma_s/\sigma_0)^2$ with T/θ in this case will be nonlinear.

Prolonged annealing, leading to equalization of the concentrations throughout the sample and, consequently, to smoothing out of the exchange interaction fluctuations should also "normalize" the magnetic characteristics, i.e., should make them similar to the characteristics of pure metals. Such "normalization" was already partially realized in the investigated alloys by the preliminary homogenizing annealing**. The curves of Fig.2 show how the coefficient β for

---

*Measurements of the saturation magnetization of the alloys at helium temperatures were carried out by A.V.Ped'ko in the cryostat of the Low Temperature Laboratory of Moscow State University with the kind permission of A.I. Shal'nikov; we take this occasion to thank them.

**Appreciably longer annealing is necessary for complete "normalization".

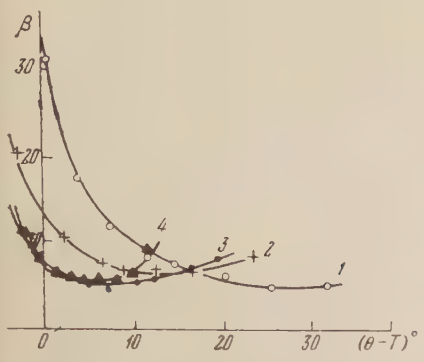

Fig.2. Temperature dependence of the coefficient β for the 80% + + 20% Cu alloy after annealing at 1000° for different lengths of time: 1) 10, 2) 20, 3) 30 and 4) 40 hours.

the 80% Ni + 20% Cu alloy varies with the annealing time; with a sufficient increase in annealing time the curves begin to exhibit the minimum characteristic of homogeneous ferromagnets, for example, pure nickel (see Ref.4).

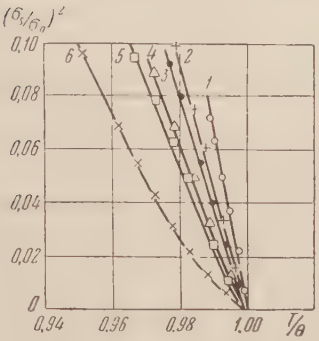

Fig.3. Same as Fig.1 but after annealing for 90 hours.

Fig.3 shows the variation of $(\sigma_s/\sigma_0)^2$ with T/θ for alloys annealed for 90 hours. It will be seen that all the curves are appreciably more rectilinear (compare with Fig. 1). The observed deviation from linearity for the 75% Ni + 25% Cu alloy apparently indicates that even the 90 hour anneal is still not sufficient in the case of this alloy for complete equalization of the concentrations. It should also be noted that the "tail" of the spontaneous magnetization determined for these alloys by the "method of lines of equal magnetization" is shortened with increasing annealing time.

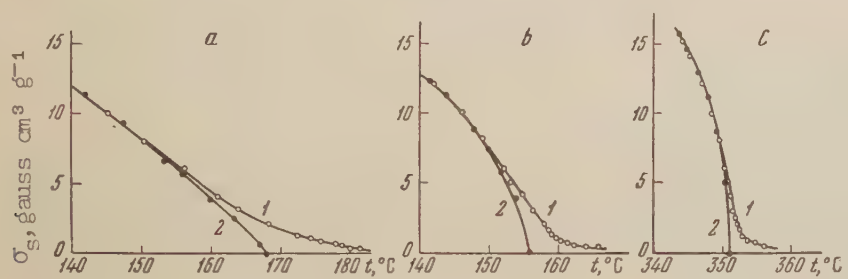

Fig.4. "Tails" of spontaneous magnetization in the 80% Ni + 20% Cu alloy after annealing for a) 10 hours at 1000°, and b) 20 hours at 1000° and 20 hours at 1200°; c) curve for pure Ni. 1 - curve obtained by the method of "lines of equal magnetization"; 2 - curve obtained by the method of "thermodynamic doefficients".

It will be seen from Fig.4 that in the case of the 80% Ni + 20% Cu alloy, the spontaneous magnetization "tail" becomes shorter with increasing annealing time and the σ_s vs temperature curve for this alloy becomes similar to the curve for pure nickel. Analogous effects have been observed by other investigators measuring the magnetic and "nonmagnetic" properties of these alloys. Thus, for example, Kussmann & Schulze[10], in measuring the temperature dependence of the conductivity and initial permeability, and Volkov & Chechernikov[11], in measuring the temperature dependence of the magnetostriction, established that in Cu-Ni alloys the "tails" of these properties in the vicinity of the Curie point are appreciably shortened as a result of prolonged annealing.

The following conclusions may be drawn from the results of our investigation of Ni-Cu alloys: 1) the temperature variation of the spontaneous magnetization and the temperature dependences of the thermodynamic coefficients α and β in the vicinity of the Curie point (in contrast to what is observed at low temperatures) are highly sensitive to inhomogeneity of concentration; 2) quantitative comparison of the values of the coefficient ξ in Eq.(2) for nickel-copper alloys with different Cu concentrations is feasible only after

prolonged annealing. The variation of $(\sigma_s/\sigma_0)^2$ with T/θ becomes linear only after such prolonged annealing.

Let us now compare the values of ξ for nickel and Ni-Cu alloys. The values of ξ deduced from our measurements are listed in Table 1. It will be evident that ξ decreases with increasing Cu content. This means that the slope of the spontaneous magnetization vs temperature curve decreases with increasing Cu concentration, i.e., that the ferromagnetic transformation is increasingly smeared out with rising Cu concentration. According to Sucksmith[1] and Went[3] the principal reason for smearing out of the ferromagnetic transformation in alloys is fluctuation of the atomic order (inhomogeneity of the Cu concentration). This factor, as we have already seen, exerts a strong influence on the temperature dependence of the spontaneous magnetization in nickel-copper alloys. The effect of this factor can be minimized by prolonged annealing. Our experiments have shown, however, that even after prolonged annealing the smearing out of the ferromagnetic transformation is still appreciable. In our opinion it is connected with the structural characteristics of the alloy, the character of the short range order and the interatomic interaction.

Table 1

Values of the Curie point and the thermodynamic coefficient ξ for Ni-Cu alloys

Alloy	θ,°K	ξ	$\sqrt{\xi}$
100% Ni	624	6,95	2,64
95% Ni + 5% Cu	575	5,34	2,31
92% Ni + 8% Cu	548	4,69	2,16
85% Ni + 15% Cu	478	3,76	1,94
80% Ni + 20% Cu	428	3,44	1,85

Vonsovskii & Vlasov[8], proceeding from the s-d exchange interaction model, attempted to give physical meaning to the coefficient ξ. Their theory leads to the following formula for the temperature dependence of the spontaneous magnetization of metals in the vicinity of the Curie point:

$$\left(\frac{\sigma_s}{\sigma_0}\right)^2 = 3\left(\frac{\theta}{\theta_d}\right)^2\left(1-\frac{T}{\theta}\right), \tag{3}$$

in other words, according to these authors,

$$\xi = 3\left(\frac{\theta}{\theta_d}\right)^2. \tag{4}$$

Here θ is the Curie point taking into account s-d exchange interaction and θ_d is the Curie point without taking it into account, i.e., the Curie point determined only by d-d exchange interaction. According to Vonsovskii-Vlasov theory $\theta/\theta_d > 1$. This means that $\xi > 3$. The experimental data for pure nickel and Ni-Cu alloys are consistent with these predictions from theory (see Table 1).

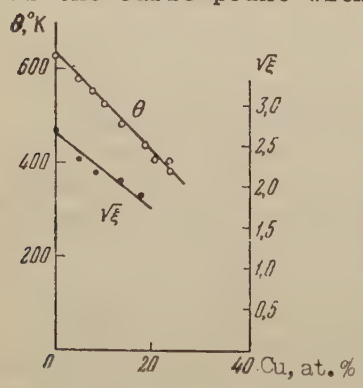

Fig.5. Variation of θ and $\sqrt{\xi}$ with the Cu concentration in Ni-Cu alloys.

As is known, the Curie point θ in Ni-Cu alloys decreases linearly with increasing Cu concentration. This decrease of θ occurs due to weakening of d-d as well as, apparently, to weakening of s-d interaction. Some confirmation of the assumption that s-d exchange interaction also decreases is furnished by the data listed in Table 1. In the table we have also listed the values of $\sqrt{\xi} \sim \theta/\theta_d$. It will be seen that $\sqrt{\xi}$ decreases with increasing Cu concentration. The tabular values are plotted against the copper concentration in Fig.5. It will be evident that $\sqrt{\xi}$ (just as θ) de-

creases approximately linearly with increasing Cu concentration.

In order to explain this decrease one must assume that the numerator in Eq.(4) decreases with rising Cu concentration more rapidly than the denominator.

In other words, according to the theory of Vonsovskii & Vlasov[8], the decrease in the slope of the $(\sigma_s/\sigma_0)^2$ vs T/θ plots for Ni-Cu alloys occurs primarily due to reduction of the s-d exchange interaction.

2. Alloy Close to Ni_3Mn in Composition

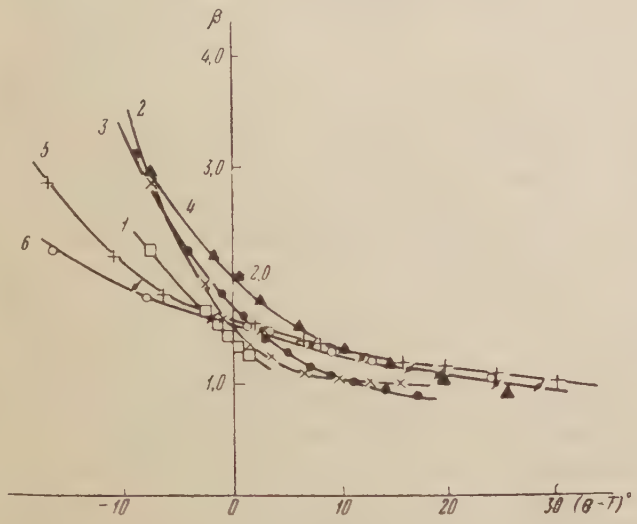

Fig.6. Temperature dependence of the coefficient β for the alloy close to Ni_3Mn in composition after different periods of annealing at 380°: 1) 40 min, 2) 1 hr, 3) 2 hr, 4) 6 hr, 5) 16 hr, 6) 36 & 84 hr.

We carried out experiments on the influence of annealing on the ferromagnetic transformation in an alloy having a composition close to Ni_3Mn (21 atomic % Mn). As is known, appropriate heat treatment results in atomic ordering in alloys of this type. Prior to measurement, the sample was first quenched (to obtain the disordered state) and then annealed at 380° for different lengths of time.

The curves characterizing the temperature dependence of β after different periods of annealing are shown in Fig.6. It will be seen that none of the curves exhibits the typical minimum indicative of "normalization" of the alloy.

It will be seen from Fig.7, where σ_s^2 is plotted as a function of $\theta - T$, that contrary to what might have been expected, the curve

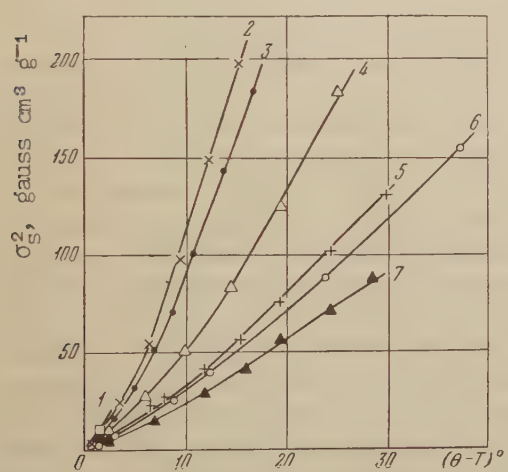

Fig.7. Temperature dependence of σ_s^2 for the alloy close to Ni_3Mn in composition after different annealing periods at 380°: 1) 40 min, 2) 1 hr, 3) 2 hr, 4) 6 hr, 5) 16 hr, 6) 36 hr, 7) 84 hr.

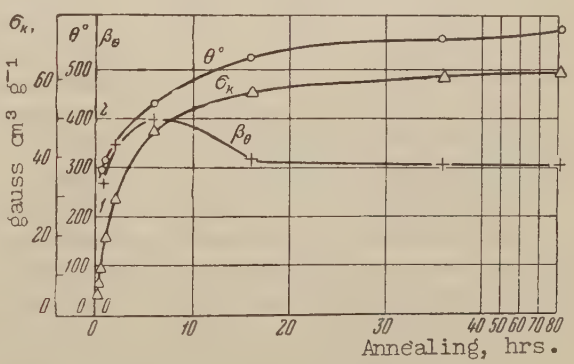

Fig.8. Variation of the Curie point θ, the saturation magnetization σ_k at room temperature and the coefficient β_θ (at the Curie point) with the annealing time for the alloy close to Ni_3Mn in composition.

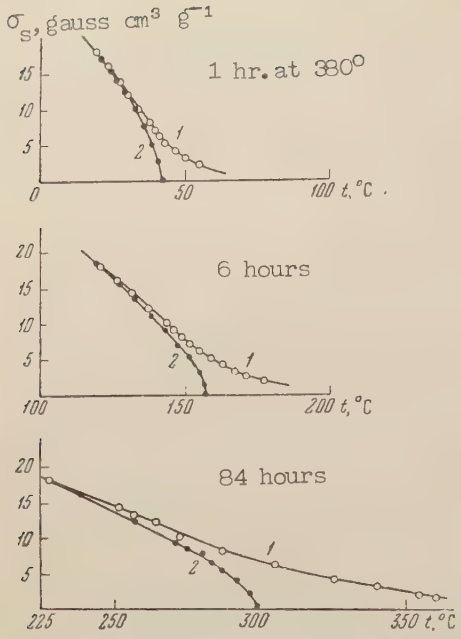

Fig.9. Influence of annealing time on the "tail" of the spontaneous magnetization in the alloy close in composition to Ni_3Mn: 1) curves obtained by the method of lines of equal magnetization and 2) curves obtained by the method of thermodynamic coefficients.

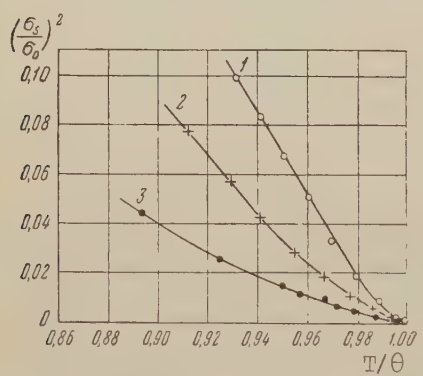

Fig.10. Temperature dependence of the square of the spontaneous magnetization in the alloy close to Ni_3Mn in composition after different annealing times at 380°: 1) 1 hr, 2) 6 hr, and 3) 84 hr.

even after 84 hours annealing does not become linear, even though as would appear from Fig.8 the process of ordering has gone to completion (by 20-30 hours annealing time) inasmuch as the Curie point θ, the saturation magnetization at room temperature and the coefficient β_θ (at the Curie point) have reached limiting (saturation) values.

It will be seen from Fig.9 that the "tails" of the spontaneous magnetization not only do not become shorter, but on the contrary become much longer with increasing annealing time.

Lastly, we must note one more interesting experimental fact. The variations of $(\sigma_s/\sigma_0)^2$ with T/θ for this alloy for three annealing times are shown in Fig.10. It will be seen that with increasing annealing time the slope of this curve decreases appreciably, which indicates that the ferromagnetic transformation is increasingly smeared out. This is apparently connected with the fact that in the alloy, in addition to the main ordered phase, there exist disordered phase "islands" which are responsible for fluctuation of the exchange interaction over the volume of the specimen and, consequently, the smearing out of the transformation. As has been noted in the literature[12], it is difficult to obtain complete ordering in the Ni-Mn alloy close to Ni_3Mn in composition.

3. Invar Type Ni-Fe Alloys

Invar alloys are characterized by distinctive magnetic anomalies and hence we felt it would be of particular interest to investigate the temperature dependence of their spontaneous magnetization in the vicinity of the Curie point. We investigated two alloys, namely, 36% Ni + 64% Fe and 35% Ni + 65% Fe. Our measurements showed that the temperature variation of the spontaneous magnetization near the Curie point in these alloys depends on the preliminary heat treatment. This, just as in the case of Ni-Cu alloys, can probably be explained by the influence of inhomogeneity of concentration over the volume due to liquation. There is, however, a heat treatment that makes the σ_s vs t curve more "normal". The temperature dependences of β and σ_s^2 for samples of the 35% Ni + 65% Fe alloy annealed for different periods are shown in Figs. 11 and 12.

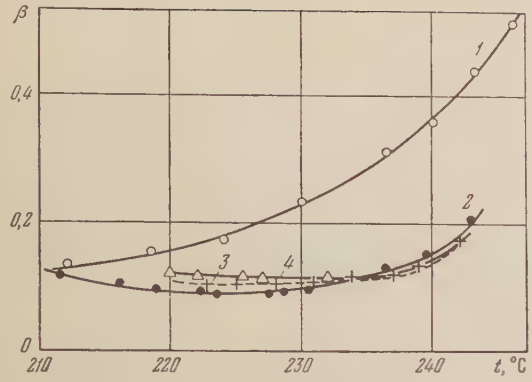

Fig.11. Temperature dependence of the coefficient β of the 35% Ni + 65% Fe invar alloy: 1) cold drawn specimen, 2) after 5 hr annealing at 1000°, 3) 10 hr at 1000°, 4) 20 hr at 1100°.

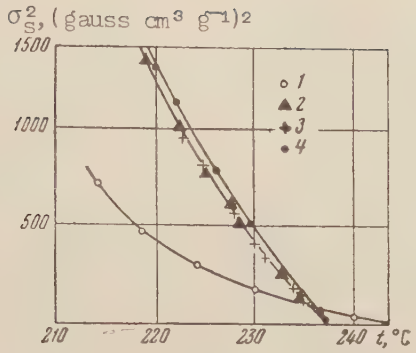

Fig.12. Temperature dependences of σ_s^2 of the 35% Ni + 65% Fe invar alloy: 1) cold drawn specimen, 2) after 5 hr annealing at 1000°, 3) 10 hr at 1000°, 4) 20 hr at 1100°.

Table 2

Values of the Curie point θ and the thermodynamic coefficient ξ for Ni-Fe alloys

Alloy	θ, °K	ξ
36% Ni + 64% Fe	571	1,44
35% Ni + 65% Fe	510	1,46

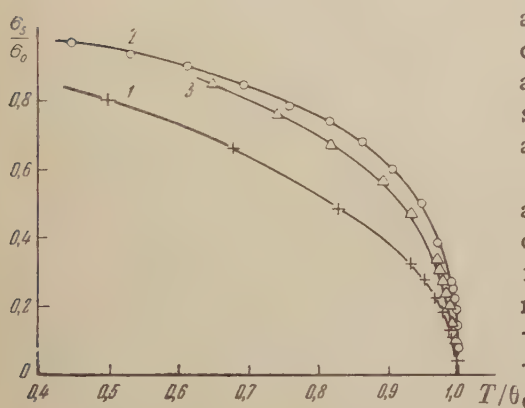

Fig.13. Variation of σ_s/σ_0 with T/θ for 1) the 36% Ni + 64% Fe alloy, 2) nickel, and 3) the 80% Ni + 20% Cu alloy.

It will be seen that as a result of annealing the β vs t curves acquire a minimum, while the σ_s^2 vs t curves straighten out. Little further change occurs when the annealing is extended beyond some 5 hrs. It was found, nevertheless, that the coefficient for the invar alloys is appreciably smaller than 3 (see Table 2); this indicates that the ferromagnetic transformation in invar type Ni-Fe alloys is greatly smeared out.

In Fig.13 we give the σ_s/σ_0 vs T/θ curve for the 36% Ni + 64% Fe alloy (after prolonged annealing) together with the corresponding curves for pure nickel and the 80% Ni + Cu alloy for purposes of comparison. It will be seen that the curve for the invar alloy is anomalously flat.

A possible reason for the anomalous character of the spontaneous magnetization curve of invar alloys may be that the ferromagnetism in these alloys is due to exchange interaction not only between atoms in the first coordination sphere but also to longer range interaction. In other words, these alloys may be characterized not by one but by several exchange inegrals, which leads to smearing out of the ferromagnetic transformation.

Department of Physics,
Moscow State University

References

1. W.Sucksmith, J.Phys.of Rad., 12, 490 (1951).
2. M.Guilland, C.R., 222, 1110 (1946).
3. J.Went, Physica, 17, 596 (1951).
4. K.P.Belov & A.N.Goriaga, FMM (Physics of Metals and Metallography), 2, 3 (1956).
5. K.P.Belov & Ia.Paches, FMM (Physics of Metals and Metallography), 4, 48 (1957).
6. S.V.Vonsovskii & Ia.S.Shur, Ferromagnetizm (Ferromagnetism), M.-L,1948.
7. Ia.S.Dorfman, Magnitnye svoistva i stroenie veshchestva (Magnetic properties and the structure of matter), M.1955.
8. S.V.Vonsovskii & K.B.Vlasov, Zhur.eksp.i teor.fiz., 25, 327 (1953).
9. K.P.Belov, Uchenye zapiski (Scientific records) Moscow State University, No.162, 21 (1952).
10. A.Kussmann& A.Schulze, Phys.ZS., 38, 42 (1937).
11. D.I.Volkov & V.I.Chechernikov, Zhur.eksp. i teor. fiz., 27, 208 (1954).
12. R.M.Bozorth, Ferromagnetism. (Cited in Russian trans., M.1956.)

INVESTIGATION OF THE MAGNETIZATION OF FERRITES IN THE VICINITY OF THE CURIE POINT

- K.P.Belov, K.M.Bol'shova & T.A.Elkina

The purpose of the present work was to investigate true magnetization (the paraprocess) in certain ferrites. Inasmuch as the intensity of the paraprocess increases with temperature, attaining the maximum at the Curie point, we strove to make all our measurements near this temperature. In this temperature region one can compare the parameters characterizing the paraprocess in different materials. The paraprocess in essence consists of the orienting action of the magnetic field on the spin magnetic moments in the magnetic domains. We felt it would be of interest to compare the true magnetization curves for ferrites and metals in order to elucidate the distinctive characteristics of the paraprocesses in these two different types of ferromagnets.

We were also interested in obtaining the curves characterizing the paraprocess in ferrites because from these one can determine the temperature variation of the spontaneous magnetization in these materials in the immediate vicinity of the Curie point. There is little information on the subject in the literature[1]. At the same time such data are necessary for investigating the character of the ferromagnetic transformation in ferrites, many details of which are as yet unclarified. Investigation of ferromagnetic transitions in ferrites is also of theoretical interest because the mechanism of the appearance of spontaneous magnetization in them differs from the mechanism in ferromagnetic metals.

1. Procedure and samples

We studied seven samples of ferrites in the Mn-Zn ferrite system with MnO contents ranging from 20 to 40% and two ferrites of the Co-Zn system. The Mn-Zn ferrites were prepared by the procedure used in obtaining commercial samples (the Co-Zn ferrites were prepared from chemically pure materials in the Department of Chemistry of Moscow State University). Ferrites with low Curie points were chosen with a view to precluding the possibility of structural changes incident to heating to high temperatures. The samples were in the form of bars of approximately square cross section, 4.5 mm on the side and about 40 mm in length.

The magnetization curves at different temperatures were recorded by the ballistic procedure. Specimens were magnetized in a solenoid yielding fields of up to 2500 oersted. The differential ballistic coil was wound on an ebonite form which was mounted over the water jacket of an electric heater. The coil consisted of two identical sections of 4500 turns each. In each case the specimen was positioned so that its center was in line with the center of one of the coil sections. Prior to measurement the differential coil system was compensated (balanced) in the absence of the specimen.

Obviously, with the given system in the case of measurements on short samples, it would be incorrect to calculate the magnetization in the specimen by means of the usual formulas inasmuch as the magnetic flux through the air gap from the ends of the sample will intersect the turns of the ballistic coil, with the result that the calculated magnetization of the sample would be lower than the true value. It was therefore necessary to calibrate the equipment, i.e., to find experimentally the factor relating the deflection of the galvanometer to the true magnetization in the specimen. To this end we prepared a single layer coil, wound of thin conductor on a form of the same shape and size

as the specimen. This coil was positioned exactly in the place of the sample and a current passed through it. Since the magnetic moment of the coil could readily be calculated, we were able to calibrate our set-up in this manner.

The temperature was measured by means of a copper-constantan thermocouple. The temperature was maintained uniform over the length of the heater within 0.15°.

2. True magnetization of ferrites close to the Curie point

Our measurements showed that the paraprocess curves for ferrites close to the Curie point are closely characterized by the thermodynamic expression that we used earlier for describing the true magnetization of metallic ferromagnets[2]:

$$\alpha + \beta\sigma^2 = \frac{H}{\sigma}, \qquad (1)$$

where $\sigma = J/\rho$ is the specific magnetization (J is the magnetization and ρ is the density) and α and β are thermodynamic coefficients, dependent on the temperature and elastic stresses.

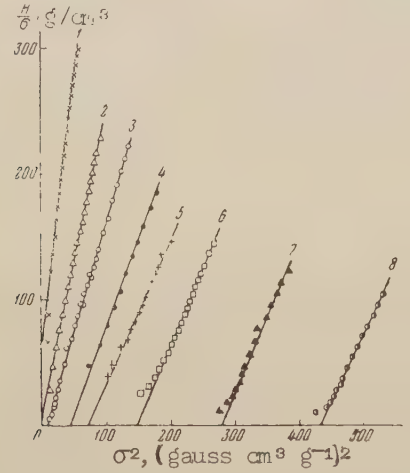

Fig.1. Variation of H/σ with σ^2 near the Curie point for the 35.5% MnO + + 15% ZnO + 49.5% Fe_2O_3 ferrite at different temperatures: 1) 185°, 2) 180°, 3) 178°, 4) 175°, 5) 173°, 6) 170°, 7) 165° and 8) 160°.

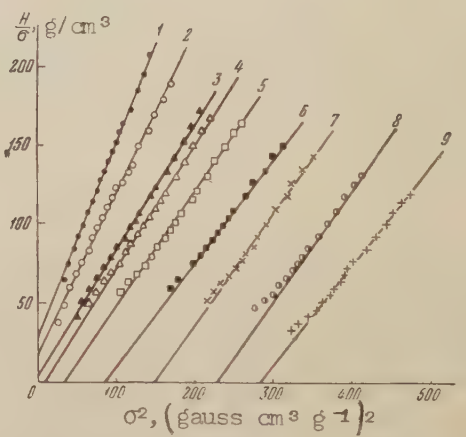

Fig.2. Same as Fig.1 but for the 28% MnO + 21.5% ZnO + 50.5% Fe_2O_3 ferrite at: 1) 110°, 2) 108°, 3) 106°, 4) 105°, 5) 104°, 6) 102°, 7) 100°, 8) 98° and 9) 96°.

The curves giving the variation of H/σ with σ^2 for two of the investigated ferrites are shown in Figs.1 & 2 (analogous results were obtained for the other ferrites including the Co-Zn ferrites*). It will be seen that in accord with (1) the plots are straight lines. The deviations in weak fields are associated with the technical magnetization processes which are not taken into account in Eq.(1). Eq.(1) holds particularly well in the temperature region close to the Curie point.

The values of the coefficients α and β can be determined graphically from the curves of Figs.1 & 2. As follows from the thermodynamic theory of ferromagnetic transformations[3,4] at $t < \theta$, the coefficient α is less than zero

---

*S.A.Nikitina participated in the measurements on the Co-Zn ferrites.

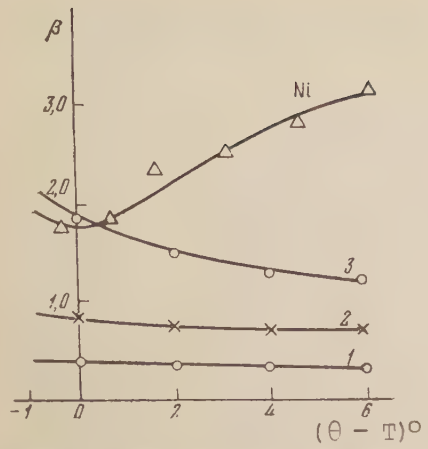

Fig.3. Temperature variation of the coefficient β for Mn-Zn ferrites of different composition: 1) 23% MnO, 2) 28% MnO, 3) 35.5% MnO. The curve for pure nickel is shown for comparison.

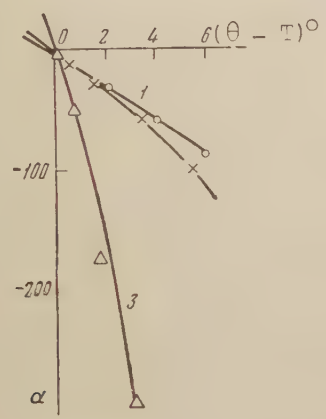

Fig.4. Temperature dependence of the coefficient α for ferrites: 1) 23% MnO, 2) 28% MnO, 3) pure Ni.

(i.e., negative, while for $t > \theta$, $\alpha > 0$). It goes through zero at the Curie point; this serves as an indication of θ. As for the coefficient β, according to the theory, it is positive at all temperatures. Variations of the experimental values of α and β with temperature have been plotted in Figs.3 & 4, from which it follows that the deductions from theory are in agreement with experiment. The general character of the temperature variation of α and β for ferrites is the same as for metallic alloys.[2]

One can effectively compare the intensity of the paraprocess in different materials only by juxtaposing the true magnetization curves in the immediate proximity of the Curie point where the paraprocess is maximal. At $t = \theta$, when $\alpha \to 0$, we have from (1):

$$\sigma = \frac{1}{\sqrt[3]{\beta_\theta}} H^{1/3}. \qquad (2)$$

The greater the value of $1/\sqrt[3]{\beta_\theta}$, the steeper will be the curve characterizing the magnetization at the Curie point and the more intense the paraprocess. Thus the magnitude of $1/\sqrt[3]{\beta_\theta}$ can serve as a parameter characterizing the intensity of the paraprocess in different materials. The values of this parameter for the investigated ferrites as well as for nickel and some nickel alloys are listed in Table 1 together with the corresponding Curie points and the values of the absolute saturation magnetization σ_0. For σ_0 we have taken the value of the magnetization saturation at the boiling point of helium, according to the measurements of A.V.Ped'ko.

It will be evident from the table that the paraprocess in the investigated ferrites is of the same order of magnitude as in metallic ferromagnets. The great intensity of the paraprocess in ferrites is due to the fact that they are characterized by high values of the absolute saturation magnetization σ_0, which is determined by the number and magnitude of the elementary magnetic moments. There is no discernible correlation between the intensity of the paraprocess and the values of the Curie point, although it might be inferred from general theoretical considerations that a relationship should obtain: it might be assumed that the lower the Curie point, the weaker the exchange interaction and the greater the perturbing influence of the external field on the elementary moments, i.e., the greater the intensity of the paraprocess.

It should be noted that the value of β_θ (as experiments with alloys have shown[5]) depends substantially on the thermal history of the sample, i.e., on whether it was subjected to homogenizing annealing. We did not anneal our ferrite samples. This may be the reason why the experiments did not bring out any apparent correlation between the intensity of the paraprocess and the Curie temperature.

3. Temperature variation of the spontaneous magnetization in ferrites near the Curie point

Table 1

Values of the intensity of the paraprocess, the absolute saturation magnetization and the Curie point for Mn-Zn ferrites

Material	$\frac{1}{\sqrt[3]{\beta_\theta}}$	σ_0, gauss $cm^3\ g^{-1}$	θ, ° K
35,5% MnO + 15% ZnO + + 49,5% Fe_2O_3	0,805	152	467,5
28% MnO + 22,5% ZnO + + 49,5% Fe_2O_3	1,07	146	387
30% MnO + 20% ZnO + 50% Fe_2O_3	0,88	144	401,5
40% MnO + 10% ZnO + 50% Fe_2O_3	0,55	102	475
23% MnO + 27,5 ZnO + + 49,5% Fe_2O_3	1,35		300
25% CoO + 25% ZnO + 50% Fe_2O_3	1,35		
20% CoO + 30% ZnO + 50% Fe_2O_3	1,12		
Nickel	0,8	55,2	628
80% Ni + 20% Cu	0,5	35,9	428
36% Ni + 64% Fe	2,14	184,4	571
Ni_3Mn (ordered)	0,87		

Having the experimental paraprocess curves, there are three ways in which one can determine the temperature variation of the spontaneous magnetization in the vicinity of the Curie point:

1) by the well-known method of "lines of equal magnetization" proposed by Weiss and Forrer,

2) by the method of "thermodynamic coefficients"[2] which follows from Eq.(1); for H = 0, we have from (1):

$$\sigma_s = \sqrt{-\frac{\alpha}{\beta}},$$

3) by extrapolation of the true magnetization isotherms to H = 0.

The results of such determinations for some of the Mn-Zn ferrites are shown in Figs.5 & 6. The spontaneous magnetization values obtained by all three methods agree in the temperature region below the Curie point θ (we take θ to be the temperature at which $\alpha = 0$). Divergences become noticeable only at temperatures some 3-5° below the Curie point: the curve for the temperature dependence of σ_s obtained by the method of thermodynamic coefficients falls steeply toward the t-axis,

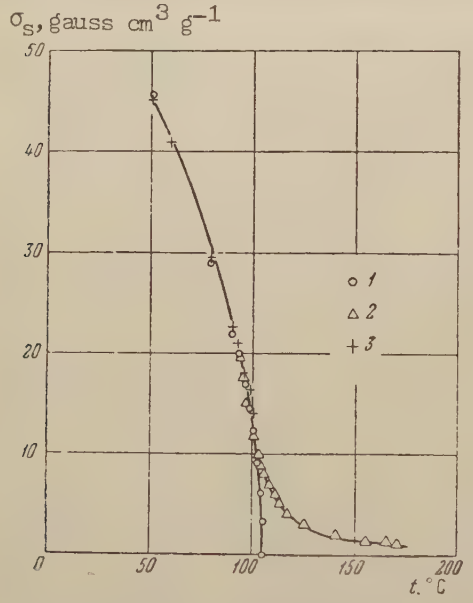

Fig.5. Temperature dependence of the spontaneous magnetization near the Curie point for the 28% MnO + 21.5% ZnO + 50.5% Fe_2O_3 ferrite: 1) spontaneous magnetization values determined by the method of thermodynamic coefficients, 2) values determined by the method of lines of equal magnetization and 3) values determined by the method of magnetization isotherms.

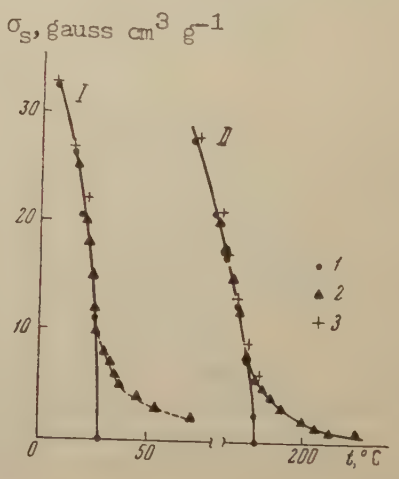

Fig.6. Same as Fig.5 but for ferrites with 23% MnO (I) and 35.5% MnO (II).

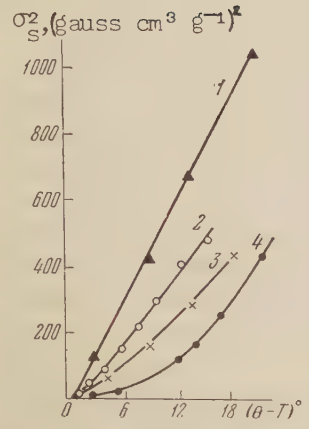

Fig.7. Variation of σ_s^2 with $(T - \theta)$ for Mn-Zn ferrites with different MnO concentrations: 1) 23%, 2) 28%, 3) 35.5% and 4) 40% MnO.

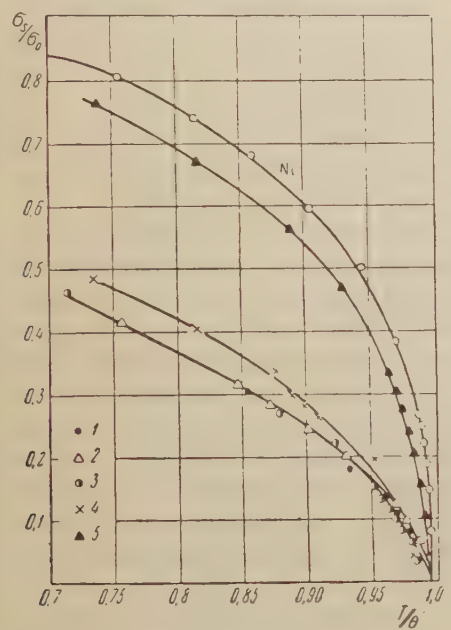

Fig.8. Variation of σ_s/σ_0 with T/θ for metals and ferrites: 1) Mn-Zn ferrite with 35.5% MnO, 2) with 28% MnO, 3) with 30% MnO, 4) with 40% MnO and 5) alloy of 80% Ni + + 20% Cu.

i.e., continues the curve obtained by the three methods in the region of lower temperatures, while the curve obtained by the lines of equal magnetization method bends over and asymptotically approaches the t-axis, forming the so-called spontaneous magnetization "tail". It becomes impossible to determine σ_s from the magnetization isotherms at temperatures from about 10° below the Curie point because the magnetization isotherms in a strong field become nonlinear as the Curie point is approached. The curvature of the magnetization isotherms increases rapidly as the Curie point is neared, consequently any attempt to extrapolate the isotherms of magnetization in strong fields to H = 0 must necessarily be highly arbitrary and conducive to misleading results.

At temperatures above the Curie point there appears a linear section in the magnetization curves in the region of strong fields; this rectilinear section increases in length with increasing temperature. However, even at temperatures 200° above the Curie point a nonlinear section persists in the magnetization curve in the region of weak fields (to ~400 oersted). Pure paramagnetic behavior is observed only at temperatures 250° above the Curie point. Analogous temperature dependences of the spontaneous magnetization were observed for all the investigated Mn-Zn ferrites.

It is of interest to compare the length of the spontaneous magnetization "tail" in ferrites and alloys. The length of the "tail" in the investigated ferrites attained as much as 70°, while in Ni-Cu alloys the length is only ~15°. It was shown in Refs.2 & 5 that such "tails" in the case of alloys are due to fluctuation of the concentration over the volume of the sample. An analogous fluctuation can, apparently, obtain in ferrites, particularly mixed ones. Recently Sucksmith and his coworkers[1] carried out measurements of the spontaneous magnetization near the Curie point in a simple ($MnO \cdot Fe_2O_3$) and in a mixed ($0.5\ MgO \cdot 0.5\ ZnO \cdot Fe_2O_3$) ferrite. They established that in the simple ferrite the spontaneous magnetization "tail" is rather short, while in the mixed ferrite it attains an appreciable length.

From the thermodynamic theory of the ferromagnetic transformation[3], it follows that

$$\left(\frac{\sigma_s}{\sigma_0}\right)^2 = \xi\left(1 - \frac{T}{\theta}\right). \qquad (3)$$

Here the coefficient ξ characterizes the "steepness" of the ferromagnetic transformation in the proximity of the Curie point. The variation of the experimental values of σ_s^2 as a function of $(\theta - T)$ for four Mn-Zn ferrites is

shown in Fig.7. It will be seen that the relationship (3) holds for only two of the samples; in the case of the ferrites with higher MnO concentrations the observed variation is nonlinear. An analogous situation obtains for alloys. In the case of alloys, disagreement between the results of measurement and Eq.(3) can be explained by the influence of concentration inhomogeneities in the alloy (liquation). Obviously, the same thing can occur in ferrites.

Vlasov made an attempt to determine the numerical value of the coefficient ξ for ferrites. He showed that whereas for metallic ferromagnets ξ must be greater than 3, for ferrites ξ must always be smaller than 3.

In actual fact, the values of ξ for all the ferrites investigated by us lie between 0.1 and 0.7. This indicates that the ferromagnetic transformation in ferrites is much more smeared out than in metallic ferromagnets. The spontaneous polarization curves for Mn-Zn ferrites in σ_s/σ_0 vs T/θ coordinates are shown in Fig.8, together with the corresponding curves for pure nickel and annealed 80% Ni + 20% Cu alloy. It will be seen that the slope of the ferrite curves is appreciably less steep. Néel[7] and Vlasov & Ishmukhamedov[6] have given qualitative explanations of the anomalous temperature dependence of the spontaneous magnetization of ferrites. It should be noted, however, that the smearing out of the spontaneous magnetization in ferrites is due not only to the sublattice structure but also to the influence of concentration fluctuations over the volume of the specimen.

4. Behavior of Mn-Zn ferrites near the Curie point in weak fields

We felt it would also be of interest to investigate the temperature dependence of the magnetic properties of our ferrite samples in weak fields. The weak field measurements were performed on a vertical astatic magnetometer by the null method. We recorded the temperature dependences of the magnetization in a weak field (0.8 oersted) as well as the coercive force and the residual magnetization in a magnetizing field of 150 [190?] oersted.

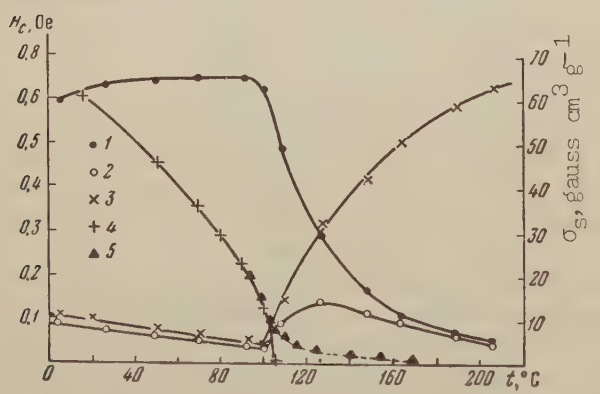

Fig.9. Temperature dependences of the residual magnetization and coercivity in Mn-Zn ferrite with 28% MnO in the region above the Curie point: 1) magnetization in a 0.8 oersted field, 2) residual magnetization in a 190 oersted field, 3) coercive force in a 190 oersted field, 4) σ_s calculated by the method of thermodynamic coefficients and 5) σ_s calculated from the equal magnetization curve.

It was found that above the Curie point (determined as the temperature at which $\alpha = 0$) the investigated Mn-Zn ferrites exhibited anomalies of a type not mentioned in the literature. The residual magnetization in approaching the Curie point from the side of lower temperatures decreases, then starts to rise from a minimal value at a temperature close to the Curie point, goes through a maximum and again falls off (Fig.9). The coercive force also shows an anomalous behavior; it too at first falls off, goes through a minimum at the same temperature as the residual magnetization and then increases, the increase being very appreciable in some cases (Fig.9).

With a view of investigating this effect in more detail, we repeated these measurements on three of the seven initially investigated ferrites some months after the first

experiments. The ferrite samples exhibited the identical anomalies. Then the three samples were sealed into glass tubes in order to eliminate the possible influence of oxygen during heating and the measurements were repeated. The anomalies persisted. In order to determine whether such anomalous behavior is characteristic of all Mn-Zn ferrites regardless of the method of preparation and the possible presence of impurities, we carried out measurements on two ferrite samples made available to us by N.N.Shol'ts and K.A.Piskarev.* The compositions of these samples were 10% ZnO + 40% MnO + 50% Fe_2O_3 and 20% ZnO + + 30% MnO + 50% Fe_2O_3. In the case of these samples only the coercive force anomaly was observed, while the temperature variation of the residual magnetization was normal.

Subsequently, we carried out similar measurements on several samples of cobalt-zinc ferrite samples; in this case no anomalies were observed.

Conclusions

1. The paraprocess in the vicinity of the Curie point in the Mn-Zn and Co-Zn ferrites we investigated is of the same order of magnitude as in ferromagnetic metals and alloys. The same thermodynamic equation, namely, $\alpha\sigma+\beta\sigma^3=H$, as was used earlier for describing the true magnetization in metallic ferromagnets can be used for describing the paraprocess in ferrites in the vicinity of the Curie point. This is as might have been expected in view of the fact that the thermodynamic theory of ferromagnetic transformation is not based on any specific model and hence the deductions following from it are general and should be applicable to all ferromagnetic materials.

2. The values of the spontaneous magnetization calculated by the method of thermodynamic coefficients (which derives from the same thermodynamic theory of ferromagnetic transformation) agree with the values of the spontaneous magnetization obtained by the method of lines of equal magnetization and by the method of magnetization isotherms. All three methods of calculating the spontaneous magnetization give identical values of σ_s up to temperatures very close to the Curie point (up to within about 10° of the Curie point).

3. In mixed ferrites, just as in metallic ferromagnets, the magnetic transformation is not a "point" process, i.e., does not occur fully at sharply defined temperature. In the case of mixed ferrites a very long (up to $\sim 70^\circ$) spontaneous magnetization "tail" extends out from the Curie point temperature, which is here understood to be the temperature at which $\alpha = 0$.

4. Anomalous increases of the coercivity and the residual magnetization were observed in the Mn-Zn ferrites above the Curie point.

Department of Physics,
Moscow State University

References

1. W.Sucksmith & C.Clark, Proc.Roy.Soc., A225,147 (1955).
2. K.P.Belov & A.N.Goriaga, FMM (Physics of Metals and Metallography) 2,3(1956).
3. S.V.Vonsovskii & Ia.S.Shur, Ferromagnetizm (Ferromagnetism) M.-L., 1948.
4. V.L.Ginzburg, Zhur.eksp.teor.fiz., 17, 833 (1947).
5. K.P.Belov & Ia.Paches, FMM (Physics of Metals and Metallography) 4,48 (1957).
6. K.B.Vlasov & B.Kh.Ishmukhamedov, Zhur.eksp.i teor.fiz., 27,75 (1954).
7. L.Neel, Ann. de phys., 3, 137 (1948).

---

*We take this occasion to thank them.

TEMPERATURE DEPENDENCE OF THE DIFFERENTIAL SUSCEPTIBILITY OF COBALT IN STRONG MAGNETIC FIELDS

- L.Pál & T.Tarnotsi

Introduction

The shape of magnetization curves near saturation for polycrystalline ferromagnetic materials in the absence of external and internal mechanical stresses is determined almost entirely by the magnetic anisotropy.

It is therefore obvious that in strong fields the differential susceptibility must be intimately related with the magnetic anisotropy. It may be assumed that the temperature dependence of the differential susceptibility in the temperature region far below the Curie point will be determined by the temperature dependence of the anisotropy constant, inasmuch as this changes much more with changes in temperature than the saturation magnetization. Hence investigation of the temperature dependence of the differential susceptibility in strong magnetic fields can yield valuable information on the temperature dependence of the anisotropy constant. Although for purposes of determining the anisotropy constants and investigating their temperature dependences the preferred procedure is torque measurements on single crystals, in many cases it may be useful to supplement such data by measurements on polycrystalline specimens.

In the case of ferromagnets with a cubic lattice we have ample experimental evidence[1] that the values of the anisotropy constants obtained from measurements on polycrystalline specimens agree well with the values obtained for single crystals.

A number of authors have investigated the temperature and field dependences of the differential susceptibility of polycrystalline ferromagnetic materials with a cubic lattice (iron, nickel and their alloys); there are, however, few reports on analogous investigations of cobalt which has a hexagonal structure. Bloch[2], Weiss & Forrer[3] and Allen & Constant[4] investigated the temperature dependence of the saturation magnetization of cobalt; their measurements, however, cannot be regarded as reliable, for, as Mayers & Sucksmith[5] have noted, the magnetic properties of cobalt near the allotropic transformation temperature are strongly dependent on the thermal history of the sample.

On the basis of the results of earlier investigations of Edwards & Lipson[6] and Troiano & Tokich[7], Mayers & Sucksmith[5] considered it expedient to carry out their measurements of the saturation magnetization of cobalt on a single crystal. Prior to the measurements of Mayers & Sucksmith, analogous measurements were performed by Kaya[8] and Honda & Masumoto[9].

Utilizing the temperature vs magnetization curves obtained by Honda & Masumoto[9], Bozorth[10] calculated the temperature dependence of the first and second anisotropy constants of hexagonal cobalt.

Edwards & Lipson[6] showed by x-ray diffraction studies that the hexagonal modification of cobalt even at room temperature contains inclusions with the cubic lattice, whose concentration depends on the previous heat treatment.

The mechanism of the allotropic transformation in cobalt became clear in 1936 as a result of the investigation of Nishiyama[11]. Nishiyama established that the formation of the (111) plane of the cubic phase proceeds parallel with the (0001) plane of the hexagonal phase, while formation of the $[110]$ direction occurs parallel with the $[11\bar{2}0]$ direction. In the $\alpha \rightarrow \beta$ transformation only one face-centered cubic crystal is formed from one hexagonal crystal, while in the reverse $\beta \rightarrow \alpha$ transformation from each face-centered cubic

crystal there may form four hexagonal crystals with different but definite orientations. However, these four hexagonal crystals formed from one cubic crystal in the case of repeat $\alpha \rightarrow \beta$ transition always transform into only one cubic crystal. Nishiyama's inferences regarding the $\alpha \rightleftarrows \beta$ transformation mechanism in cobalt were substantiated by the work of Kehrer & Leidheiser[12]. Thus from a cobalt single crystal with a hexagonal lattice one can by allotropic transformation obtain a cubic single crystal with a definite orientation. Sucksmith & Thompson[13] utilized this possibility and were the first to determine the temperature dependence of the anisotropy constant of cubic cobalt.

According to their measurements, the anisotropy constants of cubic cobalt are one order of magnitude smaller than the corresponding constants of the hexagonal modification (it is surprising to note, however, that the absolute value of the second anisotropy constant is greater than that of the first). One may therefore expect a sharp decrease in the differential susceptibility of polycrystalline cobalt in strong fields in the region of the phase transformation, inasmuch as the most important factor (the value of the anisotropy constants) in determining its magnitude apparently decreases sharply.

It was already known from the measurements of Honda & Masumoto[9] that the first anisotropy constant in the hexagonal phase changes sign at about 220°, while the second constant decreases slowly but remains positive. From this it may be inferred that the temperature variation of the differential susceptibility of cobalt should exhibit a pronounced minimum at a temperature slightly above 220°.

The purpose of our investigation was to obtain additional information on the magnetic properties of cobalt.

Measurement procedure

In principle, for measuring the differential susceptibility one can use the ballistic procedure proposed by Czerlinsky[14]. In the case of small diameter specimens, however, particularly in the region of high temperatures, the ballistic method becomes very cumbersome and insensitive. Thus the ballistic procedure is no longer applicable for determining susceptibilities of the order of 10^{-2}-10^{-3} gauss/oersted with an accuracy of 1-10% in the case of thin samples.

For the purpose of enhancing the sensitivity of differential susceptibility measurement, Akulov & Bol'shova[15] proposed a bridge set-up. Unfortunately, this procedure, as one of the present authors[16], showed is not without shortcomings and cannot be used for precise measurements.

The method developed and used by us consists of comparing the voltages induced in a measuring coil with and without the specimen.

A diagram of our set-up is shown in Fig.1. The solenoid L_1 producing a constant magnetic field (H) is supplied from a storage battery, while the solenoid L_2 producing an alternating magnetic field (h) is supplied from an audio-frequency generator (EMG, Type 1113).

The maximum amplitude of the alternating magnetic field was chosen so as to be equal to approximately 1% of the constant magnetic field in each case. The potential necessary for compensating the voltage of the measuring coil L_3 is applied through the phase shifter ϕ to the potentiometer P (pure resistance) by the transformer T_2. Balance (i.e., zero current through the coil L_3) is shown by the null indicator I. The null indicator in our set-up was a selective amplifier having a large amplification factor (10^6) and a narrow passband (±9 cps). The frequency of the audio generator G was selected

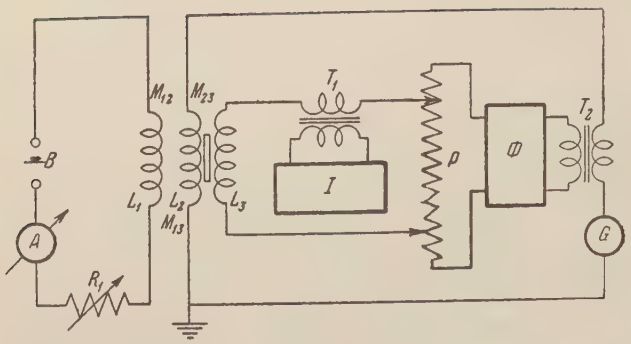

Fig.1. Diagram of measuring set-up: B - storage battery, L_1 and L_2 - solenoids, L_3 measuring coil, T_1 and T_2 - transformers, ϕ - phase shifter, P - potentiometer, I - null indicator, G - audiogenerator, R_1 - variable resistor, A - ammeter.

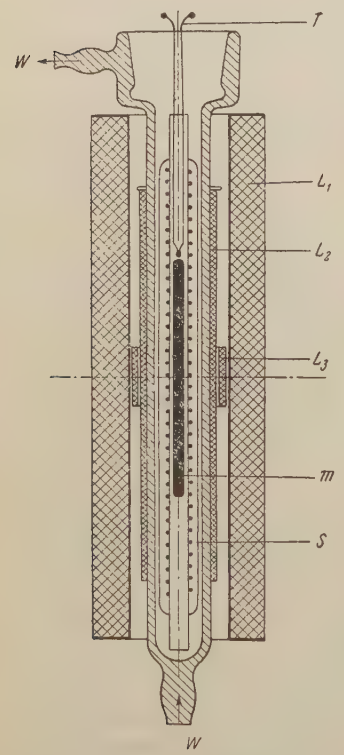

Fig.2. Arrangement of sample, coil and solenoids: L_1 & L_2 - solenoids, L_3 - measuring coil, S - heater, T - thermocouple, m - specimen, W - cooling water.

so that the skin effect in the specimen near magnetic saturation could be neglected. One of the present authors showed earlier[16] that the error produced by the skin effect in the case of cylindrical specimens up to 4 mm in diameter is negligible up to about 500 cps.

The measuring coil L_3 which was 10 mm long and 21 mm in diameter (600 turns) was centered over the investigated specimen which was 80 mm in length and 4 mm in diameter. Thus the influence of the demagnetizing field could be taken into account by means of the ballistic demagnetizing factor. Inasmuch as the measuring coil was not in contact with the specimen, it was necessary to check the influence of the air gap on the accuracy of measurement. Control measurements showed that in the case of the given experimental geometry the influence of the air gap could be neglected. The specimen was suspended by means of a fine tungsten filament inside a porcelain tube (inside diameter 5 mm; length 30 cm); the tube in turn was inserted into a heater with a bifilar winding of platinum wire (0.1 mm diameter, 20 cm long). The specimen together with the heater and porcelain tube was placed into a special double-wall glass vessel which served as the form for the solenoid L_2 producing the alternating magnetic field. L_2 was 180 cm long; its winding comprised 838 turns. The measuring coil L_3 was well insulated from the solenoid L_2 and wound so that its center coincided with the common center of coils L_1 and L_2. The entire arrangement is diagramed in Fig.2.

The space between the bifilar heater winding and the inner wall of the glass vessel was filled with heat insulation. Coils L_2 and L_3 were cooled by water circulating through the double-walled vessel. The temperature of the specimen was measured by a platinum-platinum rhodium thermocouple. The heater S was supplied from a Type Tr-500 tungsten diode voltage regulator.

The constant magnetic field of solenoid L_1 was uniform within 2% over the 80 mm section comprising the sample. By virtue of the provision for cooling, it was feasible to produce magnetic fields of up to 10,000 oersted. Details of the solenoid design are given in Ref.17.

Let us designate the cross section of the measuring coil by Q, the cross section of the cylindrical

specimen by q. Let the number of turns of the measuring coil be n_3. The voltage induced in the measuring coil without the specimen is then given by

$$E_0 = -nQ\frac{dh}{dt}, \tag{1}$$

while the voltage induced with the specimen in place is

$$E_1 = -n\left(Q\frac{dh'}{dt} + 4\pi q\frac{dJ}{dt}\right), \tag{2}$$

where $J=J(H+h)$ is the magnetization. It must be noted that $h'\leqslant h$, inasmuch as the presence of the specimen increases the mutual inductance coefficient M_{12} (see Fig.1) even in the case when the specimen is close to saturation. In view of this the amplitude of the magnetic field due to the alternating current induced in solenoid L_1 increases when the specimen is inserted in solenoid L_2. Inasmuch as the alternating field is in phase opposition with the magnetic field of solenoid L_2, we actually have $h'\leqslant h$. The inductance of coil L_2 also increases, which leads to a reduction of the current in the coil at a constant generator voltage. G.Szilvay[18] of the Mathematical Institute of the Hungarian Academy of Sciences carried out a calculation of this effect. She established that in the case of our experimental geometry one may assert with good approximation that $h'=h$.

Inasmuch as

$$\frac{dJ}{dt} = \frac{dJ}{d(H+h)}\cdot\frac{dh}{dt} \sim \chi(H)\frac{dh}{dt}, \tag{2'}$$

bearing in mind Eqs.(1) and (2), we can write

$$\chi(H) \sim \frac{Q}{4\pi q}\cdot\frac{E_1 - E_0}{E_0}. \tag{3}$$

It will be evident that in order to determine the susceptibility as the function of the field H, it is sufficient to measure the ratio of E_1 and E_0 with great accuracy which, of course, is much simpler than measuring the amplitude and the phase of the alternating voltage.

Although we could take advantage of this circumstance, it was still necessary to insure high accuracy in determining E_1/E_0, particularly in cases when small values of χ were to be measured. Obviously, it was essential to satisfy the inequality

$$\frac{\Delta E}{E} \ll \frac{4\pi\chi q}{Q}, \tag{4}$$

which in the case of the cross sections Q and q involved in our experiments and $\chi \approx 10^{-3}$ gauss/oersted means that $\Delta E/E$ would be smaller than 10^{-3}. Clearly, we had to check carefully all the factors that could possibly affect the accuracy of determining E_1/E_0.

In addition to the above mentioned sources of error, one must, in working with a set-up of this type, pay particular attention to errors stemming from the operation of the phase shifter. Design of a truly amplitude-independent phase shifter is very difficult, particularly if it is also necessary to provide for variation of the phase angle in a wide range. If in going from measurements of E_0 to measurements of E_1 a large change in the phase shift angle were necessary, the error in determining E_1/E_0 would be large. In our case, however, it was not necessary to change the phase angle much inasmuch as the specimen in a strong polarizing magnetic field has little effect on the

phase of the voltage induced in coil L_3. A series of test measurements showed that the error produced by the amplitude-dependence of the phase shifter under our conditions was always less than 0.1% of the measured voltage.

We also took particular pains to reduce the temperature dependence of the resistance of coil L_2, for changes in resistance during the course of an experiment would obviously hinder measurements. Hence, coil L_2 was wound of 0.3 mm diameter manganin wire. Coil L_2 and the transformer T_2, supplying the compensating voltage, were connected to the audio-frequency generator supplied from a Type Tr-500 voltage regulator. After all the necessary tests and adjustments, we were readily able to measure differential susceptibilities of the order of 10^{-3} gauss/oersted with an accuracy of ±10%. The measurement procedure was the following. First, we established the requisite value of the constant magnetic field H by means of the automatic rheostat R_1, then by adjustment of the potentiometer P and the phase shifter Φ we compensated the voltage E_0 induced in coil L_3 without the specimen. Next, the specimen was placed in the measuring coil L_3 and after attainment of thermal equilibrium (in heater S), we determined the voltage E_1. Inasmuch as it was assumed that the phase shifter was amplitude independent, the indication (null setting) of the potentiometer P could be used for determining E_1/E_0.

Each time in going to a different temperature, we waited long enough to insure that thermal equilibrium was established. After completion of a full temperature cycle, we set another value of the constant magnetic field and repeated the above procedure.

Results and discussion

Our measurements were carried out on a sample of electrolytic cobalt 80 mm in length and 4 mm in diameter. The chemical composition of the cobalt was 99.65% Co, 0.27% Fe and 0.08% C. Prior to measurement the sample was annealed in vacuum for two hours at 1000° and slowly cooled, particularly through the temperature range near the phase transformation temperature. The purpose of this heat treatment was both to relieve the mechanical stresses in the specimen and to reduce the number of metastable cubic inclusions in the hexagonal phase.

The curves reproduced in Fig.3 show the temperature dependence of the differential susceptibility at different field intensities. It will be seen that the differential susceptibility exhibits a pronounced minimum at about 290-300° and then, after rising to a second maximum near 450°, rapidly falls off to very low values. The temperature corresponding to the differential susceptibility minimum changes little with the field intensity.

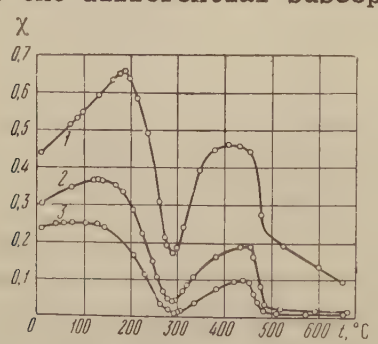

Fig.3. Temperature dependences of the differential susceptibility of cobalt at different constant field intensities: 1) 444, 2) 888 and 3) 1332 oersted.

The initial section of curve 1 clearly shows that the susceptibility increases up to about 195°. The temperature of the first maximum decreases with increasing field intensity and at the same time the maximum is increasingly smeared out. This distinctive temperature dependence of the differential susceptibility of cobalt can readily be explained if we bear in mind that rotation processes play a predominant role in the magnetization mechanism in the region of field intensities employed in our experiments.

Assuming that there are no external or internal stresses present and designating the first and second anisotropy constants of cobalt at temperature T by $K_1(T)$ and $K_2(T)$ and its saturation magnetization at T by $J_s(T)$, in the case of a sufficiently strong magnetic field H, but one in which the inequality $HJ_s/K_1 < 1$ is still fulfilled, we can write the following expression for the differential susceptibility (Gans[19]):

$$\chi \approx \frac{1}{3} \cdot \frac{J_s^2}{K_1} \left\{ 1 - \frac{9}{16} \cdot \frac{J_s}{K_1} H + \frac{3}{10} \left(1 - 4 \frac{K_2}{K_1} \right) \frac{J_s^2}{K_1^2} H^2 - \ldots \right\}. \qquad (5)$$

Inasmuch as in the temperature range from 0° to 150-200°C, J_s/K_1 is of the order of 10^{-3}, one can select a magnetic field value for which domain rotation processes will still play the predominant role in magnetization and at the same time the inequality $HJ_s/K_1 < 1$ will hold. Since $K_1(T)$ decreases much more rapidly than $J_s(T)$ with rising temperature in the range from 0 to 100° (in this interval $K_1(T)$ changes by 45.6%, while $J_s(T)$ changes by only 1.1%), the differential susceptibility in such a magnetizing field must increase with increasing temperature, as long as HJ_s/K_1 remains smaller than unity. The corresponding initial rising section is particularly evident in curves 1 & 2 (Fig.3). With increasing field intensity this section is shifted to the side of lower temperatures (see curve 3). At sufficiently high magnetic field values or sufficiently high temperatures, condition $HJ_s/K_1 < 1$ will no longer hold. If the opposite inequality obtains, i.e., if $K_1/HJ_s < 1$, then, as one of us has shown earlier, the expression for the differential susceptibility assumes the form

$$\chi = 2J_s^{-1} \left(\frac{4}{16} K_1^2 + \frac{64}{105} K_1 K_2 + \frac{128}{315} K_2^2 \right) H^{-3} +$$

$$+ 3J_s^{-2} \left(\frac{16}{105} K_1^3 + \frac{128}{315} K_1^2 K_2 \frac{512}{1155} K_1 K_2^2 + \frac{8192}{45045} K_2^3 \right) + O(H^{-5}). \qquad (6)$$

Naturally, this expression is valid only in the case of a specimen free of all mechanical stresses and provided 1) that magnetic interaction between the individual crystallites can be neglected and 2) that the susceptibility of the true magnetization (the paraprocess susceptibility) is very small. The assumption of negligible interaction between the crystallites is probably questionable; this question however has little bearing on the discussion of our results.) It follows from (6) that the value of the susceptibility will decrease if the absolute values of the anisotropy constants K_1 and K_2 decrease with rising temperature. It would be logical to assume that the sharply falling sections of the curves in Fig.3 are associated with such a decrease in the absolute values of the anisotropy constants.

It is known from measurements on cobalt single crystals that the constant K_1 changes sign near 260°, while constant K_2 slowly decreases with increasing temperature but remains positive. Let us assume that in the temperature range from 250 to 350° the first term in Eq.(6) alone gives a sufficiently good approximation of the susceptibility in strong magnetic fields. In this case it can readily be seen that the function

$$f(x) = a_2 x^2 + a_1 x + a_0, \qquad (7)$$

where

$$a_2 = \frac{4}{15}, \quad a_1 = \frac{64}{105}, \quad a_0 = \frac{128}{315},$$

does not vanish for any real values of x and has a minimum at $x = -\frac{a_1}{2a_2}$.

Taking advantage of the fact that K_2 is a very slowly varying function of the temperature, i.e., assuming that K_2 is virtually constant in the narrow temperature interval in question, we can deduce the following expression for the temperature corresponding to the minimal differential susceptibility:

$$K_1(T_K) = -1{,}14\,K_2(T_K). \tag{8}$$

Using the experimental values reported by Sucksmith & Thompson[13], we determined the temperature T_K for which K_1 and K_2 satisfy Eq.(8); it proved to be 293°. The minimum of the differential susceptibility in our experimental curves is located at 294°. It will be evident that the agreement is excellent. Further, utilizing the data of Sucksmith & Thompson[13], we calculated by means of (8) the temperature dependence of the differential susceptibility in a field of 1332 oersted in the region of T_K; the calculated curve is shown in Fig.4 together with the corresponding section of our experimental curve for 1332 oersted. It will be seen that the minima of the two curves coincide and that the curves are close, particularly in the region of higher temperatures. At temperatures below T_K the divergence is greater because K_2 is rather large. Hence, expression (6) can be regarded as only rough approximation in the range of magnetic fields used in our experiments.

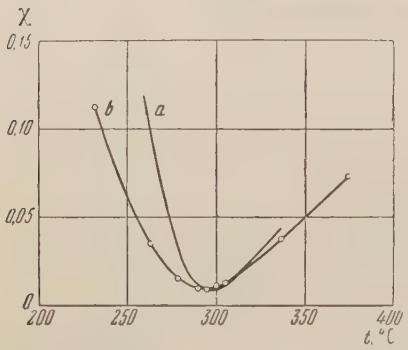

Fig.4. Temperature dependence of the differential susceptibility near 300°: a) theoretical curve calculated by means of Eq.(6) (the values of K_1 and K_2 were taken from Sucksmith & Thompson[13]) and 6) our experimental curve for 1332 oersted.

Inasmuch as the absolute value of K_1 changes slowly near 390°, the slope of the differential susceptibility curve decreases gradually with increasing temperature. Near 440° the differential susceptibility has a local maximum and

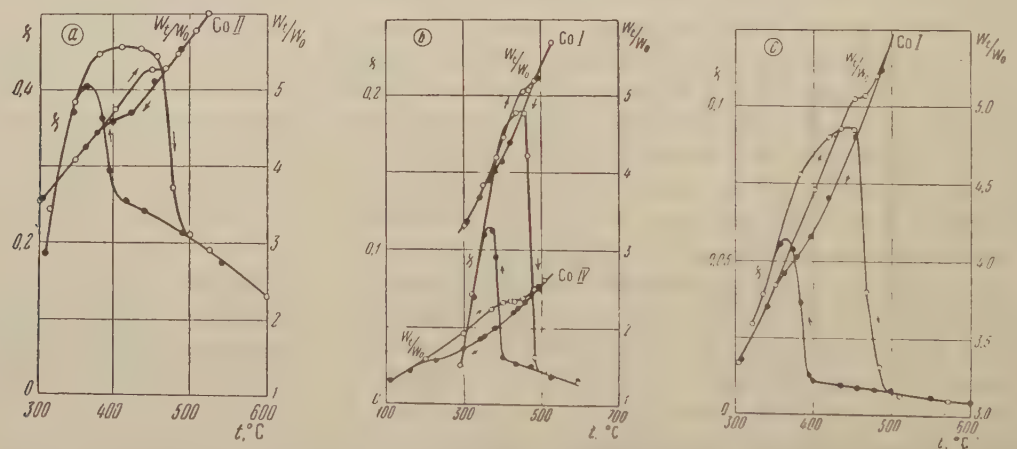

Fig.5. Influence of the $\alpha \rightleftharpoons \beta$ transformation in cobalt on the temperature dependences of the differential susceptibility and resistivity at different field values (a - H = 444, b - H = 888 and c - H = 1332 oersted). Circle points - differential susceptibility and resistivity measured during heating ; solid points - susceptibility and resistivity measured during cooling. The curves identified by Co I, Co II and Co IV represent the experimental results of Schulze[20].

then falls off sharply. The sharp decrease is connected with the transformation of hexagonal cobalt to the cubic modification.

The very appreciable change in the differential susceptibility associated with the phase transformation can be utilized for detecting and investigating the allotropic transformation itself. In Fig.5 we show the differential susceptibility curves obtained during heating and cooling in fields of different intensity. In the same figure we have plotted the data of Schulze[20] for the temperature dependence of the resistivity of cobalt specimens of different degrees of purity. Schulze investigated this dependence in the region of the phase transformation. His specimen, identified by "Co I", was of the same degree of purity as our cobalt. It will be evident from Fig.5 that the temperature dependence of the differential susceptibility is a more sensitive characteristic of the phase transformation than the resistivity. According to our measurements the temperature of the start of the $\alpha \rightarrow \beta$ transformation was 445° and the temperature of the end of transformation was 490°. For the $\beta \rightarrow \alpha$ transformation, the initial and final temperatures were 400 and 340°, respectively. We feel that these results are the most accurate so far obtained.

Central Physical Research Institute,
Hungarian Academy of Sciences.

References

1. H.Polley, Ann.d.Phys., 36, 625 (1938); I.M.Puzei, Zhur.tekh.fiz., 19, 653 (1949); N.Z.Miriasov, Vestnik (Review) Moscow State University, No.5, 65 (1951).
2. O.Bloch, ZS.Naturf.Ges., Zürich, 56, 415 (1911).
3. P.Weiss & R.Forrer, Ann.de Phys., 5, 153 (1925); 12, 279 (1929).
4. R.L.Allen & F.W.Constant, Phys.Rev., 44, 228 (1933).
5. H.P.Mayers & W.Sucksmith, Proc.Roy.Soc., A208, 427 (1951).
6. O.S.Edwards & J.Lipson, J.Inst.Mat., 69, 177 (1943); O.S.Edwards & H.Lipson, Proc.Roy.Soc., A180, 268 (1942).
7. A.R.Troiano & J.L.Tokich, Techn.Publ.Amer.Inst.Min.Engrs., No.2348 (1948).
8. S.Kaya, Sci.Rep.Tohoku Univ., 17, 1157 (1928).
9. K.Honda & M.Masumoto, Sci.Rep.Tohoku Univ., 20, 323 (1931).
10. R.M.Bozorth, J.Appl.Phys., 8, 575 (1937).
11. Z.Nishiyama, Sci.Rep.Tohoku Univ., 25, 79 (1936).
12. V.J.Kehrer & H.Leidheiser, J.Chem.Phys., 21, 570 (1953).
13. W.Sucksmith & J.E.Thompson, Proc.Roy.Soc., 225, 362 (1954).
14. E.Czerlinsky, Ann.d.Phys., 13, 80 (1932).
15. N.S.Akulov & K.M.Bol'shova, Vestnik (Review) Moscow State University, No.9, 79 (1950).
16. L.Pal, Thesis, Moscow State University, 1953.
17. L.Pal & G.Zsigmond, KFKI Kozl., 3, 300 (1955).
18. G.Szilvay, KFKI Kozl., 4, 102 (1956).
19. R.Gans, Ann.d.Phys., 15, 28 (1932).
20. A.Schulze, ZS.f.Metallk., 22, 308 (1930).

APPLICATION OF PARAMAGNETIC RESONANCE (NUCLEAR INDUCTION) TO DETERMINATION OF THE STRUCTURE OF ROCHELLE SALT AND EPOXY RESINS

- A.Lösche

Until 1945 the exact determination of nuclear magnetic moments was rather difficult. By means of an improved technique, Bloch and Purcell succeeded, in 1946, in measuring the Zeeman levels of nuclear spins by pure radiofrequency methods. During the last 10 years, these methods have been developed in different directions and today we have more than 700 publications on the subject.

It would be a pleasant task to talk about this very interesting phenomenon, but I wish to tell you how it can be utilized for exploring the structure of matter. For lack of time I shall describe only two of the investigations that have been carried out at our Institute at Leipzig. First, however, I have to mention the possibilities given by nuclear magnetic resonance absorption.

It is a well-known fact that a nuclear spin, characterized by the gyromagnetic ratio γ, precesses in a magnetic field H with the Larmor frequency

$$\omega_0 = \gamma H.$$

This precession may be detected by the absorption, which takes place in a radiofrequency field of the same frequency and a suitable polarization. Here we are not interested in either the magnitude of γ or the different line shapes that appear when we sweep through resonance at different rates (i.e., we neglect "wiggles", etc.). We shall be concerned only with the case of so-called "slow passage"; in this case the line shape will obviously be determined primarily by spin-spin interaction.

For the sake of simplicity we shall restrict our consideration to nuclei with spin 1/2 (say, protons, for example). The results can, however, be generalized to include other spins with little difficulty. These nuclei have only two possible orientations in a magnetic field: they may be parallel or antiparallel; it is possible to calculate the static magnetic field by means of which the nuclear moment of one spin acts on the other. In other words, the magnetic field, acting on any nucleus, is composed of the external field due to the electromagnet and an additional local field, created by the surrounding nuclei. For example, this additional field in the case of the two protons in a water molecule (with a separation of $\sim$1.58 A) is about 10 gauss; this means that our absorption line will be broadened by approximately this amount.

From this simplified picture, we can derive certain additional details.

1. If the molecules with the nuclei in question are rotating very rapidly, i.e., with a frequency much higher than the Larmor frequency ω_0, the mean local fields decay to zero. This mechanism is found in liquids; it can be proved by macroscopic motion. We have very narrow absorption lines; the exact line shape does not matter for the following considerations.

2. In order to calculate the line shape in the case of a rigid crystal, we have to consider the interaction of all the nuclei, the energy of which is given by

$$W_m = Hg\beta \sum_j I_{zj} + g^2\beta^2 \sum_{k>j} [r_{jk}^{-3}(I_j I_k) - 3r_{jk}^{-5}(r_{jk}I_j)(r_{jk}I_k)].$$

Here g is the g-factor, β is the nuclear magneton, I is the spin operator, and j and k are the numbers of two nuclei at a distance r_{jk}. It is hopeless to try to calculate all the eigenvalues of this system; fortunately Van Vleck showed how to calculate the second and fourth moments of the line width: ΔH^2 and ΔH^4.

I will not give here the results for different types of lattices, but one point is important: the second moment - which is the only one we shall

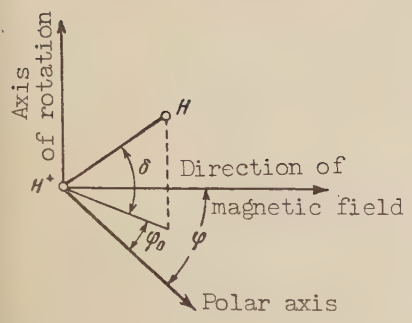

Fig.1. Position of a proton pair (H and H) in a constant magnetic field.

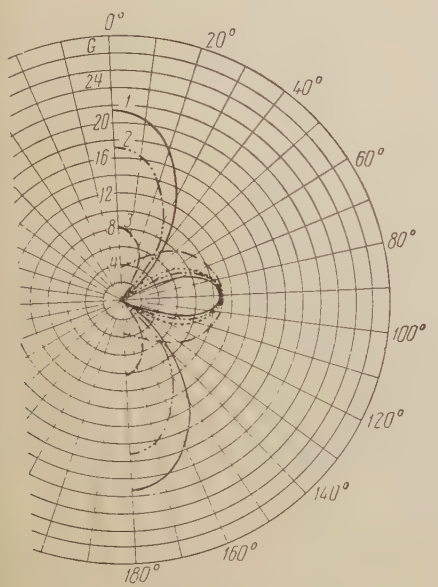

Fig.2. Splitting of doublet associated with a two-proton system having a proton-proton separation of 1.58 A as a function of the direction of the magnetic field. The circumference is scaled in values of φ. The curves correspond to different values of δ: 1) $2\Delta H = 11(3\cos^2\varphi - 1)$, 2) $2\Delta H$ & $11(3\cos^2 24^\circ\cdot\cos^2\varphi - 1)$, 3) $2\Delta H = 11(3\cos^2 40^\circ\cdot\cos\varphi - 1)$ and 4) $2\Delta H = 11(3\cos^2 62^\circ\cdot\cos^2\varphi - 1)$ gauss.

consider - depends on r^{-6}. This result tells us that in the first approximation it is possible to consider only the nearest neighbors of each nucleus: the line shape is determined primarily by the molecular groups in our probe. Let us examine the case in which only two nuclei are close together: we call it a two-proton system. We can distinguish two cases:

a) Single crystal. Here all proton-proton directions are parallel to each other; the local field of each proton is the same. We shall have a doublet with a separation between its components equal to

$$H_{\text{loc}} = \pm\alpha(3\cos^2\delta\cos^2\varphi - 1),$$

where $\alpha = \frac{3}{2}\mu a^{-3}$ (μ is the nuclear moment, and a is the proton-proton separation). The angles are defined in Fig.1.

If we rotate the crystal around the axis perpendicular to the z-direction, we will obtain the distances between the doublet components for different angles δ (Fig.2). Thus it is easy to determine the proton-proton separation and direction in this manner.

b) Powder. If all proton-proton systems are distributed randomly, we can calculate the second moment:

$$\overline{\Delta H^2} = \frac{9}{20}\gamma^2\hbar^2\frac{1}{a^6}.$$

From this quantity we again can readily deduce the proton-proton separation.

These methods were applied to crystals of gypsum by Pake and others; we shall see that they are suitable for investigation of more complicated systems as well.

Our measurements were made with an autodyne detector in the gap of a permanent magnet yielding a 3000 gauss field. A block diagram of the set-up is shown in Fig.3. The following results were obtained.

1. Rochelle-salt. The positions of the K, Na, C and O atoms are known from the x-ray diffraction measurements of Beevers & Hughes, but we know nothing about protons. On the other hand, it seems certain that the protons, or more accurately speaking, certain definite protons, are responsible for the ferroelectric behavior of this material.

In first approximation it is possible to use the derived equations for explaining the proton absorption curves; this means that the line shape is mainly determined by the protons in the H_2O molecules that are bound in the

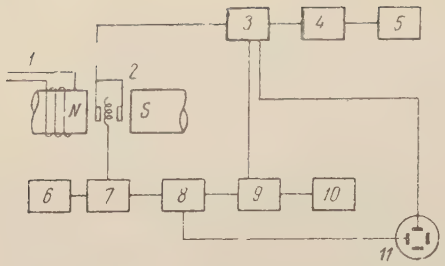

Fig.3. Block diagram of radio-frequency spectrometer: 1) magnetizing current leads, 2) modulation coil, 3) phase shifter, 4) power amplifier, 5) low-frequency oscillator, 6) indicator, 7) autodyne generator and detector, 8) low-frequency amplifier, 9) amplifier input, 10) recording unit, 11) oscilloscope.

crystal. But in this case, we have in a unit cell not just one but 16 different H_2O molecules.

First, we investigated the powder and found

$$\overline{\Delta H^2} = 18.3 \text{ gauss}^2;$$

when the temperature was raised above the upper Curie point (24°C), the second moment suddenly fell off to

$$\overline{\Delta H^2} = 15.1 \text{ gauss}^2.$$

This effect cannot be interpreted as due to an increase of the proton-proton distance; such a dilatation would be detectable macroscopically. We have to assume that some protons are beginning to oscillate.

The results of our measurements on single crystals are shown in Figs.4 & 5.

The designations A-, B- and C-crystals mean that the axis of rotation was parallel to the a-, b- and c-axis, respectively. The absorption curves were plotted from the derivatives by numerical methods. Only one doublet was observed. This result was at first rather discouraging, but, as follows from the above analysis, if we know the position of a doublet in one orientation of the crystal in the field, we can calculate the doublet separation for all other orientations. Thus, we reduced the absorption lines by subtracting the first doublet. We thus found another doublet and so on. Proceeding in this manner, we succeeded in finding the orientation of the proton-proton directions in all 16 molecules. Here is the result.

$$\begin{aligned}
7&: \varphi_{A\,7} = \pm 6^\circ, & \delta_{A\,7} &= \pm 7^\circ,\\
8&: \varphi_{A\,8} = \pm 65^\circ, & \delta_{A\,8} &= \pm 23^\circ,\\
9&: \varphi_{A\,9} = \pm 35^\circ, & \delta_{A\,9} &= \pm 33^\circ,\\
10&: \varphi_{A\,10} = \pm 30^\circ. & \delta_{A\,10} &= \pm 62^\circ.
\end{aligned}$$

These numbers of the water molecules correspond to the notation of Beevers & Hughes.

Subsequently, by applying an additional electric field to the single crystal, we were able to establish the character of the variation of the second moment, which is caused by the spontaneous polarization. Further work is in progress on single crystals with different orientations. It would appear feasible to determine the positions of the protons responsible for the ferroelectric properties of different salts.

2. Epoxy resins. We investigated the polymerization of an artificial resin; the German word is "Epoxyd-Harz". It consists of molecules of the type shown in the diagram below. These molecules are bound by other molecules, which are mixed in with them.

You see that there are two different proton groups of interest: the two protons of the benzene and the methyl group - CH_3.

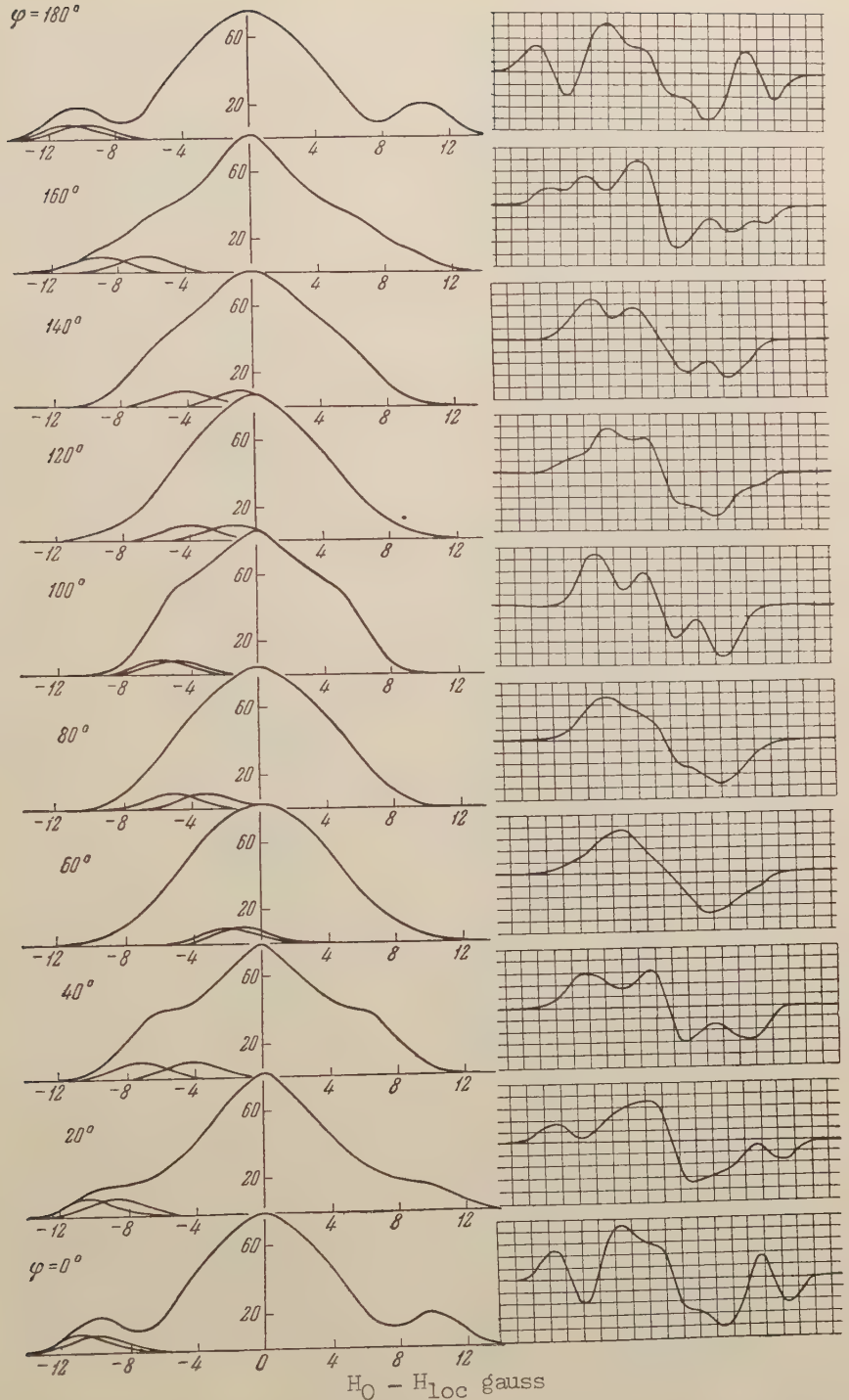

Fig.4. Absorption curves of A-crystals at different values of φ. At right - original curves made by the recorder; at left - absorption curves plotted on the basis of the recorded curves. Here φ is the angle between the b-axis and the direction of the magnetic field.

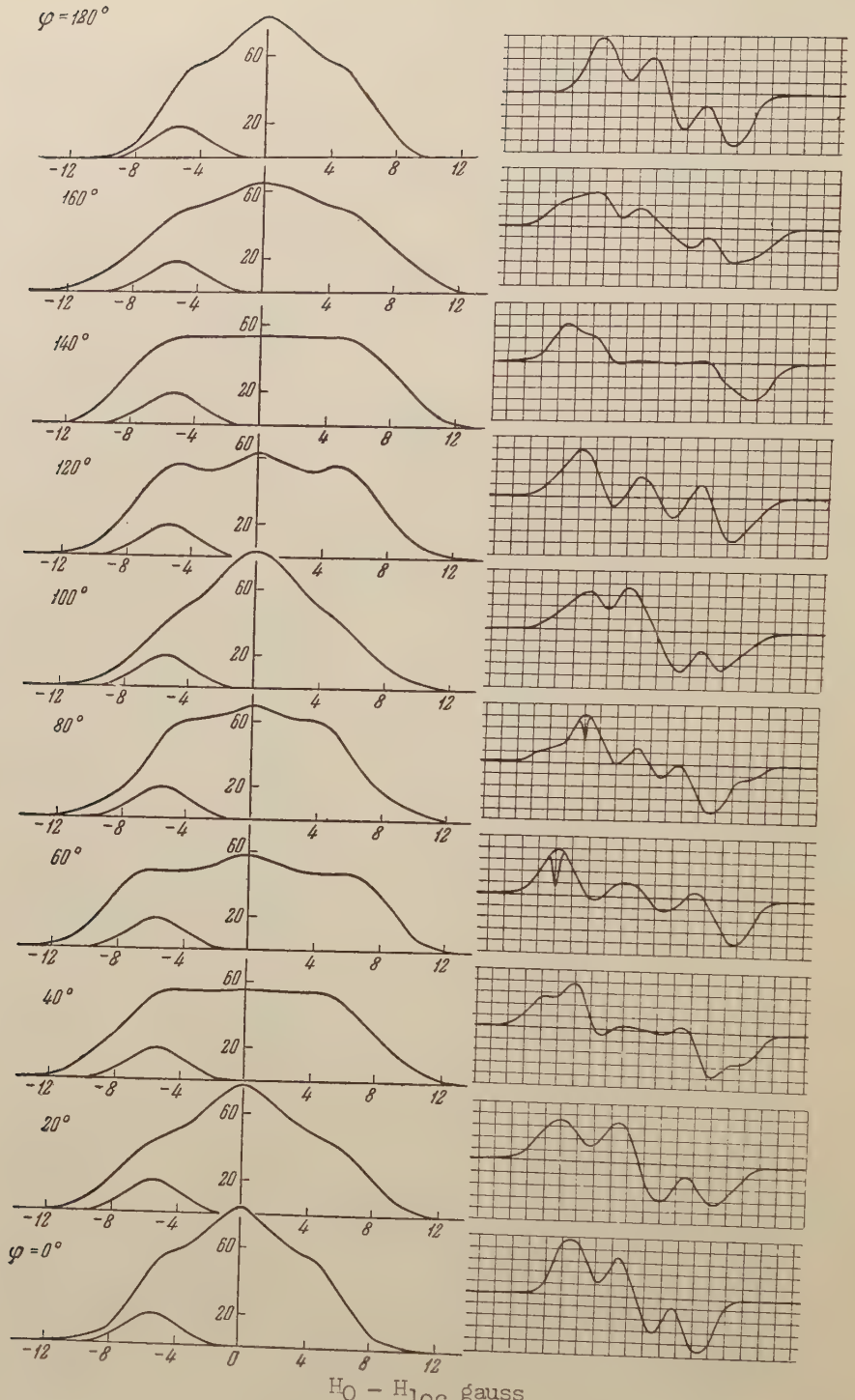

Fig.5. Same as Fig.4 but for B-crystal. Here φ is the angle between the c-axis and the magnetic field direction.

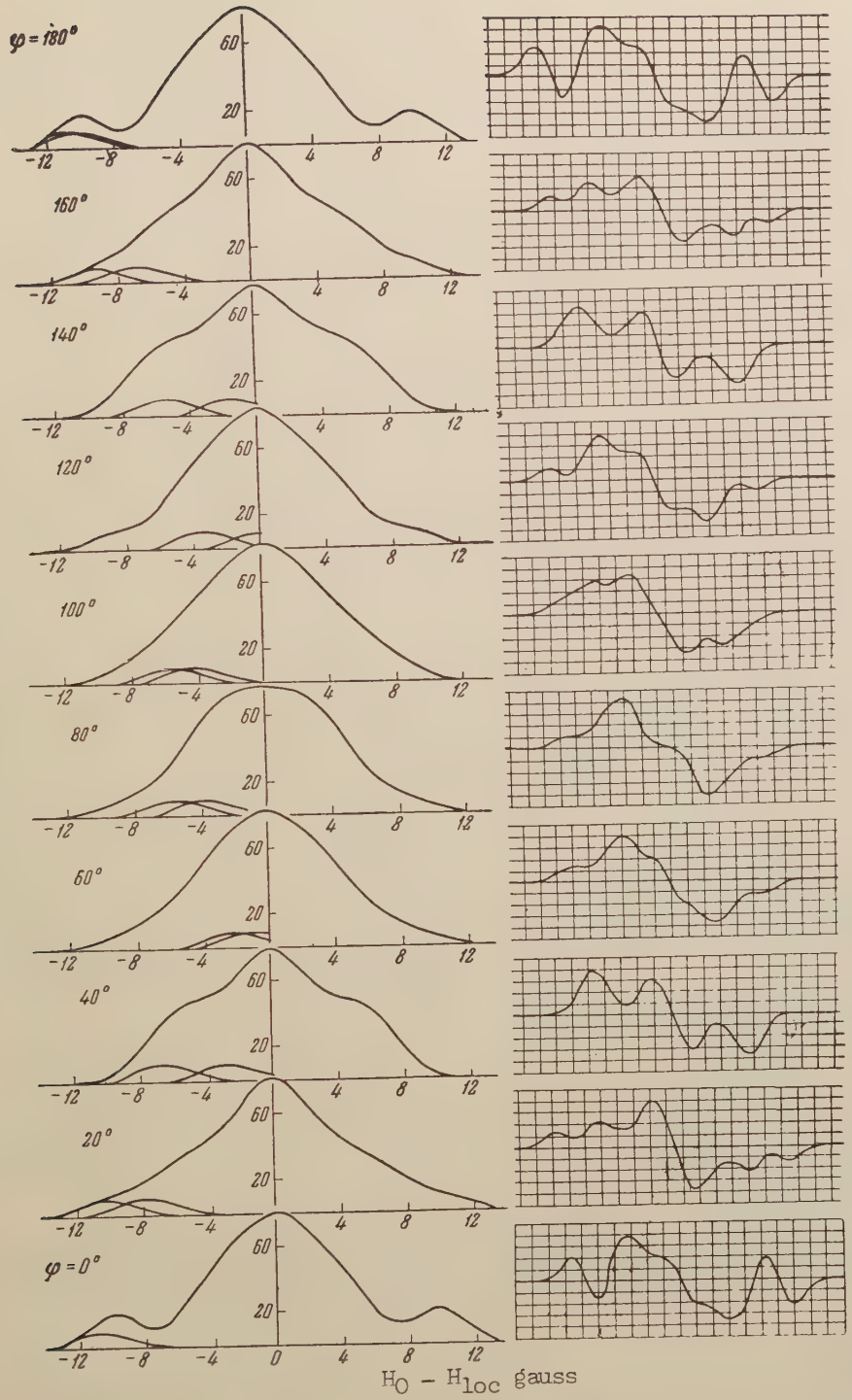

Fig.6. Same as Fig.4 but for C-crystal. Here φ is the angle between the b-axis and the magnetic field direction.

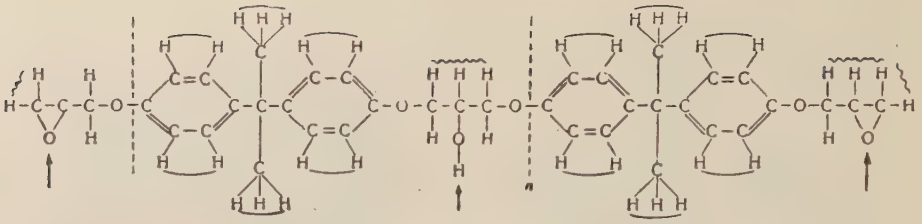

Diagram of unsolidified epoxy resin

In this case we could not obtain single crystals, so we calculated only the second moments. We obtained

ΔH^2 (cyclohexane) $= 1.6$ gauss^2 **and** ΔH^2 (methyl) $= 10$ gauss^2

In preparing a sample, we at first get a liquid - a rather difficult probe - which begins to harden macroscopically about 1.5 hours after the preparation of the mixture. Microscopically, we found that the process of polymerization begins after about 20 minutes: at the end of this period we observed broadening of the initial narrow line. Exact measurements gave the result shown in Fig.7.

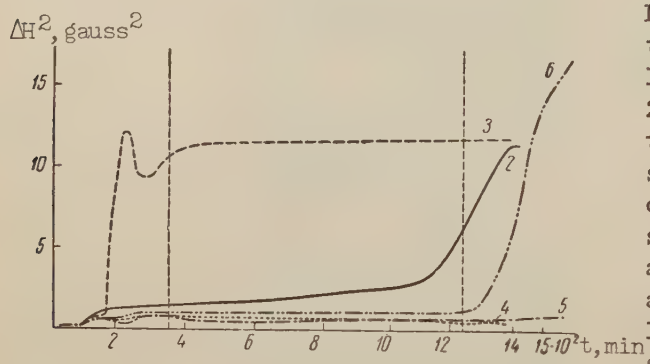

Fig.7. Variation with polymerization time of the second moment of the absorption curves of the protons in epoxy resin: 2) normal composition of the resin; 3 and 6) low proportion of epoxy molecules; 4 and 5) high proportion of epoxy molecules.

Let us examine curve 2. After 1 hour, the second moment increased to about 1.3 gauss^2. It remains constant for 20 hours and then it increases further to about 10 gauss^2. These results show that the mobility of the long chains is hindered almost from the start; the benzene rings become rigid after about 1 hour; the methyl groups are still rotating at this time. This lasts for about 24 hours when these groups too are fixed by the neighboring molecules.

The other curves pertain to other mixtures and we have no time to discuss them here. At present I cannot give more details regarding polymerization processes and the problems which may be solved by nuclear induction methods.

In principle, I wished to show that the phenomena of nuclear magnetism are applicable today to the solution of complicated problems having to do with the structure of solids.

Physical Institute
Leipzig University

RECENT DEVELOPMENTS IN THE FIELD OF PARAMAGNETIC RELAXATION

- C.J.Gorter

Summary

A few years ago it looked as if the main phenomena of paramagnetic relaxation up to frequencies of 10^8 cps could satisfactorily be described by a spin-lattice relaxation obeying the formulae of Casimir and Du Pré plus a short temperature independent spin-spin relaxation according to Waller and Broer.

In two respects this picture has now been found to fail. At liquid hydrogen temperatures rather slow temperature independent relaxations were found to occur inside the spin system. Only the old Kronig-Bouwkamp theory seems to be able to account for these relaxations.

At liquid helium temperatures the bottle-neck of the low frequency relaxation was found not to be the spin-lattice interaction but in many cases the transport of energy to the bath by a fraction of the lattice oscillators. A confrontation with the saturation of microwave resonance is being carried out.

1. Most of the data obtained on paramagnetic relaxation down to liquid air temperatures could find an adequate description by the formulae of Casimir and Du Pré. The data compiled for each substance could then be presented by giving the value of b/C and the relaxation time τ as a function of the temperature T. The dependence of τ on the external field H_c was often in agreement with the Brons-Van Vleck formula, thus only leaving the constant p, indicating the ratio of the τ-values at zero field and infinite field, to be quoted. Curie's constant C being known, the value b in the expression for the specific heat of the spin system b/T^2 can thus be determined with a good accuracy. Its value in general agrees reasonably well with the data independently obtained on this specific heat by caloric determinations, adiabatic demagnetization and the structure of microwave magnetic resonances. The relaxation time τ is, according to Waller, Fierz, Kronig and Van Vleck, determined by inelastic phonon-scattering (the socalled quasi-Raman effect), the coupling between the lattice waves and the spins being due to orbital moment coupled to the latter. Its dependence on T and H_c is not understood in all details, e.g., the anomalous temperature dependence in the Gd-salts, but there is general order-of-magnitude agreement between theory and experiment.

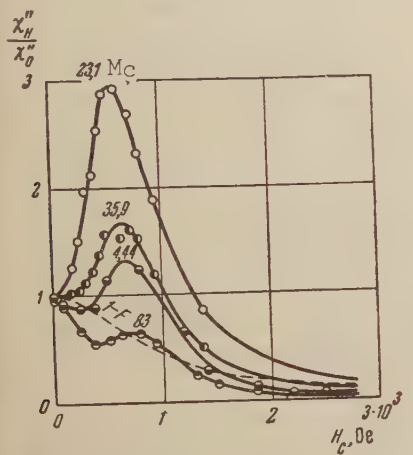

Fig.1. χ'' divided by its value at $H_c = 0$ as a function of the parallel field H_c in $CrK(SO_4)_2\cdot12H_2O$ at 20.4°K

In order to account for the data on the absorption coefficient χ'' a term $\chi_0 b\tau'\omega/(b + CH_c^2)$, ω being the angular frequency, is usually added to the Casimir-Du Pré expression for χ''. This term characterizes the (small) deviation from Casimir and Du Pré's basic assumption that the spin system is at any moment in internal equilibrium.

This term has been given a somewhat different form by Shaposhnikov.

We shall now discuss recent data which do not agree with the simple scheme sketched above as well as the theories proposed so far to account for these deviations. In section 2 the relaxation inside the spin system will be considered and in section 3 the relaxation at liquid helium temperatures.

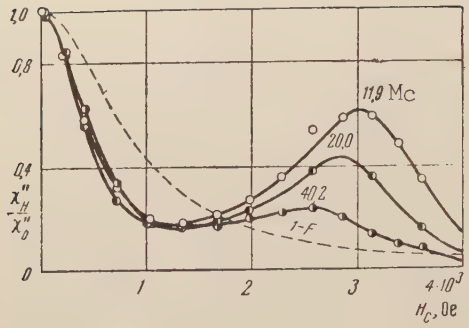

Fig.2. Same as Fig.1 but in $Mn(NH_4)_2(SO_4)_2 \cdot 6H_2O$ at 20.4°K.

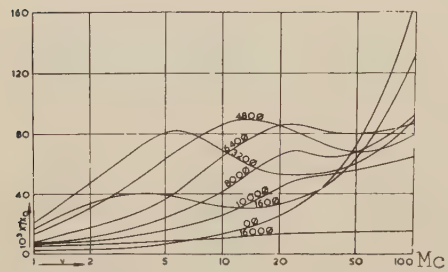

Fig.4. Ratio of χ'' to its value at $H_c = 0$ as a function of the frequency for different values of the parallel field H_c in $CrK(SO_4)_2 \cdot 12\ H_2O$ at 20.4°K.

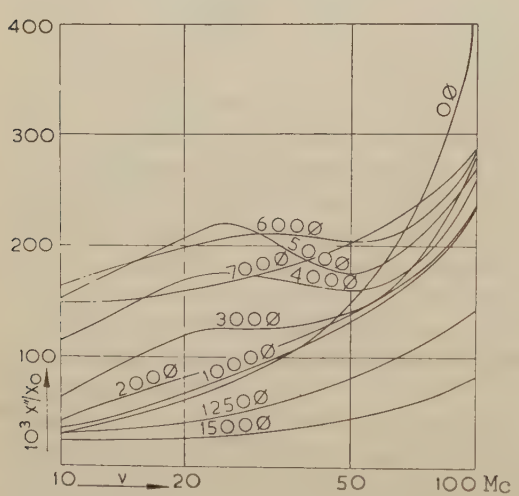

Fig.5. Same as Fig.4 but for $CrNH_4(SO_4)_2 \cdot 12\ H_2O$ at 20.4°K.

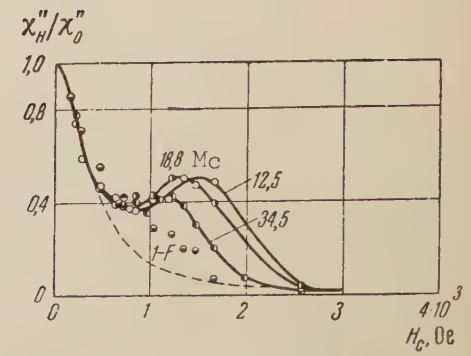

Fig.3. Same as Fig.1 but in $Cu(NH_4)_2(SO_4)_2 \cdot 6H_2O$.

2. At liquid hydrogen temperatures in many salts the relaxation times τ are of the order of 10^{-5} sec, leaving the easily attainable frequency interval between 10^5 and 10^8 Hz free from spin-lattice relaxation. Caloric measurements on χ'' have been carried out, in cooperation with Smits, Derksen and Verstelle, in a series of non-diluted and diluted powder-samples from 10^6-10^8 cps as well as heterodyne and bridge measurements on χ' and χ'' from 10^5-10^7 cps. Figs. 1, 2 and 3 give the dependences of χ'' on H_c in a number of salts, the dotted line indicating the expectation for τ' constant. Figs. 4, 5 and 6 give dependences of χ'' on the frequency while Fig.7 gives an example of data on χ' as a function of H_c.

It is possible to divide the substances in three groups:

A - those having an anomalously high χ'' at low fields (Fig.1, 4 and 5).

B - those having a rather steep decrease of χ'' in low fields but an extra contribution in much higher fields (Fig.2 and 6)

C - those having a normal behavior in low fields and

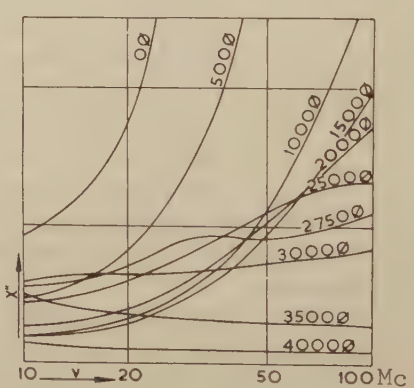

Fig.6. χ'' as a function of the frequency for different values of the parallel field H_c in $Mn(NH_4)_2(SO_4)_2 \cdot 6H_2O$

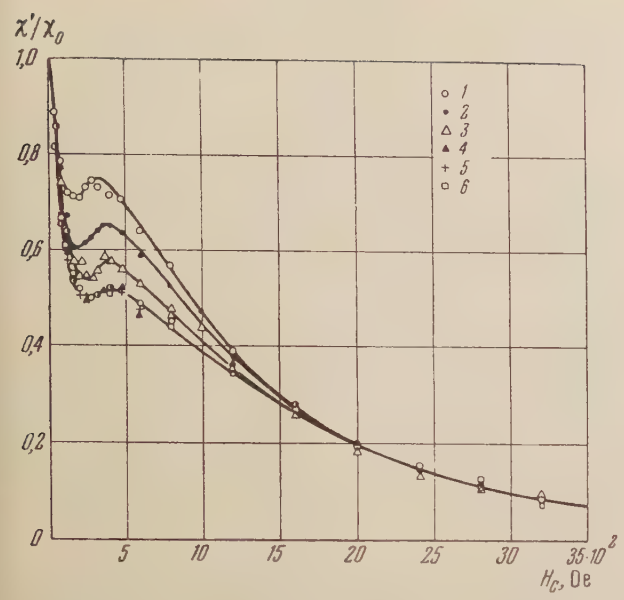

Fig.7. Variation of the ratio of χ' to its value at $H_c = 0$ as a function of the parallel field H_c in $CrK(SO_4)_2 \cdot 12\,H_2O$ diluted with Al(1 : 20) at 20.4°K and different frequencies: 1) 0.1, 2) 0.5, 3) 1, 4) 3, 5) 6 and 6) 10 Mc.

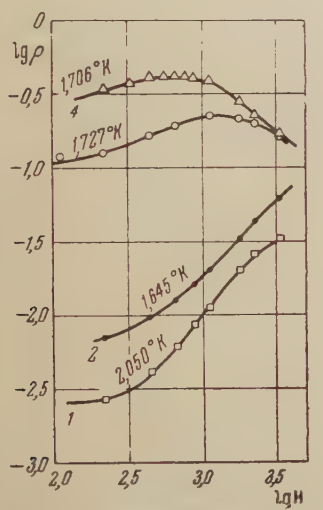

Fig.8. Logarithm of the average relaxation time ($\log \rho = \log \tau_{av} + \log 2\pi$) as a function of the logarithm of the parallel field H_c. Samples of $FeNH_4(SO_4)_2 \cdot 12H_2O$ diluted by different amounts of Al: 1) undiluted, 2) 1 to 3, 3) 1 to 18 and 4) 1 to 61.

also an extra contribution in high fields (Fig.3).

The substances of group A have electrical splittings of their basic levels which are mugh higher than their magnetic broadening. In those of group C, on the contrary the magnetic broadening is preponderant. In group B the two effects are of the same order of magnitude. That this deviation has sense is proved by the fact that a salt belonging to B joins group A if its magnetic interactions are reduced by diluting with non-magnetic material.

The first relevant theory was that of Kronig and Bouwkamp who in 1938 suggested that the decisive condition for a spin, that changes its orientation is that the vector sum of the external field and the momentary field due to its neighbours happens to be zero. This is a much rarer event if $H_c > H_i$ (the root mean square internal field) and thus τ' is expected to be proportional to $\exp(H_c^2/H_i^2)$. In 1942 Broer has remarked that this would only apply to the diagonal elements of the magnetic moment while the non-diagonal elements would give a constant non-relaxing contribution to the adiabatic susceptibility χ_{ad}. For chromic ions he made some computations leading to a dependence of χ_{ad} on the field, which appeared to be in disagreement with all then available data. Broer thus rejected the Kronig-Bouwkamp theory and later argued in a theoretical paper that τ' should not increase with rising H_c but even decrease somewhat.

Now it is found that the lowest curves of Fig.7 are almost identical with Broer's rejected 1942 prediction. So apparently the Kronig and Bouwkamp reasoning gives the right answer. The results for group B and C agree with their prediction though perhaps τ' does not increase quite so rapidly as was predicted. To understand the relaxation times found in the salts of the A group, crossing over of energy levels should be taken into account.

3. In the liquid helium region no single spin-lattice relaxation times are found but a wide region of relaxation times which are not very reproducible and are very structure sensitive. In nondiluted salts τ_{av} usually increases with H_c, while in diluted salts τ_{av} is considerably larger but often decreases in high fields proportional to H_c^{-1} (Fig.8). The dependence on the temperature varies from T^{-5} to

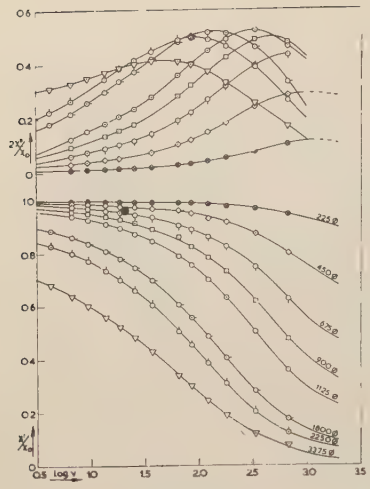

Fig.9. Absorption χ'' and dispersion χ' in a pressed pill of $FeNH_4(SO_4)_2 \cdot 12H_2O$ at 2.88°K at different values of the parallel field.

about $T^{-1.5}$ in the most diluted salts (Fig.8).

The spin-lattice relaxation at these very low temperatures would theoretically not be due to inelastic scattering but to direct absorption and emission of phonons. Thus we expect to have rather narrow bands of crystal oscillators, that are "on speaking terms" with the magnetic ions. Van Vleck has suggested that it is not the spin-lattice interaction which forms the bottleneck determining the average relaxation times but the transfer from the relatively few oscillators "on speaking terms" to the other oscillators or the liquid helium bath. As a matter of fact the spin-lattice interaction would lead to large fields and low concentrations of the magnetic ions to $\tau \sim T^{-1} H_c^{-2} c^0$, which does not at all fit with the experimental data (c is the concentration of magnetic ions). The other bottlenecks having to do with the oscillators "on speaking terms" appear to have sufficient flexibility to account for many of the complicated data (Fig.9). A provisional and rough model leads to $\tau_{av} \sim T^{-2} H_c^{-1} c$ in high fields and to $\tau_{av} \sim T^{-2}(b + C H_c^2) c^{-2}$ in low fields which account for a fair portion of the experimental data collected in cooperation with Van der Marel and Van den Broek.

Exchenfelder and Weidner have studied the saturation of paramagnetic absorption when the microwave power is increased in a few crystals. They conclude to the existence of much shorter relaxation times which have the dependence on T to be found if the bottleneck in their experiments were the spin-lattice interaction. Investigations are under way to decide whether this is due to a much stronger excitation of the oscillators "on speaking terms" than occurs in the usual measurement of paramagnetic relaxation.

Kamerlingh Onnes Laboratory,
University of Leiden

TEMPERATURE DEPENDENCE OF THE MAGNETIC ANISOTROPY ENERGY IN NICKEL

- I.M.Puzei

The energy of the magnetic anisotropy of nickel has been investigated by a number of authors. The results obtained, however, are extremely divergent owing to the fact that different techniques and specimens are used in the different investigations. This observation also applies to investigations of the temperature dependence of the magnetic anisotropy constant. Thus, for example, in the region of hydrogen temperatures Honda, Masumoto & Shirakawa[1] and Williams & Bozorth[2] obtained markedly different anisotropy constant values.

Vonsovskii[3] was the first to demonstrate the theoretical possibility of a change in the sign of the anisotropy constant. The results of Honda, Masumoto & Shirakawa[1] support this deduction. The experimental data obtained by these investigators for the region of higher temperatures are only approximate, however, due to the small values of the anisotropy and the inherent limitations of the experimental technique employed.

Hence we felt it would be of interest to investigate the temperature dependence of the magnetic anisotropy of nickel both at low and at high temperatures. In our experiments we measured the torque acting on a single crystal specimen in a magnetic field and calculated the first anisotropy constant from the recorded values.

1. Specimen

The single crystal was grown by slow cooling of a melt in a high frequency vacuum furnace. The chemical composition of the specimen was 99.8% Ni, 0.035% Co, 0.008% Fe, 0.02% Cu, 0.009% S, 0.03% C, and 0.001% Pb. The specimen was cut in the shape of a sphere and after removal of the hard surface layer by etching with acid was heat treated by heating in vacuum at 1000° for 4 hours, followed by cooling with the furnace.

The diameter of the specimen was approximately 9 mm. The maximum difference between diameters in different directions after light grinding with chromium oxide compound was reduced to ±0.0005 mm. The direction of the crystal axes was determined by means of x-rays with an accuracy of $\pm 1^{\circ}$. The density of the specimen at $+20^{\circ}$ was 8.926 g/cm^3.

2. Anisometer

A diagram of the anisometer is shown in Fig.1. It consists of a Dewar flask 1 surrounding the hermetically sealed insert 2 with the specimen holder 4 and a heating element wound on the copper cylinder 3. At the bottom end, the specimen in the holder is centered by means of the fine tungsten wire with known torsional characteristics. On top, the movable system has a mirror 6, a massive copper damper ring 7* and is centered by means of the elastic filament 8. This top filament was a length of wire made of a special watch-hairspring alloy with a small temperature coefficient of the elasticity modulus. The modulus of elasticity of the upper elastic filament was much greater than the modulus of elasticity of the lower tungsten wire.

The temperature of the specimen was measured first by a copper-constantan thermocouple (5) and then by means of a platinum thermometer which was cali-

---

*The stationary ring of the damper is assembled of permanent magnets made of magnico alloy.

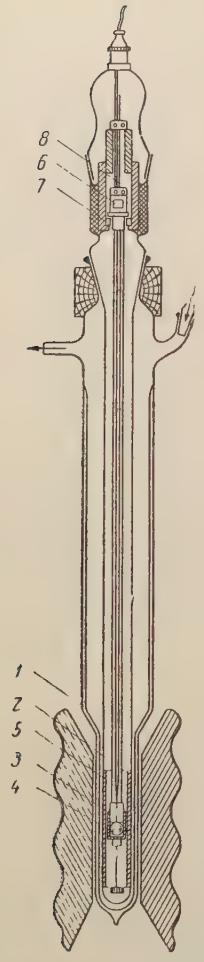

Fig.1. Cryostatic anisometer: 1) Dewar, 2) insert, 3) cylinder with heating winding, 4) specimen, 5) thermocouple, 6) mirror, 7) magnetic damper, 8) calibrated filament.

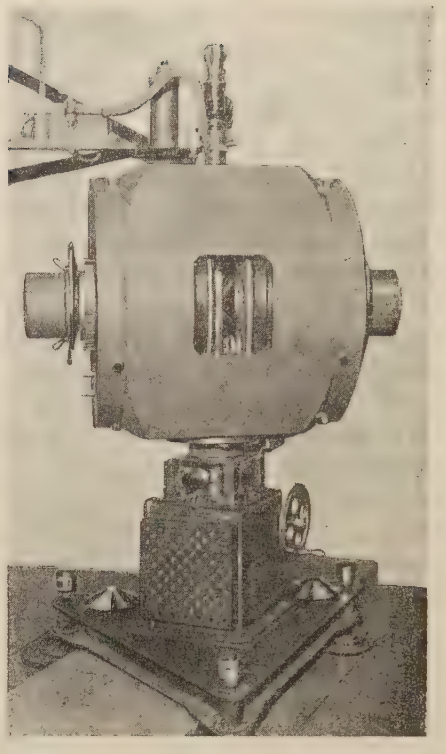

Fig.2. General view of electromagnet.

brated beforehand with reference to a standard platinum thermometer. The thermocouple and the platinum thermometer were in thermal contact with the specimen. In the low temperature region the accuracy of temperature measurement was $\pm(0.2\text{-}0.3)^{\circ}$; at temperatures above 83°K the accuracy was better.

The inside of the insert was evacuated. Upon attainment of thermal equilibrium in the Dewar between the specimen and the liquid coolant, the heater was switched on and any desired intermediate temperature established. A cryostat of this type allows of maintaining intermediate temperatures with very little change over a period sufficient for performing the necessary measurements, provided only that the current through the heater and the level of the cooling liquid in the Dewar are kept constant. We measured the temperature of the specimen at the beginning and end of each experiment and took the average value.

The entire assembly was clamped to a massive bracket built into the wall with the narrow lower part of the Dewar in the gap of the electromagnet.

3. Electromagnet

In order to obtain the requisite strong and uniform fields, we designed a special electromagnet weighing 3.5 tons. A photograph of this electromagnet is reproduced in Fig.2. It consists of a yoke 830 mm in diameter, tapered winding-carrying cores having a base diameter of 660 mm, movable insert cores 200 mm in diameter, a suitable rotating contact assembly, a blocking rheostat, a set of pole pieces and diverse accessories.

The yoke and winding-carrying cores are cast of decarbonized Armco type steel. The insert cores and pole pieces are made of a better grade carbon free forged iron. The winding is of square conductor with a cross section area of 25 mm^2; the maximum rated capacity is 170,000 ampere turns. The coils are air cooled. This electromagnet differs from an earlier version, described in Ref.5, by a more efficient shape of the magnetic components and a more regular distribution of the magnetic flux, as well as by the possibility of obtaining stronger and more uniform fields in a larger volume.

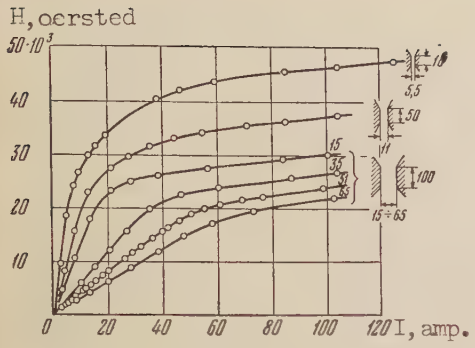

Fig.3. Influence of the gap width on the magnetization curves of the electromagnet.

The magnetization curves for the present electromagnet with different gap widths are shown in Fig.3. It will be evident from the curves that using iron pole pieces one can obtain the following fields:

Diameter, mm	Gap, mm	Field, oersted
100	50	25,000
100	15	30,000
50	10	38,000
10	6	47,000

Undoubtedly by employing Permendur pole pieces even stronger fields could be obtained.

4. Computation of the anisotropy constant

Our procedure consisted of measuring at different temperatures and field intensities the torque acting on the specimen in the (100) plane for 24 discrete orientations of the field, i.e., at 15° intervals. From the experimental data, using Bessel's equations familiar from harmonic analysis, one can calculate the amplitude of the fourth harmonic and from this readily compute the anisotropy constant. In cases when the anisotropy constant is large, this method of calculation does not give its true value, inasmuch as technical saturation is not attained in the highest available fields. In such cases it is necessary to extrapolate to an infinitely strong field. To this end, it is convenient to use the variation of the torque as a function of the field strength in the analytic form given by Akulov[6]:

$$\Psi = \arcsin\frac{M}{HJ_s} + \frac{1}{4}\arcsin\frac{2M}{K}.$$

Here it is assumed that the anisotropy constant K is field independent. This formula was fundamental for our extrapolation. An analogous extrapolation procedure was employed by Shubina[7].

5. Torque measurements

The accuracy of the torque measurements is determined by the accuracy of evaluating the resilience (stiffness) of the elastic elements (i.e., the torsion filaments) of the anisometer, the accuracy of reading the deflections of the mirror and the accuracy of measuring the angle of the magnetic field. The error in determining the resilience of the elastic system of the anisometer is evaluated to be 0.2%; the uncertainty in reading the deflection of the light beam is 0.3% on the average; the angular position of the magnet was read to within 0°7.5' (consequently, this uncertainty was appreciably smaller than the others). Thus the uncertainty as regards determination of an individual torque value amounted to about 0.5%. As was noted above, however, 24 torque values are used for determining each anisotropy constant value. In view of this the accuracy of determination is enhanced and the uncertainty amounts to only about 0.3%. The accuracy of the temperature measurements was indicated above. At high temperatures the anisotropy constant is very small. The accuracy of its determination, however, remained virtually the same inasmuch as with decreasing magnitude of the anisotropy constant (increasing

temperature), we replaced the elastic elements (the torsion filaments) successively by more sensitive ones. At low temperatures it proved necessary to take into account also the stiffness of the mounting bracket built into the wall inasmuch as at these temperatures the torque acting on the specimen and transmitted to the mounting bracket is sufficiently great to deform the bracket to a slight but noticeable degree.

6. Results and discussion

The results of our measurements of the anisotropy constant K at different temperatures and in different fields are shown in the accompanying table. In the last column we list the values of K extrapolated to H = ∞.

Temperature and field dependence of the anisotropy constant of nickel

Exp. No.	t, °C	T, °K	H, oersted	$-K_H \cdot 10^{-4}$ erg/cm^3	$-K_\infty \cdot 10^{-4}$ erg/cm^3
1			11 250	103,41	105,36
2			14 150	104,26	105,46
3	—252,8	20,4	15 200	104,60	105,63
4			16 300	104,75	105,64
5			17 120	104,84	105,65
6	—237,1	36,1	10 000	98,26	102,18
7	—195,6	77,6	7 600	74,89	76,40
8	—161,4	111,8	13 800	55,98	56,16
9	—146,6	126,6	7 530	48,69	49,10
10	—132,8	140,4	13 860	41,72	41,80
11	—109,1	164,1	7 520	31,18	31,29
12	— 90,2	183,0	7 500	25,88	25,94
13	— 38,9	234,3	7 500	13,29	13,30
14	— 16,3	256,9	13 875	9,79	9,80
15	+ 29,5	302,7	7 600	4,64	4,64
16	34,6	307,8	7 800	3,95	3,95
17	59,6	332,8	7 750	2,55	2,55
18	80,4	353,6	7 150	1,72	1,72
19	120,6	393,8	7 070	0,712	0,712
20	139,2	412,4	6 900	0,429	0,429
21	159,3	432,5	6 820	0,235	0,235
22	180,0	453,2	6 830	0,102	0,102
23	195,6	468,8	6 730	—0,042	0,042
24	218,7	491,9	7 400	—0,007	—0,007
25	235,0	508,2	7 300	—0,024	—0,024
26	256,6	529,9	7 275	—0,030	—0,030
27	271,8	545,0	7 150	—0,030	—0,030

The variation of the magnetic anisotropy constant as a function of the temperature is also shown graphically in Fig.4. The dots in the breaks in the curve are the experimental points. In plotting the curve we used values of the anisotropy constant measured in fields of as nearly the same value as possible. In principle, of course, one should use values of the constant measured in a field of exactly the same intensity. The dash line shows the curve obtained by extrapolating the values of the anisotropy constants to H = ∞.

It will be noted that the anisotropy constant has a very high value at liquid hydrogen temperature. In an 11,250 oersted field, it equals $103.4 \cdot 10^4$ erg/cm^3; the magnitude of the constant extrapolated to H = ∞ is $105.36 \cdot 10^4$ erg/cm^3. This value is in good agreement with the results of Honda, Masumoto & Shirakawa[1] who report $K = -100 \cdot 10^4$ erg/cm^3, but differs greatly from the data of Williams & Bozorth[2] who obtained a value of $K = -78 \cdot 10^4$ erg/cm^3.

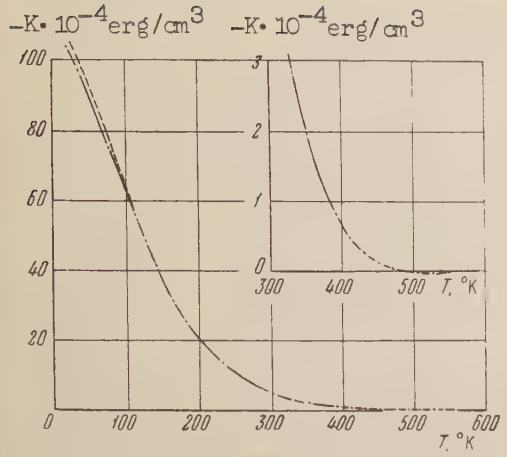

Fig.4. Temperature dependence of the anisotropy constant of nickel.

At the temperature of liquid nitrogen Briukhatov & Kirenskii[8] obtained K = $= -64.6 \cdot 10^4$ erg/cm^3. This differs appreciably from our value of K = $-74.89 \cdot 10^4$ erg/cm^3 (H = 7600 oersted). The empirical formula deduced by these investigators for the variation of K as a function of the temperature has a noticeable tendency to saturation even at 90°K. It will be seen from the curve reproduced in Fig.4 that there is no such tendency evident down to 20.4°K.

The disagreement between our data and the results of Briukhatov & Kirenskii[8] and Bozorth[9] may be explained by differences in the purity of the specimens and by the fact that these investigators apparently employed insufficiently strong fields.

As may be seen from the table and Fig.4, at high temperatures the anisotropy constant of nickel changes sign, i.e., goes through zero, at about 217°C. Above this temperature and up to 272° it is small, being equal approximately to +300 erg/cm^3. Thus the change in the sign of the anisotropy constant predicted by Vonsovskii is actually observed in nickel.

The change in sign of the anisotropy constant must be evinced in the magnetic properties of the material, specifically the initial and maximum permeabilities, which must be greatest at the temperature corresponding to K = 0. According to the data of Bozorth[9], at 200° there are observed maxima of the initial and the maximum permeabilities of nickel. This temperature is close to the temperature of the change in sign of anisotropy constant found in the present investigation. According to the data of Honda, Masumoto & Shirakawa[1], the temperature of the change in sign is 100° (see Ref.4).

In their recent theoretical work Tiablikov & Gusev[10] give a quantum mechanical calculation of the temperature and field dependence of the magnetic anisotropy constant of cubic crystals. Their treatment is based on the polar model of a metal[11]. Taking into account the symmetry of the lattice, these authors deduce a new approximate expression for the Hamiltonian and then by means of the method of approximate second quantization calculate the sum-over-states and the free energy. Expansion of the free energy in a series in terms of the direction cosines of the total magnetization vector of the system leads to a formula for the first anisotropy constant.

In the case of sufficiently strong magnetic fields, where $\cos(\hat{H}J_s) \approx 1$, the formula deduced by Tiablikov & Gusev can be written in the form

$$K = K_0\left[1 - 5\left(\frac{kT}{\theta}\right)^{3/2} e^{-2\mu H/kT}\right],$$

where $\theta = \frac{2}{3}\pi\bar{J}_2$ ($\bar{J}_2$ is the mean exchange integral).

The formula is valid at temperatures at which $J_4 < kT \ll \bar{J}_2$, where J_4 is a quantity characterizing the electron interaction in a ferromagnetic crystal.

Utilizing our tabular data one can evaluate the order of magnitude of the constant entering into the above formula and compare the experimental field and temperature dependences of the anisotropy constant with the variations predicted by theory. Most suitable for the purposes of such comparison is

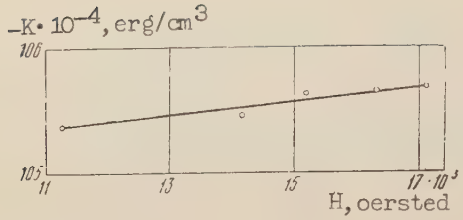

Fig.5. Field dependence of the anisotropy constant of nickel at 20.4°. Line - theoretical curve based on the data of Tiablikov & Gusev[10]; points - our experimental values.

the field dependence of the anisotropy constant of nickel at 20.4°K.

Taking $\mu = 0.927 \cdot 10^{-20}$ erg/gauss and $k = 1.372 \cdot 10^{-16}$ erg/degree, let us take the first and fourth values of K from the table for T = 20.4°K and substitute them in the formula. Eliminating K_0 from the two equations obtained in this manner, we find

$$\bar{\theta} = 4.0 \cdot 10^{-14} \text{ erg/atom and}$$
$$J_2 = 2 \cdot 10^{-14} \text{ erg/atom.}$$

From its definition θ must be of the order of the product of Boltzmann's constant by the Curie temperature; this is in fact the case.

The solid line in Fig.5 shows the variation of the anisotropy constant as a function of the field at 20.4° calculated according to the formula of Tiablikov & Gusev; the points are values taken from the last column of our table. We see that the theoretical curve gives a correct indication of the actual field dependence of the magnetic anisotropy constant of nickel.

Institute of Precision Alloys,
Central Scientific Research Institute of Ferrous Metallurgy

References

1. K.Honda, Masumoto & Y.Shirakawa, Sci.Rep.Tohuku Univ., 24, 391 (1935).
2. H.J.Williams & R.M.Bozorth, Phys.Rev., 56, 837 (1939).
3. S.V.Vonsovskii, Zhur.eksp.i teor.fiz., 8, 1104 (1938).
4. R.M.Bozorth, Ferromagnetism. (Cited in Russian trans. p.457,M.,1956.)
5. I.M.Puzei, Izv.AN SSSR, Ser.fiz., 16, 549 (1952).
6. N.S.Akulov, Ferromagnetizm (Ferromagnetism) M.-L., 1940.
7. L.A.Shubina, Izv.AN SSSR, Ser.fiz., 11, 527 (1947).
8. N.L.Briukhatov & L.V.Kirenskii, Sow.Phys., 12, 602 (1937).
9. R.M.Bozorth, Ferromagnetism. (Cited in Russian trans.p.218, M.,1956.)
10. S.V.Tiablikov & A.A.Gusev, FMM (Physics of Metals & Metallography), 2, 385 (1956).
11. N.P.Bogoliubov & S.V.Tiablikov, Zhur.eksp.i teor.fiz., 19, 256 (1949).

SUPERSTRUCTURE AND THE TEMPERATURE DEPENDENCE OF THE MAGNETIC ANISOTROPY ENERGY OF NICKEL-IRON ALLOYS

- I.M.Puzei

Introduction

Order-disorder transformations in alloys consisting of atoms with different magnetic moments have a strong influence on the character of their magnetic interaction and, consequently, on the removal of directional degeneracy, i.e., on the anisotropy of their magnetic properties. As is known, nickel-iron alloys have the ability to form ordered structures and, consequently, investigation of the magnetic anisotropy energy of the crystal lattices of Ni-Fe alloys under different conditions (structure and composition of the alloys, temperature, field, etc.) is of particular interest where elucidation of the nature of the ordering process is concerned, for the behavior of the magnetic anisotropy energy in these alloys is distinctive.

Nickel-iron alloys are now widely used in engineering and technology, primarily in the quality of high permeability alloys. Their magnetic properties as a whole depend to an appreciable extent on the magnetic anisotropy; hence the temperature behavior of these properties is closely associated with the temperature dependence of the anisotropy.

Until now there have been virtually no studies of the temperature dependence of the anisotropy energy of nickel-iron alloys. The purpose of the present investigation was to determine the temperature dependence of the anisotropy energy of binary Ni-Fe alloys as well as the variation of the anisotropy energy of permalloy type alloys, containing molybdenum, chrome and copper, with the degree of order.

Samples

The investigation was carried out on single crystal samples of spherical shape. The samples were prepared by slow cooling of the appropriate melt under vacuum (10^{-2} mm Hg). The initial materials used for the preparation of the specimens were the following:

1) Ni - 99.88%, C - 0.03%, remainder Co, Fe, Cu;
2) Fe - 99.81%, C - 0.02%, Cu - 0.04%, Mn - 0.05%;
3) Mo - 99.36%, Fe - 0.6%;
4) FeCr; Cr - 69.9%, Si - 0.14%, C - 0.07%, remainder Fe;
5) Cu - refined electrolytic.

The extent of liquation in the specimens was determined by chemical analysis. At the two diametrically opposite points of the specimen along the line of growth of the crystal the difference in local composition was less than 0.1%. The investigated samples are characterized in Table 1.

After etching in acid the samples were annealed in vacuum at 1000° for 3 hours and then cooled with the furnace.

X-ray diffraction studies by the back-reflection technique showed that the specimens had the usual structure peculiar to all crystals obtained from a melt and having an appreciable width of the Darwin curve. The same samples were used for investigating ordering effects by the neutron diffraction procedure.[1] Neutron diffraction patterns obtained by reflection from the crystal planes showed that samples Nos.1,2 & 3 had sharp maxima 30-40' wide, while samples Nos.4,5 & 6 had 2° wide maxima.

Table 1

Composition of the investigated samples

Sample No.	Ni	Fe	Cu	Mo	Cr
1	76,4	23,6	—	—	—
2	53,6	46,4	—	—	—
3	75,2	20,8	4,0	—	—
4	78,3	17,9	—	3,8	—
5	78,4	16,2	—	5,4	—
6	74,5	22,8	—	—	2,7

The character of the maxima gives us a clear indication of the structure of the specimens: in the case of sharp narrow maxima we have single crystal specimens, while in the case of broad maxima the specimens have the fragmented structure frequently obtained in growing "single crystals" from a melt. In the latter case the crystal consists of blocks disoriented by $\pm 1^{\circ}$. Where investigation of the anisotropy is concerned this structure can introduce no substantial errors and hence for our purposes all the specimens could be regarded as single crystal ones.

In order to avoid large errors in measuring small anisotropy constant values, the specimens were brought to as nearly spherical shape as feasible. The maximum diametral difference (relative to the mean diameter) did not exceed ±0.0005 mm.

In order to obtain the ordered state the samples were subjected to prolonged annealing for 600 hours with the temperature being reduced in steps in the range from 600 to 300°. In order to obtain intermediate degrees of order the specimens after the preliminary 600 hour anneal were heated at each given temperature, beginning with 300° and ending with 600°, for 3 hours and then quenched in oil. Sample No.1, in addition, was investigated after a series of isothermal anneals averaging 100 hours each (total heating duration of about 600 hours) first in the direction of ordering and then in the direction of disordering. Sample No.4 was also investigated after prolonged anneals of 48 to 72 hours each with a total heating duration of 400 hours in the direction of ordering.

After the heat treatment the samples were mounted in the anisometer holder, in each case being carefully and rigorously oriented with reference to appropriate gold lines applied electrolytically beforehand. The equipment and experimental technique as well as the accuracy of measurement are fully described in Ref.1 (the preceding article).

Neutron diffraction studies

The results of our neutron diffraction studies have been given in detail in Ref.2 and hence will only be summarized here.

In addition to the samples listed in Table 1 we also investigated three single crystal specimens having the following compositions: 82.6% Ni + 17.4% Fe, 70.4% Ni + 29.6% Fe and 49.8% Ni + 50.2% Fe. After annealing for 600 hours in the temperature range from 550-300° the Ni-Fe alloy specimens were characterized by the following values of the long-range order parameter η:

Ni content, %	82.6	76.4	70.4	49.8
Long-range order, η	0	0.8	0.9	0

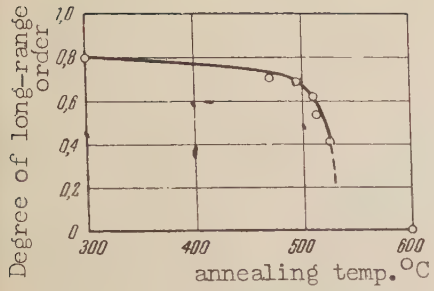

Fig.1. Variation of the degree of long-range order in sample No.1 (Ni_3Fe) with the isothermal annealing temperature.

The asymmetry of the long-range order relative to the Ni_3Fe composition is evident: increasing the Ni content by 6.2% led to complete disappearance of the long-range order, whereas reducing the Ni content by 6% resulted in a noticeable increase in the degree of long-range order as compared with the Ni_3Fe alloy. This asymmetry is characteristic of many of the properties of this system and is particularly evident in the composition dependence of the anisotropy constant of ordered alloys[3], the electric resistivity[4], the transparency of the alloys to neutrons[5], etc. In connection with this, in Ref.2 we suggested that the principal contribution to the ordering energy comes from the exchange energy.

This inference is substantiated by the fact that no superstructure is formed in the alloy with 50% Ni. If the ordering energy were primarily elastic or electrostatic in character superstructure should appear, while if this energy is of ferromagnetic origin the ordered phases would have a laminar structure and this would give rise to unfavorable conditions for the appearance of the ferromagnetic state.

The curve shown in Fig.1 is based on the results of our investigation of the degree of long-range order in the Ni_3Fe alloy (sample No.1) after different isothermal anneals. It is interesting to note that evaluation of the size of the ordered regions on the basis of the width of the neutron diffraction peaks by means of the Seliakov-Sherer formula showed that the dimensions of the ordered regions after annealing for 600 hours are of the order of 30 Å.

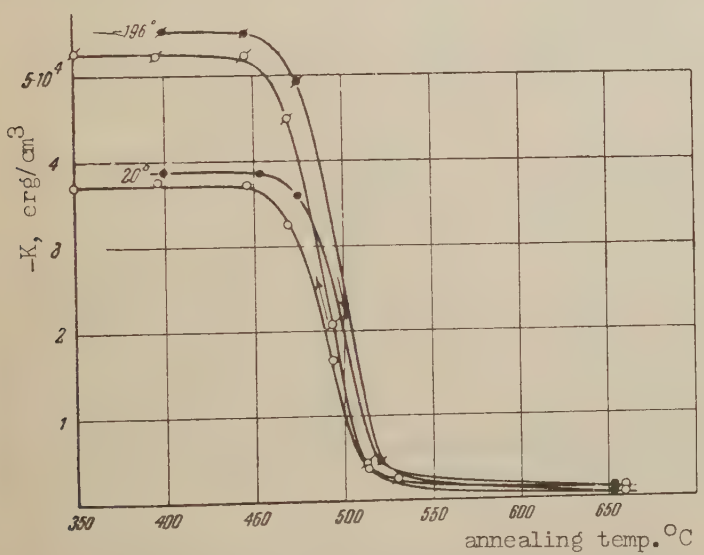

Fig.2. Variation of the anisotropy constant of Sample No.1 (Ni_3Fe alloy) with the annealing temperature as this temperature is increased and decreased.

After annealing for 600 hours samples Nos.3 & 6 had long-range order parameters $\eta = 0.3$ and 0.75. Copper and chromium have different effects on the ordering (in the case of chromium, apparently, superstructure of the $Ni_3(FeCr)$ type is formed. In alloys containing molybdenum (samples Nos.4 & 5) the long-range order after 600 hour annealing proved to be zero, but these samples exhibited a strong dependence of their physical properties on the heat treatment owing presumably to short-range ordering.

Investigation of the magnetic anisotropy energy

The curves of Fig.2 show the variation of the magnetic anisotropy constant of the Ni_3Fe alloy (sample No.1) measured at +20 and -196°C with the annealing temperature. It will be seen from the figure that there

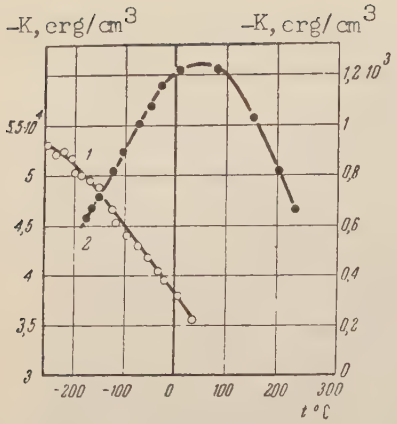

Fig.3. Temperature dependence of the anisotropy constant of sample No.1 after prolonged annealing (1) and after quenching from 600° (2).

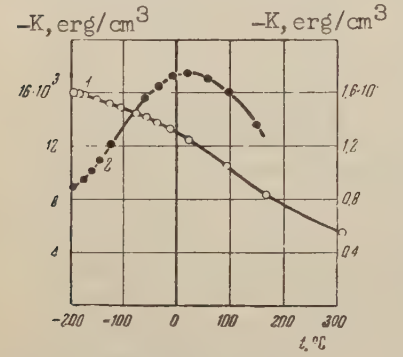

Fig.4. Temperature dependences of the anisotropy constant of sample No.3 (75.2% Ni + 20.8% Fe + 4% Cu) after prolonged annealing (1) and after quenching from 600° (2).

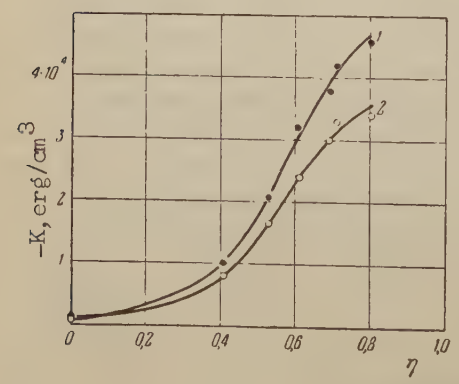

Fig.5. Variation of the anisotropy constant of sample No.1 measured at -196° (1) and at +20° (2) with the degree of long-range order.

obtains hysteresis of the order-disorder transformation. The relative displacement of the increasing and decreasing annealing temperature curves is about 10°. Although the degrees of order after annealing for a period of 600 hours differ somewhat (which, of course, also causes some difference between the anisotropy constants) one cannot explain the hysteresis by this factor alone.

The existence of transformation hysteresis is direct indication that this transformation has the character of a first order transition. This is consistent with the theory of Landau and Lifshits. As was noted above, the size of the ordered regions proved to be very small: 30 Å.

Up to an annealing temperature of 520° the anisotropy constant at the temperature of liquid nitrogen is larger than at room temperature, while after annealing at temperatures above 520° we have the opposite relationship, i.e., the constant decreases with decreasing temperature of measurement. The temperature dependences of the anisotropy constant of sample No.1 in the two extreme states - after prolonged annealing and after quenching - are shown in Fig.3. In the ordered state (annealed) the temperature variation of the constant is normal down to liquid nitrogen temperature, while in the disordered state (quenched) the curve exhibits a maximum at 60°. This is the first time such an anomalous variation of the anisotropy constant of metallic alloys with a cubic lattice has been observed. An inverse temperature dependence has hitherto been observed only in MnBi and Mn_2Sb whose lattices are characterized by a lower order of symmetry.

An analogous inverse dependence is displayed by our alloy with 4% copper (sample No.3), as may be seen from Fig.4. During the neutron diffraction studies of sample No.1, after each heat treatment we measured the degree of long-range order and the anisotropy constant. This enabled us to establish a direct relationship between the magnitude of the constant and the degree of long-range order. The dependence is shown in Fig.4. Here the state after quenching from 600° was taken for reference purposes as the state with a zero long-range parameter.

We felt it would be of interest to investigate the magnetic anisotropy of a nickel-iron alloy having a different stoichiometric composition, namely, NiFe, because many alloys having this stoichiometric proportion form superstructure (for example, Cu-Au and Cu-Pt) and because the magnetic anisotropy is highly sensitive to ordering.

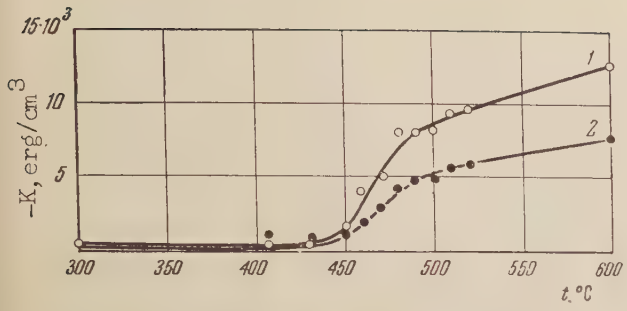

Fig. 6. Variation of the anisotropy constant of sample No.2 (53.6% Ni + + 46.4% Fe) measured at -196° (1) and at 20° (2) as a function of the temperature of isothermal annealing.

In Fig.6 we show the variation of the anisotropy constant of sample No.2 with the temperature of prolonged isothermal annealing. It will be seen that the constant falls off almost to zero, i.e., that the material becomes virtually isotropic both at room temperature and at that of liquid nitrogen. The observed variation is of practical significance inasmuch as binary alloys with 50% Ni are extensively used in engineering. In the equilibrium phase diagram of the Ni-Fe system (see Ref. 6) the γ-α transformation curve extends into the region of 50% Ni concentrations.

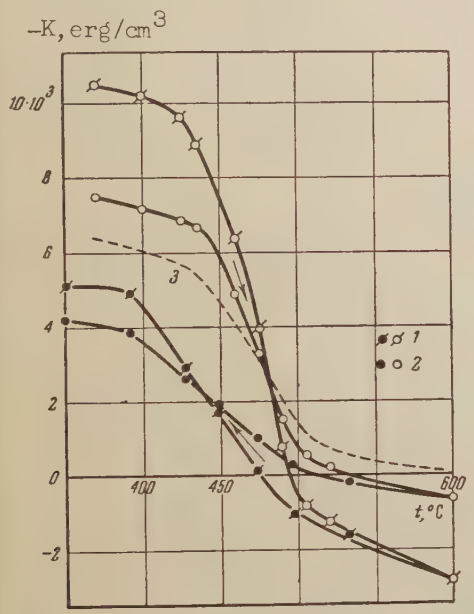

Fig.7. Variation of the anisotropy constant of sample No.4 (78.3% Ni + 17.9% Fe + 3.8% Mo) with the temperature of isothermal annealing. Constant measured at 1) -196° and 2) +20°; 3) schematic curve for temperatures above room temperature.

Offhand, one might assume that prolonged annealing would result in decomposition of the γ-phase into the α-phase with simultaneous fragmentation of the single crystal into a polycrystal. Our experiments show, however, that after heating of the specimen to 600° and subsequent quenching the monocrystalline properties of the specimen are apparently retained, inasmuch as the anisotropy constant returns to its initial value, i.e., the value obtaining prior to prolonged annealing.

The interval of concentrations, found in the work of Ref.3, in which one can make the anisotropy constant go to zero by appropriate heat treatment is thus extended from 27.5% Fe to 50% Fe.

The decrease in the magnitude of the positive anisotropy constant with ordering, noted in Ref.3, is common to nickel-iron alloys in a wide range of concentration and is in all probability due to the appearance of superstructure of the same type as in the Ni_3Fe alloy.

Long-range order in the alloy with 50% Fe was not detected by neutron diffraction, consequently the variation of the anisotropy constant with the temperature of isothermal annealing is probably due to short-range ordering. No long-range order was detected in molybdenum permalloy (samples Nos.4 & 5) after annealing for 600° hours; nevertheless heat treatment does exert a strong influence on the value of the anisotropy constant. The variation of the anisotropy constant of samples Nos.4 & 5 with the temperature of isothermal annealing is shown in Figs.7 & 8. It will be noted that the curves are generally similar for both samples.

In the case of sample No.4 we also carried out measurements of the anisotropy constant with successively reduced isothermal annealing temperatures, the sample being held at each temperature from 48 to 72 hours (total duration

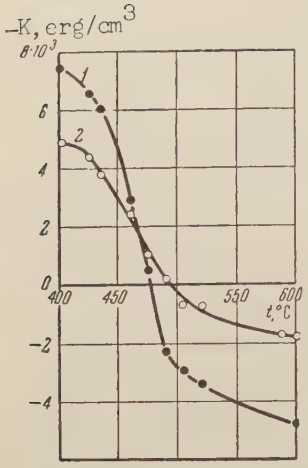

Fig.8. Same as Fig.7 but for sample No.5 (78.4% Ni + + 16.2% Fe + + 5.4% Mo).

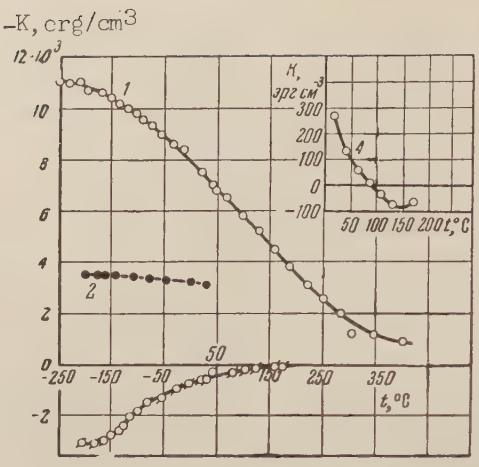

Fig.9. Temperature dependence of the anisotropy constant of sample No.4 after isothermal anneals: 1) after prolonged annealing, 2) after quenching from 477°, 3) after quenching from 600°, 4) after annealing at 570° and cooling in a current of air.

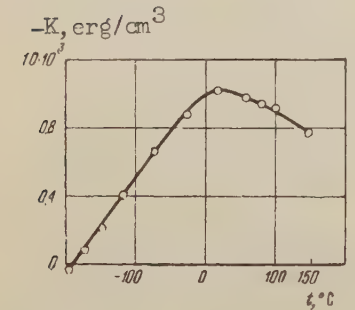

Fig.10. Temperature dependence of the anisotropy constant of sample No.4 after isothermal annealing at 495° and quenching in oil.

of heating 400 hours. The lower curves in Fig.7, drawn through the solid points, show the results of these measurements. It will be seen that these curves lie below the curves obtained in the process of disordering (3 hour anneals at successively higher temperatures). It will be seen that the maximum constants in the two cases differ by a factor of about 2. This indicates that the ordering process in the alloy with molybdenum proceeds more slowly than in binary alloys.

We see from the curves on the right in Fig.7 that quenching from temperatures up to 480° as well as from temperatures of 530° and up, yields states in which the anisotropy constant increases in absolute magnitude with decreasing temperature of measurement. In the range from 480 to 530° we have the opposite effect, i.e., an anomalous variation of the constant with the temperature of measurement.

For purposes of a more detailed investigation of the temperature dependence of the anisotropy constant, sample No.4 was again annealed for 600 hours as in the initial treatment and then subjected to a series of different heat treatments (3 hour heating at different constant temperatures followed by quenching), after each of which the temperature dependence of the anisotropy constant was determined in a separate series of measurements. The results are shown in Figs.9 & 10. It will be seen that they substantiate the above deduction drawn initially from the curves of Fig.7. The temperature variation of the constant shown in the upper right hand insert in Fig.9 becomes understandable if in Fig.7 we plot a curve for the anisotropy constant at temperatures above room temperature (the dash curve in Fig.7). It follows from Fig.7 that at an annealing temperature of 570° and in going to temperatures above room temperature the anisotropy constant changes sign.

Neutron diffraction studies of sample No.6 (74.5% Ni + 22.8% Fe + 2.7% Cr) showed that after prolonged annealing it had almost the same degree of long-range order as the Ni_3Fe alloy. In accord with this, the variation of the anisotropy energy with ordering in this alloy differs from the corresponding variation in alloys with molybdenum. The results of our anisotropy constant measure-

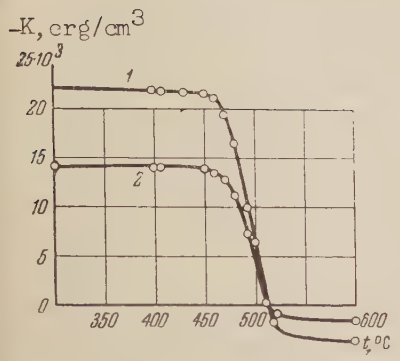

Fig.11. Variation of the anisotropy constant of sample No.6 (74.5% Ni + + 22.8% Fe + 2.7% Cr) measured at -196° (1) and +20° (2) with the temperature of isothermal annealing followed by immediate quenching in oil.

on sample No.6 are shown in Fig.11. It will be evident that at all stages of ordering, at least in the temperature range from +20 to -196°, there obtains for this alloy a normal temperature dependence of the magnetic anisotropy.

The addition of copper to Ni-Fe alloys does not eliminate the anomalous temperature dependence of the magnetic anisotropy and greatly lowers the degree of long-range order probably because of concentrational disordering. Chromium probably does not produce concentrational disordering inasmuch as the degree of long-range order in sample No.6 proved to be virtually the same as in the Ni_3Fe alloy. This is undoubtedly the reason for the different influence of chromium, as compared to copper and molybdenum, on the temperature dependence of the anisotropy constant.

Discussion

The process of ordering in Ni-Fe alloys with a high content of nickel leads to the appearance of pronounced magnetic anisotropy of the type observed in nickel. This obtains in a wide range of concentrations of binary and ternary alloys (Ni + Fe + Mo, Cr or Cu). Consequently, in the ordered state the individual properties of the component elements are lost or suppressed as regards the anisotropy.

We did not detect any discernible degree of long-range order in the alloys with molybdenum. Here all the effects leading to abnormal variations of the anisotropy must be attributed to short-range ordering. Similar effects associated with short-range ordering are observed in the binary Ni_3Fe alloy and in the alloy containing copper.

As is known, the structure of alloys in the region of short-range order is microscopically inhomogeneous, consequently there is reason to assume that the behavior of the bulk magnetic anisotropy is connected with its behavior in the microvolumes. The concentration of atoms of any given element differs in the different microvolumes and the properties of such microvolumes as regards the magnetic anisotropy are to some extent determined by the individual properties of the alloy components. This approach to the interpretation of the properties of alloys follows from the fact that in determining the free energy of a ferromagnetic alloys with components a and b, according to Vonsovskii[7], the mean exchange energy of the alloy may be regarded as consisting of four parts A_{aa}, A_{bb}, A_{ab}, and A_{ba} with the value of A being given by

$$A = \frac{A_{aa}n_{aa} + A_{bb}n_{bb} + A_{ab}n_{ab} + A_{ba}n_{ba}}{n_{aa} + n_{bb} + n_{ba} + n_{ab}},$$

where A_{aa} and A_{bb} are the exchange energies of the pure components, A_{ab} and A_{ba} are the exchange energies of the alloys and n_{aa}, n_{bb}, n_{ab}, and n_{ba} are the numbers of nearest neighbor atomic pairs.

The number of these pairs of atoms can be expressed as a function of the concentration and the short-range order. Inasmuch as with the disappearance of long-range order the uniform distribution of the atoms is disturbed, the role of A_{ab} and A_{ba} is diminished, as a result of which the individual properties of the pure components will exert an increasingly dominant additive effect

on the properties of the alloy. Taking into account the spin-spin and spin-orbit interactions when the degeneracy as regards direction is removed and the exchange integral is replaced by the exchange interaction tensor[8] does not preclude the possibility of treating the exchange energy of the alloy in the manner proposed by Vonsovskii. The energy of the magnetic anisotropy of the disordered Ni_3Fe alloy can then be regarded as the sum of the energies of Ni type and Fe type anisotropies with the normal temperature dependence

$$U = n_{Ni}U_{Ni} + n_{Fe}U_{Fe}.$$

At a certain ratio of n_{Fe} and n_{Ni}, a decisive role in determining the temperature dependence of the anisotropy will be played by the temperature dependence of the energy U_{Fe} with a negative total energy. Consequently, in this case there will be observed an "anomalous" temperature dependence.

This is the case that apparently obtains in the Ni_3Fe alloy (see Fig.3). The addition of molybdenum in all probability promotes microscopic segregation of the Ni and Fe atoms. It is known that Mo greatly reduces the saturation of alloys; for example, in nickel each molybdenum atom reduces the magnetic moment by over 5 Bohr magnetons.[9] Hence the molybdenum atoms in the alloy must be in a multiply ionized state. Inasmuch as the degree of ionization of the Ni and Fe atoms is different, the Mo atoms can further segregation of the Ni and Fe atoms. This must enhance the manifestation of the individual properties of the alloy components, as will be evident from a comparison of Figs.2 & 7. In Fig.7 we see, for example, that where the lower curves are concerned, the entire temperature range may be divided into three parts: 1) up to 440° where the temperature dependence is of the Ni type, 2) from 440 to 520° wherein the temperature variation of the constant is anomalous with the sign changing between 475 and 520°, and 3) above 520° wherein the temperature dependence is that typical for Fe.

If the interpretation suggested above is correct, one may expect that in alloys whose components are characterized by the same type of temperature dependence of the anisotropy (for example, Ni-Co alloys) no anomalous variation of the anisotropy with temperature will be observed. In the case of alloys of components with different anisotropy characteristics - for example, in the Fe-Co system - it may be expected to appear. Unfortunately, there are no data on the temperature dependence of the magnetic anisotropy of Ni-Co and Fe-Co alloys in the literature. We are now engaged in investigating these alloys.

Preparation of temperature stable permalloys

Research on the problem of temperature stabilization of permalloy has been going on for some time. The results so far show that the problem is not easy of solution.

It is known that the influence of temperature on the magnetic properties of high permeability alloys is exerted primarily through the effect of temperature on the energy of the magnetic anisotropy and the magnitostriction parameters.

Measurements of the magnitostriction of our molybdenum permalloy samples showed that after quenching from 600°, the magnitostriction equals $+1.9 \cdot 10^{-6}$, while after annealing for 600 hours it is $+5.9 \cdot 10^{-6}$. The temperature dependences in both cases are rather weak. In going from -196° to +20° the magnitostriction is reduced by 26% in the first case and by 16% in the second case.

In the temperature interval from 20 to 200° it decreases by 45% in both cases.

The actual temperature dependence of the magnetic properties of permalloy cannot be explained by this variation of the magnitostriction, particularly in the region of low temperatures (+20 to -196°) where the permeability falls off by a factor of 10.

It is obvious that the magnetic anisotropy energy has a strong and decisive influence on the permeability of permalloy. The usual low temperature heat treatment employed for molybdenum permalloy - cooling in and with an evacuated container from 600° in air - brings the alloy to a state with a strong temperature dependence of the anisotropy energy (see Fig.7); consequently, the temperature stability of the resultant material as regards magnetic characteristics is very poor.

Our reasoning was that on the basis of the curves of Fig.7 one can select a heat treatment that will result in a weak or inverse temperature dependence of the anisotropy energy and thereby modify the temperature dependence of the magnetic properties in the desired direction. To check this inference we carried out the following experiment.

We prepared two samples of standard molybdenum permalloy in the form of ribbon toroids, using 0.2 mm thick ribbon - samples Nos.1a and 2a.

These samples were first given the heat treatment usually employed in the final processing of the permalloy: heating for 3 hours at 1100° in vacuum, cooling at the rate of 200° per hour to 600° and finally cooling with the evacuated container in air. We measured the magnetic properties of the samples treated in this manner at different temperatures; specifically, we measured the initial and maximum permeabilities, the coercive force and the permeability in a constant field.

Then the same samples were subjected to a stabilizing heat treatment in conformity with the lower curves in Fig.7; 36 hours at 530°, 40 hours at 495°, 48 hours at 470°, 48 hours at 460° and finally cooling in air. Following this treatment we again measured the magnetic properties of the samples. The results of the permeability measurements in a constant magnetic field are shown in Table 2. These data characterize the temperature stability better than the initial and maximum permeability values.

Table 2

Magnetic permeability in a constant field of samples of standard molybdenum permalloy in the form of ribbon toroids after the usual heat treatment and after the stabilizing treatment

Sample No.	Usual heat treatment				Stabilizing heat treatment			
	H,Oe	−196°	+20°	+100°	H,Oe	−196°	+20°	+100°
1a	0,032	10 750	116 000	134 000	0,035	93 000	105 000	114 000
2a	0,032	10 000	110 000	130 000	0,035	100 000	114 000	120 000

It will be evident from the table that the stabilizing heat treatment greatly improved the temperature stability of the permalloy particularly in the region of low temperatures. Thus whereas in the case of sample No.1 after the usual heat treatment the permeability fell off by a factor of almost 10 in going from +20 to -196°, after the stabilizing heat treatment the corresponding decrease in permeability amounted to only 12%.

If we bear in mind that the investigated permalloy contained technological impurities (Mn and Si), we may reasonably assume that one can develop for it a

somewhat modified heat treatment that will lead to even better temperature stability. This of course does not exhaust the possibilities of stabilization by this procedure. In our opinion one can realize temperature stabilization extending to appreciably higher temperatures as well.

Conclusions

1. As a result of neutron diffraction investigation of a series of binary Ni-Fe alloys and Ni-Fe alloys with additions of Mo, Cr and Cu, we established the degree of long-range order in them after prolonged annealing and found the variation of the degree of long-range order in the Ni_3Fe alloy with the annealing temperature and the variation of anisotropy constant with the degree of long-range order in Ni_3Fe.

2. We found the dependence of the magnetic anisotropy energy on the annealing temperature for the Ni_3Fe alloy and detected order-disorder-transformation hysteresis; we established that the temperature dependence of the anisotropy energy in the disordered state has an anomalous character.

3. The dependences of the magnetic anisotropy energy of molybdenum permalloy type alloys on the annealing temperature and on the temperature of measurement are also anomalous.

4. We investigated the variation of the magnetic anisotropy energy of an iron-nickel alloy with chromium as a function of the annealing temperature.

5. Theoretical analysis of the temperature dependence of the anisotropy constant of the investigated alloys shows that the observed behavior of the constant on these alloys is consistent with theory, i.e., may be expected to be anomalous.

6. We carried out an experimental test of the efficacity of the procedure proposed by us for temperature stabilization of molybdenum permalloys.

Institute of Precision Alloys,
Central Scientific Research Institute of Ferrous Metallurgy

References

1. I.M.Puzei, Preceding article in the present issue of the Bulletin.
2. B.G.Liashchenko, D.F.Litvin, I.M.Puzei & Iu.B.Abov, Kristallografiia (Crystallography), 2, 64 (1957).
3. I.M.Puzei, Izv.AN SSSR, Ser.fiz., 16, 549 (1952).
4. S.Kaya, Journ.Fac.Sci.Hokkaido Imperial Univ., 2, 29 (1938).
5. F.C.Nix, H.C.Beyer & J.K.Dunning, Phys.Rev., 58, 1031 (1940).
6. R.M.Bozorth, Ferromagnetism, (Cited in Russian trans., p.462, M.1956).
7. S.V.Vonsovskii, Doklady AN SSSR, 26, 564 (1940).
8. S.V.Tiablikov, Zhur.eksp.i teor.fiz., 20, 661 (1950).
9. I.M.Puzei, Zhur.tekh.fiz., 19, 653 (1948).

TEMPERATURE DEPENDENCE OF SOME MAGNETIC PROPERTIES OF NICKEL

- L.V.Kirenskii, R.S.Nosova & N.V.Reshetnikova

In this report we shall give the results of two experimental investigations: a) an investigation of the magnetic field dependence of the magnetic anisotropy constant at different temperatures and b) an investigation of the temperature dependence of the galvanomagnetic effect (change in resistivity) in saturation fields.

Magnetic anisotropy

There have been relatively few investigations of the variation of the magnetic anisotropy constant of ferromagnets with the magnetic field strength. The first investigation of this line was carried out by Schlechtweg[1]. Not having available fields of sufficient intensity, however, he was unable to arrive at any reliable conclusions.

A more detailed investigation was carried out by Tarasov[2] on single crystal discs of silicon iron. His results in the range of fields from 2000-3000 oersted are described by the relationship

$$M = M_{\infty} \left(1 - \frac{A}{H}\right), \tag{1}$$

where M is the magnitude of the peak torque acting on the disc in a uniform magnetic field of intensity H, M_{∞} is the peak torque in an infinite field and A is a constant.

Inasmuch as the magnitude of the torque M is proportional to the anisotropy constant K and in the (100) plane with an angle of 22.5° between the direction of the field and the tetragonal axis of the crystal

$$K = 2M, \tag{2}$$

in the region of strong fields, we have

$$K = K_{\infty} \left(1 - \frac{A}{H}\right). \tag{3}$$

Subsequent investigations carried out by Bozorth & Williams[3] and Shubina[4] showed that although Eq.(1) does not always hold, it does remain valid for the (100) orientation of the crystal with the tetragonal axis at an angle of 22.5° to the field direction up to very strong fields[5]. It follows from the above relationship that the dependence of the anisotropy constant on the magnetic field strength will be determined by the temperature dependence of A in Eq.(3). As far as we know there have been no investigations of this dependence.

In the present work we investigated the field dependence of the magnetic anisotropy using a single crystal spherical specimen 9.75 mm in diameter in the temperature range from 20 to 300°. The investigation was carried out by the method of measuring the torque acting on the specimen in a strong uniform magnetic field. The torque was measured by means of a highly sensitive anisometer operating on the principle of torsion balance. The sensitivity of the anisometer was 4 erg per 1 mm scale deflection.

The torque corresponding to a field of 3150 oersted was compensated by torsion of the suspension filament. The increment (or decrement) of the torque with increasing magnetic field was recorded automatically on a film mounted in a cylindrical camera.[6] The film was advanced synchronously with the increase of the current in the electromagnet coils and, consequently, with increasing field intensity. The synchronization was realized by means of a drive linking

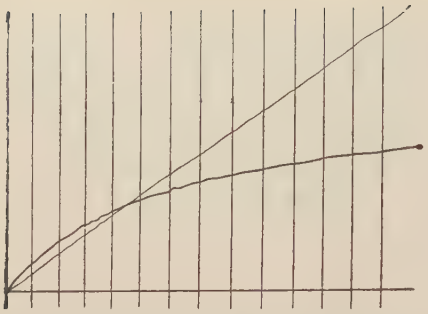

Fig.1. Magnetogram of the torque and the current in the windings of the electromagnet.

the camera shaft with the control of the electrolytic variable resistor. Simultaneously with the torque curve a record was made of the current through the electromagnet coils (proportional to the field strength) and of the so-called "null" curve characterizing the current dependence of the field corresponding to zero torque. The values of the field strength were recorded on the film in the form of ordinates. An example of such a magnetogram is shown in Fig.1.

The measurements were carried out at all eight angles corresponding to the peak values of the torque in the (100) plane.

The variation of the torque increment ΔM with the field strength at different temperatures is shown in Fig.2. As may be seen from the curves, the torque increment in the temperature range from 20 to 70° is only positive, in the interval from 80 to 180° it is at first negative and then positive and in the temperature range from 160° up it is only negative.

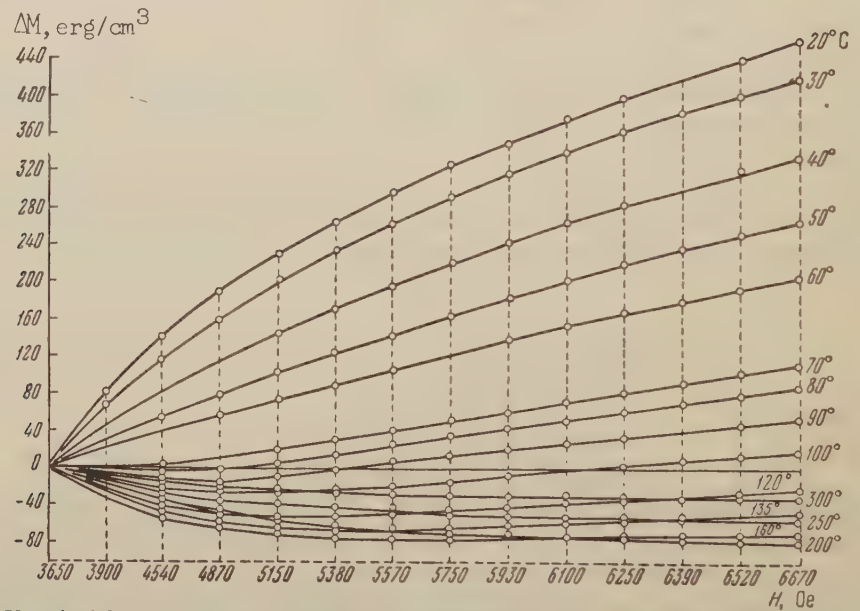

Fig.2. Variation of the torque increment as a function of the field strength at different temperatures.

In Fig.3 we show the variation of ΔK as a function of 1/H. From $1/H = 1900 \cdot 10^{-7}$ down, which corresponds to field values ranging up from 5260 oersted, the variation of ΔK as a function of 1/H proved to be linear at all temperatures in our experimental range.

From the function of dependence of the anisotropy constant on the field cited above, i.e., from Eq.(3), it follows that the slope of the $\Delta K = f(1/H)$ rectilinear plots is given by $\tan \varphi = K_\infty A$. The value of $\tan \varphi$ is readily found from experiment, while the value of K_∞ can easily be determined by extrapolation. The values of K_∞ and K are found to obey the relationship found by Briukhatov & Kirenskii[7] up to about 130-140°.

The variation of A with temperature is shown in Fig.4. As will be evident from the curve, in the temperature range from 20 to 135° is virtually

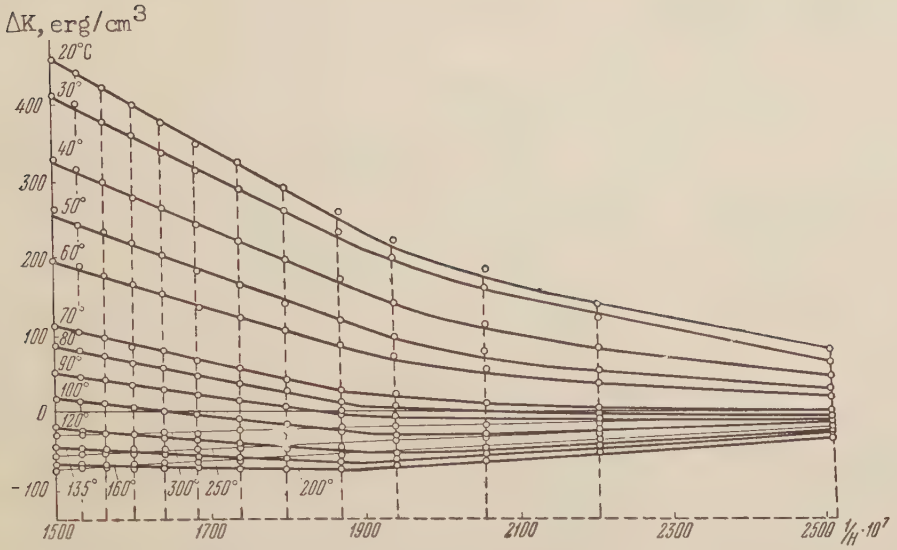

Fig.3. Variation of the change in the anisotropy constant with 1/H at different temperatures.

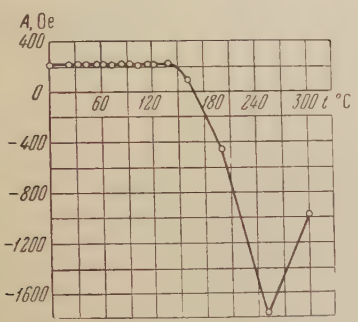

Fig.4. Temperature dependence of A.

independent of the temperature and equals approximately 208 oersted. With further increase in temperature A begins to decrease and changes sign at about 170°.

In carrying out the measurements we noted that the positions of the peak values of the torque did not come every 45° as expected but were separated alternately by 47° and 43°; the zero torques, however, repeated every 45° to within 5'. This alternation of the angles for the peak torques cannot be due to inaccurate orientation or geometric anisotropy of the sample, particularly since the maximum values of the torques at each position proved to be equal. It is reasonable to assume that this effect is due to the influence of the third anisotropy constant K_3. Taking into account the third anisotropy constant the magnitude of the torque in the (100) plane can be characterized by

$$M = \frac{K_1}{2} \sin 4\varphi + \frac{K_3}{8} \sin 4\varphi - \frac{K_3}{16} \sin 8\varphi,$$

where φ is the angle between the spontaneous magnetization vector and the tetragonal axis of the crystal.

Substituting the experimental values of the angles corresponding to the peak values of the torque in the above equation we obtain

$$K_3 = \frac{K_1}{3}.$$

It is interesting to note that the torque peaks alternate in the indicated order at all the investigated temperatures, which indicates that the temperature dependence of the constant K_3 is approximately the same as that of K_1. This may be regarded as definitely established for the temperature range from 20 to 160° within which the positions of the maxima were determined with a sufficiently high degree of accuracy. At higher temperatures the ac-

curacy in determining the positions of the peaks was lower owing to the fact that they became somewhat smeared out.

Galvanomagnetic effect

The galvanomagnetic effect was investigated by means of a sensitive bridge in conjunction with the cylindrical camera, which again enabled us to record the data automatically.

The measurements were carried out on a 0.1 mm diameter wire specimen of electrolytic nickel having a resistance of 4.75 ± 0.1 ohm at 0°. In order to eliminate possible temperature induced fluctuations of the resistivity, we used special compensators of fine copper wire. Inasmuch as the temperature coefficients of resistance of copper and nickel are different we had to utilize a number of compensators, each for a specific temperature interval. In each case the compensator was selected so that with fluctuations of up to 50 to 100° of the heater the light beam reflected from the galvanometer mirror remained virtually stationary.

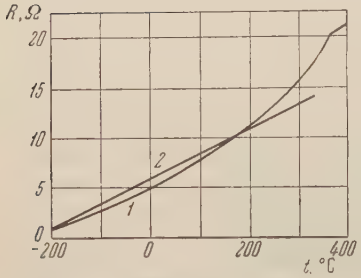

Fig.5. Temperature characteristics of the specimen and one of the compensators: 1) curve for specimen, 2) curve for compensator.

The operation of one of the compensators is characterized in Fig. 5. It will be seen from the figure

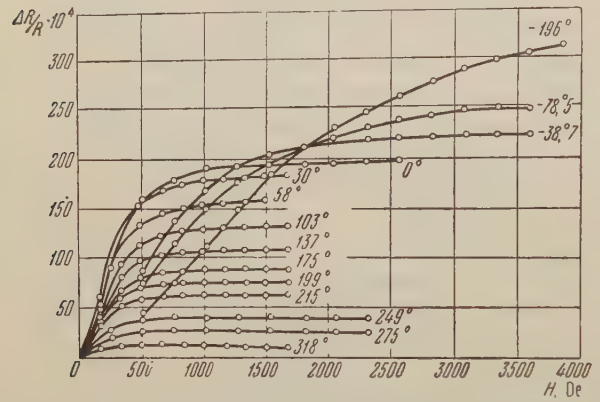

Fig.6. Isotherms of the galvanomagnetic effect in nickel in the temperature range from -196 to +318°.

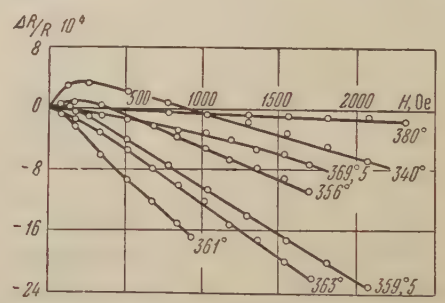

Fig.7. Same as Fig.6 but for the temperature interval from 340 to 380°.

that in the temperature range from -50 to +50° the temperature induced changes in the resistance of the compensator and specimen are equal inasmuch as their thermal characteristics are virtually parallel.

The fields of up to 400 oersted, uniform over the test length of 15 cm, were produced by means of a solenoid. The field strength was varied by means of a water rheostat; the rate of increase of the field was matched with the rate of rotation of the film drum. The heater together with the specimen was inserted into a Dewar flask which was mounted along the center line of the solenoid.

The observed dependence of the galvanomagnetic effect on the magnetic field strength at different temperatures is shown by the curves of Figs.6 & 7. It will be evident from the curves that the galvanomagnetic effect increases rapidly in weak fields corresponding to the process of displacement of domain walls; in going over to stronger fields where rotation of the walls predominates the rate of increase slows down and the effect tends to saturation. In

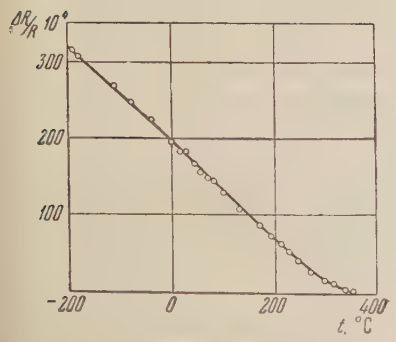

Fig.8. Temperature dependence of the galvanomagnetic effect in saturation fields.

fields exceeding technical saturation there is observed a decrease of the galvanomagnetic effect connected with the paraprocess. With increasing temperature the magnitude of the effect decreases and saturation is attained in weaker fields.

The temperature dependence of the galvanomagnetic effect in nickel in saturation fields is shown in Fig.8. As may be seen from the curve, in the temperature range from -196 to +300° the variation is linear, which is in agreement with the relation of Akulov[8] for the temperature dependence of even effects, a relation that has been substantiated in the work of D'iakov[9] and Vlasov[10]. Above 300° there is evident deviation from linearity.

In carrying out the investigation we paid particular attention to the influence of the method of demagnetization on the magnitude of the observed effect, inasmuch as according to Vlasov[10] the value of the magnetostriction depends appreciably on the method of demagnetization of the specimen before measurement. All the data cited above pertain to demagnetization by heating above the Curie point with subsequent cooling in magnetic shielding.

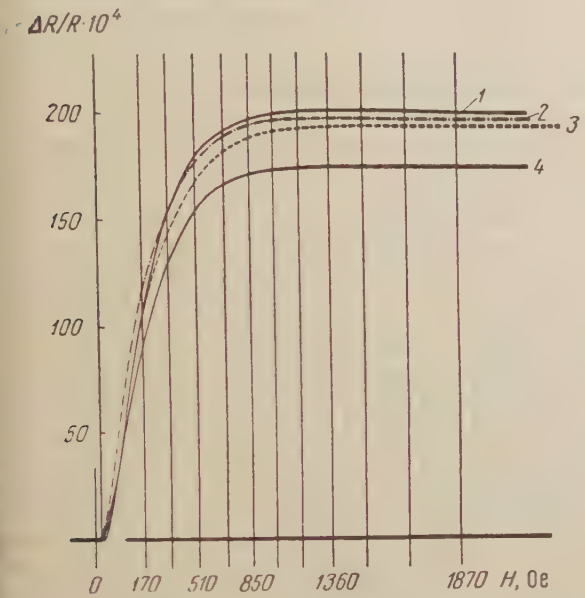

Fig.9. Magnetograms of the field dependence of the galvanomagnetic effect in nickel with different methods of demagnetization of the specimen (t = 0°): 1) heating above the Curie point with subsequent cooling in magnetic shielding, 2) heating above the Curie point and cooling without magnetic shielding, 3) dc reversals and diminishing 50 cycle ac, 4) dc reversals in the solenoid.

We investigated the influence of the method of demagnetization of the specimen on the magnitude of the galvanomagnetic effect in the temperature range from 0 to +210°. Fig.9 shows the magnetogram of the galvanomagnetic effect obtained for a nickel specimen at 0° with different methods of demagnetization. The maximum value of the effect is obtained with demagnetization by heating with subsequent cooling in magnetic shielding; a somewhat smaller value of the galvanomagnetic effect is obtained in the case of demagnetization by heating above the Curie point with subsequent cooling in the earth's magnetic field (terrestrial field normal to the axis of the specimen). A still weaker effect is obtained in the case of demagnetization by the method of reversals, using first dc and then gradually reduced 50 cycle current, through the solenoid. Lastly, the smallest effect is obtained in the case of demagnetization by reversals using dc only and gradually reducing the current to zero in the solenoid.

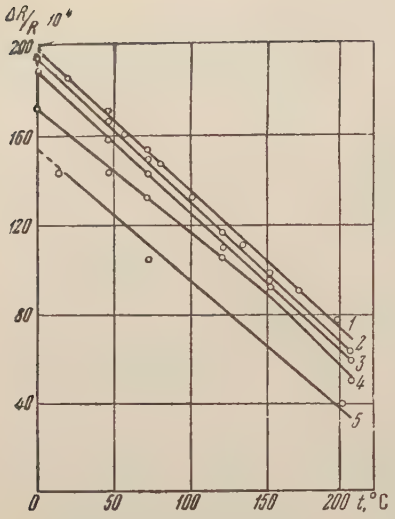

Fig.10. Temperature dependence of the galvanomagnetic effect with different methods of demagnetization: 1) heating and cooling in magnetic shielding, 2) heating and cooling without magnetic shielding, 3) dc reversals and diminishing 50 cycle ac, 4) dc reversals, 5) Potter's data (for comparison).

The temperature dependences of the galvanomagnetic effect in nickel in saturation fields with different methods of demagnetization are shown in Fig.10. It will be evident from our data that the magnitude of the effect is very sensitive to the method of demagnetization and that to obtain the true value it is expedient to carry out the magnetization by heating above the Curie point with subsequent cooling in magnetic shielding.

Krasnoyarsk State Pedagogical Institute

References

1. H.Schlechtweg, Ann.Phys., 27, 573 (1936).
2. L.P.Tarasov, Phys.Rev., 56, 1224 (1939).
3. R.M.Bozorth & H.T.Williams, Phys.Rev., 59, 827 (1941).
4. L.A.Shubina, Izv.AN SSSR, Ser.fiz., 11, 27 (1947).
5. L.V.Kirenskii, Izv.AN SSSR, Ser.fiz., 12, 121 (1948).
6. N.I.Vtiurin, Izv.AN SSSR, Ser.fiz., 16,690 (1952).
7. N.L.Briukhatov & L.V.Kirenskii, Zhur.eksp.i teor.fiz., 9, 198 (1938).
8. N.S.Akulov, Doklady AN SSSR, 15, No.8 (1937).
9. G.P.D'iakov, Izv.AN SSSR, Ser.fiz., 11, 667 (1947).
10. A.Ia.Vlasov, Izv.AN SSSR, Ser.fiz., 16, 718 (1952).

TEMPERATURE DEPENDENCE OF THE MAGNETIC SUSCEPTIBILITY OF NICKEL BASE ALLOYS

- D. I. Volkov & V. I. Chechernikov

1. There have been numerous investigations of the temperature dependence of the paramagnetic susceptibility of ferromagnetic metals.[1-3] Nevertheless, a number of important questions still remain unclarified. In theoretical treatments of the magnetic susceptibility of ferromagnetic metals of the transition group in the region of high temperatures ($T > \theta_f$, where θ_f is the ferromagnetic Curie point) it is usually assumed that the paramagnetism of these metals is due exclusively to the inner (3d) electrons; consequently, the possible role of the outer, conduction electrons is generally neglected. There is a question, however, to what extent it is allowable to disregard the influence of the s-electrons. In our opinion investigations of the temperature dependence of the paramagnetic susceptibility of ferromagnetic metals with nonferromagnetic elements of different valence should be of help in elucidating the role played by conduction electrons in the paramagnetism of such metals at temperatures above the Curie point.

Accordingly, in the present work we investigated the temperature dependence of the paramagnetic susceptibility of pure nickel and its alloys with different nonferromagnetic elements (Ni-Cu, Ni-Zn, Ni-Al, Ni-Si, Ni-Sn, Ni-Mo and Ni-Cr) in a wide temperature range extending from θ_f up to 1200°. Experiments show that in ferromagnetic transformation there is usually observed a so-called transition region. In our work we also studied the dependence of the magnetic susceptibility on the field intensity and the temperature in this transition region.

2. In our paramagnetic susceptibility measurements we utilized the Faraday-Sucksmith technique by means of which one can investigate susceptibility at rather high temperatures (up to 1200° in our experiments) under vacuum. As noted above, we investigated pure nickel and its alloys with Cu, Zn, Al, Si, Sn, Mo and Cr in wide range of concentrations. Despite the fact that the initial metals used in the preparation of the alloys were of relatively high purity, prior to the temperature dependence measurements in the paramagnetic region we checked for dependence of the susceptibility on the field. In no case was any noticeable field dependence of paramagnetic susceptibility detected.

3. The results of our experiments showed that the temperature dependence of the paramagnetic susceptibility χ of nickel alloys in the $T \gg \theta_f$ region cannot be described by the simple Curie-Weiss law

$$\chi = \frac{C}{T - \theta_p},$$

where C is the Curie-Weiss constant and θ_p is the paramagnetic Curie point.

As may be seen from Figs.1 & 2, for Ni-Cu and Ni-Mo alloys the dependence of the reciprocal of the susceptibility ($1/\chi$) on the temperature is described not by a straight line, as would follow from simple Curie-Weiss law, but by a curve with gradually decreasing slope ("downward concavity"). Similar results were obtained for all the other nickel alloys investigated. The deviation from linearity in the variation of $1/\chi$ vs T is most evident in the region of high temperatures, i.e., $T \gg \theta_p$. It is interesting to note that the deviation or curvature of the $1/\chi = f(T)$ curve is greater for alloys in which the nonferromagnetic component has a higher valence.

Hence it may be asserted that the Curie-Weiss law in its form is not applicable to the investigated alloys.

Bloch[4] and other investigators have attempted to describe the experimentally observed regularities by introducing a second constant. It will be

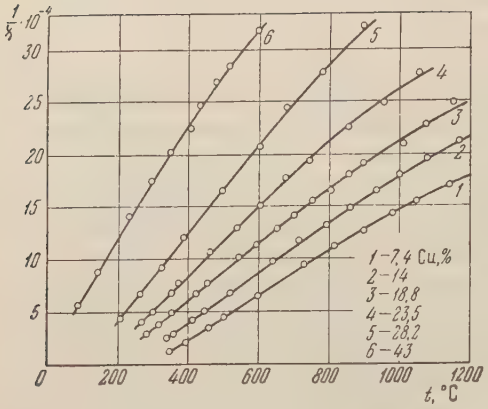

Fig.1. Variation with temperature of the reciprocal of the susceptibility of Ni-Cu alloys with different Cu concentrations (in atomic percent).

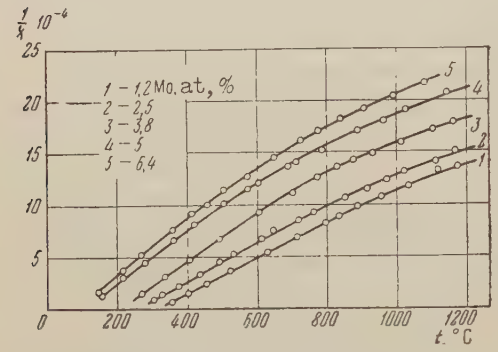

Fig.2. Same as Fig.1, but for Ni-Mo alloys.

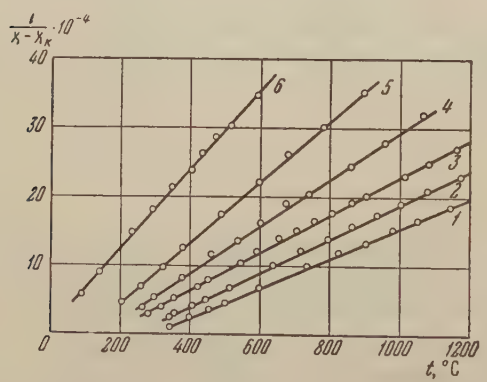

Fig.3. Variation of $\frac{1}{\chi - \chi_k}$ with temperature for Ni-Cu alloys. Numeration of curves same as in Fig.1.

evident from Figs.1 & 2, however, that the experimental curves cannot be approximated by two straight lines. Néel[5], analyzing the experimental data of Manders[1], showed that the paramagnetic susceptibility of ferromagnetic metals in the region of high temperatures ($T \gg \theta_f$) can be described by

$$\chi = \chi_k + \chi_T, \qquad (1)$$

where χ_T is a susceptibility component varying with the temperature according to the Curie-Weiss law and χ_k is a temperature independent component.

At temperatures in the vicinity of the paramagnetic Curie point χ_k is small compared with χ_T so that in this temperature region the Curie-Weiss law is approximately valid. In the region of high temperatures ($T \gg \theta_p$), however, the susceptibility χ_k becomes comparable to χ_T owing to the decrease in the value of χ_T. This circumstance allows of determining the temperature independent component χ_k. We determined the value of χ_k in this manner for all our alloys and, using Eq.(1) to calculate $1/(\chi - \chi_k)$, plotted this quantity against the temperature. By way of illustration we show the variation of $1/(\chi - \chi_k)$ vs T for the Ni-Cu and Ni-Mo alloys in Figs.3 & 4. As will be seen from the figures, in the temperature range from θ_p to about 1200° the variation is linear. It is clear therefore that the paramagnetic susceptibility of ferromagnetic alloys in the region of high temperatures is described not by the ordinary Curie-Weiss law but by the more general law (1) or

$$\chi = \chi_k + \frac{C}{T - \theta_p}.$$

Earlier investigations of the paramagnetic susceptibility of ferromagnetic alloys were concerned primarily with the question of the dependence of the Curie-Weiss constant and the magnetic moment on the composition of the alloys. In our work it was naturally of interest to establish the character of the dependence of χ_k on the content of the nonferromagnetic element in the alloy. This dependence according to the results of our measurements is shown in Fig.5. The values of χ_k for Ni-Zn alloys were calculated using the data of Wheeler[6]. It will be evident that the value of χ_k is strongly dependent on the composition of the alloy; except for Ni-Cu alloys, χ_k increases with increasing content of the nonferromagnetic component and, what is particularly

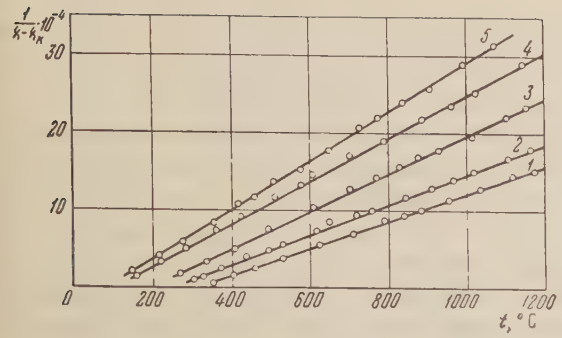

Fig.4. Variation of $\frac{1}{\chi-\chi_k}$ with temperature for Ni-Mo alloys. Numeration of curves same as in Fig.2.

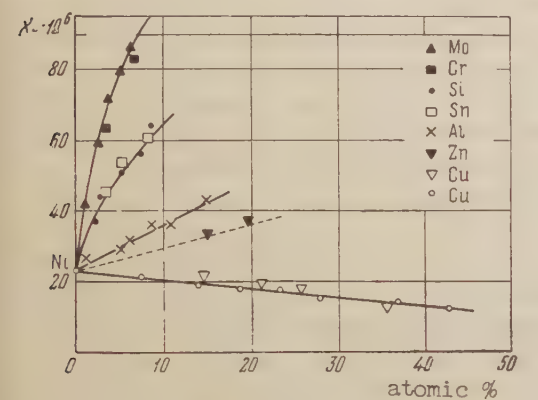

Fig.5. Variation of the temperature independent susceptibility component with the content of the nonferromagnetic element in the binary nickel alloy. The points for Ni-Zn were calculated from the data of Wheeler[6].

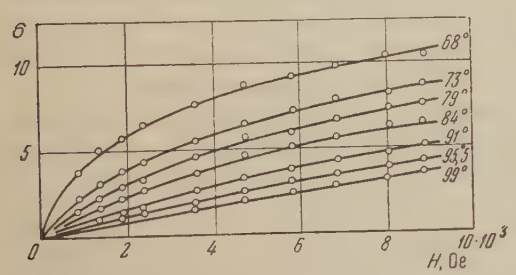

Fig.6. Variation of the magnetization with the magnetic field intensity for Ni-Mo alloy containing 5% Mo at different temperatures. Curves - calculated according to Eq.(2); points - experimental values.

important, with the valence number of the nonferromagnetic element. As regards increasing magnitude of χ_k, nickel alloys may be arranged in the following sequence:

Ni-Cu — Ni-Zn — Ni-Al — Ni-Si and Ni-Sn — Ni-Mo and Ni-Cr.

With decreasing concentration of the nonferromagnetic component, the value of χ_k approaches the value observed for pure nickel (atomic susceptibility $(\chi_k)_{Ni} = 23.6\cdot10^{-6}$). It should also be noted that the Curie-Weiss constant C and the susceptibility χ_k vary independently as functions of the concentration and valence: while C decreases with increasing concentration and the valence of the nonferromagnetic component, χ_k, on the contrary, increases. The observed regularities indicate that the presence of the χ_k term in the law of expression (1) is due to paramagnetism of the s-electron "gas", i.e., Pauli type paramagnetism. Hence in further development of the theory of paramagnetism of ferromagnetic metals and alloys it is essential to take into account not only the role of d-electrons but also that of s-electrons and their interactions.

Recently Vlasov & Vonsovskii[7] published a theoretical study in which this problem is examined on the basis of the model of interacting outer (s) and inner (d) electrons. The authors show that taking into account the influence of the outer conduction electrons on the magnitude and temperature dependence of the paramagnetic susceptibility of metals of the transitions groups leads to the additive law (1), which closely describes the regularities observed experimentally. According to this theory, the value of χ_k does not depend on the temperature and in the absence of s-d interaction goes over into the usual conduction electron susceptibility. Taking into account the interaction between s- and d-electrons also leads to variation of the constant C, whose magnitude proves to be dependent not only on the number of magnetic moment carriers but also on the s-d electron interaction energy. The existence of this interaction, as the calculations of

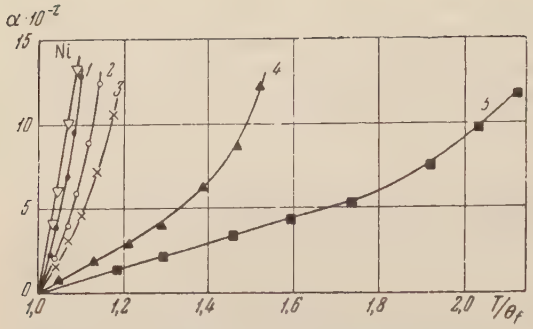

Fig.7. Variation of the coefficient α in Eq.(2) as a function of the ratio T/θ_f for Ni-Mo alloys with different Mo concentrations. Numeration of curves same as in Fig.2.

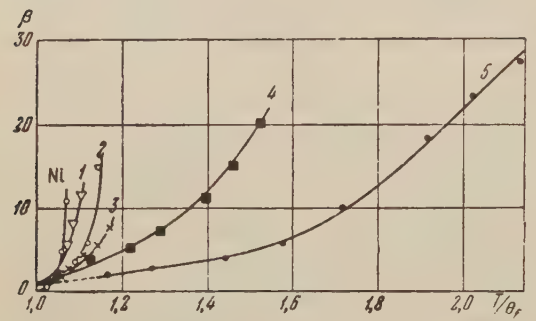

Fig.8. Same as Fig.7 but for the coefficient β.

Vonsovskii and Vlasov showed, is also evinced in changes in the Curie point θ. In the absence of interaction, the constant C agrees with the usual value of the Curie-Weiss constant and θ is equal to θ_d associated with the exchange interaction of the d-electrons. The deductions following from the theory developed by Vlasov & Vonsovskii are in qualitative agreement with our experimental results.

Investigation of the paramagnetic susceptibility at temperature close to to the Curie point showed that in this temperature range ($T \geqslant \theta_f$) the susceptibility is manifestly dependent on the magnetic field strength. The width of the temperature interval wherein this field dependence of the susceptibility obtains (the transition region) is as a rule greater for higher concentrations of the nonferromagnetic component in the alloy; for example, for Ni-Cu alloys with 23.5% Cu this temperature interval equals 170°.

The variation of the magnetization σ with the field H in the transition region, according to the results of our measurements, is satisfactorily described by a relationship of the form

$$H = \alpha\sigma + \beta\sigma^3 + \gamma\sigma^5, \qquad (2)$$

where α, β and γ are coefficients independent of both σ and H. In Fig.6 we show the isothermal magnetization curves for the Ni-Mo alloys containing 5% Mo calculated according to Eq.(2) together with the experimental data obtained for the same alloy. The values of the coefficients α, β and γ were determined from the experimental data and proved to be strongly dependent on the temperature and composition of the alloys. The dependences of α and β on T/θ_f for Ni-Mo alloys are shown in Figs.7 & 8. Analogous regularities were obtained for the other investigated alloys. Both α and β decrease in magnitude with increasing concentration of the nonferromagnetic component. In the temperature region close to θ_f the coefficient α varies linearly, going to zero at $T = \theta_f$.

Department of Physics,
Moscow State University

References

1. G.Manders, Ann.de Phys., 5, 167 (1936).
2. W.Sucksmith & R.R.Pearce, Proc.Roy.Soc., A189, 167 (1938).
3. M.Fallot, J.Phys.et Rad., 5, 153 (1944).
4. O.Bloch, Arch.Sci.phys.nat., 33, 293 (1912).
5. L.Néel, Ann.de Phys. 5, 232 (1936).
6. M.A.Wheeler, Phys.Rev., 56, 1137 (1932).
7. K.B.Vlasov & S.V.Vonsovskii, FMM (Physics of Metals and Metallography), 2, 403 (1956).

CORRELATION BETWEEN THE ELECTRIC AND MAGNETIC PROPERTIES OF CHROMIUM SULFIDES

- N.P.Grazhdankina & I.G.Fakidov

A characteristic of the magnetic properties of chromium sulfides, as of all ferromagnetic compounds, is the simultaneous existence in these substances of ferromagnetism and antiferromagnetism. The presence of exchange spin coupling between the magnetic moments leading to antiferromagnetism in these compounds cannot but affect their electric properties, just as the electric properties of ferromagnets are influenced by the interaction between outer conduction electrons and inner electrons that play an important role in ferromagnetism. Thus there can be no doubt that for a clearer understanding of the physical nature of such compounds one must study not only their magnetic but also their electric properties.

Yet, it must be admitted that the electric properties of ferromagnetic materials have so far been inadequately studied. The available scanty data are incidental in character; they do not stem from systematic investigations undertaken specifically for establishing the correlation between the magnetic and electric properties of these materials. For example, whereas the magnetic properties of such antiferromagnetic compounds as FeS, CrS and MnS have been investigated in considerable detail[1-8], the electric properties of these compounds have not been thoroughly studied by anyone.

We chose the sulfides of chromium for our investigation for the following reasons. Alteration of the chemical composition of the antiferromagnetic compound CrS by the addition of sulfur leads to the appearance of ferromagnetism in the chromium-sulfur system in a narrow range of sulfur concentrations, specifically 50-54 atomic percent (compositions close to $CrS_{1.17}$), which makes it feasible to confine the experimentation to a relatively limited number of compounds. The substantial dependence of the magnetic properties of compounds close to $CrS_{1.17}$ on such factors as annealing and quenching makes it possible to obtain samples possessing ferromagnetic (annealed samples) or antiferromagnetic properties (quenched samples) and this allows of investigating the conditions resulting in one or the other state on samples having the same chemical composition. In addition, investigation of the electric properties of $CrS_{1.17}$ makes it possible to define the temperature boundaries of the existence of the ferromagnetic state inasmuch as in contrast to ordinary ferromagnets this compound has two magnetic transition temperatures.

With the above considerations in view we undertook a comprehensive investigation of the electric properties of chromium sulfides; specifically, we investigated

1) the electric conductivity of chromium sulfides of different composition,

2) the temperature dependence of the conductivity in the range from 1.8 to 1000°K,

3) the Hall effect and the variation in resistance in a magnetic field, and

4) the thermal emf of chromium sulfides of different chemical composition.

Samples and procedure

For purposes of the investigation, we prepared chromium sulfides of different chemical compositions (50 to 59.7 atomic % S). In view of the strong dependence of the electric properties of chromium sulfide on impurities, we paid particular attention to obtaining chemically pure chromium and sulfur for the synthesis of our samples. The samples were synthesized by heating the appropriate mixture of chromium and sulfur to 900° in evacuated quartz

tubes. The chemically pure chromium was obtained electrolytically; an indication of the degree of purity of the refined chromium is given by the values of the magnetic susceptibility ($\chi = 3.6 \cdot 10^{-6}$ at 18°C), the resistivity ($\rho = 2.5 \cdot 10^{-5}$ ohm-cm at 0°C) and the relative change with temperature of the resistance in the region of low temperatures ($R_T/R_0 = 0.129$, where R_T is the resistance at 77°K and R_0 is the resistance at 0°C). The reagent grade sulfur was further purified by recrystallization in benzene followed by vacuum distillation. Spectroscopic analysis showed that the purified sulfur contained only traces of arsenic, copper and nickel. Thus the analysis of the sulfur and the comparison of the measured electric properties of the chromium with the data in the literature showed that our initial materials were of sufficiently high purity.

The samples for the electric measurements were prepared by compacting the synthesized chromium sulfide powder into tablets and sintering these at 1100°. The homogeneity of the samples was checked by examining microsections, measuring the distribution of potential over the length of the sample and by determining the sign of the thermal emf over different sections of the sample.

The resistivity and its temperature dependence, the Hall effect and the change in resistance in the magnetic field were measured by the potentiometric procedure using a Diesselhorsat compensator and a galvanometer with a sensitivity of $3 \cdot 10^{-8}$ v per 1 mm scale displacement. Measurements of the galvanomagnetic effect were carried out both under adiabatic and isothermal conditions; the highest magnetic field value used in the experiments was 22,000 oersted. The thermal emf of the chromium sulfides was measured relative to copper. The temperature difference between the hot and cold junctions was found from absolute measurements of the temperature of each junction separately.

The fact that chromium sulfides are subject to strong dissociation at high temperatures made it necessary to develop a special technique for investigating their electric properties. In order to obviate the possibility of decomposition at high temperatures the samples were mounted in special protective envelopes made of Pyrex glass (Fig.1). The mounting was arranged so that the free space above the specimen in the evacuated and sealed off ampoule would be minimal. Only by this procedure was it possible to obtain fully reproducible results.

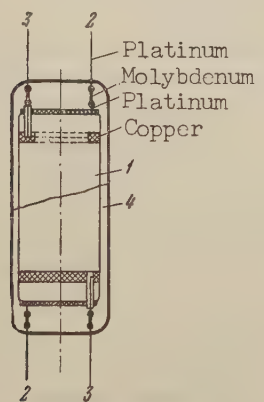

Fig.1. Ampoule used for investigating the electric properties of the chromium sulfide samples at high temperatures: 1) sample, 2) current electrodes, 3) potential electrodes, 4) protective envelope of Pyrex glass.

Results and discussion

1. As regards absolute resistivity (10^{-4}–10^{-2} ohm-cm) the investigated chromium sulfides are intermediate between metals and semiconductors. The resistivity depends greatly on the chemical composition: beginning with 50 atomic % S the resistivity decreases, goes through a minimum at 54 atomic % S and then with further increase in the sulfur content begins to increase.[9] It is worth noting that the minimal resistivity was observed in the compound exhibiting ferromagnetic properties (Fig.2).

2. Our measurements showed that chromium sulfides in the S content range from 50 to 54 atomic % are characterized by "spontaneous polarization" in the temperature range from 1.8 to 210-300°K, i.e., have a constant number of current carriers whose

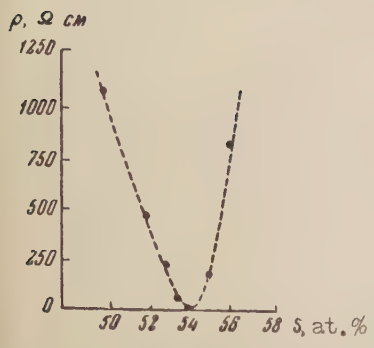

Fig.2. Variation of the resistivity ρ of chromium sulfides with the sulfur content.

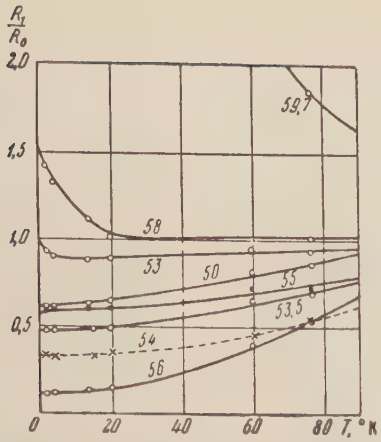

Fig.3. Variation of the relative change in resistance with temperature. The figures at the curves indicate the sulfur content in atomic percent.

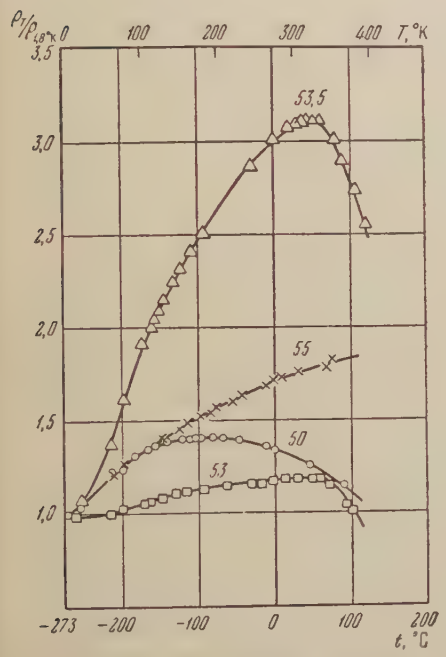

Fig.4. Temperature dependence of the resistivity of chromium sulfides. The figures at the curves indicate the sulfur content in atomic percent.

energy lies in the conduction band (Fig.3). The decrease in conductivity with increasing temperature, as in metals, is due to changes in the mobility of the conduction electrons. As the temperature is increased above 210-300°K, the current carrier concentration begins to increase exponentially, as a result of which the conductivity at high temperatures is determined, as in typical semiconductors, not only by changes in the conduction electron mobility but primarily by increase in the number of electrons in the conduction band owing to thermal ionization (Fig.4). On the basis of their temperature dependence, the investigated materials may be classed as semi-metals. From the standpoint of the character of the temperature dependence of the conductivity, the region of metallic conductivity of chromium sulfide may be divided into two intervals: an interval of low temperatures (1.8 to 80°K) in which the temperature dependence of the resistivity is characterized by $\rho = AT + BT^2$, and a higher temperature interval (80 to 300°K) in which $\rho = AT^b$, where b = = 0.2-0.5 (here A and B are constant coefficients).

3. Our results definitely demonstrate the existence of intrinsic semiconductor conductivity in the investigated materials at temperatures in the range from 420 to 620°K. Investigations in the region of intrinsic conductivity showed that the semi-metallic state of the material can exist with an electron energy band structure wherein the energy gap between the normal valence band and the conduction band is of the order of 1 ev. As the chemical composition is altered (the S content increased) the forbidden energy band gradually narrows from 0.9 ev for CrS to complete overlapping of the bands in $CrS_{1.17}$, which is ferromagnetic (Fig. 5). Our investigation of the electric properties of chromium sulfides substantiates the existence in these compounds of phases of variable composition, originally detected by x-ray diffraction studies. With change in the comcentration of the components there occurs a continuous change in the character of the chemical bonds and the electron spectrum, which can be

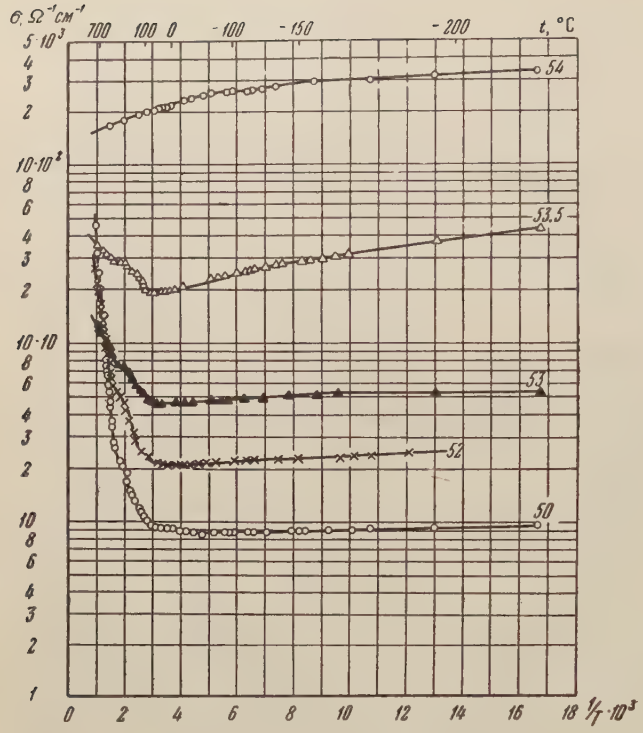

Fig.5. Temperature dependence of the resistivity of chromium sulfides in the region of high temperatures. The figures at the curves indicate the S content in atomic percent.

explained by changes in the number of atoms in the unit cell and the lattice parameters.[10]

4. On the basis of our comprehensive investigation of the conductivity, the Hall effect, the variation of the resistance in the magnetic field and the thermal emf, it may be asserted that chromium sulfides are materials in which the current carrier mobility is extremely low (of the order of 1 cm^2 v^{-1} sec^{-1}) while the concentration of current carriers is large and equal to $5 \cdot 10^{19}$-10^{22} cm^{-3}. The degeneration temperature at such high concentrations is of the order of 600°K; the electron energy in this case corresponds to the highest occupied electron level and does not noticeably change with temperature. At such high concentrations of ionized impurities, scattering from them predominates over scattering from thermal vibrations of the lattice, as a result of which the electron mobility is only weakly dependent on the temperature.

5. Investigation of the electric properties of ferromagnetic and antiferromagnetic compounds of chromium with sulfur enabled us to establish that the appearance of ferromagnetism in this system is connected with the metallic state of the material. We measured the conductivity and the temperature dependence of the conductivity of two specimens of chromium sulfide having the same chemical composition, namely, $CrS_{1.17}$ (54 atomic % S) but subjected to different heat treatments prior to measurement. One of the specimens in the process of preparation of the compound was quenched from 900°, while the other was annealed at this temperature, i.e., after synthesis was held for a prolonged period at 900° and slowly cooled with the furnace. As a result there were obtained samples with different properties: the annealed sample had ferromagnetic properties, while the quenched sample proved to be nonferromagnetic. Our measurements showed that the ferromagnetic sample had a resistivity ($\rho = 4 \cdot 10^{-4}$ ohm-cm) almost 2 orders of magnitude lower than the nonferromagnetic one ($\rho = 1 \cdot 10^{-2}$ ohm-cm). Measurements of the resistance at different temperatures indicated that the specimens differed from each other not only as regards the value of the resistivity but also as regards the character of its temperature dependence (Figs.6 & 7).

Investigation of the temperature dependence of ρ of the ferromagnetic $CrS_{1.17}$ made it possible to establish the presence of two magnetic transition temperatures, i.e., 159 and 303°K, corresponding to temperatures at which there is a break in the $\rho = f(T)$ and $(1/\rho)(d\rho/dT) = f(T)$ curves (Fig.6) as well as in the curve characterizing the temperature dependence of the magnetic susceptibility. On the basis of the available experimental data on the

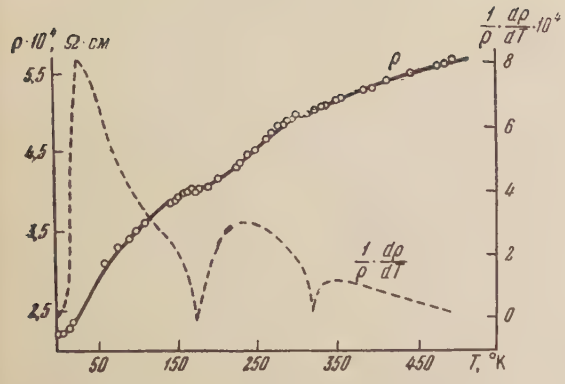

Fig.6. Temperature dependence of the resistivity of ferromagnetic chromium sulfide ($CrS_{1.17}$).

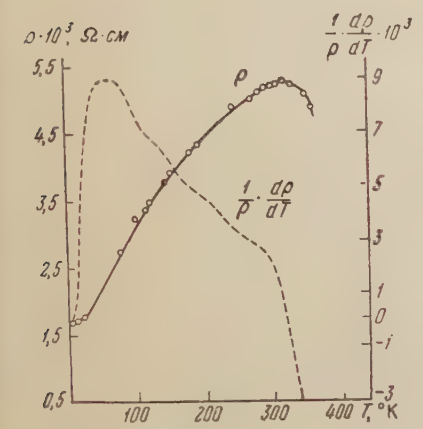

Fig.7. Same as Fig.6 but for nonferromagnetic chromium sulfide ($CrS_{1.17}$).

temperature dependences of the magnetic susceptibility, conductivity and specific heat of ferromagnetic $CrS_{1.17}$ it may be concluded that 303°K is the ferromagnetic transformation temperature at which a second order phase transition occurs (as in all other ferromagnetic substances). The character of the low temperature magnetic transformation is still unclear owing to the lack of experimental data on the physical properties of the compound and the changes they undergo in the vicinity of this magnetic transformation temperature.

It will be evident from comparison of the curves in Figs.6 & 7 that the temperature dependence of the resistivity of the ferromagnetic sulfide differs from the dependence observed for the nonferromagnetic material. The important point here is that the nonferromagnetic chromium sulfide has a temperature dependence of the resistivity characteristic of semi-metals (Fig.7), while the temperature dependence of the ferromagnetic sulfide is that typical of metals. This difference between the $\rho = f(T)$ curves is evidence of the different character of the electronic energy spectra of the ferromagnetic and antiferromagnetic samples. The energy spectrum of the ferromagnetic compound is in this case characterized by complete overlapping of the energy bands, whereas the band structure of the antiferromagnetic compound having the same chemical composition is characterized by a forbidden band some 0.045 ev in width. It must be noted that these changes are not connected with any noticeable changes in the structure of the compound inasmuch as no difference was observed between the x-ray diffraction patterns obtained from the ferromagnetic and nonferromagnetic samples. The hole ordering observed by Bertaut[11] in iron sulfide indicates, however, that such ordering may also obtain in chromium sulfide. The possible existence of such superstructure in chromium sulfide is supported by the established relation between the electric and magnetic properties and the effects of quenching and annealing producing such structural changes.

It should be noted that in chromium sulfides, as in all antiferromagnetic compounds, the character of the exchange interaction between the electron spins of different ions is indirect, i.e., the ferromagnetic and antiferromagnetic states of these compounds are determined by the form of interaction between magnetoactive ions in which a predominant role is played by magnetoneutral ions. In the case of chromium sulfides the interaction between the chromium ions occurs with the active participation of the sulfur ions inasmuch as electron transitions between the chromium and sulfur ions are involved in the interaction. It would seem to us that the above-mentioned ordering of the holes cannot exert a substantial influence on the character of the indirect exchange whether the state of the given compounds is ferromagnetic or antimagnetic.

Our experimental data substantiate the conclusion of Heikes[12], drawn on the basis of general theoretical concepts, regarding the relation between ferromagnetism and the metallic state in compounds of the transition metals with elements of groups V and VI B. It should be added that the antiferromagnetism of these compounds may be connected not only with the semiconductor state but also with the semi-metallic state of the material.

Institute of the Physics of Metals,
Ural Branch of the USSR Academy of Sciences

References

1. H.Haraldsen, ZS.Anorg.Allg.Chem.,231, 78 (1937).
2. R.Benoit, C.R., 234, 2174 (1952).
3. R.Pauthenet, C.R., 234, 2261 (1952).
4. L.Néel, Rev.Modern Phys., 25, 58 (1953).
5. H.Haraldsen, A.Neuber, ZS.Anorg.Allg.Chem., 234, 337 (1937).
6. R.Benoit, J.Chim. phys., 52, 201 (1955).
7. K.Josida, Physica, 17, 794 (1951).
8. A.Serré, J.Phys. et Rad., 8, 146 (1947).
9. I.G.Fakidov & N.P.Grazhdankina, Doklady AN SSSR, 63, 27 (1948).
10. N.P.Grazhdankina & I.G.Fakidov, Doklady AN SSSR, 102, 957 (1955).
11. F.Bertaut, C.R., 234, 1295 (1952).
12. R.Heikes, Phys.Rev., 99, 1232 (1955).

LOW-TEMPERATURE RESISTIVITY OF NICKEL ALLOYS AND ITS VARIATION IN MAGNETIC FIELDS

- E.I.Kondorskii, O.S.Galkina & L.A.Chernikova

Introduction

This report will be concerned with the results of an investigation of the resistivity and the influence of magnetic fields on the resistivity of nickel and alloys of nickel with copper, chromium and manganese in the temperature intervals from 2 to 4.2° and from 14 to 20.4°K. Investigation of the resistivity and its variation in a magnetic field in the case of ferromagnetic metals and alloys allows of checking the extant theories of the anomalous variation of the electric conductivity of ferromagnets and yields the experimental data needed for further development of our concepts in this field.

For purposes of comparison of theory with experiment, it is particularly important to obtain experimental data in the region of low (hydrogen and helium) temperatures inasmuch as at present theory gives quantitative results only in this temperature region.

Actually there is little pertinent data available for ferromagnetic metals and alloys. Meissner & Voigt[1] investigated the variation of the resistance of nickel at liquid hydrogen temperature and at 4.2°K. Van Itterbeck et al[2] studied the variation of the electric resistance of very thin films of nickel at temperatures from 1.69 to 4.2°K and in the hydrogen range. They found that the resistance increases with decreasing temperature. Smit[3] investigated the resistance of nickel and Ni_3Fe and Ni-Cu alloys in a magnetic field in the temperature range from room temperature to that of liquid hydrogen. In their report Kondorskii & Ozhigov[4] give the results of investigation of the resistance of nickel-iron alloys and the variation thereof in the region of hydrogen temperatures and at the temperature of liquid nitrogen. Masumoto & Shirakava[5] and Shirakava alone[6] studied the magnetic field dependence of the resistivity of alloys of nickel with copper, cobalt and iron in the region of nitrogen, room and higher temperatures. The cited works contain no data on the temperature dependence of the resistivity of pure nickel in the region of helium temperatures (Meissner & Voigt give data only for the 4.2°K point) or data on the electric resistivity of nickel alloys in the region of hydrogen and helium temperatures (except for nickel-iron alloys in the region of hydrogen temperatures). Aside from the sources mentioned, there are virtually no data in the literature on the variation of the resistivity in a magnetic field for nickel and its alloys at low temperatures.

The purpose of the present work was to investigate the temperature dependence of the resistivity of nickel and its alloys in the region of hydrogen and helium temperatures.

1. Procedure and samples

The resistance was measured by the conventional potentiometer procedure. We used a PPTN-1 type potentiometer fabricated by the Krasnodarsk plant by means of which one can measure resistances with an accuracy of 1 in 10,000. The magnetic field was produced by means of a solenoid which yielded a field of 3000 oersted with a current of 20 amp. The temperature was determined from the indications of a pressure guage measuring the vapor pressure in the Dewar. The measurements were carried out in the temperature intervals from 2 to 4.2° and 14 to 20.4°K.

The samples in the form of wires 0.2-0.1 mm in diameter were prepared of alloys supplied by the TsNIIChM (Central Scientific Research Institute of

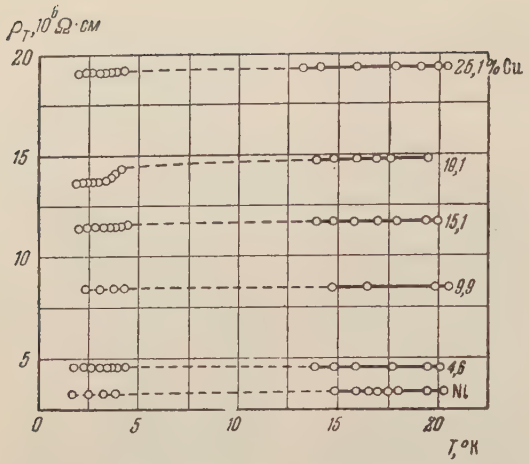

Fig.1. Temperature dependences of the resistivity ρ of nickel and its alloys with copper.

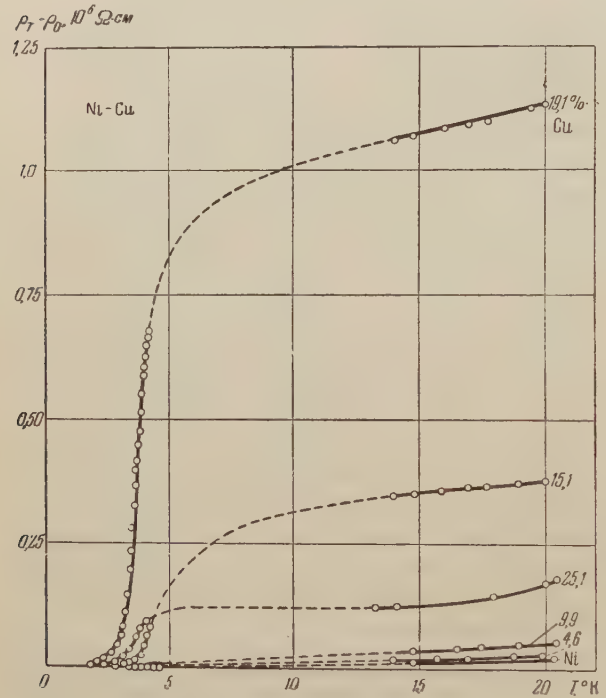

Fig.2. Temperature dependences of $\rho_T - \rho_0$ (ρ_0 is the residual resistivity) for nickel and nickel-copper alloys.

Ferrous Metallurgy). The wires were formed by cold drawing. All samples were subjected to annealing in an atmosphere of neutral gas at 900° for 1-12 hours followed by slow cooling; some of the samples were quenched from 900° in air, while the Ni_3Mn samples were quenched from 900° in water. According to chemical analysis data the Ni-Cu alloy samples had the following compositions: 1) Ni - 99.9%, 2) Ni - 95.4%, Cu - 4.6%, 3) Ni - 90.1%, Cu - 9.9%, 4) Ni - 84.9%, Cu - 15.1%, 5) Ni - 80.9%, Cu - 19.1%, and 6) Ni - 74.9%, Cu - 25.1%.

2. Resistivity of nickel and nickel-copper alloys

The curves characterizing the observed variation of the resistivity of our nickel and nickel-copper alloy samples with temperature are shown in Figs.1 & 2. "Steps" are noticeable in some of the curves in the 3 to 4°K temperature interval. The most substantial change in the resistance in this temperature region was observed in the case of the alloy with 19.1% copper which also exhibited the maximum change in resistivity in a magnetic field (see below).

It is probable that the "steps" in the resistivity curves in the 3 to 4°K interval are connected with the presence in the alloys of traces of superconducting substances, not detected in the chemical and spectral analyses. The residual resistivity of the nickel used in preparing the alloys was $1.54 \cdot 10^{-6}$ ohm-cm, i.e., 4.4 times higher than that of the samples described by Meissner & Voigt[1]. Only further investigations will show whether such "steps" appear in the resistivity curves of samples comprised of higher purity components. It is possible, however, that these "steps" are connected with the appearance of superconductivity in some parts of the ferromagnetic alloys. Recently Ginzburg[7] indicated that superconductivity may obtain in ferromagnets under certain conditions.

In describing the temperature dependence of the resistivity of nickel and its alloys in the region of helium and hydrogen temperatures it is convenient to deduct the step from the total value of the resistance, i.e., to

consider the quantity $\bar{\rho}_T = \rho_T - \Delta\rho$, where $\Delta\rho$ = the "step". In determining ρ_T one should obviously assume that $\Delta\rho = 0$ at $T < T_c$ and $\Delta\rho = \text{const} > 0$ at $T > T_c$, where T_c are the temperatures corresponding to the interval in which the "step" is observed. The resistivity of ferromagnetic metals in the region of low temperatures is described by the formula of Vonsovskii & Turov[8]:

$$\rho_T - \rho_0 = \alpha_1 T + \alpha_2 T^2 \qquad (1)$$

where ρ_0 is the residual resistivity. The values of the constants α_1 and α_2 deduced from our data* if one sets $\rho_T = \bar{\rho}_T$ are listed in the accompanying table. They cannot as yet be deduced from theory.

The temperature dependence of $\bar{\rho}_T$ can also be described by the empirical formula

$$\rho_T = \rho_0 + \alpha T^n \qquad (2)$$

Values of the residual resistivity and the constants entering Eqs. (1) and (2) for Ni-Cu alloys

Cu, %	$\rho_0 \cdot 10^6$	$\alpha_1 \cdot 10^{10}$	$\alpha_2 \cdot 10^{10}$	n
0	1,54	1	0,4	1,51
4,6	4,57	17,5	0,4	1,49
9,9	8,47	30	0,4	1,48
15,1	11,44	40	0,45	1,47
19,1	13,70	49	0,6	1,51

The corresponding values of n and ρ_0 are also listed in the accompanying table. For most of the investigated alloys the value of n is close to 3/2. The variation of the residual resistivity as a function of the Cu concentration in the alloys is plotted in Fig. 3. It will be seen that the variation is linear.

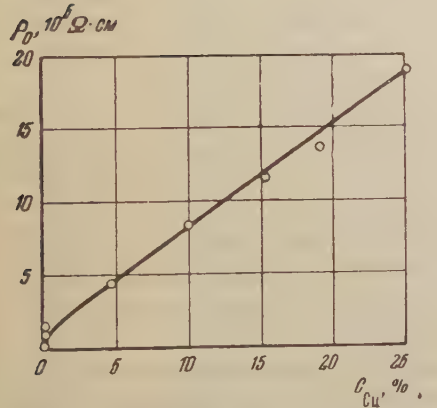

Fig. 3. Variation of the residual resistivity of Ni-Cu alloys with the Cu concentration.

In Fig. 4 we give the curves characterizing the temperature dependence of the resistivity of alloys with 15.1% and 25.1% copper in the demagnetized state in the absence of a field, with residual magnetization in the absence of a field and in different magnetic fields. In strong fields the magnitude of the "step" decreases and at H = 2000 oersted the step virtually vanishes. The smooth character of the resistivity curve in strong fields indicates that the observed "steps" are not due to magnetic texture of the samples in the initial state (with no field).**

---

*These constants were determined graphically: we plotted the variation of $(\rho_{20.4^\circ} - \rho_0)/20.4^\circ - T)$ as a function of T for the hydrogen temperature interval and drew a straight line through the points to the intersection with the y-axis.

**It might be assumed that the "steps" in the resistivity curves are due to the fact that the initial distribution of domains in the sample is not homogeneous, for example, that the domains are oriented in a plane perpendicular to the axis of the wire. Then if we assume that the absolute magnitude of the change in longitudinal resistance in a magnetic field with decreasing temperature increases sharply in a narrow temperature interval, we should expect to observe a decrease in resistance in this temperature interval in the case of specimens with the indicated nonhomogeneous domain distribution. In this case, however, in a strong field orienting the domains along the wire axis there should be observed an inverse "step" in the temperature dependence of the resistivity curves.

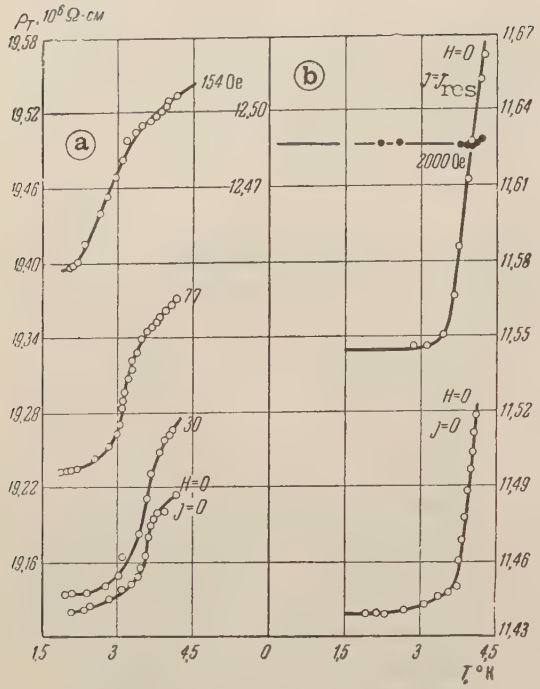

Fig.4. Temperature dependences of the resistivity of Ni-Cu alloys with 25.1% Cu (a) and 15.1% Cu (b) in the demagnetized state with no field (J = 0 and H = 0), in the state of residual magnetization with no field (J = J_{res} and H = 0) and in different fields.

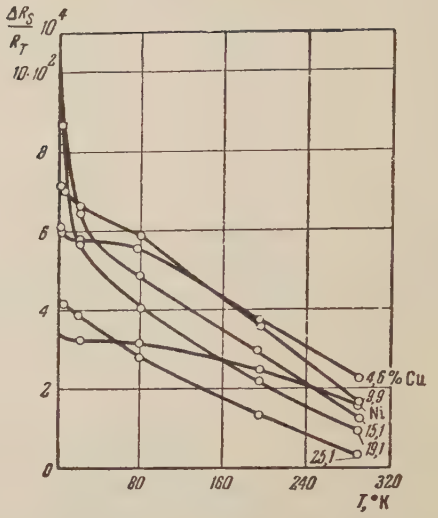

Fig.5. Variation of $\Delta R_S/R_T$ with T for Ni and Ni-Cu alloys.

4. Variation of the resistance of nickel and nickel-copper alloys in strong magnetic fields

The variation in resistivity in a magnetic field can be characterized by the quantities $\Delta\rho$, $\Delta R_T/R_T$ and $\Delta R_T/R_0$, where ΔR_T is the change in the absolute magnitude of the resistance upon the application of a magnetic field at the temperature T, R_T is the no field resistance at this temperature and R_0 is the resistance at some reference temperature, for example, at room temperature.

In the work of Kondorskii & Ozhigov[4] it was shown that ΔR_T varies little with the temperature in alloys of nickel with iron in strong fields in the region of nitrogen and hydrogen temperatures and that the temperature dependence of $\Delta R_T/R_T$ is determined primarily by the temperature dependence of the resistance itself.

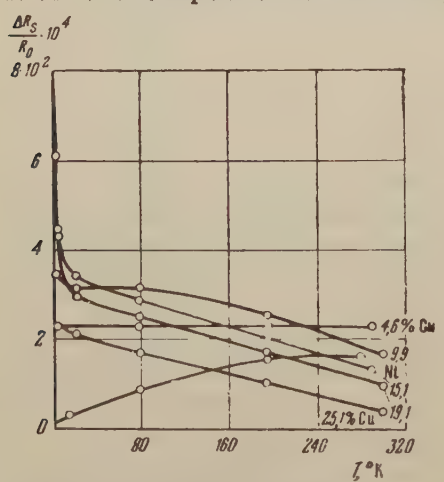

Fig.6. Variation of $\Delta R_S/R_0$ with T for Ni and Ni-Cu alloys.

Figs.5 & 6 show the curves characterizing the variation of $\Delta R_S/R_T$ and $\Delta R_S/R_0$ with the temperature for nickel and Ni-Cu alloys with different Cu concentrations; here ΔR_S is the change in resistance produced by magnetization to saturation. The value of ΔR_S is determined in each case by extrapolation of the rectilinear part of the plot of ΔR_T as a function of the field H to H = 0.

In the temperature range from 4.2-20.4°K, $\Delta R_S/R_0$ for nickel and nickel alloys containing 5, 10 and 25% copper varies little with the temperature and is approximately equal to the value obtained by Kondorskii & Ozhigov for

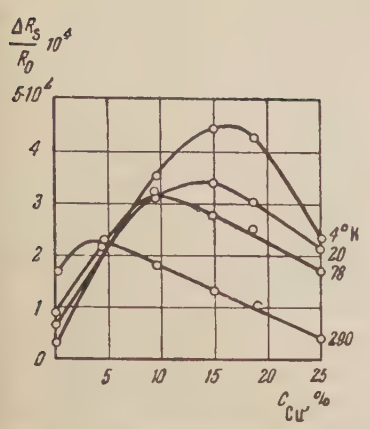

Fig.7. Variation of $\Delta R_s/R_0$ for Ni-Cu alloys with the Cu concentration at different temperatures.

nickel-iron alloys. In the case of Ni-Cu alloys with 15 and 20% Cu, however, there is observed a decrease of $\Delta R_s/R_0$ with increasing temperature in the entire range from 2 to 300°.[9] The increase of $\Delta R_s/R_T$ and $\Delta R_s/R_0$ in alloys containing 15 to 25% copper in the helium temperature range, which is connected with the decrease in the magnitude of the "step" in strong magnetic fields (see Fig.4,b), may not occur in the case of specimens of higher purity.

The variation of $\Delta R_s/R_0$ with the composition of the nickel-copper alloys at different temperatures is shown in Fig.7. It will be seen that a peak value of $\Delta R_s/R_0$ is obtained at copper contents of 15 to 20%. It is interesting to note that in nickel-iron alloys the maximum value of $\Delta R_s/R_0$ is also obtained when the alloy contains about 15% of the second component (i.e., iron).

4. Variation of the resistance of Ni-Cr alloys in magnetic fields

Curves characterizing the temperature dependence of $\Delta R_s/R_T$ with H = 2000 oersted for Ni-Cr alloys with different Cr concentrations are shown in Fig.8. In contrast to the case of other ferromagnetic metals and alloys, in these alloys the value of $\Delta R_s/R_T$ is negative in a certain temperature interval, i.e., the resistivity decreases upon magnetization to saturation in a longitudinal magnetic field. It will be evident from the curves of Fig.8 that the temperature dependence of $\Delta R_s/R_T$ for Ni-Cr alloys is rather complicated.

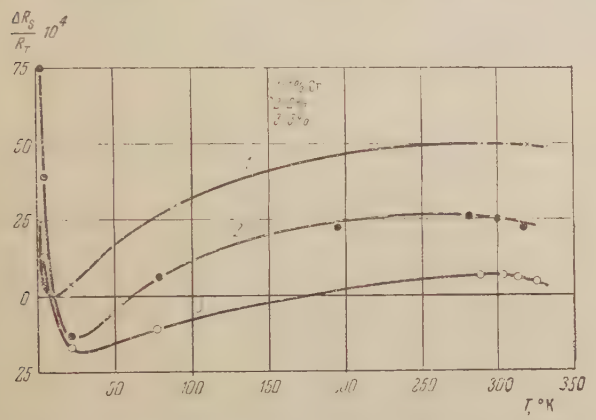

Fig.8. Variation of $\Delta R_s/R_T$ with T for Ni-Cr alloys in a 2000 oersted field.

5. Change of the resistivity of an ordered nickel-manganese alloy in a strong magnetic field

The influence of ordering on the galvanomagnetic effect in Ni-Mn alloys at room temperature has been studied by Komar & Portniagin[10] and Annaev[11]. According to Annaev ordering in the Ni_3Mn alloy leads to an appreciable increase in the change of resistivity in a longitudinal magnetic field. According to the data of Komar & Portniagin, the magnitude of $\Delta R_T/R_T$, due to orientation of the domains in a longitudinal magnetic field, decreases with ordering.

We investigated the variation of the resistance in a longitudinal magnetic field in an alloy composed of 25.6 at.% Mn and 74.4% Ni. The initial disordered state was realized by quenching in water after annealing at 900° for 1 hour. States with different degrees of ordering were obtained by reannealing the quenched samples at 450° for different periods ranging from 4 to 40 hours.

The resultant curves characterizing the variation of $\Delta R_T/R_T$ with the field at room temperature are shown in Fig.9. As regards the shape of the

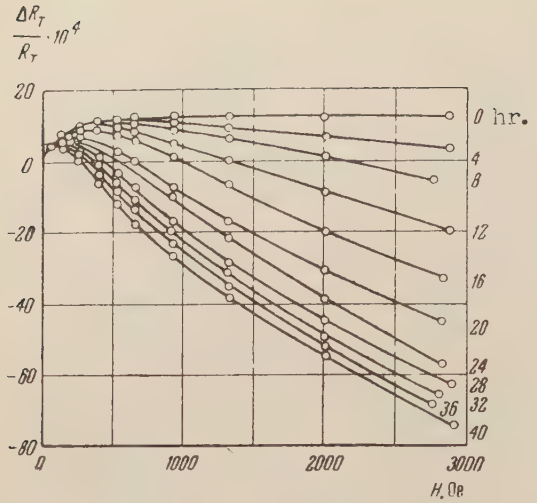

Fig.9. Variation of $\Delta R_T/R_T$ as a function of the field for Ni_3Mn samples annealed at 450° for different lengths of time.

curves, our results for room temperature are in agreement with the data of Komar & Portniagin[10].

The curves for $\Delta R_T/R_T$ vs H at four different temperatures obtained for the quenched (disordered) sample and for the (ordered) sample annealed for 40 hours at 450° are shown in Fig.10 & Fig.11. It will be seen from the curves of Fig.10 that $\Delta R_T/R_T$ for the quenched (disordered) sample increases with the field strength and remains positive in fields up to 3000 oersted. At the temperature of liquid helium the value of $\Delta R_T/R_T$ for the quenched alloy is approximately 6 times higher than at 283°K. In the case of the annealed (ordered) Ni_3Mn sample, $\Delta R_T/R_T$ at first increases somewhat with increasing field strength and then decreases, even becoming negative at higher temperatures (Fig.11).

The derivative $d(\Delta R_T/R_T)/dH$, characterizing the slope of the $\Delta R_T/R_T$ curves, decreases with decreasing temperature and hence at low temperatures the change in sign of $\Delta R_T/R_T$ occurs in stronger fields.

We desire to thank A.I.Shal'nikov for making available the cryostatic equipment of the Low Temperature Department of Moscow State University and for his valuable advice in connection with the investigation.

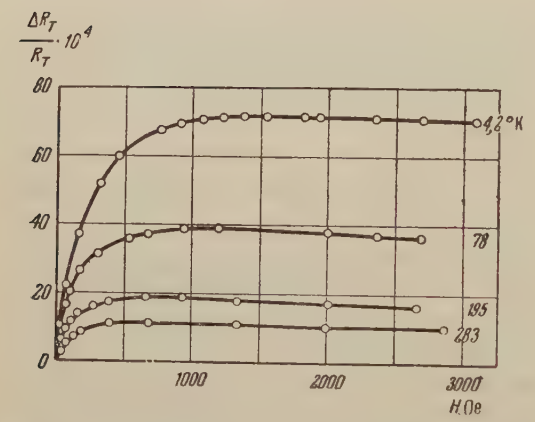

Fig.10. Variation of $\Delta R_T/R_T$ with the field strength at four temperatures for the Ni_3Mn alloy sample quenched from 900° (disordered).

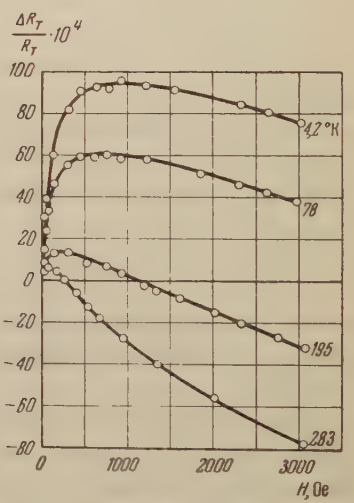

Fig.11. Same as Fig.10 but for Ni_3Mn sample annealed for 40 hours at 450° (ordered).

Physics Department,
Moscow State University

References

1. W.Meissner & B.Voight, Ann.Phys., 7, 892 (1930).
2. A.Van Itterbeck, L. Da Greve, L. Van Gerven & K.Sabbe, Physica, 20, 1 (1954).
3. D.Smit, Physica, 17, 612 (1951).
4. E.I.Kondorskii & I.E.Ozhigov, Doklady AN SSSR, 105, 1200 (1955).
5. H.Masumoto & Y.Shirakava, Sci.Rep.Tohoku Univ., 25, 104 (1938).
6. Y.Shirakava, Sci., Rep. Tohoku Univ., 27, 532 (1939).
7. V.L.Ginzburg, Zhur.eksp.i teor.fiz., 31, 202 (1956).
8. S.V.Vonsovskii & E.A.Turov, Zhur.eksp.i teor.fiz., 24, 420 (1953); E.A.Turov, Izv.AN SSSR, Ser.fiz., 19, 474 (1955). (Trans.Bulletin, 19, No.4, p.426.)
9. O.S.Galkina, Vestnik (Review), Moscow State University, No.3, 1957.
10. A.P.Komar & I.M.Portniagin, Doklady AN SSSR, 60, 569 (1948).
11. R.G.Annaev, Doklady AN SSSR, 61, 1009 (1948).

RESISTIVITY AND THE EFFECT OF A STRONG MAGNETIC FIELD ON THE RESISTIVITY OF IRON-NICKEL ALLOYS AT LOW TEMPERATURES (14-77°K)

- E.I.Kondorskii & I.E.Ozhigov

1. Investigation of the electric resistance and the galvanomagnetic effect in ferromagnetic metals and alloys in the region of low temperatures allows of checking some of the predictions of the quantum theory of the conductivity of ferromagnetic metals and thus facilitates further development of the theory. Hitherto the electric resistance of iron-nickel alloys and its variation in a magnetic field, i.e., the galvanomagnetic effect, has been investigated by Shirakava[1] down to -195°. The purpose of the present work was to investigate the resistivity and the galvanomagnetic effect $\Delta R_{\parallel}/R$ in a longitudinal magnetic field in iron-nickel alloys with nickel concentrations of 40 to 100% in the low temperature region from 14 to 90°K with a view to establishing the temperature dependences of ρ and $\Delta R_{\parallel}/R$; a further purpose was to determine the influence of heat treatments producing ordering on these parameters.

As has been shown by Bozorth[2] ordering in iron-nickel alloys close to $FeNi_3$ as regards composition results in reduction of the resistivity and in a number of cases in an increase in the magnitude of the galvanomagnetic effect.

2. The alloys for our samples were prepared in a high-frequency furnace under a layer of flux. To obtain the ordered states the samples were subjected to annealing in steps for 14 hours in the temperature range from 500 to 410° with subsequent slow cooling. The disordered state was realized by quenching the samples from 950° in vacuum-oil cooled with circulating tap water. In the case of measurements in the temperature range from 77.5 to 63.15°K the samples were surrounded with liquid nitrogen maintained at different pressures, the temperature in each case being determined from the indications of the pressure gage. For the measurements in the range from 20.4 to 14°K liquid hydrogen was employed in the same manner. The magnetic field (up to 10,000 oersted) was produced by an electromagnet.

3. The resistivity of the investigated alloys subjected to quenching (40 to 93.3% Ni) was higher than the resistivity of the alloys subjected to step annealing. The change $(\Delta\rho)_s$ in the absolute magnitude of the resistivity in a longitudinal magnetic field was greater in all cases for the quenched alloys than for the step annealed ones. Thus ordering evidently reduces $(\Delta\rho)_s$. The variation of the relative change in resistance $(\Delta R_{\parallel}/R)_s$ with the concentration is more complicated. In the region of 85-90% Ni concentrations, where the maximum of $(\Delta R_{\parallel}/R)_s$ occurs, this quantity is larger in the case of quenched alloys; in the region of 70-80% Ni concentrations, i.e., in alloys close to $FeNi_3$ as regards composition, where the resistivity falls off with ordering, $(\Delta R_{\parallel}/R)_s$ is greater in the case of alloys subjected to step annealing.

4. The temperature dependence of the resistivity in the range from 14 to 90°K for alloys containing 40.3 to 93.3% Ni in the quenched (disordered) state is described by

$$\rho_s = \rho_0 e^{\beta T^2} \approx \rho_0 (1 + \beta T^2), \tag{1}$$

where ρ_0 is the residual resistivity and β is a temperature independent parameter.

The value of $(\Delta\rho)_s$ for the investigated alloys changes insignificantly in the temperature range from 90 to 14°K; with further reduction in temperature $(\Delta\rho)_s$ decreases slightly. Thus the temperature dependence of $(\Delta R_{\parallel}/R)_s$

is determined primarily by the temperature variation of R. Consequently, the temperature dependence of $(\Delta R_{\parallel}/R)_s$ of the investigated alloys in the temperature range from 14 to 90°K is described by a formula analogous to (1), namely,

$$\left(\frac{\Delta R_{\parallel}}{R}\right)_s = \left(\frac{\Delta R_{\parallel}}{R}\right)_0 e^{-\gamma T^2} \approx \left(\frac{\Delta R_{\parallel}}{R}\right)_0 (1 - \gamma T^2), \qquad (2)$$

where $\gamma = C\beta$. For the investigated alloys the coefficient C lies between the limits 0.9 and 1.3.

Department of Physics
Moscow State University

References

1. Y.Shirakava, Sci.Rep.Tohoku Univ., 27, 532 (1939).
2. R.M.Bozorth, Phys.Rev., 70, 923 (1946).

INVESTIGATION OF MAGNETOSTRICTION AND OTHER EVEN EFFECTS IN THE REGION OF APPROACH TO SATURATION

- G.P.D'iakov

We know that under the influence of exchange forces and the forces of anisotropy there are formed in ferromagnetic crystals regions (domains) of spontaneous magnetization. The magnetic moment of each such region will tend to orient so that the total energy will be minimal. The geometric sum of the magnetic moments of all the spontaneous magnetization regions gives the resultant magnetization of the entire crystal. If we designate the direction of stable equilibrium of the moments of the spontaneous magnetization regions by L_i and the relative volume of the crystal in which the spontaneous magnetization moments are aligned with L_i by n_i, the magnetization of the crystal will be given by

$$J = J_s \sum_{i=1}^{i=k} n_i L_i. \qquad (1)$$

The quantities n_i, L_i and J_s can vary under the influence of different factors (magnetic field, elastic stresses, etc.). In all such cases there will obviously occur a corresponding change in the magnetization of the crystal. The process of change of n_i is called displacement of the boundaries between the spontaneous magnetization regions (displacement of the domain walls). The process of change in the orientation of L_i is termed rotation and the process of change in the absolute value of J_s is called the paraprocess.

The magnetization of ferromagnetic single crystals is determined primarily by the first two magnetization processes. As the strength of the applied magnetic field is increased, both the phase volume n_i and the direction of stable equilibrium L_i will change. At some value of the magnetic field H_s, i.e., the saturation field, the ferromagnet will become a single phase system and the stable equilibrium direction L_i in it will be parallel with that of the magnetic field. In other words, the single crystal in this case will be magnetized to saturation.

Magnetization of a single crystal is accompanied by alteration of its shape (magnetostriction), change in its resistivity and a number of other effects. Investigation of magnetostriction is fundamental to the general theory of ferromagnetism. In his basic work Akulov[1] established that the magnetostriction of a single crystal magnetized to stauration is characterized by the anisotropy law

$$\lambda = \frac{3}{2}\lambda_{100}\left(\Sigma s_i^2 g_i^2 - \frac{1}{3}\right) + 3\lambda_{111}\Sigma s_i s_j g_i g_j, \qquad (2)$$

where s_i are the direction cosines of the vector J_s referred to the tetragonal axes of the crystal, g_i are the direction cosines of the direction of measurement referred to the same axes and λ_{100} and λ_{111} are the saturation magnetostriction coefficients along the edge and diagonal of the cube.

Equation (2), while deduced for magnetostriction, is also applicable to calculation of the change in resistance. In fact, Akulov showed that Eq. (2) is applicable to calculation of all even effects provided the single crystal is magnetized to saturation. The anisotropy law (2) shows how the magnitude of a given even effect will change with changes in g_i if the direction cosines s_i are known. This deduction from theory has been substantiated by numerous experiments. The direction of the stable orientation of the vector J_s relative to the crystal axes is, however, not always known. It is of interest to solve the inverse problem, namely, to determine the stable position of J_s from the known value of the magnetic field. Here in calculating

the even effects one must determine the energy minima of the crystal and the position of the vector J_s relative to the crystal axes as a function of the different factors acting on the crystal. This problem has not been solved in the general case. In the region of approach to magnetic saturation, however, this problem can readily be solved.

A series of works[2-4] on magnetostriction published earlier by the writer constituted the first step in this direction and formed the basis of a theory of even effects in the region of strong magnetic fields. A general relationship for magnetostriction in the region of approach to saturation was given in Ref.2. This relationship is commonly termed the law of approach to saturation of magnetostriction and other even effects. The theory developed in Ref. 2 shows that the magnetostriction in a material devoid of texture and free of internal elastic stresses must be related to the anisotropy constant K_1, the magnetostriction coefficients λ_{100} and λ_{111}, the saturation magnetization and the intensity of the applied field H by the expression

$$\lambda = \lambda_s\left(1 - \frac{A}{H} - \frac{B}{H^2}\right), \tag{3}$$

where

$$\lambda_s = \frac{2}{5}\lambda_{100} + \frac{3}{5}\lambda_{111},$$

$$A = \frac{8}{35}(\lambda_{111} - \lambda_{100})\,\frac{K_1}{\lambda_s J_s},$$

$$B = \left(\frac{32}{7\cdot 11\cdot 13}\lambda_{100} + \frac{984}{5\cdot 7\cdot 11\cdot 13}\lambda_{111}\right)\frac{K_1^2}{\lambda_s J_s^2}.$$

Somewhat later an analogous theory of magnetostriction was developed by Lee[5]. His calculations carried out independently of the writer's, also led to Eq.(3). If we take into account the magnetostriction due to the paraprocess, we must supplement Eq.(3) by the addition of a term $\chi_{\lambda p} H$, where $\chi_{\lambda p}$ is the magnetostrictive susceptibility associated with the paraprocess. Thus Eq.(3) is brought to the form

$$\lambda = \lambda_s\left(1 - \frac{A}{H} - \frac{B}{H^2}\right) + \chi_{\lambda p} \cdot H. \tag{4}$$

Further development of the theory proceeded along the lines of taking into account internal stresses[3,4] and the influence of magnetic interaction between the crystallites[6].

In all the cited works, however, no account was taken of the second anisotropy constant K_2 and the law of approach to saturation was limited to the first and second terms of the expansion. It is clearly of interest to determine to what extent it is justifiable to leave out terms in higher powers of H from Eq.(3) and to evaluate the possible influence of the second anisotropy constant K_2. This problem is most easily solved for materials that are isotropic as regards magnetostriction.

Let us, therefore, first turn to the case of isotropic materials, bearing in mind that for them $\lambda_{100} = \lambda_{111} = \lambda_s$. We shall not dwell here in detail on the method of calculation of the magnetostriction (it is described in full in our earlier contribution), but will only recapitulate the more important steps of the calculation.

Assume that we have a ferromagnetic single crystal in an external magnetic field. If the single crystal is subject to the influence of deforming forces, the orientation of the spontaneous magnetization vector J_s will depend not only on the strength and direction of the magnetic field H but also on the magnitude and direction of the stress vector σ (Fig.1). Now misalignment of

the magnetization vector with respect to the field vector will depend to an appreciable degree on the elastic stresses arising in the given material.

In the region of strong magnetic fields the angle between the spontaneous magnetization vector J_s and the field vector H will be small: consequently, the angles

$$\alpha = \vartheta - \vartheta' \quad \text{and} \quad \beta = \varphi - \varphi'$$

will also be small. Expanding the magnetostriction into a series in terms of α and β, as described in the cited references, we obtain

$$\lambda = D_0 + D_1\alpha + D_2\beta + D_3\alpha\beta + D_4\alpha^2 + D_5\beta^2 + D_6\alpha^3 + D_7\alpha^2\beta + D_8\alpha\beta^2 + D_9\beta^3, \tag{5}$$

where

$$D_0 = \lambda_s,\ D_4 = -\frac{3}{2}\lambda_s,\ D_5 = -\frac{3}{2}\lambda_s \sin^2\vartheta',\ D_8 = -\frac{3}{2}\lambda_s \sin\vartheta' \cos\vartheta'.$$

In the case under consideration all the other coefficients vanish.

The parameters α and β in (5), which determine the spatial position of the spontaneous magnetization vector, can be found from the minimization conditions for the total energy of the crystal, which in the given case will be comprised of four parts:

1) the energy of the crystal with respect to the external magnetic field:

$$U_a = -J_s H (s_1 h_1 + s_2 h_2 + s_3 h_3), \tag{6}$$

where s_1, s_2 and s_3 are the direction cosines of the vector J_s referred to the crystal axes and h_1, h_2 and h_3 are the direction cosines of the field vector referred to the same axes;

2) the energy of the magnetic crystallographic anisotropy*

$$U_e = U_0 + K_1 (s_1^2 s_2^2 + s_2^2 s_3^2 + s_3^2 s_1^2) + K_2 s_1^2 s_2^2 s_3^2, \tag{7}$$

where K_1 is the first anisotropy constant and K_2 is the second anisotropy constant;

3) the magneto-elastic energy

$$U_\sigma = -\sigma\left[\frac{3}{2}\lambda_{100}\left(\Sigma s_i^2 v_i^2 - \frac{1}{3}\right) + 3\lambda_{111}\Sigma s_i s_j v_i v_j\right], \tag{8}$$

where v_i are the direction cosines of the stress vector.

Thus the total energy per unit volume of the crystal will be

$$U = U_a + U_e + U_\sigma. \tag{9}$$

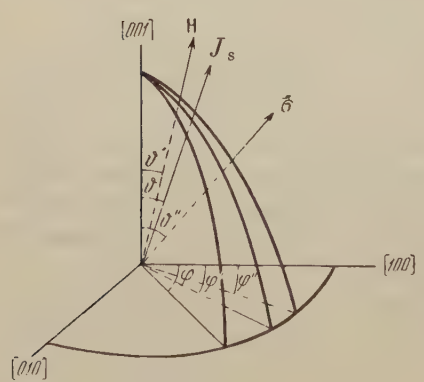

Fig.1. Orientation of the vectors J_s, H and σ relative to the crystallographic axes of the single crystal, taken here as the coordinate axes.

The parameters α and β in (5) can be determined from the condition for minimum total energy of the crystal and the additional condition that

$$s_1^2 + s_2^2 + s_3^2 = 1.$$

---

*In Refs.2-4 the magnetic anisotropy energy was taken in the form $U_e = U_0 + 2K_1 (s_1^2 s_2^2 + s_2^2 s_3^2 + s_3^2 s_1^2)$.

Substituting the expressions for α and β obtained in this manner in Eq.(5), we obtain an equaltion for the magnetostriction of a single crystal. Thus this calculation allows of determining the variation of the magnetostriction of a single crystal for any direction of the external field relative to the crystal axes.

Magnetostriction of polycrystalline materials

From the practical standpoint, however, calculation of the magnetostriction of polycrystalline specimens is more important. We determined the magnetostriction for nontextured polycrystalline materials by averaging the magnetostriction of a single crystal. We shall omit here the cumbersome intermediate computations and give only the final expression for the magnetostriction of isotropic materials with a "diffuse" (all directions equally probable) distribution of elastic stresses.

The deduced expression for the magnetostriction of isotropic materials is

$$\lambda = \lambda_s\left(1 - \frac{B_u}{H^2} - \frac{C_u}{H^3}\right), \tag{10}$$

where

$$B_u = \left[\frac{8}{35}K_1^2 + \frac{16}{385}K_1K_2 + \frac{24}{5005}K_2^2 + \frac{9}{5}\lambda_s^2\sigma^2\right]\frac{1}{J_s^2},$$

$$C_u = \left[\frac{576}{5005}K_1^3 - \frac{64}{5005}K_1^2K_2 - \frac{64}{6545}K_1K_2^2 - \frac{64}{95095}K_2^3 + \frac{126}{245}\lambda_s^2\sigma^3\right]\frac{1}{J_s^3}.$$

Thus by taking into account the elastic stresses and the second anisotropy constant, we have arrived at a more accurate description of the behavior of the magnetostriction in the region of strong magnetic fields. Further, the calculations allow of determining the magnitude of the term C_u/H^3, which was rather arbitrarily discarded in our earlier works[2-6] as a negligibly small quantity.

Let us see how many times larger the second term in (10) is than the third, previously discarded term.

It can readily be shown that in the case when $\sigma = 0$ and $K_2 = 0$

$$\frac{B_u}{H^2} : \frac{C_u}{H^3} \approx \frac{2J_sH}{K_1}.$$

Consequently, when $2J_sH > K_1$, the third term in Eq.(10) is actually small and can be neglected. Knowing the values of J_s, K_1, K_2 and σ for the investigated material, we can now in each case evaluate the relative importance of the third term in the law for approach to saturation of magnetostriction and other even effects.

An important result of the theory was that it made it possible to develop a new method for determining the important constants of ferromagnetic materials. For example, the anisotropy constant of iron-nickel alloy was evaluated by this method in Ref.7. Unfortunately, there are scarcely any data in the literature on measurements of magnetostriction in the region of approach to saturation. Actually at present we know of only one thorough investigation, namely, that of Lee[8], performed in Bates laboratory. Unfortunately, in his report Lee does not give detailed data, which naturally makes it difficult to compare the results of experiment with our theory. Yet knowing the magnetostrictive susceptibility of a polycrystalline material, one can determine λ_{100} and λ_{111}.

Thus differentiating (4) with respect to H we obtain

$$\frac{\partial\lambda}{\partial H} = \frac{A\lambda_s}{H^2} + \frac{2B\lambda_s}{H^3} + \chi\lambda_p. \tag{11}$$

The value of the magnetostrictive susceptibility associated with the paraprocess at room temperature (according to the measurements of Döring) is 10^{-11} per oersted. Hence in further calculations we can neglect $\chi\lambda_p$ in Eq.(11).

Multiplying both sides of (11) by H^2 and substituting the values for A and B, we obtain

$$\frac{\partial\lambda}{\partial H}\cdot H^2 = \frac{8}{35}\cdot\frac{K_1}{J_s}(\lambda_{111}-\lambda_{100}) + \frac{2K_1^2}{J_s^2}\left(\frac{32}{1001}\lambda_{100} + \frac{984}{5005}\lambda_{111}\right)\frac{1}{H}, \tag{12}$$

or

$$\frac{\partial\lambda}{\partial H}\cdot H^2 = a + bH^{-1}, \tag{13}$$

where

$$a = \frac{8}{35}\cdot\frac{K_1}{J_s}(\lambda_{111}-\lambda_{100}), \tag{14}$$

$$b = \frac{K_1^2}{J_s^2}\left(\frac{64}{1001}\lambda_{100} + \frac{1968}{5005}\lambda_{111}\right). \tag{15}$$

From expressions (13), (14) and (15) it follows that knowing the magnetostrictive susceptibility of a polycrystalline specimen from experiment, one can determine the magnetostriction coefficients λ_{100} and λ_{111}. In order to check these deductions, we carried out measurements of the magnetostrictive susceptibility of nickel, using a sample in the form of a strip 150 mm long, 10 mm wide and 0.1 mm thick.

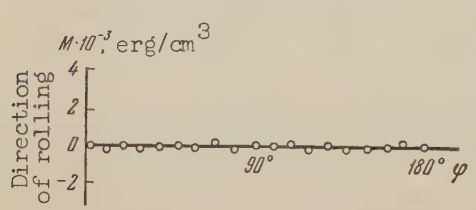

Fig.2. Torque curve obtained by the magnetic technique for the specially heat treated nickel specimen.

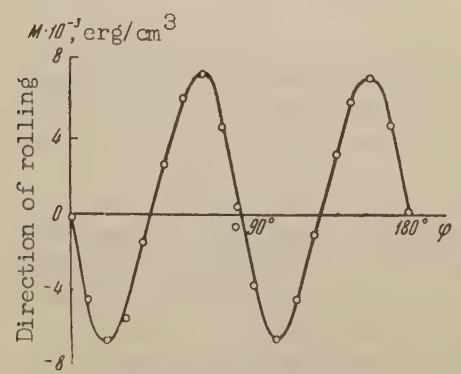

Fig.3. Magnetogram obtained for a nickel specimen heated at 1100° in vacuum.

The specimen was heat treated so as to insure complete absence of crystallographic texture. The analysis for texture was carried out by the magnetic procedure, i.e., by recording the torque curve. The magnetogram for the heat treated sample is shown in Fig.2; it will be evident that this specimen was devoid of crystallographic texture. For comparison, in Fig.3 we give the magnetogram for a similar specimen that was only annealed under vacuum at 1100°. It will be evident from the figures that the thermal and mechanical treatment to which the specimen is subjected is of paramount importance.

The magnetostriction measurements were carried out by means of resistance strain gages connected in a bridge circuit. The indicator in the diagonal of the bridge was a photoelectrooptical amplifier, which greatly enhanced the sensitivity of the set-up and made it possible to measure the magnetostrictive susceptibility with high accuracy.

The results of measurement are shown in Fig.4. It will be seen that in accord with Eq.(13) the magnetostrictive susceptibility in strong magnetic fields is a linear function of 1/H. The recti-

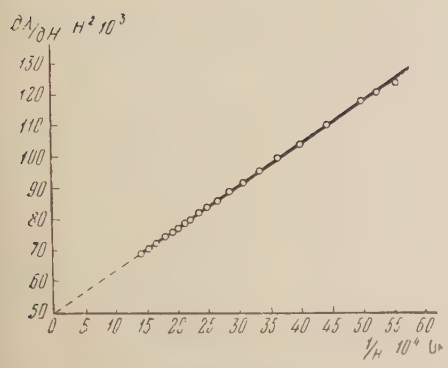

Fig.4. Variation of the magnetostrictive susceptibility of the nickel sample as a function of the magnetic field.

linear plot intercepts the y-axis at a point equivalent to the first term in (13). The magnitude of this y-intercept is

$$a = 50 \cdot 10^{-5};$$

from the slope of the line we get

$$b = 1{,}4 \cdot 10^{-1}.$$

If we take $K_1 = 5 \cdot 10^4$ erg/cm^3 and $J_s = 500$ gauss for nickel and the values of a and b from experiment, we can readily determine λ_{100} and λ_{111} by means of Eqs.(14) and (15). The values calculated in this manner are

$$\lambda_{100} = -49 \cdot 10^{-6} \quad \text{and} \quad \lambda_{111} = -27 \cdot 10^{-6}.$$

These values are in satisfactory agreement with the experimental data obtained from direct measurements on single crystals[9].

It will be noted that in deriving the law (4) of approach to saturation for polycrystalline materials, we averaged the magnetostriction of an isolated single crystal. It may be questioned, however, whether the formula for an isolated single crystal is really applicable to the microscopic single crystals of which commonly used engineering materials are comprised. Does not the interaction between these microcrystals play a sufficiently important role to invalidate the deduced law for approach to saturation where ordinary polycrystalline materials are concerned?

There can be no doubt that this is indeed a pertinent question. Néel[6] was the first to take into account the influence of magnetic interaction between crystallites. His calculations indicate that in the first approximation the influence of magnetic interaction can be taken into account in the law of approach to magnetostriction for independent crystallites by multiplying the group of terms containing H by a constant factor G_1. Further Néel showed that for anisotropic materials in the region of high fields of interest to us here, G_1 is always close to 1/2. Thus it would appear that magnetic interaction between the crystallites leads to a reduction of the magnetostrictive susceptibility.

On the other hand, in polycrystalline materials the mechanical forces in and elastic properties of the material vary from point to point, depending on the crystallographic orientations of the individual crystals. As Vladimirskii[10] has shown this circumstance should also affect the magnitude of the magnetostriction. It follows from his calculations that the mechanical interaction leads to a certain increase of the saturation magnetostriction. If we apply Vladimirskii's method in the region of fields close to saturation, then in the first approximation we must multiply the group of terms containing H by a factor G_2 taking into account the mechanical interaction. Our experimental investigation of the magnetostrictive susceptibility of nickel showed, however, that Eq.(3) deduced without taking into account magnetic and mechanical interactions is generally in agreement with experiment.

It is difficult to imagine that the comparatively weak influence of mechanical interaction can fully compensate the influence of magnetic interaction on the magnetostrictive susceptibility. It would appear, therefore,

that the assumptions (presence of free magnetic poles at the grain boundaries, etc.) invoked by Néel for his calculations of the magnetic interaction between the crystallites are highly approximate and are not validated by experiment.

Department of Physics
Moscow State University

References

1. N.S.Akulov, ZS.f.Phys., 52, 389 (1928).
2. G.P.D'iakov, Doklady AN SSSR, 68, 33 (1949).
3. G.P.D'iakov, Doklady AN SSSR, 76, 201 (1951).
4. G.P.D'iakov, Doklady AN SSSR, 82, 867 (1952).
5. E.W.Lee, Proc.Phys.Soc., A67, 381 (1954).
6. L.Néel, J.Phys.et Rad., 15, 376 (1954).
7. G.P.D'iakov & R.A.Reznikova, Doklady AN SSSR, 97, 633 (1954).
8. E.W.Lee, Proc.Phys.Soc., A65, 162 (1952).
9. R.M.Bozorth & R.W.Hamming, PhysRev., 89, 865 (1953).
10. K.V.Vladimirskii, Doklady AN SSSR, 41, 11 (1943).

SOME ASPECTS OF THE THEORY OF ELASTIC FERROMAGNETIC (MAGNETOSTRICTIVE) MEDIA

- K.B.Vlasov

In designing magnetomechanical transducers, or, more specifically, in calculating the changes taking place in a ferromagnet when it is subjected to a magnetic field, mechanical stresses and heat, one must make use of equations of electrodynamics, elasticity theory formulas and equations of state.

In a polarized ferromagnet, mechanical stresses are, in general, represented by an asymmetric tensor. As has been shown by Brown[1,2], however, one can introduce a symmetric stress tensor ($\sigma_{ij} = \sigma_{ji}$), at the same time appropriately modifying the form of the elasticity equations. In what follows we shall make use of this symmetric stress tensor.

1. Let us deduce approximate equations of state for an elastic ferromagnetic medium by expanding one of the thermodynamic potentials in powers of small parameters. We shall use this device to consider quasistatic processes. As our first or initial thermodynamic potential, let us choose the free energy per unit mass. Let us expand it in powers of the components of the deformation tensor ε_{ij}, components of the specific magnetization vector M_q (the magnetic moment per unit mass) and the temperature change ΔT. We shall carry this expansion to terms quadratic in ε_{ij} and ΔT and to sixth order terms in M_q about the state in which $\varepsilon_{ij} = 0$, $M_q = 0$ and $T = T_0$. As has been shown by Brown,[2] the change in free energy per unit mass is

$$dF = H_q\, dM_q + v\,(\sigma_{ij}\, d\varepsilon_{ij}) - s\, dT, \tag{1}$$

where the H_q are the components of the magnetic field vector, v is the specific volume,

$$v = 1/\rho = v_0(1 + \delta_{ke}\varepsilon_{ke}), \tag{2}$$

ρ is the density and s is the entropy per unit mass.

Before proceeding we make the following comments. First, the free energy per unit mass of a demagnetized ferromagnet is invariant[3] under the symmetry operation R. Second, from Eq.(1) it follows that

$$H_q = \left(\frac{\partial F}{\partial M_q}\right)_{\varepsilon T}, \quad \sigma_{fg} = \frac{1}{v}\left(\frac{\partial F}{\partial \varepsilon_{fg}}\right)_{MT}, \quad s = -\left(\frac{\partial F}{\partial T}\right)_{\varepsilon M}, \tag{3}$$

Third, when taking partial derivatives of the free energy the order of differentiation is immaterial. Also, let us introduce the new variables

$$J_q = M_q/v \tag{4}$$

which is the magnetic moment per unit volume, and

$$S = s/v, \tag{5}$$

which is the entropy per unit volume. All the above gives us the following equations of state (retaining only linear terms in ε_{ij} and ΔT, and going to fifth order terms in J_q):

$$\begin{aligned}\sigma_{fg} = \sigma^0_{fg} + C^{0*JT}_{fgij}\varepsilon_{ij} + \beta^{0*J}_{fg}\Delta T + \frac{1}{2}Q^{0*T}_{mnfg}J_mJ_n + \frac{1}{2}f^{0*T}_{mnfgij}J_mJ_n\varepsilon_{ij} + \\ + \frac{1}{2}m^{0*}_{mnfg}J_mJ_n\Delta T + \frac{1}{24}\Lambda^{0*T}_{mnpqfg}J_mJ_nJ_pJ_q + \\ + \frac{1}{24}N^{0*T}_{mnpqfgij}J_mJ_nJ_pJ_q\varepsilon_{ij} + \frac{1}{24}K^{0*}_{mnpqfg}J_mJ_nJ_pJ_q\Delta T,\end{aligned} \tag{6}$$

$$H_s = \gamma^{0\varepsilon T}_{sm} J_m + Q^{0T}_{smij} J_m \varepsilon_{ij} + p^{0\varepsilon}_{sm} J_m \Delta T + \frac{1}{6} t^{0\varepsilon T}_{smnp} J_m J_n J_p +$$

$$+ \frac{1}{6} \Lambda^{0T}_{smnpij} J_m J_n J_p \varepsilon_{ij} + \frac{1}{6} \varphi^{0\varepsilon}_{smnp} J_m J_n J_p \Delta T + \frac{1}{120} \Phi^{0\varepsilon T}_{smnpqr} J_m J_n J_p J_q J_r +$$

$$+ \frac{1}{120} L^{0T}_{smnpqrij} J_m J_n J_p J_q J_r \varepsilon_{ij} + \frac{1}{120} \Omega^{0\varepsilon}_{smnpqr} J_m J_n J_p J_q J_r \Delta T, \tag{7}$$

$$\Delta Q = Q - Q^0 = \rho C^{\varepsilon J}_0 \Delta T - T \beta^{0J}_{ij} \varepsilon_{ij} - \frac{1}{2} T p^{0\varepsilon}_{mn} J_m J_n -$$

$$- \frac{1}{2} T r^{0\varepsilon}_{mn} J_m J_n \Delta T - \frac{1}{2} T m^0_{mnij} J_m J_n \varepsilon_{ij} - \frac{1}{24} T \varphi^{0\varepsilon}_{mnpq} J_m J_n J_p J_q -$$

$$- \frac{1}{24} T K^0_{mnpqij} J_m J_n J_p J_q \varepsilon_{ij} - \frac{1}{24} T \psi^{0\varepsilon}_{mnpq} J_m J_n J_p J_q \Delta T, \tag{8}$$

where

$$Q = TS. \tag{9}$$

These equations can be obtained equivalently by transforming to the variables J_q and S in Eq.(1) and using $F' = F / v_0$ for the thermodynamic potential.

The equations of state (6)-(8) are actually expansions of σ_{fg}, H_s and $-S$ in powers of ε_{ij}, J_m and ΔT, and the tensor constants that enter into these equations are their partial derivatives at $\varepsilon_{ij} = 0$, $J_m = 0$ and $\Delta T = 0$.

Some of these tensor constants are related; in particular

$$\left.\begin{aligned}
\beta^{0*}_{ij} &= \beta^0_{ij} + S^0 \delta_{ij}, \\
Q^{0*}_{mnfg} &= Q^0_{mnfg} - \gamma^0_{mn} \delta_{fg}, \\
f^{0*}_{mnfgij} &= f^0_{mnfgij} - Q^0_{mnij} \delta_{fg} + \gamma^0_{mn} \delta_{fg} \delta_{ij}, \\
m^{0*}_{mnfg} &= m^0_{mnfg} - p^0_{mn} \delta_{fg}, \\
\Lambda^{0*}_{mnpqfg} &= \Lambda^0_{mnpqfg} - 3t^0_{mnpq} \delta_{fg}, \\
N^{0*}_{mnpqfgij} &= N^0_{mnpqfgij} - 3\Lambda^0_{mnpqij} \delta_{fg} + 3t^0_{mnpq} \delta_{fg} \delta_{ij}, \\
K^{0*}_{mnpqfg} &= K^0_{mnpqfg} - 3\varphi^0_{mnpq} \delta_{fg}, \\
C^{0*}_{fgij} &= C^0_{fgij} - \sigma^0_{fg} \delta_{ij},
\end{aligned}\right\} \tag{10}$$

where

$$\left.\begin{aligned}
C^0_{fgij} &= \left(\frac{\partial^2 F'}{\partial \varepsilon_{fg} \partial \varepsilon_{ij}}\right)^0 = \frac{1}{v_0} \left(\frac{\partial^2 F}{\partial \varepsilon_{fg} \partial \varepsilon_{ij}}\right)^0, \\
f^0_{mnfgij} &= \left(\frac{\partial Q_{mnfg}}{\partial \varepsilon_{ij}}\right)^0, \quad N^{\ 0}_{mnpqfgij} = \left(\frac{\partial \Lambda_{mnpqfg}}{\partial \varepsilon_{ij}}\right)^0.
\end{aligned}\right\} \tag{11}$$

The constants without an asterisk can be expressed in terms of partial derivatives of the free energy F or F'.

The differences between the constants with an asterisk and those without arise from the fact that unlike the usual similar treatments of magnetostrictive or electrostrictive media, our Eq.(1) for the change in the free energy includes the change in the specific volume incident to deformation. Ordinarily these differences are not great.

Let us evaluate, for instance, the difference between the constants Q^{0*}_{mnfg} and Q^0_{mnfg}, which characterize the magnetomechanical properties of isotropic polycrystalline ferromagnets. From (6) (setting $\sigma_{fg} - \sigma^0_{fg} = 0$ and $\Delta T = 0$ and restricting the considerations to quadratic terms) it follows as regards

order of magnitude $Q^{0*}_{3333} \sim \frac{\lambda_{(s)} C^0_{3333}}{J^2_{(s)}}$ where $\lambda_{(s)}$ and $J_{(s)}$ are the saturation magnetostriction and magnetization. Setting $\lambda_{(s)} \sim 10^{-5}$, $J_{(s)} \sim 1000$ gauss and $C^0_{3333} \sim 10^{12}$ dyne/cm^2, we obtain $Q^{0*}_{3333} \sim 10$. From the second of equations (10) and the fact that $\gamma^0_{33} = 1/\chi^0_{33}$, where χ^0_{33} is the reversible susceptibility ($\chi^0_{33} \sim$ 10 to 100), we are led to the conclusion that the difference between Q^{0*}_{mnfg} and Q^0_{mnfg} is of the order of a few percent or even a fraction of a percent.

The physical meaning of this difference becomes clearer if we note the following. According to (7), even in the absence of magnetostriction (i.e., when $Q^{0*}_{mnfg} = 0$ and $Q^0_{mnfg} = \gamma^0_{mn}\delta_{fg}$) deformation connected with a change in volume (at a given magnetic field strength) should lead, in a polarized ferromagnet, to a change in magnetization (but not in M_q) proportional to the polarization magnetization and to the change in volume.

Not all the components of the tensor constants in Eqs.(6)-(8) are independent of each other. The indices fg, ij and kl represent differentiation with respect to the deformations, while the indices m, n, p, q, r and s represent differentiation with respect to the magnetization. By making use of the fact that the partial derivatives of the free energy are independent of the order of differentiation, one can show that the components of all the tensors without asterisks are invariant under permutations of the indices $m, n, p, q, \ldots$ among themselves, or pairs of indices fg, $ij, \ldots$ among themselves. Since σ_{ij} and ε_{ij} are symmetric tensors, the components are also invariant with respect to interchanges between indices such as f and g, i and $j, \ldots$ within the pairs fg, $ij, \ldots$

In view of these properties and Eq.(10), we arrive at the conclusion that the second rank tensors γ^0_{ij}, β^0_{ij}, p^0_{mn}, r^0_{mn} and β^{0*}_{ij} have only 6 independent components. Among the fourth rank tensors, Q^0_{mnij}, m^0_{mnij}, Q^{0*}_{mnij} and m^{0*}_{mnij} have 36 independent components; the tensor C^0_{fgij} has 21, and t^0_{mnpq}, φ^0_{mnpq} and ψ^0_{mnpq} have 15. Of the sixth rank tensors, f^0_{mnfgij} has 126 independent components, K^0_{mnpqij}, Λ^0_{mnpqij}, K^{0*}_{mnpqij} and Λ^{0*}_{mnpqij} have 90, and Φ^0_{mnpqrs} and Ω^0_{mnpqrs} have 28. Of the tensors of rank eight, $N^0_{mnpqfgij}$ has 315 independent components, and $L^0_{mnpqrsij}$ has 168. The tensors C^{0*}_{fgij}, f^{0*}_{mnfgij} and $N^{0*}_{mnpqfgij}$ have more independent components than the corresponding ones without asterisks, since according to (10) these tensors are not invariant under interchange of the pairs fg and ij. Nevertheless, the subsidiary conditions of Eq.(10) are satisfied by these tensors.

The number of independent components of the tensor constants is also determined by the symmetry of the magnetostrictive medium. It can be shown from symmetry considerations, for example, that in the case of a medium characterized by cubic symmetry (cubic medium) and in that of an isotropic medium the respective numbers of independent tensor constant component will be the following:

Rank	Tensor constant	Number of independent components: Cubic medium	Isotropic medium
Second	All	1	1
Fourth	Q^0_{mnij}, m^0_{mnij} & C^0_{fgij}	3	2
"	t^0_{mnpq}, φ^0_{mnpq} & ψ^0_{mnpq}	2	1
Sixth	f^0_{mnfgij}	9	4
"	Λ^0_{mnpqij} & K^0_{mnpqij}	6	2
"	Φ^0_{mnpqrs} & Ω^0_{mnpqrs}	3	1
Eighth	$N^0_{mnpqfgij}$	12	6
"	$L^0_{mnpqrsij}$	4	1

2. We shall now find the equations of state for a polarized magnetostrictive medium starting from Eqs.(6)-(8) for a nonpolarized medium. We shall consider this medium in the demagnetized state to be magnetically and elastically isotropic.

Let us consider J_q to consist of two terms: a constant term J_0 (the polarization magnetization), assumed to be oriented along the z axis, and a variable term J_q'. We shall assume further that $J_q' \ll J_0$, and that J_q' is of the same order of smallness as ε_{ij} and ΔT. We shall make use of the fact that the components of the tensor constants are related as a result of the symmetry of the initial magnetically and elastically isotropic medium and of the relationships of Eqs.(10). In order to avoid considering anisotropy due to initial stresses, we shall assume these to be zero.

We drop the prime on J_q', and after appropriate mathematical operations obtain the following equations of state for a polarized magnetostrictive medium:

$$\left.\begin{aligned} \sigma_i - \sigma_i^0 &= C_{ij}^{JT}\varepsilon_j + h_{mi}^{*T}J_m + \beta_i^{*J}\Delta T, \\ H_n - H_n^0 &= h_{nj}^{T}\varepsilon_j + \gamma_{mn}^{\varepsilon T}J_m + p_n^{\varepsilon}\Delta T, \\ \Delta Q - \Delta Q^0 &= -T\beta_j^J\varepsilon_j - Tp_m^{\varepsilon}J_m + \rho C^{\varepsilon J}\Delta T, \end{aligned}\right\} \tag{12}$$

where $i, j = 1, \ldots, 6$, and $m, n = 1, 2, 3$.

The tensor constants in (12) can be expressed in terms of power series in the magnetization polarization. By comparing these series with each other, one can establish the following relations between the nonzero components of the tensor constants.

The tensor of the isothermal value of the reciprocal of the susceptibility measured at constant strain, which determines the magnetic properties of the magnetostrictive medium, is defined by the relations

$$\gamma_{mn}^{\varepsilon T} = \left(\frac{\partial H_n}{\partial J_m}\right)_{\varepsilon T}, \tag{13}$$

$$\gamma_{33}^{\varepsilon T} = \gamma^{0T} + \frac{1}{2}t_{11}^0 J_0^2 + \frac{1}{24}\Phi_1^0 J_0^4, \tag{14}$$

$$\gamma_{11}^{\varepsilon T} = \gamma_{22}^{\varepsilon T} = \gamma^{0T} + \frac{1}{6}t_{11}^0 J_0^2 + \frac{1}{120}\Phi_1^0 J_0^4. \tag{15}$$

The magnetic polarization field strength satisfies the relation

$$H_3^0 = \left(\gamma^{0T} + \frac{1}{6}t_{11}^0 J_0^2 + \frac{1}{120}\Phi_1^0 J_0^4\right) J_0. \tag{16}$$

The isothermal magnetostriction tensor constants, which determine the magnetomechanical properties, satisfy the relations

$$h_{mi}^{*T} = \left(\frac{\partial \sigma_i}{\partial J_m}\right)_{\varepsilon T}, \quad h_{mi}^{T} = \left(\frac{\partial H_m}{\partial \varepsilon_i}\right)_{JT}, \tag{17}$$

$$\left.\begin{aligned} h_{33}^{*T} &= Q_{11}^{0*}J_0 + \frac{1}{6}\Lambda_1^{0*}J_0^3 + \frac{1}{120}L_1^{0*}J_0^5, \\ h_{31}^{*T} &= h_{32}^{*T} = Q_{12}^{0*}J_0 + \frac{1}{6}\Lambda_2^{0*}J_0^3 + \frac{1}{7}\frac{1}{120}L_1^{0*}J_0^5, \end{aligned}\right\} \tag{18}$$

$$h_{24}^{*T} = h_{15}^{*T} = h_{24}^{T} = h_{15}^{T} = \frac{1}{2}(Q_{11}^{0*} - Q_{12}^{0*})J_0 + \frac{1}{24}(\Lambda_1^{0*} - \Lambda_2^{0*})J_0^3 + \frac{1}{7}\frac{1}{120}L_1^{0*}J_0^5, \tag{19}$$

$$h_{33}^{T} = h_{33}^{*T} + \gamma_{33}^{\varepsilon T}J_0, \quad h_{31}^{T} = h_{32}^{T} = h_{31}^{*T} + \gamma_{33}^{\varepsilon T}J_0. \tag{20}$$

The isothermal elastic modulus measured at constant magnetization, which determines the mechanical properties, satisfies the relations

$$C_{ij}^{JT} = \left(\frac{\partial \sigma_i}{\partial \varepsilon_j}\right)_{JT}, \tag{21}$$

$$\left.\begin{aligned} C_{33}^{JT} &= C_{11}^{0T} + \tfrac{1}{2} f_1^{0*} J_0^2 + \tfrac{1}{24} N_1^{0*} J_0^4, \\ C_{11}^{JT} &= C_{22}^{JT} = C_{11}^{0T} + \tfrac{1}{2} f_2^{0*} J_0^2 + \tfrac{1}{24} N_2^{0*} J_0^4, \\ C_{12}^{JT} &= C_{21}^{JT} = C_{12}^{0T} + \tfrac{1}{2} f_4^{0*} J_0^2 + \tfrac{1}{24} N_4^{0*} J_0^4, \\ C_{12}^{JT} &= C_{23}^{JT} = C_{12}^{0T} + \tfrac{1}{2} f_3^{0*} J_2^0 + \tfrac{1}{24} N_3^{0*} J_0^4, \end{aligned}\right\} \tag{22}$$

$$C_{31}^{JT} = C_{32}^{JT} = C_{13}^{JT} + \tfrac{1}{2}(Q_{11}^{0*} - Q_{12}^{0*}) J_0^2 + \tfrac{1}{8}(\Lambda_1^{0*} - \Lambda_2^{0*}) J_0^4, \tag{23}$$

$$C_{66}^{JT} = \tfrac{1}{2}(C_{11}^{JT} - C_{12}^{JT}), \tag{24}$$

$$C_{44}^{JT} = C_{55}^{JT} = \tfrac{1}{4}(C_{11}^{JT} + C_{33}^{JT} - C_{13}^{JT} - C_{31}^{JT}) + \tfrac{1}{24} N_5^0 J_0^4. \tag{25}$$

The stresses due to polarization in the compressed ferromagnet are

$$\left.\begin{aligned} \sigma_3^0 &= \tfrac{1}{2} Q_{11}^{0*} J_0^2 + \tfrac{1}{24} \Lambda_1^{0*} J_0^4 + \tfrac{1}{720} L_1^{0*} J_0^6, \\ \sigma_1^0 = \sigma_2^0 &= \tfrac{1}{2} Q_{12}^{0*} J_0^2 + \tfrac{1}{24} \Lambda_2^{0*} J_0^4 + \tfrac{1}{7}\tfrac{1}{720} L_1^{0*} J_0^6. \end{aligned}\right\} \tag{26}$$

The thermomagnetic constant measured at constant strain, which determines the thermomagnetic properties, satisfies the relations

$$p_n^\varepsilon = \left(\frac{\partial H_n}{\partial T}\right)_{\varepsilon J} = -\left(\frac{\partial S}{\partial J_n}\right)_{\varepsilon T}, \tag{27}$$

$$p_3^\varepsilon = p^0 J_0 + \tfrac{1}{6} \varphi_1^0 J_0^3 + \tfrac{1}{120} \Omega_1^0 J_0^5. \tag{28}$$

The specific heat measured at constant strain and constant magnetization, which determines the thermal properties, satisfies the relation

$$C^{\varepsilon J} = C_0^\varepsilon - \frac{T}{\rho}\left(\tfrac{1}{2} r_0 J_0^2 + \tfrac{1}{24} \psi_1^0 J_0^4\right). \tag{29}$$

The amount of heat liberated incident to polarization is

$$\Delta Q^0 = -T\left(\tfrac{1}{2} p^0 J_0^2 + \tfrac{1}{24} \varphi_1^0 J_0^4 + \tfrac{1}{720} \Omega_1^0 J_0^6\right). \tag{30}$$

The tensors of the temperature coefficient of mechanical stress, measured at constant magnetization, which determine the thermomechanical properties, satisfy the relations

$$\beta_i^{*J} = \left(\frac{\partial \sigma_i}{\partial T}\right)_{\varepsilon J}, \quad \beta_i^J = -\left(\frac{\partial S}{\partial \varepsilon_i}\right)_{JT}, \tag{31}$$

$$\left.\begin{aligned}\beta_3^{*J} &= \beta^0 + \frac{1}{2} m_{11}^{0*} J_0^2 + \frac{1}{24} K_1^{0*} J_0^4, \\ \beta_1^{*J} &= \beta_2^{*J} = \beta^0 + \frac{1}{2} m_{12}^{0*} J_0^2 + \frac{1}{24} K_2^{0*} J_0^4,\end{aligned}\right\} \tag{32}$$

$$\beta_3^J = \beta_3^{*J} - S^0, \quad \beta_1^J = \beta_2^J = \beta_1^{*J} - S^0. \tag{33}$$

The constant coefficients $\gamma^{0T}, \ldots, t_{11}^0, \ldots, Q_{11}^{0*}, \ldots, K_2^{0*}$ are some of the independent components of the tensors in Eqs.(6)-(8). They are considered to be independent of the polarization magnetization. They may, however, be functions of the deformation and the temperature.

In expanding the expressions for the tensor constants as functions of the polarization magnetization, the number of terms maintained varies, depending on the range of variation of J_0.

Comparison of the series of (16), (14), and (15) shows, when one recalls the definition of the reciprocal of the susceptibility, that Eq.(16) can be written*

$$H_3^0 = \int_0^{J_0} \gamma_{33}^{\varepsilon T}(J_3)\, dJ_3 = \gamma_{11}^{\varepsilon T} J_0. \tag{34}$$

From the same considerations, as well as from (18) and (28), Eqs.(26) and (30) can be rewritten

$$\sigma_3^0 = \int_0^{J_0} h_{33}^{*T}(J_3)\, dJ_3, \quad \sigma_1^0 = \sigma_2^0 = \int_0^{J_0} h_{31}^{*T}(J_3)\, dJ_3 \tag{35}$$

$$\Delta Q^0 = -T \int_0^{J_0} p_3^{\varepsilon}(J_3)\, dJ_3. \tag{36}$$

Bearing in mind the differential relations implied by (6)-(8) among the coefficients f_{mnfgij}^{0*}, $N_{mnpqfgij}^{0*}$ and Q_{mnfg}^{0*}, Λ_{mnpqfg}^{0*}, and invoking Eqs.(18) and (19), we find that we can rewrite Eqs.(22)-(25) in the form

$$C_{ij}^{JT} = C_{ij}^{0T} + \frac{\partial}{\partial \varepsilon_j} \int_0^{J_0} h_{3i}^{*T}(J_3)\, dJ_3. \tag{37}$$

From the same considerations, we may use (28) and (16) or (18), (19) and (28) to rewrite (29) or (32) and (33) in the forms

$$C^{\varepsilon J} = C_0^{\varepsilon} - \frac{T}{\rho} \frac{\partial^2}{\partial T} \int_0^{J_0} p_3^{\varepsilon}(J_3)\, dJ_3 = C_0^{\varepsilon} - \frac{T}{\rho} \frac{\partial^2}{\partial T^2} \int_0^{J_0} H_3(J_3)\, dJ_3, \tag{38}$$

$$\beta_i^{*J} = \beta_i^0 + \frac{\partial}{\partial T} \int_0^{J_0} h_{3i}^{*T}(J_3)\, dJ_3, \quad \beta_i^J = \beta_i^0 + \frac{\partial}{\partial \varepsilon_i} \int_0^{J_0} p_3^{\varepsilon}(J_3)\, dJ_3. \tag{39}$$

It is interesting to note also, as is easily seen by comparing (15) and (14) or (18) and (19), that expressions (15) and (19) can be obtained formally from the relations

$$\gamma_{11}^{\varepsilon T} = \gamma_{22}^{\varepsilon T} = \frac{1}{J_0} \int_0^{J_0} \gamma_{33}^{\varepsilon T}(J_3)\, dJ_3, \tag{15'}$$

*The factor $\gamma_{33}^{\varepsilon T}(J_3)$ in (34) is that given by (14) with J_3 replacing J_0.

$$h_{24}^{*T} = \frac{1}{J_0}\int_0^{J_0} [h_{33}^{*T}(J_3) - h_{31}^{*T}(J_3)]\, dJ_3. \qquad (19')$$

3. Let us now analyze the above relations. First, unlike the similar equations of state for piezoelectric or polarized electrostrictive media (see Refs.4-7, for example) the constants h_{mi}^{*T} and h_{mi}^{T} or β_i^{*J} and β_i^{J} are not equal, according to (20) and (33). Physically this means that if the medium is not magnetostrictive, (if $h_{mi}^{*T} = 0$) or if its coefficient of thermal expansion is zero (i.e., if $\beta_i^{*J} = 0$) deformation due to a change of the specific volume will cause a change in J_q (but not in M_q) or in the heat ΔQ per unit volume.

Second, the present method can be used to establish relations between certain constants. These relations can be established (a) between the components of any tensor constant that may have been considered independent on the basis of symmetry considerations for a transversely isotropic medium (such as the polarized magnetostrictive medium under consideration) (see, for example, (14) and (15) or (18) and (19)), and (b) between the components of different constants (see (37)-(39)). Finally, our method can be used to express the dependence of the tensor constants on the polarization magnetization.

The constants $\gamma_{11}^{\varepsilon T}$ and $\gamma_{33}^{\varepsilon T}$ as well as h_{33}^{*T}, h_{31}^{*T} and h_{42}^{*T} are in a sense dependent. To see this, let us assume that we have measured experimentally the dependence of $\gamma_{33}^{\varepsilon T}$ or h_{33}^{*T} and h_{31}^{*T} on J_0. Now we note that the expansions for $\gamma_{11}^{\varepsilon T}$ or h_{42}^{*T}, that is Eqs.(15) and (14) or (19) and (18), contain the same expansion coefficients as those for $\gamma_{33}^{\varepsilon T}$ or h_{33}^{*T} and h_{31}^{*T} (they differ only by well defined numerical factors). Therefore the experimental observations can be used with (15) and (19) (or (15') and (19')) for a direct calculation of $\gamma_{11}^{\varepsilon T}$ and h_{42}^{*T} and of their dependence on J_0.

If in the expression for the variation of the magnetostriction constant as a function of the polarization magnetization one can neglect quadratic and higher order terms, which is entirely allowable over some J_0 intervals in certain ferromagnets, the components h_{24}^{*T}, h_{33}^{*T} and h_{31}^{*T} are much more simply related. As is seen from (19) and (18),

$$h_{24}^{*T} = \frac{1}{2}(h_{33}^{*T} - h_{31}^{*T}). \qquad (40)$$

It should also be noted that, as Brown[1] pointed out, in a polarized medium the components C_{31}^{JT} and C_{13}^{JT} of the elastic modulus tensor are not in general equal, so that C_{ij}^{JT} should have six independent components. The formulas we deduced can be used to evaluate this difference. As may be seen from (23) and (26), the difference between C_{31}^{JT} and C_{13}^{JT} is of the same order of magnitude as the difference between the stresses σ_3^0 and σ_1^0 that develop due to magnetostriction in a confined (i.e., kept to constant dimensions) ferromagnet when it is magnetized from 0 to J_0. As regards order of magnitude these stresses are equal to or less than $C_{33}^{JT}\lambda_{(s)}$. Thus

$$(C_{31}^{JT} - C_{13}^{JT}) / C_{33}^{JT} \sim \lambda_{(s)}.$$

Recalling that $\lambda_{(s)} \sim 10^{-5}$-$10^{-6}$, we find that for all practical purposes

$$C_{31}^{JT} = C_{13}^{JT}. \qquad (41)$$

Thus the elastic modulus tensor has five independent components, although to terms quadratic in J_0, as is seen from (25), the number of independent components is four. Equations (22)-(25) determine the anisotropy of the so-called ΔE and ΔG effects.

In magnetostrictive media in which the volumetric magnetostriction can be neglected as compared with linear magnetostriction, we may add to the first of Eqs.(12) the restriction that when $\Delta T = 0$ and $\sigma_i - \sigma_i^0 = 0$, then $\varepsilon_1 + \varepsilon_2 + \varepsilon_3 = 0$. This restriction reduces the number of independent components of h_{mi}^{*T} still further. We then have

$$h_{31}^{*T} = -h_{33}^{*T}(C_{11}^{JT} + C_{12}^{JT} - 2C_{13}^{JT})/2(C_{33}^{JT} - C_{13}^{JT}), \tag{42}$$

or in the approximation $C_{11}^{JT} \approx C_{33}^{JT}$ and $C_{12}^{JT} \approx C_{13}^{JT}$:

$$h_{31}^{*T} = -\frac{1}{2} h_{33}^{*T}. \tag{42'}$$

4. For the purpose of design calculation it is often convenient to use variables other than J_q, ε_i and T as the independent thermodynamic variables. It is easy to transform to new variables by algebraic transformations and solve Eqs.(12) for the variables of interest.

If ε_j, H_m and T, for example, are chosen as the new variables, we obtain

$$\left.\begin{aligned} \sigma_i - \sigma_i^{0HT} &= C_{ij}^{HT}\varepsilon_j + e_{mi}^{*T}H_m + \beta_i^{*H}\Delta T, \\ J_n - J_n^{0\varepsilon T} &= -e_{nj}^{T}\varepsilon_j + \chi_{mn}^{\varepsilon T}H_m - q_n^{\varepsilon}\Delta T, \\ \Delta Q - \Delta Q_0^{\varepsilon H} &= -T\beta_j^{H}\varepsilon_j - Tq_m^{\varepsilon}H_m + \rho C^{\varepsilon H}\Delta T. \end{aligned}\right\} \tag{43}$$

If σ_i, J_n and T are chosen as the new variables, we obtain

$$\left.\begin{aligned} \varepsilon_j - \varepsilon_j^{0JT} &= s_{ji}^{JT}\sigma_i - g_{nj}^{*T}J_n - \alpha_j^{*J}\Delta T, \\ H_m - H_m^{0\sigma T} &= g_{mi}^{T}\sigma_i + \gamma_{mn}^{\sigma T}J_n + p_m^{*\sigma}\Delta T, \\ \Delta Q - \Delta Q_0^{\sigma J} &= -T\alpha_i^{J}\sigma_i - Tp_n^{\sigma}J_n + \rho C^{\sigma J}\Delta T. \end{aligned}\right\} \tag{44}$$

If σ_i, H_m and T are chosen as the new variables, we obtain

$$\left.\begin{aligned} \varepsilon_j - \varepsilon_j^{0HT} &= s_{ij}^{HT}\sigma_i - d_{mj}^{*T}H_m - \alpha_j^{*H}\Delta T, \\ J_n - J_n^{0\sigma T} &= -d_{ni}^{T}\sigma_i + \chi_{nm}^{\sigma T}H_m - q_n^{*\sigma}\Delta T, \\ \Delta Q - \Delta Q_0^{\sigma H} &= -T\alpha_i^{H}\sigma_i - Tq_m^{\sigma}H_m + \rho C^{\sigma H}\Delta T. \end{aligned}\right\} \tag{45}$$

The tensor constants in Eqs.(43)-(45) can be written in terms of those of (13)-(33) and in terms of each other. The relations are obtained automatically in the process of algebraic transformation to the new variables. They are analogous to those presented elsewhere[4-6] for the corresponding constants in piezoelectrics and polarized ferroelectrics.

If we now choose the entropy S, rather than T as one of the independent variables, we can readily find the relations between the isothermal and adiabatic values of the tensor constants.

5. In conclusion it should be noted that the above results can be used for electrostrictive media such as barium titanate ceramic. This is done by performing substitutions $H_q \to E_q$, $J_q \to P_0$ and $J_0 \to P_0$ where E_q is the electric field strength and P_q is the electric polarization (electric moment per unit volume).

Institute of the Physics of Metals,
Ural Branch of the USSR Academy of Sciences

References

1. W.F.Brown, Rev.Mod.Phys., 25, 131 (1953).
2. W.F.Brown, Am.J.Phys., 19, 290, 333 (1951).
3. L.D.Landau & E.M.Lifshits, Statisticheskaia fizika (Statistical physics), M.-L. 1951.
4. W.P.Mason, Piezoelectric crystals and their application to ultrasonics. (Cited in Russian trans. M., 1951.)
5. A.F.Devonshire, Phil.Mag., 42, 1065 (1951); Problemy sovremennoi fiziki (Problems of modern physics), No.6, 50, M. 1953.
6. J.F.Haskins & J.S.Hickman, JASA, 22, 584 (1950).
7. W.G.Cady, Piezoelectricity. (Cited in Russian trans., M. 1949).

SOME NEW EXPERIMENTS WITH BITTER FIGURES

- L.F.Bates

Maze Patterns

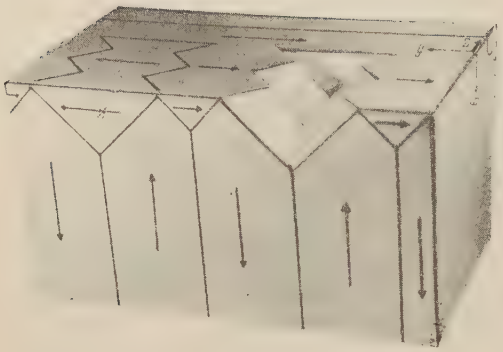

Fig.1. Model to account for maze patterns.

In this communication I wish to describe some new experiments on Bitter figures which have been made in Nottingham during the last few years, and I should first like to deal with some qualitative work on maze patterns. It is very strange that although the maze pattern was one of the earliest, if not the earliest pattern to be recorded, no quantitative or systematic work on the subject appears to have been done until 1955 when Chikazumi and Suzuki[1] published their paper on maze patterns on silicon-iron. In their work Chakazumi & Suzuki studied the changes in maze patterns as the strained surface layers responsible for them were progressively removed by electrolytic polishing.

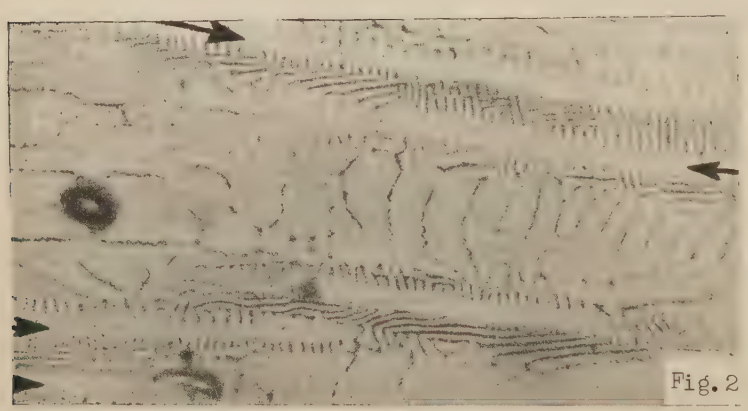

Fig.2. Maze patterns on (100) surface of silicon-iron.

They concluded from their experiments, particularly those in which strains were produced by scratches on the surface, that they could represent a maze domain as a special kind of closure domain whose purpose is to carry the magnetic flux of the underlying principal domains. The structure which Chikazumi & Suzuki suggested in a figure in their paper lends itself to reproduction in the form of a simple model which we have made in cardboard, and of which a photograph is given in Fig.1. Let us now see how far this model accounts for some new patterns photographed by P.F.Davis & P.M.Griffiths in my laboratory.

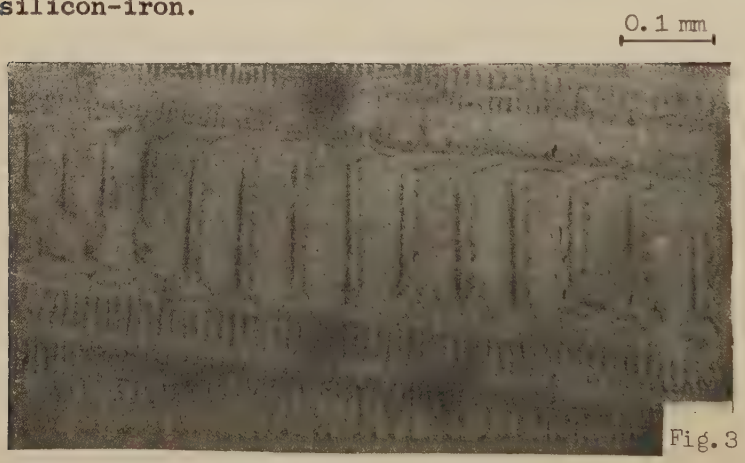

Fig.3. Maze patterns with lines probably due to free poles.

In Fig.2 are reproduced photographs of the maze patterns formed on a (100) surface of a single crystal of silicon-iron, which was lightly electropolished following the usual mechanical polishing to 0000 emery. Some

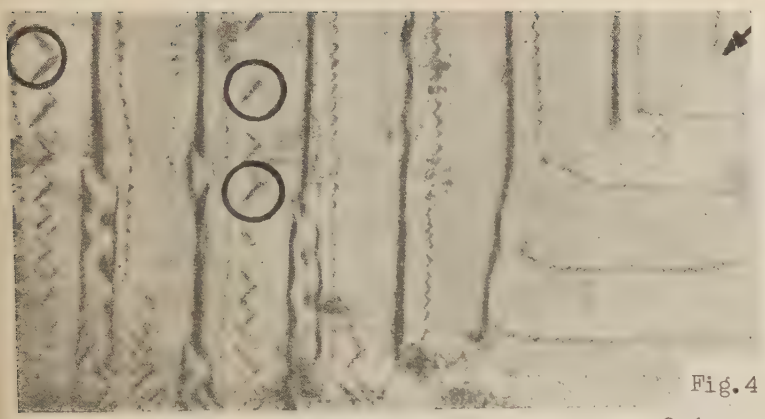

Fig.4. Two types of maze pattern.

deep scratches were deliberately made in the surface and these are indicated by arrows at the sides of the photograph; as usual, a weak magnetic field was applied normal to the surface in order to bring out the pattern more clearly. The width of the maze domains is the smaller the nearer they are to the scratches, as recorded by Chikazumi & Suzuki, who also showed that the domain width should be inversely proportional to the square root of the stress in the region in which the domain is situated. Incidentally, the maze domains are approximately parallel to the easy directions of magnetization in the surface.

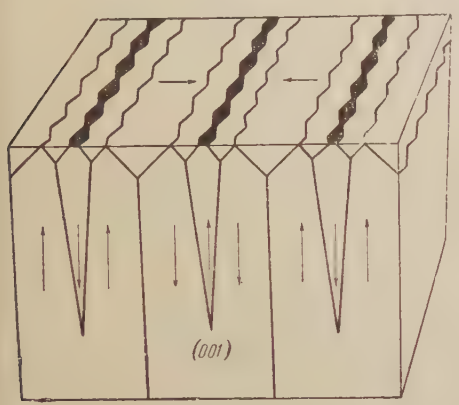

Fig.5. New model for maze patterns and line deposits.

But Fig.3, which is unfortunately rather dense, shows a feature not mentioned hitherto, and which requires modification of the model in order to provide a satisfactory picture of the phenomenon. There are lines of free poles, manifested by dense lines of deposit, parallel to some of the zig-zag boundaries which run vertically in the figure. It is, of course, possible that alternate zig-zag boundaries are suppressed by the action of the small applied normal field, and it might be suggested that the vertical field causes the appearance of the lines of free poles, but in Fig.4 we have the two types of structure present in the one picture. Here, we have the normal type of pattern running horizontally across the photograph, while running vertically we have the dense lines of colloid between alternate zig-zag boundaries. A 90° wall, marked by an arrow, runs between the two types of structure to a corner of the specimen.

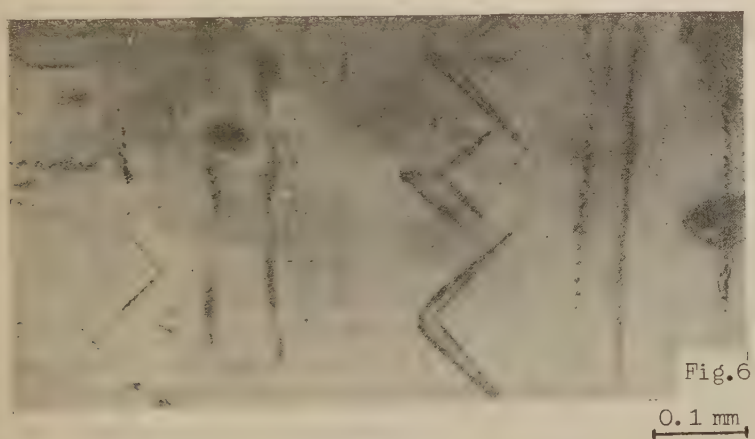

Fig.6. Spike domains attached to domains of reverse magnetization.

Fig.5 shows a modification of the first model which it is thought might explain the formation of the new lines. We think that a kind of Lifshits structure is formed in the specimen. The zig-zag closure structures are conditioned by the difference in strain energy between them and the underlying principal domains; as Lifshits showed, if this energy difference is large, one would expect branching of the principal domains near the surface.

Fig.7. Domains of reverse magnetization (Martin).

In Fig.4 there are many spike domains; some of them are ringed. At first these were thought to be ordinary Néel spike closure domains formed at inclusions, and this would of course have meant that the surface domains were magnetized longitudinally with respect to the zig-zag boundaries, which would be contrary to the Chikazumi and Suzuki model. However, Fig.6 (actually taken of a different specimen), shows that these spikes must be attacned to domains of reverse magnetization like those described by Bates & Martin[3] and illustrated in Figs.7 & 8. In the latter picture a large domain of reverse magnetization spreads downwards over the surface as a magnetizing field is reduced.

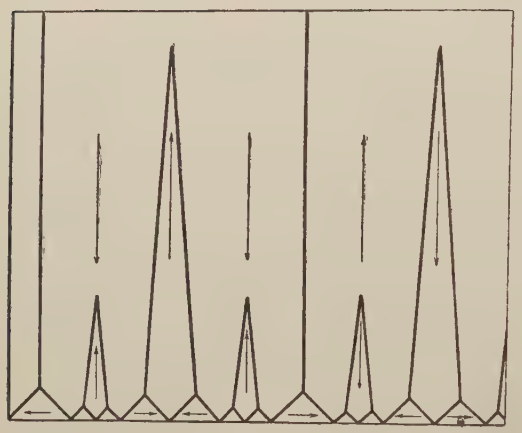

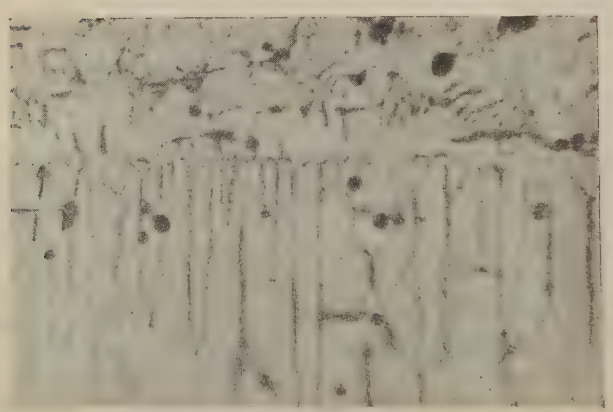

Fig.8. a) Diagram of Lifshits closure domain.
b) Bitter figures on Columax.

Lifshits Closure Structures

It is well-known that Lifshits[2] predicted that a metal like cobalt, which possesses only two directions of easy magnetization, ought to exhibit the particularly striking kind of closure domain structure shown in Fig.8a. However, this structure has never been observed in its entirety in the case of cobalt, perhaps because the anisotropy is so great that the small triangular domains are suppressed. For example, in Figs. 9a & b are reproduced pictures taken by D.J.Craik & C.D.Mee, respectively, of the surface of a circular disc cut from a side of a cobalt crystal parallel to the crystalline axis. The single crystal specimen had been slightly damaged during its mounting, and there are a few small crystal grains near one of its edges. In Fig. 9a, taken with a special phase contrast technique, three such grains are visible, while in Fig. 9b a portion

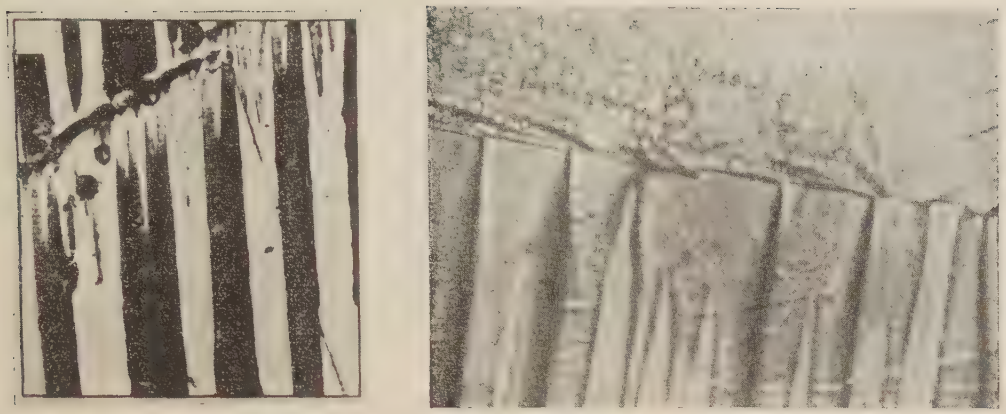

a b

Fig.9. Bitter figures on cobalt a) at grain boundaries (photographed by D.J.Craik), b) at damaged portion of surface (photographed by C.D.Mee).

of the damaged surface is shown. In neither Fig.9a nor 9b do we see the small triangular closure domains predicted by Lifshits. But we do see them in all their beauty in Fig.8b obtained by P.F.Davis on the surface of a specimen of undeveloped 'Columax' (columnar alcomax or alnico V) which had been quenched in oil after an anneal at 940°C. Running across the picture is a boundary between two crystallites and close to the boundary are the large dagger shaped domains of reverse magnetization, while at the boundary itself are the small triangular closure domains magnetized perpendicularly to the main domains. Incidentally, one may sometimes obtain on Columnax crystallites the "fir tree" patterns - like those on silicon-iron - so well explained by Bozorth and his colleagues.[6] Indeed, a crystallite adjoining that shown in Fig.8b had a (100) plane almost exactly in the surface of the specimen and gave a good "fir tree" pattern.

There are two types of daggers in Figs.8a & b and it is possible to calculate the theoretical ratio of their lengths approximately. Unfortunately, it is very difficult to obtain photographs from which satisfactory measurements can be made, but from two moderately reliable measurements which Davis was able to make, we consider that the agreement between experiment and theory is reasonably good.

Lozenge and "Tadpole" Domain Structures

In a recent publication Paxton & Nilan[4] gave photographs of what they call "lozenge" patterns on a small grain in a thin disc of silicon-iron. They found that these patterns occurred on surfaces which were approximately (110) planes but which were inclined at an agle of between 4° and 7° to the [001] direction. In Fig.10, taken by P.F.Davis, the edge of a single crystal of rectangular shape lies in the upper, dark region of the photograph. Due to the effects of electrolytic polishing the outer portions of the crystal surface were rounded, and near the edge, where the surface most deviates from a true crystal plane, are many lozenges which point toward the edge in the [001] direction. The crystal was magnetized in parallel strips, with the directions of magnetization either along the [001] or along the [00$\bar{1}$] direction, and along the line between the arrows there runs a 180° boundary between two such strips.

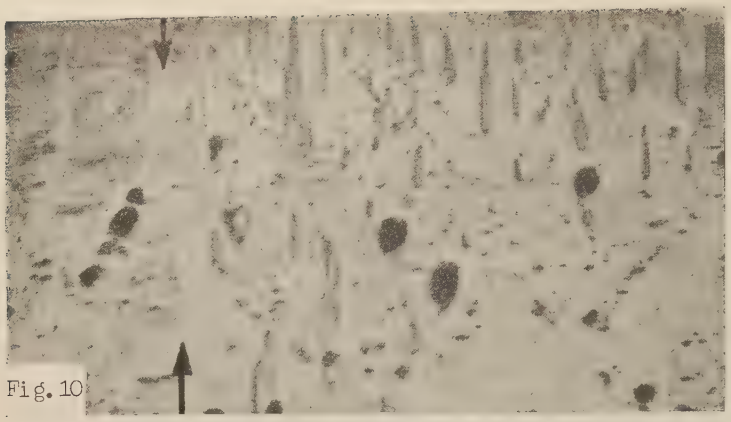

Fig.10. Lozenge patterns on surface close to a (110) plane of silicon-iron; arrows indicate 180° wall (P.F.Davis).

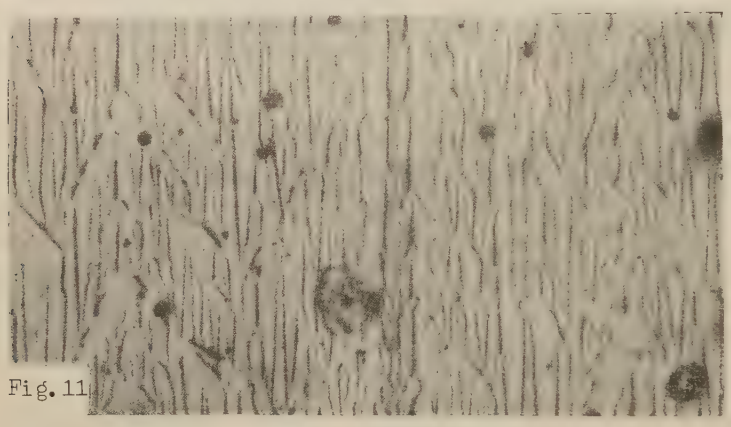

Fig.11. Large lozenge domains (P.F.Davis).

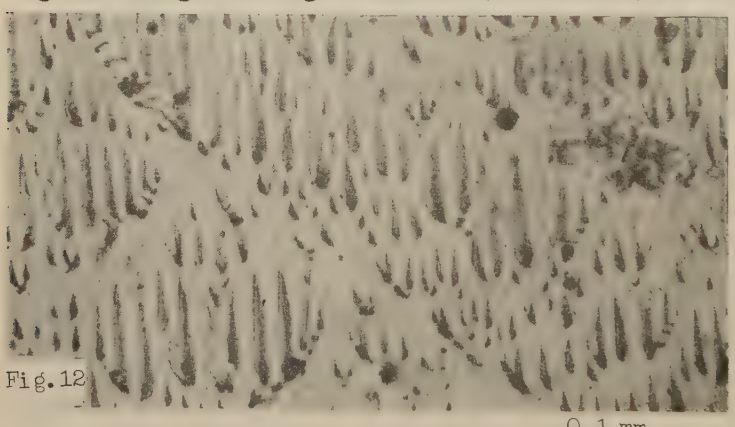

Fig.12. Lozenge patterns and some "tadpole" patterns on crystal magnetized nearly to saturation in the [111] direction (P.F.Davis).

Fig.11 was taken with another specimen which consisted of two crystals, one about three times as large as its fellow. The surface of the larger crystal was deliberately oriented to make an angle of 4° with respect to the [001] direction, and the very large lozenge seen in the picture was situated in the middle of its surface. This picture is typical of zero or low field conditions. When a field was applied along the [100] direction the lozenges changed in an irregular manner and the conditions shown in Fig.12 were reached when the crystal was nearly saturated. In this figure the lozenges seem to be arranged in bands approximately parallel to the $[1\bar{1}1]$ direction, and close inspection shows the presence in a few isolated regions of the surface of another kind of pattern, termed a "tadpole" pattern by Bates & Hart[5].

The appearance of the surface near the junction of the two crystal grains under field conditions similar to those for Fig.12 is shown in Fig.13. In the latter figure, there are many "tadpole" patterns running from the grain boundary, which is off the picture to the right, into the larger crystal. The axes of the "tadpole" patterns are inclined at about 35° with respect to the [001] direction - i.e., the "tadpoles" set themselves along the $[1\bar{1}1]$ direction. A few lozenges can be seen on the left of the photograph.

Paxton & Nilan observed that in the demagnetized state and in low fields the lozenges were arranged in rows parallel to the $[1\bar{1}0]$ direction. When they applied a small field in approximately the [001] direction, alternate

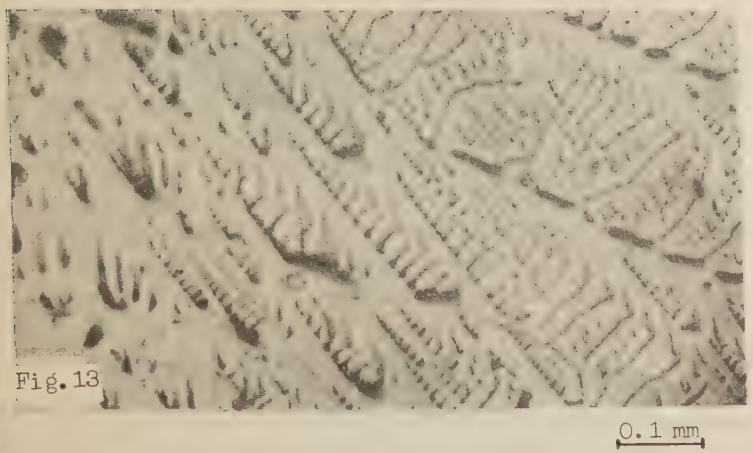

Fig.13. "Tadpole" patterns running from grain boundary between two crystals.

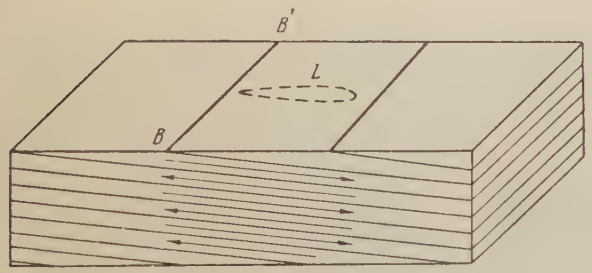

Fig.14. Illustrating conditions for formation of lozenge patterns.

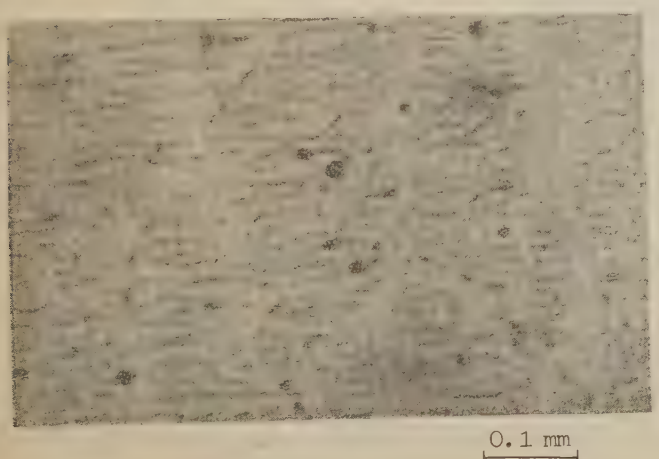

Fig.15. Bands of lozenge patterns near edge of crystal.

rows of lozenge patterns expanded at the expense of neighboring rows, yet no domain boundaries were seen between the rows of lozenges. This suggests that in low and zero fields the principal domains form layers, magnetized alternately in the $[00\bar{1}]$ and $[00\bar{1}]$ direction, so that their walls intersect the surface under observation in a series of lines such as BB' in Fig.14. As the walls make only a small angle with the surface under observation, BB' cannot be marked by a line of dense colloid, since the stray field above it would be very weak. The position of a typical lozenge is indicated in Fig.14 by the dotted outline L.

Fig.15 illustrates an interesting and unexplained phenomenon which is observed near an edge of a crystal (right edge in photograph) under zero field conditions. The lozenges form bands whose breadth increases steadily as their distance from the edge increases. Incidentally, it is found that the lozenges point downhill.

P.F.Davis has suggested a model which would explain the formation of "tadpoles". This model is pictured in Fig.16; we see that the "tadpoles" can be formed by the intersection of a large Néel spike closure domain with the surface. If the intersection were devoid of any modification, a large surface magnetization would occur. This is prevented if a set of subsidiary spikes takes care of the flux. These must be wedge shaped with small gaps between neighbors; each gap would be a narrow band of free poles and, consequently, would attract deposit and form a "tadpole". The explanation is similar to that given by Bates & Mee[6] to account for the formation of the beautiful lace patterns on the (110) surface of a Néel cut specimen of silicon-iron. The narrow bands lie parallel to the $[1\bar{1}1]$ direction as do the "tadpoles".

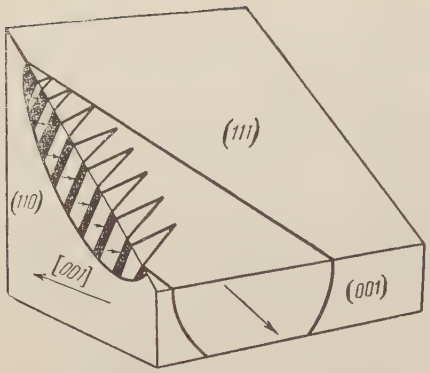

Fig.16. Model to illustrate formation of "tadpole" patterns.

Bates & Hart[5] made a special study of the patterns found on polycrystalline surfaces to see to what extent they reproduced the patterns found on single crystal surfaces. They used grain-oriented silicon-iron because the planes of intersection of many of the grains in a sheet specimen with the sheet surface are close to a (110) plane. It is therefore not surprising that they found patterns which were virtually the normal "lace" patterns observed by Bates & Mee[6] on the (110) surface of a Néel cut specimen. It was in the course of this work that "tadpole" patterns were first observed, and from the fact that these patterns always appeared near to the edge of a crystal, it was concluded that they were a special type of closure structure masking a more simple elementary domain structure and that the "blobs" or heads of the "tadpoles" were evidence of sharply localized stray fields.

Echelon Structures

If one takes a rectangular block specimen of pure iron or of silicon-iron with every face a (100) plane, and one cuts one end of the specimen so that the block terminates in a (111) surface, one finds on that surface in the demagnetized state a complicated Bitter pattern of remarkably fine texture (Fig.17) with a periodicity of about $6 \cdot 10^{-4}$ cm compared with about 10^{-1} cm for the principal domains on the adjacent surfaces. We have already seen that Lifshits suggested that principal domains should subdivide near surfaces whose orientations are such that they do not contain a direction of easy magnetization. In the course of experiments along these lines D.H.Martin attempted to correlate the fine texture patterns on (111) and more generally on (h01) surfaces with the principal domain patterns on adjacent (100) surfaces. In this way he discovered what he has termed echelon splitting of the principal domains. An example of this kind of pattern is shown in the photographs of Fig.18 with an explanatory diagram. It is clear that such a structure avoids the formation of free poles, but it must have associated with it, of course, considerable magnetostriction energy.

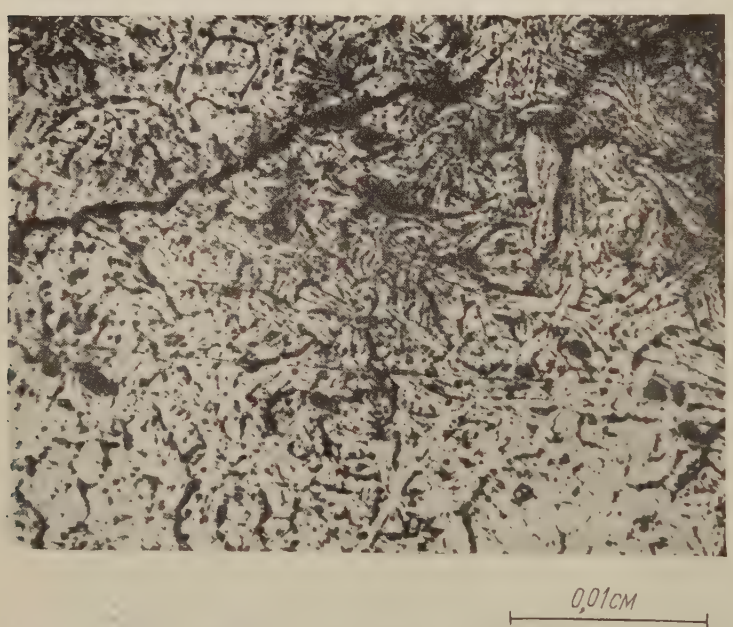

Fig.17. Fine structure pattern on a (111) surface (D.H.Martin).

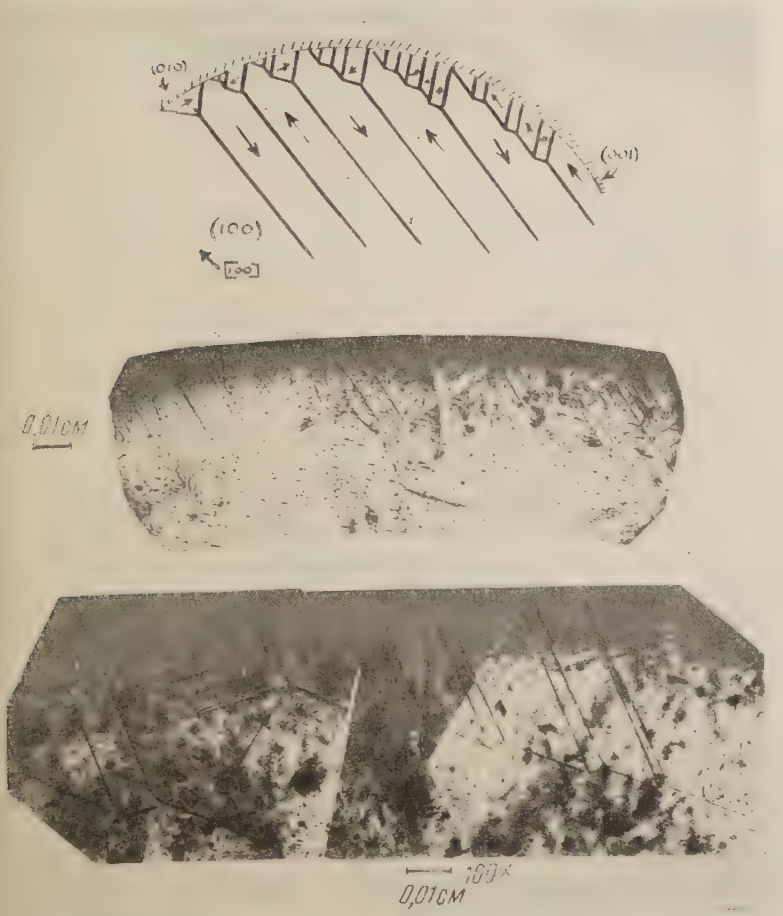

Fig.18. Echelon patterns (A.Hart) and explanatory diagram (D.H.Martin). Upper photograph - disc face near approximate (010) edge; lower photograph - disc face near approximate (001) edge.

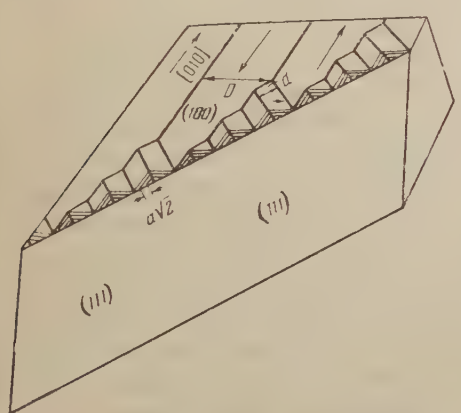

Fig.19. Theoretical aspects of the echelon structure.

The photographs of Fig.18 were obtained by A.Hart on a disc cut from a single crystal of 3% silicon-iron. Its main face was of a (100) orientation and its edges were therefore of the (h01) type. The upper and lower photographs pertain to portions of the disc face where the edges are approximately (010) and (001), respectively. "Fir tree" patterns due to rounding of the upper surface during polishing are visible on that surface, but the echelon features are nevertheless well defined. The echelons comprise two types of domains, magnetized parallel and transverse, respectively, to the magnetization of the principal domains.

As the disc was thin, it was impossible to observe patterns on its edge faces directly, but from an examination of patterns of the main face, it was possible to form conclusions about those on the edge-faces, and some support was found for a modification of the pattern predicted by Néel for the (110) face of a Néel cut specimen along lines suggested by Lawton[7].

In the light of this work, Martin has suggested the domain structure shown in Fig. 19 for the case in which the upper face of the specimen of pure iron is a (100) surface, while the sloping surface is a (111) plane. We see that we now have no less than three different domain widths to consider - D, d and a. Using the accepted values of anisotropy energy and Bloch wall energy for iron, Martin has calculated on the basis of this model the optimum domain size D and its dependence on the size of the crystal. It is not possible here to give Martin's calculations in detail, but it is very interesting to note that he

finds that the optimum domain width for a block specimen of rectangular cross section with (111) planes at both ends is nearly the same as that for a similar specimen with (010) faces at both ends. Thus far only 180° boundaries have been considered in the echelon treatment, but 90° boundaries are often found in demagnetized specimens. Martin has taken account of 90° boundaries and finds in the case of a specimen with (111) ends that if all 180° boundaries were replaced by 90° boundaries, the energy densities would differ only slightly - a truly remarkable result. These features clearly have much bearing on the optimum domain size, and therefore on magnetization processes, in polycrystalline iron. Clearly, the echelon structure deserves more experimental and theoretical investigation than it has so far been possible to give it.

Electron Microscope Studies

D.J.Craik (Boots Experimental Research Laboratories, Nottingham) in association with my laboratory has recently developed a new technique for the examination of Bitter figures, with the object of observing very much more detailed patterns and so eventually of examining the domain wall itself. For these purposes he prepared a kind of thin film replica of a pattern which could be dried without distortion and removed from the metal surface for examination either with a high power transmission microscope or with an electron microscope.

He first prepared colloidal magnetite by the Elmore recipe, peptising the deposit sufficiently for it to pass through a fine filter paper. To the filtered solution was added 0.1% of a commercial methyl ether of cellulose known by the trade name of "Celacol" and any free acid was then removed by repeated dialysis with distilled water. The "Celacol" protected the magnetite particles and maintained them in a highly dispersed state in the weak solution. A drop of the solution, on drying, formed an amorphous film sufficiently tough to be manipulated and exposed to an electron beam, even if it was only a few hundred Angstroms thick. In contrast with the colloid solutions hitherto used in Bitter figure work the new material was almost colorless, having only a faint amber tint.

The new colloid was first tried on the surface of a single crystal of cobalt, but it was found that the dry film was hard to remove and the following procedure was therefore adopted. A thin film of Formvar resin some 200 Angstroms thick was prepared by dipping a glass slide into a 0.1% solution of Formvar in ethylene dichloride and allowing the film to dry in a vertical position. By simple manipulation in water the film was floated off one end of the glass and allowed to settle on the cobalt surface. (When a silicon-iron surface was used, rusting was prevented by first coating the surface with a thin layer of quartz deposited by vacuum evaporation.) A measured quantity of the finely dispersed colloid was then placed on the film-covered surface. For examination by electron microscopy the quantity of colloid used should be sufficient to give a film some 500 Angstroms thick.

When the colloid was dry a few drops of a thick solution of collodion in amyl acetate were applied and allowed to dry; then with care the whole could be detached without damage or distortion. The great advantage of this technique is that one has a permanent film which can be examined at leisure. For electron microscope examination, chosen portions of the film were placed collodion side downwards on the standard copper grids, resting on curved strips of stainless steel mesh, below which amyl acetate could be introduced and so

the collodion removed without distorting the film.

A full account of the work has been published in the Proceedings of the Physical Society. One of Craik's pictures, an electron microscope photograph of a domain wall intersected by a scratch on a cobalt crystal (magnification - about 25,000 X), is reproduced in Fig.20. We deduce from direct measurements with the weakest possible colloid that the wall thickness is of the order of $8 \cdot 10^{-6}$ cm.

Fig.20. A 180° domain wall on a cobalt crystal intersected by a scratch (D.J.Craik). The break in the wall deposit is characteristic and has been observed very frequently.

Domain Structure and the Magnetization Curve

Akulov[8] was one of the first to use the simple concepts of reversible wall movement and the rotation of magnetization vectors in order to obtain theoretical magnetization (I vs H) curves for single crystals along chosen directions of symmetry. He considered the energy of the crystal to be the sum of its magnetocrystalline anisotropy energy and its energy in the applied field, and minimized the sum of these two energies to calculate the $I = f(H)$ curve. His work was later extended by Néel[9] and Lawton & Stewart[10] who showed independently that the energy of the crystal in its own demagnetizing field had to be taken into account. In this way a more adequate explanation could be given for example, of the shape of the experimental $I = f(H)$ curve for a single crystal of iron in the shape of an oblate spheroid.

We have, therefore, a theory which can be applied to a suitable specimen with any arbitrary direction of the crystal axes and of the applied field, but the main difficulty in the way of its application is that of calculating the demagnetization effects exactly. Because of the initial assumptions of

reversible wall movement and reversible domain vector rotations, the theoretical calculations always give a curve with infinite initial susceptibility, with kinks in regions where the mode of magnetization changes (e.g., three phase to two phase) and zero hysteresis. Nevertheless, agreement between the experimental and theoretical curves is reasonably good except in low field regions of, say, 0 to 30-40 oersteds.

Fortunately, some of the discrepancies between experiment and theory can be removed by making use of information gained from an experimental study of wall movements and surface domain structures. Some remarkably illuminating pictures of the passage of 90° and 180° domain walls across inclusions or imperfections in the surface of a silicon-iron crystal have been obtained by D.H.Martin. These pictures make it abundantly clear that only under very exceptional circumstances in ordinary, even well-annealed and carefully prepared materials, will unimpeded domain wall movements occur freely and reversibly under the action of an applied field.

A type of specimen which has provided much useful information about rotation processes, as well as about domain theory in general, is that known as the Néel cut iron or silicon-iron crystal (Fig.21). The long axis of the specimen is a [110] direction and its main upper and side faces are (100) and (110) planes, respectively. Néel postulated that when a very small effective field, in the limit tending to zero, acts upon the specimen along the [110] direction, the domain configuration is that of Fig.21a, in which the leaf-like principal domains are alternately magnetized parallel to the $[0\bar{1}0]$ and [001] directions, while on the (110) faces there exist simple closure domain systems of q-domains. When a finite effective field acts on the specimen, the principal domain vectors are forced to make an angle θ, which is less than the original 45° of Fig.21a with respect to the [110] direction, and a new set of closure domains, p-domains, are formed as shown in Fig.21b.

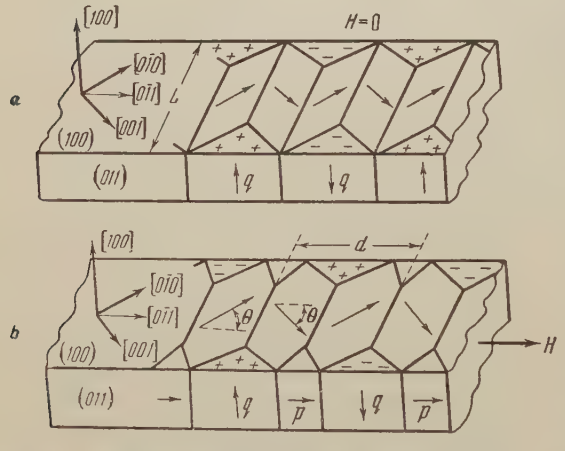

Fig.21. Illustrating the Néel cut iron crystal: a) in zero field, b) in small finite field.

Néel was able to calculate the periodicity d of the main domain system as a function of the effective field, the width L of the specimen's upper surface, and the appropriate anisotropy constants. Many experiments (Bates & Hart[5], Bates & Mee[6], Bozorth et al[11] and Bates & Neale[12]) have shown that Néel's views are essentially correct, although there is some numerical discrepancy between the calculated and observed periodicities. Moreover, the theoretical closure structure of Fig.21b is too simple, as reference to the above papers will prove. We undoubtedly get line patterns by the Bitter technique which enable us to measure the periodicity on the (100) face, but on the (110) face are found complicated "lace" patterns of the same periodicity which must be due to surface magnetization of some kind. Direct measurements by Bates & Mee of the angle between a principal domain magnetization vector and the [110] direction of different values of the effective field proved that the concept of rotation of the magnetization vectors used in the calculations was essentially correct, at any rate for a Néel cut specimen.

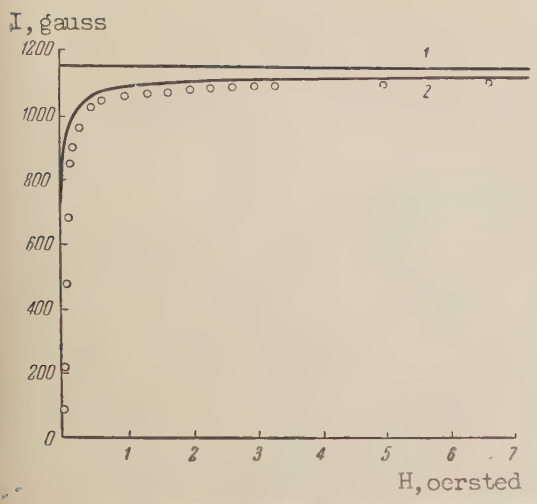

Fig.22. Calculated I vs H curves: a) Akulov, b) Lee. Experimental points by H.J.Williams.

The Néel postulation of the detailed domain structure is thus a substantial advance on earlier ideas, for it has led to a great improvement in our understanding of the detailed form of the magnetization curve. First, we have the work of Lee (1953) who suggested that the well-known lack of agreement between the experimental and theoretical magnetization curves could be due in the case of a Néel cut specimen to the neglect of the closure domain structures of Fig.21b. The closure domains are not magnetized parallel to the principal domains, and by taking account of their volumes and directions of magnetization, Lee obtained the modified magnetization curve of Fig.22 which lies considerably below the curve calculated on the theory of Akulov and of Lawton & Stewart. The new curve, which does not exhibit a sharp kink at H = 0, agrees more closely with the experimental curves, especially in the low field region up to about 40 oersteds. Another result of Lee's calculations was the prediction that the magnetization curve of the specimen would depend on the specimen depth L. The thinner the specimen, the greater the volumes of the closure domains relative to those of the principal domains and the more pronounced the depression below the Akulov curve. Thus Lee's results led to the theoretical magnetization curves such as those in Fig.23.

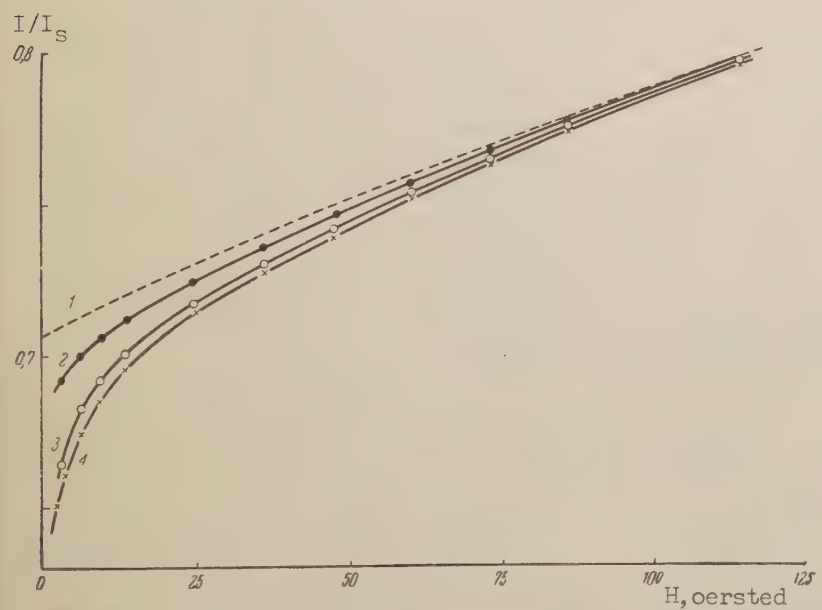

Fig.23. Theoretical magnetization curves for different specimen depths L: 1) L = ∞, 2) L = 0.6 cm, 3) L = 0.1 cm, 4) L = 0.06 cm.

Now, this predicted change of shape of the magnetization curve with specimen depth has, as far as is known, never been recorded, possibly because the expected change is small except in very low fields, and possibly because measurements of single crystal magnetization curves are rather rare and by no means systematic. Consequently, observations were recently made[13] of the domain structure of a 3.8% Si silicon-iron Néel cut specimen having an overall length 1.25 cm in the [110] direction, a (110) surface 0.58 cm wide and a depth of the (100) surface of 0.11cm. Throughout these experiments the length and width of the crystal were maintained unchanged, but the depth L was from time to time reduced by mechanical abrasion followed by electrolytic polishing,

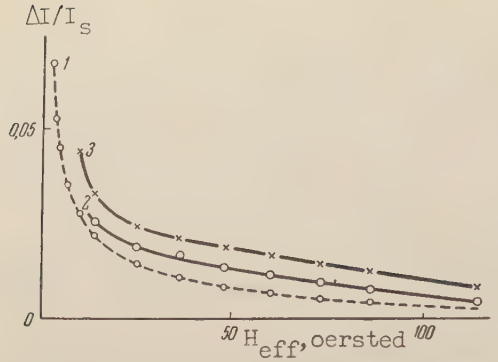

Fig.24. Difference between the Akulov magnetization curve (represented by the x-axis) and 1) the magnetization curve for L = 0.072 cm calculated from theoretical domain sizes, 2) the magnetization curve from experimentally observed domain sizes and 3) the magnetization curve obtained by direct measurement.

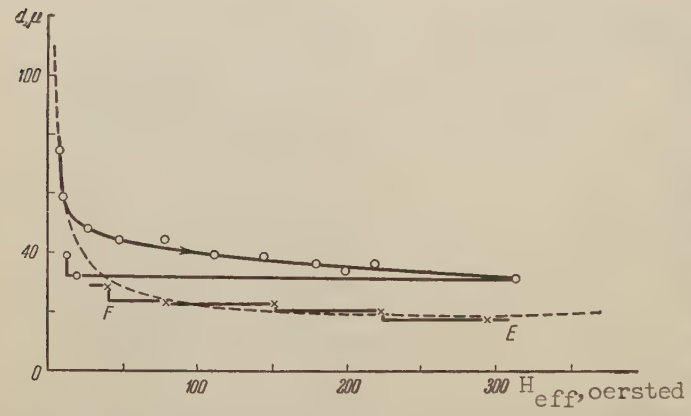

Fig.25. Hysteresis of the domain spacings on a Néel cut surface. The specimen depth is 0.072 cm. Dash-line - theoretical curve calculated by Néel; experimental points: o - H increasing, ● - H decreasing, X - H decreasing from 500 oersteds.

so that the influence of the crystal depth on the domain patterns and their periodicity, and hence on the magnetization curve, might be found. For depths L between 0.11 cm and 0.06 cm the general results were in good agreement with earlier work done at Nottingham. As can be seen from Fig.25 by comparison of the upper curve with the broken (Néel theory) curve, the experimental values of d are always greater than the theoretical ones; moreover, there is no minimum in the experimental $d = f(H)$ curve.

The first significant result of these measurements is that when the experimental values of d for different specimen depths are fitted into the appropriate form of Lee's calculations, the calculated variation of the magnetization curve with specimen depth is much less marked than before, and is, in fact, of an order which would probably remain undetected by present experimental methods. At the same time, for a specimen of depth L = 0.1 cm, the magnitude of the deviation from the Akulov curve based on the experimental values of domain size is about twice that based on theoretical domain sizes. The curves of Fig. 24 show the difference ($\Delta I/I_s$) between the Akulov curve for L = $= \infty$ and (1) the magnetization curve for L = 0.072 cm calculated using theoretical domain sizes, (2) the magnetization curve calculated using the experimentally observed domain sizes, and (3) the magnetization curve measured directly with the same crystal. It is instructive to plot curves, that might be compared with Fig. 23, showing how the variation of observed domain size with specimen depth modifies the magnetization curves originally calculated by Lee.

The measurements of domain size also provided new information concerning hysteresis phenomena in the region from technical saturation down to the zero field region. This may be seen by reference to Fig.25. The experimental values of the periodicity d shown on the continuous curve were obtained from photographs of the line patterns on the (110) surface, taken after the chosen effective field had been reversed twenty times to ensure that the specimen was in an equilibrium state. The dash-line represents the theoretical curve obtained on the basis of Néel's calculations for the stated specimen depth. The numerical discrepancy between the experimental and theoretical results is

manifest and experiment does not give the minimum spacing predicted by Néel's theory.

Now let us turn to the curve which was obtained in the following manner. The crystal was normally exposed to an effective field of 300 oersteds, the highest field which could safely be used without destroying the domain patterns. The field was then reduced slowly, and it transpired that the domain pattern or periodicity remained unchanged over wide field variations. Occasionally, however, sudden changes of periodicity occurred, and these are indicated by the crosses at the appropriate field values at which they were recorded. An excellent example is provided by the curve EF which was obtained by exposing the specimen to an effective field of over 500 oersteds, when it was technically saturated and no Bitter figures would be formed, and then reducing the field to 300 oersteds when Bitter figures could again be seen. Sudden changes in the periodicity took place as the field was reduced from 300 oersteds to low values.

The work therefore shows that there can often be two equilibrium values of domain sizes at the same field value, corresponding to two different volumes of the closure domains. Thus, although the rotation of the magnetization vectors in the principal domains may be reversible, the different volumes of the closure domains show hysteresis. The magnitude of this hysteresis may be calculated by a modified analysis, and Hart found for a specimen of depth 0.07 cm that the subsidiary hysteresis loop in a field range from 10 to 200 oersteds encloses an area corresponding to a loss of the order of 1200 ergs per cc per cycle for a maximum induction of 18,000 gauss. As the total loss measured along the [110] direction for a complete hysteresis loop with maximum fields of 200 oersteds is about 4500 ergs per cc per cycle, we see that hysteresis losses associated with closure domains may be very important.

It follows that for the special case of a Néel cut specimen we have shown that a virgin magnetization curve without sharp kinks and with a finite value for the initial susceptibility is theoretically predicted. It is obviously desirable to determine detailed domain structures for specimens of other shapes and to apply the above treatment to them.

Concluding Remarks

It is really unnecessary to emphasize further the importance of the Bitter figure technique in the elucidation of magnetization processes. In this communication I had hoped to deal also with its further application to high coercivity alloys, but the communication is already lengthy. We have already obtained domain patterns on materials with coercivities as high as 100 oersteds, and when we manage to get larger crystals cut from columnar alcomax we hope to make more fundamental experiments with them. I should like again to record my thanks to my research students whose photographs have been reproduced here, to the Department of Scientific and Industrial Research, the Electrical and Allied Industries Research Association and to all who by the provision of grants and materials have assisted us in this work. I also thank the Physical Society for permission to reproduce illustrations from the Proceedings of the Physical Society.

Nottingham University,
England

References

1. S.Chikazumi & K.Suzuki, J.Phys.Soc.Japan, 10, 523 (1955).
2. E.M.Lifshits, J.Phys.USSR, 8, 337 (1944).
3. L.F.Bates & D.M.Martin, Proc.Phys.Soc., A66, 162 (1953); Proc.Phys. Soc., B69, 145 (1956).
4. W.S.Paxton & T.G.Nilan, J.App.Phys., 26, 8, 994 (1955).
5. L.F.Bates & A.Hart, Proc.Phys.Soc., A 66, 813 (1953).
6. L.F.Bates & C.D.Mee, Proc.Phys.Soc., A64, 129, 140 (1952).
7. Lawton, Proc.Camb.Phil.Soc., 45, 145 (1949).
8. N.S.Akulov, ZS.f.Phys., 54, 582 (1931).
9. L.Néel, J.Phys. et Rad., 5, 241 (1944).
10. H.Lawton & K.H.Stewart, Proc.Roy.Soc., A193, 72 (1948).
11. R.M.Bozorth, H.J.Williams & W.Schockey, Phys.Rev., 75, 1, 155 (1949).
12. L.F.Bates & F.Neale, Proc.Phys.Soc., A63, 374 (1950).
13. L.F.Bates & A.Hart, Proc.Phys.Soc., B69, 497 (1956).

ON THE ROLE OF CLOSURE DOMAINS IN TECHNICAL MAGNETIZATION PROCESSES

- Ia.S.Shur, V.R.Abel's & V.A.Zaikova

Experimental investigations of the magnetic structure of ferromagnets by means of magnetic powder patterns (Bitter figures) have shown that there exist several types of magnetic regions or domains, namely, principal domains that may extend in the case of relatively thin crystals through the entire thickness of the ferromagnet, closure domains, located either at the edge of the specimen or distributed over its surface, that "close" the flux path to the principal domains, and subdomains which are a special form of closure domains forming near different types of defects where the homogeneity of the magnetization is disturbed.[1,2]

In the present report we shall consider questions connected with the behavior of closure domains and their role in technical magnetization. The existence of closure domains was first predicted theoretically by Landau & Lifshits[3]; subsequently, they were observed in a number of experimental studies.

We investigated the closure domains by means of powder patterns on silicon-iron crystals (4% Si). As regards preparation of the magnetic suspension, treatment of the sample surfaces and observation of the patterns we followed the procedure described earlier in Ref.1.

1. Shape of the closure domains and its relation to the natural crystallographic anisotropy

We investigated the shape of the closure domains in crystals with different crystallographic orientations of the surface. The observations were carried out on specimens in the demagnetized state. It was established that if the surface of the specimen is rigorously parallel to one of the directions of easy magnetization (i.e., if the tetragonal axis is parallel to the plane of the specimen) no closure domains appear on the surface proper; they are observed only at the ends of the principal domains (at the edge of the crystal or specimen).[1] Thus for example, closure domains in the form of triangles are observed at the boundaries of a specimen whose surface is close to a (001) plane. A photograph of the patterns on the surface of such a crystal is reproduced in Fig.1 (the arrows indicate the magnetization directions in the domains). It may be noted that such a magnetic structure was first predicted by Landau & Lifshits[3].

Fig.1. Triangular closure domains at the edges of a silicon iron crystal (4% Si). Magnification 300 X; ⟷ [100]

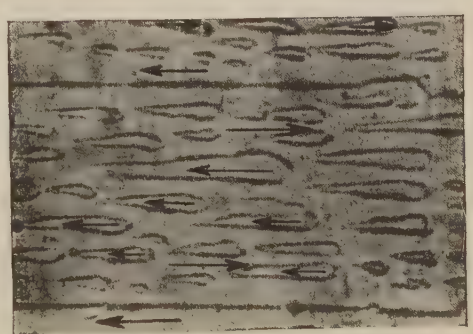

Fig.2. Drop closure domains. Magnification 300 X; ⟷ [100]

If the surface of the specimen is not parallel to one of the directions of easy magnetization, closure domains generally appear on its surface. Let us examine the forms of closure domains observed by means of powder patterns on the surface of crystals having different crystallographic orientations. Thus in the case of a specimen whose surface is close to the (011) plane, oriented so that the nearest direction of easy magnetization - the [100] direction - forms a small angle with the surface of the specimen, there are observed, in addition to the principal domains, closure domains in the shape of "drops" (Fig.2). The magnetization in the drops is oriented antiparallel to the magnetization in the principal domains.

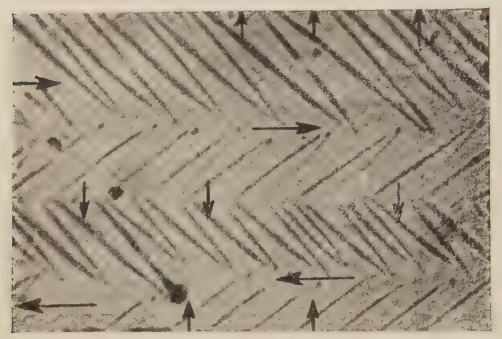

Fig.3. Fir tree closure domains. Magnification 300 X; ⟷ [100]

Fig.4. Trunk closure domains. Magnification 300 X; ⟷ [100]

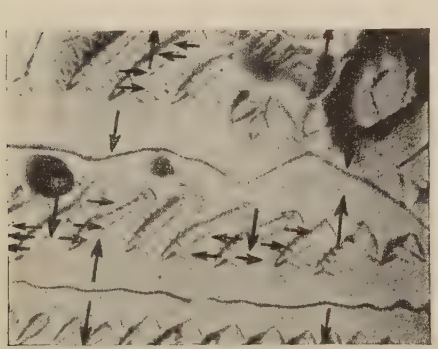

Fig.5. Comb closure domains. Magnification 300 X; ↕ [100]

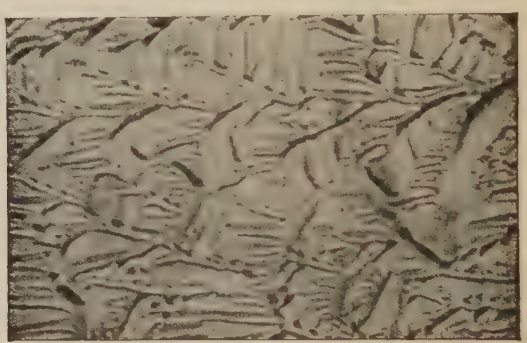

Fig.6. Closure domains in the form of complex drops. Magnification 300 X; ⟷ [100]

Closure domains exhibiting the fir tree pattern have been studied in detail by Williams, Bozorth & Shokley[4]. The fir tree pattern is observed on crystals whose surface is slightly inclined to the (001) plane and having one of the tetragonal axes parallel to the plane and the other at a small angle to it. A photograph of the pattern on a surface of such a crystal is shown in Fig.3. If the surface of the specimen is close to a (001) plane and both the tetragonal axes closest to this plane are inclined at small angles to this plane, the domains appear in the shape of "trunks" (Fig.4). Often in such cases, in addition to the "trunks", the fir tree pattern also appears.

With further deviation of one of the tetragonal axes from the surface of the specimen slightly inclined to the (001) plane there are observed closure domains in the form of "combs" (Fig.5). At large angles between the tetragonal axes on the surface of the specimen there appear closure domains of

complicated shape, specifically there may be observed domains in the form of complex "drops" (Fig.6).

It follows from these observations that closure domains appear on the surface of the specimen when none of the directions of easy magnetization coincides with the surface of the specimen. The shape of the closure domains depends on the crystallographic orientation of the specimen surface. In view of this dependence, we have the possibility (within certain limits) of determining the crystallographic orientation of crystals from the appearance of the powder patterns.

The reason for the appearance of the closure domains is the following. In crystals of silicon-iron, which has a large anisotropy constant, the magnetization vectors of the domains are oriented in the directions of easy magnetization. If these easy magnetization directions are inclined at some angle to the surface of the specimen, there develop over the entire surface of the crystal magnetic "charges" whose energy is reduced by the appearance of the closure domains.[2,4]

2. Variation of the closure domain shape with thickness of the specimen

As we go from thicker to thinner specimen the shape of the closure domains changes. The observations carried out on the same specimen gradually reduced in thickness by electrolytic etching disclose that a marked change in the shape of the closure domains occurs as the thickness is reduced below 100 μ. In the case of very thin specimens - under 5-10 μ - superficial closure domains disappear. The change observed in the magnetic structure as a specimen is reduced in thickness from 100 to 5 μ is shown in the photographs of Fig.7. As may be seen, in the initial state the specimen exhibits the complex drop pattern (Fig.7,a); with decreasing thickness the structure of the closure domains is gradually simplified (Fig.7, b & c). Finally at a thickness of 5 μ the closure domains have virtually disappeared (Fig.7,d) and only principal domains with 180° walls, similar to those shown in Fig.1 are discernible on the surface.

The change in the appearance of the closure domains occurs as though the angle α_o between the tetragonal axis closest to the surface and the surface of the specimen gradually decreased. It may be assumed that in silicon-iron crystals, characterized by a large anisotropy constant, the depth of the closure domains is the greater, the larger α_o. In thin specimens, however, this depth of the domains is limited by the thickness of the specimen itself, which leads to alteration of the domain shape and in the case of very thin specimens to vanishing of closure domains. In the process, apparently, there is no change in the direction of magnetization of the principal domains: the angle α_o remains constant. In consequence of the fact that the magnetic "charges" on the surface of the specimen remain the same, the result of vanishing of the closure domains is an increase in the total energy of the crystal. Consequently, technical magnetization of thin specimens should be more difficult and experiment shows that this is in fact the case[5].

3. Effect of tension on the shape of the closure domains

As already noted, the shape of the closure domains depends on the direction of magnetization of the principal domain orientations. Hence if the orientation of the domain magnetization is altered by stressing the ferromagnetic specimen, one may expect to observe a change in the shape of the closure domains. By way of illustration the sequence of powder patterns appearing on the surface of a gradually stretched crystal are shown in Fig.8.

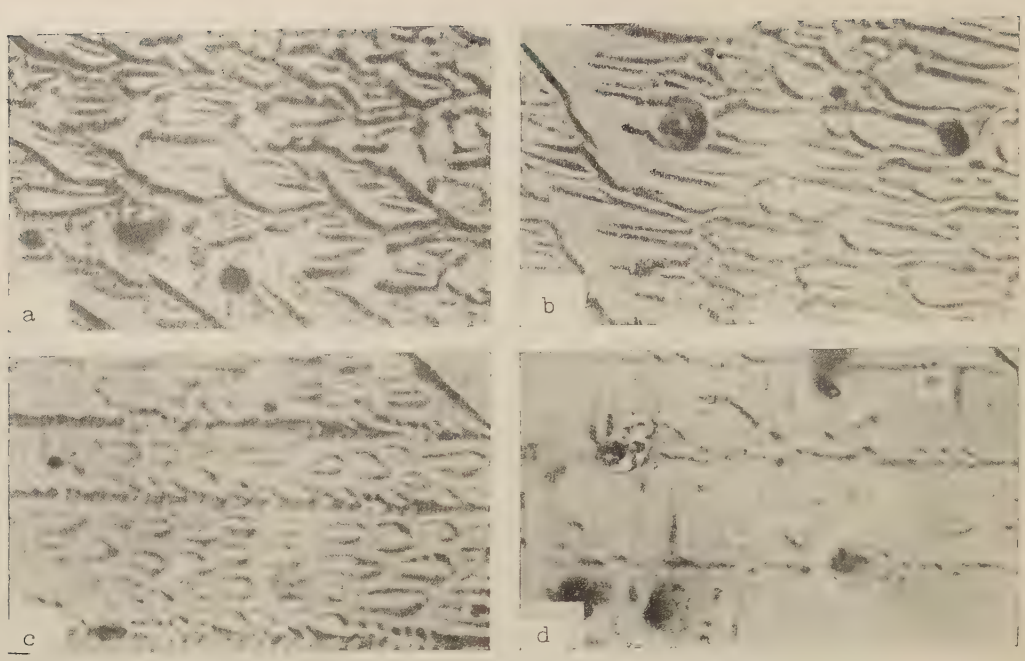

Fig.7. Variation of the closure domain shape with reduction in thickness of the specimen: a) 100 μ, b) 20 μ, c) 15 μ and d) 5 μ. Magnification 300 X; ⟷ [100]

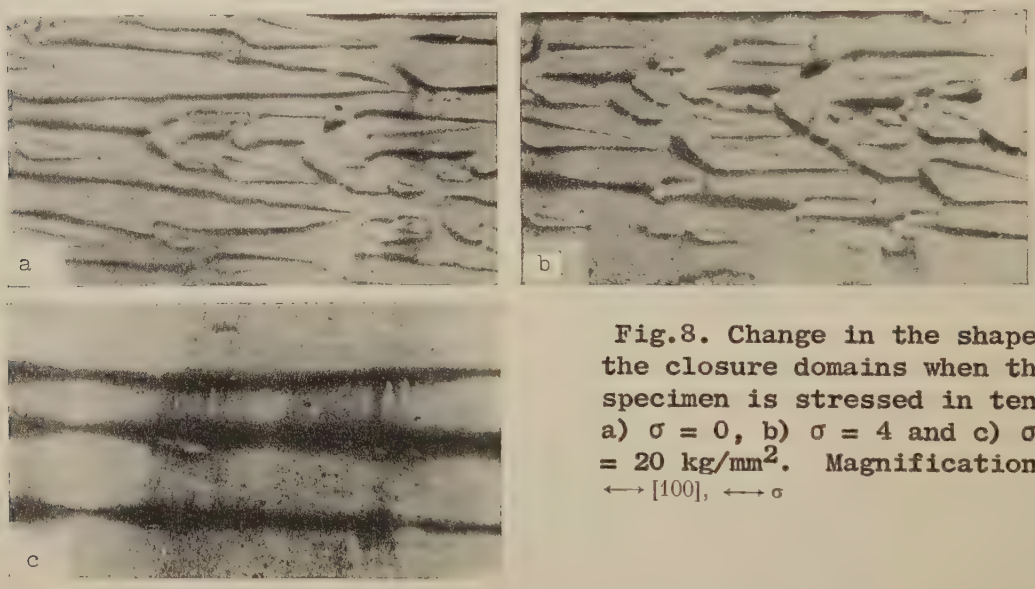

Fig.8. Change in the shape of the closure domains when the specimen is stressed in tension a) $\sigma = 0$, b) $\sigma = 4$ and c) $\sigma = 20$ kg/mm^2. Magnification 300 X; ⟷ [100], ⟷ σ

In the initial state (zero stress), we have the characteristic complex drop pattern. As the tensile load, applied in the direction parallel to that of magnetization, is increased, the magnetic structure is gradually simplified. At a stress of 4 kg/mm^2, 180° walls appear between the domains (Fig.8,b). With increasing stress the closure domains gradually disappear. At a stress of 20 kg/mm^2 only the 180° walls between the principal domains are discernible (Fig.8,c). As the load is reduced the pattern sequence is reversed.

4. Alteration of the closure domain shape with increasing magnetic field

The following sequence of changes in the magnetic structure was observed when a magnetic field of increasing intensity was applied to an initially demagnetized crystal. In weak fields there occur primarily displacements of the walls between the principal domains; the closure domains change little in the process. Where there are closure domains in the path of a shifting wall, these disappear as the wall approaches. After completion of the displacement processes, which is evinced by disappearance of the walls between the principal domains, the closure domains persist. With further increase in the field intensity the closure domains decrease in size and finally disappear. These progressive changes are illustrated in Fig.9. Here the surface of the specimen in the initial demagnetized state exhibits the magnetic structure comprised of principal domains separated by 180° walls and closure domains in the form of drops, i.e., the structure is similar to that shown in Fig.2. The increasingly strong field was applied in the direction of the domain magnetizations. At low inductions (B = 2800 and 7000 gauss), we observe gradual displacement of the principal domain boundaries (Fig.9,a & b). At B = 11,000 gauss, the walls between the principal domains have disappeared but the closure domains are still present. At B = 15,800 gauss, there is a noticeable decrease in size of the closure domains.

Fig.9. Alteration of the shape of the closure domains in an increasing magnetic field: c) B = 2800 gauss, b) 7000 gauss, c) 11,000 gauss and d) 15,800 gauss. Magnification 150 X; ↕ [100], ↑ H

It will be evident that decrease in the size of the closure domains and their eventual disappearance occur in the region of high inductions where rotation processes obtain. It follows that we must reject the commonly accepted concepts according to which in the magnetization of a ferromagnet only wall displacements occur in weak fields and rotation processes start only after full completion of the displacements. Actually, displacement processes, associated with changes in size of the closure domains, proceed simultaneously with rotation processes.

5. Alteration of the closure domains with decreasing field strength

As the applied field is reduced from the intensity producing saturation magnetization, at some point closure domain reappear. It must be emphasized that the closure domains reappear in weaker fields than those in which they vanish in the process of magnetization. Thus we have a hysteresis effect connected with the vanishing and reappearance of closure domains. This form of hysteresis is apparently one of the causes of the phenomenon of magnetic hysteresis in strong fields recently discovered by Drozhzhina et al[6].

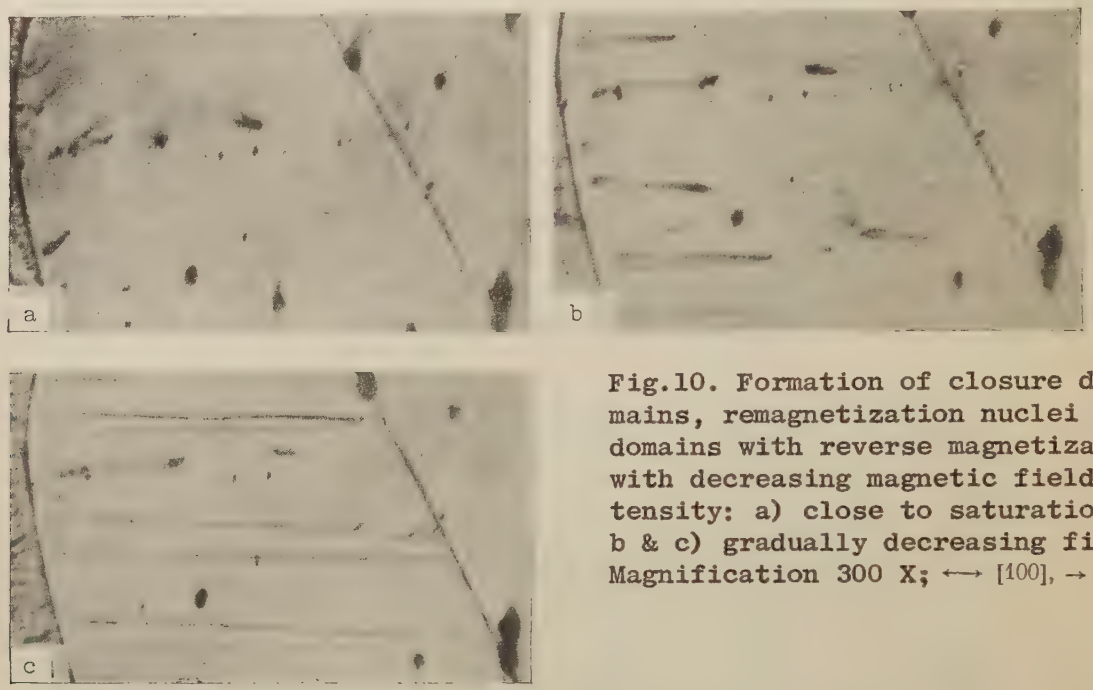

Fig.10. Formation of closure domains, remagnetization nuclei and domains with reverse magnetization with decreasing magnetic field intensity: a) close to saturation, b & c) gradually decreasing field. Magnification 300 X; ⟷ [100], → H

As the intensity of the applied field is further decreased, the closure domains increase in size. Some of them transform into principal domains with reverse magnetization. Consequently, such closure domains are nuclei of reverse polarity magnetization.

We established experimentally that such reverse magnetization nuclei form, as a rule, from closure domains located at the edge or on the surface of crystals. Subdomains (closure domains forming near different defects) usually do not act as reverse magnetization nuclei.[7]

The appearance of closure domains on the surface of a specimen initially magnetized to saturation as the applied field is gradually reduced is shown in the photographs of Fig.10. The magnetic structure of the specimen closest to saturation is shown in Fig.10,a. As the field is reduced there form near the edge of the crystal (at the left in Fig.10,b) closure domains; these increase in size and some of them serve as nuclei for the eventually forming principal domains with reverse magnetization (Fig.10,c).

6. Magnetic structure in the state of residual magnetization

The magnetic structure in the state of residual magnetization was studied on individual crystallites of ring-shaped specimens, magnetized to saturation before-hand by means of a circular magnetic field. This shape of the specimens did away with the demagnetizing influence of the ends of the specimen.

Our observations showed that in the state of residual magnetization the magnetic structure of the specimen consisted of principal domains, closure domains and in some cases of principal domains with reverse magnetization formed from reverse magnetization nuclei. In cases when none of the directions of easy magnetization are aligned with the surface of the specimen, closure domains of different shape are observed over the entire surface. The shape of the closure domains, as in the case of demagnetized specimens, is determined by the crystallographic orientation of the specimen surface. Factors influencing the formation of reverse magnetization domains are the crystallographic orientation of the specimen, its shape, the crystallographic orientation of the neighboring grains and the form of the boundary between neighboring crystallites. Because of the indicated features of the magnetic structure in the state of residual magnetization (i.e., because of the presence of closure domains and domains with reverse magnetization), the actual value of the residual magnetization is always lower than the theoretical value. The latter is usually calculated on the assumption that in the residual state, the magnetization vectors of the domains are oriented in the directions of easy magnetization closest to the orientation of the applied field by means of which the specimen was magnetized to saturation. Thus in practice the value of the residual magnetization will be the smaller, the greater the volume of the specimen occupied by closure domains and principal domains with reverse magnetization.

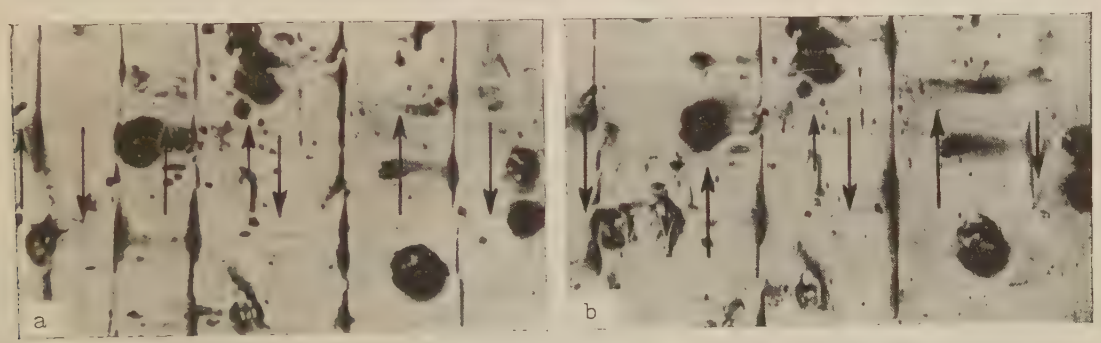

Fig.11. Magnetic structure of a specimen: a) in the demagnetized state and b) in the state of residual magnetization. Magnification 300 X; $\updownarrow$ [100], $\uparrow H_{max}$

The observed alteration in the magnetic structure in going from the demagnetized state to the state of residual magnetization is shown in the photographs of Fig.11. In the demagnetized state one can see on the surface of the crystal the principal domains separated by 180° walls (Fig.11,a). After magnetization of the specimen to saturation by a field H_{max} and removal of this field, there appear on the surface of the specimen closure domains and domains with reverse magnetization that have grown from some of the closure domains (Fig.11,b).

It will be evident from the cited data that closure domains play a decisive role in the formation of the magnetic structure and the course of technical magnetization processes in silicon-iron crystals. It may be assumed that closure domains play an analogous role in other "soft" magnetic materials, particularly in those allied to silicon-iron as regards crystal structure.

It should be noted that closure domains may also exist in high coercivity ferromagnetic materials. Thus, it has been shown by means of powder patterns[6] that in Mn-Bi alloy individual small formations can consist of one principal domain and several closure domains. The character of the technical magnetiza-

tion process in this alloy differs, depending on whether closure domains are or are not present.

Conclusions

It follows from analysis of the described experimental material that in establishing a correlation between the physical properties of ferromagnets in the region of technical magnetization and their magnetic structure, one must take into account not only the structure of the principal domains but also that of the closure domains. Hitherto in such correlation studies attention is focused primarily on the structure of the principal domains (the size of the principal domains, neighbors, etc.). In view of our results it is clear, however, that in many cases the closure domains can play a decisive role in determining the character and course of technical magnetization. Further comprehensive and detailed investigation of the magnetic structure of ferromagnets will undoubtedly lead to a deeper insight into the nature of their magnetic properties.

References

1. Ia.S.Shur & V.R.Abel's, FMM (Physics of Metals and Metallography) 1, 5 (1955).
2. Ia.S.Shur & V.R.Abel's, FMM (Physics of Metals and Metallography) 1, 11 (1955).
3. L.D.Landau & E.M.Lifshits, Sow.Phys., 8, 153 (1935).
4. H.J.Williams, R.M.Bozorth & W.Shokley, Phys.Rev., 75, 155 (1949).
5. Ia.S.Shur & V.A.Zaikova, Doklady AN SSSR, 94, 663 (1954).
6. V.I.Drozhzhina, R.I.Ianus, V.P.Kartashev & E.V.Kaplum, Izv.AN SSSR, Ser.fiz., 16, 703 (1952).
7. Ia.S.Shur & V.R.Abel's, Doklady AN SSSR, 105, 469 (1955).
8. Ia.S.Shur, E.V.Shtol'ts, G.S.Kandaurova & L.V.Bulatova, FMM (Physics of Metals and Metallography) 2, 191 (1956).

Note: In connection with presentation of this report to the Conference motion pictures were shown illustrating the changes in the powder patterns observed under the influence of different factors. Among the various processes photographed were the variation of the magnetic structure with the application and removal of a tensile load, the disappearance of the closure domains in a gradually increased magnetic field and their reappearance with induction of the field and the formation of magnetization nuclei and their growth into principal domains with reverse magnetization. A photographic record of the formation of reverse magnetization nuclei in the high coercivity Mn-Bi alloy and the role played by these nuclei in magnetization processes was also shown.

DYNAMIC BEHAVIOR OF THE DOMAIN STRUCTURE IN SILICON-IRON CRYSTALS

- L.V.Kirenskii, V.D.Dylgerov & M.K.Savchenko

According to present day concepts the process of technical magnetization consists of two stages: 1) displacement of the interdomain walls and 2) rotation of the magnetizations. It is also known that the character of the magnetization process depends on the elastic stresses in the crystal.

In this report we give the results of an investigation of the powder patterns during continuous variation of tensile stresses applied in different directions and during variation of the applied magnetic field. The work was carried out on silicon-iron single crystals cut with the observed surface parallel to the (110) planes. The influence of magnetic fields was investigated on specimens in the form of 13 mm diameter, 0.2 mm thick discs; the influence of elastic stresses was studied by observing 30 x 5 x 0.2 mm strips cut in different crystallographic directions. Prior to observation of the powder patterns all the specimens were annealed in vacuum and polished electrolytically. The alterations of the powder patterns were recorded on motion picture film.

Effect of elastic stresses

In the absence of stresses the initial structure of the domains in a (110) plane is characterized by unevenly spaced almost parallel and occasionally broken lines. The uneven spacing between the lines and the occasional breaks in them are due to the presence of small residual stresses in the specimen and inhomogeneities in its composition. The changes taking place in the powder patterns when the single crystal specimens are stretched in different crystallographic directions differ.

Stretching in the [100] direction. When the tensile stress is applied parallel to the [100] direction the domains tend to be equalized in width through parallel displacement of the walls (Fig.1); this is due to adjustment and equalization of the stresses in the specimen. The equalization in width may also occur by the growth of wedge-shaped domains, which with increasing stress become wider and gradually traverse the crystal (Fig.2). Fig.3,a shows the domain structure with σ = 10 kg/mm^2. It will be seen that with further increase of the tensile stress to 15 kg/mm^2 (Fig.3,b), marked changes occur in the domain structure: some of the domains are divided along the center line by new walls. This effect might be called remagnetization of the domains under the influ-

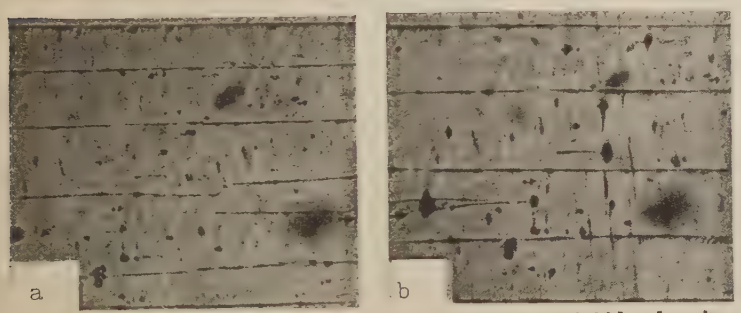

Fig.1. Equalization of domains in width during stretching in the [100] direction: a) 0 stress, b) σ = 29 kg/mm^2. Direction of tensile stress in Figs.1-4 is parallel to the horizontal edge of the pictures.

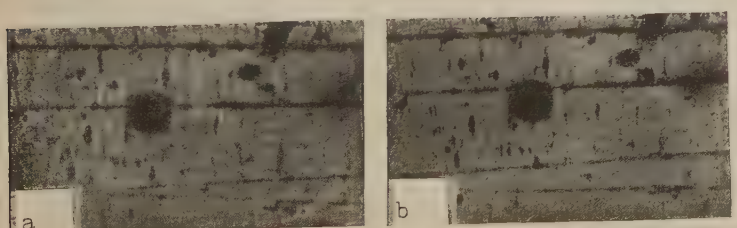

Fig.2. Growth of wedge shaped domains during stretching: a) σ = 7 and b) σ = 14 kg/mm^2.

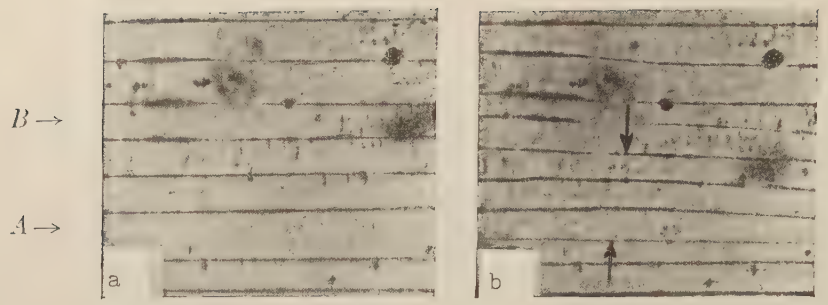

Fig.3. Division of domains by formation of new walls: a) σ = 10 and b) σ = 15 kg/mm^2; the new boundaries formed within the domains A & B in the first picture are indicated by arrows in the second picture.

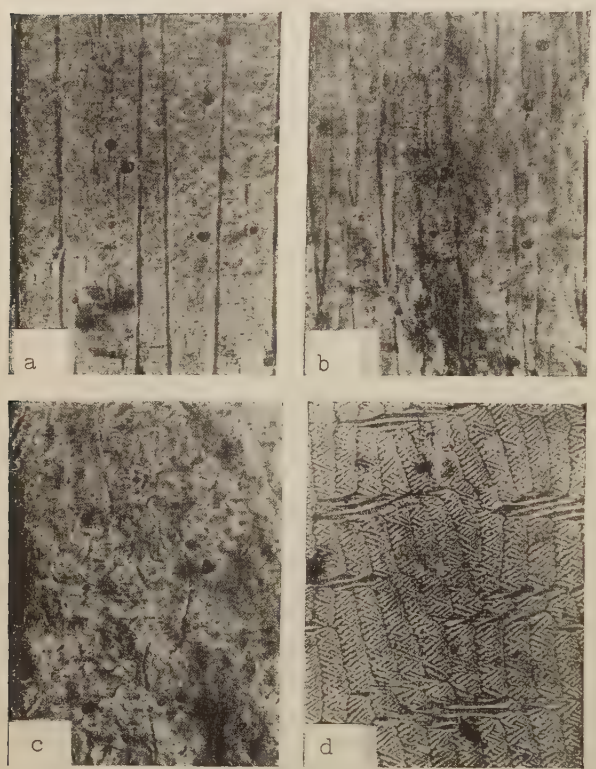

Fig.4. Alteration of the powder patterns during stretching in the [110] direction: a) σ = 0.4, b) σ = 8, c) σ = 12 and d) σ = 19 kg/mm^2.

ence of stresses. In every case an even number of new walls is formed.

Stretching in the [110] direction. When the specimen is elongated in the [110] direction the initial straight boundaries between the domains break-up or "diffuse". The structure becomes wedge-like. With further increase in stress the wedges become smaller and transform into a chaotic arrangement of line fragments. This is illustrated in Figs.4,a,b & c. As the stress is increased still further these fragments undergo a sort of ordering, forming a unique mosaic: a complex closed figure pattern (Fig. 4,c). With further stretching the horizontal bands grow at the expense of the mosaic pattern; however, we have never observed them to occupy the entire surface of the specimen. For this to occur there would, apparently, have to be extremely high stresses far exceeding the elastic limit of the material. The development of a similar mosaic pattern in a silicon-iron crystal stressed in the [110] direction has been observed by Dijxtria & Martius[1].

Stretching in the [111] direction. In the case of extension in the [111] direction the alteration of the powder pattern is similar to that observed in stretching in the [100] direction, i.e., there occur parallel displacements of the walls and at a sufficiently high stress some of the domains are divided in half by the formation of new boundaries. We also observed cases, however, when instead of new walls forming, some of the walls initially present disappeared. Such a case is illustrated in Fig.5.

In some crystals we observed "splitting" of the domain walls (Fig.6); with increasing stress the separation between the "doublet" walls increased. A similar "splitting" of the walls was observed in some cases of stretching in the [100] direction.

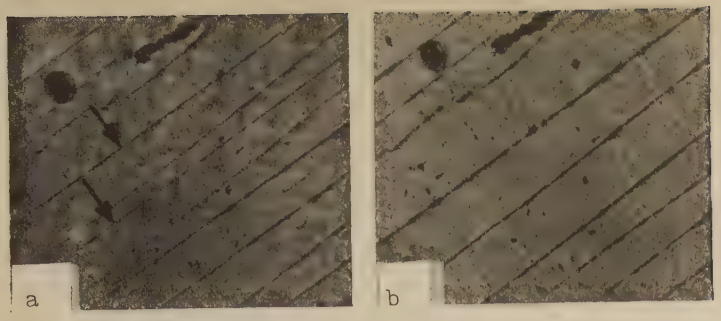

Fig.5. Disappearance of boundaries between domains in stretching in the [111] direction: a) $\sigma = 0$ and b) $\sigma = 4$ kg/mm^2. The arrows indicate the vanishing domains. The direction of tensile strength in Figs.5 & 6 parallel to the vertical edges of the pictures.

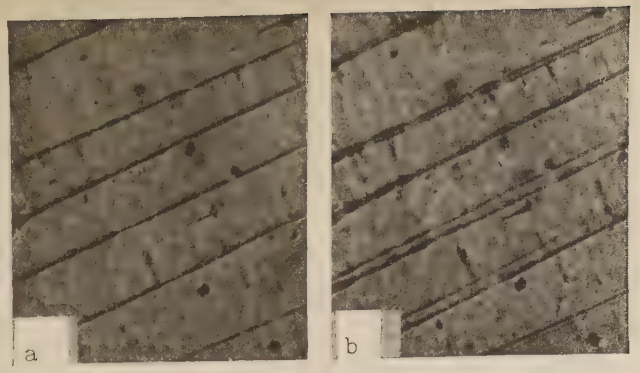

Fig.6. Splitting of domain walls during stretching in the 111 direction: a) $\sigma = 4.5$ and b) $\sigma = 10$ kg/mm^2.

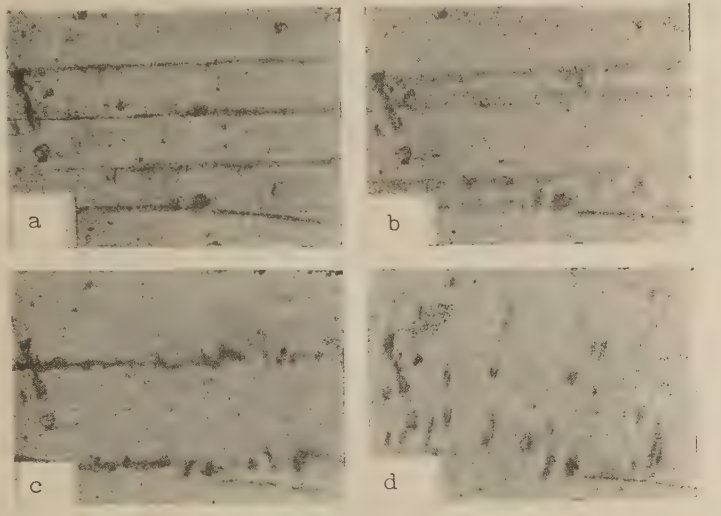

Fig.7. Frames from film taken during magnetization in an increasing field. Magnetization to saturation is realized through processes of displacement and rotation.

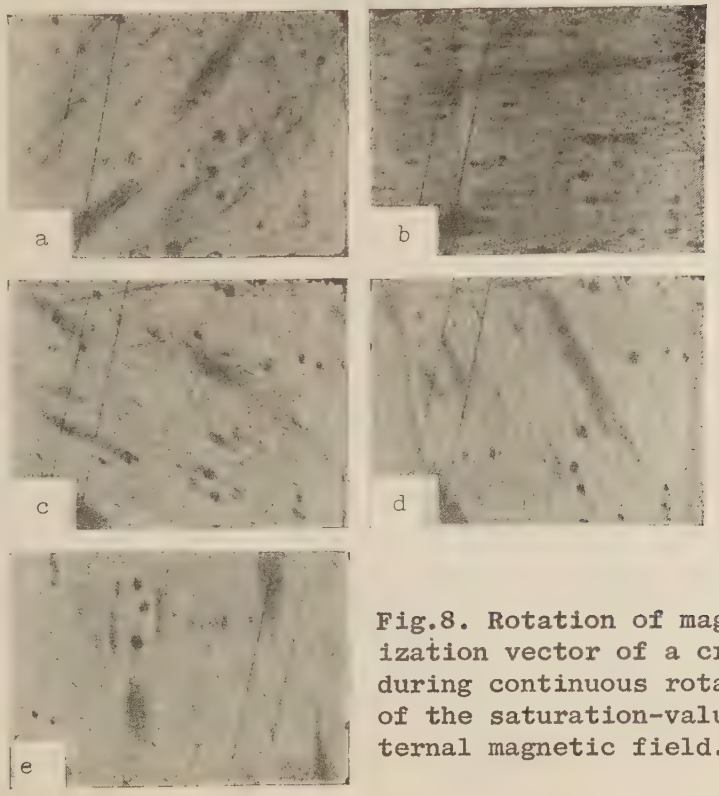

Fig.8. Rotation of magnetization vector of a crystal during continuous rotation of the saturation-value external magnetic field.

Effect of an external magnetic field

Specimens in the form of discs were stressed in the [100] direction until their magnetic structure became fully uniaxial. These magnetically uniaxial crystals were then used for investigating rotation processes. The rotation of the magnetization vector was detected from the saturation figures[2] which are always perpendicular to the magnetization vector.

In Fig.7 we reproduce some frames from the motion picture taken during the process of magnetization of a specimen in a field oriented at an angle to the direction of easy magnetization. It will be seen that magnetization is actually realized by displacement of the boundaries with subsequent rotation of the magnetization vector.

The process of rotation is clearly brought out by the powder pattern as may be seen from the photographs in Fig.8 which are frames from a motion picture taken during continuous rotation of the external saturation-value magnetic field.

Krasnoiarsk State Pedagogical Institute

References

1. L.J.Dijxtria & I.M.Martius, Rev.Mod.Phys., 25, 146 (1953).
2. H.J.Williams, R.M.Bozorth & W.Shockley, Phys.Rev., 75, 155 (1949).

DOMAIN STRUCTURE OF FERROMAGNETS AT HIGH TEMPERATURES

- J.Kaczér

Introduction

The appearance and disappearance of domain structure in ferromagnets in the vicinity of the Curie point and the variation of their domain structure as a function of temperature are of interest from both the theoretical and practical standpoints. One may expect changes in the domain structure to occur, for example, as a result of phase transitions in the material.

Investigation of the domain configuration as a function of the temperature is important from the practical standpoint also because some of the physical properties of ferromagnets that are significant in engineering application, such as the coercivity and the initial permeability, depend directly on the domain geometry and also because modern insulating materials make it feasible to extend the range of ambient temperatures in which such magnetic materials can be employed.

Until now the temperature dependence of the domain structure of ferromagnets has been studied only by a few investigators. Elschner[1] was the first to observe the behavior of the domain structure at temperatures above room temperature, specifically, in the range from 20 to 95°, by the classical colloidal suspension technique. Andrä[2] recently published two studies on the temperature dependence of the domain structure: in the first he investigated the variation of the domain structure of an Mn-Bi alloy in the temperature range from -170 to +20° by the Kerr effect procedure; in the second he investigated cobalt in the range from room temperature to 380°. In the latter investigation Andrä utilized an improved colloidal suspension technique (colloidal suspension of magnetite in paraffin).

Domain structure of magnetite

Our study of the domain structure of magnetite was carried out on a natural crystal of Ural magnetite (Fe_3O_4) which was kindly put at our disposal by Dr.Korzhimskii of the National Museum in Prague.

The crystal, which had the usual octahedral structure, was first polished with No.400 abrasive paper on a (110) plane surface. Then it was polished to a light sheen by means of fine polishing powder on a glass plate. In the course of the preliminary experiments it was found that the domains are not brought out by this technique. Nevertheless we made an attempt to detect the domains by the permalloy probe procedure.[4,5] From the very start it proved feasible to determine the individual boundaries between the domains. Measurements of the angles between the boundaries and the crystal axes showed that within the limits of the experimental error these angles were equal to the theoretical values; in magnetite the directions of easy magnetization (the [111] directions) are defined by the angles 71° and 109°.

Fig.1 is a mosaic made of 12 probe records covering the entire surface of the crystal, a microphotograph of which is reproduced in Fig.2. It will be evident from these photographs that the surface was not adequately polished.

Despite additional very thorough polishing of the surface, powder patterns were still not obtained, although the recording probe detected domains. We succeeded in observing the domain structure only after etching the crystal for several hours in boiling 30% sulfuric acid as recommended by Galt[6].

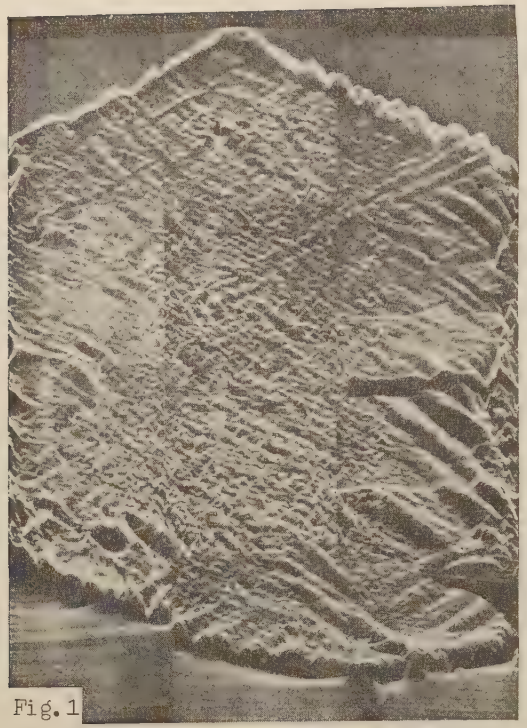

Fig.1. Mosaic composed of 12 probe records over the (110) surface of the magnetite crystal pictured in Fig.2.

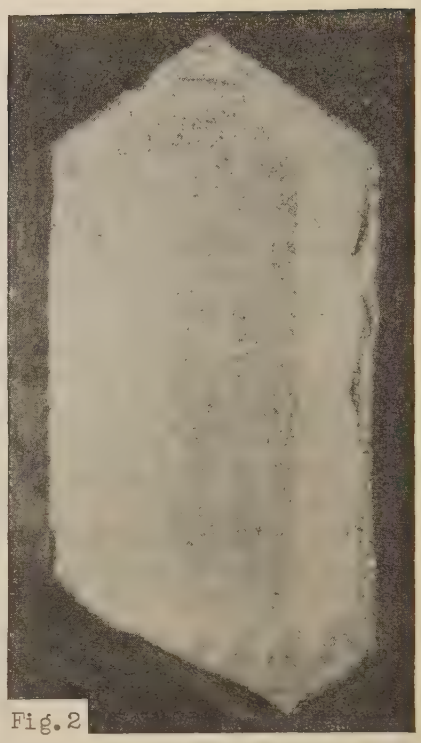

Fig.2. Microphotograph of the (110) surface of the magnetite crystal. Magnification 10 X.

The montage of 3 probe records reproduced in Fig.3 clearly shows the domain structure of one section of the surface of the crystal, microphotographs of which to different scales are shown in Figs.4 & 5. The boundaries of the sections shown in Figs.3 & 5 are outlined in Fig.4.

The photograph of Fig.6 was obtained appreciably later by means of a powder pattern. A probe record was made of the same area of the crystal; this is shown in Fig.7, where one can readily discern the laminar domain structure.

During the work with the magnetite crystal it was found that the laminar structure was not equally well developed over the entire surface. Since, moreover, at some points the crystal had a porous appearance (see Fig.2), we began to suspect that our specimen was not a true single crystal despite the fact that all the faces were fully developed. Hence we recorded transmission and back-reflection Laue diffraction patterns. These confirmed our suspicion that the specimen was not a single crystal; they showed that it was composed of at least two differently oriented crystallites having a pronounced mosaic structure.

In later experiments a crystal in the form of a thin plate was fastened to a small heater mounted on the microscope stage. The probe technique was then used to record the domain structure at different temperatures in the range from room temperature to the Curie point, which for our crystal was about 550°C. These probe records are shown in Fig.8. In the "e" photograph of this series, which was obtained at 450° or almost 0.9 x the Curie temperature on the absolute scale, the domains are still clearly discernible although their boundaries are somewhat diffused. It will be noted that the domain

Fig.3

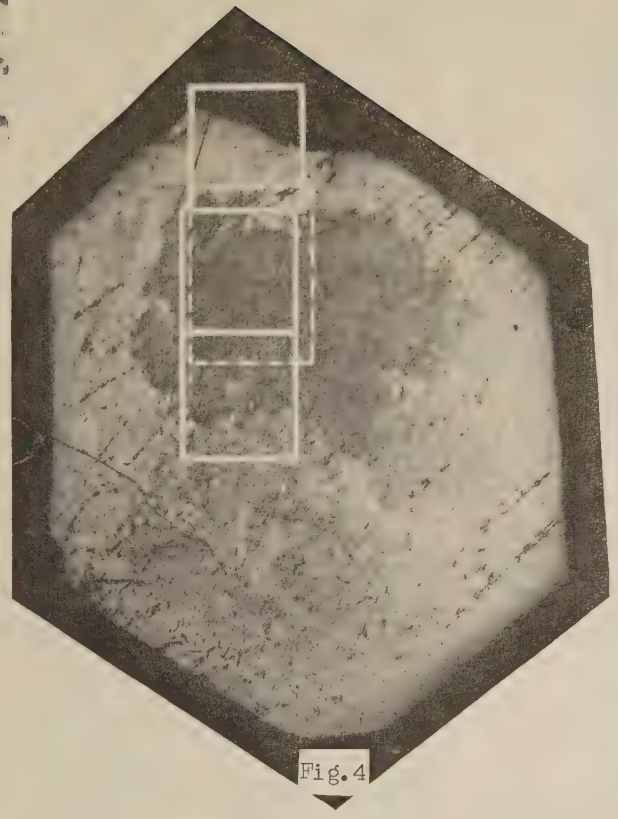

Fig.4

Fig.5

Fig.3. Mosaic made up of 3 probe records of the surface of the magnetite single crystal shown in Figs.4 & 5.

Figs.4 & 5. Microphotographs of the magnetite crystal. Magnifications 10X and 50X, respectively. The areas outlined in Fig.4 are the ones appearing in Figs. 3 & 5.

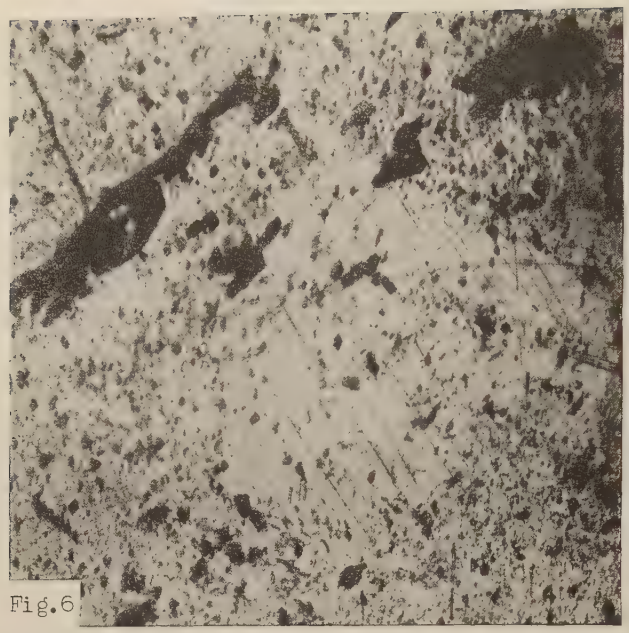

Fig.6. Powder figures of the domain structure of magnetite crystal.

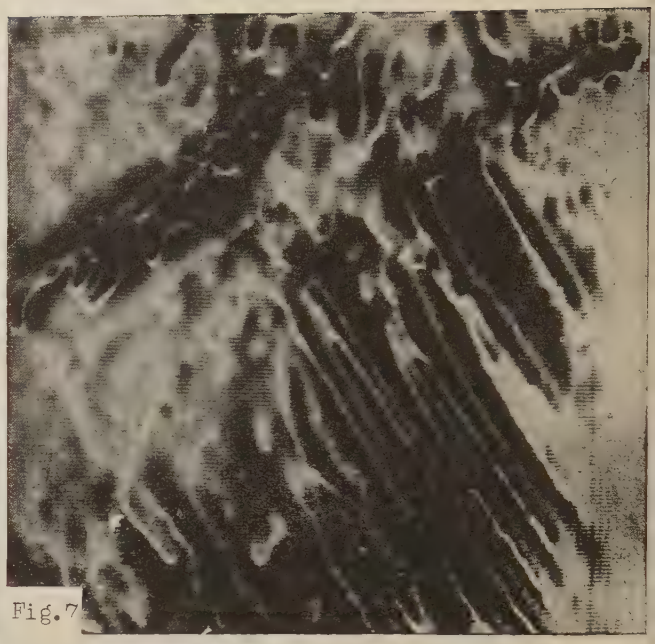

Fig.7. Record of the same area as shown in Fig.6 but obtained by means of a permalloy probe.

geometry changed very little with heating. In cooling the changes occur in reverse order, but the domain structure at the end of the experiment, i.e., after cooling to room temperature (Fig.8,f), is somewhat simpler than at the beginning.

Fig.9 shows a probe record made at an indicated temperature of 545.2°C. The domains have completely vanished, but it is interesting to note that part of the crystal is presumably above the Curie point, while part is below it. This effect is probably due to nonuniform temperature distribution in the crystal or to inhomogeneity of the crystal itself.

In view of the fact that the Curie point of our crystal measured with a probe was 545 ± 2°, while the Curie point for magnetite is reported to be 575°, we inferred that our crystal might not be pure magnetite. Chemical analysis of the specimen carried out in the Chemistry Department of our Institute yielded the following results:

Oxide	Percent	Molar proportion
FeO	28.97 ± 0.2	0.488
Fe_2O_3	70.39 ± 0.3	0.522

The excess of ferric oxide (Fe_2O_3) may be the reason for the depression of the Curie point; unfortunately, there are no reliable data in the literature[7] regarding the influence of an excess of ferric oxide on the magnetic properties of magnetite. We also do not know whether the excess Fe_2O_3 was present in the γ (magnetite) or in the α (hematite) modification.

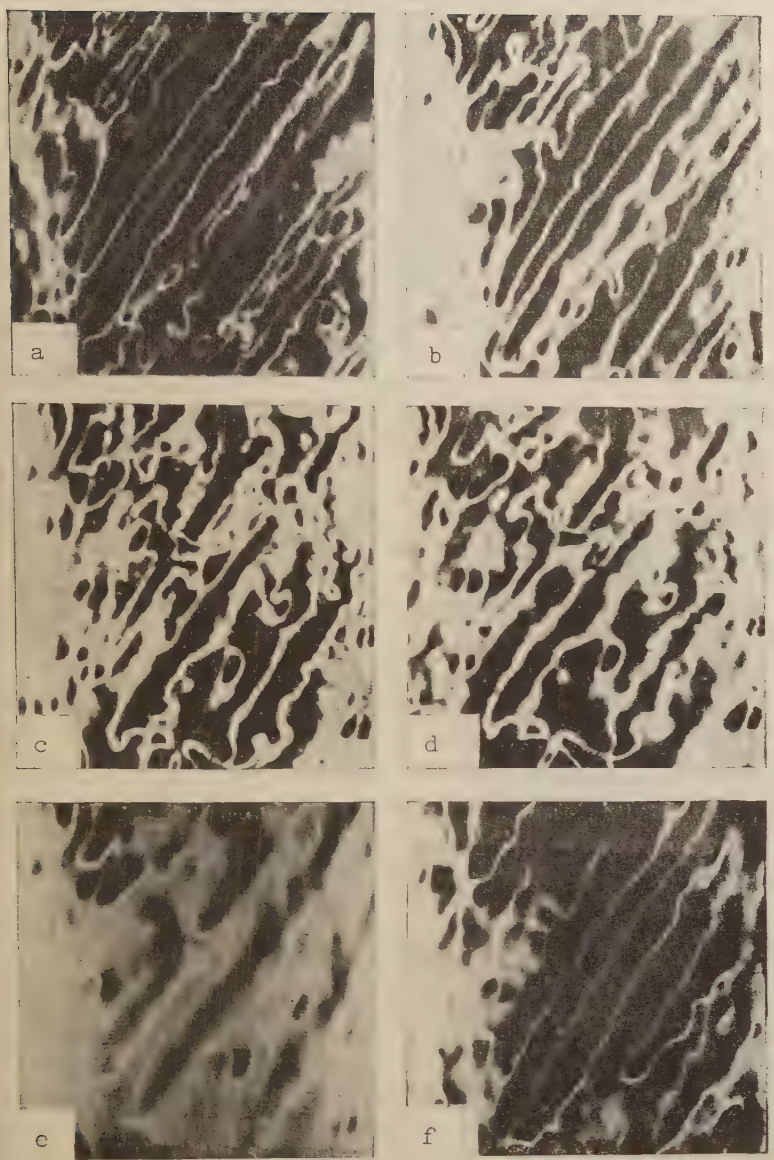

Fig.8. Variation of the domain geometry of a magnetite single crystal with the temperature (probe record): a) 20°, b) 210°, c) 328°, d) 372°, e) 450° and f) 20° C, after cooling to room temperature.

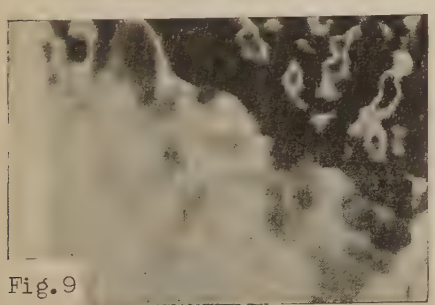

Fig.9. Transition through the Curie point at 545.2° (probe record).

Domain structure of cobalt

The domain structure of ferromagnets is strongly dependent on the anisotropy energy of the material. For a magnetically uniaxial crystal this energy is given by the formula:

$$E_a = K_1 \sin^2 \theta + K_2 \sin^4 \theta, \qquad (1)$$

where E_a is the anisotropy energy, K_1 and K_2 are the anisotropy constants and θ is the angle between the direction of easy magnetization (in cobalt this is the hexagonal axis) and the magnetization vector J. As Landau & Lifshits[8] showed the mean domain width in a magnetically uniaxial crystal is given by

$$d = \sqrt{\frac{2L\gamma}{K}}, \qquad (2)$$

where d is the domain width, L characterizes the dimensions of the crystal, γ is the wall energy and K is the anisotropy constant (in our case $K = K_1 + K_2$). It will be evident from Eq.(2) that the domain width should increase with decrease of the anisotropy constant.

At room temperature cobalt has a hexagonal structure and a large anisotropy constant: $K = 6 \cdot 10^6$ erg/cm^3. The domain structure has the form of parallel laminae or needles arranged parallel to the hexagonal axis. If the hexagonal axis is oriented normal to the surface of the crystal, there are formed closure domains in which the magnetization is either parallel or perpendicular to the surface. In the latter case the direction of magnetization in the closure domains is opposite to the direction of magnetization in the associated internal domains. As a result of incomplete closure of the domains, there develop strong stray fields on the surface.

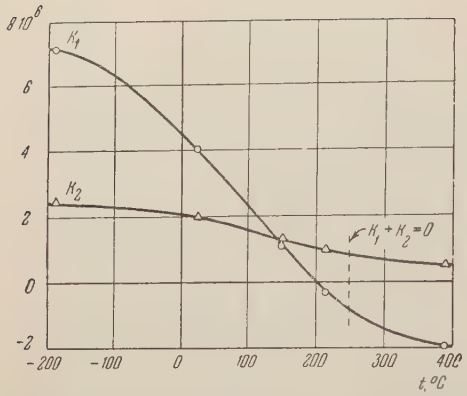

Fig.10. Temperature dependences of the anisotropy constants (after Bozorth[11]).

With increasing temperature the anisotropy constants decrease, as shown in Fig.10, and as a result the width of the internal domains gradually increases. The wedge-shaped closure domains in which the direction of magnetization is parallel to the crystal surface grow, leading to a decrease in the intensity of the stray fields.

Near 250° the sum of both anisotropy constants equals zero and the general anisotropy in the direction of the hexagonal axis also equals zero. In the temperature range from 250 to 400° cobalt is still hexagonal, but the direction of easy magnetization is no longer parallel to the hexagonal axis but lies in the plane normal to it. In this plane, however, the magnetic properties are isotropic and thus there is no preferred direction of magnetization. No domain structure theory for crystals of this type has yet been evolved.

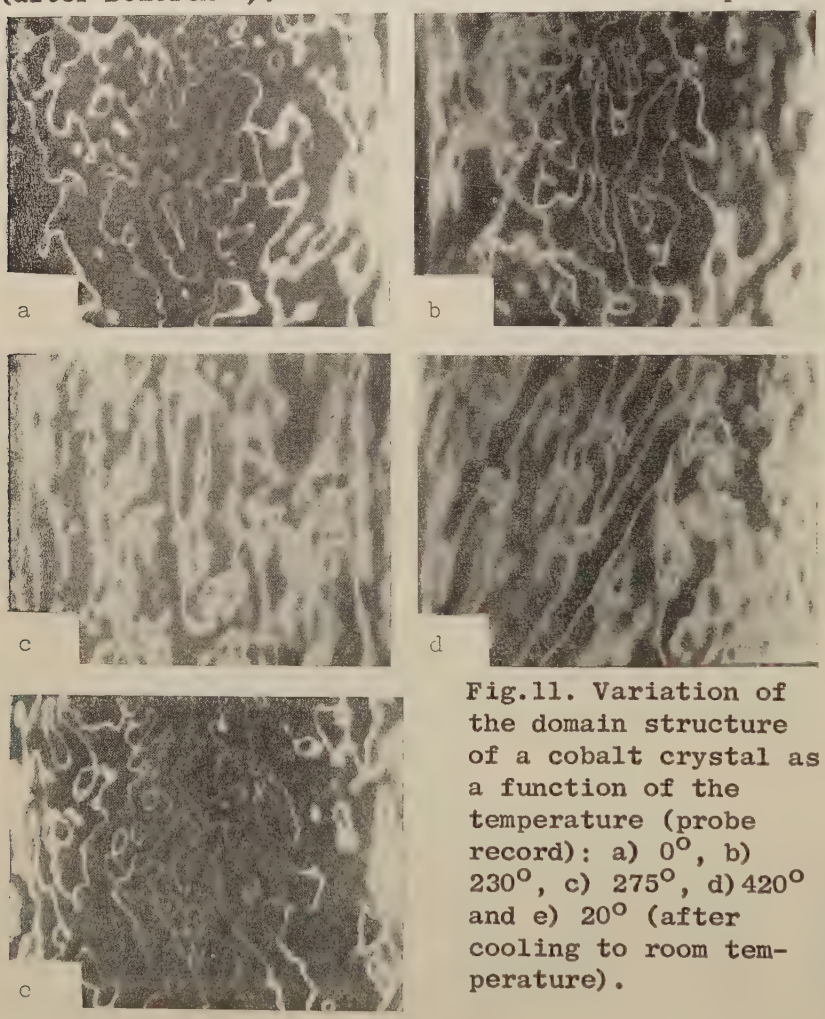

Fig.11. Variation of the domain structure of a cobalt crystal as a function of the temperature (probe record): a) 0°, b) 230°, c) 275°, d) 420° and e) 20° (after cooling to room temperature).

In the vicinity of 400° cobalt undergoes a phase transformation and goes over into the cubic modification. The magnetic properties of cobalt have not yet been determined in this temperature range and hence it is difficult to say anything definite regarding the domain structure in this temperature region.

We carried out measurements on a coarse-grained polycrystalline specimen of cobalt in the temperature interval from 20 to 420°. The results are shown in Fig.11.

Fig.11,a shows the domain structure at 20° of a cobalt grain whose hexagonal axis is approximately perpendicular to the surface of the specimen. With increase of the temperature to 230° (Fig.11,b) the character of the domain structure changes little: many of the lines in this photograph coincide with those in the first; the star-like fine structure

of the domains, characteristic of cobalt, persist. In the record made at 275° (Fig.11,c) we see an entirely different domain structure: the initial domain structure has broken up and we have a random arrangement of lines more or less parallel to the boundaries. This change is probably connected with the change in sign of the anisotropy constant. Little further change is observed in the character of the domain structure up to 400°.

The record obtained at 420° is shown in Fig.11,d. Here again we have an appreciable change in the domain structure. The roughly parallel boundaries observed at 275° have rotated and moved closer together. This change in the domain structure is probably associated with the phase transformation of cobalt occurring at about 400° in which the hexagonal modification goes over into the cubic. As the temperature is reduced the observed effects occur in reverse sequence, but the phase transformation from the cubic to the hexagonal modification occurs at a lower temperature. A photograph showing the final state of the specimen after return to room temperature is reproduced in Fig. 11,e.

Discussion

Results of our measurements show that the domain structure does not change with temperature as much as might be assumed from formula (2). Thus our observations indicate that the domain structure of magnetite virtually does not change as the temperature is increased from 20 to 100°, despite the probable decrease of the anisotropy constant. There are no experimental data on the values of the anisotropy constant of magnetite at temperatures above 20°, hence qualitative comparisons for this material are impossible. The fact that the disintegration of the domain structure occurs at the Curie point is substantiated by the recent results of Wilkinson & Shull[9] who carried out neutron diffraction studies on artificial and natural magnetite single crystals.

We also showed that for cobalt the configuration of the stray fields remains virtually unchanged at temperatures from 20 to 200°, despite the fact that the anisotropy constant changes by a factor of 6 in this temperature range. This change is so appreciable that it undoubtedly should affect the domain structure. Only when the temperature is increased from 200 to 250° does there occur a sudden change in the domain geometry. This effect can be explained if we examine the temperature dependence of the wall energy density. The energy is given by (see, for example, Kittel[10]):

$$\gamma = 2\sqrt{KA}, \tag{3}$$

where A is the exchange integral. Substituting the above value in (2), we obtain

$$d = \sqrt{\frac{2L\sqrt{KA}}{K}} \tag{4}$$

Assuming that in the first approximation the exchange integral is independent of the temperature, we obtain that the mean domain width is inversely proportional to the fourth root of K. For cobalt we obtain the values listed in the accompanying table.

In this table K_0 and d_0 are the values of the anisotropy constant and the domain width at 0°C, respectively. Thus with a temperature increase from 0 to 200° the domain width d should increase by about 60%. Actually, however, the exchange integral also decreases, so that the rate of change of d will be somewhat lower than indicated.

Table

t,C	$\frac{K}{K_0}$	$\frac{d}{d_0}$
0	1°	1
50	0,80	1,06
100	0,60	1,14
150	0,36	1,29
200	0,16	1,59
250	0	∞

Further, it follows from our measurements on cobalt, which were carried up to 680°, that above 400° the domain structure again changes noticeably. Above 400° the boundary lines become less sharp and the character of the pattern observed at 680° is similar to that obtaining at 250°. This phenomenon cannot be explained only by a decrease of the magnetization J to the value of 1150, which is equal to about 81% of the saturation magnetization at room temperature[11]. Hence we assume that simultaneously with the decrease of the saturation magnetization there occurs a decrease of the anisotropy constant to a very low value.

For a more accurate quantitative explanation of the temperature dependence of the domain structure it would be necessary to carry out measurements of the anisotropy constant both for cobalt and for magnetite in the energy interval in question.

Czechoslovak Academy of Sciences

References

1. B.Elschner, Ann.Phys., 13, 290 (1953).
2. W.Andrä, Ann.Phys., 17, 78 (1956).
3. W.Andrä, Ann.Phys., 17, 233 (1956).
4. J.Kaczer, Czechosl. J. Phys., 5, 239 (1955).
5. J.Kaczer & R.Gemperle, Czechosl. J. Phys., 6, 173 (1956).
6. J.K.Galt, Phys.Rev., 85, 664 (1952).
7. G.D.Nicholls, Advances in Phys., 4, 113 (1955).
8. L.Landau & E.Lifschitz, Sow., Phys., 8, 153 (1935).
9. M.R.Wilkinson & C.G.Schull, Phys.Rev., 103, 516 (1956).
10. Ch.Kittel, Rev.Mod.Phys., 21, 541 (1949).
11. R.M.Bozorth, Ferromagnetism. N.Y., 1951.

CONTRIBUTION TO THE THEORY OF COERCIVE FORCE IN THIN SHEETS

(Abstract - Complete report in Czechosl. Jour. of Physics, 6, 4 (1956)

- J.Kaczer

The density of the magnetostatic energy of the surface charges appearing at the intersection of a ferromagnetic interdomain boundary layer (wall) with the surface of a single crystal has been calculated on the basis of the familiar model of the boundary layer between ferromagnetic domains. It is known that this energy is not small compared with the other energies (the potential and anisotropy energies) and must be taken into account in the case of thin sheets. Consequently, the energy density in sheets is higher than in an unbounded crystal. It is shown that the thickness of the boundary layers between domains is a function of the thickness of the sheet.

The expression obtained for the dependence of the coercive force on the thickness of the sheet is in good agreement with experiment in the case of single crystal sheets. For polycrystalline sheets, however, only qualitative agreement is obtained: the calculated values are smaller than the experimental ones. It is possible to obtain agreement in the case of polycrystalline sheets as well if one takes into account the constant magnetostatic surface energy, which should probably increase the charges on the surface of the sheet. The experimental value of the energy of these charges for polycrystalline silicon steel is about 4 erg/cm^2.

DIRECT OBSERVATIONS OF THE DOMAINS IN A FERROMAGNET BY MEANS OF A SECONDARY EMISSION ELECTRON MICROSCOPE AND AN ELECTRON MIRROR

- G.V.Spivak, N.G.Kanavina, I.S.Sbitnikova, I.N.Prilezhaeva, T.N.Dombrovskaia & V.K.Azovtsev

Introduction

Back in 1947 Germer[1] showed that an electron beam passing over the face of a cobalt single crystal interacts with the domain fields. By studying the patterns recorded on photographic plates he was able to evaluate the maximum field intensity. He did not, however, obtain a picture of the domains inasmuch as a parallel or glancing beam is not suitable for this purpose.

One might also note the interesting investigations of Martin & Lochenbruch[2] who in 1949 developed an original procedure for electron optical visualization of domain fields consisting of forming an electron image of the edge of a magnetized single crystal on a suitable screen. Simultaneously with the edge of the specimen a small grid was projected on the screen. Visualization of the field was realized through the distortion of the grid image by the magnetic field at the edge of the domains. This procedure, however, did not yield an image of the domains proper. A modification of this procedure was used by Soboleva[3] for measuring local fields at the edge of a specimen.

In contrast to the above researches, we developed procedures which allow of obtaining a direct image on a screen of the domains of ferromagnets or the magnetization pattern on the surface of diverse specimens. The development is based on the idea that one can create electron-optical contrast and, consequently, actually see magnetic inhomogeneities (for example, ferromagnetic domains) if these inhomogeneities are magnetic "microlenses" incorporated in a conducting plane surface.

Interaction of a uniform electron beam with a conducting surface possessing a magnetic topography (magnetic microlenses) should result in density modulation, i.e., bunching, of the electron beam. This modulation beam can then be focused by means of another electrostatic or magnetic lens (a macrolens) to form an image of either the conducting surface itself or of a plane close to it where the influence of the local magnetic field is strongest.

Interaction of micro- and macrolenses

The problem of obtaining the requisite contrast in the image of the microlenses and the problem of the useful magnification of this image required analysis of the question of interaction of the micro- and macrolenses. Inasmuch as an enlarged image of the magnetic topography constituted by the microlenses can be obtained only by using an electron focusing macrolens, it will be obvious that not every combination of lenses will achieve the desired purpose.

In addition to magnetic microlenses there may also exist electric microlenses (local electric fields on the conducting electrode); in fact at any given spot there may simultaneously be both a magnetic and an electric microlens. Further, both the magnetic and the electric microlenses may be either "weak" or "strong". Thus we may expect to encounter four basic types of microlenses. Similarly analysis shows that there may be six types of macrolenses. Macrolenses intended to form an image of the magnetic or electric topography on the screen may under certain circumstances suppress the effect of the microlenses; in this case no image of the microlenses will be formed.

Let us, by way of illustration, consider the case of an electric microlens. For it E_z is the intensity of the accelerating field (an accelerating field is necessary, for without it there would be no luminescence of the screen), E_x is the tangential component of the microlens field of electric origin and H_z is the magnetic field of the macrolens forming the image on the screen.

A rigorous solution of the problem of the electron trajectories based on the equations of motion in the vicinity of the flat surface under investigation leads to the following equations:

$$x = \frac{m}{e} \cdot \frac{E_x}{H_z^2}\left(1 - \cos\frac{eHt}{m}\right) + \frac{m}{eH_z}\left(\dot{x}\sin\frac{eHt}{m} + \dot{y}_0\cos\frac{eHt}{m} - \dot{y}_0\right),$$

$$y = \frac{E_x}{H_z}t - \frac{m}{e}\cdot\frac{E_x}{H_z^2}\sin\frac{eHt}{m} + \frac{m}{eH_z}\left(\dot{y}_0\sin\frac{eHt}{m} - \dot{x}_0\cos\frac{eHt}{m} + \dot{x}_0\right),$$

where x and y are the electron coordinates as determined by the tangential component E_x of the electric field of the microlens and the field H_z of the macrolens.

We note two interesting circumstances:

1) with $H_z \gg E_x$, the microlens effect vanishes;

2) the character of the image (chromatic and spherical aberration, etc.) and the magnification of the electron optics depend on the initial velocity components $\dot{x}_0$ and $\dot{y}_0$ of the electrons.

These circumstances must be borne in mind in selecting the combination of macro- and microlenses. Our analysis also shows that the initial kinetics of the electron beam is an important factor where formation of the image is concerned.

Characteristics of the electron beam necessary for observation of magnetic microtopography

The sensitivity, resolution and magnification of the electron optical system necessarily depend on the characteristics of the electron beam modulated by the magnetic microlenses. Let us list these characteristics:

1) the electrons must have an optimal velocity: obviously if velocities are high the electrons will only be weakly modulated by the local magnetic fields; important here is not only the mean velocity imparted to the electrons by the electric field but also the velocity straggling of the emitted electrons;

2) the angle between the electron beam and the magnetic field over the surface of the specimen will undoubtedly have a considerable influence on the quality of the resultant image;

3) accumulation of electrons, if they are significantly slowed down, will produce a noticeable space charge and, consequently, have a deleterious effect on the sensitivity;

4) the best results should be obtainable with narrow beams when overlapping of the effects of neighboring magnetic region is minimal.

The quality of the image and degree of magnification we have achieved with each of the procedures described below are in a sense measures of how close we have been able to come to the ideal conditions formulated above. The potentialities of each procedure must be evaluated on the basis of the possibility of approaching closer to the ideal conditions.

Visualization of domains by means of secondary electron emission

The experimental arrangement for obtaining an image of the surface by means of secondary electron emission has been described.[4,5] The primary beam impinges on the hexagonal face of a cobalt single crystal. Secondary electrons released from the surface "spiral" to a greater or lesser extent about the magnetic lines of force, i.e., are deflected by the microfield, which provides the contrast in the eventually formed electron optical image.[4,5]

The electron beam modulated in density by the local magnetic fields is focused on the screen by a magnetic macrolens to form an image of the domains (Fig.1). For comparison in Fig.2 we show the powder pattern observed on the same specimen. Comparing the same area in both photographs, we can readily see that the electron optical image really does show the domain structure. [[We would like to assure the reader finding it difficult to detect any similarity between Figs.1 and 2 that the fault does not lie with our reproduction. Except for the arrows, the original photograph of Fig.1 would appear to be an underexposed, out-of-focus snapshot of a classical London fog. Translation editor.]]

Fig.1. Electron optical picture of the domains on the surface of a cobalt single crystal obtained by the secondary emission procedure. Magnification 50 X.

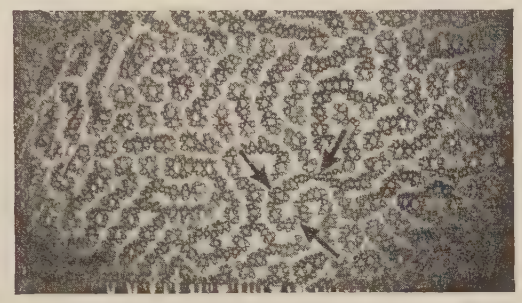

Fig.2. Powder pattern on the same surface of the cobalt single crystal shown in Fig.1. Magnification 50 X. The arrows indicate the same area in in the two photographs.

Let us evaluate the merits, shortcomings and potentialities of this electron-optical procedure.

So far we have not succeeded in eliminating geometric and chromatic aberration connected with inadequate adjustment of the instrument and the use of secondary electrons having high initial velocities. Both these factors determine and limit the useful magnification of the optics and the contrast of the image.

The procedure does in general correctly render the domain structure and, if geometric and chromatic aberration can be substantially reduced, has the potentiality of developing into a technique for obtaining greatly magnified (up to several thousand times) domain images. It should be feasible to minimize aberration by design of a special metal emission electron microscope having provision for utilizing beams of low velocity secondary electrons.

Visualization of domains by means of an electron mirror

The second promising procedure we tried for domain visualization is that of the electron mirror.

The reason for using such a mirror is to enhance the sensitivity of the

Fig.3. Electron optical picture of domains on the surface of a cobalt single crystal obtained by the electron mirror technique. Magnification 150 X.

system by increasing the interaction of the electrons with the local fields. With an electron mirror the electrons are stopped near the surface and then begin to move in the reverse direction. Thus near the surface we are dealing with relatively slow electrons so that appreciably better contrast should be obtained than when the image is formed by means of fast secondary electrons. This reasoning is substantiated by our experimental results. The experimental electron mirror set up is described in Ref.7, where a detailed comparison between the pictures obtained by this procedure and by the powder pattern technique is also given. By way of illustration we have reproduced in Figs.3 & 4 photographs of the same area of a cobalt single crystal obtained by the electron mirror and powder pattern procedures. The powder patterns were photographed by means of a metallurgical microscope.

The domain boundaries at a magnification of 150 X are seen in the form of bright very contrasty halos; much detail is discernible. The dark area at the right in Fig.3 is the region of secondary emission; the next zone is the region of reflection of electrons near the crystal surface and the zone at the left is due to reflection of the electrons from a region further away from the surface. An electron mirror with magnetic topography yields an image with specific distortions due to the peculiarities of the electron motion in the complex configuration of the micro- and macrofields. The pictures must be interpreted with great caution.

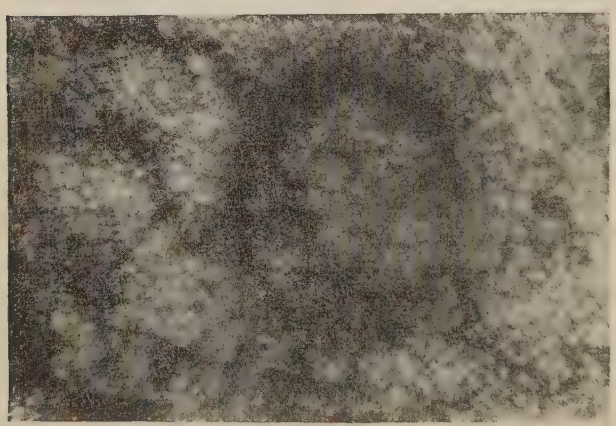

Fig.4. Powder pattern on the same surface of the cobalt single crystal as in Fig.3. Magnification 150 X.

At the same time it must be admitted that the mirror gives exceptionally contrasty images. We obtained a useful magnification of 150-200 X; with appropriate suppression of geometric aberrations the magnification can be further increased. Initially, interpretations of the photographs obtained by this procedure must be based on experimentation and comparison with powder patterns, etc. It should eventually be possible to realize quantitative evaluation of domain fields. Although the electron mirror technique seems promising, it is impossible to say now whether hyper-optical magnifications can be achieved by means of it.

Visualization of magnetic microstructure by the modulated film technique

Fig.5. Modulated film image of local magnetic fields on a cobalt single crystal. Magnification 60 X.

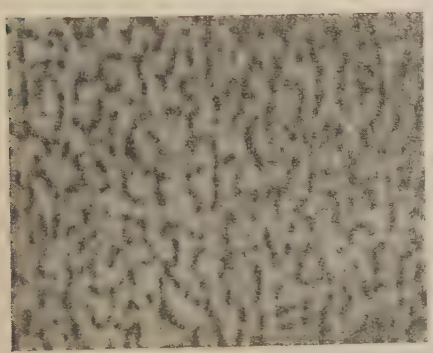

Fig.6. Modulated film image of local magnetic fields on silicon iron. Magnification 120 X.

An obvious question is whether one cannot use the modern transmission electron microscope with its great magnification for the investigation of domain boundaries. One possible procedure for such application of the electron microscope was suggested by Martin in 1944 and realized experimentally by Eckhardt & Elschner[8] in 1952.

Essentially the procedure consists of depositing a ferromagnetic powder on the crystal, obtaining a replica and then examining this replica in a transmission electron microscope. By means of this method one can make a more profound study of the magnetic microstructure than by means of an ordinary optical microscope. The procedure is relatively simple and can undoubtedly lead to interesting results. The replica procedure, however, does not yield a picture of the topography of the magnetic field on the surface of the specimen but rather a map of the contours of the ferromagnetic particles located in this field.

It may be asked whether instead of obtaining a replica of the geometric relief produced by the deposited powder one cannot cause a film to form directly under the influence of the local magnetic fields? In this case the field would act on the molecules and ions constituting the replica film rather than on the comparatively large colloidal particles of a ferromagnetic powder. It is known that films can be formed under the influence of electron bombardment. We found that such films formed under certain conditions on the surface of a ferromagnet are "modulated" by the magnetic inhomogeneities.

We established that at low magnifications there is general correspondence between such modulated film images and powder patterns. At present we are engaged in determining to what extent the modulated film images agree in detail with powder patterns. Photographs of the magnetic inhomogeneities on the surface of cobalt and silicon iron specimens obtained by the modulated film technique are reproduced in Figs.5 & 6. Our results so far are only of a preliminary character.* (See note on next page.)

We feel that side by side with indirect electron optical procedures for investigating microfields it is expedient to continue the development of direct electron optical techniques inasmuch as they should make it possible to observe dynamic behavior of the domain structure under the influence of different factors and are also promising as regards attainment of hyper-optical resolutions.

Department of Physics,
Moscow State University

---

*A good picture of the domains on the surface of the same cobalt specimen was obtained by means of photoelectrons by Spivak et al[9].

References

1. L.N.Germer, Phys.Rev., 62, 295 (1942).
2. L.Marton & S.Lochenbruch, Journ.Appl.Phys., 20, 1117 (1949).
3. L.P.Soboleva, Izv.AN SSSR, Ser.fiz., 18, 511 (1954). (Trans.Bulletin, 18, No.5, 197.)
4. G.V.Spivak, N.G.Kanavina, I.S.Sbitnikova & I.N.Chernyshev, Doklady AN SSSR, 92, 541 (1953).
5. G.V.Spivak, N.G.Kanavina, I.S.Sbitnikova & T.N.Dombrovskaia, Doklady AN SSSR, 105, 706 (1955).
6. S.V.Vonsovskii & Ia.S.Shur, Ferromagnetizm (Ferromagnetism), M.-L., 1948.
7. G.V.Spivak, I.N.Prilezhaeva & V.K.Azovtsev, Doklady AN SSSR, 105, 965 (1955).
8. A.Eckardt & B.Elschner, Naturwiss., 39, 566 (1952).
9. G.V.Spivak, T.N.Dombrovskaia & N.N.Sedov, Doklady AN SSSR, 113, 78 (1957).

* * * * * *

NATURE OF FERROMAGNETIC DOMAIN WALLS
(Abstract)

- C.P.Bean

A new method has been employed to measure accurately the surface energy associated with a ferromagnetic domain wall. A cylindrical wire of 65% nickel + 35% iron with an axial stress-induced anisotropy receives a pulse of magnetic field in a direction opposite to that of its initial magnetization.

Due to shielding of the external field by eddy currents, a cylindrical domain wall is formed, separating the outer region of the wire which has reversed its magnetization from the inner region which retains its initial direction of magnetization. In zero field this domain wall shrinks due to its surface energy, but its motion can be stopped by a field tending to make it expand. From the value of this field and the radius of the domain wall, the surface energy is calculated.

Measurements of this energy as a function of the anisotropy allow a separation of the factors which contribute to the surface energy and, in particular, give a value of the "exchange stiffness" for this alloy of $1.0 \pm .2 \times 10^{-6}$ erg/cm. This result is compared with the various theoretical predictions. In addition, an experiment has been devised to measure the thickness of the ferromagnetic domain wall. In brief, the change in balancing field caused by passing a current down the wire is proportional to the integral of the circumferential component of the magnetization over the radius of the wire. This integral is a measure of the thickness of the domain wall. Preliminary measurements of this quantity are in good accord with theoretical predictions.

General Electric Research Laboratory
Schenectady, N.Y.

THERMAL CHANGES ASSOCIATED WITH MAGNETIZATION

- L.F.Bates

1. Introduction

The results of experimental work on the thermal changes which accompany the magnetization of ferromagnetic metals and alloys on making step-by-step changes in an applied magnetic field have been reviewed on two recent occasions[1,2]. In the present communication an account will be given of some improvements in the technique of measurement and of new measurements on ferromagnetic substances. It is well-known that the observed thermal changes are very small, so that their measurement requires the detection of temperature changes of the order of 10^{-6}°C. The experimental procedure used in Nottingham has been described elsewhere and hence will only be outlined here. The specimen under investigation is usually in the form of a rod or stout wire, about 40 cm long and 0.5 cm or less in diameter. It is mounted vertically inside a water-cooled solenoid which supplies the magnetizing field, the vertical component of the earth's magnetic field being separately compensated. The magnetizing current can be changed by cutting out resistances in parallel with the solenoid; a choke of high inductance and low resistance is permanently connected in series with the main current supply in order to avoid rapid field changes which would produce eddy-current heating of the specimen.

The temperature changes accompanying magnetization are measured by a system of some 20 copper-constantan thermocouples, whose "hot" junctions are attached to the specimen, while the "cold" junctions are close to, but not in contact with, the specimen. Each thermocouple has its own primary winding on a Mu-metal core transformer, whose secondary winding is connected to a sensitive, long-period galvanometer. Formerly, the galvanometer scale distance was 8 meters, and the ballistic deflection, which occurs when the temperature of the specimen is suddenly changed, was observed with a large telescope. The temperature change causes a current to flow in each thermocouple circuit, the flux through the secondary winding of the transformer is changed and then remains constant for a short time so that the galvanometer gives a ballistic deflection, after which the galvanometer spot returns to its initial position. Subsequently, (see Ref.3), the telescope was replaced by a split photocell amplifier similar to that described by Preston (1946), except that negative feedback was not employed. While the use of the amplifier produced only a slight increase in the overall sensitivity of the apparatus, it resulted in a great improvement as regards the ease with which the thermal deflections could be read.

The thermal deflections are usually calibrated by producing a known adiabatic cooling of the specimen by suddenly hanging a weight from its lower end; in accordance with the Joule expression

$$\Delta T = -\alpha TF/J\rho SA \quad \text{or} \quad \Delta Q = -\alpha TF/A,$$

where ΔT is the change in temperature which occurs when a tension F (dynes) is applied to a rod with a thermal expansion coefficient α, S is the specific heat of the specimen, ρ is its density, A is its cross section area and T is the absolute temperature. It is often more convenient to calculate the corresponding quantity of heat ΔQ in ergs/per cc. Other methods of calibration such as the passage of low frequency alternating current through the specimen, or calculations based on Warburg's law are frequently employed in special cases. Details of the mounting of the specimens and the elimination of errors

due to eddy currents, etc. are given in the original papers. The magnetic hysteresis curves of the specimens are found by the usual ballistic method, using a coil wound on the central portion of the specimen and correcting for demagnetization effects.

Since materials of high coercivity are normally available only as short specimens and for magnetization require fields much stronger than those readily obtainable with a solenoid, a technique different from the foregoing was used by Bates & Simpson[4]. They used a single thermocouple connected to a sensitive galvanometer with a suitable amplifier. The "cold" junction of the copper-constantan thermocouple was some 2 or 3 mm from the "hot" junction. The thermocouple was cemented along the axis of an ebonite tube with the "hot" junction protruding from one end and bent over to make a disc which could rest in close contact with the flat surface of the specimen. The latter was mounted between the poles of an electromagnet with thin sheets of soft rubber between the pole faces and the specimen. The pole pieces were water cooled and great attention was paid to the thermal insulation of the specimen.

2. Theoretical Considerations

Let us now turn to the theoretical aspects. In an important treatment of the reversible processes accompanying magnetization, Stoner & Rhodes[5] showed that the reversible component of the thermal change $\Delta Q'$ for a field change from H_1 to H is given by

$$[\Delta Q']_{H_1}^{H} = a \int_{H_1}^{H} d(HJ) + b \int_{H_1}^{H} H\, dJ, \qquad (1)$$

where J is the intensity of magnetization and a and b are constants for the material under investigation. The first term on the right side of Eq.(1) gives the thermal change due to change in intrinsic magnetization, the constant a being equal to $-(T/J_o)(\partial J_o/\partial T)$, where J_o is the intrinsic magnetization. The second term represents the thermal change associated with reversible rotation processes only, and the constant b is equal to $(T/k)(\partial k/\partial T)$, where k is the modulus of the appropriate anisotropy constant, K.

Let us consider the first term in Eq.(1). Since the slope of the (J_o,T) curve is normally negative, the coefficient a is positive, and for a field decreasing from saturation the integral is negative (by convention we always start with a field described as negative). Thus the first term is negative in these circumstances and represents a cooling. Since rotation processes are very small near the saturation condition, the second term will then be either very small or zero, assuming that the coefficients a and b are of a reasonable order of magnitude. We therefore always expect an initial cooling of the specimen. With further decrease of the magnetic field rotation processes become more important, and the integral in the second term is no longer very small. The sign of the coefficient b depends on whether k increases or decreases with rise in temperature. It is clear that when the magnetic field is low, especially in the region of coercivity, irreversible processes occur and Eq.(1) is not valid until positive fields much above the coercivity value are attained.

If we subtract from the observed thermal changes those which may properly be considered due to changes in intrinsic magnetization, following Stoner & Rhodes we may write

$$Q'' = \Sigma\, dQ' - a \int d(JH) = \int b'' H dJ. \quad (2) \qquad (2)$$

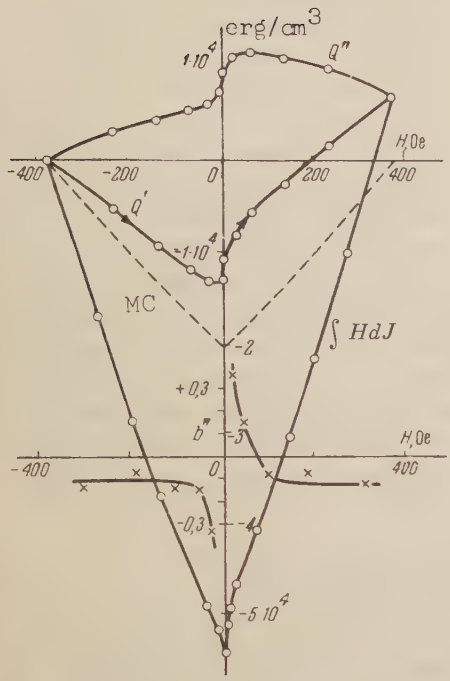

Fig.1. Results for 0.5% silicon-iron in the untreated (hard drawn) condition. Maximum field 400 oersted.

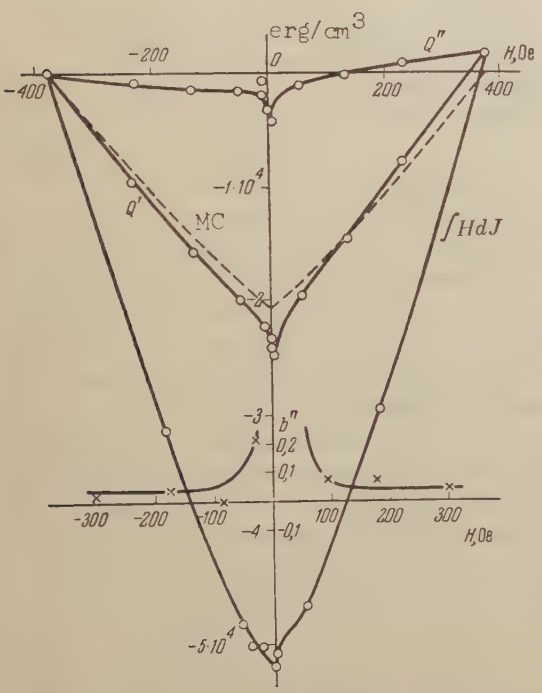

Fig.2. Results for 0.5% silicon-iron in the annealed condition. Maximum field 400 oersteds.

In this equation, b'' corresponds to b of Eq.(1), but is placed under the integral sign to allow for possible variation when calculated from Q'' experimental data. Hence, $b'' = \frac{(dQ''/dJ)}{H}$ and, in order to make quite clear how the experimental results are treated, we may write

$b'' = \frac{\Delta Q''}{\Delta \int HdJ}$. We thus see that the quantity b'' is of much interest, even though we cannot expect exact agreement between the experimental values b'' and the calculated values of b, because the latter are not exactly known and the former may be modified by other processes not accounted for in the above treatment. Nevertheless comparison of b'' and b for many materials is obviously important, and many representative values are now available[2]. Some recent attempts to separate the reversible and irreversible effects are described below.

The work of Bates & Marshall with silicon-iron provides very good examples of the application of the Stoner and Rhodes theory. We will briefly consider here their data for a 0.5% silicon-iron specimen. The results for the untreated material, i.e., in the hard drawn condition, are shown in Fig.1. The material was first magnetized in a field (negative) of some 400 oersteds. Starting from the left side of the figure, we follow the course of the Q' curve as the specimen is exposed to a magnetic field which is decreased step-by-step. We note the initial cooling, followed by a pronounced heating as the coercive point is traversed. The ordinate of the outermost point on the right side of the figure represents the heat wasted in going through a half-cycle of magnetization. (In order to save space, we have cut off the curve for the remaining half-cycle.)

The curve labelled MC, signifying magnetocaloric, is the thermal change represented by $a\int d(JH)$, calculated by assuming a definite value of $3.40 \cdot 10^{-2}$ for a. It is worth noting that the magnetocaloric effect is not a high-field phenomenon only, and that it must be taken into account at all field strengths. The curve Q'' is obtained by plotting the difference in the ordinates of the Q' and MC curves. Finally, we have the $\int HdJ$

curve; from it and the Q'' curve, the increments $\Delta Q''$ and $\Delta \int H dJ$ for chosen increments of H enable us to calculate the values of b'' shown in the lower portion of Fig.1. We see that b'' has a small, constant negative value, except in regions of low field, where the Stoner and Rhodes theory does not apply.

In Fig.2 we have the corresponding data for the same specimen of silicon-iron after a normal industrial anneal: approximately 15 hours heating up to 830°C, "in its own atmosphere", followed by approximately 48 hours in the town's gas supply. The values of b'' are now positive. Attention is directed to the shapes of the Q' and Q'' curves, and especially to the peculiar "dips" or troughs in the region of H = 0. When one compares the Q'' curves of Figs.1 & 2, the suggestion at once arises that the "dip" must be intimately connected with the occurrence of boundary movements which should be much more pronounced in the case of the annealed specimen. The "dip" is all the more interesting because it is in a region where irreversible heating would be expected. In seeking for a satisfactory explanation for its occurrence we have done much work, some of which is described below.

3. Separation of Reversible and Irreversible Changes

It is clear that a considerable advance would be made in our comparison of experimental results with the Stoner and Rhodes theory, if we could distinguish between the reversible and the irreversible components of the thermal changes which are observed when we make a change in magnetization. Three attempts have so far been made to measure reversible heat changes experimentally. The first was a direct method applied by Okamura[6] to a large number of materials, but his method does not appear to be sound although his results certainly give an indication of the magnitudes of the separate reversible and irreversible effects. More recently, Tebble, Wood & Florentin[7] used the simple thermodynamic relation of Eq.(4) given below, while Bates and Sherry[3] used the direct method analogous to the method of measuring reversible susceptibility, namely, by making small backward and forward increments at given points on the hysteresis cycle. At moderate and high fields, the last method is clearly effective, but in low fields it would be necessary to employ very small increments, especially with materials of low coercivity. However, it was found possible to use the method on a specimen of electrolytic cobalt. It is considered that this would be reliable with any material provided that the thermal sensitivity of the measuring apparatus were sufficiently high.

Let us turn to Fig.3. Here the smooth curve depicts a portion of the magnetic hysteresis curve for a ferromagnetic material that is in the cyclic state and has arrived at the conditions represented by point A. The field increment H_A to H_B is made, and the thermal effect accompanying the change is measured by the method described above. Now, instead of continuing around the cycle, the field is returned to H_A and, unless the step AB is entirely reversible, the material will now be at a condition A' which is different from A. If this subsidiary step is reversible, when the field is again increased to H_B a return should be made to B. This is only true if the step AB is vanishingly small, and in practice finite changes of sufficient magnitude must be realized to give a measurable thermal effect. The reversibility test to be applied here is that the heat change accompanying the step

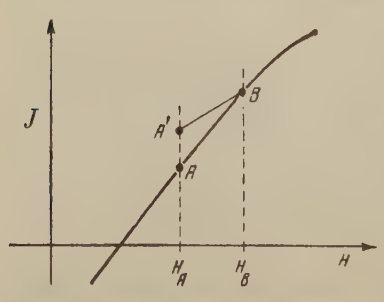

Fig.3. Method of separating reversible and irreversible changes.

BA' must be equal in magnitude but opposite in sign to the change accompanying step A'B; furthermore the associated increments in magnetization must be equal and opposite. The field increments are so chosen that the difference between the magnitude of the thermal changes BA' and A'B is smaller than the experimental error and therefore to a first approximation the area of the closed subsidiary loop is so small that irreversible effects can be neglected.

It is assumed that the step A'B represents the reversible part of the step AB since, as long as the subsidiary step is reversible, the measured $\Delta Q'_{rev}/\Delta H$ value cannot depart much from the true limiting value, and there are few irreversible jumps or the subsidiary loop would not be closed. Thus it appears that a satisfactory direct separation may be made when materials of moderate coercivity are chosen.

Measurements on the above lines were first made on a specimen of electrolytic cobalt, both the heat treated and untreated states. The irreversible heat changes were deduced from the simple relation

$$Q'_{tot} = Q'_{rev} + Q'_{irrev}. \qquad (3)$$

One set of results is shown graphically in Fig.4, from which it may be seen that the total curve Q'_{tot} exhibits the usual form for cobalt (Bates & Harrison, 1948): it rises slowly to a maximum and then descends to the value of the energy loss per half-cycle. The extreme portions of the graph are linear because the function $\int HdJ$ is linear over these regions. The overall heating was in good agreement with the value predicted by Warburg's law. The curve for irreversible changes Q'_{irrev} is satisfactory, because little change takes place at the larger field values; the major part of the heating occurs on the steep part of the hysteresis cycle and the middle of the rise is at the coercive point (34 oersteds). No irreversible cooling is observed. The curve for reversible changes is symmetrical about the zero field axis, and the net thermal effect is only -1400 erg cm^{-3}, a discrepancy which is well within the limits of experimental error in view of the fact that the observed maximum reversible heating was 42,800 erg cm^{-3}.

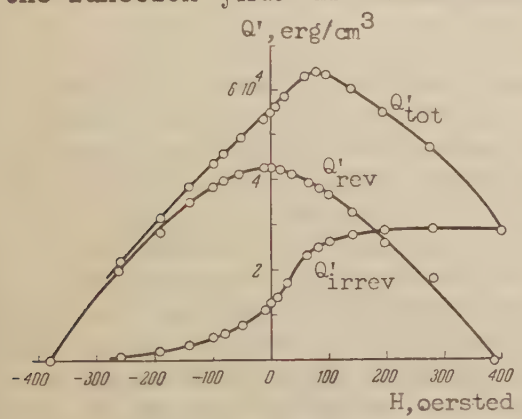

Fig.4. Cobalt (heat treated) - separation of reversible and irreversible changes.

The quantitative test of these results was obtained by the application of the Stoner and Rhodes theory, since we could now consider only the effect of the reversible rotations. The energy changes due to rotations, denoted by Q''_{rev}, could be obtained, as is seen from Eq.(1), by subtracting from Q'_{rev} the effect caused by the changes in intrinsic magnetization. Fortunately, the latter effect is small in cobalt, as dJ_0/dT is small. The results and the theory were then tested by the consistency of the coefficient b'':

$$b'' = \frac{\Delta Q''_{rev}}{\Delta \int HdJ_{rev}}.$$

The results for the reversible increments in intensity of magnetization were obtained by similar "back" steps and the value of $\Delta\int HdJ_{rev}$ evaluated. Once again, it is emphasized that the method is a first approximation only, since

the value for $\int_{-H_{max}}^{+H_{max}} HdJ_{rev}$

was not zero as would be expected, but was small and positive.

A plot of Q''_{rev} vs $\int HdJ_{rev}$ for the same specimen is given in Fig.5. In this graph the open circles represent the results from -400 oersteds to zero field, while the black circles represent the second part of the hysteresis cycle from zero to +400 oersteds; the outermost end is at the value for zero field. Within the limits of experimental error, the ascending points fall on the same straight line, which shows that the value of b'' is constant right down to the lowest fields. Previous results indicated that b'' was constant at the higher field values only, but we now have direct experimental support for the Stoner and Rhodes theory over the whole field range. The experimental results gave b'' = -1.1 which is in good agreement with the calculated value, particularly in view of the possible unreliability of the values of dK/dT.

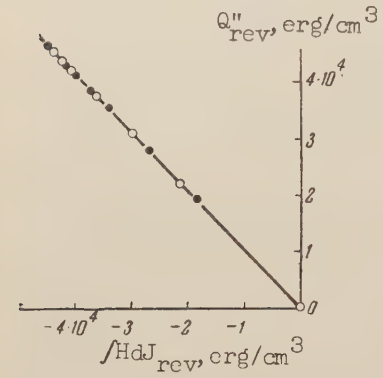

Fig.5. Cobalt (heat treated) - test of Stoner and Rhodes theory.

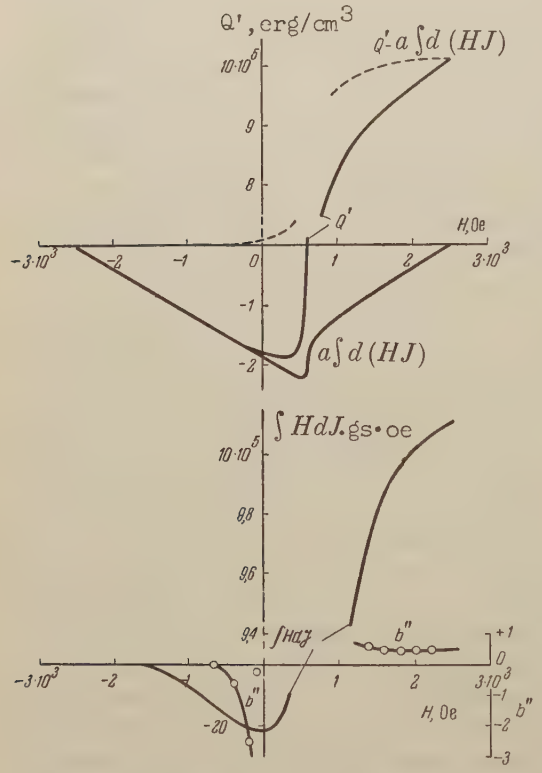

Fig.6. Analysis for Alcomax III; b'' estimated as described in text.

In the case of untreated cobalt, the results were also satisfactory: the coefficient b'' was constant over a large part of the field range, but showed a slight increase as zero field was approached. The actual value of b'' was again most satisfactory, namely, -1.3; the slight difference between the two measured b'' values is not thought to be significant, since the theoretical value is -1.27.

In the work of Ref.4 a similar attempt was made to separate reversible and irreversible processes with high coercivity alloys, but it was impossible to make the field changes sufficiently small with the available sensitivity. The work was not fruitless, however, as the experiments indicated clearly over what regions of the cycle the magnetization processes were completely reversible. For example, in the case of an alnico specimen, starting with an initially saturated specimen, the magnetization processes were found to be completely reversible from saturation (above 2200 oersteds) down to 800 oersteds.

Bates & Simpson[4] analyzed the experiments made on seven high coercivity materials in the light of Eq.(1). The results for a specimen of Alcomax III (8% Al, 13.5% Ni, 50% Fe, 24.5% Co, 3% Cu and 1% Nb) are given in Fig.6, where the variation of Q', $a\int d(HJ)$ and $\int HdJ$ with H are shown for those field values

where irreversible processes are small or zero. The integrals were found by measuring the appropriate areas within the J,H loop. The axes of the $a\int d(HJ)$ curve have been chosen to make the curve coincide with the Q' curve on the left side of the figure. This means that over the initial portions of the cycle changes in intrinsic magnetization alone are assumed to take place. The thermal changes in these regions thus enable a value for a to be calculated, and this in turn permits calculation of $a\int d(HJ)$ and the coefficient b''. We see that for negative fields from saturation to about -400 oersteds the $a\int d(HJ)$ curve and the thermal curve Q' exactly coincide, and hence taking a to be 0.094, b'' is zero over this region. The variations of b'' over the rest of the cycle are typical of the results obtained in earlier work. They are considered to be characteristic of irreversible processes in which rotation contributions are small. On the whole, the Stoner and Rhodes theory adequately fits the experimental results, although the experimental values of a are somewhat larger than expected.

4. Further Theoretical Considerations

Eq.(1) can be expressed in a more general form from free energy considerations (Teale, 1955):

$$[Q']_{H_1}^{H} = C\int_{H_1}^{H} HdJ - \frac{T}{J_0}\cdot\frac{dJ_0}{dT}[HJ - (HJ)_1], \qquad (4)$$

where C is appropriate to the type of process involved in the change of magnetization. Here we see that the second term depends only on the magnetic states at the beginning and at the end of the magnetization change responsible for the change in Q' and that it applies both to reversible and irreversible changes; whereas the first term is seen to depend on the actual path by which the magnetic change occurs and can be valid only for reversible changes. Consequently, we may picture different processes as contributing separately to the first term and may theoretically examine the contributions to Q'. Thus, if only boundary movements are involved in the change in magnetization, C in Eq. (4) is given by $(T/\gamma)(d\gamma/dT)$, where γ is the energy per unit area of domain wall. If we suppose that the motion of the domain wall is impeded by a mechanism such as that visualized in the strain theory, C is given by

$$C = \frac{T}{J_0}\cdot\frac{dJ_0}{dT} + \frac{T}{\lambda_s}\cdot\frac{d\lambda_s}{dT},$$

where λ_s is the saturation magnetostriction coefficient. Other expressions may likewise be deduced to take account of the magnetostatic energy due to free poles and of the effects envisaged by the Néel disperse field theory, which gives

$$C = \frac{2T}{\lambda_s}\cdot\frac{d\lambda_s}{dT} - \frac{T}{K}\cdot\frac{dK}{dT}.$$

These expressions for the first term have recently been discussed by Lilley (Thesis, University of Leeds, 1952) and Teale (Thesis, University of Leeds, 1955).

5. Experimental Work at Leeds University

Dr. R.S.Tebble (to whom I am indebted for much helpful information on work done at the University of Leeds) and his co-workers have endeavored to make measurements under conditions in which changes in magnetization take place reversibly so that the Stoner & Rhodes analysis may be rigorously

applied. They have avoided the difficulties of measuring $(\partial Q'/\partial H)_s$ under reversible conditions by measuring $(\partial J/\partial T)_H$ and calculating the former quantity by using the thermodynamic relation

$$(\partial Q'/\partial H)_s = -T\,(\partial J/\partial T)_H, \tag{5}$$

It is thus more convenient in this work to write Eq.(1) in the differential form

$$(\partial Q'/\partial H)_s = a\{J + H\,(\partial J/\partial H)_T\} + bH\,(\partial J/\partial H)_T. \tag{6}$$

Then b'' can be calculated using the expression

$$b'' = \frac{(\partial Q'/\partial H)_s - a\,(J + H\chi_{rev})}{H\chi_{rev}}, \tag{7}$$

where χ_{rev} is the reversible susceptibility and is equal to $(\partial J/\partial H)_T$.

Their method involved the measurement of a change in magnetization of the order of 1 e.m.u. in the specimen when it was heated and cooled by a stream of liquid through a temperature range of about 1°C. They used polycrystalline specimens in the form of long narrow ellipsoids and the changes in magnetization were measured by means of a suspension magnetometer. In addition, work was carried out with single crystal "picture frame" specimens; in these experiments the changes in magnetization were measured with a search coil connected to a galvanometer with a photocell amplifier.

They found general agreement with the results obtained in Nottingham for the total thermal Q' changes and in particular with the curves given by Bates & Sherry[3] in Fig.4. Their value for b'' for nickel in fields of the order of 100 oersteds was -4.35 in good agreement with the calculated value of -4.5 given by Stoner and Rhodes; their values for cobalt in fields of between 200 and 400 oersteds fell uniformly from -1.10 to -1.14 in good agreement with the calculated value of -1.1. They found no indication of a decrease in b'' in high fields.

Tebble and his co-workers have also attempted to estimate the effect of processes other than rotation on the value of b''; in other words, they have attempted to find the components of the coefficient C in Eq.(6) above. However, this estimation is a matter of considerable difficulty because of the smallness of some of the effects, but they hope soon to show the presence of disperse field processes as the sign of b'' is reversed, by means of experiments on strained single crystals.

6. Experimental Work on Ferrites

It is clear that examination of diverse materials in order to try to distinguish between the several processes which are responsible for changes in magnetization, as well as for the purpose of explaining the phenomenon of the "dip", is important. Hence it was felt that a study of the ferrites might well be rewarding. The first experiments with these materials were made by Bates & Sherry[3] who used four specimens of Ni-Zn ferrites of compositions ranging from 15 NiO and 35 ZnO to 48 NiO and 2 ZnO. These particular materials have low Curie points in the range 130 to 550°C and, consequently, $(T/J_o)(dJ_o/dT)$ - the first term in the expression for C - is so great, that the ordinary magnetocaloric effect is very pronounced in them.

Only in the specimen of lowest Zn content did Bates & Sherry find any marked evidence of irreversible processes, when it appeared as a kind of step superimposed on the large magnetocaloric effect in the low field region. The

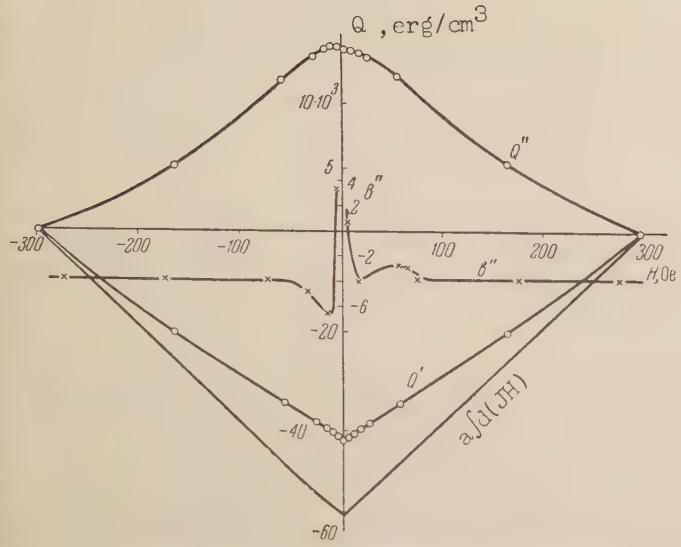

Fig.7. Results for a commercial Mn-Mg ferrite.

thermal effects were overwhelmingly due to change in intrinsic magnetization with temperature, and rotational processes were certainly very small. However, considerable evidence of the existence of the "dip" was found, and careful investigation proved that the phenomenon is a real one for which we have no completely satisfactory explanation.

The experiments on ferrites have recently been extended by D.A.Christoffel who has considerably improved the sensitivity of the measurements. Among the interesting results he has obtained, the following may be noted. First, with a commercial Mn-Zn ferrite, of coercivity 0.5 oersted and B_{max} 4,000 gauss, with low remanance, the thermal changes in fields from some hundreds of oersteds down to 15 oersteds were due almost entirely to the magnetocaloric effect, but there was a small rotational contribution, as the magnetization increased slightly with the field even when the latter exceeded 300 oersteds, and the Q", H curve gave a distinct positive peak in a field close to H = 0. It was found that the value of b'' was constant at -1.0 over the ranges ±(300 to 15) oersteds, but in the field range ±15 oersteds b'' fell sharply to a value of about -4 or -5. Hence, another process besides rotation and change of intrinsic magnetization is involved.

Second, with a commercial Mn-Mg ferrite, of coercivity 1.6 oersteds and B_{max} = 3,500 gauss, with a square hysteresis loop, and with a much lower magnetocaloric effect than the first of his specimens, Christoffel obtained the results shown in Fig.7. Here, there is a distinct "dip" in the Q' curve for fields below 10 oersteds, in which region b'' attains positive values; its value in higher fields is -4, approximately. Some of the changes in b'' in the field ranges -50 to -10 and +10 to +80 oersted seem well worth further study. These interesting experiments are being continued with other ferrites.

7. Experiments with Ferromagnetic Alloys

In the pioneer experiments of Bates & Weston (1941) and of Bates & Harrison (1948), several ferromagnetic alloys, more particularly those of moderately high coercivity were studied. However, the discovery of the "dip" in silicon-iron made it imperative to carry out a series of measurements on low coercivity alloys, as well as on single crystals of iron and silicon-iron, with apparatus of high sensitivity. Such measurements have recently been made by D.J.Sansom, and a preliminary account of some of his work will now be given. The account is preliminary because it transpires that the calibration of the thermal changes is at the moment somewhat incomplete in view of the fact that accurate values of the coefficients of thermal expansion of the alloys are not available; it is intended to measure them forthwith.

In the following table are given the approximate constitutions of some commercial alloys, supplied in the form of rods 36 cm long and 4 mm in diameter, except in the case of H.C.R. alloy which is available only in the form

Alloy	Nominal composition, %	J_{max}, gauss	H_c, oersted	$\int_{-100}^{+100} HdJ$, erg/cm^3	a
Mu-metal	77 Ni + 14 Fe *	568	0,035	80	0,267
H.C.R.	50 » + 50 »	1230	0,12	670	0,143
Radiometal	50 » + 50 »	1230	0,16	940	0,142
Rhometal	36 » + 60 »	1220	0,21	1220	0,127

*Remainder - impurities

of thin strips, of which a composite specimen consisting of 12 strips each 40 cm x 3 mm x 0.2 mm was made.

It should be understood that most of these alloys contain small quantities of other metals besides nickel and iron in order to improve their properties for commercial use. HCR alloy is particularly interesting because it is a grain-oriented, square hysteresis loop material, the long axis of the strips being roughly a [001] direction of easy magnetization. (Radiometal of similar composition is not grain-oriented.)

The coefficient $a = -T/J_0 \cdot dJ_0/dT$ was found by measuring the temperature variation of the saturation magnetization in a field of about 4,000 oersteds; it is estimated that the values of a are accurate to about 4%. J_{max}, given for comparison purposes, is the intensity of magnetization in a field of 100 oersteds.

In all cases the (Q',H) curves were linear for fields of above 100 oersteds; indeed in some cases they were linear down to about 20 oersteds, apart from a slight upward curvature, attributable to rotation. The curve for mu-metal was actually linear down to zero field, presumably because its anisotropy and magnetostriction are so small. For all the specimens the thermal changes, as tested by the Bates & Sherry method, were reversible down to about 2 oersteds and therefore with a knowledge of χ_{rev} it should be possible to make an estimate of b'' for each.

The results for the grain-oriented H.C.R. alloy are shown in detail in Fig.8 (assuming a coefficient of expansion of $\alpha = 10 \cdot 10^{-6}$ degree^{-1}). One notes the pronounced "dip" in the (Q",H) curve. There was no "dip" in the

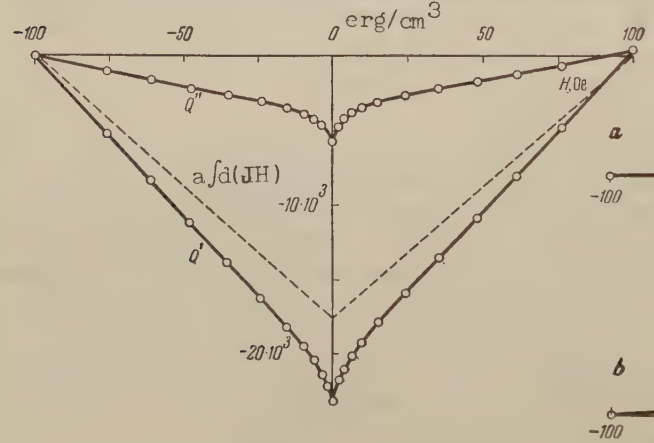

Fig.8.

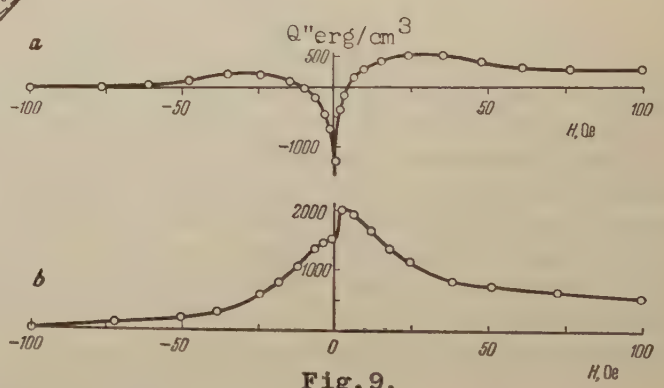

Fig.9.

Fig.8. Results for grain-oriented H.C.R. alloy.

Fig.9. a) Q" curve for grain-oriented H.C.R. alloy, b) Q" curves for Radiometal. Both alloys are approximately 50% Fe & 50% Ni.

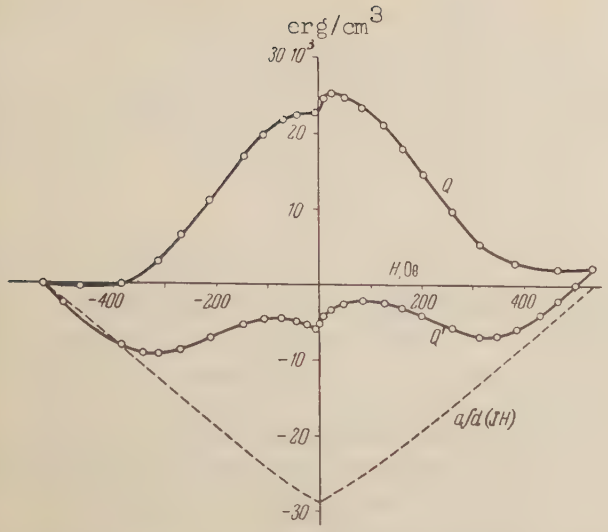

Fig.10. Results for single crystal of 3% silicon-iron.

(Q'',H) curve for Radiometal, however, in spite of the similarity in composition. For comparison the (Q'',H) curves for both specimens are shown on a large scale in Fig.9 (a & b), assuming this time that $\alpha = 8 \cdot 10^{-6}$ degree^{-1} in order that the ordinary magnetocaloric effect should be completely eliminated from the curves.

As far as the experiments have gone at present, we may say that Mumetal shows only a small rotation effect and no observable change due to boundary movements, while Radiometal gives larger rotation effects but still no boundary effects. However, H.C.R. alloy and Rhometal show large boundary effects and weak rotation effects, but the thermal changes due to boundary effects are of opposite sign in these two alloys. One suspects therefore that boundary effects are very dependent on crystal orientation. For this reason experiments are being made on single crystal specimens of silicon-iron. In Fig.10 are given some results for a single crystal of 3% silicon-iron when magnetized along a direction close to the [111] direction of difficult magnetization. Here the effects of rotation are very pronounced, and the (Q'',H) curve exhibits a broad, positive peak. Incidentally, we have just devised a new electrical method for measuring $(\partial J/\partial T)_H$ with such single crystal strip specimens, and we hope to report on such measurements soon.

8. Concluding Remarks

In this communication an attempt has been made to give an account of recent additions to our knowledge of the theoretical and experimental aspects of the heat changes accompanying magnetization processes. I should like to record my thanks to the Department of Industrial and Scientific Research and to my research students for their help in this work, as well as to the many friends, particularly Dr.E.W.Gorter of the Philips Research Laboratories, Eindhoven, and Dr.H.H.Scholefield of the Telegraph Construction and Maintenance Company, who have so willingly supplied me with the materials needed.

References

1. L.F.Bates, J.Phys.et Rad., 12, 459 (1951).
2. L.F.Bates & G.Marshall, Revs.Mod.Phys., 25, 17 (1953).
3. L.F.Bates & N.P.R.Sherry, Proc.Phys.Soc., B68, 304, 642 (1955).
4. L.F.Bates & A.W.Simpson, Proc.Phys.Soc., B68, 849 (1955).
5. E.C.Stoner & O.Rhodes, Phil.Mag., 40, 781 (1949).
6. T.Okamura, Sci.Rep. Tohoku Univ., 24, 745 (1936).
7. R.S.Tebble, J.E.Wood & J.J.Florentin, Proc.Phys.Soc., B65, 858 (1952).

REPORT ON SOME RECENT PROGRESS IN THE FIELD OF MAGNETIC INVESTIGATION IN TOKYO

- Ryogo Kubo

I would like to report here on the results of some recent experiments made by my colleagues in Tokyo. I shall speak on four topics from two different fields.

I. Magnetic Susceptibility of Transition Metals near Their Melting Points

The first topic is the change of magnetic susceptibility of transition metals and their alloys in the vicinity of their melting points. This work has been done by Y.Nakagawa[1] at Kaya's Laboratory in our Department of Physics. He made careful measurements of the susceptibility of transition metals, such as Ni, Co, Fe, Mn and their alloys up to 1600°C in an atmosphere of argon.

The results are summarized in Table 1. They are divided into several groups. Group 1 consists of those materials that do not comprise iron. Group 2 includes iron and iron-rich alloys. Group 3 consists of iron-poor alloys. Each group is further divided into subgroups. The materials in subgroups a show a decrease of χ (susceptibility per unit mass) when they melt. Subgroups b include those materials for which χ increases in melting. Finally, χ remains unchanged for the materials in subgroup c.

Table 1

Results of measurements of the magnetic susceptibility of transition metals and their alloys at their melting points (Nakagawa[1])

Group	Material	$\frac{\Delta\chi}{10^{-6}\,g}-1$	$\Delta\chi/\chi_S$ %	C_l/C_s
1a	Co	−1,5	−3	1,0
	Ni — Co (1 : 3)	−1,9	−6	1,0
	Ni — Co (1 : 1)	−1,4	−8	1,0
	Ni — Co (3 : 1)	−0,3	−3	1,0
1b	Mn	0,3	2	1,0
	Mn (γ)*	1,0	9	1,0
	Ni — Cr (3 : 1)	0,8	18	1,0
1b'	Ni — Cu (3 : 1)	0,16	5	1,3
	Ni — Mn (3 : 1)	1,2	10	1,0
	Co — Mn (3 : 1)	4,1	14	0,8
	Co — Cr (3 : 1)	1,1	10	0,6
1c	Ni	0,0	0	1,0
2a	Fe	−6,2	−20	1,5
	Fe — Cr (3 : 1)	−2,4	−14	2,3
	Fe — V (3 : 1)	−2,3	−15	3,4
2b	Fe (γ)*	1,6	7	0,4
	Fe — Ni (3 : 1)	2,0	8	0,8
	Fe — Co (3 : 1)	2,3	8	0,6
	Fe — Mn (3 : 1)	1,9	9	0,6
3a	Fe — Ni (1 : 3)	−0,5	− 3	1,0
3b	Fe — Ni (1 : 1)	1,2	5	1,0
	Fe — Co (1 : 3)	1,9	4	0,9
	Fe — Co (1 : 1)	3,8	10	0,8

*Extrapolated value.

$\Delta\chi$ in the first column of the table is the difference between the values of χ in the solid and liquid state at the melting point, that is, $\Delta\chi = \chi_l - \chi_s$.

The next column shows the percentage variation of the susceptibility referred to the solid state value. The last column is the ratio of the Curie constants, C, in the liquid and solid states. C is defined by

$$C = \frac{d(1/\chi)}{dT}.$$

for each state.

The group 1a is apparently the simplest case. The magnetic susceptibility of this group obeys the usual Curie-Weiss law, i.e.,

$$\chi = \frac{C}{T - \theta}.$$

As may be seen from the table, the experiments showed that C remains unchanged in melting for group 1a; the paramagnetic Curie temperature θ, however, shows a definite decrease, which means that χ decreases in melting.

For the groups 1b, 1b' and 1c the susceptibility preferably is described by a modified Curie-Weiss law of the type

$$\chi = \alpha + \frac{C}{T - \theta}.$$

where α is presumably independent of temperature, but increases incident to melting in all cases.

In group 1b, the first term α is predominant, so that χ is almost independent of temperature, but in other cases, the decrease of the second term may under certain circumstances cancel out the effect of the first term. This actually occurs for nickel, the susceptibility of which does not change in melting.

The materials of group 2a, including pure iron, have a body-centered cubic (b.c.c.) structure below the melting points. The large decrease of χ in this group is connected with this fact. We might say that in general the susceptibility of iron satisfies the relation

$$\chi_{\text{f.c.c.}} < \chi_l < \chi_{\text{f.c.c.}}$$

In fact, if we extrapolate the susceptibility vs temperature curve in the face-centered cubic (f.c.c.) structure region (γ-phase) of iron to the melting point, we find a value which is smaller than the susceptibility of the liquid phase. The extrapolated value is indicated in the table by an asterisk. The same phenomenon is also observed for iron-rich alloys. The atomic arrangement in the melts seems to be more like the f.c.c. than the b.c.c. structure.

Finally, an interesting remark which Nakagawa made concerning his experimental results is the following. The measured change of the susceptibility can nicely be interpreted in terms of the so-called Bethe-Slater curve (Fig.1). In this figure, the point for pure iron is different from that commonly assumed, for it corresponds here to the f.c.c. structure. This curve explains the variation of the exchange interaction constant and hence of the Curie temperature θ. θ may decrease or increase with the volume expansion at the melting point, depending on whether the material is in the state on the right or on the left side of the maximum.

The changes of the Curie constant C and of α are much more difficult to explain satisfactorily. They might be explained by some band theory considerations.

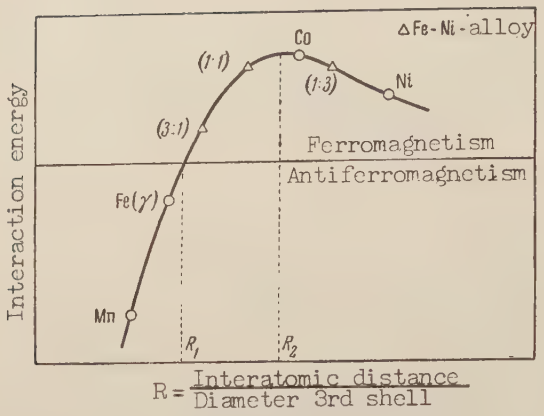

Fig.1. Bethe-Slater curve.

II. Magnetic Annealing and the Directional Order

The other topics of the present report are concerned with the mechanism of magnetic annealing and the directional order.

Magnetic annealing effect in Ni_3Fe single crystals

These experiments were made by S. Chikazumi; some of the preliminary results have been described in 1952 at the Maryland Conference by Prof.S.Kaya[2].

The effect of annealing in a magnetic field in the case of iron-nickel alloys is well known. If an Fe-Ni alloy is cooled in a magnetic field, it acquires a large permeability along the direction of the field, while the permeability in the perpendicular direction is reduced. Thus, magnetic annealing gives rise to an anisotropy, the minimum of which lies in the direction of the annealing field.

A mechanism of this effect was proposed by Prof.Néel[3] and independently by Yamamoto & Taniguchi[4]. The effect is attributed to a directional order produced by annealing. If the pseudodipolar type interactions are different between A-A, B-B and A-B atom pairs (A and B represent the components of the alloy in consideration), annealing in a magnetic field will induce an anisotropic arrangement of atoms. This is the directional order, which is frozen during the cooling process and produces an uniaxial magnetic anisotropy.

Chikazumi[5] recently made precise measurements of this effect using single crystals of Ni_3Fe. The magnetic field was applied in various crystallographic directions in the (110) plane during annealing and the anisotropy was measured at room temperature. The data can be easily analyzed to separate the uniaxial anisotropy from the other part. The dependence of the uniaxial anisotropy constant K_{uni} on the direction of annealing field can thus be determined.

The theoretical expression of the uniaxial anisotropy energy E_{uni}, according to Néel and Yamamoto & Taniguchi, is

$$E_{uni} = K_1 \sum \beta_i^2 \gamma_i^2 + K_2 \sum_{i>j} \beta_i \beta_j \gamma_i \gamma_j, \qquad (1)$$

where β_i's are the direction cosines of the saturation magnetization, and the γ_i's are those of the annealing field. The theory gives

$$K_2/K_1 = 4$$

for a f.c.c. lattice, but Chikazumi obtained 8.5 instead of 4. In Fig.2, curve A is the curve computed from the Néel-Yamamoto-Taniguchi theory, while curve B is based on Chikazumi's empirical formula, using the value $K_2/K_1 = 8.5$. It will be seen that the latter fits the experimental data very well.

The direction of the minimal uniaxial anisotropy does not generally coincide with that of the annealing field. The angle $\Delta\theta$ between these two directions can be calculated from Eq.(1), using the value $K_2/K_1 = 8.5$. The result is in good agreement with experiment (Fig.3).

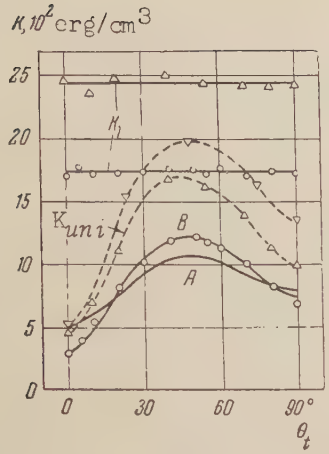

Fig.2. Variation of the crystal anisotropy energy K_1 and the uniaxial anisotropy K as functions of θ_t (the direction of the magnetic annealing field relative to the crystallographic [100] direction):
A) curve calculated according to the Neel-Taniguchi-Yamamoto theory,
B) K_{uni} computed according to Chikazumi's empirical formula using K_2/K_1 = = 8.5.
Experimental points for cooling rates of o - 14°, Δ - 5° and ∇ - 1° per min.

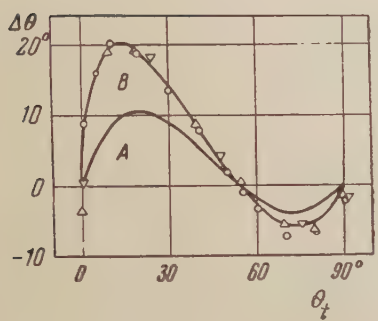

Fig.3. Variation of $\Delta\theta$ (angle of deviation of the minimum K direction from θ_t) as a function of θ_t: A) curve based on the Néel-Taniguchi-Yamamoto formula, B) Chikazumi's empirical formula with $K_2/K_1 = 8.5$. Experimental points for cooling rates of o - 14°, Δ - 5° and ∇ - 1° per min.

According to Chikazumi, the discrepancy between the 8.5 and 4 values for the ratio K_2/K_1 should be attributed to the existence of triangle nearest neighbors, the configuration characteristic of f.c.c. structure. This factor was not taken into account in the Néel-Yamamoto-Taniguchi theory. Its effect most probably is to increase the value of K_2.

Anisotropy in Ni_3Fe single crystals produced by rolling

Another interesting series of studies performed by Chikazumi is concerned with the roll-anisotropy effect.

Isoperm, which is 50-50 Fe-Ni alloy, is well known for this effect. The mechanism of this effect has also been discussed by Néel[3] and independently by Yamamoto and Taniguchi[4]. They attributed this effect to a directional ordering caused by migration of atoms under the strong influence of stresses occurring during rolling. In order to clarify the nature of this effect, Chikazumi and Suzuki[6] made experiments using single crystals of Ni_3Fe.

In connection with their work they obtained the domain patterns on the (110) surface of Ni_3Fe single crystals rolled in the [100] direction. Fig.4 shows the domain pattern for 55.2% roll reduction. The magnetization was perpendicular to the roll direction. Slip bands were also observed.

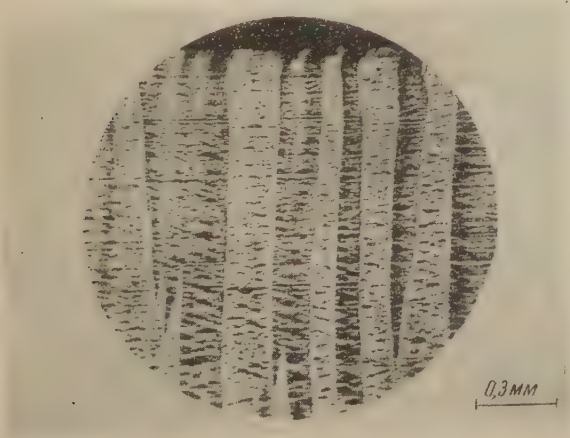

Fig.4. Domain pattern observed on the (110) surface of a rolled Ni_3Fe single crystal. Roll direction parallel to the [100] direction.

Chikazumi now suggests a new mechanism of the rolling effect. When the material is rolled out in (110) plane along [100] direction, we have only two sets of (111) planes, out of a total of four, which will

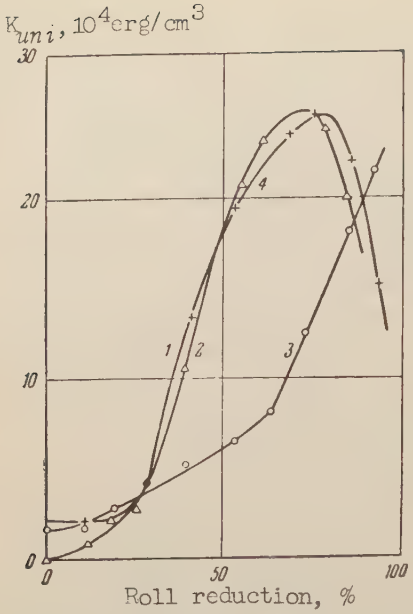

Fig.5. Uniaxial anisotropy induced in an Ni_3Fe single crystal by rolling as a function of the roll reduction for various preliminarey heat treatments. Rolling in the [100] direction. Heat treatments: 1) cooling in air, 2) annealing for 1 hr at 490°, 3) complete ordering, 4) quenching from 700°.

contribute to the deformation as the slip planes. Now suppose that there exists a certain degree of short range order before the process of rolling takes place. The slip will destroy the order between atomic planes on the two sides of the slip plane, whereas the order will remain unaffected in the slip plane. Since the slip occurs during rolling only in two sets of (111) planes, it leaves the short range order in the [110] direction unchanged, but it destroys the order in the other directions. Consequently, an anisotropy in the directional order is thus produced by rolling.

The dependence of the roll-anisotropy on the degrees of order present before rolling was examined in detail. It was expected that the roll-anisotropy would increase with increase in the degree of initial order. Actually, however, it was found that in the case of nearly perfect order before rolling, the roll-anisotropy effect becomes smaller (Fig.5).

At first glance this might seen to be a contradictory result. Actually it is not: in a perfectly ordered crystal, the dislocations run in pairs so as to "keep" the order. Consequently, plastic deformation will, in such cases, produce little effect on the directional order.

In the case of Isoperm, the rolling is carried out parallel to the (100) planes in the [100] direction. The slip now takes place equally in four (111) slip planes. The idea of Chikazumi will also apply here and shows that the directional order will be produced in the [110] direction on (100) plane. Thus the effect in Isoperm may be interpreted by means of the same mechanism.

Anisotropy of annealed cobalt-iron ferrites

The last topic of this report is also related to magnetic annealing and directional order. It concerns the magnetic annealing effect in cobalt-iron ferrites. Williams, Heidenreich and Nesbitt[7] inferred that the magnetic annealing effect in this ferrite is due to a preferential growth of precipitates. Iida, Sekizawa and Aiyama[8] in Kaya's laboratory, however, point out that it is not so, but that the effect must be related to the presence of vacant sites in the crystal and perhaps to directional ordering of the cations around the vacancies.

These investigators carefully studied the complex phase diagram of spinel and hematite[9]. They measured the oxidation and reduction of $Fe_{1-r}Co_rO_{4/3}$ at temperatures ranging from 900° to 1400°C. It was shown that the spinel phase is stabilized by the addition of Co. The oxygen pressure for the precipitation of hematite increases with increase of r, that is, the cobalt concentration. These investigators found that cobalt-iron ferrite can be cooled down from 1400°C without any precipitation of the hematite phase if the oxygen pressure is controlled in such a way that it is always kept just below the critical pressure of the hematite-magnetite transformation.

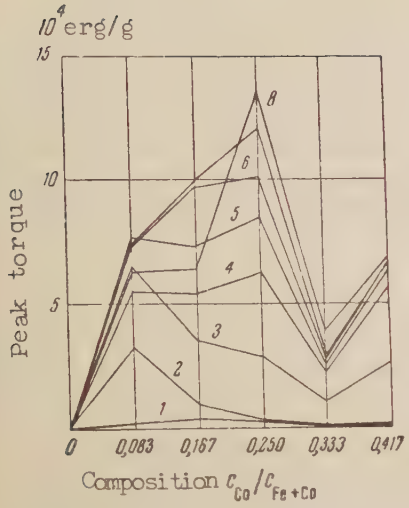

Fig.6. Peak torque vs composition curves for magnetic field-annealed iron-cobalt ferrite for different degrees of oxidation. Curve (1) is the result obtained after annealing at 1000°C for several hours in high vacuum; (2),(3),(4),(5),(6) and (7) are those after annealing further at 400° for 4 hours successively in oxygen at pressures of 0.7, 1.7, 6.5, 28, 160 and 765 mm Hg; (8) after annealing further at 500°C in the oxygen at 763 mm Hg pressure.

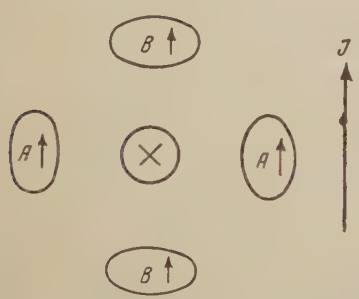

Fig.7. Schematic illustration of the configuration and symmetry of crystalline fields around a cation vacancy in a ferrite crystal.

Using this procedure Iida et al prepared a series of cobalt-iron ferrite samples, and performed x-ray studies and the conductivity measurements on them. There is no evidence of the occurrence of precipitation around 300°C, which is the effective temperature for the magnetic annealing of this material. A slight change of the activation energy of conductivity was observed. But this should not be attributed to the effect of precipitation because it also occurs in magnetite.

Iida et al found that the magnetic annealing effect is very strongly influenced by the degree of oxidation of the samples. When the samples are heated in high vacuum at high temperatures, the magnetic annealing effect completely disappears. It reappears when the samples are oxidized again.

Fig.6 shows the anisotropy, expressed in terms of the maximum torque, produced in samples with different Co concentrations by annealing in a magnetic field. The different curves are for different conditions of oxidation.

The result shows clearly that the magnetic annealing is more effective when the samples are more highly oxidized. There must therefore be cation vacancies in these crystals. Thus we may conclude that there is a close correlation between the presence of vacancies and the effectiveness of magnetic annealing.

Incidentally, the decrease of anisotropy for high oxygen pressure as shown in Fig.6 for cobalt concentrations r = 0.083 and 0.167 is attributed to precipitation of the hematite phase.

These investigators also made measurements of the relaxation process. A disc sample was cooled from 500°C down to a given temperature in a magnetic field and then kept at that temperature. The sample was turned by 45° and the torque required to keep it in this orientation was observed over a period of time. The rate of decrease of the torque represents the relaxation. The activation energy of this relaxation process was found to be about 1.4 ev, which should pertain to the process of atomic migration.

The conclusion drawn from these experiments is the following. The presence of vacancies and the presence of two cation components must be the most important factors in the magnetic annealing effect in ferrites. The atomic arrangement around a vacancy will be influenced by the applied magnetic field because the vacancy gives rise to an anisotropy crystalline field at each of the neighboring sites. The cations A and B which have oriented spins in

the direction of the applied magnetic field are influenced through spin-orbit interaction by such crystalline fields. The energy will differ for different arrangements of the two kinds of cations. Thus the atoms of one of the components will tend to take up positions next to the vacancies along the direction of the magnetic field, as illustrated schematically in Fig.7.

This shows that the cobalt ion must be the more sensitive to magnetic annealing, since its ground state is orbitally degenerate.

Department of Physics
University of Tokyo

References

1. Y.Nakagawa, J.Phys.Soc.Japan, 11, No.8 (1956).
2. S.Kaya, Revs.Mod.Phys., 25, 49 (1953).
3. L.Néel, Comp.Rend. 237, 1613 (1953); J.Phys.et Rad., 15, 225 (1954).
4. S.Taniguchi & M.Yamamoto, Sci.Rep.Res.Inst.Tohoku Univ., A6, 330 (1954); S.Taniguchi, Sci.Rep.Res.Inst.Tohoku Univ., A7, 269 (1955).
5. S.Chikazumi, J.Phys.Soc., Japan, 11, 552 (1956).
6. S.Chikazumi & K.Suzuki, Phys.Rev., 98, 1130 (1955).
7. H.J.Williams, R.D.Heidenreich & R.A.Nesbitt, Appl.Phys., 27, 885 (1956).
8. S.Iida, H.Sekizawa & Y.Aiyama, J.Phys.Soc.Japan, 10, 907 (1955).
9. S.IIda, J.Phys.Soc.Japan, 11, No.8 (1956).

ANISOTROPIC MAGNETIC CORES

- P.Denes

Compacted powder cores are used in order to reduce losses. In such cases it is generally necessary to settle for a relatively low effective magnetic permeability. The effective permeability μ_m depends primarily on the amount of insulating material in the core; the dependence is described by

$$\mu_m = \frac{3}{v}, \tag{1}$$

where v is the fraction of the volume occupied by the insulating substance. This formula follows from Ollendorf's relationship[1]

$$\mu_m = \frac{1 + (\mu + 1)\,[N(1-p) + p]}{1 + (\mu - 1)\,N(1-p)}, \tag{2}$$

where μ is the permeability of the ferromagnetic particles, N is the demagnetizing factor for these particles and p is the part of the volume occupied by the ferromagnetic material. Obviously, $p + v = 1$. Inasmuch as the demagnetizing factor for a sphere N = 1/3, for cores compressed of spherical particles, we have

$$\mu_m = \frac{3 + (\mu - 1)(1 + 2p)}{3 + (\mu - 1)(1 - p)}. \tag{3}$$

For μ = 300 and $v < 0.05$, i.e., values encountered in practice, this expression reduces to (1).

The best permeability values are obtained with cores of permalloy. An initial permeability μ = 300 (higher values do not substantially improve the effective permeability of the core) can be obtained by using binary Ni-Fe permalloy type alloys. In practice usually a third alloying element - chromium or molybdenum - is added for reducing the coercivity and increasing the resistivity. This leads to a reduction of the hysteresis and eddy current losses.

The highest core permeability that can be found in industrial catalogs is of the order of μ =120. A core of such material has the following characteristics: μ = 120, $\mu_a = 0.33 \cdot 10^{-3}$, $\mu_e = 4 \cdot 10^{-6}$ and $\mu_c = 7 \cdot 10^{-3}$, where μ_a is the hysteresis loss factor, μ_e is the eddy current loss factor and μ_c is the aftereffect loss factor. The increases in resistance ensuing in this case are 1) $R_a = \mu_a LBf$, due to the hysteresis loss, 2) $R_e = \mu_e Lf^2$, due to the eddy current loss and 3) $R_c = \mu_c Lf$, due to the aftereffect loss. Here L is the inductance of the windings in henries, B is the maximum kinetic inductance during a magnetization cycle in gauss and f is the frequency in cycles per sec.

In texts[2] we find the following extreme values of core parameters: μ = 125, $\mu_a = 0.2 \cdot 10^{-3}$, $\mu_e = 2.5 \cdot 10^{-6}$ and $\mu_c = 4 \cdot 10^{-3}$.

Can one increase the permeability of transformer cores without increasing the losses? Analysis shows that there are the following possibilities.

1. Reduction of the relative volume of the insulating material. The minimal amount of insulating substance sufficient for complete insulation of the ferromagnetic particles in the case of modern insulating materials is about 2% by volume. This represents a thin layer of the order of 10^{-4} mm uniformly surrounding the ferromagnetic particles; such layers of modern insulating materials are capable of withstanding the high pressures and heat treatment incident to the production of transformer cores. According to our experiments, some silicones are particularly suitable for insulation of permalloy powder cores in view of their excellent thermal stability.

2. Use of a ferromagnetic insulating material with a permeability μ_i. In this case the effective permeability of the core is given by

$$\mu_m = \frac{1 + (\mu - 1)[N(1-p) + \mu_i p]}{1 + (\mu - 1) N (1-p)}. \quad (4)$$

This relationship was obtained by calculation by the method of Ollendorf. If $\mu \gg \mu_i$ and v_i is the relative volume of the insulating material, where $v_i = 1 - p$, then for spherical ferromagnetic particles (N = 1/3), we have

$$\mu_m = \frac{v_i + 3\mu_i p}{v_i}. \quad (5)$$

Whence for $v_i < 0{,}1$, we obtain

$$\mu_m \approx \mu_i \frac{3}{v_i}. \quad (6)$$

The permeability of such a core increases with weak insulation in proportion to the permeability of the insulating material. Thus even a nonconducting ferromagnetic material with a susceptibility slightly greater than unity presents an appreciable advantage. This advantage can be utilized, however, only provided the part of the volume of the core corresponding to the insulating material does not have to be increased more than the increase in μ_i. Thus the requirements that must be met by a ferromagnetic insulating material are very exacting: in addition to the usual specifications (ability to form a thin and strong insulating layer, stability under pressure and heat, etc.), we have the new requirements of a high permeability and low losses.

Certain ceramic substances could in principle be used as ferromagnetic insulating core materials, but here we encounter a practical difficulty connected with the fact that the sintering conditions (temperature and atmosphere) necessary for obtaining good ferromagnetic ceramic materials differ from the conditions of heat treatment indicated for ferromagnetic metals.

3. Improvement of the basic ferromagnetic material. In principle, increases in permeability could be obtained by improving extant ferromagnetic materials. Thus, for example, by increasing the resistivity of the alloy we could obtain the same eddy current loss factor with less insulation, which would result in an increase in permeability.

To this end we experimented with Ni-Fe alloy powders. As is known the use of tin as an alloying element increases the resistivity of iron or nickel to a far greater extent than the addition of chromium or molybdenum. Thus, for example, the addition of 2% tin increases the resistivity of iron to 30 microohm·cm, while to obtain the same resistivity one must add 5% chromium or 10% molybdenum.[3] Replacement of molybdenum in Ni-Fe-Mo alloys by tin yields a 20-50% increase in resistivity.

The use of stanniferous permalloy powder for the fabrication of cores has certain technological advantages. Tin reduces the coercivity and consequently the hysteresis loss as compared with the binary permalloy. A thin layer of tin dioxide forms on the surface of stannous permalloy particles; this layer persists even after heat treatment in a reducing atmosphere and prevents the particles from coalescing. Furthermore, this dioxide coating facilitates the formation of a uniform thin insulating layer.

Tests in our laboratory yielded the following characteristics for stannous permalloy cores: $\mu = 140$, $\mu_a = 0{,}25 \cdot 10^{-3}$, $\mu_e = 2 \cdot 10^{-6}$ and $\mu_c = 5 \cdot 10^{-3}$.

4. Use of geometrically anisotropic ferromagnetic particles. An appreciable increase of the effective permeability is theoretically possible with the use of geometrically anisotropic particles in forming the cores. The

permeability of a core consisting of geometrically isotropic particles or of uniformly distributed geometrically anisotropic particles is the same in all directions. In the latter case the permeability value is the mean one, that is, it is the average value for the different permeabilities of the small constituent particles. It follows that if the geometrically anisotropic particles could be aligned in the same direction, the permeability in different directions would be different; consequently, there would be some one direction in which the permeability would be greater than the mean value.

Calculation of the effective permeability of a core comprised of oriented geometrically anisotropic particles is highly complicated and, consequently, we must introduce certain simplifications. Let us assume that the permeability μ of the principal ferromagnetic material is greater than 200, so that we can neglect $1/\mu$ compared with 1, the permeability of the insulating material. Further, let us assume for simplicity that the lines of force inside the ferromagnetic particles are rigorously parallel to the field and that the lines of force in the insulating material always follow the shortest path. Let us also assume that the relative volume of the insulating material in the cores is less than 0.05 and that consequently we can neglect the lines of force parallel to the longitudinal direction in the insulating material, i.e., the lines of force in the insulating material parallel to the surface of the ferromagnetic particles.

We calculate the effective permeability of the core from the permeance. Let us assume that the core is composed of isotropic particles consisting of ferromagnetic cubes with an edge length A, covered with insulating material in the form of plates of thickness $d/2$ (Fig.1). Then the lines of force induced by the external magnetic field will traverse a length A in the ferromagnetic material and a length d in the nonferromagnetic insulating material. The lengths are additive and the total reluctance in accord with our simplifying assumption (i.e., neglecting the lines of force parallel to the plane of the plate in the insulating material) will be given by

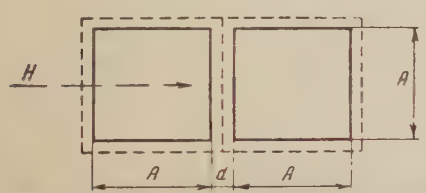

Fig.1. Relative dimensions of cubic ferromagnetic particles and the insulating material comprising the core.

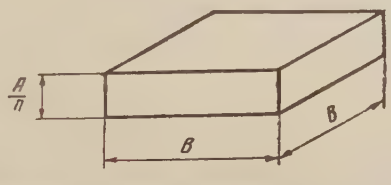

Fig.2. Dimensions of a ferromagnetic particle after rolling out a cubic particle with reduction of one of the edges by a factor of n.

$$\frac{A+d}{\mu_m} = \frac{A}{\mu} + \frac{d}{1},$$

where μ_m is the effective permeability of the core, μ is the permeability of the ferromagnetic material and 1 is the permeability of the nonferromagnetic insulating material. In view of the fact that the insulating layer thickness is very small as compared with the cube edge, we can write $A + d \approx A$, and therefore

$$\mu_m \approx \frac{A}{\frac{A}{\mu} + d} \approx \frac{A}{d}. \qquad (7)$$

The volume of the ferromagnetic particles is A^3; the volume of the insulation blocks is $3A^2 d$. Then the relative volume of the insulating material is

$$v = \frac{3d}{A}. \tag{8}$$

Then from (7) we have

$$\mu \approx \frac{3}{v}, \tag{9}$$

which is identical with (1).

Now let us see what happens if the ferromagnetic particles are geometrically anisotropic. Let us assume that we have rolled out our cube, reducing one of the edges by a factor of n to obtain a rectangular parallelepiped; its edges will be equal to A/n, B and B (Fig.2). The volume will obviously be the same:

$$A^3 = \frac{A}{n} \cdot B^2,$$

whence

$$B = A\sqrt{n}.$$

The thickness of the insulation on each face remains $d/2$, inasmuch as according to our premises this is the thickness necessary for complete insulation regardless of the shape of the ferromagnetic particles. In this case the volume of the insulation per particle will be $\frac{d}{2}\left(2B^2 + 4\frac{AB}{n}\right)$ and the relative volume of the insulating material will be

$$v_1 = \frac{3d}{A} \cdot \frac{n + 2n^{-1/2}}{3}. \tag{10}$$

Obviously, for obtaining the same insulating effect in the case of "rolled out" parallelepiped particles, we will need σ times more insulating material:

$$\sigma = \frac{v_1}{v} = \frac{n + 2n^{-1/2}}{3}. \tag{11}$$

If the direction of the external field is aligned with that of one of the edges, the effective permeability of a core comprised of a rigorously aligned arrangement of parallelepipeds will be

$$\mu'_m = \frac{B}{d} = \mu_m \sqrt{n}. \tag{12}$$

Consequently, the theoretical increase in permeability resulting from the use of aligned geometrically anisotropic particles will be very great, i.e., in the ratio $1:\sqrt{n}$. The practical difficulties, however, in the way of realizing such an improvement are appreciable: first, the anisotropic particles must be true parallelepipeds and, second, the alignment of these parallelepiped must be virtually perfect.

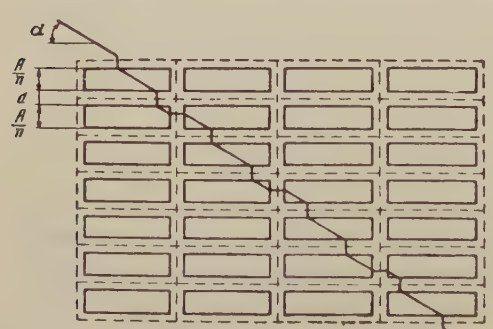

Fig.3. Diagram of a core with an ideal texture, i.e., a core consisting of a spatial network of perfectly aligned, uniformly spaced parallelepiped particles.

Inasmuch as any departure from perfect alignment will have a strong effect on the effective permeability, let us investigate this question theoretically. To this end let us first calculate the permeability of a core with an ideal texture in different directions, i.e., at an arbitrary angle α to the direction for optimal permeability

(Fig.3). In accord with our previous assumption the lines of force in the ferromagnetic particles will be at an angle α with the optimal direction and will be perpendicular to the planes of the insulating layers in the insulating material. Thus, the path length of the lines of force after traversing s vertical insulating plates will be $sB/\cos\alpha$, if we neglect the lengths of the path intercepts in the insulating material as compared with the path lengths in the ferromagnetic particles. Over this distance the lines of force will traverse h horizontal insulating layers. Consequently, the path length of lines of force in the insulating material will be $(h + s)\, d$. We thus obtain the following approximate expression for the effective permeability

$$\mu_\alpha = \frac{B_s/\cos\alpha}{(h+s)\,\alpha} = \frac{\mu'_m}{\cos\alpha}\cdot\frac{s}{h+s}. \tag{13}$$

If we take a sufficiently large number of particles, i.e., take s sufficiently large, the error resulting from our assumptions will be small; then setting

$$\operatorname{tg}\alpha = \frac{h\cdot\frac{A}{n}}{sB}, \tag{13'}$$

we will have

$$h = sn^{3/2}\operatorname{tg}\alpha. \tag{14}$$

Consequently,

$$\mu_\alpha = \frac{\mu'_m}{\cos\alpha + n^{3/2}\sin\alpha}. \tag{15}$$

If $\alpha = 0^\circ$, then from (12) we obtain:

$$\mu_0 = \mu'_m,$$

while if $\alpha = 90^\circ$, then

$$\mu_{90} = \frac{\mu'_m}{n^{3/2}} = \frac{\mu_m}{n}. \tag{16}$$

Eq.(16) can, of course, be obtained by taking the length of the magnetic flux path in the ferromagnetic material to be A/n and in the insulating material d.

Expression (15) can be used to calculate the effective permeability of a core composed of nonaligned geometrically anisotropic ferromagnetic particles. If we assume for example that the probability of orientation of the anisotropic particles is the same in all possible directions, the effective permeability will be

$$\tilde{\mu}_m = \frac{2}{\pi}\mu'_m\int_0^{\pi/2}\frac{d\chi}{\cos x + n^{3/2}\sin x} = \frac{2}{\pi}\mu'_m\sin\varphi\ln\frac{\operatorname{tg}\left(\frac{\varphi}{2}+\frac{\pi}{2}\right)}{\operatorname{tg}\frac{\varphi}{2}}, \tag{17}$$

where

$$\varphi = \operatorname{arctg} n^{-3/2}.$$

For cubic particles, $n = 1$ and $\tilde{\mu}_m \approx 0{,}91\ \mu'_m$; thus disordered orientation of cubical particles leads even theoretically to a small reduction of the permeability as compared to the case of an ordered arrangement of the cubes.

The curve of Fig.4 shows how rapidly the effective permeability of a core consisting of randomly oriented geometrically anisotropic particles decreases with increasing n (Fig.2); the thickness of the insulation in each case is assumed to be the same and equal to $d/2$. In the case of a disordered

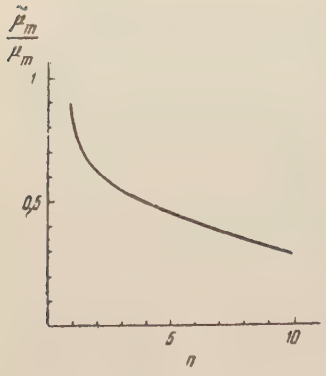

Fig.4. Dependence of the effective permeability of a core of rolled out particles separated by an insulating material on the factor n, i.e., the factor by which one of the edges of the initial cube is reduced by rolling.

arrangement, particles of symmetrical shape also give the best result.

It must be emphasized that the above result is obtained on the assumption that the thickness of the insulation is constant. On the other hand, if we assume that the relative volume of the insulating material is constant, then from (17) and (11) we obtain

$$\frac{\tilde{\mu}_m}{\mu_m} = \frac{2}{\pi} \cdot \frac{n^{3/2}+2}{3} \sin\varphi \ln \frac{\operatorname{tg}\left(\frac{\varphi}{2}+\frac{\pi}{4}\right)}{\operatorname{tg}\frac{\varphi}{2}}. \qquad (19)$$

In the region of $n = 1$ to 5, the right side of (19) differs little from unity. Consequently, formula (1) holds for strongly anisotropic (i.e., greatly elongated) ferromagnetic particles, but in this case one must generally use more insulating material.

It may be concluded from the above analysis that an attempt to use geometrically anisotropic particles is justified only provided they can be aligned with fair accuracy, for in the case of appreciable directional scattering (misalignment) the use of elongated particles may prove disadvantageous.

Let us designate the limiting misalignment angle by ψ and assume for the sake of simplicity that all particle orientations between $+\psi$ and $-\psi$ are equally probable.

Then the effective permeability will be given by

$$\tilde{\mu}_m(\psi) = \frac{1}{\psi} \mu'_m \sin\varphi \ln \frac{\operatorname{tg}\frac{\varphi+\psi}{2}}{\operatorname{tg}\frac{\varphi}{2}}. \qquad (20)$$

Let us introduce the notation $z = \frac{\psi}{\varphi}$. If z is not too large, for example, if $z < n$ and the angles $(\varphi + \psi)/2$ and φ do not exceed 20°, we can with fair approximation write

$$\frac{\sin\varphi}{\varphi} \approx 1 \quad \text{and} \quad \operatorname{tg}\frac{\varphi+z\varphi}{2} \approx (z+1)\operatorname{tg}\frac{\varphi}{2}.$$

Substituting these approximations in (20), we obtain

$$\tilde{\mu}_m(\psi) \approx \mu'_m \frac{\ln(z+1)}{z}. \qquad (21)$$

From this equation we can determine the allowable bounds for ψ. The curves given in Fig.5 show the variation of $\tilde{\mu}_m/\mu_m$ as a function of ψ for different values of n. It will be seen from the curves that the allowable bounds for the misalignment angle are of the order of 15-20°. If the "scattering" is greater, the effective permeability will be smaller than for a core composed of geometrically isotropic particles of the same thickness of insulation.

Thus the use of geometrically anisotropic particles is advantageous only within a rather narrow range of "scattering" angles. Technologically the necessary alignment may be achieved either by mechanical or magnetical procedures. The theoretical values shown in Fig.5 are, of course, realizable only when the ferromagnetic particles are in the form of regular parallelepipeds and are uniformly aligned. One may approach this ideal condition by means of appropriate

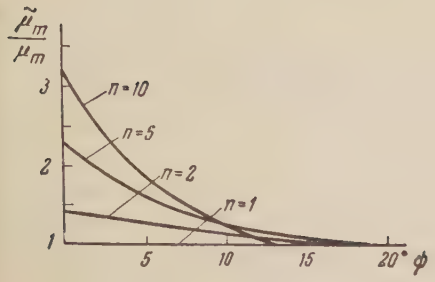

Fig.5. Variation of the relative effective permeability of a core composed of geometrically anisotropic particles as a function of the angle ψ of misalignment for different values of n.

technological procedures, for example, by repeated compressing. According to our studies one can increase the effective permeability by 30% by inducing alignment of ordinary commercial permalloy particles having a geometric anisotropy factor $n = 2$. One can also artificially increase the anisotropy factor of the particles by repeated rolling with intermediate anneals. Using such geometrically anisotropic particles, we were able to obtain in the laboratory cores with an effective permeability of the order of 200 and normal loss values. Through improved technology it should be possible to bring the experimental values closer to the theoretically possible ones.

In cores consisting of aligned, geometrically anisotropic particles, the hysteresis losses are somewhat greater than the hysteresis losses in cores of geometrically isotropic particles. The reasons for this are, first, that the coercive force in regular, geometrically anisotropic particles is greater than in symmetric particles and, second, that in the case of large geometric anisotropy factors the length of the shortest edge of the parallelepiped is so small that the coercive force is appreciably increased due to decrease in the size of the domains. This increase may be as much as 100% with $A/n \approx 10^{-3}$ mm and $n = 10$.

The shape of the particles has little effect on the aftereffect loss. In our experiment we were not able to detect any difference (within the limits of the experimental error) in the aftereffect loss in grains with different geometric anisotropies.

More significant is the influence of alignment on the eddy current loss. This loss factor according to Kornetzki & Weis[4] is

$$\mu_e = kd^2 \frac{\mu'_m}{\rho},$$

where k is a constant dependent on the shape, μ'_m is the effective permeability of the core, ρ is the resistivity of the ferromagnetic metal and d is the size of the particles measured normal to the lines of force. For spherical particles $k = 1.25$; for plates, $k = 4.13$. For perfectly aligned particles $d = A/n$ and, consequently,

$$\mu_e = 4{,}13 \frac{A^2}{n^2} \cdot \frac{\mu'_m}{\rho}; \qquad (22)$$

whence, invoking (12) we have

$$\mu_e = \frac{4{,}13}{\rho} A^2 n^{-3/2} \mu_m. \qquad (23)$$

The eddy current loss for a core of geometrically isotropic particles is

$$\mu_e = \frac{1{,}25}{\rho} A^2 \mu_m. \qquad (24)$$

If the particles have a geometric anisotropy factor n and are all perfectly aligned, the eddy current loss factor is decreased by

$$w_e = 3{,}3 \cdot n^{-3/2}. \tag{25}$$

The factor 3.3 is, of course, valid only for large values of n, inasmuch as for strongly anisotropic plates k increases from 1.25 to 4.13. The reduction of the eddy current loss factor can be very appreciable: thus for $n = 10$ from (25), we obtain in the case of perfect alignment $w_e = 0.1$.

If, on the other hand, the particles are not perfectly aligned but deviate from the optimal direction with equal probability by different angles up to $\pm\psi$, (23) reduces to the following form, provided $z \gg 1$:

$$\mu_e = 4{,}13 \cdot \frac{A^2}{n^2} \cdot \frac{\tilde{\mu}_m(\psi)}{\rho} \cdot \frac{1}{\psi} \cdot \int_0^{\psi} \frac{dx}{\cos^2 x}. \tag{26}$$

From this, taking into account (20) and (24), we obtain

$$w_e(\psi) = 3{,}3 \cdot n^{-3/2} \cdot \frac{\operatorname{tg}\psi}{\psi} \sin\varphi \cdot \ln \frac{\operatorname{tg}\frac{\varphi+\psi}{2}}{\operatorname{tg}\frac{\varphi}{2}}. \tag{27}$$

Utilizing the approximations from (21), we can simplify (27) to

$$w_e(\psi) \approx 3{,}3 \cdot n^{-3/2} \frac{\ln(z+1)}{z}. \tag{28}$$

Juxtaposition of Eqs.(21) and (28) shows that even for "scattering" angles ψ for which $\tilde{\mu}_m(\psi) = \mu_m$ & $w_e(\psi) = 3{,}3/n$. The eddy current losses decrease for highly geometrically anisotropic particles even in the case when due to imperfect alignment their permeability is smaller (rather than greater) than that of a corresponding core of geometrically isotropic particles.

Budapest, Hungary

References

1. F.Ollendorff, Arch.Electr., 25, 436 (1931).
2. R.M.Bozorth, Ferromagnetism, p.146, N.Y., 1951.
3. Ch.F.Burgess & J.Aston, Trans.Amer.Electrochem.Soc., 20, 205 (1911).
4. M.Kornetzki & A.Weis, Siem.Wiss.Ver., 15, 95 (1936).

BULLETIN OF THE ACADEMY OF SCIENCES OF THE USSR - Physical Series
Vol. 21, No. 8
Transactions of the Third Conference on the Physics of Magnetic Phenomena
(Continued from Vol.21, No.6; to be continued in Vol.21, No.9)

TABLE OF CONTENTS

	Page Orig.	Trans.
Influence of the structural characteristics of ferromagnets of the temperature dependence of the spontaneous magnetization - K.P.Belov and A.N.Goriaga	1038	1043
Investigation of the magnetization of ferrites in the vicinity of the Curie point - K.P.Belov, K.M.Bol'shova & T.A.Elkina	1047	1051
Temperature dependence of the differential susceptibility of cobalt in strong magnetic fields - L.Pal & T.Tarnotsi	1055	1058
Application of paramagnetic resonance (nuclear induction) to determination of the structure of Rochelle salt and epoxy resins - A.Lösche	1064	1066
Recent developments in the field of paramagnetic relaxation - C.J.Gorter	1083	1073
Temperature dependence of the magnetic anisotropy energy in nickel - I.M.Puzei	1088	1077
Superstructure and the temperature dependence of the magnetic anisotropy energy of nickel-iron alloys - I.M.Puzei	1094	1083
Temperature dependence of some magnetic properties of nickel - L.V.Kirenskii, R.S.Nosova & N.V.Reshetnikova	1105	1093
Temperature dependence of the magnetic susceptibility of nickel base alloys - D.I.Volkov & V.I.Chechernikov	1111	1099
Correlation between the electric and magnetic properties of chromium sulfides - N.P.Grazhdankina & I.G.Fakidov	1116	1103
Low-temperature resistivity of nickel alloys and its variation in magnetic fields - E.I.Kondorskii, O.S.Galkina & L.A.Chernikova	1123	1109
Resistivity and the effect of a strong magnetic field on the resistivity of iron-nickel alloys at low temperatures (14-77°K) - E.I.Kondorskii & I.E.Ozhigov	1131	1116
Investigation of magnetostriction and other even effects in the region of approach to saturation - G.P.D'iakov	1133	1118
Some aspects of the theory of elastic ferromagnetic (magnetostrictive) media - K.B.Vlasov	1140	1125
Some new experiments with Bitter figures - L.F.Bates	1149	1134

On the role of closure domain in technical magnetization processes - Ia.S.Shur, V.R.Abel's & V.A.Zaikova	1162	1149
Dynamic behavior of the domain structure in silicon-iron crystals - L.V.Kirenskii, V.D.Dylgerov & M.K.Savchenko	1168	1157
Domain structure of ferromagnets at high temperatures - J.Kaczer	1170	1161
Contribution to the theory of coercive force in thin sheets - J.Kaczer	1176	1168
Direct observations of the domains in a ferromagnet by means of a secondary emission electron microscope and an electron mirror - G.V.Spivak, N.G.Kanavina, I.S.Sbitnikova, I.N. Prilezhaeva, T.N.Dombrovskaia & V.K.Azovtsev	1177	1169
Nature of ferromagnetic domain walls - C.P.Bean	1183	1174
Thermal changes associated with magnetization - L.F.Bates	1184	1175
Report on some recent progress in the field of magnetic investigation in Tokyo - Ryogo Kubo	1197	1186
Anisotropic magnetic cores - P.Denes	1205	1193

Translated in 1958 by
Columbia Technical Translations
5 Vermont Avenue, White Plains, N.Y.

Number 9 Volume 21 1957

BULLETIN

of the

Academy of Sciences of the USSR

- Physical Series -

(Izvestiia Akademii Nauk SSSR)
(Seriia fizicheskaia)

Reproduction rights reserved

by

Columbia Technical Translations
5 Vermont Avenue
White Plains, New York

Single Issues
$20

Annual Subscription
$215

Transactions of the Third Conference
on the
Physics of Magnetic Phenomena

(Concluded from Vol.21, Nos. 6 and 8)

Lithoprinted in U.S.A.
EDWARDS BROTHERS, INC.
Ann Arbor, Michigan

CHARACTERISTICS OF TECHNICAL MAGNETIZATION IN GRAIN-ORIENTED FINE POWDER SPECIMENS

- Ia.S.Shur, E.V.Shtol'ts & G.S.Kandaurova

1. Correlation between the magnetic properties and the size of ferromagnets has been observed by a number of investigators[1]. In particular, it has been noted that in the case of powdered paramagnetic materials reduction of the particle size leads to an increase of the coercive force. It is natural to assume that this change in properties is connected with changes in the magnetic structure of the ferromagnet. From theoretical considerations Frankel' & Dorfman[2] predicted the existence of a critical size below which fragmentation of the material into domains becomes energetically disadvantageous, i.e., of a critical size below which all the powder particles must necessarily be single domain formations. Until now, however, we have had no detailed information on the domain structure of particles in the region of approach to critical size. There can be no doubt that the presence of a transition (from multiple to single domain) magnetic structure must be manifested in the magnetic properties of the material.

The purpose of our work was to investigate the distinctive features of the magnetic properties of ferromagnetic powders in this dimensional region. We chose a magnetically uniaxial Mn-Bi alloy for our study. Of all the ferromagnetic materials investigated to date, this alloy has the highest anisotropy constant at room temperature[3] ($K \approx 10^7$ erg/cm^3). One can artificially produce an appreciable anisotropy of the magnetic properties in powders of this alloy[4], which makes it possible to bring out more clearly the distinctive features of the magnetic structure of powders of different degrees of coarseness.

2. The manganese-bismuth alloy was prepared by sintering an appropriate mixture of powdered manganese and bismuth at about 300° and in the bulk had a coercive force of the order of 1000 oersted. The prepared alloy was crushed and pulverized mechanically and the resultant powder separated into a number of fractions by sieving. The mean particle diameter of the different fractions varied from 1 mm to a few microns. The magnetic properties were measured by the ballistic throw method on specimens in the form of discs. Magnetic texture (grain-orientation) was realized in the following manner. The powder fraction was thoroughly mixed with an appropriate binder and the mixture placed between the poles of an electromagnet; since setting occurred in the magnetic field, the particles were fixed in their field-oriented positions.

3. It was found that an appreciable change in the magnetic properties occurred with decreasing grain size of the Mn-Bi alloy particles. The curves of Fig.1 show the variation of the coercive force with the powder particle size for isotropic samples (curve 3) and textured samples (curve 1 for $\varphi = 0^\circ$ and curve 2 for $\varphi = 90^\circ$, where φ is the angle between the direction of the magnetic field during preparation of the sample, i.e., the texture axis, and the direction of the magnetic field during measurement). As may be seen the coercive force in textured samples with $\varphi = 0$ and in isotropic samples increases with decreasing particle size very appreciably, while the coercive force of textured samples with $\varphi = 90^\circ$, on the contrary, decreases with decreasing particle size. An appreciable anisotropy of the coercive force is observed in samples of fine powders. Thus in the case of the sample composed of particles with a mean diameter of 6 μ the coercive force in the $\varphi = 0^\circ$ direction is 13,200 oersted, while in the $\varphi = 90^\circ$ direction the coercive force is only 500 oersted.

Fig.2 shows the magnetization curves (after demagnetization with an alternating field at -195°) and the hysteresis loops obtained for samples of 9 μ

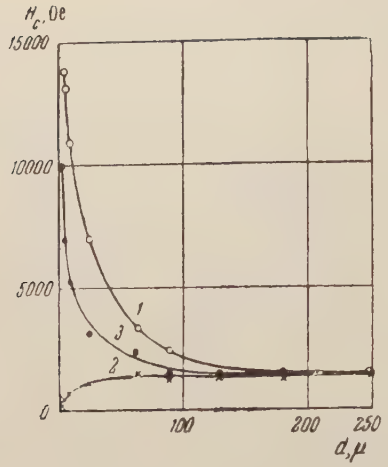

Fig.1. Variation of the coercive force with particle size: 1) textured sample with $\varphi = 0^o$, 2) with $\varphi = 90^o$, 3) isotropic samples.

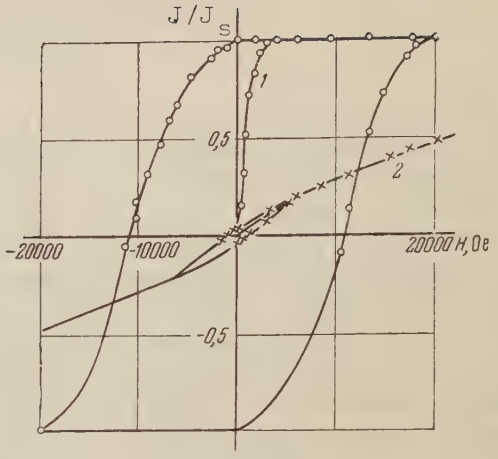

Fig.2. Magnetization curves and hysteresis loops obtained for a textured specimen of 9 μ particles: 1) $\varphi = 0^o$, 2) $\varphi = 90^o$.

diameter particles with $\varphi = 0^o$ and $\varphi = 90^o$. As may be seen from the figure, in the case of magnetization in the direction of the texture axis (curve 1) saturation magnetization is attained in a field of about 300 oersted. In the case of magnetization at 90^o to the texture axis (curve 2) a far stronger field is needed to attain saturation; in a field of 20,000 oersted the relative magnetization J/J_s amounts to only about 0.5. There is also observed a pronounced anisotropy of the hysteresis loops; in the case of magnetization along the texture axis ($\varphi = 0^o$) the area of the hysteresis loop is maximal, the remanence equals the saturation magnetization and the coercive force equals 11,000 oersted. In the $\varphi = 90^o$ case the area of the hysteresis loop is minimal, the relative residual magnetization J_R/J_s equals 0.03 and the coercive force is 700 oersted. It should be emphasized that with $\varphi = 0^o$, the field in which saturation magnetization is attained is appreciably (3-4 times) lower than the value of the coercive force.

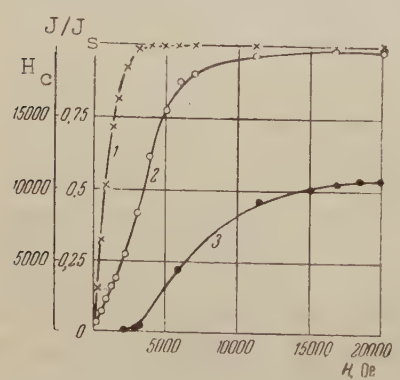

Fig.3. Variation of the 1) relative magnetization, 2) remanence, and 3) coercive force with the magnetizing field parallel to the texture axis ($\varphi = 0^o$). Particle size 9 μ.

Hereinafter we give only the results obtained in magnetizing the specimen along the texture axis, i.e., $\varphi = 0^o$.

The dependences of the relative magnetization, the residual magnetization and the coercive force on the magnetizing field for specimens of 9 μ particles are shown in Fig.3. It will be seen from the curves that the magnetization attains saturation in a field of 3000 oersted; in the same field the residual magnetization amounts to only 25% of its maximum value and the coercive force to only a few percent of its maximum magnitude. With increasing strength of the magnetizing field the remanence and coercive force increase; these parameters attain their maximum values after magnetization in a field of about 18,000 oersted.

Fig.4 shows the downward part of the hysteresis loop and the return curve obtained for a

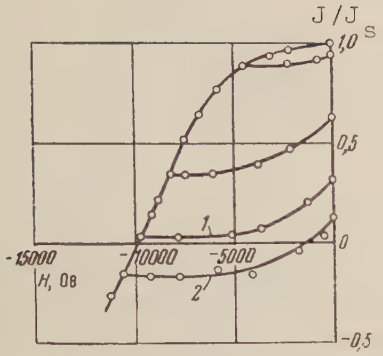

Fig.4. Descending branch of the hysteresis loop and return curves ($\varphi = 0^{o}$). Particles size 9 μ.

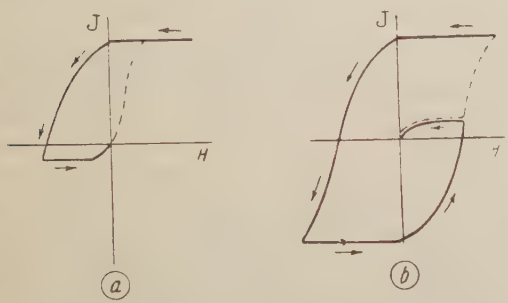

Fig.6. Diagram of demagnetization by means of a reverse field (solid line) and the corresponding magnetization curve (dash line).

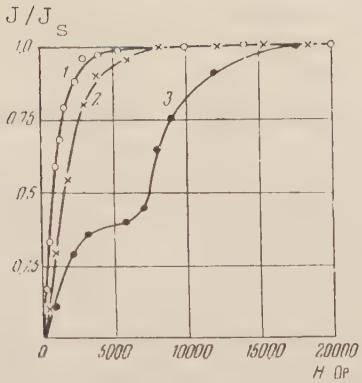

Fig.5. Magnetization curves with the field aligned with the texture axis ($\varphi = 0^{o}$): 1) after demagnetization with an alternating field at -195°, 2 & 3) after demagnetization by a reverse constant field at room temperature (see Fig.6 and accompanying text). Powder particles size 25 μ.

specimen composed of 9 μ diameter particles. It will be noted that the return curves are distinctive in that with decreasing field the magnetization remains constant over an appreciable field interval. Thus in the case of curve 1, for example, where the initial magnetization is very small, reduction of H by a factor of 2 produces virtually no change in magnetization; a noticeable increase in magnetization is observed only with further decrease in the negative field. Curves of analogous shape are obtained in the case of negative initial magnetization (curve 2). The return curves are fully reversible.

In Fig.5 are shown the magnetization curves for a specimen of 25 μ mean diameter particles after demagnetization by an alternating field at liquid nitrogen temperature (curve 1) and by a reverse constant field at room temperature (curves 2 & 3). Magnetization proceeds most easily after demagnetization by means of an alternating field. In the case of demagnetization by a reverse constant field the shape of the magnetization curves depends on the direction (polarity) of the demagnetizing field H_o relative to the field H in which the magnetization curve is recorded. Two ways of attaining the demagnetized state by means of a constant field are illustrated schematically in Fig.6. When the field H_o and H are opposite in direction, i.e., when the demagnetized state was obtained by the process illustrated in Fig.6 a, the magnetization process occurs easily. The field in which saturation magnetization is attained in this case is only somewhat higher (curve 2, Fig.5) than when the sample is demagnetized by means of an alternating field (curve 1, Fig.5). If the fields H_o and H are of the same polarity, i.e., if the demagnetized state was reached by the procedure illustrated in Fig.6 b, the magnetization process is hindered (curve 3, Fig.5); the magnetization curve has a step like shape and the initial part of the magnetization curve coincides with the return curve.

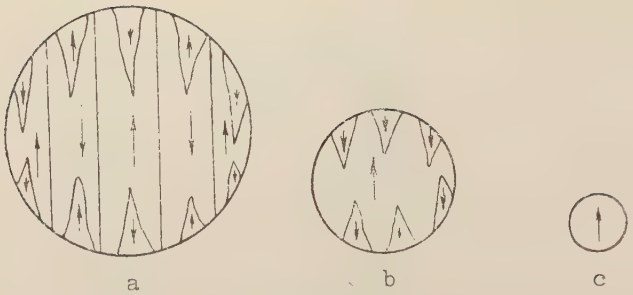

Fig.7. Domain structure of particles of different size: a) multiple domain structure characteristic of large particles, b) transition structure, c) single domain structure.

The distinctive features of the process of technical magnetization of fine powder specimens can be explained if we assume that the magnetic structure of the individual particles changes in a consistent manner with decreasing grain size. Presumably a sufficiently large particle is characterized by the multiple domain structure peculiar to magnetically uniaxial ferromagnets. Such a structure has, for example, been observed by Andrä[5] in cobalt crystals. In this case (Fig.7 a) in the demagnetized state the particle consists of a series of principal domains with 180° walls and dagger-shaped closure domains, whose magnetization is antiparallel to the magnetization of the principal domains. With decreasing particle size, the multiple domain structure becomes energetically disadvantageous, so that ultimately the smaller particles consist of only one principal domain with a number of closure domains along their edges (Fig.17 b).

Some of these closure domains in ferromagnets may, as in the case of soft magnetic materials[6], serve as nuclei of reverse magnetization. Consequently, the conditions of formation, growth and annihilation of closure domains should play a significant role in technical magnetization processes in ferromagnetic materials. That such a domain structure does exist in small particles is substantiated by our observations by means of powder patterns of the domain structure of small formations of the Mn-Bi alloy.[7] Finer powder particles should presumably have the single domain structure illustrated in Fig.7,c; in view of this, in such particles the process of reversal of magnetization can be realized only by irreversible rotation of the magnetization vector.

The magnetic behavior of our powder specimens can be explained if we assume that most of the powder particles comprising our specimens are characterized by the transition structure illustrated in Fig.7 b. If the powder is demagnetized at liquid nitrogen temperature, i.e., in the region where the anisotropy constant is very small,[3] a multiple domain structure is produced and the process of magnetization along the texture axis occurs as a process of displacement of the 180° walls accompanied by reduction of the volume and final elimination of the closure domains. The process of wall displacement occurs most easily (with the least expenditure of energy) and hence the particles are magnetized virtually to saturation in relatively weak fields (Fig.2). Apparently, a few closure domains persist, however, and these, upon removal of the field, play the part of reverse magnetization nuclei with the result that we observe a large value of the residual magnetization and coercive force (partial hysteresis cycle). The closure domains are fully eliminated only in relatively strong fields and then the maximum values of the remanence and coercive force are attained (Fig.3). Reverse magnetization of such a closure-domain-free particle may occur either through irreversible rotation of the magnetization vector or through creation and growth of nuclei. In both cases the expenditure of an appreciable magnetic-field energy will be necessary for realization of reversal of magnetism, which explains the high value of the coercive force observed in such cases (Fig.2). If, however, such reverse magnetization nuclei are already created in negative fields, they apparently persist through a certain reduction

of the negative field. This explains the invariance of the magnetization along the initial parts of the return curves (Fig.4). On the other hand, in weak negative fields and particularly in positive fields the closure domains begin to decrease in volume, so that in such cases the magnetization curve (curve 2, Fig.5) rises fairly steeply and differs little from the magnetization curve after demagnetization at -195° (curve 1, Fig.5). On the contrary, when the direction of the magnetizing field is parallel to the magnetization vector of the closure domains (curve 3, Fig.5, when the fields H_o and H coincide in direction) the magnetization occurs through the growth of reverse magnetization nuclei and appreciably stronger magnetic fields are necessary for attainment of saturation magnetization.

Thus from the magnetic behavior of fine, high coercivity powders we may infer the existence of a transition magnetic structure in particles somewhat above critical size. In such particles in addition to the principle domains, there exist closure domains. Under certain circumstances these closure domains may vanish and then the process of reverse magnetization will occur in the same way as in single domain particles. Under other conditions, these closure domains may play a significant role in the process of technical magnetization.

Institute of the Physics of Metals,
Ural Branch, USSR Academy of Sciences

References

1. V.H.Gottschalk, Physics, 6, 127 (1935); F.Bertaut, C.R., 229, 417 (1949); C.Guillaud, J.Phys.et Rad., 12, 492 (1951); Ia.S.Shur, T.D.Zotov & I.A.Chebotarev, Doklady AN SSSR, 81, 387 (1951).
2. Ia.I.Frenkel' & Ia.G.Dorfman, Nature, 126, 274 (1930).
3. C.Guillaud, Cahiers Phys., p.15 (1943).
4. E.V.Shtol'ts & Ia.S.Shur, Doklady AN SSSR, 95, 781 (1954).
5. W.Andrä, Ann.d.Phys., 15, 135 (1954).
6. Ia.S.Shur & V.R.Abel's, FMM (Physics of Metals & Metallography) 1, 11 (1955).
7. Ia.S.Shur, G.S.Kandaurova, E.V.Shtol'ts & A.V.Bulatova, FMM, 3, 191 (1956).

INVESTIGATION OF DISSOCIATION IN AN Ni-Be ALLOY

- N.N.Buinov, L.I.Podrezov & M.F.Komarova

In a number of investigations of high coercivity alloys[1-3] the magnitude of the coercive force is related to the internal stresses. Hence experimental clarification of the role played by stresses in determining the magnitude of the coercive force is of interest particularly where development of the theory of coercivity is concerned.

The role of stresses can be elucidated by investigation of the structure and measurement of the properties of ferromagnetic alloys such as Ni-Be, characterized by rapid aging and strong ordering. In the present work we investigated the aging of the Ni-Be alloy containing 1.9% Be. The phase transition in this alloy is accompanied by a large volumetric change, unusually strong ordering, considerable changes in the magnetic properties and segregation of a nonferromagnetic β-phase. The magnetic properties of this alloy have been investigated by Gerlach[4]; its structure has been studied by Lay[5]. These investigations show that the initial stage of dissociation in the alloy is homogeneous in character, while the later stages are heterogeneous. These investigators, however, did not establish any correlation between the coercive force and ordering and the structure of the alloy.

Experimental procedure

The alloy used in our investigation was prepared by melting in a high frequency vacuum furnace in the Laboratory of Precision Alloys headed by G.V. Gaidukov. According to the chemical analysis data, in addition to the Ni and the 1.9% Be, the alloy contained the following impurities: 1.25% Fe, 0.12% Al, 0.16% Cu, 0.15% Si and traces of Mg. After solidification of the melt, the alloy was subjected to hot working (forging) followed by a homogenizing anneal for 15 hours at 1100°. The structure of the alloy was investigated by means of an electron microscope by the method of oxide replicas[6] and by means of x-rays, using both the coarse-grain sample procedure[7] and back reflection[8]. In addition we measured the coercive force, the saturation magnetization, the hardness and the microhardness.

The specimens for the electron microscope investigations, for measurements of the hardness and coercive force and determination of the lattice constant by the back reflection technique measured 8 x 6 x 4 mm. In some cases the same samples were used for obtaining the x-ray patterns by the coarse-grain sample procedure. For the most part, however, the samples for the latter purpose were in the form of cylinders 0.3 mm in diameter and consisted of individual grains having a size of 0.1-0.3 mm.

To allow of direct correlation of the magnetic properties with the structure, we prepared a cylindrical sample 3 mm in diameter and 50 mm long. At one end this sample had an extension 2 mm in length and 0.5 mm in diameter. This extension served for obtaining the x-ray diffraction patterns at different stages of aging of the alloy at 500°. The coercive force, saturation magnetization and microhardness of this sample were measured at the different stages. The alloy was subject to aging at temperatures of 425, 500, 600 and 650° for different lengths of time. All measurements were performed at room temperature.

Results

The x-ray patterns of the initial hardened alloy show clear Laue spots and a few very weak two-dimensional diffraction effects. The latter may be

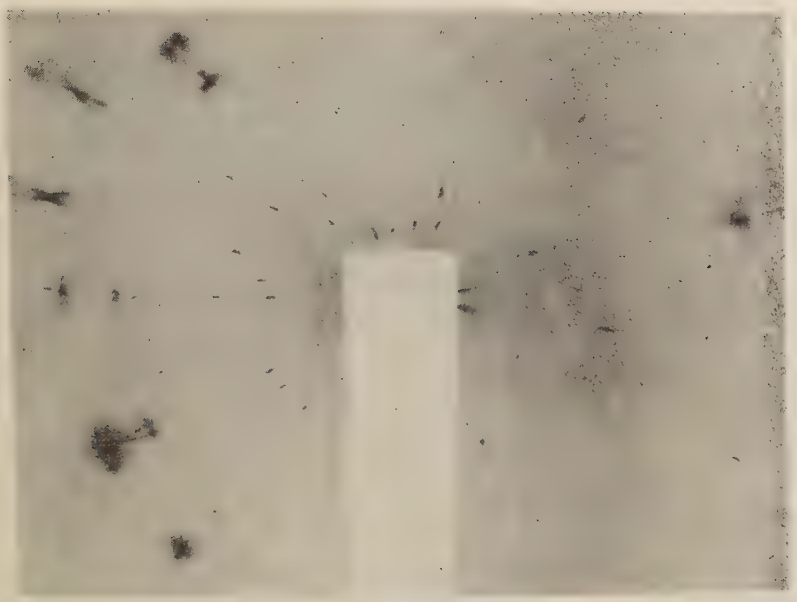

Fig.1. X-ray pattern of Ni-Be alloy sample aged at 425° for 3 hours 35 min (Ni radiation).

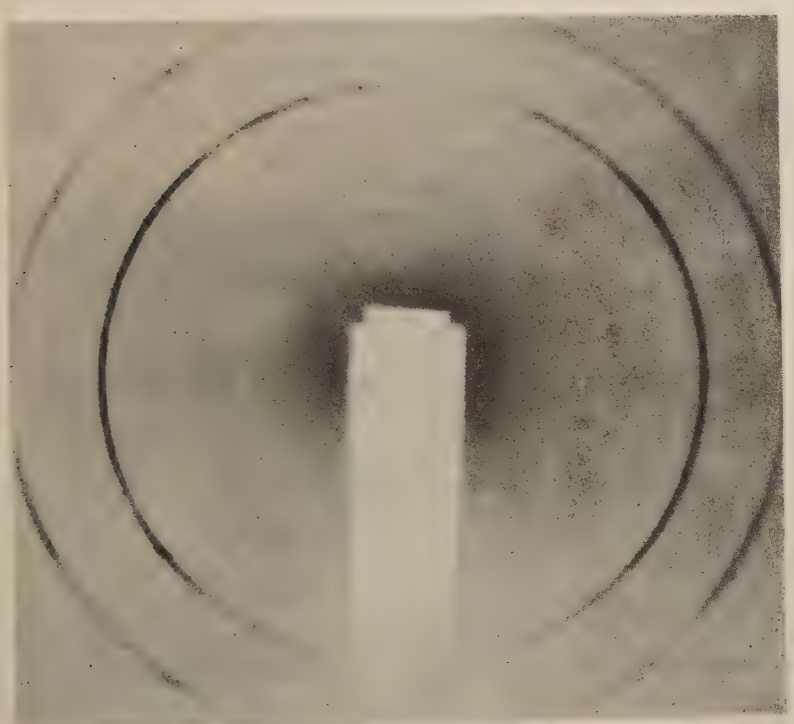

Fig.2. X-ray pattern of Ni-Be alloy sample aged at 500° for 58 hours.

regarded as proof of incomplete strain hardening of the alloy. This follows from the fact that these effects become more intense with aging and are analogous to the effects produced by subsequent aging. Short period aging of the quenched alloy, for example, for 15 min at 425°, already leads to the appearance of anomalous two-dimensional effects in the x-ray patterns. The intensity of these defects as well as the hardness of the alloy rapidly increases in the initial stages of aging, while the intensity of the Laue spots decreases (Fig.1). The Laue spots, without changing size, fade out almost entirely after aging of the alloy for 4 hours at 425° or 1-2 hours at 500°. No appreciable change in the intensity of the anomalous effects is observed at the stages of aging yielding the greatest hardness of the alloy; the coercive force also remains unchanged.

When the alloy as a result of aging attains maximum hardness, the x-ray patterns exhibit anomalous two-dimensional effects and in some cases linear effects in the form of bridges connecting neighboring two-dimension refraction spots and weak interference rings associated with the solid solution. No Laue spots are discernible in the x-ray patterns of such maximum hardness samples.

Further aging of the alloy, leading to reduction of its hardness, is accompanied by an increase of the coercive force, diffusion and weakening of the

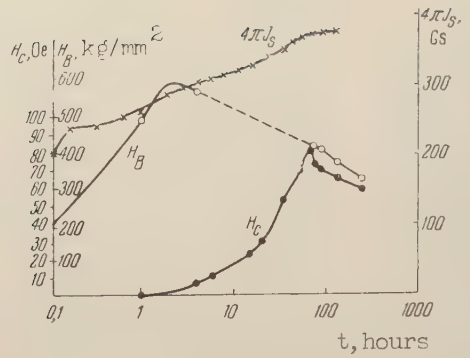

Fig.3. Variation of the saturation magnetization ($4\pi J_S$), the Brinell hardness (H_B) and the coercive force (H_C) with the aging time at 500°.

Time required by the Ni-Be alloy to reach maximum hardness and maximum coercive force at different aging temperatures

Aging temp.	Time to attain peak	
	hardness	coercive force
425	24 hrs	Maximum not reached after 105 hours
500	2 hrs	70 hours
600	10 min	3 hours
650	10 min	Not established

anomalous effects, an increase in the intensity of the solid solution interference rings and the appearance of rings associated with the β-phase. After aging of the alloy to the point where the coercive force is maximal, the anomalous effects in the x-ray patterns disappear entirely and only intense interference rings associated with the solid solution and the β-phase are observed (Fig.2)

It should be emphasized that the above results were obtained in x-raying both thin (0.3 mm) specimens and the massive samples intended for electron microscope observation and magnetic and hardness measurements.

Curves showing the variation of the Brinell hardness, the coercive force and the saturation magnetization with the aging time at 500° are shown in Fig.3. The times to attainment of maximum hardness and maximum coercive force at different aging temperatures are listed in the accompanying table. It will be seen that in all cases of aging, peak hardness in the alloy is attained earlier than the maximum coercive force.

Analysis of the anomalous two-dimensional diffraction pattern leads to a value of a = = 3.484 Å for the reciprocal lattice of the supersaturated solid solution, while from the interference rings we obtain a = 3.510 Å for the lattice constant of the beryllium-poor solid solution. The extent of the anomalous scattering regions does not very with temperature or aging time. The diameter of the rod-like regions of anomalous scattering increases with increasing distance from the reciprocal lattice sites of the solid solution, whereas according to commonly accepted concepts[9] the opposite effect should obtain.

Roundish or somewhat elongated light spots with dimensions of the order of 50 Å are observed in the electron microscope photographs of both freshly quenched and aged specimens that have not yet attained maximum hardness (Fig. 4). The elongated spots sometimes form a pattern reminiscent of the Widmanstatten structure. We have not been able to determine whether these light spots are due to Be-enriched zones or are associated with the structure of the oxide film forming on the surface of the sample.

New boundaries resembling fracture cracks form inside the grains in some sections of the alloy as a result of aging leading to the maximum hardness of the alloy at the given temperature (Fig.5). These crack-like lines also bear a certain resemblance to the block boundaries observed to form as a result of deformation at elevated temperatures in aluminum[10] and zinc[11]. With further aging of the alloy, there appear in it areas with a structure reminiscent of perlite (Fig.6). When the aging alloy has reached the state of maximum coercive force, these areas generally occupy at least 90% of the surface.

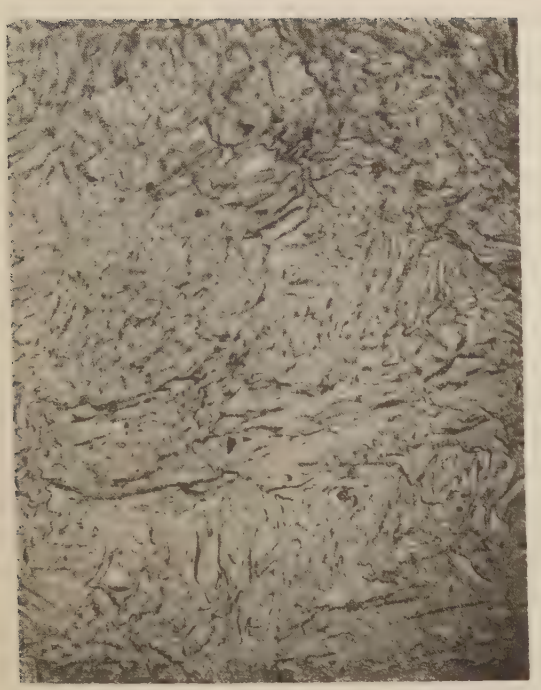

Fig.4. Electron microscope photograph of Ni-Be alloy aged at 425° for 4 hours. M 21,000 X.

Fig.5. Photograph of Ni-Be alloy quenched from 1100°. M 21,000 X.

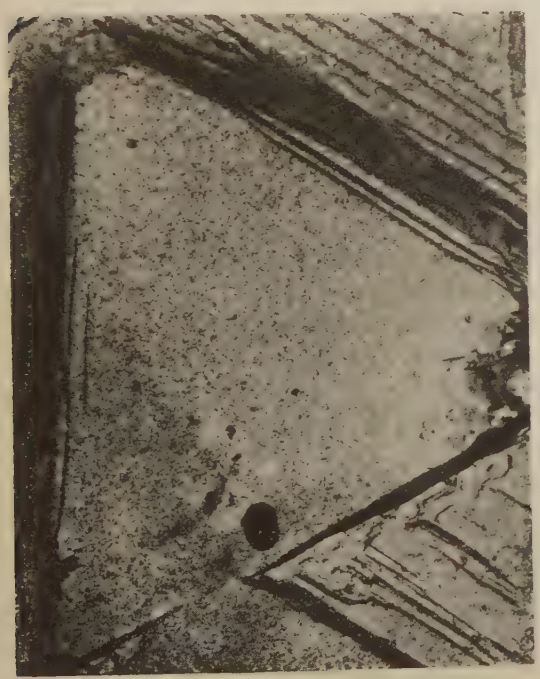

Fig.6. Photograph of Ni-Be alloy aged 5.5 hrs. at 500°. M 21,000 X.

Inasmuch as there are lines associated with the β-phase in the x-ray patterns corresponding to this stage of aging, it may be assumed that the perlite structure is formed by numerous β-phase lamillae alternating with the solid solution. The areas with plates arranged in the same direction measure about 1-2 μ. This is also probably the approximate size of the solid solution crystals yielding the continuous interference rings on the x-ray patterns. The β-phase plates have a length of 0.1-0.5 μ. The separation between them varies from 0.05 to 0.2 μ.

A regular Widmanstatten structure was observed only after slow cooling of the alloy.

Discussion of the experimental results

Aging of the Ni-Be alloy begins with the formation in it of Heine-Preston zones enriched with beryllium and having a distorted matrix lattice. This is evinced 1) by the presence in

the x-ray patterns of anomalous effects associated only with the reciprocal lattice of the supersaturated solid solution and 2) by the invariance of the lattice parameter of the solid solution during the initial stages of aging (according to Lay[5]). At this stage there develop in the alloy elastic distortions that are responsible for the anomalous effects observed in the x-ray patterns. The disappearance of the Laue spots and the widening of the diameter of the rod-like areas of anomalous dispersion towards their ends (i.e., with increasing distance from the reciprocal lattice sites) may be regarded as proof that the alloy is fragmented into blocks that are elastically compressed or elongated and but little disoriented relative to each other.

Insofar as the coercive force of the alloy remains virtually constant during the first stage of dissociation, it may be assumed that the segregated zones as well as the alloy matrix are ferromagnetic. The ferromagnetism of the zones may be due to their structure rather than to their composition.

During the second stage of dissociation, there occurs in the alloy a rearrangement of the zones into β-phase particles. This rearrangement is accompanied by the formation of greatly disoriented blocks or grains; this is evidenced by the appearance in the Laue patterns of interference rings associated with the solid solution and the β-phase. Formation of strongly disoriented blocks or grains may occur in two ways: either through rupture of the coherent bonds between the strongly elongated and compressed blocks and between the blocks and the zones transforming into β-phase particles or by recrystallization. We feel that the first alternative is the more probable if only because one can frequently observe migration or transfer of β-phase particles from one block to another.

Block formation with rupture of the coherent bonds apparently begins even before transformation of the zones into β-particles inasmuch as new boundaries resembling cracks appear in some sections of the alloy without segregation, but this process proceeds most intensely during conversion of the zones into β-phase particles. This transformation is accompanied by relief of stresses, at least stresses of the second kind, which is evinced by a decrease in the hardness of the alloy and the appearance in the x-ray patterns of a $K\alpha_1$ and $K\alpha_2$ doublet due to reflections from the (331) and (420) planes (Cu radiation). At the same time the coercive force increases from a few oersted to 80 oersted.

It follows, therefore, that the high coercive force observed in the Ni-Be alloy should be attributed to the appearance of particles of the β-phase rather than to the existence of stresses in the alloy. The thin β-phase plates, being present in large numbers (depending on the composition of the alloy they may account for as much as 25% of the total volume) divide the alloy into isolated sections. Inasmuch as the length of the β-phase lamillae exceeds the distance between neighboring lamillae, it may be assumed that the particles of solid solution between the lamillae are geometrically anisotropic. The isolation of the individual particles of solid solution and their anisotropic shape sharply increase the coercive force of the alloy.

If during aging together with alteration of the composition of the solid solution there occurs an appreciable change in the anisotropy constant, one may expect a certain additional increase in the coercive force due to this factor.

Some details of the anomalous effects require additional analysis and will be considered in a future paper. Here we only note that the anomalous effects observed in the x-ray patterns for the Ni-Be alloy are similar to the effects observed by A.M.Elistratov[12] in x-ray patterns of Cu-Be alloy.

Conclusions

1. On the basis of our electron microscope and x-ray studies and our measurements of the hardness and coercive force it may be concluded that dissociation in the Ni-Be alloy, as in Al-Cu, Al-Ag and Al-Zn alloys, proceeds in two stages.

2. The first stage of dissociation is characterized by the formation of zones rich in the alloying component (Be) and the appearance of appreciable elastic strains leading to distortion of the block structure. This stage is associated with maximum ordering of the alloy. Inasmuch as during this first dissociation stage the coercive force changes very little, it may be assumed that the zones and regions of localized elastic strain do not offer any appreciable resistance to reversal of magnetization.

3. During the second stage of dissociation, there occurs a rearrangement or transformation of the zones into particles of the β-phase. In conjunction with this, the coercive force of the alloy increases from a few oersted to 80 oersted. Thus it may be concluded that the high coercive force of the aged Ni-Be alloy is associated with the segregation of β-phase particles rather than with the presence of stresses.

We take this opportunity to thank Iu.A.Bagariatskii and A.M.Elistratov for discussion of the results of our work.

Institute of Physics of Metals,
Ural Branch, USSR Academy of Sciences

References

1. A.H.Geisler, Electr.Eng., 69, 37 (1950).
2. D.Balli & M.I.Zakharova, Doklady AN SSSR, 96, 737 (1954).
3. A.Komar & D.Tarasov, Zhur.tekh.fiz., 10, 1145 (1940).
4. W.Gerlach, Z.S.Metallkunde, 28, 80, 183 (1936).
5. H.Lay, ZS.Metallkunde, 29, 32 (1937).
6. A.A.Lebedev (editor), "Elektronnaia mikroskopiia" (Electron microscopy) (M.1954).
7. A.M.Elistratov, Doklady AN SSSR, 69, 337 (1949).
8. G.S.Zhdanov & Ia.S.Umanskii, Rentgenografiia metallov (Radiometallography) Part 1, M.-L., 1937.
9. R.W.James, Optical principles of the diffraction of x-rays, 1948. (Cited in Russian trans., M.1950).
10. J.M.Kelly & R.C.Gifkins, J.Inst.Met., 82, 475 (1954); W.A.Rachinger, J.Inst. Met., 80, 415 (1952).
11. J.A.Ramsey, J.Inst.Met., 80, 167 (1952).
12. A.M.Elistratov, Doklady AN SSSR, 88, 669 (1953); 101, 69 (1955).

CHANGES IN THE STRUCTURE AND PROPERTIES OF NICKEL SOLID SOLUTIONS DURING HEAT TREATMENT

- B.G.Livshits

The results of some recent investigations of alloys indicate that there may exist an additional distinctive state - and, accordingly, another phase transition - in homogeneous solid solutions, which is not ordered in the usual sense of the word. The existence of such a state was first noted in 1951 by Thomas[1] who investigated it in nichrome (80% Ni + 20% Cr) and other alloys by measuring their electric resistance. Thomas called this new structural state the K-state.

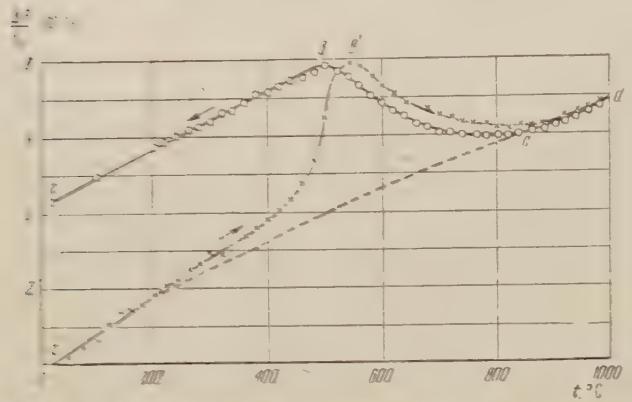

Fig.1. Temperature dependence of the resistance of 80% Ni + 20% Cr nichrome alloy: abcd - variation of the resistance in the stable state, a'b'cd - variation in the state after quenching.

The writer in collaboration with Sh.Sh.Ibragimov, A.Z.Ivanushkina and M.P.Ravdel' investigated this new phenomenon in nichrome, molybdenum permalloy and invar alloyed with molybdenum, using different procedures such as measurement of the resistance, expansion, hardness, saturation magnetization and so on; all the measurements yielded consistent results.

The curve abcd in Fig.1 shows the temperature dependence of the resistance of nichrome in a stable state. If we take the resistance values corresponding to sections ab and cd, after making the appropriate correction for the temperature coefficient, we find that the resistance at low temperature is higher than at high temperature. The existence of this difference in resistivity can also be proved directly by quenching the alloy from high temperature; that is, by such quenching one can obtain a value of the resistance corresponding to the point a'. Heating the quenched specimen yields the transition curve a'b' and then the curve b'cd. The character of the variation over the section a'b' is determined by the kinetics of the phase transformation. The section b'c, which is similar to bc, characterizes the resistance of nichrome in the stable state.

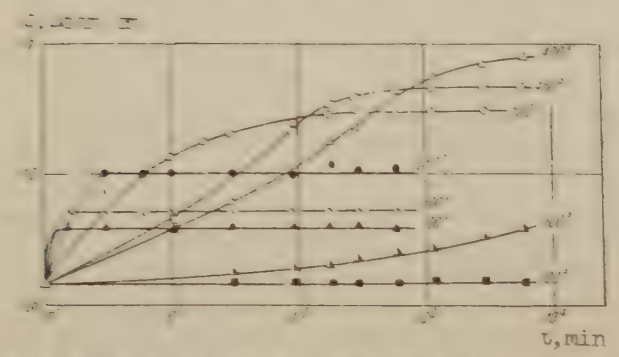

Fig.2. Variation of the resistivity of initially quenched nichrome with the annealing time at different temperatures. All measurements made at room temperature.

The character of this transformation as evinced by the variation of the resistivity measured at room temperature during reheating of quenched nichrome specimens is shown in Fig.2. The stable K-state is readily obtained by annealing at 450° for 15 hours, at 500° for 2 hours or at 550° for 5 min, followed by quenching. Calculation of the activation energy yields a value of 43 Kcal per gram atom.

The variation of the resistance

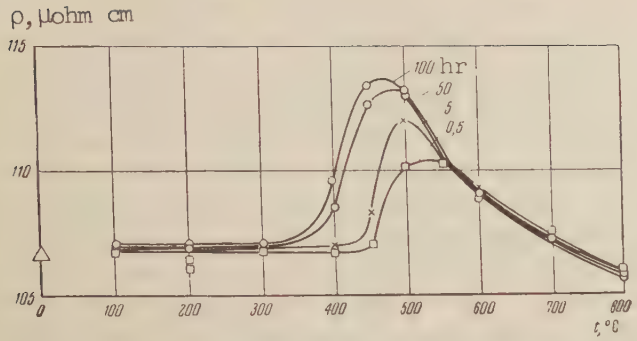

Fig.3. Variation of the resistivity of nichrome with the annealing temperature for different annealing times.

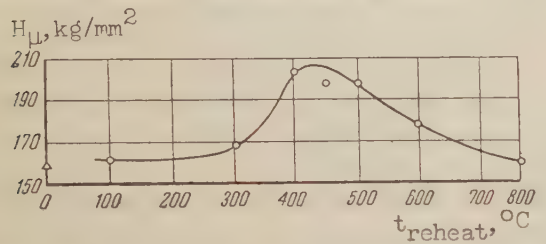

Fig.4. Variation of the microhardness of nichrome with the reheating temperature (reheating period 10 hours).

with the reheating temperature is shown in Fig.3. The extreme right and left points on each curve lie at approximately the same level and correspond to the supercooled high-temperature solid solution (each reheating was terminated by rapid cooling). It will be seen that we are dealing here with a phase transformation associated with displacement of the atoms in the solid solution.

Analogous curves can be plotted on the basis of results of measurements of the microhardness (Fig. 4), as well as on the basis of dilatometric data, measurements of the specific heat, etc.

The lattice of the high-temperature phase supercooled to room temperature is less compact than the lattice of the low-temperature phase. This is substantiated by x-ray diffraction studies.

The photograph of Fig.5 shows the microstructure of the supercooled high-temperature solid solution. Fig.6 shows the microstructure of the low-temperature K-state as brought out by a special method of preparing and etching the section.

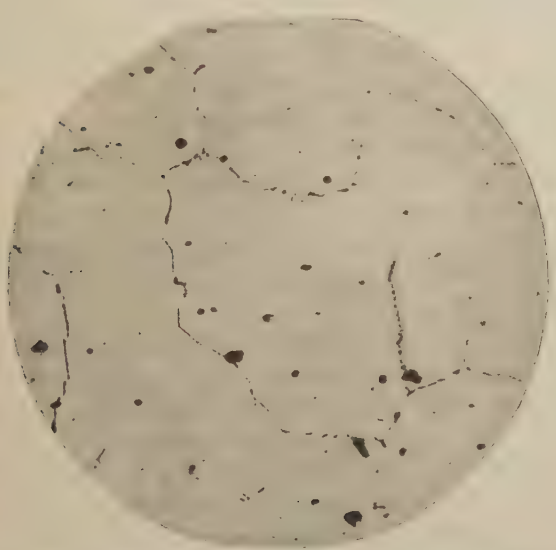

Fig.5. Microstructure of nichrome after quenching from a high temperature (supercooled high temperature solid solution). Magnification 400 X.

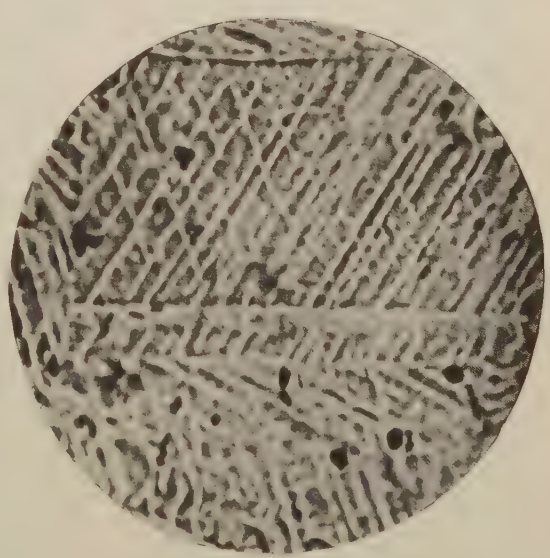

Fig.6. Microstructure of the K-state of nichrome. Magnification 400 X.

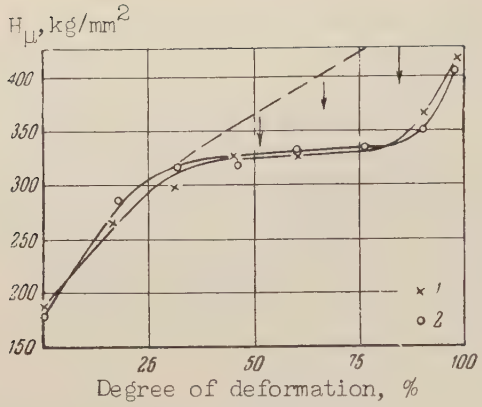

Fig.7. Influence of "strain hardening" (deformation) on the microhardness of 1) 80% Ni + 20% Cr nichrome and 2) 60% Ni + 15% Cr + 25% Fe iron nichrome after cooling of the alloys from 1100° at the rate of 25° per hour.

As a result of cold working, the K-state, just as the ordered structure, breaks down, but in this case the resistance does not increase as in the case of the ordered solution, but on the contrary decreases. The K-state is re-established by reheating, and then the resistivity increases to the stable value corresponding to the given annealing temperature. It is interesting to note that the hardness of a specimen heat treated to the K-state also apparently decreases under the influence of deformation. In the interval of reductions in thickness from 23 to 80%, the increase in hardness due to strain is compensated by the reduction in hardness due to destruction of the K-state. This is indicated by the arrows in Fig.7. It will be seen from the figure that in a certain interval of deformations the hardness does not change and that the hardness begins to increase, i.e., strain hardening becomes effective, only when the K-state is wholly destroyed. It will also be seen from Fig.7 that a similar effect is observed in Ni-Cr-Fe alloy (nichrome with 25% iron, i.e., far from Ni_3Cr as regards composition).

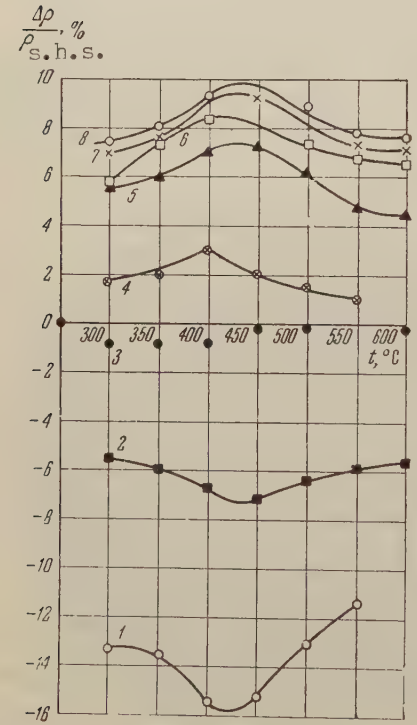

Fig.8. Variation of the resistivity (percent change in resistivity relative to the resistivity of the strain hardened state) with reheating temperature of Ni_3Fe alloys containing different amounts of molybdenum: 1) 0.2%, 2) 0.5%, 3) 1%, 4) 2%, 5) 3%, 6) 4%, 7) 5% and 8) 6% Mo.

Can the K-state be an "ordered" state of an alloy such as Ni_3Cr? This is the assumption made by Taylor & Hinton[2] who consider that in ordering the resistance need not necessarily decrease but may increase. Evidence against this inference is the anomalous variation of the resistance in molybdenum permalloy which in this respect behaves just as nichrome.

The variation of the resistivity with reheating temperature of Ni_3Fe alloy and Ni_3Fe with different amounts of Mo added is shown in Fig.8. The initial state is the disordered solid solution obtained by strain hardening (severe deformation).

Curve 1 for Ni_3Fe without molybdenum (0.2% Mo) is typical of the curves obtained for ordered alloys. It will be seen that the presence of even 0.5% Mo (curve 2) noticeably reduces the degree of order. With 1% Mo (point 3) the resistivity of the alloy becomes virtually insensitive to heat and mechanical treatment, i.e., the resistance almost does not change as a result of quenching, annealing and cold working. The introduction of larger amounts of Mo

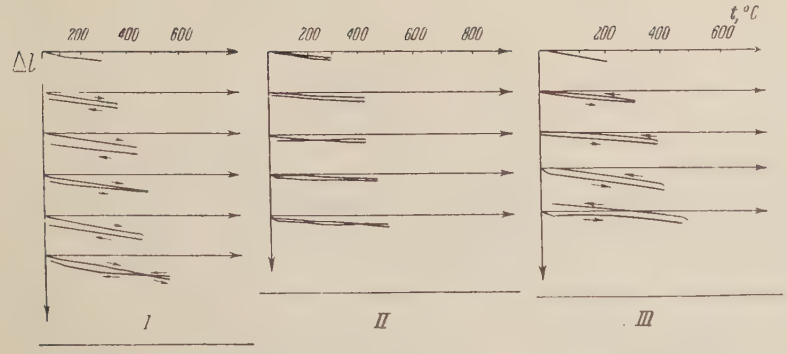

Fig.9. Dilatometric curves for I) Ni_3Fe alloy, II) Ni_3Fe + 1% Mo and III) Ni_3Fe + 5% Mo.

(2-6% - curves 4-8) results in a change of sign of the $\Delta\rho$ effect, that is, ordering gives way to formation of the K-state. The intensity of the effect increases with increasing molybdenum content. Similar changes are observed as a result of reheating after quenching from 900° except that in this case the change in ρ is somewhat smaller than after attainment of the disordered state by plastic deformation.

It is improbable that the observed effect can be the result of ordering particularly since it increases with the molybdenum concentration, which presumably can only impede ordering.

It is interesting to note that the variation of the specific volume follows the variation of the resistivity: in the case of ordering of the alloy having the Ni_3Fe composition, the specific volume decreases while with an Mo content of 2 to 5% the specific volume increases in the process of formation of the K-state.

The dilatometric curves for the three alloys having the compositions Ni_3Fe, Ni_3Fe + 1% Mo and Ni_3Fe + 5% Mo are shown in Fig.9. Prior to the measurements the alloy samples were quenched from a high temperature (homogeneous solid solution) and then reheated in the dilatometer to 300, 400, 450, 475, 550 and 600° and held at each of these temperatures for 7 hours. It will be obvious that ordering of the solid solution in the case of Ni_3Fe leads to reduction of the volume.* In the case of the alloy with 5% Mo the volume increases. The intermediate alloy with 1% Mo exhibits virtually no volumetric variation.

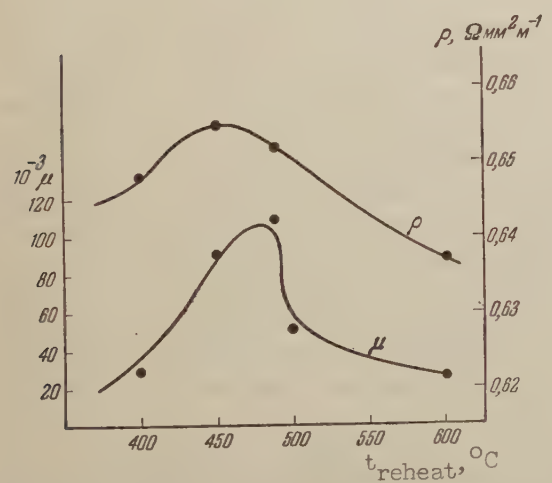

Fig.10. Variation of the resistivity and permeability of superpermalloy with the reheating temperature (1 hour heating).

The dependences of the hardness, saturation magnetization and mechanical properties on the temperature and time of reheating are in general similar to the variation of the resistance: starting with the disordered state, attained by quenching or cold working, each of these properties attains a maximum at a certain reheating temperature (around 450°) and then falls off as the heating temperature is further increased.

The variations of the magnetic permeability (according to Bozorth[3]) and of the resistivity of superpermalloy with the reheating temperature (1 hour heating) are compared in Fig.10. The correlation between the two quantities is good, particularly if we take into account the high structure-sensitivity of the permeability. For complete

---

*The curves of Fig.9 show the change in length Δl which uniquely characterizes the variation in volume.

analysis one must know how the crystal energy and the magnetostriction depend on the degree of the K-state.

This degree, i.e., the phase state, can be evaluated from the resistivity which is virtually independent of internal stresses, grain size and concentration of minor impurities.

Thomas[1] advanced the hypothesis that the K-state is a state of submicroscopic inhomogeneity of the solid solution which is obtained as a result of stable segregation of one of the solution components. In the specific case of nichrome one can speak only of local segregation of chromium. The linear dimensions of the chromium enriched regions are of the order of the free path length; hence the formation of such inhomogeneities results in an increase of the resistivity. An analogous argument was advanced with regard to permalloy by Ravdel' and the author[4]: it was shown that the introduction of molybdenum into Ni_3Fe leads to a gradual transition of the solution, stable at low temperatures, from the ordered state to the K-state (the state of segregation). This transition occurs, as is evident from what has been said above, at a Mo content of about 1%. It was suggested that the Mo atoms segregate. Dekhtiar[5] came to the same conclusion as the result of his investigation of the magnetic properties of molybdenum permalloy which after reheating exhibits two Curie points. Dekhtiar further assumes that in the case of such segregation the microregions free of Mo atoms are characterized by ordering of the Ni_3Fe type. This assumption appears plausible although it must be noted that differences in Mo concentration in different parts of the crystal per se would be sufficient for the appearance of two Curie points. Dekhtiar's work makes the concepts formulated in Ref.4 more specific in that he emphasizes the discrete character of the atomic segregation. The existence of two separate and distinct Curie points indicates that there occurs in the solid solution "intraphase dissociation" into regions with different concentrations.

A number of investigators (see, for example, Refs. 2 & 5) have suggested that the so-called K-state is a variant of ordering. True, in Ref.2 no mention is made of atomic segregation.

A natural question is whether one can produce the K-state in an alloy in which the possibility of ordering is precluded? To answer this question Ivanushkina[6] investigated the 36% Ni + 64% Fe invar alloy whose resistivity and hardness and other properties do not change as a result of quenching, reheating and other heat treatment. This alloy consists of crystals of disordered solid solution and is completely inert. If, however, niobium or molybdenum are dissolved in this alloy, it exhibits the same effect as nichrome and molybdenum permalloy: in this case upon reheating of the quenched alloy the hardness, resistivity and tensile strength increase and the specific volume, the temperature coefficient of the elasticity modulus and other characteristics decrease; in other words, the alloy becomes very sensitive to heat treatment. Furthermore, the magnitude of the variation increases with increasing molybdenum content beginning with a concentration of about 0.5% Mo. By way of illustration, the variation of the resistivity of the reheating temperature for the invar alloys with 1 and 8% Mo is shown in Figs.11 & 12.

It is highly improbable that introduction of molybdenum or niobium can produce ordering in the invar and, particularly, that the degree of order could increase with increasing Mo or Nb content.

Apparently, the K-state is a special state of the solid solution whose atomic nature it would be desirable to clarify. There is evidence that this state forms in a large number of other alloys: Fe-Al, Cu-Ni, Cu-Ni-Zn, Fe-Ni-Cr, Cu-Ni-Mn, etc. As a rule these alloys comprise transition metals. They may be ferromagnetic. Apparently, the type of the crystal lattice is of no signi-

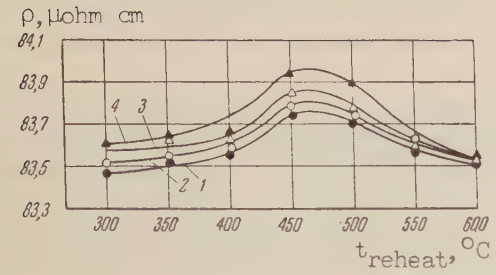

Fig.11. Variation of the resistivity of samples of 36% Ni + 1% Mo + Fe (balance) invar alloy with the reheating temperature with different reheating times: 1) 1 hour, 2) 2 hours, 3) 4 hours and 4) 10 hours.

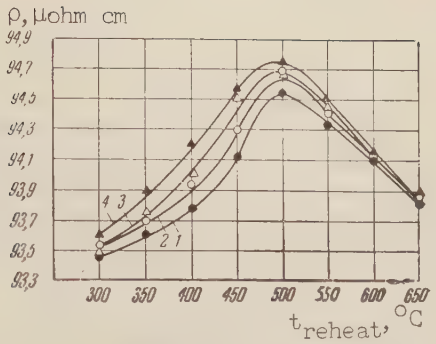

Fig.12. Same as Fig.11 but for the alloy of 36% Ni + 8% Mo + + Fe (balance.

ficance. The K-state can be produced in both alloys characterized by ordering and in alloys with a disordered lattice at all temperatures, if they are alloyed with transition metals in amounts not exceeding the solubility limit.

A significant fact that should be borne in mind in considering the problem is that the anomalous resistivity effect is obtained if the alloy undergoes concentration disordering as a result of variation of the proportion of components or the addition of a third component to a binary alloy.

We did not specifically study the thermodynamics and causes of formation of the K-state*.

In conclusion let us list the distinctive indications of the K-state or "intraphase heterogenization".

1. The kinetics of formation of the K-state indicate that it is established by diffusion, i.e., that in this respect it is similar to ordering and ordinary aging.

2. The process occurs in solid solutions without the separation of a second phase with a lattice differing from the lattice of the initial solution. In this respect the process of K-state formation is analogous to ordering.

3. Transition to or from the K-state, like other phase transitions, is accompanied by absorption or liberation of heat, changes in volume, hardness, elastic and other properties.

4. The change in resistivity incident to formation of the K-state is opposite to that occurring in ordering. Specifically, with formation of the K-state (by annealing or reheating) the resistance increases; and on the contrary, elimination of the K-state by quenching or cold working (after annealing or reheating) results in a decrease of the resistance.

5. The introduction of a third component into a binary alloy normally exhibiting a tendency to ordering (for example, Ni_3Fe) at first hinders or eliminates ordering and then with a sufficient increase in the concentration of the third component intensifies formation of the K-state, which is evinced in changes of the physical properties of the alloy. In the case of alloys that are not normally ordered (for example, 64% Fe + 36% Ni), the introduction of a third component furthers the formation of the K-state. In both cases an appreciable enhancement of the K-state is obtained upon the introduction of

---

*Note added in proof: In a paper published after the Conference the author showed that the K-state is essentially due to formation of Heine-Preston type zones in single phase alloys. The entire problem, however, still requires further investigation by a structural method.

only a few atomic percent of the third component. In this respect the K-state differs significantly from ordinary ordering, for where the latter is concerned the introduction of a third component only weakens the ordering effect by concentration disordering.

In many cases in investigating the influence of heat treatment on the properties of single phase ferromagnetic alloys, it is desirable to bear in mind the possibility of formation of the K-state at a low temperature and its transition to a statistically homogeneous solid solution at high temperatures. This transition occurs gradually with increasing temperature after the manner of second order phase transitions.

"I.V.Stalin" Moscow Steel Institute

References

1. H.Thomas, ZS. Physik, 129, 219 (1951).
2. A.Taylor & G.Hinton, J.Inst.Met., 19, 169 (1952).
3. R.M.Bozorth, Ferromagnetism (Cited in Russian trans., M., 1956).
4. B.G.Livshits & M.P.Ravdel', Doklady AN SSSR, 93, 6 (1953).
5. M.V.Dekhtiar, FMM (Physics of Metals & Metallography), 3, 55 (1956).
6. A.Z.Ivanushkina, Thesis, Moscow Steel Institute, 1956.

STRUCTURE OF Fe-Ni-Al ALLOYS IN THE HIGH COERCIVITY STATE
(Abstract)

- B.G.Livshits & V.S.L'vov

The composition of most high coercivity Fe-Ni-Al alloys lies in the two-phase region of the corresponding phase equilibrium diagram. Such an alloy in the stable state is a conglomerate of two types of crystals: crystals containing most of the iron and having the α-iron space lattice and crystals consisting predominantly of the compound Ni-Al with only a small amount of iron and having a crystal lattice of the same type but with a slightly different period.

The high temperature modification, i.e., the Fe-Ni-Al solid solution, has the same space lattice, so that dissociation of it into the Fe phase and the Ni-Al phase (both during reheating and aging) leads to coherent binding between the respective structural components regardless of the degree of dispersion (crystallite size).

The alloys of this system that are of practical value are characterized by anomalous aging. The anomaly is that the highest coercive force is obtained not after conventional quenching followed by reheating, but as a result of continuous cooling from a high temperature (from a single phase state) at a critical rate. Continuous cooling can be replaced by an equally effective procedure, namely, holding the supercooled high-temperature solid solution at two temperatures: first at 800-850° and then at 650-700°. At these temperatures we have two-stage decomposition into an Fe phase and an Ni-Al phase; the former is gradually impoverished as regards Ni and Al; the latter, as regards iron. The preliminary dissociation into two phases at 800-850° can be detected by microscopic observation: the final decomposition at 650-700° can be shown by phase analysis (chemical or x-ray) of the Ni-Al phase separated electrochemically from the alloy. The dissociation and decomposition are also evinced by variations of the electric magnetic and other properties of monolithic samples and by the results of measurements of the magnetization of the isolated Ni-Al phase. If this separated Ni-Al phase is subjected to heating, it undergoes aging consisting of further segregation of Fe accompanied by an increase of the coercive force to 160 oersted.

In the framework of the single domain theory it would appear plausible to assume that the maximum increase of the coercive force is due to enhanced isolation of the α-iron particles in the final decomposition stage, i.e., of the α-particles formed in the initial dissociation of the supercooled solid solution. It is still not clear why the conventional heat treatment - quenching followed by reheating - yields a value of the coercive force only half that obtained by means of the heat treatment described above. Investigation of the stresses arising during the phase transitions may help answer this question. Our preliminary experiments indicate that the stresses developing during dissociation at 800-850° exert a definite influence on the final decomposition process at 650-700°.

The principal contents of this report appear in FMM (Physics of Metals & Metallography) 1, 455 (1955); the complete report has been published in Sbornik trudov (Collected works) of the Moscow Steel Institute, 33, p.75, 1955.

"I.V.Stalin" Moscow Steel Institute

MAGNETIC INVESTIGATION OF ORDERING IN Ni_3Mn-BASE ALLOYS (Abstract)

- B.G.Livshits & B.V.Molotilov

The purpose of the present work was to determine the influence of Mo on the process of ordering in the Ni_3Mn alloy. It was shown earlier (Asmus & Pfeifer and Livshits & Ravdel') that the introduction of Mo into Ni_3Fe at first inhibits ordering and then, with increasing Mo concentration, leads to the formation of a distinctive inhomogeneous solid solution (called the K-state by Thomas).

For the purpose of the present investigation we chose the alloy having the composition Ni_3Mn and the same alloy with amounts of Mo up to 4%. As a first step we investigated the kinetics of the phase transition at different temperatures by measuring the resistivity and then studied this process in more detail by the thermal magnetic method on an Akulov anisometer. In addition, we investigated the elastic properties and structure of the alloys.

Investigation of the Ni_3Mn samples at different stages of ordering showed that the mechanism of the ordering process consists of the formation and growth of ordered phase nuclei at the expense of the disordered solution, which gradually vanishes.

Introduction of molybdenum into Ni_3Mn slows down the ordering and reduces the degree of possible order. This effect is not directly proportional to the Mo dilution. Apparently, the reduction of the maximum degree of order is determined not only by deviations from the stoichiometric composition but also by more fundamental changes in the character of the interatomic bonds.

With additions of molybdenum up to 4.1% at any rate, the solution still retains the capacity to attain some degree of order and the transition to the inhomogeneous solid solution (the K-state) is not observed. The kinetics of ordering of Ni_3Mn alloys with and without molybdenum are the same.

The principal contents of the report have been published in co-authorship with N.N.Miuller and N.A.Savost'ianova in FMM (Physics of Metals & Metallography), 3, 477 (1956).

"I.V.Stalin" Moscow Steel Institute

KINETICS OF SUPERSTRUCTURE TRANSFORMATIONS OF Fe_3Al ALLOY

- V.E.Rode

Investigation of ordering in alloys is of great interest both from the viewpoint of understanding the nature of processes occurring in metals and alloys and from the practical standpoint of preparing materials with desired physical characteristics. As is known the physical properties of an alloy may change with transition to the ordered state. Thus the resistivity, hardness, resistance to rupture, elasticity modulus and other attributes of many alloys undergo a marked change upon ordering. The alloy Ni_3Mn, for example, becomes ferromagnetic in the ordered state.

Although there have been numerous investigations of ordering in alloys, most of them as a rule were concerned primarily with the end result of ordering as regards changes in one or more specific physical parameters rather than with the kinetics of the process in time and as a function of the temperature. The few studies concerned specifically with the kinetics of ordering are limited either to investigation of the variation of some one physical parameter of the alloy or to determinations of the degree of order in the alloy as a function of different conditions of heat treatment with no attempt being made to correlate the variation of the physical properties with the degree of order in the alloy. Attempts to correlate the results of the former group with those of the latter are hampered by the fact that the specific conditions of heat treatment employed in the different investigations generally differ appreciably.

The purpose of our work was to investigate the variation of the different physical parameters of the alloy Fe_3Al in process of ordering and at the same time to determine the degree of order in the alloy from the intensity of the superstructure lines in the x-ray patterns.

For the purpose of investigating the kinetics of ordering of Fe_3Al, it was necessary to determine the Kurnakov point for the alloy of the given composition. For determining the Kurnakov point of this alloy as well as of alloys with an excess of iron and aluminum, we determined the temperature dependences of the specific heat C_p, the resistivity ρ, the saturation magnetization J_s and the linear expansion coefficient α. The specific heat vs temperature curves has two maxima one of which responded to the Kurnakov point, the other to the Curie point. One could decide which maximum pertained to which point from the temperature dependence curves of the saturation magnetization. The maxima in the curves in the variation of the temperature coefficient of resistance and the linear expansion coefficient as functions of the temperature coincided exactly on the temperature scale with the maximum in the C_p vs t^o curve corresponding to the Kurnakov point.

The kinetics of ordering of the Fe_3Al alloy was investigated with reference to the following parameters: 1) resistivity, 2) saturation magnetization, 3) coercive force, 4) effective anisotropy constant and 5) the lattice constant.

For investigating the resistivity of the alloy containing 13.9% aluminum, we prepared samples 2 mm in diameter and 10 cm in length in a high-frequency furnace. After preparation, the alloy specimens were annealed in vacuum at 800, 700 and 600° for several hours and quenched in water. The resistance was measured on a potentiometer set-up.

The resistance values of the samples annealed at and quenched from the different temperatures were virtually identical. We computed the resistivity to be 125 microohm-cm and took this to be the resistivity of the alloy in the ordered state. To investigate the dependence of the resistance on the time and temperature of reheating, a disordered sample was placed into a furnace

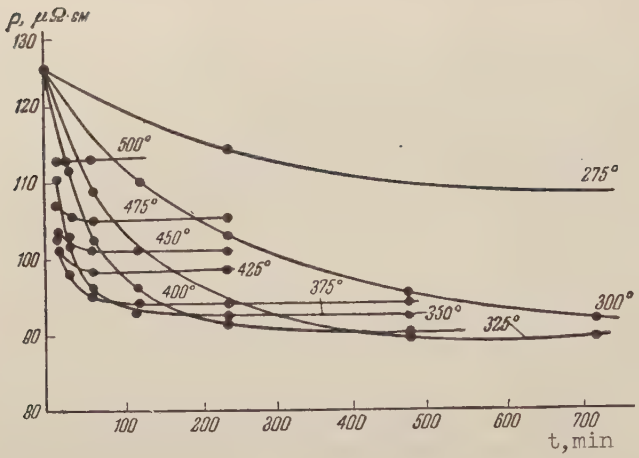

Fig.1. Variation of the resistivity of Fe_3Al alloy with the heating time at different temperature.

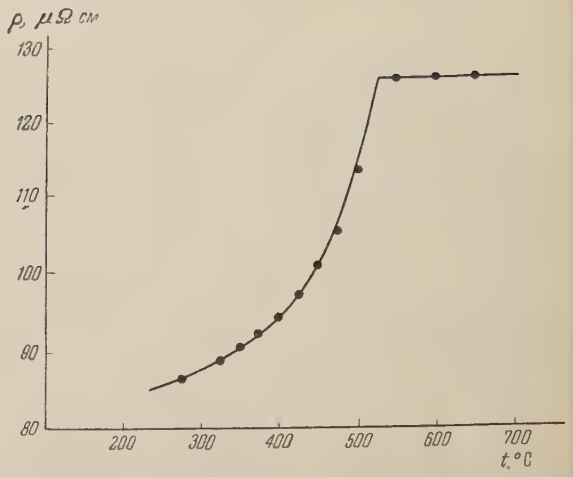

Fig.2. Variation of the equilibrium value of the resistivity of Fe_3Al alloy with the reheating temperature.

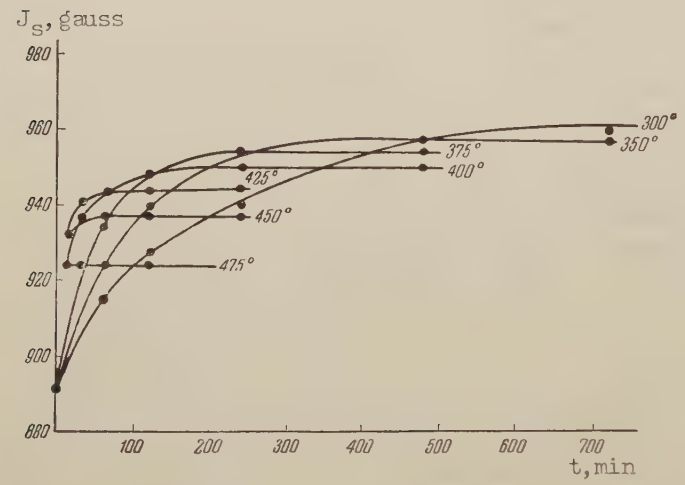

Fig.3. Variation of the saturation magnetization of Fe_3Al alloy with the duration of heating at different temperatures.

at a temperature below the Kurnatov point. The sample was heated for a certain time and then quenched in water and its resistance measured. The sample was then placed in the furnace maintained at the same temperature; the heating time was doubled, the specimen again quenched and its resistance measured. This operation was repeated until the resistance no longer changed with further heating (time). The final value of the resistance thus obtained was assumed to be the equilibrium value of the resistance for the given reheating temperature. Next the sample was heated at a temperature above the Kurnatov point (650°) for one hour and quenched in water; this brought it to the disordered state as indicated by measurement of the resistance. The disordered sample was then again heated for successively doubled periods at the next temperature of interest, etc.

The results of these measurements are shown in Fig.1. From these curves we took the equilibrium values of the resistance at each annealing temperature and plotted the variation of these resistance values as a function of the heating temperature. The results are shown in Fig.2. It will be seen that the resistance monotonically decreases with decreasing annealing temperature and, consequently, with the degree of order.

Concurrently with the resistance measurements, we also measured the saturation magnetization J_s of our alloy in fields of up to 1100-1200 oersted on a ballistic set-up. The results are shown in Figs.3 & 4. It will be seen that the saturation magnetization increases monotonically with decreasing

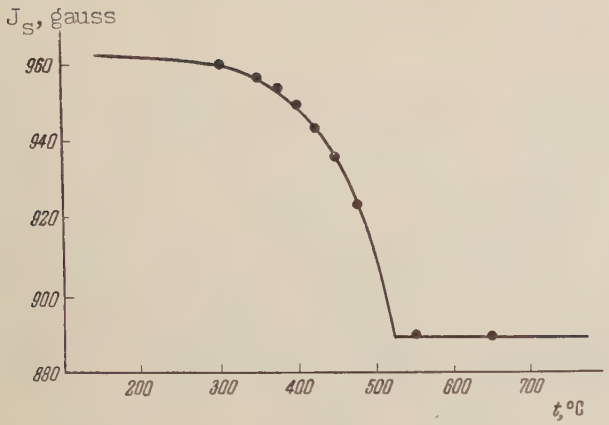

Fig.4. Variation of the equilibrium value of the saturation magnetization of Fe_3Al alloy with the reheating temperature.

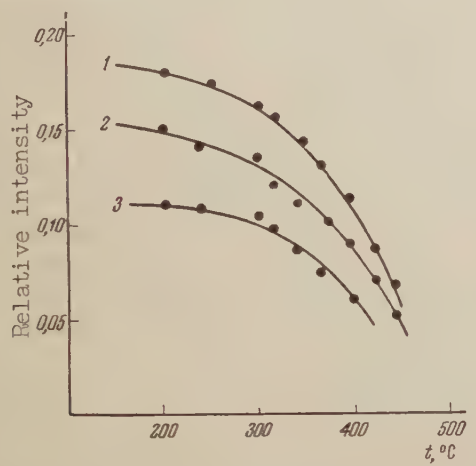

Fig.5. Variation of the relative intensities of the superstructure lines in the x-ray patterns of the Fe_3Al alloy with the reheating temperature:

$$1-\frac{I(200)_\alpha}{I(220)_\beta},\ 2-\frac{I(111)_\alpha}{I(220)_\beta},\ 3-\frac{I(311)_\alpha}{I(220)_\beta}$$

heating temperature, at first rapidly and then tending to a constant value.

From the curves of the variation of the resistivity and saturation magnetization as a function of the heating time at different temperatures we determined the relaxation times for different temperatures and calculated the activation energy for the Fe_3Al alloy. The value obtained was 29.5 Kcal per mole.

Above we have described the results of our investigation of the variation of the parameters (specifically, the resistivity and saturation magnetization) of the Fe_3Al alloy as functions of the temperature and duration of heating. The theoretical work of Akulov[1,2], defining the dependence of the saturation magnetization on the degree of order, and the theoretical calculations of Ryzhanov[3] and Smirnov[4], showing how the resistivity of an alloy should vary with the degree of order, allow of relating these parameters with the degree of order. A good indication of the degree of order obtaining in an alloy is furnished by the intensity of the superstructure lines that appear in the x-ray patterns of the alloys.

Hence to evaluate the degree of order obtaining in our samples we measured the intensities of the $(111)_\alpha$, $(200)_\alpha$ and $(311)_\alpha$ superstructure lines. In view of the fact that we had no possibility of directly determining the intensity of the x-rays reflected at different angles, we were forced to evaluate the intensity of the superstructure lines from the degree of blackening (density) of the lines on the x-ray pattern photographs. By way of reference we took the $(220)_\beta$ line since it is close in intensity to the mean intensity of the superstructure lines and is located near them conveniently.

The microphotometry of the x-ray patterns was carried out on a Type A Molle precision microphotometer, which is particularly suitable for such work inasmuch as it superimposes a grid on the photograph, thereby facilitating intensity determinations. On the basis of our intensity evaluations we were able to plot the relative intensity curves for the $(111)_\alpha$, $(200)_\alpha$ and $(311)_\alpha$ superstructure lines as functions of the reheating temperature (see Fig.5). From these data we evaluated the degree of ordering of the alloy at different heating temperatures (the degree of order is proportional to the square root of the intensity ratios). The results are shown in Fig.6.

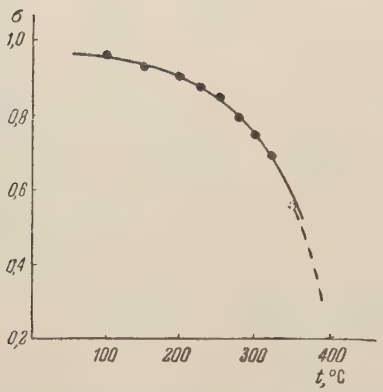

Fig.6. Variation of the degree of order in the Fe_3Al alloy with the reheating temperature.

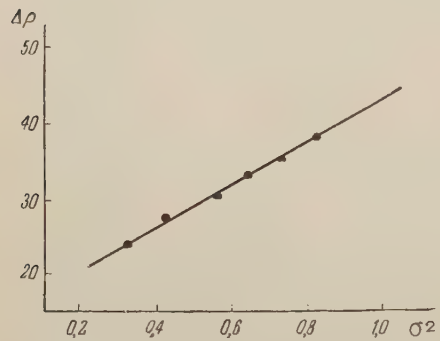

Fig.8. Variation of the increment in resistivity of Fe_3Al with the degree of order squared.

Department of Physics
Moscow State University

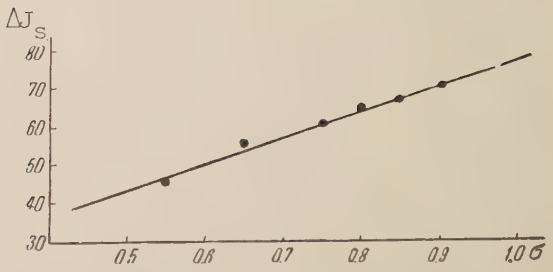

Fig.7. Variation of the change in saturation magnetization with the degree of order.

Having these data we could readily correlate the variation of the physical properties of the alloy with the degree of order. Comparing the variations of the lattice constant, the saturation magnetization and the resistivity of the alloy with the degree of order we found the following relationships: 1) the saturation magnetization varies as a linear function of the degree of order; the change in saturation magnetization is directly proportional to the degree of order - $\Delta J_s \sim \sigma$ (Fig.7) and 2) the change in resistivity is proportional to the square of the degree of order - $\Delta\rho \sim \sigma^2$ (Fig.8)

References

1. N.S.Akulov, Doklady AN SSSR, 66, 361 (1949).
2. N.S.Akulov, Doklady AN SSSR, 82, 221 (1952).
3. S.Ryzhanov, Zhur.eksp.i teor.fiz., 9, 4 (1939).
4. A.A.Smirnov, Zhur.eksp.i teor.fiz., 17, 743 (1947).

MAGNETIC PROPERTIES OF ORDERED Fe_3Al ALLOY
(Abstract*)

- V. I. Ivanovskii

The report gives the results of experimental investigations of the temperature dependences of the magnetic properties of Fe_3Al alloy.

Measurements of variations of the coercive force H_c with the temperature showed that this variation is anomalous: at room temperatures H_c is always less than 1 oersted; with increasing temperature, H_c at first decreases to 0.3 oersted at 400° and then rises rapidly, attaining a value of 200 oersted at 520°; this temperature is approximately that of the Kurnatov point. Measurements of the temperature dependence of the magnetocaloric effect showed that the curve characterizing this variation has a second maximum in the temperature region where the high value of H_c was observed.

The high coercivity state was observed only in a certain temperature interval, namely from 400° to the Curie point (590°). A study was also made of the kinetics of the growth of the coercive force at the ordering temperature. The temperature variation of the initial susceptibility was also found to be anomalous. It was found that at the ordering temperature the susceptibility falls off rapidly with time; if, however, the sample is held at the given temperature in a magnetic field no appreciable decrease of the susceptibility is observed. Indications of superductility were found at the temperature of ordering in the Fe_3Al alloy.

Department of Physics,
Moscow State University

* * * * * * *

RESIDUAL MAGNETIZATION OF NICKEL AND ITS STABILITY

- Ia. S. Shur & I. E. Startseva

The causes bringing ferromagnets to the state of residual magnetization and the factors determining the stability of this state is still inadequately understood. Recent advances in the investigation of the magnetic structure of ferromagnets, however, make it possible to make a new approach to the problem. To this end we must first investigate in detail the influence of the crystal structure of the ferromagnetic material on the magnitude and stability of the residual magnetization. As far as we know there have been no special investigations of this type hitherto.

The present investigation was devoted to determining the influence of different types of treatment altering the crystal structure of nickel on the magnitude of the residual magnetization and its stability as regards alternating magnetic fields, temperature fluctuations and mechanical vibration.

Samples and procedure

The measurements were carried out on toroidal samples assembled of flat rings 0.1 mm thick with an inner diameter of 28 mm and an outer diameter of

---

*For a more detailed report on the work see V. I. Ivanovskii, Thesis, Moscow State University, 1952; FMM (Physics of Metals and Metallography) 4, 70 & 245 (1957); also V. I. Ivanovskii & P. P. Denisov, FMM, 4, 550 (1957).

40 mm. For the purpose of producing different crystal structures in the material the samples were subjected to the following forms of treatment: anneal of the cold rolled material at different temperatures in vacuum and in air (we shall hereinafter refer to the latter as oxidizing annealing) and plastic deformation by extension or compression of the material subjected beforehand to recrystallization annealing in air or vacuum.

The magnetic properties of the samples were measured by the ballistic procedure. The specimens were magnetized by means of a circular magnetic field. In investigating the stability of the residual magnetization we studied the demagnetizing effects of 1) a circular alternating magnetic field with a frequency of 50 cps and an amplitude gradually reduced to zero, 2) mechanical vibration with a frequency of 50 periods per sec and an amplitude of 0.8 mm and 3) temperature variations in the range from +20 to -195°.

Experimental results

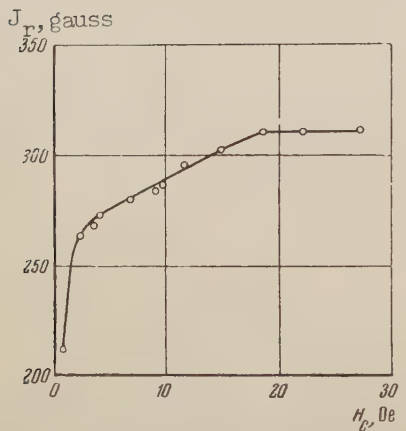

Fig.1. Residual magnetization of nickel samples subjected to annealing at different temperatures in vacuum and having different values of the coercive force.

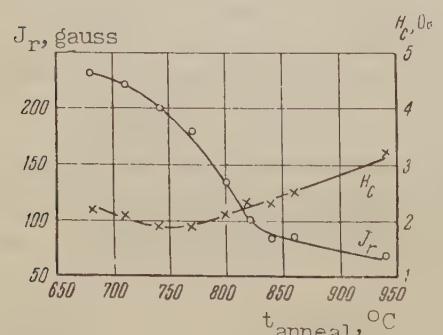

Fig.2. Variation of the residual magnetization and the coercive force of nickel specimen as a function of the temperature of oxidizing anneal (sample held at each temperature for 15 min).

By employing the treatments outlined we obtained several series of samples having different crystalline structures and different values of the residual magnetization J_r and coercive force H_c.

The principal results of our measurements are shown in Figs.1 through 4. The curve of Fig.1 shows the variation of the residual magnetization with changes in the degree of perfection of the Ni crystal lattice as a result of annealing cold rolled specimens in vacuum. By way of parameter characterizing the degree of perfection of the crystal lattice we took the magnitude of the coercive force. It will be seen that with re-establishment of the perfect lattice, distorted initially by cold rolling, (i.e., with decrease of the coercive force) the residual magnetization decreases.

The curves given in Fig.2 show the variation of the residual magnetization and the coercive force with the temperature of oxidizing annealing of the cold rolled nickel samples. It will be seen that up to an annealing temperature of 750° the coercive force decreases somewhat and then with increasing annealing temperature begins to rise. The residual magnetization, on the contrary, monotonically decreases with increasing annealing temperature; after oxidizing annealing at 940° the residual magnetization amounts to only 13% of the saturation magnetization.

The magnetic properties of samples subjected to oxidizing annealing change markedly under the influence of plastic deformation. The magnitude of the change depends on the degree of oxidization of the nickel. Deformation of a strongly oxidized sample increases both the coercive force and the remanence several fold. Plastic deformation of a weakly oxidized sample leads to a sharp increase in the coercive force but has relatively

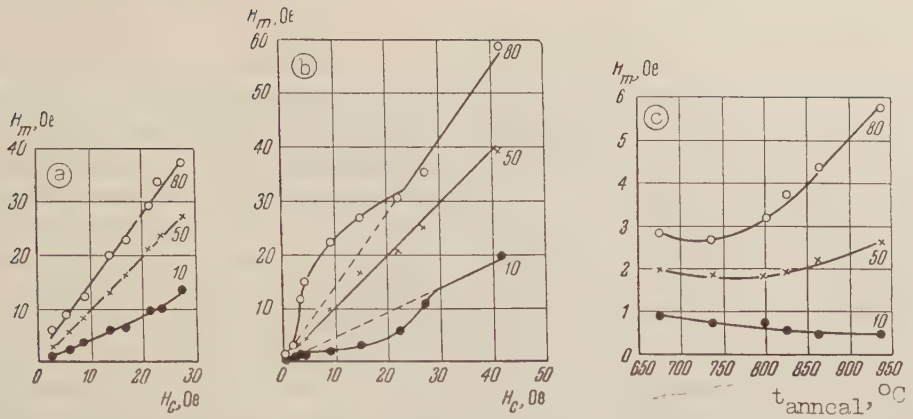

Fig.3. Effect of preliminary treatment of the nickel samples on the stability of the residual magnetization as regards the demagnetizing influence of an alternating magnetic field: a) samples made of nickel riboon plastically deformed by stretching, b) samples annealed in vacuum, c) samples annealed in air (oxidized). H_m = peak values of the alternating field demagnetizing the samples by the percentages indicated at the respective curves.

little effect on the magnitude of the residual magnetization.

Cooling the nickel specimens to the temperature of liquid nitrogen also alters their magnetic properties, but the character of the changes differs for different initial crystal structures. Thus in the case of specimens subjected to recrystallizing anneal in vacuum or in air, the remanence and coercive force are greatly increased by deep cooling (J_r by a factor of 1.5 and H_c by a factor of 2.5). Deformed specimens in which at room temperature $H_c \approx 30$ oersted exhibit little change in coercive force upon cooling, while their residual magnetization increases by about 20%.

The curves in Fig.3 illustrate the stability of the residual magnetization of different samples under the influence of demagnetizing alternating fields. Fig.3, a,b and c pertain respectively to samples subjected to preliminary annealing in vacuum and plastic deformation by stretching, cold rolling and annealing in vacuum at different temperatures (different degrees of recrystallization) and cold rolling and oxidizing annealing. The vertical axis is scaled

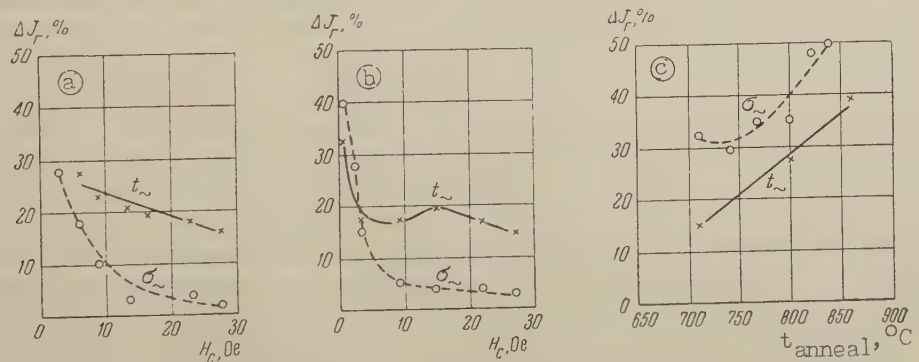

Fig.4. Effect of preliminary treatment on the stability of the residual magnetization under the influence of temperature fluctuations (solid curves) and mechanical vibration (dash curves) for the samples as in Fig.3.

in values of the maximum amplitude of the alternating field H_m demagnetizing the specimens by 10, 50 and 80%.

The results of measurements showing the influence of preliminary treatment of the samples on the stability of their residual magnetization as regards temperature fluctuations and mechanical vibration are shown in Fig.4. The data given in Fig.4, a, b and c were obtained on the same specimens as those characterized respectively in Fig.3 a, b and c. The ordinates in Fig. 4 are values of the decrease in residual magnetization relative to the initial value in percent, i.e., $\Delta J_r/J_r \times 100\%$.

It will be seen from the curves of Figs.3 & 4 that in the case of samples plastically deformed by stretching the stability of J_r as regards all demagnetizing influences increases with increasing coercive force of the material. Specifically, with increasing H_c, a higher value of H_m is required for reducing J_r by 10, 50 and 80% and the relative change in J_r under the influence of temperature fluctuations and mechanical vibration decreases. A similar increase in the stability of the residual magnetization with increasing H_c is observed in the case of the samples subjected to annealing in vacuum, in which $H_c < 3$ or $H_c > 15$ oersted (Fig.3,b and Fig.4,b). The partially recrystallized samples ($3 < H_c < 15$ oersted) exhibit a deviation from this regularity. Thus it will be seen from Fig.3,b that reduction of the residual magnetization by 10% in samples with $H_c \approx 3$ oersted and $H_c \approx 16$ oersted is realized by alternating fields having virtually the same peak value. An even more noticeable deviation from the general regularity as regards reduction of J_r of the partially recrystallized samples is observed in the case of demagnetization by temperature fluctuation (Fig.4,b). The stability of the residual magnetization of samples subjected to oxidizing annealing with respect to weak alternating fields (the lowest curve in Fig.3,b) and with respect to temperature fluctuations and mechanical vibration (Fig.4,b) decreases with annealing temperature although, as has been noted earlier, the coercive force increases with increasing annealing temperature.

Analysis of the results

If we assume that in the state of residual magnetization the magnetization vectors of the individual crystallites in a disoriented polycrystal are oriented in the directions of easy magnetization closest to the direction of the field acting on the sample (i.e., if we take into account only rotation processes), we find that the relative value of the residual magnetization of tri- or tetra-axial material defined by

$$\frac{J_r}{J_s} = \frac{\int_0^{2\pi}\int_0^{\pi/2} \cos\theta \sin\theta \, d\theta \, d\varphi}{\int_0^{2\pi}\int_0^{\pi/2} \sin\theta \, d\theta \, d\varphi} \qquad (1)$$

(where J_s is the saturation magnetization, θ is the angle between the direction of the applied external field and the direction of magnetization in the crystallite and φ is the azimuth angle) must be equal to about 0.8 J_s; or in the case of an uniaxial material to about 0.5 J_s. In practice, however, such high values of residual magnetization are rarely encountered[1]. The lower value of J_r in actual materials can be explained in the light of present day concepts regarding the magnetic structure of ferromagnets. We note the following factor that may be responsible for the reduced value of J_r:

1) the formation of closure domains in the areas of accumulation of relatively large magnetic "charges" (at grain boundaries near the surface of the sample, near extraneous inclusions, at points of nonuniform stress, etc.) and the formation of domains with reverse magnetization;[2]

2) deviation of the elementary magnetic moments from the direction of easy magnetization under the influence of stray fields due to magnetic "charges" building up near small radius defects;

3) the appearance in individual regions of the material of preferred directions of easy magnetization under the influence of residual internal stresses, with the result that the material is transformed in these regions from magnetically multi-axial to magnetically uni-axial.

On the basis of these concepts regarding the magnetic structure of a residually magnetized soft ferromagnet, one can understand the reasons for the observed effects of mechanical and heat treatment of the material on the magnitude of the residual magnetization and its stability. The reduction in the value of J_r with decrease of the coercive force in the case of samples annealed in vacuum (Fig.1) is apparently due primarily to the first factor. At room temperature nickel has a low magnetic anisotropy constant; in recrystallized regions the residual internal stresses will also be low; consequently, in such regions we will have a low value of the wall energy density

$$\gamma \sim \sqrt{aK + b\lambda_s\sigma_i} \qquad (2)$$

where K is the magnetic anisotropy constant, λ_s is the saturation magnetostriction, σ_i is the magnitude of the residual internal stresses and a and b are constants.[3] Hence in recrystallized portions of the sample near different types of defects there may form closure domains and domains with reverse magnetization. The greater the number of recrystallized regions in the sample, the greater will be the relative volume occupied by such domains and, consequently, the lower the residual magnetization of the sample. This, too, is probably the reason for the reduction of J_r of samples with increasing temperature of oxidizing annealing (Fig.2). In annealing cold rolled nickel in air, simultaneously with recrystallization there occurs oxidation of the material. The oxide film as a result of intercrystallite diffusion forms lamellar nonferromagnetic inclusions between the grain boundaries. To compensate the magnetostatic energy of the "charges" appearing on the oxide inclusions, there form near them closure and reverse magnetization domains. Raising the annealing temperature leads to increase of the area and thickness of the nonmagnetic oxide inclusions which in turn leads to an increase of the volume occupied by closure and reverse magnetization domains. As a result, again, the residual magnetization is reduced.

Increase of the residual internal stresses through plastic deformation of a strongly oxidized sample or increasing the magnetic anisotropy constant by cooling the nickel[3] leads to a sharp increase in the wall energy density. In consequence the volume occupied by closure and reverse magnetization domains changes, which results in an increase in J_r. The small change in the value of J_r incident to cooling of samples having a value of $H_c \approx 30$ oersted at room temperature shows that the role played by closure domains in this material is minor. The reduction of J_r as compared with the theoretical value in this case is apparently due primarily to the second and third factors listed above.

The state of residual magnetization is metastable; consequently, the effect of any external influence tending to alter the magnetic structure of the

ferromagnet produces a decrease of the residual magnetization. As noted earlier, in a magnetically soft polycrystalline material in the remanance state there are always present closure domains whose magnetization is oriented antiparallel to the magnetization of the principal domains. Some of these closure domains are nuclei of reverse magnetization, i.e., grow into domains with reverse magnetization. The stability of the residual magnetization is determined by the extent to which growth of the reverse magnetization nuclei and displacement of the walls between the principal domains and reverse magnetization domains are hindered. Consequently, the stability of the residual magnetization must increase with increasing domain wall energy density and increasing steepness of the residual internal stress gradients. In particular this is what occurs in samples subjected to plastic deformation by stretching (Figs.3,a and 4,a). The absence of direct correlation between the stability of the residual magnetization and the magnitude of the coercive force in partially recrystallized samples (Figs.3,b & 4,b) and oxidized samples (Figs.3,c & 4,c) is due to the distinctive features of their crystal structure (inhomogeneous recrystallization and nonuniform oxidation).

Conclusions

1. The results of our investigation show that in nickel samples, even in non-grain-oriented ones) the residual magnetization may vary over a wide range under the influence of different treatments affecting the crystal structure of the material.

2. The stability of the residual magnetization as regards different demagnetizing factors also depends on the crystal structure of the material. It must be noted that this stability is not always correlated with the magnitude of the coercive force; samples having the same value of the coercive force butsubject beforehand to different heat or mechanical treatments may exhibit very different degrees of stability of the residual magnetization.

3. The observed regularities can be qualitatively interpreted in the light of present concepts regarding the magnetic structure of soft ferromagnetic materials and the structural changes produced by various external influences.

Institute of the Physics of Metals,
Ural Branch, USSR Academy of Sciences

References

1. R.M.Bozorth, Ferromagnetism, p.502, N.Y., 1951.

2. Ia.S.Shur & V.R.Abel's, FMM (Physics of Metals & Metallography), 1, 5, 11 (1955; Doklady AN SSSR, 105, 469 (1955).

3. S.V.Vonsovskii & Ia.S.Shur, Ferromagnetizm (Ferromagnetism), N.-L., 1948.

INFLUENCE OF PLASTIC DEFORMATION ON THE BARKHAUSEN EFFECT

- K.Wotruba

Three techniques are now available for quantitative investigation of the Barkhausen effect: 1) the procedure in which the effect is viewed on an oscillograph (Tyndall[1] and Sawada[2]), 2) the statistical procedure used by Bozorth[3,4], Foerster & Wetzel[5] and Tsomakion & Ivlev[6], and 3) the direct method of Bush[7], Tebble[8], Krantz[9] and the author[10-12]. The first procedure is inadequate for quantitative measurements, while the second is predicated on the assumption of statistical independence of the effect which was disproved by the experiments of Sawada[2] and Krantz[9]. In view of this, in our work we utilized the third procedure, employing the set-up diagrammed in Fig.1. In order to reduce the experiment time, the set-up had five channels with appropriate separators and pulse counters. The current supply to the magnetizing coil was realized by means of an electrolytic potentiometer with a mechanical drive similar to that used by Foerster & Wetzel[5]. It is interesting to note that in a recent investigation Krantz[9] elected to use the same experimental procedure.

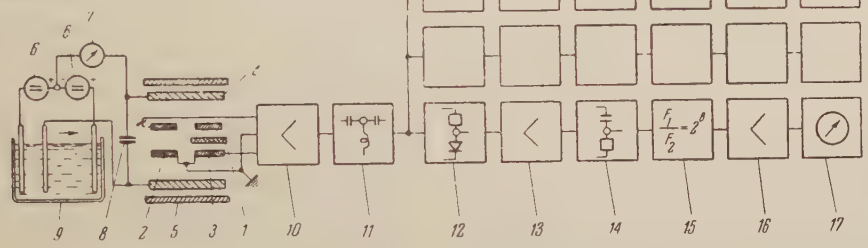

Fig.1. Set-up for investigating the Barkhausen effect: 1) ferromagnetic sample, 2) measuring coil, 3) compensating coil, 4) magnetizing coil, 5) magnetic shield, 6) battery, 7) field meter, 8) interference filter, 9) voltage divider (electrolytic potentiometer), 10) 110 db amplifier, 11) high frequency filter, 12) clipper, 13) 40 db amplifier, 14) differentiating network, 15) frequency divider - 256:1, 16) pulse amplifier, 17) recording unit.

The influence of plastic deformation on the Barkhausen effect has as yet been little studied. Bozorth & Dillinger[14] and Tebble, Skidmore & Corner[8] found that the Barkhausen effect in permalloy and iron changes after annealing. Foerster & Wetzel[5] showed that plastic deformation markedly reduces the Barkhausen effect. Ivlev notes that the Barkhausen effect vanishes in nickel after strong elastic deformation.

The purpose of our work was systematic investigation of the influence of plastic deformation on the Barkhausen effect in Mumetal, Hypernik, iron and nickel. The materials used for our samples were technically pure and hence not subject to further purification. The samples were taken in the form of wires 10 cm in length and weighing 100 mg. Prior to measurement they were subjected to annealing in an atmosphere of hydrogen for 1/2 hour at 800°. The deformation ϵ_p was varied from 1 to 20%. Each degree of deformation was represented by a separate sample on which we also measured the coercive force (Figs.2-6). This made it possible to repeat all the Barkhausen effect measurements three times on the same sample. The rate of variation of the magnetic field was 0.05 oersted/sec; the range of variation was from -120 to +120 oersted. The scatter of experimental points did not exceed 15-20%. In Figs.2-6 we have plotted the arithmetic mean values of the intensity of the Barkhausen effect. This intensity

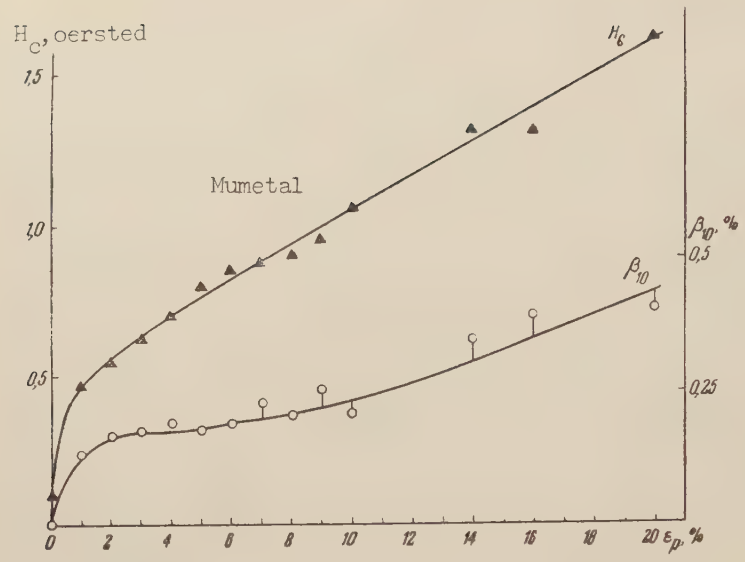

Fig.2. Variation of the coercive force H_c and the Barkhausen effect β_{10} with the percent plastic deformation (stretching) ϵ_p for Mumetal.

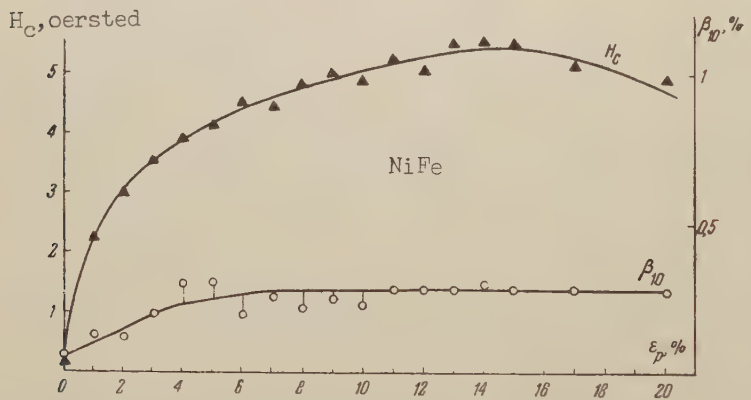

Fig.3. Same as Fig.2 but for Hypernik.

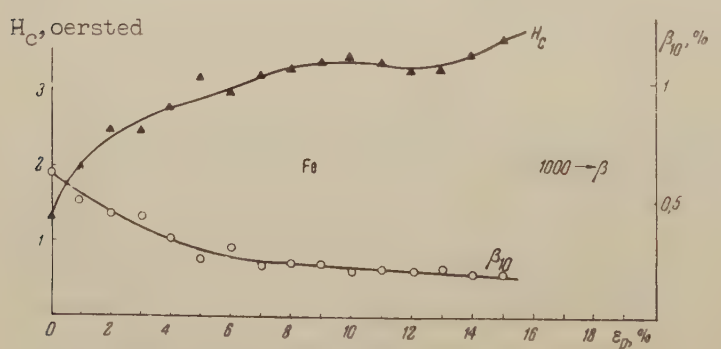

Fig.4. Same as Fig.2 but for iron.

is equal to the ratio of the change in magnetization due to the Barkhausen effect to the total change in magnetization incident to reversal of magnetization. In the case of Mumetal, Hypernik and iron we recorded jumps of the magnetic moment exceeding $10 \cdot 10^{-6}$ cgs units; in the case of nickel, wherein the effect is weaker, we recorded jumps exceeding $5 \cdot 10^{-6}$ cgs units. The curves of Figs.2-5 pertain to samples subjected to stretching; Fig.6 is for samples deformed by rolling.

It will be seen from the curves that the Barkhausen effect increases with the degree of deformation in Mumetal and Hypernik and decreases with deformation in iron (slowly) and in nickel (more rapidly). In the case of nickel the Barkhausen effect goes through a minimum at a deformation of about 10% (Figs.5 & 6). This result has a theoretical explanation. According to Tebble[14], the Barkhausen effect is caused by internal stress inhomogeneities, the dimensions of which approach the thickness of the boundary layer. This thickness is given approximately by[15,16]

$$b \approx \left(K + \frac{3}{2}\lambda\sigma\right)^{-\frac{1}{2}},$$

where K is the magnetic anisotropy constant, λ is the magnetostriction and σ is the mechanical stress. In the case of nickel K is small, while λ is large, hence the thickness of the boundary layer decreases with increasing stresses. Consequently, the intensity of the Barkhausen effect decreases accordingly. Under deformation, however, the inhomogeneity of the internal stresses increases and hence the Barkhausen effect must simultaneously increase; this explains the minimum at about 10% deformation in Figs.5 & 6.

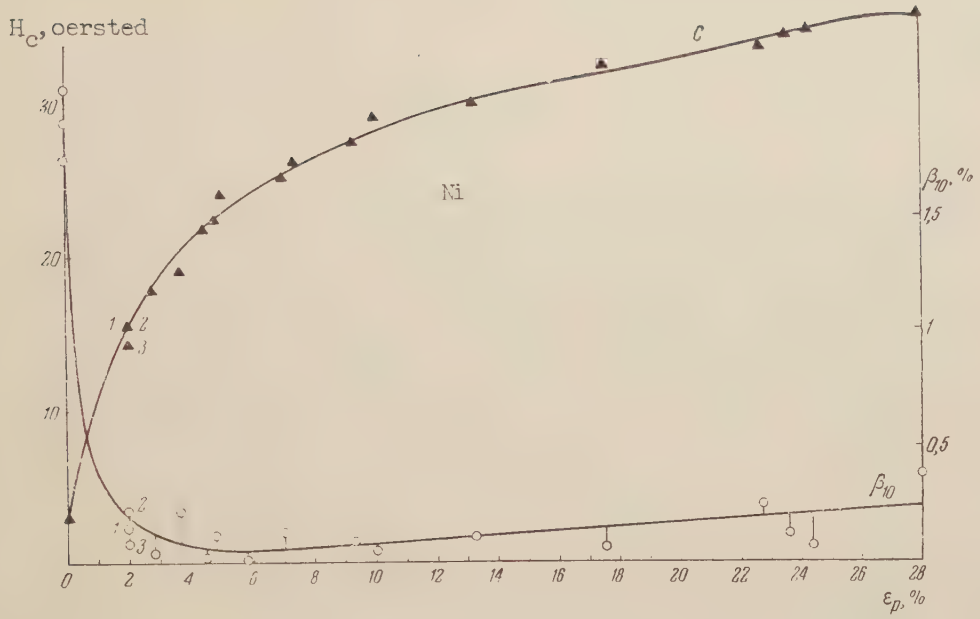

Fig.5. Same as Fig.2 but for nickel.

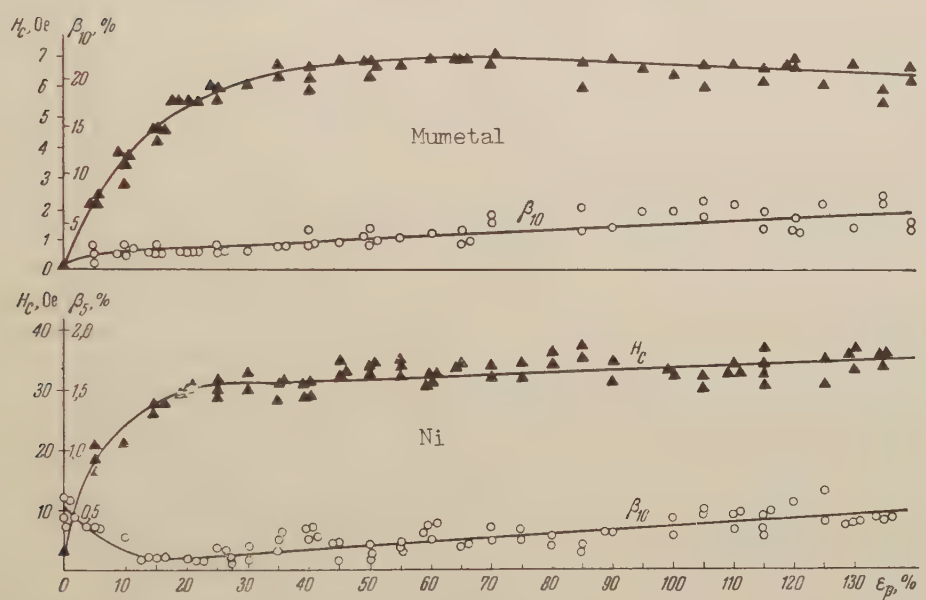

Fig.6. Same as Fig.2 but for Mumetal and nickel subjected to plastic deformation by rolling.

In iron K is larger and the thickness of the boundary layer decreases more slowly. In Mumetal and Hypernik K and λ are both small quantities. The thickness of the boundary layer is therefore large and the number of inhomogeneities of comparable dimensions is small. Consequently, the Barkhausen effect in these materials in the absence of deformation is weak and increases only with increasing number and size of the stress inhomogeneity regions under

the influence of deformation. The above is, of course, only a rough qualitative interpretation of the observed regularities.

Prague, Czechoslovakia

References

1. E.Tyndall, Phys.Rev., 24, 439 (1924).
2. H.Sawada, J.Phys.Soc.Japan, 7, 564, 571, 575 (1952).
3. R.Bozorth, Phys.Rev., 34, 34 (1929).
4. R.Bozorth & J.Dillinger, Phys.Rev., 35, 733 (1930).
5. F.Foerster & H.Wetzel, ZS. Metallk., 33, 115 (1941).
6. B.Tsomakion & V.Ivlev, Doklady AN SSSR, 66, 105 (1951).
7. H.Bush & R.Tebble, Proc.Phys.Soc.London, A60, 370 (1948).
8. R.Tebble, J.Skidmore & W.Corner, Proc.Phys.Soc.London, A63, 739 (1950).
9. J.Krantz, ZS.Phys., 139, 41 (1954).
10. K.Wotruba, Czech.Journ.Phys., 4, 375 (1954).
11. K.Wotruba, Czech.Journ.Phys., 5, 98 (1955).
12. K.Wotruba, Czech.Journ.Phys., 4, 375 (1954).
13. S.V.Vonsovskii, Usp.fiz.nauk, 46, 759 (1951).
14. R.Tebble, Proc.Phys.Soc., B68, 1017 (1955).
15. F.Bloch, ZS.Phys., 74, 295 (1932).
16. L.Landau & E.Lifschitz, Sow.Phys., 8, 153 (1935).

INVESTIGATION OF REVERSAL OF MAGNETISM (BARKHAUSEN) JUMPS IN FERROMAGNETS

- V.F. Ivlev, V.L. Il'iushenko & L.I. Aseeva

It has been shown in a number of investigations that the volume involved in a reversal of magnetism (Barkhausen) jump is of the order of 10^{-7}-10^{-9} cm^3.[1]

For purpose of clarifying the nature of the magnetism jumps one of the present authors[2] investigated the temperature dependence of the number and magnitude of the jumps in nickel. The results of this investigation showed that with increasing temperature the number and the magnitude of the jumps decrease exponentially. One of the aims of the present study was to determine whether this exponential law applies to all ferromagnets or is peculiar to nickel.

Aside from the work of Tebble & Newhouse[3] there have been virtually no investigations of the jump-like magnetization effect in single crystals. Hence a second purpose of our investigation was to determine experimentally the dependence of the number of jumps and their magnitude on the crystallographic direction and the temperature.

We used the following samples in our experiments:

Sample No.1 - iron wire (99.93% Fe), diameter 0.56 mm, length 4 cm (annealed and not annealed).

Sample No.2 - iron wire (98.59% Fe) diameter 0.2 mm, length 4 cm (annealed and not annealed); the annealing was carried out at 1000° for 5 hours followed by slow cooling in the furnace.

Sample No.3 - silicon iron single crystal (transformer iron with 3.4% silicon) in the shape of a thin round disc. The surfaces of the disc were parallel to the (110) planes which was convenient for our purposes inasmuch as all the three principal crystal directions - [100], [110] and [111] - are in the (110) plane. Investigation of the magnetization jumps in the different crystallographic directions was carried out by rotating the discs in a magnetic field. In rotating the discs we noted the angle φ between the direction of the magnetic field and the [110] direction; hence $\varphi = 90°$ corresponded to the [100] direction, $\varphi = 180°$ to the [110] direction and $\varphi = 150°$ to the [111] direction.

The experiments were carried out on a set-up similar to that described in Ref.2 which allowed of recording reversal of magnetism jumps involving volumes from $0.7 \cdot 10^{-9}$ cm^3. The present set-up differed from that described in Ref.2 only in that the undulator in the original set-up was replaced by type PS-64 scaling circuit. In addition in investigating the jumps in single crystals the amplifier circuit was improved somewhat making it possible to detect jumps from $0.3 \cdot 10^{-9}$ cm^3.

The number of jumps in the process of reversal of magnetization of the specimen was counted on one of the branches of the hysteresis loop, i.e., in the field range from -H to +H, which did not exceed 280 oersted for any of the investigated samples.

Results and discussion

The variation with temperature of the number of jumps of different size for Sample No.1 in the nonannealed state is shown in Fig.1. Similar curves were obtained for Sample No.1 in the annealed state and for Sample No.2 (annealed and nonannealed). It will be seen that in iron samples the maximum number of jumps for all sizes of jump occurred at approximately the same temperature.

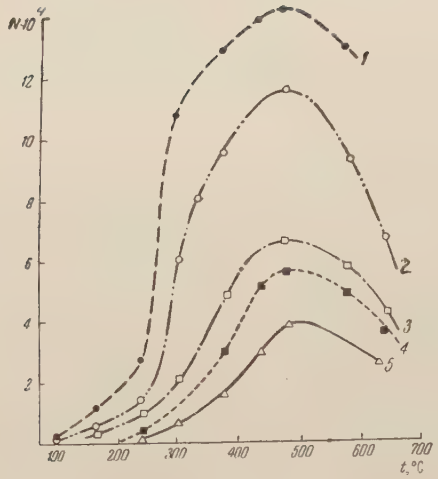

Fig.1. Temperature dependence of the number N of jumps of all magnitudes for unannealed iron specimen No.1: 1) $v = (0.8\text{-}1.0)\cdot10^{-9}$, 2) $v = (1.1\text{-}1.3)\cdot10^{-9}$, 3) $v = (1.4\text{-}1.6)\cdot10^{-9}$, 4) $v = (1.7\text{-}1.9)\cdot10^{-9}$, 5) $v = (2.0\text{-}2.3)\cdot10^{-9}$ cm^3.

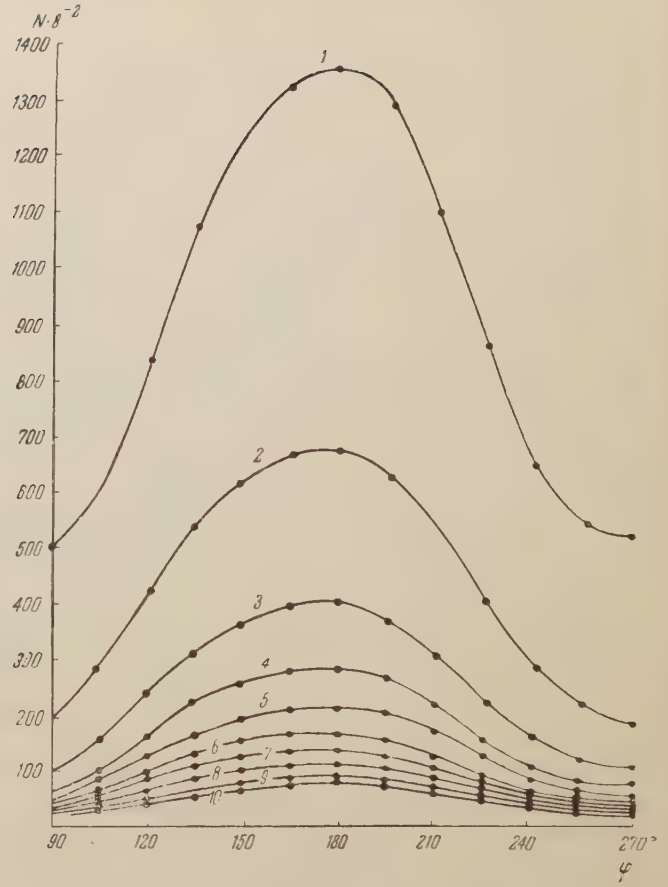

Fig.2. Variation of the number of jumps of different size with the angle φ (the angle between the magnetic field and the [110] direction) for the unannealed No.3 sample at room temperature. H = 140 oersted; 1) $v = (0.3\text{-}0.6)\cdot10^{-9}$, 2) $v = (0.6\text{-}0.9)\cdot10^{-9}$, 3) $v = (0.9\text{-}1.2)\cdot10^{-9}$, 4) $v = (1.2\text{-}1.5)\cdot10^{-9}$, 5) $v = (1.5\text{-}1.8)\cdot10^{-9}$, 6) $v = (1.8\text{-}2.1)\cdot10^{-9}$, 7) $v = (2.1\text{-}2.4)\cdot10^{-9}$, 8) $v = (2.4\text{-}2.7)\cdot10^{-9}$, 9) $v = (2.7\text{-}3.0)\cdot10^{-9}$, 10) $v \geqslant 3.0\cdot10^{-9}$ cm^3.

Fig.2 shows the variation of the number of jumps of different size at room temperature with the angle φ for unannealed Sample No.3. It will be evident from the figure that we have an appreciable anisotropy of the number of jumps, i.e., that the number of reversal of magnetization jumps depends significantly on the crystallographic direction. The maximum number of jumps occurs for $\varphi = 180^\circ$, i.e., for the [110] direction, while the minimum is observed for $\varphi = 90^\circ$ or the [100] direction.

It will be noted that the maximum and minimum number of jumps of all sizes correspond to the same crystallographic directions. As a result of annealing the number of jumps of all sizes decreases for all directions; the mean size of the jumps in the annealed sample for all directions is the same and equals $0.8\cdot10^{-9}$ cm^3.

Fig.3 shows the variation with temperature of the number of jumps of different size for the nonannealed No.3 sample with $\varphi = 180^\circ$, i.e., for the angle at which the maximum number of jumps is observed at room temperature. Similar curves were obtained for the other two crystallographic directions. It will be obvious from the figure that in the case of the single crystal silicon iron sample the number of jumps is strongly dependent on the temperature.

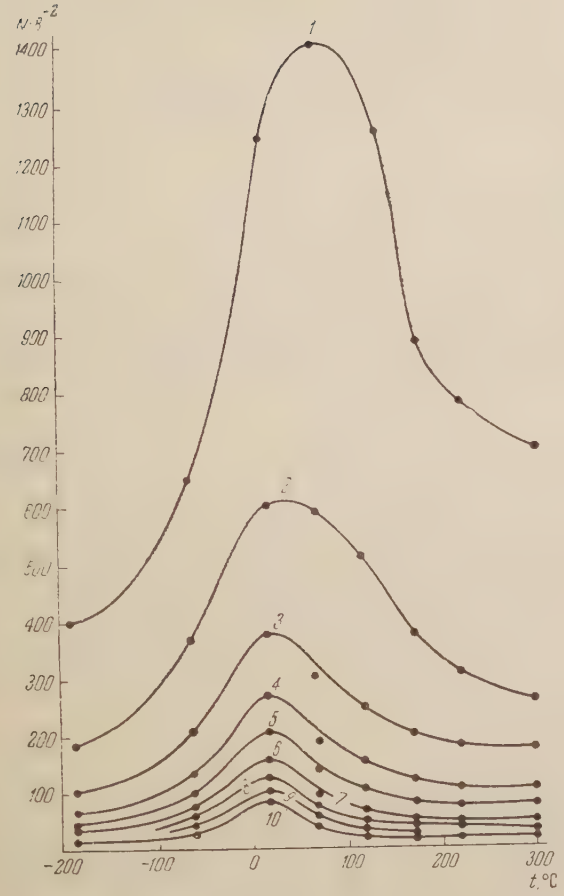

Fig.3. Temperature dependence of the number of jumps of different size for the nonannealed No.3 Sample with $\varphi = 180^\circ$ ([110] direction). Numeration of curves same as in Fig.2.

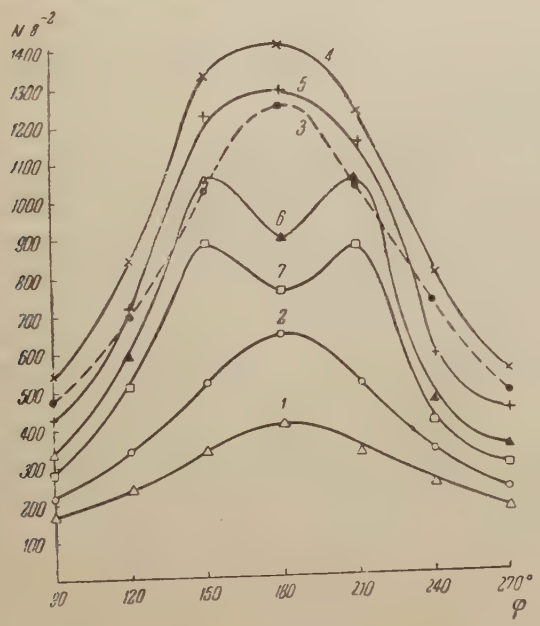

In the temperature range from -183 to 300° the total number of jumps observed in remagnetizing the specimen along any crystallographic direction at first increases with the temperature, passes through a maximum at about 70° and begins to decrease. The maxima for successively larger jumps are displaced increasingly to the side of lower temperatures. This is true of all crystallographic directions.

The variation of the number of jumps with the angle φ at different temperatures is shown in Fig.4. It will be obvious that the character of the number of reversal jumps anisotropy changes with temperature. In the temperature range from -183 to +150°, we consistently have one direction (the [110] direction) with a maximum number of jumps and one direction (the [100] direction) for which the number of jumps is minimal. At higher temperatures two maxima and two minima become evident. The maxima correspond to [111] directions, i.e., to $\varphi = 150$ and 210°; the minima correspond to the [100] and [110] directions, i.e., to $\varphi = 90$ and 180°, the former minimum being somewhat deeper than the latter.

From a comparison of Figs.1 and 3 it follows that the character of the temperature dependences of the number of jumps for polycrystalline iron samples and for the silicon iron single crystal is the same: in the case of both materials the maximum number of jumps is observed at a certain temperature. In nickel the character of the temperature dependence of the number of jumps differs, namely, the number of jumps of all sizes consistently decreases with increasing temperature in the entire range from -183° to the Curie point.[2]

The number-of-jumps peak for polycrystalline iron samples occurs in the temperature region where the absolute value of the saturation magnetostriction λ_s is lowest. To both sides of the region λ_s increases in absolute magnitude, while the number of jumps decreases.

Fig.4. Variation of the number of jumps with the angle φ at different temperatures: 1) -183°, 2) -60°, 3) 20°, 4) 70°, 5) 120°, 6) 170°, 7) 220°.

From Shtrukin's[4] investigation of the temperature dependence of the saturation magnetostriction in a silicon iron single crystal it follows that the magnetostriction constants vary with increasing temperature in a different manner for different crystallographic directions. At room temperature the inequality

$$|\lambda_{100}| > |\lambda_{111}| > |\lambda_{110}| \qquad (1)$$

obtains, i.e., as regards absolute magnitude λ_s is minimal in the [110] direction and maximal in the [100] direction.

In the same temperature range for the number of reversal of magnetization jumps we have the inequality

$$N_{100} < N_{111} < N_{110}, \qquad (2)$$

i.e., the greatest number of jumps is observed in the direction for which λ_s is minimal as regards absolute magnitude and vice versa. Tebble[3] showed that inequality (1) holds for all temperatures in the range from +20 to +150°. Inequality (2) also remains valid over this entire temperature range.

At 150° and higher temperatures (1) no longer applies and instead we have the inequality

$$|\lambda_{100}| > |\lambda_{110}| > |\lambda_{111}| \qquad (3)$$

Inasmuch as the maximum number of jumps should be observed in the direction for which λ_s is minimal, in this temperature range the maximum number of jumps should occur in the [111] direction. This is borne out by experiment as can readily be seen in Fig.4.

It also follows from (3) that the deepest minimum should be observed in the [100] direction, which again is the case. Thus in the temperature range from +150 to +300° the inequality

$$N_{100} < N_{110} < N_{111} \qquad (4)$$

obtains for the number of jumps.

Our experiments showed that the temperature dependence curves for the number of jumps in the [100] and [110] directions are similar to each other in the entire temperature range from -183 to +300°.

In the [111] direction the temperature variation of the number of reversals of magnetization jumps is somewhat different: specifically, starting with about +150° the curve lies appreciably higher than for the other two directions.

It also follows from Tebble's work that the temperature dependence curves for the magnetostriction constant λ_s for the [100] and [110] directions, just as the number of jumps vs temperature curves, are similar in the temperature range from 20 to 500°. The temperature variation of λ_s in the [111] direction in this temperature range differs from the variation for the other two directions.

Thus it is clear that the observed anisotropy of the number of jumps and the temperature dependence of the number of jumps reflect in some degree the anisotropy and temperature dependence of the magnetostriction constants λ_s for the different crystallographic directions.

In conclusion we desire to thank L.V.Kirenskii for valuable advice and suggestions in connection with the work.

Krasnoiarsk State Pedagogical Institute

References

1. S.V.Vonsovskii & Ia.S.Shur, Ferromagnetizm (Ferromagnetism), M.-L., 1948.
2. V.F.Ivlev, Izv.AN SSSR, Ser.fiz., 16, 664 (1952).
3. R.Tebble & V.Newhouse, Proc.Phys.Soc,London, B66, 633 (1953).
4. D.A.Shturkin, Doklady AN SSSR, 58, No.4 (1947).

ON THE STRUCTURE OF THE FAMILY OF SYMMETRICAL HYSTERESIS LOOPS OF FERROMAGNETS

- R.I.Ianus & V.P.Kartashov

1. One still sometimes encounters in the literature schematic diagrams showing the family of symmetrical hysteresis loops of ferromagnets in the form of inscribed loops with no common points, as shown in Fig.1,a. Experiment shows, however, that this pattern obtains only for the loops for which the maximum magnetization J_m is only a fraction of the saturation magnetization J_s for the given ferromagnet.

Actually, it was discovered years ago in connection with investigations of the shape of the so-called normal magnetization curve and the limiting hysteresis loops (loops run to saturation) for the same specimens that loops with different values of J_m may have common sections. It was found that the normal curve (the locus of the tips of the symmetrical minor loops) gradually approaches the branches of the limiting loop; at some value $J_m = \pm J_{ma}$ the normal loop comes so close to the branches of the limiting loop that the distance between the normal loop and the nearest points of the limiting loop becomes smaller than the measurement error. Further (at all values of $J_m > J_{ma}$) both curves are experimentally indistinguishable, i.e., virtually coincide (Fig.1,b).

The authors of Ref.5-7 showed that in the case of electrotechnical grade Fe and technical grade Ni coincidence of the nonlimiting or minor loops with the limiting loop occurs not only over the sections where $|J| \geq J_{ma}$ (as was assumed earlier - Fig.1,b). It was found that when $J_m > J_{ma}$, the ascending branch of a given loop (minor) becomes contiguous to the ascending branch of the limiting loop at $J = J_a$, where $J_a < J_{ma}$, and that the descending branches become contiguous from $J = -J_a$ (Fig.1,c). The greater the difference $J_m - J_{ma}$, the greater the difference $J_{ma} - J_a$ on the same loop.

At a certain value of $J_m = J_{mc}$ one obtains $J_a = 0$ (as in Fig.1,c for the loop having $J_m = J'_m$). This means that in measuring the coercive force h_c of the given material (provided $J_m \geq J_{mc}$) there will be obtained the same limiting value of the coercive force ($h_c = H_c$) regardless of whether the measurement is made with reference to the limiting loop or any of the intermediate minor loops.

At some value of $J_m = J_{mr} > J_{mc}$, one obtains $J_a = -J_r$ (as in Fig.1,c for the loop having $J_m = J''_m$). This means that in measuring the remanence j_r of the given material there will be obtained the same value ($j_r = J_r$) as in measuring with reference to the limiting loop or any minor loop for which $J_m \geq J_{mr}$ (the areas of these loops, however, will not be the same due to the variance between the initial and final apex sections of the various loops). It was found in the investigations of Refs.5-7 that J_{mc} approximately agrees with the magnetization at the "knee" of the normal magnetization curve for the same specimen (J_G).

In Ref.5 we evaluated J_{ma} for electrotechnical grade iron and also arrived at a value close to J_G. For this evaluation we used only the h_c vs J_m curve, because, failing to note the location of the normal magnetization curves relative to the limiting hysteresis loops for the same specimens, we overevaluated

---

*At one time it was even suggested that the normal loop at $J_m = \pm J_{ma}$ even intersects the limiting loop and thereafter lies outside it, merging with it only at $J_m \approx J_s$.[1] It was shown in the study of Ref.2 and later in the investigations of Refs.3 & 4, however, that there were serious, misleading errors involved in the experiments upon which this suggestion was based.

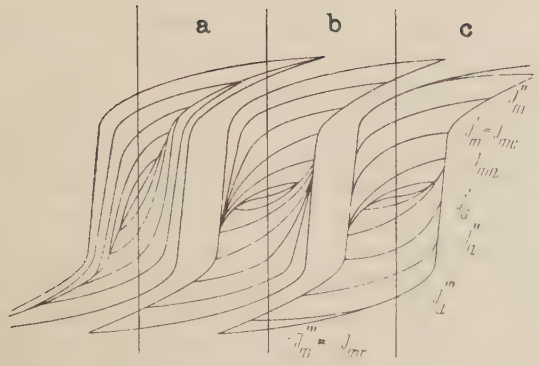

Fig.1. Families of symmetrical hysteresis loops.

the errors involved in recording the curves and comparing the hysteresis loops with different values of J_m and were unduly fearful of erring on the side of underestimating J_{ma} (this was natural in view of the fact that our thinking was influenced by the appearance of earlier diagrams of the type shown in Figs.1,a & b). If, however, one evaluates J_{ma} from the point at which the normal curve merges with the limiting loop (and such an evaluation appears to be legitimate) then the results of the experiment described in Refs.5-7 as well as the results obtained by other investigators all show that J_{ma} approximately agrees with the magnetization at which the differential permeability of the material as given by the normal curve ($\mu_{dk} = 4\pi dJ_m/dH_m$) attains its maximum value. For most technical ferromagnets $J_{ma} \approx 0.3\text{-}0.6\ J_G$.

As a result of these refinements the diagram of the family of symmetrical hysteresis loops shown in Fig.1,c differs somewhat from the diagrams given in Refs.5 & 6.

2. In order to clarify the relation between J_a and J_G in different cases one should perform experiments in which J_G changes appreciably, while the other conditions (the chemical composition and microstructure of the specimens, their shape and so on) remain entirely or almost the same. Such, for example, might be measurements on single crystal spheres or ellipsoids performed with magnetization in different crystallographic directions. Inasmuch, however, as it is difficult to prepare such specimens and to attain the requisite accuracy of measurement with them, we elected to use an easier if less perfect procedure: we prepared samples of polycrystalline but grain-oriented material (from a sheet of cold rolled electrotechnical grade iron alloyed with 3% silicon) in the form of bars pointed at both ends, having the same thickness over their entire area and bounded on the lateral sides by parabolas (the specimens are described in detail in Refs.5,6; such specimens are magnetized in a homogeneous external field almost as uniformly as ellipsoids). The direction of the length of the first specimen coincided with the direction of the <100> axes of its component crystallites; in the second specimen the length was aligned with the <110> axes and in the third with the <111> axes. The dimensions of the specimens were the following: length 2a = 25 cm, width 2b = = 3.0 cm, thickness 2c = 0.050 mm. An ellipsoid having the same length, volume and b/c ratio would have a demagnetization coefficient N = 0.011. After being cut out, the specimens were subjected to 2 hours annealing in vacuum at 800° to relieve the work hardening strains produced along by the cutting operation.

The specimens were magnetized in a uniform field of a solenoid; the strength of the field H_e was determined from the current through the solenoid winding.

The magnetic measurements were carried out by the ballistic procedure. For measuring the coercive force we used the ballistic throw method; for the other measurements we used the reversal or switching method.

The measurements of the coercive force and the recording of the normal curves were carried out by the "usual" observation system with the "usual" experimental errors. To enhance the accuracy of determining the points of confluence of the branches of neighboring hysteresis loops, we employed, as in the work of Refs.5-7, the procedure based on the "vertical sections" scheme for recording the loops. This procedure merits a brief description.

In working in this manner the measured values of the magnetization J_1 on the ascending branch of the hysteresis loop and J_2 on the descending branch are grouped in pairs; J_1 and J_2 comprising a pair are measured at the same nominal value of H_e (form a "vertical section" of the loop).

Let us assume that we are recording the loop at the tips of which nominally $H_e = \pm H_{em}$ and $J = \pm J_m$; in the k-th section $H_e = H_{ek}$, $J_1 = J_{1k}$ and $J_2 = J_{2k}$. To determine J_{1k} and J_{2k} we observe the ballistic throws of the galvanometer with jump-like changes (after appropriate "magnetic preparation") of H_e from H_{ek} to H_{em} (throws α_{1k}) and from H_{em} to H_{ek} (throws α_{2k}).

Actually, however, one cannot reproduce with absolute accuracy in all the measurements the values of H_{ek}, H_{em} and the associated quantities, to say nothing of some of the varying parameters of the measuring set-up; this obviously introduces additional errors. Providing all such quantities pertaining to α_{1k} with the additional subscript 1 and the quantities pertaining to α_{2k} with the additional subscript 2, we obtain the following obvious equations:

$$\begin{aligned} \Phi_{m1} &= 4\pi s J_{m1} + S(H_{em1} - N_{m1}J_{m1}), \\ \Phi_{m2} &= 4\pi s J_{m2} + S(H_{em2} - N_{m2}J_{m2}), \\ \Phi_{1k} &= 4\pi s J_{1k} + S(H_{ek1} - N_{1k}J_{1k}), \\ \Phi_{2k} &= 4\pi s J_{2k} + S(H_{ek2} - N_{2k}J_{2k}), \\ C_{1k}\alpha_{1k} &= \Phi_{m1} - \Phi_{1k},\ C_{2k}\alpha_{2k} = \Phi_{m2} - \Phi_{2k}. \end{aligned} \tag{1}$$

From them we obtain

$$\begin{aligned} C_{1k}\alpha_{1k} - C_{2k}\alpha_{2k} &= 4\pi s(J_{m1} - J_{m2} + J_{2k} - J_{1k}) + \\ &+ S(H_{em1} - H_{em2} + H_{ek2} - H_{ek1} + N_{m2}J_{m2} - N_{m1}J_{m1} + N_{1k}J_{1k} - N_{2k}J_{2k}. \end{aligned} \tag{2}$$

Here s is the cross section area of the specimen at the point encompassed by the measuring winding, S is the area encircled by a turn of the measuring winding ($S > s$) and C is the sensitivity of the galvanometer as regards the induction current.

In order to carry out a comparison of the corresponding differences $J_{2k} - J_{1k}$ for different loops (and this is necessary for determining the points of confluence of the branches of different loops), we must calculate the difference $J_{2k} - J_{1k}$ for another (the compared with) loop by substituting in (2) for the values of H_e, J, N and so on for the given loop the corresponding values of the quantities for the other (compared with) loop. One can readily guess how many and diverse the sources of error in such a comparison can be and how serious they may be if all possible measures are not taken to minimize or eliminate them.

In particular, in the case of specimens having the shape of rectangular section strips N not only differs for different loops but differs at different points of the same loop ($N_{1k} \neq N_{2k} \neq N_m$); in fact $N = f(J)$ even has its own hysteresis[8]. But the shape of the specimens used in our experiments makes N almost constant (as for ellipsoids). The small value of S/s in our experiments (1.2) further reduced the influence of the remaining inconstancy of N on the results. Hence for our experiments we could assume

$$N_{1k} = N_{2k} = N_{m1} = N_{m2} = N. \tag{3}$$

In order to reduce the influence of differences in the values of C, H_{ek} and H_{em} in different observations due to fluctuations of temperature, zero drift of the instruments, gradual discharge of the storage batteries and similar factors, in addition to the appropriate stabilizing devices and similar

measures, we utilized the classical procedure of measuring α_{1k} and α_{2k} pertaining to the same cross section of the loop in series in which the observations of α_{1k} and α_{2k} followed each other rapidly and in turn, being repeated numerous times without readjustment of the rheostats in the magnetizing and measuring circuits (i.e., the changes of H_e were realized solely by closing and opening the circuit switches). Cutting down the time expended on a series of measurements to a minimum reduces the possible range of variation of all the parameters during the series of measurements and alternating the observations of α_{1k} and α_{2k}, keeping the time intervals between them constant, makes the influence of any persisting variation of the parameters on the mean values of α_{1k} and α_{2k} (for the given series of measurements) almost the same so that in the difference between the mean values this influence is compensated to within a quantity of the second order of smallness. Hence we can write

$$C_{1k} = C_{2k} = C_k; \quad H_{ek1} = H_{ek2}; \quad H_{em1} = H_{em2}; \quad J_{m1} = J_{m2}. \tag{4}$$

Taking into account (3) and (4), we obtain from (2)

$$J_{2k} - J_{1k} = \frac{C_k(\bar{\alpha}_{1k} - \bar{\alpha}_{2k})}{4\pi s - NS}. \tag{5}$$

where $\bar{\alpha}_{1k}$ and $\bar{\alpha}_{2k}$ are the mean values of α_{1k} and α_{2k} for the given series of measurements.

One of the measures or criteria of the effectiveness of the procedure employed is the reproducibility of the values of $J_{2k} - J_{1k}$ in different series of measurements carried out under slightly different conditions (for example, on different days). In our results the values of J_m, J_{1k} and J_{2k} pertaining to the same nominal values of H_{em} and H_{ek} but obtained in different series of measurements differed within the limits of the "usual" errors of ballistic measurements (up to 0.5-1%), but the difference $J_{2k} - J_{1k}$ reproduced well even for such k's when the difference $J_{2k} - J_{1k}$ was appreciably smaller than the scattering of the values of J_{1k} and J_{2k} obtained in different series of measurements.

Comparison of the values of $J_{2k} - J_{1k}$ for different loops of the same specimen makes it possible to establish for some of them, with the same accuracy as the value of $J_{2k} - J_{1k}$ was determined, the points of confluence of the branches of the different loops. Thus from the inequalities

$$J'_{1k} \geqslant J''_{1k} \quad \text{and} \quad J'_{2k} \leqslant J''_{2k}, \tag{6}$$

following from the absence of the intersections of the branches of different loops of the same specimen and from the equality

$$J'_{2k} - J'_{1k} = J''_{2k} - J''_{1k} \tag{7}$$

it follows that

$$J'_{1k} = J''_{1k} \quad \text{and} \quad J'_{2k} = J''_{2k}. \tag{8}$$

This means that if some loops have in some sections identical values of $J_{2k} - J_{1k}$, then both the ascending and the descending branches of these loops in the given section coincide. But if the descending (or ascending) branches of the loops do not coincide (i.e., if, for example, $J'_{2k} \neq J''_{2k}$) then coincidence of the other branches (ascending or descending as the case may be) cannot be established by this procedure inasmuch as then $J'_{2k} - J'_{1k} \neq J''_{2k} - J''_{1k}$

even if $J'_{1k} = J''_{1k}$. Consequently, by means of this procedure one can determine the points of merging of only those loops for which $J_a \geqslant J_d$ (here J_d is the remanence of the specimen according to the limiting, magnetization-to-saturation loop not corrected for the demagnetizing effect; $J_r > J_d \approx H_c/N$).

All the loops with small values of J_m, including the loops for which $J_m = J_{mc}$, fall under this limitation, but J_{mc} can be found from the h_c vs J_m curves, while J_{ma} can be determined by comparing the normal magnetization curves with the limiting hysteresis loops.

3. In Fig.2 we show the normal magnetization curves (loci of the hysteresis loop end-points) $H_{em}(B_m) \approx H_{em}(4\pi J_m)$ for the samples listed above. It will be seen that for the first specimen the induction at the "knee" ($B_G \approx 4\pi J_G$) is ~15,000 gauss, for the second ~12,000 gauss and for the third ~1,000 gauss.

In the same figure we show the h_c vs B_m curves for these specimens. It will be seen that in all these specimens there exists the same relation between B_{mc} and B_G (or what is the same thing between J_{mc} and J_G) as was found in the investigations of Refs.5-7, namely,

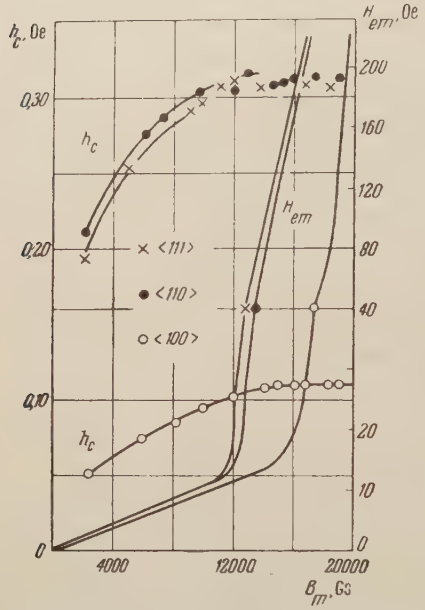

Fig.2. Normal magnetization curves $H_m(B_m) \approx H_{em}(4\pi J_m)$ and h_c vs B_m curves.

$$J_{mc} \approx J_G \qquad (9)$$

The observed variation of the difference $B_{2k} - B_{1k} \approx 4\pi(J_{2k} - J_{1k})$ as a function of H_{ek} for different loops of the first specimen is given in Fig.3; the corresponding curves for the second and third specimens are given in Figs.4 & 5, respectively. It will be seen that the character of the structure of the family of symmetrical hysteresis loops in these specimens agrees with the description given above in Section 1. In the case of the first specimen coincidence of the correspondbranches of the loops in the section where $H_{ek} = 0$ (when $-J_a = J_d$) obtains for all loops with $B_m \geqslant 14{,}200$ gauss (the corresponding values for the second and third specimens are $B_m \geqslant 12{,}100$ gauss and $B_m \geqslant 11{,}100$ gauss, respectively).

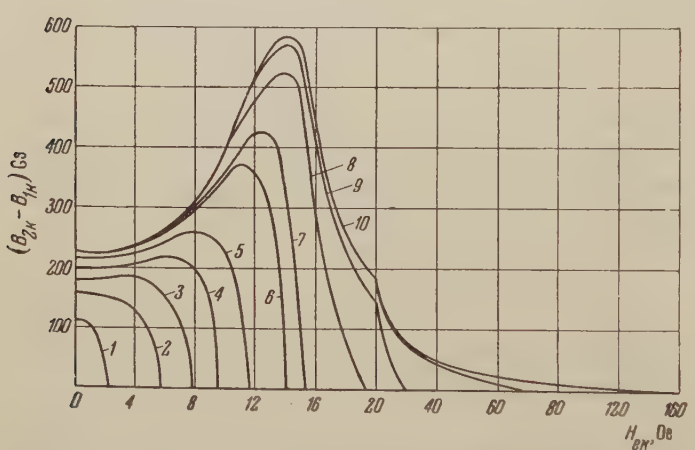

Fig.3. Variation of the difference $B_{2k} - B_{1k} \approx 4\pi(J_{2k} - J_{1k})$ with H_{ek} in magnetizing in the <100> direction with B_m = 1) 2400, 2) 6000, 3) 8200, 4) 10,000, 5) 11,900, 6) 14,200, 7) 15,100, 8) 16,100, 9) 16,800, 10) 18,300, 11) 18,900 gauss.

These values agree within the limits of the experimental error with the values of B_G for the same specimens.

The value of J_{mr} can be approximately determined in the following manner:

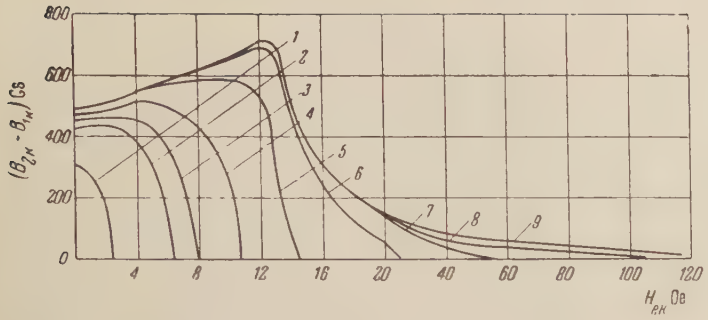

Fig.4. Same as Fig.3 but for magnetization in the ⟨110⟩ direction; B_m = 1) 2000, 2) 6000, 3) 7300, 4) 9900, 5) 12,100, 6) 12,900, 7) 13,800, 8) 15,100, 9) 18,000 gauss.

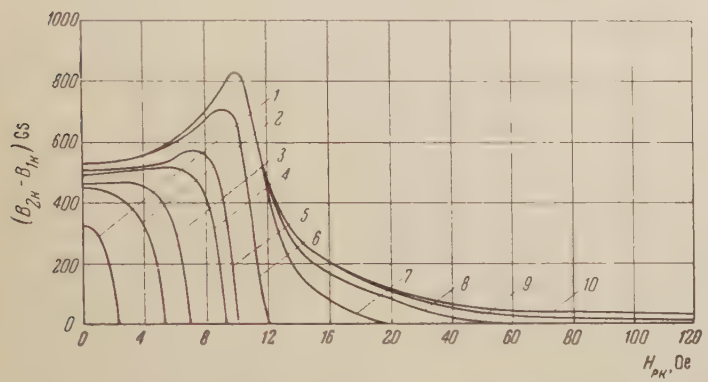

Fig.5. Same as Fig.3 but for magnetization in the ⟨111⟩ direction; B_m = 1) 2100, 2) 5200, 3) 6800, 4) 9200, 5) 10,000, 6) 11,100, 7) 11,900, 8) 13,700, 9) 16,700, 10) 18,000 gauss.

designating the value of H_{ek} at which $J_2 = J_r$ through H_{er}, we have

$$H_{er} = NJ_r. \qquad (10)$$

For our specimens $N \approx 0.011$. Assuming $J_r \approx J_G$, we find that for the first specimen $H_{er} \approx 13$ oersted, for the second ~10.5 oersted and for the third ~9.5 oersted. From Figs.3,4 & 5 we find that the values of $B_{2k} - B_{1k}$ for all the loops of the first specimen with $B_m \geqslant 18{,}000$ gauss, all the loops of the second specimen with $B_m \geqslant 13{,}000$ gauss and of the third specimen with $B_m \geqslant 12{,}000$ gauss coincide at the respective indicated values of H_{ek}. These values are therefore the approximate values of $4\pi J_{mr}$ for the given specimens. They are somewhat larger than the values of B_G; in the case of the first specimen the difference is approximately 20%; in the case of the second and third specimens the difference is about 10%.

In these specimens just as in those investigated in the work of Refs.5-7 there proved to be an appreciable magnetic hysteresis in the region of very high magnetization (even at $J > J_{mr}$) where, according to "textbook" theories of reversal of magnetization, it would appear that reversal of magnetism should occur only through reversible processes. Apparently, this hysteresis is associated with the hysteresis of nucleation and vanishing of some forms of "subdomains" in the region of high magnetization, as indicated by powder pattern (Bitter figure) studies performed in recent years by a number of different investigators.

Faculty of General Physics,
Ural State University

References

1. T.Spooner, Properties and testing of magnetic materials, p.18, N.Y. -London, 1937.

2. V.I.Ianus & L.A.Shubina, Zhur.tekh.fiz., 9, 1994 (1939).

3. J.L.Snoek, Physica, 8, 426 (1941); New developments in ferromagnetic materials, Amsterdam, 1947 (Cited in Russian trans.).

4. J.Kayser, J.Sci.Instr., 26, 60 (1949).

5. V.I.Drozhzhina, R.I.Ianus, V.P.Kartashov & E.V.Kaplun, Izv. AN SSSR, Ser.fiz., 16, 703 (1952).

6. R.I.Ianus & V.A.Kadkin, FMM (Physics of Metals & Metallography), 1, 420 (1955).

7. R.I.Ianus & V.P.Voroshilov, FMM, 1, 424 (1955).

8. R.I.Ianus, V.I.Drozhzhina & E.F.Shabalina in Sbornik (Collected articles dedicated to the Seventy-fifth Anniversary of Academician A.F.Ioffe, p.411, M., 1950.

TEMPERATURE AND ROTATIONAL HYSTERESIS IN FERROMAGNETS

- L.V.Kirenskii, A.Ia.Vlasov, N.I.Vtiurin, A.I.Drokin, V.F.Ivlev & R.I.Tukalov

When a magnetic parameter of a ferromagnet does not have a unique value for a given value of the external magnetic field, the elastic stress, the angle between the field vector and the crystal axes or the temperature but, on the contrary, is characterized by different values depending on the previous history of the specimen or the mode of approach to the given state, we have the effect commonly known as hysteresis. It is customary to distinguish between the following different types or kinds of hysteresis effects:

1) ordinary hysteresis effects occurring in cyclic variation of the magnetizing field; in this case the magnetic parameters depend on the previous magnetic history of the specimen;

2) magnetoelastic hysteresis effects occurring incident to cyclic variation of the elastic stresses; the magnetic parameters depend on the previous deformation history of the specimen;

3) temperature hysteresis effects occurring in cyclic variation of the temperature; the magnetic parameters in this case depend on the previous thermal history of the specimen;

4) rotational hysteresis effects developing as a result of cyclic variation of the direction of the field vector relative to the crystallographic axes in one sense or the other (clockwise or counterclockwise rotation).

There have been relatively few investigations of temperature magnetic hysteresis of magnetization (hereinafter TMHM), aside from the fundamental work of Shur and his co-workers[1-3]. As for temperature hysteresis of other magnetic properties, we have only the studies of Kirenskii & Vlasov[4] indicating the existence of temperature hysteresis of magnetostriction (hereinafter THMS) and of Kirenskii & Ivlev[5] on the temperature hysteresis of the galvanomagnetic effect (hereinafter THG). So far only hysteresis losses have been measured in rotating magnetic fields; other hysteresis effects in rotating fields have not been observed. The present report is devoted to the results of our experimental investigation of temperature hysteresis of magnetization in following the B cycle (cooling—heating) and temperature hysteresis of magnetostriction and the galvanomagnetic effect in following the A cycle (heating—cooling). We also discovered and investigated the effect of rotational hysteresis of magnetostriction in conjunction with an investigation of the hysteresis loss in rotating magnetic fields.

Samples and measurements

Temperature magnetic hysteresis (TMHM) in the B cycle was investigated on nickel samples with different demagnetization coefficients. The samples were cylindrical and were composed of 99.98% pure Ni. Sample No.1 with a large demagnetization coefficient was 100 mm long and 2.12 mm in diameter; sample No. 2 with a small demagnetization coefficient was 100 mm long and 1.05 mm in diameter. For the purpose of relieving the internal stresses the samples were subjected to prolonged annealing at 1100° followed by slow cooling in magnetic shielding. The measurements were carried out on a vertical astatic magnetometer provided with magnetic shielding. The vertical components of the earth's magnetic field and other extraneous fields were compensated by means of appropriate single layer coils incorporated into the set-up.

Temperature hysteresis of magnetostriction (THMS) was investigated on a wire sample of electrolytic nickel 20.99 cm in length and 2 mm in diameter. The sample was subjected to prolonged high temperature annealing. Prior to

each measurement the sample was heated to a temperature above the Curie point and cooled in magnetic shielding. The magnetostriction measurements were carried out on a set-up operating on the principle of compensating the thermal expansion of the sample. The set-up and photographic recording procedure are described in Ref.4.

The measurements comprised four separate series: in series I the initial temperature was -183° and the final temperatures were 400, 250, 150 and 10°, in series II the initial temperature was 10° and the final temperatures were 400, 250 and 150°, in series III the initial temperature was 150° and the final temperatures 400 and 250° and in series IV the initial temperature was 250° and the final temperature 400°. In all the series the magnetostriction curves were recorded in fields of 1.5, 8, 10, 12.5, 15, 20, 25, 37.5, 50, 75 and 100 oersted. The experimental points were obtained at intervals of 50°.

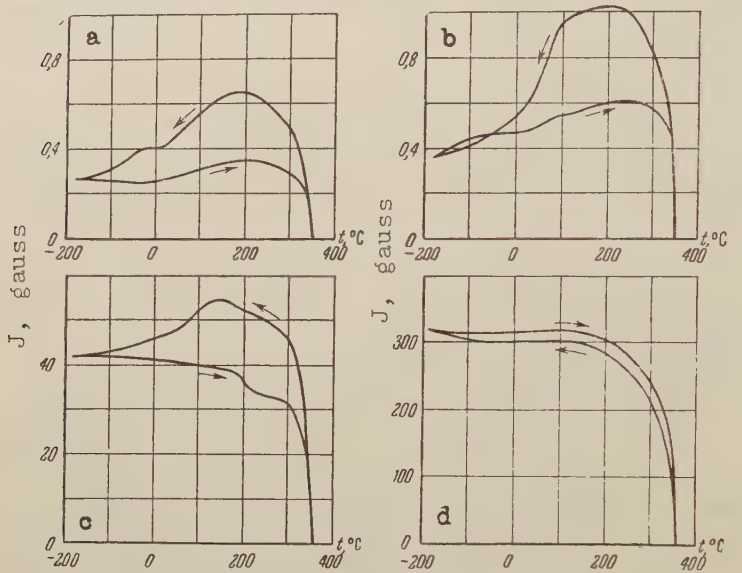

Fig.1. TMHM of nickel in the B cycle (cooling—heating). Sample No.1. Magnetizing fields: a) 0.0065, b) 0.013, c) 0.65, d) 10.4 oersted.

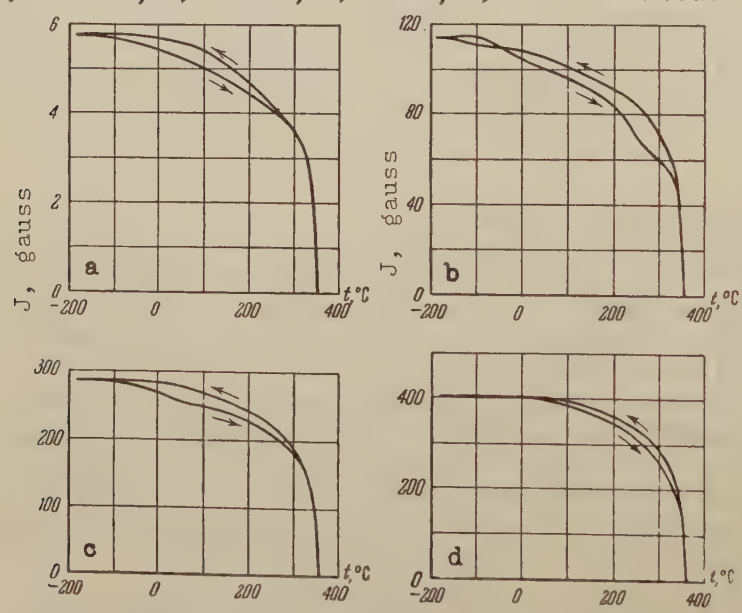

Fig.2. TMHM of nickel in the B cycle. Sample No.2. Magnetizing fields: a) 0.039, b) 0.65, c) 6.5, d) 13.0 oersted.

Temperature hysteresis of the galvanomagnetic effect (THG) was also investigated on a nickel sample - a wire with a resistance of 25.9 ohm - but in a narrower temperature range (18 to 400°) in fields of 9, 18, 27, 36, 45, 54, 64, 78, 90, 115, 136, 180 and 360 oersted.

Measurements were also carried out following the A cycle with different initial temperatures (18, 25, 50, 75, 100, 125 & 150°) and different return points (130, 220, 260 & 380°).

In order to eliminate the influence of the temperature variation of the resistance of the sample a compensator of the same material but carrying a winding positioned normal to the field vector was connected into the second arm of the bridge circuit.

Our investigation of rotational hysteresis of the magnetostriction (RHMS) was carried out on an annealed, rolled polycrystalline nickel disc at 20°C in the field interval from 100 to 4850 oersted (diameter of disc 14.2 mm, thickness 1.02 mm,

percent reduction in thickness in rolling 54.7%).

The magnitude of the magnetostriction was determined by means of a wire guage cemented to the sample in the direction of rolling. The torques were recorded by means of an Akulov type anisometer. The magnetic field produced by an electromagnet was rotated relative to the sample from 0 to 360° forward and backward (clockwise and counterclockwise).

The TMHM, THMS, THG and RHMS measurements were carried out by the method of automatic recording of the investigated parameters on photographic film. Thus the results of measurements were obtained in the form of magnetograms.

Results and discussion

The results for TMHM following the B cycle for sample No.1 are shown in Fig.1 and for sample No.2 in Fig.2. It will be evident that TMHM is far more pronounced in the thick as compared with the thin sample.

In the case of sample No.1, in contrast to that of No.2, in the curve for cooling in fields of less than 1 oersted there is first an increase of magnetization and then a decrease, so that TMHM appears. In cooling, passage through the Curie point is accompanied by increase of the magnetization due to growth of the spontaneous magnetization.

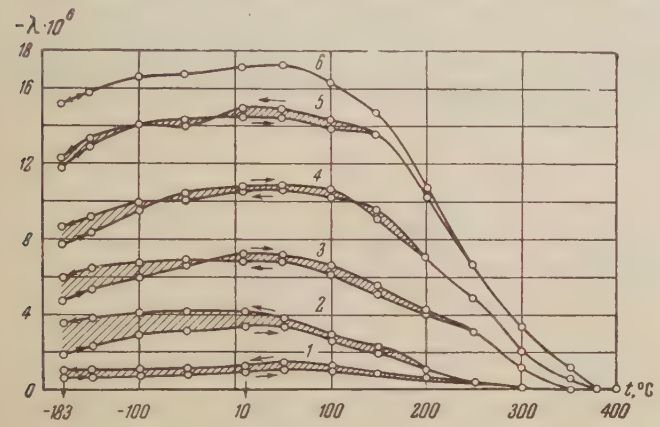

Fig.3. THMS of nickel in different fields. Measurement series I (see text). H = 1) 1, 2) 10, 3) 25, 4) 37.5, 5) 50, 6) 75 oersted.

With further cooling, in thick samples the higher demagnetization coefficient acts to further reduce the weak external field. Here the role of the anisotropy energy is enhanced so that in displacement of the domain walls the domain magnetization vectors are aligned not in the direction of the magnetizing field but in the directions of easy magnetization which may not coincide with the orientation of a weak field. In stronger fields (and in fact in all but the weakest field) in the case of samples with a small demagnetization coefficient, there is no significant drop of the magnetization over the heating part of the cycle so that the temperature hysteresis is minor; in fact in the case of very thin samples TMHM in the B cycle is not observed.

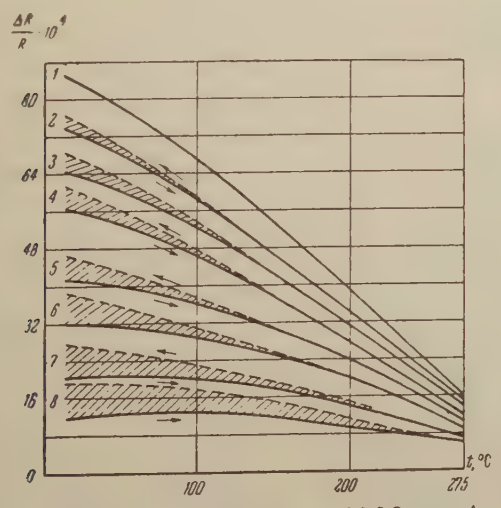

Fig.4. THG in nickel in different fields: 1) 78, 2) 64, 3) 54, 4) 45, 5) 36, 6) 27, 7) 18, 8) 9 oersted.

The THMS curves for nickel recorded in the first series of measurements at different field values are shown in Fig.3. It will be seen that in fields up to 15 oersted the curves corresponding to cooling of the sample lie below the curves for heating, i.e., positive THMS is observed. It will also be

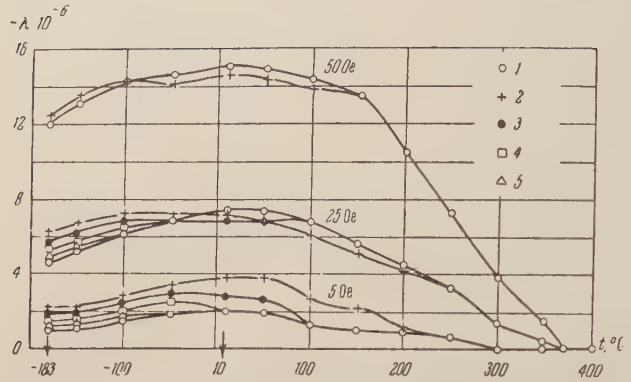

Fig.5. THG in nickel with H = 5.25 and 50 oersted. Initial temperature -183°: 1) heating to 400°, 2) cooling from 400°, 3) cooling from 250°, 4) cooling from 150°, 5) cooling from 10°.

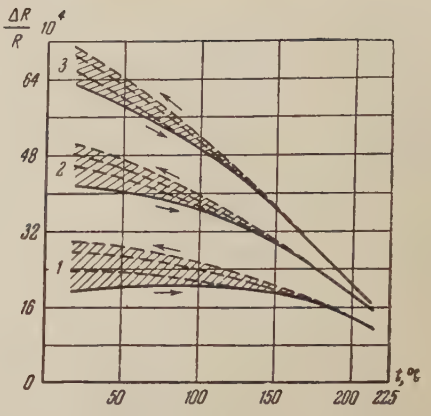

Fig.6. THG in nickel. Initial temperature 18°. Return points: 260°, 220° and 130°. Fields: 1) 18, 2) 36 and 3) 54 oersted.

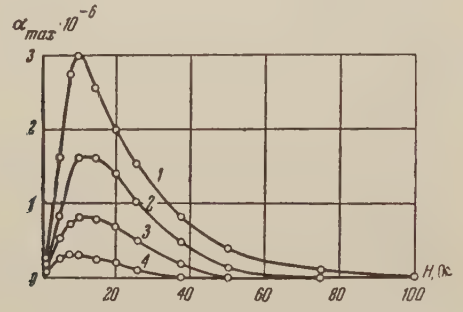

Fig.7

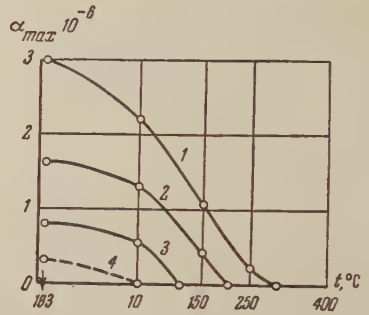

Fig.8

Fig.7. Field dependence of the maximum temperature hysteresis of magnetostriction for different heating ranges. Initial temperature -183°; final heating temperature (return points): 1) 400°, 2) 250°, 3) 150°, 4) 10°.

Fig.8. Temperature dependence of the maximum THMS. Initial temperature in all cases -183°; final temperatures: 1) 400°, 2) 250°, 3) 150°, 4) 10°.

seen that the magnitude of the hysteresis gradually decreases with increasing field strength so that in fields of the order of 100 oersted THMS is no longer observed. A similar situation was found to obtain for THG (Fig.4).

The magnitude of both THMS and THG depend on the initial temperature and on the final point of heating (return point), provided this lies below the Curie point. This is evident from Figs.5 & 6, from which we see that with decreasing return point temperatures the magnitudes of both THMS and THG decrease.

It will be clear from the curves shown in Fig.7 that THMS increases sharply in fields of the order of 8-10 oersted and then slowly falls off to zero. The field values at which THMS vanishes also decrease with decreasing end-point heating temperature. A similar picture is observed for THG.

It was found that the curves for the variation of the maximum THMS as a function of the final heating temperature (with the initial temperature kept constant) are linear in the temperature range above 10°, which is in agreement with the data obtained for THG (Fig.8). In the region of negative temperatures,

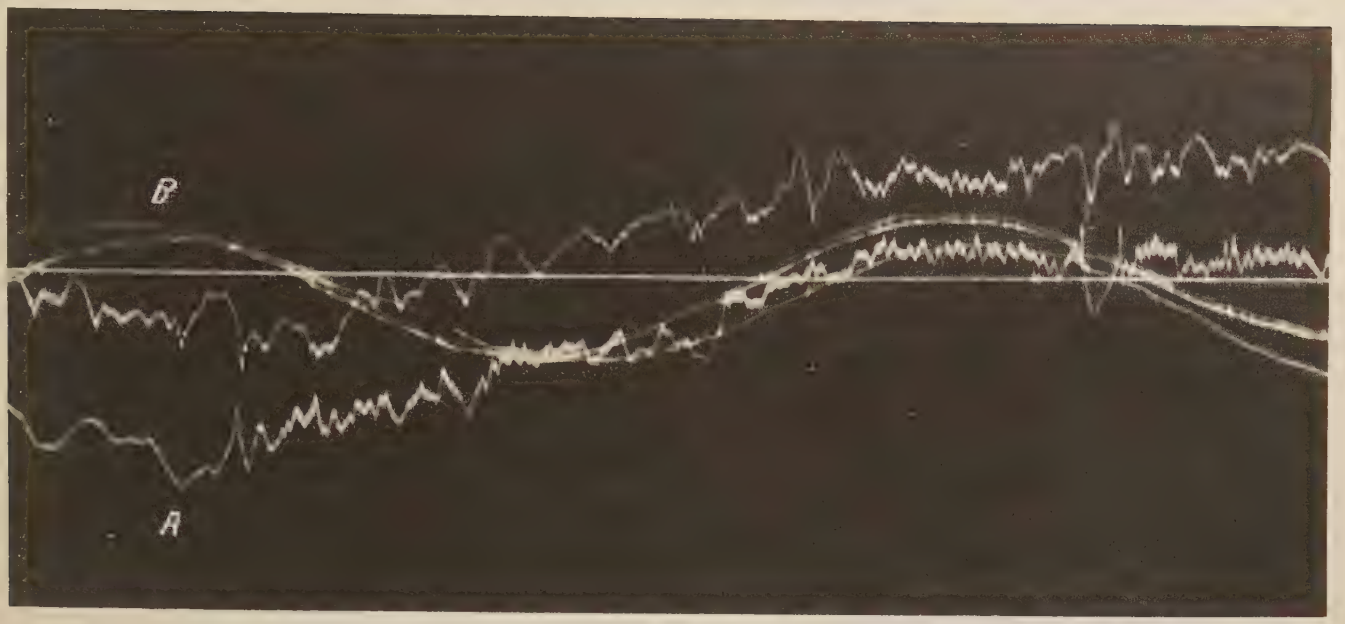

Fig.9. Automatic photographic record of the curves giving the variation of the torque (A) and the magnetostriction (B) of the nickel incident to clockwise and counterclockwise rotation of the magnetic field. H = 4850 oersted.

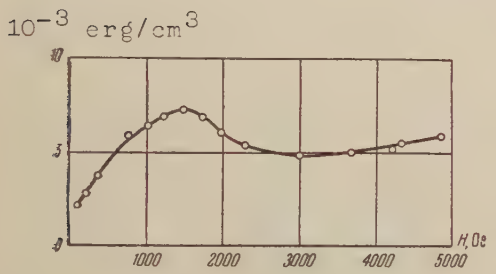

Fig.10. Magnetic hysteresis loss in rotating fields for a rolled polycrystalline sample at 20°.

however, the variation deviates from linearity. The points of intersection of the curves with the temperature axis give the temperature values at which THMS and THG disappear.

In Fig.9 we reproduce by way of illustration a magnetogram showing the photographic record of the variation of the magnetostriction and the torque acting on the specimen during rotation of the magnetic field in the plane of rolling.

The magnetization hysteresis losses per cycle in rotating fields were calculated from the areas between the torque curves. The results show that the magnetic hysteresis loss in rotating fields of from 1000 to 2500 oersted is correctly described by the theory of Akulov[6]. Our results generally substantiate the experimenta data of Baskakov & Briukhatov[7], Sarapkin[8] and other investigators, indicating that with increasing magnetic field strengths the loss increases up to a certain limit and then start to decrease (Fig.10). We found, however, that the hysteresis loss does not disappear entirely in strong fields, but on the contrary exhibits a tendency to growth at very high field values.

As noted above, we established the existence of rotational hysteresis of magnetostriction (Fig.9). Analysis of the magnetostriction magnetograms shows that both the magnetostriction itself and RHMS increase with increasing field

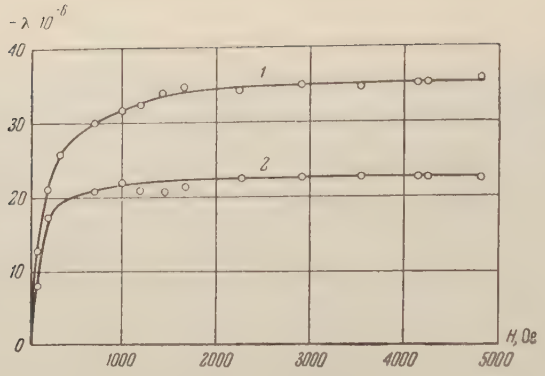

Fig.11. Magnetostriction (1) and hysteresis of magnetostriction (2) of nickel in rotating magnetic fields at 20°.

strength from 100 to 1000 oersted and then with further increase in field strength asymptotically approach a maximum "saturation" value.

Krasnoiarsk State Pedagogical Institute

References

1. Ia.S.Shur & V.I.Drozhzina, Zhur.eksp.i teor.fiz., 17, 607 (1947).
2. Ia.S.Shur & V.I.Drozhzina, Izv.AN SSSR, Ser.fiz., 11, 539 (1947).
3. Ia.S.Shur & N.A.Barapova, Zhur.eksp.i teor.fiz., 20, 183 (1950).
4. L.V.Kirenskii & A.Ia.Vlasov, Izv.AN SSSR, Ser.fiz., 16, 673 (1952).
5. L.V.Kirenskii & V.F.Ivlev, Doklady AN SSSR, 106, 419 (1956).
6. N.S.Akulov, Uch.zap. (Scientific notes) Moscow State University; N.S. Akulov, Ferromagnetizm (Ferromagnetism), 1939.
7. A.A.Baskakov & N.L.Briukhatov, Zhur.eksp.i teor.fiz., 9, 984 (1939).
8. P.S.Sarapkin, Izv.AN SSSR, Ser.fiz., 16, 688 (1952).

HYSTERESIS LOSSES IN ROTATING MAGNETIC FIELDS IN A MAGNETITE SINGLE CRYSTAL BEFORE AND AFTER PHASE TRANSITION

- N.L.Briukhatov

Introduction

Since Weiss' studies[1] of the magnetic properties of magnetite single crystals, studies that led to the discovery of magnetic anisotropy, there have been numerous investigations[2-7] which have resulted in the discovery of the low temperature phase transition in magnetite single crystals and determination of their crystal structure[8-16].

Of particular importance in this field is the work of Néel[17] who explained the magnetic properties of magnetite on the basis of the concepts of antiferromagnetism. Néel's hypotheses have been substantiated by neutron diffraction studies[18-20]. These studies confirmed the existence of two groups of magnetic cations with antiparallel spin orientations.

It is of obvious interest to investigate the problem of the interaction of these spins with the crystal lattice. The process of transition of the spin from coupling with the lattice to coupling with the external field can be followed by observing the hysteresis losses in rotating magnetic fields.[21] This, then, was the purpose of the present investigation.

Experimental part

The experiments were carried out on a Ural magnetite single crystal cut to a 10.4 mm diameter sphere. The crystal was rounded by the method of A.V. Shubnikov with his kind assistance.

The magnetic anisotropy of the crystal and hysteresis losses in rotating magnetic fields were determined by the method of measuring the torque on a magnetic dynamometer (Fig.1). The measurements were carried out at room temperature and at the temperature of liquid nitrogen in magnetic fields ranging from 10 to 10,000 oersted. The torque curves were recorded for the (100) plane. The measurements showed that at room temperature the magnetite single crystal has eight directions of easy magnetization. Its first anisotropy constant at +15° has the value $K_1 = -1.4 \cdot 10^5$ erg cm^{-3}. The corresponding torque curve is shown in Fig.2.

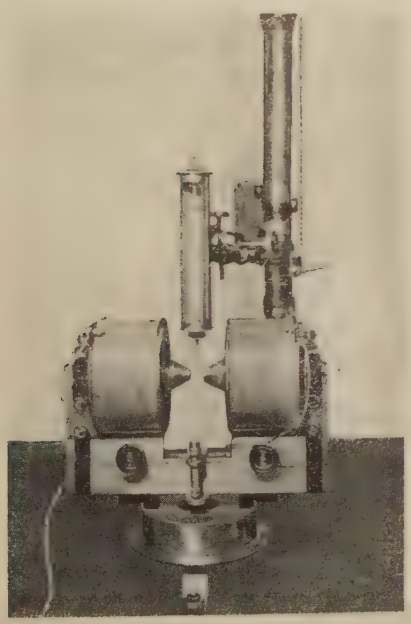

Fig.1. Magnetic structure dynamometer.

The experiments showed that the character of the magnetic anisotropy of the crystal in the (100) plane does not change, i.e., that the [110] axis remains the direction of easy magnetization both at room temperature and when the crystal is cooled below the phase transition point in the absence of an external magnetic field. The character of the magnetic anisotropy does change when the crystal specimen is cooled in a strong magnetic field. Then, instead of eight directions of easy magnetization there appears only one axis of easy magnetization. This axis is oriented parallel to the edges of the cubic lattice closest to the direction of the applied magnetic field. These results were obtained by the author

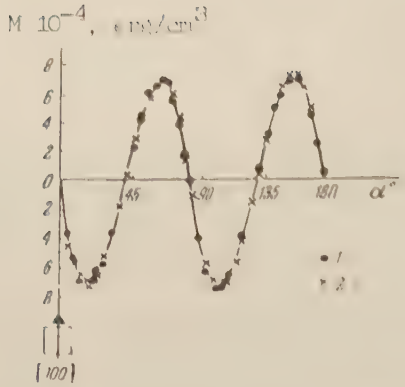

Fig.2. Torque curve for the magnetite single crystal in the (100) plane at 15° and H = 3500 oersted: 1) forward rotation (clockwise), 2) reverse rotation.

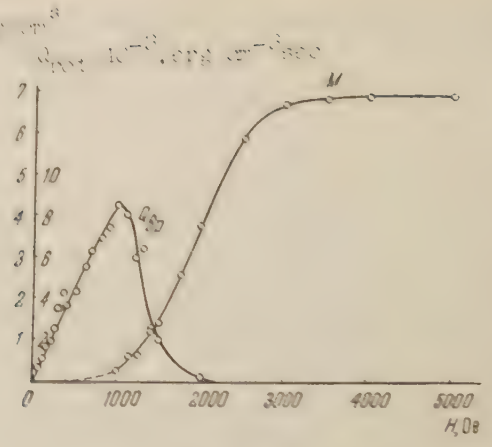

Fig.3. Variation of hysteresis loss (Q_{rot}) at room temperature and variation of the maximum torque (M) with increasing field strength.

Results of hysteresis loss measurements

Measurements of the hysteresis loss Q_{rot} in a rotating magnetic field at room temperature showed that the character of the variation is similar to that observed in nickel single crystals[21]. The hysteresis loss has a maximum at a field value of 1000 oersted (8.5 erg cm^{-3}) and falls to zero at a field of about 2000 (Fig.3) when rotation processes begin, which is in agreement with the theory of Akulov[22].

Results of hysteresis loss measurements at liquid nitrogen temperature

The development of hysteresis losses in a rotating magnetic field at temperatures below the phase transition temperature in a magnetite single crystal is more complicated than at room temperature. In the case of cooling not

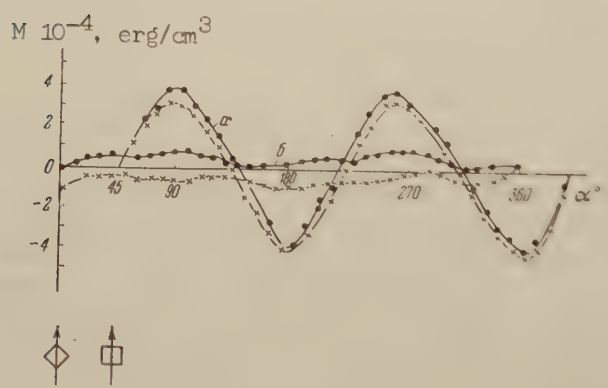

Fig.4. Torque curves recorded at -195° and H = 70 oersted: a) cooling in a magnetic field, b) cooling without a magnetic field.

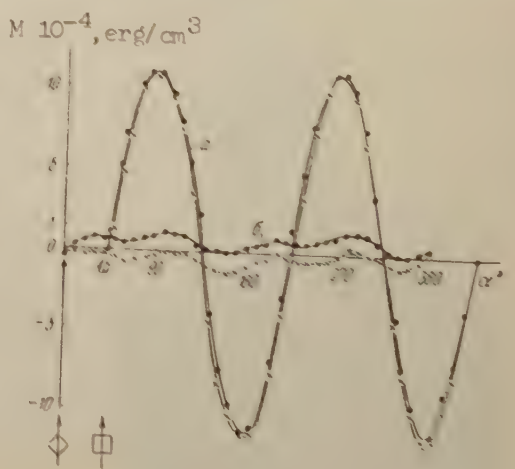

Fig.5. Torque curves recorded at -195° and H = 1000 oersted; a) and b) same as in Fig.4.

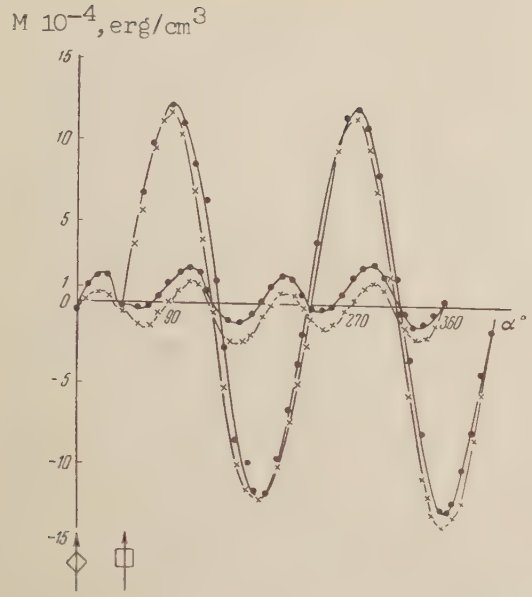

Fig.6. Torque curves recorded at -195° and H = 1500 oersted; a) and b) same as in Fig.4.

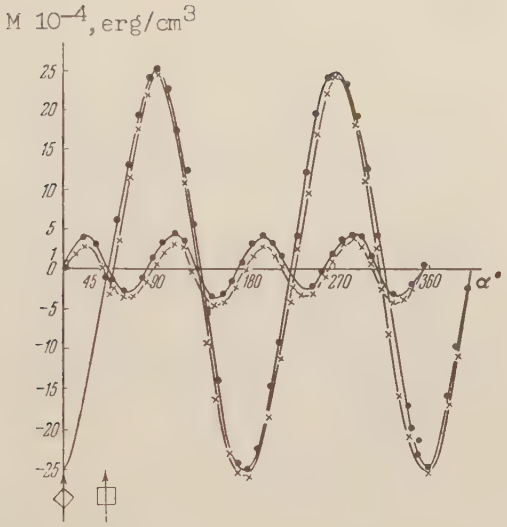

Fig.7. Torque curves recorded at -195° and H = 2000 oersted; a) and b) same as in Fig.4.

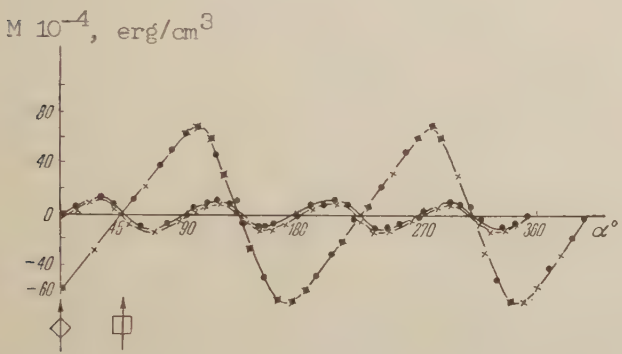

Fig.8. Torque curves recorded at -195° and H = 3000 oersted; a) and b) same as in Fig.4.

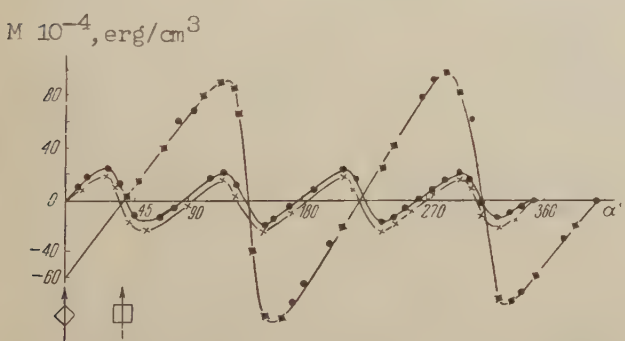

Fig.9. Torque curves recorded at -195° and H = 6000 oersted; a) and b) same as in Fig.4.

in a magnetic field, when the [110] axis remains the direction of easy magnetization, the hysteresis loss increases rapidly with increasing magnetic field strength and passes through a maximum ($70 \cdot 10^3$ erg cm^{-3}) at a field of about 1000 oersted; with further increase in the field strength the hysteresis loss decreases but does not go to zero. At a field of about 3000 oersted the loss amounts to only $20 \cdot 10^3$ erg cm^{-3}, from which point the loss begins to increase attaining the extremely high value of about $476 \cdot 10^3$ erg cm^{-3} in a field of 10,000 oersted.

The torque curves recorded at -195° in different fields of up to 10,000 oersted with the crystal cooled without a magnetic field are shown in Figs.4-10. The starting position of the crystal was with one diagonal of the lattice cube face in line with the magnetic field, which corresponds to the distribution of the eight directions of easy magnetization along the space diagonals of the cube at room temperature. The areas between the curves

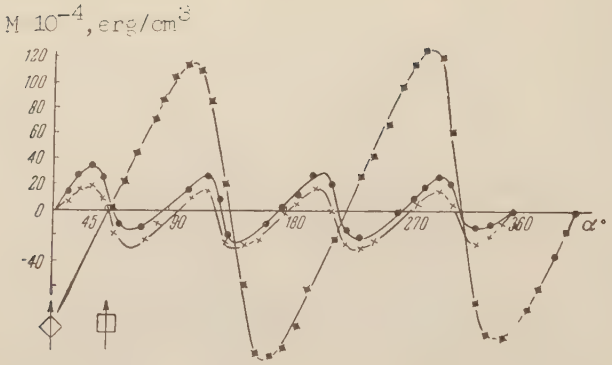

Fig.10. Torque curves recorded at -195° and H = 10,000 oersted, a) and b) same as in Fig.4.

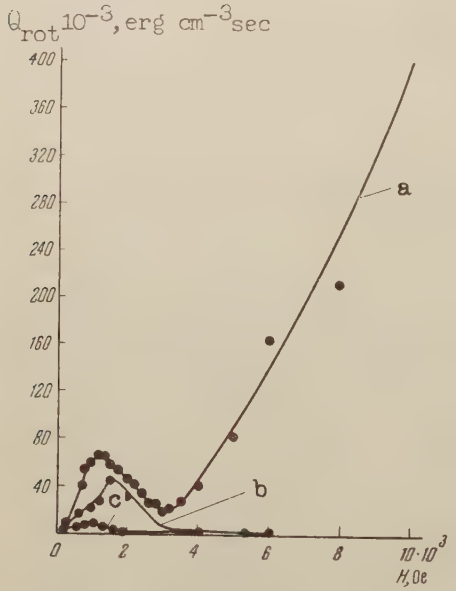

Fig.11. Variation of the hysteresis loss in rotating fields in the magnetite single crystal specimen: a) hysterelоss at -195° in the case of cooling in the absence of a magnetic field, b) hysteresis loss at -195° in the case of cooling in a magnetic field, c) hysteresis loss at room temperature. For purposes of comparison all the curves have been plotted to the same scale.

recorded for forward (clockwise) and reverse rotation of the magnetic field give the value of the hysteresis loss.

The variation of the hysteresis loss with field strength is shown in Fig.11 (curve a). For purposes of comparison we give the variation of the hysteresis loss at room temperature plotted to the same scale (curve c in Fig.11).

Cooling of the crystal in a magnetic field

The crystal was cooled in a magnetic field of 10,000 oersted prior to each series of measurements. The 10,000 oersted magnetic field was applied at room temperature with the crystal positioned with the [110] axis in the direction of the field. Then the Dewar flask containing liquid nitrogen was raised into position. Upon immersion into the liquid nitrogen, the crystal was sharply rotated to bring the edges of the cube parallel to the field direction and fixed in this position. This rotation of the crystal is shown schematically at the lower left in Figs.4-10. Then the magnetic field was reduced to the desired value and the torque curves recorded. It will be seen that these curves have a period of 180° which indicates that the crystal was transformed to a magnetically uniaxial one. The amplitude of these curves is much greater than the amplitude of the torque curves recorded with the crystal cooled in the absence of a field.

As the areas between the forward and reverse curves show, the value of the hysteresis loss has a maximum at a field value of about 1500 oersted; the loss in this field is $44 \cdot 10^3$ erg cm^{-3} per cycle. From H = 3000 oersted the areas between the curves disappear, i.e., the hysteresis loss goes to zero. The variation of the hysteresis loss with the field strength in the case of a crystal cooled in a magnetic field is shown by curve b in Fig.11.

Conclusions

The exceptionally great increase in hysteresis loss in strong rotating magnetic fields cannot be explained from the standpoint of the conventional theories and concepts of ferromagnetism.

The transformation of the torque curves in the (100) plane to sinusoidal form with a $\pi/2$ period is connected with transition from coupling of the magnetization vector with the crystal lattice to coupling of the magnetization

vector with the external magnetic field as the latter is increased. The hysteresis loss attains a maximum in fields in which the character of the spin coupling changes. In saturation fields when the spin is coupled exclusively with the external magnetic field the hysteresis loss goes to zero. It has been established by the neutron diffraction studies of Shull and his co-workers[18-20] that in magnetite $Fe^{3+}(Fe^{3+}Fe^{2+})O_4^{2-}$ the spins of the trivalent cations located at the tetrahedral interstices between the oxygen ions are antiparallel to the spins of the bivalent and trivalent cations located at the octahedral interstices, which is in accord with Néel's antiferromagnetism theory of two sublattices. In the light of these concepts one can attempt to explain the increase of the hysteresis loss in strong magnetic fields in the magnetite crystal cooled in the absence of a magnetic field. Under the influence of the low temperature there occurs a redistribution of the electron density in the lattice without the cations exchanging places, as a result of which we have a change not only of the character of the binding forces in the lattice (leading to transition from the cubic to the orthorhombic symmetry) but also a change of the strength of the coupling of the spins with the crystal lattice, i.e., a change in the anisotropy. At low temperature the change in the coupling of the trivalent cations located at the tetrahedral positions with the crystal lattice may be such that for these spins the transition from coupling with the lattice to coupling with the external field will only begin at the intensity of the magnetic field in which this transition is already virtually completed for the spins of the cations located at the octahedral positions. As the upper curve (a) in Fig.11 shows, this is the variation exhibited by the hysteresis loss in fields of about 3000 oersted.

Cooling of the crystal in a magnetic field presents a special case. The very high value of the torques in this case (see Figs.4-10) indicates a strong increase of the normal components of the magnetization of the crystal as compared with the normal magnetization component obtained in the case of cooling in the absence of a magnetic field (at the same field values). This increase of the normal magnetization component, as indicated by the ratio of the corresponding torques, in fields of 6000 to 10,000 oersted is close to the ratio of the sum of the magnetic moments of all the Fe^{2+} and Fe^{3+} cations (14 μ_B) to the magnetic moment found experimentally by Weiss & Forrer[2] (4.08 μ_B).

Calhoun's investigation[3] of the temperature dependence of the magnetization of magnetite indicates that the uncompensated antiferromagnetism (see Néel[17]), which exists in magnetite crystals both at room temperature and at low temperatures if the cooling is carried out in the absence of a magnetic field, should also persist to a significant extent when the crystal is cooled in a strong magnetic field. The sharp increase of the normal component of magnetization in this case indicates that in cooling in a magnetic field there must occur an appreciable change of the anisotropy in connection with orthorhombic distortion of the lattice. Assuming that the change in the character and strength of the magnetic anisotropy in this case is such that the magnetic moments of all the Fe^{2+} and Fe^{3+} cations can simultaneously switch to complete coupling with the relatively strong magnetic field, one can explain the diminution to zero of the hysteresis loss in rotating magnetic fields when the deep cooling is realized under the continuous influence of a strong magnetic field.

Faculty of Physics,
Moscow Institute of Railroad Engineers

References

1. P.Weiss, L'èclair. èlectr., 7, 487; 8, 56 (1896); 8, 105 (1896).
2. P.Weiss & R.Forrer, Ann.d.Phys., 12, 279 (1929).
3. R.Millar, J.Amer.Chem.Soc., 51, 215 (1929).
4. Hsien Li Ching, Phys.Rev., 40, 1002 (1932).
5. Okamura, Scient.Rpts.Tohoku Univ. 21, 231 (1932).
6. T.Barth & E.Posnjak, ZS.f.Kristallogr., 82, 325 (1932).
7. P.Khallileev, Phys.ZS.d.Sowjetun., 7, 108 (1935).
8. E.Verwey, J.of Chem.Phys., 3, 585 (1935).
9. E.Verwey & J.deBoer, Rec.d.trav.Chim.Pays.-Bas, 55, 531 (1936).
10. E.Verwey & E.Heilmann, J.of Chem.Phys., 15, 174 (1947).
11. E.Verwey, P.Haymann & E.Romeijn, J.of Chem.Phys., 15, 181 (1947).
12. C.Domenicali, Phys.Rev., 78, 458 (1950).
13. L.Bickford, Phys.Rev., 78, 449 (1950).
14. N.Tombs & H.Rooksby, Acta Crystallogr., 4, 474 (1951).
15. H.Williams & R.Bozorth, Revs.of Mod.Phys., 25, 79 (1953).
16. H.Williams, R.Bozorth & M.Boertz, Phys.Rev., 91, 1107 (1953).
17. L.Neel, Ann.d.Phys., 3, 137 (1948).
18. C.Shull, E.Wollan & W.Strausser, Phys.Rev., 81, 483 (1951).
19. C.Shull, Phys.Rev., 81, 626 (1951).
20. C.Shull, E.Wollan & W.Kochler, Phys.Rev., 84, 912 (1951).
21. A.Baskakov & N.Briukhatov, Zhur.eksp.i teor.fiz., 9, 984 (1939).
22. N.Akulov, Uch.zap. (Scientific notes) Moscow State University, 2, 137 (1934).
23. B.A.Calhoun, Phys.Rev., 94, 1577 (1954).

INFLUENCE OF ELASTIC STRESSES AND THERMOMECHANICAL TREATMENT ON THE MAGNETIC PROPERTIES OF HIGH COERCIVITY ALLOYS

- Ia.S.Shur, M.G.Luzhinskaia & L.A.Shubina

Introduction

It is now commonly accepted that the magnetic structure of "hard" (high-coercivity) materials differs substantially from the magnetic structure of magnetically "soft" materials. Consequently, there is good reason to assume that physical factors capable of altering the magnetic structure of ferromagnets will exert a different influence on magnetically hard as compared with magnetically soft ferromagnets. Until now the influence of diverse factors has been investigated experimentally and theoretically only as regards soft materials. Thus the work of Refs.1 & 2 was devoted to a detailed investigation of the influence of unilateral elastic stresses and thermomechanical treatment on the magnetic properties of a large number of different soft magnetic materials. Little attention was paid to high-coercivity materials. In light of the general concepts concerning the magnetic structure of high-coercivity alloys, it may be assumed, however, that in some cases these factors may exert an appreciable effect on their properties. These considerations induced us to undertake the present work which was devoted to experimental investigation of the influence of elastic stresses (tensile and torsional) and of thermomechanical treatment on the magnetic properties of some high-coercivity alloys. The thermomechanical treatment consisted of applying elongating loads to the specimens during heat treatment designed to produce the crystal structure corresponding to the high-coercivity state.

1. Specimens

In selecting the alloys for experimentation we turned to materials with a high elastic limit inasmuch as in such cases one might expect the greatest change in magnetic properties under the influence of stress. In addition it was desirable to have the possibility of preparing samples with a small cross section (i.e., in the form of thin wires or narrow strips) so as to be able to operate with readily realizable absolute loads. These requirements are satisfied by the chosen alloys of the Fe-Co-V and Fe-Mn systems. The Fe-Co-V alloys contained 8, 12 and 14% V and 52% Co; the Fe-Mn alloy contained 15% Mn. In these alloys the high-coercivity state is obtained by cold deformation of the specimens followed by annealing at temperatures of 500 to 600°.[3-5]

The investigated specimens were in the form of wires 0.1 and 3.0 mm in diameter and 50 to 80 mm in length. The degree of reduction obtained in the process of cold drawing was 75 to 98%. The specimens were subjected to conventional annealing at temperatures up to 700°. In the case of thermomechanical treatment the specimens were heated to temperatures in the same range and simultaneously subjected to different tensile loads (up to 90 kg/mm^2). After the thermomechanical heat treatments we determined the magnetic characteristics (magnetization curves, hysteresis loops), the longitudinal magnetostriction and resistivity and evaluated the influence of elastic stresses on the magnetic properties of the specimens. In addition, we carried out measurements on specimens stressed in torsion.

2. Influence of elastic stress

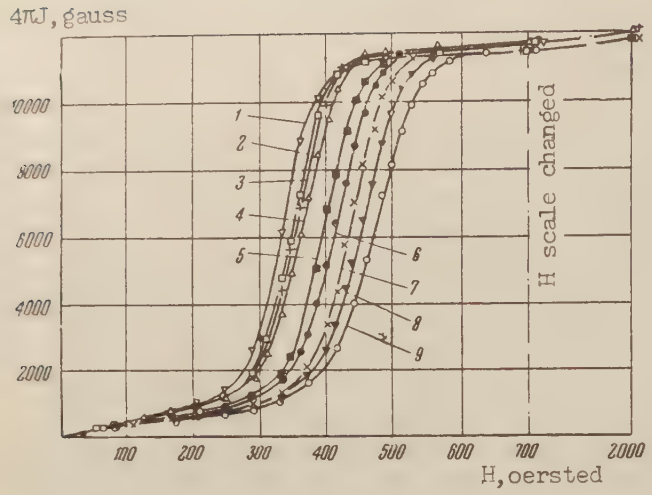

Fig.1. Influence of elastic elongation on the magnetization curves recorded for a Vicalloy specimen. The respective loading values for curves 1-9 are σ = 0, 10, 21, 32, 42, 53, 64, 74 and 85 kg/mm^2.

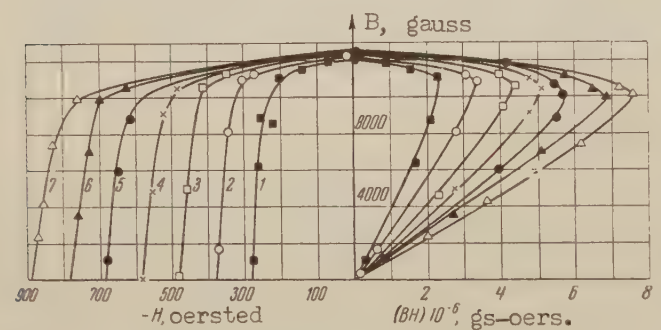

Fig.2. Variation of the demagnetization branch of the hysteresis loop and the magnetic energy curve for a 0.1 mm diameter Vicalloy specimen. The respective load values for curves 1-7 are σ = 0, 51, 101, 152, 203, 254 and 305 kg/mm^2.

Fig.1 shows the influence of elastic stress (σ) on the magnetization curves of a Vicalloy specimen (12% V + 52% Co + 36% Fe) 0.5 mm in diameter, annealed for one hour at 575°. It will be seen that the character of the magnetization curves changes under the influence of elastic stresses: with increasing elastic stress the steep rise of the magnetization curve begins at higher field values and, accordingly, saturation is also attained at higher values of the magnetizing field.

Fig.2 shows the influence of elastic stresses on the demagnetization branch of the hysteresis loop and the magnetic energy curve for a specimen of the same composition 0.1 mm in diameter. It will be seen that elastic stresses produce a very marked increase of the coercive force H_c and the maximum magnetic energy $(BH)_{max}$ and a significant increase of the remanence B_R. In the absence of a tensile load this specimen was characterized by H_c = 280 oersted, B_R = = 12,000 gauss and $(BH)_{max}$ = = $2.3 \cdot 10^6$ gauss·oersted. Under a tensile load of 305 kg/mm^2 the respective values were H_c = 880 oersted, B_R = 12,500 gauss and $(BH)_{max} = 7.7 \cdot 10^6$ gauss·oersted. It should be noted that the steeply rising section of the curves in Fig.1 corresponds to fields close to the value of H_c for the given loading. Thus in the case of the unstressed specimen H_c = 330 oersted, while with a load of 85 kg/mm^2 applied to the specimen H_c = 480 oersted.

The demagnetization branches of the hysteresis loop of a Vicalloy 0.3 mm diameter specimen annealed for 30 min at 550° are reproduced in Fig.3. Curve a was obtained for an unstressed specimen, curve b was obtained on a specimen elongated by a load of 45 kg/mm^2 and curve c was obtained for a specimen stressed in torsion (3.7° twist per 1 mm length). It will be evident from the curves that deformation by torsion, just as deformation by elongation, increases the coercive force. On the other hand, the remanence B_R decreases under the influence of torsion, while in the case of stretching it increases (compared with the unstressed specimen).

Analogous regularities were observed in the behavior of the specimens of the other investigated alloys.

3. Thermomechanical treatment

Figs.4 & 5 show the magnetization curves, the demagnetization branches of the hysteresis loops and the magnetic energy curves obtained for specimens of Vicalloy 0.1 mm in diameter annealed for 1 hour at 560° with different tensile loads (σ_A) applied to the specimen during annealing.

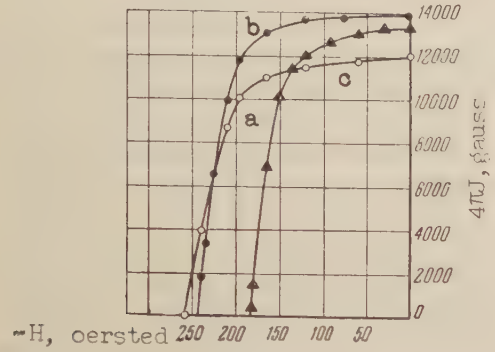

Fig.3. Demagnetization branches of the hysteresis loop of a Vicalloy specimen: a) specimen not subject to stress, b) specimen stretched by a 45 kg/mm^2 tensile load and c) specimen twisted 3.7° per mm length.

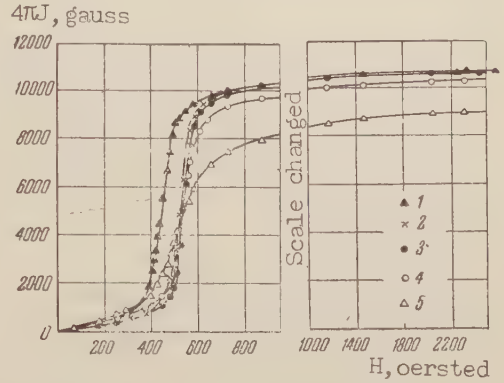

Fig.4. Influence of thermomechanical treatment on the magnetization curves of Vicalloy. Stress σ_A applied during annealing: 1) 0, 2) 20, 3) 30, 4) 40, 5) 60 kg/mm^2.

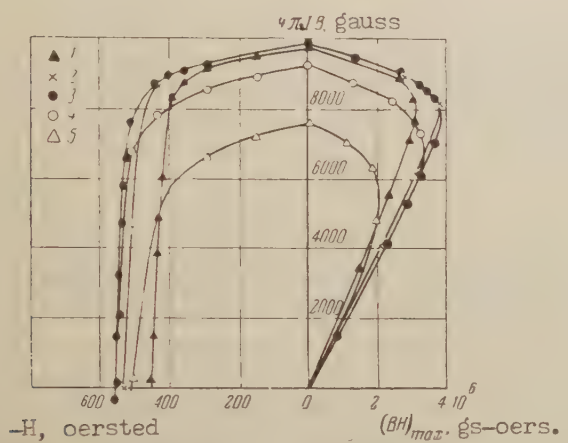

Fig.5. Influence of thermomechanical treatment on the demagnetization branches of the hysteresis loops and the magnetic energy curves of Vicalloy (curve designations same as in Fig.4).

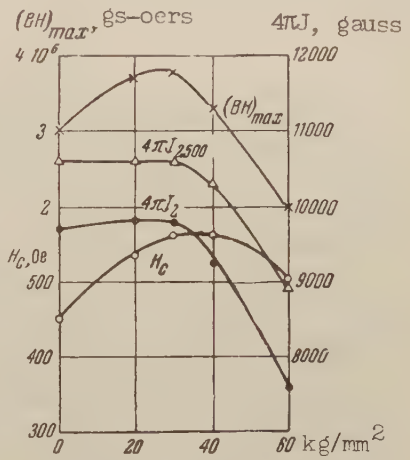

Fig.6. Influence of thermomechanical treatment on the principal magnetic characteristics of Vicalloy.

As may be seen from the figures, with increasing load during annealing, up to a stress of 30 kg/mm^2 there is observed a displacement of the magnetization curve to the side of higher fields, an appreciable increase in H_C (from 450 to 570 oersted) and a small increase in B_R; in the process the value of $(BH)_{max}$ increases from $3.1 \cdot 10^6$ to $3.8 \cdot 10^6$ gauss·oersted. With further increase of the load up to 60 kg/mm^2, the magnetization curves become less steep, B_R decreases, as does $(BH)_{max}$. At about 40 kg/mm^2, H_C stops increasing and begins to decrease with increasing load during annealing. The saturation magnetization remains fairly constant up to loads of 30 kg/mm^2 and with further increase of the tensile stress applied during annealing begins to decrease.

The variation of the principal magnetic characteristics of the Vicalloy specimens with the magnitude of the stress applied during annealing is shown in Fig.6.

Thus our results show that the magnetic properties of specimens annealed at the same temperature differ appreciably depending on the load applied in the process of annealing. It was established that increasing the annealing temperature leads to a reduction of the stress value at which the decrease of saturation magnetization and B_R begin as well as of the load at which the maximum value of H_c is attained. Increasing the annealing time at a given temperature has approximately the same effect as raising the annealing temperature.

Similar regularities were established for the other investigated alloys. The optimal values of the load, temperature and annealing time at which the highest values of H_c and $(BH)_{max}$ are obtained differ for alloys of different composition.

The magnetic properties of Vicalloy can be significantly enhanced by appropriate thermomechanical treatment. Whereas after conventional treatment at optimal conditions specimens of different diameters have values of H_c from 400 to 450 oersted and $(BH)_{max}$ from $2 \cdot 10^6$ to $3 \cdot 10^6$ gauss·oersted, after appropriate thermomechanical treatment one can obtain H_c = 500 to 550 oersted and $(BH)_{max} = 3\text{-}4 \cdot 10^6$ gauss·oersted. The material with enhanced properties has been called "termekhvako" [= termechvaco] (thermomechanically treated vanadium-cobalt alloy). The best samples of the thermomechanically treated material have $(BH)_{max} = 4.2 \cdot 10^6$ gauss-oersted with H_c = 570 oersted and B_R = 10,400 gauss.

4. Discussion

The observed regularities can be explained if we assume that the investigated alloys in the magnetically hard state have a single domain structure so that technical magnetization is realized primarily by domain rotation processes. In this case the magnetic characteristics will be determined by the magnitude of the total magnetic anisotropy.

Under the influence of elastic elongation or torsion the total magnetic anisotropy increases which leads to hindering of the technical magnetization processes. As a result with increasing stress the magnetization curves are displaced to the side of higher fields and the value of H_c increases. The investigated materials in the high-coercivity state have a pronounced longitudinal magnetic texture, as is evident from the value of the ratio J_R/J_s (attaining 0.9); this is apparently connected with the presence of crystallographic structure. Under the influence of elastic elongation the degree of longitudinal texturing (uniform orientation) increases; because of this the remanence B_R increases. In the case of torsion there arise stresses oriented at an angle of 45^o to the axis of the specimen; these stresses produce partial disintegration or disorientation of the longitudinal magnetic structure so that in the case of torsion B_R decreases.

In the process of thermomechanical treatment the tensile loads exert an influence on the character of the structural transformations during the anneal. Small loads do not change the phase composition of the alloy (J_s remains constant), but even in the case of small loads there occurs an increase of H_c which in all probability, as in the case of elastic stresses, is connected with an increase of the total magnetic anisotropy of the alloy. Under the influence of small loads during annealing there occurs a change of the longitudinal magnetic structure leading to an increase of B_R.

Heavy loads have an appreciable effect on the phase composition of the alloy; there occurs an additional transformation of the ferromagnetic phase to the nonferromagnetic, accompanied by a decrease of the saturation magnetization, B_R and H_c.

Conclusions

Elastic stresses and thermomechanical treatment (loading during annealing) exert an appreciable influence on the magnetic properties of some high coercivity alloys. By virtue of this one can appreciably increase the values of H_c and $(BH)_{max}$ of some alloys. Thus in the case of the alloy consisting of 12% V + 52% Co + 36% Fe (Vicalloy) one can through appropriate thermomechanical treatment increase the value of the coercive force H_c by 25% and of $(BH)_{max}$ by 40%. In the presence of tensile stresses H_c and $(BH)_{max}$ of Vicalloy may increase several fold. The observed regularities in the variation of the magnetic properties of the investigated alloys under the influence of elastic stresses and thermomechanical treatment are explicable in the light of present day concepts regarding the magnetic structure of high-coercivity materials.

Institute of the Physics of Metals,
Ural Branch, USSR Academy of Sciences

References

1. S.V.Vonsovskii & Ia.S.Shur, Ferromagnetizm (Ferromagnetism), M., 1948.
2. Ia.S.Shur, Izv.,AN SSSR, Ser.fiz., 11, 570 (1947).
3. E.A.Nesbitt, Met.Techn. 13, 2 TP, 1973 (1946).
4. W.Jellinghaus, Techn.Mitteil.Krupp, Forschungsber., 12, 257 (1941).
5. B.G.Livshits, Izv.AN SSSR, Ser.fiz., 12, 116 (1948).

* * * * * * *

MAGNETIZATION VISCOSITY OF Ni-Zn FERRITES WITH FREE VARIATION OF THE MAGNETIZATION (Abstract*)

- I.A.Lednev & R.V.Telesnin

A new technique was developed for measuring the magnetic viscosity by means of an electronic control circuit and a pulse oscillograph; the curve of the emf produced by viscous changes of magnetization is observed on the oscillograph screen. The magnetic viscosity of a series of commercial Ni-Zn ferrites in the temperature range from 78°K to the Curie point has been investigated. It was found that both the fast and slow parts of the viscosity can be described by variants of the formulas characterizing the first rule of magnetic viscosity.

Department of Physics,
Moscow State University

---

*Complete report in Radiotekhnika i elektronika, 1, 1186 (1956).

ON THE DECAY OF MAGNETIC PERMEABILITY IN SILICON IRON

- Iu.S.Vail'

Despite the fact that there have been numerous investigations devoted to magnetic viscosity, one cannot say that the nature and regularities of this effect have been fully clarified. Specifically, the question of the decay with time of the reversible permeability has been little studied; there is virtually nothing in the literature on this subject except the semiqualitative investigations of Snoek[1] and Ianus & Drozhzina[2] and the somewhat later work of Fahlenbrach[3]. Moreover, most of the investigations of magnetic viscosity have been carried out in a rather narrow time range, extending over only one or two orders of magnitude, so that the regularities of the variation of the permeability or magnetic induction with time could not be clearly brought out.

We undertook an investigation of the decay with time of the reversible permeability in silicon iron; in designing the experiments we took pains to encompass as wide an interval of times, temperatures and magnetic fields as feasible. The decay was investigated in specimens of silicon iron of the type used for the cores of industrial transformers. Most of the experiments were carried out on KhVP type iron (formerly designated "Hypersil") in the form of a 0.08 mm wide ribbon; we also investigated the effect in ordinary silicon steel containing 3.5% silicon (thickness 0.35 mm) and Armco iron.

We used the following procedure in order to be able to record rapidly occurring changes of the permeability. A small coil was wound about the specimen and this was connected into a T-circuit inductance bridge. The bridge was supplied from an audio-frequency oscillator through a high resistance (100 kiloohm) so that only a very weak current flowed through the coil. The field produced by this current was less than 20 microoersted and hence could have no significant effect on the magnetic state of the sample. The signal from the output of the bridge was amplified by a wide-band linear amplifier, detected by a germanium diode and viewed and recorded by means of a loop oscillograph. Prior to each experiment the set-up was calibrated so that the change in inductance of the coil and, consequently, the change in permeability of the specimen could be determined directly from the deflection of the oscillograph beam. In view of the low value of the alternating field produced by the coil the permeability measured in this fashion could be identified with the reversible permeability μ_r.

By means of the described procedure it was possible to detect changes in permeability beginning with several milliseconds after changing the state of the specimen (altering the field), but in the experiments we started observation only 0.1 sec after the field change in order to eliminate fully the influence of eddy currents and the time constants of the circuits. In prolonged experiments when the permeability changed slowly, the oscillograph was replaced by a microammeter and the permeability measurements were made by the usual null method.

As is known in the case of induction measurement by a T-circuit bridge the inductance L is found from the relationship

$$L = \frac{1}{2G\omega^2}, \qquad (1)$$

where G is a standard capacitance. Hence the accuracy of measurement of L depends primarily on the accuracy of frequency determination.

In our set-up the frequency was measured directly: the signal from the oscillator was applied to a trigger scaling circuit with a 1:64 scaling ratio

and the output pulses were counted by an electromechanical register. As a result it was possible to detect reliably changes in permeability of the order of 0.05%.

In order to eliminate magnetic interference, the specimen was surrounded by a double sheath of soft iron. This sheath also served as the thermostat housing; the temperature was maintained constant to within 0.05°.

The current for magnetizing the specimen was supplied by storage batteries. By means of appropriate switches and rheostats one could realize any desired sequence of magnetic fields. In addition, in part of the experiments the magnetization was carried out by means of a special trigger circuit which yielded rigorously square current steps with a rise time of $\leqslant 10$ μsec. Under the conditions of our experiments, however, this switching procedure did not result in any differences as compared with closing and opening the magnetizing circuit by means of ordinary knife switches.

The procedure employed in most of the experiments was the following. After the specimen had come to the desired temperature, it was magnetized almost to saturation (in a field of about 50 oersted). After being held in this state for a while, the field was almost instantaneously changed to the desired value, bringing the specimen to the selected point on the descending hysteresis loop. Measurements of the permeability, as described above, started 0.1 sec after thus changing the magnetic state of the specimen. Part of the experiments were carried out with the specimen initially in a demagnetized state, i.e., following the normal magnetization curve. In such cases the specimen was held in the demagnetized state for a sufficiently long time (several hours to several days) for all the viscosity processes to go virtually to completion.

A decrease with time of the reversible permeability was observed in all the investigated specimens of silicon iron and Armco iron. It is interesting to note that the general character of the effect was similar in different samples despite the rather appreciable differences between their magnetic properties. The magnitude of the decrease in different samples amounted to 20 to 70% relative to the stable value of the permeability.

At temperatures above 0° the major part of the change in permeability occurs during the first seconds (or even fraction of a second) after alteration of the external field. Thereafter the rate of decay of the permeability slows down appreciably so that a virtually stable state is attained only after many hours or even days.

Temperature dependence of the decay of reversible permeability

Although the temperature dependence of the magnetic viscosity has been studied in some detail, there is no unanimity of opinion regarding the character of this dependence. Most authors consider that the magnetic aftereffect is strongly temperature dependent, but Hizimura[4] and others assert the opposite. As for the decay of reversible permeability, as far as we know it has never been studied from this viewpoint.

Our investigations in the temperature range from -50 to 100° showed that there is a very strong temperature dependence of the decay of reversible permeability. The curves shown in Fig.1 are typical of the results obtained. It is noteworthy that all the curves pertaining to different temperatures can be superposed by shifting them along the x-axis which is laid off in a logarithmic time scale. It follows that the rate of decay of permeability is characterized by the factor $e^{-T_a/T}$, where T_a is a constant having the meaning of activation temperature. A similar dependence for the rate of change of the residual reduction was found by Richter[5].

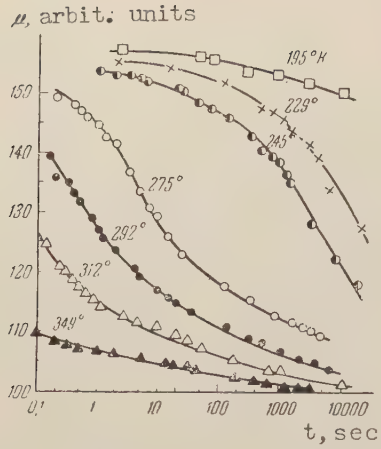

Fig.1. Decay of permeability in KhVP iron (Hypersil) at different temperatures. After demagnetization of the specimen a field of 0.06 oersted was switched on at t = 0.

A surprising and interesting result of the investigation was the virtually identical value of the activation temperature for all the investigated samples despite the appreciable differences between their chemical compositions and magnetic properties. In all cases the determined values of the activation temperature fell between 9600 and 10,800°K; the spread is within the limits of the experimental error. Virtually the same value (10,200°K) was obtained by Richter for carbonyl iron.

It is interesting that a change in temperature alone without changing the field may cause decay of the permeability. The magnitude and character of the effect in this case are equal to the change in permeability occurring after removal or application of a magnetic field. This effect can readily be explained by means of the concepts developed by Shur and his coworkers for interpreting thermomagnetic hysteresis.

Influence of the external field strength

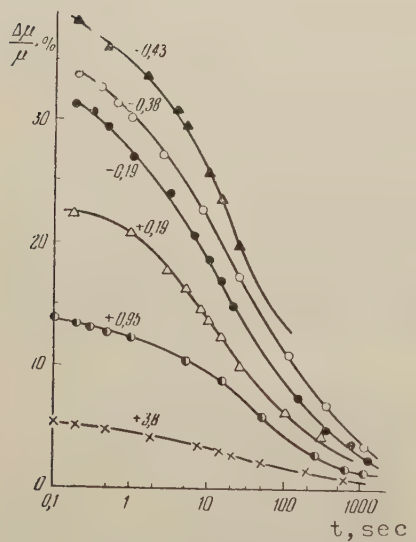

Fig.2. Decay of permeability in KhVP iron (Hypersil) at different values of the applied field. At t = 0 the field was changed from 45 oersted to the value indicated at each curve. The measurements were made at 0°C.

The influence of field strength on the magnetic viscosity has not been adequately investigated. Most authors merely indicate that the greatest magnitude of the aftereffects is attained in fields in which the differential permeability is maximal. In recent years the question has been investigated in greatest detail by Telesnin[6] who established the so-called "first rule of magnetic viscosity". According to this rule the rate of change of magnetization is always inversely proportional to the differential permeability or as Telesnin himself formulated it: the relaxation time of magnetic aftereffects is proportional to the differential susceptibility. Our investigation of the decay of the reversible permeability in different fields showed that the rate of decrease in permeability with time in all fields is in general the same (Fig.2). The change in permeability can always be described by the formula

$$\Delta\mu = a_H f(t), \qquad (2)$$

where $f(t)$ is a certain function of the time depending only on the temperature and properties of the specimen but not on the strength of the applied magnetic field and a_H is a coefficient dependent on H. This regularity holds at all

temperatures and in all field values from 0 to 45 oersted (no measurements were made in stronger fields). It follows therefore that the relaxation time for the decay of reversible permeability is the same for all field values which, of course, is in direct contradiction to Telesnin's "first rule of magnetic viscosity". Inasmuch as the decay of permeability must basically be of the same nature as the lagging change in magnetization, it would appear that the validity of the above "rule" is questionable.

Thus only the absolute value of the decrease in permeability (and not the relaxation time) depends on the applied field. This functional dependence proved to be simple:

$$\Delta\mu = k\mu_{\infty}^2 , \qquad (3)$$

where k is a coefficient dependent only on the properties of the specimen. An analogous formula was derived theoretically by Néel[7]. Thus it may be asserted that the magnetic viscosity is proportional to the reversible permeability and not to the differential permeability as most investigators assume.

In the experiments described above, the sample was brought into the "lower-field" state from a state close to saturation. In other experiments the initial state was an intermediate state characterized by a field value H'.

Inasmuch as the magnetic viscosity is presumably associated with processes developing in the ferromagnet after its transition into the new state of magnetization, it may be assumed that the viscosity measured after some change of the field will be determined only by the final and not by the initial state of the specimen, or, in other words, will not depend on the amplitude of the abrupt change in field strength ΔH (Telesnin's "second rule"). This "rule" was actually found to hold for values of ΔH up to 0.02 oersted. In the case of smaller changes, however, the absolute magnitude of the increase in permeability decreases (at $\Delta H < 0.002$ oersted the aftereffect becomes undetectable). The relative rate of decrease of permeability, however, does not change, which again is in conflict with Telesnin's data. If the sign of ΔH is opposite to that of the preceding field change, the decrease in permeability becomes undetectable at $\Delta H < 0.006$ oersted. This disappearance of decay of permeability in the case of small changes in field strength appears to be natural inasmuch as in this case the character of the change in the magnetic state of the specimen is reversible.

We observed another interesting phenomenon: in experiments with small changes in field strength ($\Delta H = 0.004$ to 0.008) - in contrast to the experiments involving a large change in field strength - the decrease in permeability fluctuated from experiment to experiment, differing sometimes by an appreciable factor. Moreover, for some 5 to 30 seconds after the change of field there were observed spontaneous jumps of the reversible permeability: the permeability increased sharply by 5-15% and then decreased in the same way as immediately after alteration of the applied field. In this case, apparently, the changes in energy due to the change in field strength were of the same order of magnitude as the energy of the potential barriers in the path of the domain walls so that conditions favorable to fluctuation obtained.

Decay of permeability upon the application and removal of elastic stresses

The application of stresses producing regroupment of the spontaneous magnetization domains should presumably be accompanied by aftereffects. In our experiments we found that the application or removal of a load was accompanied in silicon iron samples by the same decrease of the reversible permeability as was observed upon changing the field. The rate of decrease of the permeability

and the temperature dependence of the effect were the same in both cases, but the absolute magnitude of the effect under the influence of stress changes was only about half as large. The magnitude of the load in the range from 1.2 down to 0.04 kg/mm^2 made no appreciable difference, but with the application of smaller loads the magnitude of the effect decreased and at a load of 0.004 kg/mm^2 no aftereffect was detectable. Presumably the decrease of permeability observed by a number of authors incident to vibration or impact can be explained by this stress aftereffect inasmuch as vibration or impact is equivalent to application and removal of stresses.

Influence of strain hardening and heat treatment

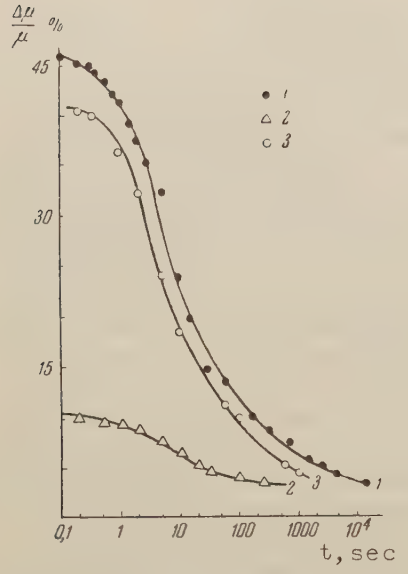

Fig.3. Influence of strain hardening on the decay of reversible permeability. Sample of transformer steel. The strain hardening was produced by stretching with a load of about 40 kg/mm^2: 1) before deformation, 2) after strain hardening, 3) after annealing at 900°. The 57 oersted magnetizing field was cut off at t ≈ 0. T = 0°.

Many investigators have noted that the character of the mechanical or heat treatment to which a ferromagnet is subjected exerts a strong influence on the magnetic aftereffects. The influence is particularly strong where plastic deformation is concerned. Cold working (strain hardening) generally drastically reduces or wholly eliminates magnetic viscosity. We obtained the same results for the reversible permeability, but there is another significant fact that emerges from our experiments. Measurements at different temperatures showed that despite the large differences between the absolute values of the effect the rate of relative decrease of the permeability and the temperature dependence of the decay effect are virtually the same for deformed and not deformed specimens; in other words, the activation temperature remains almost the same after plastic deformation.

If a plastically deformed sample is subjected to annealing, the decrease in permeability with time again increases. Comparison of the properties of samples subjected to different heat treatments showed that even brief (1-2 hours) annealing at 800° fully counteracts the influence of strain hardening (Fig.3). Additional heating in hydrogen to 1200-1250° for 3-6 hours had virtually no further influence on the aftereffect; the decay of permeability differed only insignificantly in specimens subjected to different heat treatments. An exception was Armco iron for which prolonged annealing in hydrogen led to a decrease of the aftereffect, i.e., reduced the decay of permeability.

Discussion

The most significant result of our investigation particularly from the purely practical standpoint is the fact that there does exist an appreciable decay (up to 70%!) of permeability with time in industrial silicon iron. This in itself may lead to misleading experimental values of the reversible permeability, particularly when this parameter is measured at low temperatures,

when, as was noted above, hours or even days may elapse before the stable value of the permeability is attained. The decay of permeability should also probably be taken into account in analyzing the operation of such equipment as pulse transformers and magnetic amplifiers.

A commonly accepted view in the literature is that magnetic viscosity is one of the highly structure sensitive attributes of ferromagnets. The results of our observations go contrary to this notion. While the absolute magnitude of the decrease in permeability does vary considerably from sample to sample, the relative rate of decrease (in other words, the relaxation time) and the temperature dependence of the decay (i.e., the activation temperature) proved to be remarkably close for all the investigated specimens and in remarkably good agreement with the data obtained by Richter for carbonyl iron. This would indicate that the processes responsible for magnetic aftereffects including decay of permeability are associated not with the state of the magnetic domain walls but with the structure of the iron crystal lattice. Most plausible from this viewpoint is the hypothesis of Néel[7], according to which magnetic viscosity is due to displacement of carbon atoms over the interstices of the iron lattice, accompanied by an appreciable change of the magnetocrystalline anisotropy energy and, consequently, of all the magnetic properties. An indirect confirmation of this view is the absence of any appreciable aftereffect in nickel and permalloy which are characterized by a low anisotropy energy.

One can approach this problem from another standpoint. At present the most satisfactory theory of magnetic aftereffects is the fluctuation theory advanced by Street & Wooley[8] and Néel. True, the equations proposed by these authors are not applicable for describing our results but this in our opinion can be explained by the exceedingly rough initial assumption on which the theoretical calculations are based. Specifically, these authors assume that the number of "objects" susceptible to activation is the same for any value of the energy, i.e., that the distribution in activation energy function is a constant. It would be more natural to assume that the activation energy distribution is random, for example, gaussian. It appears that assuming a gaussian distribution in energy one can satisfactorily explain from the standpoint of the fluctuation theory the results of our measurements of the decay of permeability in the entire investigated range of times and temperatures and also the results of Richter. One can in fact calculate two quantities of interest, namely, the mean activation energy and the average fluctuation frequency. Our calculations showed that for all samples regardless of their previous treatment history and specific magnetic properties these quantities are virtually the same, namely, of the order of $1.5 \cdot 10^{12}$ erg and 10^{13} sec^{-1}, respectively. These values are in good agreement with the above mentioned hypothesis of Néel. On the contrary, assumption of fluctuation of the direction of the spontaneous magnetization vector or fluctuation of the surface tension of the domain walls led to an appreciably lower characteristics frequency (of the order of 10^{10} sec^{-1} according to Néel).

The authors are sincerely grateful to Ia.S.Shur, S.V.Vonsovskii and V.I. Drozhzhina for their helpful interest in the work.

Institute of Experimental Medicine,
Academy of Medical Sciences of the USSR

References

1. J.L.Snoek, Physica, 5, 663 (1938); 6, 161 (1939).
2. R.I.Ianus & V.I.Drozhzhina, Zhur.tekh.fiz., 9, 1960 (1939).
3. H.Fahlenbrach, Ann.d.Phys., 2, 355 (1948).
4. T.Hizimura, J.Phys.Soc.Jap., 5, 358 (1950).
5. G.Richter, Ann.d.Phys., 29, 605 (1937); 32, 683 (1938).
6. R.V.Telesnin, Uch.zap.(Scientific notes), Moscow State University, 162, Bk.VI, 55 (1950).
7. L.Néel, J.Phys.et Rad., 11, 49 (1950); 12, 339 (1951).
8. R.Street & J.C.Woolley, Proc.phys.soc., 61, 391 (1948); 62A, 562 (1949); 62B, 141 (1949).

SOME MAGNETO-OPTICAL EFFECTS AT MICROWAVE FREQUENCIES

- N.N.Neprimerov

Microwave analogs of magneto-optical effects began to be studied concurrently with the beginning of investigation of magnetic resonance absorption (1948). The first optical effect to be observed at microwave frequencies was rotation of the plane of polarization of radiowaves incident to passage through a magnetized medium (the Faraday effect).[1] Soon thereafter magnetic double refraction at microwave frequencies was reported by Weiss & Fox.[2] The present report will be concerned with the results of measurements of the rotation of the plane of polarization of microwaves (9375 Mc) due to reflection from a magnetized medium (the Kerr effect). It must be emphasized that magneto-optical effects at radiofrequencies are associated not only with magnetic resonance but can also be caused by other factors. For example, the Faraday effect may be produced by 1) magnetic spin resonance in para- and ferromagnets[3], 2) diamagnetic resonance in discharge plasma and solid semiconductors[4], 3) transitions between molecular inversion sublevels[5] and 4) the high-frequency Hall effect[6].

Experimentally gyromagnetic properties of media are determined in two ways: a) by investigating individual magneto-optical effects and establishing the correlation between them and other parameters of the medium[1-6] and b) by measuring the components of the permeability and permittivity tensors and calculating the effect in question from the measured values[7].

In an earlier publication[3] the author described an experimental set-up for investigating the Faraday effect at centimeter wavelengths. The set-up is diagrammed in Fig.1. The use of measuring lines 5 instead of matched detectors made it possible to enhance the sensitivity of the set-up. The high sensitivity as regards angle of rotation (~0.1'') and the distinctive arrangement of the polarizer, specimen and analyzer make it possible to use the set-up for investigating other magneto-optical effects. This is most easily accomplished where the Kerr effect is concerned; in fact there is no difference in the arrangement of the polarizer, specimen and analyzer in investigating the Faraday and Kerr effects. In both cases the specimen in the form of a disc is mounted in the same position in a round waveguide in front of a shorted termination. If the depth of penetration of the radio wave into the specimen is greater than the thickness of the specimen the observed rotation is due to the Faraday effect and, on the contrary, if the skin depth is much smaller than the thickness of the specimen ($\delta \ll d$), the Kerr effect is responsible for the observed rotation.

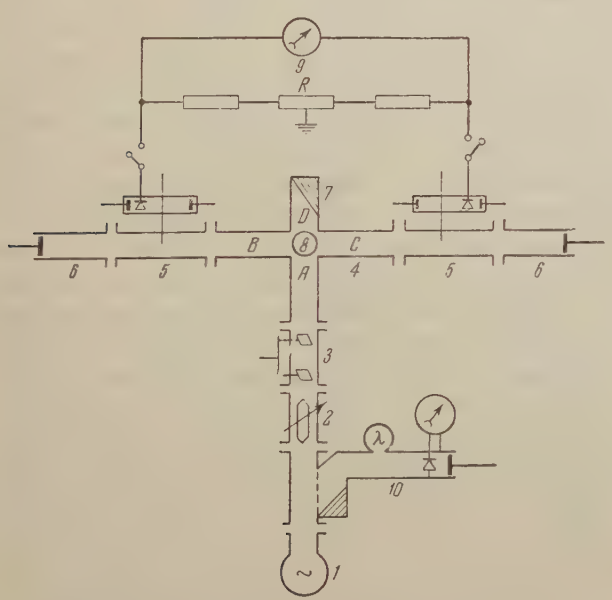

Fig.1. Diagram of set-up: 1) klystron generator, 2) decoupling attenuator, 3) matching device, 4) turnstile junction, 5) measuring line, 6) short-circuit plunger, 7) matched load, 8) specimen in round waveguide, 9) measuring unit, 10) wavemeter.

A special 1.6 kw electromagnet was designed and built in order to obtain the resonance field values necessary

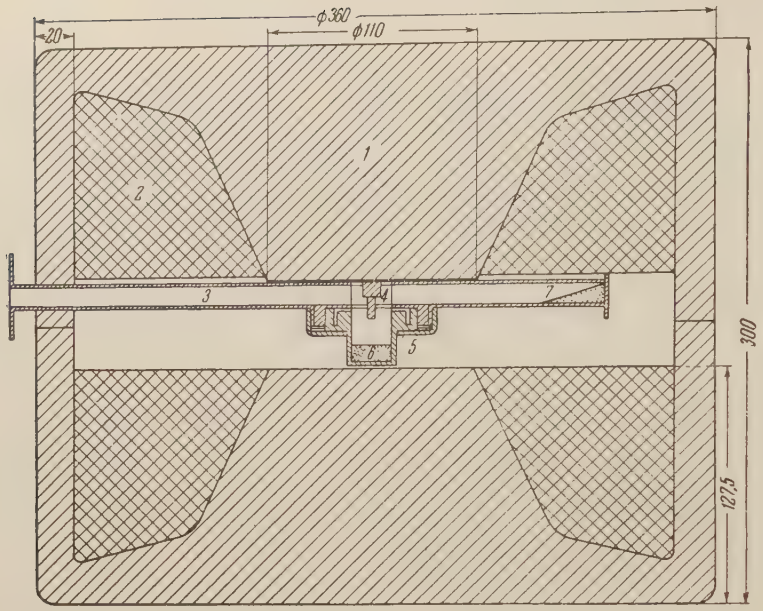

Fig.2. Section through central part of set-up with electromagnet: 1) yoke of electromagnet, 2) electromagnet coil - 2 x 2000 turns of 2 mm diameter copper conductor, 3) input waveguide, 4) matching stub of turnstile junction, 5) round waveguide with choke-flange coupling, 6) specimen, 7) matched load.

for investigating the Kerr effect. The magnet produces a uniform magnetic field of up to 9000 oersted in a 45 mm wide gap with pole pieces 110 mm in diameter. Thanks to effecient design of the magnetic circuit components, a virtually linear dependence of the field on the current through the windings is obtained for the entire useful range of magnetic fields.

A sectional view of the set-up with the electromagnet is shown in Fig.2. It will be seen that the external magnetic field is parallel to the direction of propagation of the radio waves and perpendicular to the reflecting surface of the specimen, i.e., that the necessary condition for the so-called polar Kerr effect is satisfied. Inasmuch as this effect is linear with respect to the field, we recorded the rotation curves with both polarities of the magnetic field and took the half sum of the resultant curves as the characteristic of the effect. This procedure, like that used in measuring the Faraday effect[3], minimized possible errors. In order to eliminate hysteresis effects in the electromagnet and the specimen, an additional weak alternating field with a frequency of 50 cps was superposed on the constant field so that the magnetization in all cases followed the ideal or hysteresis-less curve.

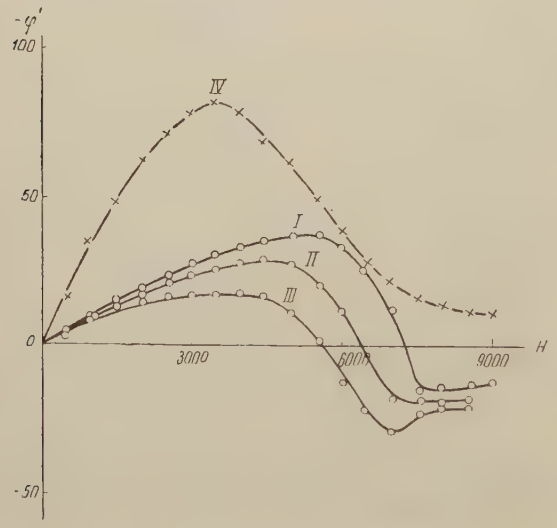

Fig.3. I, II and III - curves of the Kerr effect for magnetite obtained for specimens 23 mm in diameter and 3.6 mm, 6.2 mm and 8.4 mm thick, respectively; IV - curve of the Faraday effect for magnetite.

The limited dimensions of the pole gap and the large value of one of the demagnetization factors with such an arrangement of the field and specimen led us to choose magnetite as the subject for the first investigation. Having an electric conductivity and saturation magnetization intermediate between metallic ferromagnets and ferrites, magnetite allows of obtaining experimentally convenient demagnetization factors and a suitable magnitude of the effect with specimens of acceptable size.

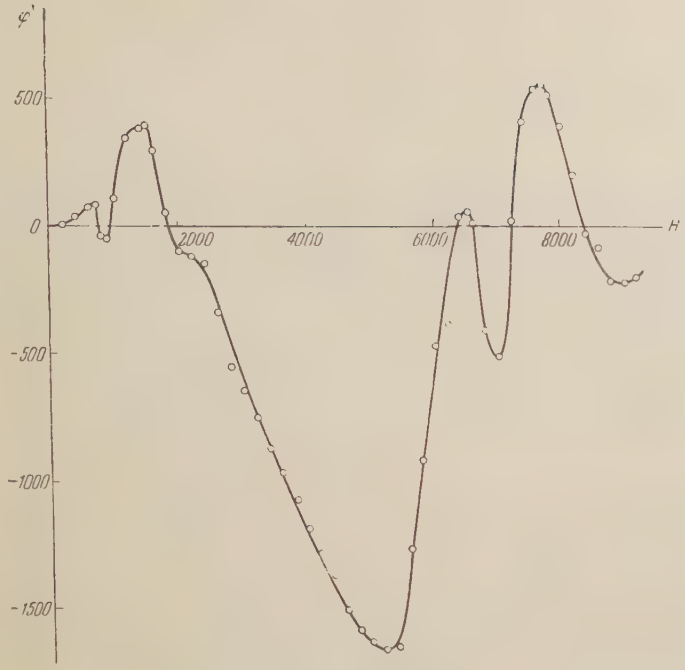

Fig.4. Curve of the Kerr effect for Ni-Zn ferrite. Diameter of specimen 23 mm, thickness 16 mm.

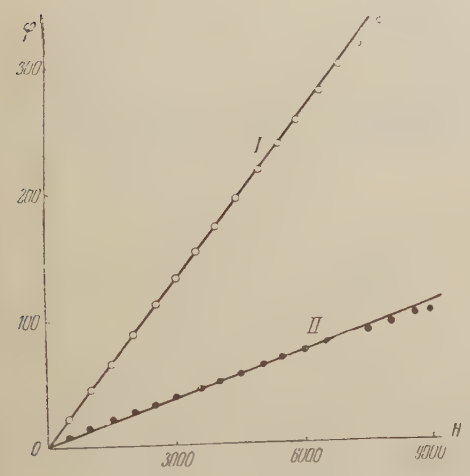

Fig.5. Field dependence of the rotation of the plane of polarization for germanium: I - plane-parallel metallic plate d = 0.5 mm, diameter = = 23 mm, II - suspension of germanium powder in paraffin; Ge particle size $r \leq 100$ μ; volumetric concentration 15%.

Measurements of the Kerr effect were carried out on three specimens in the form of discs of natural polycrystalline magnetite. All of these satisfied the above mentioned condition ($\delta \ll d$) inasmuch as for magnetite $\delta = 5 \cdot 10^{-3}$ cm. The experimental results are shown in Fig.3. The top curve (IV) in the figure is for the Faraday effect in magnetite. The variation in the amplitude of the Kerr rotation curves can be explained by the influence of a residual Faraday effect manifested, apparently, due to reflection from the back wall of the specimen or due to inhomogeneities of the investigated medium. It will be seen that this influence decreases with increasing thickness of the specimen. There may also be present distortions associated with nonuniformity of the demagnetization factors of specimens having a shape differing from ellipsoids.

The principal but, as will be shown below, not the sole cause of the Kerr effect at microwave frequencies is magnetic spin resonance. From the shape of the Faraday rotation curve (IV in Fig.3, which does not change sign in the entire range of investigated magnetic fields) it follows[8] that at the given wavelength the product of the frequency by the relaxation time for magnetite is less than unity, i.e., $\omega\tau < 1$. By analogy with the Faraday effect[8] one may assume that with $\omega\tau > 1$ the shape of the curve must change and take on a resonance-like character. To check this assumption we prepared a specimen of Ni-Zn ferrite whose electric conductivity was substantially increased (to about 0.5 mho/cm) by repeated high temperature anneals. The results of measurements on this specimen are shown in Fig.4. It will be seen that the amplitude and shape of the curve are different. The appearance of the additional peaks may be due to differences between the magnetic sublattices of the ferrite containing different magnetic ions (iron and nickel), but it is not impossible that these additional peaks may appear due to inhomogeneities formed in the specimen in the process of high temperature annealing.

In measuring the Kerr effect, in addition to the errors introduced by incomplete elimination of the Faraday effect, there may be present errors due to

additional rotation of the plane of polarization owing to the high-frequency Hall effect[6]. This effect is also linear with respect to the magnetic field and cannot be excluded in the field reversal procedure. It is difficult at present to evaluate the contribution of the high-frequency Hall effect to the total rotation.

Fig.5 gives the results of measurement on the same set-up of the specific rotation of the plane of polarization in an n-type germanium plate (curve I) and in powder of the same germanium suspended in paraffin with a volumetric concentration of 15% (curve II). In both cases the rotation is due exclusively to the high-frequency Hall effect and, as may be seen, attains an appreciable magnitude.

More detailed data on and evaluation of the microwave analog of the optical Kerr effect must await development of the theory of this effect at microwave frequencies.

"V.I.Ul'ianov-Lenin" Kazan State University

References

1. M.S.Wilson & G.F.Hull, Phys.Rev., 74, 711 (1948).

2. M.T.Weiss & A.G.Fox, Phys.Rev., 88, 146 (1952); A.Battaglia, A.Gozzini & E.Polacco, Nuovo Cim., 10, 1205 (1953).

3. N.Neprimerov, Zhur.eksp.i teor.fiz., 26, 511 (1954); Izv.AN SSSR, Ser. fiz., 18, 368 (1954). (Trans.Bulletin, 18, No.3, p.63).

4. L.Goldstein, M.Lampert & J.Heney, Phys.Rev., 82, 956 (1951); H.Suhl & G.L.Pearson, Phys.Rev., 92, 858 (1953).

5. A.Gozzini, J.Phys.et Rad., 16, 357 (1955).

6. E.R.Wicher, J.Appl.Phys., 22, 1327 (1951).

7. A.Trier, Appl.Sci.Res., B-3, 142 (1953).

8. N.Neprimerov, Izv.AN SSSR, Ser.fiz., 20, 1236 (1956) (Trans.Bulletin, 20, No.11, 1126.); L.Ia.Shekun, Izv.AN SSSR, Ser.fiz., 20, 1262 (1956) (Trans. Bulletin, 20, No.11, 1151.).

MAGNETO-OPTICAL PROPERTIES OF FERROMAGNETS IN THE INFRARED REGION

- G.S.Krinchik

Introduction

There have been numerous experimental investigations of the magneto-optical properties of ferromagnets; the results of many of these are tabulated and systematized in the monograph of Schütz[1]. The relation between diverse magneto-optical effects has been interpreted and generalized Fresnel equations for the Kerr effect and other phenomena have been deduced in the framework of the classical theory where these effects are treated phenomenologically by the introduction of tensor permittivity[2] or permeability[3]. There have also been a few studies in which the Faraday and Kerr effects have been treated from the viewpoint of quantum theory[4]. Nevertheless, the nature of magneto-optical effects in ferromagnets is still not fully clarified. This may in part be due to the fact that experimental investigations of the magneto-optical effects have been carried out only in the visible region of the spectrum (to 2-3 μ in individual cases). Hence no definitive conclusions regarding the character of the wavelength dependence of the effect could be drawn inasmuch as only narrow sections of the dispersion curves were obtained in these investigations.

In the present investigation we studied the influence of magnetization on the reflection of light from a ferromagnet in a wider range of wavelengths than has been done hitherto.

A number of experimental difficulties are encountered in extending the measurements into the infrared.

1. Since visual observations become impossible, it is necessary to have recourse to electrical means of detection and such detectors are subject to the influence and limitations imposed by the electromagnet.

2. Conventional glass lenses and polarizers become useless due to their strong absorption in the infrared region.

3. The intensity of most light sources falls off rapidly with increasing wavelength.

In our experiments the influence of the first factor was reduced by investigating the effects associated with magnetization of the samples parallel to their surface. This made it possible to reduce the size of the electromagnet and the cross section of the magnetic circuit components and to minimize the stray magnetic flux. We were able to circumvent the restricting influence of the second and third factors by virtue of the fact that we discovered the effect of the magnetization dependence of the absorption of natural (non-polarized) light by ferromagnets. This made it possible to enhance the effective intensity of the light by eliminating polarizers, auxiliary focusing devices, etc. As a result we were able to investigate the effects of interest in a rather wide range of wavelengths, namely, from 0.75 to 9 μ.

1. Apparatus and samples

An IKS-11 infrared spectrometer served as the infrared source and monochromator; the radiation detector was a vacuum type thermoelement. The output of the FEOU-15 photomultiplier was connected to an M-21/4 galvanometer. The overall sensitivity of the detecting unit was $7 \cdot 10^{-10}$ watt/mm. The electromagnet measured 100 x 100 x 140 mm and allowed of magnetizing the sample virtually to saturation with a current of 0.1-0.3 amp through the coil. The sample of technical grade iron with a polished 30 x 50 mm surface was inserted

into the magnetic circuit having a cross section of 40 x 15 mm. In another version of the experimental set-up, part of the magnetic circuit of the same iron and with a constant 30 x 2 mm cross section was polished. The spectroscope was calibrated with reference to water, benzene and polythene. In measuring the meridional Kerr effect selenium mirrors were used as polarizers.

2. Experimental results

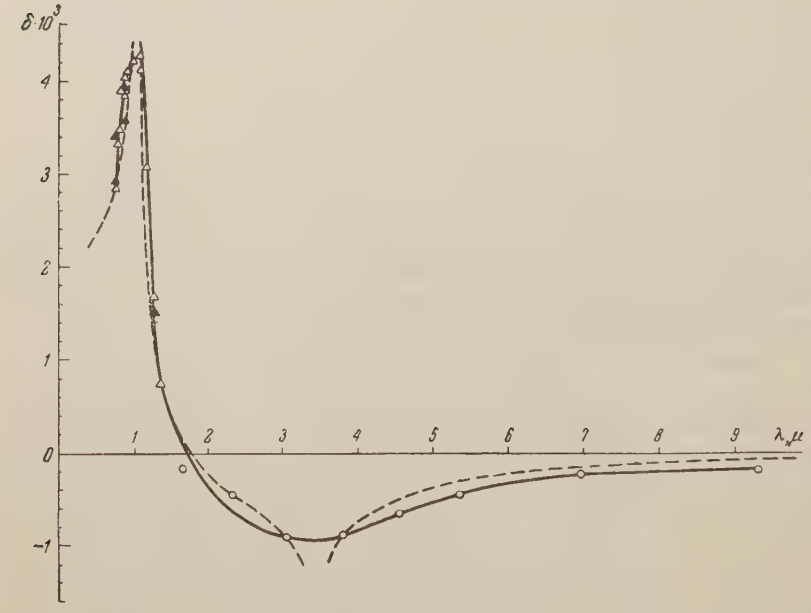

Fig.1. Change in the intensity of the reflected light of different wavelengths with reversal of magnetization of the sample (technical grade iron) magnetized to saturation: Δ) prism - glass, slit - 2 mm; ▲) prism - glass, constant light intensity; O) prism - NaCl, constant light intensity.

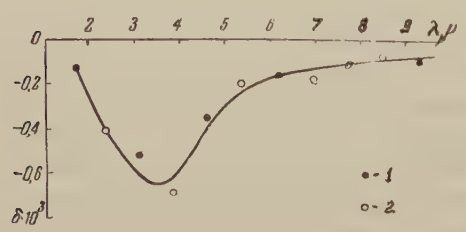

Fig.2. Change in the intensity of the reflected light with the magnetization. Sample - technical grade iron; saturation not attained: 1) prism - NaCl, slit - 2 mm; 2) same but with compensation method of measurement.

As was noted above, in investigating the reflection of light from a ferromagnetic mirror we discovered the effect of influence of the magnetization of the specimen on the absorption of natural, nonpolarized light. The magnetization vector was oriented parallel to the surface of the specimen and perpendicularly to the plane of incidence; the angle of incidence of the light relative to the surface was 45°.

Fig.1 shows the variation of the intensity of the reflected light of different wavelengths with reversal of magnetization of the sample (the ordinates are half the observed values inasmuch as in the case of reversal of magnetization the change in magnetization equals $2J_s$). Each of the points in the figure represents the arithmetic mean of 50 measurements. The average relative error of individual measurements is 15-25% in the middle portion of the curve and 20-25% at the extreme wavelengths. Most of the points were obtained with a constant slit width of 2 mm. Some of the points were recorded under different conditions in order to check on the errors associated with the strong dependence of the emission of the source on the wavelength. In these latter experiments the emission intensities were equalized by varying the slit width so that the measurements were carried out under identical intensity conditions. In addition, the presence of a maximum of the effect in the 3 to 4 μ region was verified on another sample of the same material. The results of these measurements are shown in Fig.2.

Part of the points were obtained by the usual procedure, while the other part were obtained by the compensation method, when half the light was allowed to bypass the specimen and fall on another, second thermoelement connected in opposition to the first with a view to minimizing the influence of fluctuations in the intensity of the source. The somewhat lower values of the effect shown in Fig.2 are explained by the fact that in this case it was impossible to magnetize the specimen to saturation owing to heating of the coil.

It was also found that the meridional Kerr effect with a 45° angle of incidence changes sign in the same wavelength region (3-4 μ). It was impossible to make more detailed reliable measurements of this effect inasmuch as the intensity of the light was diminished by a factor of more than 20 in this case as compared with the preceding one.

The sign of the magnetization-dependence of the light absorption effect (Figs.1 & 2) is considered to be positive when for a right-handed vector system ($\overline{IBA}$) the light absorption is less than for the left-handed system ($\overline{A}$ and $\overline{B}$ are the vectors of the incident and reflected waves).

3. Discussion

The newly detected effect, i.e., the influence of magnetization on the absorption of light, is in all probability a consequence of the equatorial Kerr effect. It follows from the generalized Fresnel equations for ferromagnets[2,3] that if the ferromagnetic mirror is magnetized perpendicularly to the plane of incidence of the light, the reflection coefficient for the component polarized parallel to J_s is independent of the magnetization, while the coefficient for the component polarized perpendicularly to J_s does depend on the magnetization. Hence the effect is not equal to zero in the case of natural light. This deduction was substantiated by experiment: the effect of change in absorption could not be detected when the light was polarized by a selenium mirror in the parallel plane and it was observed when the light was polarized in the perpendicular plane. The effect was also found to vanish in the case when the magnetization vector lay in the plane of incidence of the light. Like the polar and meridional Kerr effects and the Faraday effect, the equatorial Kerr effect is proportional to the magneto-optical parameter; hence in investigating the influence of magnetization on the absorption of light in ferromagnets we can establish general regularities common for all magneto-optical phenomena.

The curve for the magneto-optical effect shown in Fig.1 has the appearance of a smeared-out resonance curve. Its shape is apparently determined by the frequency dependence of the magneto-optical parameter inasmuch as the dispersion curves of the optical characteristics of the metal have an appreciably simpler shape in this frequency range. It must be concluded therefore that in the given case we observe a unique phenomenon which might be termed magneto-optical resonance. From general considerations one might assume the following simple form for the resonance dependence of the effect on condition that the damping decrement is equal to zero:

$$\delta = \frac{\delta_0}{\lambda_0^2 - \lambda^2}. \qquad (1)$$

The resonance wavelength λ_o is determined by the energy difference between the states between which the transition under the influence of the incident light occurs. The smeared-out character of the resonance curves shows that λ_o does not have a single unique value but is spread out over an interval λ_1 to λ_2. Assuming the simplest case of uniform distribution of wavelengths

over this interval, we obtain the following formula for δ:

$$\delta = \frac{\delta_0}{\lambda_2 - \lambda_1} \int_{\lambda_2}^{\lambda_1} \frac{d\lambda}{\lambda_0^2 - \lambda^2} = \frac{\delta_0}{2(\lambda_2 - \lambda_1)\lambda} \left(\ln \frac{\lambda + \lambda_1}{|\lambda - \lambda_1|} - \ln \frac{\lambda + \lambda_2}{|\lambda - \lambda_2|} \right). \quad (2)$$

The curve calculated according to Eq.(2), taking $\lambda_1 = 1\ \mu$ and $\lambda_2 = 3.5\ \mu$ is shown by the dash line in Fig.1. The assumed wavelength values as regards order of magnitude correspond to the electron transition energies (1.2 and 0.4 ev, respectively). In order to check the validity of the above inferences and arrive at more definitive conclusions regarding the character of the transitions responsible for the effect, one must carry out analogous measurements on different ferromagnetic materials under different conditions. Such measurements are being undertaken by the author in collaboration with R.D.Nuralieva and V.I.Riabchenko and the results will be published in a future article.

Faculty of Physics,
Moscow State University

References

1. W.Schütz, Magnetooptik.Hanb.d.exsp.Phys., 16 (1936).
2. A.V.Sokolov, Usp.fiz.nauk., 50, 161 (1953).
3. G.S.Krinchik, Vestnik (Review) Moscow State University, 12, 61 (1955).
4. H.R.Hulme, Proc.Roy.Soc., 85, 237 (1932); S.V.Vonsovskii & A.V.Sokolov, Zhur.eksp.i teor.fiz., 19, 703 (1948); P.N.Argyres, Phys.Rev., 97, 334 (1955).

CONTRIBUTION TO THE THEORY OF THE KERR AND FARADAY EFFECTS AT RADIOFREQUENCIES

- G.V. Skrotskii & V.F. Zakharchenko

A linearly polarized electromagnetic wave in propagating through a magnetically gyrotropic (gyromagnetic) medium is "separated" into two partial, circularly polarized (right and left) waves which are characterized by different absorption and different phase velocities. Consequently, the resultant wave emerging from the magnetic layer or reflected from its surface is elliptically polarized. The microstructure of the resultant wave may be described in terms of the orientation of the polarization ellipse and the ratio of its axes.

Thus we have two problems in investigating the propagation of electromagnetic waves in gyromagnetic media.

The first problem consists of determining the microstructure of the wave after its passage through the ferromagnetic material (the Faraday effect). The second problem involves describing the microstructure of the wave reflected from the surface of the magnetic material (the Kerr effect). A quantitative measure of both effects is the angle between the major axis of the polarization ellipse and the plane of polarization of the initial wave.

Both effects, as we know, are observed in the radiofrequency as well as in the optical region of the spectrum. The magnitude of the effects can be controlled by varying the intensity of the magnetic field applied to the specimen. The effect is appreciably greater in the case of ferromagnetic materials as compared with paramagnets.

The precession frequency of the magnetic moments depends on the intensity of the field H_0 in the specimen and for fields of the order of 10^3 oersted lies in the range of microwave frequencies.

While there have been numerous experimental and theoretical investigations of the Faraday effect at microwave frequencies, there have been very few studies of the Kerr effect in this frequency range.

1. In gyromagnetic media the relation between the magnetic induction vector $\mathbf{b}$ of the magnetic wave and the field intensity $\mathbf{h} = \mathbf{h}_0 \exp(j\omega t)$ is given by

$$\mathbf{b} = \mu \mathbf{h} + j[\vec{\Gamma}, \mathbf{h}], \tag{1}$$

where μ is the complex permeability and $\vec{\Gamma}$ is the complex gyration vector:

$$\mu = \mu' - j\mu'' \quad \text{and} \quad \vec{\Gamma} = \vec{\Gamma}' - j\vec{\Gamma}''. \tag{2}$$

If to these expressions we add the relation between the induction vector $\mathbf{d}$ and the electric field $\mathbf{e}$ of the wave:

$$\mathbf{d} = \varepsilon \mathbf{e} \quad \text{and} \quad \varepsilon = \varepsilon' - j\varepsilon'', \tag{3}$$

we can find all the expressions characterizing the magnitude of the Faraday and Kerr effects by solving the Maxwell equations for the medium with the appropriate boundary conditions. In the case of electrically conducting media the quantity $4\pi\sigma/\omega$ should be included in the imaginary part of ε.

For a plane wave of frequency $\omega = ck$, we readily obtain the following relation from Maxwell's equations

$$b = \frac{\mathfrak{N}^2}{\varepsilon}\{\mathbf{h} - \vec{\nu}(\vec{\nu}, \mathbf{h})\}, \tag{4}$$

wherein

$$\vec{\nu} = \frac{\mathbf{k}}{k} \quad \text{and} \quad \mathfrak{N} = \frac{c}{v}. \tag{5}$$

Comparing (4) and (1), we obtain equations for h, which determine the possible values of $\mathfrak{N}$. In the most interesting case when the wave is propagated in the direction of the gyration vector $\vec{\Gamma}$, i.e., when $\vec{\nu}$ is parallel to $\vec{\Gamma}$, we have

$$\mathfrak{N}_{\pm}^2 = \varepsilon(\mu \pm \Gamma). \tag{6}$$

$\mathfrak{N}_+$ and $\mathfrak{N}_-$ correspond to left and right circularly polarized waves.

Separating $\mathfrak{N}_{\pm}$ into real and imaginary parts,

$$\mathfrak{N}_{\pm} = n_{\pm} \mp j\varkappa_{\pm}, \tag{7}$$

we find, according to (2) and (3)

$$n_{\pm}^2 = \frac{1}{2}\{\varepsilon'(\mu' \pm \Gamma') - \varepsilon''(\mu'' \pm \Gamma'') + \sqrt{(\varepsilon'^2 + \varepsilon''^2)[(\mu' \pm \Gamma')^2 + (\mu'' \pm \Gamma'')^2]} \tag{8}$$

and

$$\varkappa_{\pm}^2 = \frac{1}{2}\{-\varepsilon'(\mu' \pm \Gamma') + \varepsilon''(\mu'' \pm \Gamma'') + \sqrt{(\varepsilon'^2 + \varepsilon''^2)[(\mu' \pm \Gamma')^2 + (\mu'' \pm \Gamma'')^2]}. \tag{9}$$

The indices of refraction $n_{\pm}$ determine the phase velocities of the right and left circularly polarized electromagnetic waves and the $\varkappa_{\pm}$ define the attenuation coefficients for these waves.

2. In the case of propagation of the electromagnetic wave in an infinite homogeneous medium in the direction parallel to the vector $\vec{\Gamma}$, the polarization ellipse monotonically rotates. The angle of rotation of ϑ_F per unit path length is given by[1]

$$\vartheta_F = \frac{\omega}{c} \cdot \frac{n_+ - n_-}{2}. \tag{10}$$

In a more complicated case, for example, when the wave passes through a finite layer of matter, one must take into account conditions at the interfaces inasmuch as the wavelengths of microwaves are commonly commensurable with the thickness of the layer[2].

Where reflection of electromagnetic waves from a plane magnetized specimen is concerned, one must distinguish between the cases of the normal and equatorial Kerr effects. In the case of the normal Kerr effect the plane polarized wave is incident on the surface of the magnetic specimen in the direction parallel to the vector $\vec{\Gamma} = \Gamma_z$.

Separating the incident wave into two circularly polarized components satisfying the boundary conditions on the surface of the magnetic specimen, we obtain

$$h_x^r = R_1 \exp(j\psi_1) \quad \text{and} \quad h_y^r = R_2 \exp(j\psi_2), \tag{11}$$

where

$$R_1 = \frac{(\varepsilon'^2 - \varepsilon''^2 - n_+n_- - \varkappa_+\varkappa_-)^2 + (n_+\varkappa_- - \varkappa_+n_- + 2\varepsilon'\varepsilon'')^2}{[(\varepsilon' + n_+)^2 + (\varepsilon'' + \varkappa_+)^2][(\varepsilon' + n_-)^2 + (\varepsilon'' - \varkappa_-)^2]} \tag{12}$$

and

$$R_2 = \frac{(\varepsilon'^2 + \varepsilon''^2)\,[(n_- - n_+)^2 + (\varkappa_- + \varkappa_+)^2]}{[(\varepsilon' + n_+)^2 + (\varepsilon'' + \varkappa_+)^2]\,[(\varepsilon' + n_-)^2 + (\varepsilon'' - \varkappa_-)^2]}. \tag{13}$$

The reflected wave is elliptically polarized with the major axis of the polarization ellipse rotated through an angle $\vartheta_к$ relative to the plane of polarization of the incident wave; this angle is defined by[3]:

$$\operatorname{tg} 2\vartheta_к = \frac{2R_1R_2}{R_1^2 - R_2^2} \cos(\psi_1 - \psi_2). \tag{14}$$

The axial ratio of the polarization ellipse of the reflected wave is found from the condition

$$\left(\frac{b}{a}\right)^2 = \frac{R_2^2 - R_1^2 \operatorname{tg}^2 \vartheta_к}{R_1^2 - R_2^2 \operatorname{tg}^2 \vartheta_к}. \tag{15}$$

Comparing the expressions for R_2 and R_1, we note that $R_2 \ll R_1$ and, consequently, according to (12) and (13)

$$\vartheta_к = \frac{A\,[\varepsilon''(n_- - n_+) - \varepsilon'(\varkappa_- + \varkappa_+)] - B\,[\varepsilon'(n_- - n_+) + \varepsilon''(\varkappa_- + \varkappa_+)]}{A^2 + B^2} \tag{16}$$

and

$$\frac{b}{a} = \frac{A\,[\varepsilon'(n_- - n_+) + \varepsilon''(\varkappa_- + \varkappa_+)] + B\,[\varepsilon''(n_- - n_+) - \varepsilon'(\varkappa_- + \varkappa_+)]}{A^2 + B^2}, \tag{17}$$

where

$$A = n_+n_- + \varkappa_+\varkappa_- - \varepsilon'^2 + \varepsilon''^2 \tag{18}$$

and

$$B = \varkappa_+n_- - n_+\varkappa_- - 2\varepsilon'\varepsilon''. \tag{19}$$

It will be noted that the expressions for the angle of rotation of the polarization ellipse are functions of the parameters ε, μ and Γ.

3. The parameters ε, μ and Γ are in general functions of the frequency of the wave field. The complex permeability μ in the microwave frequency range is a very slowly varying monotonic function of the frequency. Dispersion equations for μ and Γ can be found on the basis of the appropriate magnetic material model.

In the case of paramagnetic materials, whose magnetic properties are determined by a single spin system, the variation of the transverse part of the high-frequency magnetization (m_x, m_y) with time

$$\mathbf{m} = \frac{\mathbf{b} - \mathbf{h}}{4\pi} \tag{20}$$

is characterized by the equation[4]:

$$\dot{\mathbf{m}} + \frac{\mathbf{m}}{\tau} = \frac{\chi_0}{\tau}\mathbf{h} + \gamma[\mathbf{M}, \mathbf{H}], \tag{21}$$

where $\mathbf{M} = \mathbf{M}_0 + \mathbf{m}$, $\mathbf{M}_0 = \chi_0 \mathbf{H}_0$, τ is the intraspin relaxation time and $\mathbf{H} = \mathbf{H}_0 + \mathbf{h}$.

The solution to this equation is of the form

$$\mathbf{m} = \chi\mathbf{h} + j[\mathbf{g}, \mathbf{h}], \tag{22}$$

where

$$\chi = \chi_0 \frac{1 + j\omega\tau + \omega_1^2\tau^2}{(1 + j\omega\tau)^2 + \omega_1^2\tau^2}, \tag{23}$$

and

$$g = \chi_0 \frac{\gamma\omega\tau^2}{(1+j\omega\tau)^2+\omega_1^2\tau^2} H_0; \tag{24}$$

here

$$\omega_1 = |\gamma| H_0. \tag{25}$$

The quantities μ and Γ are related to χ and g by the expressions

$$\mu = 1 + 4\pi\chi; \quad \Gamma = 4\pi g. \tag{26}$$

Now

$$\mu' - 1 = 4\pi\chi_0 \frac{(1+\tau^2\omega_1^2)^2 + (1-\tau^2\omega^2)\,\tau^2\omega^2}{[1+\tau^2(\omega_1^2-\omega^2)]^2 + 4\tau^2\omega^2}, \tag{27}$$

$$\mu'' = 4\pi\chi_0 \frac{[1+\tau^2(\omega_1^2+\omega^2)]\,\tau\omega}{[1+\tau^2(\omega_1^2-\omega^2)]^2+4\tau^2\omega^2}, \tag{28}$$

$$\Gamma' = 4\pi\chi_0 \frac{[1+\tau^2(\omega_1^2-\omega^2)]\,\gamma\tau\omega}{[1+\tau^2(\omega_1^2-\omega^2)]^2+4\tau^2\omega^2} H_0; \tag{29}$$

$$\Gamma'' = 4\pi\chi_0 \frac{2\gamma\tau^3\omega^2}{[1+\tau^2(\omega_1^2-\omega^2)^2+4\tau^2\omega^2} H_0. \tag{30}$$

For ferromagnetic materials the time variation of the transverse part of the magnetization is also described by Eq.(21). Consequently, Eqs.(27)-(30) are applicable in this case as well.

The situation is somewhat more complicated in the case of the equatorial Kerr effect when the direction of propagation of the incident wave is perpendicular to the gyration vector. In this case we must know not only the transverse components of the magnetization m_x and m_y, but also the z-component m_z, which is defined by a more complicated expression.

In carrying out experimental observations of the Faraday and Kerr effects the measurements are usually made by varying the field H_0, while keeping the frequency constant. In this case the frequency dependences of ε and σ are unimportant. In what follows we shall assume that ε and σ are independent of the magnetic field strength.

The solutions for μ and Γ have singularities near the frequency Introducing the notation

$$\omega_0^2 = \omega_1^2 + \frac{1}{\tau^2}, \quad \xi = \frac{\omega_0 - \omega}{\omega} \quad \text{and} \quad \eta = \frac{1}{\omega\tau}, \tag{31}$$

and setting $\omega_0 + \omega \approx 2\omega$ for frequencies close to ω_0, we obtain from Eqs.(10), (8) and (27)-(30)

$$\vartheta_F = \frac{\omega}{2c}\sqrt{\varepsilon'}\{\sqrt{2A_0} - \sqrt{\pi\chi_0}\}\sqrt{\frac{\omega\tau|\xi|}{1+\omega^2\tau^2\xi^2}}, \tag{32}$$

where

$$A_0 = 2\pi\gamma\tau M_0.$$

The character of the variation of the angle of rotation of the polarization ellipse with ξ is shown in Fig.1.

In the case of the normal Kerr effect we find

$$2\sqrt{\frac{2\pi\sigma}{\omega}}\vartheta_K = \sqrt{\mu'-\Gamma''} - \sqrt{-(\mu''+\Gamma''') + \sqrt{(\mu'+\Gamma')^2+(\mu''+\Gamma'')^2}}, \tag{33}$$

and further

$$2\sqrt{\frac{2\pi\sigma}{\omega}}\cdot\frac{b}{a}=\sqrt{\mu'-\Gamma'}+\sqrt{(\mu''+\Gamma'')+\sqrt{(\mu'+\Gamma')^2+(\mu''+\Gamma'')^2}}. \qquad (34)$$

In the case of paramagnetic materials the angle of rotation close to resonance even under the most favorable conditions does not exceed a few minutes. In contrast, in the case of ferromagnetic materials on condition of good electric conductivity ϑ_K may attain several tenths of a radian in weak fields.

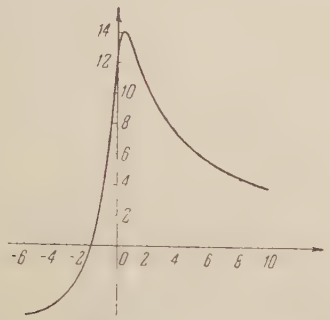

Fig.1. Variation of $\frac{100\,\vartheta_F}{\sqrt{A_0\varepsilon'}}$ as a function of $\xi=\frac{\omega_0-\omega}{\omega}$.

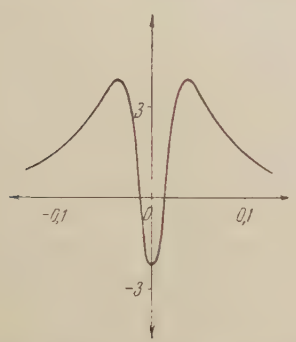

Fig.2. Variation of $2\sqrt{\frac{2\pi\sigma}{\omega}}\,\vartheta_K$ as a function of ξ.

The dependence of ϑ_K on ξ is shown in Fig.2. It will be seen that the curve characterizing this dependence is symmetrical and changes sign to either side of $\omega_0=\omega$. The exact shape of the curve characterizing the variation of ϑ_K as a function of ξ depends strongly on the relaxation time. Thus ferromagnetic materials with a long relaxation time are characterized by a sharp "resonance peak" of the angle of rotation of the polarization ellipse, while in the case of short relaxation time (10^{-8}-10^{-10} sec) the "resonance" character of the effect will be appreciably less pronounced.

4. Eq.(21) upon which the above calculations of both effects are based proves to be inadequate for many special types of magnetic materials and cannot describe their specific behavior in perpendicular fields. Thus, for example, Eq.(21) is not suitable for substances such as ferrites in which the magnetization is determined by two strongly interacting spin systems. A similar situation obtains in the case of paramagnetic solutions containing several different types of ions with different gyromagnetic ratios.

In the case of a paramagnet comprising two spin systems one can use Eq.(49) deduced in Ref.4. In this case, in consequence of the presence of two resonance frequencies, the character of the field dependences of ϑ_F and ϑ_K is appreciably more complicated.

The case of antiferromagnets will be examined in a future article.

Physical-Technical Faculty,
Ural Polytechnical Institute

References

1. A.L.Mikaelian, Usp.fiz.nauk, 51, 205 (1953).
2. M.A.Gintsburg, Doklady AN SSSR, 95, 753 (1954).
3. A.V.Sokolov, Usp.fiz.nauk, 50, 161 (1953).
4. G.V.Skrotskii & L.V.Kurbatov, Izv.AN SSSR, Ser.fiz., 21, 833 (1957).
(Trans.Bulletin 21, No.6, p.833.)

MEASUREMENT OF THE INITIAL PERMEABILITY OF FERROMAGNETS IN THE MICROWAVE REGION

- G.S.Sanyal

Introduction

It is known that the initial permeability of ferromagnets at high radio-frequencies ($\sim 10^8$ cps and higher) becomes a complex quantity. Determination of the apparent permeability from the loss and phase velocity in the electromagnetic circuit containing the ferromagnetic specimen leads to different values which are designated as μ_R and μ_L, respectively. It has been shown that μ_R is greater than μ_L and that both μ_R and μ_L decrease with frequency, approaching unity in the microwave region. Descriptions of the various techniques of measuring ferromagnetic permeability in the UHF and microwave frequency regions and analyses of the results of such measurements have been given by Alanson[1], Rado[2] and Sanyal[3].

In order to study the dispersion of the initial apparent permeability, extensive data relating to the variation of both μ_R and μ_L with frequency are required. Whereas such data are available for μ_R up to a frequency of the order of 10^{10} cps, this is not the case for μ_L. It was, therefore, thought desirable to measure μ_L in the microwave range (free-space wavelength λ = = 3.2 cm) to see whether this fits in with the value of μ_L obtained from the general trend of data at lower frequencies.

In this report we shall describe a method of determining the value of μ_L of soft iron in the form of thick plates at a wavelength of 3.2 cm. The method uses a cylindrical cavity resonator with a detachable end wall (test resonator 7 in Fig.1). The resonant frequency of the resonator is measured once when the end wall is made of a non-magnetic material, e.g., brass, and again when it is of soft iron. In each case the resonance frequency is determined, relative to a reference cavity of almost identical shape and size, by utilizing the cavity comparator technique.[4] The shift in resonance frequency gives the value of μ_L in terms of the parameters of the cavity.

The main difficulty in such a substitution method of measurement is the uncertainty introduced by the two end walls (non-magnetic and ferromagnetic) not being geometrically identical. A small difference in geometry between the two can mask the frequency shift due to the substitution. This difficulty has, however, been minimized to a considerable extent by accurate machining of the surfaces of the end walls. The measured value of μ_L at a wavelength of 3.2 cm was approximately 4.5. This is not inconsistent with the trend of lower frequency data, i.e., the measurement shows that μ_L does in fact tend to approach unity at very high frequencies.

1. Experimental Arrangement and Method of Measurement

A schematic diagram of the experimental set-up of the apparatus is shown in Fig.1. The source of microwave power is a 723 A/B klystron oscillator which is frequency modulated by a linear sawtooth waveform (400 cps) applied at its repeller. The cathode follower gives a low impedance path from the repeller electrode to ground and this together with use of a stabilized power supply insures negligible spurious frequency modulation. The sawtooth waveform is superimposed on the dc repeller voltage and the operating point of the klystron adjusted so that a linear frequency modulated signal is generated. The frequency limits of the klystron may be changed by varying the amplitude of the sawtooth wave.

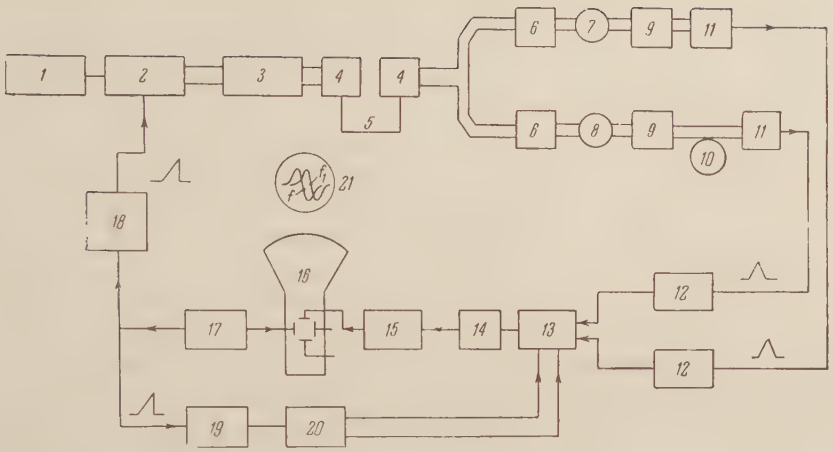

Fig.1. Block diagram of the experimental set-up: 1) stabilized power supply, 2) klystron oscillator, 3) variable attenuator, 4) waveguide to coaxial line junction, 5) coaxial cable, 6) attenuator 10 db, 7) test resonator, 8) reference resonator, 9) variable attenuator, 10) reaction type wavemeter, 11) matched crystal detector, 12) amplifier, 13) two tube amplifier with common plate load, 14) differentiator, 15) CRO vertical deflection amplifier, 16) CRO, 17) linear sawtooth generator, 18) cathode follower, 19) differentiator, 20) multivibrator, 21) display on CRO screen.

The klystron feeds rf power via an isolating attenuator (10 db approximately), a flexible coaxial cable and a shunt T-junction into two rectangular waveguide (0.9" x 0.4" I.D.) branch arms. One of these arms contains the cavity (transmission type) under test; and the other contains the similar reference cavity. Two fixed 10 db attenuators are interposed between the T-junction and each of the cavities. This is sufficient to prevent the frequency pulling due to mismatching in the input sides of the cavities. The microwave power transmitted through these cavities is detected by two separate matched crystal diodes (1N21). In order to obtain separately controllable output from these two crystal diode units, two variable attenuators are also inserted in the output sides of the cavities. A standard wavemeter cavity (reaction type) placed in the output side of the reference cavity is utilized for checking the frequency of resonance of the test and reference cavities as well as for calibrating the sweep of the cathode-ray oscilloscope.

Both the test and the reference cavities are right circular cylinders of brass and of very nearly identical dimensions with a detachable end wall. As noted above the end wall of the test cavity is interchangeable (brass or soft iron). Each of these cavities is of the transmission type and is coupled to the rectangular waveguides by two holes (0.285" in diameter) bored diametrically opposite in the middle of the cylindrical surface of the cavities. The center lines of the rectangular waveguides are aligned with a diameter of the cylinder so that the broad sides of the waveguide are parallel to the cavity axis. The end walls are made accurately perpendicular to the cavity axis to ensure that the cavities oscillate only in the TE_{011} mode.

The sawtooth frequency modulated rf signal produces video pulses, having the shape of resonance curves, at the outputs of the crystal detectors. The

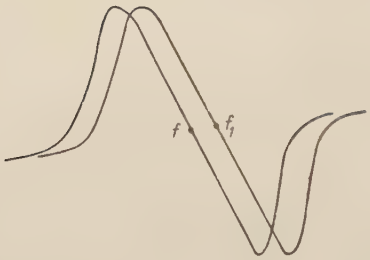

Fig.2. Display on the CRO screen showing the resonance frequencies of the cylindrical test and reference cavities.

repetition rate of these pulses equals that of the sawtooth generator. The maxima of these two waveforms correspond to the resonant frequencies of the two cavities. These video pulses are then separately amplified and fed to the grids of a two-tube amplifier stage having a common plate load. A square waveform synchronized with the sawtooth generator but of half the frequency is also applied to the two cathodes of the amplifier in phase opposition. This cuts in the video output from each cavity during alternate traces of the cathode ray oscillograph. The output of this amplifier is then differentiated and is further amplified by the vertical deflection amplifiers of the oscillograph. Thus two S-shaped curves are produced during alternate sweeps of the sawtooth wave and are superimposed on the oscillograph screen (Fig.2). The zeros of these curves are the resonant frequencies of the test and the reference cavities respectively. As the sawtooth wave amplitude applied to the klystron is reduced, these curves spread out giving greater separation between the zeros. The distance between the zeros of these two curves corresponds to the frequency difference between the two cavities. The sweep trace is calibrated in terms of frequency by a reaction type standard wavemeter placed in tandem with the reference cavity. During calibration the attenuation of the variable attenuator between the reference and the wavemeter cavity is increased to obviate frequency pulling. As the wavemeter cavity tuning is changed, a small pip superimposed on one of the curves travels along it; since the sawtooth wave amplitude applied to the repeller of the klystron is small, the wavemeter frequency tuning is linear with the distance of travel of the pip. Thus, knowing the frequency change of the standard wavemeter per its micrometer division, the sweep trace can readily be calibrated.

In the experiment three brass and three soft iron plates (1/4" thick), all accurately machined, were successively used for the end wall of the test cavity. During the initial stage of the experiment the dimensions of the reference cavity were adjusted so that both the test (with brass end walls) and the reference cavities had very nearly the same resonant frequencies as indicated by the distance between the two zeros of the S-curves. The resonance frequency of the test cavity relative to the reference cavity was then found when the three brass plates were successively used as one end wall of the test cavity. Similarly the shifts in resonance frequency caused by the substitution of soft iron plates were found. The uncertainty due to geometrical inaccuracy was small and since the measurement of only the relative shift in resonance frequency is important, the cavity comparator technique as used in this experiment eliminates the effect of humidity and temperature.

2. Theoretical Analysis

A brass cylindrical cavity resonator with a detachable end wall (Fig.3) made either of brass or a ferromagnetic material, was used in our experiments. The Q-factor[5] and the resonance frequency of the cavity depend on the permeability of the material of the end wall. We now proceed to derive the expression for the shift of the resonance frequency of the cavity oscillating in the TE_{011} mode, when the nonmagnetic, i.e., brass end wall of the cavity is replaced by a similar end wall of the ferromagnetic material under test.

Assume that an empty, cylindrical brass waveguide of radius a and of length l, carrying a TE_{011} mode, is terminated at one end by a perfectly conducting plate (end wall) perpendicular to the guide axis. The input wave impedance looking from the other end of the guide is given by

$$Z_{in} = jZ_c \operatorname{tg} \alpha l, \tag{1}$$

where

$$Z_c = \eta_i \Big/ \sqrt{1 - \left(\frac{\lambda}{\lambda_c}\right)^2},$$

here $\eta_i = \sqrt{\frac{\mu_0}{\varepsilon_0}}$ is the characteristic impedance for a plane wave in free space, $\mu_0 = 4\pi \cdot 10^{-7}$ henries per meter is the permeability of free space, $\varepsilon_0 = 10^{-9}/36\pi$ farads per meter is the dielectric constant of free space, λ is the free-space wavelength, $\lambda_c = 2\pi a/p$, where $p = 3.832$ is the first root of the equation $J_0'(x) = 0$, and $\alpha = \sqrt{\left(\frac{\omega}{c}\right)^2 - \left(\frac{p}{a}\right)^2}$ is the phase constant of the mode existing as a travelling wave; here $c = \lambda f$ is the velocity of light in free space in meters per sec; $\omega = 2\pi f$, f being the frequency of the wave.

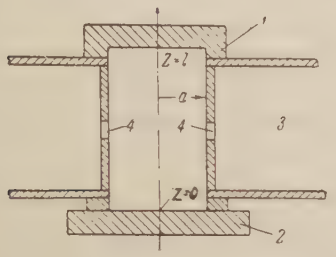

Fig.3. Cylindrical resonator: 1) fixed end wall, 2) detachable end wall, 3) rectangular waveguide, 4) coupling holes.

Eq.(1) holds to a high degree of approximation even for an end wall of finite conductivity, provided this is very high, i.e., such as that of brass.

If now the other end of the cylindrical guide is also closed by a conducting end wall perpendicular to the axis, the region enclosed by the conducting walls becomes a cylindrical cavity resonator. A criterion of resonance is that at any cross section of the waveguide the impedances looking into either side at resonance must have equal and opposite reactances. The resonant frequency of the cavity can be determined by applying this criterion at the plane of the second end wall.

If this second conducting end wall is made of a ferromagnetic material of complex permeability, the input impedance looking towards the wall is simply the characteristic wave impedance of the material

$$\sqrt{\frac{j\omega\mu\mu_0}{\sigma}},$$

where σ is its conductivity. Since μ is complex and is given by

$$\mu = \mu_1 - j\mu_2 = |\mu| e^{-j\psi},$$

where

$$|\mu| = \sqrt{\mu_1^2 + \mu_2^2} \quad \text{and} \quad \psi = \operatorname{arctg}\left(\frac{\mu_2}{\mu_1}\right),$$

the above expression reduces to

$$\sqrt{\frac{\omega\mu_0}{2\sigma}} \cdot [(|\mu| + \mu_2)^{\frac{1}{2}} + j(|\mu| - \mu_2)^{\frac{1}{2}}].$$

The relative values of the apparent permeabilities μ_R and μ_L are

$$\mu_R = |\mu| + \mu_2$$

and

$$\mu_L = \mu_R - j\mu_I.$$

Thus

$$\sqrt{\frac{j\omega\mu_0\mu}{\sigma}} = \sqrt{\frac{\omega\mu_0}{2\sigma}}\left(\sqrt{\mu_R} + j\sqrt{\mu_L}\right). \tag{2}$$

The criterion of resonance as applied to the second wall gives from Eqs.(1) and (2)

$$Z_c \operatorname{tg} \alpha l + \sqrt{\frac{\omega\mu_0\mu_L}{2\sigma}} = 0.$$

where $\sqrt{\frac{\omega\mu_0\mu_L}{2\sigma}}$ is the reactive part of the characteristic impedance of the material of the second wall.

The cavity resonates in the TE_{011} mode when

$$\alpha l = \pi - \operatorname{arctg}\left[\frac{1}{Z_c}\sqrt{\frac{\omega\mu_0\mu_L}{2\sigma}}\right].$$

Substitution for α in the above yields the cavity resonance frequency f in the transcendental form

$$\left(\frac{\omega}{c}\right)^2 - \left(\frac{p}{a}\right)^2 = \left[\frac{\pi}{l} - \frac{1}{l}\operatorname{arctg}\left(\frac{1}{Z_c}\sqrt{\frac{\omega\mu_0\mu_L}{2\sigma}}\right)\right]^2 \tag{3}$$

A similar relation can be obtained for the cavity resonance frequency $f_1 = \omega_1/2\pi$ when the second wall is of a nonmagnetic conducting material, e.g., brass,

$$\left(\frac{\omega_1}{c}\right)^2 - \left(\frac{p}{a}\right)^2 = \left[\frac{\pi}{l} - \frac{1}{l}\operatorname{arctg}\left(\frac{1}{Z_{c_1}}\sqrt{\frac{\omega_1\mu_0}{2\sigma_1}}\right)\right]^2, \tag{4}$$

where Z_{c_1} is the wave impedance for the TE_{011} mode at the frequency f_1 and σ_1 is the conductivity of the nonmagnetic material.

Subtracting Eq.(3) from (4) and putting arc tan $\alpha = \alpha$ for small values of α, we obtain

$$\frac{\omega_1^2 - \omega^2}{c^2} = \frac{1}{l}\left(\frac{1}{Z_{c_1}}\sqrt{\frac{\omega_1\mu_0}{2\sigma_1}} - \frac{1}{Z_c}\sqrt{\frac{\omega\mu_0\mu_L}{2\sigma}}\right)\left[\frac{2\pi}{l} - \frac{1}{l}\left(\frac{1}{Z_{c_1}}\sqrt{\frac{\omega_1\mu_0}{2\sigma_1}} + \frac{1}{Z_c}\sqrt{\frac{\omega\mu_0\mu_L}{2\sigma}}\right)\right]. \tag{5}$$

For most cases, the above equation can be further simplified by considering the relative values of the terms in the right hand side of the equation. Thus both Z_{c_1} and $Z_c > 120\pi$ ohms, $\sqrt{\frac{\omega_1\mu_0}{2\sigma_1}} \approx 0.05$ and $\sqrt{\frac{\omega\mu_0\mu_L}{2\sigma}} \approx 0.05\sqrt{\mu_L}$, and since μ_L is not far from unity, it is obvious that the second factor on the right is equal to $2\pi/l$ to a high degree of accuracy. Also, since the cavity diameter is such that the cylindrical waveguide is operating appreciably away from its cut-off wavelength λ_c, and f and f_1 are very close, the change in wave impedance with frequency can be neglected. Then, putting $Z_{c_1} = Z_c$ and $\omega_1 = \omega$ in the right hand side in Eq.(5) and bearing the above considerations in mind, we get

$$\frac{\omega_1^2 - \omega^2}{c^2} = \frac{2\pi}{l^2 Z_c}\sqrt{\frac{\omega\mu_0}{2\sigma}}\left(\sqrt{\mu_L} - \sqrt{\frac{\sigma}{\sigma_1}}\right)$$

or

$$\sqrt{\mu_L} = \left[\frac{4\pi j(f_1 - f)}{c^2} l^2 Z_c \sqrt{\frac{\sigma}{\pi f\mu_0}}\right] + \sqrt{\frac{\sigma}{\sigma_1}}. \tag{6}$$

Eq.(6) shows that the accuracy of measurement of $(f_1 - f)$ primarily determines the accuracy of the value of μ_L. It may also be noted that for a given value of μ_L the frequency shift $(f_1 - f)$ would be large when the cavity length l is small and its radius a large one.

2. Results and Discussion

The test cavity dimensions and parameters are: diameter $2\alpha = 4.95$ cm, length $l = 2.60$ cm, coupling hole diameter = 0.285", critical wavelength of the cylindrical waveguide = 0.04059 meters, wave impedance of the cylindrical waveguide $Z_c = 611.6$ ohms, conductivity of soft iron $\sigma = 1.0 \cdot 10^7$ mhos/meter and the conductivity of brass - $\sigma_1 = 1.57 \cdot 10^7$ mhos/meter.

The resonance frequency of the test cavity with an accurately machined soft iron plate forming one of its end walls was 9386 Mc, which corresponds to a free-space wavelength $\lambda = 0.03196$ meters. The frequency shift $(f_1 - f)$ produced by the replacement of the soft iron wall with a brass end wall was calculated from the CRT pattern to be 150 kc. An average value of the frequency shift was also obtained by using three different accurately machined brass and soft iron plates. The variation in frequency due to geometrical uncertainty of the brass and in the soft iron plates was less than ±20 kc. The relative apparent permeability μ_L of soft iron calculated from Eq.(6) is 4.5. The accuracy of measurement is estimated to be about ±20%.

The cavity comparator method used in the above described experiments is also suitable for determining the change in the Q-factor of the cavity when one of its conducting end plates is replaced by a plate of ferromagnetic metal. This change in the Q value of the cavity can be related to μ_R, as shown by Sanyal & Chatterjee in Ref.5.

To account for the decrease of initial permeability with frequency several theories have been put forward. They try to explain the phenomenon of dispersion of permeability in terms of the behavior of the ferromagnetic domains in the applied rf field. An excellent review has been given by Rado[2]. We shall, therefore, only mention these theories briefly here.

In Becker's theory[6] it is assumed that small eddy currents are induced in the domains as a result of the rapid changes in magnetization due to the rf field. This happens for both reversible and irreversible domain wall displacements and the eddy currents restrict the motion of the walls. Taking this into account Becker showed that the initial susceptibility for weak fields at a frequency f is given by

$$\chi = \chi_s \frac{1}{1 + i \frac{f}{2\pi f_c}},$$

where χ_s is the static susceptibility and f_c is a critical frequency giving a relaxation time $\tau = 1/2\pi f_c$ for the domain walls. The critical frequency is given by

$$f_c = \frac{3\rho}{\pi^2 \mu_s l^2},$$

where ρ and μ_s are the resistivity and the static initial permeability of the substance, respectively, and l is the domain size. The critical frequency for iron with an estimated domain size of 10^{-4} cm is $3 \cdot 10^9$ cps.

A different theoretical approach was made by Landau & Lifshitz[7] who studied the frequency dependence of the initial permeability in a uniaxial crystal. These authors show that the dispersion of permeability can be satisfactorily accounted for by considering the role played by the crystalline anisotropic energy in the precessional motion of the magnetic moments in the combined rf

and the internal crystalline field. The complex nature of the permeability is explained by incorporating a phenomenological damping term in the equation of motion. The theory, in particular, shows the possibility of a damped resonance being obtained in the dispersion of permeability due to the internal crystalline field. This has since been shown to be so by Birks[8] and Snoek[9] in ferromagnetic semiconductors.

According to Kittel[10] the decrease of initial permeability of ferromagnets at UHF and higher frequencies is due to the fact that the domain dimensions (10^{-4}-10^{-3}) are comparable to or larger than the skin depth at the applied frequency. There is thus a reduction of the rf field within the thickness of single domains. By taking this into account he showed that the permeabilities μ_R and μ_L at any frequency could be expressed in terms of the domain size, resistivity and the initial static permeability of the ferromagnetic metal. For a domain thickness of $2.5 \cdot 10^{-4}$ cm normal to the layer acted on by the rf field, the frequency dependence of μ_R and μ_L shows fair agreement with the theoretical data.

Döring[11] has modified Becker's theory by taking into consideration the inertia of the moving domain walls. According to this theory the eddy current damping as proposed by Becker plays a minor role and the critical frequency at which the initial permeability significantly begins to decrease does not depend on the resistivity of the metal. The critical frequency of iron has been calculated to be $6 \cdot 10^{8}$ cps. Birks' experiments on semiconductors and the dispersion of permeability of metals give critical frequencies in fairly good agreement with Döring's theory.

Kittel[10] has attributed the dispersion of the initial permeability observed in ferromagnetic resonance experiments to a damping factor of unknown origin.

It would appear from all the above theories that the critical frequency at which the initial rf permeability begins to decrease significantly is directly dependent upon the size of the domain and/or its behavior under the influence of a rapidly alternating field. It is reasonable to assume that an increase in temperature should change the value of critical frequency in a manner depending upon the mechanism involved at high frequencies and thus change the values of μ_R and μ_L for a given sample. Hence determination of μ_R and μ_L for the same samples at different temperatures should give a clearer indication of the cause of dispersion of the initial permeability with frequency. Experiments to find the temperature dependence of rf permeability at ~3 cm are in progress. It is also proposed to study how μ_R and μ_L vary with the thickness of the ferromagnetic sample.

Indian Institute of Technology,
Kharagpur, India

References

1. J.T.Alanson, J.I.E.E., 92, P.III, 247 (1945).
2. G.T.Rado, Adv. in Electr., II, 251 - Academic Press, 1950.
3. G.S.Sanyal, Symposium on Magnetism, Ind.Assoc. for the Cult. of Sci. - Calcutta, 1954.
4. G.C.Montgomery, Technique of Microwave Measurements. -McGraw Hill Book Co., N.Y., 1947.
5. G.S.Sanyal & J.S.Chaterjee, Ind.J., Phys., 27, 328 (1953).
6. R.Becker, ZW.f.tech.Phys., 19, 542 (1938).
7. L.Landau, E.Lifshitz, Phys.ZS.8, 153 (1935).
8. J.B.Birks, Nature, 158, 671 (1946); ibid., 159, 775 (1947); ibid., 160, 535 (1947); Proc.Phys.,Soc., 60, 282 (1948).

9. J.L.Snoek, Nature, 160, 90 (1947); Physica, 14, 207 (1948).
10. C.Kittel, Phys.Rev., 70, 281 (1946); ibid. (1951).
11. W.Döring, ZS.f.Naturf., 3a, 373 (1948).

* * * * * *

RADIOFREQUENCY MAGNETIC SPECTRA OF MIXED FERRITES

- L.A.Fomenko

The magnetic radiofrequency spectra of the complex permeability $\mu' = \mu_1 - j\mu_2$* of simple and mixed polycrystalline ferrites have been the subject of numerous investigations.[1-16] The purposes of the present report are to describe briefly our new experimental data on the magnetic spectra of mixed ferrites measured in very weak fields in the frequency range from 0.2 to 60 Mc, to discuss these results and to suggest methods of characterizing such spectra.

The spectra were investigated by the procedures described earlier.[4,6,14,16] The measurements were carried out on a large number of toroidal samples (over 100) of Ni-Zn, Ni-Zn-Cu, Ni-Zn-Be, Ni-Zn-Mg, Li-Zn and Mn-Zn ferrites characterized by initial permeability values from some tens to 2000 gauss/oersted. We investigated the influence on the character of the spectra of the following factors: a) the "scatter" of the technological processing conditions, i.e., the more or less minor variations of the conditions of preparation inevitable in industrial production of cores, b) significant differences in the technology of preparation, c) certain variations in the composition of the mixed ferrites, d) the cross section area of the core, i.e., the influence of turning down the core, e) quenching, f) the temperature of measurement, which was varied up through temperatures above the ferromagnetic Curie point θ, and g) other factors.

With few exceptions all the samples were investigated in the absolute zero magnetization (fully demagnetized) state and in the remanence state. Earlier measurements[14,16] on ferrites of the same composition and sintered at the same temperature showed that the relations between the spectra observed in both these states for specimens of the same type are remarkably constant, which indicates a certain regularity of these relations and makes it possible to use them as the basic criterion for evaluating the character of the magnetization processes of ferrites in weak fields, particularly, since there are no other suitable criteria for specimens of the given type which in the radio and super-high frequency ranges have "one dispersion" region spectra[10,11,13]. While the use of this criterion has not been justified theoretically[12,17], judging by the results of Rado, Wright & Emerson,[5] it is consistent in the case of ferrites with a residual to saturation magnetization ratio $J_R/J_s \approx 0.5$ with the experimental data. We feel that the qualitative agreement of our data obtained on the basis of this criterion with the general physical concepts concerning magnetization processes can serve as an added argument in favor of the validity of this method of analyzing the phenomena.

We shall first describe some of the results of our experiments.

1. We investigated the magnetic spectra in the absolute demagnetized state of ordinary commercial samples of Ni-Zn ferrites prepared both by decomposition of Ni and Zn salts (Oxifers[18]) and by the mixed oxide procedure.

---

*Or in terms of the notation used earlier[4,7,14,16] $\mu' = \mu - j\rho'$.

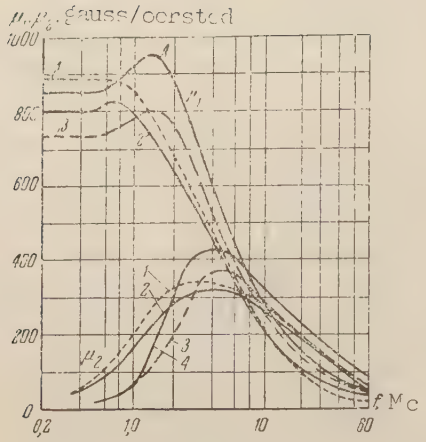

Fig.1. Magnetic spectra of Ni-Zn ferrites measured in the state of absolute demagnetization: 1,2 & 3) Oxifer-1000 samples, and 4) NTs-1000 ferrite sample.

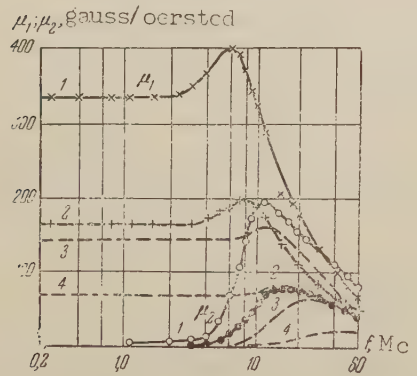

Fig.2. Magnetic spectra of 1 & 2) sample of Ni-Zn-Cu ferrite $[(NiO)_{0.21} + (ZnO)_{0.26} + (CuO)_{0.04} + (Fe_2O_3)_{0.49}]$ and 3 & 4) sample of Ni-Zn ferrite $[(NiO)_{0.25} + (ZnO)_{0.26} + (Fe_2O_3)_{0.49}]$ sintered at 1140°; curves 1 & 3 are for measurements in the absolute demagnetized state while curves 2 & 4 are for measurements in the remanence state.

It was found that samples of ferrites close as regards composition and having approximately the same values of initial permeability μ_a and saturation magnetization J_s are characterized by magnetic spectra of approximately the same type which, however, may have either a resonance or a relaxation character, presumably because of the scatter of technological processing conditions. This conclusion can, for example, be drawn from the data of Fig.1 which shows the spectra of three samples of Oxifer-1000 plotted on the basis of results of measurements on ten cores and one sample of NTs(= NiZn)-1000 ferrite prepared by the mixed-oxides procedure.

Resonance peak type spectra are typical of samples having relatively small loss tangent values, $\tan\delta = \mu_2/\mu_1 < 0.1$, in the region of the beginning of the resonance rise of the dispersion curve (μ_1 vs f) and, consequently, a comparatively small phenomenological Landau-Lifshitz[19] damping constant. Probably these samples have narrower resonance and relaxation frequency bands due to the greater homogeneity of the material. The lowest loss in this frequency range and the most pronounced resonance peak among the investigated ferrites was found[14] for one of the Ni-Zn-Cu ferrite samples (Fig.2). When the CuO in the initial composition of this ferrite is replaced by ZnO, the height of the resonance peak of the real part of the permeability μ_1 is reduced (Fig.2); this decrease may be described by the increase of the ratio of the Landau-Lifshits phenomenological damping constant to J_s, inasmuch as the value of J_s is appreciably reduced (~30%) upon replacement of the CuO with ZnO.

The values of the absorption peak frequency f_u and of the frequency f_r, at which the permeability equals half its value at low frequencies for the investigated ferrite, are given by the expression

$$f_u \approx f_r \approx C \frac{J_s}{\mu_a - 1}, \qquad (1)$$

where $C \approx ge/2\,mc \approx e/mc = 17.6$ Mc/oersted and g is the spectroscopic splitting factor, which according to Refs.20-22 may be assumed to be equal to 2 (it should be noted that in the temperature range of our investigation no "compensation" temperature[24] was detected). In view of the fact that the frequencies f_u and f_r are approximately equal to the mean resonance frequencies of the ferrite material and that the validity of Eq.(1) does not depend on the character of the magnet-

ization processes* a theoretical basis for Eq.(1) is furnished:

a) in the case of predominance of domain rotation processes, by the theory of Landau-Lifshits[19] and Snoek[1] which gives the following familiar formula

$$f_{0\mathrm{rot}} = \frac{ge}{4\pi mc} H_i \approx \frac{1}{\pi} \cdot \frac{ge}{2mc} \cdot \frac{k}{J_s} \approx \frac{4}{3} \cdot \frac{ge}{2mc} \cdot \frac{J_s}{\mu_{a\,\mathrm{rot}} - 1}\,; \tag{2}$$

b) in the case of predominance of wall displacement processes, by the theory of Landau-Lifshits[19] and Döring[23] which yields the following relationship for the 90° walls

$$f_{0\mathrm{dis}} = \frac{ge}{2mc} \sqrt{\frac{\Delta}{d}} \cdot \frac{J_s}{\sqrt{\mu_{a\mathrm{dis}} - 1}}\,; \tag{3}$$

c) in the case of approximate equality of the contribution of domain wall displacement and domain rotation processes, by the approximate equality of the mean resonance frequencies of the ferrite material due to both types of magnetization process.

In Eqs.(2) & (3) $H_i \approx 2k/J_s$ is the internal effective magnetic field in the ferrite material[25], k is the effective anisotropy constant, $\mu_{a\,\mathrm{rot}}$ is the initial rotation permeability, $\mu_{a\,\mathrm{rot}} - 1 \approx 4J_s^2/k$, $\mu_{a\,\mathrm{dis}}$ is the initial wall displacement permeability and Δ/d is the ratio of the effective thickness of the boundary layer to the average size of the ferromagnetic domains. Phenomenologically from our experimental data[9,14,16] we should write

$$\frac{\Delta}{d} \approx \frac{1}{\mu_{a\mathrm{dis}} - 1}, \tag{4}$$

which, however, is not in agreement with Vonsovskii's formulas (Ref.25, pp.258 & 260) expressing this ratio in terms of the exchange energy, the anisotropy energy, the lattice constant and the size of the crystal sample.

2. We investigated the magnetic spectra in the remanence state both of ordinary commercial samples of Ni-Zn ferrites prepared by different industrial procedures and of specially prepared samples of different composition. It was found that the quantitative relations between the spectra in the demagnetized state and the remanence state of every ferrite sample and, consequently, (taking into account that the values of J_R/J_S for most of the investigated samples were close to 0.5) the ratios of the relative contributions of wall displacement and domain rotation processes to the magnetization depend strongly on the composition, the sintering temperature t_s and the cooling procedure.

The dependence of the character of the magnetization processes in ferrites on the sintering temperature was not taken into account in our earlier investigations[2,3] although from general physical considerations it follows[14,16] that at low sintering temperatures the contribution from wall displacement processes must be small inasmuch as the large number of inclusions (impurities, cavities, etc.) present in such cases tend to "fix" the walls at many points and hinder their displacement, thereby reducing $\mu_{a\,\mathrm{dis}}$; wall displacement is further hindered in this case by large internal stresses σ_i. With increasing sintering temperature, internal stresses are relieved and the number of inclusions is reduced so that $\mu_{a\,\mathrm{dis}}$ must increase and attain a maximum value at some optimal sintering temperature t_s' and then start decreasing because of increase in the number of inclusions formed by the decomposition of the excess ferrite. Theoretical support of the above argument is furnished by Kondorskii's theory of stresses (Ref.17, p.352), Kersten's theory of inclusions (Ref.17, p.395)

---

*This follows both from our results[14,16] and from the data of Rado, Wright, Emerson & Terris[9].

and the theory of the initial rotation permeability developed by Akulov (Ref. 25, p.362). We verified the above hypothesis by measurements on a group of ferrite samples of different composition which were sintered at different temperatures. The experiments showed that for each ferrite there is a certain optimal sintering temperature t'_s corresponding to the minimum value of the ratio of the initial permeability μ_{aR} in the remanence state to the initial permeability μ_a in the demagnetized state and, consequently, to a maximal relative contribution from wall displacement processes. As regards absolute value, the optimal sintering temperature differs for ferrites of different composition. The highest value of the sintering temperature ($t'_s > 1330^\circ$) was observed for the most stable Ni-Zn ferrite composition (Oxifer-2000 - approximate molar composition 15% NiO + 35% ZnO + 50% Fe_2O_3) which is consistent with our hypothesis and the x-ray diffraction data of Erastova[26] indicating that there is little decomposition of this ferrite at relatively high sintering temperatures.

The lowest value of t'_s (about 1140°) was observed for the Ni-Zn-Cu ferrite* in which the Cu-ferrite begins to decompose at the relatively low temperature of about 850° (the magnetic spectra for this ferrite are shown in Fig.2). Investigations of the Ni-Zn ferrite having the composition $(NiO)_{0.25}(ZnO)_{0.25}(Fe_2O_3)_{0.5}$ prepared by the method of decomposition of a mixture of the salts showed (Fig.3) (as might be expected in view of the fact that the decomposition of the excess Ni ferrite begins at 1200° - Ref. 26) a somewhat higher optimal sintering temperature $t'_s \approx 1240^\circ$). Analogous results were obtained for samples of Ni ferrite of stoichiometric composition prepared by decomposition of a mixture of the salts and sintered at 1110, 1240, 1375 and 1420°; the values of the ratio μ_{aR}/μ_a for these samples proved to be 0.84, 0.56, 0.77 and 0.9, respectively. It is possible that these regularities apply also to the Ni ferrites studied by Brown & Gravel[13], although as regards absolute initial permeability our samples had values approximately 4 times greater than those of Brown & Gravel.

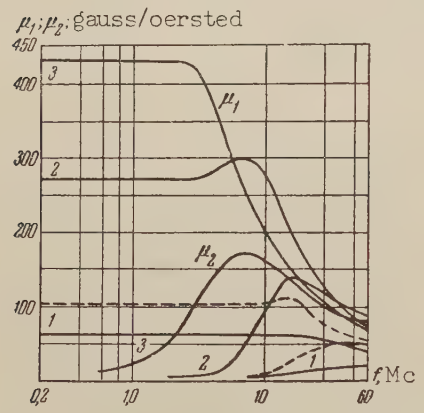

Fig.3. Magnetic spectra of Ni-Zn ferrites in the absolute demagnetized state; composition - $(NiO)_{0.25}(ZnO)_{0.25}(Fe_2O_3)_{0.5}$. Samples sintered at 1) 1110°, 2) 1240°, 3) 1420°. The values of the ratio μ_{aR}/μ_a are 0.6, 0.39 and 0.81, respectively. The dash line shows the remanence state spectrum for the specimen sintered at 1240°.

We must also note the influence of the composition of the ferrite and the method of cooling on the increase of the ratio μ_{aR}/μ_a and, consequently, on the decrease of the relative contribution from wall displacement processes in Ni-Zn ferrites (in the range of high zinc oxide concentrations) as a function of the amount of ZnO present and incident to quenching of the samples (Fig.4). The influence of ZnO, according to Snoek[1], Rado[10] and the writer[16] is evinced in a decrease of the anisotropy constant of the ferrite, while the influence of quenching is to increase the internal stresses and inclusions hindering wall displacement.

---

*The ratios μ_{aR}/μ_a and J_R/J_S in this case were equal to 0.5 and 0.55, respectively, which indicates that wall displacement processes predominate in the general magnetization of the Ni-Zn-Cu ferrite (sintered at 1140°) in very weak fields.

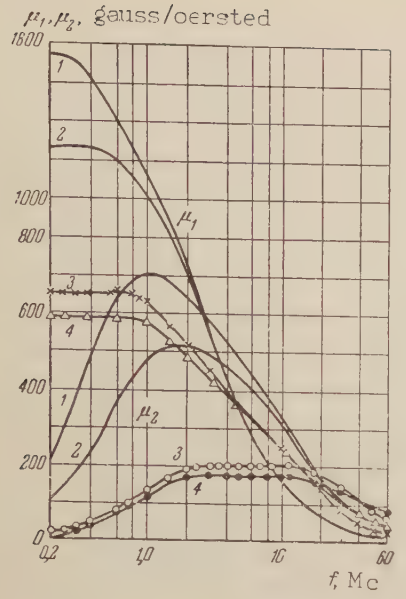

Fig.4. Magnetic spectra of Oxifer-2000-1 type Ni-Zn ferrite measured in the state of absolute demagnetization (curves 1 & 3) and in the state of remanence (curves 2 & 4). Curves 1 & 2 pertain to a sample prepared in the conventional manner, for it J_S = 195 gauss and J_R = 95 gauss. Curves 3 & 4 pertain to the same specimen after quenching from 650° in oil; for it J_S = 260 gauss and J_R = = 21 gauss.

It should also be noted that the sintering temperature and composition of the ferrite have a strong effect on the temperature coefficient of the initial permeability which apparently attains a maximum for ferrites sintered at t'_s, i.e., at the temperature yielding the maximum μ_{aR}/μ_a ratio. Quenching sharply reduces this temperature coefficient. This decrease can be understood in the framework of Kersten's theory as a result of the influence of inclusions inasmuch as according to this theory, other conditions being equal, the temperature dependence of μ_a is determined by the temperature dependence of the anisotropy constant entering into Kersten's equation to the 1/2 power, while the Kondorskii theory of stresses and the theory of the initial rotation permeability define the temperature dependence of μ_a as a linear function of the anisotropy k or the magnetoelastic energy $\lambda_s \sigma_i$.

3. In the case of some samples of Ni-Zn and other ferrites (for example, the samples characterized in Fig.2) sintered at temperatures close to the optimal, undoubtedly wall displacement processes play a dominant role; the mechanism of dispersion can be described according to Landau-Lifshits[19] and Döring[23] in terms of inertia of the effective mass of the domain walls. As further substantiation of this deduction one might consider[14] the shift of the frequency corresponding to maximum absorption for the investigated ferrite specimens in going from the demagnetized to the remanence state; this shift as determined experimentally for samples characterized by weak damping is described (see curves 1 & 2 of Fig.2) by the equality

$$\frac{f_u}{f_{uR}} \approx \sqrt{\frac{\mu_{aR}-1}{\mu_a-1}} \qquad (5)$$

and, consequently, is in agreement with Eq.(3) given by Döring. The initial permeability of these ferrites can be ascribed, in accord with the general theory of reversible wall displacement[17], to the influence of inclusions and internal stresses in the samples. Evidence in favor of the influence of the internal stresses on the initial permeability in ferrites is furnished by the observations of Rado[9,10], Brown & Gravel[13] and others[3,6] who found two dispersion regions in a number of ferrites characterized by low values of saturation magnetostriction and one dispersion region in Ni-Fe ferrites characterized by appreciably higher values of the saturation magnetostriction. Our inference that wall displacement processes play a predominant role in some Ni-Zn ferrites is also in agreement with the low calculated values of μ_c for the latter obtained from the values of the anisotropy constants and internal fields familiar from the work of Miles[21].

For some of the other ferrite samples sintered at very low or very high temperatures domain rotation processes may be assumed to predominate and the

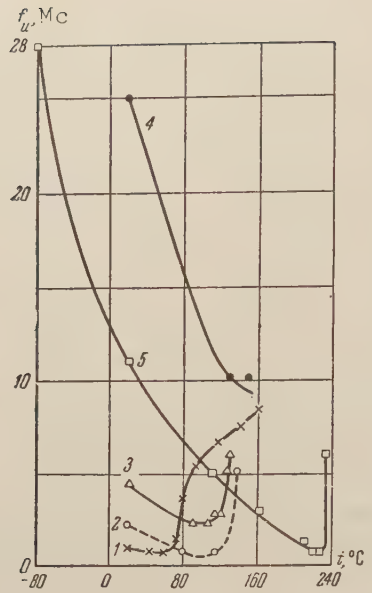

Fig.5.

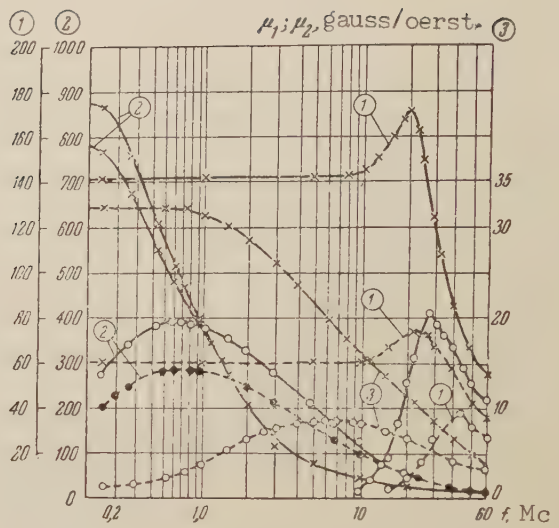

Fig.6.

Fig.5. Temperature dependence of the maximum absorption frequency f_u in the magnetic spectra of ferrites of different composition: 1) Oxifer-2000-1, $\theta \approx 70^{\circ}$; 2) NTs-2000, $\theta \approx 118^{\circ}$; 3) NTs-1000 (Ref.16), $\theta \approx 124^{\circ}$; 4) Oxifer-200, $\theta \approx 154^{\circ}$; 5) Ni-Zn-Cu ferrite, $t_s = 1140^{\circ}$, $\theta \approx 232^{\circ}$.

Fig.6. Temperature dependences of the magnetic spectra of Ni-Zn-Cu ferrite measured in the absolute demagnetized state (solid lines) and in the remanence state (dash lines): 1) -80°, $J_S = 460$ gauss, $J_R = 290$ gauss; 2) -226°, $J_S = 72$ gauss; 3) 232°, $J_S = 10$ gauss. The spectra of both states of the ferrite merge at 232°.

dispersion mechanism according to Landau-Lifshits[19] and Snoek[1] can be described in terms of the precession of the electron spins in the internal effective magnetic field of the anisotropy of the ferrite material. In the case of many of the samples, however, in describing the dispersion one should probably take into account the influence of both dispersion mechanisms.

Preliminary investigations of turned-down samples, moreover, indicate a certain nonuniformity and, consequently, we believe that the actual spectrum of a ferrite should be regarded as the sum of a certain number of more elementary spectra associated with individual layers or regions of the sample.

4. Investigations of the temperature dependence of the magnetic spectra carried out on five samples of Ni-Zn ferrite with μ_a = 200-2000 gauss-oersted and a sample of Ni-Zn-Cu ferrite with μ_a = 370 gauss/oersted showed, in accord with earlier results[1,7,9,12], that with increasing temperature the frequency f_u of the absorption peak at first goes down, attains a minimum at a certain temperature t_Δ, the "thermal maximum of the rf magnetic viscosity" of the ferrite material and then begins to increase (Fig.5). This character of the temperature dependence of the peak absorption frequency apparently is not determined by the character of the magnetization processes in the ferrites at 20° and for all of the investigated samples is approximately described by Eq.(1), which thus appears to be generally applicable. Convincing in this respect are the results of investigation of the temperature dependence of the

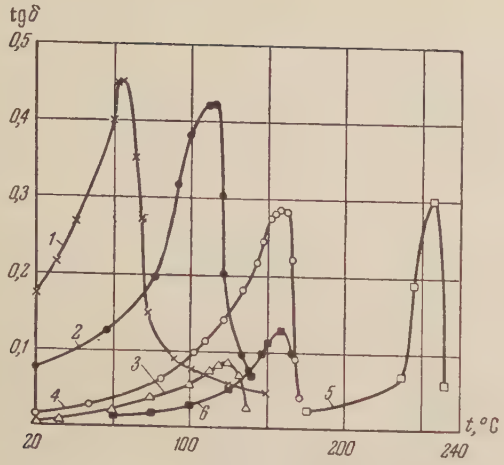

Fig.7. Temperature dependence of tan δ for mixed ferrites: 1) Oxifer-2000-1, $\theta \approx 70^{\circ}$, f = = 0.25 Mc, 2) NTs-2000, $\theta \approx 118^{\circ}$, f = 0.25 Mc, 3) NTs-1000, $\theta \approx 124^{\circ}$, f = 0.25 Mc, 4) Oxifer-200, $\theta \approx 154^{\circ}$, f = 1 Mc, 5) Ni-Zn-Cu ferrite, $t_s = 1140^{\circ}$, $\theta \approx 232^{\circ}$, f = 0.25 Mc, 6) Oxifer-400, $\theta \approx 148^{\circ}$, f = 0.39 Mc.

magnetic spectra of one of the Oxifer-2000-1 Ni-Zn ferrite samples for which the μ_a and J_s vs temperature curves are characterized by long tails in the temperature region above the Curie point and the results obtained for Ni-Zn-Cu ferrite (Fig.6) which exhibits a wide range of variation of the frequency f_u of saturation magnetization and the initial permeability.

The character of the temperature dependence of the loss tangent in the frequency range $0.01\ f_u \leqslant f \leqslant f_u$ can be determined with the aid of the expression given in Ref.4:

$$\operatorname{tg}\delta = \frac{\mu_2}{\mu_1} \approx \frac{f}{f_u} \approx \frac{f}{C} \cdot \frac{\mu_a - 1}{J_s}. \qquad (6)$$

Calculations by means of this expression, which are in agreement with the experimental data (Fig.7), show that the loss tangent in ferrites attains a maximum value at the temperature of the "thermal maximum of the rf magnetic viscosity". The temperature dependence of the magnetic spectra in the region of low temperatures for ferrite samples in which wall displacement processes predominate can be described by means of both the inclusion theory of Kersten and Kondorskii's theory of stresses as being associated with decreases of J_s, k and $\lambda_s \sigma_i$. With increasing temperature the contribution from domain rotation processes increases as follows both from general physical considerations and from the results of experiments on the temperature dependence of the magnetic spectra in the demagnetized and remanence states (Fig.6). At temperatures approximately equal to or greater than t_Δ, although the predominant role is apparently played by rotation processes, the character of the temperature dependence of the magnetic spectra cannot be described by the variation of the anisotropy constant or the spectroscopic splitting factor (inasmuch as even at the Curie temperature the anisotropy goes to zero, while in the region of anomaly of the g-factor, according to Torizuka, Kojima & Fujimura[27] the internal field of the ferrite must also vanish) and may possibly be due to precession of the electron spins in the effective field induced by internal stresses in the ferrite, if we assume that the magnetostriction of the ferrite at $t > \theta$ has a finite value and passes through a partial maximum.

In conclusion it must be noted that in the case of resonance spectra, degeneration of these into relaxation spectra is observed a) upon increase of the temperature of measurement, b) as a result of quenching the sample, c) as a result of increasing the ZnO content of the ferrite and d) in consequence of using excessively high or low sintering temperatures. These data indicate that the resonance shape of the magnetic spectra of ferrites is probably due to resonance of the domain walls.

References

1. J.L.Snoek, Philips Tech.Rev., 8, 353 (1946); Nature, 160, 90 (1947); New developments in ferromagnetic materials, Amsterdam, 1947 (M.1949).
2. E.Flegler, Arch.Electrotechn., 40, 4 (1950).
3. J.J.Welch, P.F.Nicks, A.Fairweather & F.F.Roberts, Phys.Rev., 77, 403 (1950).
4. L.A.Fomenko, Transactions, Fifth Scientific Technical Conference, Leningrad, April, 1950; Zhur.eksp.i teor.fiz., 21, 1201 (1951).
5. G.T.Rado, R.W.Wright, & W.H.Emerson, Phys.Rev., 80, 274 (1950).
6. M.Roberts, Phys.et Rad., 12, 301 (1951).
7. L.A.Fomenko, Transactions, Sixth Scientific Technical Conference, Leningrad, April, 1951; Scientific session dedicated to Radio Day, Moscow, May, 1951; Zhur.eksp.i teor.fiz., 25, 107 (1953).
8. J.J.Went & E.W.Gorter, Philips Tech.Rev., 13, 181 (1952).
9. G.T.Rado, R.W.Wright, W.H.Emerson & A.Terris, Phys.Rev., 86, 509 (1952); 88. 909 (1952).
10. G.T.Rado, Rev.Mod.Phys., 25, 81 (1953).
11. H.P.J.Wijn, M.Gevers & C.M.van der Burgt, Revs.Mod.Phys., 25, 91 (1953).
12. J.Smit & H.P.Wijn, Adv.Electron., VI, Acad.Press, N.Y. (1954).
13. F.Brown & C.L.Gravel, Phys.Rev., 97, 55 (1955).
14. L.A.Fomenko, Report at Scientific-Technical Conference at "A.S.Popov" VNOR i E, Leningrad, May, 1955; FMM (Physics of Metals & Metallurgy), 2, 22 (1956).
15. E.W.Gorter, Proc.IRE, 43, 1945 (1955).
16. L.A.Fomenko, Zhur.eksp.i teor.fiz., 30, 18 (1956); FMM, 2, 16 (1956); 2, 27 (1956); Izv.AN SSSR, Ser.fiz., 20, 1336 (1956); 1348 (1956). (Trans. Bulletin, 20, No.11, 1220, ibid., 1232.)
17. S.V.Vonsovskii & Ia.S.Shur, Ferromagnetizm (Ferromagnetism), 1948).
18. N.N.Shol'ts, Izv.AN SSSR, Ser.fiz., 18, 465 (1954). (Trans.Bulletin, 18, No.4, 155.)
19. L.D.Landau & E.M.Livshits, Sow.Phys., 8, 157 (1935).
20. E.I.Kondorskii & N.A.Smol'kov, Doklady AN SSSR, 93, 237 (1953).
21. P.A.Miles, Nature, 174, 177 (1954).
22. T.Okamura & Y.Torizuka, Nature, 167, 986 (1951).
23. W.Döring, ZS.Naturforsch., 3a, 373 (1948).
24. E.W.Gorter & J.A.Schulkes, Phys.Rev., 90, 487 (1953); E.W.Gorter, Philips Res., Rep., 9, 295 (1954).
25. S.V.Vonsovskii, Sovremennoe uchenie o magnetizme (Modern Magnetism), M.-L., 1952.
26. A.P.Erastova, Dissertation, Leningrad Institute of Precision Mechanics & Optics, 1956.
27. Y.Torizuka, Y.Kojima & T.Fujimura, Phys.Soc., Japan, 9, 298 (1954).

MAGNETIC SPECTRA OF MAGNETODIELECTRICS OF THE ALSIFER TYPE

- L.A.Fomenko

Our measurements of the magnetic spectra of TCh-60 (ТЧ-60) and TChK-55 (ТЧК-55) magnetodielectrics of the Alsifer type were carried out on toroidal samples in very weak fields according to the procedure described earlier.[1] The dimensions of both cores were approximately the following: inside diameter, 1.3 cm, outside diameter, 2.4 cm, cross section, 1.3 cm^2. From the experimental data we calculated the real μ_1 and the imaginary μ_2 components of the complex magnetic permeability $\mu = \mu_1 - j\mu_2$ and the value of the magnetic loss tangent $\tan \delta = \mu_2/\mu_1$ at different frequencies (see accompanying figure).

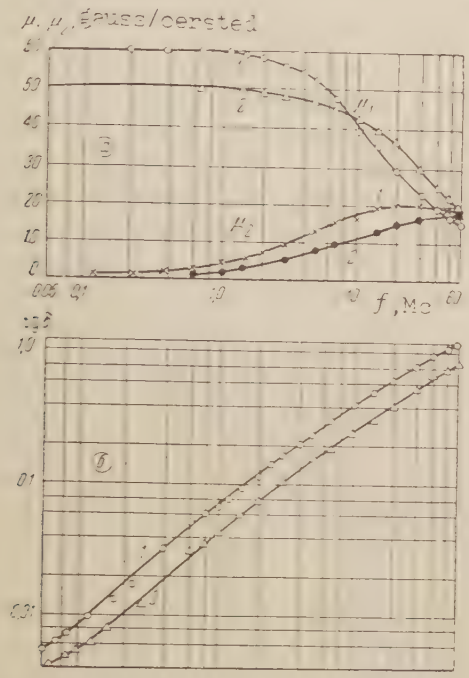

a) Magnetic spectra, b) frequency dependence of the magnetic loss tangent of magnetodielectrics of the Alsifer type: 1) TCh-60, 2) TChK-55.

In general the frequency dependence of the permeability of a magnetodielectric[2] is determined by 1) the dispersion of the material itself, due to microprocesses, 2) dispersion due to the shape of the particles and 3) dispersion due to the structure of the composite core or sample. In view of this, solution of the problem of finding the frequency dependence of the permeability in the general form is difficult.

We made an attempt to calculate the frequency characteristics of our magnetodielectrics on the assumption that the characteristics are determined primarily by the eddy currents induced in the particles of the material. By way of theoretical model we assumed the model of an idealized magnetodielectric (proposed by Kornetzki & Weis[3]) consisting of cylindrical particles of metallic ferromagnet with a length greatly exceeding the diameter and the cylinder axes oriented in the direction of the magnetic field. A certain physical justification of this model in the case of high permeability magnetodielectrics is furnished by the probability of formation of "chains" by the individual contacting metallic particles. The calculations were carried out by means of the following equations:

$$\mu_1 = C_m\mu_a, \quad \mu_2 = D_m\mu_a \quad \text{and} \quad \tan\delta = D_mC_m,$$

where C_m and D_m are coefficients determined as functions of the frequency f and the eddy current loss coefficient δ_f from the curves of Figs.1 & 5 of Ref.4. The values of tan δ were determined directly from the curve of Fig.6 in Ref.4. These curves were plotted by the writer on the basis of the data given by Arkad'ev[5]. Evaluation of the coefficients δ_f carried out on the basis of the results of low frequency measurements gave $\delta_f = 50\cdot10^{-9}$ for TCh-50 and $\delta_f = 30\cdot10^{-9}$ for TChK-55. These appear to be plausible values inasmuch as the magnitude of this coefficient for TCh-60, according to Rabkin & Shol'ts, should not exceed $200\cdot10^{-9}$.

Comparison of the results of calculation with the experimental data shows that the divergence in general is less than ±20%. It was felt that these

results may be of practical interest inasmuch as the method of calculation in this case is very simple and the results for the radiofrequency range are in satisfactory agreement with experiment despite the rough character of the model and neglect of the dispersion associated with the material itself and with the structure of the composite sample.

References

1. L.A.Fomenko, Zhur.eksp.i teor.fiz., 30, 18 (1956).
2. K.M.Polivanov, B.M.Fradkin, N.G.Katkov & V.V.Skugarev, Abstracts of Reports prepared for the Conference on the Physics of Magnetic Phenomena, Moscow, May 1956, Pub.in Sverklovsk.
3. M.Kornetzki & A.Wais, Wissenschaft Veröffent.S.W., 15, H.2, 95 (1936).
4. L.A.Fomenko, Radiotekhnika (Radio Engineering), 5, 3 (1949).
5. V.K.Arkad'ev, Elektromagnitnye protsessy v metallakh (Electromagnetic processes in metals, Part II), M.-L., 1936.
6. L.I.Rabkin & N.N.Shol'ts, Magnitodielektriki i ferrokatushki (Magneto-dielectrics and ferrocoils), M.-L., 1948.

FERROPROBE MAGNETOMETER FOR INVESTIGATING THE PROPERTIES OF SMALL SAMPLES OF MAGNETICALLY SOFT MATERIALS

- V. I. Drozhzhina & L. A. Fridman

The magnetic characteristics of ferromagnetic materials are often measured by means of magnetometers of the type in which the indicator consists of a moving astatic system of two permanent magnets suspended by a thin filament. Owing to the presence of this rotating system, magnetometers of this type suffer from a number of shortcomings: sensitivity to mechanical vibrations, zero drift and shift upon application of strong magnetic fields, etc. These shortcomings can be largely eliminated by replacing the movable astatic system by ferroprobes[1,2] the operation of which is based on the nonlinearity of their magnetization curve.

Ferroprobes with transverse excitation were first used some time ago for open magnetic circuit measurements of the coercive force H_c ($\sim$40 oersted) of relatively large specimens.[3] There is also mention in the literature[4] (but without description of the experimental conditions) of the use of ferroprobes with longitudinal excitation for measuring H_c and determining the magnetization curves of specimens of different dimensions down to very small ones, also in an open magnetic circuit.

Coil	Number of turns	Enameled wire, mm	Length of winding, mm
Indicating	828	0.15	70
Compensating	314	0.2	90
Magnetizing	314	0.2	90

We designed and constructed two magnetometers employing differential ferroprobes with longitudinal excitation as indicators and tested their suitability for measurement of the coercive force of small specimens of magnetically soft materials. Our ferroprobes consisted of two cores (90 x 3 x 0.1 mm) of 80 NkhS permalloy, mounted side by side in textolite forms carrying three coils having the following characteristics.

The excitation or magnetizing coils 2 (see accompanying figure) are connected in series so that the fluxes induced in the two cores form a continuous magnetic circuit; an appropriate generator sends an 80 milliamp, 1000 cps alternating current through these coils. The indicating circuit consists of a null indicator (an M91/A galvanometer with a sensitivity of $1.5 \cdot 10^{-8}$ amp per scale division and an internal resistance of 3500 ohm) connected in series with a symmetrical nonlinear resistance (two antiparallel connected MKV-7-1 copper oxide rectifiers) and the indicating coils 1. These coils are differentially connected[2] so that in the absence of an external constant field the sum of the electromotive forces induced in them, consisting in this case only of the odd harmonics, equals zero. In the case of magnetization of the cores by an external magnetic field the emf's in the indicated windings of each cores comprise, in addition to the odd, even harmonics which are not compensated and thus serve as a measure of the external field. The compensating coil (not shown in the figure) serves to neutralize the effect of the external constant field on the ferroprobe.

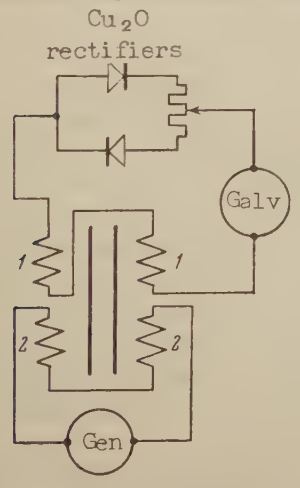

Diagram of ferroprobe magnetometer: 1) indicating coils and 2) magnetizing coils.

The arrangement described above is called a field intensity meter. The first ferroprobe magnetometer tested by us had the following design characteristics. It consisted of two identical solenoids 250 mm in length with an inside diameter of 8 mm wound on copper pipes having a wall thickness of 1 mm and located horizontally one above the other with a center line to center line distance of 20 mm. The investigated specimen was placed into one of the solenoids. The differential ferroprobe field meter was located between the solenoids; it served to indicate the presence of the stray magnetic field due to the magnetization of the specimen. The solenoid windings were connected in series-opposition so that the solenoid fields at the point of location of the ferroprobe compensated each other. The influence of the alternating stray field of the ferroprobe on the investigated specimen was obviated by the shielding action of the eddy currents in the copper pipe carrying the solenoid winding. The solenoids and the ferroprobe were mounted on a wooden board, equipped with bubble levels and screw legs for positioning in the horizontal plane. The ferroprobe was mounted parallel to the solenoid axes.

Before the beginning of measurement the magnetometer assembly as a whole was set normal to the horizontal component of the earth's magnetic field, using the indication of the ferroprobe. In measuring the coercive force H_c the specimen is first magnetized, the magnetizing field is then removed and a gradually increasing demagnetizing field is applied; with reduction of the magnetization of the specimen the constant field acting on the ferroprobe decreases. The instant when the specimen is fully demagnetized, i.e., when the field of the solenoid corresponds to H_c of the specimen, is precisely indicated by the ferroprobe.

A magnetometer of this type is sensitive to variation of any extraneous magnetic fields present (i.e., is not astatic) and hence can be used only for rough evaluation of the magnetic characteristics of materials such as permalloy.

We also constructed and tested an astatic version of the ferroprobe magnetometer. In this magnetometer the indicating unit consisted of two differential ferroprobe field meters connected into a gradient-meter circuit; one of the field meters was located between the solenoids (just as in the first version of the magnetometer) and the second in the horizontal plane, parallel to the first and at a distance of 130 mm from it, i.e., at a point where the field of the specimen is negligibly weak. The indicating coils of the two ferroprobe field meters were connected in series-opposition.

The utilized arrangement makes it possible to measure both the fields at the points where each of the ferroprobes is located and the difference between the fields at the two points. The set-up is relatively insensitive to variations of extraneous magnetic fields with a weak gradient in the vicinity of the magnetometer. In this magnetometer one division of the indicating instrument corresponded to $3.7 \cdot 10^{-5}$ oersted. By means of the described astatic ferroprobe magnetometer we were able to measure with adequate accuracy the coercive force (down to $H_c \approx 0.02$ oersted) of permalloy specimens 0.1 and 0.08 mm thick, 3 mm wide and varying in length from 40 to 100 mm (the weight of the smallest specimen was ~ 0.1 g). The lowest measureable value of H_c and the minimal size of the investigated specimen can be reduced by enhancing the sensitivity of the magnetometer, for example, by increasing the number of turns of the indicating coils or/and the frequency of the magnetizing current. The time required for individual measurements on the described magnetometer is about 30 sec. The ferroprobe magnetometer can also be used for recording the magnetization curves and hysteresis loops of specimens by the

compensation procedure. This can be done by passing a current through the compensating coils to produce an opposing field neutralizing at the point of location of the ferroprobe the stray field due to magnetization of the specimen. The process of measurement can be automatized more readily with ferroprobe magnetometers than in the case of other types.

There are already in use two coercimeter models with automatic compensation, one in which the compensation is electronic[5] and the other in which a magnetic amplifier is used[6]. These instruments are used for measuring H_c of electrotechnical iron specimens ≥ 250 mm in length and ≤ 30 mm in width in a closed magnetic circuit. With these instruments the individual measurement time is only a few seconds. The use of automatic compensation in conjunction with a ferroprobe magnetometer of the type described should make it possible to reduce the measuring time to a few seconds.

One of the outstanding positive features of the described ferroprobe magnetometers is the simplicity of the indicating circuit. The usually rather complex electronic circuits commonly employed with ferroprobes are replaced here by a simple symmetric nonlinear resistance.

Institute of the Physics of Metals,
Ural Branch, USSR Academy of Sciences

References

1. M.A.Rozenblat, Magnitnye usiliteli (Magnetic amplifiers), M.-L., 1949; F.Forster, ZS.f.Metallkunde, 46, 358 (1955); M.Wurm, ZS.f.angew.Phys., 2, 210 (1950).

2. R.I.Ianus, L.A.Fridman & V.I.Drozhzhina, Zavod.labor. (Factory Laboratory), 21, 1193 (1955).

3. M.A.Grabovskii & V.I.Skorobogatov, Zavod.labor., 13, 702 (1947).

4. F.Forster, ZS.f.Metallkunde, 46, 297 (1955).

5. V.M.Frantsevich & L.A.Fridman, Zavod.labor., 22, 590 (1956).

6. L.A.Fridman & V.P.Ankudinova, Zavod.labor., 22, 1108 (1956).

MAGNETIC MOMENTS AND CURIE CONSTANTS OF FERROMAGNETIC ALLOYS

- F.M.Gal'perin

Owing to the difficulties inherent in the many-electron problem, we still do not have relationships for quantitative calculation of even the principal magnetic characteristics of ferromagnets. In earlier publications[1,2] the author gave empirical expressions for the atomic magnetic moments, the Curie points and certain other properties of the pure ferromagnetic metals. In the present report we suggest analogous relationships for ferromagnetic alloys and show on the example of iron-chromium and iron-nickel alloys, whose structure has been investigated by the neutron diffraction method[3], that the proposed relationships are in agreement with experiment.

Let us consider the strongly coupled electron approximation.[4-7] In this case the s-electrons are preponderantly at a distance R_s from the atomic nucleus and the d-electrons are at a distance R_d from the nucleus, where R_s and R_d are the radii of the s- and d-shells of the isolated atom, respectively.

The minimum interelectron distance (along the straight line connecting the atomic nuclei) between an s-electron of an A atom and the d-electrons of neighboring A atoms is $r_1 - R_A$; the distance between an s-electron of a B atom and the d-electrons of neighboring B atoms is $r_1 - R_B$; the distance an s-electron of an A atom is from the d-electrons of neighboring B atoms is $r_1 - R_{AB}$; where r_1 is the interatomic distance in the first coordination sphere (hereinafter c.s.); $R_{AB} = f_A R_A + f_B R_B$, where f_A is the atomic concentration of component A and f_B is the atomic concentration of component B. In the case of the first transition group in the periodic tables (this includes Ni, Fe, etc.)

$$R_A = 0.13\,[(Z_A - 2)^2 - (14{,}75 - u)\,Z_A + 26\,(9{,}05865 - u)]\ \text{Å}$$

where Z_A is the atomic number of element A, $u = 0$ for $Z_A > 26$ and $u = 1$ for $Z_A \leqslant 26$. R_B is given by an analogous relationship.

These interelectrondistances are very small (see accompanying table), so that we can expand the expressions for the atomic moments, the Curie points and other parameters dependent on them in series in powers of $r_1 - R_A$, $r_1 - R_B$ and $r_1 - R_{AB}$ and limit the expansion to the first term, i.e., we can regard these parameters as being linearly dependent on the interelectron distances (see Eq.(1) in Ref.7).

Let us divide binary alloys consisting of components A and B (transition metals) into two groups. Let us class in the first group those in which the difference $r_1 - R_{AB} < 0$ and in the second in which $r_1 - R_{AB} > 0$. Among the alloys we shall consider below, the Fe-Cr alloys with an A2 type lattice, as in iron, and Fe-Ni alloys with an A1 type lattice as in nickel in the concentration range from 25 to 67 atomic percent Ni belong in the first group, while the Fe-Ni alloys with the same lattice but with a concentration of Ni exceeding 67 at.% belong in the second group. Fe-Ni alloys with a nickel concentration from 0 to 25 at.% have an A2 type lattice.

Let us tentatively assume that the empirical relations for the different properties of ferromagnetic binary disordered alloys are the same as for pure ferromagnetic metals but that the dimensionless parameters entering into these expressions are given by

$$I_{AA} = 1 \pm 0{,}641\,[n_1(r_1 - R_A) + n_2(r_2 - R_A)]\,f_A^2,\ (I_{AA} > 0), \quad (1)$$

$$I_{AB} = 0{,}641\,[n_1(r_1 - R_{AB}) + n_2(r_2 - R_{AB})]\,f_A f_B, \quad (2)$$

$$I_{0A} = -0{,}13 N_{dA}(N_{dA} - n_{sA} + \gamma)/(N_{dA} - 1), \quad (3)$$

where the upper sign (+) in (1) here and below pertains to the first group of binary alloys and the lower sign (-) to the second group; n_1 is the total number of neighbors of the atom in the first c.s., n_2 is the total number of neighbors in the second c.s., r_2 is the interatomic separation in the second c.s., $\gamma = 0$ for the first group, $\gamma = 1$ for the second group, N_{dA} is the number of unpaired d-electrons of atom A and n_{sA} is the total number of s-electrons of atom A. I_{BB} is given by an expression analogous to (1) and I_{0B} by an expression analogous to (3). For lattices of the Al type usually only the first c.s. (12 nearest neighbors) is taken into account, while for lattices of the A2 type both the first and second coordination spheres are taken into account. Accordingly, for the Fe-Ni alloys we will take into account only the first terms in the brackets in Eqs.(1) & (2), while for Fe-Cr alloys we will also take into account the second terms.

Properties of iron-chromium and iron-nickel alloys

Properties of the alloys*	Concentration of second component (atomic %)						
	iron-chromium			iron-nickel			
	14,8	30,2	48,8	40	50	60	75**
$n_1(r_1)$, Å	8 (2,4826)	8 (2,4844)	8 (2,4861)	12(2,539)	12 (2,528)	12 (2,521)	12 (2,508)
$n_2(r_2)$, Å	6 (2,865)	6 (2,867)	6 (2,869)	—	—	—	—
R_{AB}, Å	2,7813	2,8305	2,8918	2,603	2,571	2,538	2,489
$r_1 - R_{AB}$, Å	—0,299	—0,346	—0,406	—0,064	—0,043	—0,017	+0,019
I_{AA}	0,435	0,630	0,807	0,451	0,606	0,739	0,892
I_{BB}	—0,919	—0,665	—0,128	0,840	0,769	0,687	0,567
I_{AB}	—0,150	—0,345	—0,540	—0,118	—0,083	—0,031	0,028
I_{1AA}				1,549	1,395	1,261	1,108
I_{1BB}				1,157	1,231	1,313	1,433
I_{0A}/I_{1AA}				—0,335	—0,373	—0,412	—0,469
I_{0B}/I_{1BB}				—0,449	—0,422	—0,400	—0,362
m_A, μ_B	2,14	2,00	1,83	2,451	2,606	2,739	2,892
m_B, μ_B	—0,62	—0,06	0,85	0,844	0,769	0,687	0,567
$m_A - m_B - \{$calc.	2,91	2,41	1,52	1,72	1,92	2,08	2,30
$-I_{AB}$, μ_B exper	2,85± ±0,10 [3]	2,38+ +0,07 [3]	1,62± ±0,11 [3]		1,93± ±0,20 [3]	2,06± ±0,21 [3]	2,31± ±0,22 [3]
$\overline{m}$, μ_B	1,81	1,41	0,93	1,744	1,604	1,435	1,107
C_A				2,384	2,378	2,372	2,363
C_B				0,337	0,341	0,345	0,351
$\overline{C}$				1,44	1,27	1,12	0,88

---

*R_{Ni} = 2.4082 A, R_{Co} = 2.5382 A, R_{Fe} = 2.7332 A and R_{Cr} = 3.0582 A.[2] N_d = 4 for Fe and Cr, and N_d = 2 for Ni (we assume n_s = 2 for all metals). The data on n_1, n_2, r_1 and r_2 for Fe-Cr alloys are taken from Adcock[8]; the data for Ni-Fe alloys are taken from Marsh[9].

**The alloys listed in this column belong to the second group; the other alloys belong to the first group.

Hence we introduce the parameters

$$I_{1AA} = 1 \pm [0{,}641 n_1 (r_1 - R_A) f_A^2 - E_0], \quad (I_{1AA} > 0), \tag{4}$$

$$I_{2AA} = 1 \mp [0{,}641 n_1 (r_1 - R_A) f_A^2 - E_0], \tag{5}$$

where E_0 is the integral part of the first term in the brackets. Calculations show that for all ferromagnetic metals except iron $E_0 = 0$, while for iron $E_0 = -1$.

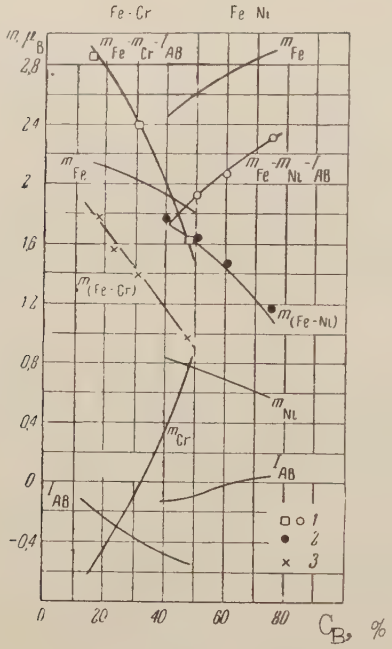

Fig.1.

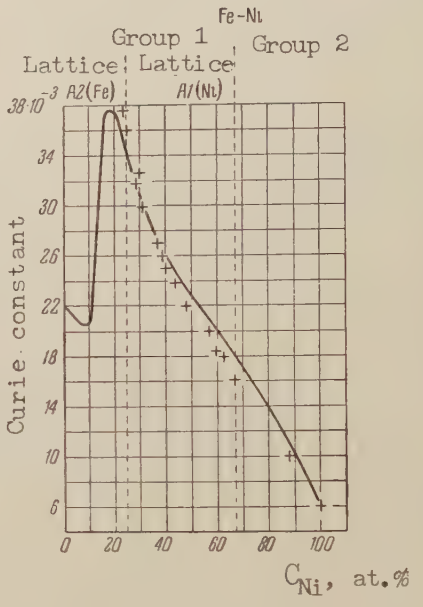

Fig.2.

Fig.1. Variation of the atomic moments of iron-chromium and iron-nickel alloys and their components with the concentration in the alloy. Curves - calculated; experimental points: 1) Shull & Wilkinson[3], 2) Kondorskii & Fedotov[10], 3) Fallot[11]. For I_{AB} read the corresponding μ_B value; m_{Fe-Ni} and $m_{Fe-Cr} = m$

Fig.2. Variation of the Curie constant per gram Fe-Ni alloy with the Ni concentration. Experimental points from the work of Peshard[12].

The atomic magnetic moment of the A component is

$$m_A / \mu_B = e (N_{dA} - n_{sA}) + I_{AA}, \tag{6}$$

and the atomic magnetic component of the alloy is

$$\overline{m}/\mu_B = f_A (N_{dA} - n_{sA}) \pm f_B (N_{dB} - n_{sB}) + f_A I_{AA} f_B \sigma I_{BB} \pm I_{AB}, \tag{7}$$

where the coefficient $e = 1$, if both components of the alloy are ferromagnetic in the pure form (+); and $e = f_A$, if the B component in the alloy is ferromagnetic in the pure form (-); μ_B is the Bohr magneton.

The data for calculating the quantities in question are listed in the accompanying table. In Fig.1 we compare the calculated (curves) with the experimental values (points). It must be noted that experiment[3] gives only the difference between the magnetic moments of the components A and B, namely, $m_A - m_B$. In order to determine each of them separately, Shull & Wilkinson[3]

compare this difference with the moment $\bar{m}$, found from saturation, assuming that $\bar{m} = f_A m_A + f_B m_B$, according to (7), however, $\bar{m}$ is comprised of the moments of the components A and B represented by the first four terms in (7) and the moment due to interaction of the A atoms with the B atoms represented by the last term in (7) (see the $m_A - m_B - I_{AB}$ type curves in Fig.1).

The atomic magnetic moments of component A and the alloy in the paramagnetic state are given by

$$m_{Ap}/\mu_B = 2{,}83\sqrt{C_A} \quad \text{and} \quad \bar{m}_p/\mu_B = 2{,}83\sqrt{\bar{C}},$$

respectively, where the Curie constant per gram-atom of component A in the general case is characterized by

$$C_A = \{[(N_{dA} + E_0)(N_{dA} + E_0 + 2) + (N_{fA} + E_0)(N_{fA} + E_0 + 2)]/t \pm \\ \pm 0{,}05\,(I_{0A}/I_{1AA} - 4) n_{sA}(n_{sA} + 2)\}\, L\mu_B^2/k; \qquad (8)$$

here the upper sign in front of the third term and $t = 3$ correspond to ferromagnetic metals in the pure form and the lower sign and $t = 1$ correspond to paramagnetic metals in the pure form (for example, γ-iron), L is the number of atoms per gram-atom and N_{fA} is the number of unpaired f-electrons in an A atom.

The Curie constant per gram-atom of alloy equals

$$\bar{C} = f_A C_A + f_B C_B + I_{AB} \text{ degree}^{-1}. \qquad (9)$$

The calculated and experimental values of the Curie constants are plotted for comparison in Fig.2.

References

1. F.M.Gal'perin, Zhur.eksp.i teor.fiz., 19, 451 (1949); Izv.AN SSSR, Ser.fiz., 13, 574 (1949).
2. F.M.Gal'perin, Zhur.eksp.i teor.fiz., 31, 150 (1956).
3. C.G.Shull & M.K.Wilkinson, PhysRev., 97, 304 (1955).
4. H.Bethe & A.Sommerfeld, Electronic Theory of Metals (Cited in Russian trans., M.-L., 1938).
5. S.V.Vonsovskii & Ia.S.Shur, Ferromagnetizm (Ferromagnetism), M.-L., 1948.
6. S.V.Vonsovskii, Sovremennoe uchenie o magnetizme (Modern magnetism), M.-L., 1953.
7. S.V.Vonsovskii & K.B.Vlasov, Zhur.eksp. i teor.fiz., 25, 327 (1953).
8. E.Adcock, J.ISI, 124, 99 (1931).
9. S.Marsh, The Alloys of Iron and Nickel, Vol.I, p.45, New York, 1937.
10. E.I.Kondorskii & L.N.Fedotov, Izv.AN SSSR, Ser.fiz., 16, 432 (1952).
11. M.Fallot, Ann.de Phys., 6, 305 (1936).
12. M.Peshard, Rev.de Met., 22, 490, 581, 563 (1925).

INVESTIGATION OF THE MAGNETIC SUSCEPTIBILITY OF IRON AND NICKEL BASE SOLID SOLUTIONS

- V.V.Parfenov

The differential susceptibility in the region of strong magnetic fields can be represented in the following form (Vonsovskii's law of approach to saturation[1,2]):

$$\chi = \frac{b}{H^2} + \frac{b}{H^3} + \chi_p(H, T), \qquad (1)$$

where the term bH^{-2} is dependent on the crystallographic anisotropy energy and the energy of the elastic stresses[3], the term bH^{-3} is associated with the presence of inclusions and inhomogeneous stresses localized in small volumes[4,5] and $\chi_p(H, T)$ is the susceptibility associated with the paraprocess, i.e., the intrinsic magnetization or change in the absolute magnetization due to alignment of the spin magnetic moments under the influence of the external field .

Akulov, Puzei and others[6-8] have carried out experimental investigations of the law of approach to saturation in solid solutions. The data of these experimentors pertain, however, primarily to the range of magnetic fields where the dominant role is played by the term bH^{-2}; these investigators did not consider the influence of impurity atoms on the other terms in expression (1).

For the sake of clarifying our understanding of magnetization processes, it is important to investigate the influence of impurity atoms on the shape of the magnetization curve in the region of high magnetic fields.

Another matter of great interest from the standpoint of the theory of ferromagnetism is investigation of the influence of impurity atoms on the paraprocess susceptibility. Present day theory gives the following dependence of the paraprocess susceptiblity on the field and temperature[9]:

$$\chi_p = \frac{J_0 - J_{T0}}{J_0} \cdot \frac{1}{2H} \left(\frac{4\pi J_0}{3H}\right)^{1/2} \left[\left(\frac{4\pi J_0}{H}\right) + \sin^{-1}\left(\frac{4\pi J_0}{H + 4\pi J_0}\right)^{1/2}\right], \qquad (2)$$

where

$$J_{T0} = J_0\left(1 - \frac{T^{3/2}}{\theta'^{3/2}}\right) \qquad (3)$$

and

$$\frac{1}{\theta'^{3/2}} = \left(\frac{k}{AZ}\right)^{3/2} \left(\frac{0.117}{2CZ}\right). \qquad (4)$$

A is the exchange energy per electron spin moment, k is Boltzmann's constant, Z is the number of electron spins per atom participating in the ferromagnetism and C is a coefficient dependent on the type of lattice.

It would appear feasible to evaluate from (2) and (3) not only the probable value of the paraprocess susceptibility but also a quantity proportional to the exchange integral. It should be noted, however, that measurement of the paraprocess susceptibility is fraught with great difficulties.

Furthermore, we feel that investigations of this kind are important for the following reasons. The saturation magnetization and the Curie point are important magnetic characteristics. The problem of determining these characteristics, however, has so far not been satisfactorily solved. For example, most investigators in determining the saturation magnetization, make use of the law of approach to saturation in the form $J = J_0(1 - AH^{-1})$. Yet the validity of this procedure is open to question and will remain so until we know exactly which magnetization processes are responsible for the behavior of different ferromagnetic materials in the region of strong fields.

The present work was devoted to investigation of the magnetic susceptibility of solid solutions in the region of high fields at different temperatures.

Experimental procedure

In recording the magnetization and susceptibility curves at room temperatures, we used the electromagnet and followed the procedure described in earlier contributions.[10,11] Most of the measurements at room temperature were carried out in fields of up to 10,000 oersted.

For measuring the temperature dependence of the magnetic susceptibility we used a solenoid with oil cooling capable of producing a fairly uniform field of up to 4500 oersted in the useful gap.

With the measuring coil and galvanometer employed in the experiments, the sensitivity as regards measurement of ΔJ was 0.05 gauss/mm, that for ΔH was 1 oersted/mm. The total uncertainty in determining the susceptibility taking into account all possible sources of error could not exceed 10-12% in the worst case. Actually, the scatter of permeability values was much less, since the resultant permeability values were based on the average for 10-12 measurements at each point.

The samples for the measurements in the electromagnet were made in the form of cylinders 42 mm in length and 6 mm in diameter. The samples for the temperature dependence measurements were made in the form of ellipsoids of revolution with a major axis of 70 mm and a minor axis of 7 mm.

Results of measurement

For analyzing the experimental values of the susceptibility we used Eq.(1) (taking into account the field dependence of the paraprocess susceptibility) in the following form

$$\left(\chi - \frac{a}{H^3}\right) \cdot H^2 = b + CH^{3/2}. \qquad (5)$$

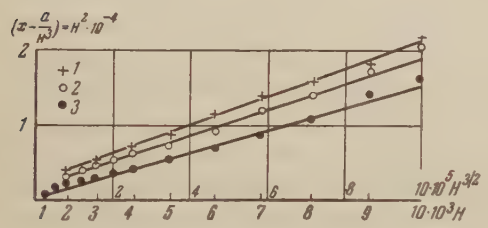

Fig.1. Variation of $\left(\chi - \frac{a}{H^3}\right) \cdot H^2$ with $H^{3/2}$ for Fe-Si alloys: 1) 2% Si, 2) 4% Si, 3) 6% Si.

It will be seen from Fig.1 that for alloys of the Fe-Si system in the region of strong fields the term on the left in Eq.(5) is a linear function of $H^{3/2}$ and that the coefficient b decreases very slowly with increasing Si concentration.

As the temperature is reduced from 290 to 77°K the coefficient a increases slightly. The paraprocess susceptibility and the coefficient b did not change in this temperature range within the limits of our experimental accuracy. Analogous regularities were observed for the paraprocess susceptibility χ_p and the coefficient b for alloys of the Ni-Cu system. The results of our measurements are summarized in the table.

The regularities observed for the Fe-Mo and Fe-W systems are entirely different. The value of the coefficient b for these alloys differs markedly from that for pure iron and increases with increasing impurity (Mo or W) concentration. Thus, whereas in the case of the Fe-Si alloy with 6% Si, $b = 0.02 \cdot 10^4$, for the Fe-W alloy with 6% W, $b = 1.0 \cdot 10^4$. The paraprocess susceptibility in these alloys, however, remains constant within the limits of our measurement error. We were note able to detect in our experiment the possible weak influence of Mo or W impurity atoms on χ_p. This is explained by the far stronger influence of the bH^{-2} term.

Table 1

Principal magnetic characteristics of the investigated ferromagnetic materials

№	Material	J_{290}	J_{77}	$a_{290}\cdot10^{-6}$	$a_{77}\cdot10^{-6}$	$b_{290}\cdot10^{-3}$	$c_{290}\cdot10^{3}$	$k^{eff}_{290}\cdot10^{-5}$*	$k^{eff}_{77}\cdot10^{-5}$*
	Alloy Fe-Ni, % Ni								
1	0	1700	1740	14,0	24,4	3,0	2,0	4,0	5,3
2	10	1670	1710	8,4	14,2		—	3,0	4,0
3	21	1600	1680	2,1	4,3		—	1,5	2,2
4	34	970	1110	—	—	3,0	8,2	—	—
5	48	1280	1330	—	—	1,0	4,3	—	—
6	58	1110	1160	—	—	0,5	3,0	—	—
7	71	960	1000	—	—	0,1	1,5	—	—
8	78	820	855	0,08	0,20	0,1		0,1	0,5
9	91	670	700	0,21	51,0	0,1	1,5	0,3	2,4
10	100	490	510	0,78	86,0	0,1	1,4	0,50	5,2
	Alloy Fe-Si, % Si								
11	1,2	1670	1710	10,7	18,0	0,2	1,8	3,5	4,5
12	1,59	1650	1685	8,9	13,0	—	—	3,2	3,8
13	2	1630	1670	6,3	9,5	—	—	2,6	3,4
14	3	1585	1610	3,6	7,2	0,15	1,6	2,1	2,7
15	4,5	1510	1535	2,9	4,3	—	—	1,7	2,1
16	6	1460	1500	2,3	3,2	0,1	1,3	1,5	1,8
	Alloy Ni-Cu, % Cu								
17	2	460	495	0,67	62,0	0,1	1,4	0,45	4,5
18	4,3	430	470	0,57	39,5	0,1	—	0,4	3,5
19	5,8	400	435	0,34	31,0	0,1	1,0	0,3	3,0
20	10	360	400	0,26	15,2	0,1	0,83	0,25	2,0

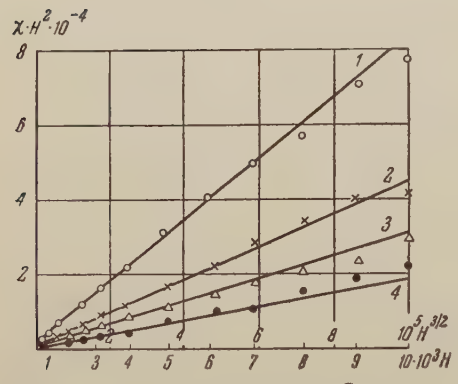

Fig.2. Variation of χH^2 with $H^{3/2}$ for alloys of the Fe-Ni system at 20°: 1) 33% Ni, 2)48% Ni, 3) 58% Ni, and 4) 71% Ni.

The results of our susceptibility measurements at room temperature for the Fe-Ni system are shown in Fig.2. It will be seen that in the range of fields from 600 to 10,000 oersted χH^2 varies linearly with $H^{3/2}$. The term aH^{-3} does not play a significant part in this field range. The paraprocess susceptibility increases with Fe concentration and attains its maximum value in the alloy containing about 30% Ni. As the nickel concentration is reduced from 100 to 30% the susceptibility in a 10,000 oersted field at 290°K increases from $2\cdot10^{-4}$ to $47.0\cdot10^{-4}$ gauss/oersted.

The law of approach to saturation holds also at low temperatures. This is evinced by the results of measurements on the alloy containing 33% Ni shown in Fig.3. The susceptibility of this alloy decreases with decreasing temperature in a wide range of magnetic fields.

Now let us see what influence ordering has on the character of the magnetization curve in the region of strong fields. We showed earlier[10] that in alloys having a composition close to Ni_3Mn, a high paraprocess susceptibility obtains even at room temperature. In order to check this further we deemed it desirable to investigate the temperature dependence of the susceptibility in different magnetizing fields. Hence in the present series of experiments we measured the susceptibility in the temperature range from 393 to 77°K in fields ranging up to 4500 oersted.

*Effective values of the anisotropy constant at 290° and 77° K.

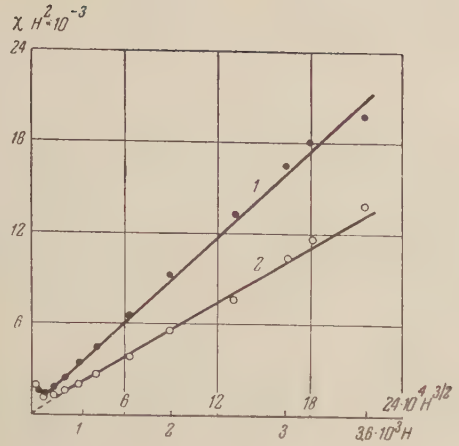

Fig.3. Variation of χH^2 with $H^{3/2}$ for alloys containing 33% Ni: 1) 290°K and 2) 77°K.

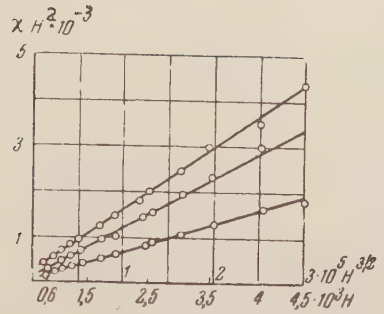

Fig.4. Variation of χH^2 with $H^{3/2}$ for alloys having a composition close to Ni_3Mn in the ordered state: 1) 393°K, 2) 290°K and 3) 77°K.

The results of measurements on the Ni_3Mn composition alloy in the ordered state are shown in Fig.4. It will be seen that in the range of fields in question the susceptibility consistently increases with increasing temperature. This variation is characteristic of the paraprocess susceptibility. It is interesting to note that in the ordered solid solution the coefficient b differs markedly from its value for pure nickel both as regards absolute magnitude and its temperature dependence. Thus for the Ni_3Mn composition alloy at 77°K, $b = 0.10 \cdot 10^5$, while at 393°K $b = 0.25 \cdot 10^5$, whereas for pure nickel $b = 150$.

Discussion of the results

Our experimental investigations of the magnetic susceptibility in different solid solutions in a wide range of magnetic fields and at different temperatures showed that the law of approach to saturation is generally borne out by experiment. The constant entering into the expressions deriving from this law are determined by the different magnetization processes and depend significantly on the nature of the impurity atoms.

The term aH^{-3}. The term aH^{-3} has been explained theoretically on the basis of the concept of rotation of the spontaneous magnetization vector; it has been shown that it must be determined by the crystallographic anisotropy energy and the magnetoelastic energy.[3,12] Numerous experimental investigations performed on pure metals and on certain alloys at different temperatures clearly substantiate this. The good agreement of the results of measurements on the magnetic anisotropy constant of Ni and Fe and of the results of our measurements of the constants of Fe-Si alloys with the values calculated on the basis of measurements on single crystals indicate that the law of approach to saturation is valid and useful for evaluating these parameters. It should be noted, however, that the values of the magnetic anisotropy constant so obtained are somewhat lower than the values measured on single crystals. It has been suggested that one of the possible reasons for this divergence is the influence of the magnetic interaction between the individual grains of the polycrystalline material[13,14] which is not taken into account in the expression for a. We shall not enter into a discussion of this problem 1) because there is little point in discussing the matter until we have more thorough investigations of this type on single crystals, 2) because there are also appreciable discrepancies between the values of the anisotropy constant

measured on single crystals by different procedures and 3) because it is still not known which magnetization processes are responsible for the behavior of a single crystal in strong fields when it is magnetized in different crystallographic directions.

Recently the law of approach to saturation has been refined by the introduction of a term $C'H^{-4}$, which allows of determining the sign of the anisotropy constant[15]. The coefficient C' is proportional to the anisotropy constant to the third power. Consequently, in the case of nickel this term must play a significant role at low temperatures. This is the case where it would appear feasible to determine its influence with the greatest accuracy. Analysis of our experimental results at 77°K as well as of the results of Polli, however, failed to substantiate the existence of this term.

The term bH^{-2}. This term in the law of approach to magnetization is due to the presence in the ferromagnetic material of supplementary forces which act to oppose attainment of saturation.

In general there are observed three kinds of regularities as regards the influence of impurity atoms on the coefficient b. In Fe-Si, Fe-Ni, Ni-Cu and certain other systems the coefficient b is small and comparable with its value for pure ferromagnets. In most of these alloys this coefficient decreases with increasing impurity concentration. In contrast, in alloys of the Fe-W, Fe-Mo and Ni-Mo systems, b increases with increasing concentration. Investigations of the temperature dependence indicate that in these alloys b is weakly dependent on the temperature. The third regularity is observed in the alloy having the composition Ni_3Mn in the ordered state and in some alloys of the Fe-Ni system. Here the value of the coefficient b is appreciably greater than in the other enumerated alloys and is strongly dependent on the temperature.

Theoretical interpretations of the term bH^{-2} have been given in the work of Brown[4] and Néel[5]. According to Brown highly inhomogeneous stresses localized in small volumes (dislocations) may be one of the factors responsible for the deviation of magnetization from saturation and, consequently, giving rise to the term bH^{-2}. Hence from this point of view the extraneous impurity atoms incorporated into the alloy solid solution lattice should be responsible for the appearance of this term. This is the view we held formerly[16]. The results of the present investigation show, however, that the mechanism of the influence of impurity atoms on the coefficient b is far more complex than has hitherto been supposed. Serious difficulties arise in attempting to explain the observed regularities in the framework of this theory. As it stands the theory cannot explain why different impurity atoms have a different effect on the value and temperature dependence of the coefficient b. The observed differences certainly cannot be explained by geometric differences in the size of the impurity atoms, i.e., the magnitude of the distortions introduced by impurity atoms of different size in the host lattice. Such distortions should also obviously affect the term aH^{-3} through the magnetoelastic constant. Nor is it feasible at present to explain the observed regularities from the standpoint of Néel's theory[5].

It is difficult to decide on the basis of the presently available scant experimental data whether the observed increase in the coefficient is characteristic of impurity atoms pertaining to the transition metals. There is a wealth of material on the problem in the work of Mariam, Fallot and Sadron (Ref.18-20) concerning measurements of magnetization in strong fields. Unfortunately, only constants obtained by extrapolation of the magnetization to $H \rightarrow \infty$ from the Weiss law $J = J_s(1 - AH^{-1})$ are given in these references. The results of the present investigation show rather convincingly that this law holds only in a rather limited range of magnetic fields. Hence without further verification, the results of such extrapolation remain open to question.

The term χ_p. Our present experimental investigation of the temperature dependence of the susceptibility in different magnetizing fields substantiated our earlier inference that in the region of high fields (where the terms with a and b are relatively unimportant) the observed variation of magnetization is due primarily to the paraprocess.

The linear variation of the paraprocess susceptibility with $H^{-1/2}$ for the investigated alloys is apparently a general regularity in the region of strong fields. This dependence must also obtain with fair accuracy for some alloys of the Fe-Ni system and also for the alloy of composition to Ni_3Mn in ordered state. One must, however, note the following. In the Ni_3Mn alloy in the ordered state in the range of fields from 200 oersted up, we are dealing with true magnetization (this is evidenced by the temperature measurements). Consequently, in this case, the susceptibility should vary linearly with $H^{-1/2}$. Actually, however, this dependence holds only in a limited field range. An analogous regularity is observed in some alloys of the Fe-Ni system. The deviation observed in the given case is due to the appreciable influence of the second term in the susceptibility equation (2). In other cases deviations from this dependence are difficult to detect for two reasons: first, the magnitude of the paraprocess susceptibility is small and, second, the weak field dependence of the susceptibility is masked by the stronger influence of the other terms in the law of approach to saturation from the side of weak fields.

Our experiments have made it possible to check the deductions from quantum mechanical theory regarding the temperature dependence of the susceptibility. Such verification is feasible only in the case of materials in which the paraprocess susceptibility is sufficiently large. In our case it probed feasible to do this in the case of the alloy having the composition close to Ni_3Mn and some of the Fe-Ni alloys that have Invar attributes[21,22]. If the law of Eq.(3) is valid for alloys, the expression for the susceptibility in a constant field can be written in the form

$$\chi = \frac{J_0 - J_{T0}}{J_0} \cdot P\left(\frac{1}{T}\right)^{3/2} = P\left(\frac{T}{\theta'}\right)^{3/2}\left(\frac{1}{T}\right)^{3/2} = P\frac{1}{\theta'} \cdot T.$$

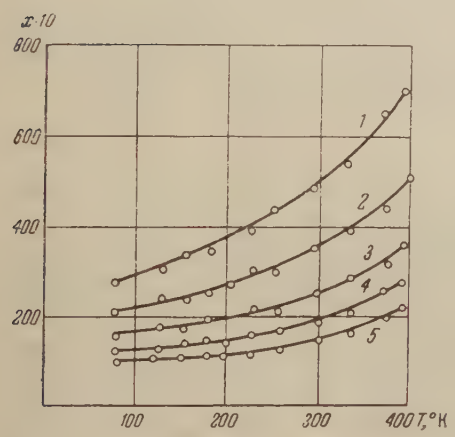

Fig.5. Temperature dependences of the susceptibility of the Ni_3Mn composition alloy in the ordered state in different fields: 1) H = = 1000, 2) 1500, 3) 2000, 4) 3000, and 5) 4000 oersted.

It follows from the above expression that the paraprocess susceptibility should increase linearly with temperature. Our experiments fail to substantiate this regularity in the temperature range from 77 to 290°K in different magnetizing fields. To be convinced of this one need only examine the results for the Ni_3Me alloy shown in Fig.5. Similar temperature dependences of the susceptibility are observed for Fe-Ni alloys with a high value of χ_p.

A natural question is: what is the reason for the observed deviation? It is difficult at present to give a definite answer. Possibly, the observed deviation is evidence of the inadequacy of the theory of Holstein & Primakoff[9]. There is yet another possibility. One cannot as yet unambiguously evaluate the validity of the deductions from quantum theory regarding the temperature dependence of the spontaneous magnetization. Investigations here encounter a serious difficulty. As was noted above, the problem of determining the spontaneous magnetization has not been satisfactorily solved. The

lack of a reliable procedure for determining the spontaneous magnetization and the nonavailability of susceptibility measurements in the region of low temperatures make it difficult to carry out a conclusive comparison of experimental results with deductions of theory.

One can on the basis of Eq.(2) give an evaluation of the paraprocess susceptibility to be expected according to the Holstein-Primakoff theory. In the case of the pure ferromagnets Fe and Ni, our results are also in good agreement this theory[9]. The lack of the necessary magnetization values makes it difficult to carry out an analogous comparison for the alloys investigated by us and, particularly, for the alloys with an anomalously high value of the paraprocess susceptibility. It is impossible on the basis of the information now available to propose a plausible explanation of the anomalously large value of χ_p and its temperature dependence observed in our experiments.

Faculty of Experimental Physics
"A.M.Gorkii" Ural State University

References

1. S.V.Vonsovskii & Ia.S.Shur, Ferromagnetizm (Ferromagnetism), M.-L.,1948.
2. S.V.Vonsovskii, Sovremennoe uchenie o magnetizme (Modern Magnetism),1952
3. N.S.Akulov, Ferromagnetizm (Ferromagnetism), M.-L., 1939.
4. W.F.Brown, Phys.Rev., 53, 736 (1940); 60, 139 (1941).
5. L.Neel, J.Phys.et Rad., 5, 184 (1948).
6. N.S.Akulov & I.M.Puzei, Izv.AN SSSR, Ser.fiz., 5, 533 (1941).
7. N.S.Akulov & K.M.Bol'shova, Zhur.tekh.fiz., 19, 8 (1949).
8. K.M.Bol'shova, Izv.AN SSSR, Ser.fiz., 16, 5, 598 (1952).
9. T.Holstein & H.Primakoff, Phys.Rev., 58, 1098 (1940).
10. V.V.Parfenov, Izv.AN SSSR, Ser.fiz., 16, 601 (1952).
11. R.I.Ianus & V.V.Parfenov, Izv.AN SSSR, Ser.fiz., 16, 611 (1952).
12. N.S.Akulov, L.V.Kirenskii, Zhur.tekh.fiz., 9, 1945 (1939).
13. L.Neel, J.Phys.et Rad., 8, 9, 184 (1948).
14. T.Holsten & H.Primakoff, Phys.Rev., 59, 388 (1941).
15. L.V.Kirenskii & L.I.Slobodskoi, Doklady AN SSSR, 69, 639 (1949).
16. V.V.Parfenov & Iu.V.Shumkov, FMM (Physics of Metals & Metallography), I, 427 (1955).
17. Ia.G.Dorfman, Magnitnye svoistva i stroenie veshchestva (Magnetic properties and the structure of matter), 1955.
18. V.Mariam, Ann.de Phys., 7, P459 (1937).
19. M.Fallot, Ann.de Phys., 6, P305 (1936); 7, 420 (1937); 10, 291 (1938).
20. C.Sadron, Ann.de Phys., 17, 10, 371 (1932).
21. K.P.Belov, Uprugie, teplovye i elektricheskie iavleniia v ferromagnitnykh metallakh (Elastic, thermal and electric effects on ferromagnetic metals), 1951.
22. V.V.Parfenov & V.P.Voroshilov, Present issue of the Bulletin, p.1319.

INFLUENCE OF ELASTIC DEFORMATION ON THE PARAPROCESS SUSCEPTIBILITY

- V.V.Parfenov & V.P.Voroshilov

One of the more important questions in the modern theory of magnetization is that of the influence of mechanical factors on the saturation magnetization. Variation of the interatomic distances under the influence of mechanical factors must necessarily affect the exchange interaction energy to some extent and, consequently, the magnitude of the saturation magnetization. Until recently it has been assumed that unilateral deformation under tension, i.e., stretching, has no such effect provided no changes in phase composition occur in the material.

Belov[1] used a new and original procedure for investigating this question and showed that stretching can change the saturation magnetization. In the case of certain alloys of the Fe-Ni system characterized by a high paraprocess susceptibility the effect can be observed from the change in the magnetization curve even at room temperature.

If the observed change in saturation magnetization is actually due to elongation induced changes in the interaction energy, rather than to changes in phase composition, these alterations must be manifested in the paraprocess susceptibility.[2] To check this we carried out some experiments to determine the influence of elastic deformation under tension on the paraprocess susceptibility. By way of material we chose molybdenum permalloy and Invar. This choice made it possible to investigate the process in relatively weak fields where changes of magnetization are caused exclusively by the paraprocess.

The samples were prepared in the form of wires 300 mm in length and 2.5 mm in diameter. The magnetic susceptibility measurements were carried out in a 1000 mm long solenoid which provided a satisfactorily uniform field in the working volume. We followed the measuring procedure described in Refs. 3 & 4. All measurements were made at room temperature with no load and with a load of 5 kg/mm^2. Heavier loads resulted in irreversible changes in the variation of the susceptibility. The uncertainty in the susceptibility measurements, taking into account all possible sources of error, did not exceed 2% where the Invar samples are concerned. Actually, the spread of susceptibility values was appreciably smaller inasmuch as the final values were obtained by averaging the data from a number of measurements. In the case of the molybdenum permalloy the uncertainty was somewhat greater.

Results

The experimental results are shown in the accompanying table. In the case of the investigated materials we did not detect any noticeable change in the paraprocess susceptibility under the influence of stretching in the elastic region. Our investigation of the temperature dependence of the susceptibility clearly proved that in the magnetic field range in question the observed changes in susceptibility are due to the paraprocess. Here the susceptibility increases with increasing temperature. Changes in susceptibility under the influence of tensile loads are observed only in the region of very weak fields where true magnetization plays a relatively insignificant role.

Our negative results as regards the influence of stretching on the paraprocess susceptibility and, consequently, on the interaction energy may be ascribed to inadequate experimental accuracy. Unfortunately, there are no data in the literature that would allow of evaluating the effect even qualitatively. It must be noted, however, that if the effect amounted to at least 2% of the measured quantity (the permeability), we would have been able to detect it in investigating the Invar alloy. It must be concluded, therefore,

H	Susceptibility · 10^4 gs/oers.				H	Susceptibility · 10^4 gs/oers.			
	Permalloy		Invar			Permalloy		Invar	
	$\sigma=0$	$\sigma=4{,}2$ кг мм$^{-2}$	$\sigma=0$	$\sigma=5{,}2$ кг мм$^{-2}$		$\sigma=0$	$\sigma=4{,}2$ кг мм$^{-2}$	$\sigma=0$	$\sigma=5{,}2$ кг мм$^{-2}$
950			42,0	42,0	350	23,0	23	163	170
900			43,5	43,5	300			220	240
850	10,5	10,5	45,5	45,5	250	30,5	30,5	300	350
800			48,0	48,0	200	39,5	39,5	680	790
750			51,0	51,0	140	62,5	62,5	—	—
700	12,0	12,0	54,5	54,5	70	156	156	—	—
650			59,0	59,0	35	350	350	—	—
600	13,8	13,8	62,0	62,0	20	690	690	—	—
550			73,5	73,5	15	1080	1080	—	—
500	16,5	16,5	86,5	86,5	13	1400	1400	—	—
450			104,0	104	10,4	1870	1890	—	—
400	20,5	20,5	128	130					

that this effect, if it exists, is small, i.e., too weak to be detected by the procedure employed by us.

In studying this question one should also bear in mind the following. In principle any change in interatomic separation produced by straining the material should lead to a change in the interaction energy and, consequently, in the paraprocess susceptibility. This reasoning is valid provided the investigated material is isotropic. Actually, however, polycrystalline ferromagnets are never entirely homogeneous as regards structure. Obviously, the presence of grains of different shape, size and orientation and of interactions between them must appreciably complicate the mechanism of the influence of stretching on the interaction energy responsible for the spontaneous magnetization. One can hardly imagine that when a polycrystalline specimen is subjected to tensile stress in the elastic region all the volumes of the individual crystallites will change in exactly the same way. Hence if the effect does exist the presence of polycrystalline structure must undoubtedly complicate the mechanism whereby the elastic deformation affects the interaction energy.

The situation is even more complicated in the case of Invar. Here the effect of influence of unilateral extension on the saturation magnetization attains an appreciable magnitude.[1] The paraprocess susceptibility, however, does not change under the influence of stretching at least within the limits of our experimental accuracy. On the basis of the information now available it is difficult to draw any unambiguous inferences regarding the effect of mechanical deformation on the saturation magnetization of this alloy. It is not impossible that the observed not inconsiderable changes in the saturation magnetization in Invar under the influence of mechanical stress are due not to changes in interatomic separation but to other factors, for example, changes in the phase composition. Admittedly, we have no direct evidence at present that such changes occur. It is to be hoped that further investigations of these alloys will help clarify this question that is of such great importance for the theory of ferromagnetism.

Faculty of Experimental Physics,
"A.M.Gorkii" Ural State University

References

1. K.P.Belov, Uprugie, teplovye i elektricheskie iavleniia v ferromagnitnykh metallakh (Elastic, thermal and electric effects on ferromagnetic metals), M., 1951.

2. T.Holstein & P.Primakoff, Phys.Rev., 58, 1098 (1940).

3. R.I.Ianus & V.V.Parfenov, Izv.AN SSSR, Ser.fiz., 16, 611 (1952).

4. V.V.Parfenov, Izv.AN SSSR, Ser.fiz., 16, 601 (1952).

BULLETIN OF THE ACADEMY OF SCIENCES OF THE USSR - Physical Series
Vol.21, No. 9
Transactions of the Third Conference on the Physics of Magnetic Phenomena
(Continued from Vol.21, Nos. 6 and 8)

TABLE OF CONTENTS

	Page Orig.	Trans
Characteristics of technical magnetization in grain-oriented fine powder specimens - Ia.S.Shur, E.V.Shtol'ts & G.S.Kandaurova	1215	1205
Investigation of dissociation in an Ni-Be alloy - N.N.Buinov, L.I.Podrezov & M.F.Komarova	1220	1210
Changes in the structure and properties of nickel solid solutions during heat treatment - B.G.Livshits	1225	1216
Structure of Fe-Ni-Al alloys in the high coercivity state (Abstract) - B.G.Livshits & V.S.L'vov	1232	1223
Magnetic investigation of ordering in Ni_3Mn-base alloys (Abstract) - B.G.Livshits & B.V.Molotilov	1233	1224
Kinetics of superstructure transformations of Fe_3Al alloy - V.E.Rode	1234	1225
Magnetic properties of ordered Fe_3Al alloy (Abstract) - V.I.Ivanovskii	1239	1229
Residual magnetization of nickel and its stability - Ia.S.Shur & I.E.Startseva	1240	1229
Influence of plastic deformation on the Barkhausen effect - K.Wotruba	1246	1235
Investigation of reversal of magnetism (Barkhausen) jumps in ferromagnets - V.F.Ivlev, V.L.Il'iushenko & L.I.Aseeva	1250	1239
On the structure of the family of symmetrical hysteresis loops of ferromagnets - R.I.Ianus & V.P.Kartashev	1255	1244
Temperature and rotational hysteresis in ferromagnets - L.V.Kirenski A.Ia.Vlasov, N.I.Vtiurin, A.I.Drokin, V.F.Ivlev & R.I.Tukalov	1262	1251
Hysteresis losses in rotating magnetic fields in a magnetite single crystal before and after phase transition - N.L.Brukhatov	1268	1257
Influence of elastic stresses and thermomechanical treatment on the magnetic properties of high coercivity alloys - Ia.S.Shur, M.G.Luzhinskaia & L.A.Shubina	1275	1263
Magnetization viscosity of Ni-Zn ferrites with free variation of the magnetization (Abstract) - I.A.Lednev & R.V.Telesnin	1280	1267

	Page Orig.	Trans.
On the decay of magnetic permeability in silicon iron - Iu.S.Vail'	1281	1268
Some magneto-optical effects at microwave frequencies - N.N.Nepremerov	1288	1275
Magneto-optical properties of ferromagnets in the infrared region - G.S.Krinchik	1293	1279
Contribution to the theory of the Kerr and Faraday effects at radiofrequencies - G.V.Skrotskii & V.F.Zakharchenko	1297	1283
Measurement of the initial permeability of ferromagnets in the microwave region - G.S.Sanyal	1302	1288
Radiofrequency magnetic spectra of mixed ferrites - L.A.Fomenko	1310	1295
Magnetic spectra of magnetodielectrics of the Alsifer type - L.A.Fomenko	1318	1303
Ferroprobe magnetometer for investigating the properties of small samples of magnetically soft materials - V.I.Drozhzhina and L.A.Fridman	1320	1305
Magnetic moments and Curie constants of ferromagnetic alloys - F.M.Gal'perin	1323	1308
Investigation of the magnetic susceptibility of iron and nickel base solid solutions - V.V.Parfenov	1327	1312
Influence of elastic deformation on the paraprocess susceptibility - V.V.Parfenov and V.P.Voroshilov	1334	1319

Translated in 1958 by
Columbia Technical Translations
5 Vermont Ave., White Plains, N.Y.

Number 10 Volume 21 1957

BULLETIN

of the

Academy of Sciences of the USSR

- Physical Series -

(Izvestiia Akademii Nauk SSSR)
(Seriia fizicheskaia)

Reproduction rights reserved

by

Columbia Technical Translations
5 Vermont Avenue
White Plains, New York

Single Issues

$20

Annual Subscription

$215

SOVIET PHYSICS AT THE FORTIETH ANNIVERSARY OF THE OCTOBER REVOLUTION

To arrive at a correct evaluation of the state of the physical sciences in the USSR forty years after the revolution it is not enough to look at absolute figures: the past 40 years brought qualitative as well as quantitative changes.

There were many outstanding names in pre-revolutionary science in Russia: Lomonosov and Lenz, Mendeleev and Stoletov, Lebedev and Golitsen, Petrov and Belopol'skii, Umov and Tsiolkovskii, Popov and Zhukovskii, Iakovi, Lodygin - inspired prophets, skilled experimenters and brilliant inventors. But all these were single isolated individuals. Organized planned research virtually guaranteeing eventual solution of any problem - the situation so characteristic of present day physics - could only be dreamed of.

No positive discipline, no science capable of benefitting humanity can develop by the endeavors of merely a score of even brilliant scientists. The history of physics is not a list of famous names or even an enumeration of brilliant discoveries. The history of science is the history of laboratories and institutes, universities and academies, journals and conferences. The spurt in the development of Russian physics after 1917 is characterized primarily not by the appearance of new academicians and laureates, but by the initiation of organized education, organized research and organized scientific effort. Such organization could be provided for only by the Soviet Government.

The need for creating a Russian scientific school was clear long ago. We know that Lomonosov placed great value on the organization of research at the University and the Academy of Sciences, but his ideas were too ambitious for his age. Mendeleev elaborated far-reaching plans for linking science with practice, but the plans of the discoverer of the periodic system were too radical for the bureaucrats and functionaries of his epoch.

The only one who had any luck in creating a physical school in pre-revolutionary Russia was Peter Nikolaevich Lebedev, but his remarkable cooperative society of scientists soon disintegrated in the reactionary atmosphere of Tsarist times.

Then came the Revolution. The fundamental rebuilding of all aspects of Russian life extended to science. In the first few years after the Revolution there were created three physical institutes: The Institute of Physics and Biophysics in Moscow (headed by P.P.Lazarev), the Physical-Technical Institute (A.F.Ioffe) and the Optical Institute (first under D.S.Rozhdestvenskii and then under S.I.Vavilov) in Petrograd. The following years were marked by the opening of the Electrotechnical, Aerodynamical and Physical-Chemical Institutes.

From the very beginning these new institutes were regarded as the bases of technical progress, as the scientific foundations for the development of socialist industry. With every year the ties between science and practice developed and strengthened. Subsequently, during the years of the Great War this close association between science and industry made it possible for most scientific collectives to devote their full energies to the solution of defense problems.

Simultaneously with the organization of research there began the reorganization of science education. A physical-mechanical department was opened at Leningrad Polytechnic Institute and physics faculties were organized in Leningrad and Moscow State Universities. The graduates of these departments and faculties were trained for scientific work in the new and expanding older physics laboratories. Thus there were prepared cadres of

new scientific workers differing as much from the prerevolutionary generation of Russian physicists as the workers and engineers of modern large-scale industry differ from the artisans of the middle ages. The new social order gave rise to new more perfect forms of organization of labor and this could not but extend to the organization of scientific work.

The principal physical schools and directions emerged clearly even in the first 10-15 years of the Soviet regime. Among these we have first the Leningrad School of A.F. Ioffe which concentrated its efforts on the problems of solid state physics. The first fruitful achievements of this school include P.E.Lukirskii's investigation of electronics and the photoeffect, the work of A.F. Ioffe and I.V.Obreimov on single crystals, and the theory of thermal breakdown of dielectrics of N.N. Semenov and V.A.Fok. This, too, was the period of the brilliant work of A.A.Fridman on the theory of relativity.

Another large physics school was that of the spectroscopists headed by D.S.Rozhdestvenskii, whose method of "hooks" is still widely used in studying dispersion. Soviet optical and light engineering and the domestic glass and optical instrument industries developed under the guidance and with the encouragement of D.S.Rozhdestvenskii and S.I.Vavilov. In Moscow the investigations of the Lebedev school expanded greatly under the leadership of P.P.Lazarev. The work done on magnetic anomalies and the ionic theory of excitation is particularly worthy of mention. Another adherent of this school was Iu. V.Vul'f, whose researches in crystallography have become world famous.

In Moscow new scientific approaches were explored by L.I.Mandel'shtam and his colleagues who worked primarily in the field of molecular physics. The principal achievement here was the discovery by Mandel'shtam and Landsberg of combined scattering of light [*the Raman effect*]. Worthy of mention, too, are the remarkable studies of Mandel'shtam, Papaleski and their students on nonlinear vibrations.

This initial period of Soviet physics also included the famous work of D.V.Skobel'tsyn on the investigation of gamma-spectra in a Wilson chamber in a magnetic field and the development of Ia.I.Fenkel's ideas regarding the movement of vacancies in a continuous medium (problems of thermoconductivity and diffusion) which subsequently led to the formulation of the concept of excited states of atomic electrons in crystals (excitons). Important studies in the field of magnetic spectroscopy of iron were carried out at the laboratory of V.K.Arkad'ev. A.A.Glagoleva-Arkad'ev and M.A.Levitskaia were the first to generate electromagnetic waves overlapping the infrared spectrum. An important discovery was made in the laboratory of S.I.Vavilov by P.A.Čerenkov: radiation emitted by electrons moving in a medium with a varying index of refraction. The theory this "Čerenkov effect" suggested was soon thereafter formulated by I.E.Tamm and I.M.Frank.

A new important physical school, the school of S.I.Vavilov on luminescence of liquids was formed during this period. S.I.Vavilov was also responsible for important investigations of weak light intensities and development of new luminophors, the phosphors upon which the production of "daylight" fluorescent lamps is based.

P.L.Kapitsa in the Institute of Physical Problems made a number of outstanding discoveries in the field of low temperatures (superfluidity of helium, etc.), theoretical interpretations for which were given by L.D.Landau and others.

I.V. and B.V.Kurchatov and P.P.Kobeko made significant progress in the investigation of the electrical analog of ferromagnetism: ferroelectricity. A further development of this work was B.M.Vul's investigation of barium titanates which play such an important role in modern engineering.

The researches of A.F.Ioffe's school on semiconductors also made important contributions in this field. Today semiconductors are one of the most intensively developing fields of practical and theoretical physics. Highly promising work is now being done in the field of semiconductor catalysis.

A large group of Ural physicsts headed by S.V.Vonsovskii is doing important work in the field of the physics of magnetic phenomena, in particular, they are successfully developing the theory of ferromagnetism and antiferromagnetism.

The work of the Kazan school of physicists led by E.K.Zavoiskii was crowned in 1944 by the discovery of paramagnetic resonance for which a Lenin prize has recently been awarded.

An important school of crystallography headed by A.V.Shubnikov was formed in Moscow.

The investigations of Soviet scientists in the field of nuclear physics date back to the Thirties. The contributions of Soviet scientists in this outstanding field of physical science include D.D.Ivanenko's hypothesis regarding the structure of the nucleus, the discovery of nuclear isomerism by I.V.Kurchatov, B.V.Kurchatov, L.I.Rusinov and L.V.Mysovskii, the work of A.I.Alikhanov on pair formation and annihilation of positrons, the cosmic ray studies of D.V.Skobel'tsyna, S.N.Vernov, V.I.Veksler, A.I.Alikhanov and A.I.Alikhanian and the theory of cosmic ray showers of L.D.Landau, I.E.Tamm and S.Z.Belen'skii. Here one must also mention the investigation of the Alikhanov brothers and B.S.Dzhelepov in the field of artificial radioactivity which served as the beginning of the intensive nuclear spectroscopy studies which are still being continued on an expanded scale today.

Of great importance for the development of physics was the theoretical work of I.E.Tamm, I.D.Landau, I.E.Pomeranchuk, Ia.I.Frenkel', V.A.Fok, N.N. Bogoliubov and many other outstanding Soviet physicists.

During the years of the War for the Defense of the Fatherland, Soviet physicists devoted all their forces, knowledge and capabilities to the defense of our country. Under trying war conditions our physicsts demonstrated their ability of combining a high level of theoretical investigation with operative solutions of urgent practical problems. Among these problems was that of radio location, based on fundamental discoveries made in our country back in the Nineteen Thirties by D.A.Rozhanskii and Iu.B.Kobazarev.

In the post war period, which brought the dawning of the atomic age, Soviet physicists moved another giant step forward.

The achievements of science cannot and should not, of course, be measured by listing the technical results attained by it. Nevertheless, we can justifiably cite a few significant facts.

The realization in the Soviet Union of a chain nuclear reaction, the construction of the first atomic electric power station in the world (for which the collective headed by D.I.Blokhintsev was awarded a Lenin prize), work on the realization of controlled thermonuclear reactions in a gas discharge (L.A.Artsimovich, M.A.Leontovich and A.D.Sakharov), the construction of the largest particle accelerator in the world - the 10 bev synchrophasotron (on the basis of the autophasing principle of V.I.Veksler), the creation of intercontinental ballistic rockets and, finally, the launching of the first artificial earth satellite, all these have been the achievements of the past 10-12 years! Increasingly rapid development of theoretical physics and mass penetration of physical methods into our socialist national economy and the methodology of allied scientific disciplines are the characteristic traits of this epoch of the flowering of Soviet physics.

Let us supplement this far from exhaustive list of the attainments of Soviet physics with a few figures.

In pre-Revolutionary Russia there were active about 100 physicists, only 20 of whom held doctor's degrees. Their yearly production of literature - about 100 reports (nearly half of which were essentially surveys or reviews) - required about nine thin issues of the only journal then published: the Journal of the Russian Physical-Chemical Society. Rare conferences of naturalists and physicians were the only occasions at which Russian physicists could meet and present papers.

Now the USSR Academy of Sciences alone publishes eleven physical journals (this number does not include numerous publications in allied fields). Several thousand specialists, including 300 doctors of physical and mathematical sciences report on their work in these journals.

By the Twenties, the general physical conferences initiated in the first years after the Revolution could no longer meet the needs of Soviet physicists. Hence regular conferences and meetings on special topics, ever more specialized and narrower, had to be called. Now we have yearly (and sometimes more frequent) conferences on atomic and molecular spectroscopy, magnetism, nuclear spectroscopy, cosmic rays, luminescence, x-rays, semiconductors, crystallography and many other branches of physics. Hundreds of reports are presented at these conferences by scientists from scores of large scientific research institutes, universities and colleges scattered through the major cities of the Soviet Union. Soviet physics today at the Fortieth Anniversary of the October Revolution is represented by the planned integrated work of this collective of many thousands of scientific workers.

TRANSACTIONS OF THE SECOND ALL-UNION CONFERENCE ON X-RAY SPECTROSCOPY

The Second All-Union Conference on X-Ray Spectroscopy was held in Moscow January 31 to February 4, 1957.

The following reports were presented at the Conference:

1. Opening address - Ia.S.Umanskii.

2. Analysis of the structure of x-ray emission spectra of ordering alloys - A.N.Orlov & A.V.Sokolov (Ural Branch, USSR Academy of Sciences).

3. Width of the inner levels and density distribution of electron states in elements of the iron transition group - M.A.Blokhin & V.P.Sachenko (Rostov State University).

4. X-Ray spectroscopic method of investigating the electron state distribution in metals and alloys - N.D.Borisov, V.V.Nemoshkalenko & A.M.Fefer (Institute of Metal Physics, Ukrainian SSR Academy of Sciences).

5. On the state of atoms in ferromagnetic iron, cobalt and nickel base alloys - I.Ia.Dekhtiar (Institute of Metal Physics, Ukrainian SSR Academy of Sciences).

6. Modern methods of recording x-ray spectra - M.A.Blokhin & A.I.Froiman (Rostov State University and Chemistry Faculty, Moscow State University).

7. X-Ray equipment power supplies with high stability characteristics - A.I.Froiman (Chemistry Faculty, Moscow State University).

8. Use of URS-50-I x-ray equipment as a double crystal spectrometer - I.B.Borovskii & V.V.Shmidt (Institute of Metallurgy, USSR Academy of Sciences).

9. Possibilities of using electrostatic recording (xerography) in x-ray spectroscopic and diffraction analysis - A.I.Froiman (Chemistry Faculty, Moscow State University).

10. On determining the density of electron states from x-ray spectra - I.Ia.Nikiforov (Rostov Institute of Agricultural Machinery Engineering).

11. Investigation of the fine structure of the K absorption and emission spectra of some elements of the iron group - I.B.Borovski, V.P.Bykov & A.I.Kozlenko (Physics Faculty, Moscow State University).

12. Correlation between certain x-ray spectroscopic and magnetic characteristics of iron base alloys - S.A.Nemnonov & K.M.Kolobova (Ural Branch, USSR Academy of Sciences).

13. X-Ray spectroscopic investigation of chemical composition in microvolumes of alloys - I.B.Borovskii, N.P.Il'in, L.E.Loseva, I.D.Marchukova & A.N.Deev (Institute of Metallurgy, USSR Academy of Sciences).

14. Investigation of bond strengths in Fe-Mo solid solutions from the fine structure of their x-ray absorption spectra - V.A.Trapeznikov and S.A. Nemnonov (Ural Branch, USSR Academy of Sciences).

15. Contribution to the theory of transition metal solid solutions - I.B.Borovskii & K.P.Gurov (Institute of Metallurgy, USSR Academy of Sciences).

16. X-Ray spectroscopic investigation of (Cr-base) solid solutions - I.B.Borovskii, K.P.Gurov, S.A.Ditsman, V.A.Batyrev & N.D.Lobanova (Institute of Metallurgy, USSR Academy of Sciences).

17. Influence of thermal vibrations of atoms on the electron energy distribution in metals and alloys - I.B.Borovskii & G.N.Ronami (Physics Faculty, Moscow State University).

18. Temperature and concentration dependence of the fine structure of x-ray absorption spectra of solids and investigation of bonding forces - V.A. Trapeznikov (Ural Branch, USSR Academy of Sciences).

19. Dependence of the x-ray absorption spectra of atoms in compounds on the character of the bonds - R.L.Barinskii, E.E.Vainshtein & K.I.Narbutt (IMGRE, GEOKhI & IGEM, USSR Academy of Sciences).

20. Investigation of the fine structure of x-ray absorption spectra of alkali halide compounds - I.S.Smirnova & K.I.Narbutt (IGEM, USSR Academy of Sciences).

21. K Absorption spectra of chlorine in alkali metal chlorides - R.L. Barinskii (IMGRE, USSR Academy of Sciences).

22. Effect of neutron irradiation on the fine structure of the K absorption spectrum of germanium - M.M.Kakhana & E.E.Vainshtein (GEOKhI, USSR Academy of Sciences).

23. L Series x-ray spectrum of germanium - G.P.Borikova & M.I.Korsunskii (Kharkov Polytechnic Institute).

24. Investigation of the L series x-ray spectra of some rare-earth element compounds - N.V.Troneva, I.D.Marchukova & I.B.Borovskii (M.S.U.) (Physics Faculty, Moscow State University).

25. Investigation of the Kβ emission lines of titanium in carbides and certain other compounds - E.E.Vainshtein & Iu.N.Vasil'ev (GEOKhI, USSR Academy of Sciences).

26. Influence of an activator on the x-ray absorption spectrum of a luminescent crystal - K.I.Narbutt & I.S.Smirnova (IGEM, USSR Academy of Sciences

27. L Absorption and emission spectra of molybdenum in molybdenum carbide and other compounds - R.L.Barinskii & E.E.Vainshtein (IMGRE & GEOKhI, USSR Academy of Sciences).

28. X-Ray spectroscopic investigation of the L spectra of molybdenum in some alloys and compounds - V.A.Batyrev, I.B.Borovskii & S.A.Ditsman (Institute of Metallurgy, USSR Academy of Sciences).

29. The $L\beta_6$ and $L\gamma_5$ lines in the spectra of Cu and Zn - I.A.Rumiantsev & M.I.Kosunskii (Khar'kov Polytechnic Institute).

30. Some spectral line satellites - T.I.Kakushadze (Georgian Pedagogical Institute).

31. X-Ray spectroscopic investigation of sulfurized samples - M.A.Blokhin, P.S.Nesterenko & A.T.Shuvaev (Rostov State University).

32. External screening and the fine structure of x-ray spectra - S.M. Karal'nik (Kiev State University).

33. Quantitative determination of titanium from secondary x-ray spectra - A.S.Ivoilov & N.F.Losev (Irkutsk State Institute of Rare Metals).

Part of these reports appears below.

Translation editor's note: No indication is given in the Russian Bulletin whether the reports not printed in the present issue of the Bulletin are being published elsewhere and, if so, where.

WIDTH OF THE INNER LEVELS AND DENSITY DISTRIBUTION OF ELECTRON STATES IN ELEMENTS OF THE IRON TRANSITION GROUP

- M.A.Blokhin & V.P.Sachenko

X-ray emission and absorption spectra yield direct information on the distribution in energy of electron states or more accurately speaking the quantity $N(E) \cdot P(E)$, where $N(E)$ is the density of states and $P(E)$ is the transition probability.

As has been shown by one of the present authors[1-3], for finding the actual form of the function $N(E)$ the x-ray spectra must be "corrected" for the distortions introduced by the finite width of the inner level participating in the transition (specifically, the K level). In order to apply this correction procedure, one must know the shape and width of the inner level. Numerous experimental and theoretical data indicate that K levels are characterized by the classical dispersion (Lorentzian) shape, at least in the case of other than the transition elements. This follows if only from the fact that the shape of the $K\alpha_{1,2}$ line of non-transition elements is closely approximated by a dispersion curve (see for example Refs.4 & 5). The above mentioned method of correcting x-ray spectra was developed in particular for this shape of the inner levels. The widths of the inner levels are known for only a very few elements. The available experimental data[6-12] on K level widths are summarized in Table 1.

Table 1

Experimental values of K level width

Element	γ, ev	Element	γ, ev	Element	γ, ev
12 Mg	0,5	27 Co	1,5	36 Kr	2,07
13 Al	0,35	28 Ni	1,9	47 Ag	8,0
18 Ar	0,58	29 Cu	1,3	74 W	37
19 K	0,73	30 Zn	1,5	79 Au	62
26 Fe	1,8	31 Ga	1,9		

The level widths determined by Beeman & Friedman[12] for the transition elements of the iron group cannot be regarded as correct inasmuch as the K absorption edge of these transition elements has a complicated character by virtue of the unfilled 3d shell which participates in the absorption. In this case application of the method of Richtmyer, Barnes & Ramberg[13] for determining the level width is unjustified.

In the present investigation we attempted to determine the width of the K levels of some elements of the iron transition group by interpolation of the experimental values of the K level widths for the non-transition elements listed in Table 1.

It is known that the level width γ is directly proportional to the probability P of transition of the atom from the given state. In determining the law characterizing the variation of the K level width with the atomic number, we took into account the two essentially different types of transitions, namely, radiative and nonradiative transitions. The total probability of an atom undergoing a transition from a given state is the sum of the radiative transition probability P_r and the nonradiative transition probability P_o.

Consequently,

$$\gamma = A(P_r + P_o). \qquad (1)$$

The specific numerical value of the coefficient A depends on the shape of the level. In particular for the dispersion (Lorentzian) shape, $A = 6.58 \cdot 10^{-16}$ (when γ is expressed in electron volts and P is the number of

transitions per sec). Hence finding the variation of the level width with the atomic number reduces to finding the dependence of P_r and P_o on the atomic number.

In view of the fact that an atom can leave a given state by different radiative and nonradiative transitions the probabilities will be given by the sums

$$P_r = \sum_{|E_k|>|E_n|} P_{kn} \text{ and } P_o = \sum_{E|_k|>|E_{nm}|} P_{k,nm},$$

where P_{kn} is the probability of a radiative transition from level k to level n and $P_{k,nm}$ is the probability of a nonradiative transition from level k to a double-ionization level nm.

For P_{kn}, calculation of the transition probability between two single-ionization levels yields the familiar relationship

$$P_{kn}(Z) \sim Z^4. \tag{2}$$

Consequently, in this approximation

$$P_r(Z) \sim Z^4. \tag{2a}$$

Taking into account the influence of screening of the electron shells on the probability P_{kn} leads to a somewhat different expression for the Z-dependence. Computations of the transition probabilities $P_{K,L_{II,III}}$ and $P_{K,M_{II,III}}$, carried out in the wave function approximation of Slater[14] using the formula

$$P_{kn} = \frac{32\pi e^2 \nu_{kn}^3}{3c^3 h} \left(\sum_{i=1}^{3} |X_{kn}^i|^2 \right),$$

where X_{kn}^i is the matrix element for the i-th coordinate, showed that these dependences are closely approximated by the expressions

$$P_{K,L_{II,III}} = BZ^{4,53} \text{ and } P_{K,M_{II,III}} = CZ^{4,83}. \tag{3}$$

The ratio $\varkappa$ of these probabilities can also be calculated from the experimental data on the relative intensities of the corresponding lines. The ratios calculated theoretically and from the experimental data show satisfactory agreement (Table 2).

Table 2

Comparison of the experimental and theoretical values of the ratio $\varkappa$ of the transition probabilities corresponding to the $K\alpha_{1,2}$ and $K\beta_{1,2}$ lines

Element	29 Cu	47 Ag	79 Au
$\varkappa_{exp}$	7,3	5,2	4,4
$\varkappa_{theo}$	5,8	5,0	4,2

Hence for finding the variation of P_r as a function of Z, we used the following method. For $K \rightarrow L_{II,III}$, we took the calculated dependence (3). For the other transitions, we based the evaluation on the experimental data obtained from the relative intensities of the corresponding lines. The dependence on Z deduced in this manner is closely approximated by the formula

$$P_r = DZ^{4,71}. \tag{4}$$

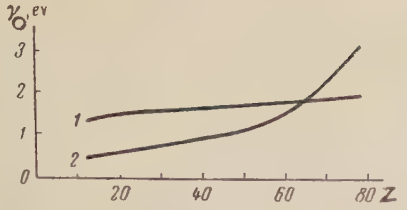

Fig.1. Variation of the nonradiative width γ_0 with the atomic number: 1) curve obtained theoretically and 2) curve obtained by means of Eq.(4) utilizing experimental K fluorescence yield values[26-31].

The nonradiative transition probability P_0 has been calculated for a number of elements by different authors and in different approximations.[17-23] The common deduction from these calculations is that P_0 is weakly dependent on Z, that is, the nonradiative transition probability appears to be virtually constant. The level width corresponding to these transitions is 0.8-0.9 ev. It should be noted that Massey & Burhop[19] calculated the probability of some nonradiative transitions taking into account relativistic corrections. The probability so evaluated is approximately twice the corresponding nonrelativistic value in the case of Au and three times the value in the case of Ag.

We felt it would be of interest to obtain the nonradiative transition probabilities for different elements, calculated in the same approximation. To this end we carried out calculations of the nonradiative probability for the K level. By way of wave functions of the electrons in the atom we took the wave functions of Slater[14]. We used a plane wave for the wave function of the ejected electron. The results of our calculations are shown in Fig.1 (curve 1). As may be seen, the use of a plane wave for the wave function of the continuous spectrum yields results approximately 1.5 times greater than those obtained through calculations[18-23] employing the precise expression for the continuum wave function. In addition, in the approximation utilized herein P_0 is weakly dependent on Z. In view of the highly approximate character of these calculations, the calculated dependence of P_0 on Z could hardly be expected to give good agreement with experiment. Actually attempts to fit the γ vs Z curve to the experimental values listed in Table 1 did not give good results. Hence for finding the Z-dependence of γ we utilized the experimental values of the K fluorescence yield

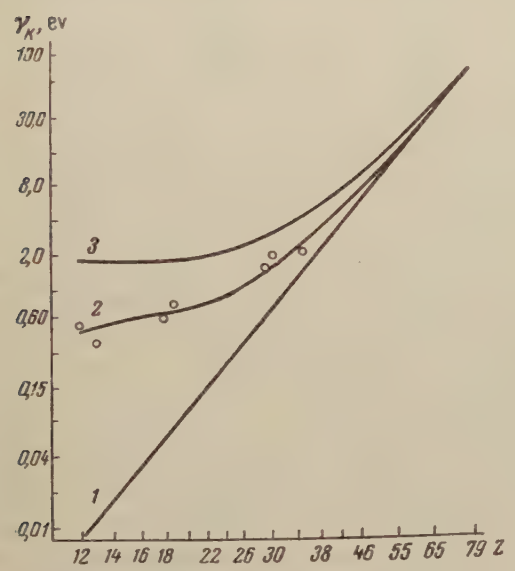

Fig.2. Variation of the K level width with atomic number. Both scales are logarithmic. 1) variation of the radiation width with Z according to Eq.(4), 2) final Z-dependence of γ_K obtained using the experimental values of the fluorescence yield from Ref. 24-29, 3) Z-dependence of γ_K obtained using Eq.(2a) on the assumption that P_0 = const, i.e., that the nonradiative transition probability is independent of the atomic number.

By definition

$$\omega = \frac{P_r}{P_r + P_0}.$$

From this we found the total probability as a function of Z using the values of P_r from Eq.(4).

In view of the arbitrary nature of the coefficient in Eq.(4) we shifted the γ curve relative to the vertical axis to obtain the best fit with the experimental values (Table 1). The value of the coefficient D determined in this manner was $1.00 \cdot 10^8$ transitions per sec. From the curve (curve 2 in Fig.2) determined in this manner we picked the values of γ for different elements listed in Table 3.

Table 3

K level widths taken from curve 2 of Fig.2

Element	γ, ev	Element	γ, ev	Element	γ, ev	Element	γ, ev
12 Mg	0,44	21 Sc	0,71	30 Zn	1,40	47 Ag	6,28
13 Al	0,48	22 Ti	0,74	31 Ga	1,53	50 Sn	7,98
14 Si	0,51	23 V	0,79	32 Ge	1,67	55 Cs	12,0
15 P	0,54	24 Cr	0,84	34 Se	1,98	60 Nd	17,7
16 S	0,57	25 Mn	0,92	36 Kr	2,37	65 Tb	26
17 Cl	0,60	26 Fe	1,00	38 Sr	2,82	70 Yb	36
18 Ar	0,63	27 Co	1,09	40 Zr	3,55	75 Re	48
19 K	0,65	28 Ni	1,19	42 Mo	4,10	79 Au	61
20 Ca	0,68	29 Cu	1,30	45 Rh	5,38		

The values of γ for elements of the iron group obtained in this manner differ appreciably from the values found by Beeman & Friedman[12]. The upper part of curve 2 (Fig.2) up to Z = 30 can be approximated by $\gamma \approx Z^4$. Zinn[24] and others give a similar dependence of the level width on Z in this range of atomic numbers. In the region of small atomic numbers, however, the $\gamma \sim Z^4$ dependence no longer obtains. Consequently, use of this dependence for finding the width of the K level of the Cl atom, as was done by Parratt & Jossem[25], is very questionable. One can find the P_o vs Z curve by using the experimental K fluorescence yield data[26-31] and Eq.(4) for P_r with $D = 1.00 \cdot 10^8$ transitions per sec. The curve obtained in this manner is represented by curve 2 in Fig.1. It is distinguished from the curve obtained by theoretical calculation by the sharp rise in the region of large values of Z. Apparently this rise is explained by the relativistic effects mentioned above.

Some authors[18,20-23,32] indicate that the variation of ω with Z can be approximated by an expression in which $P_r(Z) \sim Z^4$ and $P_o(Z) = \text{const}\ (Z)$. In this case, however, as was noted above, one cannot obtain good agreement with the experimental data on the level widths (Table 1). Curve 3 in Fig.2 was plotted on the assumption that $P_r(Z) \approx Z^4$ and $P_o = \text{const}\ (Z)$ so that the value of γ_K for Z = 79 would match the experimental value. In this case we obtained an appreciable divergence between the curve (1.7 ev) and the experimental data (0.6 ev) for light elements. On the other hand, if the curve is plotted so as to fit the experimental data for light elements, then for Z = 79, we obtain a value of 40 ev as compared with the experimental value of 62 for γ. In contrast our curve for γ vs Z is consistent with two series of independent experimental data: data on the level width and data on the fluorescence yield. It is therefore in better agreement with the true Z-dependence of γ.

Knowing the width of the K levels, one can readily calculate the width of L_{II} and L_{III} levels from the width of the $K\alpha_{1,2}$ lines. Unfortunately, the data on the $K\alpha_{1,2}$ line widths reported by different investigators[33-38] differ owing to the different procedures used in correcting for the distortion of the two crystal spectrometer. In order to obtain more consistent data we assumed, following Brogren[39], that for the most perfect crystals the correction for distortion of the crystals should be introduced according to the linear law and recalculated the basic experimental data of Refs.33-39 on this basis. The $K\alpha_{1,2}$ line widths obtained in this manner are listed in Table 4. From these values and the K level widths shown in Table 3, we calculated the widths of the L_{II} and L_{III} levels (Table 5).

Inasmuch as the $K\alpha_{1,2}$ lines for elements of the iron transition group are asymmetric, the use of the linear correction for distortion of the crystals for these lines is not entirely justified. Moreover, in this case the width of the L_{II} and L_{III} levels cannot be found as the difference between the width

Table 4

Widths of the $K\alpha_1$ and $K\alpha_2$ lines

Element	$\gamma_{K\alpha_1}$, ev	$\gamma_{K\alpha_2}$, ev	Element	$\gamma_{K\alpha_1}$, ev	$\gamma_{K\alpha_2}$, ev
22 Ti	1,38	1,90	32 Ge	2,73	2,94
23 V	1,58	2,21	38 Sr	4,5	4,6
24 Cr	1,96	2,43	40 Zr	5,2	5,4
25 Mn	2,46	2,96	41 Nb	5,8	5,4
26 Fe	2,65	3,00	42 Mo	5,86	6,18
27 Co	2,45	3,12	44 Ru	6,8	6,7
28 Ni	2,26	3,03	45 Rh	7,3	7,2
29 Cu	2,31	3,21	46 Pd	7,8	7,9
30 Zn	2,44	2,90	47 Ag	8,6	8,7
31 Ga	2,40	2,55			

Table 5

Widths of the L_{II} and L_{III} levels

Element	$\gamma_{L_{III}}$, ev	$\gamma_{L_{II}}$, ev	Element	$\gamma_{L_{III}}$, ev	$\gamma_{L_{II}}$, ev
22 Ti	0,64	1,16	32 Ge	1,06	1,27
23 V	0,79	1,42	38 Sr	1,68	1,78
24 Cr	1,12	1,59	40 Zr	1,85	2,05
25 Mn	1,54	2,04	41 Nb	2,09	1,69
26 Fe	1,65	2,00	42 Mo	1,76	2,08
27 Co	1,36	2,03	44 Ru	1,94	1,84
28 Ni	1,07	1,84	45 Rh	1,92	1,82
29 Cu	1,01	1,91	46 Pd	1,99	1,89
30 Zn	1,04	1,50	47 Ag	2,32	2,42
31 Ga	0,87	1,02			

of the $K\alpha_{1,2}$ lines and the K level. Hence the data on the L level widths for these elements shown in Table 5 must be regarded as only a first approximation.

Using the K level widths deduced as described above, we corrected the K spectra of the transition elements Cu, Ni, Co and Fe obtained by Beeman & Friedman[12] on a two-crystal spectrometer for the distortion introduced by the finite width of the K level (Fig.3). The corrections resulted in an increase of the slope of the curves particularly on the short wavelength side of the $K\beta_5$ line and the initial part of the K absorption edge. The correction also accentuated the col (double peak and dip) on the high energy side, particularly, for Cu. We cannot as yet give an unambiguous interpretation of the resultant curves. The initial section of the K absorption edge in the spectra of Cu and Ni can hardly be interpreted as being due to transitions to the 3d band.[40,41]

The most acceptable appears to be the interpretation of Beeman & Friedman[12] who base their inferences not on more or less hypothetical concepts concerning the individual s, p, etc. bands corresponding to levels of a free atom but on the actual density of states curve[42] (Fig.4). They interpret the long wavelength portion of the K absorption edge of Cu as being associated with electron transitions into the unfilled part of the 4s band, in the middle part of which there is an appreciable admixture of p states. Inasmuch as at the point M (the end of the 4s band) both the density of states and the admixture of p functions fall off, a dip or col appears in the absorption spectrum. With decreasing atomic number the overlapping of the 4s and 4p bands increases, which leads to smearing out of the dip (Fig.3,b). It will be seen from Fig.3,a that the $K\beta_5$ line of Cu has two maxima.

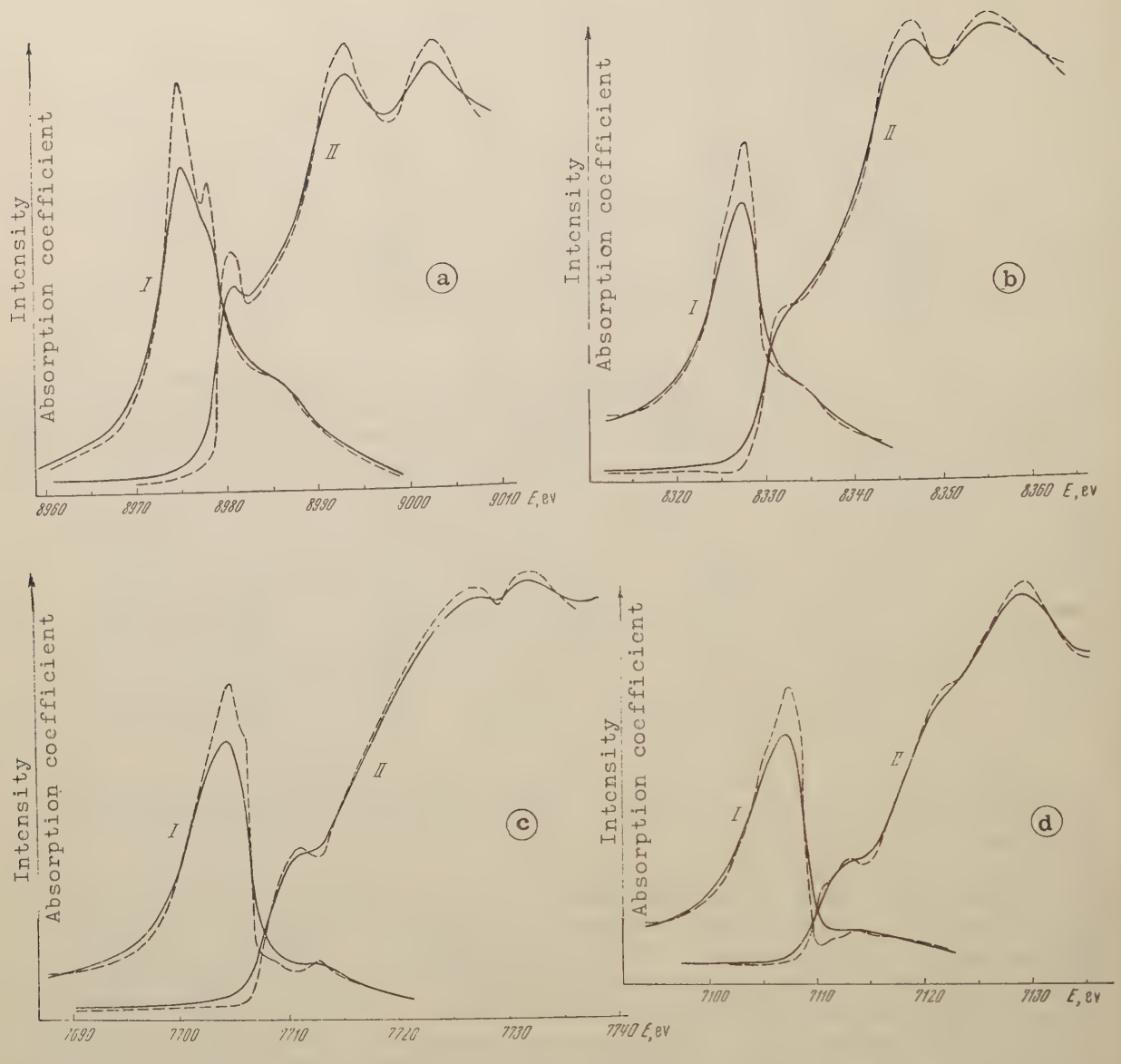

Fig.3. Results of processing the emission (I) and absorption (II) K spectra of a) Cu, b) Ni, c) Co and d) Fe. Solid lines - experimental spectra of Beeman & Friedman[12]; dash lines - corrected spectra.

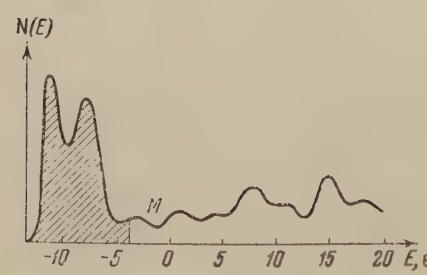

Fig.4. Distribution in energy of the density of electron states for copper.[42]

According to Beeman & Friedman the left maximum corresponds to transitions from the left maximum of the density of states curve (Fig.4) which contains a certain admixture of p states. The short-wave maximum is interpreted as being associated with transitions from the filled part of the 4s band with an appreciable admixture of p states. In addition, pure quadrupole transitions from the 3d band can make a certain contribution to the intensity of the $K\beta_5$ line. According to

Fletcher[43], in Ni the 3d band in the ferromagnetic state is filled only up to the second maximum. This explains the absence of splitting of the $K\beta_5$ line in Ni. In the case of elements with an unfilled 3d shell, one can expect fluctuations in the K absorption curve associated with quadrupole transitions to the 3d shell. In view of the low probability of quadrupole transitions and the relatively great width of the d band, however, these transitions are not evinced to any noticeable degree in the absorption spectra of pure metals. In contrast, in some compounds of transition metals the 3d band is split into a filled and an unfilled band and the density of states in each of them increases appreciably. Hence in such compounds the transitions associated with the 3d band are observed not only in the emission spectra but also in the absorption spectra.[44]

Rostov State University

References

1. M.A.Blokhin, Doklady AN SSSR, 107, 33 (1956).
2. M.A.Blokhin, Doklady AN SSSR, 107, 229 (1956).
3. M.A.Blokhin, Izv.AN SSSR, Ser.fiz., 20, 142 (1956). (Trans. in Bulletin, 20, No.1, 127.)
4. E.E.Vainshtein, Rentgenovskie spectry atomov v molekulakh khimicheskikh soedinenii i v splavakh (X-ray spectra of atoms in molecules of chemical compounds and alloys), M.-L., 1950.
5. F.K.Richtmyer & S.Barnes, Phys.Rev., 46, 352 (1934).
6. J.H.Munier, J.A.Bearden & C.H.Shaw, Phys.Rev., 58, 537 (1940).
7. L.G.Parratt, Phys.Rev., 56, 295 (1939).
8. J.B.Platt, Phys.Rev., 69, 337 (1946).
9. C.H.Shaw, Phys.Rev., 57, 876 (1940).
10. L.G.Parratt, Phys.Rev., 54, 99 (1938).
11. L.G.Parratt & C.F.Hempstead, Phys.Rev., 94, 1593 (1954).
12. W.W.Beeman & H.Friedman, Phys.Rev., 56, 392 (1939).
13. F.K.Richtmyer, S.Barnes & E.Ramberg, Phys.Rev., 46, 843 (1934).
14. J.C.Slater, Phys.Rev., 36, 57 (1930).
15. J.H.Williams, Phys.Rev., 44, 146 (1933).
16. O.Beckman, Arkiv. f. Fysid., 9, 495 (1955).
17. E.Ramberg & F.K.Richtmyer, Phys.Rev., 51, 913 (1937).
18. E.Burhop, Proc.Roy.Soc., 148A, 272 (1935).
19. H.Massey & E.Burhop, Proc.Roy.Soc., 153A, 661 (1936).
20. L.Pincherle, Atti Accad. Lincei, 20, 29 (1934).
21. L.Pincherle, Nuovo Cimento, 12, 81 (1935).
22. L.Pincherle, Nuovo Cimento, 12, 162 (1935).
23. L.Pincherle, Physica, 2, 596 (1935).
24. W.H.Zinn, Phys.Rev., 46, 659 (1934).
25. L.Parratt, E.Jossem, Phys.Rev., 97, 916 (1955).
26. C.Broyles, D.Thomas & S.Haynes, Phys.Rev., 89, 715 (1953).
27. P.R.Gray, Phys.Rev., 101, 1306 (1956).
28. G.Harrison, R.Crawford & J.Hopkins, Phys.Rev., 100, 841 (1955).
29. J.Heintze, ZS.f.Phys., 143, 153 (1955).
30. C.E.Roos, Phys.Rev., 93, 401 (1954).
31. C.E.Roos, Phys.Rev., 100, 1267 (1955).
32. G.Wentzel, ZS.f.Phys., 43, 524 (1927).
33. F.K.Richtmyer & S.Barnes, Phys.Rev., 46, 352 (1934).

34. S.K.Allison, Phys.Rev., 44, 63 (1933).
35. J.A.Bearden & C.H.Shaw, Phys.Rev., 48, 18 (1935).
36. H.H.Roseberry & J.A.Bearden, Phys.Rev., 50, 204 (1936).
37. S.K.Allison & J.H.Williams, Phys.Rev., 35, 1476 (1930).
38. L.G.Parratt, Phys.Rev., 46, 749 (1934).
39. G.Brogren, Ark.f.Fysik., 8, 391 (1954).
40. I.B.Borovskii & E.E.Vainshtein, Doklady AN SSSR, 34, 144 (1942).
41. I.B.Borovskii, Doklady AN SSSR, 26, 772 (1940).
42. J.C.Slater, Phys.Rev., 49, 537 (1936).
43. G.C.Fletcher, Proc.Rhys.Soc., 65A, 387, 192 (1952).
44. H.P.Hanson & J.R.Knight, Phys.Rev., 102, 632 (1956).

DEPENDENCE OF THE X-RAY ABSORPTION SPECTRA OF ATOMS IN COMPOUNDS ON THE CHARACTER OF THE BONDS

- R.L.Barinskii, E.E.Vainshtein & K.I.Narbutt

Introduction

In earlier publications[1,2] we showed that the fine structure of the main K absorption edge of atoms bound in molecules and of ions in solution can be interpreted and approximately calculated on the assumption that it is due to superposition of a number of selective absorption lines and the true absorption edge appearing incident to transition of the K electrons of the absorbing atom to successive np-levels of the molecule or ion* and into the region of continuous variation of the molecule's energy.

By means of the developed computation method and the expressions deduced, it proved feasible to give a quantitative interpretation of the K absorption edges of the noble gases[1,3], the atoms in a number of simple gaseous molecules[1,2] and the ions in some solutions[1,4].

In going to the x-ray absorption spectra of atoms in more complicated substances - polyatomic molecules consisting of several relatively heavy atoms or polar crystals - certain complexities appeared in the fine structure of the x-ray spectra, complexities the appearance of which could not be explained from the standpoint of the simple variant of our theory. This showed that the effects accompanying K absorption in these substances are much more complicated and that further development and refinement of the theory was indicated.

The results obtained in the work of Ref.5, devoted to investigation of the absorption spectra of potassium and chlorine in KCl crystals, have played an important role in the development of our theoretical concepts regarding the mechanism of x-ray absorption by atoms of chemical compounds and the nature of the fine structure of their x-ray spectra. It was shown in Ref.5 that the complex structure of the main K absorption edge of each of the components of the compound can be satisfactorily described if it is represented as a superposition of two series of lines converging towards the continuous absorption boundary. The intensity and energy width of these line series can be calculated by means of the same (i.e., earlier deduced) formulas, differing for each series only as regards the value of the parameter n^*. Both series of absorption lines were detected in the spectra of both components, but with inverse intensity ratios. Entirely analogous regularities in the structure of the absorption spectra of both components of the compound were subsequently established in the absorption spectra of zinc, germanium and bromine in $ZnBr_2$ and $GeBr_4$ molecules.[6,7]

This indicated that the empirical generalizations arrived at in Ref. 5 were more extensively applicable and made evident the desirability of systematically investigating this effect with a view to clarifying the principal regularities characterizing the parameters determining the relative intensity, energy width and relative positions of both series of lines in the x-ray absorption spectra of elements in compounds and the dependence of these parameters on the properties of the interacting atoms and the character of the chemical bonds linking them. It was felt that generalization of such data

---

*We are speaking here of elements with electron shells having a normal structure. In the structure of K absorption edges of atoms with defects in the nd- and nf-shells there should and do appear additional long-wave absorption maxima.

should help clarify the conditions and causes by reason of which it was feasible to represent the x-ray absorption spectra of atoms in polyatomic molecules in the form of a superposition of two hydrogen-like series of absorption lines, establish the limits of applicability of these concepts and perhaps yield a deeper insight into the nature of the phenomena accompanying the absorption of x-rays by atoms bound in polyatomic molecules and solids.

For our investigations we chose the K absorption spectra of Zn in $ZnCl_2$, $ZnBr_2$ and ZnS molecules[8], the K spectra of chlorine in the chlorides of Li, Na, K, Rb and Cs[9] and the K absorption spectra of potassium bound in KF, KCl, KBr and KI[10], which have also been studied by Kiyono[11]. All these crystals (except CsCl) form a simple lattice. Each group, in addition to the same cation or anion, contains atoms with widely varying values of nuclear charge, ionic radius and polarizability. Accordingly, the degree to which the atomic bonds in each group are predominantly ionic varies in each group.

1. Dependence of the fine structure of the K absorption edges of Zn, K and Cl in molecules and alkali halide crystals on the character of the bonds.

The K absorption spectra of zinc in $ZnCl_2$, $ZnBr_2$ and ZnS molecules and the results of analysis of these spectra by one of the methods[2] proposed by us are shown in Fig.1.

The absorption spectra of potassium in KF, KCl, KBr and KI crystals and chlorine LiCl, NaCl, KCl, RbCl and CsCl crystals and the results of their resolution by the method of Ref.1 have already been given in Refs.9 & 10. Some of them, namely, those pertaining to potassium in KF, KCl, KBr and KI and the spectra and results for sodium and chlorine in NaCl crystals are reproduced herein in Figs.2-7.

Examination of the above mentioned experimental material on the x-ray absorption spectra of both components of simple polar crystals not only fully substantiates our earlier conclusions[5,12] regarding the possibility of representing the fine structure of the x-ray spectra of these atoms in the form of a superposition of two series of absorption lines but also serves to bring out certain general regularities that help clarify the physical picture underlying this interpretation of the spectral structure.

For theoretical synthesis of the fine structure of the absorption edge of an atom in a molecule in the general case one should know four independent parameters, namely,

1) the width of the absorption lines and the true absorption edge of each of the

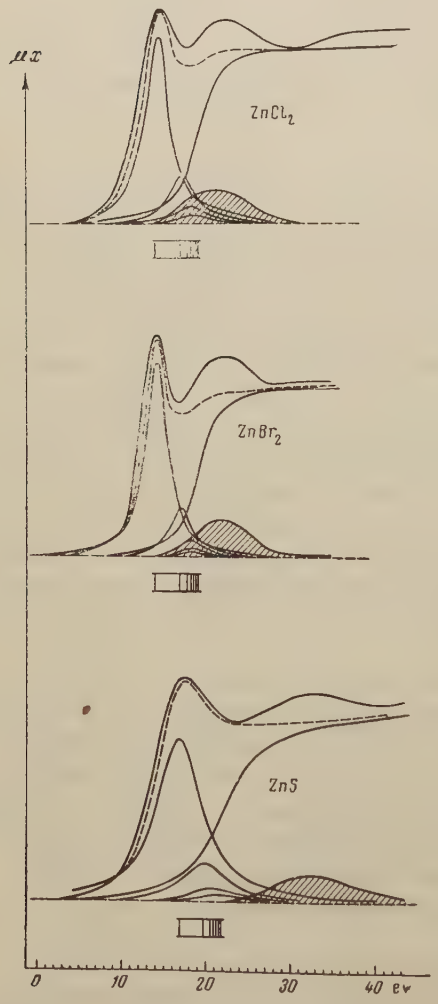

Fig.1. K absorption spectra of zinc in $ZnCl_2$, $ZnBr_2$ and ZnS gas molecules and the results of analysis of these spectra. Dash line = integral theoretical absorption curve due to the presence of selective lines of the principal series. Hatched area = portion of absorption due to the presence of the secondary absorption line series.

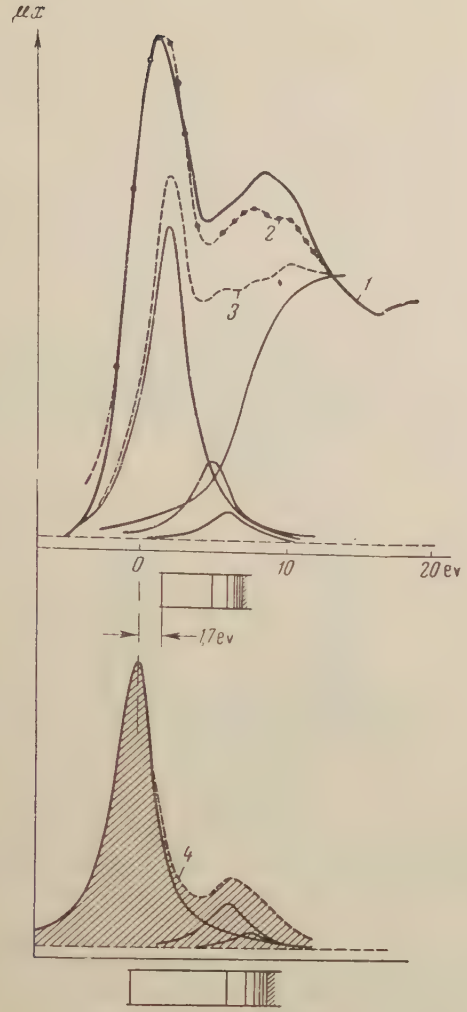

Fig.2. K absorption edge of potassium in KF crystal: 1) experimental curve; 2) integral theoretical curve, 3) integral theoretical curve for the principal line series and the true edge, 4) integral theoretical curve for the secondary series.

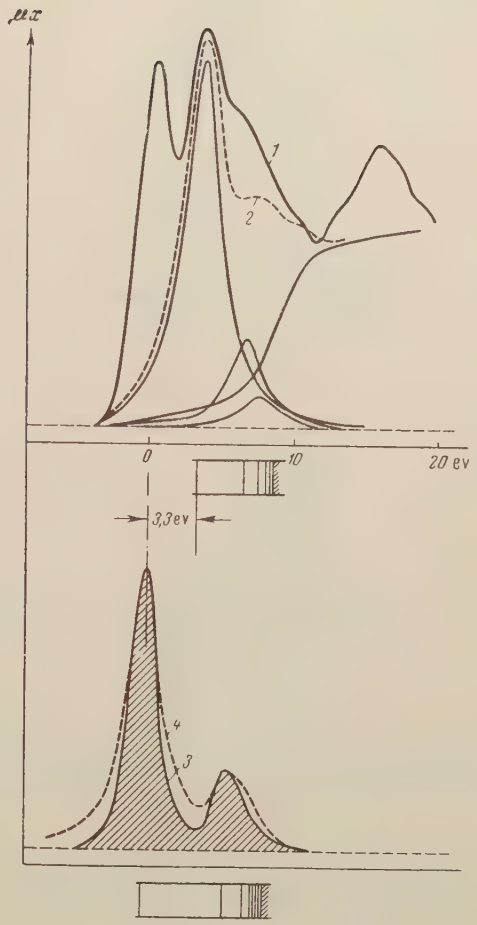

Fig.3. K absorption edge of potassium in KCl crystal: 1) experimental curve; 2) integral theoretical curve for the principal series and the true absorption edge, 3) difference between curves 1 and 2, 4) integral theoretical curve for the secondary line series.

two series of lines (the principal and the secondary),

2) the values of n_1^* and n_2^* by means of which one can calculate the relative intensity and the wavelengths of the selective absorption lines within each of the two series,

3) the relative intensity I_1/I_2 of the first absorption lines of the principal and secondary series, and

4) the energy separation δ between the first absorption lines of the principal and secondary series.

At present it is impossible to calculate all these quantities rigorously and wholly from theory. Hence in interpreting the structure of the K absorption edge of atoms in compounds one must necessarily proceed semiempirically and take certain values from experiment. As follows from analysis of the

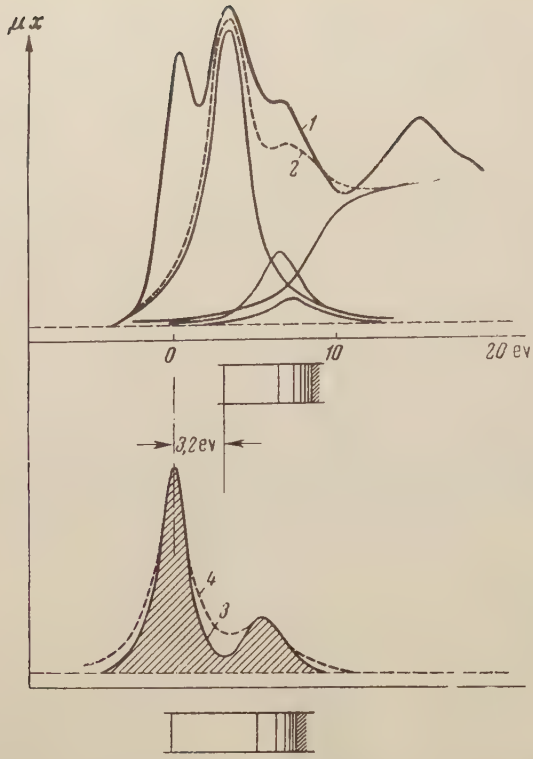

Fig.4. K absorption edge of potassium in KBr crystal. Curve designations same as in Fig.3.

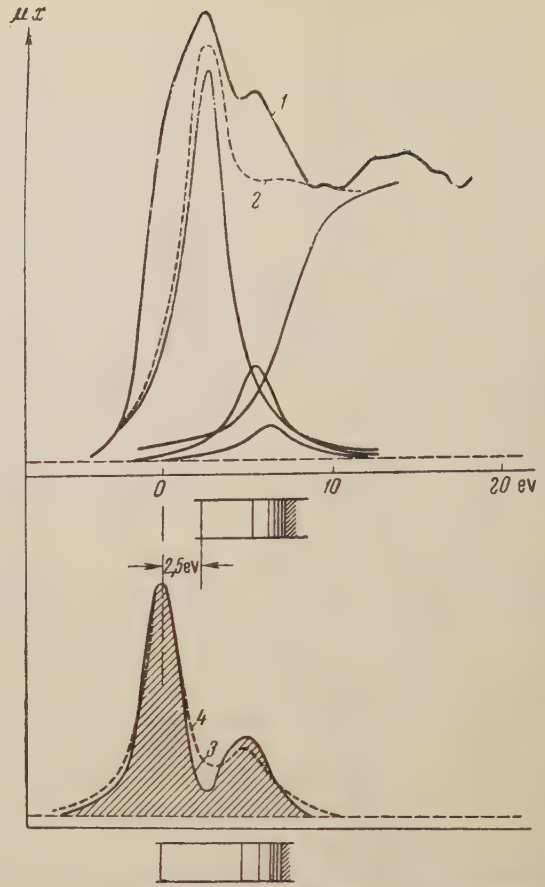

Fig.5. K absorption edge of potassium in KI crystal. Curve designations same as in Fig.3.

results obtained in Refs.9 & 10, however, the fundamental parameters determining the structure of the absorption edge of the anion or cation in different compounds, specifically, the value of the principal quantum number (n^*) and the relative intensity of the principal and secondary series (I_1/I_2) are consistently related with the polarizability and, respectively, the energy E of the electron affinity or the ionization potential J of the "partner" atoms in the compound. This will be evident from a careful examination of Figs. 8,9* and 10.

Fig.8 shows the variation of n_2^* for the secondary line series in the absorption spectra of potassium in KI, KBr and KCl crystals with the polarizability of the anion. This dependence was obtained in analyzing these spectra on the assumption that the value of the parameter n_1^*, characterizing the energy width and relative intensity of the lines of the principal series in the absorption spectrum of the cation, is invariant (in the first approximation) in all these compounds. The plots of Fig.9 and 10 show the variation of the relative intensity of the principal and secondary line series in the absorption spectra of potassium and chlorine in alkali halide crystals with the electron affinity of the anions (Fig.9) and the ionization potential of the cations (Fig.10).

---

*The straight line plot in Fig.9 (in I_1/I_2 vs E coordinates) is equivalent to the curve given in Fig.3 of Ref.10 (in log I_1/I_2 vs log Z coordinates). A misprint, however, crept into the associated text in Ref.10: $I_1/I_2 \approx Z^2$ therein should read $I_1/I_2 \approx Z^{0.2}$.

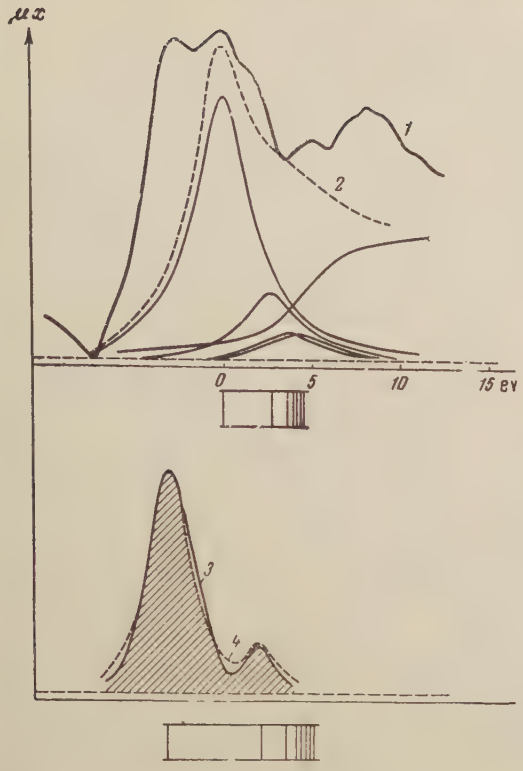

Fig.6. K absorption edge of sodium in NaCl crystal. Curve designations same as Fig.3.

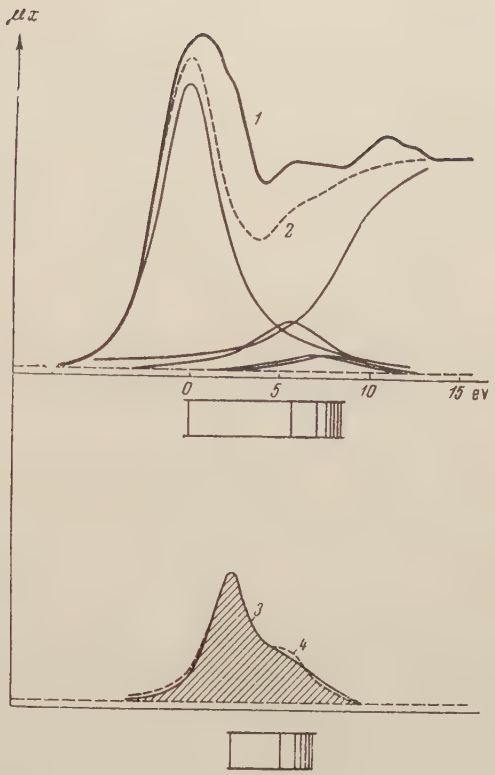

Fig.7. K absorption edge of chlorine in NaCl crystal. Curve designations same as in Fig.3.

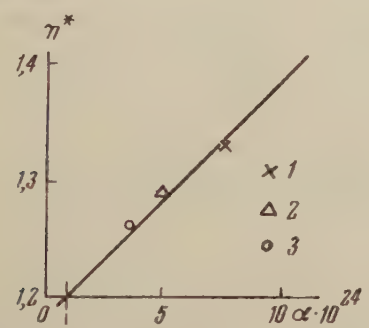

Fig.8. Variation of n^* for the secondary line series in the absorption spectrum of potassium in halide compounds with the polarizability of the anion: 1) for iodine, 2) for bromine, 3) for chlorine. The dash line gives the variation for fluorine.

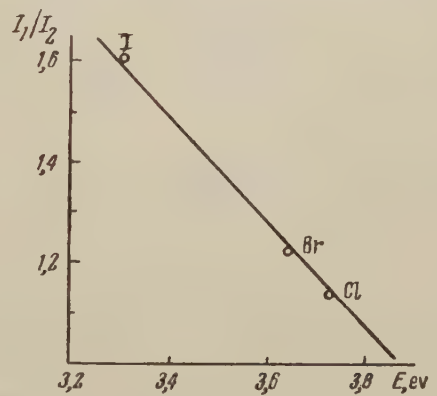

Fig.9. Variation of the relative intensity of the principal and secondary line series in the absorption spectra of potassium in KI, KBr and KCl crystals with the electron affinity of the anion.

Examination of these curves shows that the relative intensity of the secondary line series in the absorption spectra of any of the components of polar crystals is the greater, the lower the ionization potential of the cation and the higher the electron affinity energy of the anion. In other words, this means that the relative intensity of the secondary absorption line series

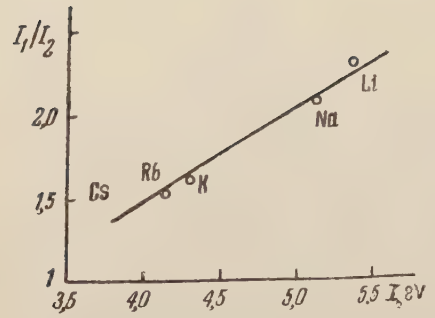

Fig.10. Variation of the relative intensity of the principal and secondary line series in the absorption spectra of chlorine in LiCl, NaCl, KCl, RbCl and CsCl crystals with the ionization potential of the cation.

in the spectra of each of the components of a polar crystal depends strongly on the heteropolarity ("ionicity") of the bonds between the atoms and is the greater, the stronger the tendency of each of the components of the compound to form ionic bonds. We come to analogous conclusions regarding the relation between the fine structure of the absorption spectra of the atoms and the character of the interatomic bonding in the compounds from analysis of the data pertaining to molecules of gases (see, for example, Fig.1) in which there is also observed a decrease of the part of the absorption associated with the presence of the secondary line series with weakening of the ionic character of the bonds between the atoms and approach to covalent bonding.

In the case of polyatomic molecules with predominantly covalent bonds, we may expect to find a radically different structure of the x-ray absorption spectra (as compared with that of polar compounds). It will probably be impossible to distinguish or separate two hydrogen-like line series in the absorption spectra of covalent molecules. In this sense one can speak of the complete disappearance of the second secondary absorption line series in the spectra of atoms bound in compounds with covalent bonds; in fact one might consider the possibility of distinguishing or detecting such secondary series in the spectra of compounds with bonds of an intermediate character as an indication of nonuniform distribution of charges within the molecules of the compound and the presence in it of atoms or groups of atoms with opposite charges. One might venture to predict that in the future, given a more thorough and comprehensive understanding of the regularities involved, this effect may be utilized even for quantitative evaluations.

2. On taking into account the role of cross transitions in the theory of the principal K absorption edge of atoms in polyatomic molecules and solids.

In the preceding section we showed that the relative intensity of the secondary line series in the absorption spectra of atoms in polyatomic molecules and polar crystals and, apparently, the very possibility of representing the fine structure of the K absorption edge in the form of a superposition of two hydrogen-like absorption line series are connected with the ionic character of the bonding in these compounds, i.e., with the presence in them of differently charged ions. Yet this fact is in no way taken into account in our simple variant of the theory of the principal absorption edge, which is based on the concepts of spherical symmetry of the field of the molecular radical remaining after K-ionization and the associated assumption of completely isotropic polarizability of this radical under the influence of the K electron ejected to the periphery of the molecule.

Whereas in the process of K-ionization of an atom composing a molecule with covalent bonds and transfer of the electron to one of the higher excited levels of the molecule, the polarizing effect of the electron on the molecular radical can in the first approximation be regarded as independent of the angular coordinates and the radical itself can be characterized by some single

mean polarizability value, in the case of compounds with predominantly polar bonding this situation will not obtain. In the case of ionic compounds the inverse polarizing effect of the electron knocked out of the K shell must depend substantially on in what region of the polar molecule it is located, i.e., on whether the electron finds itself in the field of the cation or in the field of the anion. For example, in the case of a simple diatomic polar molecule it is obvious that the polarizing influence on the molecular radical of a K electron from either of the atoms of the compound will be much greater if the electron is in the region of the molecule adjacent to the anion than if it moves in the field of the cation.

In polyatomic molecules of this type the polarizability anisotropy will be evinced in a more complicated manner and in general will depend on their structure. In all cases of homeopolar bonds, however, there must be a certain degree of anisotropy of the polarizability, the extent of which must vary within certain limits depending on the direction in which the electron is ejected from the K shell of the absorbing atom.

In view of the known relation[1] between the polarizability and the parameter n^* entering into the basic formulas of the theory, this in turn must lead to complication of the structure of the K absorption edges of the atom in such compounds as compared with the structure observed in the absence of polar bonding, i.e., in the case of simple molecules or molecules with predominantly covalent bonds. The precise dependence of the polarizability α of the molecular radical and the value of n^* associated with it on the direction of ejection of the K electron in the process of absorption of x-rays is not known. There is reason to assume, however, that the form of this functional dependence will undergo more or less appreciable changes in going from one compound to another. Nevertheless, on the basis of our more or less satisfactory semiempirical interpretation of the fine structure of the K absorption edges of atoms in a large number of different polyatomic molecules and polar crystals, it may be assumed that in compounds with predominantly ionic bonds this dependence $n^*(\vartheta, \varphi)$ will be characterized by a curve with two more or less pronounced extrema (a maximum and a minimum) corresponding to the electron ejected from the K shell of the absorbing atom being in positions associated with the two most sharply differing states of polarization of the molecular radical. In the case of a diatomic polar molecule each of these two groups of n^* values obviously corresponds to the ejected electron being near one or the other of the ions composing the molecule.

The more pronounced the ionic character of the bonds, the greater must be the distance between the centroids of the two groups of n^* values and the narrower the range of variation of the values within each group, i.e., the closer the clustering of the n^* values. Under these conditions the two groups of different states of polarization of the molecule (as follows from analysis of the experimental data) can be characterized by two mean values of the polarizability or the related parameters n_1^* and n_2^*, while the fine structure of the absorption spectra of the atoms in the compound can be represented in the form of a superposition of only two series of absorption lines, each of which corresponds to one of these values of n^*. With decreasing polarity of the bonding forces, i.e., with increasing covalence of the bonds, separation of two series of absorption lines, additively comprising the observed absorption edge, will become theoretically less justified and practically increasingly difficult. This should also be manifested in broadening of the corresponding absorption lines in each of the two series utilized for synthesizing the experimental absorption edge and in increasing deviation of their shape from the theoretical dispersion shape. In molecules with purely covalent bonds there

should, apparently, be observed only one series of absorption lines.

Thus we see that taking into account the anisotropy of the polarizability of the molecule under the influence of the electron ejected to its periphery from the K level of one of the constituent atoms enables us a) to understand the reason for the appearance of two series of absorption lines in the spectra of atoms bound in polyatomic polar molecules and polar crystals, b) to correlate this effect with the character of the bonding forces predominating in the compound and c) to approximate (with due regard to the rough character of this method of interpretation of the experimental data) the theoretical limits of applicability of our method of analysis.

From the viewpoint of model concepts regarding the absorption of x-rays by each of the ions of a polar molecule or crystal, the conclusion that the fine structure of the K absorption edge can be represented in the form of a superposition of two series of absorption lines (corresponding in the first approximation to two groups of different states of polarization of the system after K ionization of its atoms) implies that we admit that in considering the process of absorption of x-rays by the atoms of these substances we must take into account not only transitions of the K electrons to molecular levels within the absorbing ion but also the so-called cross transitions to molecular energy levels which are genetically more closely related to the other (i.e., oppositely charged) ion.

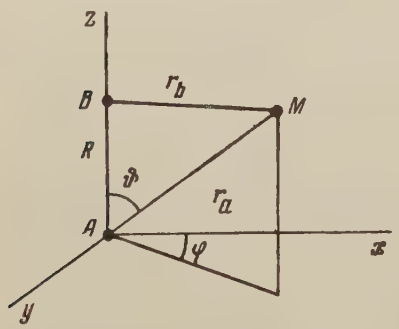

Fig.11. Diagram used in deriving Eq.(1).

With a view to evaluating the relative probabilities of direct and cross transitions in compounds with polar bonds, let us examine the simplest case of a diatomic ionic molecule. Let us assume that the z-axis of our rectangular system of coordinates (Fig.11) is directed along the axis of the molecule AB, and that atom A is located at the origin. Let R be the interatomic distance A-to-B and r_a and r_b be the distances from A and B, respectively, to an arbitrary point M, whose angular coordinates are ϑ and φ. In essence, calculation of the matrix element for the cross transition of a 1s electron of the absorbing atom to the molecular levels of np symmetry, in view of the symmetry of the problem, reduces to calculating only the integral

$$\int_V \psi_a z \psi_b d\tau,$$

inasmuch as the matrix elements of the x and y coordinates vanish identically. Since $R/r \ll 1$, the corresponding wave functions of the initial and final levels of the electron transition in the molecule can, in the first approximation, be characterized by hydrogen-like functions of the form (in atomic units):

$$\psi_{1s}^{(a)} = \frac{1}{\sqrt{\pi}} Z^{3/2} e^{-Zr},$$

$$\psi_{np}^{(b)} = \frac{1}{\sqrt{3\pi}} \sqrt{\frac{n^{*2}-1}{n^{*5}}}\, r e^{\frac{\eta}{n^*}(r - R\cos\vartheta)} \cdot \eta^{5/2} \cos\vartheta,$$

where η is the charge of the molecular radical after K-ionization of one of its atoms and n^* is the effective principal quantum number of the final level. Under the above assumptions the sought intensity of the cross transition, proportional to the square of the matrix element, is

$$I^{z}_{1s,np} = C\,\frac{\nu\eta^5(n^{*2}-1)}{Z^2 n^{*5}}\,\Phi\left(R,\ \frac{\eta}{n^*}\right), \qquad (1)$$

where Φ is given approximately by

$$\Phi\left(R,\ \frac{\eta}{n^*}\right) = \left[1 + 2R\eta/n^* + 2{,}3R^2\left(\frac{\eta}{n^*}\right)^2\right] e^{-2R\frac{\eta}{n^*}}.$$

As might be expected, Eq.(1) at the limit R→0 approaches the expression that characterizes the probability of a direct transition in the molecule. This expression, as is known, has been substantiated in analysis of the structure of the x-ray absorption spectra of atoms of noble gases and simple molecules.[1]

The variation of the function Φ with the interatomic distance in the molecule (or more precisely with the ratio R/a, where a is the Bohr radius) for different values of n^*/η is shown graphically in Fig.12.

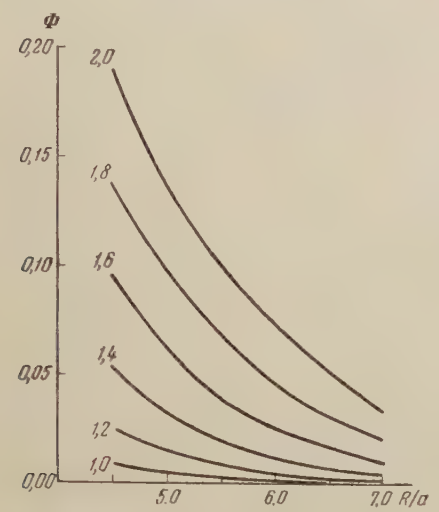

Fig.12. Variation of the function Φ with the interatomic distance in a polar molecule for different values of n^*/η; the figures at the curves are values of n^*/η.

Thus in the indicated approximation the intensity ratio of the absorption lines associated with the direct and cross transitions of an electron ejected from one of the atoms of the molecule in the process of K absorption of x-rays can be evaluated by means of the expression

$$\frac{I_2}{I_1} = \frac{C_1\eta_2^5 n_1^{*5}(n_2^{*2}-1)}{\eta_1^5 n_2^{*5}(n_1^{*2}-1)}\,\Phi\left(R, \frac{\eta_2}{n_2^*}\right) \qquad (2)$$

or approximately

$$\frac{I_2}{I_1} = C_1\left(\frac{\eta_2}{\eta_1}\right)^5 \cdot \left(\frac{n_1^*}{n_2^*}\right)^3 \Phi\left(R, \frac{\eta_2}{n^*}\right). \qquad (3)$$

Calculations of this ratio carried out by us for a number of compounds led to numerical values satisfactorily consistent with the experimental data.

Conclusions

The theoretical concepts we have examined herein make it possible to explain and unify the earlier discovered empirical regularities in the structure of the x-ray absorption edges of atoms in polyatomic compounds with predominantly polar bonds. They allow, also, of making certain quantitative evaluations which prove in satisfactory agreement with experimental data. Thus in the case of diatomic polar compounds one can from analysis of the known data on the polarizability of different anions and cations assert the following:

1. The extent of the principal absorption line series in the spectrum of the cation must always be less than the extent of the secondary series in the same spectrum; in the case of the anion spectrum the relationship is reversed.

2. The relative intensity of the secondary line series in the spectrum of the cation must always be greater than the corresponding intensity in the spectrum of the anion in the same compound.

3. The shape of the selective absorption lines within each series in the spectra of the cation and anion in compounds with predominantly ionic bonds must be close to the dispersion shape. With weakening of the ionic character of the bonds, i.e., in going to increasingly covalent bonding, the shape of

the lines must deviate increasingly from the above theoretical one.

4. The relative position of the principal and secondary absorption line series is apparently determined by which of the two extreme states of polarization of the molecule is characterized by the lowest energy. Inasmuch as $E = -R/n^{*2}$ and the polarizability of the cation is less than that of the anion, in the case of diatomic molecules the minimal energy must be associated with the absorption line series which corresponds to the electron ejected from the K shell of the absorbing atom being in the field of the anion.

5. The anisotropy of the polarizability of polyatomic molecules such as, for example, the molecules of the halide salts of some metals (Zn, Ge, etc.) depends on their structure and hence (in contrast to the case of diatomic compounds) is not directly related with the polarizability of the ions forming the compound. The considerations developed herein, however, allow of predicting the relative intensity and energy positions of the lines of both series in the spectrum of one of the components on the basis of the experimentally determined values of the parameter n^* for the principal and secondary line series in the spectrum of the other components of the molecule.

All the above deductions from our theory are satisfactorily substantiated by experiment. Or, at least, we know of no x-ray absorption spectrum of atoms in polar molecules or simple polar crystals that formed an exception to the outlined regularities.

In view of this further theoretical development of the problems touched upon in the present report and systematic accumulation and interpretation of experimental material pertaining thereto acquire added importance. In the light of further theoretical and experimental work it should be feasible to extend and refine and if necessary correct the concepts which, as we have attempted to show, already allow of deciphering and interpreting many of the details observed in the x-ray absorption spectra of atoms bound in polyatomic molecules and crystals. Essential, too, is development of more advanced mathematical methods of solving the problems arising in the field of x-ray spectroscopy. Lacking this, further progress of the theory of the fine structure of x-ray spectra of substances having a complicated structure and composition may be seriously hampered.

IMGRE, GEOKhI & IGEM,
Academy of Sciences of the USSR

References

1. E.E.Vainshtein, R.L.Barinskii & K.I.Narbutt, Zhur.eksp.i teor.fiz., 23, 593 (1952).
2. R.L.Barinskii, E.E.Vainshtein & K.I.Narbutt, Doklady AN SSSR, 82, 355 (1952).
3. J.Backovsky, Českosl.casop.fys., 4, 118 (1954).
4. E.E.Vainshtein, Doklady AN SSSR, 91, 1059 (1953).
5. E.E.Vainshtein, K.I.Narbutt, R.L.Barinskii, Doklady AN SSSR,82,701(1952).
6. K.I.Narbutt, Doklady, AN SSSR, 93, 21 (1953).
7. K.I.Narbutt, Izv.AN SSSR, Ser.fiz., 20, 780 (1956). (Trans. Bulletin, 20, No.7, p.710.)
8. K.I.Narbutt, Doklady, AN SSSR, 92, 273 (1953).
9. R.L.Barinskii, Present issue of the Bulletin, p.1369.
10. E.E.Vainshtein, R.L.Barinskii & K.I.Narbutt, Doklady, AN SSSR, 105, 1196 (1955).
11. S.Kiyono, Sci.Rep.Tohoku Univ., Ser.I, 36, No.1 (1952).
12. K.I.Narbutt, E.E.Vainshtein & R.L.Barinskii, Doklady,AN SSSR,87,381(1952)

ON DETERMINING THE DENSITY OF ELECTRON STATES FROM X-RAY SPECTRA

- I.Ia.Nikiforov

The shape of an x-ray spectrum characterizes the distribution of electron states in energy (neglecting variations in the transition probability) with a certain degree of distortion which depends on the width of the inner levels and the resolution of the spectrometer. Since the inner levels have a Lorentzian shape and since the distortion due to the apparatus is also usually close to Lorentzian[1], the problem of finding the density of electron states in the case of an emission spectrum reduces to solving the integral equation

$$F(x) = \int_{-\infty}^{+\infty} f(t)\, D(t-x, \gamma)\, dt, \qquad (1)$$

where $D(t-x,\gamma)=1/\pi\gamma\,[1+(t-x)^2/\gamma^2]^{-1}$ the function $f(x)$ is the electron state density function, $F(x)$ characterizes the experimental shape of the spectrum and γ is the sum of the half-widths of the inner level and dispersion curve associated with the apparatus distortion. In the case of an absorption spectrum, Eq.(1) must be solved twice: once for the intensity curve (to correct for apparatus distortion) and again for the absorption coefficient curve (to correct for broadening due to the width of the inner level). The present methods for solving Eq.(1) have serious shortcomings. Van Cittert's successive approximation method[2,3] requires wearisome graphic or optical integration, the latter involving construction of a complicated optical system. His method is rarely used and then only for cases of weak distortion and simple line shape.[4]

The method based on approximating $F(x)$ by arc tangent curves[5] is not used in practice because of its complexity. To find the arc tangent parameters, one must solve a cumbersome set of equations with a large number of unknowns, which is practically impossible. This is also true when one tries to approximate $F(x)$ by Lorentzian dispersion curves. The method involving a trigonometric series approximation[6] of $F(x)$ (with from 25 to 35 odd sine functions) also has serious shortcomings. The harmonic continuation of the function gives rise to edge effects, and if one tries to correct this by increasing the interval of the approximation, the harmonic series does not converge as well and the necessary number of terms becomes very large. The Gibbs effect causes a significant amount of distortion on the steep sides of the curve contours. For the above reasons, we developed a new method free of the above-mentioned shortcomings.

In our method, the plot of the $F(x)$ curve is approximated by a series of horizontal rectangles (Fig.1). Each of these rectangles can be represented in the form of the difference between two step-functions, one of which has the step on the left side of the $F(x)$ curve; the other, on the right. If we agree always to take the step-function whose step is on the left side with a minus sign, calling it a negative step function, the rectangle can be written as the sum of positive (right side) and negative (left side) step-functions, so that

$$F(x) = \sum_{i=1}^{N} a_i \delta_i(x),$$

where a_i is the height of the i-th step-function, N is the total number of steps, $\delta_i(x) = \begin{cases} 0 \text{ for } x \geqslant x_i \\ 1 \text{ for } x < x_i \end{cases}$ for a positive step-function, and $\delta_i(x) = \begin{cases} -1 \text{ for } x \leqslant x_i \\ 0 \text{ for } x > x_i \end{cases}$ for a negative one. The number of step-functions and the

height of each one is chosen so that the $F(x)$ curve will be closely approximated. Obviously, it is not neccessary to break up each rectangle into two step-functions, since all that is required is that the sum of all these step-functions approximate the curve.

To find the function which, after distortion, will give us a step-function of unit height, we can use Van Cittert's method of successive approximations.[2,3]

The n-th approximation for this function (if we locate the step at the origin) is given by

$$\Phi_n(x) = \sum_{k=0}^{n} (-1)^k C_{n+1}^{k+1} \hat{D}^k \delta(x), \tag{2}$$

where

$$\hat{D}\delta(x) = \int_{-\infty}^{+\infty} D(t-x, \gamma)\,\delta(t)\,dt,\quad \hat{D}^2\delta(x) = \int_{-\infty}^{+\infty} dt \int_{-\infty}^{+\infty} D(t-x, \gamma)\,D(s-t, \gamma)\,\delta(s)ds \quad \text{and so on.}$$

For a positive step-function, we obtain, after integration,

$$\Phi_n(x) = \frac{1}{2}\left[1 - \frac{x}{|x|}(n+1)\right] + \frac{1}{\pi}\sum_{k=1}^{n} (-1)^{k+1} C_{n+1}^{k+1} \operatorname{arctg} \frac{x}{k\gamma}. \tag{3}$$

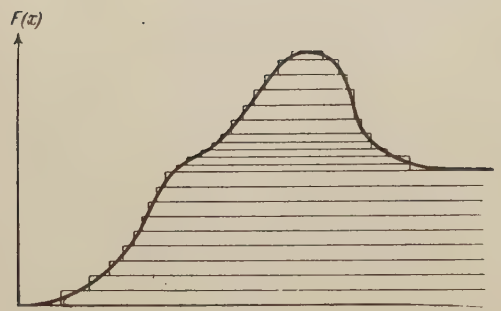

Fig.1. Approximating the $F(x)$ curve by rectangular step-functions.

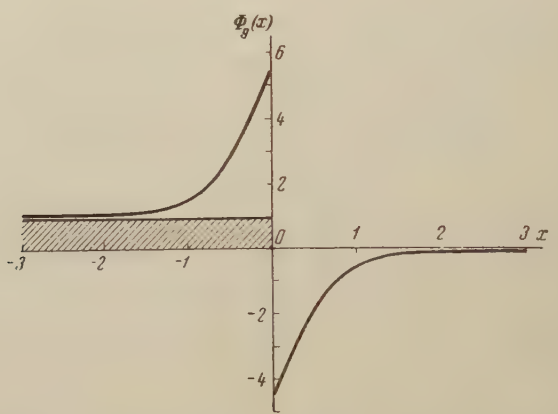

Fig.2. The ninth approximation $\Phi_9(x)$ for the function which gives a step-function after distortion. The horizontal axis is scaled in γ units.

For a negative step-function, $\Phi_n(x)$ has the opposite sign. The function $\Phi_n(x)$ was calculated in the ninth approximation, with the step-function itself being taken as the zeroth approximation, which means that $F(x)$ is taken as the zeroth approximation of $f(x)$. It will be seen from Fig.2 that this function is symmetric about the center point of the step boundary. For correcting a curve it is convenient to use the difference $\Phi_n(x) - \delta(x)$; this quantity should be added to the ordinate of the point on the distorted curve for which we seek the true ordinate.

It is most convenient to carry out the calculations if the curve is plotted with the x-axis scaled in units of γ; this γ-unit should always be taken of the same length, say, 20 mm. The values of $\Phi(x)-\delta(x)$ may be laid off on a rule (straight-edge) in both directions from the center, using the figures given in the table. The rule laid out in this manner can be used to correct any and all curves plotted to the selected γ-unit scale.

We now place the rule so that its center (origin) lies on the abcissa of the point of interest and note the number on the rule appearing opposite

Calculated values for the spectrum shape correcting rule with γ = 20 mm and a step height a = 1

$\Phi_9(x) - \delta(x)$	x, мм	$\Phi_9(x) - \delta(x)$	x, мм	$\Phi_9(x) - \delta(x)$	x, мм	$\Phi_9(x) - \delta(x)$	x, мм
4,00	1,6	0,80	16,9	0,30	24,9	0,09	63,0
3,50	3,3	0,75	17,4	0,25	26,4	0,08	76,4
3,00	5,1	0,70	17,9	0,20	28,4	0,07	90,0
2,50	7,0	0,65	18,5	0,15	31,8	0,06	105,0
2,00	9,2	0,60	19,1	0,14	33,2	0,05	126,0
1,50	11,7	0,55	19,8	0,13	34,6	0,04	159,0
1,00	15,1	0,50	20,6	0,12	36,0	0,03	204,0
0,95	15,5	0,45	21,4	0,11	38,4	0,02	320,0
0,90	15,9	0,40	22,4	0,10	44,4	0,01	640,0
0,85	16,4	0,35	23,5				

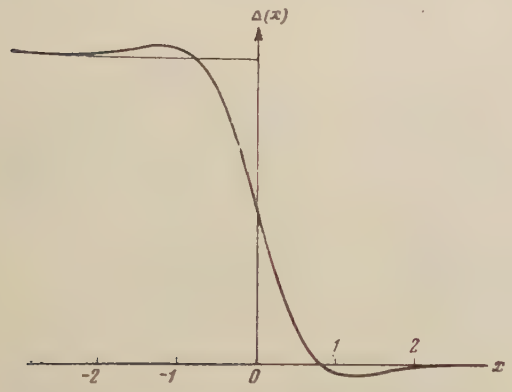

Fig.3. The function $\Delta(x)$ obtained after analytic distortion of

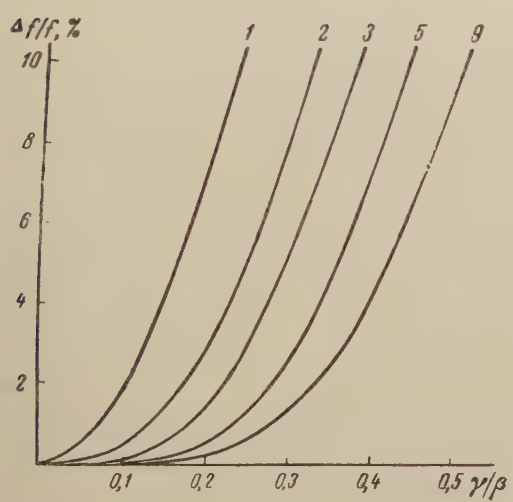

Fig.4. Relative error in the correction at the peak of the dispersion curve as a function of the order of approximation of $\Phi(x)$ (numbers at the curves) and the ratio of the broadening γ to the half-width β of the corrected line contour.

the center of the edge of the given step-function. We repeat the process for successive step-functions and then multiply each of these numbers by the height of the step-functions. Finally, we sum up the products with signs determined by the sign of the step-function. This gives the ordinate of the points on the corrected $F(x)$ curve. This method requires that the point we wish to correct be at the center of the edge of some step-function, or else we get further distortion. This limits the number of points for which one can obtain the "true" ordinate with a given set of step-functions. Tests show that for simple curves (with one or two maxima) it is sufficient to take 20 to 25 step-functions of equal height for each branch of the curve.

After distortion, the function $F(x)$ should give a step-function. Analytic distortion of $\Phi_9(x)$ shows that $F(x)$ is actually approximated not by step-functions, but by functions $\Delta(x)$ having the form shown in Fig.3. This characterizes the degree of approximation of the solution and shows that there is no advantage in taking a large number of step-functions of smaller height.

In order to estimate how the error of this method depends on the order of approximation of $\Phi(x)$ and the relative width of the corrected line, we calculated the relative error in finding the ordinate of the peak of a corrected dispersion curve for different ratios of γ to the half-width β of the distorted line and for several orders of approximation of $\Phi(x)$ (Fig.4). As can be seen, the relative error at the peak is no greater than 1.5%

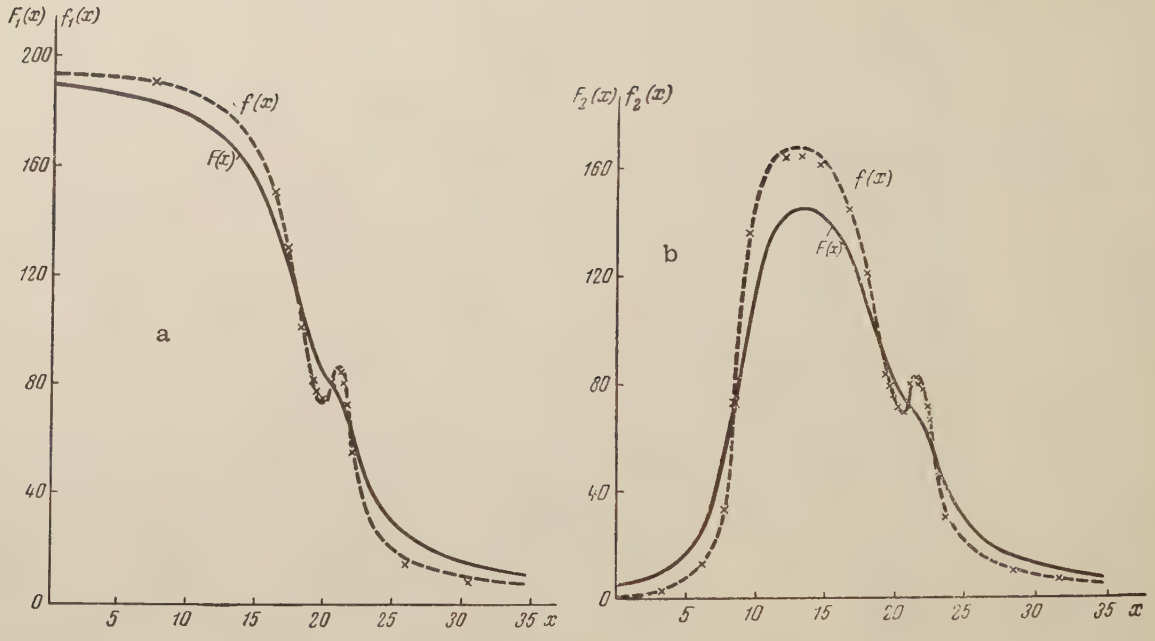

Fig.5. Test of the method: a) simulated absorption spectrum, b) simulated emission band.

for $\gamma/\beta = 0.3$ and obviously is much smaller at the other points of the curve. As β increases, the error decreases rapidly. The method was tested in the following way. The $F(x)$ curve was taken as the sum of an arc tangent and a dispersion curve (Fig.5), namely,

$$F_1(x) = 100\left(1 - \frac{2}{\pi}\operatorname{arctg}\frac{x-15}{2}\right) + \frac{25}{1+\left(\frac{x-28}{2}\right)^2},$$

a curve whose shape is similar to that of actual x-ray absorption lines. We also used a curve obtained from this one and approximating an actual x-ray emission band, namely,

$$F_2(x) = \frac{-200}{\pi}\left(\operatorname{arctg}\frac{x-15}{2} - \operatorname{arctg}\frac{x-25}{3}\right) + \frac{25}{1+\left(\frac{x-28}{2}\right)^2}.$$

The mathematically determined corrected shapes

$$f_1(x) = 100\left[1 - \frac{2}{\pi}\operatorname{arctg}(x-15)\right] + \frac{50}{1+(x-28)^2}$$

and

$$f_2(x) = \frac{-200}{\pi}\left[\operatorname{arctg}(x-15) - \operatorname{arctg}\frac{x-25}{2}\right] + \frac{50}{1+(x-28)^2}.$$

are shown on the same figure.

The points obtained by our method for $f_1(x)$ and $f_2(x)$ are also shown on the plots (crosses). It will be evident that in spite of the fact that γ/β was as large as 0.5 the points depart from the calculated $f_1(x)$ and $f_2(x)$ curves by no more than 5% at the maximum ordinates and that for the most part the error is even less than 1%.

The advantages of this method over those mentioned at the beginning of the article are obvious, since no calculations are required to obtain the step-function parameters, as is necessary when using the arc tangents, dispersion curve and trigonometric series methods. Unlike the last named, our method is free of edge distortion. Shortcomings of our method are that it can be used only for dispersion type distortion and that its accuracy falls off as the ratio of the line broadening to the half-width of the corrected line increases. In addition, it must be admitted that in the case of a complicated spectrum with many close peaks, the number of computational operations becomes rather great.

In conclusion, I express my sincere gratitude to Dr. M.A.Blokhin for advice and aid in writing the present article.

Rostov Institute of Agricultural Machinery Engineering

References

1. E.E.Vainshtein, Rengenovskie spektry atomov v molekulakh khimicheskikh soedenenii i splavakh (X-ray spectra of atoms in molecules of compounds and alloys). M. 1050.
2. P.H.Van Cittert, ZS fur phys. 69, 289 (1931).
3. P.H.Van Cittert & H.C.Burger, ZS f. Phys. 79, 722 (1932).
4. V.M.Chulanovskii & A.V.Timoreva, Izv. AN SSSR, Ser.fiz., 11, 376 (1947).
5. E.E.Vainshtein, Usp. khimii, 15, 269 (1946).
6. M.A.Blokhin, Doklady AN SSSR, 107, 229 (1956).

INFLUENCE OF AN ACTIVATOR ON THE X-RAY ABSORPTION SPECTRUM OF A LUMINESCENT CRYSTAL

- K.I.Narbutt & I.S.Smirnova

Over a period of years Barinskii, Vainshtein and one of the present authors[1-6] have been engaged in developing methods of analyzing the fine structure of x-ray absorption spectra. According to the concepts upon which these methods are based, the experimentally observed fine structure may be regarded as a superposition of lines of selective absorption corresponding to allowed transitions of inner electrons to free excited levels and continuous absorption associated with transition of inner electrons into the energy continuum. Other investigators[7,8] have expressed a different view regarding the nature of the fine structure of x-ray absorption spectra; they assert that the fine structure can appear only in the spectra of defect containing ionic crystals and that it is connected with the transfer of inner electrons to local levels associated with lattice defects.

Although the methods of analysis of the fine structure of absorption spectra developed in Refs.1 through 6 have already been successfully applied to a wealth of experimental material, convincing proof of the validity of this interpretation of the nature of the fine structure could be furnished only by experimental determination of the position of local levels in the fine structure of an x-ray absorption edge. Theoretically the position of lines of selective absorption associated with transitions to local defect levels was predicted for the case of a KCl crystal in Ref.3. It was shown in this theoretical investigation that these lines should appear between the shortest wavelength emission line and the first selective absorption line. Recently an attempt was made to find evidence of defect levels in the fine structure of the K absorption edge of chlorine in a KCl crystal subjected beforehand to heavy x-irradiation.[9] Evidence of the expected defect levels was not found in these experiments and thus the question remained open. Nevertheless, we felt that it might be feasible to detect the x-ray absorption associated with local levels in the crystal by subjecting the crystal to a stronger influence than x-irradiation, namely, by introducing into it an activator, thereby creating in it local activator levels. This therefore was the motivation of the present investigation.

At the same time one could expect the influence of the activator to extend to the entire crystal lattice with resultant modification of the entire structure of the x-ray absorption spectrum. From this viewpoint the present investigation was related to studies concerned with the influence of small amounts of impurities on the fine structure of x-ray spectra in general.

For the subjects of our investigation we chose NaI(Tl) and CsI(Tl) crystals of the type used in scintillation counters for detecting x-rays. In addition to regard for the practical importance of these crystals in x-ray spectroscopy, we were motivated in our choice by the fact that we had already investigated[10] experimentally and theoretically the fine structure of the L_{III} absorption spectra of both components in an unactivated CsI crystal and of iodine in unactivated NaI and therefore already had on hand some of the necessary data.

Experimental procedure

The L_{III} absorption spectra of iodine in NaI, CsI, NaI(Tl) and CsI(Tl) and of cesium in CsI and CsI(Tl) crystals were obtained on a long-wave focusing x-ray spectrograph with a quartz crystal analyzer. We used reflection

from the $(10\bar{1}0)$ planes in the second order; the dispersion was 6.91 X/mm in the region of the L_{III} edge of cesium and 6.53 X/mm in the region of the L_{III} edge of iodine. The spectra were recorded photographically and the densities measured on an MF-2 microphotometer. All the final results were the average values for five curves. We used extremely fine-grained photographic film, so that even single curves satisfactorily brought out the structure of the absorption edge. The reference lines for wavelength determinations in the region of the L_{III} edge of iodine were the III Co $K\alpha_{1,2}$ and IV Cu $K\beta_1$ lines; the reference lines for the L_{III} edge of cesium were the IV W $L\beta_2$ and III Co $K\beta_1$ lines. For our investigation we selected NaI(Tl) and CsI(Tl) crystals tested beforehand in a scintillation counter and found to be effective x-ray photon detectors. The approximate thallium content of the crystals was 0.01-0.1%.

Selecting a procedure for preparing the absorbers presented particular difficulties. It was necessary to prepare thin screens consisting of undamaged fine crystals of the luminophor and, in addition, it was necessary to take into account the highly hygroscopic nature of NaI. The absorbers were prepared by grinding the crystal in vacuum type "Vaseline" (petroleum jelly) and applying the resultant mixture to cigarette paper in a uniform thin layer. For control purposes, absorbers of unactivated substances were prepared in the same manner. With this method of preparation it was difficult to determine the thickness of the absorber, hence the absorption spectra of both activated and unactivated crystals with absorbers of different thickness were photographed numerous times.

Experimental results and analysis

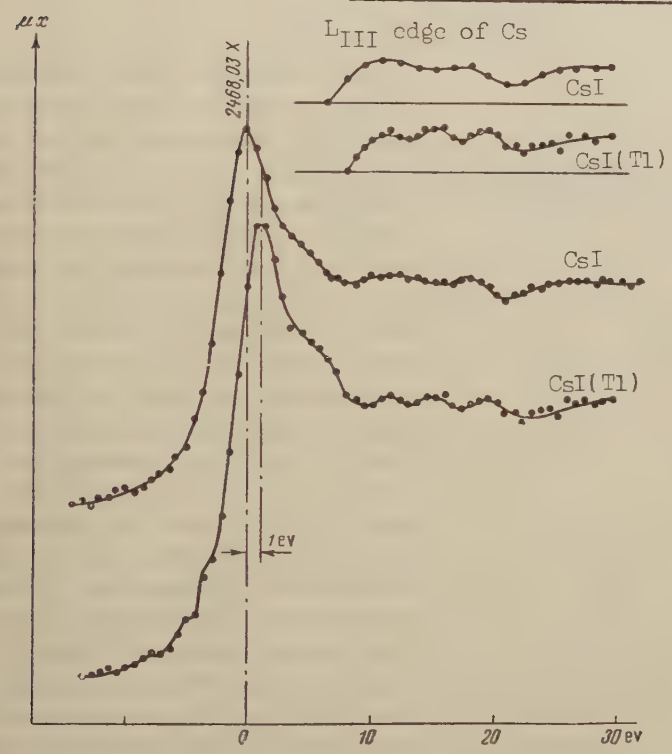

Fig.1. Experimental L_{III} absorption spectra of cesium in CsI and CsI(Tl) crystals. The upper insert shows the remainders left after subtraction of the selective absorption lines; these residual spectra are associated with transition of 2p electrons to s-symmetry levels.

The absorption spectra of cesium in the vicinity of the L_{III} absorption edge in activated and unactivated CsI crystals are shown in Fig.1. As was done in Ref.10 in the case of an unactivated CsI crystal, the L_{III} absorption edge of cesium in the activated CsI(Tl) crystal can be resolved into lines of selective absorption corresponding to transitions of 2p electrons to free d-symmetry bands and a remainder corresponding to transitions of 2p electrons to free s-symmetry bands. The remainders obtained in this manner are shown in the upper part of Fig.1; these remainders represent the absorption associated with transitions to s-symmetry bands beginning with 6s. As may be seen from the figure, introduction of the activator leads to splitting of the 6s band. In addition, as was expected, there appear on the long wavelength side of the edge, a weak absorption maxima which we associated with transitions of 2p electrons to local levels.

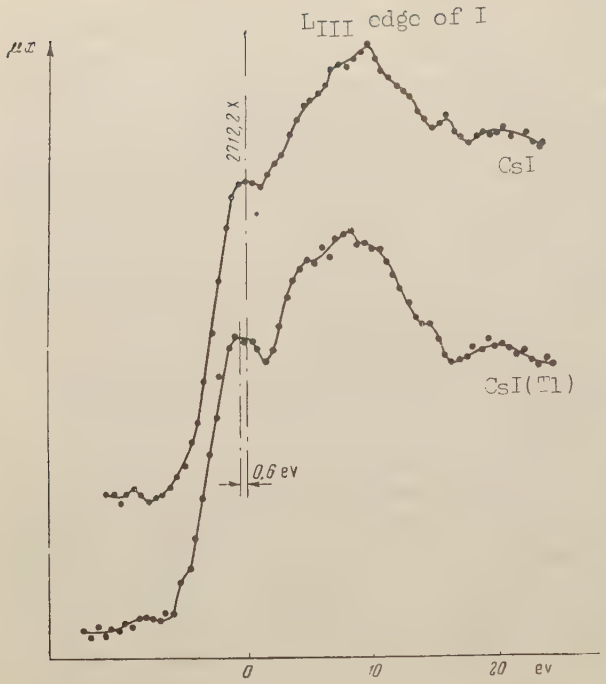

Fig.2. Experimental L_{III} absorption spectra of iodine in CsI and CsI(Tl) crystals.

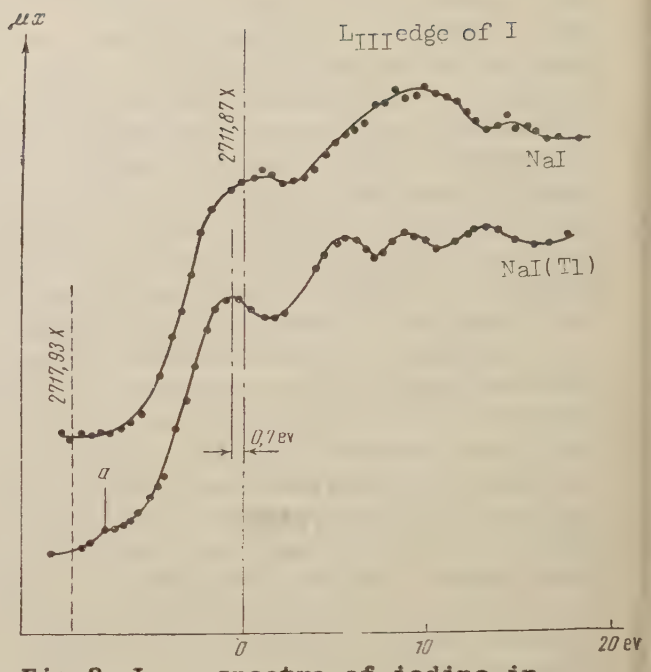

Fig.3. L_{III} spectra of iodine in NaI and NaI(Tl) crystals obtained with the minimum thickness of the absorbing screen (layer).

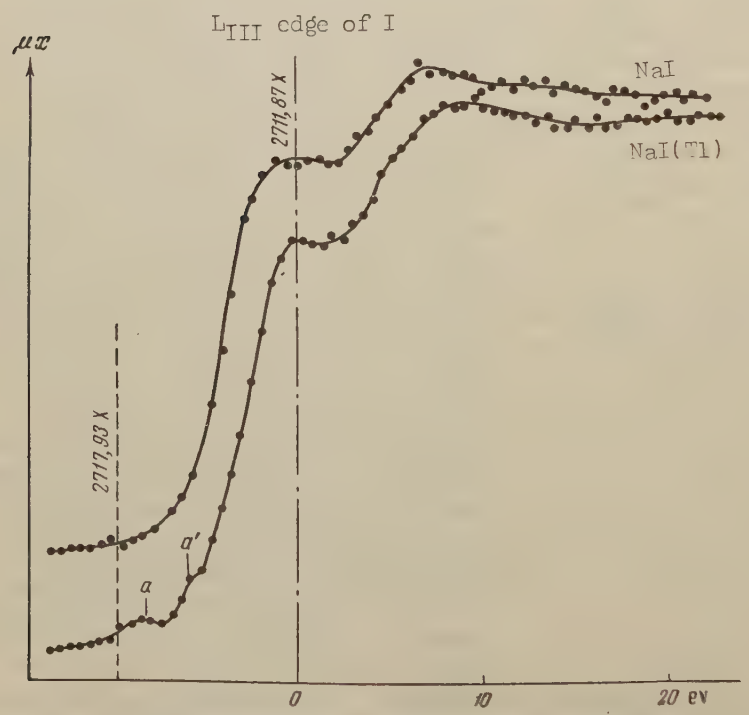

Fig.4. L_{III} absorption spectra of iodine in NaI and NaI(Tl) crystals obtained with the maximum thickness of the absorbing screen.

Analogous evidence of local levels is observed in the L_{III} spectrum of iodine in CsI(Tl) (Fig.2). The influence of the activator on the s bands in this case, however, is less pronounced.

With a view to eliminating any possibility that the observed alteration in structure was due to the influence of absorber thickness, the L_{III} absorption spectra of iodine in NaI and NaI(Tl) were photographed with the minimum and maximum possible thicknesses of the absorbing layer. The results are shown in Figs.3 & 4. It will be obvious from a comparison of the curves that the difference in structure of the L_{III} edges of iodine in the activated and unactivated absorbers is due to the influence of the activator and not to any variation in thickness of the

layer. In the case of NaI introduction of the activator leads to the appearance of additional absorption maxima on the long wavelength side of the edge and noticeable splitting of the 6s band.

Thus we note the following changes in the structure of the L_{III} absorption edges of iodine and cesium in NaI and CsI crystals as a result of introduction of the activator:

1. Additional fine structure in the form of weak absorption maxima or inflections in the spectral curve appears on the long wavelength side of the L_{III} discontinuity.

2. The structure associated with transitions of 2p electrons to the free s-symmetry bands (beginning with 2p→6s) is noticeably modified.

3. The absorption edge of the halide is displaced to the long-wave side, while the absorption edge of the metal is displaced in the opposite direction; the magnitude of the shift amounts to 0.6-1 ev. The last two effects are apparently manifestations of the general influence of the impurity on the system of energy bands in the crystal.

As was noted above, in the work of Ref.9 it proved impossible to find any evidence of local levels produced by heavy x-irradiation of the crystal in the fine structure of the K absorption spectrum of chlorine in KCl. In that study the x-ray dosage was such that one could expect the appearance in the crystal of local levels in the amount of 0.1% relative to the total number of atoms in the crystal. In the activated crystals used in the present investigation the number of local levels was not greater than in the x-irradiated crystals of Ref.9, inasmuch as the thallium content in our crystals did not exceed 0.1%. Yet, in the case of the activated crystals, evidence of local levels was detected in the x-ray spectra. Thus where manifestiation of local levels in x-ray spectra is concerned, it would appear that what is important is not the quantitative aspect but the qualitative difference of the local levels produced by the activator.

As was shown in Ref.2, one can calculate the wavelengths of the lines in the ultraviolet spectrum of a material from analysis of the structure of the absorption edge provided the energy level of the last filled band in the crystal is known. This energy value can be determined if we know the wavelength of the last emission line of the x-ray spectrum of the given series.

In the case of iodine the transition from the last filled $O_{II,III}$ band to the L_{III} level is forbidden by the selection rules so that direct determination of the relative position of the last filled band is impossible. One can, however, artificially determine the position of the last emission line utilizing the value of the term for the $\gamma_4\gamma_4'$ line corresponding to the $O_{II,III}$ →L_I transition and the relationship

$$O_{II,III}\rightarrow L_{III} = (O_{II,III}\rightarrow L_I) - (L_{III}\rightarrow L_I).$$

By way of illustration we give the calculation for NaI below.

For determining the $L_{III} - L_I$ term difference one cannot use the tabular values of the L_{III} and L_I terms, calculated, as is usually done, from the points of inflection in the long wavelength side of the absorption edge curve. Inasmuch as the first absorption peaks in the L_I and L_{III} edges correspond to transitions from the L_I and L_{III} levels to the $P_{II,III}$ and $O_{IV,V}$ bands, respectively, the difference taken in this manner includes the difference between the final bands of the transition, i.e., the difference

$$(P_{II,III} - L_I) - (O_{IV,V} - L_{III}) = (L_{III} - L_I) - (O_{IV,V} - P_{II,III}).$$

Hence in order to determine the difference $L_{III} - L_I$ from the L_I and L_{III} absorption discontinuities one must take not the points of inflection in the long wavelength side of the absorption curve but the points of inflection of arc-tangent curves obtained in resolving the edges corresponding to continuous absorption. Proceeding in this manner, we obtained the following values for the points of inflection of the true absorption edges:

for the true L_I edge: $\lambda = 2378.76$ X; $\nu/R = 383.08$, and
for the true L_{III} edge: $\lambda = 2708.18$ X; $\nu/R = 336.48$.

We obtained the $\gamma_4\gamma'_4$ line by the primary method with the x-ray tube operated at reduced power. In calculating its wavelengths we used the IV W $L\beta_2$ and II Cu $K\alpha_2$ lines as reference. We obtained

$\lambda = 2386.22$ X and the corresponding term value $\nu/R = 381.88$.

Using the term difference $(L_I - L_{III})$ and the term value for the $\gamma_4\gamma'_4$ line evaluated as described above, we determined the relative absorption (with reference to the L_{III} edge) of the last emission line characterizing the position of the last filled band:

$$(\nu/R)_{L_{III} - O_{II,III}} = 381.88 - (383.08 - 336.48) = 335.28,$$
$$\lambda_{L_{III} - O_{II,III}} = 2717.93 \text{ X}$$

The position of this line in the spectrum is shown by dash lines in Figs. 3 & 4.

Using the above value, we calculated the wavelength of the band in the optical spectrum of NaI(Tl) corresponding to the weak absorption peak α (see Figs.3-4) appearing in the long wavelength part of the L_{III} edge as a result of introduction of the activator. We obtained $\lambda = 5600$ Å, which is in good agreement with the experimental value[11] for the wavelength of the F absorption band in NaI(Tl), namely, $\lambda_{exp} = 5880$ Å. The analogously calculated wavelength of the band in the optical spectrum corresponding to the weak absorption maximum α'(Fig.4), which is more clearly evident in the case of a thick absorber, is 2900 A. Hilsh[12] reports observing a band at 2930 Å in the spectrum of NaI(Tl). The agreement of the calculated wavelengths with the experimental values may be considered fully satisfactory inasmuch as the accuracy of our measurements was no better than 0.11 ev, which corresponds to an uncertainty of ±300 Å in calculating the wavelengths in the optical region.

On the basis of the experimental data obtained for the absorption spectrum of the NaI(Tl) crystal and analysis of this spectrum, we constructed the energy diagram shown in Fig.5. In this diagram we have indicated the position of the last filled band as well as the positions of the local levels; the arrows in the lower part of the diagram denote the electron transitions corresponding to bands that should be observed in the optical spectrum of this crystal.

A similar energy diagram was also constructed for the CsI(Tl) crystal and is shown in Fig.6. It should be noted that in the case of CsI(Tl) the local levels were evinced both in the L_{III} absorption spectrum of the iodine and in the L_{III} absorption spectrum of cesium; their energetic location relative to the selective absorption lines of the d series was the same in both cases within the limits of the experimental error. It follows from our calculations that there should be observed bands at 2990, 1800, and 1170 A in the optical

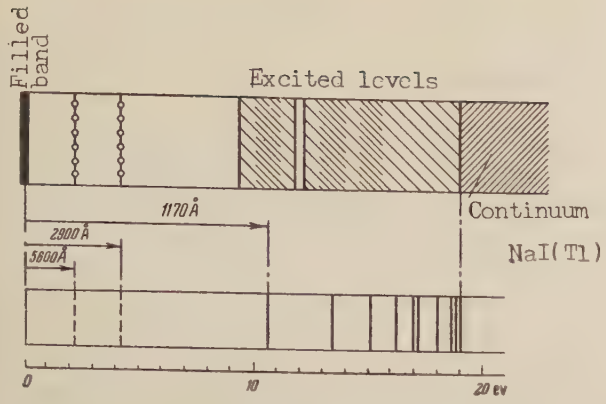

Fig.5. Energy diagram for NaI(Tl) crystal constructed on the basis of the x-ray spectroscopic data.

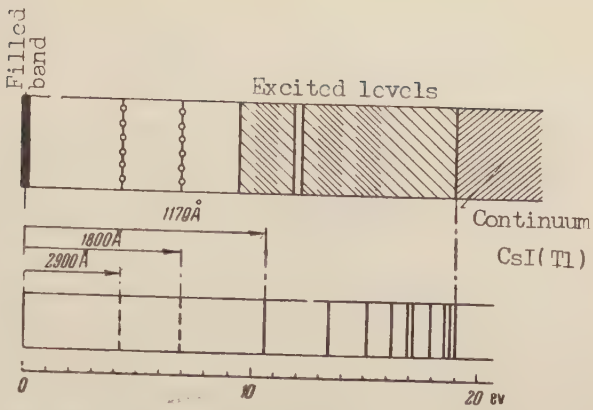

Fig.6. Energy diagram for CsI(Tl) crystal constructed on the basis of the x-ray spectroscopic data.

spectrum of CsI(Tl). According to the data in the literature a band at about 2900 A has been observed in the spectrum of this crystal.[12]

Conclusions

1. The investigation provided experimental evidence of the influence of an activator on the x-ray absorption spectrum of luminescent crystals in the case of NaI and CsI crystals activated with thallium.

2. We observed the appearance of additional absorption maxima on the long wavelength side of the absorption discontinuity in the L_{III} spectra of iodine and cesium in CsI(Tl) and of iodine in NaI(Tl); we inferred that these new peaks are associated with electron transitions to local levels.

3. The wavelengths of the bands that should appear in the optical region of the spectrum have been calculated on the basis of analysis of the long-wave portion of the L_{III} absorption spectrum of iodine in NaI(Tl) and the L_{III} absorption spectra of iodine and cesium in CsI(Tl) crystals. The calculated values are in satisfactory agreement with optical experimental data, in particular with the wavelength reported for the F band in NaI(Tl).

4. The alterations observed on the short-wave side of the discontinuity in the L_{III} absorption spectra of iodine and cesium in NaI and CsI crystals upon the introduction of an activator (Tl) amount to splitting of the second intense absorption peak, which according to our analysis indicates splitting of the 6s band into at least two bands.

5. With introduction of the activator the absorption edge of the halide is shifted to the long-wave side and that of the metal to the short-wave side by ~1 ev.

6. Energy diagrams for the NaI(Tl) and CsI(Tl) crystals have been constructed on the basis of the x-ray spectroscopic data obtained in the present investigation.

IGEM, Academy of Sciences of the USSR

References

1. E.E.Vainshtein, R.L.Barinskii & K.I.Narbutt, Zhur.eksp.i teor.fiz., 23, 593 (1952).
2. E.E.Vainshtein, K.I.Narbutt & R.L.Barinskii, Doklady AN SSSR, 82, 701 (1952).
3. K.I.Narbutt, E.E.Vainshtein & R.L.Barinskii, Doklady AN SSSR, 87, 381 (1952).
4. E.E.Vainshtein, R.L.Barinskii & K.I.Narbutt, Zhur.eksp.i teor.fiz., 27, 521 (1954).
5. E.E.Vainshtein, R.L.Barinskii & K.I.Narbutt, Doklady AN SSSR, 105, 1196 (1955).
6. R.L.Barinskii, E.E.Vainshtein & K.I.Narbutt, Present issue of the Bulletin, p.1341.
7. A.I.Kostarev, Zhur.eksp.i teor.fiz., 22, 628 (1952).
8. A.I.Kostarev & I.B.Borovskii, Zhur.eksp.i teor.fiz., 26, 377 (1954).
9. R.L.Barinskii, Tezisy dokladov V Vsesoiuznogo soveshchaniia po primeneniiu rentgenovykh luchei k issledovaniiu materialov (Abstracts of reports presented at the Fifth All-Union Conference on the Application of X-rays to the Investigation of Materials), p.84, L.1955.
10. I.S.Smirnova & K.I.Narbutt, Present issue of the Bulletin, p.1363.
11. Landolt-Börnstein, Atom und Molekularphysik, Teil 4, Kristalle, p.982, Springer-Verlag, 1955.
12. R.Hilsh, Phys.f.ZS., 38, 1031 (1937).

INVESTIGATION OF THE FINE STRUCTURE OF X-RAY ABSORPTION SPECTRA OF ALKALI HALIDE COMPOUNDS

- I.S.Smirnova & K.I.Narbutt

The most fruitful approach to the study of the structure of x-ray absorption spectra, in our opinion, is through investigation and analysis in proper sequence of the spectra of materials of increasing complexity, i.e., starting with gases and proceeding to more complicated compounds. Positive results have already been obtained in this way.[1-4]

Where the absorption spectrum of solids are concerned, we come first to the group of alkali halide compounds. Investigations of the spectra of potassium and chlorine in ionic KCl crystals[5,6] and analysis of the K spectra of potassium halides[7] have shown that not only can systematically accumulated experimental data on ionic crystals be analyzed from a consistent viewpoint but that such analysis allows of bringing out certain important regularities. A number of different investigators have studied the fine structure of the x-ray absorption spectra of alkali halide compounds. In the accompanying table, listing all the alkali halide compounds, we have underlined the elements whose absorption spectra have already been investigated. Thus the K spectra of sodium in all sodium halides have been investigated by Rule[8]; the L_{III} spectra by O'Bryan[9]. The K spectra of potassium in all potassium halides was investigated in the above mentioned work of Vainshtein, Barinskii & Narbutt[7], as well as by Trishka[10], and Kiyono[11]. The K spectra of chlorine were investigated experimentally and theoretically by Barinskii[12].

LiF	LiCl	LiBr	LiI
NaF	NaCl	NaBr	NaI
KF	KCl	KBr	KI
RbF	RbCl	RbBr	RbI
CsF	CsCl	CsBr	CsI

The purpose of the present work was to complete the experimental investigation of this group of compounds insofar as the possibilities available to us allowed. If we exclude from consideration the ultralong wavelength region of the x-ray spectrum (the absorption spectrum of lithium and fluorine), it will be seen from the table that the following absorption spectra had not been previously investigated: iodine in the iodide series, bromine in the bromide series, and cesium and rubidium in the respective halides. In the present report we shall give the results of investigation of the structure of the L_{III} absorption spectra of iodine in the iodides of all the alkali metals (LiI, NaI, KI, RbI and CsI) and the L_{III} absorption spectra of cesium in all its halides (CsF, CsCl, CsBr and CsI). We also investigated the absorption spectra of bromine in the alkali bromides and of rubidium in its halides, but the results obtained will be set forth in another article.

Experimental procedure

The absorption spectra of iodine in the alkali iodides and of cesium in its halides were obtained on a long-wave curved quartz crystal spectrograph in the second order of reflection from the $(10\bar{1}0)$ planes with a dispersion of 6.913 X/mm in the region of the L_{III} edge of cesium and 6.53 X/mm in the region of the L_{III} edge of iodine. The spectra were recorded photographically and measured by means of an MF-2 microphotometer; the final values in each case were averages for five photometric curves. The use of extremely fine-grained photographic film minimized the harmful influence of grain so that

even individual curves satisfactorily brought out the structure of the absorption edge. The reference lines used in determining the wavelengths in the L_{III} edge of iodine were the III Co $K\alpha_{1,2}$ and IV Cu $K\beta_1$ lines, while the reference lines for determining the wavelengths in the L_{III} edge of cesium were the IV W $L\beta_2$ and III Co $K\beta_1$ lines. The absorbers (samples) were prepared by soaking sheets of cigarette paper in aqueous solutions of the respective salts. The best absorber thicknesses were found empirically. In investigating the L_{III} edges of iodine the effective thickness of the absorber was of the order of 5 μ iodine, while for the L_{III} edges of Cs it was 5-8 μ cesium.

Results and analysis

The experimental L_{III} absorption spectra of Cs in all the halides and the L_{III} spectra of I in all the iodides are reproduced in Fig.1.

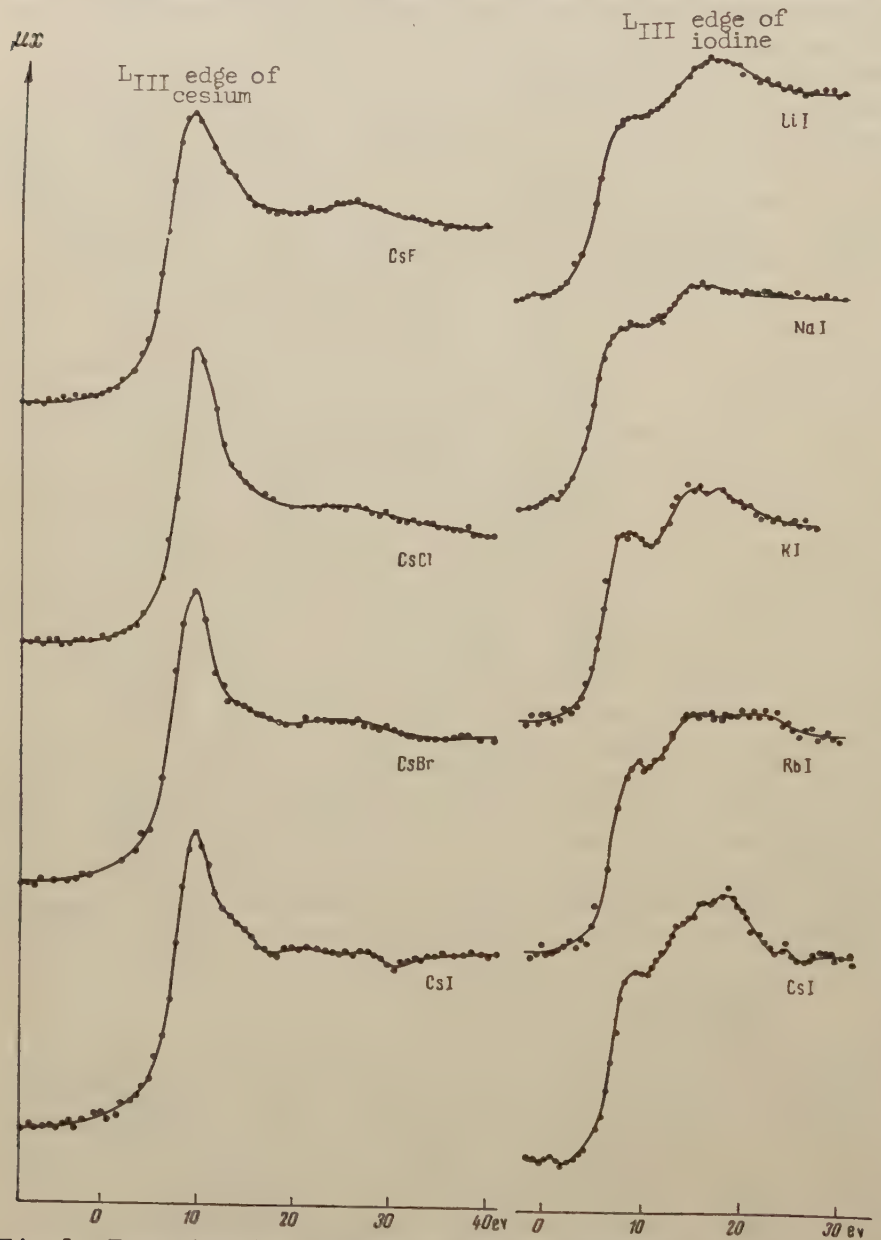

Fig.1. Experimental L_{III} absorption spectra of cesium and iodine in the indicated alkali halides.

In turning to interpretation of the results we must note that only availability of systematic data, i.e., the results of investigation of the L_{III} spectra of cesium in all its halides and of the L_{III} spectra of iodine in all the iodides made it possible to decipher the results by means of the method of analysis of absorption edges developed in the above-cited investigations (Refs.2,3,5 & 7). The distinction was that in this case we were dealing with the L_{III} absorption spectra whereas in the earlier investigations only the K spectra were analyzed.

We treat the L_{III} absorption spectra as being the result of superposition of the selective absorption lines corresponding to allowed transitions of 2p electrons to free s- and d-symmetry bands (2p→ns and 2p→nd). The L_{III}

spectrum is comprised of at least two series of lines: an s and a d series; this, however, is true only in the simplest case. As was shown in Ref.5 for the specific case of the K absorption spectra of potassium and chlorine in KCl crystals, the K spectrum of each of the components of the crystal consists of a superposition of two series of selective absorption lines: a principal and a secondary series. Applying these concepts to the given case, we must expect to find in the L_{III} spectrum four series of lines, namely, two s series (a principal and secondary one) and two d series (again, a principal and secondary one).

These were the concepts utilized in analyzing our experimental data. For purposes of illustration and more detailed analysis here we have selected the data for CsI inasmuch as in this case we investigated both the components. Examining the L_{III} edges of cesium, we note the presence of a clearly pronounced intense white line in all the edges. It is natural to infer that this line is associated with 2p→5d electron transitions. This gives us the beginning of the principal d series. We associate the "hump" in the short wavelength part of the L_{III} absorption spectrum, whose intensity is greatest in the case of the most ionic compound CsF and falls off in going to the less ionic compounds (i.e., to CsI), with transitions to the s state. The first maximum of the principal d series is clearly evident; we identified the bulge on the short wavelength side of the principal maximum with the second line of the principal d series and on the basis of this identification calculated the effective quantum number n^* for the principal d series ($n^* = 1.41$). Next we plotted the entire principal d series and the true edge. We subtracted this total curve from the experimental one and obtained a remainder in the form of two lines indicating the existence of the second d series. This remainder was represented in the form of a series with $n^* = 1.55$.

The described resolution is shown in Fig.2. Here we show the selective absorption lines of the principal d series and have hatched the area under the secondary d series. The integral (total) curve for the d series is given by the dash line. The remainder obtained in the short wavelength part of the spectrum is by inference associated with transitions to s states, beginning with 6s and comprises two s series (a principal and a secondary).

Let us now turn to the L_{III} spectrum of iodine. On the basis of the general concepts developed in Ref.5 & 7, it may be assumed that the order of arrangement of the series must be the same as in the L_{III} spectrum of cesium. Consequently, we aligned the first peak of the L_{III} edge of iodine with the first peak in the L_{III} edge of cesium. This enabled us to determine the position of the first line of the secondary d series in the L_{III} spectrum of iodine. The position of the first line of the principal line of the d series of iodine was determined from the position of the first line of the secondary d series in the cesium spectrum. Using the same effective quantum numbers as in the case of the L_{III} edge of cesium ($n^*_{Cs} = 1.41$ and $n^*_I = 1.55$), we constructed the principal and secondary d series. The remainder, obtained after subtracting the integral curve from the experimental one, contains two s series (it is shown in the upper part of Fig.2).

There are a number of noteworthy features in the structure of the L_{III} edges of cesium and iodine in CsI. In the spectrum of cesium the principal d series is much more intense than the secondary one, whereas in the L_{III} spectrum of iodine the secondary d series approaches the intensity of the principal d series. The explanation for this must be sought in the different configurations of the 5d shells of iodine and cesium (the atomic numbers of Cs and I are 55 and 53, respectively) and in the fact that the filling of the 5d shell begins with the atomic number 57.

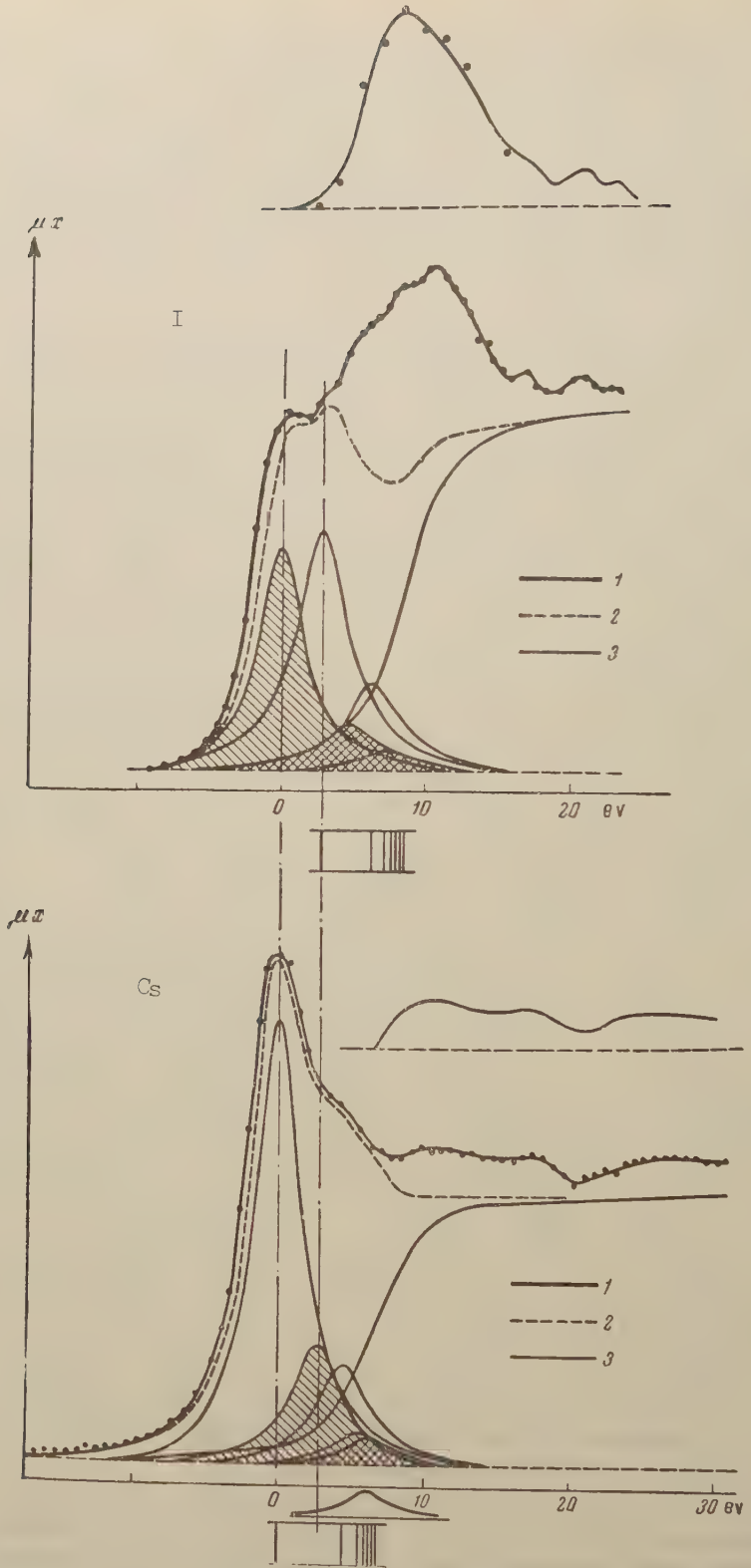

Fig.2. Analysis of L_{III} absorption spectra of iodine and cesium in crystalline CsI: 1) experimental curves, 2) theoretical total curve for the principal and secondary d series, 3) lines of selective absorption of the principal d series and continuous absorptions; the secondary d series is hatched. In the upper part of each figure are shown the s remainders obtained after subtraction of the integral theoretical curves for the principal and secondary d series from the experimental absorption curves; these comprise the principal and secondary s series.

From our analysis of the absorption spectra of cesium and iodine (Fig.2) it will be evident that the s states are more strongly manifested in the L_{III} spectrum of iodine as compared with the L_{III} spectrum of cesium, which, of course, is consistent with the fact that the 6s shell of iodine is vacant, while the 6s shell of cesium is partially filled.

An analogous analysis can be carried out for the other compounds, but even without going through the process, from an examination of the shape of the experimental curves shown in Fig.1, one can readily see that in the L_{III} spectra of cesium and its halides as we go from iodine to fluorine the remainder which we associate with 2p→ns transition ($n \geqslant 6$) increases; this is undoubtedly related with the increasingly ionic character of the compounds as we go to CsF. Or, more accurately speaking, one can say that with increasing heteropolarity of the compound the intensity of the principal s series must increase. In contrast, in the L_{III} spectra of iodine the degree to which the compound is ionic should not have much effect on the total magnitude of the s remainder inasmuch as the 6s shell of iodine in the compounds in question does not participate in the chemical bonding. Variation in the degree of heterpolarity should, however, exert some influence on the intensity of the secondary s series which may lead to some change in shape of the s remainder.

We determined the wavelengths corresponding to the characteristic points of the investigated spectra. It was found that the wavelengths of the principal peak in the L_{III} spectra of cesium remains the same in all the cesium compounds and equals 2468.03 ± 0.05 X-units. In the light of what has been said regarding the structure of the L_{III} spectrum of cesium, this means that the wavelength of the 2p→5d line of the principal series, which essentially determines the position of the principal peak, remains unchanged in all the cesium compounds. In contrast, the wavelength of the first (lower) absorption peak in the L_{III} spectra of iodine changes appreciably as we go from lithium to cesium iodide. We obtained the following values:

LiI 2711.55 ± 0.06 X	RbI 2711.87 ± 0.06 X
NaI 2711.87 ± 0.06 X	CsI 2712.20 ± 0.06 X
KI 2712.13 ± 0.06 X	

In the light of the concepts developed here and taking into account the invariance of the wavelength of the first peak in the L_{III} absorption spectrum of cesium, the variation of the wavelength of the first peak in the L_{III} spectrum of iodine can be interpreted as the result of changes in the ratio of the intensities of the principal and secondary d series (Fig.2). It also follows from the above that the energy values of the selective absorption lines associated with 2p→nd type transitions do not depend on the character of the chemical bonds. It is interesting to compare this result with the fact, established in the investigation of Ref.13 (the preceding article) that the entire spectrum of NaI and CsI crystals is shifted upon the introduction of an activator (Tl).

Conclusions

1. We investigated the L_{III} absorption edge of cesium in all cesium halides and the L_{III} absorption edge of iodine in all alkali iodides.

2. The structures of the cesium and iodine L_{III} edges in CsI have been analyzed on the basis of the hypothesis that the L_{III} spectrum is the result of superposition of four series of selective absorption lines (a principal and secondary d series and a principal and secondary s series) and continuous absorption.

3. The L_{III} absorption spectra of cesium in its halides are characterized by an intense first absorption peak and a weak second peak. In contrast, in the L_{III} spectra of iodine in the alkali iodides the first absorption peak is lower than the second. These distinctive features can be explained by

a) the ratio of intensities of the principal and secondary d series: in the spectra of cesium the secondary series is strongly suppressed, while in the spectra of iodine the intensities of the principal and secondary d series are approximately equal; and

b) the difference in the filling of the 6s shells of iodine and cesium: in iodine this shell is vacant, while in cesium it is partially filled, thus giving rise to an appreciable intensity of the s series in the spectra of Cs and I.

4. The variation in the structure of the L_{III} absorption spectra of Cs and I in going from compound to compound amounts essentially to variation in intensity and shape of the second absorption maximum which we associate with $2p \rightarrow ns$ transitions.

5. The wavelength of the first peak in the CsI L_{III} absorption spectra remains the same for all the cesium halides. The wavelength of the first peak in the L_{III} spectra of iodine varies over a range of about 0.65 X (1.4 ev). These data, together with the proposed interpretation of the structure of the spectra lead us to conclude that the position of the lines of selective absorption does not depend on the character of the chemical bonds: the nature of the bonds (the degree to which ionic bonding predominates) affects only the relative intensities of the lines of the principal and secondary series. This leads to displacement of the experimentally observed peak which is the sum of the principal and secondary line series as one goes from less to more ionic crystals.

IGEM, Academy of Sciences of the USSR

References

1. K.I.Narbutt, Izv. AN SSSR, Ser.fiz., 15, 231 (1951).
2. E.E.Vainshtein, R.L.Barinskii & K.I.Narbutt, Zhur.eksp.i teor.fiz., 23, 593 (1952).
3. K.I.Narbutt, Doklady AN SSSR, 93, 21 (1953).
4. K.I.Narbutt, Izv.AN SSSR, ser.fiz., 20, 780 (1956). (Trans. in Bulletin, 20, No.7, 710.)
5. E.E.Vainshtein, K.I.Narbutt & R.L.Barinskii, Doklady AN SSSR, 82, 701 (1952).
6. K.I.Narbutt, E.E.Vainshtein & R.L.Barinskii, Doklady AN SSSR, 87, 381 (1952).
7. E.E.Vainshtein, R.L.Barinskii & K.I.Narbutt, Doklady AN SSSR, 105, 1196 (1955).
8. K.C.Rule, Phys.Rev., 66, 119 (1944).
9. H.M.O'Bryan, Phys.Rev., 57, 995 (1940).
10. J.Trischka, Phys.Rev., 67, 313 (1945).
11. S.Kiyono, Sci.Rep.Tohoku Univ., Ser.1, 36, 1 (1952).
12. R.L.Barinskii, Present issue of the Bulletin, p. 1369.
13. K.I.Narbutt & I.S.Smirnova, Present issue of the Bulletin, p.1356.

K ABSORPTION SPECTRA OF CHLORINE IN ALKALI METAL CHLORIDES

- R.L.Barinskii

Introduction

It has been shown in Refs.1-4 that the x-ray K absorption spectra of certain alkali halide crystals and gas molecules containing two different atoms can be represented in the form of a superposition of two series of absorption lines and continuous absorption. In resolving the spectrum, i.e., in plotting each line series and the continuous absorption, it was considered essential to adhere to the formulas derived for the hydrogen-like atom. The only arbitrary quantities in the analysis were the relative positions of the two series and their relative intensities. Where experimental data on the K absorption spectra of both components of the molecule or crystal were available even this arbitrariness fell away and the K absorption spectra of both components could be represented unambiguously in the form of two series of selective lines.

As a result of resolution of the K absorption spectra of potassium in KF, KCl, KBr and KI crystals[4], it was found that the extent of the secondary line series and the relative intensities of the principal and secondary series are subject to certain definite regularities, namely, depend on the polarizability and atomic number of the anion. This deduction, it must be noted, was reached for the specific case of the K absorption spectra of potassium in the enumerated halide crystals and its physical meaning as well as the validity of the basic hypothesis regarding the possibility of representing K absorption spectra of molecules and ionic crystals in the form of a superposition of two line series remained open to some question.

It was felt, therefore, that the availability of additional experimental material on the K absorption spectra of molecules and crystals in a series with continuously varying properties of one of the components (as for example in the series KF, KCl, KBr and KI) would allow of checking and refining the earlier deductions and provide the basis for a specific theoretical model that would lead to and thus substantiate the earlier empirical conclusions.

Hence by way of subject for the present investigation we chose the K absorption spectra of chlorine in the halides of Li, Na, K, Rb and Cs. All these halide crystals (except CsCl) have a simple cubic lattice and comprise cations with gradually changing parameters (ionic radius, polarizability, ionization potential, etc.) which should be evident in the character of the fine structure of the K absorption spectra of chlorine bound in these crystals.

Experimental results

The K absorption spectra of chlorine in the various chlorides were investigated on a vacuum x-ray spectrograph with quartz crystal bent to a radius of 0.5 meters. The spectra were recorded in the first order on fine-grain positive motion picture film. The dispersion of the instrument was 14 X/mm (9 ev/mm). The x-ray tube with a tungsten anode was operated at 30 to 50 ma and 5.5 kv. The exposure time varied from 5 to 8 hours. The spectra were measured on an MF-2 microphotometer, the scanning being repeated at 4-5 different heights and the final results being taken as the average for 3 to 5 films.

The specimens were prepared by compressing C.P. powders of the various compounds between two sheets of cigarette paper. The thickness of the absorbing layer prepared in this manner was determined by weighing and varied from 3 to 7 mg/cm^2. The best results were obtained with the thin absorbers ($\sim$ 3 mg/cm^2).

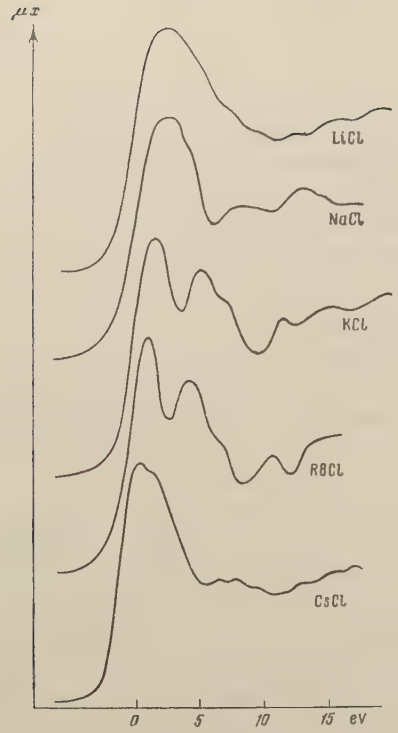

Fig.1. Absorption spectra of chlorine in LiCl, NaCl, KCl, RbCl and CsCl.

In view of the fact that LiCl is strongly hygroscopic a special procedure had to be developed for preparing and weighing the specimens of this compound; the final stages of drying of the LiCl specimens were carried out under high vacuum in the spectrograph tank itself. In Fig.1 we give the photometric curves of the K absorption spectra of chlorine in LiCl, NaCl, KCl, RbCl and CsCl reduced by means of the calibration curve for the photographic to the μx scale, where μ is the absorption coefficient and x is the thickness of the absorbing specimen.

It will be seen from the figure that in going from Li to Cs the long wavelength "branch" and the maximum of the fine structure of the K absorption spectra is displaced further to the long wavelength side. There also occurs an appreciable change in the fine structure itself, although at first glance there appears to be no consistent regularity in the nature of the changes.

Interpretation of the results

As the basis for resolution of the K absorption spectra of chlorine in the above enumerated compounds into two line series and continuous absorption we took the K spectrum of chlorine in KCl inasmuch as such a resolution for the K spectra of both components (K and Cl) had been carried out in an earlier investigation[1]. The results of this resolution are shown in Fig.4, where in the upper part of the figure the experimental K absorption edge of chlorine in KCl is shown by the heavy solid line, the individual components (the absorption lines through the fourth in the series and the continuous absorption) are shown by the light solid lines and the integral theoretical curve for the principal series is indicated by the dash line. In the lower half of Fig.4 the hatching (heavy solid line) represents the secondary series, i.e., the difference between the experimental curve and the integral theoretical curve for the principal series; the dash line indicates the integral theoretical curve for the secondary series. The locations of the lines on the energy scale are indicated by the vertical lines in the "spectra" under the curves. The values of the parameter n^* (principal quantum number) for the principal and secondary series and the values of the relative intensities of the series obtained in the present resolution were virtually identical with those arrived at in the analysis of Ref.1.

In order to realize the resolution of the K absorption spectra of chlorine in the other compounds it was necessary to assume in the first approximation (as was done earlier in Ref.4) that the principal series in the K spectra of Cl undergoes little variation in going from LiCl to CsCl, that is, that all the observed changes in the structure of these spectra occur primarily in the secondary series. Further from the appearance of the K spectra shown in Fig.1, it follows that the width of the absorption lines progressively increases in going from CsCl to LiCl and that it can be gaged from the experimental data.

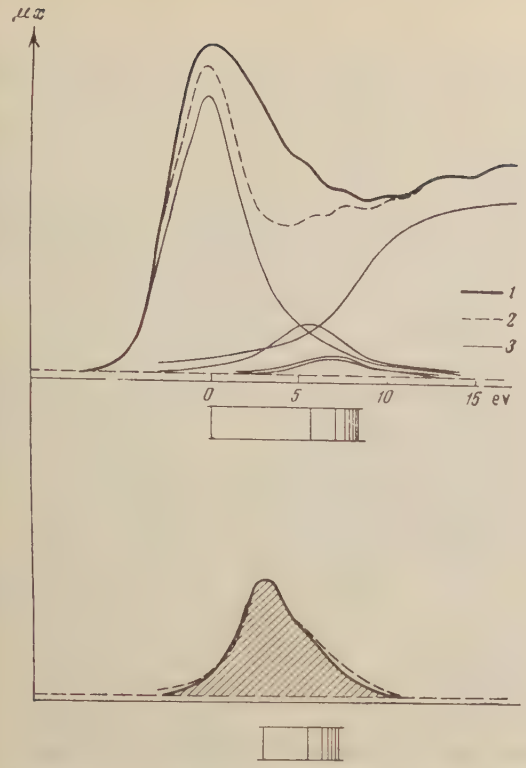

Fig.2. K absorption spectrum of Cl in LiCl.

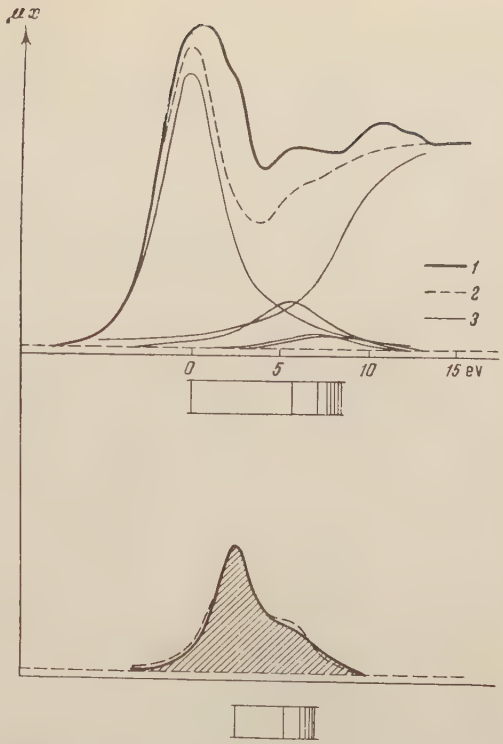

Fig.3. K absorption spectrum of Cl in NaCl.

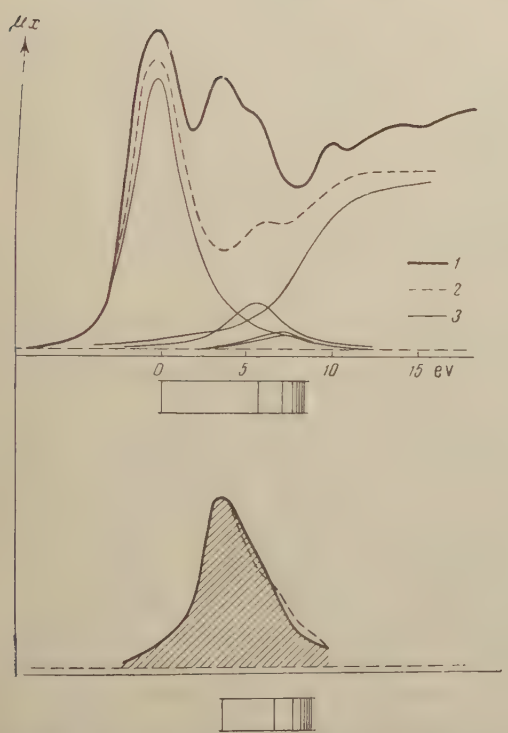

Fig.4. K absorption spectrum of Cl in KCl.

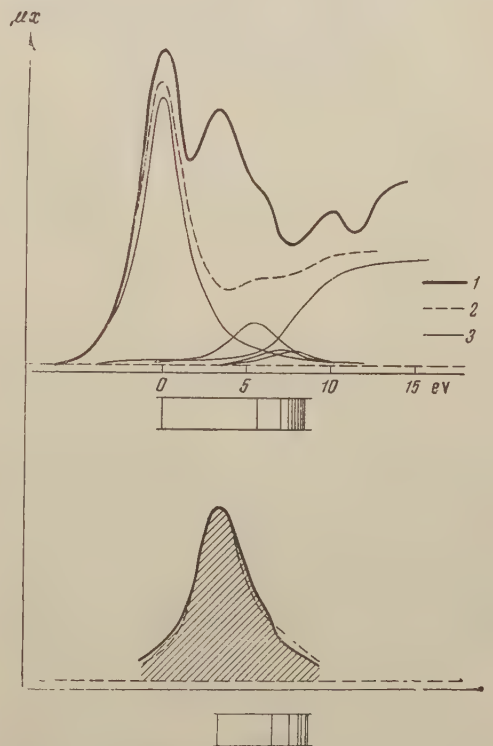

Fig.5. K absorption spectrum of Cl in RbCl.

Note: In all the above figures and Figs.6 & 9: 1) experimental curve, 2) individual "resolution" components of the principal line series, 3) integral theoretical curve for the principal series. In lower half of each figure: hatched area = difference between the experimental and the integral theoretical curves for the principal series; dash line = integral theoretical curve for the secondary line series.

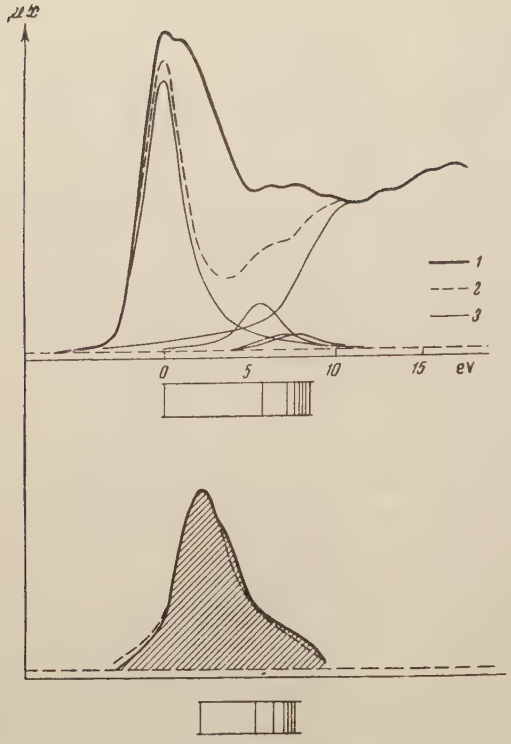

Fig.6. K absorption spectrum of Cl in CsCl.

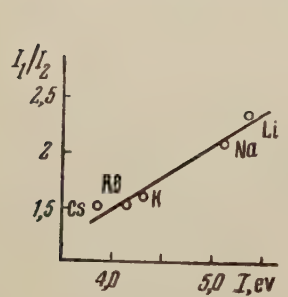

Fig.7

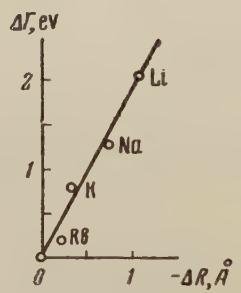

Fig.8

Fig.7. Plot of the ratio of intensities I_1/I_2 of the principal and secondary line series in the K absorption spectra of Cl in LiCl, NaCl, KCl, RbCl and CsCl vs the ionization potential of the alkali metal ions.

Fig.8. Plot of the difference between the absorption line widths $\Delta\Gamma$ vs the difference between the ionic radii of the alkali metal ions ΔR.

The K absorption spectra of chlorine in LiCl, NaCl, RbCl and CsCl were resolved accordingly and the results obtained are shown in Figs.2,3,5 & 6.

Analysis of the resultant data showed, in agreement with the earlier results of Ref.4, that the value of the principal quantum number n^* of the secondary line series is directly proportional to the polarizability of the cation. The slope of the straight line plot characterizing the relationship, however, is somewhat less steep than was found in the work of Ref.4. The same relationship, as in Ref.4, was found between the ratio of intensities (I_1/I_2) of the principal and secondary line series and the atomic number of the cation.

The physical meaning of this relationship becomes more clearly apparent if we plot I_1/I_2 vs J the ionization potential of the cation (Fig.7). In this case the dependence also proves to be linear and shows that the intensity of the secondary line series increases with increasing ionic character of the bonds.

Let us see what influence the magnitudes of the ionic radius of the cation has on the fine structure of the K absorption spectra of chlorine in its alkali metal compounds. As we noted above, the absorption line width progressively increases in going from CsCl to LiCl. The character of this growth can readily be followed in Figs.2-6. A similar effect has been noted earlier in the case of the 2p, 3s and 4p emission bands of alkali halide crystals[5] and is connected with decrease of the radius of the metallic ion in the Cs—Li series. With decreasing radius of the cation, the halide ions come closer together and the overlapping of their electron shells in creases. This leads to a broadening of the spectral lines. The effect is quantitatively illustrated in Fig.8 wherein the difference in line width $\Delta\Gamma$ (difference between the line width in the indicated compound and the width in CsCl) is plotted against ΔR (the radius of the indicated alkali ion minus the radius of Cs^+.

The correctness of the above description of the resolution of the K absorption spectra of chlorine was checked for the case of NaCl using the K absorption spectrum of sodium in NaCl obtained

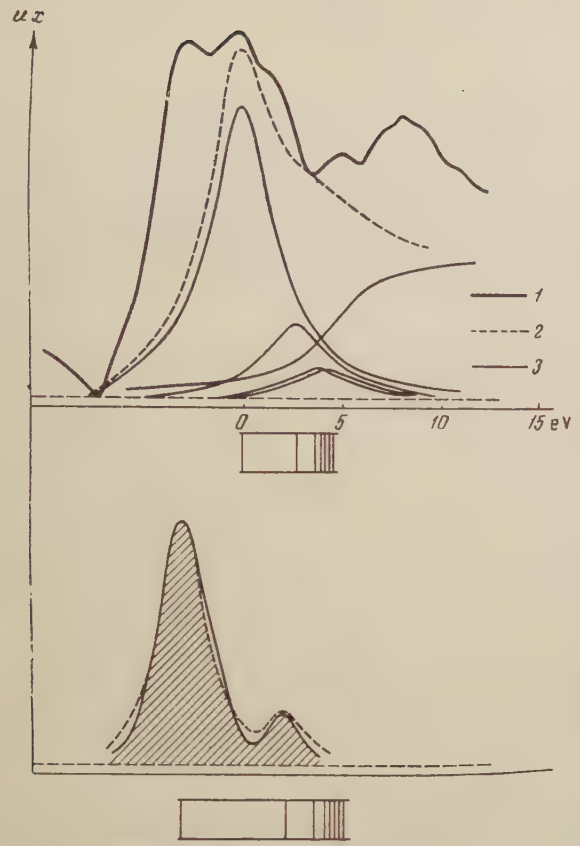

Fig.9. K absorption spectrum of Na in NaCl.

by Rule[6]. As the first step Rule's experimental curve was replotted to the same scale as the curves in Figs.2-6 (heavy solid curve in Fig.9). As the basis for the resolution of this spectrum, we used the secondary series separated out in the K spectrum of chlorine in NaCl and shown in the lower half of Fig.3. In the case of the K spectrum of sodium, this series must be the principal series and is therefore plotted as such (light solid line) in the upper half of Fig.9. The dash line in the upper part of Fig.9 is the integral theoretical curve for this principal line series. Naturally, the remainder obtained after subtracting the principal line series from the experimental K absorption curve for Na in NaCl (indicated in the lower part of Fig.9 by the hatching) and the integral theoretical curve of the secondary line series in the K spectrum of Na in NaCl must agree with the principal line series in the K spectrum of Cl in NaCl. That this is so will be evident from a comparison of Fig.3 (principal line series) and Fig.9 (secondary line series). This proves both the correctness of our resolution and the validity of the initial assumption upon which it is based.

Conclusions

1. We recorded the K absorption spectra of chlorine in LiCl, NaCl, KCl, RbCl and CsCl in the first order on a quartz crystal x-ray spectrograph.

2. The experimental curves exhibit a gradual shift to the side of longer wavelengths in going from LiCl to CsCl. The fine structure of the spectra also undergoes appreciable changes which at first glance appear to be characterized by no apparent regularity.

3. The K absorption spectra of Cl in the enumerated compounds were resolved into a principal and secondary line series and the true edge in accordance with earlier developed concepts and procedures.[1-4]

4. The correctness of this method of resolution was demonstrated for the case of the K absorption spectrum of Na in NaCl obtained some years ago by Rule[6] under entirely different experimental conditions. This demonstration again proved the validity of our method of analysis.

5. The resolution of the K absorption spectra of chlorine in its alkali metal compounds made it feasible to bring out certain regularities in the variation of the structure of the K spectra and to correlate the observed variations with such crystal parameters as the polarizability of the cation, its ionization potential and the ionic radius.

6. We give a physical interpretation of the detected regularities based on taking into account the variation in the ionic character of the bonds in alkali halide crystals and in the degree of overlapping of the electron shells of the chlorine ion.

7. The results obtained in the present investigation together with the earlier available data led to the formulation of a new theoretical model characterizing the processes occurring incident to K absorption of x-rays in gas molecules and alkali halide crystals (see Ref.7). All the deductions following from this model are in satisfactory agreement with the empirical generalizations arrived at earlier concerning x-ray absorption in such molecules and crystals.

Institute of Mineralogy, Geochemistry and Crystal Chemistry
of the Rare Elements ("IMGRE"), Academy of Sciences of the USSR

References

1. E.E.Vainshtein, K.I.Narbutt & R.L.Barinskii, Doklady AN SSSR, 82, 701 (1952).

2. K.I.Narbutt, Doklady AN SSSR, 93, 21 (1953).

3. K.I.Narbutt, Izv.AN SSSR, Ser.fiz., 20, 780 (1956) (Trans. Bulletin, 20, No.7, 710.)

4. E.E.Vainshtein, R.L.Barinskii & K.I.Narbutt, Doklady AN SSSR, 105, 1196 (1955).

5. N.F.Mott & R.W.Gurney, Electronic processes in ionic crystals (Cited in Russian trans., M., 1950).

6. K.Rule, Phys.Rev., 66, 199 (1944).

7. R.L.Barinskii, E.E.Vainshtein & K.I.Narbutt, Present issue of the Bulletin, p. 1341.

L ABSORPTION AND EMISSION SPECTRA OF Mo IN MOLYBDENUM CARBIDE AND OTHER COMPOUNDS

- R.L.Barinskii & E.E.Vainshtein

Introduction

The question of the nature of the chemical bonding forces between the atoms in carbides, nitrides and other "interstitial phases" of the transition elements and the question of the degree and character of participation of the nd electrons of the metal in the chemical bonds are among the most interesting and as yet obscure questions in the realm of chemistry and metallurgy. There have been advanced a number of more or less plausible hypotheses[1,2] regarding the character of the bonding forces between the atoms of the metal and the nonmetal in these compounds which, as we know, are characterized by a number of exceptional properties, properties that make them of great practical value. It has as yet been impossible to verify or disprove the different rival hypotheses due to the lack of sufficiently accurate, unambiguous experimental procedures. Indirect deductions, such as those drawn on the basis of analysis of data on the magnetic and electric properties of these substances or from crystallochemical considerations, often lead to contradictory or ambiguous results.

New and as yet unutilized possibilities as regards solution of these problems are offered by the methods of x-ray spectroscopy, based on experimental investigation and theoretical interpretation of the data on the fine structure of the x-ray spectra in different series of compounds. The present level of development of x-ray experimental techniques and the progress made in recent years in the field of the theory of x-ray spectra makes the spectroscopic method one of the most direct and promising experimental means for investigating the energy structure of solids and the allied question of the nature of the chemical bonds in them.

The first systematic investigations of the fine structure of the x-ray spectra of atoms of the transition elements in carbides, nitrides and some other "interstitial phases" were undertaken in two recently published studies (Ref.3 & 4) of the K emission spectra of titanium in a number of compounds and in alloys of the Ti-C system. The K absorption spectra of these substances are now being studied in our laboratory. However, even more clear cut results can apparently be obtained in investigating the fine structure of the L_{III} spectra of the transition metal in the corresponding carbide and other compounds. The most intense lines in the L_{III} spectra must be precisely the absorption and emission lines associated with electron transitions to the excited levels of d and s symmetry. This makes the L_{III} absorption edge and the corresponding emission spectra of the transition elements with unfilled nd shells particularly convenient for investigation of processes associated with involvement of the electrons of these atoms in the chemical bonds. Hence these spectra should be especially sensitive to changes occurring in the nd shells of the metal atoms incident to the formation of the bonds. The possibility of investigating the properties of transition elements in compounds with reference to their L_{III} absorption spectra has already been illustrated in the work of Ref.5.

The principal aim of the present study was investigation of the fine structure of the L_{III} absorption edge of molybdenum in Mo_2C with a view to clarifying certain controversial theoretical questions relating to the character of the chemical bonds linking the atoms in this compound. To facilitate and enhance the reliability of interpretation of the results we also investigated under identical conditions the fine structure of the L_{III} spectra of Mo

in four other compounds, namely, $(NH_4)_2MoO_4$, MoO_3, MoS_3 and MoS_2, inasmuch as the chemical bonds in these compounds have been investigated fairly thoroughly. For the same reason we also investigated the structure of the shortest wavelength L_{III} emission band of Mo (the $L\beta_2$ line) in the spectra of the carbide and certain other molybdenum compounds.

In ammonium molybdate the Mo atom has a valence of 6 and is located at the center of a tetrahedron. In it, according to Kimball[6], there must obtain sp^3-hybridization. Thus $(NH_4)_2MoO_4$ is a compound in which there are ten vacancies in the 4d shell of the Mo atoms, vacancies capable of receiving, under favorable conditions, 2p electrons ejected in the process of absorption of x-rays. The structure of the L_{III} absorption edge in this case should obviously be the most complicated and evince the maximum possibility of absorption of x-rays in the region of the spectrum associated with transition of Mo 2p-electrons to excited levels of the compound, having primarily d symmetry. The two other compounds investigated in this study, namely, MoO_3 and MoS_2, in which the nonmetal atoms form, respectively, a strongly deformed octahedron and a triangular prism with d^2sp^3 and d^4sp hybridization about the hexavalent and tetravalent molybdenum atom, are examples of compounds with successively increasing participation of the 4d electrons of the central atom in the chemical bonds. Accordingly, one should expect a regular change in the appearance of the fine structure of the L_{III} absorption edge of Mo in these compounds as compared with $(NH_4)_2MoO_4$: a decrease in the relative intensity as well as a change in the width and appearance of the corresponding regions of the spectrum within the main absorption edge of the element.

Measurement procedure

The spectroscopic work was carried out on a type DRUS (1956 model) long-wavelength vacuum spectrometer. The analyzer was a quartz slab having a working length of 15 mm and bent to a radius of 0.5 meters. The radiation was recorded by means of an RM-3 Geiger counter. The preliminary focusing of the crystal was carried out in air (photographic recording) by means of a sealed x-ray tube; the quality and accuracy of focusing on the Rowland circle was checked in the second, third and fourth orders of the Cu $K\alpha_{1,2}$ doublet. The line broadening at the focus due to defocusing and the Johansson mounting amounted to 0.7 X as compared with the calculated value of ~1 X. Further adjustment of the crystal was carried out in the tank of the spectrometer also by means of a sealed x-ray tube and was realized by turning the adjustment screws of the crystal-holder stage and the counter slit. The width of the counter slit was 0.05 mm. The final adjustment, determining the resolving power of the instrument, was checked by comparing the width of the $K\alpha_{1,2}$ lines of copper in the third order with the width of these lines as measured on a two-crystal spectrometer. It was found that the width of the $K\alpha_{1,2}$ copper doublet in the third order as measured by means of the DRUS spectrometer exceeded the true width of these lines by 0.7 X. Thus the resolution of the instrument for a wavelength of 4600 X was ~7000; the dispersion in the investigated region of the spectrum was 15.1 X per dial division; the accuracy of reading the dial was 0.01 division.

The L_{III} absorption spectra of molybdenum were recorded with a tungsten anode with the tube operated at a potential of 5 kv and a current of 15 to 20 ma. In investigating the emission spectra, the material was applied to the surface of a copper anode. The $L\beta_2$ emission bands of molybdenum were recorded with the tube operated at 3-3.5 kv and 4 to 5 ma.

The tube anode current was stabilized by means of an electronic regulator to within ±0.5% (with line voltage fluctuation of ~10%). The stabilization of the input voltage to the high voltage transformer and the entire supply circuit was realized by means of a ferroresonance regulator. The stability of the rectified high voltage was monitored by a S-96 kilovoltmeter. In the process of operation the voltage fluctuations at the output did not exceed 0.5%. The Geiger counter was operated from a special power supply unit; the rectified voltage (1500 v) was maintained stable within ±0.5%. The slope of the Geiger counter plateau (200 v) did not exceed 5-7%. The pulses from the counter were applied to a B-2 type scaling circuit and an integrating circuit with RC = 1 min. The last also served for coarse adjustment of the instrument.

The intensity of the x-irradiation varied with the operating regime of the tube and on the average did not exceed 500 pulses per min. To enhance the accuracy of wavelength determination (taking into account the possibility of play in the counter displacement mechanism) all the curves were recorded with the counter being displaced in the same direction. The possible error in wavelength measurement did not exceed 0.5 X (0.3 ev). In recording the curves from 3000 to 5000 pulses were counted for each point. In order to check the reproducibility of the results we usually recorded several curves (3 to 5) which were then averaged; in this case the total number of counts per point were not less than 10,000. Thus the statistical uncertainty was 0.8-1%.

Under the above described experimental conditions the reproducibility of the results was fully satisfactory. To illustrate the reproducibility, the points obtained in three series of measurements of the L_{III} absorption spectrum of molybdenum in $(NH_4)_2MoO_4$ are shown in Fig.1. The averaged results are represented by the solid line. The continuous spectrum from the tungsten anode is shown in the upper part of the figure (experimental points and averaged curve).

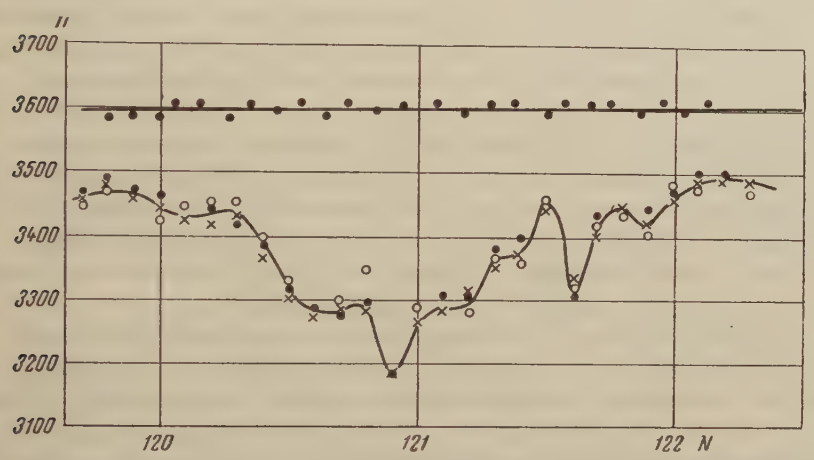

Fig.1. L_{III} absorption spectrum of Mo in $(NH_4)_2MoO_4$; experimental points for three series of measurements and the averaged curve. Above - continuous spectrum from the tungsten anode.

In preparing the absorber for recording the absorption spectra of molybdenum, we used the procedure of pressing the finely powdered specimen material into the pores of cigarette paper. This procedure is relatively simple and has a number of advantages over other procedures described in the literature: it obviates deterioration of the material and makes it possible to obtain a uniform absorbing layer 0.2 to 0.5 μ thick. The question of choosing the optimum thickness of the absorber in recording of absorption spectra containing a very intense line in the main absorption edge was analyzed by us in an earlier contribution[7] with respect to photographic recording. In the presence of a background, the conclusions reached in Ref.7 are valid for ionization type

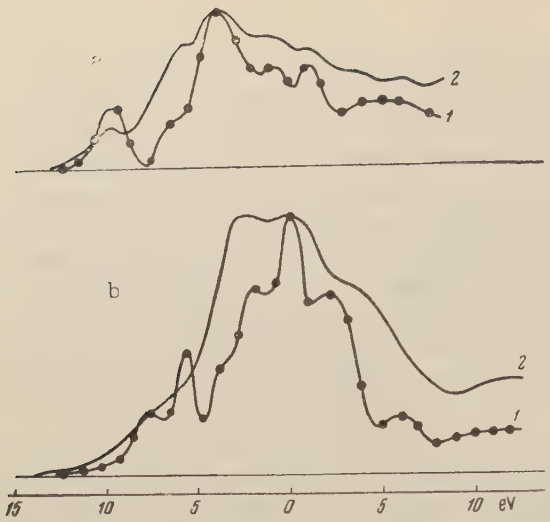

Fig.2. Comparison of the L_{III} absorption edges of Mo in MoS_2 (a) and $(NH_4)_2MoO_4$ (b) obtained in the present investigation (1) and in an earlier investigation using a photographic recording (2).

recording; consequently, the present study was carried out with absorbers having a thickness of 0.5 μ. Proof of the absence of any changes in the specimen inside the spectrograph was furnished, on the one hand, by the identity of the curves recorded at intervals of several days and, on the other hand, by the unaltered appearance of the absorber.

By way of illustration of the superiority of the above described equipment as compared with that used earlier[5] we have juxtaposed in Fig.2 the L_{III} absorption edge of molybdenum in $(NH_4)_2MoO_4$ and MoS_2 recorded in the present investigation by means of a Geiger counter and in the earlier investigation on a similar spectrograph but with photographic recording. Another purpose of this juxtaposition was to determine the degree of correspondence of the results obtained by different procedures.*

As may be seen in Fig.2 curves 1 and 2 obtained by different procedures are in good qualitative agreement. The positions of the individual fluctuations within the main edge coincide. Their relative intensities differ, however, as might be expected, taking into account the higher resolution of the instrument used in the present investigation (curves 1) and the effects[7] due to the influence of photographic recording and the thickness of the absorber on the structure of the absorption edge.

As was noted above, in investigating the $L\beta_2$ emission band of molybdenum we used the method of primary excitation. For this part of the investigation we chose MoS_2 and Mo_2C which we thought would not undergo any appreciable changes in the process of electron bombardment on the anode. The criterion for the absence of such transformations (aside from no change in the appearance of the material) was similarity of a number of successive curves recorded at intervals. From a comparison of such consecutive curves it was found that some 1-1.5 hours after the beginning of recording, material freshly applied to the anode did undergo appreciable changes. Thus, from the curves, we have reason to assume that the Mo_2C was gradually transformed into metallic molybdenum. In view of this, in averaging we used only the curves obtained for freshly applied material not exhibiting any of the above mentioned changes. For the thermally less stable compounds $(NH_4)_2MoO_4$ and MoO_3, we made an attempt to obtain the requisite data by the fluorescence method. In view of the low intensity of the fluorescence spectra and the strong distorting influence on them of reabsorption, however, we have so far not been able to obtain dependable, reproducible results. Hence in the present report we must restrict our consideration to the emission data obtained by the primary method for MoS_2 and Mo_2C.

---

*The energy scale in Figs.1 & 2 of Ref.5 was given incorrectly. The correct scale is shown in Fig.2 above.

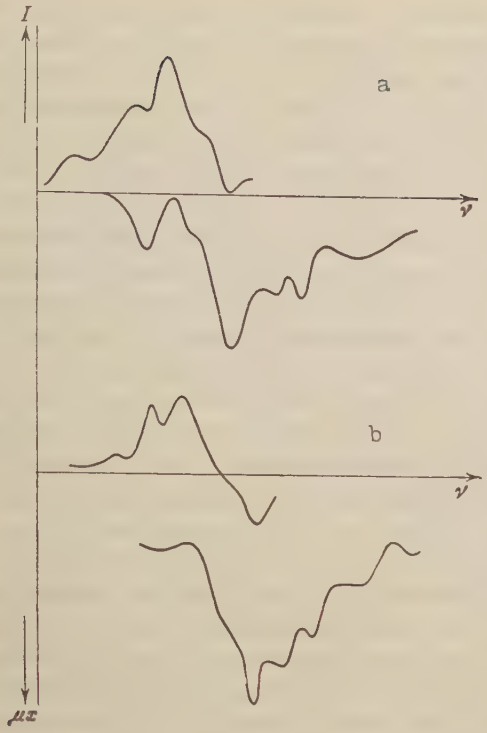

Fig.3. L_{III} absorption spectra and $L\beta_2$ bands of Mo: a) in MoS_2, b) in Mo_2C.

There are a number of reports in the literature (see, for example, Ref.8) that the presence of a bright absorption line in the absorption edge leads to strong distortions in the structure of the last emission band recorded at a voltage greatly exceeding the excitation potential (due to the so-called reabsorption effect). Analogous distortions were observed in the present investigation. For this reason the lowest possible tube voltage was used in recording the $L\beta_2$ band of molybdenum. Nevertheless, a decrease in intensity going well below the usual background level was observed on the short wavelength side of the $L\beta_2$ band of Mo in Mo_2C. An even more curious effect was observed in the fine structure of the $L\beta_2$ band of molybdenum in MoS_2. To illustrate it, the L_{III} absorption spectra and the $L\beta_2$ bands of molybdenum in MoS_2 and Mo_2C are reproduced in Fig.3. Aside from the above mentioned anomalous decrease of the background on the short wavelength side of the $L\beta_2$ band of Mo in Mo_2C, one is immediately struck by the exact coincidence of the wavelengths of the intensity minima in the $L\beta_2$ band of Mo in MoS_2 with the absorption peaks in the L_{III} edges of this compound. This is apparently the same reabsorption effect, but here its distorting influence is manifested in the fine structure of the emission band over its entire extent and leads to the appearance of false fine structure. This phenomenon proved possible in this case by virtue of the strong overlapping of the $L\beta_2$ band and the L_{III} edge, overlapping that is so great that the $L\beta_2$ band of Mo in MoS_2 actually lies within the limits of the main edge of the metal in this compound. As far as we know an analogous effect was noted only once previously[9], specifically in the case of the $M_{IV,V}$ absorption spectra and $M\alpha$ and $M\beta$ emission bands of Br. In view of the fact that Er is a rare earth, it may be concluded that this phenomenon is peculiar to the emission and absorption spectra of "defective" elements.

Experimental results and discussion

Our experimental results pertaining to the L_{III} absorption spectra of Mo in $(NH_4)_2MoO_4$, MoO_3*, MoS_2 and Mo_2C are juxtaposed in Fig.4. The zero of the energy scale in the figure is arbitrary; the vertical scale is laid off in units proportional to the absorption coefficient. The curves in the figure identified by hatching are the contours of the $L\beta_2$ band of Mo obtained by the method of primary excitation.

---

*The structure of the L_{III} absorption spectrum of Mo in MoS_3 is virtually identical with that observed in MoO_3.

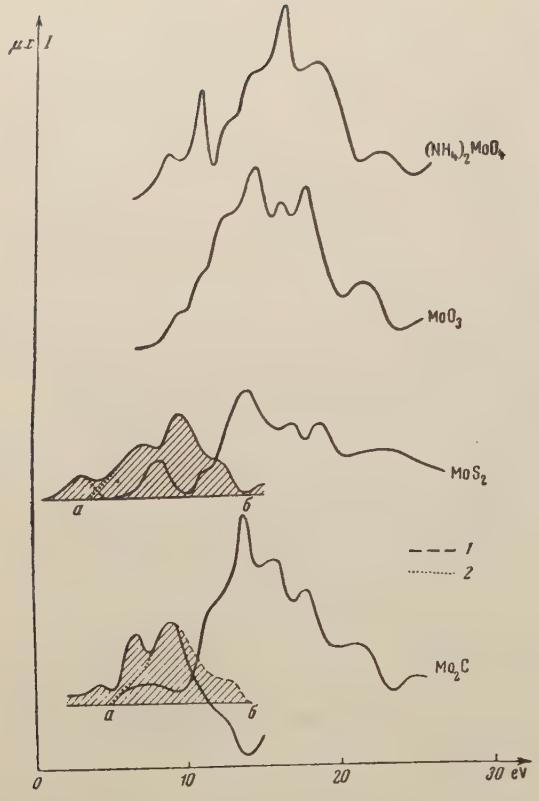

Fig.4. L_{III} absorption spectra and $L\beta_2$ bands of Mo (hatched) in different compounds: 1) result of correction of the short wavelength edge of the emission band to allow for the effective reabsorption, 2) approximate resolution of the emission band into two components.

A feature common to all the absorption spectra of Mo is the presence in them of a group of selective lines located in the long wavelength part of the spectrum (extending 11-15 ev from the limit of the edge) and having intensities appreciably greater than the intensity of the rest of the edge. These lines appear in the spectrum as a result of transitions (allowed by the dipole selection rules) of 2p electrons of the absorbing atom to excited levels of the compound, having primarily d symmetry. These levels are characterized, as is known, by a relatively small energy width and a high density. To the right of this line group is the region of the spectrum associated with transitions of the same electrons to excited levels of primarily s symmetry. As might have been expected this short wavelength part of the spectrum is characterized by an appreciably lower intensity than the long wavelength group of lines and (except in the case of Mo in MoS_2), it shows little variation in going from one compound to another. These compounds differ as regards the valence and coordination number of the absorbing atom, crystal structure and the type of interatomic coupling (bonds).

The behavior of the long wavelength group contrasts sharply with that of the short wavelength section of the spectrum mentioned above. In going from one compound to another the structure of the spectra in this region changes regularly and consistently with changes in the character of the bonds and the type of hybridization determining the ensemble of electrons participating in the formation of stable σ-bonds. Let us analyze the changes in the structure of the spectra in more detail and see what deductions may be drawn from the analysis.

1. In going from $(NH_4)_2MoO_4$ to MoS_2 and then to Mo_2C, the valence of Mo changes from 6 to 4 and then to 2. In the ammonium compound the 4d band is entirely unoccupied. In MoS_2 there obtains d^4sp hybridization and the only 4d orbit of the Mo atom in this compound not participating in the bonding is occupied by two electrons. In bivalent Mo in Mo_2C not more than three 4d orbits, which can accommodate six electrons, are free or are capable of participating in the chemical bonds. Two 4d orbits of Mo in Mo_2C are occupied by four electrons.

These changes in the degree of filling of the 4d bands of Mo in the enumerated compounds are reflected in the structure of the Mo absorption spectra. Richest in detail is the structure of hexavalent Mo in $(NH_4)_2MoO_4$. In addition to the wide triple-peaked absorption band (with minor fluctuations on the long wavelength side), characteristic of all these spectra, the spectrum of ammonium molybdate contains two additional absorption lines situated on the long wavelength side of the main absorption band. Precisely these

two lines prove to be particularly sensitive to changes in valence of the metallic atom in the compounds. The intensity of absorption in this region of the spectrum falls off appreciably in going over to tetravalent Mo in MoS_2, in the spectrum of which at this position there is observed only one line of appreciably lower intensity; the intensity in this region of the spectrum falls off to zero in the spectrum of Mo_2C in which the valence of Mo becomes formally equal to two. In view of the above, it may be assumed that the appearance in the absorption spectrum of Mo in $(NH_4)_2MoO_4$ of the two longest wavelength absorption maxima, forming virtually a separate line group, is due to transitions of 2p electrons of the absorbing atom to the two (of the five) deepest lying 4d orbits of the metal in the compound, which, in principle, are capable of accomodating four electrons. In $(NH_4)_2MoO_4$, in which the 4d band of Mo is entirely vacant, this possibility is wholly realized; in MoS_2 the possibility is only half realized, while in the carbide - in which the corresponding 4d orbits of Mo are occupied by its own electrons - transition of 2p electrons to this band becomes impossible.

The same absorption spectra of Mo in the three compounds, characterized by different valences of the molybdenum atom, can, we feel, also be used to illustrate the idea that the excited energy levels comprising the 4d band of a transition element in the crystal can be naturally divided into two categories depending on the degree of influence on them of the fields of their neighbors in the compound. One group of levels is formed by excited (hybrid) energy states of the electron in the compound, participating in the chemical bonds; the other group is made up of "quasi-atomic levels" characterized by an appreciably lower energy, levels which in the free state of the atom are occupied by its electrons.

In our case the presence of two such groups of energy levels is manifested in the appearance of the long wavelength group of absorption lines (which are very narrow and which it may therefore be assumed are relatively free of the influence of the crystal lattice field) and one broad (triple-peaked) absorption band.

If with constant valence of the transition element atom, its 4d levels are even partially involved in the chemical bonds (hybridized), this leads to further perturbation of the corresponding levels, i.e., their further broadening, and can result in their losing their "quasi-atomic" character in whole or in part. An example illustrating this is the absorption spectrum of Mo in MoO_3. The structure of this spectrum and the way it differs from the spectrum of hexavalent Mo in ammonium molybdate can be qualitatively explained if we take into account the fact that d^2sp^3 hybridization obtains in this compound. In consequence, the structure in the long wavelength part of the L_{III} absorption edge of Mo, which is well resolved in $(NH_4)_2MoO_4$, loses its initial sharpness and independence (due to the "quasi-atomic" character of the deeper 4d levels of Mo in the compound) and in the spectrum of Mo in MoO_3 almost merges with the neighboring triple-peaked absorption band. This leads to the appearance of a single absorption band appreciably wider than in the spectrum of $(NH_4)_2MoO_4$ and to a certain redistribution of the intensity fluctuations on the long wavelength side of the band.

It is significant that participation of the 4d orbital electrons of Mo in the formation of hybrid bonds in the compound does not lead to complete disappearance of the corresponding lines in the absorption spectra but results only in a sharp decrease of their intensity relative to the other parts of the spectrum. This is clearly brought out by comparison of the long wavelength structure of the absorption spectra of Mo in $(NH_4)_2MoO_4$ and MoO_3 and, particularly, by examination of the absorption spectrum of Mo in MoS_2. In

the last compound d^4sp hybridization is realized and the greater part of the 4d levels of the metallic atom participate in the chemical bonding. Yet this does not lead to complete disappearance of the long wavelength structure in the absorption spectra or even to a radical change of the structure, but results only in a sharp decrease of the relative intensity of this portion of the spectrum as compared with the shorter wavelength part (in contrast to what occurs when the corresponding 4d levels of Mo are filled by "its own" electrons). In the case of MoS_2 this is also accompanied by a general reduction of the L_{III} absorption discontinuity as compared with that in the spectrum of Mo in all the other investigated compounds.

Thus involvement of the 4d levels of a transition element atom in hybrid bonds results only in a reduction of the probability of electron transitions to the corresponding levels, the decrease in probability being the greater, the greater the participation of these levels in the chemical bonds.

2. For the purpose of independent verification of the conclusions drawn from our analysis of the x-ray absorption spectra of Mo in the above-named compounds, we also investigated the structure of the shortest wavelength L_{III} emission bands of Mo, namely, the $L\beta_2$ lines. The contours of these lines are indicated in Fig.4 by hatching of the area under them. In the case of Mo_2C, in addition to the experimental $L\beta_2$ line contour, we show by means of the dash line the short wavelength portion of this emission line after correction of the influence of reabsorption on its shape. No such correction for the short wavelength side of the emission line of Mo in MoS_2 was made since apparently due to the general weakening of the absorption discontinuity in this compound, the distorting influence of reabsorption here proved to be less appreciable.

As will be evident from Fig.4, the emission bands of Mo in MoS_2 and Mo_2C differ from each other both as regards intensity distribution within the bands and as regards their overall width. In this case, too, the considerations set forth above regarding the character of the 4d state of Mo in the investigated compounds allow of interpreting the structure of these emission bands and lead to conclusions that are in good agreement with the deductions drawn from analysis of the absorption spectrum. By analogy with the absorption spectra, of Mo in these compounds, the $L\beta_2$ emission bands can also be thought of as consisting of two parts: 1) a short wavelength wide band (section ab in Fig.4), reminiscent, as regards shape, of the wide absorption peak in the L_{III} spectra of Mo in MoS_2 and Mo_2C, and 2) a group of narrow emission bands (one in the case of MoS_2 and two in the case of Mo_2C) forming the long wavelength portion of the $L\beta_2$ line. The section ab in the emission band can be associated with electron transitions from the hybridized orbits of Mo in MoS_2 and Mo_2C. As for the longer wavelength narrow peak within the emission band of Mo in MoS_2 and the two similar narrow maxima in the spectrum of Mo_2C, they can be interpreted (in complete accord with the data on the absorption spectra) as "quasi-atomic" emission lines appearing incident to the transition of two 4d electrons of Mo in MoS_2 and of four 4d electrons of Mo in Mo_2C to the 2p levels of Mo vacated in the process of absorption of the x-rays. These narrow peaks are the manifestation in emission of the same two lowest energy levels within the 4d band of the transition element in compounds, whose degree of filling in different compounds we were able to follow earlier by the decrease in intensity of the corresponding selective lines in the absorption spectra of Mo.

A further argument in favor of the above interpretation of the structure of the $L\beta_2$ bands of Mo in MoS_2 and Mo_2C is that it allows of understanding the fact (strange at first glance) of appreciable overlapping of the emission

bands and absorption spectra of Mo in these compounds.* To this end we need only assume that the excited "quasi-atomic" 4d levels of Mo in the compounds can possess an appreciably lower energy than the corresponding excited hybridized states and that the value of this energy can be comparable with the energy of the hybridized levels of the compound occupied by electrons. From this viewpoint, we can readily understand such characteristic features of the phenomenon as the approximately similar shape of the main absorption edge and the emission band,** the fact that this phenomenon is peculiar to the soft x-ray spectra of the L and M series and the fact that this phenomenon has so far been observed only (and probably can be observed only) in the spectra of transition elements.

3. On the basis of the above analysis of the x-ray spectra of Mo in the carbide and the other investigated molybdenum compounds and our interpretation of the present data, we can evaluate the plausibility of the theoretical concepts advanced in the past by different authors regarding the nature of the chemical bonds between the atoms in Mo_2C and the degree of participation of the 4d levels of the transition metal in the carbide bonding. From a comparison of the absorption data it may be asserted that the appearance in the 4d shell of Mo in the investigated compounds of two (in MoS_2) or four (in Mo_2C) electrons leads, as might have been expected, to gradual weakening of the two longest wavelength peaks observed in the absorption spectrum of Mo in $(NH_4)_2MoO_4$ in which these levels are vacant.

A similar process is evident in the variation of the structure of the $L\beta_2$ emission band of the metal in these compounds. If, as is assumed in certain theories, in the process of formation of the chemical bonds between the metal and the nonmetal in Mo_2C the carbon electrons were even partially utilized for screening the charge of the Mo atom and went to fill its incomplete 4d band, this would inevitably lead to further weakening of the intensity of the long wavelength part of the L_{III} absorption edge of Mo in the carbide. This effect was not observed in the experimental spectrum. On the contrary, the width and the relative intensity of the corresponding groups of lines in the L_{III} absorption edge of Mo in the carbide and in the other investigated compounds proved to be nearly the same. As for the small differences in the relative intensity of the individual variations of the absorption coefficients within the limits of the group of lines in question, it must be noted that they are observed only in the short wavelength part of the L_{III} spectra and cannot be due to filling of the 4d levels of Mo in the carbide by carbon electrons. On the other hand, the great width of the emission band and the very appreciably overlapping of the short wavelength part of the emission band and the long wavelength section of the absorption spectrum of Mo in Mo_2C can be regarded as arguments in favor of the assumption of partial hybridization of the bonds in this compound and participation in them of the 4d levels of the Mo atom.

---

*It will be obvious that we are not speaking here of the partial overlapping of the emission lines and absorption edges, connected with the finite width of the L_{III} energy levels in the atom.

**We note the similarity of the effect in question with the law of mirror symmetry of absorption and emission spectra established by Levshin in investigating the luminescence of certain classes of organic molecules.[10]

Conclusions

1. The L_{III} absorption spectra and $L\beta_2$ emission bands of Mo in molybdenum carbide and other molybdenum compounds have been investigated by means of a focusing vacuum x-ray spectrograph. The investigation brought out the influence of the valence of the metal atoms and the character of the chemical bonds between the atoms in the compounds on the fine structure of these spectra.

2. For the instance of the x-ray spectra of Mo in MoS_2 we have shown the possibility of appreciable overlapping of the $L\beta_2$ emission band and the L_{III} absorption spectrum of the metal. Hitherto a similar effect has been observed only once in investigating the $M_{IV,V}$ absorption spectra and $M\alpha$ and M_β emission bands of Er. We suggest the possible reasons for the effect and outline the conditions necessary for its appearance.

3. The experimental data obtained for Mo_2C cannot be reconciled with the hypothesis advanced by a number of authors, according to which formation of the carbides of transition elements involves partial filling of the nd energy levels of the metal atoms. The degree to which this conclusion is generally applicable can only be decided on the basis of further extensive experimental investigation of the Mo-C system and the carbides of other transition elements.

Institute of Mineralogy, Geochemistry and Crystallochemistry of Rare Elements and "V.I.Vernadskii" Institute of Geochemistry and Analytical Chemistry, Academy of Sciences of the USSR

References

1. D.Bernal, Metal Physics (Cited in Russian trans., M., 1933).
2. Ia.S.Umanskii, Karbidy tverdykh splavov (Solid solution carbides), M., 1947.
3. E.E.Vainshtein, Iu.N.Vasil'ev, Doklady AN SSSR, 114, 53 (1957).
4. E.E.Vainshtein & Iu.N.Vasil'ev, Doklady AN SSSR, 114, 741 (1957).
5. R.L.Barinskii, Doklady AN SSSR, 83, 381 (1952).
6. G.Kimball, J.Chem.Phys., 8, 188 (1940).
7. K.I.Narbutt, R.L.Barinskii & E.E.Vainshtein, Doklady AN SSSR, 82, 567 (1952).
8. R.L.Barinskii, Dissertation, Moscow, 1951.
9. E.A.Stewardson & J.E.Wilson, Proc.Phys.Soc., A69, 93 (1956).
10. V.L.Levshin, Fotoliuminestsentsiia zhidkikh i tverdykh veshchestv (Photoluminescence of liquids and solids), M.1956.

INFLUENCE OF THERMAL VIBRATIONS OF ATOMS ON THE ELECTRON ENERGY DISTRIBUTION IN METALS AND ALLOYS

- I.B.Borovskii & G.N.Ronami

Through investigation of frequency variation of the intensity $I(\omega)$ in their x-ray emission and absorption spectra one can determine so important a characteristic of solids as the energy distribution of electron states $N(\omega)$. The relationship between $I(\omega)$, $N(\omega)$ and the frequency dependence of the transition probability $f(\omega)$ is given by the following expression:[1]

$$I(\omega) = \frac{e^2h^3\omega^2N_0\Omega G^3}{6\pi^3m^2c^3}\int\int\left\{\left(\frac{\partial E}{\partial k_1}\right)^{-1}\left[\int\psi_k^*\Delta\psi_0 d\tau\right]^2\right\}dk_2dk_3 = AN(\omega)f(\omega).$$

Numerical evaluation of $N(\omega)$ and $f(\omega)$ is feasible only in the rough approximations of entirely free or strongly bound electrons at absolute zero; the results of such computations have been discussed by a number of authors[2,3].

Attempts have been made to evaluate the influence of atomic vibrations with changes in temperature in solids on the so-called fine structure of absorption spectra on the short wavelength side of the main absorption edge[4] and on the structure of the emission bands in the ultralong wavelength region of the x-ray spectrum[5,6].

In the work of Bethe & Sommerfeld[4] and Kostarev[5] the interaction of an electron, ejected in the process of absorption from an atom in the crystal lattice, with the phonon field of the lattice is treated as a small perturbation. A consequence of this theoretical treatment was prediction of the effect of disappearance ("melting") of the fine structure of the absorption spectra on the short wavelength side of the main edge with increasing temperature (increase in the amplitude of the atomic vibrations). Thus for copper Kostarev[5] evaluated the temperature of "melting" of the fine structure as 800°, which is in agreement with the experimental data.

The purpose of our investigation was to check the conclusions drawn in earlier theoretical and experimental studies[4,6] inasmuch as for physical reasons it appeared clear that vibrations of atoms in the crystal lattices of metals and alloys, the amplitudes of which attain values equal to 15-20% of the interatomic distances at high temperatures (i.e., near the fusion point of the metal), should influence not only scattering processes and, consequently, should not be treated as a small perturbation.

Of particular interest to us was determining the influence of "small" admixtures (impurities) on the process of "melting" of the fine structure of absorption spectra in connection with the recently developed concepts[7] regarding the formation in dilute solid solution of "atomic blocks" with decreased mobility of the atoms entering into the sphere of influence of these blocks.

The L_{III} absorption spectra of lead in the form of the pure metal and in alloys of lead with tin, containing 0.2, 0.5, 2, and 10% Sn were investigated on a bent crystal spectrograph by the transmission method. The linear dispersion was 4 X mm^{-1}; the tube was operated at 21.5 kv and 20 ma; the exposure times were 5 to 12 hours.

The structure of the alloys was determined from x-ray diffraction patterns which showed that all the alloys were solid solutions (the Pb alloy with 10% Sn was obtained by quenching from 200°). The absorption spectra were recorded at 4-5 temperatures in the temperature range from -190 to +300°. All the spectra were photographed using a special vacuum camera (pressure - 1.10^{-5} mm Hg). We checked for the absence of oxidation at elevated temperatures by rephotographing the spectra of the same specimen at room temperature following the high temperature exposures. For supplementary control purposes we also recorded the L_{III} absorption spectra of lead in PbO and PbO_2.

Energy values (ev) of the principal L_{III} edge and the maxima and minima in the fine structure of the absorption spectrum of lead

Material	Maximum and minimum	Temperature, °C				
		300	200	100	20	—190
Alloys						
Pb	Edge		13037	13037	13036	13036
	A		—	—	13046	13047
	α		—	—	13050	13050
	B		—	13059	13060	13059
	β		—	13070	13070	13070
	C		—	13085	13085	13084
	γ		—	13100	—	13100
	D		—	—	—	13114
PbSn (0,2% Sn)	Edge	13036	13036		13036	13037
	A	13048	13048		13047	13048
	α	13051	13051		13051	13051
	B	—	13062		13061	13062
	β	—	13071		13071	13071
	C	—	13085		13084	13085
	γ	—	—		—	13101
	D	—	—		—	13114
PbSn (0,5% Sn)	Edge		13037		13037	13037
	A		13048		13047	13047
	α		13050		13050	13050
	B		13060		13060	13060
	β		13070		13070	13069
	C		—		13084	13084
	γ				—	13100
	D		—		—	13114
PbSn (2% Sn)	Edge	13037	13037		13036	13037
	A	—	13048		13046	13047
	α	—	13050		13050	13050
	B	—	13062		13059	13061
	β	—	13071		13071	13071
	C	—	—		13084	13085
	γ	—	—		—	13100
	D	—	—		—	13114
PbSn (10% Sn)	Edge		13037		13036	13037
	A		—		13046	13048
	α		—		13049	13050
	B		—		13059	13060
	β		—		13070	13070
	C		—		13084	13084
	γ		—		—	13100
	D		—		—	13114
Oxides						
PbO_2	Edge				13044	
	B				13064	
	β				13086	
	C				13121	
O	Edge				13042	
	B				13058	
	β				—	

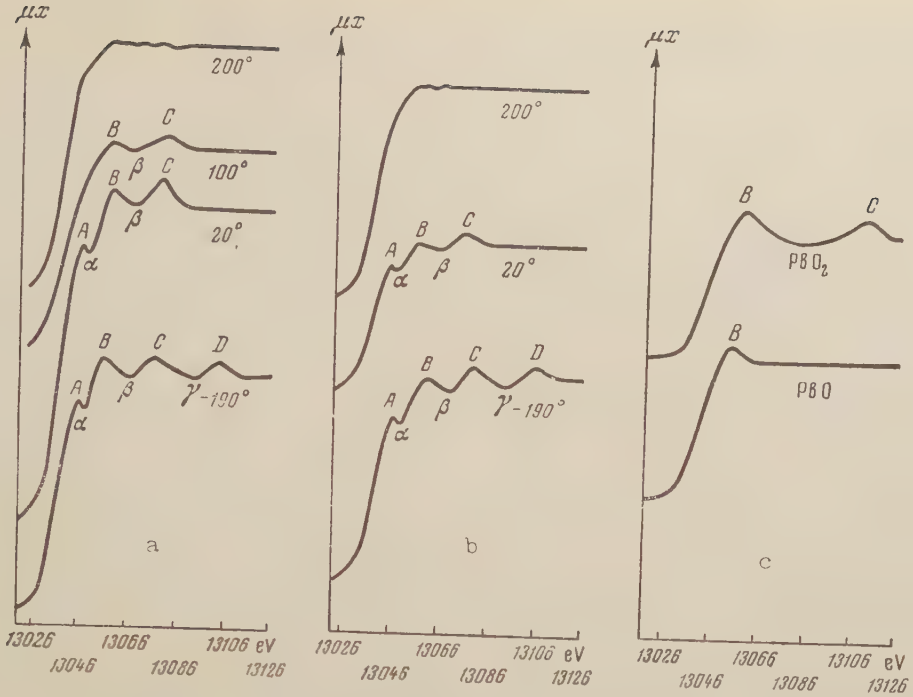

Fig.1. L_{III} absorption spectra of lead in the form of metallic lead (a), in the Pb alloy with 10% Sn (b) and in the oxides PbO and PbO_2 (c).

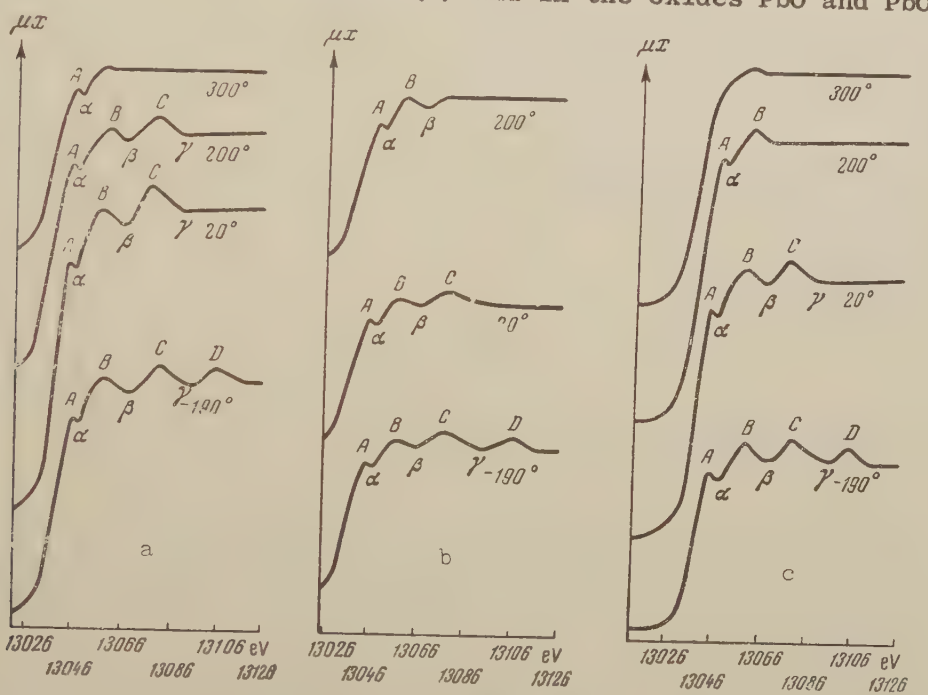

Fig.2. L_{III} absorption spectra of lead in Pb alloys with 0.2% Sn (a), 0.5% Sn (b) and 2% Sn (c).

The absorption spectra as given by the averaged photometric curves (each curve was the average for 4-5 spectrograms) are shown in Figs.1 & 2. The wavelengths (in ev) of the characteristic points of the L_{III} absorption spectra of lead in the metal and the investigated alloys are given in the accompanying table.

Analysis of the experimental results leads to the following conclusions.

1. In addition to the effect of "melting" of the fine structure on the short wavelength side of the main absorption edge with increasing temperature of the metal, there also occurs a change in the structure of the absorption edge itself. Consequently, changes in the frequency and amplitude of the atomic vibrations influence not only scattering processes (small perturbation) but also affect the entire energy spectrum of the crystal lattice of the metal.

2. The intensity of the "melting" of the fine structure of the absorption spectrum and the extent of the changes in the main absorption edge of lead in alloys with tin with increasing temperature depend strongly on the content of the alloying element (Sn). Thus whereas in the case of pure metallic lead and its alloy with 10% Sn the entire structure of the absorption spectrum disappears entirely at a temperature under 200°, for alloys with 0.2 to 0.5% Sn the structure of the main absorption edge persists up to 300° (i.e., to within less than 27° of the melting point). Hence the presence of small amounts of impurities (to 1%) appreciably changes the variation of the frequency and amplitude of atomic vibrations with increasing temperature as compared with the pure metal. Consequently, the presence of impurities in the metal affects both scattering processes (for example, the well-known impurity dependences of the residual resistance at low temperatures, the specific heat, etc.) and the entire energy spectrum of the alloy.

On the basis of a very rough evaluation of the influence of the amplitude of atomic vibrations at a given temperature on the distortion of the interaction potential between the atoms in the pure metal, it may be asserted that this distortion may be the reason for "diffusion" of the levels at the Fermi brim, which leads to disappearance of the structure of the main absorption edge.

The monotonically decreasing influence of impurities with increasing impurity content can be explained in the framework of the theory of "atomic blocks".[7]

More detailed conclusions require more extensive analysis of the various factors involved and hence will be given in the following report.

Physics Faculty,
Moscow State University

References

1. P.Dirac, Quantum Mechanics; W.Heitler, The Quantum Theory of Radiation (Cited in Russian trans.), M.1956.

2. N.Mott & H.Jones, Theory of the Properties of Metals and Alloys, Oxford, 1945.

3. Wilson, Quantum Theory of Metals (Cited in Russian trans. M, 1940).

4. Bethe & Sommerfeld, Electronentheorie der Metalle (Cited in Russian trans.M, 1938); A.I.Kostarev, Zhur.eksp.i teor.fiz., 20, 811 (1950).

5. A.I.Kostarev, Zhur.eksp.i teor.fiz., 21, 917 (1951); Dissertation, 1953.

6. H.W.Skinner, Phil.Trans.Roy.Soc., A.239, 95 (1940); J.Serpe, C.R.202, 1979 (1936).

7. I.B.Borovskii & K.L.Gurov, FMM (Physics of Metals & Metallography), 4, No.1, (1957).

X-RAY SPECTROSCOPIC INVESTIGATION OF SOLID SOLUTIONS

- I.B.Borovskii, K.P.Gurov, S.A.Ditsman, V.A.Batyrev, & N.D.Lobanova

Fundamental investigation of the atomic-electronic structure of alloys is possible only through comprehensive application of different methods of studying the properties of alloys (x-ray spectroscopic, x-ray diffraction, diffusion, optical, magnetic, electric, thermophysical, etc.). Among these methods the x-ray spectroscopic one is important for investigation of the electron structure of metals and alloys. Its importance stems from the fact that there is a direct dependence between the distribution in frequency of the x-radiation intensity and the density of electron states. Hence the x-ray spectroscopic method can serve as a sensitive indicator of variation of the electron structure of alloys as a function of their composition, temperature and other factors.

The present study was devoted to investigation of the variation of the distribution in energy of the electron states in continuous series of binary solid solution alloys of the transition elements as typified by the Cr-Mo system. An additional specific aim of the study was to determine the influence of relatively small concentrations of one of the components on the electronic energy spectrum of the atoms of the other, basic component.

Our particular interest in "dilute" solid solutions (as we shall hereinafter refer to solid solutions with a small content of one of the components) is connected with the fact that particularly pure metals exhibit physical properties that differ sharply from the properties exhibited by the same metal with a small amount of impurity. Outstanding illustrations of the influence of small amounts of impurities on the properties of a metal are furnished by Ti, Cr and Mo. We are all familiar with the great influence of small additions of alloying elements on different physical properties of alloys. Finally, in developing a modern theory of alloys one should, in principle, start with an examination of infinitely diluted solid solutions. Hence it was logical to begin our investigation with a study of the x-ray spectra of samples of metallic chromium of different degrees of purity. For the purposes of this investigation we chose chromium obtained by the iodide method* (the greatest impurities in it are nitrogen and oxygen), electrolytic chromium prepared in the TsNIIChERMET having a purity of 99.90-99.85% and commercial chromium prepared by the hydride procedure and having a purity of 99.5%.

In addition, owing to the fact that there are no sufficiently reliable data in the literature on the x-ray spectra of molybdenum, we deemed it desirable to investigate pure metallic molybdenum as well.

From our point of view the most complete data on the character of the changes of the electron energy spectrum of alloys or chemical compounds can be obtained only by investigating the changes in the structure of the lines and absorption edges of all the components of the given alloy or compound in all the attainable regions of the x-ray spectrum. Hence in investigating Cr, Mo and Cr-Mo alloys we recorded the following emission lines: the $K\alpha_{1,2}$ ($K \rightarrow L_{II,III}$ transition) and $K\beta_1$ ($K \rightarrow M_{II,III}$ transition) lines of Cr and the $K\beta_5$ ($K \rightarrow M_{IV,V}$ transition), $L\alpha_{1,2}$ ($L_{III} \rightarrow M_{IV,V}$ transition) and $L\beta_1$ ($L_{II} \rightarrow M_{IV,V}$ transition) lines of Mo. These lines are associated with transitions between

---

*We take this opportunity to thank N.V.Ageev and V.A.Trapeznikov for making available the high-purity chromium specimens.

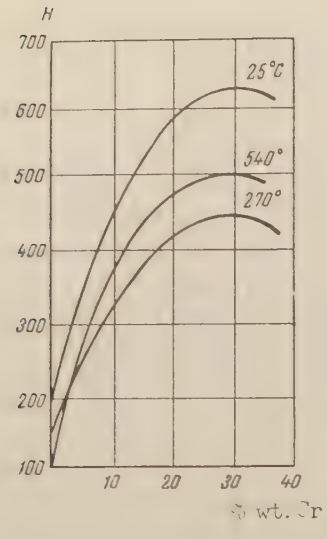

Fig.1. Microhardness of Cr-Mo alloys.[1]

deep atomic levels. In addition, we investigated the $K\beta_5$ ($K \rightarrow M_{IV,V}$ transition) line of chromium and the $L\beta_2$ ($L_{III} \rightarrow N_{IV,V}$ transition) line of molybdenum, which are associated with transitions from the 3d and 4d shells of chromium and molybdenum to the inner 1s and 2p levels. Further, we also investigated the K and L_{III} absorption spectra of chromium and molybdenum which are associated, respectively, with electron transitions from the 1s and 2p levels to the conduction band and also to the 3d and 4d shells.

The Cr-Mo alloys with up to 35% Mo were melted in an induction furnace under vacuum. These alloys were made with the electrolytic chromium. Alloys containing 0.5 to 22% of the commercial hydride process chromium were melted in an arc furnace in an atmosphere of argon. Thus there were prepared alloys containing the following percentages of Mo by weight: 0.1, 0.14, 0.6, 0.8, 1.17, 1.93, 2.64, 16.8, 30.7, 80, 94, 97, 99, 99.4 and 100%. The alloys containing up to 35% Mo were subjected to a homogenizing anneal at 1200° for 24 hours; the alloys with 0.5 to 22% Cr were annealed for 12 hours at 1400°. The solid solutions of the alloys were "fixed" by quenching in ice water after holding for 2 hours at 1200°.

Metallographic analysis of microsections of the prepared alloys etched for 30-40 sec electrolytically (25 ma current) in a 10% solution of oxalic acid showed that all the alloys were single phase solid solutions.

Investigation of the microhardness as a function of the chromium concentration showed that the microhardness varied in accord with the established regularity for variation of the hardness in continuous series of solid solutions. The position of the maximum in the hardness curve was consistent with the data of Kessler & Hansen[1] (Fig.1).

The K spectra of chromium were investigated by the primary excitation method on a spectrograph employing Johann focusing (R = 500 mm) in the second order of reflection from the $(10\bar{1}0)$ plane of the quartz crystal. As reference lines we used the $K\alpha_1$ line of Fe and the $K\alpha_1$ line of Mn in the second order. To avoid oxidation of the specimen during recording of the emission spectra the tube was operated at reduced power (1-2 ma at 25 kv). Metallographic examinations of microsections of chromium mounted on the anode of the x-ray tube

Table 1

Positions of the $K\beta_1$, $K\beta_5$ lines and the K absorption edge in the spectra of the iodide, electrolytic and hydride chromium specimens

Grade chromium	K_{β_1}		K_{β_5}		K-edge		Asymmetry index $K\alpha_1$
	X	ev	X	ev	X	ev	
Iodide	2080,41 ±0,04	5946,1 ±0,1	2066,45 ±0,03	5986,3 ±0,1	2065,76 ±0,08	5988,3 ±0,03	1,30 ±0,06
Electrolytic	2080,61 ±0,05	5945,5 ±0,1	2066,59 ±0,03	5986,0 ±0,1	2066,03 ±0,06	5987,5 ±0,2	1,4 ±0,06
Hydride	2080,79 ±0,04	5945,0 ±0,1	2066,73 ±0,05	5985,5 ±0,1	2066,1 ±0,1	5987,5 ±0,1	1,20 ±0,04

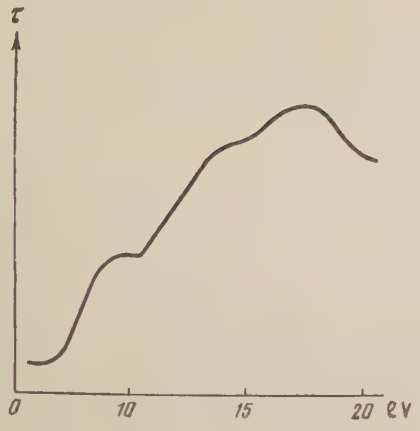

Fig.2. K absorption edge of Cr. Curve obtained for the iodide chromium; similar curves were obtained for the other specimens.

showed no sign of changes in structure of the surface or traces of oxidation after being subjected to the influence of the electron beam.

The absorption spectra of chromium were investigated with an absorber thickness of 4-5 mg/cm^2, using a tungsten anode with the tube operated at 25 kv and 30 ma; the exposure times were 0.25 to 1 hour. The wavelength data on the $K\beta_1$ and $K\beta_5$ lines and the K absorption edge of the different grades of chromium are shown in Table 1; the indicated values are averages for 8-10 spectra.

The variation of the absorption coefficient in the region of the K absorption edge of the iodide chromium is shown in Fig.2 (the variations of the absorption coefficients of the electrolytic and hydride chromiums were analogous).

The L emission and absorption spectra of molybdenum were investigated on the above mentioned spectrograph in the first order. The purity of the molybdenum was 99.1%.

Table 2

Positions of characteristic points of the L_{III} absorption edge of molybdenum

Points	Metallic Mo	MoO_3	MoS_2
A	2519,3 ± 0,1	2521,3 ± 0,1	2520,1 ± 0,1
B	2522,8 ± 0,1	2525,0 ± 0,1	2523,6 ± 0,1
C	—	2527,2 ± 0,2	—

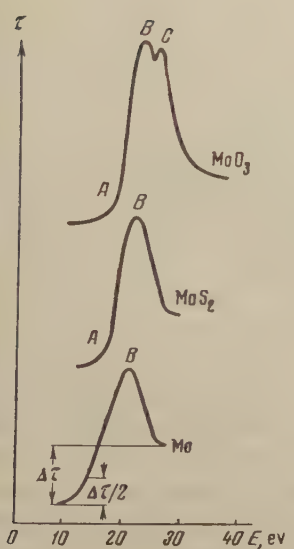

Fig.3. L_{III} absorption edge of Mo for metallic molybdenum and in MoS_2 and MoO_3.

The following reference lines were used: for the Mo emission $L\alpha_{1,2}$ doublet - the Ti $K\alpha_1$ (second order) and S $K\alpha_1$ (first order) lines; for Mo $L\beta_1$ and $L\beta_2$ - the Ba $L\beta_1$ and $L\beta_2$ lines; for the L_{III} absorption of molybdenum - the V $K\alpha_{1,2}$ (second order) and Cl $K\alpha_1$ (first order) lines. The tube was operated at 15 kv and 5 ma in recording the emission spectra and at 5.5 kv and 30 ma in recording the absorption spectra. The variation of the absorption coefficient in the region of the L_{III} absorption edge of Mo in the form of metallic molybdenum and in MoS_2 and MoO_3 is shown in Fig.3. The positions of the characteristic points of the absorption edge in the energy scale are listed in Table 2.

In investigating the enumerated alloys of the Cr-Mo system, the spectra of chromium and molybdenum in the alloys were obtained under the same experimental conditions as used in investigating the spectra of pure chromium and molybdenum, respectively. Specifically, we investigated the $K\beta_1$, $K\beta_5$ and $K\alpha_{1,2}$ lines and the $K\beta'$ satellite in the emission spectrum and the K absorption edge of chromium and the $L\alpha_{1,2}$, $L\beta_1$, $L\beta_2$, $K\beta_1$ and $K\beta_2$ emission lines and the L_{III} absorption edge of molybdenum. The data on the wavelengths of the emission lines peaks and the absorption edges have been given in Ref.2. The shape of the Cr $K\beta'$ satellite for pure chromium and some of the alloys

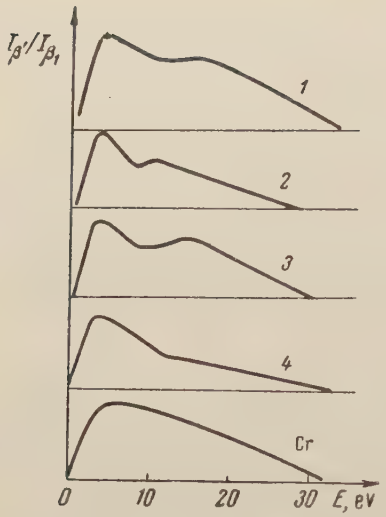

Fig.4. Shape of the Cr Kβ' satellite in the spectra of pure chromium and Cr-Mo alloys: 1) 97% Mo, 2) 94% Mo, 3) 80% Mo, 4) 30% Mo.

Fig.5. Shape of the Mo $L\beta_2$ line as a function of the tube voltage: 1) 3.6 kv, 2) 5 kv, 3) 5.2 kv, 4) 10 kv, 5) 30 kv.

is shown in Fig.4. The variation with wavelength of the absorption coefficient near the K and L_{III} absorption edges of chromium and molybdenum in the alloys is similar to the variation in the spectra of pure chromium and molybdenum (Figs.2 & 3).

The positions of the $K\beta_1$ and $K\beta_2$ emission lines of molybdenum in the alloys remain the same within the limits of the experimental error.

We carried out a special series of experiments with a view to determining the influence of the conditions of excitation on the principal parameters of the Cr $K\beta_5$ and Mo $K\beta_2$ lines and the effect of superficial density of the absorber on the L_{III} spectrum of molybdenum.

The variation of the shape of the Mo $L\beta_2$ line as a function of the tube potential (Fig. 5) shows that the short wavelength edge of this line is distorted by reabsorption of the radiation in the material of the anode at voltages above 3.6 kv. An analogous distortion is obtained in the case of the short wavelength part of the Cr $K\beta_5$ line. The data on the tube potential dependence of the index of asymmetry and the width of the Cr $K\beta_5$ and Mo $L\beta_2$ lines are listed in Tables 3 & 4.

In light of the facts established in our investigations, it is clear that one must approach the data in the literature on changes in the shape of the last emission line, such as Cr $K\beta_5$ and Mo $L\beta_2$, with due caution. In order to avoid erroneous interpretation of displacements of the center of the short wavelength part of such lines as being due to differences in number of filled electron states in different chemical compounds and alloys, one must in each specific case take into account the changes in the position and structure of the corresponding absorption edge.

Investigation of the variation of the character of the L_{III} absorption edge of molybdenum as a function of the density of the absorber showed the following. Use of the usual superficial density of 2-4 mg/cm^2 leads to appreciable distortion of the shape of the L_{III} absorption edge and to complete disappearance of the selective absorption line (Fig.6). Use in the present work of absorbers with a density of the order of 1 mg/cm^2 (preparation of such absorbers in the case of substances with a high volume density such as Mo and MoS_2 presents appreciable difficulties) made it possible to obtain the true wavelength variation of the absorption coefficient in the region of the L_{III} absorption edge (see

Table 3

Variation of the asymmetry index of the Cr $K\beta_5$ line with tube voltage

Tube voltage, kv	7	8	9	10	30
Asymmetry index Cr $K\beta_5$ line	1,8	1,7	2	2,4	2

Table 4

Variation of the shape of the Mo $L\beta_2$ line with tube voltage

Tube voltage, kv	3,6	5	5,2	6	10	30
Asymmetry index Mo $L\beta_2$	1	1,2	1,2	1,2	1,5	1,6
Width of Mo $L\beta_2$ line, ev	6	5,3	5,3	5,3	5,4	4,9

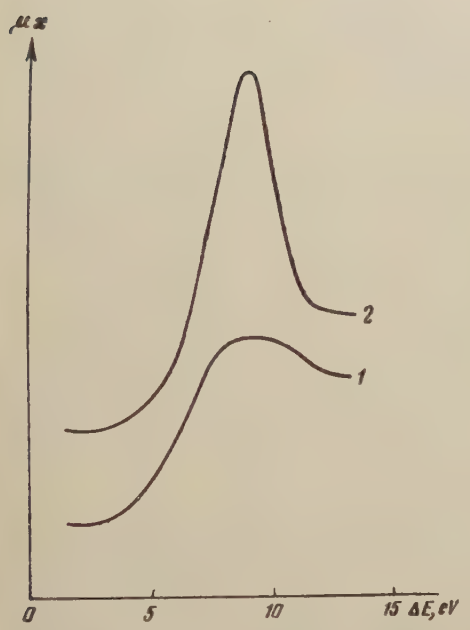

Fig.6. L_{III} absorption spectra of Mo obtained with absorbers of different thickness: 1) 3 mg/cm^2 and 2) 1 mg/cm^2.

Fig.3); the actual variation differed significantly from the data on coefficient in the literature[3].

Analysis and examination of the results of our investigations lead to the following conclusions.

1. There were observed definite differences in the parameters of the $K\alpha_1$, $K\beta_1$ and $K\beta_5$ lines in the emission x-ray spectrum of the three samples of metallic chromium having different degrees of purity. The first two lines ($K\alpha_1$ & $K\beta_1$) are due to transitions between deep atomic levels: $K \rightarrow L_{III}$ ($1s \rightarrow 2p$) and $K \rightarrow M_{II,III}$($1s \rightarrow 3p$), respectively; the $K\beta_5$ line is associated with electron transitions from the 3d band, overlapping with the conduction band, to the inner K level (1s).

With decreasing impurity content in the chromium (i.e., in going from the Cr refined by the hydride procedure to that refined by the iodide method) the $K\beta_1$ and $K\beta_5$ lines are displaced to the side of shorter wavelengths. At the same time the asymmetry index of the $K\alpha_1$ line changes appreciably. The position and shape of the K absorption edge, however, remain virtually unaltered.

2. For the purpose of characterizing the behavior of the electron energy spectrum in going from pure metals to alloys one can conveniently use the change in the absolute value of the level energies in Cr and Mo in Cr-Mo alloys relative to the energies of the corresponding levels in pure Cr and Mo. For the purposes of our comparitive evaluation we assumed that the energy of the K level (1s) is the same for the atoms in both the pure metal and alloy. On the basis of this assumption it is found that the energy of the $M_{II,III}$ level of Cr increases in going from electrolytic Cr to alloys containing from 0.14 to 1% Mn and then remains constant up to an Mo content of 31%. An analogous energy increase is observed for the $M_{IV,V}$ level of chromium, except that

in this case after a noticeable shift in the region of small impurity contents the energy value of this level remains constant up to an Mo concentration of 2.5%. With further increase in Mo concentration the energy of the $M_{IV,V}$ level again rises, going to a maximum value in the alloy with 80% Mo.

Turning to the behavior of the $M_{IV,V}$ and $N_{IV,V}$ levels of molybdenum, we find that with a low concentration (up to 1%) of Cr in the alloy the energy of the $M_{IV,V}$ and $N_{IV,V}$ levels increases, relative to the energy value in pure Mo. Further increase in Cr concentration reduces the absolute value of the energies of the $M_{IV,V}$ and $N_{IV,V}$ levels. More specifically, the $M_{IV,V}$ levels show little energy variation in the range of low Cr concentrations but do exhibit a tendency to decrease in energy in alloys with a high Cr concentration, while the $N_{IV,V}$ levels are characterized by an appreciable decrease in energy even in the 20-70% Cr concentration range.

The virtually constant value of the asymmetry index of the Cr $K\alpha_1$ line in all the investigated alloys (except the alloy with 0.07% Mo) can be taken, in our opinion, as experimental substantiation of the above assumption that the energy of the K level in Cr atoms remains constant in all the alloys and equal to the value in the pure metal.

Further, it may be noted that in a series of alloys with increasing Mo content the shape of the Cr $K\beta'$ satellite changes substantially and at high concentrations of Mo is characterized by an intensity distribution virtually identical with that observed for the $K\beta'$ satellite of Mn (the atomic number of this element is one greater than that of Cr).

The above described behavior of the electron energy levels can be explained as follows. An increase in the absolute value of the level energy is connected primarily with increase in the effective charge of the nucleus, which can occur, for example, due to loss of part of the 3d electrons as a result of spatial redistribution of the electrons under the influence of changes in the concentration of the second component of the solid solution. Thus any increase in the absolute value in the energy of the atomic levels is evidence that the atom has acquired an additional positive charge as compared with its charge in the pure metal, and, vice versa, a decrease in the absolute level energy value is an indication of a decrease in the effective charge of the nucleus.

Analysis of the experimental data from this viewpoint leads us to infer that in Cr-Mo alloys, Mo as an impurity has an excess negative charge, while the chromium as the host material has a positive charge; the change in charge does not, however, affect the shape of the Cr $K\beta_5$ and Mo $K\beta_2$ lines inasmuch as in the average (per atom) the change in charge is small.

In alloys with a small Cr content, the Cr as the impurity also has a certain excess negative charge.

In alloys in the range of Mo concentrations from 1 to 30%, chromium has an excess positive charge and the molybdenum an excess negative charge.

* * *

The established facts - the noted influence of impurities on the electron energy distribution in the atoms of the element constituting the base of the alloy and the resultant deformation of almost all the electron levels of the atom, including the deepest lying ones - have led us to formulate certain new concepts in the theory of dilute solid solutions based on elements of the transition groups (elements with incomplete (n - 1)d and (n - 1)f shells.

As we have noted in earlier publications[4,5], small concentrations of substitutional impurities exert a strong influence on the properties of the base

metal and, in particular, on its electron energy spectrum. The experimental data cited above allow of elaborating our original theoretical concepts. According to these concepts[6], the most important effect of impurities in transition metals is the formation of "atomic blocks" having dimensions of the order of 10^{-7} cm and characterized by an enhanced strength of the interatomic bonds. In the present report, we are interested not so much in the magnitude of this additional interatomic coupling but in the character of the changes in the electron spectrum. These changes are the primary cause of formation of these stronger bonds.

Fundamental in our theoretical treatment is the model for an infinitely diluted solid solution ("one impurity in a metal").

Let the charge of the atomic kernels of the base metal be +Ze, where e is the absolute value of the electron charge; consequently, Z is the number of electrons surrendered by each atom into the common conduction zone. On the basis of the experimental data obtained in our x-ray spectroscopic investigation, it may be concluded that the metallic impurity atom entering into the base metal lattice loses its weakly bound valence electrons, i.e., gives them up into the conduction band of the electron spectrum of the base metal. Thereby the impurity atom acquires a certain positive charge.

If, however, the impurity is a transition element having an incomplete inner electron shell, the situation as regards determination of the charge of the impurity becomes complicated in view of the fact that there may occur either a loss or acquisition of electrons by the incomplete shell of the impurity atoms with a corresponding change in the "usual" charge, depending on the relative positions of the electron energy spectrum of the base metal and the electron spectrum of the unfilled shell of the impurity.[7] Thus the charge of the impurity may prove to be either greater or smaller than the charge of the atomic kernels of the base metal.

It is most convenient to approach the question of the degree of the perturbing effect of a substitutional impurity on the electron spectrum of the base metal on the assumption that in the pure metal there is the same charge at all lattice sites, the charge giving rise to the ideal periodic potential of the lattice characterized by the normal unperturbed spectrum of the base metal. At a site where an impurity atom is lodged, in addition to the normal charge, there will be an additional "excess charge" perturbing the electron spectrum. Thus the problem reduces to determining the perturbing influence of the excess charge on the known unperturbed spectrum of the pure base metal. The excess charge is defined as the difference between the true charge of the impurity and the true charge of the atomic kernel of the base metal. Obviously, the excess charge can be either positive or negative.

The excess charge is screened by the conduction electrons (and partially by the electrons of the unfilled shells). This screening gives rise to a change in the spatial density of the electrons: closer packing of the electrons in the vicinity of impurity atoms with a positive excess charge and a reduction in density about impurity atoms with a negative excess charge. From the energy standpoint this amounts to local variations in the density of the quasi-levels in the conduction band.[8] In the case of such local deformation of the conduction band there occurs a displacement of all the quasi-levels comprising the conduction band. In the case of local "crowding" of the quasi-levels, part of the unoccupied levels lying above the Fermi level will be displaced downward to below the Fermi level; analogously, in the case of "thinning out" of the quasi-levels, part of the occupied levels in the given local region will be displaced upward from under the Fermi level to above it. In both cases there will occur a spatial redistribution of the electrons for

equalization of their energy with reference to the Fermi level. As a result we obtain the above mentioned screening of the excess charge of the impurity.

Outside this screening region the influence of the impurity is virtually negligible. The region of screening is limited to the more or less immediate neighborhood of the impurity atom. Thus the perturbing potential proves to be a short-range one. The shape and magnitude of the deformation of the electron spectrum is determined primarily by the form of this potential. As both theoretical and experimental investigations[4,8-10] show the perturbing potential in the case of an infinitely diluted solid solution can be satisfactorily approximated by

$$W(r) = \frac{Z'e}{r} e^{-qr}, \qquad (1)$$

where r is the distance from the impurity, $Z'e$ is the excess charge (which may be positive or negative) of the impurity, and q is a parameter depending in general on Z' and determining the effective radius R_{eff} of action of the impurity. In the case of finite impurity concentrations the form of the potential is, of course, more complicated. If, however, the impurity concentration is such that between the impurity particles there is only statistical correlation as regards uniformity of distribution but no direct interaction (i.e., if the distance between impurities is greater than their effective radius of action) one can use Eq.(1) for the perturbing potential for rough qualitative evaluation of different characteristics. The range of concentrations wherein this approximation is allowable can be determined empirically, for example, from the experimental data on the dependence of the self-diffusion coefficient of the base metal element on the impurity concentration (see Ref.11).

Mathematical evaluations of the results of the influence of impurities can at present be carried out in the so-called "rigid band" approximation in which it is assumed that all quasi-levels of the electron spectrum bands of the base metal at a given spatial point are displaced under the influence of the impurity by the same amount, determined simply by the potential energy of the perturbing influence of the impurity on an electron located at the given point (or more accurately at the given atomic kernel).

If we denote the magnitude of the displacement through ΔE, then in the given approximation (see Refs.1 & 6):

$$\Delta E = -eW(r) \qquad (2)$$

for any level (with any value of E^0, the energy of the level in the absence of perturbation).

This formula cannot, however, be deduced in the framework of the general perturbation theory. In connection with this it is important to analyze the character of the assumptions recently made in utilizing this approximation even in cases when it was not assumed that $|eW(r)|$ is small compared with the Fermi level energy.[9]

Our theoretical analysis[2] showed that the rigid band approximation is obtained only in the case when the periodic part of the Bloch functions can be approximated by means of atomic functions subject to very rigorous localization conditions. Consequently, this approximation is more suitable for inner rather than for outer electrons, as is also obvious from physical considerations. A certain degree of applicability of the approximation to deep inner electrons is assured, however, by the fact that the influence of the impurity on them is masked by the stronger influence of changes in the energy spectrum of the electrons of the neighboring shell (the next inner one).

Furthermore, the effective influence of the impurity is reduced for electrons in deeper shells (in many-electron atoms the influence of the impurity may be considered to be negligibly small for 1s electrons).

On the other hand, for outer electrons and primarily for electrons in the conduction band, the rigid band approximation can serve only for rough qualitative evaluations. The most interesting and valuable evaluations will be those for electrons of unfilled shells having a common Fermi level with the conduction electrons.

As was noted above, electrons from the unfilled shells of the base metal atoms, for example, the 3d electrons of chromium, also participate in the screening of the excess charge of the impurity. This means that in the process of equalization of the electron energy with respect to the Fermi level some of the atomic kernels of chromium in the vicinity of the impurity atoms may lose or acquire 3d electrons. In general, these atomic kernels will now have a new value of charge so that they may be regarded as induced impurities with an excess charge having a polarity opposite that of the excess charge of the main impurity.

This excess charge can be evaluated by means of the rigid band approximation in the following manner. Let R_{eff} be the effective radius of action of the main impurity. Then the total value of the screening charge attributable to the 3d electrons will be given by

$$(Ze)_{3d} = \int e \{\rho_{3d}(E_\Phi) - \rho^0_{3d}(E_\Phi)\}\, d\tau, \tag{3}$$

where $\rho^0_{3d}(E_\Phi)$ and $\rho_{3d}(E_\Phi)$ are, respectively, the spatial densities of the 3d electrons in the pure metal and in the case when an impurity is present. Further, we have

$$\rho_{3d}(E_\Phi) = \rho^0_{3d}(E_\Phi + \Delta E_\Phi). \tag{4}$$

The magnitude of the shift ΔE is negligibly small; hence

$$\rho_{3d}(E_\Phi) = \rho^0_{3d}(E_\Phi) \approx \Delta E_\Phi \left(\frac{\partial \rho^0_{3d}}{dE}\right)_{E=E_\Phi}. \tag{5}$$

In the "rigid band" approximation

$$\Delta E_\Phi = -eW(r). \tag{6}$$

Moreover, $\left(\frac{\partial \rho^0_{3d}}{\partial E}\right)_{E=E_\Phi} = n^0_{3d}(E_\Phi)$, the level density in the 3d band near the Fermi level in pure metal. Furthermore, inasmuch as the atomic dimensions are small, the distribution of 3d electrons may be assumed to be spherically symmetrical relative to the main impurity in all cases. Then we obtain

$$(Ze)_{3d} = -4\pi e^2 n^0_{3d}(E_\Phi) \int^{R_{eff}} W(r)\, r^2 dr. \tag{7}$$

This screened charge is distributed in a sphere of radius R_{eff}. The number of atomic kernels of the base metal in this sphere is

$$x \frac{\frac{4\pi}{3} R^3_{eff}}{V_{uc}}, \tag{8}$$

where V_{uc} is the volume of the unit cell; for chromium with a body centered cubic lattice $V_{uc} = a^3$; x is the number of atoms per unit cell (two in the

case of chromium). Thus the mean induced 3d charge per atomic kernel of the base metal in the region where the action of the impurity is effective is given by

$$(\overline{Ze})_{3d} = \frac{-4\pi e^2 n^0_{3d}(E_\Phi)\int_0^{R_{eff}} W(r)\, r^2 dr}{x\,\frac{\frac{4\pi}{3}R^3_{eff}}{a^3}}. \qquad (9)$$

In the optimal case of action of the impurity, when the atomic blocks encompass the total volume of the system, but the main impurities do not interact with each other, the value of $(\overline{Ze})_{3d}$ will be the average excess induced charge per atomic kernel in the system. Such a change of the mean charge must, according to Moseley's law, affect the magnitudes of the x-ray terms; the direction of change of these terms gives a unique indication of the sign of the induced excess charge of the atomic kernels and, consequently, of the sign of the excess charge of the impurity.

In the light of these theoretical considerations one can satisfactorily describe the character of the changes observed in the x-ray spectra of transition metals as a function of the impurity concentration.

Thus for determining the charge of the impurity atoms and the atoms of the base metal one must determine the magnitude of $n^0_{3d}(\Xi_{Coff})$ from the x-ray spectra. Unfortunately, one cannot carry out such an evaluation on the basis of the experimental data given above. To permit of such an evaluation one must extend the investigation to the region of the ultralong wave x-ray spectrum, i.e., investigate the L and M spectra of Cr and Mo. An appreciably better resolution in energy (0.05-0.1 ev) is obtainable in the long-wave x-ray region; only with such resolutions can one hope to obtain quantitative data.

The value of the charge of the impurity atoms can be obtained directly in investigating the electrolysis of atoms of elements in solid solutions.[12]

Conclusions

As a result of our x-ray spectroscopic investigation of the electron energy spectrum of solid solutions and theoretical analysis of the problem of dilute solid solutions we come to the following conclusions.

1. In dilute solid solutions there are formed in the vicinity of impurity atoms having a negative excess charge "atomic blocks" with an effective radius of action of 10^{-7} cm (in the case when the base metal is an element of the transition group). Within the boundaries of these blocks there appear addiotional interaction forces; the potential of these forces has the character of a short-range (cut-off) potential.

2. The influence of these "blocks" on the electron energy spectrum is evinced most strongly as long as there is no interaction between the impurity atoms.

3. The additional bonding, which is polar in character, persists over an appreciable range of concentrations in solid solutions of the Cr-Mo system, although in the higher-than-dilute range of concentrations, no blocks are formed and the additional bonding is weaker than in dilute solutions. In the case of Cr base solutions this interval of "constant additional binding" extends from 2 to 30 atomic percent Mo; in the case of Mo base solutions it extends from 3 to 20 atomic percent Cr.

4. When Mo or Cr is the impurity each of these atoms has an excess negative charge relative to the atoms of the base metal (Cr or Mo, respectively).

5. In the range of Cr concentrations from 38 to 70% in Cr-Mo solid solutions, the Cr has a positive and the Mo has a negative excess charge as compared with the respective charges in the pure metals.

Laboratory of Physical Methods of Investigation,
"A.A.Baikov" Institute of Metallurgy,
Academy of Sciences of the USSR

References

1. Kessler & Hansen, Trans. Am. Soc. Met., 42, 1008 (1953).
2. I.B.Borovskii, K.P.Gurov, S.A.Ditsman, V.A.Batyrev & H.A.Lobanova, Sbornik "Issledovanie po zharoprochnym splavam" (Collected articles on "Investigations in the field of heat-resistant alloys), Vol.III, M., 1957.
3. R.L.Barinskii, Doklady AN SSSR, 83, 381 (1952).
4. I.B.Borovskii & K.P.Gurov, Sb. "Issledovanie po zharoprochnym splavam" (see 2 above), Vol.II, M.1957.
5. I.B.Borovskii, S.A.Ditsman & V.A.Batyrev, ibid.
6. I.B.Borovskii & K.P.Gurov, FMM (Physics of Metals and Metallog.), 4, 187 (1957).
7. H.Jones, Phil.Mag., 44, 355 (1953).
8. J.Friedel, Adv. in Phys., 3, 12 (1954).
9. L.C.R.Alfred & N.H.March, Phil.Mag., 46, 759 (1955).
10. N.F.Mott & H.Jones, Theory of the properties of metals and alloys, Oxford, 1945.
11. I.B.Borovskii, K.P.Gurov & Iu.G.Miller, Doklady AN SSSR, 118, 1958.
12. I.N.Frantsevich & D.F.Kalinovich, Sb."Voprosy poroshkovoi metallurgii i prochnosti materialov" (Collected articles on "Problems on powder metallurgy and strength of materials"), Kiev, 1956.

USE OF THE URS-50-I X-RAY EQUIPMENT AS A DOUBLE CRYSTAL SPECTROMETER

- I.B.Borovskii & V.V.Shmidt

Use of the double crystal spectrometer in x-ray spectroscopic and other work has made it feasible to solve a number of problems not susceptible of solution by means of other monochromators. The principal advantages of the double crystal spectrometer are the possibility of accurately taking into account imperfections of the monochromator crystal and rigorous monochromatization of the radiation. These features make it possible to determine such important physical characteristics as inherent line widths in the x-ray spectrum[1], the diffraction pattern at very small angles[2], and the number of growth defects in single crystals (so-called dislocations)[3] and to make precision measurements of the lattice parameters of organic crystals (of the order of 450-500 A).

Despite the obvious importance of such investigations and the fact that they have been extensively carried on abroad, until now there has not been available in the USSR a single x-ray spectrometer of the double type suitable for such investigations. Shortly after the beginning of production of the URS-50-I equipment in the USSR, we undertook to make certain improvements in this apparatus with a view to making it suitable for use as a double spectrometer. Let us briefly recall the fundamental positions of a double crystal spectrometer.

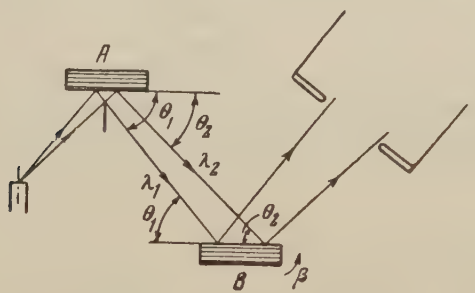

Fig.1. The (1, -1) position.

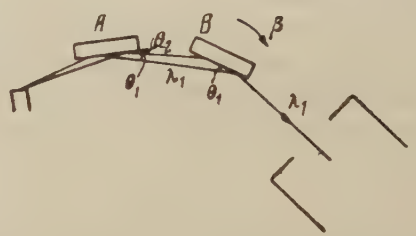

Fig.2. The (1, +1) position.

In the (1, -1) position (Fig.1) both crystals are parallel and the reflection is in the first order. Crystal A diffracts the incident radiation into parallel beams according to wavelength. If beam λ_1 is reflected from the crystal at an angle θ_1, it will be incident on crystal B at the same angle and, consequently, can be reflected. The same thing may be said regarding ray λ_2. Hence, in this position the dispersion of the instrument is zero.

Let us assume that both crystals are perfect, i.e., that there is not only no mosaicity but also no dynamic interference (i.e., that the reflection is exactly at the Bragg angle). Then even a slight rotation of the crystal B about its axis will completely cut off the radiation to the counter. If, on the other hand, the crystals are not perfect, then the intensity recorded by the counter as a function of the angle β of rotation of the crystal B will be characterized by some curve with a maximum. The width of this reflection curve in the (1, -1) position characterizes the quality of the reflecting surfaces of both crystals.

In the (1, +1) position (Fig.2) the crystals are antiparallel; the reflection is in the first order. Now if the crystal B is at the Bragg angle θ_1 to the ray λ_1, the ray λ_2 cannot be reflected. Now the instrument has dispersion and the reflection curve will characterize the shape of the spectral line.

The basic component of our two-crystal spectrometer set-up is a GUR-3 goniometer. The goniometer has a monochromator and crystal A is clamped in its crystal holder. Crystal B is clamped in the specimen-crystal holder of the URS-50-I equipment. With the equipment used as a double spectrometer all the slits were completely removed. A knife-edge was mounted on the first crystal. In investigating the fine structure of x-ray spectra we used calcite crystals prepared by the procedure described in Ref.4. In a double crystal spectrometer one must be able to determine the rotation of the second crystal within a few seconds. Inasmuch as each division on the circle of the GUR-3 goniometer equals 1', it was necessary to install an auxiliary worm gear. A drive yielding 18" rotation of the second crystal per revolution of the worm proved to be fully satisfactory.

Satisfactory operation of the URS-50-I equipment as a two-crystal spectrometer can be assured only through very careful and thorough adjustment. The most important adjustments are 1) bringing the axis of rotation of crystal B exactly into its reflecting plane and 2) alignment of the axis of crystal B with a plane parallel to the reflecting plane of crystal A. We undertook a special theoretical analysis of the accuracy of indication of a double crystal spectrometer and the influence upon it of misalignments. The principal results of this analysis were the following. Let the axis of rotation of crystal B form an angle δ with its reflecting plane; then in the (1, -1) position the reflection curve will be wider than the reflection curve for the ideal adjustment by an amount

$$\Delta\beta \approx k\varphi_m\delta + \frac{\varphi_m^2\delta^2}{b}, \quad 0 \leqslant k \leqslant 1,$$

where φ_m is the maximum vertical divergence, b is the width of the diffraction pattern from the calcite crystal ($\sim 10^{-5}$ radians).

If we take $\varphi_m \approx 10^{-2}$ and $\delta \approx 1'$, we obtain $\Delta\beta \approx 1''$. Disadjustment as regards the second above-mentioned alignment leads to an analogous result.

If we assume that the subject of investigation is a spectral line having the classical dispersion shape and a half-width β_0, the relative broadening of the line due to disadjustment in the (1, +1) position, again taking $\varphi_m \approx 10^{-2}$ and $\delta \approx 1'$, it is evaluated to be

$$\frac{\Delta\beta}{\beta_0} \approx k\varphi_m\frac{\delta}{b} + \frac{\varphi_m^2\delta^2}{b^2} \approx 0{,}1$$

It will be obvious from these calculations that the adjustment must be carried out with an accuracy of $\delta = 1'$. The necessary adjustment was carried out by means of a KM-5 cathetometer. After this adjustment, the width of the reflection curve obtained in the (1, -1) position with Mo Kα radiation was 6.5", while the theoretical value of this width on the assumption of complete absence of mosaicity is 4.5" according to Nordling[5].

According to Beeman & Friedman[6] in recording an absorption spectrum one must carry out the intensity measurements at each point of the spectrum two times, once with the absorber and then without it. In addition, one must have an appropriate device for placing the absorber back in exactly the same position each time. We improved this procedure by introducing an auxiliary control counter (see Fig.3). In our set-up the auxiliary crystal 5 separates out a portion of the "white" radiation in the investigated wavelength interval. Crystal 5 and counter 6 are always stationary so that the indications of the auxiliary control counter depend only on the operating regime of the set-up. Hence if the indication of counter 4 is divided by the indication of counter 6, we obtain a quantity that is independent of chance variations of the

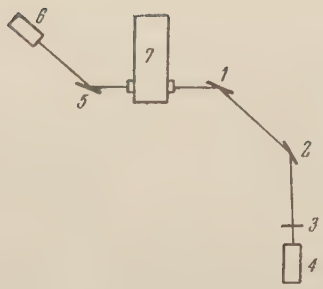

Fig.3. Diagram of set-up for investigating absorption spectra: 1) first crystal, 2) second crystal, 3) absorber, 4) Geiger-Müller counter, 5) auxiliary crystal, 6) auxiliary control counter, 7) x-ray tube.

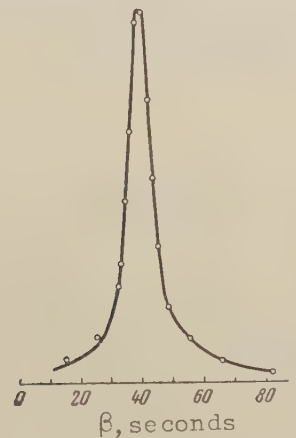

Fig.5. Reflection curve in the (1, -1) position. Solid line - dispersion curve; points - experimental values.

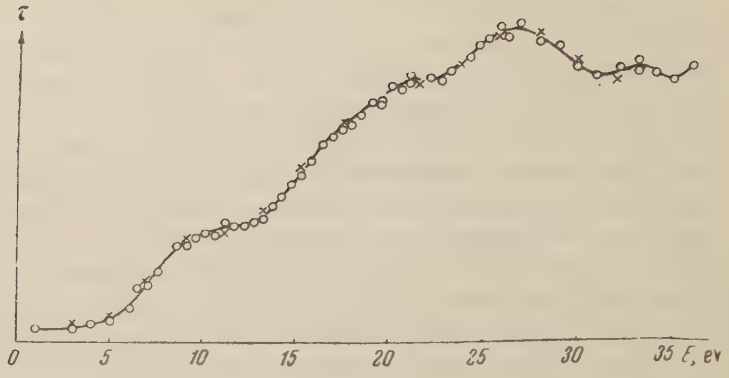

Fig.4. K absorption edge of Fe.

operating conditions in the process of recording the given point. The two counters have a common control so that they start and stop at the same time. Incorporation of the control counter into the circuit made it possible to obtain the curve of the white radiation in the investigated wavelength interval, i.e., $I_4/I_6 = f(\lambda)$ with the absorber 3 withdrawn from the beam, where I_4 and I_6 are the indications of counters 4 and 6, respectively. This curve is entirely independent of the operation of the set-up and is constant for the given angular interval. Experiments showed that the plot of this function is a straight line parallel to the x-axis.

Hence thereafter the entire spectrum could be recorded with the absorber in place. Obviously, this substantially reduced the time required for recording a spectrum.

With respect to the K absorption edge of Fe (λ = 1.74 A) our instrument has a dispersion D = = 0.35 A/mm, a reflection curve width in the (1, -1) position W = 11.5", and a resolution in the (1, +1) position of $\lambda/\delta\lambda = \lambda D/W$ = 10,000. In this position the homogeneity of the monochromatic ray separated from the continuous spectrum is characterized by $\Delta\lambda \approx 0.2$ X.

By way of illustration, the curve obtained for the K absorption edge of Fe is reproduced in Fig.4.

We repeatedly checked the reproducibility of the results obtained with the apparatus. In the case of the absorption edge of Fe the results for the repeat recording are indicated by the crosses. It will be evident that the reproducibility is fully satisfactory.

As may be seen from Fig.5 the reflection curve obtained in the (1, -1) position has the classical dispersion shape.

Laboratory of Physical Methods of Investigation
"A.A.Baikov" Institute of Metallurgy
Academy of Sciences of the USSR

References

1. A.H.Compton & S.K.Allison, X-rays in Theory and Experiment, 1935 (Cited in Russian trans., M., 1941).
2. E.A.Porai-Koshits, Usp.fiz.nauk, 39, 573 (1949).
3. A.D.Kurtz, S.A.Kulin & B.L.Averbach, Phys.Rev., 101, 1285 (1956).
4. Manning, Rev.Sci.Inst., 5, 316 (1934).
5. C.Nordling, Ark.f.Fys., 11, 79 (1956).
6. W.W.Beeman & H.Friedman, Phys.Rev., 56, 392 (1939).

X-RAY SPECTROSCOPIC INVESTIGATION OF CHEMICAL COMPOSITION IN MICROVOLUMES OF ALLOYS

- I.B.Borovskii, N.P.Il'in, L.E.Loseva, I.D.Marchukova & A.N.Deev

In the present report we shall give some of the results obtained in investigating the microcomposition of complex samples and show on the basis of these the possibilities offered by x-ray spectroscopic methods of determining the chemical composition in microvolumes as regards solution of diverse problems in metallography, the physics of metals and allied fields.

This method has been under development since 1951 by Castaing in France and simultaneously here in the Soviet Union. At present one can already clearly delineate its possibilities and potentialities.

Briefly, the method may be described as follows. The investigated microsection is mounted in a special x-ray tube in the place of the anode so that the target "speculum" is the surface of the microsection whose structure may then be examined by means of a metallomicroscope incorporated in the tube. The specimen can be displaced in the plane of the anode by means of special micrometer screws, thereby bringing any desired point (microvolume) into the electron beam. The electron beam is focused, the diameter of the focal spot in the plane of the anode being 2-3 μ. Thus the electrons excite the atoms of the material in a microvolume of about 10 μ^3, which corresponds to an analyzed mass of the order of 10^{-10} g. Thus given an average analytic sensitivity of 0.1% one can detect the presence in the anode-section of as little as 10^{-13} g of the element. The analysis of the chemical composition at the "point" of the focal spot is realized by the usual procedures of x-ray spectroscopy.

As developed in France the procedure is based on using a specially designed spectrograph with focusing of the monochromatic x-ray radiation by means of a bent crystal by the Johansson method and employing a microfocus tube with electrostatic focusing of the electron beam. In the Institute of Metallurgy of the USSR Academy of Sciences the work led to the development of the RSASh-2 x-ray spectrograph for determination of the elements from Fe^{26} to Mo^{42} and from Hf^{72} to U^{92} in microsections. Recently, there has also been developed the RSASh-ZD model spectrograph by means of which microsections can be analyzed for the elements from Fe^{26} to Mg^{12} inclusive.

The RSASh-2 equipment consists of the x-ray spectrograph proper, a microfocus x-ray tube, a power supply and a detecting-recording unit.

For spectral resolution of the x-ray radiation use was made of a modification of the transmission method developed by DuMond for analysis of the x-ray spectra of radioactive elements. The short wave x-ray spectrograph has a stationary $(10\bar{1}0)$ reflecting plane quartz crystal curved to a radius of 300 mm and two moveable arms, one carrying the x-ray tube and the other the radiation detector, a Geiger-Müller counter.

The microfocus x-ray tube is an electron optical system with electromagnetic focusing of the electron beam. With the optimal diameter of the focal spot (2-3 μ) and a current of 10^{-7}-10^{-8} amp at 35-50 kv, the specific power load on the anode-section is several kilowatt per square millimeter. At this specific loading the temperature at the focal spot does not exceed 50°.

In working out the design of the specimen "stage", it was assumed that of greatest practical interest would be investigation of the continuous distribution of the elements in the samples, i.e., continuous "point" analysis. The developed design allows of precision displacement (accuracy ~1 μ) of the sample under the electron beam at rates from 10 to 150 μ/min. With simultaneous continuous recording of the intensity of the characteristic lines of the

element being determined on the roll chart of the recording potentiometer, there is obtained a concentration curve for the scanned strip of the sample with a magnification from 1000 to 20,000. The actual magnification is determined by the ratio of the rate of displacement of the sample to the rate of advance of the potentiometer chart.

Below we give the results of some of the investigations carried out by means of the described equipment.

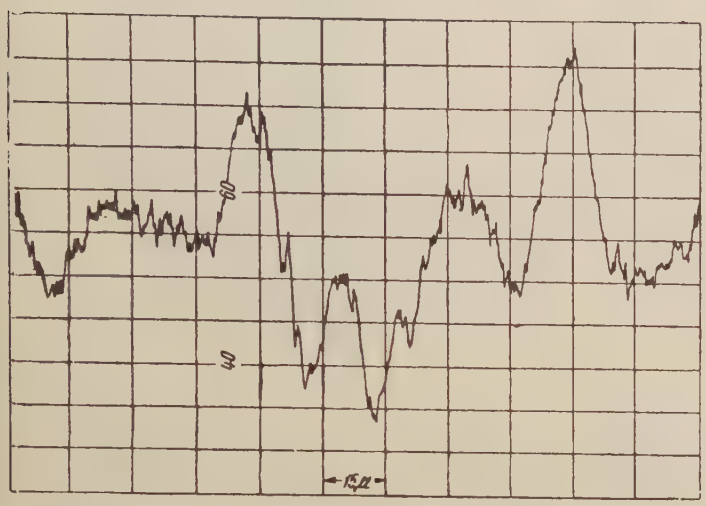

Fig.1. Distribution of rhenium in an Re-Ni solid solution.

Analysis for homogeneity. Using continuous recording for a given element while scanning across the specimen in a selected direction, one can check the degree of homogenization of an alloy and investigate the distribution of different elements in the process of crystallization of ingots. Important here is the fact that it is not necessary to etch or otherwise treat the specimen to bring out the microstructure, which is particularly advantageous in investigating solid solutions of variable concentration or, for example, certain metalloceramic specimens. By way of illustration of the results obtained in such investigations, the distribution of rhenium in an Re-Ni solid solution is shown in Fig.1.

Analysis for phase composition. In Fig.2. we show a photograph of a microsection of a multiple component Ni base alloy to which an additional amount of rhenium was added. The addition of rhenium to the initial alloy led to the separation of a new phase discernible as light grains in the photograph. Next to the microphotograph we show the concentration curve obtained in scanning across one of the grains of this new phase. It will be obvious from the distribution curves for Re, Mo, W and Ni that the segregated phase is appreciably enriched with rhenium, tungsten and molybdenum. Results of quantitative analysis of the phase composition of this alloy are listed in Table 1.

Table 1

Phase composition, atomic %	Element			
	Ni	Re	W	Mo
Basic phase	60 ± 2	14	2,8	2,6
Segregated phase	11 ± 0,5	75	11	6,1
Initial alloy	65 ± 2	—	3,3	2,7

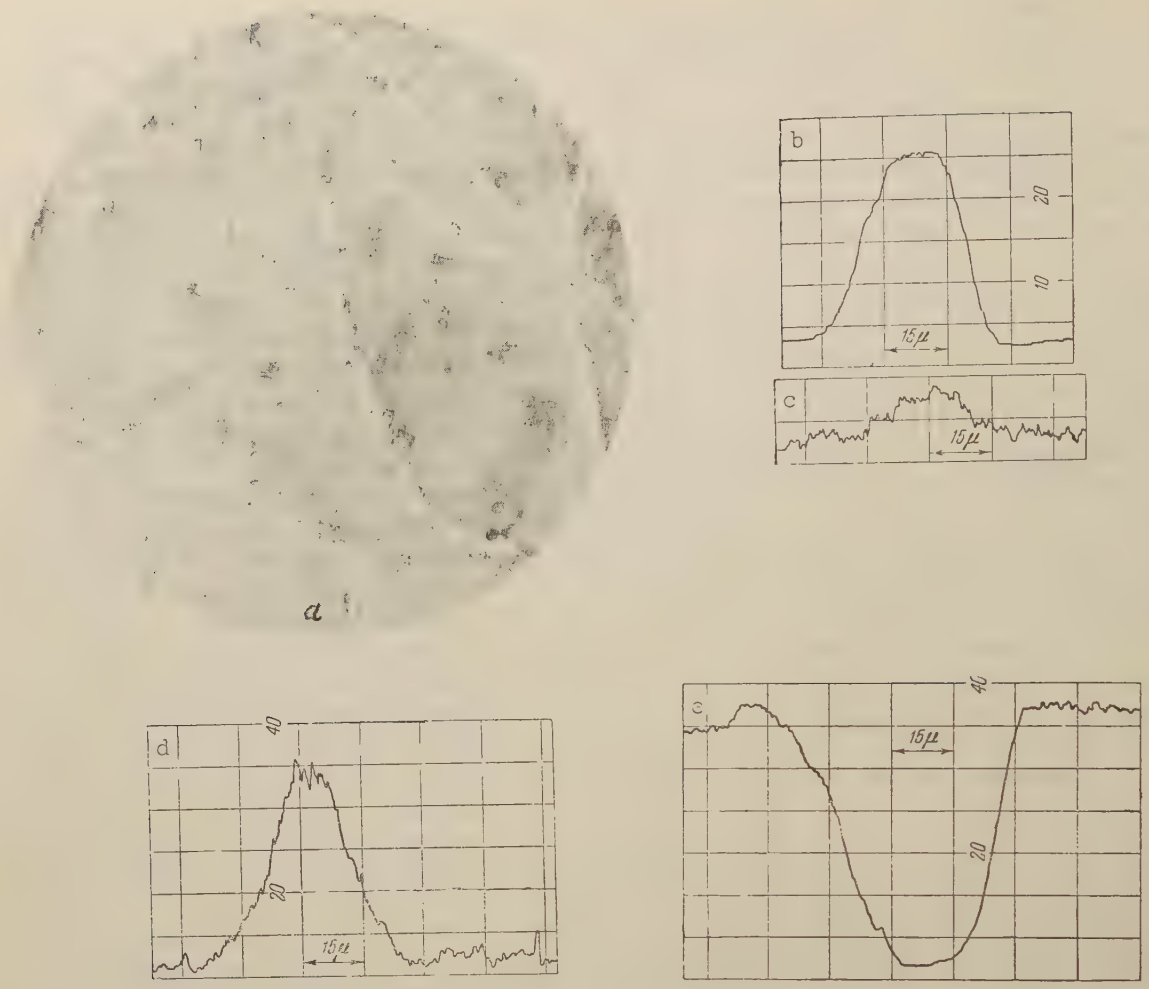

Fig.2. Phase composition analysis of a multiple component alloy to which rhenium was added: microstructure (a) and distribution curves of Re (b), Mo (c), W (d) and Ni (e).

Analysis of welded and soldered joints. By way of illustration of investigations in this category we give the results for a weld obtained in fusing copper onto cold steel. Metallographic analysis (Fig.3 a) showed that in this case there is formed an intermediate layer having a variable width ranging from 15 to 40 μ. From the upper distribution curve (Fig.3 b) across this layer, recorded on the basis of the variation of the intensity Cu $K\alpha_{1,2}$ line, it will be seen that this layer is a metastable phase of constant composition containing approximately 12% Cu.

The RSASh-2 equipment made it possible for the first time to investigate the microcomposition of soldered joints of heat resistant alloys. The samples were prepared by gas-torch soldering with three different types of brazing solder. The investigation comprised determining the distribution of Ni, Fe, Co, W, Mo and Mn in the different phases of the solder alloy as well as the variation in chemical composition of the applied solder across and along the length of the joints. The microphotograph of one of the soldered joints is shown in Fig.4 a; it will be seen that there are two phases - a light one and a dark one - present. Fig.4 b gives the curve characterizing the variation of Mo in the solder of the joint.

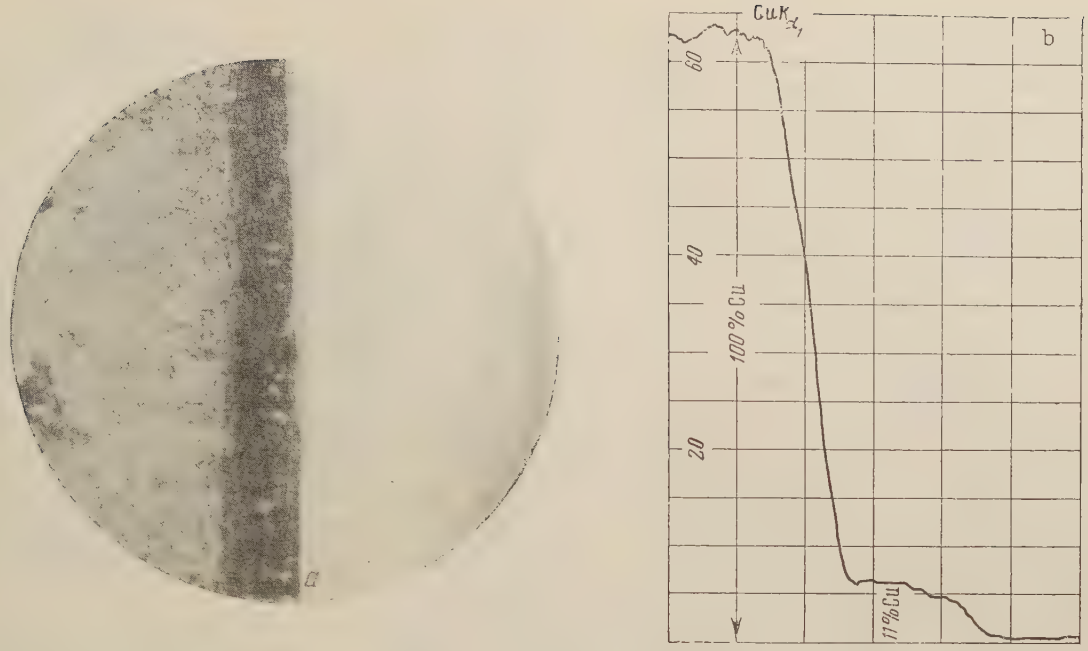

Fig.3. Welded joint: a) microstructure, b) Cu distribution in the weld.

From a comparison of the concentration curve with the microstructure photograph, it was deduced that the areas with an enhanced Mo concentration correspond to the dark phase. The concentration curves characterizing the Ni and Mn distributions, respectively, at the beginning and end of the soldered joint are shown in Fig.4,c & d. It will be obvious from these curves that the amount of nickel decreases, while the amount of manganese increases towards the end of the joint, i.e., where the solder runs out. Quantitative analysis showed that in the light phase of these samples there is 62% Ni and 2% Mn at the beginning of the joint and 50% Ni and 5.5% Mn at the end. Semi-quantitative analysis by continuous recording of the distribution of the elements over the joint and quantitative "point" analysis using suitable references for all the samples led to the following deductions: 1) there is less nickel and iron and more molybdenum and manganese in the dark phase than in the light one; 2) as the solder flows from the point of application to the edges the amount of Ni, W and Fe decreases and the amount of Mo and Mn in it increases; 3) in soldering Ia-1-T steel the solder is appreciably enriched with iron (to 26% instead of the initial 1-2%); 4) in the process of soldering an appreciable amount of manganese is burnt out.

Certain recommendations leading to improved composition of the brazing solders were made on the basis of the described investigation.

Investigation of diffusion layers. For the purpose of determining the possibilities of the method for investigating diffusion processes a series of studies of the Cu-Ni and Cu-Zn systems were carried out. The components of the first system, according to the phase diagram, form a continuous series of solid solutions; in agreement with this the copper concentration curve (Fig.5) obtained in scanning across the diffusion layer (produced at a temperature of 600° with an annealing time of 4 hours) shows a characteristic continuous variation of the Cu concentration.

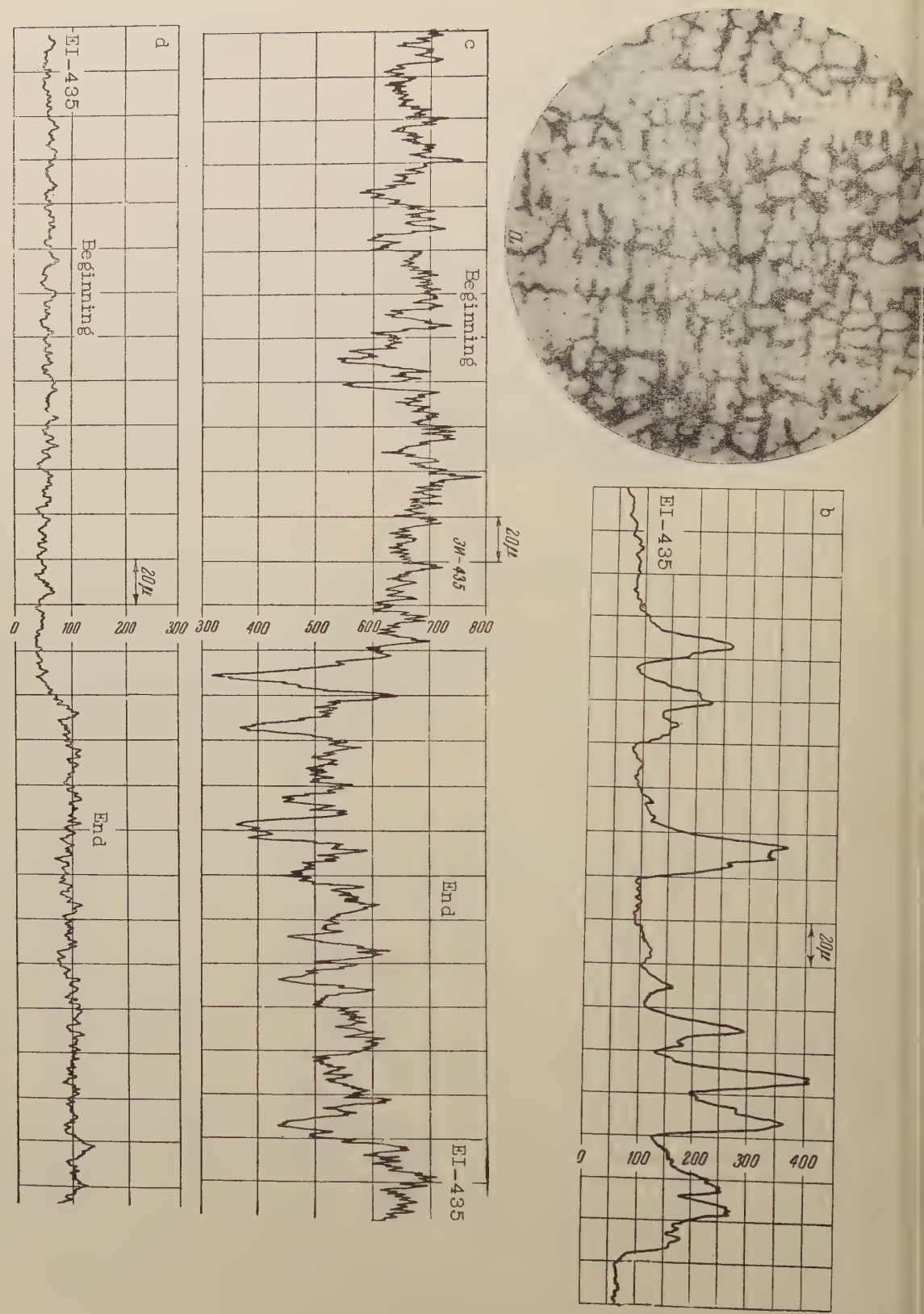

Fig.4. Soldered joint: a) microstructure, b) distribution of Mo in the joint; c & d) distribution of Ni and Mn at the beginning and end of the joint, respectively.

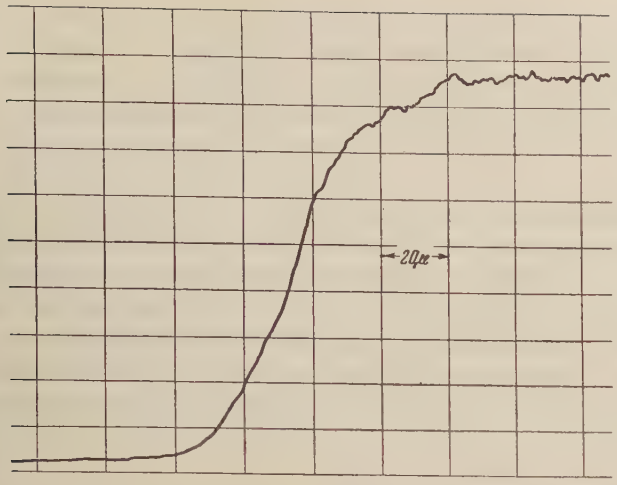

Fig.5. Distribution of Cu in a copper-nickel diffusion layer (4 hour diffusion heating at 600°).

According to the state diagram for the Cu-Zn system these elements form both solid solutions and a number of phases of constant composition. Experimental concentration curves characterizing the distribution of copper and zinc across the diffusion layer were obtained for samples heated at temperatures below the melting point of zinc; further the quantitative composition of the diffusion layers at different sections was determined.

It will be seen from the microphotograph reproduced in Fig.6,a that the diffusion layer consists of two sharply bounded phases. The copper and zinc concentration curves (Fig.6,b) recorded in scanning over the same section of the diffusion layer also indicate the presence of two phases of constant composition in the diffusion layer formed during 3 hour 10 min heating at 320°. The abrupt jumps in the concentration curves in going from the pure metal to the first phase and from one phase to the other indicate that there are no regions of mutual solid solution or mixtures of phase, at least within the limits of resolution, i.e., approximately 2-3 μ, which for a diffusion layer some 200 μ wide equals about 1%. The minor deviations of the concentration curves from the vertical in the transition regions are fully explained by the finite dimensions of the focal spot. From the concentration curves one can make semiquantitative determinations of the elements in question. The accuracy of such analyses is 5-10 relative percent. Thus in the present case it was established for the phase richest in zinc that the zinc content in it is approximately 85%, which corresponds to the ε-phase; the zinc content in the second phase was evaluated to be 65% which corresponds to the γ-phase.

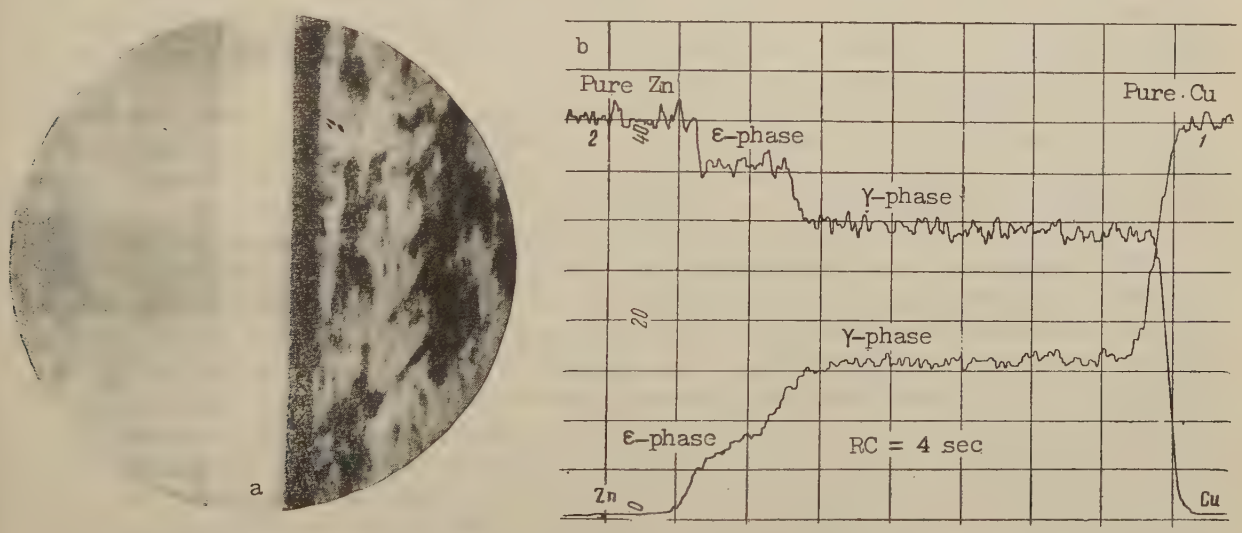

Fig.6. a) Microstructure of copper-zinc diffusion layer and b) corresponding concentration curves: 1) copper and 2) zinc. Diffusion layer obtained by 3 hours 10 min heating at 320°.

Recordings of the concentration curves across the phase layers made with maximum magnification brought out variations in the composition within the bounds of one phase and showed that the variation is linear. Concentration curves recorded for samples heated at different temperatures and for different times allow of determining the width of the phase layers and thus calculating the diffusion coefficients.

It should be noted that in measuring the width of phase layers with the RSASh-2 equipment a much higher accuracy than with other methods is obtained inasmuch as the effective magnification of the concentration curve (20,000 X) appreciably exceeds the possible optical magnification in observing the microstructure; moreover, by virtue of the continuous recording feature of the equipement one can with great accuracy establish the boundaries between individual phases particularly between the solid solution and the adjacent constant composition phase, which, of course, cannot be done by means of a conventional metallographic microscope.

The calculated values of the diffusion coefficients are listed in Table 2; these values are in good agreement with the data of other authors.

Table 2

Values of the diffusion coefficients obtained for the γ- and ϵ-phase layers

Instrument	γ-phase		ϵ-phase	
	$Q, \frac{cal}{g \cdot atom}$	D_o, cm^2/hr	$Q, \frac{cal}{g \cdot atom}$	D_o, cm^2/hr
RSASh-2	11740 (±8%)	11.0	20680 (±26%)	93
Microscope	13400 (±12%)	9.84	20800 (±25%)	93

In addition to investigation of the concentration curves, we carried out an analysis of the quantitative composition in different parts of the layer of each of the phases by comparison with standards. Thus, in the case of the γ-phase we found a change in the Zn concentration in going from the boundary with copper to the ϵ-phase interface from 66 to 68% (the Cu concentration decreased accordingly from 34 to 32%).

By virtue of the high degree of localization of the analysis, we were able to investigate different diffusion layers (down to 10 μ thick); it was found that the kinetics of phase growth in thin layers differs from that in thick layers. These results may be helpful in the investigation of processes occurring on grain boundaries in multiple component heterophase alloys.

Thus from our experience with the new method it may be concluded that whereas until recently x-ray spectroscopy developed along the line of theoretical investigations connected with studies of the character of interaction between atoms as evinced by the fine structure of the spectra and along the line of practical application of x-ray spectroscopy for total analysis of chemical composition, the new method of analysis in microvolumes opens a whole new field of applications of x-ray spectroscopy in the field of the physics of metals. Many important problems that hitherto could not be solved due to the lack of quantitative methods of investigation of microcomposition can be readily and reliably solved by means of this method. Such problems include analysis of the phase composition of complex alloys, investigation of the degree of homogenization of alloys, investigation of the detailed distribution of alloying additions and impurities in alloys and their redis-

tribution in the processes of aging, deformation and heat treatment, and investigation of diffusion and other intermediate layers, in particular, grain boundaries and the processes occurring thereon. The high local sensitivity of this method of quantitative analysis (down to 10^{-13} g) makes it feasible to utilize it as well for determining small amounts of different elements in minerals, slags and ores.

In conclusion the authors desire to express their thanks to E.M.Savitskii, M.Kh.Shorshov and V.A.Gorokhov for making available the various samples used in the investigation.

Laboratory of Physical Methods of Investigation,
"A.A.Baikov" Institute of Metallurgy
Academy of Sciences of the USSR

X-RAY SPECTROSCOPIC METHOD OF INVESTIGATING THE ELECTRON STATE DISTRIBUTION IN METALS AND ALLOYS

- N.D.Borisov, V.V.Nemoshkalenko & A.M.Fefer

Introduction

Metallurgists are increasingly called upon to "create" new alloys with different, often rigorously specified properties to meet the diversified needs of modern engineering and industry. One of the important factors hampering such development of alloys "to specification" is the lack of a complete, consistent physical theory of metals.

The present band theory even with the use of the method of a self-consistent field is incapable within the framework of the one-electron model to take into account interaction between electrons. Thus one of the urgent problems in the field of the physics of metals is development of a complete many-electron theory. The development of such a theory is predicated on a better knowledge of the distribution in states of electrons in metals and alloys and the variation in this distribution occurring under the influence of different factors.

It is natural therefore that the early theoretical calculations of Mott, Jones & Skinner[1] connected with distribution in energy of electrons called for immediate experimental verification and served as the basis of the development of a new method of metal studies, aptly named "spectroscopy of the solid state" by Skinner[2]. The principles underlying this method are the following. In view of the fact that transformations of a material into different physical and physical-chemical states are accompanied by definite changes in the state of the atoms in it, changes leading to modifications of the electron states of the atoms comprising the material, it may be assumed that all such processes will produce detectable changes in the structure of the x-ray spectroscopic lines. Thus it may be assumed that investigation of the structure, shape, width, intensity and position of the lines in x-ray spectra should allow of establishing a unique correlation between the changes in the spectral characteristics and intra-atomic processes occurring incident to "transition" of the material from one state to another.

Research in this field has consequently been directed towards creating a new method of metal study, a method capable of aiding the solution of practical problems in the "metallurgy of the future".

From the standpoint of modern solid state theory the structure of the electronic energy spectrum is the key to understanding the basic physical and physical-chemical properties of solids.

Modern solid state spectroscopy is concerned with investigation of the character of interatomic bonds linking the constituent particles of solids, the density of electron states, the filling by electrons of the conduction band in semiconductors with increasing temperature, the energy distribution of electrons in the conduction band of metals and alloys, the influence of temperature on this distribution and a number of other factors specific to metals and alloys, factors associated with the variation of the energy state of their atoms (polymorphic transformations, phase transitions, decomposition in the solid state, influence of alloying impurities, degree of ordering, transformation into ionic oxide compounds, etc.).

Development of research in this field of solid state spectroscopy abroad was initiated by Skinner and Farino who utilized diffraction-grating x-ray spectrometers that allowed of investigating the spectra in the soft and ultrasoft x-ray regions (50 to 500 A).

Systematic research in the field of spectroscopy of the solid state in the Soviet Union has been carried out over a period of years in Kiev, Moscow, Odessa, Rostov-on-the-Don, Sverdlovsk and Khar'kov. In our laboratory work in the field has been carried on since 1940 on bent crystal spectrographs operating in the central region of the x-ray spectrum. The design and construction of x-ray tubes for recording emission spectra in a wide range of temperatures and the development of large x-ray spectrographs with a high resolution have enabled us to expand our work in the field of solid state spectroscopy, although unfortunately our investigations are still limited to a certain region of the spectrum.

In a report presented at the Fifth All-Union Conference on the Application of X-rays to the Investigation of Materials we outlined the general aims and purposes of the new method, namely,

1) to explain the physical and physical-chemical properties of solids (in particular, of metals and alloys) on the basis of the electron energy spectrum and

2) to establish laws and regularities that would make possible formulation and realization of alloys with desired specific properties.

In our report we examined the various approaches to solutions of the problems involved, evaluated the possibilities connected with investigation of the $K\beta_5$ emission bands of elements of the iron transition group and considered the various physical factors affecting the intensity, width and shape of x-ray emission bands.

The research reported on herein is a direct continuation of our earlier work and had as its purpose investigation of the characteristics changes in the structure of the electron spectrum of chromium and iron in Fe-Cr alloys occurring under the influence of variation in concentration of the alloy components and transition (along the composition axis) of the γ to α solid solution.

1. Samples and Lines Investigated

Specifically, we investigated the following lines: the $K\beta_5$ lines of chromium and iron associated with electron transitions from the conduction band to the K level and the $K\beta_1$ lines (together with the long wavelength $K\beta'$ satellite) associated with electron transitions from the 3p shell to the K level.

These spectral lines were recorded at 1000° for samples of the pure metals and samples Nos.1 through 8 of Fe-Cr alloys containing 4, 5.8, 8, 20, 30, 45, 50 and 75% Cr by weight, respectively.

The $K\beta$ lines of chromium were not obtained for samples Nos.1, 2, 3 and 4 owing to their low intensity in the spectra of these alloys.

The initial metals were electrolytic high purity chromium and iron. The Fe-Cr alloys were prepared by the technological department of the Institute of Metal Physics of the Ukrainian Academy of Sciences in a vacuum h-f induction furnace.

The samples were prepared in the form of special plates which were then mounted on the primary target of the x-ray tube.

2. Equipment and Procedure

The high voltage equipment was a four-Kenotron rectifying assembly based on the Gratz circuit. The power was supplied from a ferroresonance regulator maintaining the primary voltage constant to within 0.5%.

All the x-ray spectra were obtained by means of the x-ray tube designed earlier by us[3] for obtaining the fluorescent spectra of specimens at high temperatures. After appropriate modification of the electrode, this tube was used for obtaining the x-ray spectra by the method of primary excitation. The tube was evacuated by an oil forepump, a mercury diffusion pump and a high-vacuum MM-40 type oil vapor pump connected in series. The vacuum maintained in the system was of the order of $2\text{-}3\cdot10^{-5}$ mm Hg and was measured and monitored by HG-200 and VI-3 ionization pressure gages.

The diffraction apparatus was a nonvacuum x-ray large aperture spectrograph of our design,[4] equipped with a quartz crystal slab bent to a radius of 500 mm. The reflection was from the $(10\bar{1}0)$ plane. In contrast to the procedure employed in our earlier investigations the entire spectrum was obtained using a rocking angle close to 2°. The need for using a rocking crystal in investigating the fine structure of the x-ray bands obtained by the method of primary excitation was dictated by the difficulties of subtracting the background (Brehmsstralung spectrum) which, as is known, has a distinct shape and is superimposed on the x-ray band of interest. In selecting the rocking angle for this crystal we were guided by the rules listed in Ref.5.

The linear aperture of the crystal was controlled by means of a knife edge (slit) and did not exceed 1.5 mm. The reasons making it necessary to use so small an aperture have been discussed in an earlier publication[6].

The exposure conditions for recording the x-ray spectra of the investigated sample were selected by measuring their temperature by means of a Pt--PtRh thermocouple, whose hot junction was welded directly to the samples at the center of the focal spot.

This method of determining the temperature of the emitting part of the sample, however, is not perfect inasmuch as it does not guarantee that the temperature is uniform across the entire focal spot. Only forced heating of the sample with the secondary method of excitation can assure a uniform, stable temperature over the entire focal spot. With a view to minimizing the temperature gradient along the diameter of the focal spot, the latter was not allowed to exceed 1 mm and was controlled by the focusing cup of the cathode. The temperatures of the emitting samples were recorded by means of a "Kent" thermorecorder.

The filament of the tube was a tungsten spiral wound of 0.25 mm diameter wire. The service life of the spiral was about 500-700 hours.

The samples were in the form of metal plates 3 mm thick cut in the form of equilateral trapezoids with beveled edges and were tightly fitted into a mating swallow-tail recess in the copper adapter at the end of the anticathode.

All the spectra were recorded on "Agfa" film, emulsion coated on one side only; the development was carried out in a thermostat at 18° for 15 minutes, using fresh metol-hydroquinone developer of standard concentration. In determining the exposures, account was taken of the necessity of obtaining photographic densities lying on the linear section of the characteristic curve for the given film:

$$t_{exp}=\frac{\lg \frac{S_p}{S_b}}{S_p-S_b}\,t, \qquad (1)$$

The optimal exposure time was calculated according to the equation given by Blokhin[7], where S_p and S_b are, respectively, the photographic densities of the line peak and the background obtained with an exposure time t. Under these conditions the optimal values of the photographic densities of the background and line peak are given by

$$S_b = \frac{\lg|\chi+1|}{\chi}, \quad (2)$$

$$S_p = \frac{\chi+1}{\chi}\lg|\chi+1|, \quad (3)$$

where χ is the ratio of the line intensity to the background intensity.

It can be shown that the highest contrast for weak spectral lines is obtained in exposing the background to a photographic density of 0.2-0.4.

The spectrograms were measured on an MF-4 recording microphotometer using a magnification of 7 X, a 20 to 1 record to film motion ratio and a slit setting of 0.7 x 14 mm; the photometric procedure followed was that described in Ref.8. The rate of scanning of the photographic film was 60 mm per min. Prior to the final photometry of each double spectrogram, we obtained on one photographic plate the complex microphotograms consisting of six microphotograms at different levels across the $K\beta_5$ bands. This photometric procedure brought out the structure of all the lines in height and minimized the possibility of chance photometric errors.

3. Experimental Data

As noted above we recorded the $K\beta_5$ and $K\beta_1,\beta'$ lines of Fe of the pure iron and Fe-Cr alloy samples and the $K\beta_5$ and $K\beta_1,\beta'$ lines of Cr of pure chromium and the Fe-Cr alloys containing 30, 45, 50 and 75% Cr at a temperature of 1000°. The Fe lines were obtained in the fourth order; the Cr lines in the third order of reflection.

The experimental conditions employed in recording the double spectrograms are listed in Table 1.

Table 1

Material	Line designation	Recording conditions		
		kv	ma	ma/hr
Iron	IV FeKβ′, β₁, β₅	35	6,4	60
Alloy № 1 (4% Cr)	IV FeKβ′, β₁, β₅	35	5,0	60
Alloy № 2 (5,8% Cr)	IV FeKβ′, β₁ β₅	35	7,4	60
Alloy № 3 (8% Cr)	IV FeKβ′, β₁ β₅	35	4,6	60
Alloy № 4 (20% Cr)	IV FeKβ′ β₁, β₅	35	4,5	80
Alloy № 5 (30% Cr)	IV FeKβ′, β₁ β₅	35	4,5	90
	III CrKβ′ β₁ β₅			100
Alloy № 6 (45% Cr)	IV FeKβ′, β₁ β₅	35	4,4	115
	III CrKβ′ β₁ β₅			115
Alloy № 7 (50% Cr)	IV FeKβ′, β₁, β₅	35	4,5	120
	III CrKβ′, β₁, β₅			100
Alloy № 8 (75% Cr)	IV FeKβ′, β₁, β₅	35	5,0	150
	III CrKβ′, β₁, β₅			80
Chromium	III CrKβ′, β₁, β₅	35	6,0	50

4. Calculated Data

For calculating the wavelength of the spectral lines we used the formula

$$\lambda_X = \frac{2d_n}{n}\sin\varphi_X = \frac{2d_n}{n}\sin\left[|l_0 \mp \Delta l|\frac{90}{\pi r}\right], \quad (4)$$

where d_n is the lattice constant of the crystal taking into account the order of reflection (n), l is the calculated distance from the center of the crystal

to the standard spectral line, Δl is the measured distance from the sought to the standard line in mm and $90/\pi r$ is a constant.

The value of this constant was determined by means of the formula

$$l_1 - l_2 = \frac{\pi r}{90} |\varphi_1 - \varphi_2|, \tag{5}$$

where $l_1 - l_2$ is the measured distance in mm between the known standard spectral line recorded on the photographic film and φ_1 and φ_2 are the calculated Bragg angles for these lines. On the basis of photometric measurements of the spectrograms the distance Δl between the III Cr $K\alpha_1$ (λ = 2285.00 X) and the IV Fe $K\beta_1$ (λ = 1752.99 X) lines was found to be 16.01 mm.

Substituting this value in Eq.(5) and the corresponding values of the Bragg angles for the two lines we find

$$\frac{90}{\pi r} = \frac{\Delta\varphi}{\Delta l} = 0.11456 \text{ degree/mm}.$$

That this value remains constant throughout the work was checked by periodic determinations at appropriate intervals.

By way of standard lines for determining the positions of the chromium and iron lines we chose the IV Cu $K\alpha_1$ and III Cr $K\alpha_1$ lines, respectively.

For calculating l_0 (the distances of the $K\alpha_1$ lines of chromium and copper from the center of the crystal) we took the tabular values:[9] λ_{Cr} = 2285.00 X and λ_{Cu} = 1537.40 X.

The distances were determined by means of the expression

$$l_0 = \frac{\pi r}{90} \varphi_0, \tag{6}$$

where φ_0 is given by the relationship

$$\sin\varphi_0 = \frac{\lambda_{0n}}{2d_n}. \tag{7}$$

In our case the distances from the center of the crystal to the $K\alpha_1$ lines of chromium and copper were calculated to be 469.864 and 405.026 mm.

Further calculations for the positions of the $K\alpha_1$ and $K\beta_5$ line peaks of chromium and iron were carried out by means of Eq.(4).

The other quantities associated with the determined wavelength were calculated by means of the equations

$$\lg \nu/R = 5{,}9596486 - \lg\lambda, \tag{8}$$

$$\lg V = 7{,}0914911 - \lg\lambda, \tag{9}$$

where λ is in X-units.

Table 2 lists the dispersion data in the region of the $K\beta_5$ lines of Cr and Fe calculated by means of the equations

$$\frac{\Delta\lambda}{\Delta l} = \frac{2d_n}{nR}\cos\varphi \text{ X/mm} \tag{10}$$

$$\frac{\Delta V}{\Delta l} = \frac{\text{ctg}\varphi\,|n\lambda|}{8{,}09\,R\lambda}\,10^8 \text{ ev/mm} \tag{11}$$

$$\frac{\Delta\nu/R}{\Delta l} = \frac{\text{ctg}\varphi\,|n\lambda|}{R\lambda}\,9{,}1245\cdot10^5\,\frac{\nu/R}{\text{mm}} \tag{12}$$

The calculated values of the wavelength of the $K\beta_1$ and $K\beta_5$ lines and the short wavelength edge of chromium and iron based on measurements of the corresponding spectrograms are summarized in Table 3. It will be evident from

Table 2

Line	$\Delta\lambda/\Delta l$, X/mm	$\Delta V/\Delta l$, ev/mm	$\frac{\Delta\nu}{R}/\Delta l$, $\frac{\nu}{R}$/mm
III Cr $K\beta_5$	4,144	11,195	0,826
IV Fe $K\beta_5$	2,430	9,917	0,732

the data in Table 3 that only in the case of the Cr $K\beta_5$ line is there an appreciable displacement of the peak to the side of longer wavelengths with increasing iron concentration in the Fe-Cr alloys. The positions of the peaks of the other lines remained the same in all cases within the limits of the experimental error.

Table 3

Material	Line	Data source	λ X	λ ev	λ ν/R	Short-wave edge
Iron	$FeK\beta_1$	Tabular	1752,99	—	519,84	—
	$FeK\beta_5$		1740,54	—	523,56	1739,83
Iron & alloys Fe-Cr № 1, 2, 3, 4, 5, 6, 7, 8	$FeK\beta_1$	Exper.	1752,99	7042,25	519,84	—
	$FeK\beta_5$		1740,43	7093,06	523,59	1739,97
Chromium	$CrK\beta_1$	Tabular	2080,60	—	437,98	—
	$CrK\beta_5$		2066,53	—	440,97	2065,95
Chrom.&alloys Fe-Cr № 5, 6, 7,8	$CrK\beta_1$	Exper.	2080,48	5933,73	438,01	—
Chromium	$CrK\beta_5$	Exper.	2066,53	5973,77	440,97	2065,92
Alloy № 8	$CrK\beta_5$	"	2066,64	5973,46	440,94	2065,89
Alloy № 7	$CrK\beta_5$	"	2066,69	5973.32	440,93	2065,84
Alloy № 6	$CrK\beta_5$	"	2066,88	5972,77	440,89	2065,88
Alloy № 5	$CrK\beta_5$	"	2067,16	5971,96	440,83	2066,11

5. Photometric Curves

Some of the photometric curves of the $K\beta_5$ lines of chromium and iron obtained from the double spectrograms recorded at 1000° for samples of the pure metals and the Fe-Cr alloys are shown in Figs.1-4.

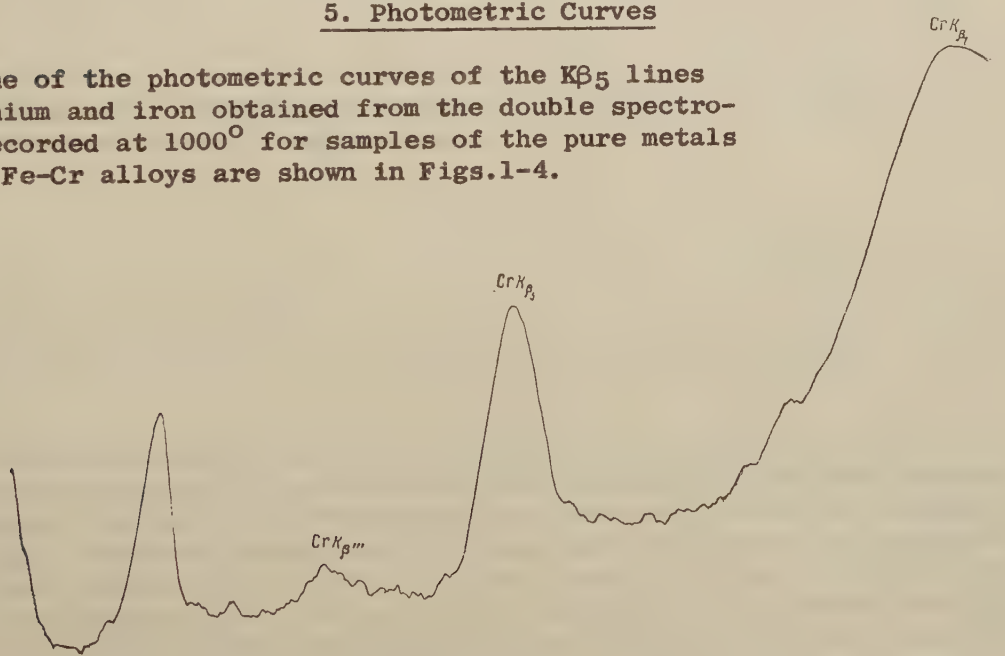

Fig.1. Photometric curve of the Cr $K\beta_5$ line obtained for pure chromium.

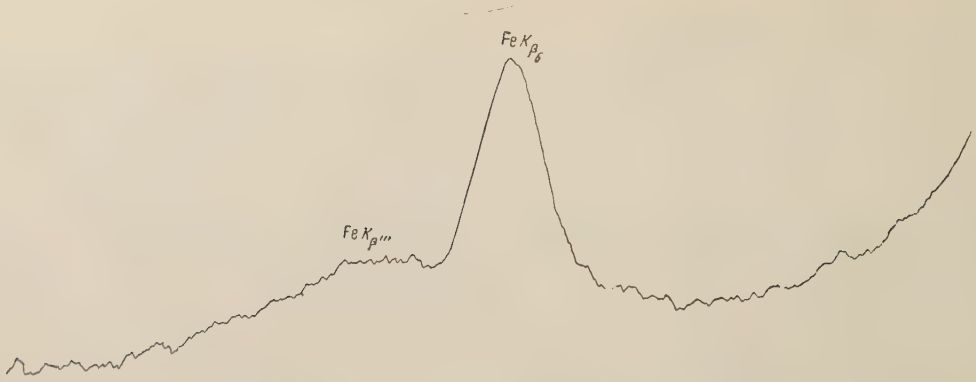

Fig.2. Photometric curve of the Fe $K\beta_5$ line obtained for pure iron.

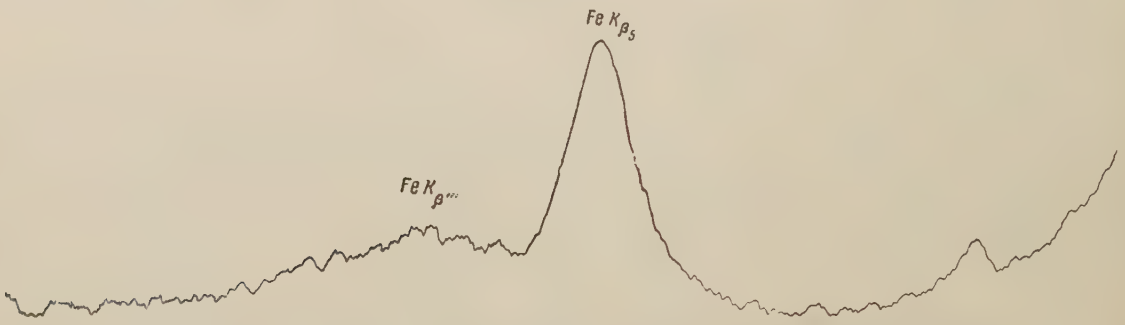

Fig.3. Photometric curve of the Fe $K\beta_5$ line obtained for the No.6 alloy sample (50% Cr).

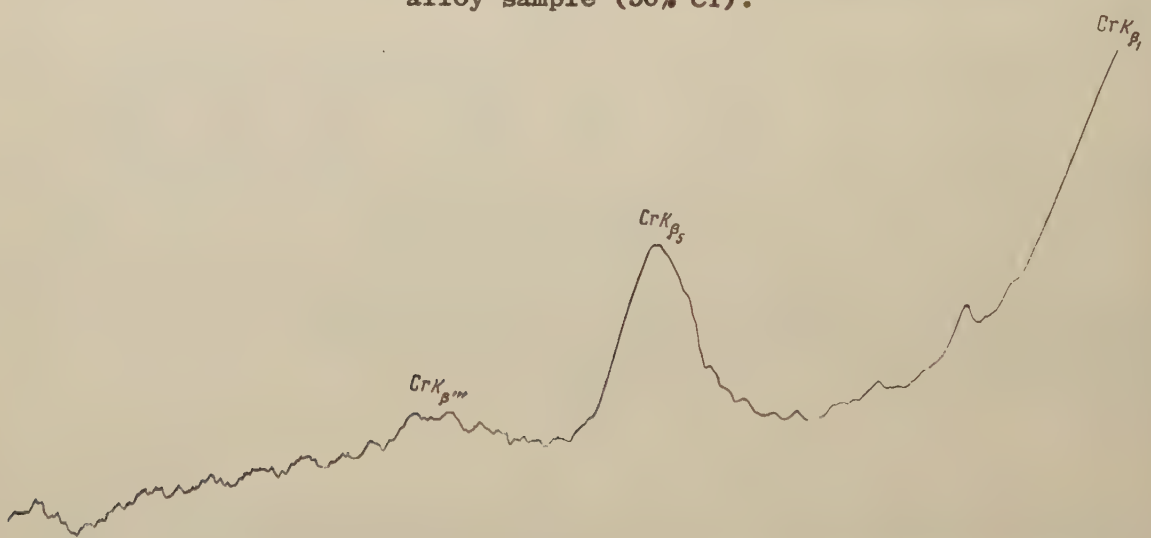

Fig.4. Photometric curve of the Cr $K\beta_5$ line obtained for the No.6 sample (50% Cr).

It will be evident from an examination of the photometric curves that only in the case of Cr is the $K\beta_5$ band free of the $K\beta'''$ satellite and therefore discernible in its pure form. In the case of iron the $K\beta'''$ satellite is already clearly superposed on the short wavelength side of the $K\beta_5$ band and has a simple shape. In other words the microphotograms show that in investigating the shape and width of the Fe $K\beta_5$ line it is essential to resolve it into components.

6. Results of Processing the Photometric Curves

The microphotograms were processed as follows. For the purpose of allowing for the intensity of the short wavelength branch of the $K\beta_{1,3}'$ lines superposed on the intensity of the $K\beta_5$ band, a straight line was drawn tangent to the two branches of the band. Then a straight line was drawn through the point of minimum background density parallel to the "dark" (zero density) datum line in the microphotogram. This line was taken to be the fog level. The entire photogram was then subdivided into equal strips by vertical lines every 1.5 mm, which with the 20 to 1 motion ration used equals 0.075 mm on the film. Then for each point of intersection of the verticals with the contour of the band we calculated the photographic density S_c' with the background subtracted by means of the formula

$$S_c' = S_c - S_b = \log i_b/i_c \qquad (13)$$

where i_b and i_c are the distances from the dark datum line to the corresponding points of the background and band contour as measured on the microphotogram. For finding the values of S_c', we determined the values of i_c', i.e., the distances from the dark datum line to the corresponding points on the contour of the $K\beta_5$ band referred to the total fog by means of the formula

$$\log i_c' = \log i_f - S_c', \qquad (14)$$

where i_f is the distance from the dark datum line to the fog level line. On the basis of the values of i_c' so determined we plotted the contour of the $K\beta_5$ band (less background) referred to the fog level.

Resolution of the complex contour of the Fe $K\beta_5$ band into components was carried out by the method of successive subtraction at each point of the $K\beta_5$ band contour of the corresponding photographic densities of the $K\beta'''$ satellite. In view of the complete symmetry of the resolved Cr $K\beta'''$ satellite it was assumed that the Fe $K\beta'''$ satellite is also symmetric.

The width of the $K\beta_5$ band was determined as the sum of two terms: $T = T_1 + T_2$, where T_1 is the width of the short wavelength branch measured at half the maximum intensity (i.e., from the point of inflection of the short wavelength branch corresponding to the Fermi level to the maximum of the band) and T_2 is given by Vainshtein's formula[10]

$$T_2 = \frac{\gamma_{2n}}{1 - \frac{1}{n^{2/3}}}, \qquad (15)$$

where γ_{2n} is the width of the long wavelength branch of the $K\beta_5$ band measured at different heights with

$$n = \frac{I_{max}}{I_n} = \frac{S_{max}}{S_n}.$$

The resultant value for the width of the $K\beta_5$ band was corrected for broadening of the band due to the finite width of the K level and the oblique incidence of the x-rays on the film. This corrected value of the $K\beta_5$ band width was taken as $T_{max} = |E_{max} - E_0|$, the kinetic energy of the electrons in the conduction band.

The calculations for one of the microphotograms are listed in Table 4, from which it will be seen that Eq.(15) satisfactorily describes the shape of the long wavelength branch of the $K\beta_5$ band.

Table 4

n	$1-\frac{1}{n^{3/2}}$	S_n	$\lg i_n$	i_n	$\gamma_2 \times 20$, мм	γ_2, мм	γ_2, ev	T_2, ev
1,00	0,00000	0,16080	1,88138	76,1	0,000	0,000	0,000	—
1,50	0,23686	0,10720	1,93498	86,1	5,5	0,275	3,076	12,986
2,00	0,37004	0,08040	1,96178	91,6	7,0	0,350	3,915	10,579
2,50	0,45712	0,06432	1,97786	95,0	8,1	0,405	4,530	9,909
3,00	0,51926	0,05360	1,98858	97,4	9,2	0,460	5,145	9,908
3,50	0,56620	0,04594	1,99624	99,2	9,9	0,495	5,537	9,779
4,00	0,60315	0,04020	2,00198	100,5	10,6	0,530	5,928	9,828
4,50	0,63312	0,03573	2,00645	101,5	11,1	0,555	6,208	9,805
5,00	0,65801	0,03216	2,01002	102,3	11,6	0,580	6,487	9,858
7,00	0,72672	0,02297	2,01921	104,5	12,6	0,645	7,214	9,926

Notes: $T_{2cp} = 9.859$ ev for $n = 2.5, 3.0, 3.5, 4.0, 4.5, 5.0, 7.0$;
$T_1 = 2.908$ ev for $\gamma_1 \times 20 = 5.2$.

The calculated values for T_{max} the kinetic energy of the electrons in the conduction band and n the number of "outer" electrons per atom in the conduction are summarized in Table 5.

Table 5

Material	Composition, %		T_{max}, ev		V_a, Å³	n	
	Fe	Cr	Fe K_{β_5}	Cr K_{β_5}		Fe	Cr
Feγ	100	0	10,70	—	12,250	1,94	—
Alloy № 1	96	4	9,93	—	12,241	1,71	—
Alloy № 2	94,2	5,8	9,85	—	12,239	1,73	—
Alloy № 3	92	8	10,59	—	12,236	1,91	—
Alloy № 4	80	20	10,19	—	11,932	1,76	—
Alloy № 5	70	30	9,72	11,04	11,904	1,63	1,98
Alloy № 6	55	45	9,17	11,08	11,857	1,49	1,98
Alloy № 7	50	50	9,08	10,67	11,857	1,47	1,87
Alloy № 8	25	75	10,43	9,56	—	—	—
Cr	0	100	—	8,49	12,470	—	1,40

The latter values were calculated by the means of the Blokhin[7] formula

$$n = 0.00453\, V_a T_{max}^{3/2}, \qquad (16)$$

where V_a is the atomic volume in Å³.

The tabular values of the lattice constants of chromium, γ-iron and the Fe-Cr alloys were recalculated for the 1000° temperature of the measurements using the appropriate linear expansion coefficient obtained from dilatometric curves.

The Cr concentration dependences of T_{max} and n are plotted in Figs.5 & 6.

It will be seen from the plots that the width of the $K\beta_5$ band attains a maximum value for chromium and a minimal value for iron in the region of middle (approximately equal) concentrations of the alloy components. The width of the $K\beta_5$ band and the number n remain different for chromium and for iron at all concentrations of the Fe-Cr alloy components (except for two, apparently). Transition along the composition axis from the γ to the α solid solution is characterized by a sharp break in the T_{max} vs component concentration curve for iron.

The demonstrated difference between the energy states of the chromium and iron atoms in the investigated range of concentrations of Fe-Cr alloys

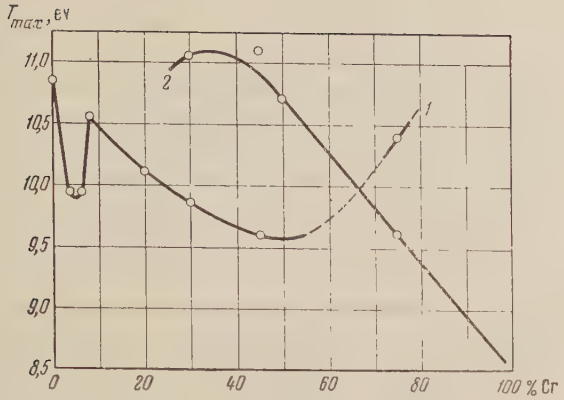

Fig.5. Variation of T_{max} with the Cr concentration for 1) Fe and 2) Cr.

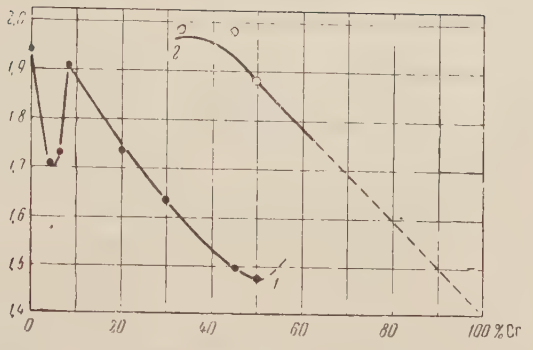

Fig.6. Variation of n with the Cr concentration in the alloy for 1) Fe and 2) Cr.

would appear to open a new approach to investigation of metals and alloys. The results of the present work point up the importance of detailed investigation of the fine structure of the electron energy spectrum of metals and alloys and the character of the changes produced in it under the influence of different factors affecting the energy state of the constituent atoms.

Conclusions

1. We obtained the Kβ group emission lines in the x-ray spectra of pure chromium and iron and the Fe-Cr alloys containing 4, 5.8, 8, 20, 30, 45, 50 and 75% chromium by means of a bent crystal spectrograph and a special tube designed for recording the x-ray spectra of samples at elevated temperatures. The spectra were obtained by the method of primary excitation at a temperature of 1000°, employing the rocking crystal technique.

2. The transition of chromium and iron into Fe-Cr alloys in the investigated range of component concentrations and transition along the composition axis from the γ to the α solid solution does not affect the position of the peaks of the Fe $K\beta_1$, Fe $K\beta_5$ and Cr $K\beta_1$ lines.

3. With increasing iron concentration, however, the position of the Cr $K\beta_5$ band peak is displaced to the side of longer wavelengths. The position of the short wavelength edge of the Cr $K\beta_5$ band, on the other hand, is displaced to the side of shorter wavelengths with increasing Fe concentration.

4. The width of the conduction band and the number of "outer" electrons per atom in the conduction band remain different for chromium and for iron at all concentrations of the alloy components (except, apparently, two). These quantities attain a minimal value for iron and a maximal value for chromium in the region of approximately equal concentrations of the two components in Fe-Cr alloys.

5. The character of the determined variations in the width of the $K\beta_5$ bands of chromium and iron and of the position of the short wavelength edge of the Cr $K\beta_5$ band may be regarded as evidence of complicated variation of the electron structure of the Cr and Fe atoms in Fe-Cr alloys with changes in the relative concentration of the alloy components.

6. Transition along the composition axis from the γ to the α solution for iron is characterized by a sharp break in the curve characterizing the variation of T_{max}, the kinetic energy of the electrons in the conduction band, with the relative concentration of the components in the investigated Fe-Cr alloys.

7. The demonstrated differences in the energy states of the Cr and Fe atoms in the investigated range of component concentrations clearly indicate the need for further detailed investigation of the fine structure of x-ray bands particularly with a view to establishing the influence of various individual factors on this structure. We believe that the results of our work offer a new approach to establishing correlation between the physical properties of metals and alloys and the structure of their energy spectra.

Institute of Metal Physics,
Academy of Sciences of the Ukrainian SSR

References

1. N.F.Mott, H.Jones & H.W.B.Skinner, Phys.Rev., 45, 370 (1934).
2. H.W.B.Skinner, Phil.Trans.Roy.Soc. A, 239, 801, 95 (1940).
3. N.D.Borisov & Ia.M.Fogel', Zhur.tekh.fiz., 16, 1471 (1946).
4. N.D.Borisov & Ia.M.Fogel', Zhur.tekh.fiz., 7, 164 (1937).
5. N.D.Borisov, Zhur.eksp.i teor.fiz., 6, 433 (1936).
6. N.D.Borisov, Trudy Instituta chernoi metallurgii (Transactions of the Institute of Ferrous Metallurgy, Academy of Sciences of the Ukrainian SSR, Vol.6 (1953).
7. N.M.A.Blokhin, Fizika rentgenovykh luchei (Physics of X-rays), M., 1953.
8. N.D.Borisov, in "Voprosy fiziki metallov i metallovedeniia" (Collected articles on the Physics of Metals and Metallography), 8, 1957.
9. E.E.Vainshtein & M.M.Kakhana, Spravochnye tablitsy rentgenovskoi spektroskopii (Reference tables for x-ray spectroscopy), M., 1953.
10. E.E.Vainshtein, Rentgenovskie spektry atomov v molekulakh khimicheskikh soedinenii i v splavakh (X-ray spectra of atoms in molecules of chemical compounds and in alloys), M.-L., 1950.

THE $L\beta_6$ AND $L\gamma_5$ LINES IN THE SPECTRA OF Cu AND Zn

- I.A.Rumiantsev & M.I.Korsunskii

In the present report we give the first results of our investigation of the L series lines in the x-ray spectra of Cu and Zn.

In free copper and zinc atoms the 3d shell is filled and the 3s electrons are valence electrons. In the solid state of these elements, however, transitions to the 4s level have not been detected. In the K series, transitions to this level are ruled out, while in the L series, they have not yet been observed.

Inasmuch as the K series of Cu includes a $K\beta_2$ line corresponding to the $K \rightarrow N_{II,III}$ transition, it is not clear whether there are electrons at the N_I level in Cu in the solid state.

The purpose of our research was to determine whether $L_{II,III} \rightarrow N_I$ transitions exist in Cu and Zn in the solid state. In this connection it may be recalled that in the case of germanium, as is evident from the work of Borovikova & Korsunskii[1], these transitions do exist and the lines corresponding to them are very intense.

The $L\beta_6$ line is associated with the transition from the L_{III} to the N_I level, while the $L\gamma_5$ line is associated with the $L_{II} \rightarrow N_I$ transition.

The $L\beta_6$ and $L\gamma_5$ lines in the spectra of germanium are located rather close to the $L\alpha_{1,2}$ and $L\beta_1$ lines, respectively. Hence we reasoned that these lines in the spectra of Cu and Zn will also be close to the $L\alpha_{1,2}$ and $L\beta_1$ lines. Consequently, we investigated the L spectra of Cu and Zn in the regions close to the $L\alpha_{1,2}$ and $L\beta_1$ lines of these elements.

The Cu and Zn L series spectra have been studied by a number of investigators[2-6], but the $L\beta_6$ and $L\gamma_5$ lines were not observed. Different investigators report different line shapes for the $L\alpha_{1,2}$ and $L\beta_1$ lines of Cu and Zn. The disagreement as regards the general appearance of the spectra may be due to the fact that the different investigators used different excitation conditions, i.e., the divergences may be due to the formation of compounds - in particular, oxides - on the surface of the specimens.

In view of this we decided first to investigate the variation in appearance of the Cu and Zn spectra with the excitation conditions. The diverse excitation conditions employed differed primarily as regards degree of heating of the anode and duration of its operation.

The spectra were recorded photographically on a bent crystal vacuum spectrograph (see Ref.1). In investigating the spectra of Cu the anode was made of electrolytic copper. The zinc was used in the form of plates 2 mm thick mounted on the copper anode and also in the form of a thin layer sputtered on the anode surface.

The tube voltages used were 5 to 7 kv; the current values 10 to 15 ma; the exposure times 2 to 6 hours. The temperature of the anode was monitored by means of a copper-constantan thermocouple. A vacuum of $1.2\text{-}1.5 \cdot 10^{-5}$ mm Hg was maintained. The spectrograms were measured on a recording MF-4 microphotometer.

Our measurements showed that the shape of the $L\alpha_{1,2}$ and $L\beta_1$ lines of Cu depend on the excitation conditions. Under some conditions the $L\alpha_{1,2}$ and $L\beta_1$ lines are double; the "second" line is characterized by a strong dependence of its intensity on the excitation conditions.

The photometric curve of the L series spectrum of Cu obtained at a rather low temperature of the anode (about 100°) is shown in Fig.1. It will be evident that there is noticeable doubling of the $L\alpha_{1,2}$ line. We believe that the second (the shorter wavelength) line is the $L\beta_6$ diagram

Fig.1

Fig.2

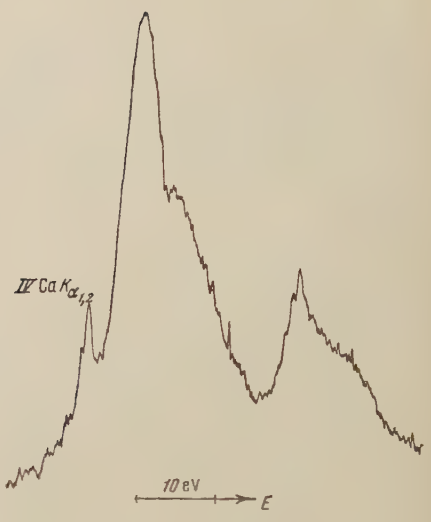

Fig.3

Fig.1. $L\alpha_{1,2}$ and $L\beta_6$ lines of Cu.

Fig.2. $L\alpha_{1,2}$ and $L\beta_6$ lines of Cu; sample partially oxidized. The high intensity of the IV Ca $K\alpha_{1,2}$ line is due to the large amount of calcium salt applied to the anode.

Fig.3. $L\beta_{1,2}$, $L\beta_6$, $L\beta_1$ and $L\gamma_5$ lines of Cu; surface of sample appreciably oxidized.

Fig.4

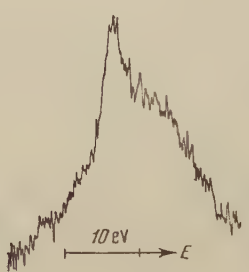

Fig.5

Fig.4. $L\alpha_{1,2}$ and $L\beta_6$ lines of Zn.

Fig.5. $L\alpha_{1,2}$ and $L\beta_6$ line of Zn; sample partially oxidized.

line, i.e., the line due to the $L_{III} \rightarrow N_I$ transition. Similarly the $L\beta_1$ line in the spectrum is also split; we identify the short wavelength component of this line as $L\gamma_5$.

The decrease in intensity of the $L\beta_6$ and $L\gamma_5$ lines (relative to the intensity of the $L\alpha_{1,2}$ and $L\beta_1$ lines, respectively) with increasing oxidation of the surface of the sample (Figs.2 & 3) is explained by transfer of the 4s valence electrons to the oxygen.

The $M_{IV,V}—N_I$ energy interval as evaluated from the relative positions of the $L\alpha_{1,2}$ and $L\beta_6$ lines in the spectrum is about 4.5 ev which is consistent with the expected value.

Fully analogous results were obtained for zinc (Figs.4 & 5). In this case the brightest $L\beta_6$ and $L\gamma_5$ lines were obtained under conditions of best cooling of the Zn surface (the layer of zinc sputtered on the face of the copper anode). In the case of zinc the $M_{IV,V}—N_I$ energy interval as evaluated from the line positions is about 5.5 ev.

Conclusions

1. The shape of the L spectra of Cu and Zn is strongly dependent on the excitation conditions. In view of this, all the data in the literature regarding the L series x-ray lines of the middle atomic number elements (i.e., from Fe^{26} to Br^{35}) require verification.

2. The $L\beta_6$ and $L\gamma_5$ lines, corresponding to transitions from the N_I level to the L_{III} and L_{II} levels, respectively, were observed and identified in the emission spectra of copper and zinc.

Kharkov Polytechnic Institute

References

1. G.P.Borovikova & M.I.Korsunskii, Present issue of the Bulletin, p.1426.
2. J.Farineau, Nature, 140, 508 (1937).
3. J.Farineau, Ann.de Phys., (11), 10, 20 (1938).
4. E.Gwinner, ZS. f. Phys., 108, 523 (1938).
5. Y.Cauchois, Acta crystallogr., 5, 348 (1952).
6. Y.Cauchois, Phil. mag., 44, 173 (1953).

L SERIES X-RAY SPECTRUM OF GERMANIUM

- G.P.Borovikova & M.I.Korsunskii

It is a familiar fact that transformations of a material to different physical and chemical states are accompanied by changes in the state of its atoms. Changes in the energy state of the electrons in the atoms must be evinced in the structure of the corresponding x-ray spectral lines. Of greatest interest in spectroscopy of the solid state are the spectral lines associated with transitions of valence electrons whose energy states are subject to the greatest alterations incident to transition of the atoms of the material from one state to another. In view of the fact that the energy dispersion increases with increasing wavelength, the lines most suitable for investigation in the case of elements in the intermediate range of atomic numbers (Mn^{25} to Mo^{42}) are the lines of the L series.

The wavelengths of the L series lines of these elements lie in the 5 to 18 Å region. This region can be investigated by means of mica crystal spectrometers, characterized by high efficiency and good resolution.

It must be noted that investigation of the L series lines of the elements from Mn^{25} to Mo^{42} is highly important. The L series contains three sublevels (the 2s and 2p states); hence investigation of the electron transitions giving rise to the L series can yield detailed information on the level structure. In particular, there may be detected the $L_{II} \rightarrow N_I$, $L_{III} \rightarrow N_I$ and $L_I \rightarrow N_{II,III}$ transitions involving valence electrons (in the group of elements from Mn^{25} through Ge^{32} transitions of valence electrons to the K level are forbidden). Unfortunately, the L series spectra of the group of elements extending from Mn^{25} to Br^{45} have not been fully investigated.

It is evident from the L series wavelength table for the elements from yttrium to copper given in Blokhin's book[1] that the $L\beta_6$ and $L\gamma_5$ lines corresponding to $L_{III} \rightarrow N_I$ and $L_{II} \rightarrow N_I$ transitions do not appear in the spectra of copper, zinc, gallium, arsenic, germanium and selenium. The $L\gamma_{2,3}$ line corresponding to the $L_I \rightarrow N_{II,III}$ transition is also absent from the spectra of these elements. Investigators have failed to observe the $L\beta_3$ and $L\beta_4$ lines in the spectra of gallium, germanium and selenium, which appears surprising since these lines are present in the spectra of the neighboring elements. Even more surprising is the absence of electron transitions from the N_I to the $L_{II,III}$ levels ($L\gamma_5$ and $L\beta_6$ lines).

The purpose of the present work was investigation of the L series lines of the x-ray spectrum of germanium. Germanium was chosen inasmuch as in the free Ge atom the N_I level must be completely filled.

1. Apparatus and Procedure

The x-ray L series spectrum of germanium was obtained by means of a Krasnikov type[2] tube for fluorescence analysis. We cannot, however, assert that the spectrum was a purely fluorescent one inasmuch as a certain if rather small number of electrons still impinged on the secondary anode. The direct current amounted to 1/20 of the total current through the tube and equaled 0.5 ma. So low a current with a wide focus and intense cooling with circulating water could not appreciably heat the secondary cathode on which the sample was mounted. The temperature of the material was measured by means of a thermocouple whose hot junction was in direct contact with the anode. In our experiments the temperature of the germanium did not exceed 50-60°.

The primary anode of the tube was covered with aluminum plate. The principal exciting x-radiation was that of the Al $K\alpha_1$ and $K\alpha_2$ lines whose

wavelengths are 8321.37 and 8323.82 X, respectively. Owing to the location of the secondary anode near the crystal inside the focal circle, the entire focal spot area participated in formation of the spectrum. The tube was operated at 3.5-5 kv and 10 ma. The radiation was dispersed and analyzed by means of a high-vacuum bent mica crystal spectrograph. The dimensions of the crystal were 10 x 40 mm; the radius of curvature was 990 mm. A vacuum of $5\text{-}6 \cdot 10^{-6}$ mm Hg was maintained in the common system of the spectrograph and tube. The spectra were photographed on Agfa Isopan film. The film was shielded from stray radiation by 2 μ thick aluminum foil. The photographed spectra were scanned by means of a recording MF-4 microphotometer.

2. Experimental Results

A. The $L\beta_3$ and $L\beta_4$ lines in the Ge spectrum.

The wavelength of the possible $L\beta_3$ line of Ge was found by plotting λ vs Z; interpolation yielded a value of 9570 X.

Accordingly, in photographing the x-ray spectrum with a view to detecting the $L\beta_3$ and $L\beta_4$ lines, the spectrograph was focused for this wavelength. In all the photographs in this region of the spectrum, obtained under different excitation conditions, (voltage from 3.5 to 5 kv, current 10 to 16 ma, exposure time 9-12 hours) there appeared two lines in close proximity to each other (Fig.1). The wavelengths of the $L\beta_3$ and $L\beta_4$ lines as evaluated from the photometric curves proved to be 9561 and 9620 X. The linear dispersion in this region of diffraction angles was 35.4 X/mm. The reference lines were the $K\alpha_1$ and $K\beta_1$ lines of calcium in the third order. The calcium was used in the form of the compound $CaCO_3$. In calculating the wavelength an appropriate correction was made for deviation from the Bragg law. The temperature correction was less than 0.1 X and hence was neglected. The error in determining the wavelength was estimated to be ~2 X. Comparison of the determined wavelength values with the tabular wavelength values for all elements (in all possible orders) showed that the detected lines do belong to germanium. This was further substantiated by the fact that the investigated single-crystal germanium samples were of a high degree of purity.

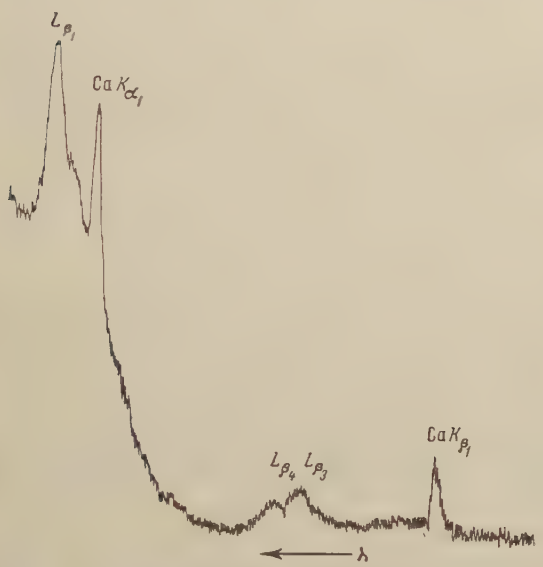

Fig.1. Investigated region of the L spectrum of germanium.

It will be evident from the photometric curve of Fig.1 that the shorter wavelength line is more intense than the longer wavelength one. It is known from the data in the literature that the shorter wavelength $L\beta_3$ line ($L_I \rightarrow M_{III}$) is the more intense line of the $L\beta_3$-$L\beta_4$ doublet; its intensity is approximately 1.5 times greater than the intensity of the longer wavelength $L\beta_4$ line, corresponding to the $L_I \rightarrow M_{II}$ transition. Inasmuch as the wavelength of the shorter wavelength line was the closer one to the wavelength obtained for $L\beta_3$ by interpolation, we took this more intense line at 9561 X to be the $L\beta_3$ line of germanium and assumed the less intense line at 9620 X to be the $L\beta_4$ line.

It should be noted that with this identification of the observed lines, the doublet separation in germanium proved to be somewhat greater than might be expected. In elements heavier than germanium, beginning with Rb^{37}, the wavelength difference between the lines of the $L\beta_3$-$L\beta_4$ doublet is 35 X. Our experimental value is 9620 - 9561 = 59 X. It must be borne in mind, however, that germanium is not far from the group of elements in which the M shell becomes filled; consequently, in this group the separation between the M_{II} and M_{III} levels may actually be somewhat greater than the usual value characteristic of heavier elements.

It is difficult to establish the ratio of intensities of the $L\beta_1$ line to the $L\beta_3$-$L\beta_4$ doublet inasmuch as there is an appreciable difference in the densities of the respective lines in the spectrograms. At a density of the $L\beta_3$-$L\beta_4$ doublet sufficient to allow of photometry, the $L\beta_1$ line is overexposed. Hence we evaluated the ratio of these intensities of the $L\beta_3$-$L\beta_4$ and $L\beta_1$ lines only by recalculating the intensity of the $L\beta_1$ line on the basis of the exposure times for a photograph in which all three lines were discernible and a photograph in which the density of the $L\beta_1$ line was equal to 0.44. According to this evaluation the intensity ratio of the $L\beta_3$ to $L\beta_1$ lines is 0.13. As noted above, the intensity of the $L\beta_4$ line is about 1.5 times less. It will be clear therefore that the relative intensities of the doublet lines are very low. In view of this low intensity of the lines and the appreciable background present in the case of primary excitation, it is not surprising that previous investigators did not succeed in detecting these lines.

B. The $L\beta_6$ and $L\gamma_5$ lines in the Ge spectrum

The reported absence of the $L\beta_6$ and $L\gamma_5$ lines from the spectrum of germanium makes it questionable whether there are any electrons at the N_I level in the solid state of germanium. Inexplicable, too, is the absence of the $L\gamma_{2,3}$ line, inasmuch as the $K\beta_2$ line ($K \rightarrow N_{II,III}$) has been observed in the spectrum of germanium and its wavelength measured with relatively high accuracy. The existence of the $K \rightarrow N_{II,III}$ transition proves that there are electrons at the $N_{II,III}$ levels of germanium, making the reasons for the presumed absence of electrons from the N_I level even more obscure.

In the present investigation we searched the L series for the $L\beta_6$, $L\gamma_5$ and $L\gamma_{2,3}$ lines with a view to determining whether the $L_{III} \rightarrow N_I$, $L_{II} \rightarrow N_I$ and $L_I \rightarrow N_{II,III}$ transitions occur in solid germanium. Even visual examination of our photographs of the $L\alpha_{1,2}$ and $L\beta_1$ regions of the spectrum showed that they differed radically from the spectral photographs given in the literature, in particular from the photographs of Gwinner[3] who investigated the dependence of the shape of the $L\alpha_{1,2}$ and $L\beta_1$ lines and their satellites on the character of the bonds. Gwinner's studies were carried out by means of a spectrograph with a plane mica crystal and an ionic tube with hydrogen cooling and a sharp focus. The linear dispersion of his instrument was 55.2 X/mm. He investigated metallic germanium and GeO_2.

Gwinner established that for metallic germanium and GeO_2 the $L\alpha_{1,2}$ and $L\beta_1$ lines are single symmetric lines with satellites on the short wavelength side. The intensity of the satellites with reference to the main lines decreases in going from metallic germanium to GeO_2. In addition, he noted that the satellites in pure germanium are sharp, while the satellites in GeO_2 are diffused; moreover the α' and α'' satellites in GeO_2 are not separated, i.e., appear as one satellite, whose distance from the main line agrees with the mean distance for α' and α'' for pure germanium.

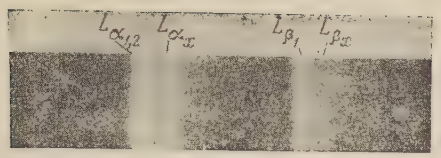

Fig.2. Enlarged photograph of the $L\alpha_{1,2}$ and $L\beta_1$ lines in the spectrum of germanium.

The $L\alpha_{1,2}$ and $L\beta_1$ lines in the spectrum of pure single-crystal germanium obtained by us exhibit a distinct doublet character (Fig.2). The intensities of the satellites of the $L\alpha_{1,2}$ and $L\beta_1$ lines (for the purpose of the present discussion we designate them as $L\alpha_x$ and $L\beta_x$, respectively) are comparable with the intensities of the main lines (Fig.3). There is no description in the literature of such sharp and intense satellites of the $L\alpha_{1,2}$ and $L\beta$ lines in metallic germanium.

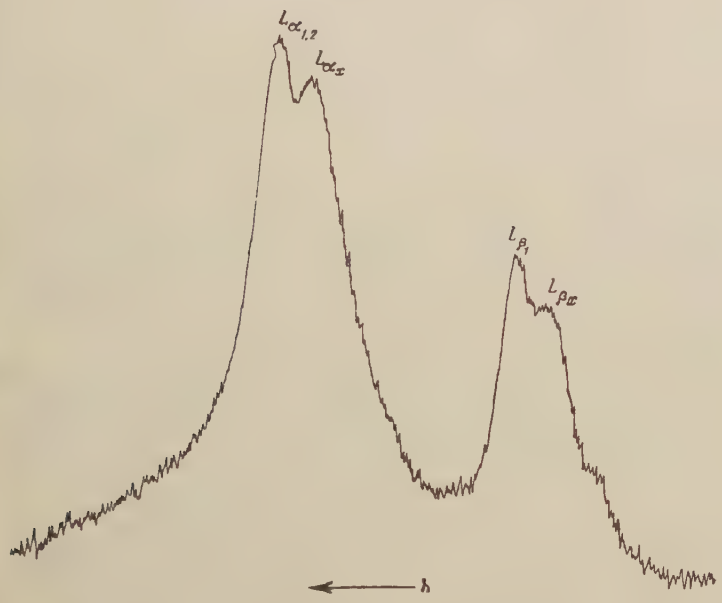

Fig.3. Photometric curve of the $L\alpha_{1,2}$ and $L\beta_1$ region of the Ge spectrum. Magnification 4X.

Whereas the failure of the earlier investigators to detect the $L\beta_3$ and $L\beta_4$ lines in the spectrum of germanium could be explained by the low intensity of these lines, we felt that the reported absence of such bright lines was difficult to explain and required further investigation. In order to verify the actual existence of the detected $L\alpha_x$ and $L\beta_x$ lines, we photographed the $L\alpha_{1,2}$ and $L\beta_1$ section of the spectrum under different conditions of excitation and using different exposure times. The spectrum was excited at a potential lower than the excitation potential for the K series, but somewhat higher than the minimal excitation potential for the L series: specifically, voltages of 3 to 5 kv, currents of 10 to 16 ma and exposure times from 2 to 4 hours were used. The doublet character of the $L\alpha_{1,2}$ and $L\beta_1$ lines was evident in all the spectrograms. The maximum blackening of the spectral photographs was relatively low. The blackening density for $L\beta_1$ was 0.34, that for $L\alpha_{1,2}$ was 0.51.

An enlarged photograph of the $L\alpha_{1,2}$ and $L\beta_1$ section of the spectrum obtained at a voltage of 3.5 kv, a current of 10 ma and exposure time of 3 hours is reproduced in Fig.2; the corresponding photometric curve is shown in Fig.3. It will be evident from the photometric curve that the double lines are asymmetric and that the assymetry indicates that the satellites are wider than the corresponding main lines.

In view of the relatively high intensity of the $L\alpha_x$ and $L\beta_x$ lines it may be asserted that these lines cannot be satellites but must be diagram lines. Inasmuch as the only possible diagram lines in this region of the spectrum are the $L\beta_6$ and $L\gamma_5$ lines corresponding to the $L_{III} \rightarrow N_I$ and $L_{II} \rightarrow N_I$ transitions, we felt it necessary to check further whether the detected $L\alpha_x$ and $L\beta_x$ linex were not actually $L\beta_6$ and $L\gamma_5$. If the L_{III}--N_I and L_{II}--N_I transitions do occur, these two lines must appear in the germanium spectrum at energy positions characterized by the following relationship:

$$E_{L\beta_6} - E_{L\alpha_{1,2}} = E_{L\gamma_5} - E_{L\beta_1}.$$

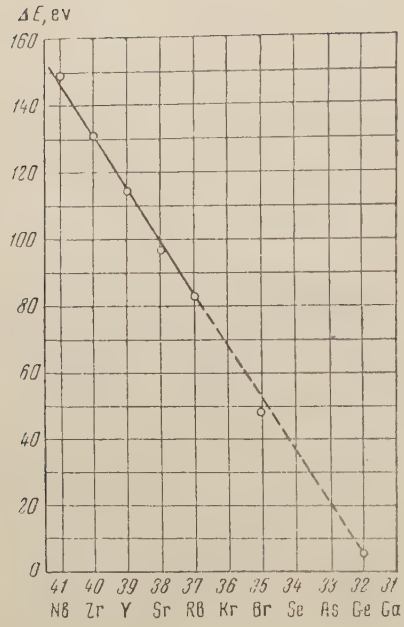

Fig.4. Variation of the energy difference ΔE between the M_{IV} and N_I levels with atomic number.

We found that this relationship does hold for the detected $L\alpha_x$ and $L\beta_x$ lines. To verify this we extrapolated the value of the energy difference ΔE between the N_I and M_{IV} levels for elements from Rb^{37} to Mo^{42}. Unfortunately, there are no data in the literature on the energy of the N_I level in elements closer to germanium. The ΔE vs atomic number plot is shown in Fig.4; it will be seen that the energy difference between the N_I and M_{IV} levels decreases approximately linearly with atomic number for this group of elements.

Thus large values of ΔE should obtain only for elements far from germanium, while for germanium and elements close to it ΔE should be small and, consequently, the $L\beta_1$ and $L\gamma_5$ lines should be close to each other in the energy scale. The experimental value of ΔE found by us for germanium was 4.9 ev. This value for ΔE is in good agreement with that obtained by extrapolation of the ΔE = f(Z) curve.

We found that the ratio of the "satellites" to the main line intensities depended strongly on whether the given specimen had been exposed to electron bombardment. After a sufficiently prolonged exposure of the germanium single crystal at a vacuum of $1 \cdot 10^{-4}$ mm, the intensity of the $L\alpha_x$ and $L\beta_x$ lines fell off appreciably relative to the intensity of the $L\alpha_{1,2}$ and $L\beta_1$ lines.

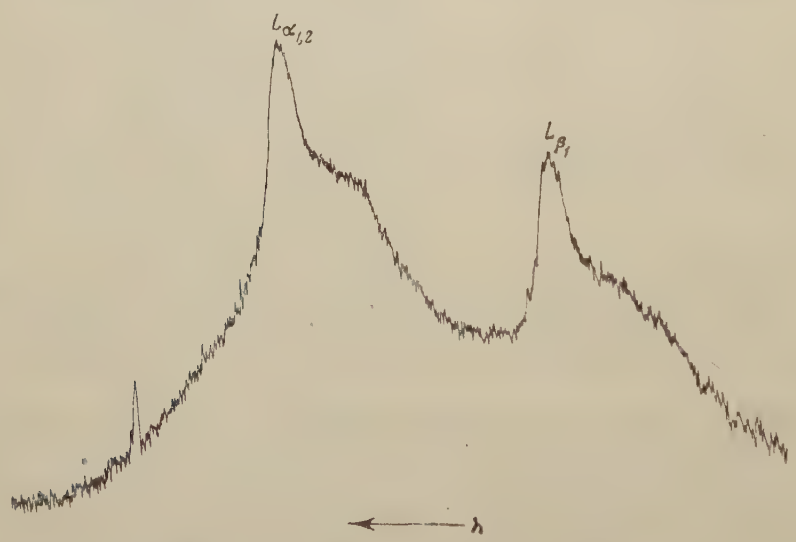

Fig.5. Photometric curve of the $L\alpha_{1,2}$ and $L\beta_1$ section of spectrum of GeO_2. Magnification 4X.

We attributed this decrease in relative intensity of the $L\alpha_x$ and $L\beta_x$ lines to gradual oxidation of the germanium surface. For the purpose of checking this inference and clarifying the influence of the chemical bonds on the detected $L\alpha_x$ and $I\beta_x$ lines, we investigated the x-ray spectrum of GeO_2. Photometric curve for this spectrum is reproduced in Fig.5.

From a comparison of the figures it will be evident that the spectrum of GeO_2 differs markedly from the spectrum for pure single crystal germanium obtained by us (Fig.3) and is very similar to the spectrum obtained by Gwinner[3] for metallic germanium (Fig.6). The intensity of the $L\alpha_x$ and $L\beta_x$ "satellites"

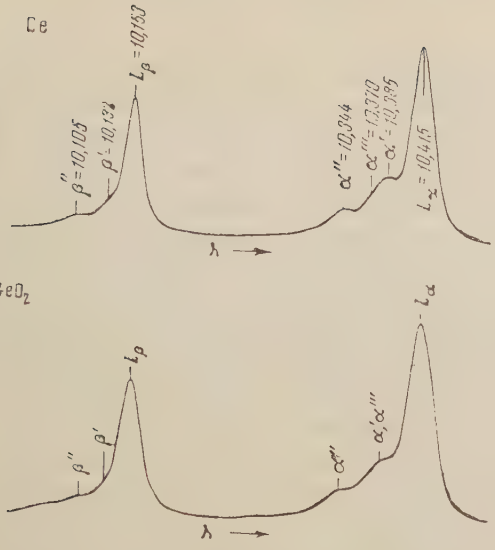

Fig.6. Spectra of metallic germanium and GeO_2 according to Gwinner[3].

is sharply reduced in the spectrum of GeO_2. This decrease in the intensity of the $L\alpha_x$ and $L\beta_x$ lines in the spectrum of GeO_2 can be explained by the absence of electrons on the N_I level of germanium atoms bound in GeO_2. In GeO_2 the germanium is tetravalent and the bonding of the germanium atoms with the oxygen atoms is realized by the transition of four germanium atoms from the N_I and $N_{II,III}$ levels to the oxygen atoms. Consequently, the $L\alpha_x$ and $L\beta_x$ lines should vanish from the spectrum of GeO_2, i.e., only the short wavelength satellites of the $L\alpha_{1,2}$ and $L\beta_1$ lines should appear next to these lines in the spectrum of GeO_2.

Thus the fact that the $L\alpha_x$ and $L\beta_x$ lines are present in the spectrum of pure germanium and absent from the spectrum of GeO_2 gives reason to assume that these lines are associated with the $L_{III} \rightarrow N_I$ and $L_{II} \rightarrow N_I$ transitions, that is, that they are actually the $L\beta_6$ and $L\gamma_5$ lines.

As noted above the $K\beta_2$ line, corresponding to the $K \rightarrow N_{II,III}$ transition has been observed in the spectrum of germanium in the solid state. We observed a line having a wavelength of 9709 ± 5 X in the L spectrum of germanium; as regards position, this corresponds to the $L\gamma_{2,3}$ line associated with the $L_I \rightarrow N_{II,III}$ transition.

The presence in the spectrum of solid germanium of the $K\beta_2$ and $L\gamma_{2,3}$ lines, associated with transitions from the $N_{II,III}$ levels gives reason to assume that there should be L lines connected with transitions from the N_I level in the spectrum of Ge. In view of all the above, it may be asserted that our $L\alpha_x$ line is $L\beta_6$ and our $L\beta_x$ is $L\gamma_5$. We determined the wavelengths of these lines from the photometric curves and obtained 10365 X for $L\beta_6$ and 10103 X for $L\gamma_5$.

The dispersion in the given spectral region was about 32 X/mm. The reference lines were the Mn $K\alpha_1$ and $K\alpha_2$ lines in the fifth order and the Cu $K\alpha_1$ and $K\alpha_2$ in the seventh order. In calculating the wavelength we introduced the requisite correction for the deviation (due to refraction) from the Bragg law. The uncertainty is evaluated as ~2 X.

It should be borne in mind that the radiation of the L series spectrum is emitted from a surface layer some 10^{-5} cm thick. The absence of the $L\beta_6$ and $L\gamma_5$ lines in the spectrum of metallic germanium obtained by Gwinner[3] and other investigators[4] can be explained by the formation of a thin oxide layer on the surface of the germanium during excitation of the spectrum.

From our results it may be inferred that the apparent absence of the $L\beta_6$ and $L\gamma_5$ lines from the spectra of elements from Mn^{25} to Ge^{32} may be due to oxidation of the metallic surface in the process of excitation of the x-ray spectra.

Kharkov Polytechnic Institute

References

1. M.A.Blokhin, Fizika rentgenovskikh luchei (Physics of X-rays)M, 1953.
2. A.I.Krasnikov, Zavod. labor. (The Factory Laboratory), 4-5, 1939.
3. E.Gwinner, ZS.f.Phys., 108, H.7-8 (1938).
4. R.Thoraeus, Phil.Mag. 7, 2, 1007 (1926).

EXTERNAL SCREENING AND THE FINE STRUCTURE OF X-RAY SPECTRA

- S.M.Karal'nik

In a report presented at the Fifth Conference on the Application of X-rays to the Investigation of Materials we pointed out the importance of taking into account variations in the degree of "external screening" (screening of the inner electrons by the outer electrons) incident to changes in the character of the atomic bonds in alloys, where interpretation of observed changes in the x-ray absorption spectra of the alloy components is concerned.

Our argument was based on the assumption that there is a small but finite probability of finding an outer electron in the region of the inner electron shells. By virtue of this the outer electrons can screen the interaction between inner electrons and the atomic nucleus to a certain extent. The degree of such screening varies with the strength of the interatomic bonds due to the participation of the outer electrons. In consequence the effective influence of the nucleus on the inner electrons of the atom changes and this is evinced in the characteristic fine structure of the atomic x-ray spectra.

The present report is an attempt to develop this approach to interpretation of the fine structure of x-ray spectra, an approach that might prove useful for understanding the changes in the x-ray spectra of components not only of metal alloys but of substances having other types of bonds as well.

As the first step we must evaluate the magnitude of this screening for different electrons of the atom. Such an evaluation - true, rather approximate - was carried out in Ref.2.* For describing the electron states in the atom we utilized the radial part of the Bethe[3] hydrogen-like function constructed for different electrons:

$$R_{nl}(r) = \frac{1}{(2l+1)}\sqrt{\frac{(n+l)!}{(n-l-1)!\,2n}}\left(\frac{2Z}{n}\right)^{3/2} e^{-\frac{Zr}{n}}\left(\frac{2Zr}{n}\right)^{l} F\left[-(n-l-1),\, 2l+2,\, \frac{2Zr}{n}\right], \qquad (1)$$

where $F(\alpha,\beta, x)$ is a hypergeometric function. After substitution of dimensional quantities we obtain

$$R_{nl} = \frac{1}{(2l+1)!}\sqrt{\frac{(n+l)!}{(n-l-1)!\,2n}}\left(\frac{2}{na_{nl}}\right)^{3/2} e^{-\frac{r}{na_{nl}}}\left(\frac{2r}{na_{nl}}\right)^{l} F\left[-(n-l-1),\, 2l+2,\, \frac{2r}{na_{nl}}\right], \qquad (2)$$

where $a_{nl} = a_B/Z^*$ is a quantity dependent on the effective value of the nuclear charge for the corresponding atomic electron. It is determined from an expression deduced by analogy with Bethe's equation for the radius of the Bohr orbit of a hydrogen atom:

$$r^2 = \frac{n^2}{2Z^2} a_B^2 [5n^2 + 1 - 3l(l+1)]; \qquad (3)$$

in our case

$$r_{nl}^2 = \frac{n^2}{2} a_{nl}^2 [5n^2 + 1 - 3l(l+1)], \qquad (3')$$

The value of r_{nl} was determined according to Slater[4]:

$$r_{nl} = \frac{n^{*2}}{Z^*} a_B,$$

where n^* and Z^* are the appropriately determined values of the quantum numbers n and l. The r_{nl} values for Z = 26 determined in this manner are:

---

*The work was carried out at the suggestion of M.A.Krivoglaz.

$$r_{4s} = 1.95 \text{ Å},\ r_{3d} = 0.77 \text{ Å},\ r_{3p} = 0.326 \text{ Å},\ r_{3s} = 0.326 \text{ Å},$$

$$r_{2p} = r_{2s} = 0.098 \text{ Å},\ r_{1s} = 0.021 \text{ Å}.$$

Substituting these values in Eq.(3'), we determine a_{nl}.

Further we calculate $\int_0^{r_{ik}} r^2 R_{nl}\, dr$, the probability that the nl electron will be inside a sphere of radius r_{ik}. Finally, we determine the fraction of the charge of the nl electron in the volume of the sphere of radius r_{ik}.

Numerical calculations carried out in this manner led to the values listed in Table 1 for the charges of the various outer electrons in the indicated inner shells of a Z = 26 atom.

Table 1

Outer electrons	Inner electrons				
	1 s	2 s	3 s	2 p	3 p
2 *s*	0,0445	0,631	0,999	0,631	0,999
3 *s*	0,0325	0,0445	0,69	0,0445	0,65
4 *s*	0,001 (0,007)	0,003	0,036	0,003	0,036
2 *p*	0,0055	0,63	0,999	0,63	0,999
3 *p*	0,0002	0,088	0,594	0,088	0,594
3 *d*	$1{,}5 \cdot 10^{-7}$	0,008			

The values listed in the table must be regarded as only indicative, not only because the hydrogen-like function approximation was used in obtaining them, while the radius of the corresponding inner shells was taken according to Slater for isolated atoms (the latter approximation, for example, affected the value of the screening of the 1s shell by the 4s electrons, for which, if we take the atomic radius of iron, ~1.3 A, as the radius of the 4s shell, we obtain the charge value of 0.007), but also due to the fact that for a complex atom, where there are many electrons, the external screening is undoubtedly characterized by qualitatively new, as yet unknown traits. Inasmuch, however, as at present we do not have more accurate data*, we shall continue to use the present values, since they are suitable for qualitative comparisons and allow of drawing certain interesting and helpful deductions.

At this point it is appropriate to emphasize the important circumstance that the magnitude of the external screening proves to be finite even for peripheral electrons having a large principal quantum number. If these are s symmetry electrons, for example, they will screen even the "deepest" 1s shell and the degree of screening will increase with decreasing value of the principal quantum number. The p shell electrons do not produce such screening of the "deepest" shell at large values of their quantum number. Further, 3d type electrons do not screen the 1s shell electrons although they do screen the other inner shells to an appreciable extent. Thus the outer electrons of different shells screen the inner electrons of the atom to different degrees.

In the condensed state of the material the atoms are already interbound. Regardless of the type of the interatomic bond, it leads to a redistribution of the electron density with a resultant change in the degree to which a given outer electron "belongs" to its original atom. Here we can distinguish different cases: "withdrawal" of outer electrons from the atom, i.e., excitation of the outer electrons to higher energy states, "penetration" of the outer

---

*It has been suggested that more accurate results can be obtained by using the Thomas-Fermi method.

electrons to deeper inner shells of their own atom, transfer to some extent of the electrons into the possession of the other component atoms, the partners in the bonds (this does not necessarily mean complete liquidation of the binding of these electrons with their own atom) or entry of the outer electrons into the collective possession of a number of neighbors, etc. In all these cases, together with the changes in the degree or manner in which the outer electrons are involved in the bonds, there occurs a change in the magnitude of the screening by them of the inner electrons, i.e., the electrons which are primarily responsible for the x-ray spectrum. This is why, in our opinion, x-ray spectra are "sensitive" to changes in the interatomic bonding realized by the outer electrons. We must emphasize that participation in the bonding of electrons of different symmetries (for example, s, p or d) will be evinced in different ways in the fine structure of the x-ray spectra. Thus, for example, "withdrawal" of 4s electrons from an atom will be accompanied by a reduction of the screening by them of the 1s electrons (as well as of all the others) which will lead to stronger binding between the latter and the atomic nucleus; this in turn will result in lowering of the K energy level as compared with its position when the 4s electrons are not involved in the interatomic bonds or participate in them to a lesser extent.

On the other hand, the transfer of an electron to a given atom incident to a change in the nature or strength of the interatomic bonds and its "adoption" by the atom in the ns form leads to an increase in the degree of screening of the inner electrons and hence to a decrease of their binding with the nucleus of their atom, which in turn leads to a rise of the energy levels of the atom compared with their position prior to the arrival of the additional electron. A different situation arises when a 3d electron enters into the bonding and is thus removed from the atom. Inasmuch as the 3d electrons screen all the inner electrons, except the 1s electrons, all the energy levels (except the K level) will be "lowered" to a certain extent. The opposite occurs in the case of filling of the 3d shell (for example, in transition elements): all the energy levels (except the K level) are "raised" to a certain degree. The energy separation between the other levels and the K level is reduced in the former case and increased in the latter. The x-ray photons emitted or absorbed as the result of electron transitions between these levels will be less energetic in the former case and more energetic in the second, as compared with the photons emitted when the 3d electrons do not participate in the bonds. In other words, the associated x-ray spectral characteristic will be shifted to the side of longer or shorter wavelengths.

The examined four cases are characterized in Fig.1 in which the energy levels of atoms with atomic numbers Z - 1, Z and Z + 1 are shown schematically; the level positions for the four cases considered are designated by the figures 1, 2, 3 and 4, respectively.

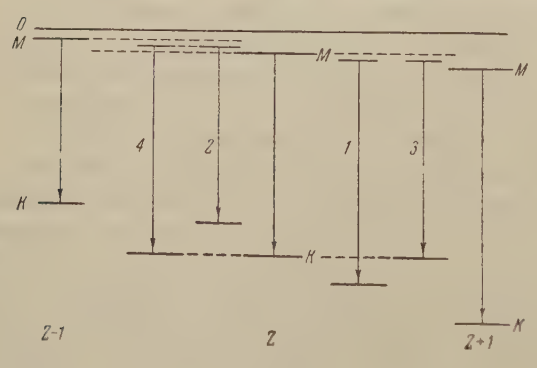

Fig.1.

The effect on the x-ray spectrum of involvement of np electrons in the bonding is analogous to that when ns or 3d electrons participate in the interatomic bonds, the extent of the effect depending on the degree of screening produced by them.

There may also be a cumulative or total effect. For example, we can imagine the formation of interatomic bonds in which the 4s electrons will be excited and become 4p electrons. In this case, in view of the disappearance of the 4s electrons, all the levels in the atom will be lowered, while due to the fact that there appear 4p electrons, all the levels (except 1s) may be raised; thus the total energy difference between the K level and the higher levels will be increased with the result that the x-ray spectral characteristics will be shifted to the side of shorter wavelengths. An analogous result will obtain in the case of transition of 4s electrons to the 3d (defective) shell of their own atom. The energy difference between the levels in this case may become greater than in the case of simple removal or ejection of 4s electrons.

The magnitude of the change in the energy separation (and, consequently, the magnitude of the displacement of the x-ray spectral characteristics in the frequency scale) with a given type of interatomic bonds will be the greater, the stronger the interatomic bonding. Apparently, an increasing degree of involvement of an electron in the bonding and an increase in the number of electrons of a given symmetry in the bonding with a lesser degree of involvement of each one lead to similar results. Thus in many cases an increase in the magnitude of a given change in the x-ray spectral characteristics, i.e., a shift of structure features to the side of shorter or longer wavelengths, may occur in parallel with changes in the strength of the interatomic bonds.

We note in passing that the above may offer an approach to physical interpretation of Kunzl's rule.

For the purpose of illustrating what has been said above let us turn to some experimental data such as those recently compiled by Faessler[5].

Experimental data relative to the displacement of the K edge of an element in its compounds can be used for determining the magnitude of the external screening. Thus if we have a monovalent element, in the case of ionic bonds there will be a maximum withdrawal of the outer (valence) electron from its atom (cation), so that in this case the external screening of the 1s shell by this electron vanishes and the displacement of the K edge resulting from bond formation will be maximal. If the element in the given compound is multivalent, the total displacement of the K edge will be due to the removal of all the valence electrons. The magnitude of the displacement referred to unit valence and divided by the difference in energies of the K level of the given element and the neighboring element in the Mendeleev periodic table* will give us an indication or measure of the magnitude of the external screening per electron.

Let us determine this quantity for a number of elements of the iron transition group. For example, for vanadium the displacement of the K edge relative to its position in the pure element is 7.5 ev in VO, 9.7 ev in V_2O_3 and 15.5 ev in V_2O_5 (see Ref.7); thus the magnitude of the displacement referred to unit valence is 3.75, 3.23 and 3.1 (3.4) ev, respectively, or 3.4 ev on the average. The sought quantity is therefore

$$\left(\frac{e_{outer}}{1s}\right)_{exper} = \frac{3.4 \text{ ev}}{520 \text{ ev}} = 0.0065$$

---

*If there appears an additional electron in the region of the K shell this is equivalent to having an element with atomic number Z - 1 (or if a K electron is removed, it will be equivalent to dealing with an element with the atomic number Z + 1.

(the denominator in the expression above is the difference between the K level energy for vanadium and the neighboring element in the periodic table).

The values obtained in this manner for some elements* for which experimental data on the magnitude of the displacement of the K edge in compounds are available[5] are listed in Table 2.

Table 2

Element	Mean displacement of the K edge per unit valence, ev	Magnitude of the screening of the 1s shell by one outer electron
Vanadium	3.4	0.0065
Chromium	3.2	0.006
Manganese	4.0	0.007
Iron	4.5	0.008
Nickel	5.2	0.008
Sodium	4	0.018

We see that for all the elements of the iron group we obtain for the screening of the inner electrons by an outer electron a value of the order of 0.007. It is interesting to note that theoretical calculations for an atom with Z = 26 yielded a value of the same order of magnitude (see Table 1). For sodium we obtain a value approximately three times greater than for the other elements, but this is understandable inasmuch as the outer electron participating in the bond in the case of sodium is the 3d electron which screens the inner electron to an appreciably greater degree than a 4s electron. Again the value here is of the same order of magnitude as that obtained by theoretical calculations (see the value for 3s electron screening of the 1s inner shell in Table 1).

It is important to note that while the absolute value of the external screening by the peripheral electrons is much smaller for the deeper shells than for those further out from the nucleus the actual magnitude of the displacement of the deepest levels may be appreciable because the absolute value of the energy of the deeper levels is considerably greater than that of the outer ones. Thus, for example, for Z = 26 we have $E_K/E_L = 9$, while $E_K/E_M =$ = 100. Hence, although the magnitude of the external screening of the K shell for a 4s electron amounts to only approximately 0.01, upon the removal of the electron the K level will be displaced by 0.01 x 520 ev (the energy difference between the K levels in two neighboring elements) or about 5 ev. On the other hand, calculation of the screening of the M level by a 3p electron yields a value of 0.6 x 4 = 2.4. In other words, we find that the experimentally observed shifts of the K edges are due to an appreciable extent to changes in the position of the deeper levels of the atom even though the actual magnitude of the change in energy of these levels as compared with their absolute energy is minor.

* *
*

The data listed in Table 3 substantiate the fact that in the case of strong bonds, as a rule we observe a greater displacement of the K edge of the component relative to its position in the pure element than in the case of weak bonds.

---

*The tacit assumption that in the compounds of these elements the same sort of screening obtains for the 3d electrons as for the 4s electrons stems from the familiar concept of overlapping of the 3d and 4s levels in transition elements.

Table 3

Substance	Bond energy Kcal g/mol	Wavelength of K-edge as comp.X
Na_{met}		11545 (11516)
NaBr	172	11504.8
NaJ	161	11505
NaF	215	11501
NaCl	182,7	11501.6
K_{met}		3431.0
KCl	164	3427,9
KBr	156	3427,9
KJ	154	3427,7
Cl_2		4393,8
KCl	164	4385,0
RbCl	157	4385,2
NaCl	183	4383,9
LiCl	200	4383,8

The same direction of the shift of the K edge for cations and anions with increasing strength of the interatomic bonds can in a number of cases be explained by the fact that the cations give up s electrons, while the anions add electrons to their 3p shells. As we indicated above, in both the former and the latter cases the K absorption edge must be displaced to the side of shorter wavelengths. Analysis of other data[5] shows that the K edge of the cation is shifted most strongly to the side of shorter wavelength in the solid and into the region of long wavelength in the gaseous state. This is the situation obtaining in the case of NaCl. The K edge of chlorine in the solid state is displaced to the side of shorter wavelength, while in solutions it moves to the side of longer wavelengths with decreasing concentration. These facts also substantiate the rule formulated above to the effect that the greatest displacement of the absorption edge is observed when the bonding between the constituent atoms is strongest.

The question of the quantitative relation between the magnitudes of the observed shifts of the K edge and changes in the bonding energy (sublimation energy) has been discussed earlier in Ref.1. Here we must again emphasize that it would be vain to seek a direct relationship between the shift and binding energy inasmuch as the change in the position of the K edge in different types of compounds depends directly on the change in binding between the inner electrons and the atomic nucleus and this change in turn is only indirectly dependent on changes in the strength and character of the interatomic bonds.

It is worth noting that in compounds of the transition metals the K edge of the metal is displaced to the side of shorter wavelengths as compared with its position in the pure metal, while the $K\beta_5$ line is displaced to the side of longer wavelengths. Some data relative to these shifts taken from Faessler[5] are given in Table 4.

These facts can be explained by the circumstance that in these compounds not only the 4s but also the 3d electrons of the metal atoms are involved in the bonds; these electrons are "withdrawn" from the atom which, as is indicated above, leads to lowering of all the levels except the K level and hence to a decrease of the energy difference between the K and M levels, i.e., to a shift of the $K\beta_5$ line to the side of longer wavelengths.

Table 4

Compound	Shift, ev	
	K-edge	$K\beta_5$ line
Cr_2O_3	+10,4	—4,6
MnO	+ 5,4	—1,4
Fe_2O_3	+12,1	—2,5
Ni_2O_3	+ 9,9	—1,1

This is shown schematically in Fig.2 where (1) represents the case of the pure metal, (2) the case of a compound in which only the 4s electrons are involved in the bonds and (3) illustrates the case when both the 4s and 3d electrons participate in the bonds. It will be evident that in case (3) the $K\beta_5$ line may have a longer wavelength and the K edge a shorter wavelength than in the pure metal (case 1).

It must be noted that in some cases changes in the magnitude of the external screening may have a more noticeable effect

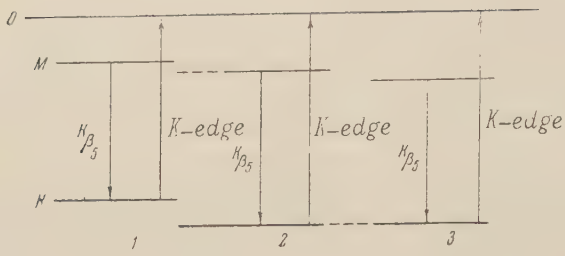

Fig.2

on the deep-lying inner levels than on those further from the nucleus. Thus, for example, if as a result of formation of an interatomic bond, a 3s electron goes over into the 3p shell of the atom, there will be an effective change in the external screening of the 1s shell but very little change in the screening of the other inner shells inasmuch as these shells are screened almost to the same degree by 3s and 3p electrons. Whence we have the important conclusion that in the case of formation of some types of interatomic bonds one may observe a greater change in the K than in the L spectra. This may be the explanation of the fact observed by Seigbahn & Magnus (see Ref.7) that in elements from Z = 21 to 30 the magnitude of the frequency shift of the absorption edges and spectral lines of the L series is appreciably greater (rather than smaller) than the shift of the K series lines.*

We used the above described approach for calculating the satellites in x-ray spectra[2]. Among other things we found that this made feasible a consistent, unified explanation of both short wavelength and long wavelength satellites. In the present article we have not touched upon such problems as the variation in width, intensity distribution and shape of x-ray lines.** We feel that the described method of analysis should also prove useful in interpreting these detailed features of x-ray spectra.

The proposed approach allows of interpreting the details of x-ray spectra, taking into account changes in the degree of external screening with changes in the strength and character of the interatomic bond. The precise ways in which these changes can and should be taken into account are as yet unclear, but there is reason to assume that just as the principal x-ray characteristics - the diagram lines and absorption edges - reflect the basic electron distribution in atoms, the fine details of x-ray spectra furnish evidence of the finer aspects of the electron distribution in atoms and, in particular, of the "penetration" of outer electrons into the region of the inner electron shells.

In conclusion I take this opportunity to express my gratitude to P.P.Kuz'menko for discussion and valuable suggestions and Prof.S.D.Gertsriken for his interest in the work.

"T.G.Shevchenko" Kiev State University

References

1. S.Karal'nik, Izv.AN SSSR, Ser.fiz., 20, 815 (1956). (Trans. Bulletin, 20, No.7, 739.)

2. S.Karal'nik & S.Nizhnik, Ukr.fizichnii zhurnal (Ukrainian Physics Journal), 2, No.4 (1957).

3. H.Bethe, Quantum Mechanics of One- and Two-Electron Systems. (Cited in Russian trans., M.1935.)

---

*From the standpoint of the band structure model the energy shift should be at least equal in both cases.

**These problems, specifically, the asymmetry of the Kα lines in transition metals, have been examined in Ref.8.

4. J.Slater, Phys.Rev., 36, 1, 57 (1930).

5. A.Faessler, Rentgenspektrum und Bindungzustand, in Handbook edited by Landtold & Börnstein, 6th edition, Vol.1, part 4, p. 769-868, 1955.

6. R.Evans, Introduction to Crystal Chemistry. (Cited in Russian trans. M. 1948.)

7. I.Borovskii & M.Blokhin, Rengenospektral'nyi analiz (X-ray spectroscopic analysis) pp. 71 and 77, M., 1939.

8. S.Karal'nik, Naukovi povidomlennia Kiivs'kogo universitetu, Fizika (Scientific notes of Kiev University, Physics), No.1, p.41, 1956.

ON THE STATE OF ATOMS IN FERROMAGNETIC IRON, COBALT AND NICKEL BASE ALLOYS

- I.Ia.Dekhtiar

One of the approaches to determining the electron structure of alloys of transition elements is through investigation of their magnetic properties. As a rule, however, such investigations allow of characterizing the electron structure in terms of a macroscopic quantity (for example, the magnetic moment) representing an average over all the components of the alloy, but do not allow of determining the states of the individual atoms.

In principle, the neutron diffraction method developed in recent years makes it possible to obtain information on the structure of the outer electron shells of different atoms and, consequently, on the state of the different atoms.

In scattering of neutrons by a disordered ferromagnetic alloy there occurs disorder scattering, appearing in the diffuse background. The intensity of this disorder scattering by an alloy of given composition proves to be proportional to $(m_a - m_b)^2$, the square of the difference between the atomic moment of the alloy components.[1] If, on the other hand, we know the average magnetic moment per atom of the alloy from magnetic saturation data, i.e., if we know

$$\bar{m} = Cm_a + (1 - C)\, m_b, \tag{1}$$

where C is the concentration of type atoms, then, as has been shown by Shull & Wilkinson[1] for the case of alloys of the Fe-Cr, Co-Cr and Fe-Ni systems, we can determine m_a and m_b.

Knowledge of the magnetic moments of the atoms of the different alloy components makes it possible to determine their states in terms of the filling factors for the d vacancies.[2] Until now, however, the filling factors q have been determined from the average magnetic moment per atom of the alloy by means of the formula

$$\bar{q} = \frac{d_0 - \bar{m}}{d_0}, \tag{2}$$

where d_0 is the number of d vacancies calculated per atom of the alloy in the free state by means of the expression

$$d_0 = Cd_{0a} + (1 - C)\, d_{0b}.$$

The values of d_{0a} and d_{0b} characterizing the electronic structure of the isolated atoms are known from microscopic data. For the purpose of determining the filling factors of individual atoms one can make use of the analogous formula

$$q_i = \frac{d_{0i} - m_i}{d_{0i}}, \tag{3}$$

where m_i are the magnetic moments of the atoms of the different components of the alloy, which can be determined from magnetic neutron scattering.[1]

Thus using the data for the positive values of m_{Fe} and m_{Cr} for alloys of the Fe-Cr system (also see Ref.3) and the known values for d_0, namely, $d_{0\,Fe} = 4$ and $d_{0\,Cr} = 5$, we computed the values of q_i for a number of alloys in the Fe-Cr system; the results are shown in Fig.1. The dash line in the figure gives the filling factor values per atom of the alloy calculated according to Eq.(2) on the basis of the average atomic magnetic moments of the alloys of the Fe-Cr system, obtained from magnetic saturation measurements.[4] The data

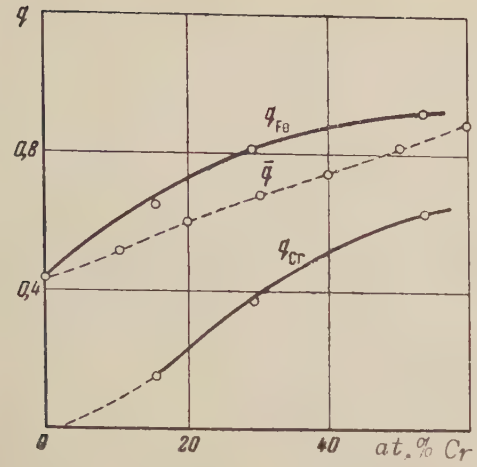

Fig.1. Variation of the d-vacancy filling factors with the Cr concentration in Cr-Fe alloys.

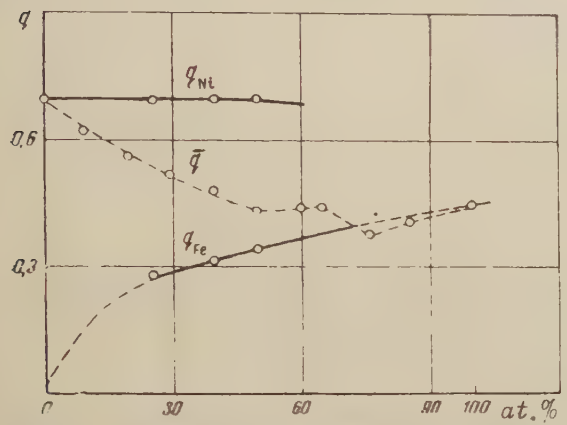

Fig.2. Variation of the d-vacancy filling factors with Fe concentration in Fe-Ni alloys.

of Fig.1 show that with increasing Cr concentration there occurs "filling" of the vacant d states in the atoms of both elements. At the same time there is an increase in the effective value of the filling factor $\bar{q}$. Analogous conclusions can be drawn from the available data on Co-Cr alloys.

A somewhat different picture is obtained for Fe-Ni alloys (Fig.2). In this case it is found that increase of the iron content up to almost 50 atomic percent does not change the filling factor for the nickel atoms but does lead to an increase of the factor for the iron atoms; at the same time the effective value of the filling factor varies in a more complex manner over the entire range of concentrations.

Another method of investigating the states of the component atoms in alloys of the given type is by studying their x-ray spectra; from these one can draw certain deductions regarding the electron distribution. In an earlier contribution[5] it was shown that the displacement of the absorption edge in the spectra of atoms in transition element alloys can be related with the effective value of the filling factor $\bar{q}$. It was found that the shift of the K edges of the alloys components to the same, short wavelength side can be explained by the fact that in the process of fusion of the components the degree of "defectiveness" of the d states for atoms of different types decreases and that the displacement of the edge is the greater, the higher the degree of "filling" of the vacancies of the atoms or the lower their degree of "defectiveness". The last was determined by means of a formula in which use was made of the effective value of the filling factor $\bar{q}$ (see Eq.(2)), which made it possible to determine also a certain mean value of the defectiveness

$$\bar{n}_{di} = d_{0i}(1 - \bar{q}). \qquad (4)$$

If, however, one uses the now available values of q_i for atoms of type i, Eq.(4) can be more accurately written in the form

$$n_{di} = d_{0i}(1 - q_i). \qquad (5)$$

Assuming in the first approximation that the magnitude of the displacement of the K edge (see Fig.3 for displacement of the K edge of Co in Co-Cr alloys) is proportional to the change in the degree of defectiveness in going from the pure metal to the alloy, one can use Eq.(5) for certain evaluations and comparisons.

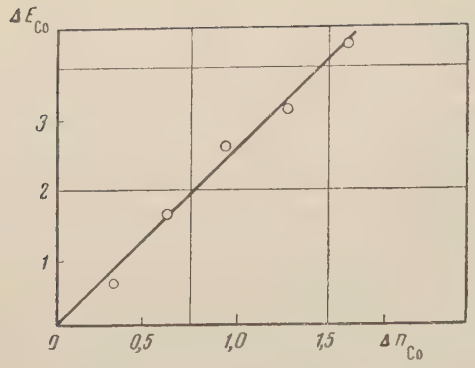

Fig.3. Variation of the displacement of the K edge of Co in Co-Cr alloys with the degree of defectiveness.

Let us consider a binary alloy of composition $C_i + C_j = 1$. Let d_{0i} and d_{0j} be the number of vacancies in the d shells of atoms of types i and j in their isolated (free) states, q_{0i} and q_{0j} will be the filling factors corresponding to transition to the condensed state of the pure metals and q_i and q_j be the filling factors for the atoms in the alloy. Then the change in degree of "defectiveness" in going from the pure metal to the alloy for atoms of different kinds, according to Eq.(5), will be characterized by

$$\left.\begin{aligned}\Delta n_i &= d_{0i}(q_i - q_{0i})\\ \Delta n_j &= d_{0j}(q_j - q_{0j})\end{aligned}\right\}. \qquad (6)$$

Assuming in accord with what has been said above that the displacements of the K edges of the components (in the alloy with respect to their positions in the pure metal)

$$\Delta E_i = k\Delta n_i \quad \text{and} \quad \Delta E_j = k\Delta n_j, \qquad (7)$$

where k is a proportionality factor, we obtain

$$p = \frac{\Delta E_i}{\Delta E_j} = \frac{d_{0i}(q_i - q_{0i})}{d_{0j}(q_j - q_{0j})}. \qquad (8)$$

From Eqs.(1), (3) and (8) we can deduce expressions by means of which we can evaluate the magnetic moments of the atoms in the alloy:

$$\left.\begin{aligned}m_i &= \frac{p\bar{m} + [C_j d_{0i}(1 - q_{0i}) - pC_j d_{0j}(1 - q_{0j})]}{C_i p + C_j}\\ m_j &= \frac{\bar{m} - [C_i d_{0i}(1 - q_{0i}) - pC_i d_{0i}(1 - q_{0j})]}{C_i p + C_j}\end{aligned}\right\}. \qquad (9)$$

The results of measurements of the positions of the K edges of nickel and manganese in Ni_3Mn alloy brought to the ordered state by annealing at 450° for 150 hours are listed in Table 1. In the table λ is the wavelength corresponding to the K absorption edge and ΔE is the displacement of the edge relative to its position in the pure metal.

Table 1

State of the alloy or metal	λ_{Ni}, X	ΔE, ev	λ_{Mn}, X	ΔE, ev
Metal in the solid state	1484.01	---	1891.50	---
Alloy ordered at 450° and slowly cooled	1483.29±0.15	3.9	1889.60±0.15	6.5

For the ordered alloy, the average ferromagnetic moment $\bar{m} = 1.02\ \mu_B$. The values of the other parameters of interest are

$$p = \frac{\Delta E_{Ni}}{\Delta E_{Mn}} = 0{,}61, \quad q_{0\,Ni} = 0{,}7, \quad q_{0\,Mn} = 0{,}29, \quad d_{0\,Ni} = 2 \quad \text{and} \quad d_{0\,Mn} = 5.$$

On the basis of these data we can evaluate m_i and m_j and then compare them with the measured values obtained from neutron scattering[1]. The data in Table 2 show satisfactory agreement of the values of m_i and m_j, determined from displacement of the K edge and from neutron scattering.

Table 2

From displacement of the K edge of Ni	From neutron scattering	From displacement of the K edge of Mn	From neutron scattering
0.32	0.3	3.17	3.2

It will be evident from the data of Ref. 5 that the displacement of the K edge of cobalt in Co-Cr alloys with variation in the degree of "defectiveness" is linear (Fig.3); the maximum displacement is observed for the alloy of critical composition C_{cr} for which $q_{alloy} = q_{Co} = 1$.

Then determining all the values of ΔE_i for cobalt with respect to the maximum displacement of the K edge of Co in Co-Cr alloys ($\Delta E_{max} = 4.5$ ev), we can, according to Eq.(8), write

$$p_1 = \frac{\Delta E_i}{\Delta E_{max}} = \frac{d_{0i}(q_i - q_{0i})}{d_{0i}(1 - q_{0i})}. \qquad (10)$$

From Eqs.(3) and (10) we can evaluate the magnetic moment of cobalt atoms in Co-Cr alloys:

$$m_i = d_{0i}(1 - q_{0i})(1 - p_1). \qquad (11)$$

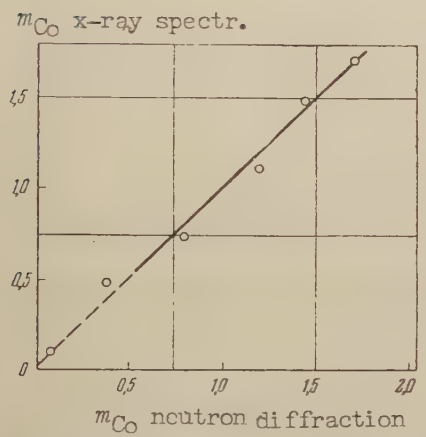

Fig.4. Comparison of the values of m_{Co} obtained by different methods.

In our cases $C_{cr} = 0.73$* and for cobalt $d_{0i} = 3$ and $q_{0i} = 0.43$. Using the values of ΔE_i, given in Ref.5, we can be means of Eq.(11) calculate the values of m_i for cobalt and compare them with the data obtained for some Co-Cr alloys from neutron diffraction studies.** The results, shown in Fig.4, despite the approximate character of the calculations and the experimental errors, show satisfactory agreement between the data obtained from x-ray spectroscopic measurement and neutron diffraction.

A similar evaluation of the atomic magnetic moments of Fe in Fe-Cr alloys was made on the basis of Karal'nik's[6] investigation of the K absorption edge of iron in these alloys. The results of this evaluation are compared in Table 3 with the data obtained by Shull & Wilkinson from neutron scattering. In this case, too, the agreement may be regarded as satisfactory.

Thus one may judge of the states of the atoms in alloys of ferromagnetic metals both on the basis of magnetic neutron diffraction data and from the results of investigations of the x-ray spectra.

---

*For Co-Cr alloys at a Cr concentration of 27 atomic percent the magnetic moment per atom of the alloy is ~0, (Ref.4).

**The magnetic neutron scattering values for alloys with 80 and 75 atomic percent Co were obtained by us by extrapolation of the results of Shull & Wilkinson.[1]

Table 3

Fe, at.%	From displacement of the K edge	From neutron scattering
100	2.22	2.22
92	1.96	1.75
84	1.85	1.65
70	1.46	1.37

It may be noted that our concept of the "filling" factor q, which to a certain degree characterizes the change in the state of the atoms in going from the free state to the solid state, does not conflict with the more consistent model of ferromagnets developed by Vonsovskii and Vlasov on the basis of the many-electron theory.[7,8] According to this model, the inner d electrons, by virtue of exchange forces, are oriented parallel to and, in addition, interact with free s electrons. Due to this interaction some fraction of the s electrons becomes oriented parallel or antiparallel to the inner electrons and thereby gives rise to a certain fractional addition to the saturation moment. According to the theory[8], the average magnetic moment of absolute saturation per atom of the metal is given (in the notation introduced above) by

$$m = d_0 + \varkappa s, \tag{12}$$

where d_0 and s are the numbers of d and s electrons per atom and $\varkappa$ is a coefficient characterizing the degree of interaction of the d electrons with the s electrons. In the case of alloys this coefficient, according to the Vonsovskii-Vlasov theory[8], is a complex function of the composition and structure; at present it cannot be calculated. From Eq.(12) we readily obtain

$$\frac{d_0 - m}{d_0} = -\varkappa \frac{s}{d_0}. \tag{13}$$

The left side of (13) is our "filling" factor (see Eq.(2)). Hence, we have

$$q = -\varkappa \frac{s}{d_0}. \tag{14}$$

The values of the coefficient $\varkappa$ for Fe, Co and Ni (from Ref.9) are -0.94, -0.65 and -0.7, respectively; whence the values of q for Fe, Co and Ni are, respectively, 0.47, 0.44 and 0.7.

Thus, the "filling" factor indicates the degree of interaction between the d and s electrons and depends also on d_0 and s, quantities characterizing the normal state of the atoms.

In the case of alloys the moment per atom of alloy $m_{\text{alloy}} = (\bar{d}_0 + \bar{s}\varkappa_{\text{alloy}})$, where d_0 and s are calculated according to the displacement rule. Hence, by analogy with Eq.(14), the effective value of the filling factor can be written as

$$\bar{q} = -\frac{\bar{s}}{\bar{d}_0}\varkappa_{\text{alloy}}. \tag{15}$$

The considerations developed above throw additional light on the results obtained from neutron diffraction studies for the case of Fe-Cr alloys. The results of these studies allow of determining the magnetic moment of atoms of different types. Hence if we express the moment for an atom of type i in terms of the coefficient characterizing the interaction of the d and s electrons, i.e., $m_i = d_{0i} + \varkappa_i s_i$, we can deduce the following expression for the filling factor q_i

$$q_i = -\varkappa_i \frac{s_i}{d_{0i}}, \tag{16}$$

where s_i and d_{0i} are the numbers of s and d electrons per atom of component i in the normal state. Thus, if with increasing chromium concentration in the Fe-Cr alloy the absolute value of $\varkappa$ increases, the magnitude of q_i must also increase (Fig.1). This means that with increasing Cr concentration in the alloy the interaction between the d and s electrons is enhanced.

It is important to note that results of neutron diffraction determinations of magnetic moments indicate that the magnetic moment has nonintegral values not only for pure metals but also for alloy components. This is due to the interaction between the d and s electrons.

It follows from the above that in cases when the magnetic moment of an atom in an alloy depends on the degree of long-range order, the magnitude of the displacement of the K absorption edge of the atom must exhibit a functional dependence on the degree of long-range order. For our purposes we can make use of the variation of the coefficient $\varkappa$ (taking into account the s and d electron interaction) with the degree of long-range order (η) deduced by Vonsovskii & Vlasov[8]:

$$\varkappa = A' [1 + B' (g - c)^2 \eta^2] = \varkappa_0 [1 + B' (g - c)^2 \eta^2], \tag{17}$$

where $g = c/\nu$, c is the concentration of the atoms of the first component in the alloy, ν is the concentration of lattice sites of the first type, $\varkappa_0 [\varkappa]_{\eta=0} = A'$ and A' and B' are coefficients that are independent of c and η.

Thus for the filling factor of the i component as a function of the degree of long-range order, we obtain

$$q_i = -\varkappa_{0i} \frac{s_i}{d_{0i}} [1 + B' (g - c)^2 \eta^2]. \tag{18}$$

Making use of Eqs.(6) and (7), we find the following expression for the dependence of the shift of the K absorption edge in the spectrum of the i component on the degree of long-range order:

$$(\Delta E_i)_{\text{ord.}} = -kd_{0i} \left\{ \varkappa_{0i} \frac{s_i}{d_{0i}} [1 + B' (g - c)^2 \eta^2] + q_{0i} \right\}, \tag{19}$$

whence, we find

$$\frac{(\Delta E_i)_{\text{ord.}}}{(\Delta E_i)_{\text{disord.}}} = 1 + \frac{\varkappa_{0i} \frac{s_i}{d_{0i}} B' (g - c)^2 \eta^2}{\varkappa_{0i} \frac{s_i}{d_{0i}} + q_{0i}}. \tag{20}$$

This expression shows that the ratio of the shift of the K absorption edge of the component i in an ordered alloy to the shift in a disordered alloy is a function of the square of the degree of long-range order. Unfortunately, there are no data in the literature for verifying this expression.

It must also be emphasized that the above calculations of the magnetic moments in the Ni_3Mn alloy are valid only within the framework of the assumptions made. In particular, if the proportionality factors in Eqs.(7) are different for the two components of the binary alloy then in Eq.(9) instead of p (obtained from experiment), we must write $p' = p(k_j/k_i)$. Then using the data from neutron diffraction studies one can evaluate the factors k_i and k_j, characterizing the energy dependence of the level density in the d shell. Unfortunately theory as yet does not allow of calculating these factors.

In the case of the Co-Cr and Fe-Cr alloys evaluation of the atomic magnetic moments for cobalt and iron, as is evident from the computation procedure, does not require knowing the value of the proportionality factor.

The results obtained demonstrate the need for further investigation of the state of atoms in alloys of the given type by means of diverse procedures and methods.

Institute of Metal Physics,
Academy of Sciences of the Ukrainian SSR

References

1. G.G.Shul & M.K.Wilkinson, Phys.Rev., 97, 304 (1955).
2. I.Ia.Dekhtiar, Doklady AN SSSR, 85, 3, 583 (1952).
3. N.S.Akulov, Doklady AN SSSR, 105, 5 (1955).
4. R.M.Bozorth, Ferromagnetism. (Cited in Russian trans., M., 1956).
5. I.Ia.Dekhtiar, Doklady AN SSSR, 108, 6, 1069 (1956).
6. S.M.Karal'nik, Naukovi zapiski KDU (Scientific notes Kiev State University), 14, Fizichnii zbirnik (Physics collection), 7, 105 (1955); Izv. AN SSSR, Ser.fiz., 20, 815 (1956). (Trans. Bulletin, 20, No. 7, 739.)
7. S.V.Vonsovskii, Zhur.eksp.i teor.fiz., 16, 981 (1946).
8. S.V.Vonsovskii & K.B.Vlasov, Zhur.eksp i teor.fiz., 25, 3 (9), 327 (1953).
9. Ia.G.Dorfman, Manitnye svoistva i stroenie veshchestva (Magnetic properties and structure of matter), p.322, M., 1955.

EFFECT OF NEUTRON IRRADIATION ON THE FINE STRUCTURE OF THE K ABSORPTION EDGE OF GERMANIUM

- M.M.Kakhana & E.E.Vainshtein

Despite the fact that the influence of irradiation on the physical properties and structure of solids has attracted the attention of numerous investigators and is of great practical and scientific interest,[1] there are almost no data in the literature on the effect of different radiations on the x-ray spectra of atoms in solids and, in particular, on the fine structure of these spectra. The only work along this line reported in the literature is that carried out a few years ago by Cauchois[2] in France. This work involved investigation of the K absorption spectra of nickel atoms in the pure metal and in an Ni-Cu alloy containing 5% nickel; no decisive results were obtained however.

The present report is a preliminary one in which we give some of the results of the researches carried out in our laboratory on the influence of neutron bombardment on the x-ray spectra of elements in different compounds. Here we shall deal specifically with the results of the investigation of the K absorption spectrum of germanium in the n-type semiconductor form and in its dioxide. The spectra were obtained by means of a focusing Cauchois type x-ray spectrograph with a quartz crystal analyzer employing reflection from the $(10\bar{1}0)$ plane. The dimensions of the bent crystal were 10 x 40 mm. The radius of curvature was 1 meter.

The crystal was bent in a special crystal holder[3] in which it was held in the bent state by the forces of molecular cohesion. The spectra were photographed in the second order. The dispersion was 4.5 X/mm. The tube was operated at 20 kv and 25 ma. A layer of uranium oxide was applied to the surface of the copper anode in order to enhance the intensity of the continuous spectrum. The spectrograms were scanned by means of an MF-2 microphotometer at three levels and the results averaged. The Pt $L\beta_1$ line was used as reference. In carrying out the work great attention was paid to finding the optimal absorber thickness and rigorous control of its uniformity.

Inasmuch as in photographic recording of x-ray spectra there may occur distortion of the relative intensity of individual fluctuations in the long wavelength fine structure and the true absorption edge[4] and inasmuch as the magnitude of the distortion in different parts of the spectrum and, consequently, the details of the fine structure depend on the thickness of the absorber (see Fig.5 below), the work was carried out with different absorber thicknesses depending on the specific problems involved at different stages of the investigation. The superficial density of the absorber was gaged by weight. The absorbing layers were prepared in the form of gelatin suspensions of finely dispersed powders of the nonirradiated and neutron irradiated material. It proved impractical to irradiate prepared absorbers since it was found that they broke down under the bombardment conditions. The neutron flux in one of the utilized reactors was 10^{11} n cm^{-2} sec^{-1}; that in the other reactor was five times heavier. Approximately 90 and 60%, respectively, of the neutrons were thermal and slow neutrons. The energy of the fast neutrons in the flux was 2 to 5 Mev. In view of the relatively high specific activity of germanium after neutron irradiation and the fact that we were primarily interested in the radiation induced irreversible changes in the lattice of the material and the effects such changes produce in the structure of the x-ray spectrum, we investigated the x-ray spectra some 1-1.5 months after irradiation.

The results pertaining to pure germanium and its dioxide (averages for three independent spectrograms) are shown in Figs.1, 2 & 3. The absorption

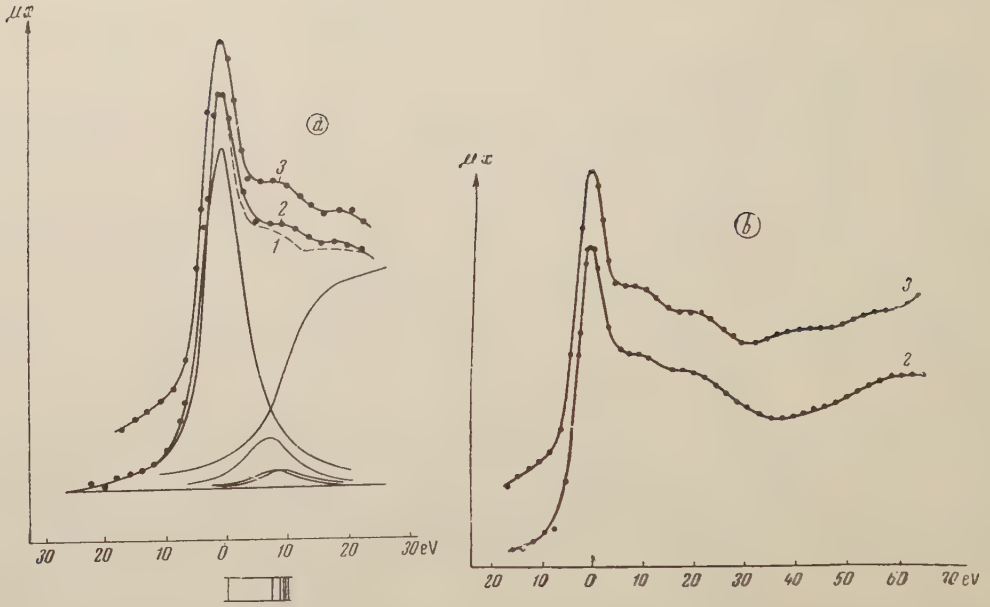

Fig.1. Fine structure of the K absorption edges of germanium in the nonirradiated and neutron irradiated dioxide and the results of calculation of the structure of the spectra by the method of Ref.5: a) region of main absorption edge; 1) total theoretical absorption curve in the vicinity of the main edge, 2) experimental curves for the nonirradiated dioxide, 3) experimental curves for the neutron irradiated dioxide; b) general appearance of the fine structure of the absorption edge. Absorber thickness 2.5 μ.

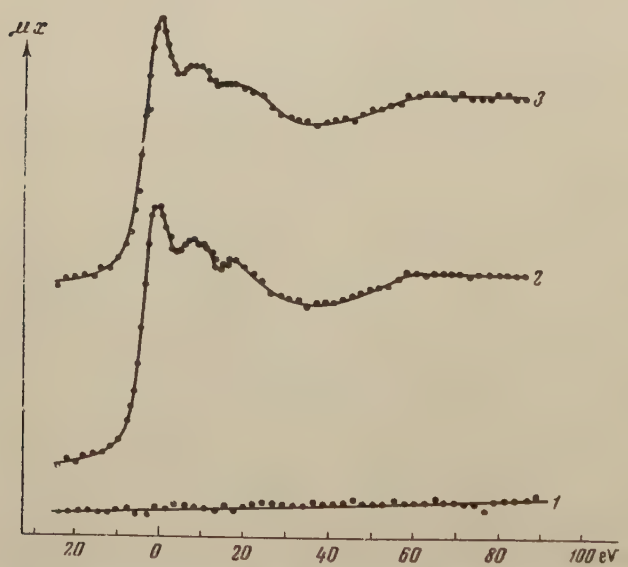

Fig.2. Comparison of the fine structure of the K absorption edges of germanium in the nonirradiated and neutron irradiated dioxide with an absorber thickness of 10 μ; 1) spectrogram background, 2) K absorption edge of germanium in the nonirradiated dioxide and 3) K absorption edge of germanium in the irradiated dioxide.

spectra shown in Fig.1 were obtained with an absorber thickness of 2.5 μ; the spectra of Figs.2 & 3 were recorded with absorbers having a thickness of 10 μ. In the first figure we also give the results of calculations of the K absorption edge of germanium in the nonirradiated dioxide by the method proposed earlier by one of us.[5] The degree of stability and reproducibility of the fine structure of the K edge of germanium with the selected absorption thicknesses and the extent of change of the spectrum as a function of the superficial density of the absorber are characterized by the curves of Figs. 4 & 5. The absorber was prepared anew for each of the curves reproduced in Fig.4.

Examination and analysis of the experimental results led to the following conclusions:

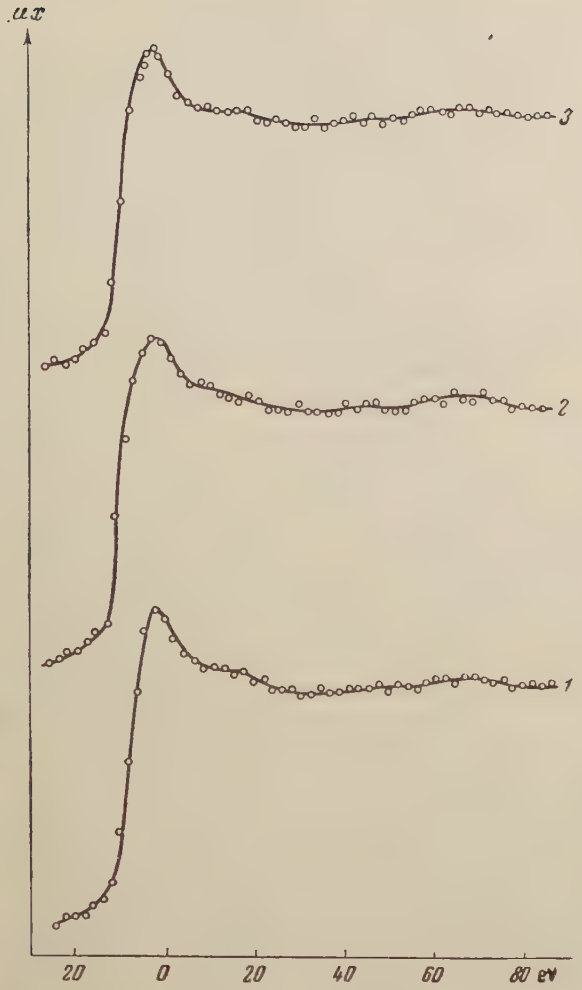

Fig.3. Comparison of the K absorption edges of germanium before and after irradiation of the material: 1) K absorption spectrum of germanium before irradiation, 2) K absorption spectrum of germanium after irradiation with a neutron flux of $\sim 10^{11}$ n cm^{-2} sec^{-1} density containing 90% slow neutrons, 3) K absorption edge of germanium after irradiation in a neutron flux of $\sim 5 \cdot 10^{11}$ n cm^{-2} sec^{-1} density containing 60% slow neutrons. Absorber thickness 10 μ.

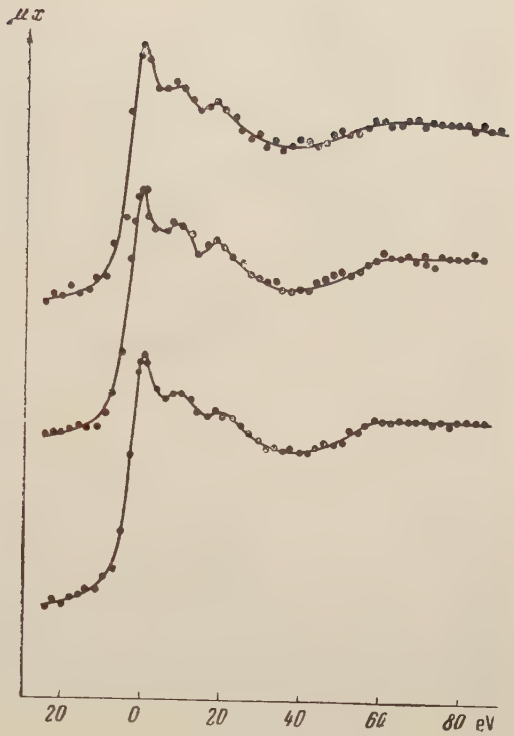

Fig.4. Producibility of the fine structure of the K absorption edge edge of germanium in the dioxide: spectra as obtained in three independent experiments. Absorber thickness 10 μ.

1. The fine structure of the main absorption edge of germanium in its dioxide, as in the case of gaseous molecules of halide compounds of this element ($GeCl_4$ and $GeBr_4$)[6,7], comprises three more or less (depending on the absorber thickness) clearly defined absorption peaks and can satisfactorily be computed (resolved) by the method described in Ref.5. Hence one may still regard as valid the earlier interpretation of this structure and, particularly, the deduction that the appearance of the third absorption peak within the main K absorption edge of Ge in the dioxide (which is particularly well defined in the spectra obtained with 10-12 μ thick absorbers) is associated with so-called cross transitions[8] of the K electrons of the absorbing atoms.

Just as is observed in the case of other compounds in the gaseous and solid states, the absorption spectrum of germanium in the solid dioxide is characterized by a lower value of the theoretical parameter n^* as compared

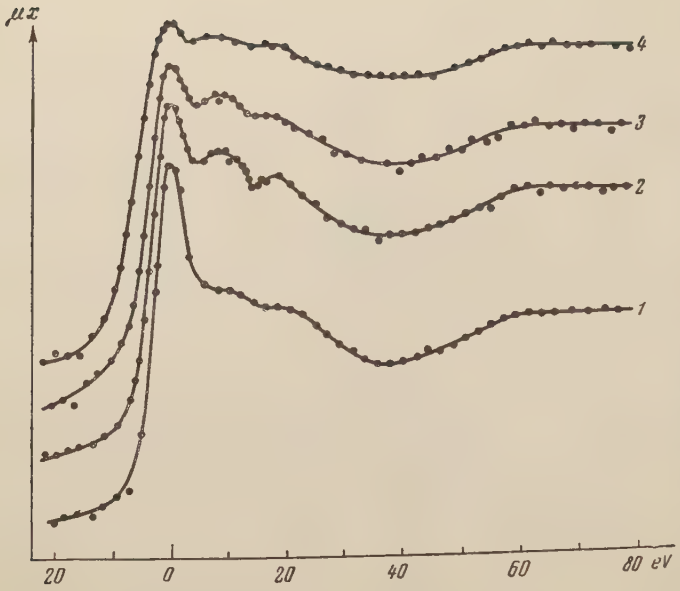

Fig.5. Fine structure of the K absorption edge of germanium in the dioxide with different absorber thicknesses: 1) 2.5 μ, 2) 10 μ, 3) 12 μ and 4) 20 μ.

with the gaseous state.* In the spectrum of germanium in the solid dioxide this is evinced in a more rapid weakening of the intensity of successive selective absorption lines and a greater energy span of the principal series of absorption lines, as compared with the spectra of gaseous molecules.

2. The position of the long wavelength limit of the K absorption edge and the ratio of the intensities of the first two fluctuations of the absorption coefficient (peaks) within the main absorption edge remain the same within the limits of the experimental error for irradiated and nonirradiated samples of germanium dioxide. As for the third peak, as may be seen from the curves in Fig.2 (obtained under the most favorable conditions for bringing out this peak), neutron irradiation leads to diffusion of this maximum, i.e., to a change in its form and intensity by an amount appreciably exceeding the experimental error (Fig.4).

In addition to the above mentioned changes in the structure of the long wavelength part of the K absorption edge of germanium in its dioxide, there is observed in irradiated samples a relatively small decrease in the amplitude of fluctuation of the absorption coefficient in the region of the so-called far fine structure. It should be noted, however, that the conditions under which our experiments were carried out (specifically, spectroscopy only some 1-1.5 months after irradiation of the samples) were not favorable for observation of this effect, which should be appreciably stronger immediately after neutron irradiation.

In pure germanium (Fig.3) no changes susceptible of detection under our experimental conditions occur in the structure of the K absorption edge of the element under the influence of neutron irradiation.

3. In the present report we have recounted the first results of our research into the influence of neutron irradiation on the fine structure of the x-ray spectra of atoms in solids. These results are, of course, only a beginning; it is therefore imperative to continue systematic investigations which would allow of characterizing the state of the material in the first stages of its life after irradiation. It is also needful to determine the influence of neutrons of different energies on the fine structure of the x-ray spectra and to establish the degree and character of the structural changes occurring in the samples. Only then will it be possible to interpret reliably the observed experimental facts and make an attempt to relate them with changes in the energy structure of the material subjected to neutron irradiation. Even

---

*Thus in the absorption spectrum of germanium dioxide in the solid state the parameter is 1.16, whereas in the spectrum of Ge in $GeCl_4$ vapor, $n^* = 1.34$.

our first results, however, and, particularly, the fact that the greatest change in the structure of the absorption spectrum of germanium in its dioxide involves the third absorption peak, whose appearance according to the latest data[9] cannot be explained by transitions of K electrons only within the absorbing atom, indicate that the observed effect is associated primarily with the influence of "impurity" atoms produced incident to capture of slow neutrons by germanium nuclei and with the irreversible dislocations (vacancies) produced in the lattice by the impact of fast neutrons. These are the very factors, as is known, that serve to explain the change in the conductivity of the investigated materials, occurring as a result of neutron bombardment.

"V.I.Vernadskii" Institute of Geochemistry and Analytic Chemistry,
Academy of Sciences of the USSR

References

1. A.I.Zakharov, Usp.fiz.nauk, 57, 525 (1955).
2. Y.Cauchois,C.R., 241, 942 (1955).
3. E.E.Vainshtein, K.I.Narbutt & A.V.Gil'varg, Trudy Instituta kristallografii (Transactions of the Institute of Crystallography), No.6, 207 (195?).
4. K.I.Narbutt, R.L.Barinskii & E.E.Vainshtein, Doklady AN SSSR, 82, 567 (1952).
5. E.E.Vainshtein, R.L.Barinskii & K.I.Narbutt, Zhur.eksp.i teor.fiz., 23, 593 (1952).
6. H.Glaser, Phys.Rev., 82, 616 (1951).
7. K.I.Narbutt, Izv.AN SSSR, Ser.fiz., 20, 780 (1956). (Trans. Bulletin, 20, No.7, 710.)
8. E.E.Vainshtein, R.L.Barinskii & K.I.Narbutt, Zhur.eksp.i teor.fiz., 27, 521 (1954).
9. R.L.Barinskii, E.E.Vainshtein & K.I.Narbutt, Present issue of the Bulletin, p.1341.

QUANTITATIVE DETERMINATION OF TITANIUM FROM SECONDARY X-RAY SPECTRA

- A.S. Ivoilov & N.F. Losev

The use of secondary x-ray spectra for purposes of chemical analysis has been described and evaluated by a number of both Soviet and foreign authors.[1-9]

M.A. Blokhin designed a number of practical fluorescent spectrographs and investigated the theoretical aspects of utilizing secondary spectra for quantitative analysis.[4,5 & 10]

The present work was devoted to development of a procedure for quantitative determination of titanium by means of a Blokhin type fluorescent long-wave x-ray spectrograph of domestic manufacture. By way of high voltage source we used a single Kenotron x-ray power unit with no stabilization of the high voltage. The voltage applied to the x-ray tube was monitored by means of an S-96 kilovoltmeter.

Among the various procedures for quantitative x-ray spectroscopic analysis with reference to secondary spectra, we chose the external standard technique.[10] The analytic line was the $K\alpha_1$ line of titanium in the second order. The width of the detecting slit was 0.2 mm. The titanium spectra were excited by radiation from chromium electrolytically deposited on the face of the copper anode. The tube was operated at 24 kv and 15 ma.

The analyzed material was titanium ore or crude concentrate. Examination of the available chemical and optical spectroscopic analysis data showed that the samples varied appreciably as regards composition due to the fact that they were from different deposits and had been subjected to different concentration treatments.

The sample preparation procedure was the following. A certain weight of the powdered assay material was applied, using liquid gelatin as the adhesive, to an aluminum plate, which served as the radiator. After drying, the layer of material on the radiator was subjected to 100-150 kg/cm^2 pressure in an hydraulic press and then heated to burn out the adhesive. In this manner there was obtained a very smooth, uniform and strong layer of the assay material on the radiator plate.

In view of the analytic procedure selected, it was necessary as a first step in developing the procedure to determine the influence of different factors associated with the conditions of excitation and the composition of the sample on the analytic results. In a series of special experiments we determined the effect of such factors as the stability of operation in the x-ray tube, the uniformity of application of the material on the radiator plate, selective excitation and absorption and the composition of the sample. The results of these experiments were the following:

1. In the process of operation the high voltage on the x-ray tube varied over a range of ±0.5 kv from its initial 24 kv value. This resulted in a variation of the counting rate in recording the intensity of the $K\alpha_1$ line of titanium not exceeding 3-4% of the mean value.

2. The above described method of preparing the radiator plates yielded fairly uniform "standardized" samples. The scatter in the counting rate in recording the intensity of the $K\alpha_1$ line of titanium for 10 different radiator-samples of the same initial material did not exceed 4-5%.

3. The effects of selective excitation and absorption due to the presence of iron and calcium in the samples had an appreciable distorting effect on the analytic results.

In the case of samples with the same titanium content, increasing the iron concentration from 0 to 30% increased the intensity of the titanium line by

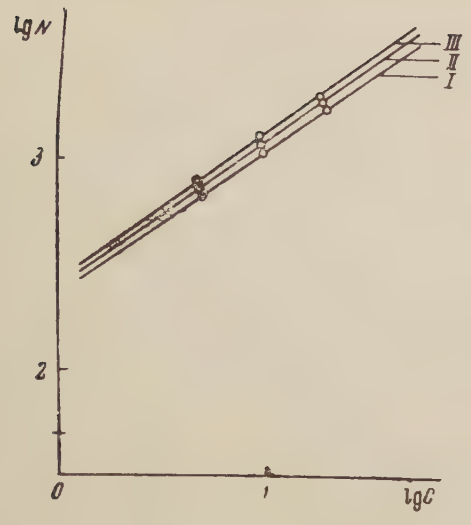

Fig.1. Influence of iron on the intensity of the $K\alpha_1$ line of titanium: I) 0% Fe, II) 30% Fe and III) 60% Fe.

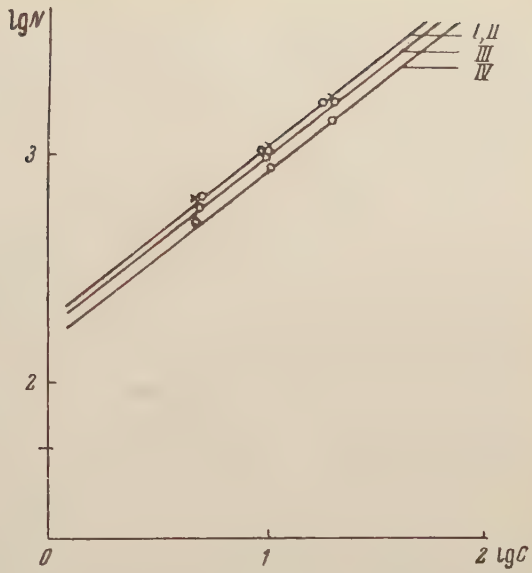

Fig.2. Influence of calcium on the intensity of the titanium line: I) 0% Ca, II) 5% Ca, III) 15% Ca and IV) 30% Ca.

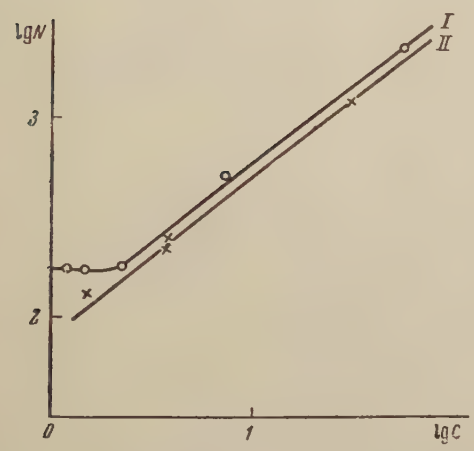

Fig.3. Variation of the intensity of the Ti $K\alpha_1$ line with the titanium content in different ores.

about 10% (Fig.1), while increasing the calcium concentration from 0 to 30% reduced the intensity of the titanium line by as much as 30% (Fig.2).

4. The density of the "filler", i.e., the medium containing the sample analyzed for titanium, affected the intensity of the $K\alpha_1$ line to a far greater degree than all the other factors listed above. As the density of the filler was increased from 2 to 4.5 g/cm^3 the intensity of the analytic line (other conditions being equal) fell off by a factor of 2-3.

From the results of the investigation of the influence of different factors on the intensity of the $K\alpha_1$ line of titanium, it was concluded that direct analysis of ore material by the external standard procedure was impossible. Thus our experiment on direct determination of the titanium content in ores led to results differing by as much as 60-100% from the data of chemical analysis. There is no need to cite here the precise results of these determinations. Instead, in Fig.3, we show the character of the variation in the intensity of the titanium line with the Ti content in the analyzed samples. It will be seen that the intensity of the analytic line varies in a different way with the Ti concentration for samples originating from different deposits. In addition, curves I and II show that there is no direct proportionality between the line intensity and the Ti concentration.

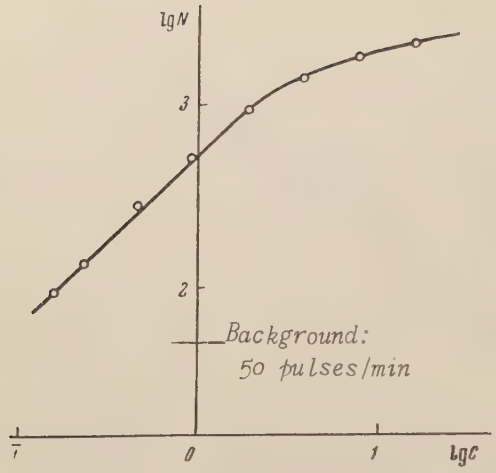

Fig.4. Working curve.

In order to be able to use the external standard technique we resorted to the procedure of diluting the samples to a uniform composition with a buffer. We chose for this purpose an ore consisting primarily of quartz (~70% SiO_2).

By way of references we used "standards" prepared by successive dilution of ilmenite with the above buffer. The analytic (working) curve plotted on the basis of these standards is reproduced in Fig.4.

Experimental work with the diluted samples showed that satisfactory agreement with the data from chemical analysis is obtained for all the forms of the analyzed material at a 5-fold dilution thereof.

The results of determination of titanium with 5-fold dilution of the samples are compared with chemical and spectroscopic analysis data in the accompanying table.

Results of quantitative fluorescence determination of titanium and comparison of these results with the data of chemical and optical spectroscopic analyses

Sample No.	TiO_2 (%), from analyses						Scatter x-ray data, %	Divergence of x-ray data from	
	x-ray spectro.				Chem.	Spectr.		chem. analys.	spectr. analysis
	1	2	3	Mean					
32	3,8	3,5	3,2	3,5	3,72	3,7	5,7	5,9	5,4
33	1,4	1,5	1,6	1,5	1,48	—	4,7	1,4	—
35	3,2	3,1	2,9	3,1	3,60	—	3,2	13,9	—
36	25	26	25	25	27,5	23	0,12	9,1	8,7
37	2,5	2,3	2,0	2,3	2,45	2,5	7,4	6,1	8,7
38	1,6	1,3	1,3	1,4	1,45	—	12,1	3,4	—
40	1,7	1,5	1,5	1,6	1,87	—	6,3	14,5	—
47	7,2	7,0	7,4	7,2	7,20	6,9	2,8	0,0	4,4
52	1,7	1,5	1,9	1,7	1,47	—	8,8	15,6	—
54	53	52	52	52	55,0	—	0,6	5,5	—
55	2,3	2,2	2,3	2,3	2,21	—	1,3	4,5	—
56	7,7	7,5	—	7,6	7,33	—	1,3	3,7	—
81	46	44	40	43	43,6	—	4,7	1,4	—
83	3,2	3,2	3,0	3,1	3,08	—	3,2	0,7	—
85	44	45	42	44	47,4	—	1,6	7,2	—
86	1,2	1,2	1,2	1,2	1,18	—	0,0	1,1	—
87	9,6	10,2	9,8	9,8	9,50	—	2,0	3,2	—
122	13	14	14	14	15,3	—	2,1	8,5	—
123	3,3	3,0	3,2	3,2	3,20	—	3,1	0,0	—
124	0,9	0,8	0,8	0,8	0,92	—	3,8	13,0	—
128	3,2	3,3	3,1	3,2	2,79	2,1	2,2	14,7	52,0
169	37	38	33	36	38,0	48	5,6	5,3	25,0
171	3,3	3,2	3,2	3,2	3,15	3,2	0,0	1,6	0,0
246	57	49	50	52	52,0	—	9,6	0,0	—
252	39	42	41	41	43,8	36	2,5	6,4	13,7

Note: The results of chemical and spectroscopic analyses are characterized by relative errors of 1-2% and 10-12%, respectively.

It will be evident from the table that the scatter of x-ray spectroscopic determinations does not exceed 10% and amounts to only about 5% relative to the mean value for all the analyzed samples listed in the table. Divergence from the data of chemical analysis in the range of titanium oxide concentrations from 1 to 50% exceeds 10% only in the case of five samples, attaining a maximum of 16%.

The cited results show that by use of the dilution technique (i.e., by reduction of the sample composition to that of the standard employed) one can obtain an acceptable accuracy of quantitative determination of titanium in ore samples by fluorescence analysis.

Using the developed technique, 8 to 10 determinations can be made per working day. Taking into account the necessity of dilution of the assay samples, the sensitivity of the developed procedure equals about 0.7-0.8% of the titanium in the initial sample.

Conclusions

We developed a procedure for quantitative fluorescence determination of titanium in ores and concentrates containing from 1 to 50% titanium oxide. The accuracy of the procedure is characterized by a mean relative error not exceeding 10%. The analytic sensitivity is 0.7-0.8%. The speed of the procedure is such that it allows of carrying out 8 to 10 analyses per working day.

In conclusion we desire to express our gratitude to G.M.Skirpkina, student at Irkutsk University, for her help in carrying out the experimental part of the work.

Irkutsk State Institute of Rare Metals

References

1. N.D.Borisov & Ia.M.Fogel', Zhur.eksp.i teor.fiz., 5, 744 (1935).
2. N.D.Borisov & Ia.M.Fogel', Zhur.tekh.fiz., 7, 931 (1937).
3. N.D.Borisov & Ia.M.Fogel', Zhur.tekh.fiz., 17, 599 (1947).
4. M.A.Blokhin, Zavod.labor., (The Factory Laboratory), 16, 681 (1950).
5. M.A.Blokhin, ibid., 16, 941 (1950).
6. L.S.Birks & E.J.Brooks, Anal.Chem., 22, 1017 (1950).
7. L.S.Birks, E.J.Brooks & H.Fridman, Anal.Chem., 25, 5, 692 (1953).
8. A.Herman Liebhafsky, Anal.Chem., 26, I, 26 (1954).
9. J.William Campbell & F.Howard Carl, Anal. Chem., 26, 5, 800 (1954).
10. M.A.Blokhin, Dissertation, Rostov-on-the-Don, 1954.

Bulletin of the Academy of Sciences of the USSR - Physical Series
Volume 21, Number 10

TABLE OF CONTENTS

	Page Orig.	Trans.
Soviet Physics at the Fortieth Anniversary of the October Revolution - Editorial	1337	1325
Transactions of the Second All-Union Conference on X-Ray Spectroscopy		
Complete list of reports presented at the conference	1342	1329
Width of inner levels and density distribution of electron states in elements of the iron transition group - M.A.Blokhin and V.P.Sachenko	1342	1333
Dependence of the x-ray absorption spectra of atoms in compounds on the character of the bonds - R.L.Barinskii, E.E.Vainshtein & K.I.Narbutt	1351	1341
On determining the density of electron states from x-ray spectra - I.Ia.Nikiforov	1362	1351
Influence of an activator on the x-ray absorption spectrum of a luminescent crystal - K.I.Narbutt & I.S.Smirnova	1367	1356
Investigation of the fine structure of x-ray absorption spectra of alkali halide compounds - I.S.Smirnova & K.I.Narbutt	1375	1363
K absorption spectra of chlorine in alkali metal chlorides - R.L.Barinskii	1381	1369
L absorption and emission spectra of Mo in molybdenum carbide and other compounds - R.L.Barinskii & E.E.Vainshtein	1387	1375
Influence of thermal vibrations of atoms on the electron energy distribution in metals and alloys - I.B.Borovskii & G.N.Ronami	1397	1385
X-ray spectroscopic investigation of solid solutions - I.B.Borovskii, K.P.Gurov, S.A.Ditsman, V.A.Batyrev & N.D.Lobanova	1401	1389
Use of the URS-50-I x-ray equipment as a double crystal spectrometer - I.B.Borovskii & V.V.Shmidt	1412	1400
X-ray spectroscopic investigation of chemical composition in microvolumes of alloys - I.B.Borovskii, N.P.Il'in, L.E.Loseva, I.D.Marchukova & A.N.Deev	1415	1404
X-ray spectroscopic method of investigating the electron state distribution of metals and alloys - N.D.Borisov, V.V.Nemoshkalenko, & A.M.Fefer	1424	1412

The $L\beta_6$ and $L\gamma_5$ lines in the spectra of Cu and Zn - I.A.Rumiantsev & M.I.Korsunskii 1435 1423

L series x-ray spectrum of germanium - G.P.Borovikova & M.I.Korsunskii 1438 1426

External screening and the fine structure of x-ray spectra - S.M.Karal'nik 1445 1432

On the state of atoms in ferromagnetic iron, cobalt and nickel base alloys - I.Ia.Dekhtiar 1452 1440

Effect of neutron irradiation on the fine structure of the K absorption edge of germanium - M.M.Kakhana & E.E.Vainshtein 1459 1447

Quantitative determination of titanium from secondary x-ray spectra - A.S.Ivoilov & N.F.Losev 1465 1452

Translated in 1958 by
Columbia Technical Translations
5 Vermont Ave., White Plains, N.Y.

Number 11 Volume 21 1957

BULLETIN

of the

Academy of Sciences of the USSR

- Physical Series -

(Izvestiia Akademii Nauk SSSR)
(Seriia fizicheskaia)

Reproduction rights reserved

by

Columbia Technical Translations
5 Vermont Avenue
White Plains, New York

Single Issues

$20

Annual Subscription

$215

Lithoprinted in U.S.A.
EDWARDS BROTHERS, INC.
Ann Arbor, Michigan

Transactions of the First Conference on the Spectroscopy of Light-Scattering Media

The First Conference of the Spectroscopy of Light-Scattering Media, organized by the Commission on Spectroscopy of the Academy of Sciences of the USSR, was held in Moscow, March 29-30, 1956.

Representatives from a number of scientific organizations of Moscow, Leningrad and Minsk participated in the Conference. All the reports were followed by lively discussion, testifying to the great current interest in the subject.

In addition to the papers published in the present issue of the Bulletin, the Conference heard the following reports:

"Present day status of the question of light scattering by large particles" by K. S. Shifrin.

"Problems in the investigation of the spectra of reflection from the surface of the earth" by K. S. Lialikov, V. V. Kol'tsov and I. N. Belononova.

"The light field in strongly scattering media" by V. A. Timofeeva.

"Light scattering in a two-dimensional colloid and the optical properties of monomolecular and translucent metallic coatings" by G. V. Rozenberg.

At the request of the Commission the transactions have been prepared for publication by G. V. Rozenberg.

OPENING ADDRESS

- B. I. Stepanov

Spectroscopic methods have long been extensively used in various fields of physics, chemistry, biology, medicine and engineering. As a rule, however, they have been applied to homogeneous and only very weakly dispersive media, such as solutions, vapors and single crystals. Yet, actually most natural substances - powders, fibers, suspensions, colloids, films and so on - are inhomogeneous. While a great deal of valuable data can be obtained by studying such substances in solution, unfortunately the properties of most such substances change when they are dissolved, so that the spectra of solutions yield only indirect evidence. Moreover, many substances simply cannot be brought into solution.

In recent years, an entirely new kind of spectroscopy has developed: the spectroscopy of scattering media. Much of the current work in this field involves collation and classification of experimental material. In some cases the experimental data are used to solve specific analytic problems, in others to elucidate the structure of diverse substances. Here we can list only a few of the infinite variety of vexing problems in this field.

One of the most fundamental problems is that of finding the wavelength dependence and the numerical values of the absorption coefficient and the index of refraction of dispersive media. In our practical work we constantly find that there are no reliable data on the indices of refraction and absorption coefficients of scintillators, dyes, metals, quartz and other substances, particularly, in the infrared region. In many regions of the spectrum, even thin films of quartz (and other optical materials) are entirely opaque, so that absorption by quartz must be studied using layers of very fine particles. With little or no justification, the spectra obtained in this way are identified with the true absorption spectrum of the bulk material. In general, infrared spectroscopy is shifting more and more towards studying the transmission characteristics of strongly dispersive films obtained by compressing powders or fibers. Yet the peculiarities of light propagation in such substances are generally not taken into account.

Where nondispersive media are concerned, it has been established that every change in the spectrum is related to some change in the composition of the molecules or to some change in the nature of the intermolecular interaction. In dispersive media, however, a change in the spectrum may be due to changes in the character of the light propagation laws. This often makes it very difficult to interpret the observed spectra. As an example, when strongly absorbing molecules are adsorbed on silica gel or some other porous medium, their absorption (or reflection) spectrum is often altered. Without knowing the optical properties of dispersive media, it would be impossible to establish whether this change is due to a change in the properties of the molecules when they are adsorbed or whether it is a purely optical effect associated with multiple scattering. This is why we have still not been able to interpret the spectrum of a living leaf. The position of the characteristic band of chlorophyll is not the same in a leaf as in its solution, and the nature of the difference has not been established.

The reflection and transmission spectra of dispersed materials depend not only on the optical constants of the basic substance, but also on the dimensions of the light-scattering particles, the index of refraction of the binding medium, on the relative proportions of the absorbing substance and the binding medium and the thickness of the investigated layer. Variation of one or all of these parameters can radically alter the spectrum and change the absolute values of the reflection and transmission coefficients and thus, of

course, the apparent color of the substance. Thus, for instance, when very greatly fragmented all materials, even strongly absorbing ones, become whitish. This possibility of modifying the color and spectrum of substances is very important in the varnish, textile, paper and phosphor industries. Sometimes it is necessary to produce a coating with distinctive, specific properties, say, with a large reflection coefficient in the infrared region and a small one in the visible region. Such problems can be solved only if one knows how the spectrum depends on the primary parameters of the dispersed substance.

Many important problems also arise in studying luminescent powders, a group of substances including all crystal phosphors. Development of a correct theory of the luminescence of crystal phosphors is predicated on a knowledge of the true absorption spectrum of luminophors. For all practical applications one must also know how the luminescence spectrum depends on the degree of dispersion, the properties of the binding medium and the thickness of the layer when dealing with the transmitted light, as well as on the nature of the backing when using screens. It should also be borne in mind that due to overlapping of the absorption and luminescence spectra, the observed luminescence yield of a powder is not identical with the true yield of the primary substance. In working with powders it is often necessary to consider not only reabsorption, but also secondary luminescence. All of these important problems are just beginning to be studied.

The phenomena encountered when using dispersive light filters also belong to this field of spectroscopy. Their theory, based on concepts of interference, has as yet hardly been developed. Interference effects often arise in studying the reflection and transmission spectra of powder layers and this leads to the appearance of entirely new bands that are in no way connected with the intrinsic properties of the bulk substance. The fact that these effects are as yet inadequately understood is retarding the development, in particular, of infrared spectroscopy.

We must limit our listing to the above few examples. The list could readily be extended butthis would serve little purpose. It is quite clear that while spectroscopy of scattering media reached maturity a long time ago, it is still developing relatively slowly. The experimental investigations have so far been largely random, that is, devoted to the solution of particular rather than general problems. Yet experimentation is undoubtedly being held back by the slow rate at which the basic theory is developing, as well as by the lack of necessary communication between the experimentalists and the theoreticians.

The present meeting on the spectroscopy of dispersive media has been called in an attempt to eliminate these faults, to discuss the results already obtained, and to mark the directions for further investigation. The purely spectroscopic aspects of our problem are closely coupled to the wider problem of the optics of dispersive media, and we have therefore invited scientists of other specialties to our Conference. Their wealth of experience and knowledge will no doubt help us in solving our spectroscopic problems.

SOME ASPECTS OF SPECTROSCOPIC ANALYSIS OF LIGHT-SCATTERING MEDIA AND THE REFLECTING POWER OF COLORED POLYDISPERSIVE MEDIA

- G. V. Rozenberg

We all know how very important spectroscopic analysis has become in industry in the last few decades and what an important tool it is for scientific research. There exists, however, a field extremely important from the practical point of view and involving very many kinds of substances, in which the present methods of spectroscopic analysis are nearly if not entirely impotent. I refer here to analysis of substances in a dispersed state which, because of their nature, can be investigated only by absorption methods. In this article I shall try to clarify the reasons for the difficulties which arise in this field, and to point out ways in which these difficulties may be overcome. Incidentally, I shall present some results of the attempts made to solve certain spectroscopic problems in this field.

Since the optics of light-scattering media has several peculiar properties, and since the fundamental concepts of this field are, for historical reasons, heavily burdened with widely accepted misconceptions, I shall have to start my discussion somewhat far afield.

Spectroscopic analysis must necessarily be based on an understanding of the laws governing the interaction between radiation and matter, but until rather recently, theoretical investigation of this interaction has been virtually restricted to two limiting cases. One of these involves the propagation of radiation in quasi-homogeneous media, when the radiation field parameters are smoothly and relatively slowly varying functions of the coordinates. The other involves emission, absorption, and scattering of radiation by single particles or inhomogeneities imbedded in a homogeneous medium. In the latter case investigation centered on the single event of sudden local transformation of the radiation field through its interaction with the matter. Closely related to such problems are those involving local transformations of the radiation field at simple discontinuous boundaries of a quasi-homogeneous medium (reflection, refraction, etc.).

The intermediate case of the propagation of radiation in scattering (turbid) media, media that cannot be considered quasi-homogeneous, has still hardly been investigated.

The restriction to quasi-homogeneous media is dictated by the fact that one can apply Maxwell's phenomenological equation to them so that the propagation of electromagnetic waves can be described by solving these equations with the appropriate boundary conditions. The development of molecular optics essentially did not alter the matter, since all it contributed to the theory of propagation was definition of the so-called material constants of the medium, determined by its structure and based on the theory of absorption, emission, and scattering of light by individual molecules. In other words, when solving problems of propagation in quasi-homogeneous media, the solution does not involve scattering and dispersion theories.

When dealing with scattering media, however, this is no longer true. The deciding factor which ultimately controls the propagation of radiation in a scattering medium is the way in which the scattering inhomogeneities irradiate each other. Therefore, although it is still possible to keep the theories of scattering and propagation strictly separated, the principal problem as regards the latter is to define the effective field in which the individual inhomogeneities are located and to take into account the interference of the waves scattered by them. Since the most important property of turbid media is their irregular structure, our problem is a statistical one, which does not allow of using the equations of phenomenological electrodynamics or separating the theory of dispersion from that of propagation.

More detailed considerations show, however, that this statistical problem can be greatly simplified. It is found that the interaction of the inhomogeneities breaks up essentially into two parts, a coherent and an incoherent one. The coherent part, due almost entirely to the nearest neighbors of a given scattering inhomogeneity, is important only in dispersion effects, i.e., is evinced only in the form of a change of index of refraction (in general a matrix) of the medium. At the same time, the incoherent part of the interaction, which is due to events occurring throughout the entire volume of the medium, is evinced in the form of multiple scattering, and in most theoretical treatments it is separated artificially from dispersion effects as such.

Let us consider a plane wave, whose mean electric field is $\tilde{\mathbf{E}}$, propagating through a medium containing randomly distributed inhomogeneities. We then have

$$\frac{d\tilde{\mathbf{E}}}{dl} = -\nu\tilde{\mathbf{E}}, \tag{1}$$

where l is the coordinate measured along the direction of propagation of the wave, and ν is a matrix whose components are of the form[1,2]

$$\nu_{ij} = ik_0 n_0 + A(N)\frac{2\pi N}{k_0^2 n_0^2} g_{ij}(0,0) \quad (i,j=1,2). \tag{2}$$

Here N is the number of scattering particles per unit volume, n_0 is the index of refraction of the medium in which the particles are suspended, k_0 is the wave number in vacuum, $g_{ij}(0,0)$ is the mean value of the plane-wave expansion coefficient of the (complex) scattering amplitude matrix (which depends on the scattering angles and is proportional to the 1/2-power of the scattering cross section of the particle, corresponding to a plane wave with the same direction of propagation as the incident wave, and A(N) is a coefficient which accounts for the difference between the effective and mean fields and depends on the concentration and scattering coefficient of the particles and on the form of the scattering indicatrix.

If $g_{ij}(0,0)$ can be diagonalized, then one can introduce the concept of an effective complex index of refraction for each of the two differently polarized components, writing

$$n_i = n_0\left[1 + \frac{2\pi N}{k_0^3 n_0^3} g_{ii}(0,0)\right], \tag{3}$$

which follows from (1) and (2). In particular, if the mean separation between the scattering particles is greater than the wavelength then A(N) = 1, and

$$n_i = n_0\left[1 + \frac{2\pi N}{k_0^3 n_0^3}\operatorname{Im} g_{ii}(0,0)\right] - i\frac{2\pi N}{k_0^3 n_0^2}\operatorname{Re} g_{ii}(0,0). \tag{4}$$

For isotropic scattering, ν_{ij} degenerates to a scalar whose real part is $\frac{1}{2}(\alpha + \sigma)$ where α and σ are the volume coefficients of absorption and scattering of the turbid medium. As for the effective index of refraction of such a medium, it becomes

$$n = n_0\left[1 + \frac{\alpha+\sigma}{2k_0}\cdot\frac{\operatorname{Im} g(0,0)}{\operatorname{Re} g(0,0)}\right] - i\frac{\alpha+\sigma}{2k_0}. \tag{5}$$

We note that while the experimental determination of the imaginary part of the index of refraction, i.e., the coefficient of extinction $(\alpha + \sigma)$, is usually rendered difficult by the presence of multiple scattering (see below), the determination of the phase shift due to the scattering particles is not masked by multiple scattering. Hence in some cases determination of the phase shift may be more expedient from the standpoint of solving certain spectroscopic problems.

Let us now see how we can take account of multiple scattering. The separation of the mutual irradiation of the particles into the coherent (local) and incoherent (distant) parts allows us to make the approximations of geometrical optics, and to reduce the solution of this statistical problem to the formulation of the so-called transfer equation.

As is known, the transfer equation in its application to the optics of dispersive media was first formulated by Hvolson and Schwarzschild about a half-century ago on the basis of rather obvious intuitive considerations, seeing in it only a statement of energy conservation.

The physical content of this equation is very simple. It implies that the change in intensity of a light beam along its length is due to attenuation associated with absorption and scattering, and to intensification as a result of scattering in the beam's direction of light propagating in all other directions. Here it is important that the scattered beams be incoherent relative to each other, so that their intensities will be additive. This is not as obvious as it may seem at first, and requires a detailed analysis which is still far from complete. If, however, it is possible to separate the mutual irradiation of inhomogeneities into a coherent and an incoherent part, then, as was stated above, the coherent part is involved only in absorption and scattering of the direct ray, while multiple scattering involves only the incoherent part.

We should now direct our attention to the fact that what happens to the luminous flux in the scattering, absorption, and double refraction to which it is subjected depends strongly on its polarization. Therefore if one formulates the transfer equation entirely in terms of energy conservation, which means that one is ignoring the the polarization-dependence (and also other conservation laws), the results will unavoidably be incorrect. On the other hand, in attempting to take account of the polarization properties of the light, we are faced with a new problem.

Essentially what we wish to do is to develop a mathematical pro-

cedure which would make it possible to include the dynamic characteristics of the photon flux (its energy and spin) in a geometrical optics description. This is an important and still largely unsolved problem. The situation is made more complicated when we note that the incoherence of the scattered waves will not allow us to describe the luminous flux in terms of the electric and magnetic field strengths. We must use statistical parameters that are additive for an incoherent flux. It is found that the so-called Stokes parameters will serve this purpose, inasmuch as they completely describe the state of the luminous flux from the point of view of both its intensity and its polarization and are closely related to the quantum mechanical density matrix.[2] In their generalized form, the Stokes parameters S_i are defined by

$$S_i = \mathbf{E} \cdot \sigma_i \mathbf{E}^* \quad (i = 1, 2, 3, 4) \tag{6}$$

and can be combined into a single four-dimensional vector-parameter S. Here σ_1 is the unit matrix, and σ_2, σ_3 and σ_4 are the Pauli matrices in the cyclic permutation starting with the third. It is significant that by using these parameters we can now associate every interaction event between radiation and matter with a matrix describing a finite or differential transformation of the vector-parameter. In addition, it becomes possible to include not only the energy conservation law, but other conservation laws (in particular, the law of conservation of angular momentum) and thus to formulate a complete transfer equation. This new equation not only takes into account the polarization of the radiation, but unites (in consistent mathematical terms) the coherent and incoherent part of the interaction between the particles, which means that dispersion phenomena and multiple scattering are treated together.

Strictly speaking, this is no longer a single equation but a set of four linear integro-differential equations of the form[1,2]

$$\frac{dS_i(\bar{l})}{dl} = \sum_j \left\{ -\varkappa_{ij} S_j(\bar{l}) + \frac{\sigma}{4\pi} \int f_{ij}(\bar{l}, \bar{l}') S_j(\bar{l}')\, d\bar{l}' + S_i^0(\bar{l}), \right. \tag{7}$$

where f_{ij} is the scattering indicatrix tensor, $\varkappa_{ij}$ is the extinction matrix whose components are real homogeneous linear functions of the components of the dispersion matrix ν_{ij} and $S_i^0(\bar{l})$ is a function of the radiation of the scattering medium itself, if such radiation is present.

It is easily seen that these equations contain terms of the same order of magnitude as the basic terms in the usual transfer equation although these terms do not appear in the latter. This is a clear indication that the polarization effects should not be neglected.

It should be noted that the deduced equations are valid not only for photons but also for any particles with spin 1/2 and open the way to possible solution of previously insoluble problems such as those involving electro-optical phenomena in colloids, the optics of polycrystalline bodies, etc.

What, then, is the situation as regards spectroscopic analysis of scattering media? It is clear that by investigating the luminous field in the scattering medium or at its boundaries and using the transfer equation we can arrive at an evaluation of the magnitudes and frequency dependence of α and σ. These quantities, referred to a unit volume, can be thought of as characteristics of the scattering medium.

Thus propagation theory may serve as the basis for experimental determination of the volumetric optical characteristics of a scattering medium. If the mean distance between particles is greater than the wavelength, i.e., if A(N) = 1, these characteristics are related to the individual optical characteristics of the isolated scattering particles in a simple and direct manner. Specifically, we can write

$$\sigma = N\sigma^0, \quad \alpha = N\alpha^0, \quad f_{ij} = f_{ij}^0, \tag{8}$$

where σ^0, α^0 and f_{ij}^0 are the scattering coefficient, absorption coefficient and scattering indicatrix for an individual particle. If, however, the separation between the particles is small or comparable to the wavelength, i.e., if $A(N) \neq 1$, Eqs.(8) become invalid and must be replaced by more general equations which can be deduced by generalizing the theory of dispersion to include scattering media. This generalization involves not only clarifying the form of A(N), but also taking into account the very important and peculiar changes in the scattering indicatrix, resulting from interference of waves scattered by neighboring particles.[1] It must be noted that up to the present only preliminary and far from conclusive attempts have been made to solve this problem.

Lastly, we note that the transition from the optical properties of the scattering particles to those of the substance of which they are composed is a different problem lying wholly outside the framework of propagation and dispersion theory. Actually, in a sense it is the inverse of a scattering theory problem.

The clear difference between the three problems - that of determining the optical characteristics of scattering media, that of the transition from these to the individual characteristics of the scattering inhomogeneities and that of going to the optical properties of the substance of which they are composed - is, I believe, a profound one. Not only the theoretical treatment, but also the experimental methods for studying these problems must be entirely different. Yet traditionally these three problems are often combined, which obviously serves only to confuse the situation and hamper their solution. In what follows we shall speak only of the first of these: determination of the optical characteristics of the medium.

Propagation theory developed essentially along two paths. Improved formulations of the transfer equation itself led to mathematical methods for solving it for different turbid-medium models and thus gave rise to an extensive, almost independent branch of mathematical physics. The use of this mathematical apparatus, however, is greatly limited by its computational complexity; hence its application has been restricted to the simplest cases. Computers, it is true, can be used to solve many "direct" problems, but the inverse problems, which are of most interest from the spectroscopic point of view, are still practically insoluble.

At the same time there has been a wide development of methods using very rough approximations whose validity has yet to be demonstrated. In many cases, however, this method of attack has led to very satisfactory results, representing a significant forward step. But the reasons for such individual and sometimes surprising successes remain unclear and the limits of applicability of the various simplifying assumptions have yet to be established.

Therefore, although these methods must be rendered their due, we can hardly hope to use them as the basis for further development of spectroscopic analysis of light-scattering media. It would seem that the only correct path lies in the most rigorous and general formulation of the transfer equation, followed by a search for particular conditions which can be used to obtain a sufficiently accurate approximate solution in relatively simple analytic form. This approach although it necessarily limits the experimental possibilities, may open much greater potentialities for a quantitative solution of the inverse problem.

One of the simplest examples which allows of a completely satisfactory approximate treatment, at least for strongly absorbing media, is the problem of reflection from a semi-infinite medium whose volume characteristics are independent of the coordinates.

In this case one can use the method developed by Kuznetsov[3] in dealing with theory of visibility. Without going into the details of the mathematics, we note only that this method consists of calculating the successive contributions to the reflecting power by scattering of different degrees of multiplicity. Application of this method to an isotropic medium gives an expression for the light reflected by the medium which, in the n-th approximation is*

$$S_i^{\text{ref}}(\vartheta, \varphi) = S_1^0 \sum_{t=1}^{n} \frac{a_{it}(\vartheta, \varphi)}{(1+\beta)^t}, \tag{9}$$

where ϑ and φ are the coordinate angles defining the direction of the line of sight (observation), S_1^0 is the intensity of the incident beam illuminating the medium, $\beta = \alpha/\sigma$ is the ratio of the volume coefficients of absorption and scattering, and

$$a_{it}(\vartheta, \varphi) = \sum_{j=1}^{4} a_{ij_t}(\vartheta, \varphi)\, c_j^0(\vartheta_0, \varphi_0), \tag{10}$$

wherein the $c_j^0(\vartheta_0, \varphi_0) = S_j^0/S_1^0$ characterize the polarization of the incident beam, and $a_{ijt}(\vartheta, \varphi)$ are coefficients depending only on the angles of incidence ϑ_0 and φ_0 and observation ϑ and φ and on the form of the scattering indicatrix.

Let R be the energy reflectivity of the medium, and let us introduce the coefficients $c_i = S_i/S_1$ characterizing the polarizations of the light reflected from the medium. We then obtain

$$c_i R = \sum_{t=1}^{\infty} \frac{a_{it}}{(1+\beta)^t}. \tag{11}$$

---

*In earlier contributions[4] we considered the case where the scattering particles in the lower half-space are suspended in the same medium as that which fills the upper half-space. This is valid, for instance, for media such as powders. If the media differ on the two sides of the interface (say, air and milk), there is an additional regular reflection on the boundary, which leads to an additional term depending on ϑ and φ in Eq.(9). If perfect mirror reflection takes place at the surface and the angle of observation differs from the angle of mirror reflection, we can neglect the surface reflection, although in this case the $a_{it}(\vartheta, \varphi)$ will be different than if there were no mirror surface.

This shows immediately that as β increases the higher multiplicities of scattering become less important, which should change the intensity, the spectral composition, and the polarization of the reflected light. This β-dependence of the relative importance of the different scattering multiplicities is a fundamental effect determining the optical properties of colored turbid media.

As has been shown by Ambartsumian[5], the mean multiplicity of scattering in the case of reflection from a semi-infinite turbid medium is $\sqrt{1+1/\beta}$, i.e., when $\beta \geqslant 1/3$, we obtain adequate accuracy from just the third, or even the second approximation. In addition, for polydispersive media with sufficiently large inhomogeneities, we may assume that the form of the scattering indicatrix is practically independent of the particles themselves, i.e., is independent of β. In particular, this should generally obtain in the case of mixing two or more polydispersive media with different α and σ, as when adding dye to a suspension. Then by simple mathematical operations we obtain[4]

$$\frac{R_0}{R} \approx \frac{(1+\beta)^2}{1+\frac{\beta}{Q}}, \tag{12}$$

where R_0 is the reflecting power of the medium when $\beta = \beta_0$ and

$$Q = 1 + \sum_{t=1}^{\infty} \frac{a_{1,\,t+1}}{a_{11}(1+\beta_0)^t}. \tag{13}$$

It is important to note that R_0 and Q, a quantity which defines the relative contribution of higher multiplicities of scattering when $\beta = \beta_0$, depend on the angles of incidence and observation and on the scattering indicatrix, but must be independent both of the character of the dye and of the dilution of the medium. Thus the simple relation obtained, which fully takes into account secondary scattering and largely also tertiary scattering, is a generalization of Lambert's law to the case of colored media and can serve as the basis, for instance, for solving problems in color engineering as well as problems related to the use of dyes and pigments in the textile industry, architecture, color photography, painting, etc.

If the scattering particles are sufficiently large, that is, if we can neglect the difference between the mean effective field and the mean field in the medium (A(N) = 1), we can use Bouguer's law to describe the mixture of two components whose volume concentrations are C_1 and C_2, i.e., in agreement with (8), write

$$\left.\begin{aligned} \alpha &= C_1\alpha_1 + C_2\alpha_2, \\ \sigma &= C_1\sigma_1 + C_2\sigma_2. \end{aligned}\right\} \tag{14}$$

If we then measure R_0/R as a function of C_2/C_1, we can find the absorption coefficients (α_i) and scattering coefficients (σ_i) of both components in terms of the scattering coefficient of one of them. This fact can be used as a basis for spectroscopic analysis of scattering media where determination of the individual optical properties of the scattering particles is concerned.

The relations obtained can also be used to find the polarization of the reflected light. Restricting ourselves to the second approximation, we obtain[4]

$$p = p_0 \frac{1 + \frac{p_\infty}{p_0} \cdot \frac{\beta - \beta_0}{(1+\beta_0)Q}}{1 + \frac{\beta - \beta_0}{(1+\beta_0)Q}}, \tag{15}$$

where p_0 and p_∞ are the degrees of polarization of the reflected light for $\beta = \beta_0$ and in the limit $\beta \to \infty$. The β-dependence of the polarization found in this way is the well known Umov[6] effect. Also, it can be used for independent determination of β as a functio of the concentration, and thus can serve as the basis for the spectroscopic analysis of polydispersive scattering media.

Experiments to test the relations obtained were undertaken by Il'ina and Rozenberg[7] in the laboratory of E.V.Shpol'skii. The experiments were performed on polydispersive media with different structures, namely, on mixtures of powders, milk, rubber, and para fin. Soluble dyes or pigments were introduced into these media an the reflecting powers were measured (in relative units) as a function of the concentration of the coloring substance; R_0 was taken as the reflecting power of the uncolored substance or of MgO powde The measurements were performed on an FM-1 photometer with wide-ba filters. The light was incident on the surface at an angle of 45° The observations were made at 90° to the surface.

Figure 1 gives the variation of R_0/R with C_{dye}/C_{milk} for milk, c lored by non-scattering (soluble) dyes. The solid line is the the retical curve for Q = 2.3 and $\gamma = \alpha_{dye} / \sigma_{milk} = 0.32$. The theory pr dicts (see Eqs.(12) and (14)) that the experimental curves for the different soluble dyes or different wavelengths should be transformed into each other when the relative concentration is multipli by a factor equal to the ratio o the appropriate values of γ ; th factor is dependent only on the wavelength and the nature of the dye, but not on its concentratio Figure 1 shows some experimental results which have been reduced this way. The agreement obtaine is obviously very good.

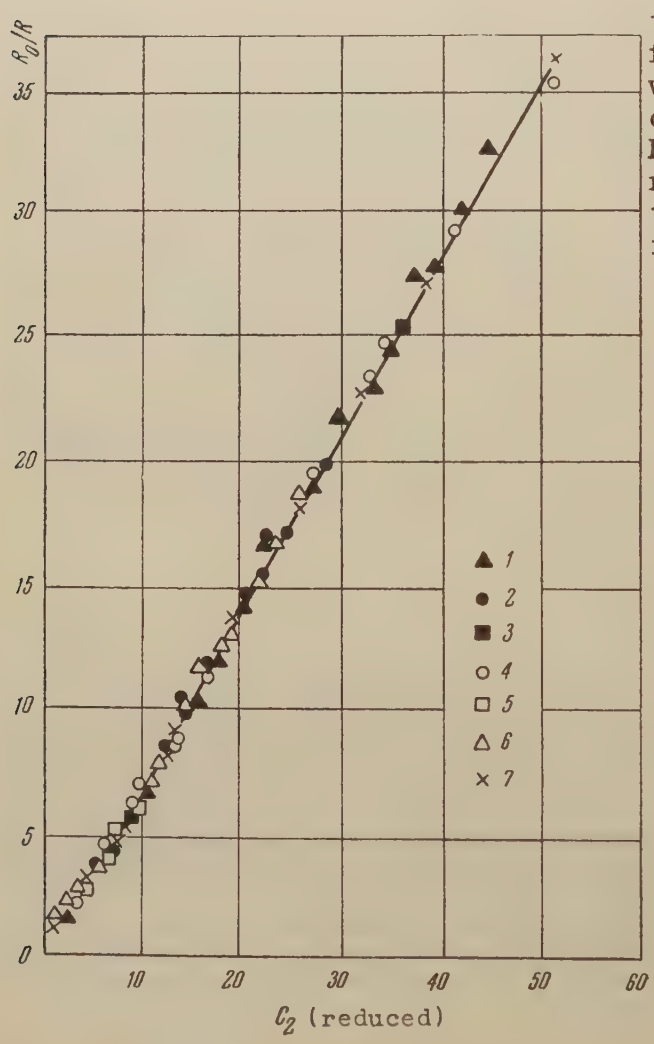

Fig.1. Comparison of measured R_0/R values for colored milk with the theoretical curve for Q = 2.3 and γ = 0.32. The dyes and light filters used were 1) black India ink, green filter, γ = 0.077; 2) black India ink, blue filter, γ = 0.062; 3) red India ink, green filter, γ = = 0.145; 4) methylene blue, red filter, γ = 0.32; 5) methylene blue, green filter, γ = 0.053; 6) points according to Eq.(12) for γ = 0.32. The reduced curves (7) were obtained by multiplying the concentration c by the factor γ /0.32.

We note that if $\beta \gg 1$, we can write $R_0/R \approx Q\beta$, which simplifies the analysis to a large extent. In particular, if $\beta \gg 1$, the wavelength dependence of R_0/R should approximately reproduce (for a fixed angle of observation) the wavelength dependence of α (so long as σ and f_{ij} are independent of the wavelength.

If the dye has an appreciable scattering power, the variation of R_0/R with C_2/C_1 is altogether different, as may be seen from Fig.2. This figure shows the results of measurements on powders and vulcanized rubber colored before vulcanization by ultramarine blue. As C_2/C_1 increases, R_0/R does not tend to infinity in this case, but to some limit. It is therefore more convenient to draw a different kind of graph, namely, one whose x-axis is laid off in values of C_2/C_1 from 0 to 1 and values of C_1/C_2 from 1 to 0.

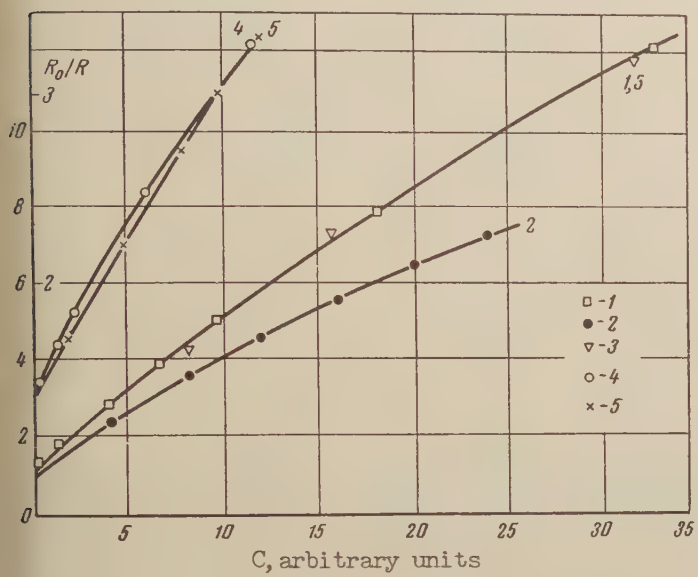

Fig.2

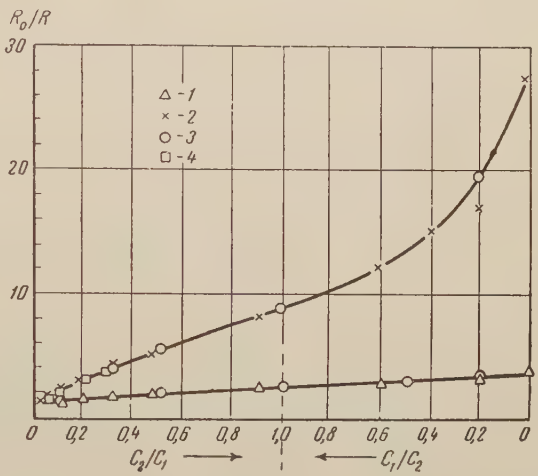

Fig.3

Fig.2. The dependence of R_0/R on the concentration of an insoluble pigment; 1) MgO and ultramarine, yellow light filter; 2) MgO and lamp black; 3) same, but with a different light filter; 4) rubber colored with ultramarine (the reflection coefficient was measured with respect to MgO powder); 5) theoretical value.

Fig.3. Variation of R_0/R with C_2/C_1 for mixtures of MgO and ultramarine powders; 1 & 2) experimental values for MgO and ultramarine in different parts of the spectrum, 3) theoretical values, 4) points on curve (2) reduced according to Eqs.(12) and (14).

In Fig.3 we compare the theoretical predictions with the measured dependence of R_0/R on the concentration for a mixture of MgO powder and ultramarine in two regions of the spectrum. The abcissae in Fig.4 are values of $\beta(C_2/C_1)$, as calculated by Eq.(14) (Bouguer's law) and the ordinates are values of $\beta(C_2/C_1)$, as calculated from our Eq.(12) on the basis of the experimental dependence of R_0/R on C_2/C_1. The experimental data fall close to the bisector of the angle formed by the coordinate axes, which may be taken as substantiation of the basic theoretical propositions.

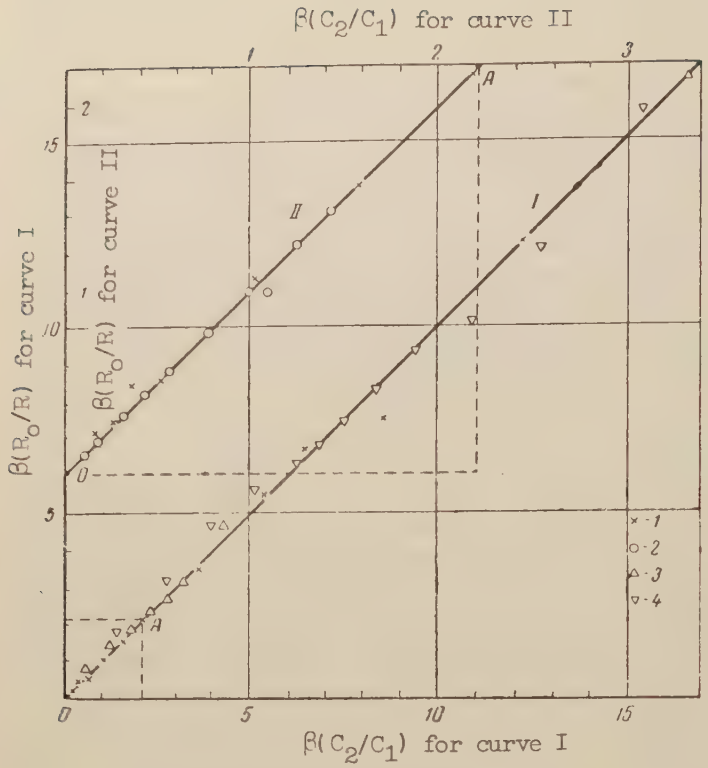

Fig.4. Comparison of values of β calculated from experimental values of $R_0/R[\beta(R_0/R)]$ and for the known concentrations of the coloring powder $[\beta(C_2/C_1)]$. The upper curve II in insert A represents the low-concentration section (A) of curve I plotted to a larger scale. 1 & 2) MgO + ultramarine for different parts of the spectrum; 3 & 4) MgO + lampblack.

We felt it would be of interest to compare the coefficients of absorption of the coloring substances, as determined from the chang in the reflecting power of a polydispersive medium colored by them, with the values obtained according to Bouguer's law by measuring th attenuation of light in a non-scattering solution of the same dye. We did this by coloring milk with crystal violet and black India in and measuring the dependence of R on the concentration, as well as by direct determination of α for these two substances by measuring their transparency in two regions of the spectrum. In the experiments on reflection from colored milk, the value of σ for crystal violet was used to find σ for milk, and this value was then used to find α for India ink. The results of measurements in two regions of the spectrum are given in the table.

α_{dye} according to Bouguer's law	corresponding value of σ_{mol} from measurements of R_0/R	$\alpha_{Ind.ink}$ from R_0/R measurements	$\alpha_{Ind.ink}$ according to Bouguer's law
0.061	1.52	0.117	0.135
0.037	0.545	0.075	0.075

As may be seen, the results are quite satisfactory. Even in the first (worst) case the divergence lies within the experimental error in determining α for India ink as given by Bouguer's law. This experimental error is due to the fact that India ink hardly scatters light.

Thus the experimental tests show the following.

1. Equation (12) is a good description of the experimentally observed variation of the reflecting power of a colored polydispersive medium with the concentration of the dye, at least for values of β that are not too small. From the nature of this variation one can immediately establish whether the dye is in solution.

2. This makes it possible not only to determine the relative concentration of the dye but also to make separate determinations of the volume coefficients of absorption and scattering of the medium, i.e., to find the individual characteristics of the scattering particles.

Thus we now have a way of solving the basic problem of absorption spectroscopic analysis of dispersed media.

Let us now see what conclusions can be drawn from the above.

First, it is clear that the method we have chosen for obtaining approximate solutions of the rigorously formulated equation is validated as a means for solving the inverse problem of propagation theory. Obviously, the work here presented can only be regarded as a first step. There is every reason to believe, however, that under different experimental conditions and with the appropriate theoretical analysis, the reliability of the results can be greatly increased. In other words, it is necessary to find the optimum conditions for solving the various particular problems. This involves among other things the developement of efficient methods of calculation and simplified experimental procedures. It would also be desirable to develop a theoretical basis and means for applying our method to solving problems in the field of luminescence. It is very important to find experimental procedures which would not involve "interfering" with the medium itself by such expedients as varying the dye concentration.

Further, the results obtained make it pressing to develop methods for solving the inverse theoretical problem of scattering from individual particles, without which it is impossible to carry out complete spectroscopic analyses. The situation is still far from satisfactory in this regard. The specific theoretical difficulties holding back solution of this problem give reason to believe that the relations obtained above (or analogous ones) can be used successfully for the experimental determination of the dependence of α^0, σ^0 and f_{ij}^0 on the dimensions of the particles and on the optical properties of the substance of which they are composed, as well as of the dependence of α, σ and f_{ij} on the concentration and size distribution of the particles.

In any case, definite possibilities exist here for the development of spectroscopic analysis of dispersed, scattering media and the urgent need for such analytic procedures lends purpose to further intensive study of these possibilities.

References

1. G.V.Rozenberg, Rasprostranenie elektromagnitnykh voln v mutnykh sredakh (Propagation of electromagnetic waves in turbid media), Thesis, M., 1955.

2. G.V.Rozenberg, Usp.fiz.nauk, 56, No.2 (1955).

3. E.S.Kuznetsov, Izv.AN SSSR,Ser.geog.i geofizika, 5,247 (1943).

4. G.V.Rozenberg, Doklady AN SSSR, 98, 2 (1954); in Sbornik (Symposium) in memory of Academician P.P.Lazarev, M., 1956.

5. V.A.Ambartsumian, Doklady AN Armenian SSR, 8, 101 (1948); J.phys.USSR, 8, 65 (1944).

6. N.Umov, Phys.Zeits., 6,674 (1950); A.S.Toporets, Izv.AN SSSR,Ser.fiz., 14, 594 (1950).

7. A.A.Il'ina & G.V.Rozenberg, Doklady AN SSSR, 98,3 (1954); in Sbornik (Symposium) in memory of Academician P.P.Lazarev, M., 1956.

BASIC PROBLEMS IN THE SPECTROSCOPY OF SCATTERING MEDIA

- B.I.Stepanov

There are two fundamental problems involved in spectroscopic analysis. A spectrum may be thought of as a photograph of the internal properties of the examined system, a photograph in the symbolic sense, for intrinsic properties of atoms, molecules, and crystals are manifested only indirectly. By measuring the intensities of absorption and emission one can determine the positions of energy levels, transition probabilities between them, and their populations and densities. Conversely, if one knows the internal properties of the system, one can learn to predict its spectrum. The basic problems involved in the spectroscopy of scattering media are quite similar. The first problem is to find the intrinsic properties of the substance, i.e., the absorption coefficient of the given substance in the nondispersed state, from the transmission and reflection spectra. At the same time, one must find the index of refraction, on which all the basic properties of these spectra depend. For luminescent substances one must also find the true luminescence spectrum. Spectroscopic methods will be widely used for analyzing scattering materials only when this basic problem has been solved. Only then will it be possible to identify scattering substances unambiguously from their spectrum, clarify the structure of their molecules, observe chemical transformations, and evaluate the effects of intermolecular forces. The second basic problem in the spectroscopy of scattering materials is to calculate the transmission and reflection coefficients and the luminescence intensity of a thick layer as a function of the wavelength from the absorption coefficients and indices of refraction of the main dispersed substance and the "suspending" medium, the degree of dispersion, the thickness of the layer, the properties of the support or backing, and the luminescent characteristics of the main substance. There is also a third, more specialized problem, namely, that of determining the optical properties of a layer of dispersed material of arbitrary thickness from its properties in specific individual cases. In the past few years this last problem has been most thoroughly treated.

Let us consider briefly the different theoretical concepts relating to this problem and see to what extent they may be of help in solving the fundamental problems of the spectroscopy of dispersed media. All the works in this field with which I am familiar can be divided into four basic groups.

1. The general theory of homogeneous light-scattering layers and of diffuse illumination.

2. The theory developed by Gurevich[1], Gershun[2], Kubelka[3,4], Munk[4], and others[5,6].

3. Transfer theory[7-11].

4. The theory based on the model of a light-scattering layer, as developed by Antonov-Romanovskii[12], Stepanov[13,14], Girin[13,14], Bodo[15], and Chekalinskaia[14,16].

Let us start by considering the first theory, which is very general and therefore very important. We subdivide the whole light-scattering layer into separate layers of arbitrary thickness and

consider two neighboring layers of thickness z_i and z_{i+1}. Let $R(z_i)$, $R(z_{i+1})$, $T(z_i)$ and $T(z_{i+1})$ denote the reflection and transmission coefficients of these layers. Then the reflection and transmission coefficients of the combined layer of thickness $z_i + z_{i+1}$ are

$$R(z_i + z_{i+1}) = R(z_i) + R(z_{i+1}) \frac{T(z_i)^2}{1 - R(z_i) R(z_{i+1})}, \tag{1}$$

$$T(z_i + z_{i+1}) = \frac{T(z_i) T(z_{i+1})}{1 - R(z_i) R(z_{i+1})}. \tag{2}$$

These exact formulas are easily derived and are used by almost all authors. If we now assume that the medium is entirely homogeneous (which means that $R(z_i) = R(z_j)$ and $T(z_i) = T(z_j)$ if $z_i = z_j$ for all i and j, and further that R(0) = 0 and T(0) = 1), then Eqs. (1) and (2) lead immediately to

$$R(z) = R(\infty) \frac{1 - e^{-2Lz}}{1 - R_\infty^2 e^{-2Lz}}, \tag{3}$$

$$T(z) = \frac{(1 - R_\infty^2) e^{-Lz}}{1 - R_\infty^2 e^{-2Lz}}. \tag{4}$$

Equations (3) and (4) were first deduced by Stokes for a stack of plane-parallel plates. Later they were derived by Schuster[5] and Gurevich[1] for light-scattering layers. Although these authors considered only special cases, it turns out that Eqs.(3) and (4) are applicable to all scattering layers so long as the scattering medium is entirely homogeneous and the illumination is completely diffuse. They are inapplicable to very thin layers containing only a few scattering particles, since in this case the intrinsic inhomogeneity of the layer will be evidenced.[14] These equations also fail to take account of the distinctive conditions at the outer boundaries of the scattering layer; these, however, can readily be taken into account separately.

It follows from (3) and (4) that the properties of any homogeneous scattering layer can be specified by just two parameters. These may be R_∞ and L. Knowing these parameters, one can calculate the reflection and transmission coefficients for a layer of any thickness. Let us call these the external parameters. Now the external parameters depend in a complicated way on the internal parameters of the scattering layer, which are the indices of refraction and absorption coefficients of the dispersed substance and of the medium in which it is suspended, the size and shapes of the scattering particles and their packing density. The values of R_∞ and L for a given substance are different for different degrees of dispersion. In the general theory we are now discussing, the relations between the external and internal parameters are not made specific. The external parameters must be determined from experiment.

Let us now turn to the papers of Gurevich[1], Kubelka[3,4] and Munk[4], which have given rise to a great deal of work and have been used widely by experimenters.[6,18] All these authors all start with the relations

$$R(\Delta z) = k_1 \Delta z, \qquad (k_2 > k_1) \tag{5}$$

and

$$T(\Delta z) = 1 - k_2 \Delta z, \tag{6}$$

that is, assume that for sufficiently thin layers T and R depend linearly on z. In these equations k_1 and k_2 are coefficients which characterize the light-scattering layer. It is easily shown that Eqs.(5) and (6) are applicable only within very narrow limits. From Eq.(6) it follows that $k_2 \Delta z \ll 1$. It is also clear that Δz cannot be made arbitrarily small, for it obviously must be very large compared to the dimensions l of the scattering particles. Hence

$$l \ll \Delta z < \frac{1}{k_2}$$

or

$$k_2 l \ll 1,$$

which means that when light passes through a layer of thickness l the resultant decrease in intensity must be very small compared to unity. For this reason (5) and (6) can be applied only to weakly absorbing and weakly scattering media.

In any case, proceeding from (1), (2), (5) and (6) and using the boundary conditions R(0) = 0 and T(0) = 1, Gurevich arrives again at (3) and (4) and thus obtains

$$k_1 = \frac{2R_\infty L}{1 - R_\infty^2}, \quad k_2 = \frac{1 + R_\infty^2}{1 - R_\infty^2} L. \tag{7}$$

This means that k_1 and k_2 in (5) and (6) are a new pair of possible external parameters for scattering layers. In his later work[3,4,6] Gurevich restates his results in a different form, but presents nothing fundamentally new. Gershun[2] further develops this work to obtain an expression for the luminance within the layer, and moreover took the influence of the external boundaries into account.

It has recently been shown[14] that Eqs.(5), (6) and (7) follow directly from the very general expressions (3) and (4) if one considers only weakly scattering and weakly absorbing media. The derivation was obtained by expanding (3) and (4) in series in powers of z.

Let us now briefly state the results given by transfer theory. The fundamental radiative transfer equation is

$$dI = \left[-k_2 I(\theta, \varphi) + \frac{k_1}{4\pi} \int f(\theta, \varphi, \theta', \varphi') I(\theta', \varphi') \, d\omega' \right] ds. \tag{8}$$

Here I is the light intensity, ds is the path length of the light, k_2 is the coefficient characterizing the attenuation due to absorption and scattering, k_1 is a coefficient characterizing the energy of the scattered light, and $f(\theta, \varphi, \theta', \varphi')$ is the scattering indicatrix. Unlike the previous equations, (8) is formulated for heterogeneous media, for arbitrary boundary conditions and for any direction of the incident radiation. Like (5) and (6), however, it is also not applicable for strongly absorbing and strongly scattering media in which one cannot assume that the energy absorption and scattering are proportional to ds. It should be noted that (5) and (6) and all that follows from them constitute a particular case in the theory of radiative transfer, namely, the special case of diffusely illuminated homogeneous media.

The transfer equation is very difficult to solve in general,

and so far only some special cases have been treated. On the whole, most of the work done has been in application to astrophysics and the physics of the atmosphere. Rozenberg alone[7] has treated the problem from the purely spectroscopic point of view. He considered a colored turbid medium and developed a method for determining the external parameters k_1 and k_2 separately. This method served as the basis for an original procedure for quantitative determination of the concentration of a colored impurity[19].

All the above attempts to describe the optical properties of scattering layers are purely phenomenological. They involve two (and if we include the scattering indicatrix, even more) parameters of the scattering medium that must be determined experimentally. Their relation to the internal parameters previously mentioned is not considered. This makes it almost impossible to use the results of these theories for solving typical spectroscopic problems. In particular, these theories do not explain the changes induced in spectra when the suspended substance is further fragmented. Essentially, they can be used only to predict the variation of optical properties of a given type of scattering layer as a function of its thickness.

Let us now discuss the possible ways of establishing the relation between the internal and external parameters. For weakly scattering media, the problem consists of finding the laws characterizing the scattering and absorption by an element of volume. To do this one must determine the scattering and absorption laws for a single elementary particle and then take into account their mutual effect. Many investigations particularly those of Mie[20], Fock[21], and Shifrin[22], have been devoted to scattering by simple elementary heterogeneities. The results obtained are quite important in principle. In most important cases, from the practical viewpoint, however, the relation between the external and internal parameters as given by Mie's theory is too complicated to be useful for actual calculations. This situation might be changed somewhat if electronic computers can be utilized for the computations.

A simpler way to establish the relation between the internal and external parameters has been suggested by the fourth group of authors[12-16] (reviewed in Ref.23), who propose matching a specific model with an actual scattering layer. No single model will do for all scattering layers. Hence, for different types of layers one must use different models, determining their suitability experimentally. After comparing with experiment one can either refine the model or discard it and turn to a new one. It seems to me that this is the only reasonable way to attempt to solve the problem, and that it can be used as a basis for interpreting and systematizing the experimental data.

Let us consider the basic model proposed in all of the cited works. Another model, suggested by Antonov-Romanovskii[12], for particles with total internal reflection, has been studied in less detail. Let us compare a real light-scattering layer with a set of elementary layers; the thickness l of an elementary layer equals the mean dimensions of the scattering particles and characterizes the degree of physical dispersion of the given substance. The elementary layers are separated from each other by boundaries whose coefficient of reflection is $2r_0/(1+r_0)$, where r_0 is the coefficient of reflection at the boundary between the main dispersed substance

and the medium in which it is suspended. The coefficient of absorption of the dispersed substance is k, and the binding or suspending medium is assumed transparent. The reflection and transmission coefficients of the system of elementary layers can be calculated using the Stokes[17] formulas deduced for a stack of plane-parallel plates. These formulas can be used if the coefficient of reflection is the same at all boundaries, or strictly speaking when the light is fully diffused. The Stokes formulas are

$$\frac{R_m}{b^m - b^{-m}} = \frac{T_m}{\frac{1}{R_\infty} - R_\infty} = \frac{1}{\frac{b^m}{R_\infty} - R_\infty b^{-m}}, \tag{9}$$

where $m = z/l$ is the number of elementary layers (z is the thickness of the layer), and

$$R_\infty = 2R_1 \frac{1}{1 + R_1^2 - T_1^2 + \Delta}, \qquad b = \frac{1}{2T_1}(1 + T_1^2 - R_1^2 + \Delta), \tag{10}$$

$$\Delta = \sqrt{(1 + R_1 + T_1)(1 + R_1 - T_1)(1 - R_1 + T_1)(1 - R_1 - T_1)}.$$

Here

$$R_1 = r_0 + \frac{(1 - r_0)^2 r_0 e^{-2kl}}{1 - r_0^2 e^{-2kl}}, \tag{11}$$

$$T_1 = \frac{(1 - r_0)^2 e^{-kl}}{1 - r_0^2 e^{-2kl}}.$$

are the reflection and transmission coefficients of a single elementary layer. Girin and Stepanov[13] and Bodo[15] obtained other but equivalent expressions which are more convenient for the numerical calculation of R_∞ in some cases. Computation by means of Eqs.(9) to (11) is rather cumbersome, so that it became necessary to construct appropriate tables. This was done by Chekalinskaia[16] for R_m and T_m for all possible values of kl and r_0. We note that (9) becomes identical with (3) and (4) if we introduce the notation

$$L = \frac{\ln b}{l} \quad \text{and} \quad z/l = m. \tag{12}$$

Eqs. (9)-(12) can be used, in principle, to solve both the fundamental problems in the spectroscopy of dispersed media. The internal parameters r_0,k and l can be used to find $T(z)$ and $R(z)$ for all values of z. One need only know the equations relating r_0 to the indices of refraction of the main substance and the binding or suspending medium. In the literature cited above, it is assumed that one may write approximately

$$r_0 = \frac{(n_1 - n_2)^2}{(n_1 + n_2)^2} \tag{13}$$

where n_1 and n_2 are the indices of refraction of the dispersed main substance and of the binding medium, respectively.

So far Eqs.(9)-(13) can also be used to find the internal parameters of a scattering layer. In this case, there arises, however, an additional fundamental difficulty. As will be explained below, the reflection and transmission coefficients of a given scattering layer are determined by just two external parameters, say R_∞ and L, which can be calculated from experimental data. At the same time, there are three basic internal parameters (r_0, k, and l) related to the two external ones by Eqs.(10)-(12). Hence knowledge of R_∞ and L is not sufficient for calculation of all three

internal parameters. One of them must be determined from other, independent measurements. Stepanov, Chekalinskaia, and Girin[14] have constructed tables and nomograms which can be used to find k and r_0 from R_∞, L, and l, or k and l from R_∞, L, and r_0, or r_0 and l from R_∞, L, and k. The necessary calculations can all be performed very rapidly. Unfortunately, in the last case there arises a further difficulty. Calculations show that for weakly absorbing and weakly scattering layers one can determine only the ratio r_0/l, rather than the two parameters individually.

This procedure for finding two internal parameters of a scattering layer has not yet been tested in practice. The absorption coefficient k alone, however, has been determined for several cases. This was done by measuring the coefficient of reflection R_∞ of an infinitely thick layer and independently determining both r_0 and l. Equations (10)-(12) were then used to calculate k. Antonov-Romanovskii[12] transformed these formulas and obtained simple expressions especially designed for calculating the absorption coefficient. Stepanov, Chekalinskaia, and Girin[14] have tabulated Eqs.(10)-(12), which, of course, does away with the need for numerical computation. Bodo[15] was the first to calculate the absorption coefficient in this way; he calculated the coefficient for powdered violet glass at three wavelengths. When the values of k obtained were compared with experimental data for bulk glass, it was found that the accuracy is about 20%. Similar results were obtained later by Antonov-Romanovskii[12] for certain crystal phosphors. In the accompanying figure we give the results[14] obtained for powdered PS-5 glass using Zhidkova's experimental data.[24] The figure shows the k vs λ curves as calculated from the reflection spectra for powders with different degrees of dispersion and in different binding media. The circles give experimental values. The agreement is almost perfect for curve 2. For the others, the error amounts to as much as 30-40%. It should be noted that the shape of the k vs λ curve is very well reproduced in all cases; this is significant since in most spectroscopic problems, one is interested only in the shape of the curve. Similar results were obtained for powdered SZS-8 glass.

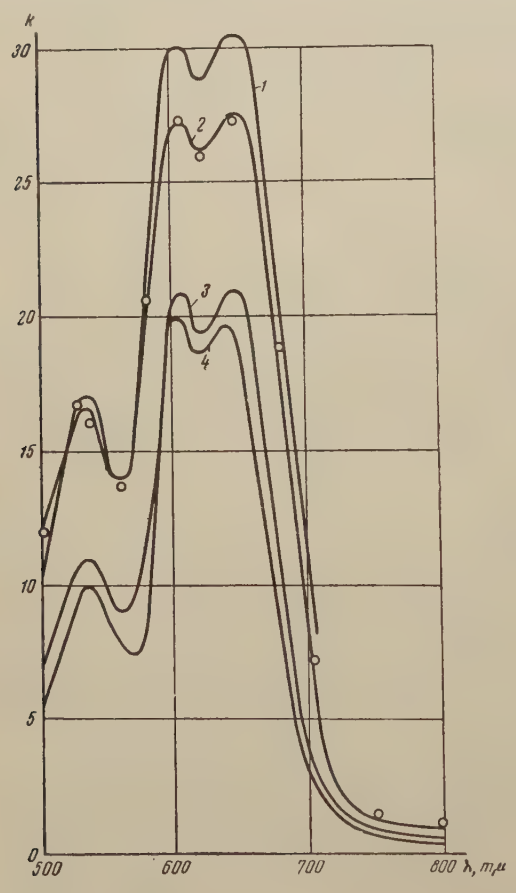

Fig. Curves for $k = f(\lambda)$ as calculated from the reflection spectra of PS-5 glass powder: 1) in air, $l = 50\mu$, 2) in air, $l = 115\mu$, 3) octoil, $l = 50\mu$, 4) anise oil, $l = 50\mu$. The circles denote experimental values of $k(\lambda)$.

Comparison with experiment thus shows that this model correctly represents the fundamental properties of certain scattering layers. The extent of its applicability can be found only by systematic experimental research. Antonov-Romanovskii has already given examples of substances for which this model will not do (substances with a large index of refraction). It is also quite obvious that it can be used only when the particles are densely packed in the scattering layer. For colloids and other media with sparsely distributed particles, the constants k, l and r_0 will not be the true internal parameters, but will only be related to them in some complicated, as yet unknown, manner.

Let us now discuss the relation between the outlined concept and all the other purely phenomenological theories. Before going on, it should be noted that it is very closely related to the general theory of a homogeneous light-scattering layer. Both theories are predicated on complete homogeneity of the layer and the radiation passing through it and do not take account of changes in the properties of the light as it passes through the medium (actually the directed incident radiation is transformed into diffused, and polarized light into nonpolarized). This last situation is described only by transfer theory in taking into account the scattering indicatrix. The similarity of the two theories is evinced in the identical thickness dependences of R and T, i.e., by the fact that Eqs.(3) and (4) are identical to (9) and (12). The unique property of our theory is that it clarifies the relation between the internal and external parameters, as given by Eqs.(10)-(12). Since this relation is hardly a universal one valid for all layers, it follows that the theory itself is of a rather special character.

There is also a close connection between our theory and the theories of Gurevich and other authors. We have already seen that Gurevich's theory is applicable only to weakly scattering and weakly absorbing media and that it is obtained as the first approximation in expanding $R(z)$ and $T(z)$ in Eqs.(3) and (4) in powers of z, with k and k_2 in Eqs.(5) and (6) being defined in terms of R_∞ and L by (7). If we now express R_∞ and L in Eq.(7) in terms of the internal parameters k, l and r_0 using (10) and (12), then for weakly dispersive and weakly absorbing media we arrive at

$$k_1 = \frac{2r_0}{1+r_0} \cdot \frac{1}{l}, \tag{14}$$

and

$$k_2 = \frac{2r_0}{(1+r_0)\,l} + k\frac{1-r_0}{1+r_0}. \tag{15}$$

Now the meaning of Eqs.(14) and (15) is very simple. The quantity $2r_0/(1+r_0)$ is the coefficient of reflection of the interface between two neighboring elementary layers, $1/l$ is the total number of such layers per unit thickness, and $2r_0/(1+r_0)\,l$ is the total reflection coefficient for all the elementary layers in a unit thickness. Thus Eq.(5) is valid only for weakly scattering media in which we need take into account only single scattering within each elementary layer. This deduction is substantiated by analysis of the transition[14] from the exact formulas (3) and (4) to the approximate ones (5) and (6). Further, it is seen from (15) that the coefficient in (6) is the sum of k_1 of Eq.(15) and the ordinary coefficient of absorption multiplied by $\frac{1-r_0}{1+r_0}$. Thus the parameters k_1 and k_2 which

Gurevich and all other authors up to Kortüm & Schöttler[6] (1953) classified as external, are actually internal parameters and characterize directly the index of refraction and the coefficient of absorption of the dispersed substance. The difference k_2-k_1 found in experiment is almost exactly equal to the coefficient of absorption and is independent of the degree of fragmentation.*

The above comparison of all the extant theories leads to the conclusion that they have much in common. They are almost all identical in their description of the properties of homogeneous weakly absorbing and weakly scattering media under diffuse illumination. Only the general theory and the "specific model" theory are applicable to strongly absorbing and strongly scattering homogeneous media with diffuse illumination. The transfer theory is the only one that can take into account the changes in the degree of diffuseness of the light. It is, however, applicable only to weakly absorbing media.

None of these theories can describe the scattering of incident nondiffuse radiation in a strongly absorbing or strongly scattering medium. Their application to such media, where allowable, involves making some very rough approximations.

One may ask why theories formulated with regard to diffuse illumination of homogeneous light-scattering layers give more or less satisfactory agreement with experiment even when the incident radiation is nondiffuse, i.e., a directed light beam. There appear to be two reasons for this. First, as the light penetrates into the layer it is rapidly diffused. Second, r_0 would appear to be virtually independent of the degree of diffuseness of the light. The existing divergence between theory and experiment is undoubtedly due to the use of directed illumination. If the illumination were diffuse, the agreement would probably be much better.

Finally, I should like to say a few words about interference. It is extremely important to take it into account, since interference phenomena are frequently encountered. They must be allowed for in studying the properties of dispersive light filters, in interpreting the reflection and transmission by powders, when $n_1 \approx n_2$ (see Eq.(13)), and in investigating infrared reflection and transmission spectra, when $l \approx \lambda$. In its general form, transfer theory includes this problem, although no conrete results have yet been obtained. All of the other theories we have considered are entirely inapplicable where interference is a major consideration, since in such problems the incident radiation is never diffuse (i.e., is always unidirectional), the coefficient of reflection is small and the scattering indicatrix is highly singular. A separate, distinctive theory is needed to treat interference phenomena in turbid media. At present one can mention only the work of Raman[25], Prishivalko & Stepanov[26], Sethy[27], and Sogani[28] on the theory of dispersive light filters. Now it is not even clear under what experimental conditions one must (or need not) take account of interference phenomena. One of the basic problems is to study many-particle layers possessing interference properties.

---

*These considerations are valid only when the particles are densely packed. Eqs.(14) and (15) cannot be applied to turbid media with loosely packed (i.e., sparsely distributed) particles.

There exist at present a number of different approaches to theoretical treatment of the spectroscopy of scattering media. One of the purposes of my discussion has been to compare the different theories and explain how they are related, in what ways they are similar and in what ways different. This has been a relatively simple goal. It is much more difficult to clarify the range of applicability of any of these theories to specific scattering media. This is because there is still very little experimental data available. Most of it is of a very specialized nature and devoted to unrelated problems. What is needed now is systematic research to test the existing theories and determine their shortcomings. We will then be able to improve the existing theories, construct new models for light-scattering layers, develop new methods for calculating their spectra and optical parameters and evaluate the potentialities of spectroscopic analysis with respect to turbid media.

Institute of Physics and Mathematics,
Academy of Sciences of the Belorussian SSR

References

1. M.M.Gurevich, Trudy GOI (Transactions, State Optical Inst.) 6, No.57 (1931); Phys. ZS., 31, 753 (1930).
2. A.A.Gershun, ibid., 11, No.99 (1936).
3. P.Kubelka, JOSA, 38, 448 (1948); 44, 330 (1954).
4. P.Kubelka & F.Munk, ZS.Techn.Phys., 12, 593 (1931).
5. A.Schuster, Astrophys. J., 21, 1 (1905).
6. G.Kortüm & H.Schöttler, ZS.für Elektrochemie, 57, 353 (1953).
7. V.G.Rozenberg, Doklady AN SSSR, 98, 201 (1954); Thesis, M., 1955.
8. V.A.Ambartsumian, Zhur.eksp.i teor.fiz., 13,9 (1943); Doklady AN SSSR, 38, 81 (1943).
9. V.V.Sobolew, Izv.AN SSSR,Ser.geogr.i geofiz., 8, 273 (1944).
10. E.E.Kuznetsov, ibid., 5, 247 (1943).
11. K.Chandrasekhar, Transfer of Radiant Energy (Cited in Russian trans., M, 1954).
12. V.V.Antonov-Romanovskii, Zhur.eksp.i teor.fiz., 26, 459 (1954).
13. O.P.Girin & B.I.Stepanov, Zhur.eksp.i teor.fiz., 27, 467 (1954).
14. B.I.Stepanov, Iu.I.Chekalinskaia & O.P.Girin, Trudy (Transactions, Inst. of Phys. & Math., No.1, 152, 1956.
15. Z.Bodo, Acta Phys. Hung., 1, 135 (1951).
16. Iu.I.Chekalinskaia, Trudy (Transactions, Inst. of Phys. & Math., No.1, 1956).
17. G.Stokes, Mathemat. and Phys. Papers, 4, 145 (1904).
18. F.Braun, Chim.Peintures, 16,368 (1953); Rayone et fibres synthet., 9, 39 (1953).
19. A.A.Il'ina & G.V.Rozenberg, Doklady AN SSSR, 98, 365 (1954).
20. G.Mie, Ann.d.Phys., 25, 377 (1907).
21. V.A.Fock, Usp.fiz.nauk, 36, 308 (1948); 43, 587 (1951).
22. K.S.Shifrin, Rasseianie sveta v mutnoi srede (Light-scattering in a Turbid Medium, 1951).
23. G.Gergely, Magyar Fiz.Foluoirat, 4, 77 (1956).
24. Z.V.Zhidkova, Zhur.eksp.i teor.fiz., 27, 458 (1954).
25. C.Raman, Ind.Acad.Sci.Sect.A, 29, 381 (1949).
26. A.P.Prishivalko, Present issue of the Bulletin, p. ; B.I.Stepanov & A.P.Prishivalko, Trudy (Transactions, Inst. of Phys. & Math., No.2, 189, 1957); A.P.Prishivalko, ibid., p.206.
27. N.Sethy, Proc.Ind.Cult.Sci., 6, 121 (1920).
28. C.Sogani, Phil.Mag., 1, 32, (1926).

ON THE MULTIPLICITY OF LIGHT SCATTERING

- Iu.I.Chekalinskaia

Investigations devoted to the optics of scattering media can be divided into two groups. In the one group (dealing with transparency and visibility and the optical properties of colloidal systems[1-5]) only single scattering of light is treated, while in the other group multiple scattering is considered. The results of the first group can be used to describe the optical properties of weakly scattering media. In dealing with strongly dispersive media and thick layers of weakly scattering media, one must take into account multiple scattering.[6-20] It is natural to inquire about the bounds of applicability of single-scattering theory. Or, more broadly, one can raise the question of the relationships between the different multiplicities of scattering.

This question has already been discussed in the literature (Rozenberg[8] and Theissing[17]). In the present report we deduce expressions for the intensity of light which has undergone different multiplicities of scattering taking into account the absorption of the medium. In addition, we investigate the relative intensities of the light scattered with different multiplicities in the reflected flux as a function of the coefficient of absorption and the intensity of forward scattering at different depths.

Consider a light-scattering layer contained between two infinite planes. We shall assume that the scattering particles are distributed uniformly throughout the layer and that the number of particles per unit volume is quite large. Then the intensities are (approximately) continuous functions of the layer thickness, and we can use differential calculus. We shall describe the light intensity within the layer in terms of two light fluxes, one propagating forward in the direction of incident radiation, and the other backward. The first flux is composed of the unscattered light and the light which has undergone one, two, three or more scatterings, whereas the second flux consists only of scattered light. Following Theissing[17] and Dexter & Beeman[18], we shall characterize the scattered light as the sum of singly, doubly,...scattered light. We shall denote the light fluxes that have undergone k scatterings forward (1) and backward (2) by $I_k^{(1)}$ and $I_k^{(2)}$, $(k = 1,2,3...)$. When light passes through a layer of infinitesimal thickness dz at a depth z, part of it is scattered, part absorbed and part simply transmitted. We shall assume that the forward and backward scatterings (the latter may be called reflection) as well as the absorption in the elementary layer are proportional to its thickness dz. If the intensity of light incident on this layer is $I^{(1)}$, the intensity reflected is $I^{(1)}rdz$, that scattered in the forward direction is $I^{(1)}tdz$, and that absorbed is $I^{(1)}\mu dz$ leaving $I^{(1)}[1-(r+t+\mu)]$ as the portion transmitted without scattering. Here r, t and μ are empirical constants dependent on the difference between the indices of refraction of the dispersed substance and the suspending medium, the size of the scattering particles, and the index of absorption of the dispersed substance; r characterizes the reflection, t the forward scattering, and μ the absorption in a layer of unit thickness. The relation between the forward and backward scattering coefficients is determined by the shape of the scattering indicatrix for a single parti-

cle. The quantity $\alpha = r + t + \mu$ determines the attenuation due to scattering and absorption in a layer of unit thickness.

The change in intensity of the direct (unscattered) forward light in the layer of thickness dz is therefore

$$\frac{dI^{(1)}}{dz} = -\alpha I^{(1)}.$$

The intensity of the singly scattered forward light is decreased due to absorption and high-order scattering and increased by scattering of the "direct" light in the layer dz, so that we can write

$$\frac{dI_1^{(1)}}{dz} = -\alpha I_1^{(1)} + tI^{(1)}.$$

The intensity of the scattered k-th multiplicity light changes for the same reasons as that of the singly scattered light, except that $I_k^{(1)}$ is further increased by the reflection of the $(k-1)$-st multiplicity light propagating backward, so that we have

$$\frac{dI_k^{(1)}}{dz} = -\alpha I_k^{(1)} + rI_{k-1}^{(2)} + tI_{k-1}^{(1)}. \qquad (1)$$

Similarly, we obtain the set of equations for the backward flux, namely,

$$-\frac{dI_k^{(2)}}{dz} = \alpha I_k^{(2)} + rI_{k-1}^{(1)} + tI_{k-1}^{(2)} \text{ and } -\frac{dI_1^{(2)}}{dz} = -\alpha I_1^{(2)} + rI^{(1)}. \qquad (1')$$

Unlike Theissing's equations, these include absorption as well as scattering. Equations (1) are valid if one can choose a layer of thickness dz such that only single scattering takes place within it. Otherwise, light of the k-th multiplicity can be transformed in the layer not only into the $(k+1)$-st but also into higher multiplicity components. This restriction makes the theory inapplicable to strongly scattering media.

We now integrate (1) with the boundary conditions

$$I^{(1)}(0) = I_0, \quad I_k^{(1)}(0) = 0 \text{ and } I_k^{(2)}(d) = 0,$$

where d is the thickness of the entire scattering layer. This gives

$$\begin{aligned} I^{(1)}(z) &= I_0 e^{-\alpha z}, \\ I_1^{(1)}(z) &= I_0 tz e^{-\alpha z}, \\ I_2^{(1)}(z) &= I_0 e^{-\alpha z}\left[\frac{(tz)^2}{2} + \frac{r^2 z}{2\alpha} + \frac{r^2}{4\alpha^2} e^{-2\alpha d}(1 - e^{2\alpha z})\right], \end{aligned} \qquad (2)$$

. . . . . .

$$\begin{aligned} I_1^{(2)}(z) &= \frac{I_0 r}{2\alpha} e^{\alpha z}(e^{-2\alpha z} - e^{-2\alpha d}), \\ I_2^{(2)}(z) &= \frac{I_0 rt}{2\alpha^2} e^{\alpha z}[\alpha z(e^{-2\alpha z} + e^{-2\alpha d}) + e^{-2\alpha z} - e^{-2\alpha d}(1 + 2\alpha d)], \end{aligned} \qquad (2')$$

As $\alpha d \to \infty$, the solutions become

$$\begin{aligned} I^{(1)}(z) &= M_0, I_1^{(1)}(z) = M_1, I_2^{(1)}(z) = M_2 + \frac{r^2}{2\alpha t} M_1, \\ I_3^{(1)}(z) &= M_3 + \frac{r^2}{\alpha t} M_2 + \frac{r^2}{2\alpha^2} M_1, \end{aligned}$$

$$I_4^{(1)}(z) = M_4 + \frac{3}{2}\frac{r^2}{\alpha t} M_3 + \frac{r^2}{2\alpha^2}\left(2 + \frac{r^2}{2t^2}\right) M_2 + \frac{r^2}{2\alpha^3}\left(t + \frac{r^2}{4t}\right) M_1, \qquad (3)$$

$$I_1^{(2)}(z)=\frac{r}{2\alpha}M_0,\ I_2^{(2)}(z)=\frac{r}{2\alpha}M_1+\frac{rt}{2\alpha^2}M_0,$$
$$I_3^{(2)}(z)=\frac{r}{2\alpha}M_2+\frac{r}{2\alpha^2}\left(\frac{r^2}{2t}+t\right)M_1+\frac{r}{2\alpha^3}\left(t^2+\frac{r^2}{4}\right)M_0,$$
$$I_4^{(2)}(z)=\frac{r}{2\alpha}M_3+\frac{r}{2\alpha^2}\left(t+\frac{r}{t}\right)M_2+\frac{r}{2\alpha^3}\left(t^2+\frac{5}{4}r^2\right)M_1+\frac{r}{2\alpha^4}\left(t^3+\frac{3}{4}r^2t\right)M_0, \quad (3')$$
$$\ldots\ldots\ldots\ldots\ldots\ldots\ldots\ldots\ldots\ldots\ldots\ldots\ldots\ldots$$

where $M_n=I_0\frac{(tz)^n}{n!}e^{-\alpha z}\ (n=0,1,2,3\ldots)$.

For the particular case of strong forward scattering ($t\gg r$), when we can neglect terms of order r^3, the expressions for the forward and backward components of any given multiplicity can be written in the form

$$I_k^{(1)}=M_k+\frac{r^2}{2}\sum_{p=1}^{k-1}\frac{(k-p)\,t^{p-2}}{\alpha^p}M_{k-p},$$

$$I_k^{(2)}=\frac{r}{2\alpha}\sum_{p=1}^{k}\left(\frac{t}{\alpha}\right)^{p-1}M_{k-p}. \quad (4)$$

Analysis of the above solutions leads to the following.

1. The intensity of the reflected light depends explicitly on the coefficient of absorption. Thus, if we set $z=0$ in (3'), we have

$$I_1^{(2)}=\frac{I_0r}{2\alpha},\quad I_2^{(2)}=\frac{I_0rt}{2\alpha^2},\quad I_3^{(2)}=\frac{I_0r}{2\alpha^3}\left(\frac{r^2}{4}+t^2\right),$$
$$I_4^{(2)}=\frac{I_0r}{2\alpha^4}\left(t^3+\frac{3}{4}tr^2\right),\quad I_5^{(2)}=\frac{I_0r}{2\alpha^5}\left(t^4+\frac{3}{2}t^2r^2+\frac{r^4}{8}\right),$$
$$I_6^{(2)}=\frac{I_0r}{2\alpha^6}\left(t^5+\frac{5}{2}t^3r^2+\frac{5}{8}tr^4\right),$$
$$I_7^{(2)}=\frac{I_0r}{2\alpha^7}\left(t^6+\frac{15}{4}t^4r^2+\frac{15}{8}t^2r^4+\frac{5}{64}r^6\right), \quad (5)$$

Figure 1 shows the functional dependence of the intensity of reflected light of different multiplicities on the coefficient μ characterizing the absorption (for $r=0.1$ and $t=0.9$). As may be seen the portion of reflected light decreases with increasing μ which is qualitatively borne out by experiment.

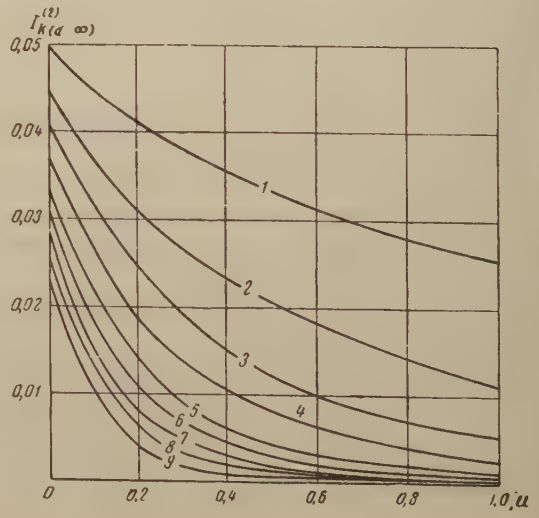

Fig. 1. Intensity of the reflected light as a function of the absorption coefficient (the numbers of the curves indicate the different multiplicities of scattering).

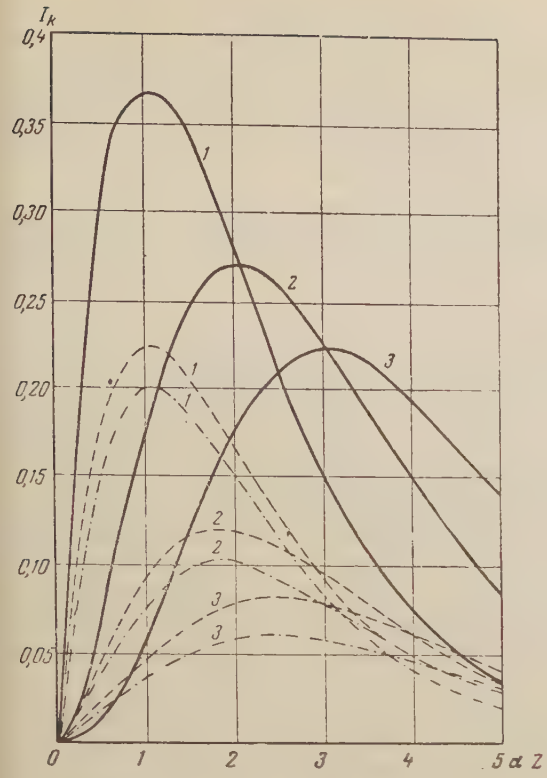

Fig.2. Variation of the intensity of the forward scattered light as a function of the optical depth (the numbers at the curves indicate the different multiplicities of scattering). Solid lines - $t = 1$, $r = 0$, and $\mu = 0$. Dash lines - $t = 0.5$, $r = 0.4$, and $\mu = 0$. Dot-dash lines - $t = 0.6$, $r = 0.4$, and $\mu = 0.1$.

Theissing's equations do not take account of absorption. He attempted to allow for absorption at the last stage of his development, replacing $e^{(r+t)z}$ by $e^{-(r+t+\mu)z}$, and arrived at the incorrect conclusion that the coefficient of reflection of an infinitely thick layer is independent of μ.

2. It follows both from the curves of Fig.1 and Eq.(5) that the intensities of the different multiplicities of scattered light decrease unequally with the increase in μ; the higher multiplicities decrease more rapidly. Thus if μ is sufficiently large, one need consider only the first two orders of scattering, i.e., single and double.

3. The intensities of the different multiplicities of forward scattered light in an infinitely thick medium first increase with the optical depth, reach a maximum value, and then begin to decrease. Fig.2 shows the variation of the scattered light intensity with the optical thickness αz of the layer for a number of different values of μ, r and t. It is seen that the different multiplicities have maximum intensities at different αz values. As we go to higher multiplicities, the maxima are gradually flattened out. Media with $r = 0$ have maximum $I_1^{(1)}$ at $\alpha z = 1$, maximum $I_2^{(1)}$ at $\alpha z = 2$, and maximum $I_k^{(1)}$ at $\alpha z = k$. If $r \neq 0$ and $t \neq 0$, the maxima of all the multiplicities except that for the singly scattered light move towards smaller αz. The maximum of the singly scattered light always remains at $\alpha z = 1$.

It is interesting to compare the above results with Timofeeva's experimental data[21], which has been qualitatively explained by Shuleikin[20]. The curves of Fig.2 have some resemblance to those of Timofeeva, which give the intensity of scattered light at various angles of observation as a function of the optical thickness αz. We have already explained how in our case the magnitude and position of the maxima depend on the multiplicity. Now Timofeeva found a similar dependence on the angle of observation. This makes it reasonable to suppose that the light scattered at a given angle has been scattered a definite number of times. Small scattering angles correspond primarily to low multiplicities; large angles to high scattering orders. Thus, for instance, it is established by Timofeeva that for a scattering angle of 10° the intensity of scattered light has its maximum value at a depth $\alpha z = 2$, the αz value at which the maximum for double scattering occurs. Thus it may be inferred that the light observed at an angle of 10° is due primarily to double scattering.

The curves of Fig.2 do not explain why Timofeeva observed a decrease in the depth at which the maxima occur in the case of observation at angles greater than 50°. There is reason to suppose that a like result will be obtained if one includes not only the absorption, but the change in r and t for the different multiplicities of scattering in setting up and solving the equations.

4. The greater the thickness of the light-scattering layer, the larger the contribution of the higher multiplicities to the forward scattered light flux.

It will be evident from Fig.2 that in a nonabsorptive medium scattering only in the forward direction ($\mu = 0$, $r = 0$, $t \neq 0$) the doubly scattered light is more intense than the singly scattered even at $\alpha z > 2$, while at $\alpha z > 3$, the triply scattered light gives the main contribution together with the light of higher orders. For $r \neq 0$ and a fixed value of $(r + t)$, the greater the absorption coefficient the deeper one must go before the higher multiplicities become predominant. Thus, if $t = 0.6$ and $r = 0.4$ in a nonabsorptive medium, the intensity of the doubly scattered light is greater than that of the singly scattered starting with $\alpha z = 2.8$. If, on the other hand, $r = 0$, this occurs at $\alpha z = 2$. Further, it will be seen from the curves of Fig.2 that absorption also retards the predominance of the multiply scattered light.

5. In the special case when $r = 0$ (nonreflecting medium) Eqs. (4) are simplified and become

$$I^{(1)} = I_0 e^{-\alpha z}, \quad I_1^{(1)} = I_0 t z e^{-\alpha z}, \quad I_2^{(1)} = I_0 \frac{(tz)^2}{2!} e^{-\alpha z}, \ldots \quad I_n^{(1)} = I_0 \frac{(tz)^n}{n!} e^{-\alpha z}, \ldots$$

Similar expressions were obtained by Dexter & Beeman[18] who treated an analogous problem, but without taking reflection into account.

6. If we are not interested in the multiplicity of the forward scattered light, but wish only to differentiate between the transmitted and reflected light, we can deduce the following expression for the coefficient of reflection for an infinitely thick layer

$$R_\infty = \frac{r}{2(r+\mu)} + \frac{r^3}{8(r+\mu)^3} + \frac{r^5}{16(r+\mu)^5} + \frac{5r^7}{128(r+\mu)^7} + \ldots$$

This expression is identical with the infinite series obtained by Gurevich.[19] Thus each term in Gurevich's formula for R_∞ represents the contribution from successive odd multiplicities of scattering.

7. If one considers only the first two multiplicities of scattering in the reflected light and assumes that a colored medium scatters in the same way as a colorless one, the ratio of the coefficient of reflection for noncolored and colored media is

$$\frac{R_\infty(\mu = 0)}{R_\infty(\mu \neq 0)} = \left(1 + \frac{\mu}{r+t}\right)^2 \cdot \frac{\left(1 + \frac{t}{r+t}\right)}{\left(1 + \frac{t}{r+t}\right) + \frac{\mu}{r+t}}.$$

This is the same as Rozenberg's[8] equation (1). In Rozenberg's notation $\frac{\mu}{r+t} = \beta$ and $1 + \frac{t}{r+t} = Q$. We have assumed hitherto that r and t are the same for the scattered and direct light and that these coefficients are independent of the multiplicity of scattering. This assumption is strictly valid only when the scattering

medium is illuminated by completely diffuse light. In general, the forward and backward scattering coefficients are not equal for directed and diffuse light. In further work we intend to take this into account and investigate the dependence of r and t on the multiplicity.

Institute of Physics and Mathematics
Academy of Sciences of the Belorussian SSR

References

1. E.V.Piaskovskaia-Fesenkova, Doklady AN SSSR, 61, 1035 (1948).
2. E.V.Piaskovskaia-Fesenkova, Astr.zhurn. (Journ. of Astronomy),24, 2, 119 (1947).
3. V.G.Fesenkov, Astr.zhurn., 20, 2 (1943).
4. V.G.Fesenkov, Trudy (Transactions, "Sternberg" State Astronomical Institute) 6, 3, 3 (1935).
5. K.S.Shifrin, Rasseianie sveta v mutnoi srede (Light scattering in a turbid medium), M., 1951.
6. O.P.Girin & B.I.Stepanov, Zhur.eksp.i teor.fiz., 27, 467 (1954).
7. V.V.Antonov-Romanovskii, Zhur.eksp.i teor.fiz., 26, 459 (1954).
8. G.V.Rozenberg, Doklady AN SSSR, 98, 201 (1954).
9. E.S.Kuznetsov, Izv.AN SSSR, Ser.georg.i geofiz., 5, 247 (1943).
10. V.A.Ambartsumian, Zhur.eksp.i teor.fiz., 13, 323 (1943).
11. K.Chandrasekhar, Transfer of Radiant Energy (Cited in Russian trans., M., 1954).
12. Z.Bodo, Acta Phys. Hung., 1, 135 (1951).
13. A.A.Gershun, Trudy GOI (Transactions, State Optical Inst.),11,No.99, 43 (1936).
14. V.V.Sobolev, Izv.AN SSSR, Ser.geogr. i geod., 8, 273 (1944).
15. P.Kubelka & F.Munk, ZS.tech.Phys., 12, 593 (1931).
16. P.Kubelka, JOSA, 38, 448 (1948).
17. H.Theissing, JOSA, 40, 232 (1950).
18. D.Dexter & W.Beeman, Phys.Rev., 76, 1782 (1949).
19. M.M.Gurevich, Trudy GOI (Transactions, State Optical Inst.) 6, No.57, 1 (1931).
20. V.V.Shuleikin, Fizika moria (Physics of the Sea), M., 1953.
21. V.A.Timofeeva, Doklady AN SSSR, 76, 6, 831 (1951).

ON DETERMINING THE TRUE ABSORPTION OF ADSORBED SUBSTANCES FROM THE DIFFUSE REFLECTION SPECTRA (Abstract*)

- Z. V. Zhidkova

The report describes further research on the determination of the true absorption spectrum $K(\lambda)$ of dispersed substances by the diffuse reflection procedure. The previous experiments[1] were performed on opaque, completely colored powders (pigments, paints, powdered colored glass, etc.). It was established both experimentally[1] and theoretically[2] that the case of weakly absorbing substances in the dispersed state the plot of -log R vs the wavelength λ qualitatively reproduces the $K(\lambda)$ curve for the substance in the bulk (here R is the coefficient of reflection). The maxima and minima of -log R and K occur at the same values of λ, but are more smeared out in the case of -log R because of the characteristics of light transmission through scattering media. The similarity of these curves is greater for higher degrees of dispersion of the powder and for larger values of the index of refraction of the powdered substance and the binding medium.

In the present work the investigation was extended to adsorption phenomena, the experiments being performed on adsorbate powders, whose particles are colored only on the surface.

This complicates the problem by making it necessary to take into account and evaluate physico-chemical factors affecting the absorption spectrum of the adsorbed substance. These factors must be distinguished and separated from the optical ones.**

The experiments were performed on powders consisting of fused and unfused particles of glass and quartz with coloring materials adsorbed on them.

The experiments established the following.

A. The diffuse reflection spectrum, that is, the -log $R(\lambda)$ curve of the adsorbate reproduces qualitatively the absorption curve $D(\lambda)$ of a film of the adsorbed substance, in that 1) maxima and minima occur at the same values of λ and 2) if there is more than one maximum, their relative magnitudes correspond.

B. In view of the light-transmission characteristics of scattering media, the shape of -log $R(\lambda)$ curve is always somewhat different from that of the $D(\lambda)$ curve.

If the dispersion curves of the adsorbent and binding medium are parallel or almost parallel, a decrease of the relative index of refraction n_o of the adsorbent and the medium leads to an increase in the half-width of the -log $R(\lambda)$ curves and smearing out of the maxima and the minima. The greater n_o, the greater the similarity between the two curves mentioned in paragraph A.

---

*Complete report in Sb."Primenenie metodov spektroskopii v promyshlennosti prodovol'stvennykh tovarov i sel'skom khoziaistve" (Use of Spectroscopic Methods in the Food Industry and Agriculture) Leningrad State University Press, 1957.

**Among the optical factors affecting the reflection spectrum are the size of the powder particles, the relative index of refraction, the angle of incidence of the light, the angle of observation, etc.

If the dispersion curves of the binding medium are far from parallel to those of the adsorbent, the -log R curve may be very different from the D curve in that the positions of the minima and maxima will occur at different values of λ and the relation between the heights of the maxima will be changed.

C. As opposed to powders in which the particles are colored throughout their volume, in the present case, variation of the geometric size of the adsorbent grains is not an optical factor; if one varies the grain size without changing the character of their adsorptive surface, the -log $R(\lambda)$ curves will not change. This was observed for fused particles and is true for monomolecular and even non-monomolecular adsorbed layers.

D. If the physico-chemical properties of the adsorbed layer change with variation in the degree of dispersion of the adsorbent, the -log $R(\lambda)$ curves may be greatly altered. This alteration reflects an actual change in the state of the coloring material adsorbed on the powder with increase or decrease of the size of the powder grains. This is the situation that arises in the case of powders of nonfused particles and particles having a well developed adsorptive surface (highly porous adsorbents).

References

1. Z.V.Zhidkova, Zhur.eksp.i teor.fiz., 27, 459 (1954).
2. O.P.Girin & B.I.Stepanov, Zhur.eksp.i teor.fiz., 27, 467 (1954).

SPECTROPHOTOMETRIC INVESTIGATION OF MIXTURES OF POWDER SPECIMENS (Abstract*)

- A.P.Ivanov & A.S.Toporets

There are cases in which one must deal with reflecting layers consisting of particles that differ as regards both their absorbing and scattering powers. By varying the relative concentration of the components of such a system one can to some extent change both the reflected spectrum and the integral reflection coefficient.

There are no theoretical investigations of such systems. Therefore attempts to calculate the reflection spectrum of such a mixture from the reflection spectra of its components are necessarily based on regularities established for systems of identical particles. Authors treating the subject generally assume that the coefficients of absorption and scattering are additive, i.e., that the absorption and scattering coefficients of a mixture are a linear combination of the coefficients of the components.

That these coefficients are additive cannot be doubted when the absorption and scattering are continuous functions of the thickness. Actually, however, light-scattering media consist of particles of finite dimension. To satisfy the continuity condition, therefore, it is necessary that an "element of volume" contain a sufficiently large number of particles and that these particles be characterized by weak absorption and weak scattering. It follows that the scattering and absorption need not always be additive.

We attempted to approach this problem from the point of view of studies taking into account the actual characteristics of scattering media, including their lack of continuity.

Our investigations were performed on the reflection spectra of mixtures of glass powders, because their fundamental properties are known or can be easily found.

Using earlier work by Bodo[1] and Girin & Stepanov[2] as a basis, we propose a new method for calculating the reflection coefficient of a mixture from the known coefficients of the component substances. The values obtained in this way are in good agreement with the experimental data.

During the course of the work we also discovered that the shape of the reflection spectrum depends not only on the composition of the mixture, but also on the degree of dispersion of the powder. For mixtures with the same composition but with different particle dimensions, the maxima and minima of the curves may occur at different wavelengths.

References

1. Z.Bodo, Acta Phys. Hung., 1, 135 (1951).
2. O.P.Girin & B.I.Stepanov, Zhur.eksp.i teor.fiz., 27, 467 (1954).

*No information regarding publication of the full report given. Translator.

INVESTIGATION OF THE REGULARITIES OF EMISSION OF FINELY DISPERSED LUMINESCENT MEDIA

- A.P.Ivanov

The present communication deals with the dependence of the luminescence of a scattering layer on its optical parameters.

Assuming as an approximation that the scattering, absorption, and emission are continuous functions of the layer thickness, we deduced formulas characterizing the luminescence output both on the side of excitation and on the opposite (back) side of the screen. These formulas are applicable to the excitation of luminescence by ultraviolet as well as by elementary particles (α- and β-particles).

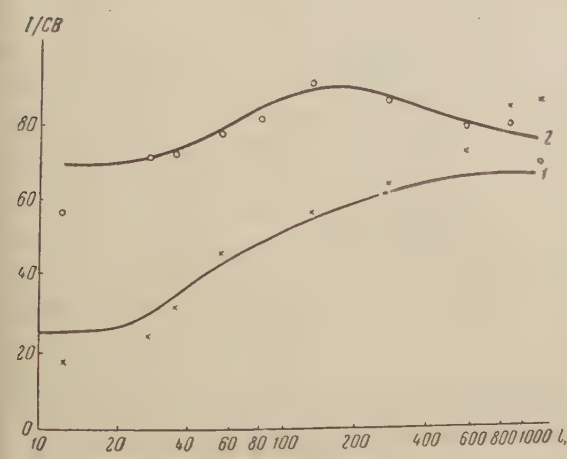

Fig. Luminescence output of powdered ZhS-9 glass as a function of the particle dimensions for two values of the index of refraction and wavelength of the incident radiation: 1) K = 0.5 mm^{-1}, λ = 365 mμ; 2) K = 10 mm^{-1}, λ = 312 mμ.

Analysis of our results brought out the regularities characterizing the variation of the luminescence output as a function of the degree of dispersion, the index of refraction, the coefficient of absorption, the thickness of the layer, etc. It was established that depending on the type of excitation greater fragmentation of the luminophor powder may lead either to an increase or to a decrease of the effective luminance. We also investigated the question of determining the optimum conditions for maximum luminescence output.

The results of our investigation can be used to estimate the true luminescence spectrum and output from the measured spectrum and output. The problem was treated both experimentally and theoretically.

The experiments were performed on powdered ZhS-9 glass with particles from 5 to 1000 μ in diameter. The monochromatic exciting radiation in the range from 230 to 365 mμ was obtained by means of a two crystal (quartz) monochromator.

The accompanying figure shows the theoretical curves and experimental points characterizing the variation of the luminescence output as a function of the particle size for two values of the index of refraction. These results as well as those of other tests show good agreement between experiment and theory and indicate that our method of calculation is applicable to most powdered luminophors.

INDICATRICES OF LIGHT SCATTERING BY DEVELOPED PHOTOGRAPHIC EMULSIONS ON A TRANSPARENT BASE

- Iu.N.Gorokhovskii & I.M.Davydkin

Introduction

Light passing through a developed black-and-white photographic emulsion undergoes appreciable scattering owing to the dispersed distribution of the blackened silver grains. In view of this, in photographic densitrometry it is the practice to distinguish between a number of different blackenings, comprising a set[1] of density values and defined by the values of the angle ω_1 of the beam illuminating the film and the angle ω_2 subtended by the photometer viewing the film. These different densities are defined in the table below.

	$\omega_2 = 0$	$0 < \omega_2 < 2\pi$	$\omega_2 = 2\pi$
$\omega_1 = 0$	Regular density $D_\parallel$		Integral density D_Σ
$0 < \omega_1 < 2\pi$		Effective density D_φ	
$\omega_1 = 2\pi$	$D_\perp$	Diffuse density	$D_\perp$

In all cases $D_\parallel > D_\varphi > D_\Sigma \approx D_\perp$.

In the present article and the one which follows[2], we shall, extending the work of other authors[3-7], consider in detail the physical processes involved in light scattering by photographic blackenings under various conditions. In addition, we shall calculate the integral and effective densities on the basis of measured values of the scattering indicatrix.

1. Procedure

The experiments were performed on two emulsions of very different graininess, namely, very fast Aerorapid aerial film and slow Printon K commercial photographic film. Forty-three samples of blackening were prepared with different diffuse optical densities, obtained by developing the films in different developers to different degrees of contrast.

The diffuse optical densities were measured on an IFT-11 wedge densitometer, carefully calibrated by means of a set of density standards[8] and the integral densities were measured by means of an integrating sphere.

A special wedge goniophotometer was constructed to measure the scattering indicatrix. The instrument is diagramed in Fig.1. Here S is the light source (an STs-62 point source), the light from which is collected by the two-lens condenser L_1 and focused in the plane of the diaphragm A. This diaphragm has a circular

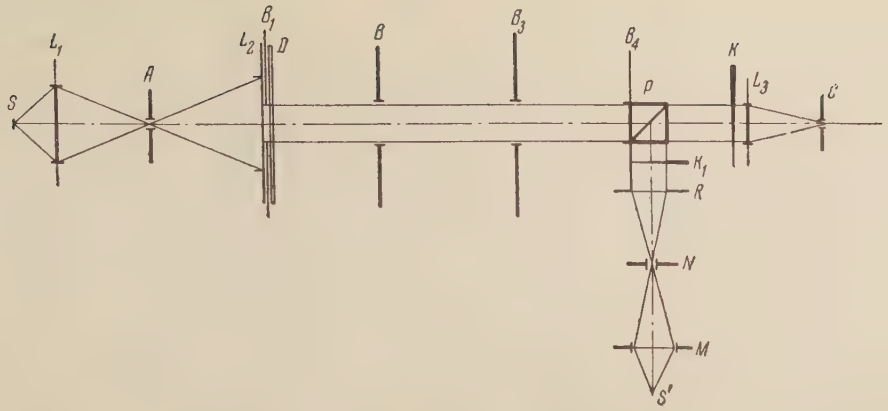

Fig.1. Diagram of the set-up for measuring the scattering indicatrix.

aperture, 1.4 in diameter, in the principal focus of lens L_2 (f = 100 mm; relative aperture 1:4.5). The almost parallel beam from L_2 falls on the face of the photometer cube P. The ocular L_3 (f = 75 mm) is focused on the face of the cube and forms an image of the source on the plane of the viewing slit C. The light from the comparison source S' is similarly focused by condenser M in the plane of the aperture N, which is situated in the principal focal plane of the lens R. The almost parallel light beam leaving R is incident on the other face of the photometer cube. Diaphragms B_1, B_2, B_3 and B_4 with openings 8 mm in diameter define the beam and suppress stray light.

The aperture angle of the illuminator is 0.8° and equal to that of the "receiver", i.e., the viewing system.

The blackening sample D being measured was inserted at diaphragm B_1. The illuminating part of the apparatus from S to L_2 together with the sample D could be rotated through different angles about a vertical axis in the plane of the sample. The brightness B of the sample was measured by comparing it with the constant brightness field from the standard source by using a neutral gray wedge K with a constant of 0.225 between the photometer cube P and the ocular L_3. To increase the range of measurement another wedge K_1 was used in the beam from the standard source.

The brightness B of the samples was measured at angles of 0, 1, 2, 4, 6, 8, 10, 12, 15, 20, 25, 30, 35, 40, 45, 50, 60 and 70° with the normal to the blackening plane.

We note that the measurements at 0° give the regular optical density of the emulsion.

The results of the scattering indicatrix measurements were plotted in polar coordinates in the form of log B_φ vs φ; that is, each value of the logarithm of the transmission coefficient was laid off in the corresponding angular direction.

2. Experimental Results

Figures 2 and 3 show two representative families of scattering indicatrices for blackenings of various densities in Aerorapid film, obtained by developing in developer No.1, according to GOST (State Standard) 2817-50,[8] to gammas of 0.73 and 1.5.

It is seen that the scattering indicatrices are always highly peaked in the forward direction (due essentially to the scattered

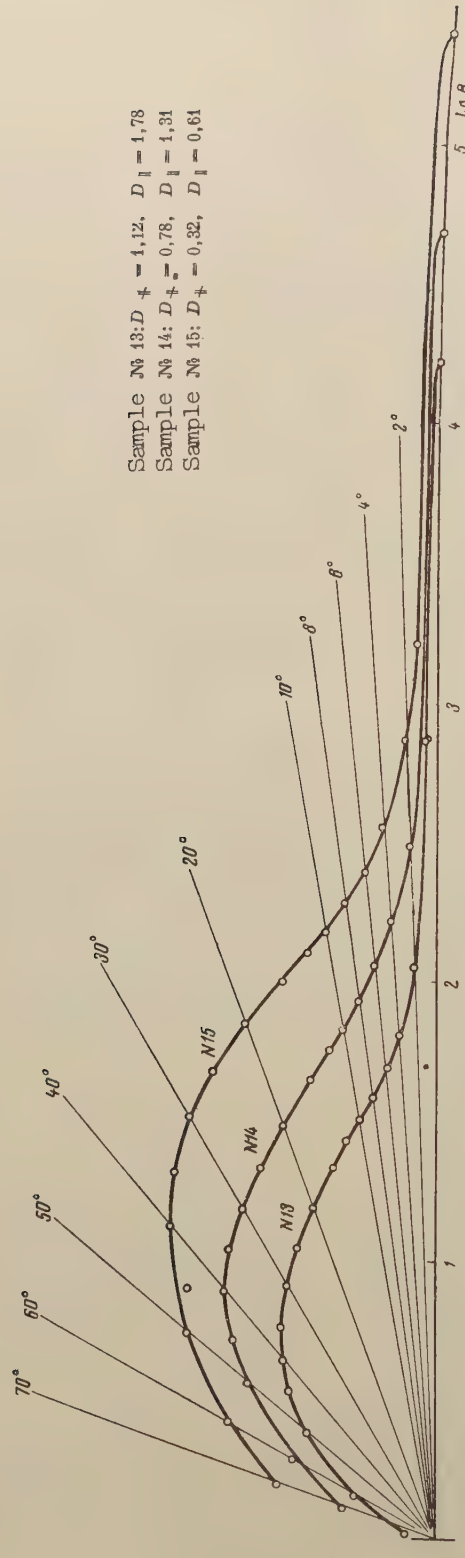

Fig. 2. Aerorapid film; developer No. 1; $\gamma = 0.73$.

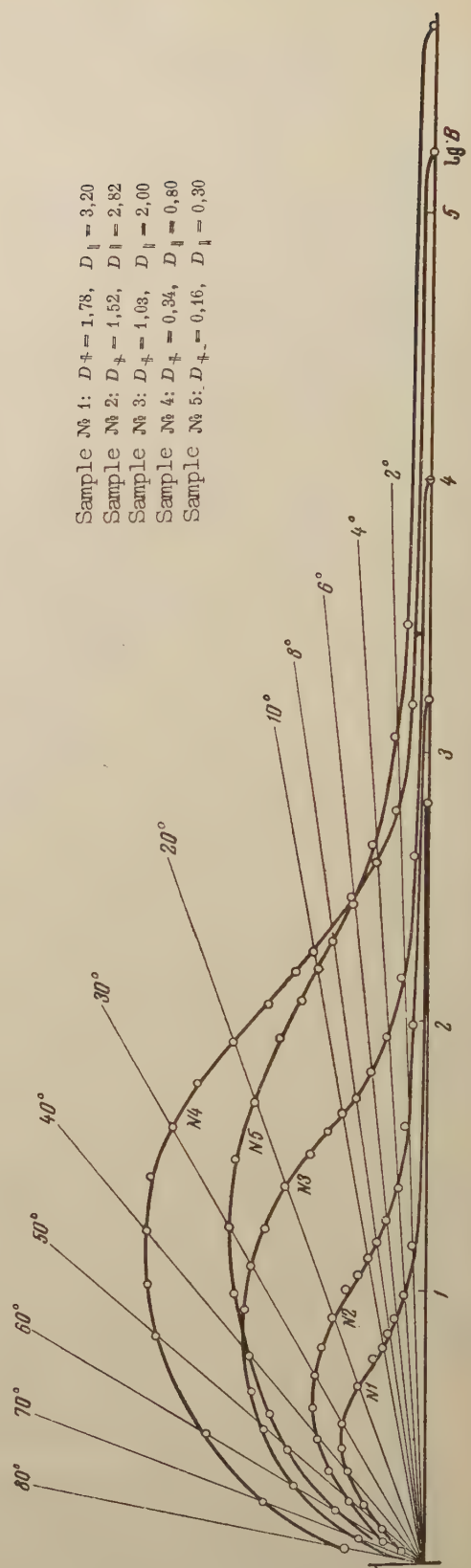

Fig. 3. Aerorapid film; developer No. 1; $\gamma = 1.5$.

light) and that for optical densities greater than 0.3 the scattering indicatrices do not in general intersect (that is, the indicatrix for a higher optical density lies entirely within the indicatrix for any lower optical density).

Such scattering indicatrices are, however, not the most convenient ones for comparing light scattering by different blackenings. Therefore all the indicatrices in a given family were normalized to the same value at $\varphi = 0$.

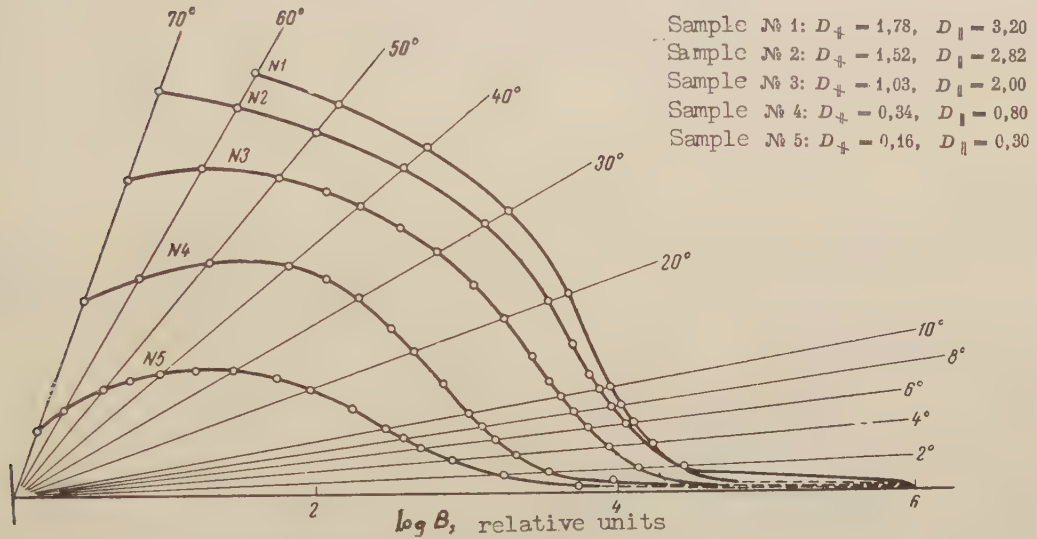

Fig. 4. Aerorapid film; developer No. 1; $\gamma = 1.5$.

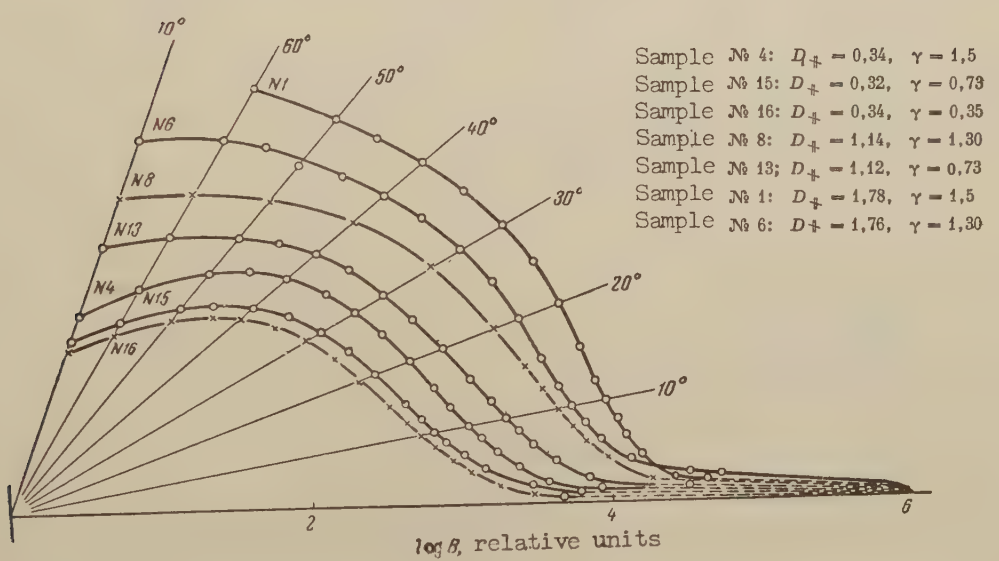

Fig. 5. Aerorapid film; developer No. 1; $D_{\perp}$ = const.

Figure 4 shows the normalized indicatrices corresponding to those in Fig.3. It shows clearly that as the diffuse optical density increases for a given gamma, the scattering power of the blackening also increases.

Figure 5 shows three families of normalized scattering indicatrices of photographic blackenings of the same optical density, but obtained by developing to different gammas. It turns out that as the gamma is increased the blackenings of a given density yield convex scattering indicatrices, i.e., are characterized by a higher scattering power.

Figures 6 and 7 compare blackenings of equal optical densities developed to equal gammas but in emulsions with different graininess. It will be seen that for these the scattering indicatrices are quite different. The more grainy emulsion is characterized by more convex scattering indicatrices.

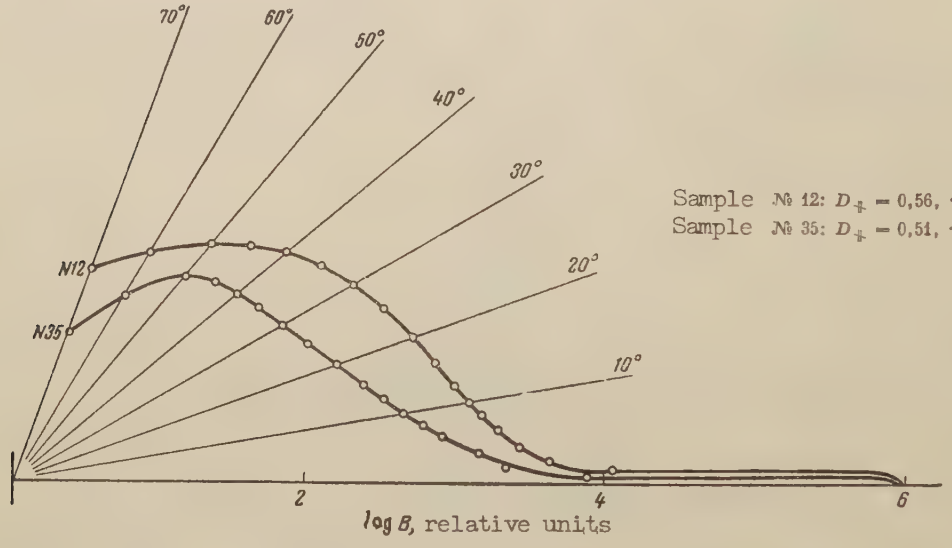

Sample № 12: $D_{\frac{1}{2}} = 0{,}56$, $\gamma = 1{,}00$. Aerorapid
Sample № 35: $D_{\frac{1}{2}} = 0{,}51$, $\gamma = 1{,}00$. Printon K

Fig. 6. Different emulsions; developer No. 1.

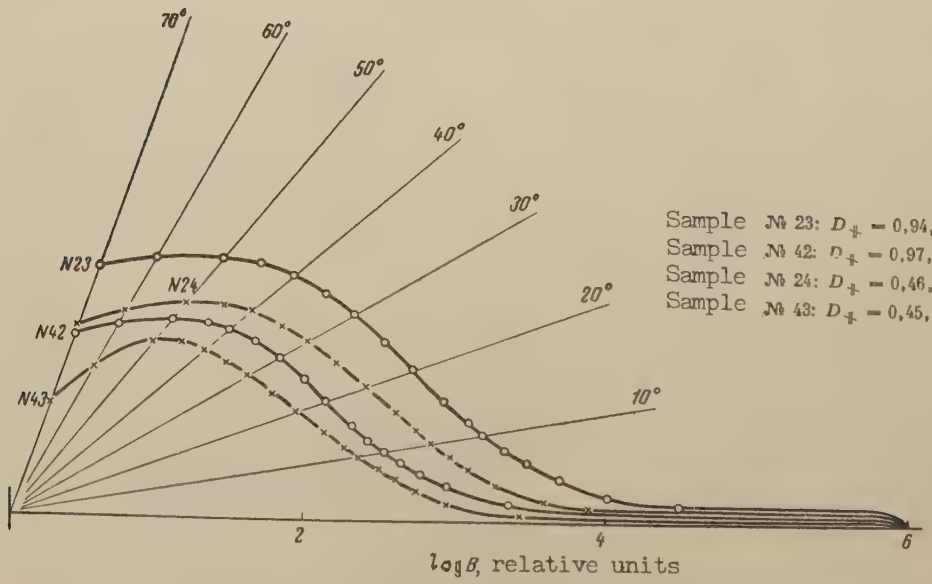

Sample № 23: $D_{\frac{1}{2}} = 0{,}94$, $\gamma = 0{,}80$. Aerorapid
Sample № 42: $D_{\frac{1}{2}} = 0{,}97$, $\gamma = 0{,}70$. Printon K
Sample № 24: $D_{\frac{1}{2}} = 0{,}46$, $\gamma = 0{,}80$. Aerorapid
Sample № 43: $D_{\frac{1}{2}} = 0{,}45$, $\gamma = 0{,}70$. Printon K

Fig. 7. Different emulsions; Siza developer.

Comparison of the scattering indicatrices of blackenings of equal density in a given emulsion developed to the same gamma in different developers (metol hydroquinone developer No.1, metol developer No.2, and glycin-paraphenylene developer Siza-IIIA) showed that the influence of the developer on the scattering indicatrix is negligible.

3. Determination of the Integral Optical Density of Blackening

The scattering indicatrix can be used to calculate the fraction of the total light flux which passes through the blackening, and from this one can determine the integral optical density of the blackening and calculate the effective densities for illumination by parallel light beams.

The total light flux F emitted from the viewing side of an area S is given by

$$F = 2\pi S \int_0^{\pi/2} B_\varphi \sin\varphi \cos\varphi d\varphi, \tag{1}$$

where φ is the direction of viewing for which the brightness B_φ is obtained.

We break up the integral from 0 to $\pi/2$ into a sum of integrals, writing

$$F = 2\pi S \sum_0^{\pi/2} \int_{\varphi_i}^{\varphi_{i+1}} B_{\varphi_i} \sin\varphi \cos\varphi d\varphi = \pi S \sum_0^{\pi/2} \int_{\varphi_i}^{\varphi_{i+1}} B_{\varphi_i} \sin 2\varphi d\varphi.$$

If we now consider the brightness B_{φ_i} to be constant within the solid angle ω_i in which the light flux is determined, we have

$$F = \pi S \sum_i B_{\varphi_i} \int_{\varphi_i'}^{\varphi_{i+1}'} \sin 2\varphi d\varphi = \frac{\pi S}{2} \sum_i B_{\varphi_i} (\cos 2\varphi_i' - \cos 2\varphi_{i+1}'), \tag{2}$$

where φ_i' and φ_{i+1}' are the rectilinear boundaries of the solid angle ω_i in which the brightness is assumed constant, and φ_i is the direction of measurement.

We shall consider the boundary of the solid angle between two neighboring directions of measurement φ_{i-1} and φ_i to be the generatrix of the cone that bisects the solid angle subtended by these two directions. Now the solid angle defined by φ_{i-1} and φ_i will be

$$\omega = 2\pi \int_{\varphi_{i-1}}^{\varphi_i} \sin\varphi d\varphi = 2\pi (\cos\varphi_{i-1} - \cos\varphi_i),$$

and half of this angle will be the angle bound by φ_{i-1} and φ_i' or φ_i' and φ_i.

Therefore the boundary of the solid angle will be given by

$$\cos\varphi_i' = \frac{1}{2}(\cos\varphi_{i-1} - \cos\varphi_i). \tag{3}$$

The difference in the cosines of the boundary angles will obviously be

$$\cos\varphi_i' - \cos\varphi_{i+1}' = \frac{1}{2}(\cos\varphi_{i-1} - \cos\varphi_{i+1}). \tag{3a}$$

If we now use the double-angle formula for the cosine and insert the values from (3a) in (2), we obtain an expression for the light flux in terms of the measured brightness values observed in the various directions, namely,

$$F = \frac{\pi S}{2} \sum \frac{1}{2} B_{\varphi_i} (\cos 2\varphi_{i-1} - \cos 2\varphi_{i+1}) = \frac{\pi S}{2} \sum_i B_{\varphi_i} C_i, \tag{4}$$

where $\varphi_{i-1}, \varphi_i,$ and φ_{i+1} are neighboring directions of measurement and the $C_i = \frac{1}{2}(\cos 2\varphi_{i-1} - \cos 2\varphi_{i+1})$ are the so-called angular coefficients.9

With our directions of measurement, Eq.(4) becomes

$$F = \frac{\pi}{2} S \left\{ B_0 \frac{\cos 0° - \cos 2°}{2} + B_1 \frac{\cos 0° - \cos 4°}{2} + B_2 \frac{\cos 2° - \cos 8°}{2} + \right.$$
$$+ B_4 \frac{\cos 4° - \cos 12°}{2} + \ldots + B_{12} \frac{\cos 20° - \cos 30°}{2} + B_{15} \frac{\cos 24° - \cos 40°}{2} +$$
$$+ B_{20} \frac{\cos 30° - \cos 50°}{2} + \ldots + B_{45} \frac{\cos 80° - \cos 100°}{2} + B_{50} \frac{\cos 90° - \cos 120°}{2} +$$
$$\left. + \ldots + B_{80} \frac{\cos 140° - \cos 180°}{2} + B_{90} \frac{\cos 160° - \cos 180°}{2} \right\}. \tag{5}$$

This is the expression we used in our calculations.

The integral optical density of the blackening is defined by

$$D_\Sigma = \lg \frac{F_0}{F_\Sigma}. \tag{6}$$

Here F_Σ is the total flux passing through the blackening as given by Eq.(5), and F_0 is the incident flux on the blackening, which is obtained by measuring the brightness in all directions in the absence of the sample. In the latter case all the B_{φ_i} except that for $\varphi_i = 0$ are zero and only the first term in Eq.(5) remains. Then

$$F_0 = B_0 \frac{\pi S}{2} \frac{\cos 0° - \cos 2°}{2} = \frac{\pi}{2} S B_0 C_0,$$

where $C_0 = \frac{1}{2}(\cos 0° - \cos 2°)$, and B_0 is the brightness of the photometer cube face for $\varphi = 0$ in the absence of the sample.

Therefore

$$D_\Sigma = \lg \frac{B_0 C_0}{\sum_i B_{\varphi_i} C_i} = \lg B_0 C_0 - \lg \sum_i B_{\varphi_i} C_i.$$

Setting $B_0 = 1$, we obtain

$$D_\Sigma = -3{,}5157 - \lg \sum_i B_{\varphi_i} C_i. \tag{7}$$

We used this equation to calculate the integral optical density of blackening of our samples. The results are given in the table.

We compared our calculated integral optical densities of blackening with the values obtained in measurements by means of an integrating sphere. The difference was no greater than 0.05.

Diffuse and integral optical densities of blackening of Aerorapid and Printon K film samples

Sample	γ	$D_{\downarrow}$	D_{Σ}, calculated	D_{Σ}, experimental
		Aerorapid, developer No.1		
1	1,5	1,78	1,755	1,767
2	1,5	1,52	1,519	1,520
3	1,5	1,03	1,018	1,019
4	1,5	0,34	0,320	0,322
5	1,5	0,16	0,148	0,151
6	1,30	1,76	1,796	1,807
7	1,30	1,41	1,412	1,460
8	1,30	1,14	1,113	1,129
9	1,30	0,73	0,702	0,750
10	1,30	0,26	0,245	0,252
11	1,00	1,31	1,295	1,321
12	1,00	0,56	0,531	0,550
13	0,73	1,12	1,117	1,149
14	0,73	0,78	0,751	0,790
15	0,73	0,32	0,282	0,292
16	0,35	0,34	0,298	0,296
17	0,35	0,14	0,124	0,126
		Aerorapid, developer No.2		
18	0,95	1,65	1,663	1,670
19	0,95	0,78	0,800	0,820
20	0,67	1,26	1,231	1,279
21	0,67	0,82	0,800	0,820
22	0,67	0,36	0,339	0,353
		Aerorapid, Siza developer		
23	0,80	0,94	0,913	0,949
24	0,80	0,46	0,439	0,434
25	0,80	0,28	0,260	0,276
26	0,58	1,03	1,003	1,036
27	0,58	0,51	0,496	0,519
28	0,58	0,32	0,299	0,319
		Printon K, developer No.1		
29	2,0	1,73	1,729	1,741
30	2,0	0,48	0,454	0,454
31	2,0	0,28	0,258	0,272
32	1,35	0,98	0,939	0,975
33	1,35	0,39	0,365	0,373
34	1,00	1,07	1,039	1,040
35	1,00	0,51	0,490	0,480
36	1,00	0,34	0,306	0,320
		Printon K, Siza developer		
37	1,25	1,26	1,215	1,209
38	1,25	0,32	0,292	0,314
39	1,00	0,90	0,873	0,915
40	1,00	0,47	0,440	0,451
41	1,00	0,32	0,284	0,305
42	0,70	0,97	0,949	0,941
43	0,70	0,45	0,426	0,450

4. Effective Optical Density of Blackening Under Parallel Illumination as a Function of the Solid Angle of the Viewer

The effective optical densities for different solid angles ω_2 of the viewer, with $\omega_1 \approx 0$, can be calculated using the analogous equation

$$D_\omega = \lg \frac{F_0}{F_\omega}, \tag{8}$$

where F_ω is the flux incident on the "radiation receiver" with a solid viewing angle ω_2.

Proceeding in exactly the same way as for the integral optical density, we obtain

$$D_\omega = -3{,}5157 - \lg \sum_0^{\varphi_i'} B_{\varphi_i} C_i. \tag{9}$$

Figures 8 and 9 give the solid-angle dependence of the optical density determined in this manner.

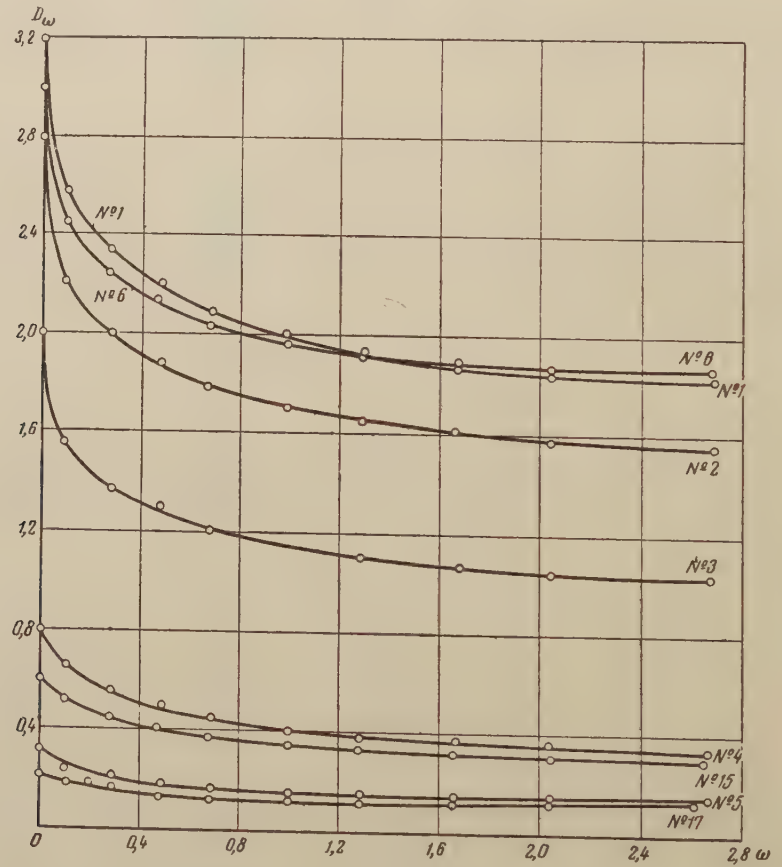

Fig. 8. Optical density of blackening as a function of the solid angle of the receiver. Aerorapid film, developer No. 1.

Sample № 1: $D_\text{ф} = 1{,}78$
Sample № 2: $D_\text{ф} = 1{,}52$
Sample № 3: $D_\text{ф} = 1{,}03$
Sample № 4: $D_\text{ф} = 0{,}34$
Sample № 5: $D_\text{ф} = 0{,}16$
} $\gamma = 1{,}5$

Sample № 6: $D_\text{ф} = 1{,}76$, $\gamma = 1{,}30$
Sample № 15: $D_\text{ф} = 0{,}32$, $\gamma = 0{,}73$
Sample № 17: $D_\text{ф} = 0{,}14$, $\gamma = 0{,}35$

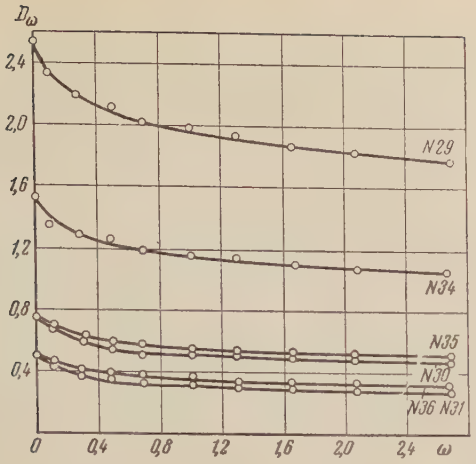

Fig.9

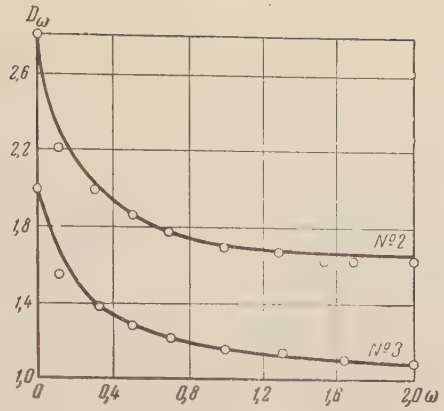

Fig.10

Fig.9. Optical density of blackening as a function of the solid angle of the receiver. Printon K film, developer No.1

Sample № 29: $D_\Sigma = 1,73$, $\gamma = 2,0$ Sample № 34: $D_\Sigma = 1,07$, $\gamma = 1,00$
Sample № 30: $D_\Sigma = 0,48$, $\gamma = 2,0$ Sample № 35: $D_\Sigma = 0,51$, $\gamma = 1,00$
Sample № 31: $D_\Sigma = 0,28$, $\gamma = 2,0$ Sample № 36: $D_\Sigma = 0,34$, $\gamma = 1,00$

Fig.10. A comparison of the solid viewing angle dependence obtained experimentally with the empirical formula. Curves = data from Eq.(10); points = values calculated from scattering indicatrix measurements.

Sample № 2: $a = 0,24$, $b = 0,18$
Sample № 3: $a = 0,165$, $b = 0,17$

These curves show that the effective optical density depends significantly on the solid viewing angle, with the largest change occurring at relatively small angles (up to about 1.0 steradians). The higher the diffuse optical density, the greater the rate of change of the effective optical density. Further, for a given D_Σ the variation is more rapid for higher gamma values.

The curves also show that for each blackening there is a certain limiting value of ω_2 above which the optical density remains practically constant and equal to the integral value. Obviously this limiting solid angle takes in almost all of the light transmitted by the blackening. It follows, therefore, that in order to measure the integral optical density it is sufficient for the densitometer "receiver" to have a solid angle equal to this limiting angle.

According to our data, the limiting solid angle will be equal to about 3.6 steradians, corresponding to an aperture angle of about 130°. This important practical conclusion agrees with Korndorf's recent data.

The solid-angle dependence of the optical density of blackening can in many cases be represented by the empirical formula

$$D_\omega = \frac{a}{b + \omega_2} + D_\Sigma, \qquad (10)$$

where a and b are constants depending on the blackening, and ω_2 is the solid angle of the "receiver".

In Fig.10 we compare the values given by Eq.(10) with the results of calculations based on measurements of the scattering indicatrix.

Conclusions

1. We constructed a visual goniophotometer for measuring the scattering indicatrix of blackening samples and used this instrument to determine the distribution of light scattered by black-and-white photographic emulsions on a transparent base.

2. The scattering indicatrices obtained indicate the following facts about the scattering power of such "blackenings". a) Different photographic emulsions have similar general features, although blackenings of the same optical density but with different degrees of graininess have measurably different scattering indicatrices. b) When the emulsions are developed to a given gamma, the scattering increases with the optical density. c) For equal optical densities, the scattering is greater for higher values of gamma.

3. We calculated integral optical densities of blackening from the scattering indicatrices and compared the calculated values with the results of direct measurements. We also established the dependence of the optical density on the solid viewing angle of the "receiver". From this we obtain information on the allowable minimum solid angle of a receiver for practical measurement of integral optical densities.

Department of General Photography and Film Processing,
Leningrad Institute of Motion-Picture Engineers

References

1. GOST 2653-44 (State All-Union Standard) Osnovnye poniatiia i velichiny fotograficheskoi sensitometrii (Fundamental concepts and Constants of Photographic Sensitometry).

2. Iu.N.Gorokhovskii & I.M.Davydkin, Present issue of the Bulletin, p.

3. A.Callier, ZS.wiss.Phot., 7, 257 (1909).

4. P.Heinisch, Untersuchungen über die Zerstreuung des Lichtes durch entwickelte Emulsionsschichten, Diss., Berlin, 1931.

5. G.Boutry, Publ.Scient.Techn.de Ministère de l'air, No.38, 1934.

6. K.Weaver, Journ. Opt. Soc. Am., 40, 524 (1950).

7. V.A.Korndorf, Uspekhi nauchnoi fotografii (Advances in Scientific Photography), 4, 67 (1955).

8. GOST 2817-50 (State All-Union Standard) on Photographic Emulsions on a Transparent Base. Method of General Sensitometric Testing.

9. P.M.Tikhodeev, Svetovye izmereniia v svetotekhnike (Light Measurements in Light Engineering), M. 1936.

NUMERICAL EVALUATION OF LIGHT SCATTERING IN PHOTOGRAPHIC BLACKENINGS ON A TRANSPARENT BASE

- Iu.N.Gorokhovskii & I.M.Davydkin

That the scattering power of photographic blackening affects the value of the optical density measured under different conditions of illumination and observation was noted when optical methods were first being introduced for degree-of-blackening measurements. At the time this question gave rise to lively discussion between Hurter and Driffield on the one hand, and Abney on the other. In modern terms one may say that Hurter and Driffield measured a quantity close to what we now call the regular density, whereas Abney measured the diffuse density.

Hurter and Driffield suggested that blackening be characterized by two values of the optical density, one for measurements in contact with opal glass (the density of a negative in contact printing), and the other for measurements under the conditions of projection printing.[1]

Maksimovich[2,3] investigated light scattering in the process of measuring optical densities of emulsions and showed that the experimental value was influenced by the particular conditions of measurement. On the basis of his results he suggested certain improvements in the design of the familiar Martens polarization densitometer.

Later Callier[4] undertook an investigation of the reasons for inconsistencies in measured optical densities. Considering these differences to be caused by the scattering properties of developed photographic film, he demonstrated that there is a difference between $D_{\parallel}$ and $D_{\perp}$ for the same blackening and introduced this notation in the sense in which we use it today.[5]

Callier assumed that one could write

$$D_{\parallel} = QD_{\perp}. \tag{1}$$

On the basis of measurements performed on a specially adapted Martens photometer, Callier concluded that the mean value of Q for a given emulsion remains approximately constant.

This quantity Q, now called the Callier coefficient and firmly established in photographic theory and practice,* is accepted as the parameter characterizing the scattering power of developed photographic emulsion.

---

*In distinction to Callier's own definition, certain investigators have taken the Callier coefficient as the ratio between the regular and integral optical densities. In our opinion, this latter definition is more meaningful physically. Further, this hardly changes the numerical value of the Callier coefficient, since it is firmly established (see, in particular, Korndorf[6] and Section 3 of our preceding article[7]) that the diffuse and integral densities $D_{\perp}$ and D_{Σ} are equal to within 0.05.

In later work it was found that the Callier coefficient depends on many other factors in addition to the physical properties of the emulsion. For this reason it can be used only as a rough indicator of the scattering properties of an emulsion.

In order to obtain a more descriptive characteristic of scattering, several investigators[8,9] suggested other parameters which, if only because of their complexity, could not possibly compete with the Callier coefficient.

In the present paper we use the results of our investigation of the physical nature of light scattering in developed photographic emulsions (outlined in the preceding article) to clarify to what extent the Callier coefficient actually characterizes the light-scattering properties of blackenings. Further, we attempt to introduce a new parameter which we think has important advantages over the Callier coefficient.

1. Determination of the Fraction of Light Scattered by the Blackened Grains in an Emulsion

By measuring the scattering indicatrix of developed film[7] we have found the values of the regular optical densities of blackenings in Aerorapid and Printon K films, which, in addition to differing greatly as regards graininess (the degree of dispersion of the silver halide grains), were developed to different gammas. From these regular optical densities we were able to calculate the Callier coefficient for each of the samples.

The dependence of the Callier coefficient on the diffuse optical density under different conditions of development is shown in Figs.1 and 2. We see that as the diffuse optical density decreases, Q increases to a maximum (occurring at D_{Φ} = 0.25-0.35 in the case of Aerorapid film). We also note that Q increases rapidly with gamma. In the case of the fine grain Printon K film (i.e., an emulsion in which the solid phase is highly dispersed) the dependence of Q on D_{Φ} and gamma is much weaker.

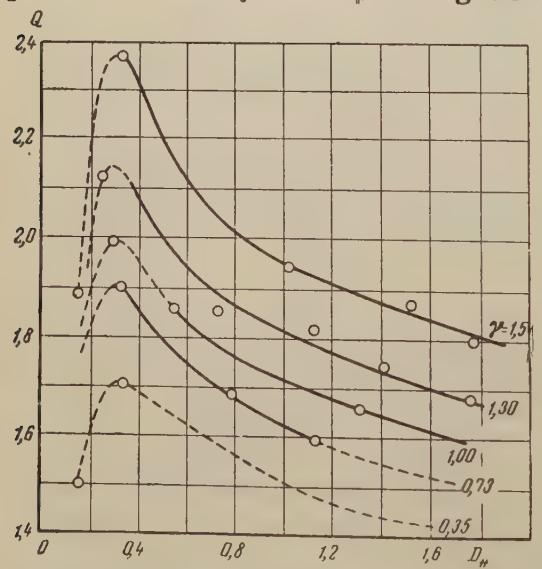

Fig.1. Variation of the Callier coefficient Q with the diffuse optical density at different values of gamma: Aerorapid film, developer No.1.

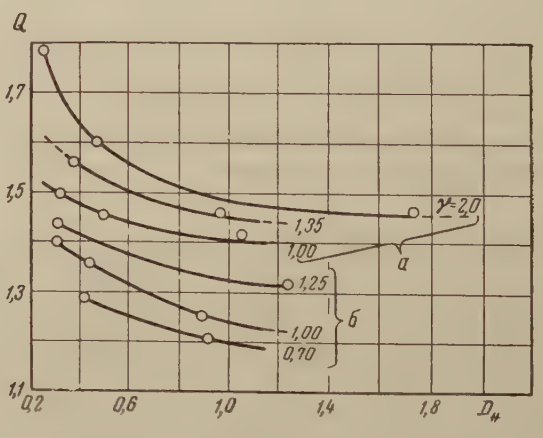

Fig.2. Variation of the Callier coefficient Q with the diffuse optical density at different values of gamma; Printon K; a) developer No.1, b) Siza developer.

Because of the way the Callier coefficient depends on the diffuse optical density and the gamma, it is difficult to use in judging of the scattering properties of the photographic blackening or for determining the spatial distribution of the transmitted light. The reason for this lies in the nature of the Callier coefficient itself. Indeed, if

$$Q = \frac{D_\parallel}{D_\perp} = \frac{D_\parallel}{D_\Sigma},$$

then

$$Q = \frac{\lg \frac{F_0}{F_\parallel}}{\lg \frac{F_0}{F_\Sigma}} = \frac{\lg \frac{F_0}{F_\parallel}}{\lg \frac{F_0}{F_\parallel + F_*}}, \qquad (2)$$

where F_0 is the incident parallel-beam flux and $F_\parallel$ and F_* are the values of light flux transmitted without change of direction and of the scattered light flux, respectively.*

We see that Q depends not only on the ratio of $F_\parallel$ to F_*, which alone characterizes the degree of light scattering, but also on the ratio between the sum of these and F_0, that is, on the degree to which light is absorbed by the blackened emulsion layer.

One may, however, suggest another light scattering parameter which is free of these shortcomings. Indeed, the difference between the regular and diffuse (or integral) densities

$$\Delta D = D_\parallel - D_\Sigma = \lg \frac{F_0}{F_\parallel} - \lg \frac{F_0}{F_\parallel + F_*} = \lg \frac{F_\parallel + F_*}{F_\parallel} \qquad (3)$$

does not contain F_0 and therefore is independent of the absorption.

We suggest calling the scattering factor q a quantity deriving from the above density difference and defined as

$$q = \frac{F_*}{F_\Sigma} = \frac{F_*}{F_\parallel + F_*} = 1 - \text{antilg}\,(D_\Sigma - D_\parallel) \qquad (4)$$

Thus the principal difference between the Callier coefficient Q and our coefficient q is that whereas our coefficient depends only on the light that has passed through the blackening, the Callier coefficient is also dependent on the incident flux, i.e., on the absorption of the investigated layer.

Table 1

Comparison of Q with q for various blackenings

D_Σ	$D_\parallel$	Q	q
0,5	0,75	1,5	0,44
	1,0	2,0	0,68
	1,5	3,0	0,90
1,0	1,5	1,5	0,68
	2,0	2,0	0,90
	3,0	3,0	0,99
2,0	3,0	1,5	0,90
	4,0	2,0	0,99
	6,0	3,0	1,00

Table 1 illustrates the difference between the Callier coefficient and q. It can be seen that blackenings with very different Callier coefficients can scatter almost identically, while those which have almost the same Callier coefficient may have very different scattering properties.

In the case of a nonscattering medium ($F_* = 0$), we have q = 0, while for an ideal fully scattering medium ($F_\parallel = 0$), we obtain q = 1.

*$F_* + F_\parallel = F_\Sigma$ the total light flux leaving the sample.

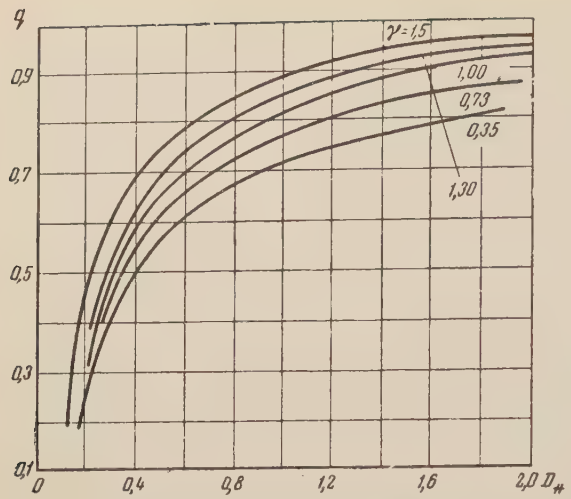

Fig.3. Variation of q with the diffuse optical density; Aerorapid film; developer No.1.

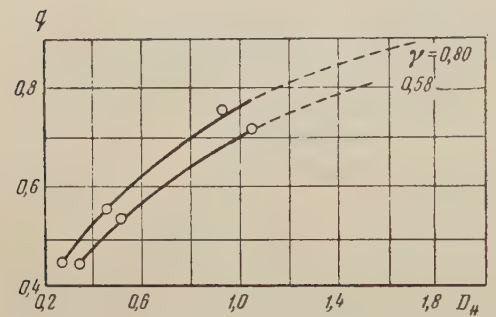

Fig.4. Variation of q with the diffuse optical density; Aerorapid film; Siza developer.

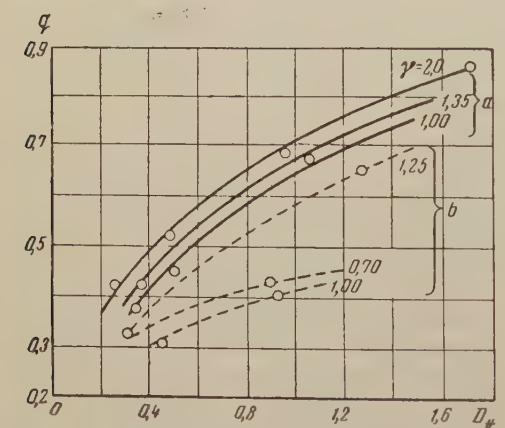

Fig.5. Variation of q with the diffuse optical density; Printon K, a) developer No.1, b) Siza developer.

By analogy with q, which characterizes the ratio between the integral and regular optical densities we may define another coefficient q_ω to characterize the ratio between any effective optical densities.

Thus, for example, having determined the effective optical density

$$D_\omega = \lg \frac{F_0}{F_\omega},$$

with the "receiver" viewing the solid angle ω_2, we obtain

$$q_\omega = 1 - \text{antilg}\,(D_\Sigma - D_\omega) = \frac{F_\omega - F_\parallel}{F_\Sigma}, \quad (5)$$

where F_ω is the flux transmitted through the emulsion and emerging within the solid angle ω_2.

Let us investigate the factors on which q depends and find the dependence of q on these factors.

Figs.3,4 & 5 show the dependence of the scattering factor q on the diffuse optical density and the gamma of the blackening (emulsion). We can draw the following conclusions from analysis of these figures

As the diffuse optical density of emulsions, developed to the same gamma, increases, the relative light flux in the normal direction decreases. At first, for low densities, the fraction of this normal (directly transmitted light) decreases very rapidly and then, as the density increases, this change becomes more gradual.

In different emulsions and for different methods of development, the general character of the variation of the scattering factor q is about the same, except that in Aerorapid film, which is coarse grained, these variations are much more pronounced than in Printon K, which is characterized by fine grain.

As the gamma increases with the diffuse optical density remaining constant, q increases. In this case also, the variations of q are less pronounced in the finer grain emulsion.

The relationship between the scattering factor q and the Callier coefficient Q is

$$\lg (1 - q) = (1 - Q)\, D_\Sigma = \frac{1 - Q}{Q} D_\parallel. \quad (6)$$

2. Separation of the Transmitted Light into Components

The indicatrices of light scattering by a photographic emulsion are curves characterizing the spatial distribution of the scattered light. The flux plotted in the direction normal to the plane of the emulsion is generally given as the total flux, although actually it consists of two components: the light scattered directly forward and the unscattered, directly transmitted light.

In some investigations[6,10-12] devoted to light scattering by photographic blackening, some account has been taken of the presence of scattered light in the forward beam. It seems to us, however, that less importance has been assigned to this fact than it merits.

If one separates the forward propagating beam into its components, one can obtain the actual angular distribution of the light scattered by the blackening and thus determine the true regular blackening density.

Thus, denoting by $F_{\parallel}^{0}$ the flux of the purely transmitted beam, which does not include scattered light, we obtain

$$D_{\parallel}^{0} = \lg \frac{F_0}{F_{\parallel}^{0}}, \tag{7}$$

where $D_{\parallel}^{0}$ is the optical density of blackening if one considers only the unscattered transmitted light.

Hence $D_{\parallel}^{0}$ is the true regular optical density associated only with actual absorption and reflection of light by the blackening, as opposed to the usual value $D_{\parallel}$ obtained by means of instruments which do not separate out the forward scattered light.

Obviously, $D_{\parallel}^{0} > D_{\parallel}$.

Let us denote by $1-q_0$ the normal emergent light that is not scattered, (i.e., the direct transmitted component), then

$$1 - q_0 = \frac{F_{\parallel}^{0}}{F_{\Sigma}} = \frac{F_{\parallel}^{0}}{F_{\parallel}^{0} + F_{*}^{0}} \tag{8}$$

and

$$q_0 = \frac{F_{*}^{0}}{F_{\parallel}^{0} + F_{*}^{0}}. \tag{9}$$

We then find that q_0 is analogous to our previously introduced scattering factor q; in fact it is a more accurate scattering factor inasmuch as it accounts for all the scattered light including that scattered directly forward. The relative magnitude of the scattering factors is given by $1 > q_0 > q > 0$.

The new scattering factor q_0 is related to $D_{\parallel}^{0}$ by

$$q_0 = 1 - \operatorname{anti}\lg (D_{\Sigma} - D_{\parallel}^{0}). \tag{10}$$

The experimental separation of the direct beam into its components was performed using a technique suggested by Gurevich and Chakhrov[13]. Thus we were able to determine $F_{\parallel}^{0}$ and $F_{\parallel}$, and these values were then used to find q_0 and $D_{\parallel}^{0}$.

The dependence of q_0 on the diffuse optical density and gamma for samples of Aerorapid film are shown in Fig.6.

A comparison of Figs.3 and 6 shows that although q_0 and q have very different numerical values, they exhibit similar variations, except that the increase of q_0 with the diffuse optical density and the gamma is sharper than that of q.

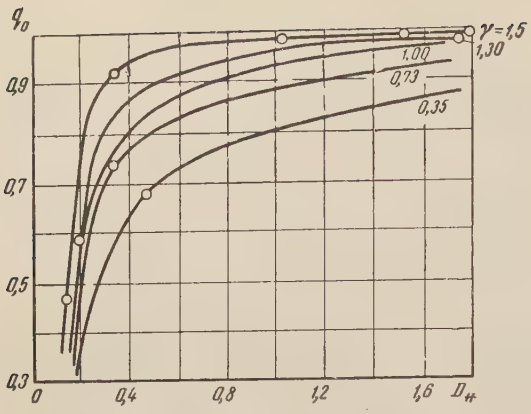

Fig.6. Variation of q_0 with the diffuse optical density; Aerorapid, developer No.1.

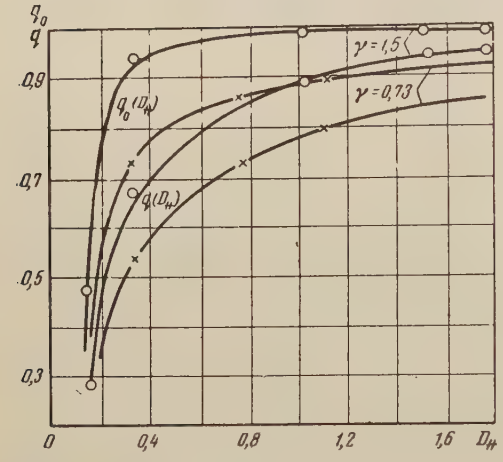

Fig.7. Comparison of q_0 and q for samples of Aerorapid film with γ = = 1.5 and γ = 0.73.

Fig.7 shows the dependences of q_0 and q on the diffuse optical density for equal degrees of blackening, obtained under the same sensitometric conditions of film development, i.e., for γ = const. We see that their absolute values are quite different.

If we assume that in passing through developed photographic film the light intensity is attenuated approximately according to Bouguer's law, the value of q_0 takes on clearer physical meaning.

Indeed, since the total light flux F_Σ scattered and directly transmitted through the blackening is determined by the absorbing properties of the substance,* we have

$$F_\Sigma = F_0 e^{-\beta l}, \qquad (11)$$

where F_0 is the incident light flux, β is the coefficient of absorption, and l is the thickness of the layer.

The unscattered flux $F_{||}^0$ of the direct beam depends both on the absorbing and on the scattering properties of the substance, which means that

$$F_{||}^0 = F_0 e^{-\beta l - \sigma l}, \qquad (12)$$

where σ is the scattering coefficient.

It follows from this that

$$1 - q_0 = e^{-\sigma l}. \qquad (13)$$

Therefore 1 - q_0 gives the weakening of the light beam due to scattering, on the assumption that this attenuation is characterized by Bouguer's law. The difference $\Delta D = D_{||}^0 - D_\Sigma$ between the optical densities turns out in this case to depend only on the scattering properties of the film and to be proportional to σ.

It follows from the above that the laws which describe the properties of blackenings should be based on studies of either q or the difference between the optical densities, since these are quantities which truly characterize the scattering properties of the substance.

3. Numerical Characterization of the Scattering Indicatrix

The factor q_0, although it determines the fraction of scattered light in the beam passing through the blackening, does not characterize the distribution of the scattered light and hence gives

*We are neglecting scattering and reflection to the rear.

no indication on how one should compare the scattering properties of different blackenings.

We should like to suggest the possibility of characterizing the scattering power of blackenings by comparing their scattering indicatrix with that of an ideal diffuser transmitting the same amount of radiant energy. This may be done by constructing equal-area graphs of these scattering indicatrices (Fig.8) and finding the angle α with respect to the incident beam at which the brightness of the sample is equal to that of the ideal diffuser (on the graph this is the angle between the polar axis and the radius vector to the point of intersection of the curves).

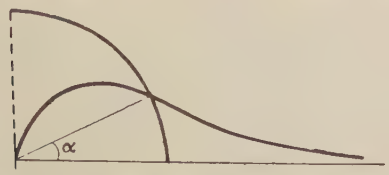

Fig.8. Definition of the scattering half-angle α.

It is then clear that for all angles $\varphi > \alpha$, the brightness of the sample is lower than that of the diffuser, while for $\varphi < \alpha$, it is greater.

Let us call 2α the scattering angle. This angle, which defines the zone containing most of the light scattered by the blackening (always more than is scattered by the diffuser within the same zone) can be used to characterize the scattering power of a blackening.

We have used our earlier scattering-indicatrix investigations to determine the scattering angles 2α for the blackenings studied.

Also, to get an idea of the amount of light scattered into the solid angle defined by 2α, we have calculated $1 - q_\alpha = F_\alpha/F_\Sigma$ for the same samples.

The values of the scattering half-angles α and of $1 - q_\alpha$ for the various samples are listed in Table 2.

Table 2

Scattering half-angle α and fraction $1 - q_\alpha$ of the transmitted light flux in the cone defined by the scattering angle 2α

Sample	γ	D_Σ	α°	$1-q_\alpha$	Sample	γ	D_Σ	α°	$1-q_\alpha$
	Aerorapid, developer No.1					Printon K, developer No.1			
1	1,5	1,755	38,5	0,72	29	2,0	1,729	33	0,63
2	1,5	1,519	36	0,76	30	2,0	0,454	18	0,72
3	1,5	1,018	33	0,76	31	2,0	0,258	14,5	0,76
4	1,5	0,320	28	0,78	32	1,35	0,939	23,5	0,69
5	1,5	0,148	14	0,87	33	1,35	0,365	15	0,74
13	0,73	1,117	29	0,74	34	1,00	1,039	23	0,66
14	0,73	0,751	27	0,74	35	1,00	0,490	17	0,78
15	0,73	0,282	23	0,78	36	1,00	0,306	14	0,79

The following conclusions on the nature of light scattering by photographic blackenings may be drawn on the basis of the experimental data.

1. The major part of the scattered light lies in a region of relatively low scattering angles. This part comprises 70 to 80% of the total light passing through the blackenings and is concentrated in the range of scattering angles 2α from 20 to 80°. It follows from this that a photographic blackening always scatters about the same fraction of light; the difference between different blackenings lies mostly in the different angular distribution of the scattered light.

2. As the integral optical density increases, the scattering angle increases.

3. Blackenings of equal integral optical densities have larger scattering angles when the emulsion is developed to a higher gamma.

4. As the dispersion is decreased, i.e., in going to finer grain emulsions, the scattering angle decreases.

Conclusions

1. An analysis of the Maksimovich-Callier phenomenon has been performed on the basis of measurements of scattering indicatrices of photographic blackenings, and it has been established that the Callier coefficient cannot serve as a rigorous characteristic of the scattering power of blackenings and cannot be used as a guide in judging of the distribution of total transmitted light.

2. We suggest a new parameter q, which we call the scattering factor, to characterize the scattering properties of blackenings. This factor gives the fraction of scattered light in the total flux transmitted by the blackening, or the difference between the regular and integral (or diffuse) optical densities, quantities which depend only on the scattering properties of the blackening.

3. The value of the regular optical density as usually determined should be corrected to allow for the scattered light in the forward beam. One should, accordingly, differentiate between the true and the apparent regular density.

4. We introduce the concept of the scattering angle for the purpose of evaluation of the relative scattering properties and indicatrices of photographic blackenings.

Department of General Photography and Film Processing,
Leningrad Institute of Motion Picture Engineers

References

1. K.V.Chibisov, Teoriia fotograficheskikh protsessov (Theory of Photographic Processes), Vol.1 (1935).

2. S.O.Maksimovich, Fotograf-liubitel' (The Amateur Photographer) 6, 177 (1909).

3. S.O.Maksimovich, ibid., 7, 198 (1909).

4. A.Callier, ZS.wiss.Phot., 7, 257 (1909).

5. GOST 2653-44 (State All-Union Standard) Fundamental concepts and Constants of Photographic Sensitometry.

6. V.A.Korndorf, Uspekhi nauchnoi fotografii (Advances in Scientific Photography) 4, 67 (1955).

7. Iu.Gorokhovskii & I.M.Davydkin, Present issue of the Bulletin, p. 1496.

8. O.Bloch & F.Renwick, Phot.Journ., 56, 49 (1916).

9. L.Silberstein & C.Tuttle, Journ.Opt.Soc.Am., 14, 365 (1927).

10. P.Heinisch, Untersuchungen über die Zerstreuung des Lichtes durch entwickelte Emulsionsschichten, Diss.,Berlin (1931).

11. K.Weaver, Journ.Opt.Soc.Am., 40, 524 (1950).

12. F.Pitt, Phot.Journ., 78, 486 (1936).

13. M.M.Gurevich & L.Ia.Chakhrov, Trudy (Transactions) State Optical Inst., 9, No.99 (1936).

SCATTERING OF LIGHT BY PHOTOGRAPHIC EMULSION LAYERS

- P.Kh.Pruss

Introduction

A light-sensitive photographic emulsion is essentially a thin layer of gelatin with silver halide microcrystals dispersed throughout it. By virtue of this, an emulsion is a layer of turbid, light-scattering medium.

Exposed photographic emulsion scatters light incident on it, and this phenomenon is responsible for many of the properties characteristic of photographic materials. Among these properties are the limitation as regards detail reproducible in a photograph and the decrease in optical density of small image elements with decreasing linear dimensions.[1-4] Thus, there is a limit to the resolution in photographic reproduction of a linear grid or a pair of closely spaced optical slits (the resolving power of a photographic emulsion).

We investigated light scattering in photographic emulsion layers primarily with a view to clarifying the nature of the resolving power of photographic materials.

The present article presents a summary of our data. Some of the earlier results have already been published[5,6] and will therefore be only mentioned briefly here. Other data, partaining to a method for finding the mean dimensions of crystals in an emulsion and to study of the flux distribution in emulsion layers are published for the first time and will therefore be presented in somewhat more detail.

1. Parameters Characterizing Scattering and Some Comparisons with Theory

We characterize the light scattering in an emulsion layer by the quantity $\Delta D = D_f - D_n$, where D_n is the measured optical density when the sensing photoelectric cell gaging the flux transmitted by the layer is in direct contact with the film (i.e., near the film) and D_f is the optical density when the photocell is at a large distance (far) from the film. This quantity (ΔD) is directly related to the parameter generally used to characterize the scattering, i.e., the scattering coefficient.

This can be shown by analyzing the dependence of ΔD on C, the concentration by weight of the silver halide in the layer. As may be seen from Fig.1, there is a range of concentrations in which this dependence is linear. This means that for these concentrations the light intensity is attenuated according to the $I = I_0 e^{-kC}$ law. If we write $k = k_a + k'_s + k''_s$ (where k_a is the absorption coefficient, k'_s accounts for forward scattering and k''_s accounts for backward scattering), then $\Delta D = k'_s C$, and the values of ΔD for different layers with the same silver halide concentration will be proportional to the forward scattering coefficients k'_s for these layers. Shifrin[7] has presented data on the way the ratio of the forward to the backward scattered fluxes depends on the quantity $\rho = 2\pi r/\lambda$ where r is the radius of the particles and λ is the wavelength. With this data one can use the values of ΔD measured for a constant silver halide concentration to calculate the total scat-

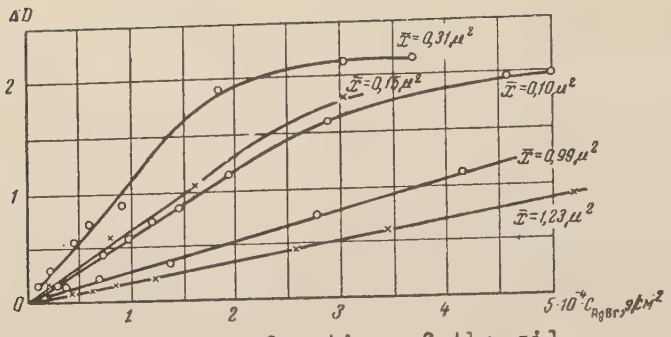

Fig.1. ΔD as a function of the silver halide concentration.

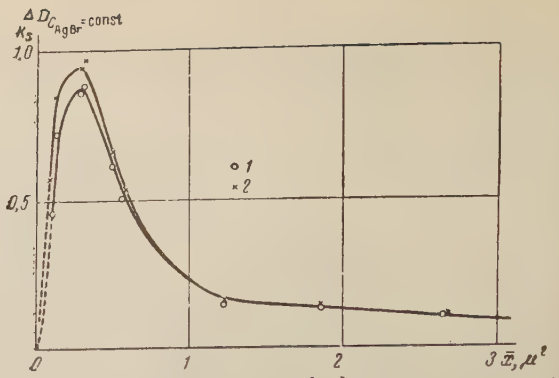

Fig.2. Variation of ΔD (1) and the scattering coefficient k_s (2) as functions of the mean AgBr crystal size.

tering coefficient $k_S = k'_S + k''_S$. Shifrin's data is calculated for a system consisting of "water droplets in air", whose relative index of refraction m = 1.33 is different than that for our system of "silver bromide crystals in gelatin". Shifrin states, however, that the dependence on ρ is much stronger than on m.

Having calculated the total scattering coefficients on the basis of our experimental values for ΔD we could then compare them with the theoretical data.

We investigated the way ΔD (with a constant silver halide concentration) and k_S depend on the mean dimensions $\bar{x}$ of the crystals* for ammonium type emulsions whose silver halide crystals are approximately spherical.[8]

Figure 2 shows the curves obtained. These are in agreement with the theory,[9] which requires that as the crystal dimensions increase the scattering should increase for fine-grain and decrease for coarse-grain emulsions.

In addition, the relative scattering coefficients of the films were used to calculate the relative scattering coefficients for individual silver halide crystals, and curves were constructed giving the dependence of K on ρ, where $K = k_S/\pi r^2$ is the so-called dimensionless scattering coefficient. This curve is shown in Fig. 3, and it strongly resembles the curve obtained by Stratton and Haughton[10] for water droplets in air. The positions of the extrema (the first principal maximum and the first minimum) are in good agreement with the theoretical calculations[11] for systems in which the relative index of refraction m = 1.55 (this is the value for a system of "silver bromide crystals in gelatin").

Thus when ΔD is used to characterize the scattering, the experimental data is in good agreement with the theory.

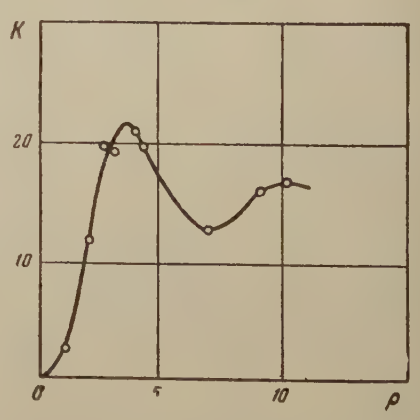

Fig.3. Variation of the scattering coefficient of AgBr crystals as a function of ρ.

*The parameter usually chosen to characterize the dimensions of the crystals is the area of their projection onto the film base. This is because this area determines the amount of light absorbed by a crystal and therefore its sensitivity to light.

2.Wavelength Dependence of Light Scattering by an Emulsion Layer

The wavelength dependence of the light-scattering properties of a number of different photographic emulsions was measured on an SF-11 spectrophotometer. Contrary to the assertions of Kilinskii[12] and others that primarily high-frequency light is scattered, we found that the range of frequencies scattered varies greatly and depends significantly on the degree to which the silver halide is dispersed in the emulsion. Fig.4 shows the wavelength dependence of scattering for a number of films with different degrees of dispersion. It is seen that primarily short wavelengths are scattered only in highly dispersed media, and that as the dimensions of the silver halide crystals increase, the scattering maximum moves towards the long-wavelength end of the spectrum. When $\bar{x} = 0.5\ \mu^2$, mainly red light is scattered, and as the crystals become still larger the scattering tends to become wavelength-independent over the entire visible region of the spectrum.

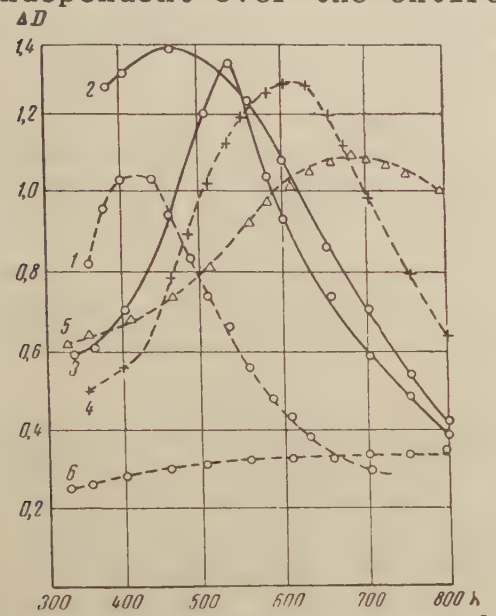

Fig.4. Wavelength dependence of light scattered by emulsion layers with different sizes of AgBr crystals. The curves correspond to equal to 1) 0.09, 2) 0.18, 3) 0.38 4) 0.53, 5) 0.58, 6) 1.50 μ^2.

On the basis of these measurements Breido and the writer[6] were able to explain the wavelength-dependence of the resolving power of photographic materials and the effect of optical sensitization of photographic film on its resolving power.

3.Determination of the Degree of Dispersion of Silver Halide in Photographic Emulsions from Measurements of Light Scattering

The mean size of silver halide crystals in photographic emulsions is usually determined by a very laborious procedure which involves microphotography of single-layer emulsions, enlarging the photographs obtained, measuring the very enlarged photographic images of the crystals and, finally, statistical analysis of the experimental data.

Because this method is so onerous, its use is highly limited. Now both the wavelength dependence of the scattering and the scattering of light of any given wavelength have been shown above to vary regularly with the crystal dimensions. Hence it is natural to ask whether one cannot find the mean crystal dimensions simply by measuring scattering. It is evident from Fig.2 that for a constant silver halide concentration ΔD depends strongly on the size of the crystals up to $\bar{x} \approx 1.5\ \mu^2$, so that it can be used to find the degree of dispersion of an emulsion in which the average size of the crystals is no greater than $1.5\ \mu^2$. Because there is a maximum in the ΔD vs $\bar{x}$ curve, however, determination of the crystal size from a measured value of ΔD alone may be ambiguous. This ambiguity can be eliminated by making use of the way the color of the scattered light varies with the crystal size. Thus when observed through a

highly dispersed film, which scatters primarily in the short wavelengths, the filament of an incandescent bulb appears red. As the average crystal size increases, the observed color changes to orange, purple, blue, and finally white (colorless). When viewed by transmitted light emulsions with an average grain size $\bar{x} < 0.3\ \mu^2$ appear red or orange. With $\bar{x} \geqslant 0.3\ \mu^2$ the transmitted color is purple, blue or whitish. Hence if one uses a light filter for which ΔD as a function of $\bar{x}$ has a maximum at $0.3\ \mu^2$, one can eliminate the ambiguity in the measurement of $\bar{x}$, since in this case all films transmitting red, orange, or yellow light will correspond to the left-hand side of the curve (to the left of the peak), while those transmitting purple, blue, or colorless light correspond to the right-hand side. A green light filter meets the above requirement, as does the curve obtained with white light under our conditions (using a selenium photocell). In general, it is expedient to have three (or at least two) curves of ΔD as a function of $\bar{x}$ for each given silver halide concentration in the blue, green, and red regions of the spectrum; then in doubtful cases, $\bar{x}$ can be determined from three (or two) measurements of ΔD, all of which, theoretically, should give the same value of $\bar{x}$.

This method of finding the degree of dispersion of the silver halide in an emulsion has been found very useful under industrial conditions since it provides a rapid means of grain-size control in the course of film production. In addition, it should be useful in research.

4. Angular Distribution of the Light in a Photographic Emulsion

Procedure

In order to understand the nature of the resolving power of photographic films, it is necessary to know how the light incident on an emulsion is distributed within it. Measuring the light transmitted or reflected by a film of emulsion does not tell much about the intensity distribution within the film. The indicatrix of the transmitted light is usually close to that of an ideal diffuser.

Many authors have proposed theoretical treatments of the problem of light passing through a light-scattering layer. There is, however, little experimental work on this subject. One may mention the work of Ginzburg, Pul'ver, and Fabrikant[13], who investigated the way the light scattered through an angle of 90° varies with the depth of penetration in opal glass illuminated by a parallel beam. These investigators observed that the scattered light intensity attains a maximum value at a certain depth, and falls off at greater and lesser depths. Timofeeva[14] performed a thorough experimental study of the light distribution in strongly scattering liquid media.

Unfortunately, the intensity distribution in a layer having a thickness of the order of 20 μ cannot be measured by the methods of Ginzburg et al or by immersing the photometer in the medium as Timofeeva in her liquid media. We did the only thing possible, which is to measure the brightness of light transmitted by emulsions of different (increasing) thickness. From this one can judge how the intensity varies in different directions as the light penetrates into the emulsion layer.

The layer thickness was varied by varying the amount of emulsion applied. Thus, when 0.5, 1.0, 2.0, 3.0, 4.0, and 8.0 milliliters of emulsion were coated on standard 3 x 12 cm glass plates, the air-dried layers obviously had thicknesses varying in the proportions 1/16, 1/8, 1/4, 3/8, 1/2 and 1. The absolute thickness of the layers depends on the gelatin concentration in the emulsion. For a 6% concentration of gelatin, the thickness of the air-dried film obtained by spreading 1 cm^3 of emulsion over a 3 x 12 cm plate is of the order of 20 μ.

A visual photometer was used to measure the relative brightness of the layers in transmitted light as viewed from different angles. The incident light was almost parallel, and the angles of measurement were 0, 10, 20, 30, 40, and 50° to the incident beam. The limitations of our apparatus precluded making measurements at angles greater than 50°.

Results

Figure 5 is a polar plot of the logarithm of the brightness B for emulsion layers of different thickness.

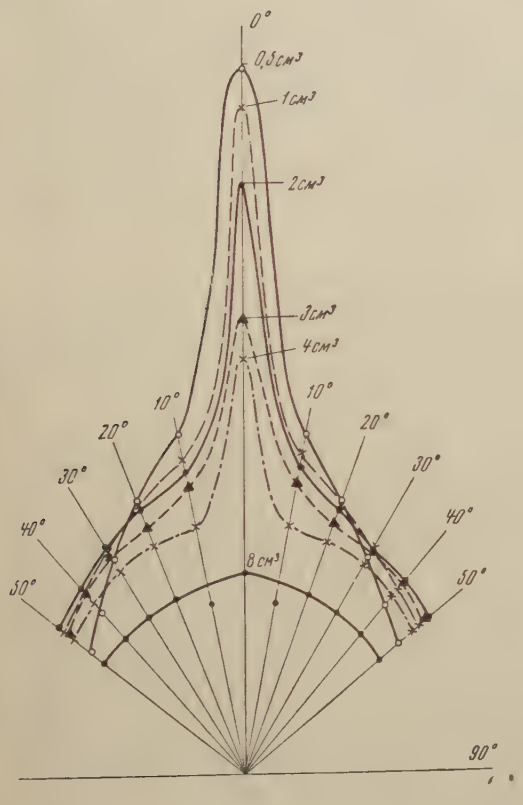

Fig.5. Scattering indicatrices for emulsion layers of different thickness (polar radii = log B).

For better accuracy, the visual photometric measurements were made with a green light filter. It will be seen from the figure that as the thickness of the emulsion increases, the scattering indicatrix of the transmitted beam becomes less and less peaked, and that at a certain thickness (actually the one corresponding to 8 ml of emulsion) the brightness becomes almost the same in all directions.

Curves characterizing the variation in brightness as a function of thickness for several directions of the measurement are plotted in Fig. 6. These curves, therefore, furnish an indication of the variation in intensity with depth of penetration into the layer. The ordinates are values of the brightness B per se (not log B). Since the brightness is particularly high at 0°, we were not able to include this curve in the figure. It is seen that in the directions at 30, 40, and 50° to the incident beam the brightness goes through a maximum. At 10 and 20°, the maximum values apparently obtain at the very surface of the layer.

Figure 7 shows the distribution in brightness with depth for the same emulsion but with different silver halide concentrations. The crystal concentrations were varied

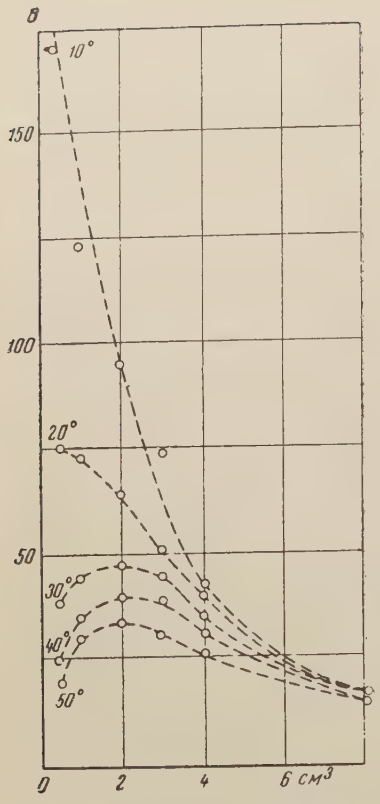

Fig.6

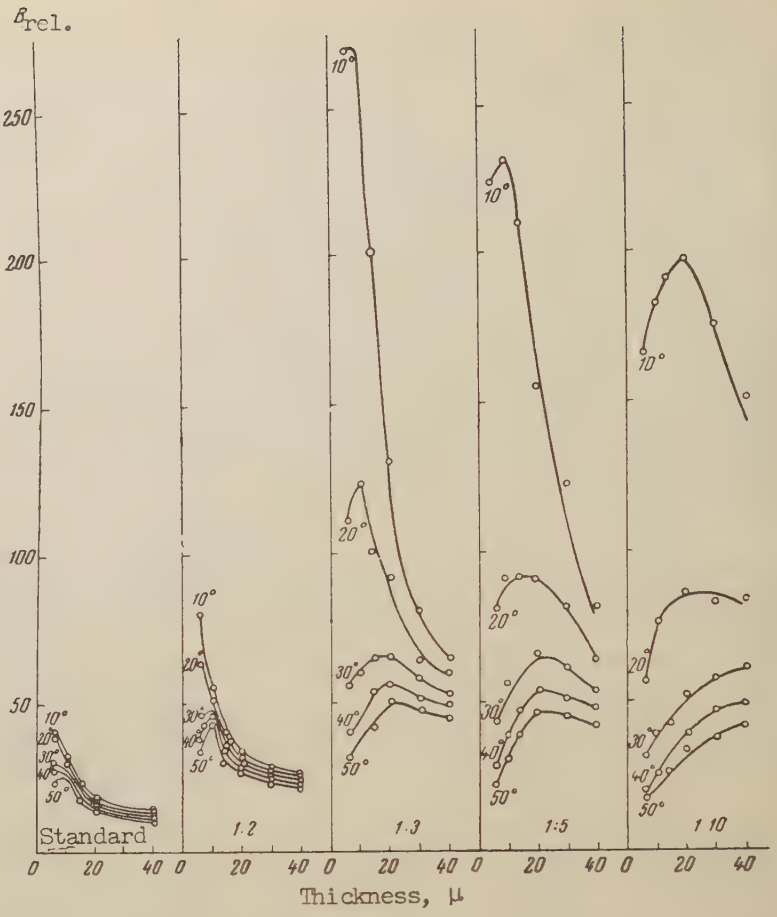

Fig.7

Fig.6. Brightness B as a function of emulsion layer thickness for different angles of observation.

Fig.7. Curves similar to those in Fig.6 for emulsion layers with different silver halide concentrations.

by diluting the standard emulsion with a gelatin solution of the same strength as that used in preparing the standard emulsion. It will be evident that for all silver halide crystal concentrations the general regularities remain the same, but that the depth at which the maximum brightness value is attained increases with decreasing silver halide grain concentration. The brightness levels per se at first increase rapidly and then begin to decrease with further dilution. Thus, while in the undiluted emulsion the brightness values of the scattered light are comparatively low and the maxima are attained near the surface of the layer, as the emulsion is increasingly diluted the scattered light intensities become greater and the maxima occur deeper in the layer.

The representation of the intensity distribution in depth based on our measurements is only qualitative and only approximates the picture that would be obtained if one could plunge a microscopic photoelectric cell to different depths in an emulsion. We do, however, obtain good agreement with Timofeeva's results. We also find qualitative agreement with the simple theoretical formulas deduced by Boldyrev & Aleksandrov.[15] The layer depth at which the maximum brightness in some given direction is attained was expressed in units of 1/k, where k is the light attenuation factor in the layer, and this was compared with the theoretical value. The

experimental depth values for the brightness maxima were found to be larger than the theoretical ones. This may be because Boldyrev & Aleksandrov deduced their theoretical formulas for a weakly scattering medium in which the absorption is much greater than the scattering; our emulsions are strongly scattering, while the absorption in them in the investigated spectral region is weak.

Further experiments, which will be described in a separate communication, showed that the way the resolving power depends on the film thickness and the concentration of silver halide is consistent with the deduced pattern for the flux intensity distribution in emulsion layers.

Conclusions

In the present report we have summarized the results of our studies of light scattering in photographic emulsion layers.

1. We compare the experimental results with the deductions of theory.

2. We established the correlation between the scattering of light of a given wavelength and the concentration of silver halide in the emulsion and found the character of the concentration dependence of the scattered spectral range.

3. On the basis of our results, we developed a procedure for determining the mean dimensions of crystals in photographic emulsions from the light scattered by such emulsions.

4. We investigated the flux intensity distribution in emulsion layers.

References

1. I.I.Breido, Usp.nauchn.fotogr. (Advances in Scientific Photography), 1,118 (1951).
2. L.Falla, Sc.Ind.Phot., 20, 449 (1949).
3. A.Narath & G.Schimmel, Sc.Ind.Phot., 23A, 280 (1951).
4. G.S.Baranov, Usp.nauchn.fotogr., 1, 106 (1951).
5. P.Kh.Pruss, Zhur.tekh.fiz., 24, 50 (1954).
6. I.I.Breido & P.Kh.Pruss, Zhur.tekh.fiz., 22,515 (1952).
7. K.S.Shifrin, Trudy GGO (Transactions, Main Geophys.Observatory), 27, 77 (1951).
8. I.R.Protas, P.KhPruss & Iu.A.Krakau, Zhur.prik.khim. (Journal of Applied Chem.) 22, 823 (1949).
9. K.S.Shifrin, Rasseianie sveta v mutnoi srede (Light scattering in a turbid medium), M.-L., 1951.
10. I.Stratton & H.G.Haughton, Phys.Rev.,38, 159 (1931).
11. D.Sinclair, JOSA, 37, 9, 475 (1947).
12. I.M.Kilinskii, Trudy NIKFI (Transactions,Motion Picture & Photograph Scientific Research Institute), 7, 69 (1949).
13. V.Ginzburg, V.Pul'ver & V.Fabrikant, Trudy GOI (Transactions, State Optical Institute), 11, 24 (1936).
14. V.A.Timofeeva, Doklady AN SSSR, 76, 677; 831 (1951).
15. N.Boldyrev & A.Aleksandrov, Trudy GOI (Transactions, State Optical Institute), 11, 56 (1936).

PROCEDURE FOR INVESTIGATING THE REFLECTIVITY OF COLOR-PRINT PHOTOGRAPHIC PAPER

- V.M.Bakhvalov

Photographic paper used for making color prints by the three-color process has the following structure. The backing is a high quality paper with baryta coating which gives the paper a smooth surface and acts as a diffuse reflector, increasing its coefficient of reflection and its whiteness. On top of the baryta coating are three layers of emulsion, containing different substances which in the process of color development form transparent dyes similar to those used at present in color motion picture photography. Thus the final color print consists of transparent dyes in a gelatinous medium in optical contact with a diffuse reflector. Different amounts and proportions of the dyes on the backing result in the reflection of different wavelengths, thus forming the color image.

Transparent dyes on a white opaque backing absorb and transmit light selectively in the same way as dyes on a transparent film base; but in this case there are factors which complicate the measurement of the reflected light. These are reflection at the surface and multiple internal reflection at the gelatin-air interface. According to the data in the literature,[1] the index of refraction of the color-print gelatin is 1.53. When light is incident on the surface of the gelatin, part of it is reflected, but most of it is refracted and reaches the backing. Since the backing reflects light diffusely in a complete hemisphere, the reflected light reaches the gelatin-air interface at all angles from 0 to 90° relative to the surface. The fraction of the light striking the gelatin-air surface at angles greater than the critical is totally reflected and returns to the backing. When there is no dye in the gelatin, multiple internal reflection takes place and as a result the brightness of the baryta backing is almost the same as if there were no gelatin film covering it.

In order to characterize the processes of modern color photography quantitatively, it is important to have an accurate determination of the absorption curve of color photographic paper and to find the superficial densities of the dyes (even if only in relative units) which give rise to absorption curves.

The experimental data given below show the effect of surface reflection on the absorption curve obtained by reflected light measurements.

Operational Comparison of Spectrophotometers

We tested several existing spectrophotometers for the purpose of determining their applicability in measuring the absorption curves of color-print photographic paper. The tests were made on paper samples containing different amounts of one of the dyes and consisted of finding the extent to which the data obtained with a given spectrophotometer agreed with Baer's law, which is fundamental to quantitative spectrophotometry. Since the actual concentration of the dye in a gelatin film cannot be determined, the extent to which the dyes conform to Baer's law can be judged from the variation in the shape of the absorption curve (as observed with

different instruments) when the amount of each of the dyes is varied.

According to the data in the literature,[2] the given dyes on a transparent base (motion picture film) obey Baer's law in the range of concentrations in practical use.

Because of surface reflection and multiple internal reflection (which are not the same for diverse intensities of the dyes) there is reason to suppose (see Ref.3) that when these dyes are viewed under reflected light, the absorption curve will change somewhat as the dye concentration is varied and that therefore Baer's law does not fully hold.

To verify this assertion, the same samples with different amounts of each of the three dyes were measured on suitable spectrophotometers with reference to a baryta backing coated with a gelatin film containing no dye. The absorption curves obtained were used to find the spurious absorption over the spectrum as a function of the absorption at the maximum. We define the "spurious absorption" as the absorption at other wavelengths of the visible spectrum.

Figure 1 shows the attachments used with the SF-2, SF-4, and Beckman spectrophotometers, on which the absorption curves were measured. It will be seen that in the SF-4 and Beckman spectrophotometers the incidence of light beam is normal to the sample surface, while in the SF-2, the angle of incidence is about 6° from the normal.

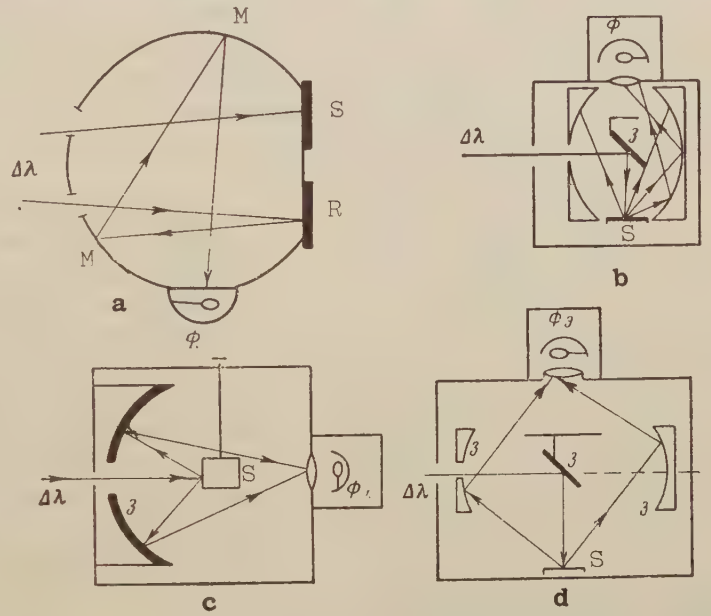

Fig.1. Spectrophotometer attachments for making measurements in reflected light: a) for the SF-2, b & c) for the SF-4 and d) for the Beckman. φ - photocell, S - sample, R - reference standard, M - mirror.

Figs.2 & 3 show the variations of spurious absorption over the spectrum as a function of the absorption at the maximum for purple dye as determined by means of the SF-2 and the SF-4 with a spherical mirror. It will be seen that the SF-2 yields curved lines, while the SF-4 gives straight lines up to $D^{r}_{\lambda max} = 2.00$, which means that the readings on the SF-4 are consistent with Baer's law. Similar dependences were obtained for the other dyes.

These data indicate that when the SF-2 spectrophotometer is used for measurements on samples such as a baryta coating covered with a gelatin film, some surface reflected light enters the receiving part of the instrument with the result that there is apparent deviation from Baer's law.

In order to find the direction of propagation of the surface reflected light from the gelatin surface, we measured the reflec-

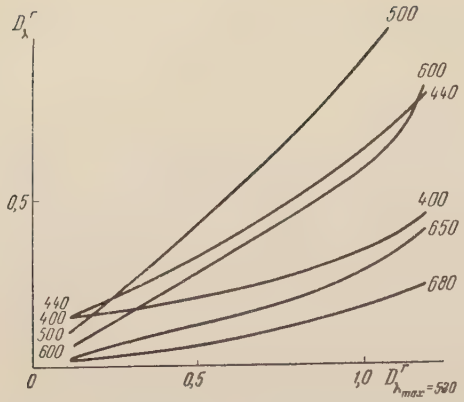

Fig.2. Spurious absorption over the spectrum as a function of the absorption at the maximum, as measured on an SF-2 spectrophotometer.

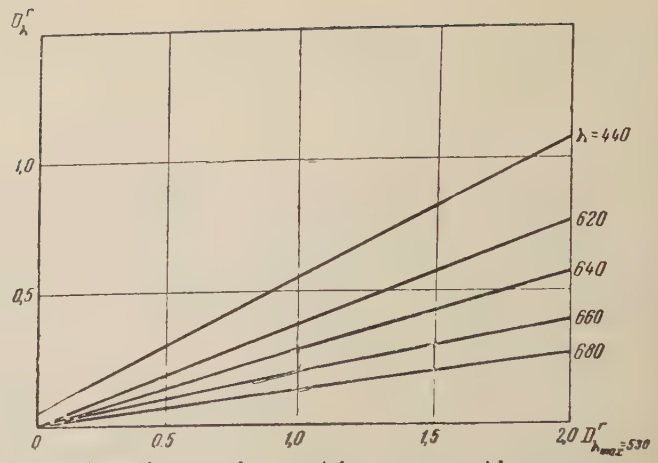

Fig.3. Spurious absorption over the spectrum as a function of the absorption at the maximum as measured on an SF-4 spectrophotometer with a spherical mirror.

tion indicatrix for paper coated with gelatin film containing the maximum amount of all three dyes, which together absorbed all the visible light. The set-up used for these measurements is diagramed in Fig.4. A narrow beam of white light from the lamp is incident on the virtually black gelatin surface. The measurements were performed in a dark room.

The surface reflection from this sample was measured at various angles with respect to the normal using a selenium photocell connected to a highly sensitive galvanometer (GPZ-2).

The light intensity was chosen so that when the beam was directed at the sample through a special aperture in the photocell, the scale reading was 100. Figure 5 shows the reflec-

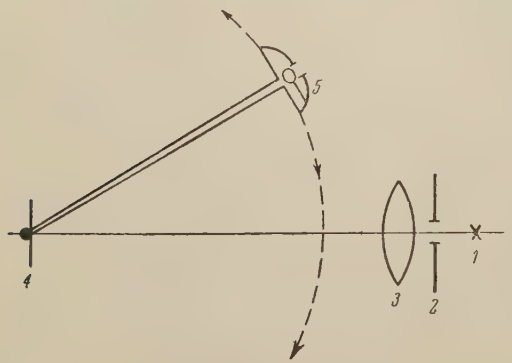

Fig.4. Diagram of the set-up for measuring the reflection indicatrix. 1) light source, 2) slit, 3) lens, 4) sample, 5) photocell on circular mounting.

tion indicatrix for gelatin surfaces and the baryta backing. The solid angle of the photocell was 0.125 sterad.

It will be seen from the figure that the glossy gelatin surface, and, particularly, the rolled-on gelatin coating are characterized by practically mirror reflection. Therefore absorption curve measurements should be performed on spectrophotometers

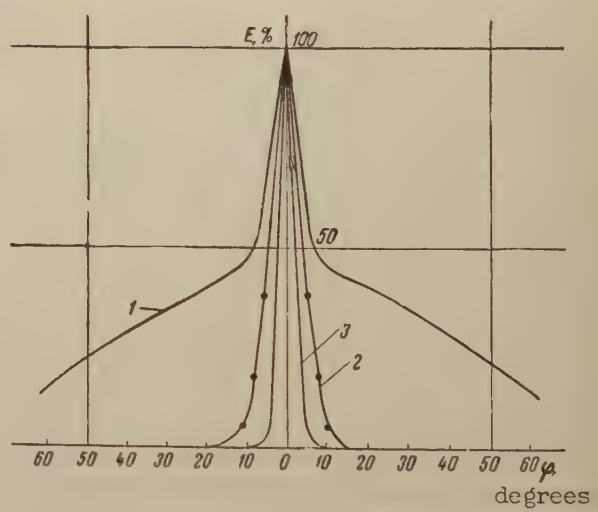

Fig.5. Reflection indicatrix for normal incidence of light on the baryta backing (1), a glossy gelatin surface (2), and a rolled-on gelatin coating (3). φ = measurement angle relative to the normal.

in which the light reflected from the surface does not enter the measuring section.

To evaluate the worth of the different instruments for purposes of absorption curve measurements, samples with different amounts of purple dye were measured with illumination by three different wavelengths on all the instruments described above. As in all other cases, the measurements were performed with reference to a baryta backing coated with a gelatin film containing no dye. The accompanying table gives the optical density values obtained for the purple samples in reflected light of 440, 530 and 680 mμ. It will be evident that up to $D_\lambda^r = 1.00$ the different attachments give virtually the same results. At densities above 1.00, the values obtained with the different instruments begin to diverge; the SF-2 and SF-4 with an ellipsoidal mirror stand out particularly. Fig.6 is a plot of the spurious absorption as a function of the absorption at the 530 mμ maximum, based on the tabular data. It will be evident that on the basis of the tests with samples having a high optical density and virtually mirror reflection at the surface, the instruments can be graded in the following descending order of desirability: 1) Beckman spectrophotometer, 2) SF-4 with a spherical mirror, 3) SF-4 with an ellipsoidal mirror, and 4) SF-2 (automatic spectrophotometer).

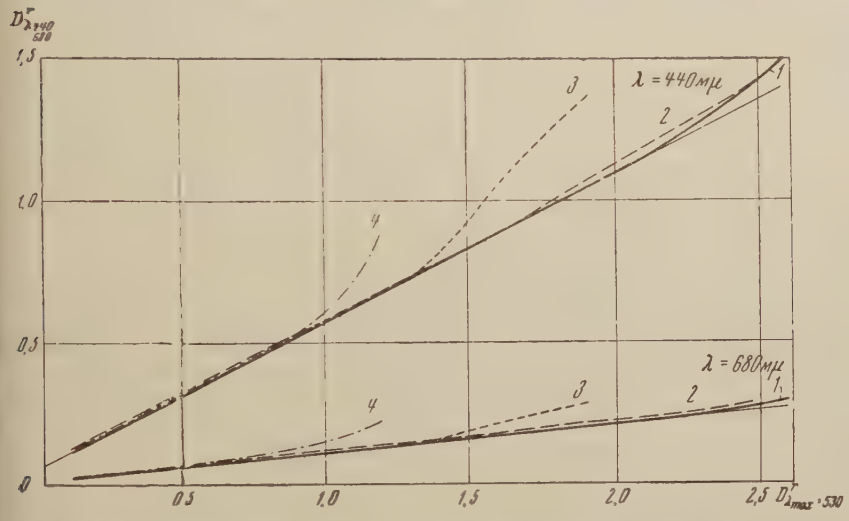

Fig.6. Spurious absorption of purple dye as a function of the absorption at the 530 mμ maximum, based on determinations with the different spectrophotometers: 1) Beckman, 2) SF-4 with spherical mirror, 3) SF-4 with ellipsoidal mirror, and 4) SF-2.

If we subtract the surface reflection, which is 4.3% for a gelatin film, the SF-2 readings for high densities are brought closer to those of the SF-4 and the Beckman spectrophotometer, while for low densities the divergences increase (see table).

It will be seen from the table that the attachment with the ellipsoidal mirror for the SF-4 gives high-density values that are considerably lower than those obtained with the spherical mirror attachment and by means of the Beckman spectrophotometer. The reason is that the baffle over the mirror directing the incident beam onto the sample in this attachment is too small and does not completely shield the photocell from the surface reflected light.

This attachment was designed for the purpose of measuring ordinary light scattering samples which commonly have diffuse surface reflection.

In the spherical-mirror attachment for the SF-4 the sample holder arm is located in the path of the beam from the spherical mirror to the photocell, which results in additional light scattering.

Optical Densities in the Reflected Light of Identical Samples as Determined by the Different Spectrophotometers Tested

Sample	Beckman spectrophotometer			SF-4 with ellispoidal mirror			SF-4 with spherical mirror			SF-2			SF-2		
	D_λ^r			D_λ^r			D_λ^r			D^r			D_λ^r		
	440	530	680	440	530	680	440	530	680	440	530	680	440	530	680
	slit width			slit width			slit width						subtracting 4.3% of the surface		
	0,40	0,25	0,30	0,10	0,05	0,20	0,11	0,05	0,14						
1	0,167	0,118	0,023	0,165	0,12	0,025	0,165	0,115	0,025	0,15	0,115	0,02	0,18	0,14	0,04
2	0,222	0,30	0,04	0,22	0,30	0,04	0,22	0,30	0,04	0,21	0,28	0,04	0,24	0,30	0,06
3	0,45	0,75	0,08	0,45	0,74	0,09	0,45	0,75	0,08	0,41	0,65	0,09	0,46	0,71	0,12
4	0,55	0,96	0,11	0,55	0,94.	0,11	0,55	0,96	0,113	0,49	0,80	0,114	0,56	0,90	0,14
5	0,64	1,18	0,13	0,64	1,13	0,13	0,64	1,15	0,13	0,56	0,93	0,13	0,63	1,13	0,17
6	0,82	1,48	0,16	0,81	1,38	0,16	0,82	1,42	0,16	0,69	1,07	0,16	0,77	1,37	0,22
7	1,12	2,03	0,22	1,06	1,59	0,22	1,11	1,96	0,22	0,88	1,18	0,21	1,06	1,65	0,27
8	1,51	2,60	0,30	1,38	1,91	0,30	1,43	2,30	0,30						

This lowers the high-density readings somewhat with resultant departure from Baer's law.

Thus the difficulties in the high-density measurements are caused by 1) surface reflected light entering the receiving section of the photometer and 2) light scattering in the attachments.

Conclusions

1. A baryta backing covered by a gelatin film reflects light at its surface. In the case of an even gelatin coating applied by rolling onto glass the surface reflection approximates mirror reflection.

2. When determining the absorption (or reflection) curve of color-print photographic paper care must be taken that the spectrophotometer attachments used are designed to prevent the surface reflected light from entering the measuring part of the instrument.

3. Two basic conditions must be borne in mind in designing attachments for spectrophotometers for the purpose of measuring the reflection curves of photographic paper:

a) The angle of incidence of the light on the sample must be confined to the range from 0° to 40-50° to the normal since at higher angles the surface reflection rises sharply, and

b) The observation angle should not be less than 15° with respect to the direction of mirror reflection.

Aerial Methods Laboratory,
Academy of Sciences of the USSR

References

1. F.C.Williams & F.R.Clapper, JOSA, 43, 595 (1953).

2. Iu.N.Gorokhovskii, D.K.Balabukha & T.M.Levenberg, Usp. nauchn. fotogr. (Advances in Scientific Photography), 2,96 (1954).

3. R.M.Evans, W.T.Hanson & W.L.Brewer, Principles of Color Photography, New York, 1953.

SOME ASPECTS OF THE THEORY OF DISPERSIVE LIGHT FILTERS

- A.P.Prishivalko

Dispersive light filters have various advantages over others, such as high monochromaticity and comparatively high transmission. The half-width of the transmission band of such light filters in the visible spectrum can be of the order of 30-40 Å with a transmission coefficient of the order of 90%. By combining several such filters, the half-width of the transmission band can be brought down[1] to 20-15 Å. Such filters are, however, highly sensitive to temperature changes, so that their temperature must be maintained stable to within 0.1°.

The operation of dispersive light filters is based on an effect discovered by Christiansen[2] in 1884. Later Sethy[3], Sogani[4], and others[5-8] have contributed to this field. Nevertheless the theory of dispersive light filters has not yet been adequately developed.

In 1949 Raman[9] published an article in which the transmission curve of a light filter was given as

$$I = I_0 e^{-\frac{p^2\pi^2 (n_1 - n_2)\, z\Delta}{\lambda^2}}, \qquad (1)$$

where $(n_1 - n_2)$ is the difference between the indices of refraction of the dispersed substance and the binding medium, p is a factor of the order of unity, Δ is the mean dimension of the particles, and z is the thickness of the light filter. In Raman's treatment the light filter is considered to be composed of a large number of independent elementary layers and the intensity is assumed to be a continuous function of the thickness.

Raman restricted his considerations to the narrow region of the spectrum transmitted by the light filter and disregarded the light of other wavelengths scattered through large angles and forming a halo. Yet a study of this part of the spectrum is of interest not only in that it can help explain the behavior of dispersive light filters, but also because it can be useful in solving certain other problems related to reflection and scattering of light in absorbing and nonabsorbing scattering media.

Further, in finding the transmission coefficient, Raman replaced the square of the sine in the exponent by the square of its argument. This approximation greatly limits the validity of Eq. (1). It is easily shown that this formula is valid only if

$$n_1 - n_2 \ll \frac{\lambda}{\Delta} \cdot \frac{\sqrt{3}}{\pi} \approx 0{,}55\, \frac{\lambda}{\Delta}. \qquad (2)$$

This means that if $\Delta = 0.01$ cm and $\lambda = 0.6 \cdot 10^{-4}$ cm, we must have $n_1 - n_2 \ll 0.0033$. For larger particles and shorter wavelengths, for instance for $\Delta = 0.2$ cm and $\lambda = 0.45 \cdot 10^{-4}$ cm, we must have $n_1 - n_2 \ll 0.00012$, which would hold only for a very narrow wavelength range. Outside of this wavelength interval the formula becomes invalid and cannot be used for determining how much of the light is directly transmitted and how much is scattered into the halo. Raman's derivation involves integration. As a result his equations can be used only for sufficiently thick layers in which $z \gg \Delta$ which means that the number of elementary layers must be large.

The present article is a more detailed investigation of the interference phenomena taking place in light-scattering layers (not necessarily in a dispersive light filter, but in any scattering medium).

Following Raman, we subdivide the entire light-scattering layer into a series of elementary layers (or films) whose individual thickness is given by the mean dimensions of the particles. We assume further that each of these films acts independently of the others and that each film consists of a large number of cells of equal size but filled in different ways by the dispersed substance and the binding medium.

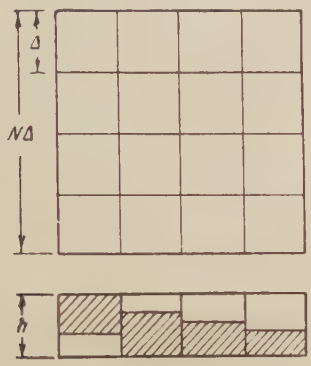

Fig.1. Model of an elementary film (top and side views).

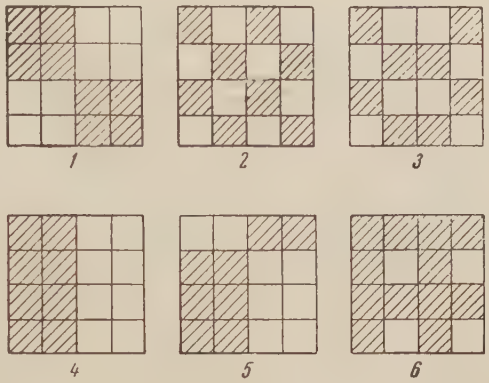

Fig.2

The intensity of light passing through a film in any direction can be calculated by adding the perturbations due to the separate cells, taking into account their phase differences. These phase differences are due to differences in the cells (which consist of a solid and the medium - a liquid or gas) and their different locations with respect to the observer. Each cell has some mean index of refraction which depends on the proportion of the dispersed substance to the medium within it or what might be termed its filling factor. The cells are chosen so that within each one we may consider the index of refraction constant (or varying according to some definite law).

Bearing in mind diffractive phenomena in such a structure and neglecting reflection, we arrive at the expression

$$I = [D(\varphi, \psi)]^2 \sum_{p,q,l,m=1}^{N} \cos k\left\{\frac{A}{N}[(p-l)\sin\varphi + (q-m)\sin\psi] + h\,(n_{pq} - n_{lm})\right\}, \qquad (3)$$

where

$$[D(\varphi, \psi)]^2 = I_0\left(\frac{\sin\frac{kA\sin\varphi}{2N}}{\frac{kA\sin\varphi}{2N}}\right)^2\left(\frac{\sin\frac{kA\sin\psi}{2N}}{\frac{kA\sin\psi}{2N}}\right)^2, \qquad (4)$$

here A represents the linear dimensions of the film surface, φ and ψ are the angles of diffraction in two mutually perpendicular planes, $k = 2\pi/\lambda$ is the wave number, h is the thickness of the film, n_{pq} and n_{lm} are the mean indices of refraction of a cell denoted by the two subscripts (one for the x axis, and the other for the y axis), and N is the number of cells along one of the dimensions.

This expression can be calculated if one knows how the index of refraction varies through the film.

The light intensity transmitted by a light-scattering layer has been calculated for some special models of elementary films, differing from each other as regards their filling factor or the way the cells are distributed in the film (Fig.2). In the most general form the results obtained can be written

$$I_{\varphi,\psi} = I_0\left\{\left(\frac{\sin\frac{kA\sin\varphi}{2}}{\frac{kA\sin\varphi}{2}}\right)^2\left(\frac{\sin\frac{kA\sin\psi}{2}}{\frac{kA\sin\psi}{2}}\right)^2 F(\varphi,\psi,\Delta,\lambda) + C(\varphi,\psi,\Delta,\lambda)\right\}. \quad (5)$$

Whenever the index of refraction distribution is symmetrical, as in models 1, 2, 3, 4, and 6 (Fig.2), we find that $C(\varphi,\psi,\Delta,\lambda) = 0$. For model 5 and similar ones, this function does not vanish. It therefore characterizes the degree of disorder in the distribution of the index of refraction. The greater the disorder, the greater $C(\varphi,\psi,\Delta,\lambda)$, and therefore the greater its influence in the intensity distribution. Unlike this function, $F(\varphi,\psi,\lambda,\Delta)$ depends on the filling factor. It can be shown that the intensity of the light directly transmitted always depends only on the filling factor. All of the models with a filling factor of 1/2 regardless of the arrangement of the cells give

$$I = I_0\cos^2\frac{kh(n_1-n_2)}{2}. \quad (6)$$

Models having a 3/4 filling factor give

$$I = I_0\frac{1+3\cos^2\frac{kh(n_1-n_2)}{2}}{4}. \quad (7)$$

for the directly transmitted light. The arrangement of the cells affects only the distribution of the scattered light.

Usually in the preparation of dispersive light filters an attempt is made to obtain as homogeneous a distribution of the solid particles in the liquid as possible. Thus models 2 and 6 are those which correspond closest to reality in Fig.2. Model 2 is an idealization of so-called mosaic light filters. A mosaic light filter is made of small plates of two kinds of glass bonded in a checkerboard pattern on a transparent base. Such light filters are used to obtain a desired energy spectrum from a given light source. Nagel[10] suggests that the spectrum of the transmitted light depends on the positions of the individual squares in the mosaic. The results of our calculations contradict this influence.

The aggregate light-scattering layer is comprised of a set or series of elementary films. Each successive elementary film scatters some part of those wavelengths of the light for which $n_1 - n_2$ is sufficiently large. As a result, these wavelengths are scattered or, in effect, filtered out. The thicker the light-scattering layer, the more films it contains, and therefore the narrower the band transmitted by it.

Consider a light-scattering layer consisting of m elementary films. Than taking into account the discrete structure of the layer, we obtain

$$I = I_0\left[\cos^2\frac{kh(n_1-n_2)}{2}\right]^m \quad (8)$$

for the direct transmitted light intensity when the filling factor is 1/2, and

$$I = I_0\left[(1-p^2) + p^2\cos^2\frac{kh(n_1-n_2)}{2}\right]^m \qquad (9)$$

for any degree of filling.

Eqs.(8) and (9) are valid for all values of $n_1 - n_2$, i.e., in a wide range of wavelengths. Because the discrete structure of the light-scattering layer has been taken into account, these equations are valid for layers of any thickness, including very thin ones for which m is small.

It is easily shown that for wavelengths close to the transmission band (i.e., in the region where $n_1 - n_2$ is small) and a sufficiently large number of films, Eqs.(8) and (9) go over into Raman's Eq.(1). Knowing h, λ_0 and the shape of the dispersion curves, one can calculate the necessary thickness of a light filter.

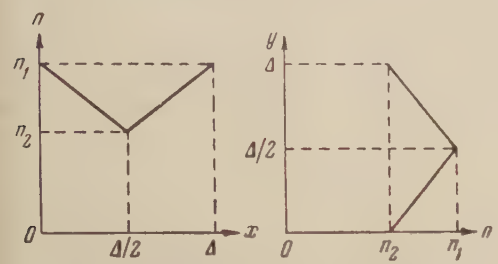

Fig.3. Variation of the mean index of refraction along the x and y axes.

Simple results for the angular distribution of the light are obtained if we assume that the mean index of refraction varies continuously. A numerical calculation was performed for a model of a film in which all of the cells are the same, and in each of which the mean index of refraction varies as shown in Fig.3. The intensity of the light transmitted along the x axis is

$$I = I_0\left[\left(\frac{\sin\frac{k(a-R)\Delta}{4}}{\frac{k(a-R)\Delta}{4}}\right)^2 + \left(\frac{\sin\frac{k(a+R)\Delta}{4}}{\frac{k(a+R)\Delta}{4}}\right)^2 + 2\left(\frac{\sin\frac{k(a-R)\Delta}{4}}{\frac{k(a-R)\Delta}{4}}\right)\left(\frac{\sin\frac{k(a+R)\Delta}{4}}{\frac{k(a+R)\Delta}{4}}\right)\cos\frac{ka\Delta}{2}\right]\left(\frac{\sin\frac{ka\Delta N}{2}}{\sin\frac{ka\Delta}{2}}\right)^2, \qquad (10)$$

where $k = \frac{2\pi}{\lambda}$, $R = h\frac{n_1-n_2}{\Delta}$, $a = \sin\varphi$, and h is the thickness of the layer.

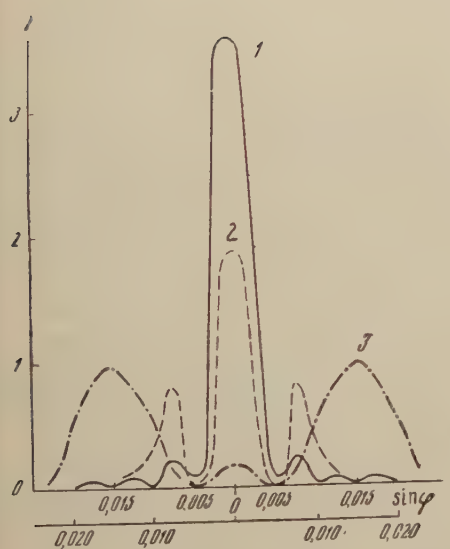

Fig.4. Variation of the transmitted light intensity as a function of φ for h = 0.01 cm, Δ = 0.01 cm, $\lambda = 0.5\cdot10^{-4}$ cm, and for $n_1 - n_2$ equal to 1) 0.001, 2) 0.005, and 3) 0.015.

Fig.4. shows graphs of the expression in brackets as a function of a for three particular cases. The shape of the curves depends strongly on $n_1 - n_2$. When this difference is small, there is one sharp central maximum and side maxima are virtually absent. When the difference is increased, the central maximum begins to drop and side maxima appear. They move further from the center as $n_1 - n_2$ increases; finally, at some values of $n_1 - n_2$ there is no central maximum. The sequence of colors in the halo depends on the spectral composition of the light. These results agree with the experimental data of Sethy[3] and Sogani[4].

Of particular interest is the case in which the dispersed substance absorbs light. Calculations with the above models including absorption of light by the dispersed substance show that only the character of the scattering depends on the distribution of the cells. The directly transmitted light depends only on the coefficient of absorption and the filling factor.

When the dispersed substance absorbs light, the intensity of the light directly transmitted through m elementary films with a filling factor σ is given by

$$I = I_0\left\{\sigma^2 e^{\frac{-4\pi\varkappa h}{\lambda}} + (1-\sigma)^2 + 2\sigma(1-\sigma)\, e^{\frac{-2\pi\varkappa h}{\lambda}} \cos\frac{2\pi h(n_1-n_2)}{\lambda}\right\}^m. \tag{11}$$

Now, the absorption coefficient for a continuous medium is

$$k_\lambda = -\frac{1}{z}\ln\frac{I}{I_0}. \tag{12}$$

Hence by analogy, we can introduce the concept of an attenuation coefficient K_λ which includes both absorption and sidewise scattering. This will then be

$$K_\lambda = -\frac{1}{h}\ln\left\{1-\sigma\left[(2-\sigma)-\sigma e^{-\frac{4\pi\varkappa h}{\lambda}} - 2(1-\sigma)\, e^{-\frac{2\pi\varkappa h}{\lambda}}\cos\frac{2\pi h(n_1-n_2)}{\lambda}\right]\right\} \tag{13}$$

where h is the thickness of the layer and $\varkappa$ is the absorption coefficient. Writing

$$\sigma\left[(2-\sigma)-\sigma e^{\frac{-4\pi\varkappa h}{\lambda}} - 2(1-\sigma)\, e^{\frac{-2\pi\varkappa h}{\lambda}}\cos\frac{2\pi h(n_1-n_2)}{\lambda}\right] = \alpha,$$

we obtain

$$K_\lambda = -\frac{1}{h}\ln\{1-\alpha\}. \tag{14}$$

If $\alpha \ll 1$, then $-\ln(1-\alpha) \approx \alpha$.

In this case $K_\lambda \approx \frac{\alpha}{h}$, and we may say with sufficient accuracy that the light intensity varies according to

$$I = I_0 e^{-\frac{\alpha}{h}z}. \tag{15}$$

This approximation is valid if $\varkappa$ and $n_1 - n_2$ are small, i.e., only for weakly absorbing and weakly scattering substances. In general for arbitrary values of $\varkappa$ and $n_1 - n_2$ the intensity varies in a more complicated way.

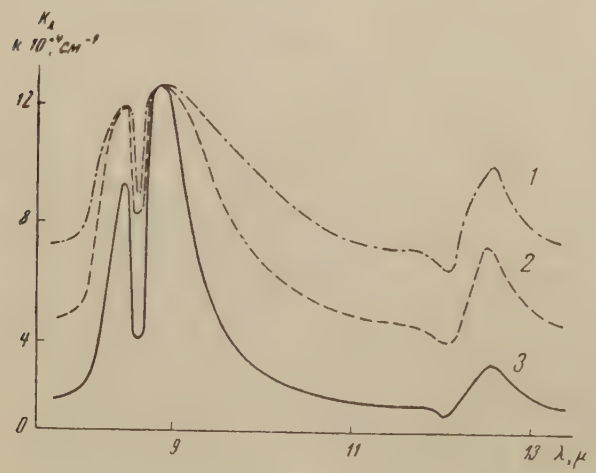

A plot of Eq.(13) shows that variation of the filling factor σ does not alter the position of the attenuation maxima (see Fig.5).

The wavelength dependence of the attenuation coefficient is strongly related to the degree of inhomogeneity of the medium.

Fig.5. Wavelength dependence of the attenuation coefficient K_λ for 1) $\sigma = 0.5$; and 2) $\sigma = 0.9$; curve (3) corresponds to $k = \frac{4\pi\varkappa}{\lambda}$ with $\sigma = 1$.

So long as the inequality

$$\frac{2\pi h}{\lambda}(n_1 - n_2) < \frac{\pi}{2}, \qquad (16)$$

is fulfilled, the K_λ curves reproduce approximately the absorption coefficient curve of the dispersive substance in the continuous (solid) state, i.e., the maxima of the attenuation and true absorption curves coincide. When $\frac{2\pi h}{\lambda}(n_1 - n_2)$ becomes greater than $\frac{\pi}{2}$, $\cos\frac{2\pi h(n_1 - n_2)}{\lambda}$ becomes negative. In other words pronounced heterogeneity of the material results in strong scattering. New maxima then appear in the curves, while the old maxima are deformed and displaced. Fig.6 shows the wavelength dependence of K_λ for various values of h. The calculations are performed for a substance whose index of refraction and absorption coefficient vary as shown in Fig.7. The condition of Eq.(16) is fulfilled only for the solid curve in Fig.6.

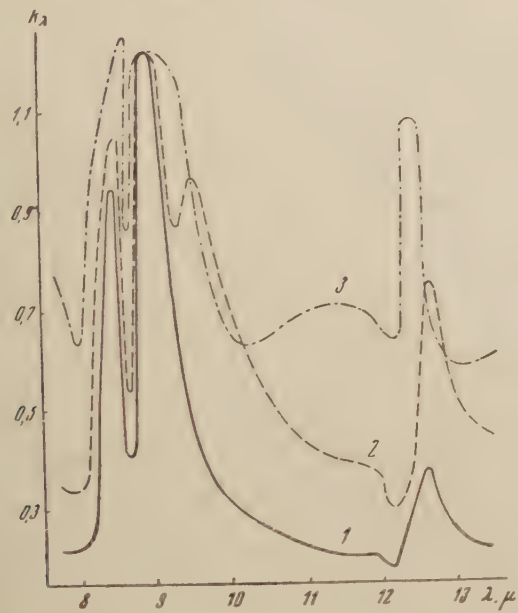

Fig.6. Wavelength dependence of K_λ for different values of the layer thickness h: 1) 1 μ, 2) 5 μ, 3) 10 μ.

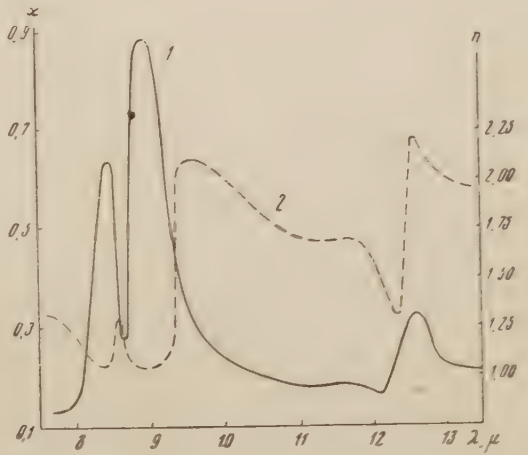

Fig.7. Wavelength dependence of $\varkappa$ (1) and n (2) of the material for which the curves of Fig.6 were calculated.

The different curves show how important it is to take into account the degree of inhomogeneity of the medium when investigating the spectrum of a substance in a dispersed state.

The questions touched upon above are discussed in more detail in the publications listed under Ref.6.

Institute of Physics and Mathematics,
Academy of Sciences of the Belorussian SSR

References

1. F.A.Korolev, A.Iu.Klement'eva, Doklady AN SSSR, 94, 1025 (1954).
2. C.Christiansen, Ann.d.phys.Chem., 23, 298 (1884); 24,439 (1885).
3. N.K.Sethy, Proc.Ind.Cult., Sci., 6, 121 (1920).
4. C.M.Sogani, Phil.Mag., 1, 32 (1926).
5. H.S.Denmark & W.M.Cady, JOSA, 25, 330 (1935).
6. E.Elvegard, H.Staude, F.Weigert, ZS.f.phys.Chem.,B2,149 (1929).
7. K.Fragstein, Ann.d.Phys., 17, 22 (1933).
8. R.B.Barnes & I.G.Bonner, Phys.Rev., 49, 732 (1936).
9. C.V.Raman, Proc.Ind.Acad.Sci., A29, 381 (1949).
10. M.Nagel, JOSA, 44, 621 (1954).
11. B.I.Stepanov & A.P.Prishivalko, Trudy (Transactions) Inst. of Phys. & Math., No.2, 189; A.P.Prishivalko, ibid., p.206.

RESOLUTION ADOPTED BY THE FIRST CONFERENCE ON THE SPECTROSCOPY OF LIGHT-SCATTERING MEDIA

The Conference notes the very great theoretical and practical importance of the spectroscopy of light-scattering media. This importance results from the fact that the overwhelming majority of substances occurring in nature and used in industry are dispersed light-scattering materials that are not susceptible of analysis and investigation by conventional optical procedures.

The present state of the theory in this field allows of solving individual spectroscopic problems, but we still have far to go before we can develop universal spectroscopic techniques applicable to light-scattering materials. The existing experimental data exhibit many important regularities but are still too sparse to serve as a reliable foundation for working out the theoretical problems. The Conference notes that the research in the field being carried out by different groups is not adequately correlated.

This Conference deems it necessary to expand scientific research in the optics and spectroscopy of light-scattering media. The most important goals to work for are a) further experimental research in the optics and spectroscopy of light-scattering media, including detailed experimental verification of the existing theories; b) further development of the theory, both general and as applying specifically to substances of different types and the diverse spectroscopic problems encountered in practice; c) further development of the phenomenological theory of propagation of radiation in the scattering media to serve as a basis for the spectroscopic analysis of light-scattering media; d) elaboration of the theory of light dispersion in light-scattering media; e) development of the theory of light-scattering by individual isolated particles (primarily absorbing particles of irregular shape) and by particle complexes and many-particle layers; f) working out detailed methods for solving important practical problems (dispersive light filters, luminescent powders, methods of spectroscopic analysis in the visible and infrared regions of the spectra, etc.); g) publication of charts and atlases of reflection and transmission spectra of light-scattering media (natural substances, pigments, colloids, etc.); h) design and construction of specialized measuring equipment; i) development of quality control and inspection methods based on the optical properties of light-scattering substances.

The Conference finds that one of the most important problems is more effective communication with industry, with a view to insuring more prompt utilization in practice of the results already achieved by researchers.

With a view to stimulating the maximum expansion in research on the optics and spectroscopy of light-scattering media and in the interests of efficient further progress, it is desirable that the research performed by different organizations be carefully coordinated. The Conference considers it necessary to call a second conference on the optics of light-scattering media in 1958, this conference to be devoted to wider problems, including spectroscopy, astrophysics, geophysics, and colloid physics, and to be attended by representatives from industrial laboratories.

The Conference turns to Comrades E.V.Shpol'skii, M.V.Savost'ianova, B.I. Stepanov, K.S.Shifrin and G.V.Rozenberg with the request that they assume the initiative for preparing the Second Conference on the Optics and Spectroscopy of Scattering Media and furthering coordination of the relevant work of different organizations in the interval between conferences.

The Conference expresses its gratitude to the Committee on Spectroscopy of the USSR Academy of Sciences for the successful organization of the present conference.

* * *
* *
*

Bulletin of the Academy of Sciences of the USSR - Physical Series
Vol. 21, No. 11

Transactions of the First Conference on the Spectroscopy of Light-Scattering Media (Moscow, 29-30 March 1956)

TABLE OF CONTENTS

	Page Orig.	Trans.
Opening address - B. I. Stepanov	1471	1463
Some aspects of spectroscopic analysis of light-scattering media and the reflecting power of colored polydispersive media - G. V. Rozenberg	1473	1465
Basic problems in the spectroscopy of scattering media - B. I. Stepanov	1485	1477
On the multiplicity of light scattering - Iu. I. Chekalinskaia	1494	1486
On determining the true absorption of adsorbed substances from the diffuse reflection spectra (Abstract) - Z. V. Zhidkova	1500	1492
Spectrophotometric investigation of mixtures of powder specimens (Abstract) - A. P. Ivanov & A. S. Toporets	1502	1494
Investigation of the regularities of emission of finely dispersed luminescent media - A. P. Ivanov	1503	1495
Indicatrices of light scattering by developed photographic emulsions on a transparent base - Iu. N. Gorokhovskii & I. M. Davydkin	1505	1496
Numerical evaluation of light scattering in photographic blackenings on a transparent base - Iu. N. Gorokhovskii & I. M. Davydkin	1517	1507
Scattering of light by photographic emulsion layers - P. Kh. Pruss	1526	1515
Procedure for investigating the reflectivity of color-print photographic paper - V. M. Bakhvalov	1534	1522
Some aspects of the theory of dispersive light filters - A. P. Prishivalko	1541	1528
Resolution adopted by the First Conference on Spectroscopy of Light-Scattering Media	1548	1534

Translated in 1958 by
Columbia Technical Translations
5 Vermont Ave., White Plains, N.Y.

Number 12 Volume 21 1957

BULLETIN

of the

Academy of Sciences of the USSR

- Physical Series -

(Izvestiia Akademii Nauk SSSR)
(Seriia fizicheskaia)

Reproduction rights reserved

by

Columbia Technical Translations
5 Vermont Avenue
White Plains, New York

Single Issues

$20

Annual Subscription

$215

Transactions

of the

Seventh All-Union Conference on Nuclear Spectroscopy

(Continued from Vol. 21, No. 7)

FINE STRUCTURE OF α-DECAY OF EVEN-EVEN NUCLEI

- V.G.Nosov

1. A characteristic of α-decay of deformed heavy nuclei is excitation of rotational states of the daughter nucleus. It can readily be demonstrated that the relative probability of excitation of the individual rotational states of the daughter nucleus can be expressed in terms of its equilibrium deformation. The mathematical proof is particularly simple in the case of even-even nuclei.

In this case the α-particle wave function in the system of coordinates rotating with daughter nucleus satisfies the following expression:[1]

$$\frac{1}{r}\cdot\frac{\partial^2}{\partial r^2}(r\psi)+\left(\frac{m}{I}+\frac{1}{r^2}\right)\frac{\partial}{\partial\mu}\left[(1-\mu^2)\frac{\partial\psi}{\partial\mu}\right]+\frac{2m}{\hbar^2}[E-U(r,\mu)]\psi=0. \qquad (1)$$

Here E is the decay energy, m is the reduced mass, I is the moment of inertia of the daughter nucleus, U is the potential energy of the electrostatic interaction of the α-particle with the nucleus, r is the distance between the daughter nucleus and the α-particle and $\mu=\cos\vartheta$ is the cosine of the angle between the direction of emission of the α-particle and the symmetry axis of the nucleus.

Let us seek a particular solution for ψ_l, which at great distances describes an α-particle with momentum l moving away from the nucleus. Substituting

$$\psi_l(r,\mu)=\frac{\sqrt{2l+1}}{2}P_l(\mu)\,e^{\sigma(r,\mu)} \qquad (2)$$

in (1) gives us the following equation

$$P_l\left\{\left(\frac{\partial\sigma}{\partial r}\right)^2+\frac{2}{r}\frac{\partial\sigma}{\partial r}+\frac{\partial^2\sigma}{\partial r^2}+\frac{2m}{\hbar^2}(E-U)-l(l+1)\left(\frac{m}{I}+\frac{1}{r^2}\right)\right\}+$$

$$+\left(\frac{m}{I}+\frac{1}{r^2}\right)\left\{P_l\left[(1-\mu^2)\left(\frac{\partial\sigma}{\partial\mu}\right)^2-2\mu\frac{\partial\sigma}{\partial\mu}+(1-\mu^2)\frac{\partial^2\sigma}{\partial\mu^2}\right]+2(1-\mu^2)\frac{dP_l}{d\mu}\frac{\partial\sigma}{\partial\mu}\right\}=0, \qquad (3)$$

which it is convenient to solve in the quasi-classical approximation

$$\sigma=\sigma_{-1}+\sigma_0+\sigma_1+\sigma_2+\cdots\cdots$$

Thus we can write

$$\left(\frac{\partial\sigma_{-1}}{\partial r}\right)^2+\left(\frac{m}{I}+\frac{1}{r^2}\right)(1-\mu^2)\left(\frac{\partial\sigma_{-1}}{d\mu}\right)^2=-\frac{2m}{\hbar^2}(E-U)+l(l+1)\left(\frac{m}{I}+\frac{1}{r^2}\right);$$

$$P_l\left[2\frac{\partial\sigma_{-1}}{\partial r}\frac{\partial\sigma_0}{\partial s}+\frac{2}{r}\frac{\partial\sigma_{-1}}{\partial r}+\frac{\partial^2\sigma_{-1}}{\partial r^2}\right]+\left(\frac{m}{I}+\frac{1}{r^2}\right)\left\{P_l\left[2(1-\mu^2)\frac{\partial\sigma_{-1}}{\partial\mu}\frac{\partial\sigma_0}{\partial\mu}-\right.\right.$$

$$\left.\left.-2\mu\frac{\partial\sigma_{-1}}{\partial\mu}+(1-\mu^2)\frac{\partial^2\sigma_{-1}}{\partial\mu^2}\right]+2(1-\mu^2)\frac{dP_l}{d\mu}\frac{\partial\sigma_{-1}}{\partial\mu}\right\}=0. \qquad (4)$$

Solution of Eq.(4) becomes easier in the case of a weakly deformed daughter nucleus. In this case the equation for the surface of the nucleus can be conveniently written in the form

$$R(\mu)=R_0+\xi(\mu)=R_0\left\{1+\sum_n\alpha_nP_n(\mu)\right\}. \qquad (5)$$

The σ_k are sought in the form of series in powers of ξ:

$$\sigma_k=\sigma_k^{(0)}+\sigma_k^{(1)}+\sigma_k^{(2)}+\ldots$$

The electrostatic potential produced by the daughter nucleus can readily be calculated in the form of an analogous series. As a result of simple operations, we obtain

$$\left.\begin{aligned} &\sigma_{-1}^{0)} = i\int_{a_l}^{r} k_l dr;\ \sigma_0^{(0)} = -\ln\sqrt{-ik_l}r; \\ &\sigma_{-1}^{(1)} = \frac{3}{2}\ i\varkappa_b^2 \sum_n \frac{\alpha_n}{2n+1} P_n(\mu)\int_r^{\infty}\left(\frac{R_0}{r}\right)^{n+1}\frac{dr}{k_l}. \end{aligned}\right\} \tag{6}$$

Here

$$k_l = \sqrt{k_\varepsilon^2 - \varkappa_b^2\frac{R_0}{r} - \frac{l(l+1)}{r^2}},$$

where

$$\varkappa_b^2 = \frac{4mZe^2}{\hbar^2 R_0},\ k_\varepsilon^2 = \frac{2m\varepsilon}{\hbar^2},\ \varepsilon \equiv \varepsilon_l = E - \frac{\hbar^2}{2I}l(l+1).$$

The double point a_l is found from the equation

$$k_l^2(a_l) = k_\varepsilon^2 - \varkappa_b^2\frac{R_0}{a_l} - \frac{l(l+1)}{a_l^2} = 0.$$

Eq.(6) are also valid for $r < a_l$, if we bear in mind that in this region $k_l = i\varkappa_l = i\sqrt{\frac{l(l+1)}{r^2} + \varkappa_b^2\frac{R_0}{r} - k_\varepsilon^2}$. The higher order terms of the double series $\sigma = \sum_{km}\sigma_k^{(m)}$ are negligibly small.

Going to the limit $r \to \infty$ one can readily show that the α-particle flux, corresponding to the ψ_l state, through a closed sphere is independent of l. Hence if we write the true α-particle wave function in the form $\psi = \sum_l c_l\psi_l$, the relative probability of excitation of a rotational level with momentum l will be $c_l{}^2$.

The coefficients c_l can readily be expressed in terms of the values of the wave function $\psi(S)$ at the surface of the nucleus. Thus, inasmuch as only relatively small values of l are significant, we can write in the requisite approximation

$$\left.\begin{aligned} &\sigma_{-1}^{(0)}(S) = \sigma_{-1}^{(1)}(R_0)|_{l=0} - \varkappa_0(R_0)\cdot\xi + \frac{\gamma}{2}l(l+1); \\ &\sigma_{-1}^{(1)}(S) = \sigma_{-1}^{(1)}(R_0)|_{l=0};\ \sigma_0^{(0)}(S) = \sigma_0^{(0)}(R_0)|_{l=0}. \end{aligned}\right\} \tag{7}$$

Here

$$\gamma = \frac{2\varkappa}{\varkappa_b^2 R_0} + \frac{\frac{m}{I}}{k^2}\left(\frac{\varkappa_b^2 R_0}{k}\operatorname{arc\,tg}\frac{\varkappa}{k} + \varkappa R_0\right), \tag{8}$$

where

$$k \equiv k_E = \sqrt{\frac{2mE}{\hbar^2}};\ \varkappa \equiv \varkappa_0(R_0) = \sqrt{\varkappa_b^2 - k^2}.$$

Utilizing the orthogonality of Legendre polynomials, we readily obtain

$$c_l = \sqrt{\varkappa R_0}\, e^{-\sigma_{-1}^{(0)}|}\sqrt{2l+1}\, e^{-\frac{\gamma}{2}l(l+1)}\int_{-1}^{1}\psi(S)\, e^{\varkappa\xi - \sigma_{-1}^{(1)}|}P_l(\mu)\, d\mu. \tag{9}$$

Here $r = R_0$ throughout and the vertical bar at the right of a term indicates that the expression should be taken for $l = 0$.

It is convenient to normalize the relative probability $w_l = |c_l|^2$ using the condition $w_0 = 1$. In this case Eq.(9) yields

$$w_l = (2l+1)\, e^{-\gamma l(l+1)} \frac{\left| \int_{-1}^{1} \psi(S)\, e^{\sum \beta_n P_n(\mu)} P_l(\mu)\, d\mu \right|^2}{\left| \int_{-1}^{1} \psi(S)\, e^{\sum \beta_n P_n(\mu)}\, d\mu \right|^2}, \tag{10}$$

where

$$\beta_n = \left\{ \varkappa R_0 - \frac{\frac{3}{2}\varkappa_0^2}{2n+1} \left[\int_{R_0}^{a_0} \left(\frac{R_0}{r}\right)^{n+1} \frac{dr}{\varkappa_0} + i \int_{a_0}^{\infty} \left(\frac{R_0}{r}\right)^{n+1} \frac{dr}{k_0} \right] \right\} \alpha_n. \tag{11}$$

Although α-particles in a nucleus are not stable structural units (in the sense of neutrons and protons), the α-particle wave function can be generalized to the region inside the nucleus. Thus from a purely formal standpoint the parent nucleus can be regarded as a composite system consisting of an α-particle and the daughter nucleus.

If we denote the wave function of the i-th steady state of the α-particle by χ_i^{α} and the wave function of the k-th state of the daughter nucleus by χ_k, the total wave function of the ground state of the parent nucleus can be written

$$\sum_{ik} \psi_{ik}(\mathbf{r})\, \chi_i^{\alpha} \chi_k,$$

where r is the radius vector of the α-particle relative to the center of gravity of the daughter nucleus.

The term corresponding to unexcited states of the daughter nucleus and the α-particle will be $\psi_{00}(\mathbf{r})\, \chi_0^{\alpha}\chi_0$. Obviously, the function $\psi_{00}(\mathbf{r})$ is a natural generalization of the α-particle wave function to the region inside the nucleus; it must be continuous inside and outside the nucleus and hence must transform smoothly into the ψ function deduced above at the surface of the nucleus. On the basis of the concept of homogeneity of nuclear matter and the shortness of the α-particle path length in it, we can naturally assume $\psi_{00}(\mathbf{r}) = \text{const}$. Substituting in (10) accordingly, we obtain

$$w_l = (2l+1)\, e^{-\gamma l(l+1)} \frac{\left| \int_{-1}^{1} e^{\sum \beta_n P_n(\mu)} P_l(\mu)\, d\mu \right|^2}{\left| \int_{-1}^{1} e^{\sum \beta_n P_n(\mu)}\, d\mu \right|^2}. \tag{12}$$

2. In heavy nuclei quadrupole deformation of the form

$$\xi = R_0 \alpha_2 P_2(\mu).$$

is most important. If, therefore, in Eq.(5) we limit our consideration to quadrupole deformation, Eqs.(11) and (12) become

$$w_l = (2l+1)\, e^{-\gamma l(l+1)} \frac{\left| \int_{0}^{1} e^{\beta P_2(\mu)} P_l(\mu)\, d\mu \right|^2}{\left| \int_{0}^{1} l^{\beta P_2(\mu)}\, d\mu \right|^2},$$

$$\beta \equiv \beta_2 = \left[\frac{4}{5} \varkappa R_0 \left(1 - \frac{k^2}{2\varkappa_b^2}\right) - i \frac{2}{5} \frac{k^3 R_0}{\varkappa_b^2} \right] \alpha_2. \tag{13}$$

On the basis of the available experimental data[2-4] on the excitation of the 2+ rotational level in α-decay it is feasible to calculate deformation α_2 of the various daughter nuclei in question by means of Eqs.(13) and (8). The quantities entering into the computation are all available directly from experiment except for the nuclear radius R_0 for which one must take two alternative values: $1.0\ A^{1/3}\cdot 10^{-13}$ and $1.4\ A^{1/3}\cdot 10^{-13}$ cm.

The results of such calculations are listed in Table 1. It would be best to check the predicted variation of the quadrupole deformation α_2 with reference to the quadrupole moment Q_0 determined from Coulomb excitation of the 2+ level. Unfortunately, at present we do not have sufficiently reliable and extensive data on Coulomb excitation of α-active nuclei, hence we must seek other methods for comparing theory with experiment.

Table 1

Nucleus	α_2		$Q_0=\frac{6}{5}\,Z\,R_0^2\,\alpha_2\cdot 10^{24}$	
	$R_0=1{,}0A^{1/3}\cdot 10^{-13}$	$R_0=1{,}4A^{1/3}\cdot 10^{-13}$	$R_0=1{,}0A^{1/3}\cdot 10^{-13}$	$R_0=1{,}4A^{1/3}\cdot 10^{-13}$
Ra^{222}	0,24	0,20	9	15
Ra^{224}	0,30	0,24	12	18
Ra^{226}	0,26	0,21	10	16
Ra^{228}	0,30	0,24	12	19
Th^{226}	0,27	0,22	11	17
Th^{228}	0,26	0,21	10	17
Th^{230}	0,21	0,17	9	14
Th^{232}	0,23	0,19	9	15
Th^{234}	0,21	0,17	9	14
U^{230}	0,13	0,11	5	9
U^{232}	0,15	0,13	6	11
U^{234}	0,20	0,16	8	13
U^{236}	0,18	0,15	8	12
U^{238}	0,16	0,14	7	12
Pu^{238}	0,18	0,15	8	13
Pu^{240}	0,17	0,15	7	13
Cm^{242}	0,15	0,13	7	11
Cm^{246}	0,13	0,11	6	10
Cm^{248}	0,12	0,10	5	9
Cf^{250}	0,12	0,10	6	9

One of the quantities readily determinable from experiment is the moment of inertia I of the daughter nucleus. It can be found directly from the excitation energy $E_2 = 3\hbar^2/I$ of the 2+ level; this energy has been measured with great accuracy in a number of cases. From the theoretical viewpoint, however, comparison with the moment of inertia values is not very rigorous, since the moment of inertia depends, apparently, not only on the deformation but also on other details of the nuclear structure. At present we have no theory giving the dependence of the moment of inertia on the deformation and on the structure of the nucleus (in particular, we have no theory for the precise dependence of the moment of inertia on the number of nucleons outside the outer closed shell). Nevertheless, we can reasonably assume that, other conditions being equal, the moment of inertia will increase with increasing deformation.

The experimental data on the excitation energy of the 2+ level of uranium, plutonium and curium isotopes, assembled by Hollander[5] from different sources, are plotted in the accompanying figure. It will be seen that in the case of uranium isotopes the moment of inertia exhibits a sharp maximum for U^{234}. An analogous maximum, but less sharply pronounced, is observed in the case of the plutonium isotopes. In contrast, in the case of plutonium, I monotonically increases in going to the heavy nuclides. Comparison of these experimental

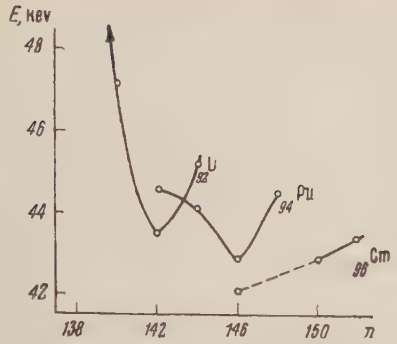

Energies of the first excited states of heavy even-even nuclei. Here n = number of neutrons in the nucleus.

data with the values in Table 1 shows fair quantitative agreement. Thus in the case of uranium isotopes the deformation α_2 does show a sharp maximum for the U^{234} nucleus. For plutonium there is no agreement, but it must be noted that the data in question require refinement. In addition, it would be desirable to measure the deformation of the Pu^{242} nucleus from α-decay of Cm^{246}. For curium there is again good agreement: the monotonic decrease of the moment of inertia is paralleled by a monotonic decrease of the deformation α_2 in Table 1. Thus it may be said that the deformation determined from the fine structure of α-decay is in good qualitative agreement with the experimental data on the moments of inertia.

The deformation values listed in Table 1 can be utilized for calculating the probability of excitation of the 4+ level. The results of calculation by means of Eqs.(13) and (8) are juxtaposed with the available experimental data in Table 2. It will be seen that at the beginning of the table there is relatively good agreement with experiment except for Ra^{222}, but that starting with U^{234} there becomes evident a definite divergence which amounts to an order of magnitude for Pu^{238}.

Table 2

Nucleus	w_4		w_4 exp	α_2		α_4	
	$r_0=1,0$	$r_0=1,4$		$r_0=1,0$	$r_0=1,4$	$r_0=1,0$	$r_0=1,4$
Ra^{222}	0,0011	0,0013	0,0078				
Ra^{224}	0,0026	0,0030	0,0028				
Ra^{226}	0,0014	0,0016	0,0026				
Th^{228}	0,0054	0,0062	0,0044				
Th^{230}	0,0028	0,0033	0,0041				
U^{234}	0,0047	0,0054	0,0013	0,25	0,20	—0,05	—0,04
U^{236}	0,0027	0,0032	0,0011	0,21	0,17	—0,03	—0,03
Pu^{238}	0,0043	0,0050	0,0005	0,23	0,19	—0,06	—0,04

It should be borne in mind, however, that in all the calculations only the quadrupole deformation α_2 was taken into account in Eq.(5). The divergence between theory and experiment can be eliminated by additionally taking into account the small deformations α_4 The values of the deformations α_2 and α_4 determined from the excitation data for the 2+ and 4+ levels according to Eqs. (8), (11) & (12) are listed for U^{234}, U^{236} and Pu^{238} in the last columns of Table 2. It will be evident from the α_4 columns that very small values of are sufficient to re-establish agreement between theory and experiment.

Thus the probability of excitation of the 4+ level proves to be very sensitive to fine details of the form of the nuclear surface. It may therefore be predicted that excitation of the 6+ level will prove sensitive to even finer details of the shape of the daughter nucleus.

References

1. V.Nosov, Doklady AN SSSR, 112, 414 (1957).
2. Annual Review of Nuclear Science, Vol.4, Stanford, 1954.
3. F.Asaro, F.Stephens, B.Harvey & I.Perlman, Phys.Rev., 100, 137 (1955).
4. F.Asaro, F.Stephens, S.Thompson & I.Perlman, Phys.Rev., 98,19(1955).
5. J.Hollander, Phys.Rev., 103, 1590 (1956).

INVESTIGATION OF THE INTERNAL CONVERSION ELECTRON SPECTRUM OF LONG-LIVED Eu^{152} AND Eu^{154}

- B.V.Bobykin & K.M.Novik

The sharp increase in the deformation of nuclei as the neutron number is increased from N = 88 to N = 90 (Mottelson & Nilsson[1]) lends particular interest to investigation of the activity of Eu^{152} and Eu^{154}. The decay products of these nuclides are Sm^{152} (N = 90), Gd^{152} (N = 88), Gd^{154} (N = 90) and possibly Sm^{154} (N = 92). The half-lives of Eu^{152} are 9.2 hours* and 13 years; the half-life of Eu^{154} is 16 years.[2]

At the time the present experimental work was being started (1954), there was considerable uncertainty in the data regarding the γ-radiation accompanying the decay of these isotopes. This can be explained by the serious diffficulties encountered in investigating their radioactivity. Among such difficulties are the possible contamination of the europium sources by other rare earth isotopes and the fact that both isotopes when prepared by neutron bombardment of natural europium are produced in mixture, while the products of their decay comprise four isotopes. Identification of the various γ-transitions is hampered by the great abundance of such transitions accompanying the decay of Eu^{152} and Eu^{154}. Our data on the identification of the γ-transitions were published in Ref.3; this report also contains references to the earlier results of other authors. Since then a number of new investigations have been reported in the literature. Grodzins & Kendall[4] published a summary of their work with separated Eu^{152} in the form of a decay scheme, Dzhelepov, Zhukovskii, Nelovesov & Shchukin[5] investigated the relative intensities of the γ-rays, Nathan & Waggoner[6] describe the results they obtained with a source free of rare earth impurities and Cork and his co-workers[7] published a communication describing their investigation with separated Eu^{152} and Eu^{154}.

The results of the present investigation show that some of the data on the decay characteristics of Eu^{152} and Eu^{154} appearing in the above listed publications are in need of revision and amplification.

Experimental procedure

The internal conversion electron spectrum of a mixture of long-lived Eu^{152} and Eu^{154} was investigated on a double-focusing spectrometer. This spectrometer is characterized by good resolution and a large acceptance angle and allows of using large sources.

The electromagnet of our spectrometer is similar to that described by Kurie et al[8]. With the realized magnetic field distribution in the magnet gap, the spectrometer was adjusted for operation in the 100 to 700 kev electron energy region, i.e., the region most densely populated by conversion lines.

For adjusting the instrument we used the monoenergetic electrons of the F-line of ThB. Using a solid acceptance angle of 0.002 of 4π, we investigated the character of the apparatus line as a function of the angular separation between the source and detector. The optimal angle proved to be 258°. In its initial state the magnet had a residual field of about 11.8 oersted at the central trajectory. In the subsequent measurements this initial residual field was retained by appropriate "aging" of the magnet.

It was found in the preliminary studies that the radius of the electron-optical axis is not critical. The source and detector slit were positioned

---

*We did not investigate the short-lived isomer Eu^{152m}.

with a radius of r_o = 243 mm corresponding to the center of the slanted part of the pole pieces. We also investigated the influence of the source width on the line shape. The character of the vertical image was determined by photographing the ThB F-line using a 1.5 x 19.5 mm source. It was found that the resultant image had a height of 20-21 mm and was curved with a radius of curvature of about 110 mm. The photograph of the F-line image was used for determining the shape of the receiving slit over the detector. The aperture slit, subtending a solid angle of 0.002 of 4π, was located at the midpoint of the angular separation between the source and detector (i.e., at 129°) and had the shape of an ellipse with semi-axes of 40 mm and 22.6 mm. All the measurements on the europium isotopes were carried out with this aperture slit using sources of the same 1.5 x 19.5 mm dimensions. The detector assembly consisted of two Geiger-Müller counters in coincidence. The curved receiving slit over the detector had a width of 2 mm.

Generally, the resolution of a spectrometer of this type is greatly reduced in working with electrons of low energy. The resolution of our instrument was improved by appropriate modification of the pre-operational preparation of the magnet. The spectra of 10 to 100 kev electrons were studied after preliminary demagnetization of the magnet. The resolution of the instrument and the shape of the instrument line obtained with different preliminary treatments of the magnet are shown in Fig.1.* The different europium lines are taken from the corresponding series of measurements. The electron line with energy 1362.5 kev had a half-width of 0.32%.

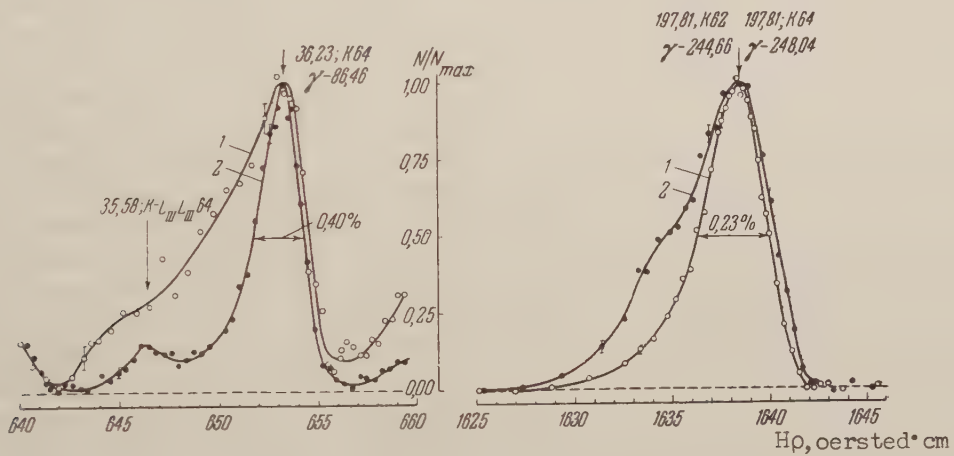

Fig.1. Shape of the apparatus line with different regimes of preparation of the magnet for operation: 1) "aging", 2) demagnetization.

If our spectrometer had provision for smooth regulation of the angular separation between the source and detector, there would have been no need for varying the preliminary treatment of the magnet and the resolution would have remained virtually constant in a wide range of magnetic fields. Unfortunately, in our case the separation between the source and detector could not be changed during operation of the instrument.

The internal conversion electron spectrum was recorded as a function of the current flowing through the windings of the magnet. The magnet current was measured by means of a PPTV-1 type potentiometer. For determining the

---

*In all figures and tables the number following the line designation denote Z (thus for K 64 read K, Z = 64; for $L_{III}62$, read L_{III}, Z = 62, etc.).

europium line energies, we used the standard lines of Th(B + C + C''), Cs^{137} and Co^{60} (Ref.9,I). In using this procedure in conjunction with iron spectrometers, the accuracy of energy determination is limited by the fact that the variation of the ratio between the strength of the magnetic field and the current through the magnet windings differs in different series of measurements. The influence of this factor in our experiments was wholly eliminated. The standard lines and the europium lines were recorded as a single spectrum without turning off the magnet. In the procedure followed, upon approach to the position (field value) of a standard line the europium source was removed from the spectrometer and replaced by the appropriate standard β- line source; after recording the given standard line the sources were again interchanged and the investigation of the europium lines continued. To facilitate this interchange all the source holders were standardized to the same size and each source had its own holder. In this special calibration series of measurements the weak lines of europium were not recorded. In subsequent series of measurements the principal europium lines served as the references for calibrating the spectrum as a whole. Appropriate measures were taken in the process of measurement to insure a smooth magnetization curve. To this end the rate of change of the current through the windings was kept as uniform as possible and the current was kept stable to better than 1 part in 10^5. The smooth regulation of the current was realized by two series-connected rheostats.

Interpolation between the reference points (the initially calibrated europium lines) was carried out by means of cubic parabolas each of which requires 4 given points for plotting. The cubic parabolas were distributed so as to insure adequate overlapping of the curves. It was found that with this method of interpolation the uncertainty in determining the energy is due primarily to the uncertainty in localizing the line peaks. Even in the most unfavorable case this factor was always less than 0.1%.

The β-sources were prepared by electrolysis of europium chloride dissolved in ethyl alcohol, following the procedure described earlier[3].

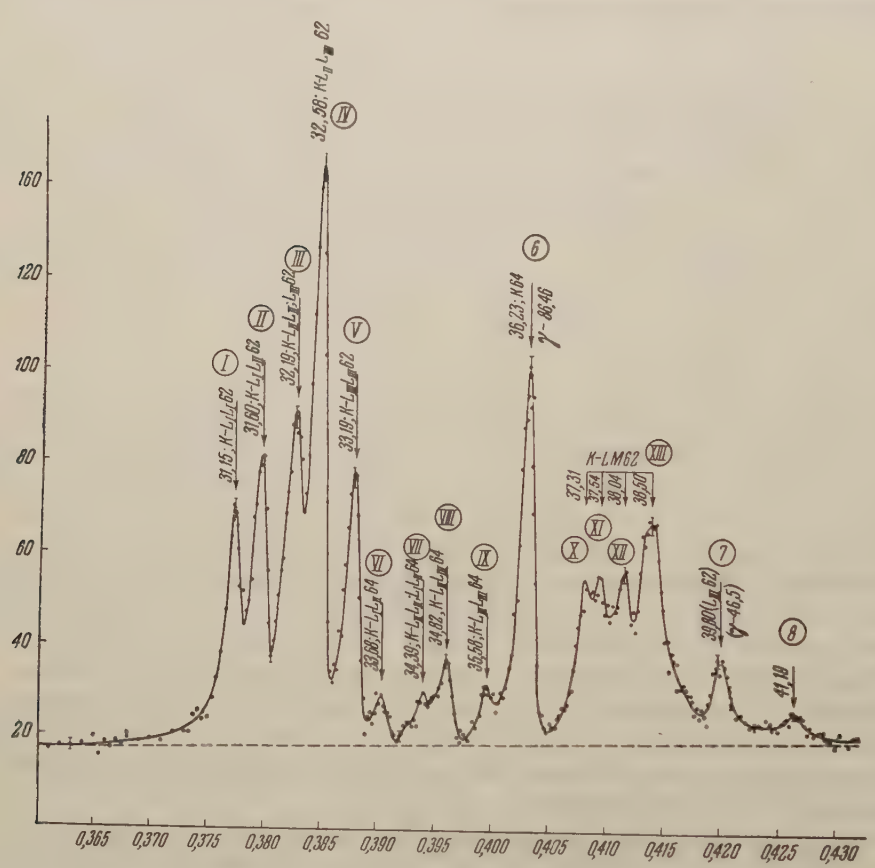

Fig.2. Auger electron spectrum of samarium (Z = 62) and gadolinium (Z = 64) observed in the decay of Eu^{152} and Eu^{154}. Correction: the inscription above line III should read "32, 19; K - $L_{II}L_{II}$; $L_IL_{III}62$".

Results

The electron lines observed incident to decay of Eu^{152} and Eu^{154} are shown in Figs.2 through 5. The lines are arranged in order of increasing energy and are numbered (in the circles). The horizontal scales in the figures are laid off in potentiometer readings; the vertical scales in terms of the counting rate, the unit being 16 counts per 3 min. Characteristics of the lines are indicated in each figure. The double repetition of the potentiometer indication values is due to replacement of the standard resistance in the external circuit of the PPTV-1 potentiometer. The resistance was divided into two sections and the change was usually made in the process of operation of the spectrometer. The ratio of the resistance sections was 1:5.5186. Thus by using this factor the potentiometer indications could be brought to the same scale where necessary.

The lines shown in the figures are taken from different series of measurements. The lines reproduced in Figs.4 & 5 were recorded with a β-source having an average thickness of 0.1-0.2 mg/cm^2, prepared on an aluminum foil backing 5 μ thick. Beta-sources one eighth this thickness were used in recording the lines shown in Figs.2 & 3. In the latter case the source support was 1.5 μ aluminum foil. As may be seen from the figures, the utilized β-sources were sufficiently thin to preclude any serious energy loss in the material itself.

Lines Nos.1-24 were recorded with the magnet demagnetized beforehand; lines Nos.25-73 were recorded with the magnet "aged" beforehand. The root mean square errors indicated at the experimental points were evaluated taking into account the different corresponding counting times; where no uncertainty is shown the magnitude of the evaluated error is commensurate with the dimensions of the solid point.

All the internal conversion electron lines rise above the rather high background of the continuous β-spectrum. The level of the β-background was plotted taking into account the experimental background points obtained in all the series of measurements. The background is shown in all the figures by the dash lines. In determining the energy of the γ-transitions we used only the K conversion lines; the L lines, in view of their triplet structure and generally low intensity are less suitable for this purpose.

The relative intensities of the conversion lines are listed in Table 1. Next to the intensity values of some of the lines we have indicated the magnitude of the probable errors taking into account the reproducibility of the observed intensity in several series of measurements. Their magnitudes do not reflect the systematic errors that might have been involved in these measurements. If there were such systematic errors, however, they must be so small as not to lead to any serious distortion of the results listed in Table 1. For purposes of comparison we also give the conversion line data published in 1957 by Nathan & Waggoner[6]. Appropriate corrections for electron absorption in the counter window are included in the relative intensity values of the conversion lines from No.1 (10.45 kev) to No.30 (122.9 kev).* The window of the counter consisted of a silvered collodion film having a density of 0.16 mg/cm^2. Strictly speaking, accurate corrections for the absorption of the film could be made only on the basis of a special investigation of its transmission with the given geometry. To determine the approximate corrections we used the transmission curve shown in Fig.6. This curve was plotted on the basis of the data of von Ardene[10] and Saxon[11].

---

*The electrons were recorded by the coincidence technique only in investigating the high energy (> 600 kev) part of the spectrum.

Table 1

Identification and relative intensity of the conversion lines observed in the decay of Eu^{152} and Eu^{154}

Nos. of lines as given in Figs. 2–5	Energy of conversion lines, kev	Identification		Relative intensity	Number of measurements	Data from Ref. 6	
						Relative intensity	Energy of conv. line, kev
1	2	3		4	5	6	7
1	10,45	L_I 64	γ-18,8	150 ~50	1	—	—
2	10,81	L_{II} 64	γ-18,8	150 ~100	1	—	—
3	11,54	L_{III} 64	γ-18,8	120	1	—	—
4	17,19	M 64	γ-18,8	45	2	—	—
5	21,15	K 63	γ-69,7	14*	1	—	—
I	31,15	$K-L_IL_I$ 62		610 80	2	—	—
II	31,60	$K-L_IL_{II}$ 62		610 100	2	—	—
III	32,19	$K-L_{II}\ L_{II}$, L_IL_{III} 62		610 120	2	—	—
IV	32,58	$K-L_{II}L_{III}$ 62		610 205	2	—	—
V	33,19	$K-L_{III}L_{III}$ 62		610 105	2	—	—
VI	33,68	$K-L_IL_{II}$ 64		72 —	2	—	—
VII	34,39	$K-L_{II}L_{II}$, L_IL_{III} 64		72 —	2	—	—
VIII	34,82	$K-L_{II}L_{III}$ 64		72 —	2	—	—
IX	35,58	$K-L_{III}L_{III}$ 64		72 —	2	—	—
6	36,23	K 64	γ-86,46	120	2	—	—
X	37,31	$K-LM$ 62		285 —	2	—	—
XI	37,54	$K-LM$ 62		285 —	2	—	—
XII	38,04	$K-LM$ 62		285 —	2	—	—
XIII	38,50	$K-LM$ 62		285 —	2	—	—
7	39,80	(L_{III} 62)	(γ-46,52)	16,5	2	—	—
8	41,19	—		5	2	—	—
9	43,73	—		17	2	—	—
10	44,98	(M 62)	(γ-46,52)	7,5	2	—	—
11	48,90	K 63	(γ-97,4)	9,5*	1	—	—
12	51,59	(L_I 64)	(γ-60,00)	23 —	2	—	—
13	52,09	(L_{II} 64)	(γ-60,00)	23 —	2	—	—
14	54,66	K 63	γ-103,2	34*	1	—	—
15	55,06	K 64	γ-105,3	50	2	—	—
16	72,79	K 64	γ-123,02	1010	3	640	73,1
17	74,92	K 62	γ-121,77	2690	3	2960	75,3
18	78,20	L_IL_{II} 64	γ-86,46	21 18	5	—	—
19	79,34	L_{III} 64	γ-86,46	21 3	5	—	—
20	84,77	M 64	γ-86,46	6	2	—	—
21	95,25	L_IL_{II} 63	γ-103,2	6*	1	—	—
22	97,0	L_IL_{II} 64	γ-105,3	8,7 6,7	5	—	—
23	97,7	L_{III} 64	γ-105,3	8,7 2,0	5	—	—
24	101,4	M 63	γ-103,2	1,6*	1	—	—
25	114,7	L_IL_{II} 62	γ-121,77	2100 —	3	—	—
26	115,2	L_IL_{II} 64 + L_{III} 62	γ-123,02+ +γ-121,77	2100 —	3	1770	115
27	116,0	L_{III} 64	γ-123,02	2100 —	3	395	116
28	120,4	M 62	γ-121,77	595 324	2	296	120
29	121,6	N 62 + M 64	γ-121,77+ +γ-123,02	595 236	2	93	121
30	122,9	N 64	γ-123,02	595 35	2	—	—
31	197,81	K 62 + K 64	γ-244,66+ +γ-248,04	100±1	5	100	198

*Relative intensity not constant; see text.

Table 1 (continued)

Nos. of lines as given in Figs. 2–5	Energy of conversion lines, kev	Identification		Relative intensity	Number of measurements	Data from Ref. 6	
						Relative intensity	Energy of conv. line, kev
1	2	3		4	5	6	7
32	237,08	*L* 62	γ-244,66	21,1	2	30	237
33	239,72	*L* 64	γ-248,04	5,9	2	—	—
34	243,22	*M* 62	γ-244,66	5,7	2	—	—
35	246,56	*M* 64	γ-248,04	1,0	1	—	—
36	294,09	*K* 64	γ-344,32	109,1±1,4	4	123	294
37	336,20	*L* 64	γ-344,32	22,8±0,3	3	30	336
38	342,67	*M* 64	γ-344,32	6,0	1	—	—
39	361,00	*K* 64	γ-411,23	6,04±0,14	4	4,9	360
40	397,38	*K* 62	γ-444,23	2,67±0,07	4	3,3	395
41	403,46	*L* 64	γ-411,23	1,27±0,04	4	—	—
42	436,40	*L* 62	γ-444,23	0,7	1	1,1	431
43	442,30	*M* 62 + *K*(?)	γ-444,23+γ(?)	0,8	1	—	—
44	536,2	*K* 62 or *K* 64	γ-583,1 or 586,5	1,27±0,05	4	1,7	531
45	565,3	*K* 62 or *K* 64	γ-612,1 or 615,5	1,18±0,04	4	1,1	564
46	629	*K* 62 or *K* 64	γ-676 or 679	~0,4	1	—	—
47	642,3	*K* 62 + *K* 64	γ-689,1+ + γ-692,5	6,94±0,10	6	6,3	641
48	673,4	*K* 62 + *K* 64	γ-720,2+ + γ-723,6	1,53±0,04	5	—	—
49	681,6	*L* 62	γ-689,1	0,90± ~0,50	5	—	—
50	684,7	*L* 64	γ-692,5	±0,02 ~0,40	5	—	—
51	707,5	*K* 64	γ-757,7	0,70±0,03	4	1,2	705
52	712,9	*L* 62	γ-720,2	~0,5 —	1	—	—
53	715,4	*L* 64	γ-723,6	~0,5 —	1	—	—
54	729,3	*K* 64	γ-779,5	2,90±0,07	5	3,0	725
55	763,7	(*K* 62 or *K* 64)	(γ-810,6 or 813,9)	0,25	1	—	—
56	771,0	*L* 64	γ-779,5	0,3	2	—	—
57	821,6	*K* 62	γ-868,5	3,12± ≤1,56	5	2,8	815
58	823,5	*K* 64	γ-873,7	±0,08 ≥1,56	5	—	—
59	860,6	*L* 62	γ-868,5	0,2	1	—	—
60	865,0	*L* 64 + *M* 62	γ-873,7+ + γ-868,5	0,2	1	—	—
61	917,9	*K* 62	γ-964,8	4,60±0,10	5	4,0	916
62	946,4	*K* 64	γ-996,6	1,07±0,03	4	—	—
63	955,2	*K* 64 + *L* 62	γ-1005,4+ + γ-964,8	2,60± 1,94 ±0,04 (0,66)	4	2,0	955
64	988,5	*L* 64	γ-996,6	0,15	1	—	—
65	997,3	*L* 64	γ-1005,4	0,3	1	—	—
66	1039,8	*K* 62	γ-1086,6	3,01±0,07	5	1,4	1032
67	1065,8	*K* 62	γ-1112,7	3,13±0,08	5	2,7	1056
68	1079,6	*L* 62	γ-1086,6	0,43	2	—	—
69	1105,1	*L* 62	γ-1112,7	0,47±0,04	3	—	—
70	1225,8	*K* 62 (or *K* 64)	γ-1272,6(or 1276,0)	0,75±0,03	3	—	—
71	1266,4	*L* 62 (or 64)	γ-1272,6(or 1276,0)	0,08	1	—	—
72	1362,5	*K* 62	γ-1409,4	1,39±0,02	3	1,7	1369
73	1402,6	*L* 62	γ-1409,4	0,23	2	—	—

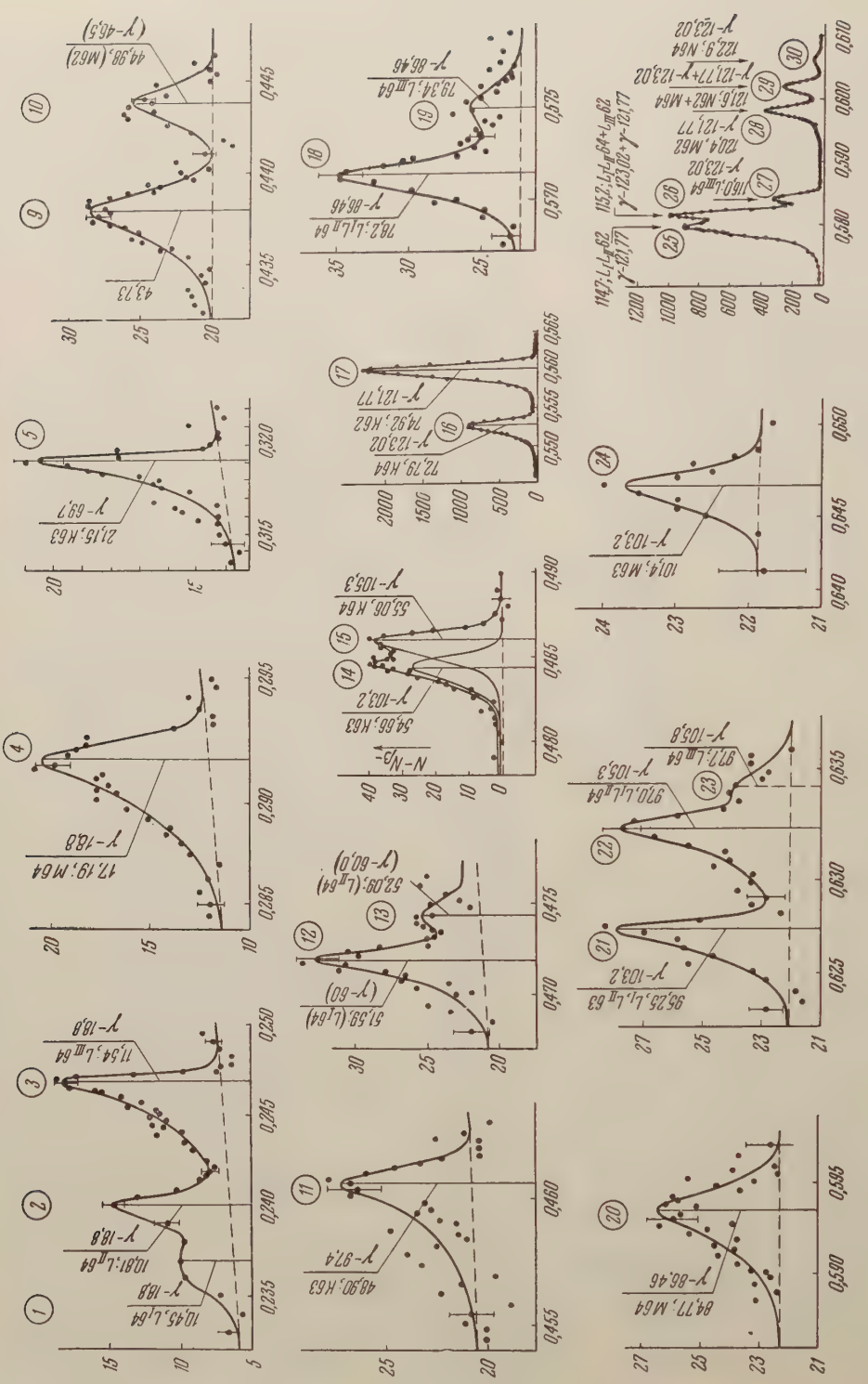

Fig.3. Internal conversion lines of Eu152,154; average thickness of source (0.1-0.2)/8 mg/cm^2; backing - 1.5 μ thick aluminum foil.

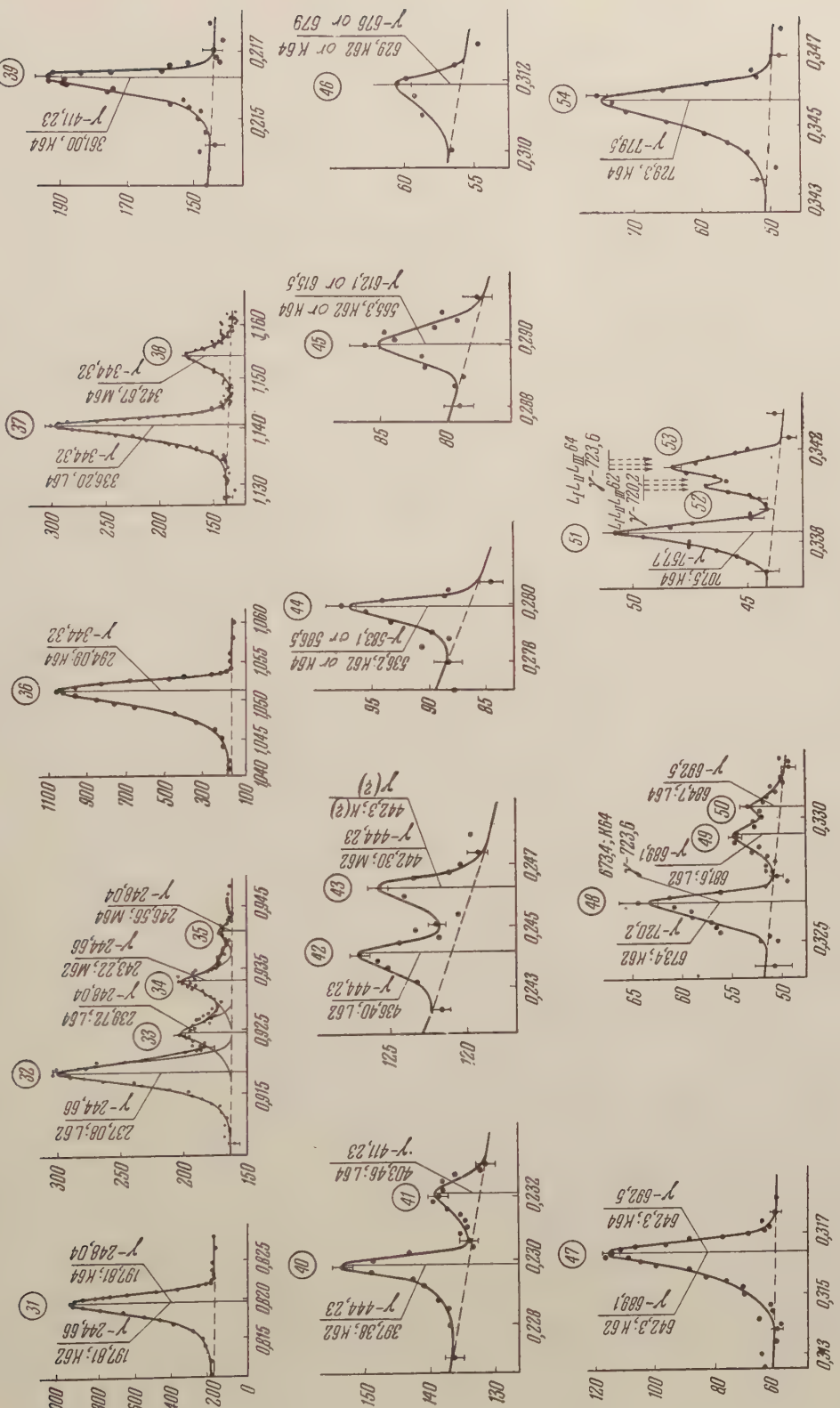

Fig.4. Internal conversion lines of $Eu^{152,154}$; average thickness of source 0.1–0.2 mg/cm^2; backing – 5 μ thick aluminum foil.

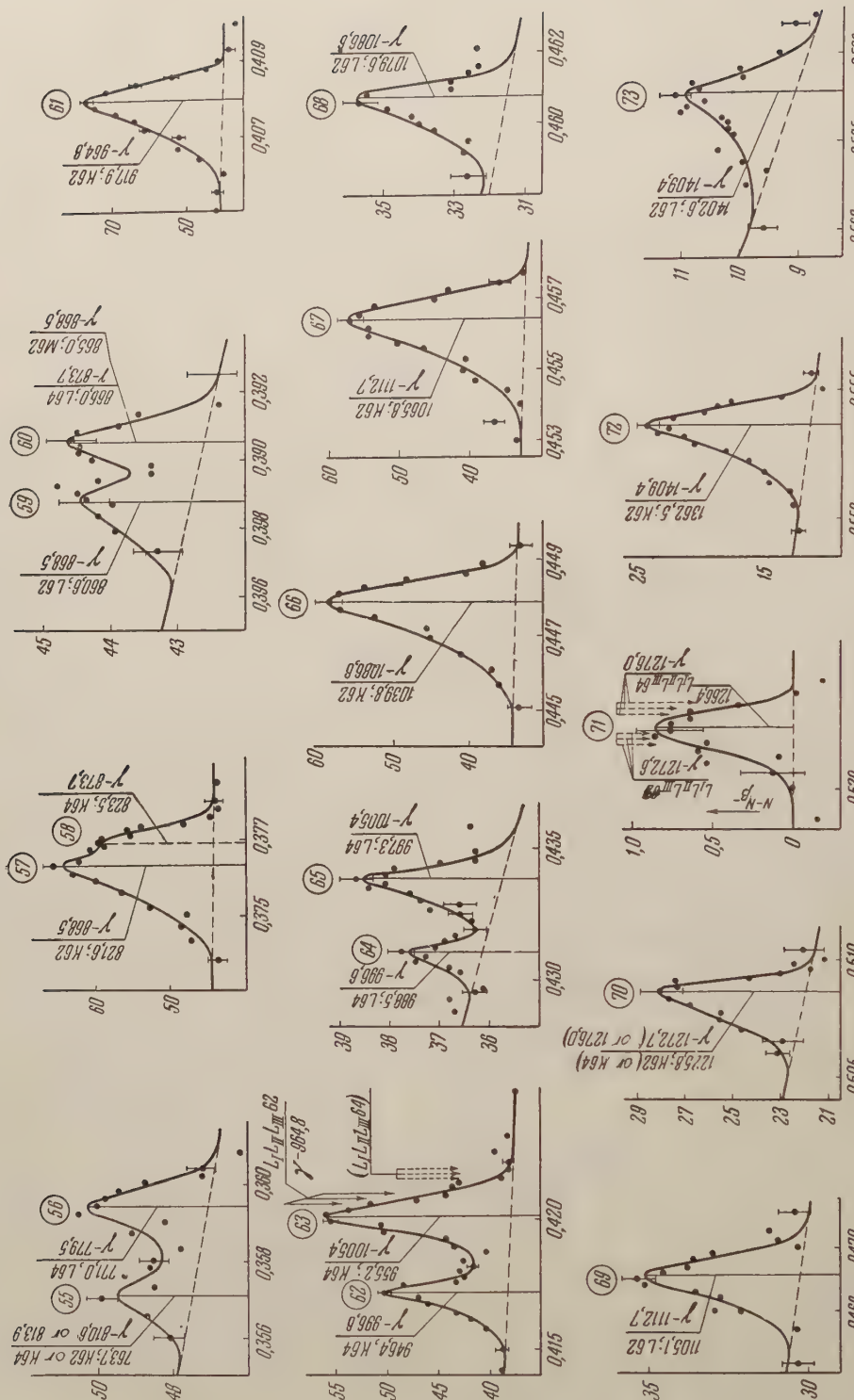

Fig.5. Internal conversion lines of $Eu^{152,154}$; average thickness of source 0.1–0.2 mg/cm^2; backing – 5 μ thick aluminum foil.

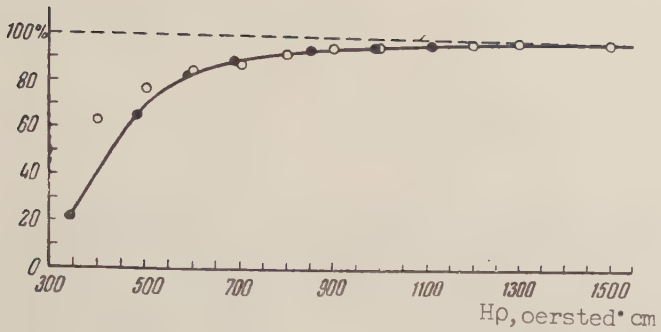

Fig.6. Plot of electron transmission by counter window film having a thickness of 0.16 mg/cm^2: ●) according to the data of von Ardene[10] and ○) points obtained by interpolation of Saxon's data[11].

Table 1 also lists the relative intensities of the Auger electron lines.

Bergström & Hill[9,II] proposed the following simple formula for determining the energy of the K-LL Auger electrons:

$$K\text{-}L_pL_q = (K - L_p)_Z - (L_q)_{Z+\Delta Z},$$

where K is the binding energy of the electrons in the K shell, and L_p and L_q are the binding energies in the L subshells. For determining the energy with an accuracy of 0.1% the authors recommend using $\Delta Z = 0.54$ for the L_I and L_{II} subshells and $\Delta Z = 0.76$ for the L_{III} subshell (the experimental verification was carried out for Z = 80 and 83). The energy values obtained in the present investigation for Z = 62 and 64 satisfy the given formula if one sets $\Delta Z = 0.65$ for the L_I and L_{II} shells and $\Delta Z = 0.85$ for the L_{III} shell.

Our investigation of the internal conversion spectrum was carried out in two stages. The principal measurements, allowing of identification of the major part of the conversion lines, were carried out during the first stage when the source was about two years old. The second stage or control measurements were carried out 280 days later for the purpose of checking the isotope assignments of the doubtful lines. It was established that the conversion lines Nos.5, 11, 14, 21, and 24 exhibit an intensity decrease more than 50% greater than the decrease of the intensity of the $Eu^{152,154}$ lines.*

The fact that the intensities of these lines all fell off at the same rate suggests that the listed lines are associated with the decay of the same isotope with a period of approximately 230 days. That the Nos. 14, 21 and 24 lines are converted in europium (Z = 63) is evidence that the 69.7 kev, 97.4 kev and 103.2 kev γ-transitions accompany the decay of Gd^{153}. Eu^{152} (N = 90), which is a product of this decay, is a deformed nucleus. The transition energies and relative intensities of the conversion lines listed in Table 1 do not conflict with the results published by Marty & Vergnes[12].

There is some doubt whether lines Nos. 12 and 13 belong to $Eu^{152,154}$ inasmuch as there is an appreciable uncertainty in the evaluation of the intensity of these lines. The identification of these lines is tentative, particularly since no attempt was made to detect the K line of 9.75 kev energy associated with the implied γ-transition. As for the other conversion lines, no anomalous changes in their relative intensities were noted in the control measurements.

Some observations regarding the 18.8**, 86.46 and 105.3 kev γ-transitions are indicated. In the β-decay of 1.7-year Eu^{155} there occur transitions having energies of 18, 84 and 102 kev in Gd^{155} (Ref.13). We cannot categorically assert that there was no Eu^{155} impurity in our $Eu^{152,154}$ sample inasmuch as the neutron-irradiated natural europium was not spectroscopically pure. Eu^{155}

---

*The intensity values for these lines listed in Table 1 pertain to the results of the control (second series) measurements.

**The L lines associated with this transition were not detected in the principal series of measurements.

could form in two ways: by the (n,γ) second order reaction on Eu^{153} and by the (n,γ) first order reaction on Sm^{154}, the product of which decays according to the following scheme

$$_{62}Sm^{155} \xrightarrow[23.5\,min]{\beta^-} {}_{63}Eu^{155} \xrightarrow[1.7\,year]{\beta^-} {}_{64}Gd^{155}.$$

The results of our control measurements show that the 18.8, 86.46 and 105.3 kev transitions belong either to $Eu^{152,154}$ or to Eu^{155}, if it is assumed that the lifetime of the latter is comparable with the lifetime of $Eu^{152,154}$.*

The inferred existence of the 46.52 kev γ-transition (lines Nos.7 & 10) is only tentative; the L_I and L_{II} lines associated with this transition may be masked by the M Auger lines of samarium.

There are a number of interesting cases when the K lines associated with some of the γ-transitions coincide almost exactly (within the 0.3% resolution of the instrument). Among these are the K lines associated with the 244.66 (Z = 62) & 248.04 (Z = 64), 689.1 (Z = 62) & 692.5 (Z = 64), 868.5 (Z = 62) & 723.6 kev (Z = 64) transitions. The first three cases have been discussed earlier[3]; the last case was spotted in a supplementary investigation carried out after we became acquainted with the results obtained by Dzhelepov et al[6] on the γ-spectrum of $Eu^{152,154}$. The intensity of the 720 kev γ-transition proved to be appreciably higher than would follow from its position in the generally accepted level diagram of Sm^{152}. We found the L lines associated with this transition: lines Nos.52 & 53 (Fig.4). While there may be some uncertainty regarding the precise contour there can be no doubt regarding the doublet character of the rise. The expected location of the L lines was determined from the known position of the K line and the known x-ray absorption energies. These L lines are indicated in the figure by dash-line arrows. The distribution of experimental points in this region substantiates the existence of two transitions; the larger fraction of conversion electrons in this group are associated with the 723.6 kev transition (Z = 64). In view of its low intensity the No.46 line was disregarded in the principal series of measurements. The results of the last series of measurements showed, however, that it cannot be attributed to the short-lived activity.

Lines Nos.70 & 71 represent the conversion lines associated with the 1272.6 kev (Z = 62) or the 1276.0 (Z = 64) transition. The dash-line arrows above the No.71 line (and the No.63 line) have the same meaning as the arrows above Nos.52 & 53. In view of the low intensity of the No.71 line, its contour could not be brought out clearly and hence the curve in the figure must be regarded as only approximate. Nevertheless it must be noted that there is a clustering of points in the region of the left-hand dash-line arrows. This cannot, however, serve as the basis for definitive identification of the γ-transition inasmuch as, in view of the prolonged recording of the electrons in this region of the spectrum, there may have been a "break" in the magnetization curve (although in our estimation this is doubtful). For this reason we give two possible identifications for the Nos.70 & 71 lines (the Z = 62 identification appears preferrable).

In determining the relative intensity of the K line (No.63) associated with the 1005.4 kev γ-transition, we took into account the fact that in the spectrum, this line includes the L line of the 964.8 kev γ-transition, the multipole order of which is E2 (see Table 3). To evaluate the intensity of the L line of the

---

*Two transitions have already been noted by Cork et al[7], namely, a transition of 104.5 kev energy pertaining to Gd^{152} and a transition of 84.2 kev pertaining to Gd^{154}.

964.8 kev γ-transition, we used the theoretical value of the K/L conversion ratio, namely, 7.0.

The decay scheme for long-lived Eu^{152} proposed by Grodzins & Kendall[4] includes γ-transitions of 550 and 1200 kev energy in Sm^{152} and of 1100 and 1240 kev energy in Gd^{152}. We did not observe any conversion lines corresponding to these transitions. If they do exist they could be detected only in a special investigation with much longer recording times at each point.

Some of the relative intensity values listed in Table 1 were used for calculating the corresponding conversion coefficient ratios. These experimental ratios are compared with the theoretical ones in Table 2. In computing the theoretical conversion coefficient ratios we used the data of Rose[9,III] for conversion on the L shell and the very detailed and accurate tables[14] concerning conversion on the K shell, calculated by Sliv & Band taking into account screening and finite nuclear size. There is some uncertainty in the values of the L conversion coefficients for Z = 62, 63 & 64. This uncertainty is due, on the one hand, to the fact that Rose's calculations were carried out for a point nucleus (but taking screening into account) and, on the other hand, to errors involved in interpolating between the rather widely spread points in Rose's tables.

The theoretical conversion ratios listed in Table 2 for the 18.8 kev transition are highly approximate because in evaluating the coefficients we had to use extrapolation, inasmuch as there are no values for the L coefficient at such low energies in Rose's tables. The multipole order of this transition can therefore be indicated only tentatively. The experimental conversion ratios for the 86.46 and 105.3 kev γ-transitions may contain an uncertainty of the order of 10-15%. For this reason these transitions have been identified as either E1 or a mixture of M1 + E2. From the formal standpoint the proportion of the two components in the mixture can readily be found[15] if one knows the conversion ratio for any two shells (or subshells) and the absolute values of the conversion coefficients for pure transitions on the same shells (or subshells). The mixture proportions for the nonconverted γ-rays of the 86.46, 103.2 and 105.3 kev transitions evaluated in this manner are listed in Table 2. The 121.77 and 123.02 kev γ-transitions were very accurately investigated on a prism β-spectrometer by Kel'man et al[16]. Our value of the ratio $\Sigma K/\Sigma L$ does not conflict with their results. There can be little doubt regarding the multipole order assignments for the 244.66, 248.04, 344.32 and 411.23 kev γ-transitions.

The absolute values of the K conversion coefficients for some of the γ-transitions are listed in Table 3. These values were calculated on the basis of our data regarding the relative intensities of the K lines and the data on the relative intensities of the γ-rays reported by Dzhelepov et al[5]. In normalizing the computed values we took the theoretical K conversion coefficient $\alpha_K = 3.1 \cdot 10^{-2}$ for the 344.32 kev γ-transition (Eu^{152}) which is known to be E2 (see Table 2). For lack of more appropriate data this normalizing K coefficient was also used in calculating the conversion coefficient of the γ-rays emitted by Eu^{154}. For this reason the values in Table 3 must be treated with some circumspection. We infer that the 859 and 873 kev transitions of Ref.5 are actually the 868.5 and 873.7 kev transitions listed in Table 1 inasmuch as there are no other conversion lines in the spectrum close to the K lines associated with these transitions.

The decay scheme for Eu^{152} proposed by Nathan & Waggoner[6] agrees in many respects with the decay scheme given by Grodzins & Kendall[4]. Nathan & Waggoner[6] also give a decay scheme for Eu^{152} taken from an unpublished work by Stephens. In these schemes Gd^{154} is assumed to have excited levels at 123, 371, 1010, 1140

Table 2

Comparison of the experimental and theoretical conversion ratios

γ-transition energy, kev	Experimental conversion coefficients ratios	Theoretical coefficient ratios					Transition type
		E1	*E2*	*E3*	*M1*	*M2*	
18,8	$\frac{L_1}{L_{11}} \approx 0,5$	1,1*	0,003*	0,001*	1,1*	13*	(*E1*)
	$\frac{L_{11}}{L_{111}} \approx 0,8$	0,8*	1,3*	2,3*	6*	0,09*	(*E1*)
86,46	$\frac{K}{\Sigma L} = 5,7$	6,6	0,9	0,13	6,7	3,5	*E1* or 4% *E2*+96% *M1*
	$\frac{L_1 + L_{11}}{L_{111}} = 6,1$	4,5	1,2	0,7	80	5,2	*E1* or 8% *E2*+92% *M1*
103,2	$\frac{K}{\Sigma L} = 4,7$	6,8	1,3	0,22	6,9	3,8	15% *E2*+85% *M1*
105,3	$\frac{K}{\Sigma L} = 5,8$	6,7	1,25	0,21	6,7	3,7	*E1* or 5% *E2*+95% *M1*
	$\frac{L + L_{11}}{L_{111}} = 3,4$	4,8	1,4	1,1	80	6,5	*E1* or 20% *E2*+80% *M1*
121,77 123,02	$\frac{\Sigma K}{\Sigma L} = 1,76$	7,0 6,7	1,8 1,6	0,4 0,3	7,0 6,8	4,0 3,9	*E2* *E2*
244,66 248,04	$\frac{\Sigma K}{\Sigma L} = 3,70$	7,2 7,1	3,7 3,5	1,5 1,3	7,0 6,8	5,1 5,0	*E2* *E2*
344,32	$\frac{K}{\Sigma L} = 4,8$	7,1	4,5	2,3	6,9	5,6	*E2*
411,23	$\frac{K}{\Sigma L} = 4,7$	7,1	5,0	3,0	7,0	5,9	*E2*

*Found for Z = 64 by graphic extrapolation in energy to 18.8 kev.

Table 3

Absolute values of the K shell conversion coefficients obtained on the basis of the relative intensities of the K lines listed in Table 1 and the relative intensities of the γ-rays reported in Ref.5

γ-transition energy, kev	Relative intensity of K line	γ-rays: Ref.5		Experiment. conversion coefficient (10^{-3})	Theoretical K conversion coefficient (10^{-3})			Type of radiation	
		relative intensty	energy, kev		E1	E2	M1	Our data	Data of Ref. 6
344,32	109,1±1,4	118±8	344			31		E2	E2
411,23	6,04±0,14	—	—						
444,23	2,67±0,07	23±6	436	3,9±1,0	4,75	14,5		E1	
583,1 or 586,5	1,27±0,05	8±2	583	5,3±1,4	2,6*	7,2*	12,5*	E1 or E2	
612,1 or 615,5	1,18±0,04	—	—						
676 or 679	~0,4	8±2	681	29±8	1,9*	5,0*	8,65*		
689,1	6,94±0,10				1,85	4,8	8,25		
692,5					2,0	5,2	9,4		
720,2	1,53±0,04	21±2	720	2,4±0,4	1,7	4,35		E2	
723,6					1,8	4,7		(E1)	
757,7	0,70±0,03	10±4	755	2,3±1,0	1,65	4,25	7,6	(E2)	
779,5	2,89±0,07	61±4	779	1,59±0,12	1,6	4,0		E1	E1
(810,6 or 813,6)	0,3	—	—						
868,5	3,12±0,08	11±2	859	3,0±0,3	1,17	2,85	4,75	(E2 +M1)	M1
873,7	⩽1,56 / ⩾1,56	24±2	873		1,25	3,1	5,4	(E2+M1)	
964,8	4,60±0,10	61±2	964	2,53±0,10	0,95	2,25	3,7	E2	
996,6	1,07±0,03	29±2	1003	3,48	0,985	2,35	3,9	(E2)	
1005,4	1,94				0,965	2,3	3,8	(E2+M1)	
1086,6	3,01±0,06	50±7	1086	2,0±0,3	0,76	1,75	2,75	E2	(E2)
1112,7	3,13±0,08	63±7	1111	1,7±0,2	0,73	1,68	2,65	E2	(M1)
—	—	7±2	1212						(E1)
1272,6 (or 1276,0)	0,75±0,03	35±3	1280	0,72±0,07	0,62*	1,3*	—	E1	(E1)
—	—	8±3	1300						
1409,4	1,39±0,02	100	1411	0,47	0,475	1,05	—	E1	E1

*Normalized to Z = 62.

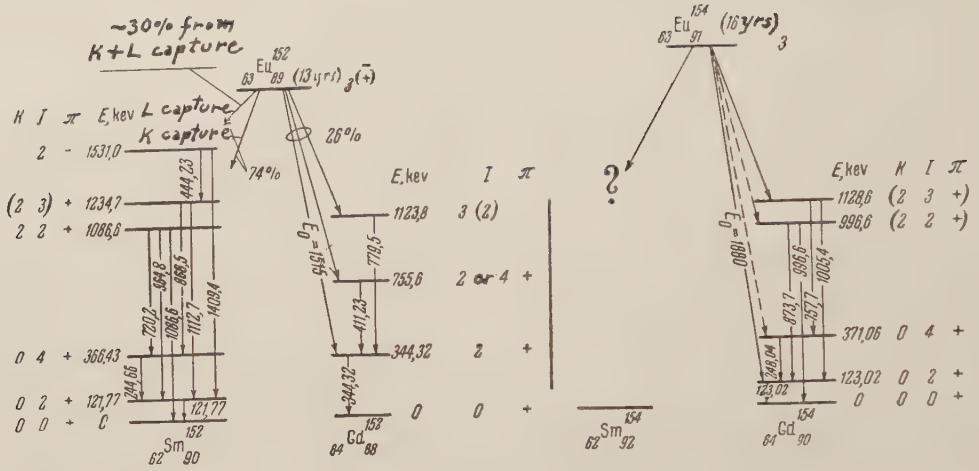

Fig.7. Decay scheme for long-lived Eu^{152} and Eu^{154}.

and 1740 kev. Where the first four levels are concerned, this does not conflict with the level diagram proposed by us in Ref.3, wherein we indicated levels at 123.02, 371.06, 996.6 and 1128.6 kev. The data of the present investigation are not adequate to substantiate the existence of levels at 1140 and 1740 kev. The precise energy values of the γ-transitions indicate, however, that the combination of cross-over and cascade transitions proposed by Stephens for de-excitation of the 1740 kev level is erroneous. The same observation may be made regarding the 1121 kev state introduced by Nathan & Waggoner in the level diagram for Sm^{152}. It is, in fact, questionable whether this level actually exists.

The parts of the level diagrams that may be regarded as reasonably certain are shown in Fig.7. The spins of 13-year Eu^{152} and (16-year) Eu^{154} have been determined by the method of paramagnetic resonance by Manenkov et al[17] and Kedzie et al[18], respectively. The energies of the β^--groups shown in the figure have been taken from the work of Nathan & Waggoner[16]. The quantum characteristics K, I and π (parity) were determined on the basis of the data listed in Tables 1, 2 & 3. From the given quantum characteristics of the ground states of Eu^{152} and Sm^{152}, one may expect the K capture branch to the ground state of Sm^{152} to be very weak or nonexistent (see also Gd^{152} and Gd^{154}). In this case the ratio of the sum of the intensities of the 121.77 and 1086.6 kev γ-transitions to the intensity of the 344.32 kev transition equals the ratio of the K + L capture branch to the β^--decay branch. The intensity of L capture is Sm^{152}* (possibly a minor fraction may be attributable to Sm^{154}) was evaluated on the basis of the empirical curve of Gray[19] for the fluorescence yield as a function of Z and the relative intensities of the Auger electron

---

*The sum of the intensities of the 444.23 and 1409.4 kev transitions according to the data of Table 1 and the theoretical K conversion coefficients amounts to 34% of the total intensity of the 121.77 and 1086.6 kev transitions.

Note added in proof: Bhattacheriee & Raman[20] recently published a report on their investigation of the activities of Eu^{152} and Eu^{154}. It is impossible on the basis of the new data appearing in this reference to refine or amplify the decay schemes shown in Fig.7.

and K conversion lines for isotopes with Z = 62.

The decay schemes as shown in Fig.7 do not include a certain number of γ-transitions, some of which are known to have an appreciable intensity.

The authors wish to express their gratitude to V.M.Kel'man for his attention to the work and valuable suggestions made in the course of discussing the results.

Leningrad Physico-Technical Institute,
Academy of Sciences of the USSR

References

1. B.R.Mottelson & S.G.Nilsson, Phys.Rev., 99, 1615 (1955).
2. D.G.Karraker, R.J.Hayden & M.C.Ingraham, Phys.Rev., 87, 901 (1952).
3. B.V.Bobykin & K.M.Novik, Doklady AN SSSR, 115, 263 (1957).
4. Nuclear Sci. Abstr., 10, 12B, 254 (1956).
5. B.S.Dzhelepov, N.N.Zhukovskii, V.G.Nedovesov & G.E.Shchukin, Izv.AN SSSR, Ser.fiz., 21, 966 (1957). (Trans. Bulletin, 21, No.7, 968.)
6. O.Nathan & M.A.Waggoner, Nuclear Phys., 2, 548 (1957).
7. J.M.Cork, M.K.Brice, R.G.Helmer & D.E.Sarason, Bull.Am.Phys.Soc., 2, Ser.II, 1, 16E3 (1957).
8. F.N.D.Kurie, J.S.Osaba & L.Slack, Rev.Sci.Instr., 19, 771 (1948).
9. Beta- and Gamma-Ray Spectroscopy, Ed. by K.Siegbahn, Amsterdam, 1955; I - A.Mitchell & H.Slätis, p.227; II - I.Bergström, p.624; III - M.E.Rose, p.905.
10. M. von Ardene, Tabellen Elektronenphysik, Ionenphysik und Übermikroskopie, Bl.1, p.153, Berlin, 1956.
11. D.Saxon, Phys.Rev., 81, 639 (1951).
12. N.Marty & M.Vergnes, Compt.Rand., 242, 1438 (1956).
13. V.S.Dubey, C.E.Mandeville & M.A.Rothman, Phys.Rev., 103, 1430 (1956).
14. L.A.Sliv & I.M.Band, Tablitsy koeffitsientov vnutrennei konversii (Tables of internal conversion coefficients), M.-L., 1956.
15. E.L.Church & J.E.Monahan, Phys.Rev., 98, 718 (1955).
16. V.M.Kel'man, V.A.Romanov, R.Ia.Metskhvarishvili & V.A.Koliunov, Zhur.eksp.i teor.fiz., 32, 39 (1957).
17. A.A.Manenkov, A.M.Prokhorova, P.S.Trukhliaeva & G.N.Iakovleva, Doklady AN SSSR, 112, 623 (1957).
18. R.W.Kedzie, M.Abraham & C.D.Jeffries, Bull.Am.Phys.Soc., Ser.II, 1, 8, M11 (1956).
19. P.R.Gray, Phys.Rev., 101, 1306 (1956).
20. S.K.Bhattacheriee & S.Raman, Nuclear Phys., 4, 44 (1957).

ON THE DECAY SCHEME OF Lu^{171}

- K.Ia.Gromov, B.S.Dzhelepov, A.G.Dmitriev & B.K.Preobrazhenskii

The results of our investigation of neutron-deficient isotopes of lutetium formed by spallation of tantalum were described in Refs.1 & 2. In the conversion electron spectra of these isotopes we detected lines whose intensity fell off with a period of about 7 days. These lines could be attributed to two lutetium isotopes, namely, Lu^{171} and Lu^{172}, whose periods are 8.5 and 6.7 days, respectively. Under the circumstances it was impossible to determine to which of these lutetium isotopes the observed lines belonged.

We have now investigated the electron conversion spectrum of a lutetium sample isolated from hafnium formed in the spallation reaction on tantalum. The investigation was carried out on a Ketron type magnetic β-spectrometer under the same conditions as obtained in the work of Ref.2. Some 12 hours after 2-hour proton bombardment of the tantalum the hafnium formed in the reaction was separated from the rare earth elements. Three days after this the daughter lutetium was isolated from the hafnium. The following lutetium isotopes can form from hafnium: 2-day Lu^{170}, 8.5-day Lu^{171}, 6.7-day Lu^{172}, 200-500-day Lu^{173} and the Lu^{175} isomers. The corresponding hafnium isotopes have the following periods: Hf^{170} - 112 min, Hf^{171} - 16 hours, Hf^{172} - 5 years, Hf^{173} - 28 hours, and Hf^{175} - 70 days.

Investigating the lutetium samples separated from hafnium, we observed a number of conversion lines whose intensity fell off with a period of 7-8 days. Taking into account the genetic relationships between lutetium and hafnium, one can unambiguously attribute these conversion lines to Lu^{171}. The experimental results obtained in the present investigation are juxtaposed with the pertinent results of the work of Ref.2 (investigations of the radiations from neutron deficient lutetium isotope with a period of ~7 days) in the accompanying table.

The lutetium sample separated from hafnium was appreciably weaker than the samples isolated directly from tantalum. Hence in the spectrum of the present lutetium sample we observed only the more intense or favorably located conversion lines from among those previously detected. We can now assert that the 75.8 and 90.6 γ-transitions and the earlier unidentified E_e = 56.6, 57.9 and 62.3 kev conversion lines observed in the spectrum of the lutetium samples separated from hafnium belong to lutetium 171. One cannot, however, say anything definite regarding the other lines; i.e., the conversion lines observed in the earlier investigation, but not detected in the present one, may belong to either Lu^{171} or to Lu^{172}. In the last columns of the accompanying table we list the identifications and possible multipolarities of the associated γ-transitions as determined on the basis of the results of Ref.2.

One can draw certain deductions regarding the decay scheme of Lu^{171} on the basis of the data obtained. The spin of the ground state of Yb^{171} has been measured by Mack[3] and is 1/2. The Lu^{171} nucleus has 71 protons and 100 neutrons; consequently[4] its spin must be the same as that of Lu^{175} (71 protons and 104 neutrons), i.e., 7/2. Thus we obtain a scheme very similar to that for the disintegration of Yb^{169} (spin 7/2) to Tm^{169} (spin 1/2). Hence there is reason to assume that the decay scheme of Lu^{172} will be similar to that of Yb^{169} (see, for example, Ref.5).

The level diagram of the lowest rotational band of Lu^{171} was accordingly constructed by analogy with the decay scheme for Yb^{169}. The following experimental data are fully consistent with this diagram.

1. According to the diagram the 75.6 kev transition must be E2. It has in fact been established experimentally that this transition is of the E2 type.

Table

Comparison of the results of the present investigation of the conversion electron spectrum of lutetium separated from the hafnium fraction with the results of Ref.2.

Electron energy, kev		Identification	Transition type
Ref. 2	Lu from Hf		
14,5±0,1	—	K-75,8	$E2$
21,2±0,25	—		
24,3±0,2			
26,2±0,25			
29,3±0,2	—	K-90,6	$E2$ or $M2+E3$
30,2±0,25	—		
40,2±0,25	—		
42,1±0,25	—		
45,3±0,2	—		
48,0±0,3	—		
49,6±0,3	—		
53,4±0,3	—		
56,6±0,15	56,6±0,2		
58,1±0,4	57,9±0,2		
62,1±0,2	62,3±0,2		
66,1±0,3	66,0±0,2	$(L_I + L_{II})$-75,8	
67,3±0,3		L_{III}-75,8	
69,0±0,2	—		
70,2±0,3			
74,2±0,2	73,1±0,2	M-75,8	
80,9±0,3	81,6±0,4	L-90,6	
88,5±0,4	—		
120,4±0,3	—	K-181,7	$E2$, $M3$ $M1+E2$
171,9±0,4	—	L-181,7	$E2+M3$
209,9±1,0	—		
753,7±1,5	—		
846,6±1,5	—	K-906,9	
903,1±2,0	—	K-964,1	

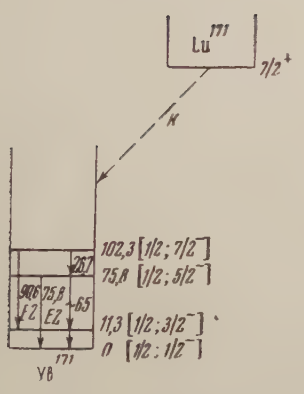

Rotational levels of Lu^{171}. γ-transition energies - experimental. Level energies calculated on the basis of known energies of the 90.6 and 75.8 kev γ-transitions.

2. The 90.6 kev transition must be E2. According to the experimental data this transition is either E2 or M2 + E3.

3. The energy of the levels of rotational band with ground state spin 1/2 is characterized by

$$E = A[I(I+1) + a(-1)^{I+1/2}(I+1/2)] + E_0.$$

We calculated the parameters A and a, using the known transition energy values 90.6 and 75.8 kev. We obtained A = 8.32 kev and a = -0.546. Then, using these values, we calculated the energy of the other transitions in the rotational band. For the energy of the transition from the (1/2; 5/2⁻) to the (1/2; 3/2⁻) level we obtained 64.4 kev. On the basis of this value one can identify the 56.6, 57.9 and 62.3 kev electron lines as the $(L_I + L_{II})$, L_{III} and M line associated with the 65-66 kev γ-transition. The computed value for the transition from the (1/2; 7/2⁻) level to the (1/2; 5/2⁻) level was 26.5 kev.

Using this value one can identify the 24.3 and 26.2 kev electron lines as the M and N lines of this transition. The experimental value for the energy of this transition consistent with this identification is 26.7 ± 0.5 kev. The calculated value of the transition energy from the (1/2; 3/2-) level to the (1/2; 1/2-) level is 11.3 kev. It was difficult to observe the electrons associated with this transition in our experiments because they are close in energy to the L Auger electrons and because our instrument is not adapted to measurements in this low energy region.

In considering the complete decay scheme of Lu^{171} one should bear in mind that K capture of Lu^{171} to the levels of the lower rotational band of Yb^{171} is forbidden with respect to the quantum number K. Thus disintegration of Lu^{171} goes apparently primarily to the higher excited states with $K > 1/2$ and it is highly probable that all or part of the γ-transitions and unidentified conversion lines associated with the base rotational band of Yb^{171} appear incident to the de-excitation of these excited states.

Conversion lines corresponding to $h\nu = 11.3$ (M shell) and 26.6 kev (L, M and N shells) were observed in the spectrum of Lu^{171} by I.M.Rogachev (Leningrad State University) by means of a lens spectrometer with a very thin counter window. The M-11.3 line is poorly discernible since it is located close to the L-MM and L-NN Auger electron lines.

"V.G.Khlopin" Radium Institute,
Academy of Sciences of the USSR

References

1. G.M.Gorodinskii, A.N.Murin, V.N.Pokrovskii & B.K.Preobrazhenskii, Izv.AN SSSR, Ser.fiz., 21, 1004 (1957). (Trans., Bulletin, 21, No.7, 1005).

2. Iu.G.Bobrov, K.A.Gromov, B.S.Dzhelepov & B.K.Preobrazhenskii, Izv. AN SSSR, Ser.fiz., 21, 940 (1957). (Trans., Bulletin, 21, No.7, 942.)

3. I.E.Mack, Revs.Mod.Phys., 22, 64 (1950).

4. Mottelson & Nilsson, Problemy sovremennoi fiziki (Problems of Modern Physics), No.1, (1956).

5. B.S.Dzhelepov & L.K.Peker, Skhemy raspada radioktivnykh iader (Decay schemes of radioactive nuclei), M.-L., 1957.

$0+ \rightarrow 0+$ TRANSITION IN Zr^{90}

- T.Yuasa, J.Laberrigue-Frolow & L.Feuvrais

It is known that $0+ \rightarrow 0+$ transitions can occur by emission of internal conversion electrons, pair formation or emission of several photons or a continuous photon spectrum.[1-7] This effect has been investigated in rare cases: O^{16} (6.04 Mev), RaC' (1.42 Mev), Ge^{72m} (0.72 Mev), Be^{8} (17 Mev) and Ca^{40} (3.35 Mev).

Until recently the disintegration of Y^{90} has been regarded as a pure β-decay ($\Delta I = 2$, yes)[8-10].

Some authors in investigating the decay of Y^{90} detected the presence of high energy photons[11], others[12-14] report observing a positron spectrum and internal conversion lines which possibly correspond to a $0+ \rightarrow 0+$ transition in Zr^{90}.

We thought it would be of interest to determine whether the $0+ \rightarrow 0+$ transition does occur in Zr^{90}, inasmuch as cases in which this transition does occur are comparatively rare. A further purpose of our work was to search for γ-quanta, particularly in the 1.7 Mev region[15], and internal conversion electrons (Ref.15) and positrons (Ref.16) corresponding to this γ-ray energy.

For such work it is important to have a very pure source with a high specific activity. We had available a source with a specific activity of up to 15 mc/mg prepared from Y^{90} in equilibrium with Sr^{90} by Bonnin by ion exchange chromatography.[17] The purity of the source was $C_{Sr}/C_Y < 10^{-7}$.

We investigated the γ-radiation accompanying the decay of Y^{90} by means of a scintillation γ-spectrometer with a NaI(Tl) crystal and a 50 channel pulse height analyzer.

The spectrum obtained (Fig.1) shows that above the internal and external brehmsstralung limit there are no observable γ-rays (the β-particles were absorbed by a centimeter thick layer of plexiglass). It may be concluded that the intensity of the 1.74 Mev γ-transition, if it exists, is less than $4.3 \cdot 10^{-6}$ relative to the intensity of the β-particles. The intensity of the 1.4 Mev γ-rays does not exceed $3 \cdot 10^{-6}$ relative to the intensity of the β-particles.*

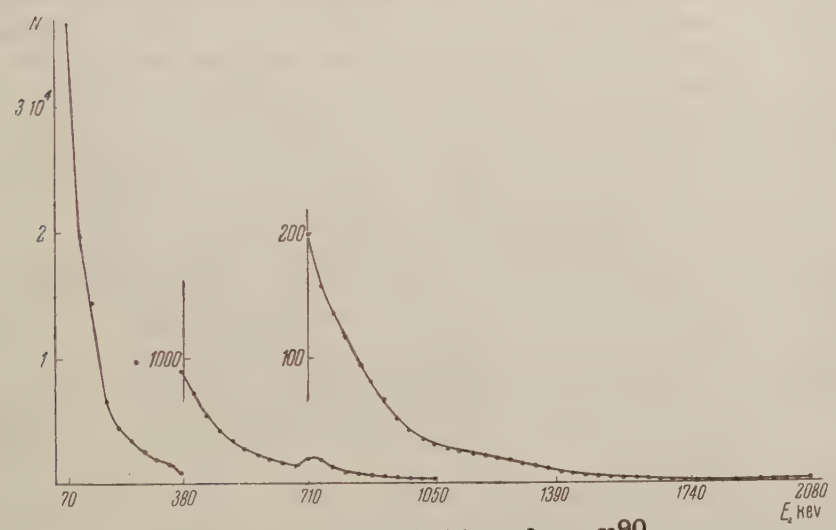

Fig.1. γ-Radiation from Y^{90}.

---

*Subsequent to this communication we carried out further measurements by means of a large (3.4 x 5.08 cm) NaI(Tl) crystal and a single-channel analyzer. Thus we were able to detect annihilation γ-radiation, the intensity of which proved to be in agreement with the intensity of the internal pair of positrons observed by means of a β-spectrograph. The full results of our investigations of the decay of Y^{90} will be published in the Journal de Physique et de Radium.

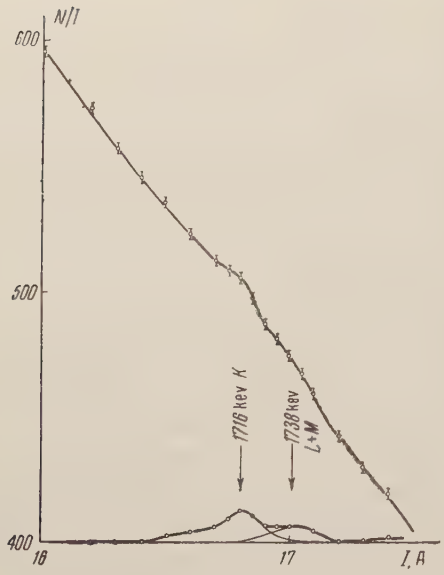

Fig.2. Internal conversion electrons associated with the 1.74 Mev 0+ → 0+ transition in Zr^{90}

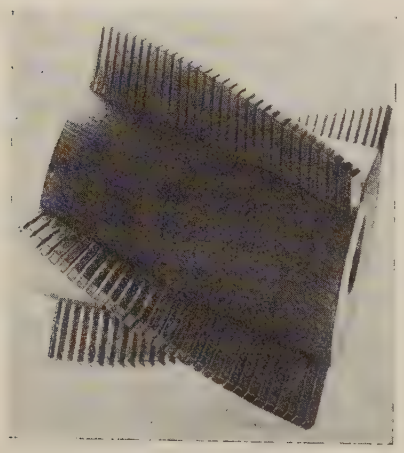

Fig.3. Modified helical slit assembly.

We investigated the decay of Y^{90} by means of a β-spectrometer with a thick magnetic lens. (Ref.15-16). The source was 3 mm in diameter, had a superficial density of 0.3 $\mu g/cm^2$ and was appled to a backing having a thickness of 20 $\mu g/cm^2$. The resolution was 0.9%. The counter was a 90 $\mu g/cm^2$ formvar window.

The investigated β-spectrum according to the Fermi theory corresponds to a $\Delta I = 2$ transition.

We carried out a very detailed investigation of the spectrum in the energy region from 1.4 to 1.75 Mev: four series of measurements were made, during which at least 10^5 counts for each point were recorded. These measurements prove the existence of two weak peaks having an intensity of $(1.6 \pm 0.3) \cdot 10^{-4}$ electrons per disintegration in the region between 1.7 and 1.756 Mev (Fig.2). These peaks are associated with internal conversion of the 1.74 Mev transition on the K and L + M shells. The indicated energy value agrees with the results of Johnson et al[13]. The intensity in our case is somewhat higher than the value given by these investigators, but taking into account the possible experimental errors involved the agreement may be considered satisfactory.

The 0+ → 0+ transition of 1.74 Mev energy can also give rise to internal pair production. There are, however, certain divergences between the experimental results pertaining to the intensity of the positron spectrum. The very low intensity of this spectrum makes it difficult to investigate it on a magnetic lens spectrometer owing to β-particle scattering.

By appropriate modification of the helical slit assemblies (Fig.3), we succeeded in reducing the scattered electron background to $1.5 \cdot 10^{-6}$ of the total number of electrons.

In these experiments we utilized a Y^{90} source with a total activity of 4 mc and a specific activity of 5 mc/mg, applied to a 30 mg/cm^2 foil.

In the positron field we observed a small peak with an upper bound of 720 ± 10 kev, rising above the general background (Fig.4). This peak was observed with two different sources in three series of individual measurements for each source.

The scattered electron background was evaluated by using an Ir^{194} source, the end-point energy of whose β-spectrum is 2.2 Mev, i.e., is approximately equal to the end-point energy of the Y^{90} β-spectrum. These experiments enabled us to determine (by subtraction) the positron spectrum, the shape of which is in good agreement with the theoretical shape predicted by Thomas[18] and calculated by Greenberg & Deutsch[12] and ourselves. We obtained the ratio

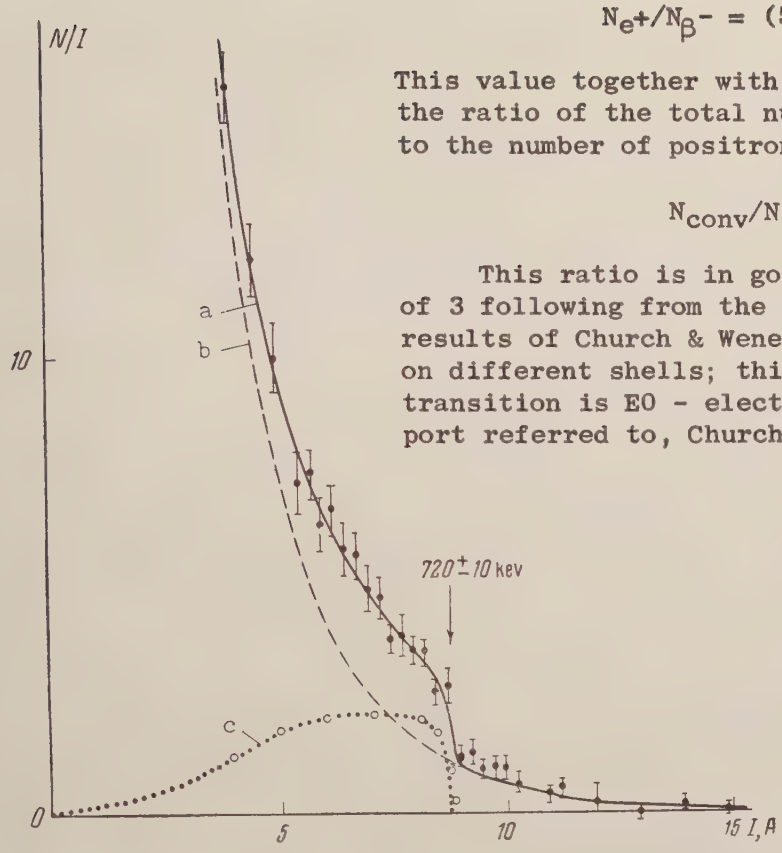

Fig.4. Internal pair production positron spectrum: a) experimental curve, b) curve obtained by means of Ir^{194}, c) theoretical e+ spectrum (•) and difference between curves a and c (o).

$$N_{e^+}/N_{\beta^-} = (5.4 \pm 0.8)\cdot 10^{-5}.$$

This value together with our preceding result yields the ratio of the total number of conversion electrons to the number of positrons:

$$N_{conv}/N_{e^+} = 3 \pm 1.$$

This ratio is in good agreement with the value of 3 following from the theory of Thomas[18] and the results of Church & Weneser[19] on internal conversion on different shells; this indicates that the given transition is E0 - electric-monopole.[19] In the report referred to, Church & Weneser also calculate the E0 transition probability W taking into account finite nuclear size. Using ρ to denote the "nuclear strength" parameter, their calculations yield for our case

$$\frac{W_{conv}}{\rho^2} = 2.5\cdot 10^9 \text{ sec}^{-1}$$

Taking into account the already known value of the ratio N_{conv}/N_{e^+}, we find

$$\frac{W_{conv + n}}{\rho^2} = 3.3\cdot 10^9 \text{ sec}^{-1}.$$

Together with the result of Deutsch[20], namely, $W_{conv + n} = 0.12\cdot 10^9$ sec^{-1}, our results allow of determining the value of ρ^2, i.e., $\rho^2 = 0.036$. This is of the same order of magnitude as the values of ρ^2 for 0+ → 0+ transitions in other nuclei.

On the other hand, Zyrianova & Krutov[21] calculated the probability of internal pair production in the 0+ → 0+ transition taking into account finite nuclear size. Interpolation of their results yields $W_n/\rho^2 \approx 1.0\cdot 10^9$ sec^{-1} for our case.

Taking into account the results of Church & Weneser for W_{conv}/ρ^2, we find

$$\left(\frac{W_{conv}}{W_n}\right)_{theo} = 3.4.$$

This value is of the same order of magnitude as the theoretical value predicted by Thomas and calculated by us.

The existence of a first excited state with 0+ in Zr^{90} inferred by Ford[14] can be explained by excitation of two particles in the unfilled nuclear shells. This is not inconsistent with the deductions of Scharff-Goldhaber[22] that the

first excited state in nuclei with magic numbers of protons and neutrons are 0+ states inasmuch as Z = 40 can be regarded as a "quasimagic number".

In view of the perplexing fact reported by Nock[23] and Lazar & O'Kelly[24] that there is a γ-transition having an energy less than 1.75 Mev in Zr^{90} formed in the decay of Nb^{90}, we consider it important, on the one hand, to check again for the presence of these γ-rays* and, on the other hand, to examine theoretically the possible origin of this excited 0+ level. Possibly a certain role is played in the structure of this 0+ level by collective excitations which correspond to radial oscillations of nuclear matter just as apparently occurs in a more overt manner[25] in O^{16}.

Laboratoire de physique et chimie nucléaires,
Collège de France, Paris and
Laboratoire de synthèse atomique, Ivry, France

References

1. R.H.Fowler, Proc.Roy.Soc., London, A129, 1 (1930).
2. H.Yukawa & S.Sakata, Proc.Phys.Math.Soc., Japan, 397 (1935).
3. J.R.Oppenheimer & J.Schwinger, Phys.Rev., 56, 1066 (1939).
4. J.R.Thomas, Phys.Rev., 58, 714 (1940).
5. T.Nakano, Prog.Theor.Phys., Japan, 6, 440 (1951).
6. S.D.Drell & M.E.Rose, Prog.Theor.Phys., Japan, 7, 125 (1952).
7. R.H.Dalitz, Proc.Roy.Soc., 206, 521 (1951).
8. A.Pohm, R.C.Waddell & E.N.Jensen, Phys.Rev., 101, 1315 (1956).
9. B.Saraf, J.Varma & C.E.Mandeville, Phys.Rev., 98, 1206 (1955).
10. H.Mark, C.McClelland & C.Goodman, Phys.Rev., 98, 1245 (1955).
11. Storrust, Thesis, Univ.Oslo, 1951.
12. G.Greenberg & M.Deutsch, Phys.Rev., 102, 415 (1956).
13. O.E.Johnson, R.G.Johnson & L.M.Langer, Phys.Rev., 98, 1517 (1955).
14. K.W.Ford, Phys.Rev., 98, 1516 (1955).
15. T.Yuasa, J.Laberrigue-Frolow & L.Feuvrais, J.de Phys.Rad., 17, 558 (1956), C.R.Acad.,Sci., Paris, 242, 2129 (1956).
16. T.Yuasa, J.Laberrigue-Frolow & L.Feuvrais, C.R.Acad.Sci.Paris, 243, 2045 (1945).
17. Bonnin, Mémoires de la Société Chimique, 5-e serie, p.1563, 1956.
18. R.Thomas, Phys.Rev., 58, 714 (1940).
19. E.L.Church & J.Weneser, Phys.Rev., 103, 1035 (1956).
20. M.Deutsch, Nuclear Physics, 3, 1, 83 (1957).
21. A.A.Zyrianova & V.A.Krutov, Izv.AN SSSR, Ser.fiz., 20, 312 (1956). (Trans., Bulletin, 20, No.3, 288.)
22. G.Scharff-Goldhaber, Phys.Rev., 90, 587 (1953).
23. Ong Ping Nock, Physica, 20, 1200 (1954).
24. N.H.Lazar & G.D.O'Kelly, BAPS, 1, No.4, 163 (1956).
25. M.Jean, Private communication.

---

*Note added proof: We have just learned (private communication) of the investigation of Sheling (Copenhagen) of the level diagram of Zr^{90} in the decay of Nb^{90}. His results are in conflict with those of Refs.23 & 24 and indicate that the 1.75 Mev 0+ level is the first excited level of Zr^{90}.

GAMMA-HODOSCOPE

- B.S.Dzhelepov

In constructing the decay schemes of radioactive isotopes it is important to be able to measure the energy and intensity of hard but weak γ-rays. The usual methods of γ-spectrometry, however, prove to be inadequate if the relative intensity of the γ-rays is less than 10^{-5} photons per decay.

In 1951 the author proposed a method by means of which the sensitivity of γ-ray measurements could be enhanced. The proposed instrument has come to be called a gamma-hodoscope. A gamma-hodoscope was constructed and partially tested at Leningrad State University by O.V.Chubinskii.[1]

Principle of operation of the gamma-hodoscope

The investigated γ-rays fall on a thin cellophane target and eject recoil electrons. These electrons move along helical trajectories in a suitable homogeneous magnetic field. Along their path the electrons pass through three arrays of Geiger counters (Fig.1). Each array consists of many counters; each counter is connected to an amplifier and neon bulb. The bulbs are arranged on a suitable display panel and whenever there occurs a triple coincidence among the counter arrays, the display panel is photographed. From the photograph one can readily tell which counters in each array were triggered. From the three counter points one can readily establish the circle that forms the projection of the helical path on a plane perpendicular to the magnetic field. Knowing the magnetic field one can find $H\rho$ and, consequently, the projection of the electron velocity v_{pr} on the plane perpendicular to the magnetic field. If the height of the counters is small, the electrons will only be insignificantly deflected from this plane and for all practical purposes v_{pr} will be equal to the actual electron velocity v.

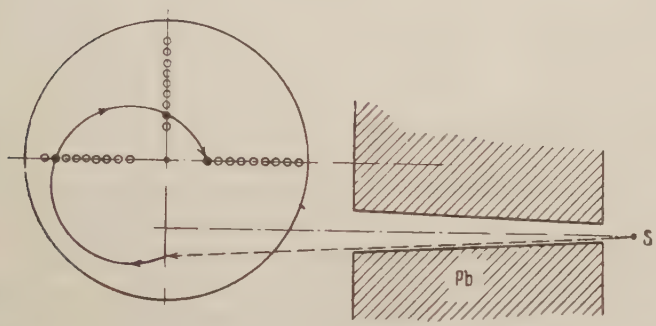

Fig.1. Principle of operation of the gamma-hodoscope.

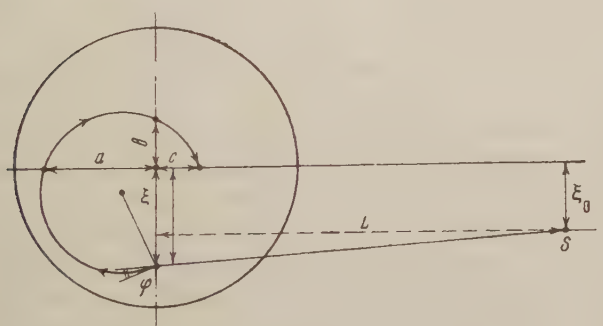

Fig.2. Diagram for derivation of the plane case equations.

Thus we readily obtain the electron energy. In addition we can find the point of intersection of the circular trajectory with the target, i.e., the point of origin of the recoil electron. Connecting this point with the point at which the source is located, we can find the narrow limits for the angle at which the electron is ejected and then, since its energy is known, we can determine the energy of the γ-ray.

This is the distinctive feature of the gamma-hodoscope as a spectrometer: for each triple coincidence one can determine the energy of the photon producing it.

Equations for the plane case

Let us situate the origin of our coordinates at the center of the instrument and designate the distances to the three triggered counters by a, b, and c (Fig.2). Then the radius of the circle passing through the counters is

$$\rho = \frac{1}{2}\sqrt{a^2 + b^2 + c^2 + \frac{a^2c^2}{b^2}},$$

the distance from the center to the point of ejection of electron is

$$\xi = \frac{ac}{b},$$

and the projection of the Compton recoil angle is

$$\varphi = \operatorname{arc\,tg}\frac{a - c}{b + \xi} - \operatorname{arc\,tg}\frac{\xi - \xi_0}{L},$$

where ξ_0 and L are the coordinates of the source.

The energy $h\nu$, as defined by the values of φ and $H\rho$, is given by

$$\frac{2\left(\frac{h\nu}{m_0c^2}\right)^2\cos^2\varphi}{1 + 2\frac{h\nu}{m_0c^2} + \left(\frac{h\nu}{m_0c^2}\right)^2\sin^2\varphi} = \sqrt{1 + \frac{e^2}{m_0^2c^4}(H\rho)^2} - 1.$$

Optimum field for a given energy

It is clear from what has been said above that the γ-spectrum can be obtained with one value of the field H. The efficiency of the system, however, is not the same for different photon energy values. Roughly speaking, the efficiency will be highest for the values of $h\nu$ for which the electrons ejected from the center point of the target pass through the middle counters of each array. Hence by adjusting the instrument for recording hard γ-rays we can, setting the appropriate high field value, "tune out" all the low energy photons.

Technical difficulties

The following difficulties are encountered in practical design of a gamma-hodoscope.

1. The electrons must pass through three counters, i.e., must traverse five counter windows. There inevitably occurs multiple scattering in the windows and this leads to an error in determining $h\nu$, due to smearing out of the experimental line. There are two ways in which this error can be reduced: either one must maintain a high vacuum in the instrument and make the window films sufficiently thick to withstand the pressure in the counters or one can fill the instrument with helium to the counter pressure and make the window films very thin or even do away with them altogether. To judge from the experiments made along this line with the Ritron and Elotron one can hope to obtain better results by the former expedient, but it must be recalled that in the Elotron the slits are narrow whereas in the gamma-hodoscope the slits are wide and in this case the technical difficulties of preparing vacuum tight thin windows are appreciably aggravated. Hence in the hodoscope that will be described in the following report[1] the latter means were employed: the instrument was filled with helium and windowless counters were used. This limits the range of application of the instrument; it is expedient to use it only for investigating γ-rays of more than 1.5 Mev energy.

2. A second source of error in determining $h\nu$ is the finite size of the counters. Of course, it is advantageous to make them as narrow as possible, that is, to increase the number of counters in each row, but this calls for a corresponding increase in the number of amplifiers.

In conclusion I would once more like to call attention to the potentialities of the gamma-hodoscope stemming from the fact that with it the energy of a γ-ray is determined from each triple coincidence. Let us assume that where we have shown the source in Fig.1, we have, instead, a target being bombarded by some particles and that we want to investigate the spectrum of the resultant γ-rays. If we are working with a conventional scintillation or magnetic spectrometer in which the spectrum is recorded section by section (i.e., a spectrometer not equipped with a multiple channel analyzer) we would have to follow carefully the intensity of the nuclear reaction while recording the spectrum. In working with the gamma-hodoscope, in contrast, there is no necessity for doing this: even though the intensity of the nuclear reaction varies over a wide range, the gamma-hodoscope will still record the true γ-spectrum.

References

1. O.V.Chubinskii, Present issue of the Bulletin, p. 1572.

THE GAMMA-HODOSCOPE AT THE SCIENTIFIC RESEARCH INSTITUTE OF PHYSICS OF LENINGRAD STATE UNIVERSITY*

- O.V.Chubinskii

In this report we shall describe a gamma-spectrometer of a new type - the gamma-hodoscope - constructed at a Scientific Research Institute of Physics of Leningrad State University at the suggestion of B.S.Dzhelepov. The principle of operation of the hodoscope has been described in the preceding report.[1]

The instrument is intended primarily for investigation of high energy γ-radiation having a very low intensity.

1. Description of the Gamma-Hodoscope

Chamber

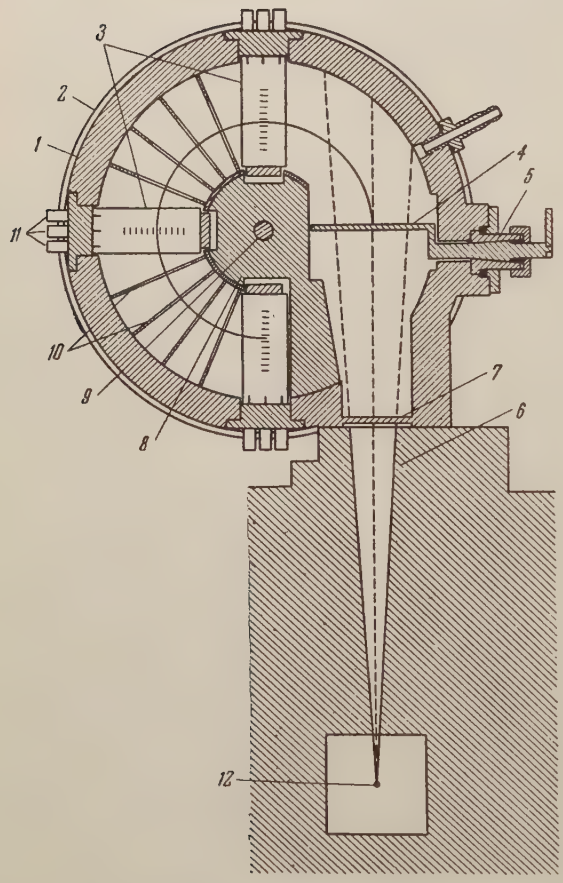

Fig.1. Chamber and collimator of the gamma-hodoscope: 1) cylindrical housing of plexiglass, 2) bottom and base of instrument, 3) counter arrays, 4) aluminum frame with target, 5) control arm, 6) collimator, 7) entry window, 8) lead shielding plates, 9) central support, 10) aluminum baffles, 11) counter terminals, 12) γ-ray source.

Fig.1 shows a section through the chamber of the instrument and the collimator (view from above). The chamber consists of a cylindrical housing (1) (inside diameter 340 mm) made of thick plexiglass, a brass bottom (2) and cover (20 mm and 10 mm thick, respectively). The inside height of the chamber is 80 mm. The bottom of the instrument also serves as the base on which the other components are mounted. The cylindrical housing is accurately positioned and attached to the bottom by bolts. The edge of the cover enters into an angular groove milled in the cylindrical housing.

Three arrays of Geiger-Müller counters (3) are inserted into the chamber through appropriate openings in the housing. The three arrays or rows of 10 counters each and the target are positioned along two mutually perpendicular axes passing through the center of the chamber. The counter assemblies are positioned by means of grooves milled in the bottom of the instrument.

Airtight seals between the bottom of the instrument and the housing and at the lead terminals of the counters are provided by rubber gaskets, while the points of contact of the cover and

---

*The present description of the gamma-hodoscope is based on reports presented at conferences of the USSR Academy of Sciences 1955 to 1957.

counter assemblies with the housing are coated with "plastilene".

The target, a celluloid film 150 μ thick, is mounted in an aluminum frame (4) which is connected with the control (5) by means of which the target can be inserted or withdrawn from the γ-ray beam without disturbing the vacuum.

The γ-ray beam defined by the collimator (6) enters the chamber through the window (7) covered with a plexiglass plate 8 mm thick.

The lead shielding plate (8), the central support (9) of brass and eight aluminum baffles (10) are mounted on the bottom of the instrument. The baffles serve to stop stray electrons. The bottom and cover of the instrument as well as the lead plate are lined with plexiglass.

Collimator

The γ-ray source (12) is mounted outside the instrument in a lead collimator (6) which defines the divergent beam of rectangular cross section.

In the initial version of the instrument the source was placed at a distance of 654 mm from the target, the length of the collimator was 400 mm, the entry window measured 8 x 8 mm and the working spot on the target had an area of 80 x 35 mm.

In 1955 the design of the collimator was modified: the target to source distance was decreased to 554 mm and the length of the collimator to 300 mm, while the dimensions of the entry aperture were changed to 14 x 8 mm. Under these conditions the effective area of the spot on the target as determined by photography is 72 x 33 mm and the solid angle of the collimator equals 0.06% of 4π. The axis of the collimator passes at a distance of 109 mm from the center of the instrument and is normal to the plane of the target.

The collimator and lead plates provide good shielding of the counters from direct γ-rays. The first row of counters, however, is heavily loaded due to the passage of scattered electrons and photons.

Counters

The counters are an important component of the gamma-hodoscope and determine its spectroscopic qualities to a significant degree.

Prior to 1955 cylindrical counters 8 mm in diameter were used in the instrument. The cathode of each counter consisted of a brass case and a cellophane film 17 μ thick coated with a thin layer of bismuth. The effective area of the counter windows was 7.2 x 50 mm. These cylindrical counter assemblies were used to study the operating characteristics of the gamma-hodoscope and were employed in investigating the hard γ-radiation from Sb^{124} and Na^{24}. These experiments showed that the background from electrons scattered in the counter walls greatly hampers measurement of very low intensity γ-rays. This point will be discussed in more detail below. In order to reduce the probability of recoil electron scattering in the counter walls, the writer suggested using rectangular section counters with open windows, i.e., counters without window films. The design of such counters was developed by the writer in collaboration with Iu.N.Podkopaev. A rectangular counter of this type and a schematic view of an array of ten such counters are shown in Fig.2.

The cathode of a rectangular counter is formed by two parallel brass strips 6 mm wide and 0.5 mm thick. The separation between the strips is 6 mm. The anode is made of tungsten wire 0.057 mm in diameter. The windows measure 6 x 50 mm. The windows of the counters of the second array are narrowed on both sides by slit strips to 4 mm.

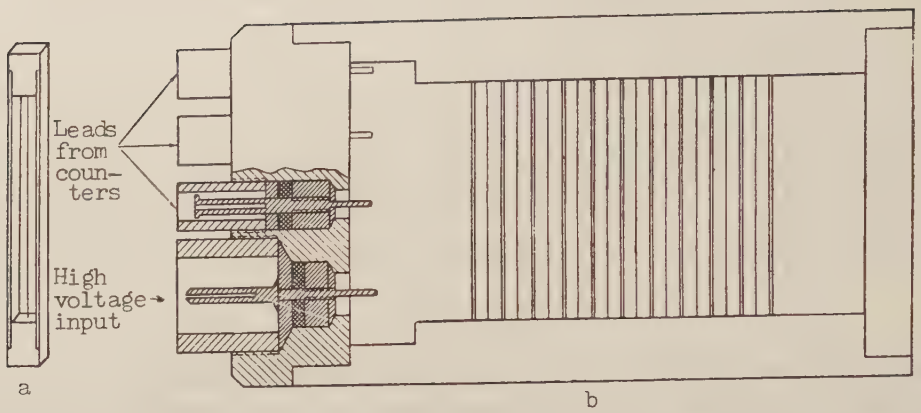

Fig.2. a) Rectangular counter, b) counter array consisting of ten rectangular counters. One rectangular brass strip serves as a common side wall for two neighboring counters.

Each counter unit (Fig.2,b) consists of an assembled frame of plexiglass in which the array of ten counters is clamped. The upper and lower members of the plexiglass frames have grooves for receiving the carefully shielded leads from the external terminals to the individual anodes of the counters.

The arrays are set in the instrument so that the center of the fifth counter* is 109 mm from the center of the instrument. The complete set of counters defines an electron beam 64.5 mm wide (from ρ = 80 mm to ρ = 144.5 mm).

The high voltage for the cathodes is supplied from a single source (dry-cell B-battery) with individual controls for each array. A small positive bias is applied to the anode of each counter; this is individually adjusted by means of potentiometers so that all counters will operate under the same conditions (see Fig.4). The operation of the counters is monitored by means of an oscilloscope.

The entire volume of the instrument (chamber and counters) is filled with a gas mixture of helium - 26 cm Hg - and methane - 4 cm Hg. With this gas mixture the threshold voltage is ~1100 v, the length of the plateau is 70 v with a slope of 3% per 10 v; the rated efficiency of the counters for relativistic electrons is ~79%; the pulse amplitude is 0.3-0.4 v. The efficiency of three counters connected in coincidence is ~49%. The coincidence background in the absence of a γ-ray source is 3-5 pulses/min. The operation of these rectangular counters is very stable at loads of several thousand pulses per minute. The gas mixture in the instrument should be changed two or three times a year.

Associated electronic equipment

The electronic equipment used in conjunction with the gamma-hodoscope fulfills the following functions.

1. Discriminates the triple coincidences among the counters of the three arrays.

2. Indicates the counters through which the recoil electron producing the triple coincidence passes.

---

*Here and below counter numbers are reckoned going out from the center of the instrument.

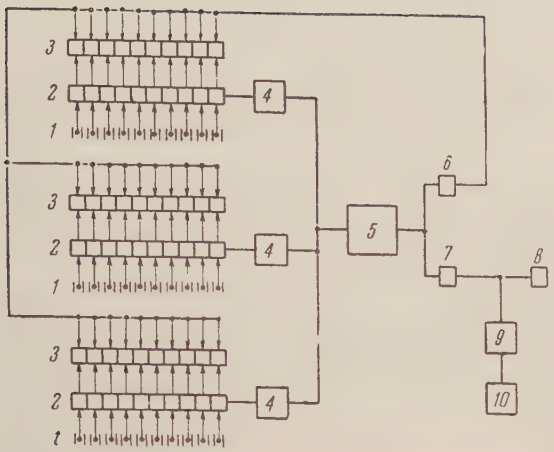

Fig.3. Block diagram of electronic equipment: 1) counters, 2) collector unit, 3) neon cells, 4) collector unit amplifier, 5) unit discriminating triple coincidences, 6) neon cell control unit, 7) unit controlling mechanical register and motion picture film advance, 8) mechanical register, 9) delay unit, 10) mechanism advancing motion picture film.

Accordingly, the electronic equipment consists of two principal parts: a triple coincidence amplifier and a recording-indicating device. The block diagram of the installation is shown in Fig.3; in principle it is similar to that described in Ref.2.

The triple coincidence amplifier assembly consists of three collector units (2) three associated amplifiers (4) a coincidence discriminator (5) and two control units (6) and (7).

The recording arrangement consists of three rows of neon cells (one cell for each counter), a display panel carrying the neon bulbs, a mechanical register (8), a delay unit (9) and a mechanism (10) advancing the motion picture film on which the flashing of the neon tubes is recorded.

The pulses from the counters are fed by individual coaxial cables to the corresponding neon cells (Fig.4). A pulse V_C arriving at the resistance R_C is applied to the input of the collector amplifier. Only the pulses from the one corresponding counter are applied to the input of a given neon cell, while the pulses from all the counters of a given array go to the input of the collector amplifier associated with the given array.

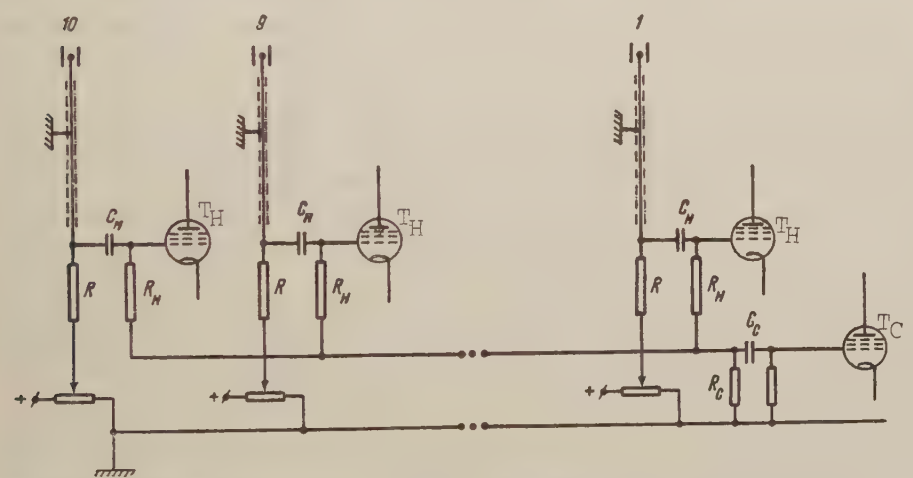

Fig.4. Collector unit. R = 10 megohm; C_H = 3000 μμf; R_H = 1 megohm; R_C = 100 kilohm; C = 1500 μμf. T_H - first neon cell tube 6Zh7 (= 6J7); T_C - first collector amplifier tube 6Zh4 (= 6AC7). V_H - amplitude of pulse applied to control grid of T_H; V_C - amplitude of pulse arriving at control grid of tube T_C. $V_C \approx 0.1\ V_H$.

Each neon cell (3) consists of a two-stage amplifier with an Mn-5 neon bulb coupled to its output.

The collector amplifiers (4) are two-stage amplifiers designed about 6Zh4 (= 6AC7) tubes. The pulses from the collector amplifier are applied to the Rossi triple coincidence circuit (5). The resolving time of the coincidence amplifier is $\sim 10^{-6}$ sec.

The triple coincidence pulses are applied to the two control units. One of them (6) shapes a high level positive pulse which is applied to the inputs

of all the neon cells. When this pulse coincides with a pulse from the corresponding counter the given neon bulb lights up. The resolving time of the neon cells is $\sim 5 \cdot 10^{-4}$ sec. Thus, with each triple coincidence three neon bulbs light up. The bulbs are mounted in three rows of ten bulbs each on the display panel. A camera suspended over the display panel photographs the flashing bulbs on motion picture film.

The control unit (7) shapes the pulses applied to the mechanical counter (8) and the delay unit (9). This delay unit is an assembly consisting of a relay and appropriate capacitors and resistors; it serves to actuate the film advance mechanism (10) 0.1 sec after the instant of a triple coincidence.

After development of the film the photographs are interpreted by means of a very simple apparatus. The interpretation consists in determining the numbers of the counters triggered by a given recoil electron.

Magnet

The requisite magnetic field is produced by an SP-9 electromagnet. Special pole pieces measuring 460 x 500 mm were designed for the magnet in order to insure a uniform field over the entire region of the recoil electron beam. The gap between the pole pieces is 116 mm. The pole pieces are parallel to within ±0.05 mm.

The field topography was measured by K.A.Baskova by means of an exploring coil connected to a sensitive galvanometer. Deviation of the field from the mean value over the entire region of the recoil electron trajectories was found to be less than 0.5%.

The absolute intensity of the magnetic field as a function of the current through the magnet windings was measured by V.S.Sadkovskii by the proton resonance technique. The error in determining the field intensity depended primarily on the error of measuring the resonance frequency by means of a wavemeter and did not exceed 0.05%.

The effective hysteresis loop was plotted on the basis of 33 experimental points from 0 to 13 amp and 18 points from 13 to 0 amp. This is the plot we now use for finding H from the indications of the ammeter connected to the magnet winding. After several 0→13→0 amp cycles, the correspondence between the field intensity and the current strength is fully reproducable to within ±0.05%.

In measuring the field distribution the magnet was supplied from storage batteries. In measuring the γ-spectra the magnet is supplied from a special dc generator. The magnet current is controlled and monitored by means of a PPTV-1 potentiometer and an M91/A galvanometer. The current is maintained constant within ±0.1 amp. Current values from 1.5 to 6 amp are commonly employed in operating the instrument.

2. Processing of the Experimental Data

Each series of measurements with the gamma-hodoscope is carried out with a constant value of the magnetic field. As a result, there is obtained a certain number of frames, i.e., photographs of the lit-up neon bulbs. The number of frames per experiment varies from only a few to several thousand depending on the specific problem and the experimental conditions involved. The energy of the corresponding primary γ-ray is determined from each frame, i.e., for each recorded recoil electron. To find this energy one must determine the energy E_e or the momentum $H\rho$ of the electron and the Compton angle φ, then

$$h\nu = \frac{E_e + \cos\varphi \sqrt{E_e^2 + 2m_0c^2E_e}}{\left(2 + \frac{E_e}{m_0c^2}\right)\cos^2\varphi - \frac{E_e}{m_0c^2}} \tag{1}$$

We cannot determine the true trajectory of the electron from the numbers of the triggered counters; we can only determine with a certain uncertainty the projection of this trajectory on a plane perpendicular to the magnetic field. For purposes of calculation we assume that for each combination of three counters we have a single circle passing through the centers of the three counters, i.e., the so-called central trajectory. The parameters of the central trajectory, including ρ and φ, are determined from the known coordinates of the centers of the three counters (a, b, c) and the source (ξ_0, L) by solving the usual equation for a circle. The coordinates of the center of the circle are given by

$$x_0 = \frac{1}{2b}(ac - b^2), \tag{2}$$

$$y_0 = \frac{a - c}{2}; \tag{3}$$

the coordinate of the point on the target where the recoil electron originated is given by

$$\xi = \frac{ac}{b}, \tag{4}$$

then the trajectory parameters are defined by

$$\rho = {}^1/_2\sqrt{a^2 + b^2 + c^2 + \xi^2}, \tag{5}$$

$$\varphi = \operatorname{arctg}\frac{a - c}{\xi + b} - \operatorname{arctg}\frac{\xi - \xi_0}{L}. \tag{6}$$

Since there are ten counters in each row, we have in all 1000 possible combinations of three counters and consequently 1000 possible central trajectories. Tables have been computed according to Eqs.(2)-(6) for all the combinations. Counter combinations corresponding to trajectories that pass more than 4 mm outside the boundary of the working spot on the target are regarded as "nonoperative" and in plotting the γ-spectrum the photographic frames containing such combinations are disregarded. There are 238 such "nonoperative" combinations.

In processing a film strip a table is made out showing the numbers of the triggered counters and the tabular values of the central trajectory parameters $H\rho$ and $E_\gamma = h\nu$.

The value of E_γ is found by interpolation of the curves for $h\nu = f(\varphi)$ (Fig.5) constructed according to Eq.(1) for different values of $H\rho$ in steps of 150 gauss cm. The accuracy of interpolation is ±5 kev. Thus we obtain a set of values for E_γ which can be used for plotting the experimental γ-ray spectrum, i.e., the variation of the number of frames within a given spectral interval ΔE_γ with E_γ. With the given method of plotting the magnitude of ΔE_γ is ~3% of E_γ. The smooth curve drawn through the plotted points is the experimental line contour (Fig.6).

A certain number of triple coincidences is produced by electrons originating not in the target but in the gas filling the instrument and in the walls and other parts of the instrument. To determine this background for the purpose of subtracting it from the experimental lines, measurements are made with

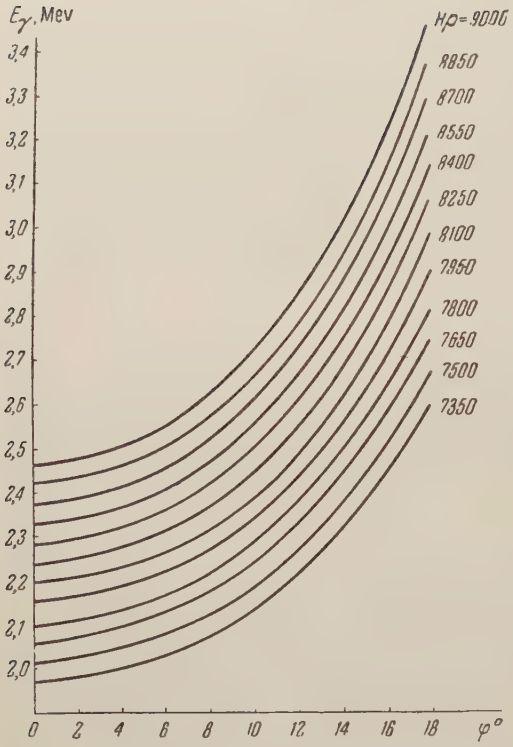

Fig.5. Variation of E_γ as a function of φ for different values of Hρ.

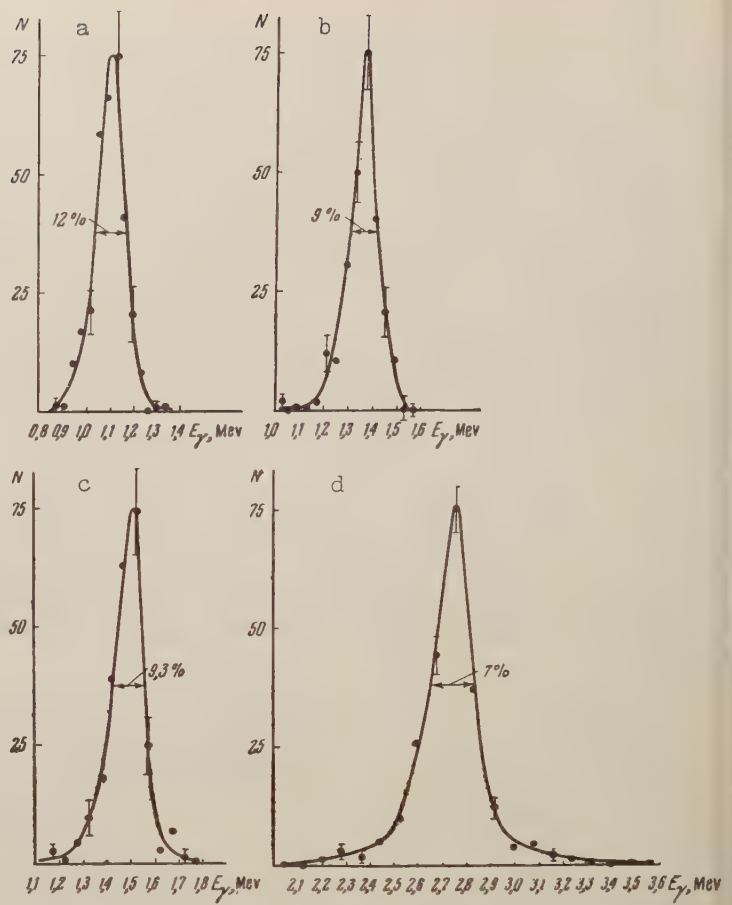

Fig.6. Experimental γ-lines obtained with H/H_0 = = 1: a) 1.118 Mev line of Zn^{65}, H = 405 oersted, b) 1.368 Mev line of Na^{24}, H = 487 oersted, c) 1.520 Mev line of K^{42}, H = 525 oersted, d) 2.754 Mev of Na^{24}, H = 917 oersted.

the target withdrawn from the γ-ray beam. The results of the background measurements are processed in the same manner as those of measurements with the target in place. In this case, too, the frames in which "nonoperative" combinations appear are also discarded in plotting the background spectrum.

Below all the experimental γ-lines are shown with the background already subtracted.

3. Some characteristics of the Gamma-Hodoscope

At a given value of the field H the gamma-hodoscope records a certain interval of the γ-ray spectrum whose width depends on the geometry of the instrument (the position and size of the working spot on the target, the angle subtended by the counters, etc.) and on H. For example, with H = 600 oersted the recorded γ-energy interval extends from ~1.2 Mev to ~2.4 Mev, while with H = = 1200 it extends from ~2.7 Mev to ~5.2 Mev.

At the same time, γ-rays of a given energy can be recorded by the hodoscope at different values of H. By way of illustration in Fig.7 we show the dependence of the counting rate for the 2.75 Mev γ-rays of Na^{24} on the field strength H. It will be seen that the hard Na^{24} γ-line can be measured at all

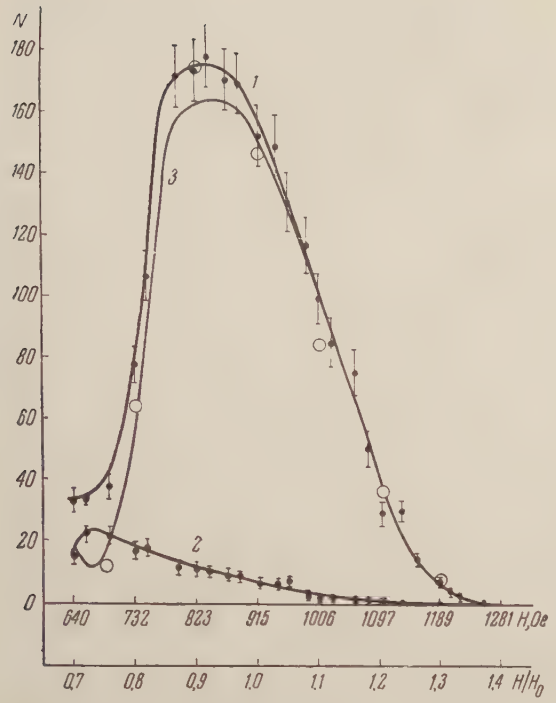

Fig.7. Variation of the counting rate for the 2.7 Mev Na^{24} γ-line with the field strength: 1) counting rate N_t when the γ-rays are incident on the target, 2) counting rate N_b when the target is withdrawn from the beam, 3) experimental curve with the background subtracted, i.e., $N_t - N_b$. The open circles indicate the calculated relative probability of recording γ-rays of 2.75 Mev energy.

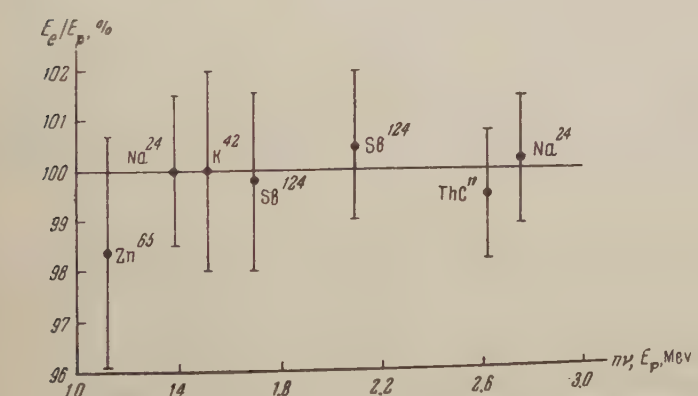

Fig.8. Calibration of the gamma-hodoscope in energy with $H/H_o = 1$. E_e - value corresponding to the peak of the experimental line; E_p - most accurately known value of the γ-ray energy.

field values from ~650 to ~1230 and that the probability of recordings strongly depends on H and attains a maximum at $H \approx 800$-900 oersted. The shape of the spectral line also depends on H.

We can characterize the measuring conditions by the ratio H/H_o, where H is the magnetic field at which the measurements are made and H_o is the magnetic field at which an electron ejected by a photon of the given energy from the central point of the target (ξ = 109 Mev) directly forward ($\varphi = 0$) will follow a circle of radius of ρ = 109 Mev, i.e., will pass through the centers of the fifth counters in each array. Obviously for the given γ-line, the field H_o is close to the optimum one at which the probability of recording is highest.

In investigating low intensity hard γ-radiation we may encounter the following cases:

1) The case when there are no softer lines close to the investigated γ-line; in this case it is expedient to carry out measurements with $H \approx H_o$, utilizing the maximum effectiveness ("transmission") of the hodoscope.

2) The case when there is a relatively intense softer γ-line near the investigated γ-line; in this case in order to be able to observe the relatively weak hard γ-line in "pure" form, one must carry out the measurements with $H > H_o$ at some sacrifice of detecting efficiency. Hence in order to be able to choose the best conditions for measurement and analysis of the experimental results one must know how the spectral characteristics of the instrument depend on the energy of the γ-rays at a given H/H_o ratio or on H/H_o with a given $h\nu$ value. Let us examine the dependence of the experimental line shape on $h\nu$ at $H \approx H_o$. The lines in this case (see Fig.6) are not quite symmetrical: the slope of the contour on the high energy side is somewhat steeper than on the low energy side and the lines have an appreciable tail on both sides.

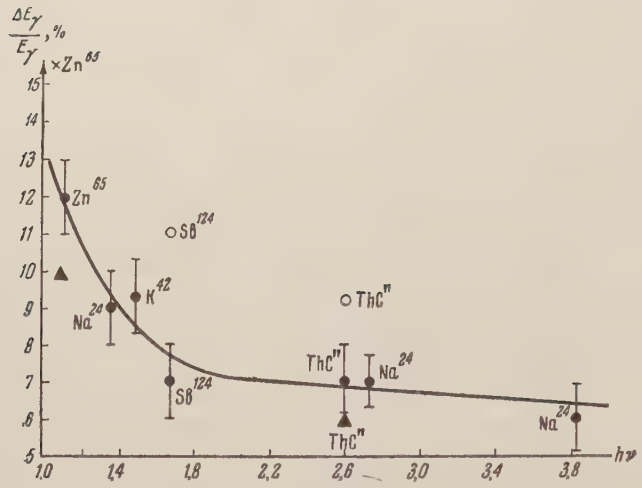

Fig.9. Variation of the relative half-width of the experimental line with the γ-ray energy ($H/H_o = 1$): - rectangular counters, × & O - cylindrical counters and ▲ - at a gas pressure of 15 cm Hg in the instrument (rectangular counters).

The energy of the γ-rays is determined from the maximum of the experimental line, the position of which can be found with an accuracy of 1-3% of $h\nu$. Fig.8 shows the variation of E_e/E_p with the γ-ray energy; here E_e is the energy corresponding to the peak of the experimental curve and E_p is the most precise value of $h\nu$ from the literature. The greatest difference between E_e and E_p does not exceed the error in determining the position of the peak of the experimental curve.

The variation of the relative line width at half-height with γ-ray energy is shown in Fig.9. Above ~1.7 Mev the experimental line half-width changes little with increasing energy. As may be seen from Fig.9 conversion to the rectangular counters with no film over the windows improved the spectral characteristics of the hodoscope to the extent of reducing the line half-width by a factor of 1.3-1.4.

Let us examine, using the Na^{24} γ-line of 2.75 Mev energy, the functional dependence of the line shape, half-width and position on H/H_o (Figs.10,11 & 12).

As usual in such cases, due to multiple scattering the recoil electrons ejected at different angles φ from the target are characterized by different energies.[3] The probability of detecting low energy recoil electrons multiply scattered through a large angle in the target increases for small values of H/H_o. This explains the shift of the entire line to the side of low energies, the increase in the line half-width and the presence of the low energy tail.

The line half-width noticeably decreases with increasing H/H_o. This is due to a decrease in the number of counter combinations that can record the recoil electrons ejected by photons of the given energy. The shift of the line peak to the side of higher energies at large values of H/H_o apparently occurs due to the fact that the values of ρ and φ calculated for the central trajectories exceed the true values of the parameters. In addition, multiple scattering of electrons in the target in this case also leads to an elevated value of E_γ.

As noted above, the lines obtained by means of the gamma-hodoscope are characterized by tails on both sides of the line. Hence it is important to investigate the shape of the high energy tails and the reason for their formation.

By way of example let us examine the results of measurement of the 2.75 Mev γ-line of Na^{24} at H = 1200 oersted ($H/H_o = 1.33$). With this field the recoil electrons not scattered in the target, the gas in the instrument or the counter walls will pass mainly through counters Nos.1—1—1 and with a somewhat lower probability through counters Nos.1—2—1 (here and below the counter numbers are for arrays I, II and III reckoning from the target, the

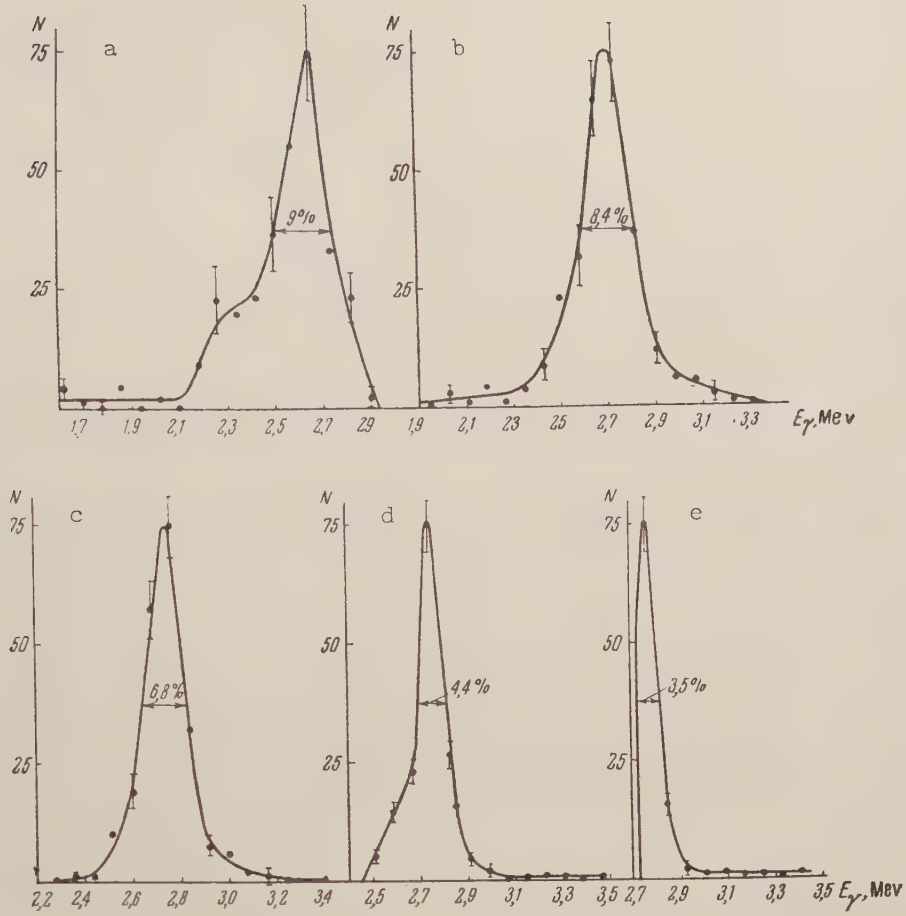

Fig.10. Experimental 2.75 Mev γ-line of Na^{24} recorded at different H/H_o values: a) H = 732 oersted, H/H_o = 0.8; b) H = 824 oersted, H/H_o = 0.9; c) H = 1007 oersted, H/H_o = 1.1; d) H = 1100 oersted, H/H_o = 1.2, e) H = 1186 oersted, H/H_o = 1.3.

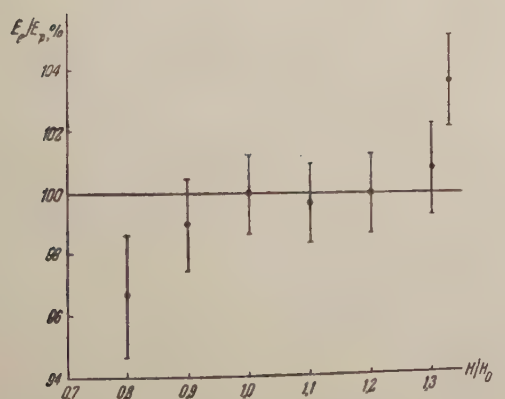

Fig.11. Variation of E_e/E_p with H/H_o for the 2.75 Mev Na^{24} gammas.

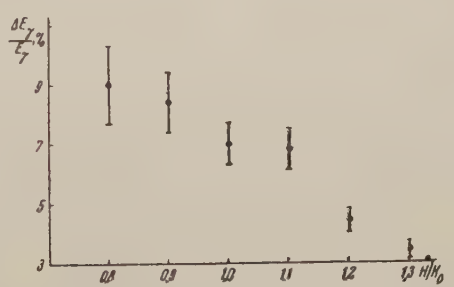

Fig.12. Variation of $\Delta E\gamma/E\gamma$ with H/H_o for the 2.75 Mev Na^{24} gammas.

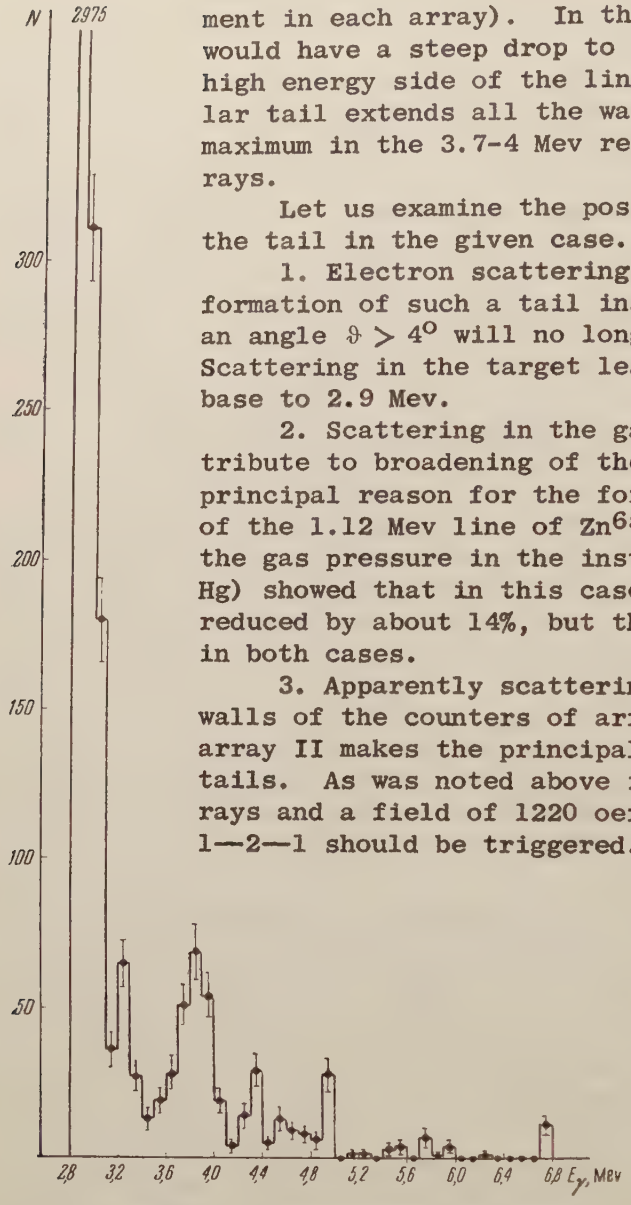

Fig.13. Results of measurement of the Na^{24} γ-spectrum with H = 1220 oersted (background subtracted). The maximum in the 3.6-4 Mev region is partially due to 3.85 Mev γ-rays.

numbering in each case being out from the center of the instrument in each array). In the ideal case the experimental line would have a steep drop to zero at ~2.85 Mev. Actually the high energy side of the line is less steep and a highly irregular tail extends all the way out to ~7 Mev (Fig.13). The minor maximum in the 3.7-4 Mev region is associated with 3.85 Mev γ-rays.

Let us examine the possible reasons for the appearance of the tail in the given case.

1. Electron scattering in the target cannot lead to the formation of such a tail inasmuch as electrons scattered at an angle $\vartheta > 4^\circ$ will no longer be detected by the instrument. Scattering in the target leads only to broadening of the line base to 2.9 Mev.

2. Scattering in the gas filling the instrument does contribute to broadening of the experimental line but is not the principal reason for the formation of the tail. Measurements of the 1.12 Mev line of Zn^{65} and the 2.62 Mev line of ThC'' with the gas pressure in the instrument reduced by half (to 15 cm Hg) showed that in this case the line width at half-height was reduced by about 14%, but the tails remained virtually the same in both cases.

3. Apparently scattering of the recoil electrons in the walls of the counters of array I and particularly in those of array II makes the principal contribution to the experimental tails. As was noted above in the ideal case for 2.75 Mev γ-rays and a field of 1220 oersted only counters 1—1—1 and 1—2—1 should be triggered. Scattering of electrons in the first counter of row I, however, leads to the appearance of counter combinations of the types 1—3—1, 1—4—1, 1—5—1, etc. (Fig.14 a) (the divergent electron beam from the first window of counter No.1 of array I is focused through 180° to arrive at the window of the No.1 counter of array III). As may be seen from the curve of Fig.15 a, however, the scattering in the counters of array I leads to relatively small error in determining E. Moreover, it will be recalled that counter combinations 1—4—1, 1—5—1,....,1—10—1, associated with scattering through very large angle ϑ, correspond to trajectories that when traced back fall outside the area of the target and are consequently disregarded in plotting the experimental line.

Scattering of electrons in the counters of array II leads to flashing of the following combinations (Fig.14,b): 1—1—2, 1—1—3,....,1—1—10 and 1—2—2, 1—2—3,....,1—2—10. An appreciable number of such combinations is recorded in practice (Fig.16). The greater the scattering angle ϑ, the higher the number of the discharging counter in array III. The tabular value of the Compton angle φ for the given combination increases rapidly with in-

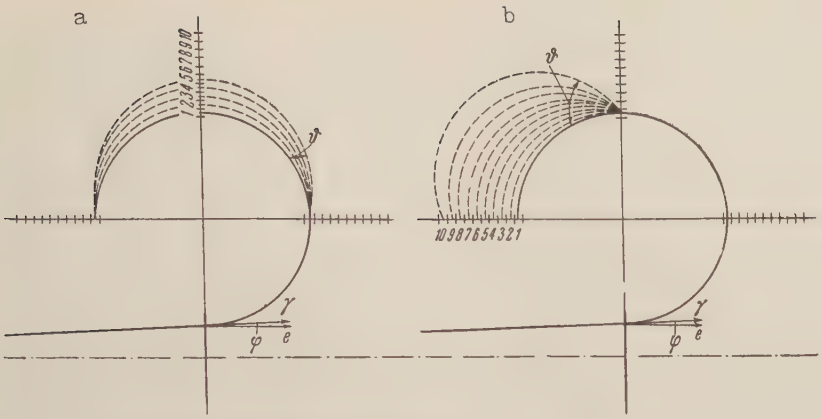

Fig.14. Electron scattering: a) in counter array I and b) in counter array II.

creasing number of the triggered counter of array III. Hence as curve b in Fig.15 shows, the value of E_γ is strongly dependent on the activated counter number in array III. It is noteworthy that combinations corresponding to the same E values but smaller Compton angles φ are not observed (except in the 3.6-4.0 Mev region, where there is a 3.85 Mev γ-ray). It will be clear from the above that in the case of our example the broadening of the line near its base occurs due to electron scattering in the target, in the gas and in the counters. The high energy tail is formed primarily due to scattering in the counters of array II. If in plotting the line we restrict ourselves to trajectories with angles $\varphi \leqslant 6^\circ$, thereby excluding all frames corresponding to

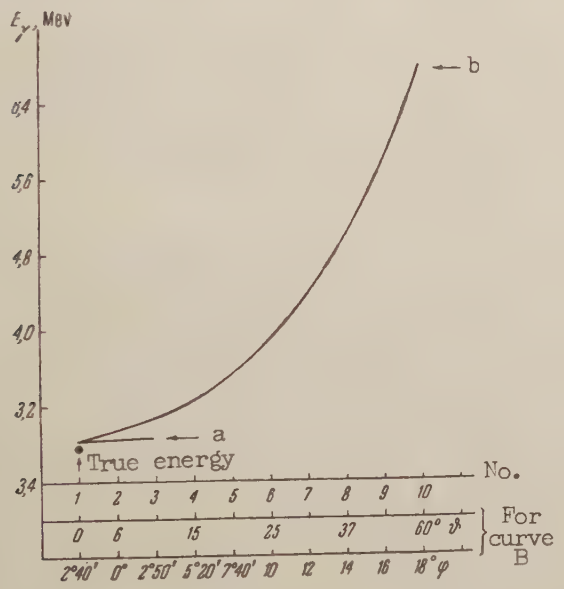

Fig.15

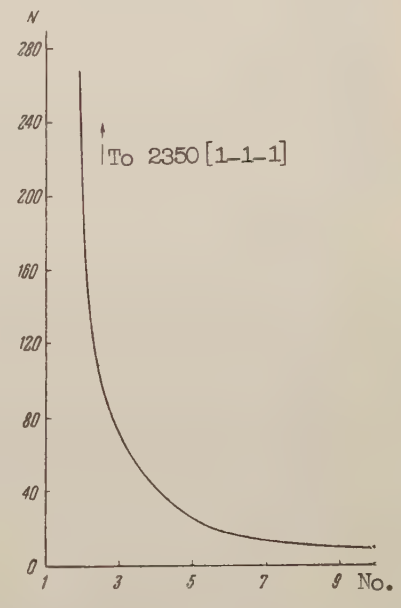

Fig.16

Fig.15. Dependence of E_γ on the counter number: a) on the number of the counter in array II when the electron passes through the first counter of array I and the first counter of array III (combination of the 1—n—1 type) and b) on the counter of array III when the electron passes through the first counter of array I and the first counter of array II (combination of the 1—1—n type). ϑ - scattering angle, hν = 2.75 Mev, H = 1220 oersted; E_γ, φ and ϑ calculated for central trajectories.

Fig.16. Dependence of the number of frames N on the number of the counter triggered in array III (combinations of the 1—1—n type); H = 1220 oersted, hν = = 2.75 Mev (Na^{24} γ-line).

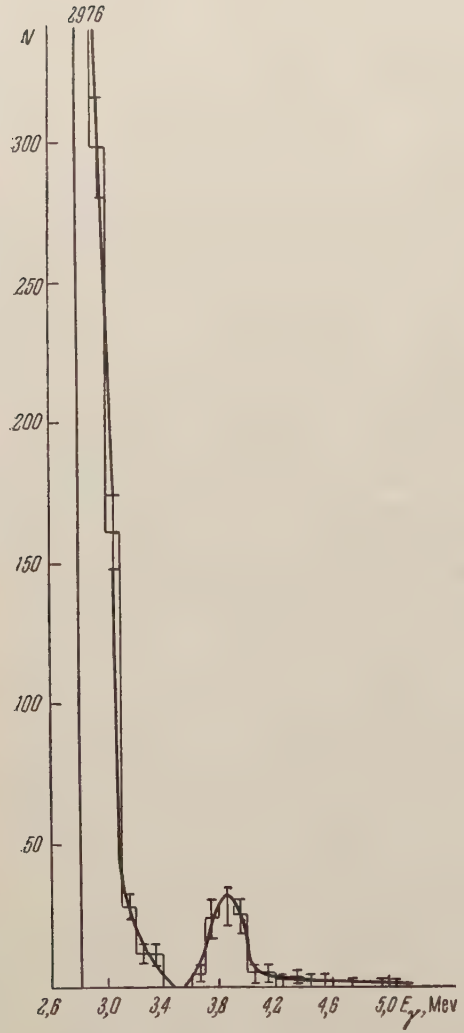

Fig.17. Experimental γ-spectrum of Na^{24} with H = 1220 oersted after subtraction of the background and exclusion of frames with $\varphi > 6^o$.

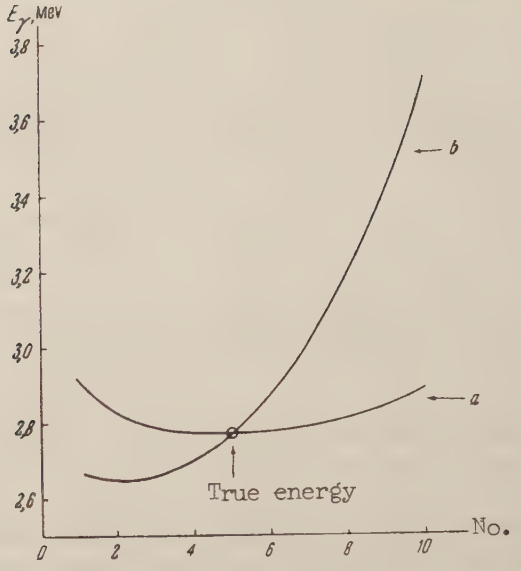

Fig.18. Dependence of E_γ on the counter number: a) on the counter in array II when the electron passes through the fifth counter of array I and the fifth counter of array III (combinations of the 5—n—5 type) and b) on the counter in array III when the electron passes through the fifth counters of arrays I and II (combinations of the 5—5—n type). 2.75 Mev Na^{24} γ-rays, H = 917 oersted.

larger scattering angles ϑ, the tail at the base of the line is almost entirely eliminated (Fig.17).

This observation applies to other measurement conditions as well, i.e., for other values of H/H_o. Fig.18 shows the variation of E_γ with the counter number in arrays II and III in the case of measurement of the 2.75 Mev Na^{24} γ-rays at H = 9.7 oersted ($H/H_o = 1$). It must be noted, however, that with decreasing H/H_o the contribution of multiple scattering in the target to tail formation increases.

Let us now see what role the background plays in measurements with the gamma-hodoscope. The background counting rate N_b when the target is withdrawn from the γ-ray beam, the ratio of the background rate to the rate with the target in place N_b/N_t and the shape of the background spectrum depend on H and on the composition of the γ-radiation emitted by the source. N_b will obviously be the greater, the higher the activity of the source. Curve 2 in Fig.7 shows that the highest value of N_b is attained in weak fields when the counting rate N_t with the target in the beam is low. In the specific case of Na^{24} the increase in N_t in fields $H < 640$ oersted is due to the soft 1.37 Mev γ-line of Na^{24}, while at the same time the background from this line is negligible. After passing through a maximum at field value slightly above

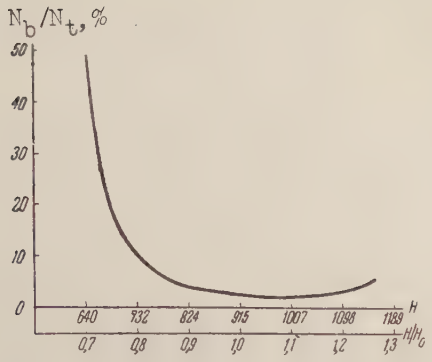

Fig.19. Variation of the relative background N_b/N_t with H and H/H_0 for $h\nu$ = = 2.75 Mev (Na^{24}). N_b - - number of triple coincidences per unit time with the target out of the beam; N_t - number of triple coincidences with the γ-rays from Na^{24} incident on the target. The curve should be shifted half a division to the right along the horizontal axis.

640 oersted, N_b monotonically decreases with increasing H/H_0 and tends to a constant value of 1 count per 6-7 hours. The counting rate N_t with the target in place with $H/H_0 > 1.35$ also tends to the same limit. The curve of Fig.19 shows how the relative background N_b/N_t varies with H and H/H_0. It will be seen that the background amounts to a small fraction of the total effect with $H/H_0 > 0.9$. With $H/H_0 < 0.9$, N_b/N_t increases rapidly owing both to decrease of N_t and increase of N_b. Finally at high values of H/H_0 the growth of N_b/N_t occurs primarily due to the rapid increase in N_t.

Essentially the background spectrum "repeats" the shape of the γ-spectrum. The peak of the background line with $H/H_0 < 1$ is shifted to the low energy side.

The ratio N_b/N_t is only weakly dependent on the gas pressure in the instrument. When the pressure of the gas mixture was reduced by half, N_b/N_t decreased by only 13% for the 1.12 Mev γ-rays of Zn^{65} and remained virtually unchanged for the 2.62 Mev radiation from ThC" ($H/H_0 = 1$). Apparently, the principal source where the background is concerned is not the gas but the walls and other components of the instrument directly irradiated by the γ-ray beam (primarily the edges of the entry window and the chamber wall directly opposite it.

4. Spectral Response of the Gamma-Hodoscope

For the purpose of determining the relative intensity of γ-transitions from the areas under the experimental line contours one must obviously know the spectral sensitivity of the hodoscope, i.e., the energy dependence of the relative probability of recording γ-rays. A characteristic of the gamma-hodoscope distinguishing it from other spectrometers is that its spectral response cannot be characterized by a single curve (as can, for example, be done in the case of the Ritron*). One must have a whole set of curves each characterizing the spectral sensitivity of the gamma-hodoscope at a given magnetic field value.

For direct experimental determinations of the spectral sensitivity curve it would be necessary to have a large assortment of different γ-sources having accurately known activities. In addition, inasmuch as resolution of the hodoscope is not large, it would be necessary to have sources having single lines or at least lines separated at least 0.4-0.5 Mev from the nearest neighbors. The number of suitable γ-sources is so small that use of the experimental procedure for determining the spectral sensitivity curve of the gamma-hodoscope is virtually precluded. Thus the only course left was to calculate the spectral sensitivity curve for a number of values of H and then to check them at individual points experimentally.

---

*See Bulletin, 18, No.5, 285 for a description of the Ritron. Trans. editor.

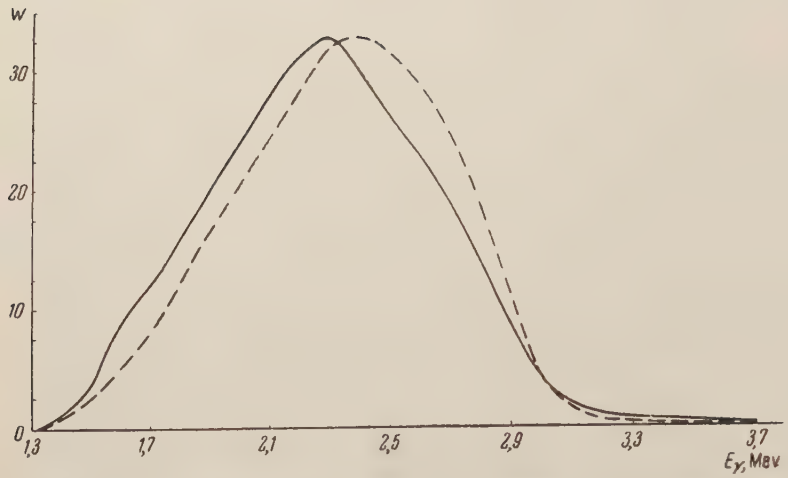

Fig.20. Spectral sensitivity curves of the gamma-hodoscope for H = 740 oersted (cylindrical counters). W - probability of recording γ-rays of the given energy in relative units. Solid line - curve from precise calculations; dash line - from rough calculations.

The solid line in Fig.20 shows the spectral sensitivity curve of the gamma-hodoscope for H = 740 oersted calculated for a point source (L = = 654 mm, effective area of the target spot S = = 80 x 35 mm, slit width 80 mm, cylindrical counters) taking into account the Compton recoil distribution in angles and energies. Scattering and stopping of the recoil electrons in the target and gas were neglected. The precise method of calculation was developed by the writer and the spectral sensitivity curve for H = 740 oersted was computed by G.F.Dranitsyna. Calculation of such a curve for even one field value is extremely laborious. Hence calculations for the requisite large number of H values would have required an excessive amount of time. Consequently, for practical purposes it was decided to use a rough method of calculation of the sensitivity curve using the following simplifying assumptions:

1. The recoil electron source is assumed to be only the center line of the target (the line of intersection of the target with the plane perpendicular to H and passing through the geometric center of the instrument).

2. Electron beam is assumed to be a plane beam.

3. The acceptance angles of all counter combinations are assumed to be identical.

4. As in the precise calculations the influence of scattering and stopping of the electrons in the target gas and counter are neglected.

The spectral sensitivity curve calculated on the basis of these assumptions for H = 740 oersted (cylindrical counters) is shown in Fig.20 by the dash line. It will be seen that the "rough" curve is basically similar to the "precise" curve. As might have been expected, primarily due to assumption 3 above, the probability of recording for low E_γ (i.e., small ρ) is somewhat lower and for large E_γ (i.e., large ρ) is somewhat higher than indicated by the "precise" curve. At very high energies ($E_\gamma > 3$ Mev) the precise values lie somewhat higher than those given by the rough curve. In this E_γ region there operate counter combinations recording electrons ejected at very large angles φ ($>16^\circ$). The Compton scattering cross section at large φ changes slowly, consequently the relative contribution from recoil electrons ejected at an angle to the central plane increases.

As noted above (assumption 2) in the rough calculation the spatial distribution of electrons is not taken into account. This part of the spectral sensitivity curve has no practical significance inasmuch as plotting the experimental γ-spectrum the counter combinations with large φ are discarded. The greatest difference between the "precise" and "rough" curves is 45% and occurs at E_γ = 1.6 Mev.

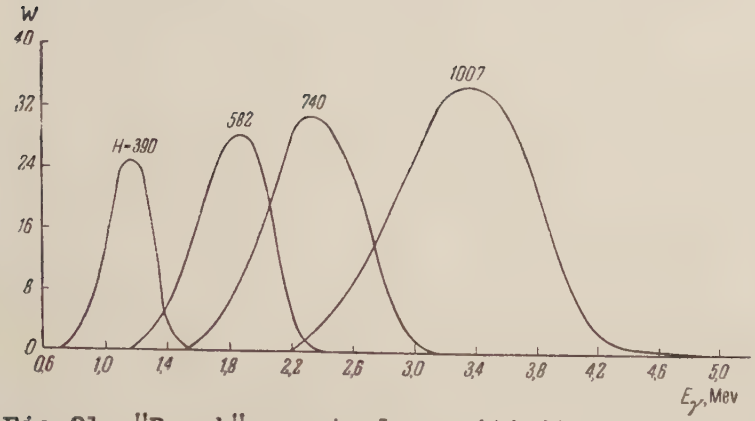

Fig.21. "Rough" spectral sensitivity curves of the gamma-hodoscope (rectangular counters).

A number of spectral sensitivity curves for the rectangular counter version of the hodoscope calculated by the rough method for a series of H values are shown in Fig.21.

The relative intensity of a γ-line is determined in the following manner. Let us assume that two γ-lines from the same source have been measured with the gamma-hodoscope: a line of energy $E_{\gamma 1}$ at H_1 and a line of energy $E_{\gamma 2}$ at H_2. During equal measurement periods there have been obtained N_1 frames for $E_{\gamma 1}$ (after subtraction of the background) and N_2 frames for $E_{\gamma 2}$. From the spectral sensitivity curves for fields H_1 and H_2, we find the probability of recording the $E_{\gamma 1}$ and $E_{\gamma 2}$ lines, namely, W_1 and W_2. Then the ratio of intensities I_1/I_2 is obviously given by the formula

$$\frac{I_1}{I_2} = \frac{N_1}{N_2} \cdot \frac{W_2}{W_1} \qquad (7)$$

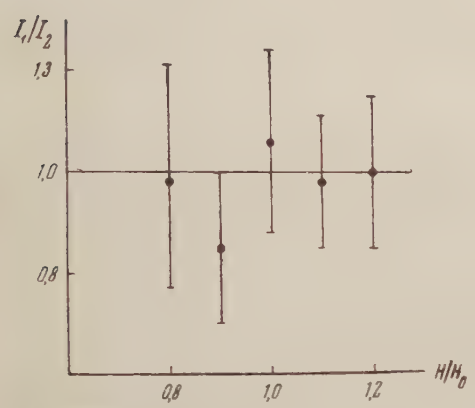

Fig.22. Relative intensity of the 1.37 Mev and 2.75 Mev γ-lines of Na^{24}. The straight horizontal line at $I_1/I_2 = 1$ indicates the true intensity ratio. The points were obtained from the experimental data using the spectral sensitivity curves calculated for the corresponding H values. I_1 is the intensity of the 1.37 Mev line and I_2 is the intensity of the 2.75 Mev line.

When the difference between the line energies is appreciable, one must take into account the difference in absorption of the γ-rays in the source itself and in the entrance window of the instrument.

The results obtained in calculating the relative intensities of the 1.37 Mev and 2.75 Mev γ-lines of Na^{24} on the basis of measurements at different values of H are shown in Fig.22. Curve 3 in Fig.7 gives the variation of the counting rate with H for the 2.75 Mev γ-rays of Na^{24}. The open circle points in Fig.7 indicate the corresponding probability of recording the 2.75 Mev γ-rays as determined from the spectral sensitivity curves. It will be seen from Figs.22 and 7 that relative intensities can be determined with an accuracy of the order of 10-30% by means of the spectral sensitivity curves.

5. Conclusions

Extensive work with the gamma-hodoscope has shown that this instrument is fully suitable for investigation of very low intensity hard γ-radiations. The γ-spectra of the radioactive isotopes Na^{24}, K^{42}, As 76, Ag^{110}, Sb^{124} and Cs^{134} have already been investigated on the gamma-hodoscope.

The efficiency of the instrument depends on the γ-ray energy, on the field H used, (i.e., on H/H_o) and on the form and size of the source. We define the efficiency of the instrument as the ratio of the number of triple coincidences (i.e., number of frames) obtained per second after subtraction of the background to the number of γ-rays of the given energy emitted by the source per second. Some data on the efficiency of the gamma-hodoscope with $H/H_o = 1$ are listed in the accompanying table. The corresponding values for the Ritron[4] are also shown for purposes of comparison. No special measurements of the activity of the sources were made.

Material	Energy, Mev	Gamma-hodoscope		Ritron		Remarks
		Dimensions of source, cm	Efficiency, number of coincidences per photon	Dimensions of source, cm	Efficiency, number of coincidences per photon	
Na^{24}	1.37	dia = 1.4 l = 15	$1.6 \cdot 10^{-9}$	dia = 1.4 l = 8	$0.9 \cdot 10^{-10}$	Standard conditions 1951
Na^{24}	2.75		$3.2 \cdot 10^{-9}$		$1.8 \cdot 10^{-10}$	

It will be seen from the table that the efficiency of the gamma-hodoscope is not high although it is superior to that of the Ritron. The possibility of using the gamma-hodoscope to investigate γ-radiation of very low intensity (10^{-5} to 10^{-6} quanta per decay) is due primarily to the following distinctive features of the instrument.

1. The energy of the corresponding γ-ray is determined from each triple coincidence, i.e., from each recorded Compton recoil.

2. The procedure of recording triple coincidences between widely separated and well shielded arrays of counters reduces the background from cosmic rays and spurious radioactivity to 1 count (frame) per 6-7 hours. This makes it possible to detect very weak effects at a counting rate equal to one coincidence every 2-3 hours.

3. In view of the fact that the γ-ray source is located outside the instrument, one can use samples having a very high total activity without fear of overloading the counters.

Thus with a source having an activity of 1000 millicurie one can investigate 2-4 Mev γ-radiations having intensity of the order of 10^{-6} γ-rays per decay.

The effective transmission (efficiency) of the gamma-hodoscope could be increased by using a thicker cellophane or beryllium target. As experience with the Ritron shows, however, the use of a beryllium target having a thickness of 400 μ reduces the resolution by an appreciable factor (in the case of the Ritron up to 13-14% at ~2.5 Mev). Hence where measurements such as those cited above are concerned this procedure for enhancing the efficiency of the instrument is expedient only for the hard γ-radiation of Na^{24}; in all the other cases (K^{42}, As^{76}, Ag^{110}, Sb^{124} and Cs^{134}) the weak γ-lines of interest are located close to far more intense softer lines.

To improve the resolution of the instrument without sacrifice of efficiency one could 1) obtain a higher degree of precision as regards the electron trajectories by reducing the size of the counters and increasing the number of counters in each array or 2) reduce the electron scattering in the instrument (gas, counter walls and target). In practice, however, not much improvement can be attained by the first measure inasmuch as 1) reducing the size of

the counters is necessarily accompanied by a decrease of their efficiency and 2) increasing the number of counters in each array will result in increased scattering in the counter walls.

Electron scattering in the instrument could be reduced by vacuum separation of the counters from the instrument chamber, i.e., by using thin windows on the counters and evacuating the instrument. Although this procedure is promising in theory[5], in the case of the gamma-hodoscope it is fraught with substantial technical difficulties.

With further technical improvement of the instrument, including the recording equipment, and more accurate determination of the spectral sensitivity, it should be feasible to use the gamma-hodoscope for a solution of a number of specific problems in the field of γ-spectroscopy.

I desire to express my gratitude to B.S.Dzhelepov for his general guidance and inspiration and to P.A.Tishkin for supervising the installation of the electronic equipment. In the course of designing the instrument I received much valuable advice from V.S.Sadkovskii, G.S.Kvater, G.S.Rusinov, A.V.Zolotavin and A.A.Bashilov, L.V.Gustov, Iu.N.Podkopaev, Iu.A.Lakomkin, G.F.Dranitsyna, P.F.Ermolov, V.I.Skopina and others participated in various stages of the work. I take this opportunity to express my heart-felt thanks to all of them.

References

1. B.S.Dzhelepov, Present issue of the Bulletin, p. 1569.

2. A.Alikhanian, A.Alikhanov, V.Morozov, G.Muskhelishvili & A.Khrimian, Zhur.eksp.i teor.fiz., 18, 673 (1948).

3. B.S.Dzhelepov, Izv.AN SSSR, Ser.fiz., 18, 95 (1954).

4. B.S.Dzhelepov, N.N.Zhukovskii & Iu.V.Khol'nov, Izv.AN SSSR, Ser.fiz., 18, 599 (1954). (Trans.Bulletin 18, No.5, 285).

5. I.B.Golovanov, B.S.Dzhelepov, A.S.Lebedev, V.P.Prikhodtseva & Iu.V.Khol'nov, Report at the Seventh Conference on Nuclear Spectroscopy, 1957.

INVESTIGATION OF THE DECAY OF Ce^{144} BY THE β-γ COINCIDENCE METHOD

- V.P.Parfenova, N.V.Forafontov & V.S.Shpinel'

Introduction

A number of authors have investigated the decay of Ce^{144} produced in fission of uranium.[1-5] The published data, however, disagree on many points and the decay scheme for $Ce^{144} \rightarrow Pr^{144}$ has not been definitively established. Certain difficulties are encountered in investigating the decay of Ce^{144}; these difficulties stem from the fact that the β and γ-transitions are close in energy and lie in the soft region so that resolution of the β-spectrum, as well as of the γ-lines, is not an easy task.

The latest published data on the β- and γ-ray energies are summarized in Tables 1 and 2; the data from coincidence experiments are listed in Tables 3 and 4.

Table 1

β-transition energies and intensities

Component	E_β, kev					I, %
	[1]	[2]	[4]	[5]	Our data	
β_1	—	100?	100?	—	130±10	7±2
β_2	170	170	160	175	175±5	26±4
β_3	—	223?	258	—	230±15	6±1
β_4	304	304	327	309	310±5	61±9

Table 2

γ-ray energies in kev

From conversion electron spectrum					Scintillation spectrometer
[1]	[2]	[4]	[5]	Our data	
29,2 Auger	29,2 Auger	28,5 Auger	— Auger	29,2 Auger	—
33,7	34	33,4	33,8	33,7	—
34 Auger	34,2 Auger	— Auger	— Auger	— Auger	36
—	41	40,8	42	41,0	—
53,5	53	53,2	53,9	53,0	—
—	—	59	—		
80,7	81	79,9	81	81,0	80
—	94	95	—	94,7	95—100
100,3	100	—	100,3	100,6	
134,2	134	133,5	134,5	134,1	134
—	—	145	—	—	

Table 3

γ-γ coincidence data

Energies of coinciding quanta, kev	
[3]	[5]
80—33; 40; 145 134—33; 40	80 X-rays 134 — no coincidences

As may be seen from Table 1, at present two β-transitions of energies ~310 and 170 kev may be regarded as firmly established. A β-spectrum of 220-250 kev energy was observed by Emmerich, Auth & Kurbatov[2] and Cork, Brice & Schmid[4], but was not detected by Pullman & Axel[5]. The 100 kev β-spectrum has not been reliably observed by anyone, but all the above listed authors infer the possibility of its existence.

In the present work we used the β-γ coincidence technique to detect the low intensity β-transitions.

Table 4

γ-β coincidence data

E_γ, kev	$E_{\beta\,max}$, kev	E_γ, kev	$E_{\beta\,max}$, kev
[5]		Our data	
		30—40	130 175 230
80	175	75—85	130 175 230
134	175	130—140	130 175

With this technique partial β-spectra should be evinced more clearly inasmuch as the β-particles of the Ce^{144} transition to the ground state of Pr^{144} and the β-transitions in Pr^{144}, which usually hamper deciphering of the primary β-spectrum, are not recorded in such measurements.

Experimental equipment

The β-γ coincidence measurements were made on a set-up consisting of a two-lens β-spectrometer and a scintillation γ-spectrometer, as described in Refs.6 & 7. The following modifications were made in the earlier described set-up.

1. In order to increase the solid acceptance angle of the β-spectrometer the internal coils which seriously limited the beam were removed and an annular slit was installed in the region of the ring image, as described in Ref.8. This increased the transmission of the instrument to 2% (line half-width = 3.3%).

2. The original plexiglass light pipe was replaced by a polystyrene one which made it possible to record electrons of >70 kev energy without loss.

In the γ-spectrometer employed in the set-up (FEU-29 photomultiplier and NaI crystals) the half-width of the Cs^{137} line photopeak was 12%.

The resolving time of the coincidence circuit was $3\cdot10^{-8}$ sec.

The Ce^{144} source was prepared by evaporation of a solution of $CeCl_3$ (stored for a period of 2 years) on a 6 mg/cm^2 mica support mounted on the bottom of an aluminum cup. The superficial density of the source was 30 μg/cm^2.

Measurements

A. β-spectrum and conversion electron spectrum

The β-spectrum and conversion electron spectrum of Ce^{144} + Pr^{144} were recorded by means of a two-lens β-spectrometer.* In the rectified (Kurie) plot obtained after subtraction of the hard β-spectra of Pr^{144} one can readily discern the 310±5 kev β-transition which, according to our data, accounts for 61% of the total number of β-transitions in Ce^{144}. Determination of the end-point energies of the other β-spectra from the rectified plot is hindered by the presence of a large number of conversion lines in this part of the spectrum. Hence the energies of the other β-spectra can be reliably established only from the coincidence data. The γ-line energies inferred from the conversion electrons are listed in the last column of Table 2. The conversion electron spectrum was recorded on another β-spectrometer of analogous design[8] which yielded a relative line half-width of 1%. All the known γ-transitions except the 145 kev transition, which has so far been observed only in one investigation[4], were evinced in the conversion electron spectrum. The intensities of the β-transitions were evaluated from the Kurie plot of the β-spectrum of Ce^{144}—Pr^{144}. In resolving the partial β-spectra, the end-point energies of the β-spectra

---

*The primary spectrum of $Ce^{144}\rightarrow Pr^{144}$ is shown in Ref.9 (the next article in the present issue of the Bulletin).

were taken from the results of the β-γ coincidence measurements. This method of determining intensities is, of course, not accurate.

B. Scintillation spectrometer measurements

The γ-spectrum of Ce^{144} is shown in Fig.1. The peaks at 36, 80 and 134 kev are clearly discernible.

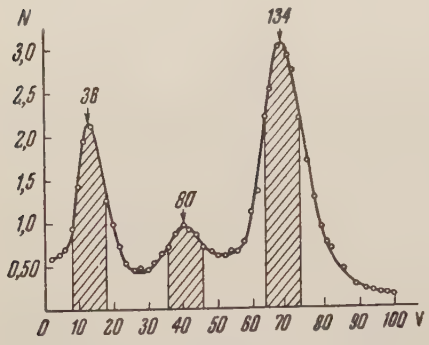

Fig.1. γ-spectrum of Ce^{144} obtained by means of the scintillation spectrometer. Hatching indicates the areas discriminated by the pulse height analyzer in investigating β-γ coincidences.

The first peak comprises x-radiation from Pr^{144} of 36 kev energy as well as 34 and 41 kev γ-rays. The resolution of the scintillation spectrometer is insufficient to resolve these γ-rays or the γ-radiation in the 95-100 kev region.

The relative intensities of the γ-rays were determined from the photopeak areas. For the ratio of the intensity of the 134 kev γ-rays to the 80 kev γ-rays we obtained a value of 4.3 ± ± 0.5 and for the ratio of the 134 kev γ-rays to the 95-100 kev γ-rays we obtained 7.1 ± 1. In calculating these values appropriate corrections were made for absorption in the aluminum plate mounted in the γ-ray beam for absorption of fast electrons from the source and for the yield of x-radiation of iodine from the NaI crystal.[10]

C. β-γ coincidences

To obtain the partial β-spectra the pulse height analyzer gate was set to discriminate the appropriate γ-ray energy interval and then the spectrum of the β-particles yielding coincidences with given γ-rays were studied. Thus we investigated the β-coincidences with γ-rays in the 30-40, 75-85 and 130-140 kev energy regions. The position of the analyzer gate in each case is shown by hatching in Fig.1

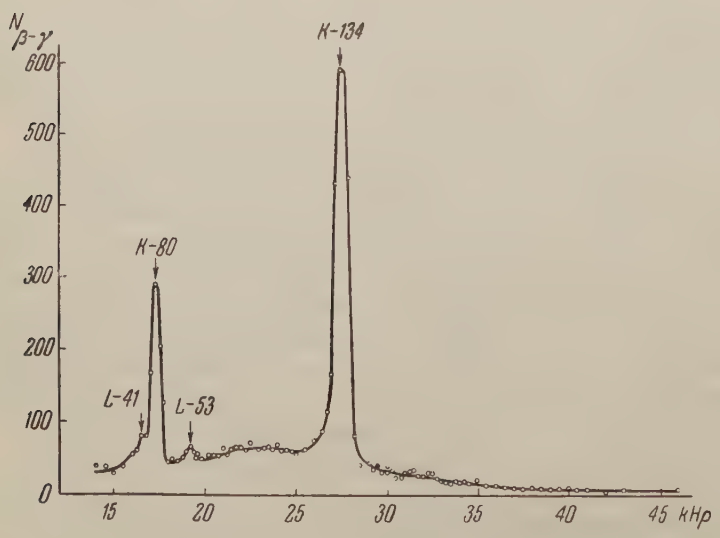

Fig.2. Spectrum of β-particles coinciding with x- and soft γ-rays.

Inasmuch as the γ-radiation of interest is soft, the absorption of the γ-rays in the NaI crystal is due primarily to the photoeffect. The Compton effect, leading to a continuous light pulse distribution in the crystal, amounts to less than 15% of the total effect at 134 kev. This circumstance makes it possible to disregard the contribution from high-energy γ-rays in the region of softer γ-lines (the magnitude of this contribution from the 134 kev line in the region of the 80 and 36 kev lines as gated by the analyzer does not exceed 2-3%; the contribution of the 80 kev γ-rays to the 36 kev peak is even smaller).

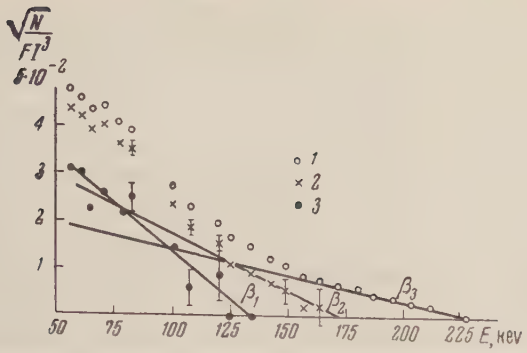

Fig.3. Kurie plot of β-ray spectrum coinciding with the x- and soft γ-rays (36 kev peak in Fig.1) and resulting resolution into partial β-spectra: 1) total β-spectrum ($E_{\beta\ max}$ = 230 kev, 2) result of first subtraction ($E_{\beta\ max}$ = 175 Kev), 3) result of second subtraction ($E_{\beta\ max}$ = 130 kev).

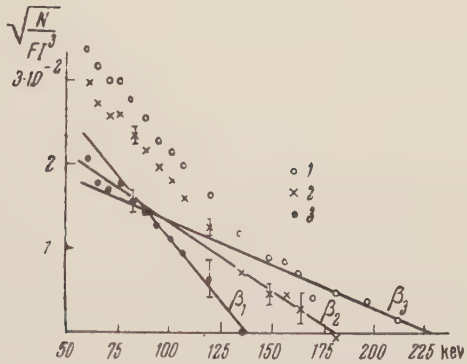

Fig.4. Kurie plot of β-spectrum in coincidence with the 80 kev γ-radiation and results of resolution into partial β-spectra. Line designation same as in Fig.3.

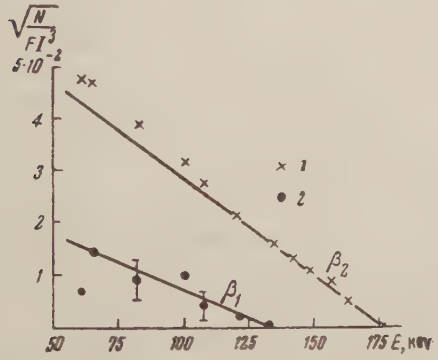

Fig.5. Kurie plot of spectrum of β-particles coinciding with the 130 kev γ-radiation: 1) total β-spectrum ($E_{\beta\ max}$ = 175 kev), 2) result of subtraction of the β-spectrum with 175 kev end-point energy ($E_{\beta\ max}$ = 130 kev.

We carried out three series of coincidence measurements. The results obtained in one series are shown in the accompanying figures. The spectrum of β-coincidences in the region of x- and soft γ-radiation is given in Fig.2. There are evident in the figure K conversion peaks corresponding to the 80 and 134 kev γ-rays as well as lower L conversion peaks associated with the 41 and 53 kev radiations. The rectified β-γ coincidence plots are shown in Figs.3, 4 & 5 together with the results of resolution into the partial β-spectrum.

It will be seen from Figs.3 & 4 that the β-particle spectra yielding coincidences with the x- and γ-radiation in the 36 kev region and with the 80 kev γ-rays are comprised of three partial β-spectra: β_1, β_2 and β_3. It will be evident from Fig.5 that the 134 kev γ-rays coincide with a β-particle spectrum consisting of two components: β_1 and β_2.

The determined end-point energies ($E_{\beta\ max}$) and the relative areas under the β-spectra coinciding with the γ-rays of different energies are listed in Table 5, wherein the values are the averages for the three series of measurements.

The uncertainty in determining the relative areas under the partial β-spectra is 15-20%.

Our β-γ coincidence data are juxtaposed with the corresponding data in the literature in Table 4.

Discussion

The results of our study show that the β-spectra yielding coincidences with three different sections of the γ-spectrum are complicated. These spectra do not include the β_4 component (Table 1) of ~310 kev energy which may therefore be assumed to be due to a transition to the ground state of Pr^{144} (no isomeric levels were detected).

Table 5

	$E_{\beta\ max}$, kev	Relative areas under β-spectra coinciding with the γ-rays, %		
		E_γ = 36 kev	E_γ = 80 kev	E_γ = 134 kev
β_1	130±10	53	28	10
β_2	175± 5	33	45	90
β_3	230±15	14	27	—

From the observed β-γ cascades it may be concluded that the β_3 ($E_{\beta\ max}$ = 230 kev) and β_2 ($E_{\beta\ max}$ = 175 kev) transitions feed the Pr^{144} levels at 80 and 134 kev, respectively. The existence of the β_1 component ($E_{\beta\ max}$ = 130 kev) was established from the break in the curve appearing in all the Kurie plots (Figs.3,4 & 5). In cases of soft, low intensity spectra such as the present, there can always be some doubt regarding the actual existence of certain components. Thus the deviation of the experimental points from the straight line in Fig.5 could be due to apparatus distortion of the β_2 spectrum. If this were the case, a like deviation should be observed in the other plots. Actually the deviation of the experimental points from the straight line in the soft part of the spectrum in Figs.3 and 4 is appreciably greater than the corresponding deviation in the spectrum pictured in Fig.5 (see Table 5). Moreover, such large deviations can hardly be explained under our experimental conditions solely by the influence of scattering and absorption. In view of this it may be concluded that the 130 kev end-point energy β_1 component actually does exist.

The presence of a β-spectrum of energy less than 175 kev indicates that there exists an excited level in Pr^{144} located above the 130 kev level.*

Our results are in best agreement with the decay scheme shown in Fig.6 which is identical with that proposed by Emmerich, Auth & Kurbatov[2].

The authors desire to thank Z.I.Anan'eva for her invaluable assistance in the work.

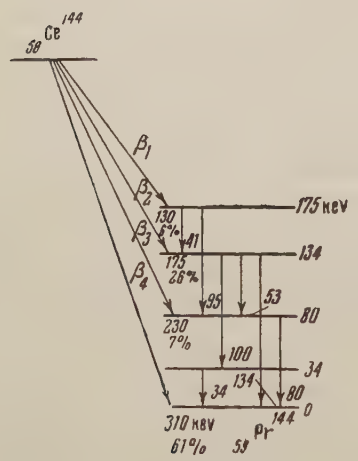

Fig.6. Decay scheme of Ce^{144}.

References

1. F.T.Porter & C.S.Cook, Phys.Rev.,87,464(1952).
2. W.S.Emmerich, W.J.Auth & J.D.Kurbatov, Phys.Rev., 94,110 (1954).
3. W.E.Kreger & C.S.Cook, Phys.Rev.,96,1276 (1954).
4. J.M.Cork, M.K.Brice & L.C.Schmid, Phys.Rev., 96,1295 (1954).
5. I.Pullman & P.Axel, Phys.Rev., 102,1366 (1956).
6. V.Shpinel', Zhur.eksp.i teor.fiz., 22, 255 (1952).
7. N.Deliagin & A.Sorokin and others, Izv.AN SSSR, Ser.fiz., 20, 913 (1956) (Trans., Bulletin, 20, No.8, 828.)
8. Ia.Gaziev, K.Mitrofanov & V.Shpinel', Izv.AN SSSR, Ser.fiz., 20, 1407 (1956). (Trans., Bulletin 20, No.12a, 1288.)
9. K.P.Mitrofanov & V.S.Shpinel', Present issue of the Bulletin, p.1595.
10. P.Axel, Rev.Sci.Instr., 25, 391 (1954).

---

*This result is in agreement with the inferences made in Refs.2 & 4 and is not consistent with the decay schemes proposed in Refs.1 & 5.

FURTHER INVESTIGATION OF ELECTRON FOCUSING IN A TWO-LENS β-SPECTROMETER

- K.P.Mitrofanov & V.S.Shpinel'

Introduction

The characteristics of two-lens β-spectrometers are strongly dependent on the shape and relative position of the magnetic lenses. In view of the difficulty of solving the theoretical equations of motions for electrons in complicated magnetic fields, the optimal operating conditions for spectrometers of this type are usually selected on the basis of experimental data. Commonly, the necessary information is obtained by photographing an electron beam or by using an electron gun and a fluorescent screen for visual observation. In the present work we used an electron gun to investigate the focusing properties of a two-lens BML-1 β-spectrometer for different positions of the lenses and studied the effect of an external correcting coil on the performance of the spectrometer.

The procedure used in the present work was employed earlier in investigating the characteristics of a spectrometer with one possible arrangement of the lenses and has been described in detail in Ref.1. Hence below we shall only outline the experimental technique and in most cases will give only the results. BML type spectrometers produced by the "Fizpribor" Plant have standard dimensions, hence the results of our investigation can be applied to any spectrometer of this series and used for adjusting the instrument and selecting the most suitable operation conditions.

1. Investigation of electron focusing

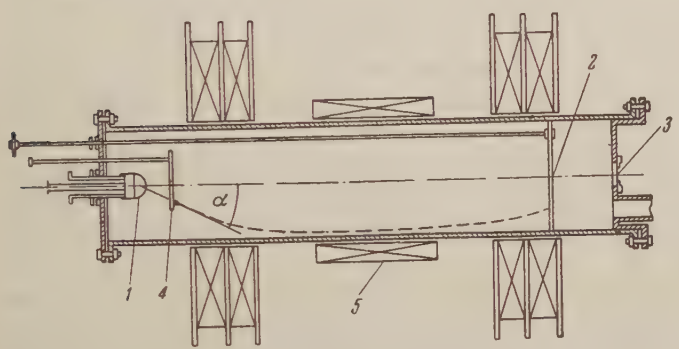

Fig.1. Diagram of experimental set-up: 1) electron gun, 2) fluorescent screen, 3) viewing window, 4) entrance aperture disc, 5) correcting coil.

The set-up for investigating the focusing of the electrons is diagramed in Fig.1. As compared with the set-up used earlier[1], the present set-up has an electron gun of improved design and a moveable entrance aperture disc 4 by means of which angle φ of divergence of the electron beam can be varied without disturbing the vacuum. By measuring the displacement of the luminous spots on the screen incident to variation of the focusing current (the current through the magnet coils) or shifting of the screen, we were able to determine the operating characteristics of the spectrometer and plot electron trajectory curves for different positions of the lenses.

The spherical aberration curves obtained with different distances (d) between the lenses are shown in Fig.2. The curves give the variation of $(I_o - I_\alpha)/I_o$ with α, where I_α is the focusing current for electrons with an angle α, and I_o with the focusing current for $\alpha \to 0$.

It will be seen that as the interlens distance is increased, the spherical aberration decreases and at $d \approx 44$ cm becomes less than the aberration of a solenoid spectrometer[2].

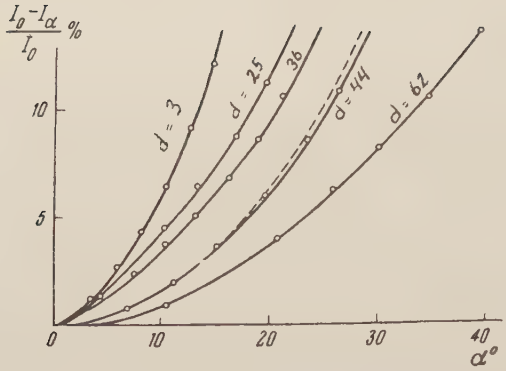

Fig.2. Curves characterizing the spherical aberration of the β-spectrometer with different positions of the lenses. The numbers at the curves indicate the distance d between the lenses at which the given measurements were made. The dash line is the spherical aberration curve for a solenoid β-spectrometer.

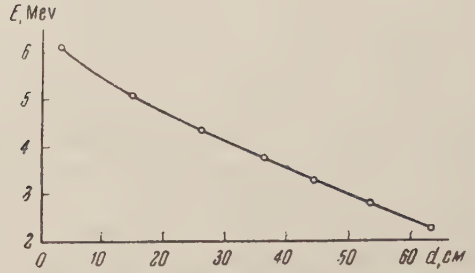

Fig.3. Functional dependence of the maximum energy of the focused electrons on the separation between the lenses.

In addition to reducing the spherical aberration, however, moving the lenses further apart also leads to a reduction of the focusing power of the spectrometer, i.e., to a reduction of the constant k in the formula $H\rho = kI$.

Fig.3 shows the variation of the maximum energy of electrons satisfactorily focused by the spectrometer at the maximum allowable current I = 50 amp through the magnet windings as a function of the interlens distance.

Improvement of the experimental technique made it possible to determine with great accuracy the variation of the electron trajectories in the spectrometer. Knowledge of the trajectories allows of selecting the range of emission angles α giving the best relationship between the transmission (acceptance angle) ω and the resolution η and of determining the optimum size and position of the spectrometer slits. The results of the investigation of the electron trajectories at different values of the interlens distance d are shown in the form of curves in Fig.4, wherein the distance R of the electron from the axis of the instrument is plotted as a function of Z the distance from the counter.

Inasmuch as the best relation between η and ω is obtained for large angles of emission α, with each new position of the lenses the entrance aperture was adjusted so that the trajectories of the electrons having a maximum angle α_{max} would pass about 1 cm from the inside wall of the chamber.

It will be seen from Fig.4 that as the lenses are moved further apart the value of α_{max} increases rapidly and the shape of the trajectories changes appreciably. The points of intersection of the electron beams forming the ring image in the case of small values of d are located close to the counter, while when the lenses are moved apart to d = 62 cm the points of intersection move back, spreading into the mid-section of the spectrometer chamber. Under given operating (field) conditions, the resolution of the spectrometer depends on the accuracy of setting the annular slit. If the annular slit is properly positioned

$$\eta = \frac{\Delta R_k}{D},$$

where ΔR_k is the width of the annular slit equal to the width of the ring image and D is the dispersion of the electron beam, equal to the magnitude of the radial displacement of the beam incident to a 1% change in the focusing current

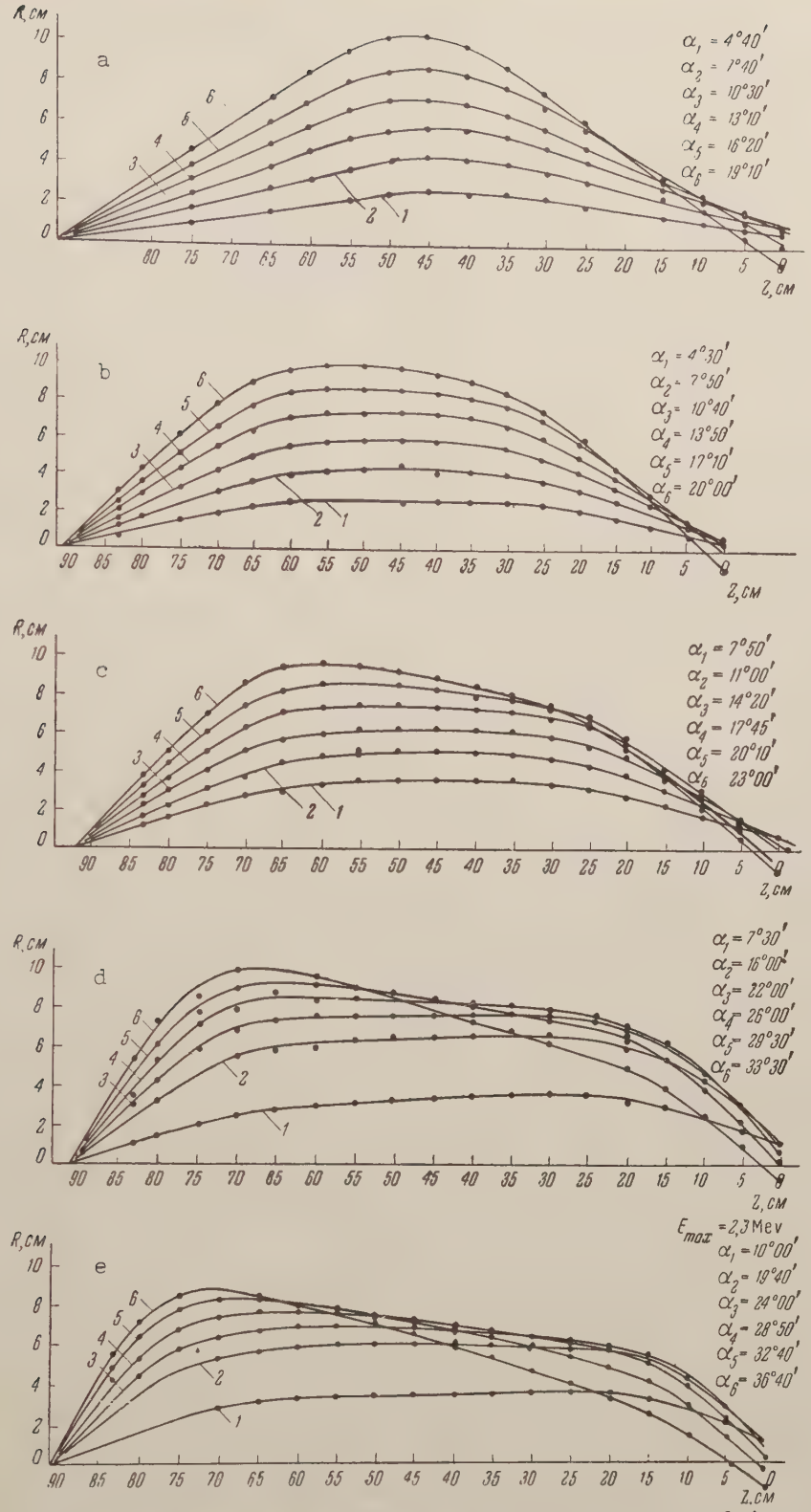

Fig.4. Electron trajectories in the two-lens β-spectrometer determined for the following interlens distances: a) 3 cm, b) 25 cm, c) 36 cm, d) 52 cm and e) 62 cm. The values of α, the angle of emission of the electrons, are shown at the right; the subscripts correspond to the numbers at the curves.

The magnitude of ΔR_k can readily be determined from the trajectory curves by measuring the width of the electron beams at the point of their greatest narrowing. Special measurements were carried out to determine the dispersion.

2. Measurement of the dispersion and determination of the resolution

For the purpose of measuring the dispersion, a narrow annular slit was cut in the entrance aperture disc (4 in Fig.1). The electron beam passing through this annulus formed a luminous ring 0.5 to 2 mm wide on the screen. Knowing the change in current ΔI producing a given change in the radius of the ring ΔR one can readily calculate the dispersion, i.e., $D = \Delta R/(\Delta I/I)$.

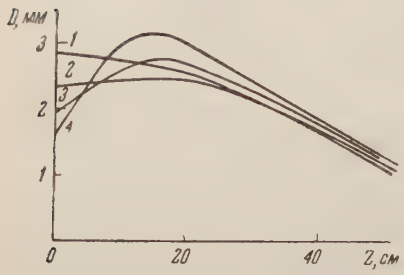

Fig.5. Dispersion of electrons having an emission angle of 20° for interlens distances of 1) 15 cm, 2) 36 cm, 3) 52 cm and 4) 62 cm.

In view of the strong dependence of the ring image position on d and α, measurements of the dispersion at different distances from the counter were carried out for several different values of d and α.

The dependence of D on Z for different interlens distances d with $\alpha = 20°$ is shown in Fig.5.

It will be seen that when the separation between the lenses is greater than 36 cm the dispersion curves exhibit a maximum some 15-20 cm from the counter.

Increasing the angle of emission α with a constant position of the lenses leads to an increase of the dispersion (Fig.6). The dependence of D on α is described with fairly good accuracy by the formula $D = C \cdot \alpha$, where C is a coefficient dependent on Z and d. The maximum value of this coefficient (C = 0.17) was obtained with d = 62 and Z = 18 cm (where α is in degrees and D in mm).

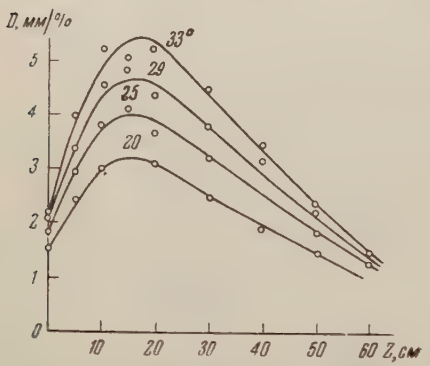

Fig.6. Dispersion in spectrometer with lenses set 62 cm apart. The figures at the curves are values of α at which the given measurements are made.

Using the trajectory and dispersion curves, one can with fair accuracy evaluate the operating characteristics of the spectrometer. The values of the various parameters corresponding to the best ratio of ω to η for some positions of the lenses are summarized in the accompanying table.

d, см	α, degree	Z, см	ΔR_k, мм	D, мм	ω, %	η, %	E_{max}, Mev
3	17—13	15	2,5	1,7	1,1	1,4	6,3
25	17—10	6	2,5	2,2	1,4	1,1	4,5
36	20—14	10	2,5	2,3	1,5	1,1	3,8
53	29—22	30	4	3,2	2,8	1,3	2,8
62	29—20	20	4	3,8	3,3	1,1	2,2
62	33—20	27	6,5	3,5	5	1,9	2,2

The listed values of η correspond to the ideal case of the point source. A source of diameter S reduces the resolution by an amount of the order of S/D %

In order to obtain good resolution, it is most desirable to use electron beams with large angles of emission, but as may be seen from the trajectory curves, with an appreciable separation between the lenses these beams form images at Z > 30 cm, where the dispersion is small. In the case of a distance of 62 cm between the lenses the maximum in the dispersion curve is most pronounced and the best relation between η and ω is obtained with an electron beam forming a ring image in the region of the maximum value of D.

We could not investigate the focusing for interlens distances d > 62 cm because our instrument had no provision for further displacement of the lenses, but it may be assumed that further increase in the separation would be accompanied by continued increase of the dispersion, particularly at values of Z corresponding to maximum D. Together with further decrease of spherical aberration and increase of the angle α_{max}, this would lead to enhanced resolution of the spectrometer.

The best relation between the transmission ω and the resolution η should be obtained when the lenses are located so that their centers coincide with the positions of the source and detector. For the BML-1 spectrometer this would obtain with d = 76 cm. In this case it would be feasible to focus electrons of up to $E_{max} \approx 1$ Mev energy.

3. Effect of an external correcting coil

The strong dependence of the electron trajectories on the configuration of the magnetic field makes it possible to improve the focusing characteristics of the spectrometer by means of relatively small correcting coils.

In principle it is possible to enhance the resolution of a spectrometer by means of coils located inside the vacuum chamber[3,4]; in practice, however, the use of such correcting coils is hampered by a number of practical difficulties connected with cooling the coils, maintaining a good vacuum in the spectrometer chamber, the necessity of using large solid angles, etc. External correcting coils are more convenient from the operational standpoint and have been successfully used in conjunction with many spectrometers[5,6].

In order to determine the effect of an external correcting coil (5 in Fig.1) on the electron focusing, we carried out measurements with a coil 25 cm in diameter and 30 cm in length consisting of 1000 turns of 2 mm conductor. The tests were carried out with the main lenses 62 cm apart.

The magnitude of the current I_{cor} through the correcting coil was measured in percent of the current I_{lens} through the main lens coils and was taken as positive when the direction of I_{cor} was the same as that of I_{lens}. It was found that the field of the correcting coil has a strong effect on the shape of the trajectories but does not noticeably alter the magnitude of the dispersion. Some of the results of the electron trajectory determinations with the correcting coil in operation are shown in Fig.7.

From a comparison of the trajectories shown in Fig.7 with the trajectories plotted in Fig.4 it will be evident that the general diffusion of the electron beam due to spherical aberration is decreased with positive values of I_{cor} and increased with negative values. At the same time with positive I_{cor} there is observed a certain decrease in the width of the ring images (ΔR_k) together with some displacement of these images towards the counter. This leads to an increase of the dispersion of electron beams with large angles of emission in the plane of the ring image.

Thus application of a correcting field makes it possible to improve the resolution of the spectrometer primarily through increase of D without sacrifice of transmission. Comparison of the values of η and ω obtained with the

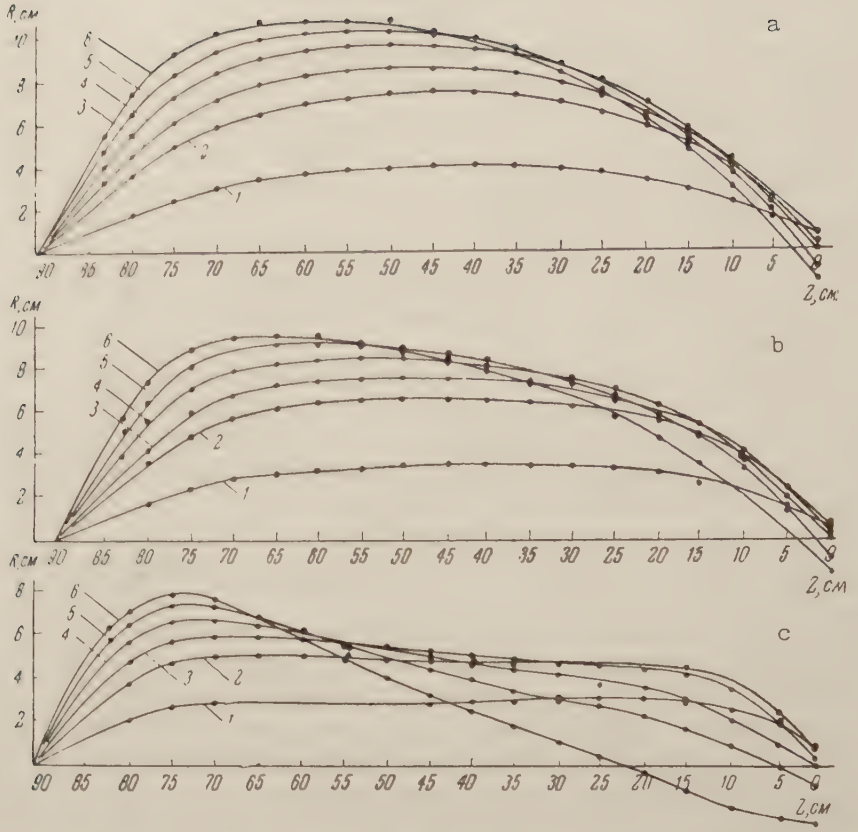

Fig.7. Electron trajectories in the spectrometer with the correcting coil in use. Distance between lenses 62 cm: $\alpha_1 = 10^\circ\ 00'$, $\alpha_2 = 19^\circ\ 40'$, $\alpha_3 = 24^\circ\ 00'$, $\alpha_4 = 28^\circ\ 50'$, $\alpha_5 = 32^\circ\ 40'$, $\alpha_6 = 36^\circ\ 40'$. Current through correcting coil: a) +6.5%, b) +3.5% and c) -6.5%.

coil with those listed in the table above shows that with I_{cor} = +3.5% the resolution was improved by 20% and with I_{cor} = +6.5% by 30%.

In the last case, however, the outer electron trajectories virtually brushed the chamber walls inasmuch as R increases with increasing I_{cor}.

4. Operating characteristics of the spectrometer

For the operation tests the lenses were set at a distance d = 62 cm; the correcting coil was connected parallel to the lens coils and the current through it I_R was set equal to +4%. A special circuit employing a Wheatstone type bridge with a sensitive microammeter as the indicator was employed to monitor and compensate changes in the resistance of the lens and correcting coils incident to heating.

On the basis of the results obtained in the above-described electron gun experiments, we prepared two sets of aperture discs passing electron beams in solid angles of 5 and 1.8% of 4π with ring images formed in the region of the maximum dispersion. To determine more accurately the proper positions of the entrance apertures, we photographed conversion electrons of the F line ThB. The annular slits, selected and positioned on the basis of the results of photographing the F line, had widths of 10 and 4 mm and were located 15 and

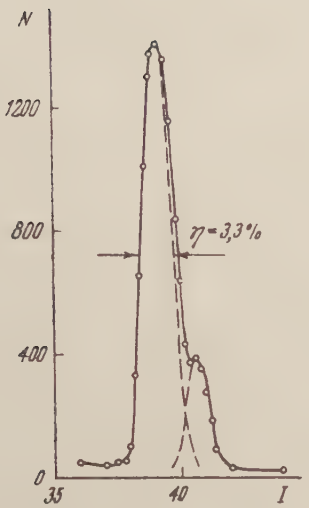

Fig.8. Conversion lines of Cs^{137}. Measurements made with a 5 mm diameter source and $\omega = 5\%$.

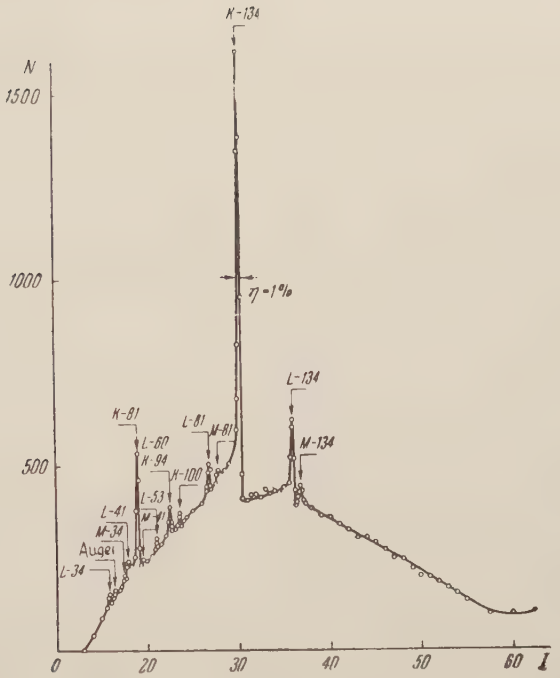

Fig.9. β-spectrum of Ce^{144}, measured with $\omega = 1.8\%$ and a 1.5 diameter source.

and 16 cm from the counter for $\omega = 5\%$ and $\omega = 1.8\%$, respectively. Measurements made under these conditions show that with $\omega = 5\%$ and a source 5 mm in diameter the effective resolution of the spectrometer was 3.3% (see Fig.8).

Measurements with $\omega = 1.8\%$ and a source 1.5 mm in diameter give a value of 1.0% for η. The β-spectrum of Ce^{144} recorded under these conditions is shown in Fig.9.

Counters with a window 20 mm in diameter were used in all the measurements.

The values of η obtained under the described conditions are in good agreement with the values of 3.0% and 1.0% obtained from the electron gun measurements.

We desire to thank A.P.Alekseev, student at the University, and N.I.Ivanova, laboratory technician, for aid in carrying out the measurements.

Scientific Research Institute of Nuclear Physics,
Moscow State University

References

1. Ia.I.Gaziev, K.P.Mitrofanov & V.S.Shpinel', Izv.AN SSSR, Ser.fiz., 20, 1407 (1956). (Trans., Bulletin 20, No.12b, 1288.)
2. G.Rundle, T.Ellis, T.Griffith & H.Tomlinson, Rev.Sci.Instr., 20,869 (1949).
3. P.Hubert, Ann.de Phys., 8, 662 (1953).
4. B.S.Dzhelepov, No Sen Chan & N.A.Tishkin, Izv.AN SSSR, Ser.fiz., 20, 947 (1956). (Trans., Bulletin 20, No.8, 857.)
5. R.Bent, W.Bonner & R.Sippel, Phys.Rev., 98, 1237 (1955).
6. R.Nichols, A.Pohm, J.Talboy & E.Jensen, Jr., Rev.Sci.Instr., 26, 580 (1955).

NEW DATA ON THE γ-SPECTRUM OF Sb^{124}

- B.S.Dzhelepov, N.N.Zhukovskii & F.A.Predovskii

With a view to refining our earlier data[1] on the relative intensities of the γ-lines of Sb^{124}, we carried out a repeat investigation of the Sb^{124} radiation on the Elotron under new, more favorable (enhanced resolution and efficiency) conditions[2]. For the purposes of the study we had available a neutron activated sample of metallic antimony weighing ~1.5 gram and having an activity of 1.5 curie. The measurements were started 40 days from the time of preparation of the sample.

We took particular pains to investigate 1) the $H\rho$ = 2500 to 3300 gauss·cm soft region of the spectrum in which the 603 and 646 kev γ-lines could not be satisfactorily resolved by the Elotron under the earlier gas-filled conditions[2] and 2) the $H\rho$ = 4800 to 6300 gauss·cm region where we detected new, hitherto unknown γ-lines whose intensity fell off with a period of 60 days.

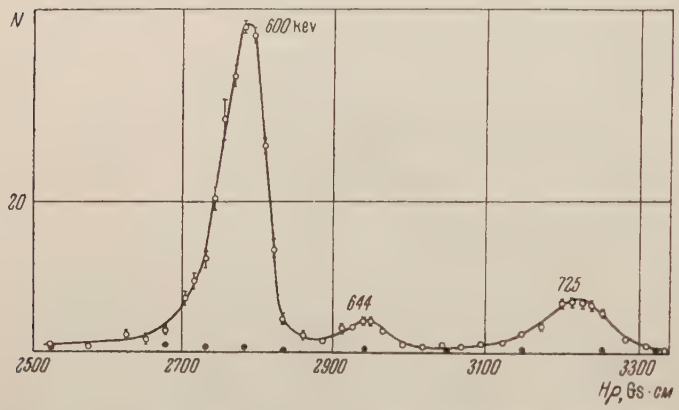

Fig.1. Experimental curve obtained for the $H\rho$ = 2500 to 3300 gauss·cm region of the Sb^{124} γ-spectrum.

We checked and revised the values of the relative intensities of all the γ-lines of Sb^{124} by means of the spectral sensitivity curve determined for the new conditions[2].

The experimental γ-spectrum in the 2500-3300 gauss·cm region is shown in Fig.1. Open circles give the number of coincidences per minute with the target in the γ-ray beam; the solid dots show the background due primarily to spurious and cosmic ray coincidences and stray electrons ejected from the instrument walls by the γ-radiation. As in the previous investigation, we observed γ-lines of 603, 646 and 723 kev energy. Here and below we give the most probable energy values based on the recorded conversion electron spectrum; our values, which agree within 0.5% with the most reliable values cited in the literature, are given in Table 1 and the figures. The ~723 kev line is 0.8% wider than the apparatus line expected in this energy region. It is, we believe, the result of superposition of γ-lines of 714 and 723 kev energy, the ratio of whose intensities according to Zolotavin, Grigor'ev & Abroian[3] is 1.0:2.7.

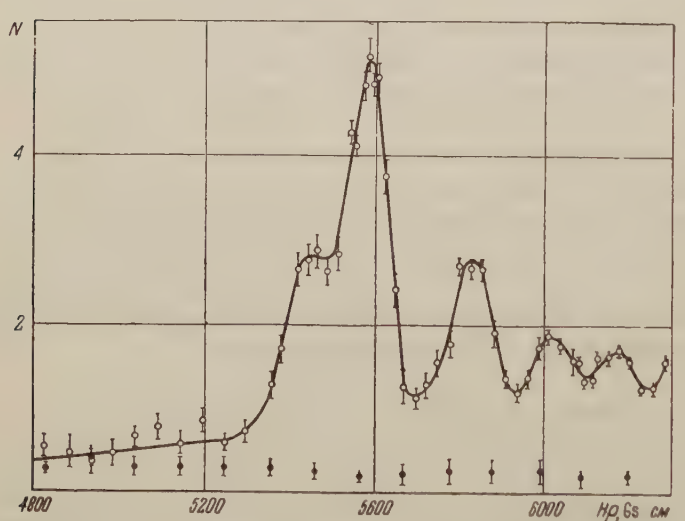

Fig.2. Experimental curve for the $H\rho$ = = 5200 to 6300 gauss·cm section of the γ-spectrum of Sb^{124}.

The $H\rho$ = 5200 to 6300 gauss·cm section of the γ-spectrum lying to the left of the low energy rise of the intense 1692 kev γ-line is shown in Fig.2.

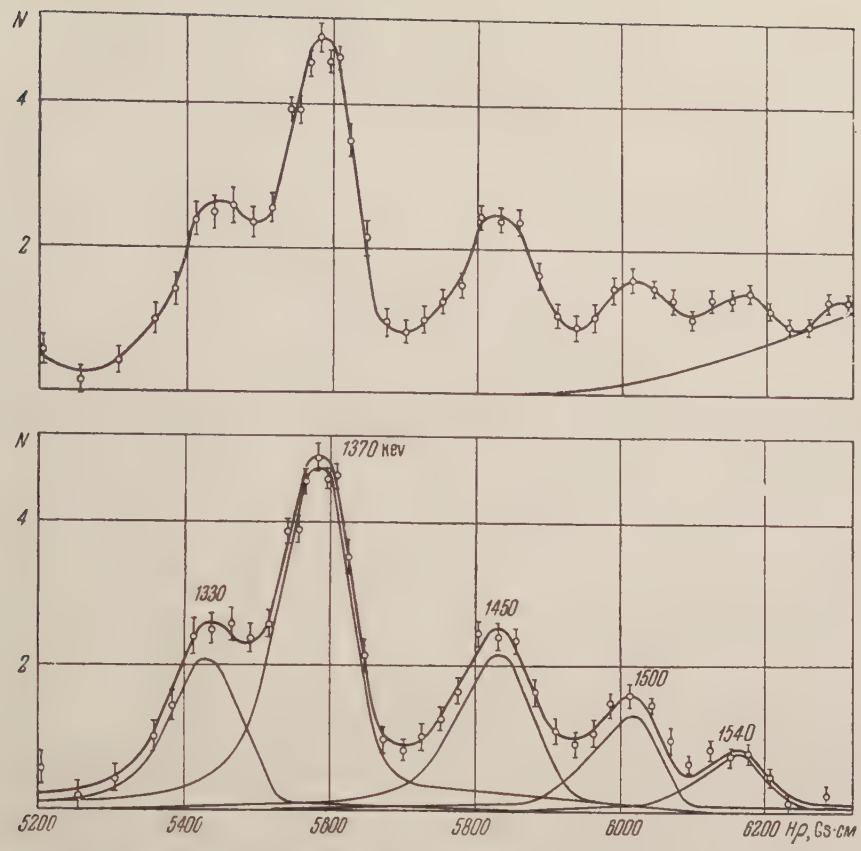

Fig.3. Resolution of the 5200 to 6300 gauss·cm section of the Sb^{124} γ-spectrum.

The resolution of this section of the spectrum into individual components is illustrated in Fig.3. The spectrum in the upper part of Fig.3 is the experimental curve with the background subtracted; the solid line at the lower right indicates the portion of the spectrum attributable to the left (low energy) rise of the 1692 kev line. The points in the lower diagram show the spectrum after subtraction of the rise associated with the 1692 kev line; here we have inscribed the individual lines corresponding to $h\nu$ = 1330, 1370, 1450, 1500 and 1540 kev. The resolution of the lines here is better than in Ref.1. It should be noted that the half-width of the 1370 kev γ-line is appreciably greater (0.3-0.4%) than the apparatus half-width for lines in this region. The observed broadening is due to the fact that this line is the result of superposition of γ-lines of 1361 and 1370 kev energy.[3] Lines at 1442 and 1525 kev were found in the previous investigation of Sb^{124} on the Elotron[1]; now the latter has been found to be a double line and the position and intensities of the lines have been refined.

A repeat measurement of this portion of the spectrum one and a half months after the first series of observations showed that the number of coincidences at the line peaks fell off in accord with the period of Sb^{124}.

In Table 1 we list the revised values of the relative intensities of the γ-lines as well as the multipole orders of some of the γ-transitions calculated on the basis of our intensity data and the data of Zolotavin, Grigor'ev & Abroian[3] on the relative intensities of the K conversion lines of Sb^{124}. The two scales of relative intensities were matched on the assumption that the 603 kev γ-line corresponding to the transition from the first excited level of Te^{124} is pure electric quadrupole radiation. The uncertainties in the relative intensities indicated in the table are made up of the uncertainty in plotting the spectral sensitivity curve ($\sim$5% - Ref.2), the statistical measurement error and the inaccuracy in resolving the spectrum into components.

Level diagram of Te^{124}

The decay scheme for $Sb^{124} \rightarrow Te^{124}$, based on all the data accumulated up to May 1956 and shown in Refs.3 & 5, is reproduced in Fig.4 with some revision

Table 1

Relative intensities and multipole orders of the γ-transitions

Adopted transition energy value, hν kev	Our data: hν, kev	Our data: relat. intens.	Rel. intens. of K conv. line (Ref.3)	Experimental value of $\alpha_K \cdot 10^3$	Theoretical value of $\alpha_K \cdot 10^3$ (Ref.4): E1	E2	E3	M1	M2	Multipole order assignment	No. γ-rays per decay, %
603±1	600	197±10	100	4,27	1,5	4,27	10,5	5,24	15,5	E2*	98,6
646±1	644	15±1	7,4	4,21	1,29	3,54	8,50	4,46	12,9	M1	4,5
714±2	725	27±2**	2,6	2,92**	1,05	2,76	6,31	3,46	9,55	E2, E2+M1	3,7
723±1			7,8	3,26**	1,02	2,69	6,03	3,39	9,33	M1	10,0
970±2	967	5,0±0,8	0,6	1,03	0,56	1,35	2,82	1,70	4,26	E1+E2	2,5
1047±3	1048	4,8±0,8									2,4
1298±4											
1326±4	1330	4,6±0,4									1,4
1361±4	1370	9,2±0,6									4,6
1370±4											
1450±14	1450	4,1±0,4									2,1
1505±15	1505	2,2±0,3									
1540±16	1540	1,2±0,3									
1692±2	1700	100	2,9	0,24	0,21	0,42	0,80	0,49	1,05	E1	50,0
2088±4	2090	13,0±2,0	—	—	—	—	—	—	—	—	6,5

*Normalization assignment

**Values taking into account the γ-line intensities given in Ref.3.

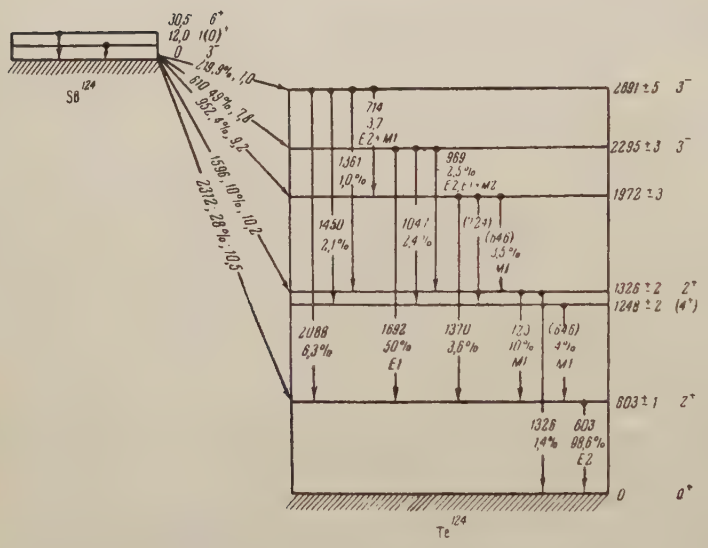

Fig.4. Decay scheme for Sb^{124}. The values of the energy of the β-components, γ-lines and levels of Te^{124} and of the intensity of the β-components are averages of all the data available in the literature. The indicated intensities and multipole orders of the γ-transitions are based on our data.

of the former level energy values. Whereas formerly the levels were assumed to be situated at 603, 1319, 1960, 2283 and 2693 kev, we have now assigned them values of 603, 1326, 1972, 2295 and 2691 kev, respectively. The 603, 646, 714, 723, 970, 1326, 1361, 1370, 1692 and 2088 kev γ-lines observed by Zolotavin et al and us, as before, fit satisfactorily into the scheme shown in Fig.4. The weak 1047, 1295, 1450, 1505 and 1540 kev lines do not correspond to any differences between the indicated levels and hence require the postulation of additional levels in order to fit them into the scheme.

Analyzing the energy differences between the above mentioned weak lines one can readily find the approximate equality 1450 - 1047 = 403 ≈ 2691 - - 2295 = 396, which allows of fitting in the 1047 and 1450 kev γ-lines by introducing one additional level with an energy of 1248 ± 2 kev. The introduction of this level makes possible a new arrangement of the 646 and 723 kev

lines inasmuch as 1972 - 1248 = 724 kev and 1248 - 603 = 645 kev.

An obvious question is whether these lines are not close doublets? The question can only be answered by a special investigation of the corresponding conversion lines on a high resolution instrument.

Multipole orders

The E1 assignment for the 1692 kev line following from Table 1 substantiates the deduction made earlier in Refs.3 & 5. The spin and parity assignments of 2+ and 3- for the 603 and the 2295 kev levels may be regarded as reliably established. The quantum characteristics of the other levels are less definite partly because of the uncertainty connected with the possible doublet structure of the 646 and 723 kev lines. Comparison with other even-even nuclei shows that two-quantum vibrational excitation of Te^{124} should form a 0+ 2+ 4+ triplet in the 1320 kev region ($E_2^*/E_1^* \approx 2.2$). Of the three possible choices one must attribute 2+ to the 1326 kev level inasmuch as there is observed a 1326→0 transition and a 2295→1326 transition (969 kev γ-line) of the E1 + M2 type.

The data on the 646, 1047 and 1450 kev lines support the inference that the 1248 kev level is 4+.

Intensity balance

Table 2

Balance of intensities for the different levels of Te^{124}

Level, kev	Transitions to the level	Transitions from the level
603	+101,9 %	—98,6 %
1248	+9,5 %	—4,0 %
1326	+12,0 %	—11,4 %
1972	+7,7 %	—7,1 %
2295	+49 %	—54,9 %
2691	+9,0 %	—13,1 %

If the 1248 and 1326 kev levels have spins 4+ and 2+ and belong to the same triplet, the probabilities of β-decay of Sb^{124} (the ground state of which is 3-) to these levels should be almost equal. Let us assume that 5% of the decays feed each level. Then the intensity balance to all the levels will be as shown in Table 2.

The divergence is 3% on the average and nearly 6% in one case (the 2295 kev level).

For the higher levels the discrepancies may be due to inaccurate determination of the intensities of the soft components of the β-spectrum in view of the fact that its precise shape is not known. For the lowest 603 kev level, however, the balance is determined primarily by the ratio of intensities of the 603 and 1692 kev γ-lines. The present experimental inaccuracy in determining this ratio still precludes more accurate intensity balancing for the 603 kev level.

"V.G.Khlopin" Radium Institute,
Academy of Sciences of the USSR

References

1. B.Dzhelepov, N.Zhukovskii, V.Nedovesov, I.Uchevatkin & V.Chumin, Izv. AN SSSR, Ser.fiz.,20,925 (1956). (Trans.Bulletin 20, No.8, 838.)

2. B.Dzhelepov, N.Zhukovskii, V.Nedovesov & G.Shchukin, Izv.AN SSSR, Ser. fiz., 21,966 (1957). (Trans.Bulletin 21, No.7, 968.)

3. A.Zolotavin, E.Grigor'ev & M.Abroian, Izv.AN SSSR, Ser.fiz., 20,289(1956). (Trans.Bulletin 20, No.3, 271.)

4. L.Sliv & I.Band, Tablitsy koeffitsientov konversii gamma-izlucheniia (Tables of internal conversion coefficients) M.-L., 1956.

5. F.Metzger, Phys.Rev., 93, 253 (1954).

6. B.S.Dzhelepov & L.K.Peker, Skhema raspada radioaktivnykh izotopov (Decay schemes of radioactive isotopes), M., 1957.

SPECTRA OF INTERNAL CONVERSION ELECTRONS EMITTED IN THERMAL NEUTRON CAPTURE BY SAMARIUM, CADMIUM AND GADOLINIUM

- L.V.Groshev, A.M.Demidov & V.A.Naidenov

Internal conversion data for (n,γ) reactions have been reported by Hibdon & Muehlhause[1], Church & Goldhaber[2] and Motz[3]. Hibdon & Muehlhause measured the internal conversion lines emitted promptly in neutron capture by Cd, Sm, Gd, Dy and Hg by means of a constant magnetic field β-ray spectrograph. Church & Goldhaber carried out a similar investigation for Gd. Motz employed a magnetic lens spectrometer to study the internal conversion spectrum associated with the Cd^{113} (n,γ) Cd^{114} reaction.

In our investigation we used a magnetic spectrometer with electric recording of the electrons by means of two widely separated counters connected in coincidence. This spectrometer is commonly used on our laboratory for measuring (by observation of Compton recoils) of the γ-rays emitted in thermal neutron capture by diverse nuclei.[4] It must be noted that this instrument is not ideally suited for investigation of internal conversion electrons inasmuch as it has a relatively low transmission factor for spectrometers of this type, together with only moderate resolution. The work was carried out primarily for the purpose of evaluating the possibility of investigating such spectra by using the above mentioned method of recording with a view to utilizing it in a special instrument to be designed for internal conversion studies.

Experimental Procedure

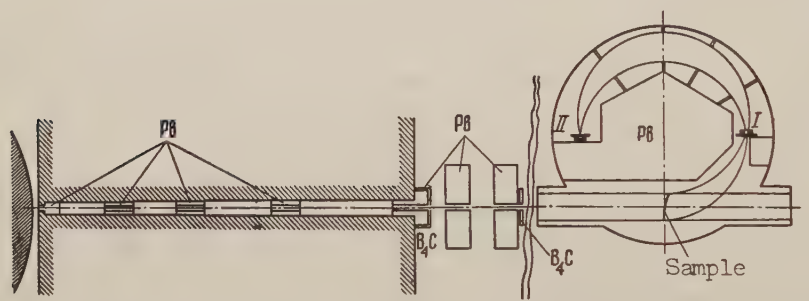

Fig.1. Experimental arrangement for measuring spectra of internal conversion electrons from the (n,γ) reaction.

The experimental procedure and equipment have been described in Ref.4. The only difference in this case was that the neutrons from one of the channels of the RTF (Reactor, physico-technical) reactor were brought directly into the spectrometer chamber and there impinged on the investigated sample (3 x 4 cm). The sample was mounted in the usual position of the radiator foil (see Ref.4 and Fig.1). The internal conversion electrons emitted from the sample were recorded by two counters connected in coincidence. Inasmuch as the sample was also a source of γ-rays, it must be noted that the counters were subjected to appreciable loads due to the proximity of the sample and inadequate shielding, particularly in the case of counter I (Fig.1). With a resolving time of $\tau = 0.5 \cdot 10^{-6}$ sec of the coincidence circuit, the spurious coincidence count amounted to 3-4 pulses per 5 min. The background due to electrons ejected from the sample by γ-rays from the reactor did not exceed 2-3 pulses per 5 min.

Scattering and stopping of electrons in the sample itself imposes a limit of 1-2 mg/cm^2 on the sample thickness. In fact, for electron energies under 150 kev even superficial densities of this magnitude result in a certain amount of line broadening. The scattering and stopping appear to have less effect on the areas under the lines. Investigation of the 130 kev line in

the spectrum of Gd using sample thicknesses of 0.78 mg/cm^2 and 0.31 mg/cm^2 showed that in this range of superficial densities, the areas under the line peaks still increase linearly with the sample thickness.

With the available neutron flux from the RTF reactor and the relatively low transmission factor of our instrument, the limitations imposed on the sample thickness allow of carrying out measurements only on strongly absorbing isotopes with a neutron capture cross-section of 1000 barns or more.

The data on our Sm_2O_3, Cd and Gd_2O_3 samples are listed in Table 1.

Table 1

Sample	Capturing isotope	Isotope content, %	Contrib. of isotope to cross section*, %	σ, barns per atom of natural mixture	Thickness of sample, mg/cm^2	Neutron absorption in sample, %
Sm_2O_3	Sm^{149}	13,8	100	9200±350	1,25	2,8
Cd	Cd^{113}	12,3	100	2400±200	2,3	2,9
Gd_2O_3	Gd^{155}	14,8	30	44000±2000	0,78	12,9
	Gd^{157}	15,7	70			

The Sm_2O_3 and Gd_2O_3 samples were prepared by settling from an alcohol suspension of the oxide powders onto a 10 μ thick aluminum backing. The cadmium sample was prepared by thermal sputtering of the metal under vacuum on similar 10 μ aluminum foil.

It must be noted that thermal neutron capture γ-rays can eject photoelectrons from the sample and that these electrons will have the same energy as the internal conversion electrons. Evaluations showed, however, that the contribution by photoelectrons to the conversion peaks did not exceed 1% in the case of our samples.

Experimental Results

The conversion electron spectra of Sm_2O_3, Cd and Gd_2O_3 are shown in Figs.2, 3 & 4. The line half-width is 1.6% at electron energies of 150 kev.

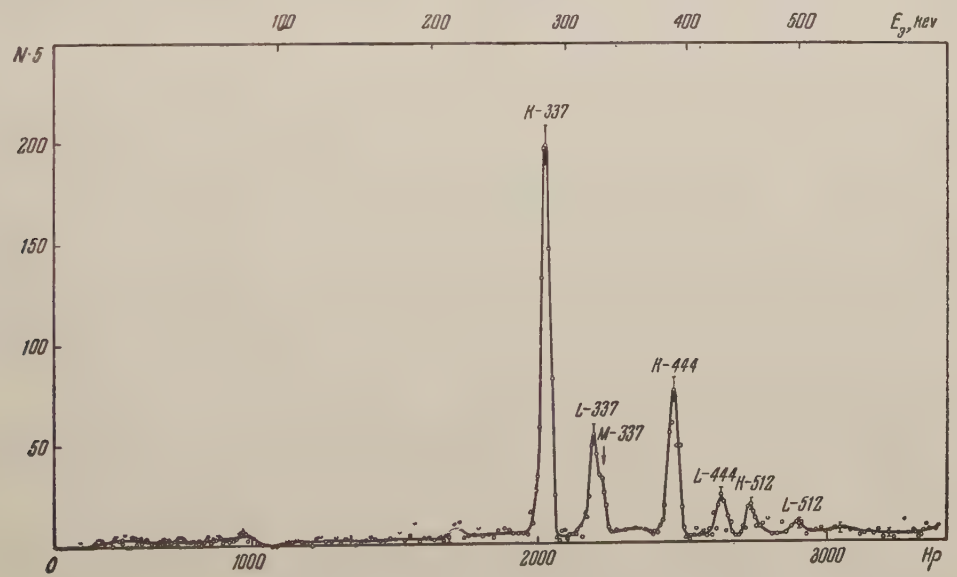

Fig.2. Conversion electron spectrum of Sm^{150}.

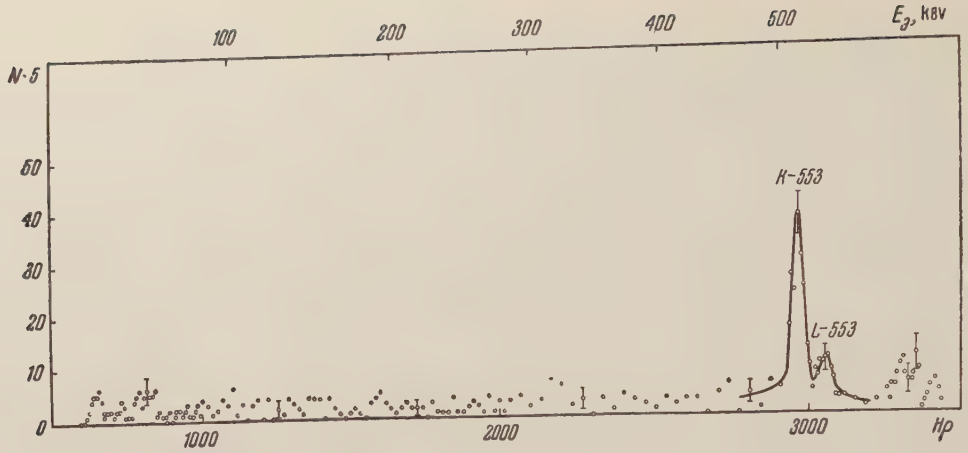

Fig.3. Conversion electron spectrum of Cd^{114}.

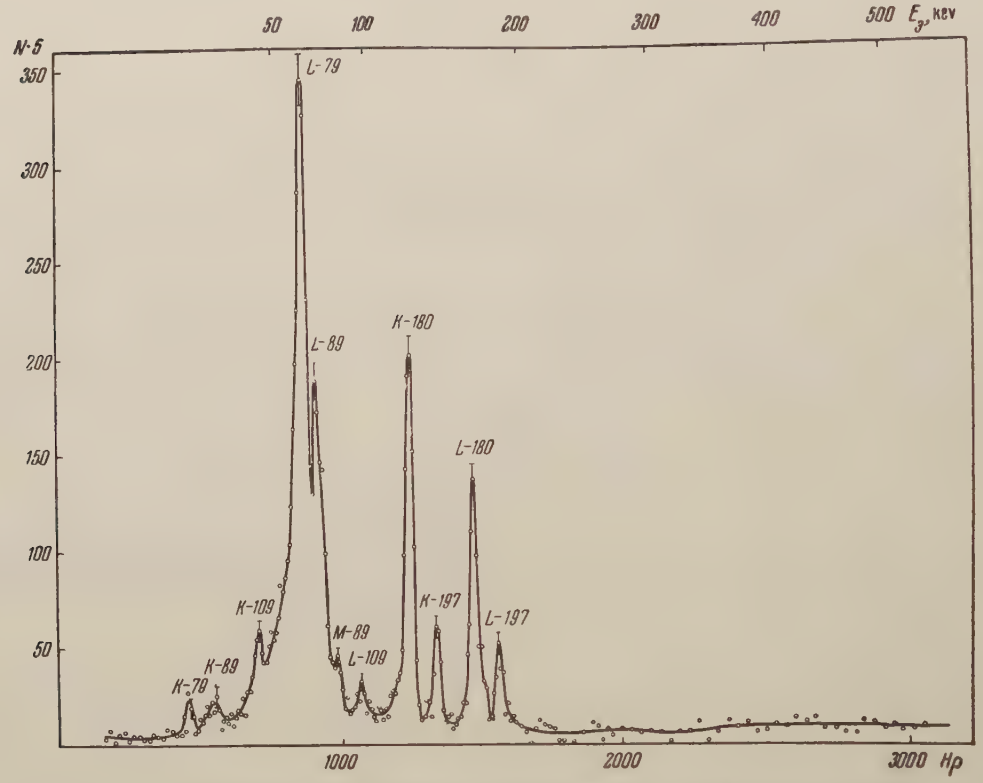

Fig.4. Conversion electron spectrum of Gd^{156} and Gd^{158}.

The data on the energies and multipole orders of the transitions in the investigated nuclei are summarized in Table 2. The multipole orders were determined by comparing the ratios of the areas under the K and L conversion lines, i.e., the experimental K/L ratios, with the theoretical ratios obtained by interpolation of Rose's data[5].

The multipole orders of the transitions were also established by another method, namely, by determining the K shell conversion coefficients (α_K) experimentally and comparing these values with the computed values given by Sliv & Band[6]. By comparing the areas under the K peaks pertaining to the same isotope (or different isotopes) one can determine the K conversion coefficients for different γ-transitions if the coefficient for one of them is known. For the last we chose the 337 kev γ-transition in Sm^{150} for which we assumed the conversion coefficient to be equal to the theoretical one.

Table 2

Isotope	I*, %	E_γ, kev	K/L, exp.	K/L, theoretical					α_K, exp	α_K, theoretical					Type transition
				E1	E2	E3	M1	M2		E1	E2	E3	M1	M2	
Sm^{150}	38	337±4	4,1±0,5	~8	~4,2	~2,5	~7,5	~6	—	—	3,2*** (-2)	—	—	—	E2
	33	444±4	4,8±1,5**	~8	~5,4	~3,5	~7,5	~6	1,3±0,5 (-2)	5,1 (-3)	1,2 (-2)	4,2 (-2)	2,5 (-2)	8,8 (-2)	E2
Cd^{114}	42	553±4	6,0±1**	~8	~6,5	~5	~8	~8	5,5±2,5 (-3)	1,4 (-3)	4,5 (-3)	1,18 (-2)	4,6 (-3)	1,48 (-2)	E2
Gd^{156}	—	89±2													
	—	197±3	1,6±0,5**	~7	~2	~1	~7	~5							(E2)
Gd^{158}	—	79±2													
	—	180±2	1,7±0,3	~7	~2	~1	~7	~5							(E2)
Gd	—	109±5													
Hg^{200}	20	368±5													
Dy^{165}	—	~106													

*I=intensity in terms of number of γ-transitions per neutron capture.

**Actually K/(L + M).

***In all cases figure in ( ) is the exponent for 10, i.e., $(-2) \approx 10^{-2}$, etc.

The areas S under the K peaks reduced to equal Hρ intervals are proportional to the number q_σ of absorbed neutrons, the γ-transition intensity I expressed in terms of number of γ-transitions per neutron capture (for Sm and Cd the values of I were taken from Ref.4), the K conversion coefficient α_K and a certain factor δ which takes into account the effect of electron scattering in the sample and in the first counter:

$$S \sim q_\sigma I \alpha_K \delta.$$

With this method of determining the conversion coefficients one must know the transition intensities and in comparing the K peaks pertaining to different isotopes one must also know the thermal neutron capture cross sections and the number of nuclei in the sample (we took the value of the capture cross section for Sm^{149} to be 66,200 ± 2500 barns - Ref.7).

The factor δ can be regarded as a double one: $\delta = \delta_1 \cdot \delta_2$, where δ_1 takes into account the effect of electron scattering in the sample and δ_2 the effect of scattering in the first counter. We took $\delta_1 = 1$ for electron energies above 100 kev in view of the results of the above mentioned experiments with Gd samples of different thickness. The value of δ_2 was calculated making certain approximations. The greatest effect of taking this factor into account for electron energies above 100 kev was ~15%. For a more accurate evaluation of the effect of scattering in the first pass-through counter, it would be necessary to determine the electron energy dependence of δ_2 experimentally.

At electron energies under 100 kev, in addition to the line broadening effect, there was observed an appreciable decrease of the factor δ_2. Here determination of the line intensities became unreliable and, consequently, we did not attempt to determine the multipole orders of the transitions associated with the peaks due to electrons of under 100 kev energy.

The multipole orders were determined for the 337 and 444 kev transitions in Sm^{150}, the 553 kev transition in Cd^{114}, the 197 kev transition in Gd^{156} and the 180 kev transition in Gd^{158}. The resultant assignments for all these transitions are E2. This deduction is in agreement with the results of other investigations (Refs.1-3). Since the uncertainty in the theoretical values of the conversion ratios is not known accurately, however, our results do not preclude the assignment E3 for the 197 kev transition in Gd^{156} and the 180 kev transition in Gd^{158}. This is why the E2 assignment for these transi-

tions is given in parentheses in Table 2.

Notes:

1. In the spectrum of Sm_2O_3 (Fig.2) there appear conversion lines corresponding to γ-rays of 512 ± 4 kev energy which appear as a result of the photoeffect on the atoms of the sample, due to annihilation quanta from the reactor channel.

2. Hibdon & Muehlhause[1] observed a 97 kev transition in the spectrum of Cd^{114}, which corresponds to a K electron energy of 70 kev. Our experimental statistics in this energy region do not allow of resolving this peak clearly.

At an electron energy of ~630 kev there appear in the spectrum of Cd conversion electron peaks from a 660 kev transition[3,4]. Owing to the low transmission of our instrument, we were not able to resolve these peaks.

3. In identifying the isotopes responsible for the conversion lines in the spectrum of Gd (Fig.4), we used the data of Refs.8 & 9 on Coulomb excitation of gadolinium isotopes. The low-intensity 109 kev transition remained unidentified.

Preliminary measurements of the internal conversion electrons emitted in thermal neutron capture by Dy and Hg indicate the presence of an isomeric transition of ~106 kev energy in Dy 165 ($T_{1/2} \approx 1$ min) and a 368 ± 5 kev γ-transition in Hg^{200}.

References

1. C.T.Hibdon & G.O.Muehlhause, Phys.Rev., 88, 943 (1952).
2. E.L.Church & M.Goldhaber, Phys.Rev., 95, 626 A (1954).
3. H.T.Motz, Phys.Rev., 104, 1353 (1956).
4. L.V.Groshev, B.P.Ad'iasevich & A.M.Demidov, Fizicheskie issledovaniia (Physical investigations) in Reports of the Soviet Delegation at the International Conference on the Peaceful Uses of Atomic Energy. 1955.
5. Beta- and Gamma-Ray Spectroscopy, K.Siegbahn, editor, Amsterdam, 1955.
6. L.A.Sliv & I.M.Band, Tablitsy koeffitsientov vnutrennei konversii γ-izlucheniia (Tables of internal conversion coefficients), M., 1956.
7. E.A.Melaika, M.I.Parker, I.A.Petruski & R.H.Tomlinson, Canadian J. Chem., 33, 830 (1955).
8. N.P.Heydenburg & G.M.Temmer, Phys.Rev., 100, 150 (1955).
9. T.Huus, Bierregard & Elbeck, Kong.Danske Vidensk, Selsk. Mat.-Fys.Medd. 30, 17 (1956).

NEUTRON-DEFICIENT ISOTOPES OF THE RARE EARTH ELEMENTS FORMING AS A RESULT OF SPALLATION OF Ta UNDER BOMBARDMENT WITH 660 Mev PROTONS. Part II*

- G.M.Gorodinskii, A.N.Murin, V.N.Pokrovskii & B.K.Preobrazhenskii

The investigated elements of the rare earths group were separated from a tantalum target bombarded in the Joint Institute for Nuclear Research synchrocyclotron with 660 Mev protons and separated chromatographically. The experimental procedure and the results obtained for the isotopes with mass numbers from A = 173 to A = 165 were described in Part I (Ref.1). In the present article we shall describe the results for the isotopes with mass numbers from 160 to 134. The omission of mass numbers in what follows means that no corresponding isotopes with periods allowing of investigation were found among the reaction products.

A = 160. The observed Er and Ho isotopes with mass number 160 form a genetic chain (Fig.1). According to Nervik & Seaborg[2] the decay of Er^{160} is not accompanied by γ-rays. This was confirmed by our observations. Thus the disintegration of Er^{160} goes directly to the ground and isomeric levels of Ho^{160}. The existence of the isomer Ho^{160m} ($T_{1/2}$ = = 5 hours) was definitively established in the investigation of Ref.3; the energy of the transition (electric) is 60 kev.

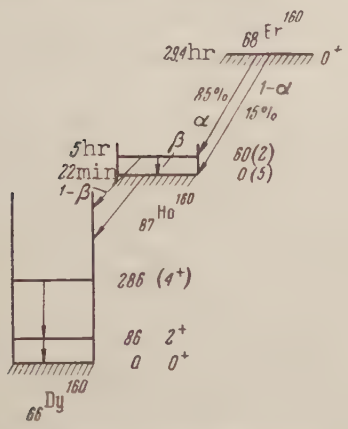

Fig.1. Decay scheme for A = 160.

In order to determine the relative transition probabilities to the isomeric and the ground levels of Ho^{160} we carried out the following experiment. The Er^{160} sample was chromatographically separated from the daughter elements. We followed the intensity of the γ-lines associated with the transitions between the levels of Dy^{160}. The intensity of these lines at first increased with accumulation of Ho^{160} + Ho^{160m} and then fell off with a period equal to that of the parent Er^{160}. We chose the most intense 86 and 198 kev lines for observation (see Fig.1). The observations were started 1-2 minutes after purification of the Er^{160} and were continued without interruption for two hours with the period of each measurement being 12 min. After the initial 2 hours the intervals between measurements were increased. In all, the measurements were made over a period of 5 days.

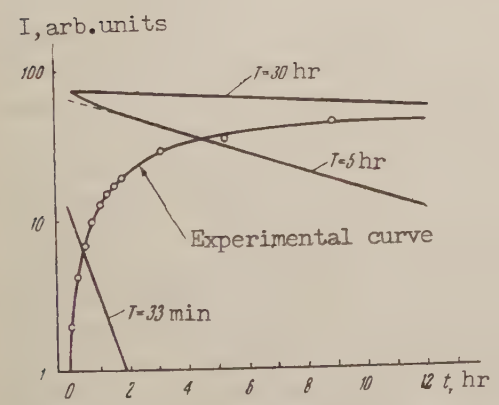

Fig.2. Variation of the intensity of the 86 kev γ-line from the Er^{160} sample chromatographically separated from Ho^{160} (zero on the time scale for the experimental curve is the time of beginning of measurements).

Fig.2 shows the results of the measurements made during the first 12 hours on the 86 kev line (the 198 kev line yields the same picture). For the sake of simplicity, we show only the initial part of the curve. The $T_{1/2}$ = = 30 hour exponential curve was obtained by extrapolation of experimental data not shown in the figure; the other exponentials were

---

*For Part I see Bulletin of the USSR Academy of Sciences, Physical Series, Vol.21, No.7, 1005.

obtained by analysis and resolution. It can readily be shown that the general analytic expression characterizing the variation in intensity given by the curves of Fig.2 is of the form

$$I = Ae^{-\lambda_1 t} + Be^{-\lambda_2 t} + Ce^{-\lambda_3 t},$$

where

$$A = \alpha(1-\beta)\frac{\lambda_1\lambda_2}{\lambda_2-\lambda_1} + (1-\alpha)\frac{\lambda_1\lambda_2}{\lambda_3-\lambda_1} + \alpha\beta\frac{\lambda_1\lambda_2\lambda_3}{(\lambda_1-\lambda_2)(\lambda_3-\lambda_2)},$$

$$B = \alpha(1-\beta)\frac{\lambda_1\lambda_2}{\lambda_1-\lambda_2} + \alpha\beta\frac{\lambda_1\lambda_2\lambda_3}{(\lambda_1-\lambda_2)(\lambda_3-\lambda_2)},$$

$$C = (1-\alpha)\frac{\lambda_1\lambda_3}{\lambda_1-\lambda_3} + \alpha\beta\frac{\lambda_1\lambda_2\lambda_3}{(\lambda_1-\lambda_3)(\lambda_2-\lambda_3)}.$$

Here α is the relative abundance of the decays of Er^{160} (T_1 = 29.4 hours) leading to formation of Ho^{160m} (T_2 = 5 hours); (1 - α) is the fraction of decays to the ground state of Ho^{160} (T_3 = 22 min); β is the fraction of isomeric transitions in the decay of Ho^{160m} ($Ho^{160m} \rightarrow Ho^{160}$), (1 - β) is the fraction of decays of the Ho^{160m} isomeric state to the levels of dysprosium ($Ho^{160m} \rightarrow Dy^{160}$) and $\lambda_i = 0.693/T_i$.

By analytic resolution of the curves shown in Fig.2, we obtained three exponential curves with periods of 30 hours (Er^{160}, $T_{1/2}$ = 29.4 hours), 5 hours (Ho^{160m}, $T_{1/2}$ = 5 hours) and 33 min (Ho^{160}, $T_{1/2}$ = 22.5 min). The excessively high value of the last period can be explained by the difficulties of resolution. Resolution of the curve of Fig.2 allows of finding the values of A, B and C, i.e., of calculating α and β. For α we obtain 0.85. This means that about 15% of the disintegrations of Er^{160} feed the ground level of Ho^{160}. This evaluation is admittedly rather rough, but the error involved can hardly exceed 8% (1 - α = 15 ± 8%). Thus under the most extreme assumptions, the fraction of decays to the isomeric level must lie within the range from 76 to 92%.

The presence of an appreciable decay branch to the ground level of Ho^{160} appears somewhat strange inasmuch as the spin of this level is apparently 5. Thus according to Peker[4] the spin of the odd-odd ${}_{67}Ho^{160}_{93}$ is given by $|\Omega_p \pm \Omega_n|$ where Ω_p and Ω_n are, respectively, the momenta associated with the odd proton or odd neutron. In our case Ω_p = 7/2- (spin of ${}_{67}Ho^{161}_{94}$, see Ref.5) and Ω_n = 3/2- (spin of ${}_{64}Gd^{157}_{93}$, see Ref.6), i.e., Ho^{160} may have spin 2 or 5, but spin 2 should be attributed to the isomeric level inasmuch as the major portion of the decay of Er^{160} goes to this level.

The γ-spectrum of Ho^{160m} + Ho^{160} consists of lines of 86, 198, 300, 525, 650, 730, 880 and 965 kev energy and a doubtful line at 400 kev. In our measurements we did not detect the 60 kev γ-line associated with the isomeric $Ho^{160m} \rightarrow Ho^{160}$ transition inasmuch as its intensity is low (the transition is strongly converted) and it is not resolved from the intense Dy x-radiation (45 kev). Our data on the spectrum of Ho^{160} are in agreement with those of Nervik & Seaborg[2]. True, these investigators do not list the 300 and 525 kev γ-lines which are weaker than the others. We note that the 525 kev γ-line is apparently a doublet.

With the data available it is still impossible to construct a level diagram for Dy^{160}. At present we can only indicate that the 86 and 198 kev lines apparently form a rotational band of the type common to even-even nuclei. We note further that the higher energy γ-lines do not fit the level scheme for Dy given in Ref.7.

A = 159. Among others we separate the long-lived isotope Dy^{159} ($T_{1/2}$ = 134 days); no γ-rays from it were observed, which is consistent with the information in the literature.[5]

A = 157. In the Dy fraction (separated from Y) we observed an activity falling off with a period of 8.5 hours. In accord with Handley & Olson[8] this activity was attributed to Dy^{157} (8.2 hours). The γ-spectrum of Dy^{157} consists solely of a 325 kev line as reported by Handley & Olson. We note that in Seaborg's Table of Isotopes[5] the γ-spectrum of Dy^{157} is erroneously shown to have a 177 kev line although in their original reference article, Handley & Olson[8] state that this is a Compton peak due to the 325 kev γ-ray.

A = 156. The separated Tb fraction may have contained Tb^{156} (see below under A = 155).

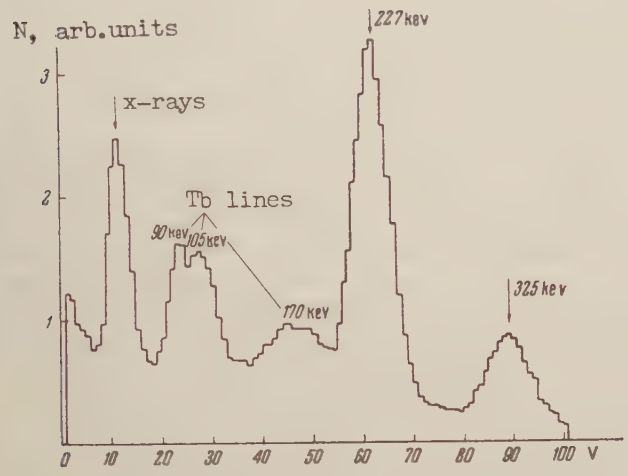

Fig.3. Gamma-spectrum of the Dy fraction, plotted in the form of a histogram. Each "step" is equivalent to 1 v. The x-radiation was attenuated by a 0.3 mm Cu + 0.15 mm Sn absorber. The identified Tb lines in the soft region are from Tb that accumulated in the Dy sample between the time of separation and the time of measurement.

A = 155. In the γ-spectrum of the Dy fraction we observed a distinct 227 kev line (see Fig. 3 which also illustrates one of the techniques employed in the present investigation, namely, automatic recording of the γ-spectrum), the intensity of which fell off with a period of 10 hours.

Further we found that as a result of decomposition of the Dy isotope with $T_{1/2}$ = 10 hours there is formed a Tb isotope whose half-life is ~5 days. This was established both by means of chromatographic separation of the Tb from the Dy fraction and by observation of the increase in intensity of the Tb lines in the γ-spectrum of the Dy fraction.

According to Seaborg's Table[5] and Handley & Lion[9] the ~5 day activity could belong either to Tb^{156} or Tb^{153}. We note that according to Seaborg's Table this activity could also be attributed to Tb^{157}, but it has been established by Handley and his co-workers[8,9] that the half-life of Tb^{157} is either less than 30 minutes or greater than 25 years. Inasmuch as Dy^{156} is stable, it was natural to assume A = 153 for the Tb; this assumption was seemingly substantiated by the fact that Gd^{153} was separated from the Dy fraction (see below under "A = 153"). It is shown in a recent communication[10], however, that the period of the isotope Tb^{155} is 5.6 days and that it had a complicated γ-spectrum comprised of the following lines: 18.9, 26.7, 31.6, 45.6, 60.2, 86.7, 101.4, 105.6, 148.8, 160.8, 161.5, 163.4, 180.4, 181.6, 221.2, 239.7, 262.6, 340.8, 368.3 kev.

According to our data the γ-spectrum of the Tb isotope with $T_{1/2} \approx 5$ days consisted of lines having the following energies 90, 170 (group), 270 (group) and 365 kev. Taking into account the limitations of the scintillation spectrometer and the complex character of the spectrum (which incidentally included activities with other periods), we feel that the agreement is sufficient to attribute mass number A = 155 to the Dy and Tb isotopes in question.

The above listed γ-lines were observed by us not only in the spectrum of Tb separated from Dy but also in the spectrum of the Tb fraction; furthermore no other lines falling off in intensity with a period of ~5 days were observed in these spectra. Hence, since the presence of Tb^{156} isotopes in the

Tb fraction is possible (in contrast to the case of the Tb sample separated from Dy), one can in principle assume that if Tb^{156} was present among the products of fission of Ta, its γ-spectrum is similar or identical with the γ-spectrum of Tb^{155}. This inference is partially substantiated by the data on the γ-spectrum of Tb^{156} given by Handley & Lion[9].

A = 154. Tb^{154} could be present in the Tb fraction (see below under A = = 151).

A = 153. Together with the Tb^{155} (~5 day), two other activities with periods of ~3 and 8 days were separated from the Dy fraction (for more details on these see below under "Unidentified A values"). Exactly the same activities were detected in the Tb fraction. Further, 10 days after the initial separation we succeeded in separating from the Dy fraction a Gd isotope which was reliably identified as Gd^{153}. This same Gd^{153} isotope was present among the daughter elements separated from the Tb.

Thus among the Dy isotopes there was present Dy^{153} which decays without emission of γ-rays and has a period close to 10 hours. We cannot as yet decide between the alternative values for the period of Tb^{153}: 3 or 9 days. In any case its half-life differs from the 5.1 day value given in Seaborg's Table[5].

The Gd A = 153 isotope (~200 days) was detected not only among the daughter nuclides of Dy and Tb but also in the Gd fraction itself. The observed γ-spectrum of Gd^{153} consisted of a weak 70 kev line and a 100 kev line, which is in agreement with Ref.7. The 97 and 103 kev lines listed in Ref.7 were naturally not resolved in the present measurements.

A = 151. In investigating the Tb fraction, we detected an activity with a period of 20 hours. According to Seaborg's Table[5] and Handley & Lion[9] it may belong to either Tb^{154} or Tb^{151}. The γ-spectrum of this isotope is very complicated and hence very difficult to analyze. It may be said that it comprises a ~270 kev line (probably a group), a 345 kev line (the most distinct one) and numerous higher-energy lines.

Long-lived (150 day) Gd^{151} was present in the Gd fraction and probably among the daughter elements separated from Tb. The observed γ-spectrum consisted of lines of 154 and 247 kev energy. This does not conflict with the fact that Seaborg's Table[5] lists a 265 kev line (based on absorption measurements).

A = 149. A 9-day activity present in the Gd fraction was attributed to Gd^{149} on the basis of the indications of Seaborg's Table. According to our measurements the γ-spectrum of Gd^{149} contains lines of 150, 300, 347 and 520 kev energy (the last is probably a doublet).

A = 147. In the radiation from the Gd fraction we observed activities with periods of about 1.5 and 60 days which we could not associate with any of the known isotopes of gadolinium. At the same time the characteristic lines of Eu^{147} (see below) appeared in the γ-spectrum of the Gd fraction sometime after separation. Through a number of consecutive chromatographic separations of Eu from the Gd fractions (for control purposes the main Gd fraction was separated into several parts and the Eu was separated therefrom at different intervals), we firmly established that the parent of Eu^{147} is the Gd isotope with $T_{1/2} \approx 1.5$ days. According to our record the γ-spectrum of ~1.5 day Gd^{147} consists of lines at 230, 370 and 390 kev (the last two lines were poorly resolved). The presence of Eu^{147} among the daughter nuclides separated from Gd and in the Eu fraction was established both from its period (24 days) and on the basis of the γ-spectrum, which contains lines of 120 and 200 kev energy. The intensity ratio of these lines is 1.0 : 1.56.

Through analysis of the spectrum of Eu^{147} (Fig.4) recorded with the "0" geometry (i.e., with the sample in the immediate proximity of the scintillation

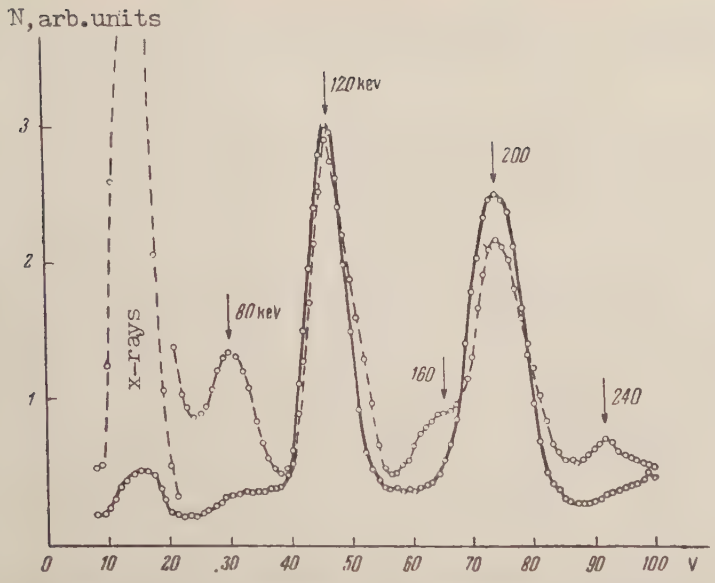

Fig.4. Eu^{147} γ-spectrum recorded using the "0" geometry with a 0.3 mm Cu + 0.15 mm Sn absorber (solid line) and without the absorber (dash line). The peaks in the recorded spectrum are due to coincidences of K capture x-rays with x-rays from conversion and to coincidences of 120 and 200 kev γ-rays with x-radiation.

crystal - see Part I) under the usual conditions and with a 0.3 mm Cu + 0.15 mm Sn absorber, which sharply reduced the intensity of the x-radiation, we were able to draw a number of important deductions in addition to evaluating the relative intensities of the lines. First, the fact that there exist peaks due to coincidences of the 120 and 200 kev γ-rays with the x-radiation (40 kev) indicates that the 120 and 200 kev γ-rays from Eu^{147} coincide with the x-rays from Sm^{147}. This deduction was substantiated by experiments on a γ-γ coincidence set-up (resolving time 10^{-6} sec). It may be noted here that the 120 and 200 kev γ-rays themselves do not give coincidences. Second, the 80 kev γ-line, which in an earlier investigation[11] we took to be a true line, is actually a peak due to coincidence of x-rays from K capture and from conversion. Finally, having evaluated the intensity of this peak one can determine the conversion coefficients. Thus the area under the coincidence peak

$$S_{Xe+XK} = A\omega_K K_{40}^2 (N_{X,\gamma\text{-}120} + N_{X,\gamma\text{-}200}),$$

where A is the relative probability of K electron capture (referred to probability of L_I electron capture), ω_K is the K shell fluorescence yield, K_{40} is the efficiency of the scintillator in detecting 40 kev photons and $N_{X,\gamma}$ is the number of x-ray quanta produced in the conversion of the γ-rays. Having determined $N_{X,\gamma\text{-}120} + N_{X,\gamma\text{-}200}$ from our data and knowing the ratio of these quantities, which is equal to the ratio of the K line intensities associated with the corresponding transitions in the conversion spectra, we could readily determine $N_{X,\gamma\text{-}120}$ and $N_{X,\gamma\text{-}200}$ separately and calculate the K conversion coefficient:

$$\alpha_K = N_{X,\gamma} / \omega_K N_\gamma \ ;$$

also $\alpha_K = N_{eK}/N_\gamma$, where N_{eK} is the number of conversion electrons from the K shell and N_γ is the number of γ-rays, but $N_{eK} = N_{X,\gamma}/\omega_K$. Utilizing the fact that $N_{X,\gamma\text{-}120}/N_{X,\gamma\text{-}200}$ = 4.4 (Ref.12), we obtained from our data α_K-120 = 1.34 and α_K-200 = 0.195.

These values are in satisfactory agreement with the theoretical values of α_K-120 = 0.9 (M1) and α_K-200 = 0.22 (E2) given by Sliv & Band[13] for the indicated multipole orders. The tabular values of α_K for radiation of other multipole orders differ appreciably from the above values deriving from our experimental data.

Further, taking K/L from Ref.12 and adding ~30% for conversion in the M shell one can calculate the total coefficients for the 120 and 200 kev transitions and then the population of the levels (the total number of transitions

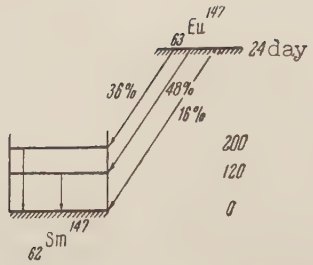

Fig.5. Decay scheme for Eu^{147}.

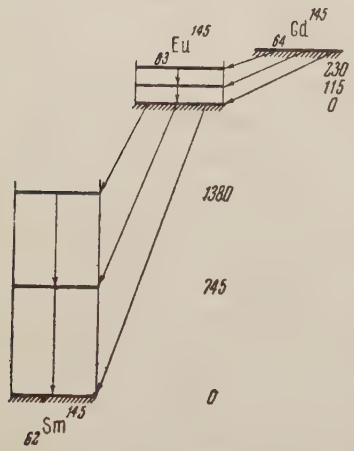

Fig.6. Decay scheme for A = 145.

is determined from the intensity of the x-radiation). The results obtained in this manner are shown in Fig.5.

A = 145.* We attributed an activity with a period of ~60 days, observed in the Gd fraction to Gd^{145}, an isotope not hitherto described in the literature. The mass number of this isotope was established in the same way (and with the same degree of dependability) as in the case of A = 147 (see below). We note that the daughter element Eu^{145} was identified only from its period inasmuch as its γ-spectrum has not been described.

The γ-spectrum of Gd^{145} has only one line located at 115 kev. Earlier[11] we also attributed γ-lines of 640 and 750 kev energy to Gd^{145}; a more careful investigation showed however that these lines belong to Eu^{145}. According to Anton'eva et al[12], the 115 kev line is a narrow doublet with energies 114.5 and 115.1 kev. The observed "self-coincidences" of the 115 kev gammas substantiate this and also indicate that these transitions are in cascade.

According to our revised data, the γ-spectrum of ~5 day Eu^{145} consists of a 636 and a 745 kev line with an intensity ratio of 1.0 : 2.3. The increase in the intensity of these lines in the spectrum of Gd chromatographically separated from Eu substantiates the data on the periods of the parent and daughter elements. On the basis of all the data now available we propose the decay scheme shown in Fig.6.

A = 140. We attributed an activity with $T_{1/2} \approx 3.5$ days observed in the Nd fraction to Nd^{140} ($T_{1/2}$ = 3.3 days). In agreement with the assumed genetic series $Nd^{140} \xrightarrow{K} Pr^{140} \xrightarrow{\beta^+} Ce^{140}$, we observed a 510 kev annihilation line in the γ-spectrum of the Nd fraction (incidentally, this is the only clearly distinguishable line in this spectrum) and also detected positrons with an end-point energy of 2.3 Mev (2.23 Mev in Seaborg's Table[5]).

Inasmuch as earlier[11] other lines were also noted in the γ-spectrum of Nd, we made a special attempt to establish the presence of lines belonging to Pr^{140} and fitting into the level diagram of Ce^{140} (Ref.7). We detected a line at 1600 kev associated with the transition from the first excited level to the ground level of Ce^{140}; however, the very low intensity of this line and the presence of a large number of other lines (apparently belonging to other Nd isotopes - see below) precludes unambiguous interpretation of the experimental results).

A = 139. In the γ-spectrum of the Pr fraction we observed an annihilation line at 510 kev whose intensity fell off with a period of ~4 hours. It was ascribed to the decay of Pr^{139} ($T_{1/2}$ = 4.2 hours[5]). At the same time, we observed an increase in intensity of the 166 kev line belonging[14] to 140 day Ce^{139} which was also detected in the Ce fraction.

---

*Note added in proof. We are now of the opinion that the Cd and Eu isotopes described in this section actually have mass number 146.

A = 134. For this mass number we substantiated the existence of the genetic series $Ce^{134} \xrightarrow{K} La^{134} \xrightarrow{K\beta} Ba^{134}$ with the characteristics described in the literature[5].

Unidentified A values. In this paragraph we shall describe some of the observed activities which for diverse reasons could not be identified.

1. In the Tb fraction and also in Tb seperated from Dy we observed activities with periods of about 3 and 8 days. The ~3 day activity includes lines of ~100 and 205 kev energy; the ~8 day activity consisted of a 100 kev γ-line. The structure of the γ-spectrum in the 100 kev region (as, incidentally, of the entire γ-spectrum of Tb) is very complicated. The intensity of this "line" in the spectrum of the Tb sample separated from Dy at first fell off with a period close to 5 days and then at an appreciably slower rate. Resolution of the intensity decay curve yielded the half-life values of ~3 and ~8 days, which does not necessarily exclude the possibility of there being a line with $T_{1/2} \approx 5$ in this region (according to the data of Ward, Jacob & Mihellich[10], for example, the spectrum of Tb^{155} includes 101.4 and 105.6 kev lines). Analysis of the γ-spectrum for the Tb fraction leads to the same deductions except that in this case there is also the possibility that there may be a Tb γ-line with a period of ~20 hours in the 100 kev region.

Inasmuch as the data in the literature on the radioactive isotopes of Tb are somewhat conflicting (see, for example, Refs.5, 9 & 10), we hesitate to make positive identification of the observed activities. One of them (~3 days) may belong to Tb^{153} (see under A = 153 above). It should also be noted that the ~8 day Tb isotope has as its parent Dy decaying without emission of γ-rays and having a period of several hours. The daughter of ~8 day Tb must be a stable or very long-lived Gd isotope.

2. Lines at 275, 330, 434 and 524 kev (the last two probably multiplets) were found in the spectrum of the Eu fraction, recorded an appreciable time after separation. A check (i.e., an attempt to separate the daughter elements from the Eu fraction) substantiated the attribution of these lines to Eu isotopes - probably 120 day Eu^{149} or 59 day Eu^{148} or a mixture thereof. The daughter activity separated from Eu had a negligible intensity and was not investigated.

It was established in the investigation of Ref.15 that the fission products of Ta include Gd and Eu isotopes with A = 146. These isotopes were not clearly evinced in our experiments but there are indications that the inferences of Ref.15 are correct.

3. In the γ-spectra of the Nd, Pr and Ce fractions we observed a rather large number of very weak γ-lines which it is difficult to attribute to definite isotopes inasmuch as in this region of Z and A values the situation is complicated by the fact that here in irradiation of Ta with fast protons there may form not only neutron-deficient but also neutron-rich nuclei. Thus, for example, (according to preliminary data), in the Nd fraction there may be present both the neutron-deficient isotopes Nd^{139} and Nd^{141} and the neutron-rich isotopes Nd^{147} and Nd^{149}; in the Pr fraction both neutron-deficient Pr^{137} and Pr^{138} and neutron-rich Pr^{142}, Pr^{134}, etc. The low intensity and complex character of the observed γ-spectra made it impossible to substantiate or disprove the presence of neutron-rich isotopes.

In conclusion, instead of a review of the mass spectrum of the rare earth isotopes obtained from spallation of Ta by 660 Mev protons, we give the appropriate section of the Segré diagram (Fig.7), wherein the isotopes observed by us are identified.

We desire to express our gratitude to V.P.Dzhelepov and the entire technical personnel of the Joint Institute for Nuclear Research synchrocylotron

Fig.7. Section of Segré chart for Z = 56 to 71: 1) stable and long-lived nuclei, 2) neutron-rich nuclei and neutron-deficient nuclei not observed by us, 3) neutron-deficient nuclei observed by us, 4) new isotopes, 5) daughter nuclei not observed by us, 6) mass number doubtful.

for their assistance in the work and to V.N.Mekhodov and V.A.Khalkin for facilitating the prolonged irradiations. We are very thankful to B.S.Dzhelepov and V.P.Dzhelepov for their interest in the work and valuable suggestions. We are indebted to N.M.Anton'eva, A.A.Bashilov and B.S.Dzhelepov for communicating their data prior to publication and for valuable discussion. Finally, we wish to thank A.V.Kaliamin and O.M.Lilova for their help in carrying out the numerous chromatographic separations

"V.G.Khlopin" Radium Institute,
Academy of Sciences of the USSR

References

1. G.M.Gorodinskii, A.N.Murin, V.N. Pokrovskii & B.K.Preobrazhenskii, Izv. AN SSSR, Ser.fiz., 21, 1004 (1957). (Trans., Bulletin 21, No.7, 1005.)

2. W.E.Nervik & G.T.Seaborg, Phys. Rev., 97, 1092 (1955).

3. J.W.Mihelich, B.Harmatz, T.H. Handley & J.J.Pinajion, Bull.Am.Phys. Soc., Ser.II, 1, 330 (1956).

4. L.K.Peker, Izv.AN SSSR, Ser.fiz., 21, 1029 (1957). (Trans., Bulletin 21, No.7, 1030.)

5. J.M.Hollander, I.Perlman & G.T. Seaborg, Table of Isotopes, Revs.Mod.Phys., 25, 469 (1953). (Cited in Russian trans. M., 1956.)

6. A.Bohr & B.Mottelson, Problemy sovremennoi fiziki (Problems of Modern Physics), 1, 173 (1956).

7. B.S.Dzhelepov & L.K.Peker, Skhemy raspada radioaktivnykh izotopov (Decay schemes of radioactive isotopes), M.-L., 1957.

8. T.H.Handley & E.L.Olson, Phys.Rev., 90, 500 (1953).

9. T.H.Handley & W.S.Lion, Phys.Rev., 99, 1415 (1955).

10. T.J.Ward, K.P.Jacob & J.W.Mihelich, Bull.Am.Phys.Soc., Ser.II, 2, 259 (1957).

11. G.M.Gorodinskii, A.N.Murin, V.N.Pokrovskii, B.K.Preobrazhenskii & N.E. Titov, Doklady AN SSSR, 112, 405 (1957).

12. N.M.Anton'eva, A.A.Bashilov, B.S.Dzhelepov & B.K.Preobrazhenskii, Materialy VII Ezhegodnogo soveshchaniia po iadernoi spektroskopii (Transactions of the Seventh Annual Conference on Nuclear Spectroscopy, Leningrad, 1957.)

13. L.A.Sliv & N.M.Band., Tablitsy koeffitsientov vnytrennei konversii γ-luchei (Tables of internal conversion coefficients), M.-L., 1956.

14. B.H.Ketelle, H.Thomas & A.R.Brosi, Phys.Rev., 103, 190 (1956).

15. I.A.Gusev, O.M.Lilova, A.N.Murin, B.K.Preobrazhenskii & V.A.Iakovlev, Zhur.eksp.i. teor.fiz., 32, 1585 (1957).

INVESTIGATION OF THE DECAY OF Pr^{144}, Rh^{106} AND Cs^{134} BY MEANS OF A SCINTILLATION SPECTROMETER

- E.I.Firsov & A.A.Bashilov

Procedure and equipment

We constructed a single channel spectrometer employing NaI(Tl) and CsI(Tl) crystals and FEU-19 M and FEU-12 photomultiplier tubes. The resolution of the instrument is characterized by the following data: half-width of the Cs^{137} 661 kev line - 6.7% for the NaI(Tl) and FEU-19 M (specially selected tubes) combination, 9% for the FEU-19 M and CsI(Tl) combination and about 10% for the FEU-12 tubes with NaI(Tl) and CsI(Tl) crystals; in the last case the stability of operation is appreciably better than in the other cases. The instrument is characterized by good linearity from 84 kev (Tm^{170}) to 2.7 Mev (Na^{24}). In addition, in the work we used a 50-channel pulse height analyzer based on a storage tube designed by O.V.Viazemskii (Leningrad Electrotechnical Institute) and a 56-channel analyzer with a mechanical register designed and constructed in our laboratory. We also used a fast-slow coincidence circuit with energy discrimination, having a resolving time of $5 \cdot 10^{-8}$ sec. For investigating the different γ-ray energy intervals we made extensive use of absorbers of different thickness and sources having different activities. All the samples were subject to careful chemical purification.

Pr^{144}

Pr^{144} is a link in the radioactive chain $Ce^{144} \xrightarrow{\beta} Pr^{144} \xrightarrow{\beta} Nd^{144}$ deriving from the fission of uranium.[1] The half-life of Ce^{144} is 282 days[2]; that of Pr^{144} is 1.5 min.[1]

1. The β-spectrum of Pr^{144} has been investigated by a number of authors[3-8]; according to the reports it comprises components with end-point energies of 0.8 Mev (3%), 1.3 Mev, 2.3 Mev (12%) and 2.97 Mev (85%).

2. The γ-spectrum of Pr^{144} was studied in the investigations of Refs.5, 6, 9, 10 & 11 and is reported to comprise γ-rays of 0.695, 1.49 and 2.185 Mev energy. There are indications[5,11] of the existence of γ-rays having an energy greater than 2.25 Mev.

3. Angular correlation measurements of the γ-rays of Pr^{144} were made by Alburger & Kraushaar for the purpose of making spin assignments. Of the two possibilities allowed by the observed correlation, they give preference to 1-2-0 (D-Q). Accordingly the ground state of Nd^{144} has spin 0+ (even-even nucleus). The energy of the first level is 0.695 Mev[3,5], the 2.185 Mev level has spin 1- according to Emmerich, Auth & Kurbatov[8], who also note that the 2.185 Mev level may be the third or a higher level. It is inferred that there may be a level with spin 4+ between the 0.695 and 2.185 Mev levels.

Our results

We investigated the γ-ray spectrum of Pd^{144} in the range from 0.7 to 2.2 Mev using the 50-channel storage-tube pulse height analyzer. We observed peaks at 2.18, 1.49, 1.1 and 0.7 Mev, having relative intensities of 100, 30, 2 and 150, respectively. In investigating the spectrum in the 2 to 3 Mev interval on the single channel and 50-channel analyzers, we also detected weak lines with energies of 1.7 and 2.8 Mev and relative intensities of 2 and 2.5 (referred to 100 for the 1.18 Mev line); the 1.7 Mev line was poorly resolved because it is overlapped by the Compton effect from the 2.18 Mev line. The

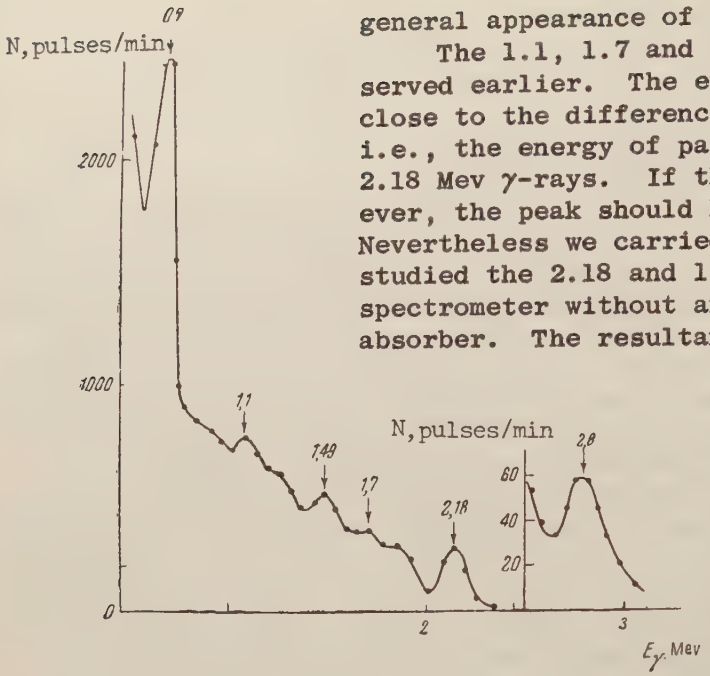

Fig.1. General appearance of the γ-spectrum of Pr^{144}.

general appearance of the γ-spectrum is shown in Fig.1.

The 1.1, 1.7 and 2.8 Mev γ-rays have not been observed earlier. The energy of the 1.1 Mev peak is close to the difference 2.18 Mev - 2 mc^2 = 1.16 Mev, i.e., the energy of pair formation in the crystal by 2.18 Mev γ-rays. If this were actually the case, however, the peak should have been lower than observed. Nevertheless we carried out a control experiment: we studied the 2.18 and 1.1 Mev lines on the 1-channel spectrometer without an absorber and with a 4.5 cm lead absorber. The resultant spectra are shown in Fig.2. The relative weakening of the line (by a factor of three) is somewhat lower than the calculated value; thus, apparently, the peak at 1.1 Mev should be regarded as the combined peak due to 1.1 Mev γ-rays and the absorption maximum associated with electron-positron pair production by the 2.185 Mev γ-rays.

Using the slow-fast coincidence two-channel spectrometer we observed coincidences between the 0.7 & 1.49 Mev and the 1.1 & 1.7 Mev γ-rays. The results of these measurements are shown in Fig.3. A further series of measurements carried out after careful chemical repurification of the samples substantiated the given results.

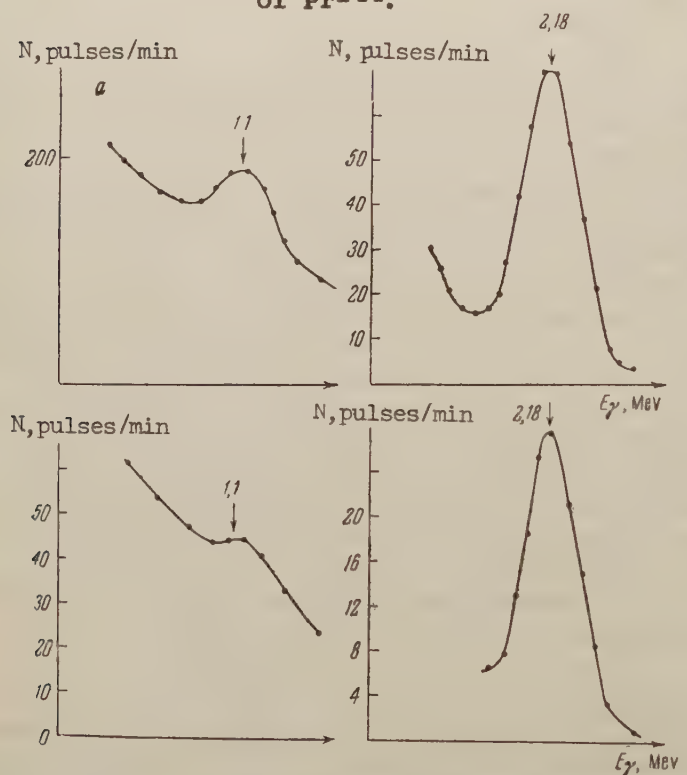

Fig.2. a) 1.1 and 2.18 Mev γ-lines recorded on the single-channel spectrometer without an absorber; b) the same γ-lines recorded under the same conditions but with a 4.5 cm Pb absorber.

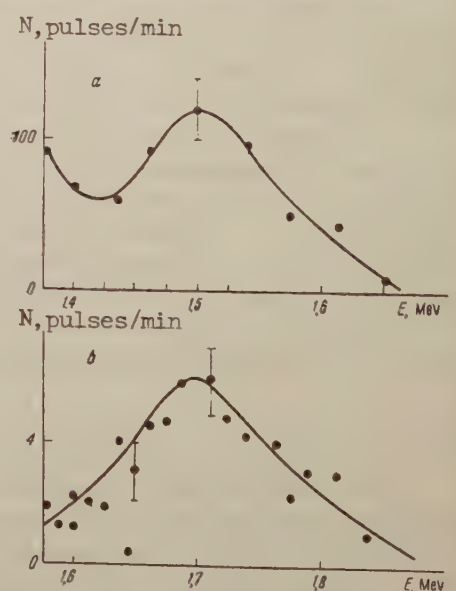

Fig.3. Pr^{144} coincidence spectrum (chance coincidences subtracted) obtained by means of the slow-fast coincidence circuit ($\tau = 5 \cdot 10^{-8}$ sec): a) with first channel set for the 0.7 Mev γ-line; second channel swept; b) with first channel gated for the 1.1 Mev γ-line

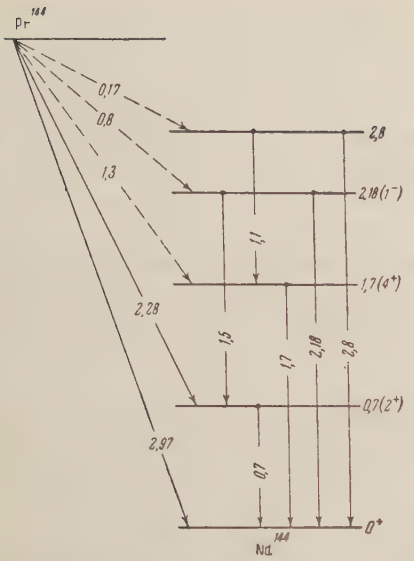

Fig.4. Decay scheme of Pr^{144}.

Decay scheme of Pr^{144}

The decay schemes proposed in Refs.2, 4 & 5 are similar as regards arrangement of part of the excited levels of Nd^{144} and apparently do picture the actual level diagram of Nd^{144}. Our results are not in conflict with these schemes, but they do allow of supplementing them in detail. Thus to situate the 2.8 Mev transition one must introduce a level with an appropriate energy which may be excited by a β-transition with an end-point energy of 200 kev. That such a β-component may exist is indicated by Cheng, John & Kurbatov[4]. In view of the coincidences between the 1.1 and 1.7 Mev γ-rays it may be assumed that these γ-rays are due to a cascade transition from the 2.8 Mev level. In analyzing the results on the coincidences of the 1.1 and 1.7 Mev γ-rays, we note that no other true coincidences should be observed (in the light of the extant decay schemes for Pr^{144}) in these energy intervals. In this case we have an alternate choice for the energy of the intermediate level, but in view of the data of Cork, Brice & Schmid[3] who observed a β-component with an end-point energy of 1.3 Mev, it is more plausible to place this level at 1.7 Mev. Emmerich, Auth & Kurbatov[8] speak of the possibility of a level with spin 4+ between 2.18 and 0.7 Mev. Thus the 1.1 Mev γ-transition may logically be situated between the 2.8 and 1.7 Mev levels. The proposed scheme is shown in Fig.4. Approximate balancing of the transition intensity does not conflict with the scheme.

Rh^{106}

Radioactive Rh^{106} is a member of the series $Ru^{106} \xrightarrow{\beta} Rh^{106} \xrightarrow{\beta} Pd^{106}$ occurring as a result of uranium fission. The half-life of Ru^{106} is 280 days, that of Rh^{106} is 30 sec.[1] The existence of an isomeric state of Rh^{106} with period of 117 min has been inferred.[12]

1. The β-spectrum of Rh^{106} has been investigated by Alburger[13] and Peacock[14]. It is reported to comprise components with end-point energies 3.53, 3.1, 2.44 and 2.0 Mev.

2. The γ-transitions in Rh^{106} have been investigated by a number of authors[13,15-19]. Gamma-rays of the following energies have been observed: 0.51, 0.624, 0.87, 1.045, 1.13, 1.55, 1.77, 1.96, 2.1, 2.42 and 2.66 Mev.

3. γ-γ Coincidences have been studied by Kraushaar & Goldhaber[18], Arfken, Klema & McGowan[20] and Klema & McGowan[21]. Coincidences between the 0.513 & 0.624 Mev γ-rays and the 0.513 & 1.045 Mev γ-rays are reported; there are no coincidences between the 0.87 & 1.045 Mev γ-rays.

4. The angular correlation of the γ-radiation was investigated repeatedly (Refs.18,21,23-26). The results show good agreement as regards multipole order assignments: 0.513 Mev - E2, 0.624 Mev - E2 and 1.045 Mev - E2 & M1.

Our results

We investigated the spectrum of Rh^{106} by means of the single-channel spectrometer and the 50-channel pulse height analyzer. The spectrum was studied in sections using appropriate lead absorbers and samples having different

activities. The γ-spectrum was investigated up to about 4.5 Mev. Sixteen γ-lines having the following energies were observed: 0.513, 0.624, 1.045, 1.13, 1.55, 1.77, 1.85, 1.96, 2.09, 2.28, 2.42, 2.93, 3.05 and 3.42 Mev. The respective relative intensities were 100, 50, 8, 1, 1, 1, 0.5, 0.3, 0.5, 0.07, 0.3, 0.1, 0.01, 0.008 and 0.005. The results are shown in Fig.5.

A second series of measurements was made after chemical purification of the Ru^{106} sample; the results were identical with those of the first series.

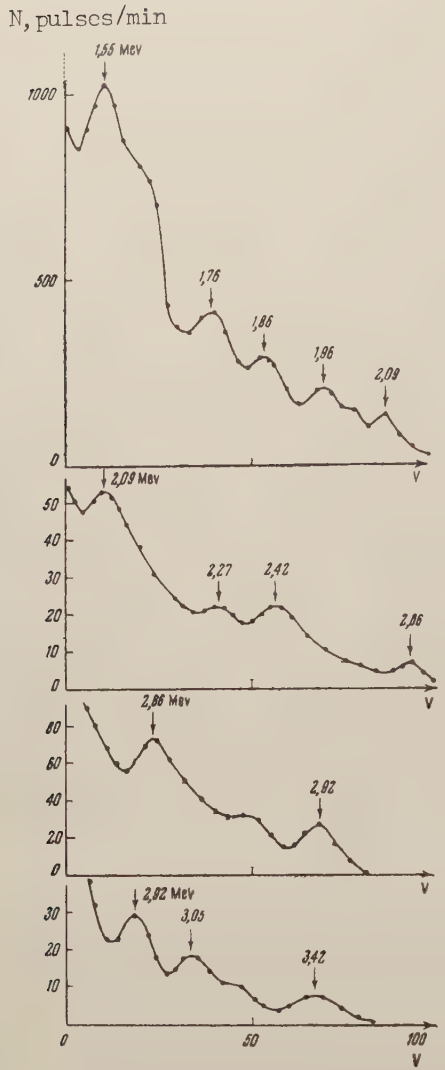

Fig.5. Sections of the γ-ray spectrum of Rh^{106} in the range from 1.5 to 3.5 Mev. The x-axis is scaled in pulse heights in volts. The sections overlap to permit comparison of intensities.

Decay scheme of Rh^{106}

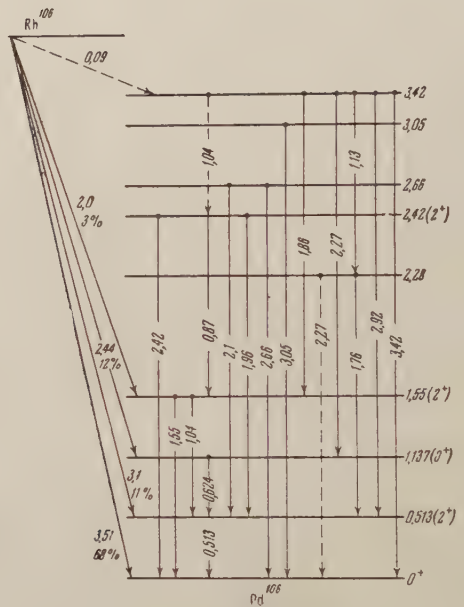

Fig.6. Decay scheme of Rh^{106}.

Analysis of the decay schemes for Rh^{106} given in the literature[15,18 & 19] shows that one may regard as reliably established the existence of the following excited levels of Pd^{106}: 0.513 Mev (2+), 1.137 Mev (0+), 1.55 Mev (2+), 2.28 Mev, 2.42 Mev (2+) and 2.66 Mev. The spin of the ground state of Pd^{106} is 0+ (even-even nucleus). In order to fit the 3.05 and 3.42 Mev γ-transitions into the decay scheme one must introduce a couple of levels with appropriate energies. The introduction of such levels is obviously predicated on the presence in the β-spectrum of Rh^{106} of components with end-point energies 0.1 and 0.14 Mev. The 1.76 and 1.85 Mev levels were introduced by Alburger[15] in order to account for the 1.24 and 1.85 Mev transitions observed by him in the decay of Ag^{106}; as was noted above, however, γ-rays of 1.85 Mev energy were observed by us in the decay of Rh^{106} and can be regarded as due to a transition between the 3.42 and 1.55 Mev levels in Pd^{106}. Similarly, the 1.76 Mev γ-rays may be associated with the transition between the 0.513 and the 2.28 Mev levels. In this case the existence of excited levels

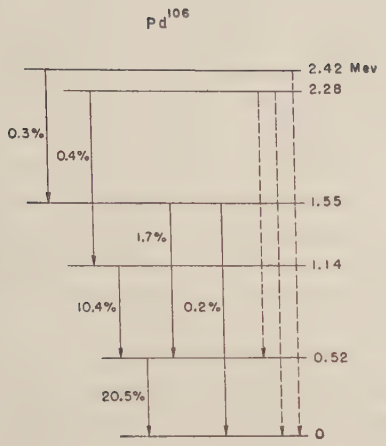

Fig.6a. Gamma-rays in the decay of Rh^{106} (from Kahn & Lyon[19]).

at 1.76 and 1.85 Mev is not necessary (but not excluded). The intensity balance in the decay scheme with the indicated arrangement of the transitions is satisfactory without the introduction of additional levels.

Thus the proposed decay scheme has the form shown in Fig.6.

Cs^{134}

Radioactive Cs^{134} is produced in neutron bombardment of natural Cs^{133}. Cs^{134} disintegrates by β^--decay into Ba^{134} with a period of 2.3 years.[1] The probability of β^+-decay to Xe^{134} is $\leqslant 0.1\%$; the probability of K-capture is $\leqslant 1\%$.

1. The β-spectrum of Cs^{134} has been investigated by a number of authors[27,30,33-36]; it is reported to comprise components with end-point energies of 0.083, 0.3, 0.655 and 0.683 Mev.

2. The γ-radiation of Cs^{134} was investigated in the work of Refs.27,30-36 & 43. Gamma-rays with energies of 1.96, 1.401, 1.368, 1.168, 1.039, 0.802, 0.796, 0.605, 0.569, 0.563, 0.475 and 0.200 Mev were observed. The relative intensities of these respective rays are $7 \cdot 10^{-5}$ (Ref.35), 0.1 (Ref.34), 2.5, 1.5, 1.0, 7, 93, 90, 16, 9 (Ref.31), and 1.8 (Ref.30).

3. β-γ coincidences were investigated by Keister et al[30] and Bertolini et al[36]. Coincidences of the 0.794, 0.604 and 0.569 Mev γ-rays with the β-spectrum of maximum energy were observed[30]. Also, there are reported to be coincidences of β-rays with end-point energies 0.33 and 0.69 Mev with the 1.37 Mev γ-rays.

4. γ-γ Coincidences were investigated by Bertolini et al[36] and Everett & Glaubman[38]. Coincidences between the following pairs of γ-rays were observed: 0.560 & 0.604 Mev, 0.604 & 0.800 Mev, 0.604 & 1.37 Mev and 1.17 & 0.8 Mev.

5. It follows from the work of Refs.27, 30, 38-41 that the following multipole order assignments obtain for the γ-rays from Cs^{134}: 0.604 Mev - E2, 0.796 Mev - E2, 0.801 Mev - E2, 0.475 Mev - E2 and 0.563 Mev - E2.

Our results

We investigated the γ-radiation from Cs^{134} in two energy intervals: 0 to 1.4 Mev and 1.3 to 2.1 Mev. In the former interval we observed peaks corresponding to γ-rays having energies of 1.37, 1.17, 1.039, 0.8, 0.6, 0.32, 0.21 and 0.1 Mev.

Interpretation of the peaks at 0.32, 0.21 and 0.1 Mev is difficult in view of the presence in this region of peaks due to back scattering and x-radiation.

In investigating the 1.3 to 2.1 Mev interval we encountered a number of difficulties stemming from the low intensity of the γ-radiation in this energy range, the low cross section for its interaction with the scintillator crystals and the presence of intense radiation in the adjacent lower-energy part of the spectrum. The investigation was carried out with sources having an activity up to 200-300 millicurie and with lead absorbers up to 10-12 cm in thickness.

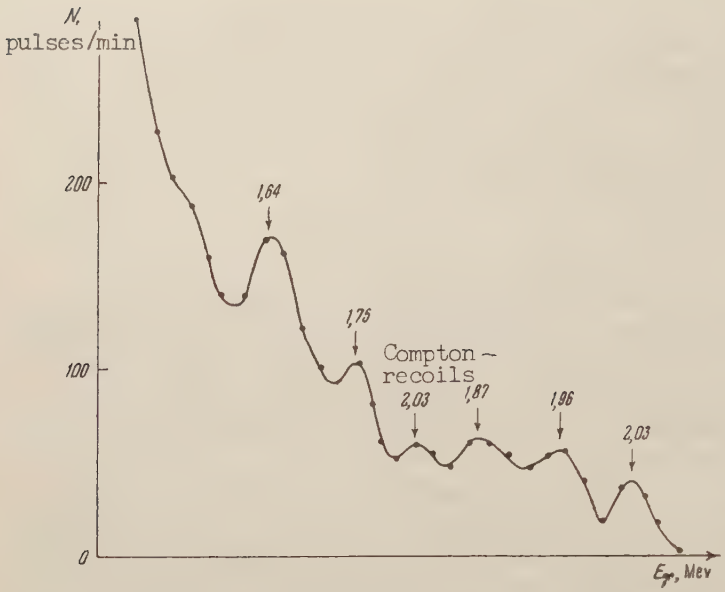

Fig.7. Section of the γ-spectrum of Cs^{134} in the 1.4 to 2.1 Mev interval recorded by means of the 56-channel analyzer.

As a result we detected a number of low intensity lines having energies of 1.64, 1.75, 1.87, 1.96 and 2.03 Mev. The appearance of the spectrum obtained on the 56-channel analyzer is shown in Fig.7.

Approximate evaluation of the intensity of these lines leads to a value of the order of 10^{-6} photons per decay for each of the lines in this hard region of the spectrum. We carried out a series of control experiments to check the possibility of formation of the observed peaks as a result of the additive effect of γ-rays of lower energies. Further the spectrum was again recorded after careful chemical repurification of the samples. Control experiments fully substantiated the above described results of the first series of measurements.

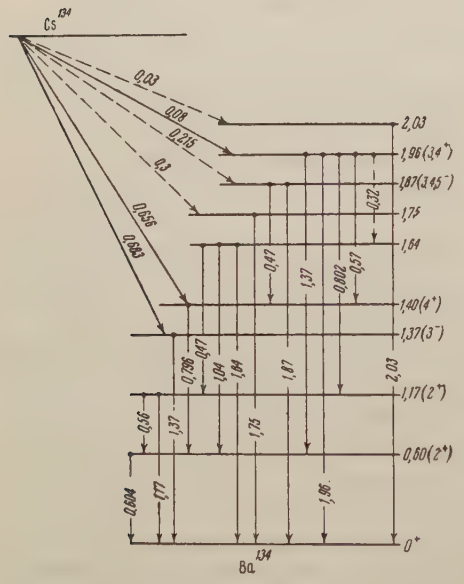

Fig.8. Decay scheme of Cs^{134}.

Decay scheme of Cs^{134}

The decay schemes for Cs^{134} proposed by different authors[27,30,31,34 & 36] contain much conflicting or contradictory data as regards both the arrangement of the excited levels of Ba^{134} and the level energies. Some of the proposed schemes (see, for example, Ref.34) do not allow of fitting in all the observed γ-transitions. There are insufficient data for determining the sequence of probable cascade γ-transitions.

The results of our work confirm the existence of a number of levels inferred or postulated earlier by different authors. The 1.64, 1.75, 1.85 and 2.03 Mev γ-transitions detected by us should be regarded as cross-over transitions from levels of these energies. There can be little doubt regarding the existence of the 0.6, 1.4 and 1.96 Mev levels included in their decay schemes by most authors. In the light of the latest data on the β-spectrum and β-γ coincidences, it would appear desirable to introduce a 1.367 Mev level and regard the 1.367 Mev γ-ray as being associated with a cross-over transition from this level to the ground state of Ba^{134}, particularly since Bertolini et al[36] observed coincidences of γ-rays of this energy with the β-spectrum component of end-point energy 0.69 Mev.

The 1.17 Mev level introduced by Cork et al[27] allows of fitting in a number of γ-transitions including that of 0.802 Mev energy for which there is no place in the decay schemes proposed in Refs.34 & 36.

Very recently Chandra[42] published the result of his work in which he observed coincidences of the 0.604 and 1.368 Mev γ-rays. Chandra carried out his measurements using a coincidence circuit with a resolving time of 10^{-8} sec. The obvious contradiction in the published coincidence investigations can be resolved by postulating the existence of two γ-transitions of close energies: either ~1.367 Mev or ~0.6 Mev.

The decay scheme for Cs^{134} based on all the currently available data is shown in Fig.8.

Central Scientific Research
Roentgen-Radiological Institute

References

1. A.N.Nesmeianov, A.V.Lapitskii & N.P.Rudenko, Poluchenie radioaktivnykh izotopov (Preparation of Radioactive Isotopes), M., 1954.
2. R.P.Schuman & A.Camilli, Phys.Rev., 84, 158 (1951).
3. J.M.Cork, M.K.Brice & L.C.Schmid, Phys.Rev., 96, 1295 (1955).
4. L.Cheng, G.John & J.D.Kurbatov, Phys.Rev., 85, 487 (1952).
5. D.E.Alburger & J.J.Kraushaar, Phys.Rev., 87, 448 (1952).
6. F.T.Porter & C.Sharp-Cook, Phys.Rev., 87, 464 (1952).
7. F.T.Porter & C.Cook, Phys.Rev., 85, 733 (1952).
8. W.S.Emmerich, W.J.Auth & J.D.Kurbatov, Phys.Rev., 94, 110 (1954).
9. W.E.Kuger & C.Sharp-Cook, Phys.Rev., 96, 1279 (1954).
10. C.Sharp-Cook, Bull.Amer.Phys.Soc., 29, 6, 20 (1954).
11. D.E.Alburger, E.der Mateosian & M.Goldhaber, Phys.Rev., 82, 332 (1951).
12. G.B.Baro, W.Seelman-Eggebert & I.E.Zabala, Z.S.f.Natur.wiss., 10a, 80 (1955).
13. D.E.Alburger, Phys.Rev., 88, 339 (1952).
14. W.C.Peacock, Phys.Rev., 72, 1049 (1947).
15. D.E.Alburger, Phys.Rev., 100, 1361 (1955).
16. D.E.Alburger, E.der Mateosian & M.Goldhaber, Phys.Rev., 82, 332 (1951).
17. R.W.Hayward, Phys.Rev., 86, 760 (1952).
18. J.J.Kraushaar & M.Goldhaber, Phys.Rev., 89, 1081 (1953).
19. A.H.Kahn, Bernd & W.S.Lyon, Phys.Rev., 92, 902 (1953).
20. G.B.Arfken, E.D.Klema & F.K.McGowan, Phys.Rev., 86, 413 (1952).
21. E.D.Klema & F.K.McGowan, Phys.Rev., 92, 1469 (1953).
22. M.Goldhaber & R.Hill, Rev.Mod.Phys., 24, 179 (1952).
23. R.M.Steffen, Phys.Rev., 80, 115 (1950).
24. A.H.Williams & M.L.Wiedenbeck, Phys.Rev., 78, 822 (1950).
25. F.Metzger & M.Deutsch, Phys.Rev., 78, 551 (1950).
26. R.M.Steffen, Phys.Rev., 86, 632 (1952).
27. J.M.Cork, J.M.Le Blank, W.N.Nester, D.W.Martin & M.Brice, Phys.Rev., 90, 445 (1953).
28. R.M.Kloepper, E.S.Lennox & M.L.Wiedenbeck, Phys.Rev., 88, 695 (1952).
29. A.W.Sunyar, J.W.Mihellich & M.Goldhaber, Phys.Rev., 95, 570 (1954).
30. G.L.Keister, E.B.Lee & F.H.Schmidt, Phys.Rev. 97, 451 (1955).
31. A.A.Bashilov, N.M. Anton'eva & B.S.Dzhelepov, Izv.AN SSSR, Ser.fiz., 18, 43 (1954).
32. H.H.Forster & J.S.Wiggins, Phys.Rev., 99, 660 (1955).
33. G.Bertolini, Nuovo Cimento, 1, 4, 744 (1955).
34. M.C.Joshi & B.V.Thosar, Phys.Rev., 96, 1022 (1954).
35. R.Wilson, Phys.Rev., 79, 1004 (1950).
36. G.Bertolini, M.Bettoni & E.Lazzarini, Nuovo Cimento, 2, 2, 273 (1955).

37. B.L.Robinson & L.Madansky, Phys.Rev., 84, 604 (1951).
38. A.E.Everett & M.J.Glaubman, Phys.Rev., 100, 955 (1955).
39. M.A.Waggoner, M.L.Moon & A.Roberts, Phys.Rev., 80, 420 (1950).
40. E.D.Klema, Phys.Rev., 100, 66 (1955).
41. M.G.Stewart, R.P.Scharenberg & M.L.Wiedenbeck, Phys.Rev., 99, 691 (1955).
42. J.Chandra, Proc.of the Indian Acad.of Sci., 14, sec.A, 4 (1956).
43. K.Gromov & B.Dzhelepov, Doklady AN SSSR, 85, 299 (1952).

ON THE RELATIVE INTENSITY OF Po^{210} γ-RAYS

- V.V.Ovechkin

Experimental evaluation of the relative intensity of the 803 kev γ-rays emitted from the first excited level of Pb^{206} in α-decay of Po^{210} is of undoubted interest. In view of the divergence in the data published prior to 1952 (Refs.1-3) we undertook[4] a repeat measurement of the ratio

$$k_\gamma = \frac{N_\gamma}{N_\alpha}. \qquad (1)$$

1. The polonium source was prepared by precipitation from a Po^{210} nitrate solution after repeated purification to remove all extraneous impurities. The source was sealed in a brass tube 8 mm long and 5 mm in diameter with a wall thickness of 0.5 mm and had an α-activity N^0_{Po} = 4.10 ± 0.5 microcurie according to a calorimetric determination.

Comparison of the γ-radiation intensities of the Po^{210} source and the reference Co^{60} source (N^0_{Co} = 5.63 ± 0.20 microcurie) was carried out by means of an end-window brass counter with an outside diameter of 20 mm; the 12 mm diameter window of the counter was covered with a 1.5 mm thickness of brass for absorption of the conversion electrons (E = 710-800 kev) and the 75 kev x-ray quanta emitted by Po^{210}. In calibrating the cobalt source with reference to β-γ coincidences an appropriate correction for γ-γ coincidences was made.

The ratio of the counting rates obtained at different distances from the counter, as determined in order to exclude the influence of the geometry, was $n_{Po}:n_{Co}$ = 2.24 ± 0.04. Bearing in mind the data of Bradt[5] et al on the efficiency of a brass counter for energies of 1.25 and 0.8 Mev ($\epsilon_{1.25}:\epsilon_{0.8}$ = = 1.85 ± 1.5%) and taking into account the self-absorption of the Po^{210} γ-rays (~ 7.5%), using the formula

$$k_\gamma = \frac{2N^0_{Co}\varepsilon_{1,25}n_{Po}}{N^0_{Po}\varepsilon_{0,8}n_{Co}}, \qquad (2)$$

we finally obtain $k_\gamma = (1.22 \pm 0.09)\cdot 10^{-5}$ quanta per decay.

2. The results of determinations of k_γ published to date by different authors are summarized in the accompanying table.

Authors	Year	$k_\gamma \cdot 10^5$	Method of α-detection
Grace et al[1]	1951	1.80 ± 0.14	Ionization chamber
Barber et al[2]	1952	1.5 ± 0.4	Scintillation counter
Riou[3]	1952	1.6 ± 0.2	Calorimeter
Our data[4]	1952	1.22 ± 0.09	"
Shintl'meister & Kunts	1952	1.32 ± 0.08	"
Shimanskaia[6]	1954	1.2 ± 0.2	"
Hayward et al[7]	1955	1.21 ± 0.06	Scintillation counter
Rojo et al[8]	1955	1.2 ± 0.1	"
Ascoli et al[9]	1956	1.21 ± 0.08	

As was recently shown by Shimanskaia[6], who discusses the results of only five investigations (Refs.1-3,6 & 7), the elevated values obtained in the first three investigations are apparently due to the inadequate accuracy of measurements of high α-intensities directly by counting particles. That our data are in good agreement with later determinations substantiates Shimanskaia's conclusion.

Averaging the results of the last six investigations listed in the table, we obtain as a weighted average $\bar{k}_\gamma = (1.21 \pm 0.05) \cdot 10^{-5}$ quanta per decay (the 0.05 is the root mean square error of these measurements). It will be seen that except for the data of Shintl'meister & Kunts (private communication), all the other five results are in good agreement with this mean value.

Taking into account the experimentally determined[10] value of the conversio coefficient for Po^{210} γ-rays ($\alpha = 0.015 \pm 0.002$), the relative intensity of the short-range group of 4.5 Mev α-particles from Po^{210} is $(1.23 \pm 0.05) \cdot 10^{-5}$.

3. Inasmuch as the Po^{210} nucleus is almost spherical in shape, the decisive factor as regards inhibition of α-decay to the second excited level of Pb^{206} ($E'' = 1.34$ Mev)[11] is the low energy of the corresponding α-particles; hence for evaluation of their intensity one may use the approximate Geiger-Nuttall relation in the form

$$\log \lambda = C - \frac{D}{\sqrt{E}} \qquad (3)$$

where λ is the probability of α-decay in sec^{-1}, E is the α-particle energy in Mev and C and D are constants pertaining to the isotopes of each α-active element. Specifically, Bohr, Fröman & Mottelson[12] recommend using C = 50.15 and D = 128.8 for polonium isotopes (Z = 84).

In the case of Po^{210}, however, it is more expedient to determine D from Eq.(3), using the experimentally determined ratio of the intensities of the first short-range and principal group of α-particles ($1.23 \cdot 10^{-5}$:1) and their energies ($E_\alpha^1 = 4.5$ and $E_\alpha^0 = 5.3$ Mev); in this case the constant C is automatically excluded. We obtained D = 132.6, which is somewhat higher than the recommended value.

Taking into account our value of D, the relative intensity of the second group of α-particles ($E_\alpha'' = 3.96$ Mev) is found to be $1.3 \cdot 10^{-9}$, whereas if we take D = 128.8, the relative intensity turns out to be $2.3 \cdot 10^{-9}$. In any case it is virtually impossible at present to detect so negligibly low an intensity of α-particles; more hopeful may be a search for the corresponding γ-rays ($E_\gamma'' = 534$ kev) emitted in cascade with the 803 kev γ-rays.[11]

I am grateful to Z.V.Ershov and E.M.Tsenter for their interest in the work and discussion of the results.

References

1. M.A.Grace & R.A.Allen, et al, Proc.Phys.Soc., 64A, 493 (1951).
2. W.C.Barber & R.H.Helm, Phys.Rev., 86, 275 (1952).
3. M.Riou, Journ.phys.et rad., 13, 244 & 487 (1952).
4. V.V.Ovechkin, Otchet (Report) USSR Academy of Sciences, 1952.
5. Bradt, et al, Helv.Phys.Acta, 19, 77 (1946).
6. N.S.Shimanskaia, Zhur.eksp.i teor.fiz., 31, 174 (1956).
7. R.W.Hayward, D.D.Hoppes & W.B.Mann, Jour.Res., Nat.Bur.Stand., 54, 1, 47 (1955).
8. O.Rojo, M.A.Hakeem & M.Goodrich, Phys.Rev., 99, 1629 (1955).
9. A.Ascoli, M.Asdente & E.Germagnoli, Nuovo Cimento, 10, 4, 946 (1956).
10. V.V.Ovechkin, Thesis, 1954; V.V.Ovechkin & E.M.Tsenter, Atomnaia energiia (Atomic energy), 2, 282 (1957).
11. D.E.Alburger & M.H.L.Pryce, Phys.Rev., 92, 514 (1953).
12. A.Bohr, P.O.Fröman & B.R.Mottelson, Dan.Mat.Fys.Medd., 29, 10 (1955).

INVESTIGATION OF THE LIFETIMES OF LOWER NUCLEAR LEVELS EXCITED IN ELECTRON CAPTURE

- E.E.Berlovich, K.M.Gvotovskii, M.P.Bonits, B.I.Breslav & B.K.Preobrazhenskii

Introduction

Experimental measurements of the lifteimes of excited states of nuclei - essentially direct determination of the probability of transitions between two nuclear levels - has proved to be a powerful tool in the investigation of nuclear structure.[1-2]

The present work was devoted to determination of the lifetimes of the states of certain nuclei formed as a result of orbital electron capture. All the parent nuclei are numbered among the neutron-deficient nuclei produced by spallation under bombardment by high energy protons. Specifically, the parent nuclei Tm^{167}, Eu^{147} and Gd^{145} were obtained in a tantalum target by irradiation with 660 Mev protons on the synchrocyclotron at the Joint Institute for Nuclear Research. The thulium, europium and gadolinium sources were prepared by chromatographic separation. The parent Ir^{190} nuclei were obtained by irradiation of a bismuth target from which they were separated by means of an iridium carrier.

Experimental Procedure

The lifetime measurements were carried out by the method of delayed coincidences on a set-up described earlier by one of us[2-4]. This set-up which includes a "fast" coincidence circuit with a variable spiral delay line and a "slow" triple coincidence circuit, differs from the set-up of Bell, Graham & Petch[5] by the incorporation in the side channels of the triple coincidence network of differential pulse height analyzers which allow of energy discrimination of the coinciding radiations.

It was shown in an earlier contribution by one of the authors[2] that the shape and position of the coincidence curve may be affected by the character of the pulse varying under the influence of the coinciding radiations, which leads to distortion of the pulse, particularly in the case of short times. It was indicated that to eliminate this effect one can either carry out coincidence measurements with energetically equivalent intervals or when this is impossible determine the coincidence curve for the investigated transition and for a prompt transition in the same intervals even though these are not energetically equivalent.

In the present experiments we measured coincidences between characteristic x-rays and γ-rays (x-γ and γ-x coincidences) or with internal conversion electrons (x-e and e-x coincidences). The end-point energy of the recoil electrons produced in the phosphor under the influence of characteristic x-rays amounts to less than 8 kev for the rare earth elements, which in some of the investigated cases is appreciably lower than the energy of the conversion electrons and the energy of the recoil electrons produced in the phosphor by the γ-rays. Hence it was not always possible to carry out the measurements in energetically equivalent intervals.

In measuring the coincidences between the electromagnetic radiations the method of "self-comparison" which had been employed previously[2] for measuring β-γ (or e-γ or e-β) coincidences and consisting of comparing the coincidence curves obtained with two positions of the β-ray (or conversion electron) absorber, was replaced by another procedure which will be described below.

In the present investigation an additional difficulty arose owing to the presence of a large number of additional types of coincidences in addition to those investigated: for example, coincidences of conversion electrons with the x-rays accompanying them, coincidences of x-rays accompanying K-capture with x-rays accompanying conversion or with Auger electrons and the like.

In the measurements we used FEU-IV type photomultiplier tubes which have 10 aluminum-magnesium alloy dynodes arranged in a circle and a flat end-type semitransparent cesium antimony photocathode. The pulse rise time of these photomultipliers is $1\text{-}2\cdot10^{-9}$ sec.[6] We worked at voltages of 2600-2700 V. The resolving time of the coincidence circuit in working with stilbene crystals was $2\text{-}3\cdot10^{-9}$ sec.

Measurements

A. $Tm^{167} \rightarrow Er^{167}$ transition

The source was prepared by evaporation of a drop containing the thulium fraction from the ion column on an aluminum foil.

The measurements were carried out a month after proton bombardment when all the 8-hour (Tm^{166}) and 1-day (Tm^{165}) activities had died out and the persisting activity was due virtually entirely to Tm^{167} with a period of 9.6 days. The activity of 100-day Tm^{168} in the sample was negligibly small. The decay scheme of Tm^{167} proposed by Gromov, Dzhelepov & Preobrazhenskii[7] and subsequently confirmed by Gorodinskii et al[8] is shown in Fig.1. The 207 Mev state is isomeric. The de-excitation of the upper level occurs only by a 56.7 kev transition to the 207 kev state.

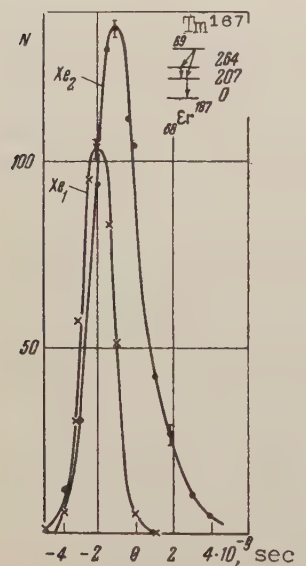

Fig.1. Coincidence curves: xe_2 - for the 56.7 kev transition; xe_1 - for the 207 kev transition. Insert - decay scheme. Here and in the other figures the abscissae are delay times in secs; the ordinates - numbers of coincidences.

We measured coincidence between the x-rays and the conversion electrons (47 kev) from the L shell of Er^{167} for the 56.7 kev transition. For detecting the x-rays we used a stilbene single crystal (d = = 35 mm; h = 20 mm) in a glass envelope with a magnesium oxide reflector. The glass completely absorbed all conversion and Auger electrons. The conversion electrons were detected by a stilbene plate 5 mm thick covered with a 1 μ thick aluminum foil reflector. The stilbene crystals were bonded to the photocathode windows by means of clear petroleum jelly.

The requisite energy intervals were selected in each channel (branch) of the coincidence system by means of appropriate differential analyzers.

By virtue of the high amplification of the photomultipliers at the operating voltages utilized, it was feasible to obtain sufficiently strong pulses (for shaping in the limiting pentode) from the recoil electrons produced by the x-rays in the stilbene crystal.

Fig.1 shows the coincidence curve obtained in the case when the electron gate was set for the pulse height of the conversion electrons from the 56.7 kev transition (curve xe_2); it will be seen that the right side of the curve has an exponential shape.

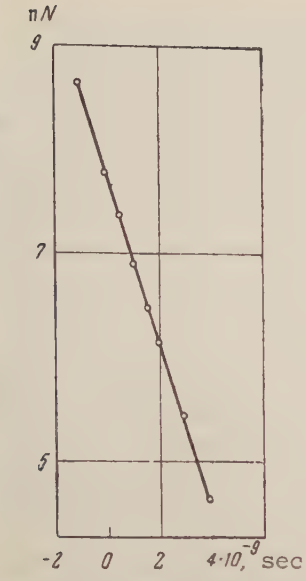

Fig.2. Exponential portion of the xe_2 curve of Fig.1 plotted in semilogarithmic coordinates.

This exponential section of the curve, investigated separately with good statistical accuracy, is shown plotted in semilogarithmic coordinates in Fig.2. From this curve we obtain a value of $(2.0 \pm 0.5) \cdot 10^{-9}$ sec for the half-life. The excess "prompt" coincidences mentioned at the end of the "Experimental Procedure" section above correspond to the region of short delays near the peak of the curve in Fig.1.

For control purposes we carried out measurements of the coincidences between the x-rays and conversion electrons associated with the 207 kev transition. Inasmuch as the 207 kev level is isomeric, there should be no coincidences of the capture x-rays with conversion electrons from the 207 kev transition. There should, however, be "prompt" coincidences of these electrons with the x-rays accompanying the conversion. The coincidence curve for these electrons is shown in Fig.1 (curve xe_1); in contrast to curve xe_2, the shape of this curve is symmetrical.

By virtue of the fact that the lifetime (which proved to be comparitively large) was determined not from the relative displacement of the curves but from the exponential branch of the coincidence curve, the influence of the energy difference between the effective intervals in the two branches of the circuit was relatively small.

B. $Gd^{145} \rightarrow Eu^{145}$ transition

Our measurements with a gadolinium source having a period of 60 days (this period was attributed by Gorodinskii et al[10] to Gd^{145}) were performed 3 months after irradiation when the ~1.5-day (Gd^{147}) and 9-day (Gd^{149}) activities were virtually exhausted.

According to the data of Gorodinskii et al[10] and Anton'eva et al[11] electron capture in Gd^{145} is accompanied by two γ-transitions of equal energy (115 kev) in cascade. The radiation from the daughter Eu^{145}, consisting of one γ-ray of high energy, does not interfere with measurements of the type in question. In the amplitude spectrum of the Compton distribution this radiation is evinced in the form of a low intensity long tail following the end of the principal Compton recoil distribution from the 115 kev γ-rays.

We measured coincidences the x-γ and γ-x type by means of two large (d = = 35 mm; h = 20 mm) stilbene crystals in containers. The effective gate of the amplitude analyzer in the γ-ray channel was set for an appropriate section of the Compton recoil distribution. In one group of measurements the γ-rays were recorded by the right-hand counter (x-γ coincidences); in the other series of measurements by the left-hand counter (γ-x coincidences). The experimentally observed relative displacements of the two coincidence curves could be due to two factors: a) a difference between the pulse fronts due to a difference in the amplitude intervals in the γ-ray or x-ray channel (displacement to the side of the x-ray detector, for, as was shown in Ref.2, the apparatus shift always occurs to the side of the detector registering the rays or particles of lower energy) and/or b) an appreciable lifetime of the level (displacement to the side of the γ-ray detector inasmuch as the delay is introduced into the channel carrying the radiation preceding the excitation of the level). In order to exclude the effect of the first "procedure" factor, in addition to

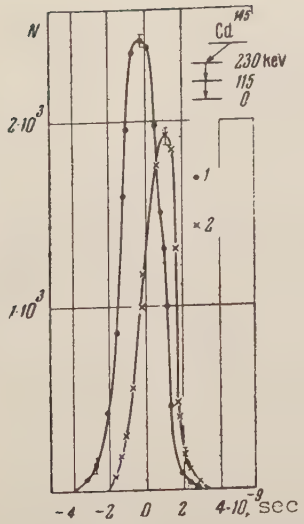

Fig.3. Decay of Gd^{145} to Eu^{145}. Coincidence curves: 1) x-γ and 2) γ-x.

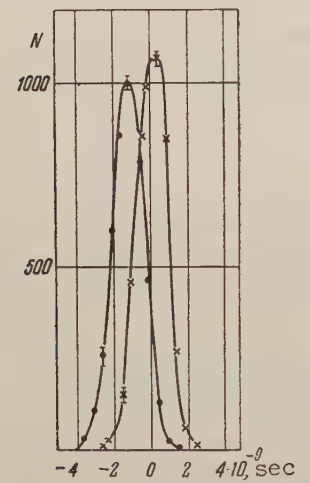

Fig.4. Coincidence curves for $Co^{60}\rightarrow Ni^{60}$ obtained with light filters.

the measurements with the investigated source, we carried out measurements (using the same intervals) of the γ-γ coincidences associated with the $Co^{60}\rightarrow Ni^{60}$ transition which was chosen because according to the work of Metzger[12] the lower level of Ni^{60} has a very short lifetime ($\tau = 10^{-12}$ sec). Inasmuch as the end-point energy of the Compton electrons from the γ-rays of Ni^{60} is almost 30 times higher than the energy of the Compton distribution for the investigated γ-rays with the result that the height of the pulses arriving (after amplification) at the differential analyzers exceeded the operating range of the analyzers, light filters were installed between the scintillator crystals and the phosphors; these were selected so that the extent of the amplitude distribution for the Ni^{60} γ-rays would be close to that for the investigated Eu^{145} γ-rays.

The results of our measurements for the $Gd^{145}\rightarrow Eu^{145}$ and $Co^{60}\rightarrow Ni^{60}$ transitions are shown in Figs.3 & 4.

We determined the relative displacements of the centers of gravity of each pair of curves (method of Bay[13]); these proved to be $2\tau' = 2.1\cdot10^{-9}$ sec for the $Gd^{145}\rightarrow Eu^{145}$ transition and $2\tau'' = 3.1\cdot10^{-9}$ sec for the $Co^{60}\rightarrow Ni^{60}$ transition. The smaller value of the displacement in the former case indicates that the lifetime of the Eu^{145} levels has a measureable value (the displacement associated with the lifetime is directed to the side opposite to that of the apparatus shift). The difference between the two displacements gives double the lifetime: $2\tau = 1.0\cdot10^{-9}$ sec.

Finally, we arrived at the value $\tau = (5.0 = 10^{-10}$ sec.

The reliability of this value is substantiated, on the one hand, by numerous repeated determinations and, on the other hand, by analogous measurements with a europium source carried out in the same effective intervals which did not give any displacement of the curves (see below). We made an attempt to attribute the determined lifetime to one of the two levels of Eu^{145}. To this end we recorded the γ-γ coincidence curve for this transition in energetically equivalent amplitude intervals located outside the x-ray region; the shape (slope of the sides) of this curve was compared with that of the $Co^{60}\rightarrow Ni^{60}$ transition recorded under the same conditions. There was no detectable difference as regards the slopes of the curve sides. Nevertheless, in view of the very small value of the lifetime obtained we cannot unequivocally assert that the determined lifetime is not associated with the lower level.

C. $Eu^{147}\rightarrow Sm^{147}$ transition

The investigated europium fraction, which was separated from the gadolinium fraction after complete exhaustion of the ~1.5-day Gd^{147}, contained only

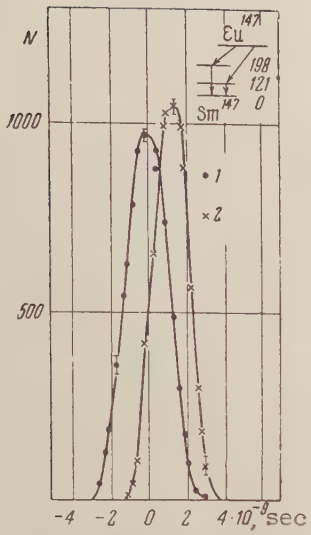

Fig.5. Eu^{147}. Coincidence curves: 1) x-γ and 2) γ-x.

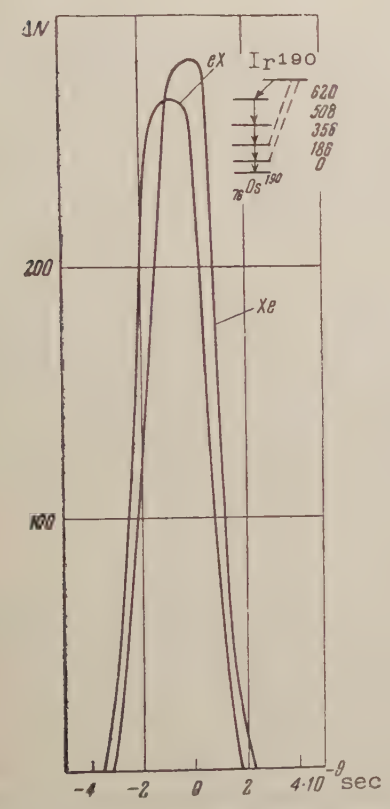

Fig.6. Ir^{190} e-x and x-e coincidence curves obtained as the differences between the experimental curves (ex + xγ + γx + $\gamma\gamma$) - (γx + xγ + $\gamma\gamma$) and (xe + xγ + γx + $\gamma\gamma$) - (γx + xγ + $\gamma\gamma$), respectively. The averaged initial curves rather than the experimental points per se were used in plotting the e-x and x-e curves.

24-day Eu^{147}.

The decay scheme of Eu^{147} established in the experiments of Gorodinskii et al[10] and Anton'eva et al[11] is shown in Fig.5. No transition is observed between the 198 kev and 121 kev levels.

We measured the lifetime of the lower (121 kev) level whose energy is very close to the energy of the γ-rays of the $Gd^{145} \rightarrow Eu^{145}$ transition (115 kev). We measured x-γ and γ-x coincidences; the effective gate of the analyzer in the γ-ray channel was set far from the maximum of the Compton recoil distribution due to the 198 kev γ-rays so that the influence of the upper transition on the result of measurement was minimal.

From the very start, the experiments with Eu^{147} and Gd^{145} were correlated: a) the measurements were carried out in the same amplitude intervals with all other conditions being equal and b) the measurements with the Co^{60} source were always performed in the interval between measurements with the isotopes. Hence, in calculating the lifetime in the case of the europium source we could use the same results for cobalt as in the case of the gadolinium source.

The displacement of the centers of gravity of the curves (x-γ and γ-x coincidences) obtained with a europium source (Fig.5) was virtually identical with the displacement of the curves for the cobalt source (in contrast with the result obtained for the gadolinium source). These measurements, which at the same time, served as a check on the validity of the results obtained for Eu^{145}, yielded a value of $2 \cdot 10^{-10}$ sec for the upper bound of the lifetime of the 121 kev level of Sm^{147}.

D. $Ir^{190} \rightarrow Os^{190}$ transition

Electron capture by Ir^{190} results in excitation of rotational levels of the deformed Os^{190} nucleus.[14]

We felt it would be of interest to measure the lifetime of the first excited state of 186 kev energy (Fig.6) with a view to determining the internal quadrupole moment of Os^{190}.

The iridium solution was applied to filter paper which was cemented to an aluminum backing 2 mm thick.

It proved expedient to carry out measurements of the x-e and e-x type for the following reasons: 1) the conversion coefficient for the lower transition is rather large (~0.63) - in fact, a whole order of magnitude greater than

the sum of the conversion coefficients for all the higher lying transitions - and 2) the fraction of conversion electrons from the higher transition whose pulses pass through the analyzer gate set for recording the electrons from the lower transition is insignificant in consequence of the large difference between the energies of the electrons of the two groups.

By virtue of the relatively large thickness of the source, in which the energy spectrum conversion electrons was smeared out due to multiple scattering, it proved possible to carry out the measurements in energetically equal intervals situated in the region of the Compton distribution from the x-rays.

The measurements were carried out by means of two unpackaged stilbene crystals with reflectors of 1μ thick aluminum foil. In view of the fact that in addition to e-x type coincidences there were recorded γ-x and γ-γ coincidences for each of the two orientations of the source on its backing, the measurements were carried out with an open source and with a thin foil for absorbing conversion electrons of the investigated transition. The coincidences with electrons were obtained as the difference between the counts in the two cases.

The results obtained for the x-e and e-x coincidences are shown in Fig.6. The value obtained for half the displacement of the centers of gravity of the curves was $(3.6 \pm 1.5) \cdot 10^{-10}$ sec. It can be shown, however, for obtaining the mean lifetime this value must be multiplied by a factor of 2.

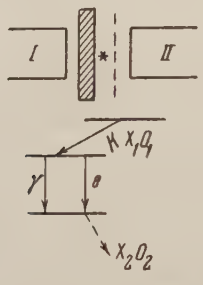

Fig.7. X_1 and O_1 - x-rays and Auger electrons accompanying K capture; X_2 and O_2 - x-rays and Auger electrons accompanying conversion. I & II - photomultipliers; the star represents the source; the shaded rectangle is the backing; vertical dash-line - thin foil absorber.

Let us consider the case when the source is oriented with the thick backing to the left as shown in Fig.7. Let us denote the x-rays and Auger electrons accompanying K capture by X_1 and O_1 and the x-rays and Auger electrons accompanying internal conversion by X_2 and O_2, respectively. Then under our conditions (after subtraction of the number of coincidences obtained with the thin absorber foil at the right), we will have recorded coincidences of the following types:

$$\underrightarrow{X_1e},\ \underrightarrow{X_1O_2},\ \underline{X_2e} \text{ and } \underleftarrow{X_2O_1};$$

the arrows above indicate the direction of displacement of the corresponding coincidence curve; the bar indicates no displacement.

Let us designate the solid angles of the left and right counters by ω_1 and ω_2, respectively, their efficiency in detecting x-rays by ε, fraction of transitions following the conversion branch by $K = \alpha/(\alpha - 1)$, where α is the conversion coefficient, the fluorescent yield through W and the number of decays from the source per unit time through M; then assuming that all the radiations are isotropic, the number of recorded coincidences of each type can be written as

$$1)\ C(\underrightarrow{X_1e}) = N\omega_1\omega_2 W\varepsilon K,$$

$$2)\ C(\underrightarrow{X_1O_2}) = N\omega_1(1-\omega_2)\omega_2 W(1-W)\varepsilon K,$$

$$3)\ C(\underline{X_2 e}) = N\omega_1\omega_2 W\varepsilon K,$$

$$4)\ C(\underset{\leftarrow}{X_2 O_1}) = N\omega_1(1-\omega_2)\omega_2 W(1-W)\varepsilon K.$$

The number of coincidences of the second and fourth types will be small inasmuch as for the Z = 76 case, 1 - W = 0.05 (Bergström[15]); moreover the two numbers will be equal and tend to produce displacements of the center of gravity of the coincidence curve in opposite directions, i.e., nullifying each other. The coincidences of the third type are "prompt" and, consequently, their centers of gravity are not displaced. They have a tendency to reduce the displacement of the center of gravity of the resultant coindicence curve. Inasmuch as the number of these coincidences is exactly the same as the number of $X_1 e$ coincidences of interest to us, the experimentally observed displacement of the center of gravity of the coincidence curve will be halved. Consequently, for the experimental value of the lifetime of the first excited state of Os^{190} we must take

$$\tau = (7.2 \pm 3.0)\cdot 10^{-10} \text{ sec}$$

or

$$T_{1/2} = (5.0 \pm 2.1)\cdot 10^{-10} \text{ sec}.$$

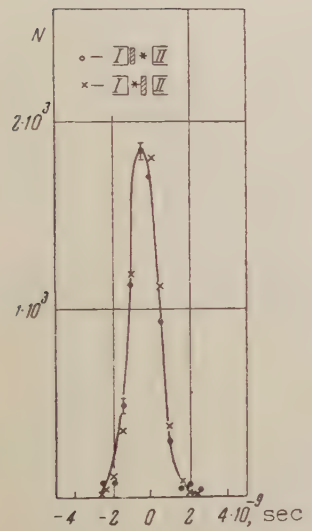

Fig.8. Coincidence curves obtained for Co^{60} with light filter. Designations same as in Fig.7.

Fig.8 shows the result of the control experiment carried out with a Co^{60} source with the same equivalent effective intervals as used with the Ir^{190} source but with a light filter. It will be seen that the points for the β-γ and γ-β coincidences fit well on the same curve.

Discussion

In cases when the multipole orders of the transitions are known certain information regarding the structure of the nucleus can be deduced from the experimentally determined lifetimes of the states.

According to the data of Gromov et al[7] the 56.7 kev transition in Er^{167} is a mixed transition characterized by 25% E2 + 75% M1. Utilizing the interpolation tables of Dranitsyna[16] for the L shell conversion coefficients (tables based on Rose's[17] data), we obtain for the given transition $\alpha_L = 5.05$ or $\alpha_{total} = 6$. Then for the radiative half-life we have

$$T_\gamma = T_{exp.}(1+\alpha) = 2.0\cdot 7\cdot 10^{-9} = 1.4\cdot 10^{-8} \text{ sec}.$$

For the partial radiative half-lives we obtain

$$T_\gamma(E2) = 5.6\cdot 10^{-8} \text{ sec}$$

and

$$T_\gamma(M1) = 1.87\cdot 10^{-8} \text{ sec}.$$

Calculations according to the formulas of Weisskopf[18] based on the single-particle model yield

$$T_{\gamma,W}(E2) = 1.73 \cdot 10^{-5} \text{ sec}$$

and

$$T_{\gamma,W}(M1) = 1.2 \cdot 10^{-10} \text{ sec.}$$

Thus the electric quadrupole transition proves to be greatly "speeded up". The "acceleration" factor

$$F = \frac{T_{\gamma,W}(E2)}{T_{\gamma}(E2)} = \frac{1.73 \cdot 10^{-5}}{5.6 \cdot 10^{-8}} = 310.$$

This is entirely natural for the Er^{167} nucleus which contains 17 neutrons outside the last closed shell and is among the highly deformed nuclei.

On the contrary, the magnetic dipole transition proves to be greatly slowed down. Here the retardation factor

$$F = \frac{T_{\gamma,W}(M1)}{T_{\gamma}(M1)} = \frac{1.2 \cdot 10^{-10}}{1.87 \cdot 10^{-8}} = 6.7 \cdot 10^{-3} \approx \frac{1}{160}.$$

This transition obviously belongs in the group of slow magnetic dipole transitions.[19] The slowing down is apparently connected with the collective nature of such magnetic transitions.

Gromov et al[7] assign a spin and parity of 1/2- to the 207 kev state of Er^{147} and characterize the 267 kev state as 1/2+, 3/2+ or 3/2-. Gorodinskii et al[8], however, indicate that the 3/2- assignment is the most probable.

In the case of the deformed Er^{167} nucleus (17 neutrons outside the last filled shell) the assumption that the rotational band begins with the first excited level and that the component of the total angular momentum along the nuclear symmetry axis $\Omega = 1/2$ leads to a value of $17 \cdot 10^{-24}$ cm^2 for the internal quadrupole moment Q_0. This is appreciably lower than the value of the quadrupole moment in the given mass number region ($Q_0 \approx 8 \cdot 10^{-24}$ cm^2).

It is not impossible that this divergence is to be explained by the inaccuracy of the above mentioned proportion of 25% E2 and 75% M1 for the mixed transition given in Ref.7 and that the actual percentage of E2 type transitions is appreciably lower.

Interpretation of our experimental results for the $Gd^{145} \rightarrow Eu^{145}$ transition is impossible not only because nothing is known regarding the multipole order of Eu^{145} γ-transitions but also because there is uncertainty as regards identification of the investigated γ-rays (115 kev). According to the data of A.A.Bashilov there exist two 5-day activities of Eu: one of them apparently belongs to Eu^{145}, the other to some other europium isotope.

The value for the upper bound of the lifetime of the first excited state of Sm^{147} deduced above, upon the assumption that the transition is (E2 + M1) leads to an appreciably higher value for the upper bound for the radiative lifetime taking conversion into account, namely, $\tau_{\gamma} \leqslant 5 \cdot 10^{-10}$ sec.

Calculations carried out by means of Weisskopf's formula yield

$$T_{\gamma,W}(M1) = 1.8 \cdot 10^{-11} \text{ sec}$$

and

$$T_{\gamma,W}(E2) = 6.7 \cdot 10^{-7} \text{ sec.}$$

Inasmuch as the Sm^{147} nucleus, which has only three neutrons outside the last filled shell, is a spherical nucleus, the "acceleration" factor for E2 type transitions must be equal to about 10. On the other hand, M1 type transitions, as a rule, are slowed down by a factor of 2 orders or more. In this case, it

is apparent that our result for the upper bound of the lifetime is in conflict with the assumption that the radiation is of the mixed E2 + M1 type.

Calculations of the same kind carried out for E1 and M2 transitions showed that the experimental bound for the lifetime is not in conflict with almost pure E1 ($\tau_{\gamma,W}(E1) \approx 2.6 \cdot 10^{-13}$ sec), if one allows for the fact that transitions of this type can be slowed down by 3 orders of magnitude as, for example, is reported[20] to be the case for the 146 kev transition in Lu^{177}. The E1 assignment, however, is not consistent with the value of the K/L ratio which according to the measurements of A.A.Bashilov equals ~3.5 (theoretically it should be appreciably higher for an E1 transition).

From the observed value of the mean lifetime of the first excited state of Os^{190}, taking into account conversion on all shells (the conversion in the K shell was calculated from tables of Sliv and Band[21]) and taking $\alpha = 0.71$, we obtain $\tau_\gamma = 1.2 \cdot 10^{-9}$ sec. Calculations according to Weisskopf's formulas yield $\tau_{\gamma,W}(E2) = 5.6 \cdot 10^{-8}$ sec and an "acceleration" factor $F \approx 47$. Utilizing Bohr's formula[1] for even-even nuclei

$$B(E2) = \frac{15}{32\pi} \cdot e^2 Q_0^2 \frac{(I+1)(I+2)}{(2I+3)(2I+5)},$$

for the given probability, we obtain $Q_0 = (4.2 \pm 0.9) \cdot 10^{-24}$ cm^2 and for the deformation parameter

$$\frac{\Delta R}{R_0} = \frac{5Q_0}{4zR_0^2} = 0.14,$$

instead of 0.3 in the region of large deformations.

In the case of Os^{186} and Os^{188}, which have 110 and 112 neutrons, respectively, the internal quadrupole moments are equal to $5.5 \cdot 10^{-24}$ cm^2 and $5.1 \cdot 10^{-24}$ cm^2, respectively.[22] In this region nuclear deformation already decreases with filling of the last shell and upon the addition of two more neutrons, i.e., upon going to Os^{190}, it should become even smaller. The decrease, in fact, is observed to be appreciable, for in going from 114 neutrons (Os^{190}) to 116 neutrons (Os^{192}), the deformation increases with a jump and the rotational structure of levels transforms into the vibrational one.[23]

The authors desire to express their gratitude to B.S.Dzhelepov, A.A.Bashilov and A.N.Murin and their co-workers for taking the trouble to familiarize themselves with our experimental data prior to publication. We are indebted to V.P.Dzhelepov and the service personnel of the synchrocyclotron whose generous help has made our investigations[23] possible.

Leningrad Physico-Technical Institute,
Academy of Sciences of the USSR

References

1. A.Bohr, Rotational States of Atomic., Copenhagen 1954; Problemy sovremennoi fiziki (Problems of modern physics), 1, 5 (1956).

2. E.E.Berlovich, Izv.AN SSSR, Ser.fiz., 20, 1438 (1956). (Trans., Bull. 20, No.12a, 1315.)

3. E.E.Berlovich, Izv.AN SSSR, Ser.fiz., 19, 343 (1955). (Trans.Bull. 19, No.3, 305.)

4. E.E.Berlovich, PTE (Instruments and Experimental Technique), 1, (1958).

5. R.Bell, R.Graham & H.Petch, Canad.J.Phys., 30, 35 (1952).

6. E.E.Berlovich & B.K.Shiliaev, PTE, 1 (1958).

7. K.Ia.Gromov, B.S.Dzhelepov & B.K.Preobrashenskii, Izv.AN SSSR, Ser.fiz., 21, 918 (1957). (Trans., Bull.21, No.7, 920.)

8. G.M.Gorodinskii, A.N.Murin, V.N.Pokrovskii & B.K.Preobrazhenskii, Izv. AN SSSR, Ser.fiz., 21, 1004 (1957). (Trans., Bull.21, No.7, 1005.)

9. R.Bell, in Beta- and Gamma-Ray Spectroscopy. Edit. K.Siegbahn, 1955.

10. G.M.Gorodinskii, A.N.Murin, V.N.Pokrovskii & B.K.Preobrazhenskii, Report at the Seventh All-Union Conference on Nuclear Spectroscopy, 1957.

11. N.M.Anton'eva, A.A.Bashilov, B.S.Dzhelepov & B.K.Preobrazhenskii, ibid.

12. Franz R.Metzger, Phys.Rev., 103, 983 (1956).

13. Z.Bay, Phys.Rev., 77, 419 (1950).

14. A.H.W.Aten, G.D.deFeifer, M.J.Sterk & A.H.Wapstra, Physica, 21, 990, 740 (1955).

15. I.Bergström, in Beta- and Gamma-Ray Spectroscopy, Edit. K.Siegbahn, 1955.

16. G.F.Dranitsyna, Koeffitsienty vnutrennei konversii na L_I-L_{II}-L_{III}-podobolochkakh (Internal conversion coefficients on the L_I, L_{II} & L_{III} shells), 1957.

17. M.E.Rose, in Beta- and Gamma-Ray Spectroscopy, Edit. K.Siegbahn, 1955.

18. J.Blatt & V.Weisskopf, Theoretical Nuclear Physics, 1952 (Cited in Russian trans., M., 1954.)

19. R.Graham & R.Bell, Canad.J.Phys., 31, 377 (1953).

20. H.DeWaard, Philos.Mag., 46, 375, 445 (1955).

21. L.A.Sliv & I.M.Band, Tablitsy koeffitsientov vnutrennei konversii gamma-izlucheniia (Tables of internal conversion coefficients)., Part I, 1956.

22. K.Alder, A.Bohr, T.Huus, B.Mottelson & A.Winter, Revs.Modern Phys., 28, 4, 432 (1956).

23. L.K.Peker & L.A.Sliv, Report at the Seventh All-Union Conference on Nuclear Spectroscopy, 1957.

NEW COMMERCIAL PHOTOMULTIPLIER TUBES

- L.G.Leiteizen, A.G.Berkovskii, I.Ia.Breido, B.M.Glukhovskoi, O.S.Korol'kova & E.I.Tarasova

Currently a number of new types of photomultiplier tubes developed by the authors have been put into production or will be shortly.

Spectrometric photomultipliers

Some time ago production was started on FEU-29 type photomultipliers intended for scintillation spectrometers (Fig.1,d). The pulse height resolution of a batch of these multipliers measured using Cs^{137} and an NaI(Tl) crystal is shown in Fig.2. Measurements were made using the individually specified (rating certificate) voltages on the first stages. Tests made over the first few months of production of the FEU-29 showed that the optimal regimes for the tubes are close to each other as regards interstage potentials. In the future it is planned to carry out a mass test on the basis of our preliminary experiments[1], using an averaged operating regime; determination of such standard operating conditions is necessary to permit use of the tube in geological survey and other mass-produced equipment.

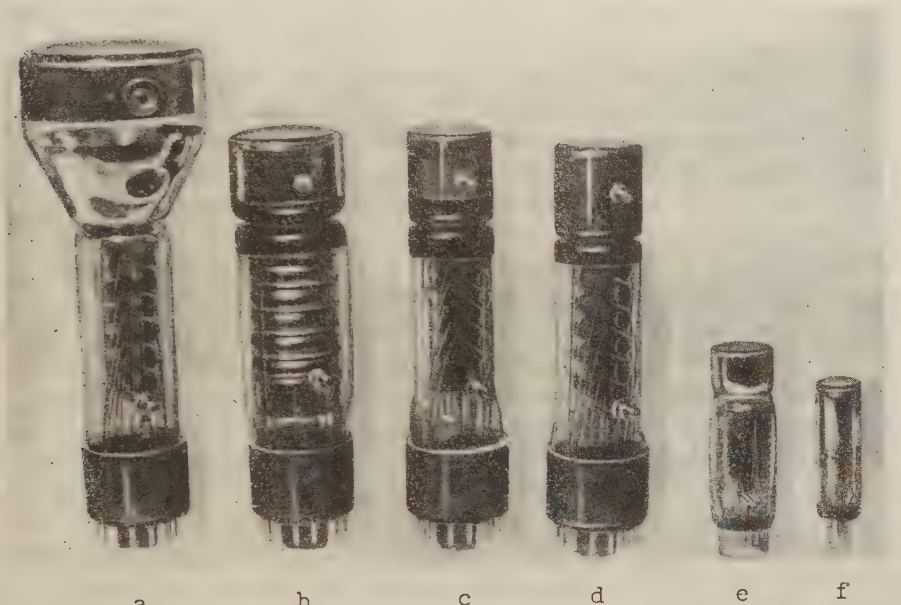

Fig.1. New photomultiplier tubes: a) FEU-24, b) prototype photomultiplier with toroidal dynodes, c) FEU-133, d) FEU-29, e) photomultiplier with bismuth-silver-cesium cathode, f) miniature photomultiplier tube.

The good pulse height resolution of the FEU-29 tubes is assured by the relatively high sensitivity of their cathodes: the integral sensitivity averages 40-45 microamp/lumen, with none below 30 microamp/lumen; the "blue" sensitivity is better than 6 microamp/lumen which corresponds to a quantum efficiency of better than 9% at $\lambda \approx 4000$ A.

Furthermore, the electron optics of the multiplier input section insure good electron collection from the cathode to the first dynode and minimal losses in the first stages. The noise amplitude measured with respect to the Cs^{137}--NaI(Tl) photopeak at an operating level of 50 pulses/sec does not exceed 5-8 kev and in an appreciable percentage of the produced tubes is ~3 kev.

The light characteristic is linear up to an output pulse amplitude of 7-8 v at a load of about 50 kilohm with a spurious capacitance $\leqslant 10$ μμf with the tube operated according to the specifications of the rating certificate.

An important characteristic of all photomultipliers is their stability. So far there is no testing procedure for stability that would yield consistent

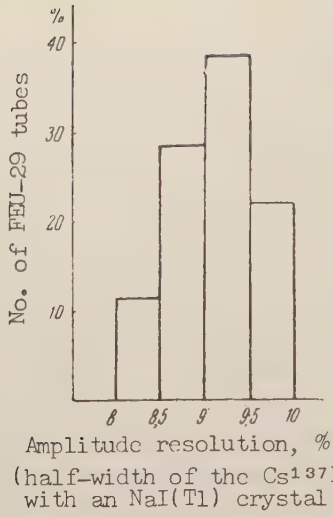

Fig.2. Amplitude resolution of a batch of 1000 FEU-29 tubes.

and unambiguous results. But according to data on hand, based on measurements carried out in a number of scientific research institutes and other organizations, most of the FEU-29 photomultipliers exhibit good stability in γ-spectrometers. Tests carried out at the tube plant show most of the tubes after a 30 minute warm-up, together with the associated apparatus, show a drift of the Cs^{137}—NaI(Tl) photopeak of less than 1.5% over a period of an hour.

With a view to improving the stability characteristics, an experimental lot of photomultiplier tubes of the same design was recently manufactured with dynodes of different alloys. The basic parameters, noise and amplitude resolution of these experimental photomultipliers are the same as those of the "standard" FEU-29, but their operating voltage is higher than average by 30-50%. These tubes are now undergoing exhaustive testing at the plant and a number of scientific organizations with a view to determining if they actually have superior stability characteristics. Experiments are also being carried out at the plant to determine the influence of technological factors and variations in design of the dynodes on the stability of the FEU-29 tubes.

Photomultipliers with an enlarged cathode

For a number of applications it is desirable to have a photomultiplier tube with a cathode 70-80 mm in diameter. Such a photomultiplier (FEU-24 - Fig.1,a) is now being put out in experimental lots preparatory to series production. This photomultiplier has a flat cathode 75 mm in diameter; hence optical contact with a large crystal can be realized without the need for an intermediate adapter pipe.

The electron optical cathode-first dynode system was designed and selected by modeling in an electrolytic bath. The quality of the focusing was checked for the experimental photomultipliers in a special set-up designed to detect inhomogeneities of the cathode sensitivity. This set-up comprises two electron beam tubes - an illuminating tube and a viewing tube - with synchronized raster scans. The raster of the illuminating tube is focused by means of a suitable lens on the photocathode of the photomultiplier. The output signal from the photomultiplier may be applied either to a modulator or to the X or Y deflecting plates of the viewing tube. In the first case one can observe the zonal distribution of sensitivity over the cathode; in the latter case one can make a quantitative evaluation of the heterogeneity by "lines" or "frames".

After tests on a number of different variants, we chose the cathode lens design diagrammed in Fig.3. Particular attention was also paid to design of the input stages of the multiplier system inasmuch as it was found in tests that the uniformity of the zonal characteristic also depends on this factor. This multiplier has 13 dynodes. The cathode, focusing ring and anode are brought out into the envelope. The overall length of the multiplier is 235 mm; it is mounted on a 14-prong base (the first two leads are brought out to button contacts).

According to preliminary test data, the FEU-24 tube has the following averaged parameters: integral sensitivity - 35-40 microamp/lumen; "blue" sensitivity - 7 microamp/lumen; amplification - about $(2-5)\cdot10^5$ at an overall potential of 1400-1500 v. At higher voltages the gain may be as high as 10^7.

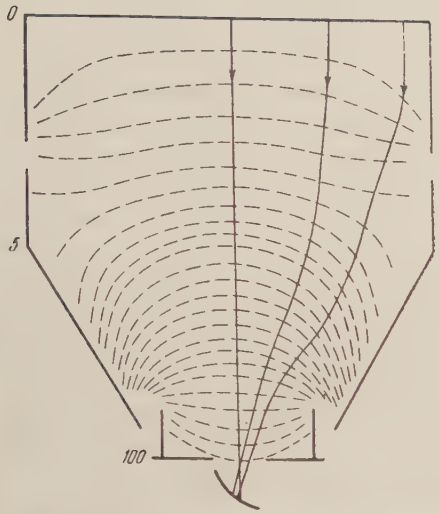

Fig.3. Cathode lens of the FEU-24 tube.

The average current density from the cathode is about $5 \cdot 10^{-15}$ amp/cm^2. The above static characteristics are for the case of equal interstage voltages (the potential across the focussing ring-cathode gap is a few volts). The pulse characteristics were measured using the individually specified (individual tube rating certificate) voltages on the first stages, assuring the best amplitude resolution. It is planned in the future to establish an average "standard" regime for general use.

The pulse height resolution, measured with an NaI(Tl) crystal 30 mm in diameter detecting the radiation from Cs^{137}, equals 9-11% in the center of the cathode and falls off by not more than 1-1.5% towards the edges of the cathode. The noise measured using the same crystal does not exceed 10 kev for most tubes with an appreciable percentage having a noise level under 5 kev. Linearity of the light characteristic is retained to pulse heights of 7 v at a load of 50 kilohm and a spurious capacitance of $\leqslant 10$ μμf.

We carried out tests with three large NaI(Tl) crystals 55, 65 and 75 mm in diameter kindly made available to us by L.M.Beliaev and V.I.Startsev. With the particular multiplier whose pulse height resolution with the 30 mm diameter crystal was 9% at the center and $\leqslant 10.5\%$ at the edge, we obtained half-widths of the Cs^{137} γ-line of 9.8, 11.0 and 11.5% with the respective crystals.

The same multiplier when illuminated by flashes from a gas discharge tube equal in brightness to the scintillations of $Cs^{137} \rightarrow$NaI(Tl) yielded a resolution of approximately 6%.

High time-resolution photomultiplier

For certain important investigations in the field of nuclear physics it is desirable to have photomultipliers with a high resolution in time. In addition to the usual requirements, such photomultipliers must meet the added requirement of minimum straggling in the passage time of the "electron packet" through the multiplier together with that of the maximum steepness of the pulse front at the output. More stringent requirements are also imposed as regards the current characteristics: the tubes must be capable of an output pulse current of the order of 0.5 amp.

Good time resolution can be attained if the design provides for 1) satisfactorily isochronous collection of photoelectrons on the first dynode and 2) low straggling of the flight time of the electrons through the multiplier system.

For isochronous collection one must have a high initial gradient at the emitting surface. Although this can be achieved by reducing the cathode-baffle (slit) distance this solution is generally unacceptable because it involves reducing the effective surface of the cathode. Hence we made an attempt to assure isochronous collection of the photoelectrons by introducing auxiliary electrodes mounted on the baffle system. After modeling a number of variants, we found a simple system that yielded good results. A cylindrical electrode maintained at the potential of the baffle was introduced between the cathode and the defining baffle. According to measurements carried out by A.S.Belousov

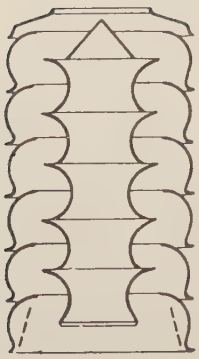

Fig.4. Multiplier system employing toroidal dynodes.

in the "Lebedev" Physical Institute of the USSR Academy of Sciences, the use of this type of intermediate cylindrical electrode in FEU-19 photomultipliers improved the time resolution by a factor of about 2 (see curve 2 in Fig.7).

Development of multiplying systems assuring minimal flight-time straggling proceeded in two directions: a) development of systems with torroidal dynodes (Fig.1,b and Fig.4) and b) systems with accelerating grids (Fig.1,c).

A system with toroidal dynodes was first described by M.Biermann[2]. Its advantages are a) a large effective working surface of the dynodes (allowing of large effective load currents), b) a large diameter entry aperture improving the isochronism of electron collection and c) the absence of edge effects distorting the field and the absence of sharp dynode edges, which eliminates one of the possible sources of instability at high potentials. This allows of improving the time characteristic by increasing the interstage voltage differences.

The shape of the dynodes assuring minimal time of flight straggling was selected by the electrolytic bath procedure. The maximum spread in the one-stage flight time with the developed system does not exceed $1.5 \cdot 10^{-9}$ sec (200 v difference per stage); furthermore the time dispersal is not increased after passage through several stages.

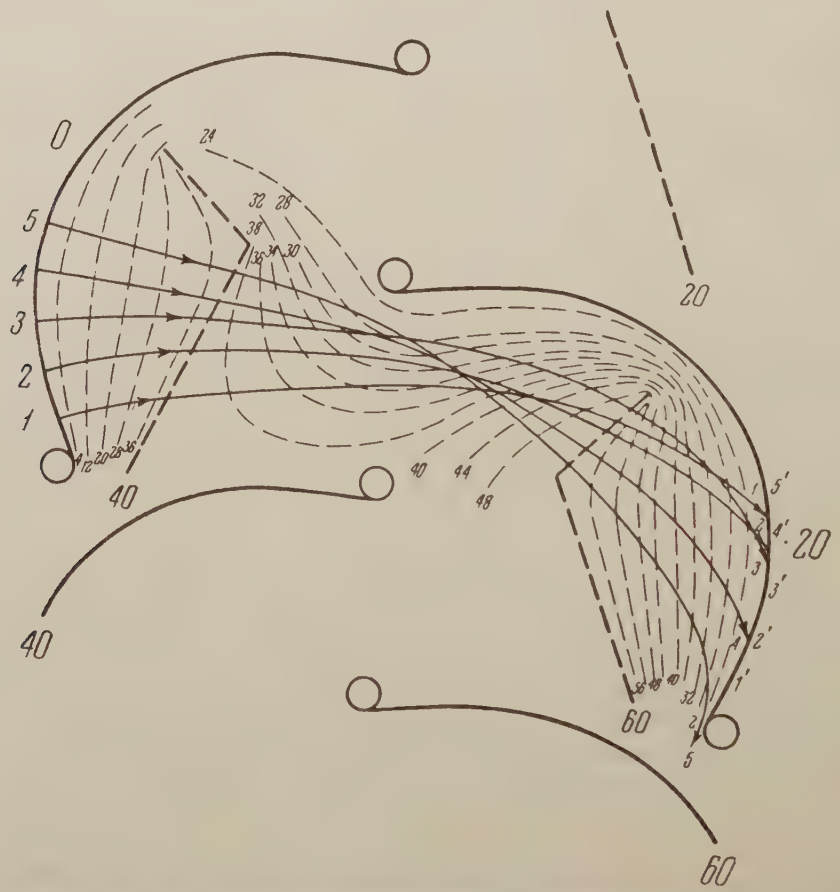

Fig.5. Diagram of multiplier system with accelerating grids (FEU-33). The figures at the dynodes and grids indicate the potentials of the electrodes in relative units.

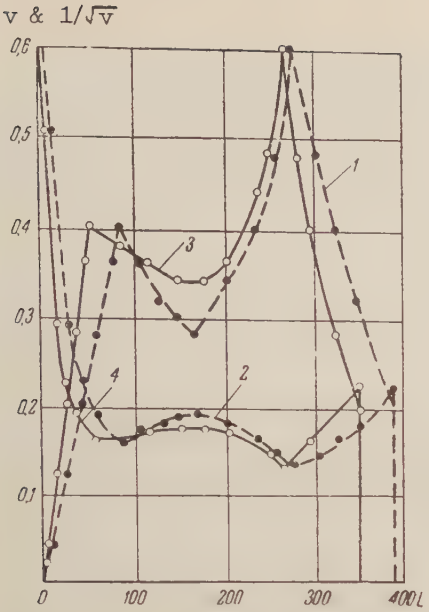

Fig.6. Variation of the potentials (V) and functions $1/\sqrt{V}$ over the electron paths with extreme flight time values: 1) variation of the potential over the longest plotted path, 2) function $1/\sqrt{V}$ corresponding to curve 1, 3) variation of the potential along the shortest plotted path, 4) function $1/\sqrt{V}$ corresponding to curve 3.

Decrease of the electron flight time and of its fluctuation can be attained by increasing the field intensity particularly over the initial part of the electron trajectories (primarily by neutralizing the influence of the initial velocities of the secondary electrons). Increasing the field gradient also furthers dissipation of the space charge in the last stages, which allows of obtaining a higher output current.

Introduction of a special grid, maintained at the potential of one of the following dynodes, in front of each dynode, produces a strong and adequately uniform accelerating field at the emitting surfaces, assuring the requisite low electron time of flight straggling. The dynode-grid voltage was selected to be twice the stage voltage.

Modeling of the first version of the multiplier system with grids showed that a strong accelerating field at the dynode surfaces appreciably complicates focusing of the primary electrons for which the field at the dynodes is a retarding one. After experimentation with a large number of possible variants we found a system insuring good focusing of the electrons and minimum time of flight straggling (Fig.5).

The variation of the potentials along the electron paths with maximum and minimum times of flight in the multiplier system pictured

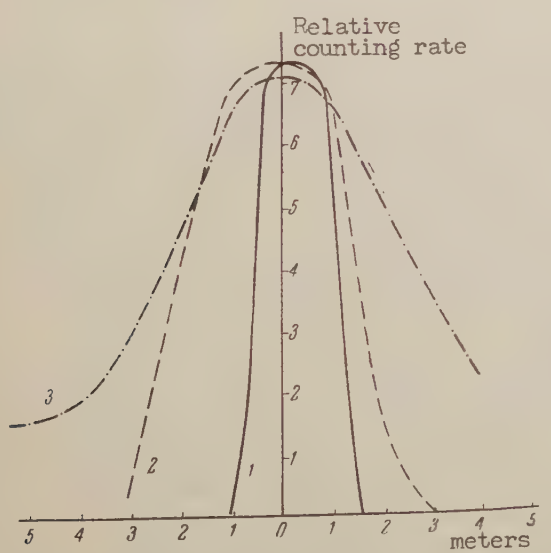

Fig.7. Delayed coincidence curves for a FEU-19 photomultiplier (1), an FEU-19 tube with an accelerating cylinder (2), and an experimental FEU-33 tube with accelerating grids (3). 1 meter of delay cable is equivalent to a delay of $4 \cdot 10^{-9}$ sec.

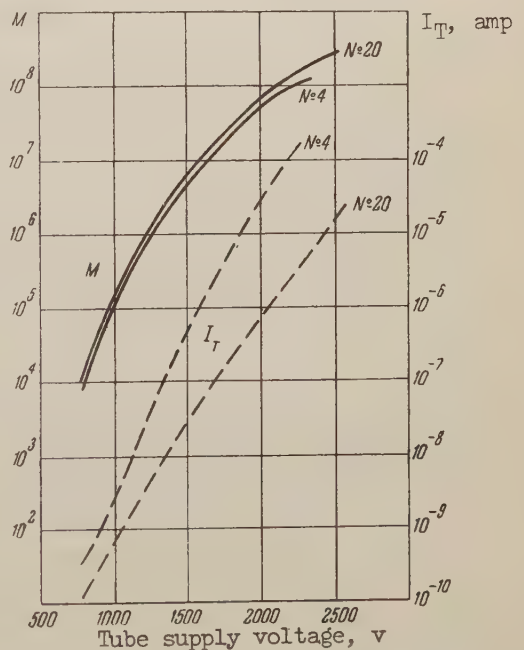

Fig.8. Amplification (M) and dark current (I_T) characteristics of some FEU-33 photomultiplier tubes.

in Fig.5 is shown in Fig.6. In the same figure we have plotted corresponding functions $1/\sqrt{V}$ defining areas proportional to the flight times.

Calculations of the maximum difference between flight times for the multiplier system with grids gives a value of $4.4 \cdot 10^{-10}$ sec (with a voltage differential of 100 v/stage) which is 3-4 times smaller than in the multiplier system of the H4646 tube[3].

Comparative measurements of the time characteristics of several photomultipliers with accelerating grids (FEU-33) and FEU-19 tubes in a double coincidence circuit carried out by A.S.Belousov at the Physical Institute of the USSR Academy of Sciences showed that for the former the width of the "hill" is smaller by a factor of 3-4 (Fig.7).

The pulse height resolution of the experimental FEU-33 photomultiplier tubes with accelerating grids, measured under the conditions described above, proved to be 9-10%. The experimental models of the photomultiplier with accelerating grids were found to have an amplification of the order of 10^8 at overall voltages of 2.5-3.0 kv (Fig.8).

Photomultiplier with a bismuth-silver-cesium cathode

Conventional photomultipliers with a cesium-antimony cathode are suitable for work in the red region of the visible spectrum inasmuch as their long wave sensitivity limit lies at 5800-6000 Å. The best signal-to-noise ratios in the wavelength region from 5500 to 8000 Å are obtained with Bi-Ag-Cs cathodes. Experimental photomultiplier models with such cathodes have been prepared in two sizes: a normal size (FEU-29 - Fig.1,d) and a smaller size (Fig.1,e).

Both multipliers have 11 amplification stages. The integral sensitivity of the cathode averages 45-50 microamp/lumen. The amplifications are of the order of 10^5-10^6 at an overall supply voltage of 1400-1600 v. The small size photomultiplier is characterized by excellent vibration resistance.

Miniature photomultipliers

In a number of photomultiplier applications, size is an important consideration. In view of this we have recently developed an 8-stage miniature photomultiplier (Fig.1,f) with a maximum outside diameter not exceeding 22.5 mm and a height of 65 mm (not including the prongs). The flat cesium-antimony semitransparent cathode of this tube has an effective diameter of 18 mm. Its sensitivity is not less than 25 microamp/lumen.

This photomultiplier provides an amplification of up to 10^5 at overall voltage of 900-1000 v. The dark current is of the order of 10^{-8} amp.

References

1. L.G.Leiteizen, B.M.Glukhovskoi & I.Ia.Breido, Kristallografiia (Crystallography), 2, 290 (1957).

2. M.Biermann, Radio und Fernsehen., 10, 292 (1955).

3. J.A.Morton, Advances in Electronics, 4, 69 (1954).

BULLETIN OF THE ACADEMY OF SCIENCES OF THE USSR - PHYSICAL SERIES
Vol. 21, No. 12 - December 1957

Transactions of the Seventh All-Union Conference on Nuclear Spectroscopy
(Continued from Vol. 20, No. 7)

TABLE OF CONTENTS

	Page Orig.	Trans.
Fine structure of α-decay of even-even nuclei - V.G.Nosov	1551	1541
Investigation of the internal conversion electron spectrum of long-lived Eu^{152} and Eu^{154} - B.V.Bobykin & K.M.Novik	1556	1546
On the decay scheme of Lu^{171} - K.Ia.Gromov, B.S.Dzhelepov, A.G.Dmitriev & B.K.Preobrazhenskii	1573	1562
$0+\rightarrow 0+$ transition in Zr^{90} - T.Yuasa, J.Laberrigue-Frolow & L.Feuvrais	1576	1565
Gamma-hodoscope - B.S.Dzhelepov	1580	1569
The gamma-hodoscope at the Scientific Research Institute of Physics of Leningrad State University - O.V.Chubinskii	1583	1572
Investigation of the decay of Ce^{144} by the β-γ coincidence method - V.P.Parfenova, N.V.Forafontov & V.S.Shpinel'	1601	1590
Further investigation of electron focusing in a two-lens β-spectrometer - K.P.Mitrofanov & V.S.Shpinel'	1607	1595
New data on the γ-spectrum of Sb^{124} - B.S.Dzhelepov, N.N. Zhukovskii & F.A.Predovskii	1614	1602
Spectra of internal conversion electrons emitted in thermal neutron capture by samarium, cadmium and gadolinium - L.V.Groshev, A.M.Demidov & V.A.Naidenov	1619	1606
Neutron-deficient isotopes of the rare earth elements forming as a result of spallation of Ta under bombardment with 660 Mev protons - Part II. - G.M.Gorodinskii, A.N.Murin, V.N.Pokrovskii & B.K.Preobrazhenskii	1624	1611
Investigation of the decay of Pr^{144}, Rh^{106} and Cs^{134} by means of a scintillation spectrometer - E.I.Firsov & A.A.Bashilov	1633	1619
On the relative intensity of Po^{210} γ-rays - V.V.Ovechkin	1641	1627
Investigation of the lifetimes of lower nuclear levels excited in electron capture - E.E.Berlovich, K.M.Grotovskii, M.P.Bonits, V.I.Breslav & B.K.Preobrazhenskii	1643	1629
New commercial photomultiplier tubes - L.G.Leiteizen, A.G.Berkovskii, I.Ia.Breido, V.M.Glukhovskoi, O.S.Korol'kova & E.I.Tarasova	1653	1639

Subject summary - Vol. 21 of the Bulletin of the Academy of Sciences of the USSR - Physical Series 1660 1649

Translated in 1958 by
Columbia Technical Translations
5 Vermont Ave., White Plains, N.Y.

SUMMARY OF THE CONTENTS

of

VOLUME XXI

of the

BULLETIN OF THE ACADEMY OF SCIENCES OF THE USSR

- Physical Series -

COLUMBIA TECHNICAL TRANSLATIONS
5 VERMONT AVENUE
WHITE PLAINS, N. Y.

SUBJECT SUMMARY - VOLUME 21

Page
(Trans)

Transactions of the Eighth All-Union Conference on Semiconductors

Number 1

Section on the theory of semiconductors

The method of traces for conduction electrons in semiconductors. Part I. Weak interaction between electrons and vibrations. - M.A.Krivoglaz & S.I.Pekar 1
The method of traces for conduction electrons in semiconductors. Part II. Variational method - M.A.Krivoglaz & S.I.Pekar 13
Influence of the polaron effect on the thermodynamics of conduction electrons in semiconductors (Part III) - M.A.Krivoglaz & S.I.Pekar 29
Interaction of excitons with a molecular lattice - E.I.Rashba 33
Investigations in the microscopic theory of crystals - K.B.Tolpygo 44
Theory of excitons in ionic crystals - I.M.Dykman 60
Interaction of localized electrons with acoustical vibrations in homeopolar crystals (Abstract) - M.F.Deigen 63
State of an impurity-center electron in an anisotropic crystal (Abstract) - A.I.Ansel'm & L.I.Korovin 64
Contribution to the theory of recombination of electrons with impurity centers in ionic crystals (Abstract) - Iu.E.Perlin 64
Thermomagnetic and galvanomagnetic effects in semiconductors taking into account variations in the current carrier concentration (Abstract) - G.E.Pikus 64
Recombination in semiconductors incident to collision of current carriers - L.Sosnowski 65
Excited states of two-electron color centers in ionic crystals and the α and β absorption bands - O.F.Tomasevich 69
On the exciton energy spectrum in an ionic crystal - I.P.Ipatova 73
On a current carrier recombination mechanism in strongly alloyed semiconductors - V.L.Bonch-Bruevich 82
Some aspects of the thermodynamics of electron and phonon gas in solids - Iu.N.Obraztsov 92
Mean free path of electrons in liquid and amorphous conductors - A.I.Gubanov 98
Interaction of semiconductor electrons with lattice vibrations at ultralow temperatures - L.E.Gurevich 99
Concerning certain electroacoustical effects - L.E.Gurevich 106

Section on the chemistry of semiconductors

Some aspects of the crystal chemistry of compounds with the zincblende structure - N.A.Goriunova 114
Contribution to the theory of phases of variable composition with the zincblende structure (On the possible region of homogeneity of $A^{III}B^{V}$ type compounds) - B.F.Ormont, N.A.Goriunova, I.N.Ageeva & N.N.Fedorova 128
Physico-chemical analysis of some semiconductor systems - N.Kh.Abrikosov 136

Growth of single-crystal layers of silicon and germanium from the vapor phase - N.N.Sheftal', N.P.Kokorish & A.V.Krasilov 140
Preparation of single-crystal specimens of cuprous oxide - Iu.I.Gritsenko 151
Investigation of the coefficients of self-diffusion of I & K ions in x-ray irradiated alkali halide crystals - V.V.Mumladze 157

Number 2

Section on semiconductor catalysis

Some problems in the field of semiconductor catalysis - S.Z.Roginskii 163
On problems arising in the theory of semiconductors as catalytic agents - F.F.Vol'kenshtein 177
On some questions of semiconductor analysis - F.F.Vol'kenshtein 180
Investigations of the catalytic properties of NiO-base solid solutions - N.P.Keier, S.Z.Roginskii & I.S.Sazonova 184
Relation between the catalytic activity and electric conductivity of zinc oxide and the influence of optical radiation on these properties - I.A.Miasnikov 192
Summary of results of investigations of the relation between the electronic surface states in a semiconductor and catalytic effects - V.I.Liashenko & I.I.Stepko 201
Investigation of adsorption of gases on manganese dioxide by the electric conductivity method - S.Iu.Elovich & L.Ia.Margolis 206
Influence of adsorption on the conductivity and work function of semiconductors - V.B.Sandormirskii 211

Section on the optical properties of semiconductors

Absorption of light in mercury halide crystals - E.F.Gross & A.A.Kaplianskii 220

Transactions of the Fifth Conference on the Application of X-Rays to the Investigation of Materials (Concl. from Vol.20, Nos.6 & 7)

Number 2

Experimental verification of the influence of anisotropy of the crystallites on the shape of the Debye ring in the x-ray pattern of stressed specimens - G.I.Aksenov & V.A.Moshchanskii 229

Transactions of the First Conference on Ferroelectricity

Number 2

Survey of some of the results of recent investigations of ferroelectric materials - G.A.Smolenskii 235
Orientation of the domains and macrosymmetry of the properties of ferroelectric single crystals - I.S.Zheludev & L.A.Shuvalov 266
Crystallochemistry of ferroelectrics with the perovskite structure - Iu.N.Venevtsev & G.S.Zhdanov 277
Character of the changes in the domain structure of Rochelle salt in alternating electric fields - I.S.Zheludev & R.Ia.Sit'ko 288

Some details of the domain structure of Rochelle salt crystals as determined by optical observation - M.A.Chernysheva 293

Number 3

Growth and investigation of ferroelectric single crystals - N.S.Novosil'tsev, A.L.Khodakov, M.L.Sholokhovich, E.G.Fesenko & O.P.Kramarov 303
Some characteristics of single crystals of $PbTiO_3$ and $(Ba,Pb)TiO_3$ solid solutions - E.G.Fesenko, O.P.Kramarov, A.L.Khodakov & M.L.Sholokhovich 314
Structure of the OH band in the spectra of crystals containing hydrogen bonds - A.I.Stekhanov 319
On the shape of the potential curve of the hydrogen bond in certain crystals - A.N.Lazarev 329
Ferroelectric characteristics of Rochelle salt crystals subjected to radioactive radiation - V.A.Iurin 336
On certain characteristics of dielectric hysteresis in Rochelle salt - I.Ia.Eisner 341
On microscopic theories of the ferroelectric properties of barium titanate - R.E.Pasynkov 346
Ion dynamics and electrostatic energy of ferroelectrics - V.Kh.Kozlovskii 358
Towards a theory of orientation ordering in molecular crystals - V.I.Kliachkin 364
Towards a theory of hysteresis in $BaTiO_3$ - L.P.Kholodenko 372
Relation between the dielectric, piezoelectric and elastic properties of polycrystalline ceramic and those of a single crystal - S.V.Bogdanov, B.M.Vul & A.M.Timonin 378
Nonlinear properties of ferroelectrics - B.M.Vul 383
Behavior of certain ferroelectrics in strong electric fields - V.A.Bokov 386
Piezoelectric properties of barium titanate ceramic with certain additives - S.V.Bogdanov 392
Inverse piezoeffect in polycrystalline $BaTiO_3$ under static conditions - G.M.Kovalenko 396
A method of determining the piezoelectric coefficient from the radial vibrations of a disc - S.V.Bogdanov & A.M.Timonin 399
Pyroelectric and piezoelectric effects in polycrystalline barium titanate - M.S.Kosman & Z.A.Shamro 401
Dielectric properties of the niobates and tantalates of bivalent metals - V.A.Isupov 404
Investigation of the antiferroelectric properties of some solid solutions containing lead zirconate - N.N.Krainik 412
Investigation of $(Ba,Pb)(Ti,Sn)O_3$ solid solutions with ferroelectric properties - I.E.Myl'nikova 423
Additional data on solid solutions of the $PbTiO_3$-$SrTiO_3$ system - A.G.Bogdanov & R.A.Khomutetskaia 432
Variation of the dielectric constant of polycrystalline ferroelectrics with time under the influence of a mechanical load and a dc electric field - M.S.Lur'e 437
Investigation of ultrasonic projectors employing Rochelle salt crystals - K.A.Minaeva 442
Stabilized piezoceramic materials - R.E.Pasynkov & V.V.Vinogradov 447

Use of ferroelectrics in frequency multipliers - D.M.Kazarnivskii & V.P.Sidorenko 452
On equipment for research in the field of ferroelectrics using small specimens - I.S.Rez 463

Transactions of the Fifth Conference on Luminescence

Number 4

Opening address - V.L.Levshin 475
Certain characteristics of sublimate phosphors and methods of preparing them (A) - F.D.Klement 482
New results in the field of phosphorescence research - V.V.Antonov-Romanovskii 483
On the possibility of two-stage excitation of photosemiconductor effects - N.A.Tolstoi & A.V.Shatilov 493
Flash luminescence of zinc sulfide phosphors - N.A.Tolstoi, A.M.Tkachuk, N.N.Tkachuk & Z.S.Mansurova 494
On the luminescence of ZnS:Mn phosphors under excitation (A) - V.L.Levshin, N.S.Borodin & G.P.Neronova 499
On the phosphorescence decay law for crystal phosphors (A) - G.M.Eliashberg 501
New procedures for investigating relaxation processes and trapping centers in crystal phosphors (A) - Ch.B.Lushchik 502
Afterglow of the Eu^{3+} ion in thorium oxide phosphors (A) - M.V.Fok 504
Decay law for zinc sulfide phosphors in and near the thermoquenching region (A) - F.I.Vergunas 506
Luminescence decay of ZnS:Cu and ZnS:Cu:Co phosphors in the region of the thermoquenching of the luminescence (A) - V.V.Nuvar'eva 508
Investigation of electron trapping levels in ZnS:Cu phosphor - Iu.L.Lukantsever & L.R.Krasovskaia 509
Kinetics of the infrared luminescence of cuprous oxide (A) - N.A.Tolstoi, N.N.Tkachuk & R.K.Preobrazhenskii 519
Semiconductor processes in organic dye layers (A) - A.T.Vartanian 521
Influence of adsorption of gases on the luminescence of zinc oxide (A) - K.V.Tagantsev & A.N.Terenin 523
On candoluminescence of crystal phosphors (A) - V.A.Sokolov 525
Luminescence of some "pure" salts - V.A.Arkhangel'skaia & P.P.Feofilov 528
Line luminescence near the principal absorption edge of crystals (A) - A.A.Kaplianskii 529
Luminescence of silver halide salts - S.I.Golub 531
On effects observed in alkali halide phosphors under the influence of intermittent light (A) - I.A.Parfianovich 533
On the quenching of ZnS:Cu:Co and ZnS:Cu:Ni phosphors by infrared light (A) - L.A.Vinokurov & M.V.Fok 535
Variation of the luminescence efficiency of ZnS:Cu with the wavelength of the exciting light (A) - M.N.Alentsev 536
Sensitivity of "fluorescent lamp" luminophors to short ultraviolet - F.A.Butaeva & V.A.Fabrikant 537
Spectral distribution and absolute value of the photoluminescence output of thallium-activated alkali iodides (A) - Z.L.Morgenshtern 540
On calculation of the luminescence spectra of crystal phosphors (A) - N.D.Potekhina 541
Influence of infrared radiation on the luminescence of zinc sulfide phosphors (A) - K.K.Rebane 542

Effect of activator concentration on the γ- and photoluminescence efficiencies of thallium-activated alkali iodides (A) - L.M.Beliaev, M.D.Galanin, Z.L.Morgenshtern & Z.A.Chizhikova 544
Kinetics of γ-scintillation in Tl-activated sodium iodide crystals (A) - I.K.Pliavin' 545
Atomic absorption and luminescence centers in alkali halide phosphors activated with heavy metal ions and their formation under the influence of hard radiation (A) - M.L.Kats 546
Influence of x-rays on the absorption and emission of Sn-activated alkali halide phosphors (A) - A.S.Andrianov & M.L.Kats 547
On the mechanism of selective absorption of the activator in KCl:Ag phosphors (A) - M.L.Kats & V.K.Nikol'skii 548
Luminescence of different types of luminophors under excitation by short pulses (A) - A.A.Bundel', M.F.Popov & Iu.A.Chizhunova 549
Surface-activated phosphors - L.M.Shamovskii & Iu.N.Zhvanko 551
Luminescence and distribution of trapping levels in alkali halide crystals with excess halide - M.N.D'iachenko 565
Visible luminescence of subtractively colored rock salt crystals at different temperatures - D.M.Eremin 573
Photochemical transformations of color centers in heated alkali halide crystals (A) - A.A.Shatalov 580
Influence of polarized light on color centers in alkali halide crystals (A) - O.A.Shmit 581
Thermal ionization energy of traps in alkali halide phosphors (A) - I.A.Parfianovich 582
Luminescence lifetime of color centers in ionic crystals (A) - A.M.Bonch-Bruevich, G.A.Tishchenko & P.P.Feofilov 583
On the stability of F-centers in NaCl:Ni phosphors (A) - E.I.Shuraleva 584
Luminescence of color centers in CsI:Tl crystals (A) - Z.L.Morgenshtern & I.P.Shchukin 586
Ultrataumeter - N.A.Tolstoi, A.M.Tkachuk & N.N.Tkachuk 588
Persistent luminescent coatings activated by artificial β-active isotopes - V.L.Levshin, E.I.Panasiuk & L.A.Pakhomycheva 606
Procedures and instruments for measuring luminescence - D.A.Shklover & R.S.Ioffe 613
Equipment for investigating the luminescence of crystal phosphors - Z.M.Sverdlov 617
Equipment for ultraviolet irradiation of luminescent coatings and materials - N.V.Gorbachev 625
Use of scintillation counters in radiometric equipment for prospecting for radioactive ore deposits - A.L.Iakubovich 628

Number 5

Stimulation and quenching of photoconduction in cadmium sulfide - B.T.Kolomiets 639
Determination of the polarity of the photoconductivity current carriers in ZnS phosphors (A) - E.E.Bukke 644
On the capacitor procedure for determining the polarity of the photocurrent carriers in crystal phosphors (A) - U.Kh.Nymm & L.Ia.Uibo 644
Determination of dielectric constant of excited ZnS:Cu and ZnS:Cu:Fe phosphors (A) - O.V.Agashkin 649
Electric and optical properties of ZnS:Cu phosphor (A) - F.I.Vergunas & O.V.Agashkin 650

On procedures for obtaining inorganic materials of high purity for luminophors (A) - I.I.Angelov 651
Purification of concentrated solutions of salts to "luminophor purity" by the chromatographic method (A) - E.A.Bozhevol'nov & V.V.Trusov 652
Chromatographic method of purifying raw materials for the synthesis of luminophors (A) - A.M.Gurvich, T.B.Gapon & M.S.Rabinovich 653
New chemical procedures for determining small amounts of impurities (A) - I.G.Shafran 660
Some questions of the chemistry of sulfide luminophors (A) - A.A.Bundel' & A.I.Rusanova 661
Investigation of the correlation between the luminescence and the catalytic and adsorption properties of "self-activated" ZnO and ZnS crystals (A) - L.N.Shekter, I.A.Miasnikov & S.Ia.Pshezhetskii 663
Some distinctive features of the luminescence spectra of sulfide--selenide luminophors (A) - A.A.Bundel' & Z.I.Guretskaia 666
Zinc sulfide-selenide luminophors and their technical applications (A) - E.I.Blazhnova 668
Some regularities in the cathodoluminescence of luminophors (A) - Z.I.Klabukova 669
Investigation of the thermal stability of sulfide phosphor screens (A) - T.V.Korovkina 669
Radii and concentrations of activator ions in crystal phosphors (A) - M.A.Konstantinova-Shlezinger 671
Role of physical-chemical systems in zinc sulfide luminophors - A.A.Cherepnev 672
Structure of alkali halide phosphors and the mechanism of luminescence processes - L.M.Shamovskii, A.A.Dunina & Iu.N.Zhvanko 673
On the nature of luminescence centers in zinc sulfide luminophors (A) - Z.A.Trapeznikova 677
Infrared photoluminescence of lead sulfide (A) - L.N.Galkin 679
Luminescence of microporous glass activated with heavy metals (A) - E.V.Pershina & A.N.Terenin 680
Phosphate type photoluminophors - N.A.Gorbacheva 681
Investigation of the luminescent properties of some borophosphate compounds (A) - L.Ia.Markovskii & R.A.Shtrikhman 683
Manganese-activated lithium-magnesium tungstate phosphors (A) - Iu.S.Leonov 686
On the causes responsible for the distinctive characteristics of cadmium sulfate crystal phosphors (A) - G.V.Maksimova 688
Cadmium sulfate phosphors (A) - B.M.Nosenko, L.S.Revzin & V.Ia.Iaskolko 692
Investigation of trapping centers and the kinetics of relaxation processes in alkali halide crystal phosphors (A) - Ch.B.Lushchik, F.N.Zaitov, V.Ia.Kark, L.A.Teiss & I.V.Iaek 694
Nature of trapping levels in ZnS:Cu:Co phosphors and their filling under different excitation conditions (A) - V.L.Levshin & V.F.Tunitskaia 696
On the formation of trapping levels in ZnSlMn phosphors (A) - V.L.Levshin & B.D.Ryzhikov 697
Investigation of thermostimulated emission of crystalline quartz excited by x-rays (A) - L.G.Chentsova, B.N.Grechushnikov & E.N.Batrak 700
Luminescence of crystal phosphors under excitation by ions (A) - B.N.Nosenko, N.A.Strukov & M.D.Iagudaev 702
On the choice of luminophors for television screens (A) - B.M.Gugel' & I.S.Vekeler 705

Improving the quality of luminous coatings in fluorescent lamps (A) - B.M.Gugel' & M.M.Shapochnik 704
Physical-chemical principles of application of luminophors to screens by the method of settling (A) - L.A.Saminskii 707
Investigation of the luminescence of uranium activated sodium fluoride (A) - Z.M.Sverdlov 708
Thermoluminescence of minerals - G.F.Komovskii, V.S.Nikol'skii & O.N.Lozhnikova 709
Introductory address (Section on electroluminescence) - V.V.Antonov-Romanovskii 713
Some results of investigations of electroluminescence - E.E.Bukke, L.A.Vinokurov, V.E.Oranovskii & Z.A.Trofimov 714
Zinc sulfide type electroluminophors - A.N.Kazankin, F.M.Pekerman & L.N.Petroshina 719
Zinc sulfide base electroluminophors - I.N.Orlov 728
Influence of crushing on the properties of some crystal phosphors (A) - F.D.Klement & R.I.Gindina 744
Influence of the activator-salt anion on the luminescence of alkali halide phosphors (A) - N.I.Ivanova 744
X-ray studies of NH_4Cl:Tl and NH_4Br:Tl phosphors (A) - A.Ia.Pae 745
Investigation of the properties of KI:In and KI:Ga phosphors (A) - Iu.N.Zhvanko, Z.L.Morgenshtern & L.M.Shamovskii 747
On the spectral characteristics of some sublimate phosphors (A) - A.F.Malysheva 747
Effect of compression on the luminescence spectra of some crystal phosphors (A) - Ia.Ia.Kirs 748
Investigation of the regularities of emission of finely dispersed luminescent media (A) - A.P.Ivanov 752
Investigation of the diffusion of rare earth activators in different crystals on the basis of luminescence spectra - A.K.Trofimov 754
A luminescence method of observing certain crystallochemical transformations in solids (A) - A.K.Trofimov & S.S.Tolkachev 759
Preparation of luminous paints and their use in motion picture production - M.N.Agranian & N.V.Gorbachev 761
Use of luminous paints in the theatre - B.M.Baranov 769
On luminescent decorative painting - A.M.Mandel'berg 772
Use of paramagnetic resonance techniques for investigating the state of the activator in phosphors - A.A.Manenkov, A.N.Prokhorov, Z.A.Trapeznikova & M.V.Fok 776
Nature of luminescence centers in artificial fluorite crystals activated with rare earths and uranium (A) - P.P.Feofilov 776
Closing address - V.L.Levshin 778
Resolution adopted by the Conference 779

Transactions of the Third Conference on the Physics of Magnetic Phenomena

Number 6

The de-Haas-van Alphen effect - D.Shoenberg 789
Influence of pressure on the galvanomagnetic properties of bismuth - N.E.Alekseevskii, N.B.Brandt & T.I.Kostina 792
On determination of the individual components of the magnetic susceptibility of a semiconductor - Ia.G.Dorfman 798
On the transverse photomagnetic effect in n- and p-type germanium (Abstract) - I.K.Kikoin & Iu.A.Bykovskii 803

Towards a theory of ferromagnetism in a nonideal lattice (Abstract) - V.L.Bonch-Bruevich 803
Paramagnetic behavior of some salts of the iron group of elements - A.Bose 804
Magnetochemistry of diamagnetic compounds and the role of polarizing paramagnetism - Ia.G.Dorfman 817
Cyclotron and plasma resonance in solids - A.F.Kip 821
Hyperfine structure of paramagnetic resonance in supercooled solutions of salts of the iron group - N.S.Garif'ianov 824
Electron paramagnetic resonance in electrolyte solutions - B.M.Kozyrev 828
Thermodynamic theory of relaxation and resonance effects in two-spin systems - G.V.Skrotskii & L.V.Kurbatov 833
Resonance paramagnetic absorption of ultrasound in some salts of the rare earth elements - S.A.Al'tshuler, M.M.Zaripov & L.Ia.Shekun 844
An approximate method of second quantization in the quantum theory of magnetism - N.N.Bogoliubov & S.V.Tiablikov 849
Quantum mechanical treatment of ferromagnetism in metals of the transition groups - S.V.Vonsovskii 854
Some remarks concerning the Bloch spin wave theory - Z.Semadeni 862
Dispersion formula for spin waves in ferromagnets - G.Czofta 865
Ferromagnetism of conduction electrons - G.S.Krinchik 869
Towards a theory of spontaneous magnetization of thin films - L.Valenta 879
On the temperature and field dependence of the magnetic anisotropy constants of a cubic crystal (A) - A.A.Gusev & S.V.Tiablikov 886
Concerning the spectrum of elementary excitations and some kinetic processes in ferromagnetic crystals (A) - E.A.Turov 886
Phase transitions and phase diagrams in a rhombic antiferromagnetic crystal - C.J.Gorter & T.van Peski-Tinbergen 887
Metamagnets or antiferromagnetic substances with a threshold field - L.Néel 889
A new form of ferromagnetic material: rare earth ferrites of the garnet type - L.Néel, F.Berteau, F.Forra & R.Pothené 903

Number 8

Influence of the structural characteristics of ferromagnets on the temperature dependence of the spontaneous magnetization - K.P.Belov & A.N.Goriaga 1043
Investigation of the magnetization of ferrites in the vicinity of the Curie point - K.P.Belov, K.M.Bol'shova & T.A.Elkina 1051
Temperature dependence of the differential susceptibility of cobalt in strong magnetic fields - L.Pal & T.Tarnotsi 1058
Application of paramagnetic resonance (nuclear induction) to determination of the structure of Rochelle salt and epoxy resins - A.Lösche 1066
Recent developments in the field of paramagnetic relaxation - C.J.Gorter 1073
Temperature dependence of the magnetic anisotropy energy in nickel - I.M.Puzei 1077
Superstructure and the temperature dependence of the magnetic anisotropy energy of nickel-iron alloys - I.M.Puzei 1083
Temperature dependence of some magnetic properties of nickel - L.V.Kirenskii, R.S.Nosova & N.V.Reshetnikova 1093

(A) = Abstract

Temperature dependence of the magnetic susceptibility of nickel base alloys - D.I.Volkov & V.I.Chechernikov 1099
Correlation between the electric and magnetic properties of chromium sulfides - N.P.Grazhdankina & I.G.Fakidov 1103
Low-temperature resistivity of nickel alloys and its variation in magnetic fields - E.I.Kondorskii, O.S.Galkina & L.A.Chernikova 1109
Resistivity and the effect of a strong magnetic field on the resistivity of iron-nickel alloys at low temperatures (14-77°K) - E.I.Kondorskii & I.E.Ozhigov 1116
Investigation of magnetostriction and other even effects in the region of approach to saturation - G.P.D'iakov 1118
Some aspects of the theory of elastic ferromagnetic (magnetostrictive) media - K.B.Vlasov 1125
Some new experiments with Bitter figures - L.F.Bates 1134
On the role of closure domain in technical magnetization processes - Ia.S.Shur, V.R.Abel's & V.A.Zaikova 1149
Dynamic behavior of the domain structure in silicon-iron crystals - L.V.Kirenskii, V.D.Dylgerov & M.K.Savchenko 1157
Domain structure of ferromagnets at high temperatures - J.Kaczer 1161
Contribution to the theory of coercive force in thin sheets - J.Kaczer 1168
Direct observations of the domains in a ferromagnet by means of a secondary emission electron microscope and an electron mirror - G.V.Spivak, N.G.Kanavina, I.S.Sbitnikova, I.N.Prilezhaeva, T.N.Dombrovskaia & V.K.Azovtsev 1169
Nature of ferromagnetic domain walls - C.P.Bean 1174
Thermal changes associated with magnetization - L.F.Bates 1175
Report on some recent progress in the field of magnetic investigation in Tokyo - Ryogo Kubo 1186
Anisotropic magnetic cores - P.Denes 1193

Number 9

Characteristics of technical magnetization in grain-oriented fine powder specimens - Ia.S.Shur, E.V.Shtol'ts & G.S.Kandaurova 1205
Investigation of dissociation in an Ni-Be alloy - N.N.Buinov, L.I.Podrezov & M.F.Komarova 1210
Changes in the structure and properties of nickel solid solutions during heat treatment - B.G.Livshits 1216
Structure of Fe-Ni-Al alloys in the high coercivity state (Abstract) - B.G.Livshits & V.S.L'vov 1223
Magnetic investigation of ordering in Ni_3Mn-base alloys (Abstract) - B.G.Livshits & B.V.Molotilov 1224
Kinetics of superstructure transformations of Fe_3Al alloy - V.E.Rode 1225
Magnetic properties of ordered Fe_3Al alloy (Abstract) - V.I.Ivanovskii 1229
Residual magnetization of nickel and its stability - Ia.S.Shur & I.A.Startseva 1229
Influence of plastic deformation on the Barkhausen effect - K.Wotruba 1235
Investigation of reversal of magnetism (Barkhausen) jumps in ferromagnets - V.F.Ivlev, V.L.Il'iushenko & L.I.Aseeva 1239
On the structure of the family of symmetrical hysteresis loops of ferromagnets - R.I.Ianus & V.P.Kartashev 1244
Temperature and rotational hysteresis in ferromagnets - L.V.Kirenski, A.Ia.Vlasov, N.I.Vtiurin, A.I.Drokin, V.F.Ivlev & R.I.Tukalov 1251
Hysteresis losses in rotating magnetic fields in a magnetite single crystal before and after phase transition - N.L.Brukhatov 1257

Influence of elastic stresses and thermomechanical treatment on the magnetic properties of high coercivity alloys - Ia.S.Shur, M.G.Luzhinskaia & L.A.Shubina 1263
Magnetization viscosity of Ni-Zn ferrites with free variation of the magnetization (Abstract) - I.A.Lednev & R.V.Telesnin 1267
On the decay of magnetic permeability in silicon iron - Iu.S.Vail' 1268
Some magneto-optical effects at microwave frequencies - N.N.Nepremerov 1275
Magneto-optical properties of ferrmagnets in the infrared region - G.S.Krinchik 1279
Contribution to the theory of the Kerr and Faraday effects at radio-frequencies - G.V.Skrotskii & V.F.Zakharchenko 1283
Measurement of the initial permeability of ferromagnets in the micro-wave region - G.S.Sanyal 1288
Radiofrequency magnetic spectra of mixed ferrites - L.A.Fomenko 1295
Magnetic spectra of magnetodielectrics of the Alsifer type - L.A.Fomenko 1303
Ferroprobe magnetometer for investigating the properties of small samples of magnetically soft materials - V.I.Drozhzhina & L.A.Fridman 1305
Magnetic moments and Curie constants of ferromagnetic alloys - F.M.Gal'perin 1308
Investigation of the magnetic susceptibility of iron and nickel base solid solutions - V.V.Parfenov 1312
Influence of elastic deformation on the paraprocess susceptibility - V.V.Parfenov & V.P.Voroshilov 1319

Transactions of the Seventh All-Union Conference on Nuclear Spectroscopy

Number 7

Alpha decay of Pu^{238} - L.N.Kondrat'ev, G.I.Novikova, V.B.Dedov & L.L.Gol'din 909
Energy of α-particles from Po^{210} - I.I.Agapkin & L.L.Gol'din 911
A grid type ionization chamber - S.A.Baranov, A.G.Zelenkov & Iu.F. Rodionov 915
Conversion electron spectra of neutron-deficient thulium isotopes - K.Ia.Gromov, B.S.Dzhelepov & B.K.Preobrazhenskii 920
Conversion electron spectra of neutron deficient lutetium isotopes - Iu.G.Bobrov, K.Ia.Gromov, B.S.Dzhelepov & B.K.Preobrazhenskii 942
Internal conversion electron spectrum of radiothorium. Part III. ($H\rho$ = 1380-2700 and 3500-9000 gauss-cm regions). - V.D.Vorob'ev, K.I.Il'in, T.I.Kol'chinskaia, G.D.Latyshev, A.G.Sergeev, Iu.N. Trofimov & V.I.Fadeev 956
Spectrum of conversion electrons from Ho^{160} - B.S.Dzhelepov, B.K. Preobrazhenskii, I.M.Rogachev & P.A.Tishkin 964
Gamma-radiation from $Eu^{152,154}$ - B.S.Dzhelepov, N.N.Zhukovskii, V.G.Nedovesov & G.E.Shchukin 968
Gamma-radiation from Ag^{110} - B.S.Dzhelepov, N.N.Zhukovskii & Iu.G.Kondakov 975
Positrons in the radiation from radioactive In^{114} - B.S.Dzhelepov, O.E.Kraft & V.B.Zhinkina 980
Gamma-spectrum of In^{114*} - I.B.Golovanov, B.S.Dzhelepov, L.S.Lebedev, V.P.Prokhodtseva & Iu.V.Khol'nov 987

Refinement of the relative intensities of the lines in the gamma-spectrum of Ta^{182} - O.I.Sumbaev 989
Investigation of the gamma-spectrum of RaC - B.S.Dzhelepov & S.A.Shestopalova 992
New lines in the spectrum of RaC - I.F.Uchevatkin & S.A.Shestopalova 1003
Neutron deficient isotopes of the rare earth elements forming as a result of spallation of Ta under bombardment with 660 Mev protons. Part I - G.M.Gorodinskii, A.N.Murin, V.N.Pokrovskii & B.K.Preobrazhenskii 1005
Rotational levels of Mg^{24} - L.K.Peker, L.V.Gustova & O.V.Chubinskii 1014
Investigation of the (α,n) reaction on oxygen - I.A.Serdiukova, A.G. Khabakhpashev & E.M.Tsenter 1018
Procedure for measuring the activity of nuclei undergoing K-capture - M.Ia.Kuznetsova & V.N.Mekhedov 1021
Characteristics of the jumps in the equilibrium shape of nuclei - L.K.Peker 1026
Spins and parities of deformed odd-odd nuclei - L.K.Peker 1030
Amplitude and time characteristics of a new photomultiplier - G.S.Vil'dgrube, A.P.Zharkov & E.D.Teterin 1035

Number 12

Fine structure of α-decay of even-even nuclei- V.G.Nosov 1541
Investigation of the internal conversion electron spectrum of long-lived Eu^{152} and Eu^{154} - B.V.Bobykin & K.M.Novik 1546
On the decay scheme of Lu^{171} - K.Ia.Gromov, B.S.Dzhelepov, A.G. Dmitriev & B.K.Preobrazhenskii 1562
$0+\rightarrow 0+$ transition in Zr^{90} - T.Yuasa, J.Laberrigue-Frolow & L.Feuvrais 1565
Gamma-hodoscope - B.S.Dzhelepov 1569
The gamma-hodoscope at the Scientific Research Institute of Physics of Leningrad State University - O.V.Chubinskii 1572
Investigation of the decay of Ce^{144} by the β-γ coincidence method - V.P.Parfenova, N.V.Forafontov & V.S.Shpinel' 1590
Further investigation of electron focusing in a two-lens β-spectrometer - K.P.Mitrofanov & V.S.Shpinel' 1595
New data on the γ-spectrum of Sb^{124} - B.S.Dzhelepov, N.N.Zhukovskii & F.A.Predovskii 1602
Spectra of internal conversion electrons emitted in thermal neutron capture by samarium, cadmium and gadolinium - L.V.Groshev, A.M. Demidov & V.A.Naidenov 1606
Neutron-deficient isotopes of the rare earth elements forming as a result of spallation of Ta under bombardment with 660 Mev protons. Part II - G.M.Gorodinskii, A.N.Murin, V.N.Pokrovskii & B.K.Preobrazhenskii 1611
Investigation of the decay of Pr^{144}, Rh^{106} and Cs^{134} by means of a scintillation spectrometer - E.I.Firsov & A.A.Bashilov 1619
On the relative intensity of Po^{210} γ-rays - V.V.Ovechkin 1627
Investigation of the lifetimes of lower nuclear levels excited in electron capture - E.E.Berlovich, K.M.Grotovskii, M.P.Bonits, V.I.Breslav & B.K.Preobrazhenskii 1629
New commercial photomultiplier tubes - L.G.Leiteizen, A.G.Berkovskii, I.Ia.Breido, V.M.Glukhovskoi, O.S.Korol'kova & E.I.Tarasova 1639

Transactions of the Second All-Union Conference on X-Ray Spectroscopy

Number 10

Complete list of reports presented at the conference 1329
Width of inner levels and density distribution of electron states in elements of the iron transition group - M.A.Blokhin & V.P.Sachenko 1333
Dependence of the X-ray absorption spectra of atoms in compounds on the character of the bonds.- R.L.Barinskii, E.E.Vainshtein & K.I.Narbutt 1341
On determining the density of electron states from x-ray spectra - I.Ia.Nikiforov 1351
Influence of an activator on the x-ray absorption spectra of a luminescent crystal - K.I.Narbutt & I.S.Smirnova 1356
Investigation of the fine structure of x-ray absorption spectra of alkali halide compounds - I.S.Smirnova & K.I.Narbutt 1363
K absorption spectra of chlorine in alkali metal chlorides - R.L.Barinskii 1369
L absorption and emission spectra of Mo in molybdenum carbide and other compounds - R.L.Barinskii & E.E.Vainshtein 1375
Influence of thermal vibrations of atoms on the electron energy distribution in metals and alloys - I.B.Borovskii & G.N.Ronami 1385
X-ray spectroscopic investigation of solid solutions - I.B.Borovskii, K.P.Gurov, S.A.Ditsman, V.A.Batyrev & N.D.Lobanova 1389
Use of the URS-50-I x-ray equipment as a double crystal spectrometer - I.B.Borovskii & V.V.Shmidt 1400
X-ray spectroscopic investigation of chemical composition in micro-volumes of alloys - I.B.Borovskii, N.P.Il'in, L.E.Loseva, I.D. Marchukova & A.N.Deev 1404
X-ray spectroscopic method of investigating the electron state distribution in metals and alloys - N.D.Borisov, V.V.Nemoshkalenko, & A.M.Fefer 1412
The $L\beta_6$ and $L\gamma_5$ lines in the spectra of Cu and Zn - I.A.Rumiantsev & M.I.Korsunskii 1423
L series x-ray spectrum of germanium - G.P.Borovikova & M.I.Korsunskii 1426
External screening and the fine structure of x-ray spectra - S.M.Karal'nik 1432
On the state of atoms in ferromagnetic iron, cobalt and nickel base alloys - I.Ia.Dekhtiar 1440
Effect of neutron irradiation on the fine structure of the K absorption edge of germanium - M.M.Kakhana & E.E.Vainshtein 1447
Quantitative determination of titanium from secondary x-ray spectra - A.S.Ivoilov & N.F.Losev 1452

Transactions of the First Conference on Spectroscopy of Light-Scattering Media

Number 11

Opening address - B.I.Stepanov 1463
Some aspects of spectroscopic analysis of light-scattering media and the reflecting power of colored polydispersive media - G.V.Rozenberg 1465
Basic problems in the spectroscopy of scattering media - B.I.Stepanov 1477

On the multiplicity of light scattering - Iu.I.Chekalinskaia 1486
On determining the true absorption of adsorbed substances from the diffuse reflection spectra (Abstract) - Z.V.Zhidkova 1492
Spectrophotometric investigation of mixtures of powder specimens (Abstract) - A.P.Ivanov & A.S.Toporets 1494
Investigation of the regularities of emission of finely dispersed luminescent media - A.P.Ivanov 1495
Indicatrices of light scattering by developed photographic emulsions on a transparent base - Iu.N.Gorokhovskii & I.M.Davydkin 1496
Numerical evaluation of light scattering in photographic blackenings on a transparent base - Iu.N.Gorokhovskii & I.M.Davydkin 1507
Scattering of light by photographic emulsion layers - P.Kh.Pruss 1515
Procedure for investigating the reflectivity of color-print photographic paper - V.M.Bakhvalov 1522
Some aspects of the theory of dispersive light filters - A.P. Prishivalko 1528
Resolution adopted by the First Conference on Spectroscopy of Light-Scattering Media 1534

Translated in 1958 by
Columbia Technical Translations
5 Vermont Avenue
White Plains, New York, U. S. A.

Annual subscriptions $215
Single issues $20

Lithoprinted in U.S.A.
EDWARDS BROTHERS, INC.
Ann Arbor, Michigan